FROM TSUNAMI SCIENCE TO HAZARD AND RISK ASSESSMENT: METHODS AND MODELS

EDITED BY: Stefano Lorito, Jörn Behrens, Finn Løvholt, Tiziana Rossetto and Jacopo Selva

PUBLISHED IN: Frontiers in Earth Science and Frontiers in Built Environment

frontiers Research Topics

frontiers

ISSN 1664-8714
ISBN 978-2-88971-794-1
DOI 10.3389/978-2-88971-794-1

About Frontiers

Frontiers is more than just an open-access publisher of scholarly articles: it is a pioneering approach to the world of academia, radically improving the way scholarly research is managed. The grand vision of Frontiers is a world where all people have an equal opportunity to seek, share and generate knowledge. Frontiers provides immediate and permanent online open access to all its publications, but this alone is not enough to realize our grand goals.

Frontiers Journal Series

The Frontiers Journal Series is a multi-tier and interdisciplinary set of open-access, online journals, promising a paradigm shift from the current review, selection and dissemination processes in academic publishing. All Frontiers journals are driven by researchers for researchers; therefore, they constitute a service to the scholarly community. At the same time, the Frontiers Journal Series operates on a revolutionary invention, the tiered publishing system, initially addressing specific communities of scholars, and gradually climbing up to broader public understanding, thus serving the interests of the lay society, too.

Dedication to Quality

Each Frontiers article is a landmark of the highest quality, thanks to genuinely collaborative interactions between authors and review editors, who include some of the world's best academicians. Research must be certified by peers before entering a stream of knowledge that may eventually reach the public - and shape society; therefore, Frontiers only applies the most rigorous and unbiased reviews.
Frontiers revolutionizes research publishing by freely delivering the most outstanding research, evaluated with no bias from both the academic and social point of view. By applying the most advanced information technologies, Frontiers is catapulting scholarly publishing into a new generation.

What are Frontiers Research Topics?

Frontiers Research Topics are very popular trademarks of the Frontiers Journals Series: they are collections of at least ten articles, all centered on a particular subject. With their unique mix of varied contributions from Original Research to Review Articles, Frontiers Research Topics unify the most influential researchers, the latest key findings and historical advances in a hot research area! Find out more on how to host your own Frontiers Research Topic or contribute to one as an author by contacting the Frontiers Editorial Office: frontiersin.org/about/contact

FROM TSUNAMI SCIENCE TO HAZARD AND RISK ASSESSMENT: METHODS AND MODELS

Topic Editors:
Stefano Lorito, Istituto Nazionale di Geofisica e Vulcanologia (INGV), Italy
Jörn Behrens, Universität Hamburg, Germany
Finn Løvholt, Norwegian Geotechnical Institute, Norway
Tiziana Rossetto, University College London, United Kingdom
Jacopo Selva, Istituto Nazionale di Geofisica e Vulcanologia (INGV), Italy

Citation: Lorito, S., Behrens, J., Løvholt, F., Rossetto, T., Selva, J., eds. (2021). From Tsunami Science to Hazard and Risk Assessment: Methods and Models. Lausanne: Frontiers Media SA. doi: 10.3389/978-2-88971-794-1

Table of Contents

frontiers in Earth Science

EDITORIAL
published: 08 October 2021
doi: 10.3389/feart.2021.764922

Editorial: From Tsunami Science to Hazard and Risk Assessment: Methods and Models

Stefano Lorito[1]*, *Jörn Behrens*[2], *Finn Løvholt*[3], *Tiziana Rossetto*[4] and *Jacopo Selva*[5]

[1]Istituto Nazionale di Geofisica e Vulcanologia (INGV), Rome, Italy, [2]Department of Mathematics, Universität Hamburg, Hamburg, Germany, [3]Norwegian Geotechnical Institute, Oslo, Norway, [4]EPICentre, Department of Civil, Environmental and Geomatic Engineering, University College London, London, United Kingdom, [5]Istituto Nazionale di Geofisica e Vulcanologia (INGV), Bologna, Italy

Keywords: tsunami, observations, numerical modelling, probabilities, hazard, risk, early warning

Editorial on the Research Topic

From Tsunami Science to Hazard and Risk Assessment: Methods and Models

The tsunami disasters of 2004 in the Indian Ocean and 2011 along the Tohoku coast of Japan revealed severe gaps between the anticipated risk and consequences (e.g., Okal, 2015), resulting in an enormous loss of life and property. The possibility that earthquakes with a moment magnitude exceeding Mw 9 would occur at the specific location of these earthquakes was probably overlooked. Moreover, both events are end members of the empirical scaling relations linking earthquake fault size, rupture duration, and slip distribution over the subduction interface.

Similarly, the two smaller yet disastrous tsunamis with unusual source characteristics that affected Indonesia towards the end of 2018 were painful reminders that we don't have to pay attention only to large mega-thrust earthquakes which cause giant tsunamis. The first one on September 28th in Palu Bay, Sulawesi Island, was caused by a primarily strike-slip earthquake, hence not expected to be highly tsunamigenic. The damaging tsunami was likely due to the complexity of the earthquake source process, possibly triggering tsunamigenic landslides, and to the propagation inside the narrow bay. This tsunami hit after minutes, leaving almost no time for evacuation. The damage and the death toll were also due to the intense ground shaking and liquefaction, for a combined number of victims higher than 4,300 (Reliefweb, 2019). The second one occurred on December 22nd in the Strait of Sunda between Java and Sumatra Islands because of the eruption and significant collapse of the Anak Krakatau Volcano. This tsunami attacked Indonesian coasts without prior notice. It caused more than 400 fatalities and considerable damage related to the tsunami inundation, as documented by several post-event surveys and event analyses (e.g., Muhari et al., 2019; Syamsidik et al., 2020).

We did not anticipate such large and diverse events and their severe consequences, in part due to the lack of rigorous and accepted hazard analysis methods as well as considerable uncertainty in forecasting the tsunami sources, and in part due to incompleteness or absence of tsunami warning systems, or lack of implementation of their "last-mile," including capillary diffusion of alert messages and preparation of the population. Population response to recent small tsunamis in the Mediterranean also revealed a lack of preparedness and awareness.

While there will never be absolute protection against tsunamis, accurate analysis of the potential risk can surely help minimise losses by providing scientific guidance to coastal planning, warning systems, awareness-raising and preparedness activities.

Hazard assessments tend to be conducted more and more by adopting a probabilistic framework, in part following the example of the long-established seismic hazard analysis practice (Gerstenberger et al., 2020). We may say that the methodology for Probabilistic Tsunami Hazard Analysis (PTHA)

OPEN ACCESS

Edited and reviewed by:
Chong Xu,
Ministry of Emergency Management, China

***Correspondence:**
Stefano Lorito
stefano.lorito@ingv.it

Specialty section:
This article was submitted to Geohazards and Georisks, a section of the journal Frontiers in Earth Science

Received: *26 August 2021*
Accepted: *23 September 2021*
Published: *08 October 2021*

Citation:
Lorito S, Behrens J, Løvholt F, Rossetto T and Selva J (2021) Editorial: From Tsunami Science to Hazard and Risk Assessment: Methods and Models. Front. Earth Sci. 9:764922. doi: 10.3389/feart.2021.764922

has now reached a high level of maturity (Geist and Parsons, 2006; Grezio et al., 2017; Mori et al., 2018). Yet, some open issues exist, mainly due to the relative rarity of the phenomenon, resulting in the sparsity and incompleteness of tsunami source and effects observations, which is a strong uncertainty driver (Selva et al., 2016; Davies et al., 2018). For these reasons, hazard analysts almost invariably adopt a computation-based approach. They first address the probability of the variety of all credible sources. Then, they model tsunami generation and propagation numerically to eventually combine the tsunami intensity with the source probability (González et al., 2009).

PTHA focuses most often on seismic sources. For feasibility reasons, it usually adopts simplified modelling assumptions as far as both the earthquake and the numerical tsunami modelling are concerned (Geist and Lynett, 2014). On the other hand, the Probabilistic Tsunami Risk Analysis (PTRA) methodology is evolving fast, but PTRA is perhaps less mature. Likely reasons include a certain lack of availability of well-constrained and general enough vulnerability data, which is another effect of the rarity of tsunamis. The complexity of tsunami consequences in the physical and social dimensions adds to the already considerable uncertainty characterising PTHA.

During the past 2 decades, the tsunami community has put significant efforts into understanding also tsunami hazard from non-seismic sources and tsunami risk. Additionally, many recent events provided essential data on tsunami sources, tsunami features, and tsunami impact at many different places. Tsunami features have been analysed and addressed through theoretical, experimental and numerical approaches.

In this Research Topic, we aimed to contribute to the ongoing scientific progress and the process of assessing and providing community-based standards, good practices, benchmarking tools and guidelines, based on the most recent observations and scientific findings. This purpose is in line with several community-based efforts like those of the "GTM—Global Tsunami Model" and "AGITHAR—Accelerating Global science In Tsunami Hazard and Risk analysis" scientific networks. We aimed to help better address the link between tsunami science and the Probabilistic Tsunami Hazard and Risk Analysis.

This Topic includes numerous Original Research papers, one Brief Research Report and one Review. Overall, we gathered 20 articles contributed by more than 200 authors. We consider this a strong indication from the research community.

Some papers on this Topic present specific hazard and risk analyses using rather innovative methods. Others address specific methodological components or provide a better understanding of recent tsunami events. Both of these aspects provide a sound scientific basis for future hazard and risk assessment efforts.

Well-documented historical events are the experimental basis for tsunami hazard assessment. Maramai et al. present a historical catalogue organised starting from the effects on a specific coastline, providing the local "tsunami history." Traditional tsunami catalogues are a collection of tsunamis classified by the generating cause, providing a general description of the effects observed for each tsunami. Strupler et al. introduce a new classification scheme for tsunami generation in lakes due to subaqueous and subaerial landslides by focusing on relative tsunami potential in Swiss perialpine lakes. The results are helpful to prioritise and rank the lakes within large regions for more detailed investigations.

A better understanding of the fundamental phenomena involved in tsunami generation, particularly their effect on the tsunami impact, can be achieved by using two different and complementary "angles," namely the laboratory-scale physical modelling and the numerical modelling assisted by high-performance computing. Chandler et al. review the evolution across three generations of pneumatic tsunami simulators and deal in particular with calibration for long period tsunamis.Wirp et al. perform a three-dimensional simulation of the earthquake dynamic rupture, informed by a model of the seismic cycle in the subduction zone. They test the sensitivity of the tsunami to dynamic effects of supershear and tsunami earthquakes, hypocenter location, shallow fault slip, and higher Poisson's ratio, pointing out the importance of dealing with earthquake source complexity for a better understanding of tsunami hazard.

Observations and numerical modelling for past or hypothetical tsunamis generated by non-seismic sources are essential for a better understanding of their mechanism, allowing better modelling of related tsunami hazard. Esposti Ongaro et al. compare different landslide-induced tsunami modelling approaches with a real event. They take as a benchmark the observations of the volcanic eruption, subaerial and submarine landslide, and consequent tsunami that occurred in 2002 at the island of Stromboli (Italy). Schambach et al. explore combinations of a dual earthquake and landslide sources for the simulation of the devastating 2018 Palu tsunami and approximate the observed inundation features; in particular, an additional landslide further than those mapped helps to generate the considerable tsunami inundation heights observed in the southeast of Palu Bay. Waldmann et al. present a complete and highly interdisciplinary reconstruction of two of the most important historical catastrophic tsunamis generated by landslides in Norway, namely the Lake Loen events in 1905 and 1936. Despite these being significant events, they have been analysed only sparsely. Hence, the review of the events is essential in its own right. Zaniboni et al. provide an assessment of potential landslide-induced tsunami hazard in a critical area—the eastern slope of the Gela Basing, Strait of Sicily. They identify historic landslides from high-resolution bathymetric data. Numerical simulations for specific events provide potential wave heights for the Coasts of Malta and the southern coast of Sicily (Italy). Salamon et al. confront themselves with a very complex geological setting. They use a worst-case oriented modelling of an earthquake and a tsunamigenic induced landslide. They model the combined effect of shaking and tsunami inundation enhanced by coastal subsidence for the Head of the Gulf of Elat–Aqaba, Northeastern Red Sea.

The feasibility issue of computation-based PTHA is related to its relatively high computational cost. This issue stems from the fact that many numerical simulations are needed to address the natural source aleatory variability. The necessity of running alternative models to quantify epistemic uncertainty increases the computational cost. Physics-reduced models, statistic data analysis, emulators and neural networks are usually employed to reduce the computational cost. Davies et al. deal with the

simulation of very long tsunami propagation necessary to address the hazard from trans-oceanic tsunamis. They propose a low-computational-cost simplified (delayed linear friction) model to approximate the Manning-friction model for long durations, which can be applied to create tsunami Green's functions. Williamson et al. deal with the "dual" problem of the very local high-sensitivity of tsunami inundation to mega-thrust source details. To limit the number of fine-resolution simulations, they propose a source clustering approach based on importance sampling focusing on the tail of the probability distribution where the number of scenarios would be excessive without sample reduction. Giles et al. propose to use tsunami emulators trained with numerical simulations to efficiently quantify the hazard in the context of a real-time tsunami warning, providing a workflow that allows uncertainty quantification hence tsunami hazard forecasting in a short time.

Long-term PTHA models can use different spatial scales, from the relatively low-resolution regional scale useful for homogenous planning at the transnational level to the high-resolution scale needed for local planning. Several methodological flavours exist, and new ones are constantly being developed. They differ in the source treatment, hydrodynamics aspects, and the approach to uncertainty quantification. Additionally, different tsunami intensity metrics may be of interest depending on the specific application. Basili et al. present NEAMTHM18, the first probabilistic hazard model that covers all the coastlines of the North-eastern Atlantic, the Mediterranean, and connected seas (NEAM). They consider subduction zones where they model shallow slip amplification, diffuse background seismicity, and a stochastic approach to inundation modelling based on local coastal amplification factors. The epistemic uncertainty treatment relies on a multi-expert protocol for the management of subjective choices. Gibbons et al. developed a workflow that allows the evaluation of high-resolution probabilistic inundation maps. Starting from a background regional PTHA such as NEAMTHM18, a disaggregation procedure allows focusing on the relevant sources for the specific location of interest. The workflow uses massive high-resolution nonlinear shallow water simulations with Tsunami-HySEA on Tier-0 GPU clusters to approach the detail and the number of scenarios needed to mimic natural variability. González et al. incorporate tides into PTHA, treating them as an aleatory variable rather than crudely adding tidal levels to the hazard curves. This PTHA considers meso- and macro-tidal areas of Cádiz Bay in Spain. Zamora et al. present microzoning tsunami hazard combining flow depths and arrival times, which is crucial, for example, for pedestrian evacuation. They advocate for a semi-qualitative approach for the sake of simplifying hazard communication related to planning.

PTHA estimates the probability that a tsunami of a certain intensity would affect a given location in a given amount of time. It is the first step for rational coastal planning. Sometimes it is followed by risk analysis. Tonini et al. present the methodology, based on the combination of scientific assessment—the PTHA—with political choices, for the definition of tsunami inundation maps used for coastal and evacuation planning in Italy. They evaluate the level of conservatism adopted by the decision-makers in the frame of the uncertainty related to tsunami source characterisation and tsunami inundation simulations. Baiguera et al. introduce a new relative tsunami risk index for (single and networks of) hospitals made of reinforced concrete. They illustrate the approach for selected hospitals in Sri Lanka. Different scenarios allow testing potential interventions by decision-makers to improve the resilience of healthcare provision. Goda presents a computational framework adopting a renewal model for conducting a time-dependent loss estimation of a building portfolio. He refers to megathrust subduction earthquakes and tsunamis affecting the Miyagi Prefecture in the Tohoku region, Japan. The study considers both seismic and tsunami fragilities in a multi-hazard scheme.

The Research Topic ends with a review by Behrens et al. of the current PTHA and PTRA methods. This review is one of the first results of the networking activities in the AGITHAR framework, where we conceived this Research Topic. The study identified numerous research gaps to foster and direct future efforts to improve tsunami risk understanding and facilitate more effective mitigation measures.

AUTHOR CONTRIBUTIONS

All authors contributed to the critical review of the papers published in this Research Topic. SL has provided an initial draft of this Editorial which was revised and approved by all the authors.

FUNDING

This article is based upon work from COST Action CA18109 AGITHAR, supported by COST (European Cooperation in Science and Technology).

ACKNOWLEDGMENTS

We warmly thank all authors for their contributions that in our opinion made up in a very valuable set of papers. We acknowledge the reviewers for valuable comments, the Frontiers Editorial Office, and especially Josie Langdon, for the continuous support during all phases of the realization of this Research Topic.

REFERENCES

Davies, G., Griffin, J., Løvholt, F., Glimsdal, S., Harbitz, C., Thio, H. K., et al. (2018). A Global Probabilistic Tsunami hazard Assessment from Earthquake Sources. *Geol. Soc. Lond. Spec. Publications* 456, 219–244. doi:10.1144/SP456.5

Geist, E. L., and Parsons, T. (2006). Probabilistic Analysis of Tsunami Hazards*. *Nat. Hazards* 37, 277–314. doi:10.1007/s11069-005-4646-z

Geist, E., and Lynett, P. (2014). Source Processes for the Probabilistic Assessment of Tsunami Hazards. *Oceanog* 27 (2), 86–93. doi:10.5670/oceanog.2014.43

Gerstenberger, M. C., Marzocchi, W., Allen, T., Pagani, M., Adams, J., Danciu, L., et al. (2020). Probabilistic Seismic Hazard Analysis at Regional and National

Scales: State of the Art and Future Challenges. *Rev. Geophys.* 58, e2019RG000653. doi:10.1029/2019RG000653

González, F. I., Geist, E. L., Jaffe, B., Kânoğlu, U., Mofjeld, H., Synolakis, C. E., et al. (2009). Probabilistic Tsunami hazard Assessment at Seaside, Oregon, for Near- and Far-Field Seismic Sources. *J. Geophys. Res.* 114, 37. doi:10.1029/2008JC005132

Grezio, A., Babeyko, A., Baptista, M. A., Behrens, J., Costa, A., Davies, G., et al. (2017). Probabilistic Tsunami hazard Analysis: Multiple Sources and Global Applications. *Rev. Geophys.* 55, 1158–1198. doi:10.1002/2017RG000579

Mori, N., Goda, K., and Cox, D. (2018). "Recent Process in Probabilistic Tsunami Hazard Analysis (PTHA) for Mega Thrust Subduction Earthquakes," in *The 2011 Japan Earthquake and Tsunami: Reconstruction and Restoration. Advances in Natural and Technological Hazards Research*. Editors V. Santiago-Fandiño, S. Sato, N. Maki, and K. Iuchi (Cham: Springer), 47, 469–485. doi:10.1007/978-3-319-58691-5_27

Muhari, A., Heidarzadeh, M., Susmoro, H., Nugroho, H. D., Kriswati, E., Supartoyo, S., et al. (2019). The December 2018 Anak Krakatau Volcano Tsunami as Inferred from Post-Tsunami Field Surveys and Spectral Analysis. *Pure Appl. Geophys.* 176, 5219–5233. doi:10.1007/s00024-019-02358-2

Okal, E. A. (2015). The Quest for Wisdom: Lessons from 17 Tsunamis, 2004-2014. *Phil. Trans. R. Soc. A.* 373 (2053), 20140370. doi:10.1098/rsta.2014.0370

Reliefweb (2019). Available at: https://reliefweb.int/report/indonesia/central-sulawesi-disasters-killed-4340-people-final-count-reveals (Accessed August 21, 2021).

Selva, J., Tonini, R., Molinari, I., Tiberti, M. M., Romano, F., Grezio, A., et al. (2016). Quantification of Source Uncertainties in Seismic Probabilistic Tsunami hazard Analysis (SPTHA). *Geophys. J. Int.* 205, 1780–1803. doi:10.1093/gji/ggw107

Syamsidik, B., Luthfi, M., Suppasri, A., and Comfort, L. K. (2020). The 22 December 2018 Mount Anak Krakatau Volcanogenic Tsunami on Sunda Strait Coasts, Indonesia: Tsunami and Damage Characteristics. *Nat. Hazards Earth Syst. Sci.* 20, 549–565. doi:10.5194/nhess-20-549-2020

Conflict of Interest: The authors declare that the research was conducted in the absence of any commercial or financial relationships that could be construed as a potential conflict of interest.

Publisher's Note: All claims expressed in this article are solely those of the authors and do not necessarily represent those of their affiliated organizations, or those of the publisher, the editors and the reviewers. Any product that may be evaluated in this article, or claim that may be made by its manufacturer, is not guaranteed or endorsed by the publisher.

frontiers in Earth Science

ORIGINAL RESEARCH
published: 30 September 2020
doi: 10.3389/feart.2020.564783

A Simplified Classification of the Relative Tsunami Potential in Swiss Perialpine Lakes Caused by Subaqueous and Subaerial Mass-Movements

Michael Strupler[1], Frederic M. Evers[2], Katrina Kremer[1], Carlo Cauzzi[1], Paola Bacigaluppi[2], David F. Vetsch[2], Robert M. Boes[2], Donat Fäh[1], Flavio S. Anselmetti[3] and Stefan Wiemer[1]*

[1] Swiss Seismological Service (SED), Swiss Federal Institute of Technology Zurich, Zurich, Switzerland, [2] Laboratory of Hydraulics, Hydrology and Glaciology (VAW), Swiss Federal Institute of Technology Zurich, Zurich, Switzerland, [3] Institute of Geological Sciences and Oeschger Centre for Climate Change Research, University of Bern, Bern, Switzerland

OPEN ACCESS

Edited by:
Finn Løvholt, Norwegian Geotechnical Institute, Norway

Reviewed by:
Emily Margaret Lane, National Institute of Water and Atmospheric Research (NIWA), New Zealand
Jia-wen Zhou, Sichuan University, China
Carl Bonnevie Harbitz, Norwegian Geotechnical Institute, Norway

***Correspondence:**
Michael Strupler
michael.strupler@sed.ethz.ch

Specialty section:
This article was submitted to Geohazards and Georisks, a section of the journal Frontiers in Earth Science

Received: *22 May 2020*
Accepted: *24 August 2020*
Published: *30 September 2020*

Citation:
Strupler M, Evers FM, Kremer K, Cauzzi C, Bacigaluppi P, Vetsch DF, Boes RM, Fäh D, Anselmetti FS and Wiemer S (2020) A Simplified Classification of the Relative Tsunami Potential in Swiss Perialpine Lakes Caused by Subaqueous and Subaerial Mass-Movements. Front. Earth Sci. 8:564783. doi: 10.3389/feart.2020.564783

Historical reports and recent studies have shown that tsunamis can also occur in lakes where they may cause large damages and casualties. Among the historical reports are many tsunamis in Swiss lakes that have been triggered both by subaerial and subaqueous mass movements (SAEMM and SAQMM). In this study, we present a simplified classification of lakes with respect to their relative tsunami potential. The classification uses basic topographic, bathymetric, and seismologic input parameters to assess the relative tsunami potential on the 28 Swiss alpine and perialpine lakes with a surface area >1 km^2. The investigated lakes are located in the three main regions "Alps," "Swiss Plateau," and "Jura Mountains." The input parameters are normalized by their range and a k-means algorithm is used to classify the lakes according to their main expected tsunami source. Results indicate that lakes located within the Alps show generally a higher potential for SAEMM and SAQMM, due to the often steep surrounding rock-walls, and the fjord-type topography of the lake basins with a high amount of lateral slopes with inclinations favoring instabilities. In contrast, the missing steep walls surrounding lakeshores of the "Swiss Plateau" and "Jura Mountains" lakes result in a lower potential for SAEMM but favor inundation caused by potential tsunamis in these lakes. The results of this study may serve as a starting point for more detailed investigations, considering field data.

Keywords: classification, lake tsunami, subaqueous mass movements, subaerial mass movements, earthquakes, perialpine lakes

INTRODUCTION

Background

Historical reports and recent studies have shown that tsunamis do not only occur in the ocean, but also in lakes where they may cause large damages and casualties. The cause for the displacement of large amounts of water can be due to a large variety of triggers, including subaqueous and subaerial mass-movements (SAQMM and SAEMM, respectively) triggered by earthquakes. The occurrence of tsunami events within Swiss lakes of various size and depths is documented in several reports (**Table 1**).

TABLE 1 | Characteristics of the Swiss lakes with surface areas >1 km (reservoirs excluded), sorted by lake area. Information extracted from swisstopo data.

Index	Name	Lake level (m.a.s.l.)	Maximum depth (m)	Shoreline length (km)[a]	Lake area (km^2)[a]	Historical tsunami year and height (m)	Trigger (SAEMM/SAQMM)
1	Lake Geneva	372	310	229.7	580	AD 563: 8–13 m (Kremer et al., 2012)	SAEMM triggered SAQMM (cascading effect)
2	Lake Constance	395	252	340	539.8	AD1720: "Unusual wave action" (Gisler and Fäh, 2011)	SAQMM (earthquake-triggered)
3	Lake Maggiore	193	372	214.1	215.6		
4	Lake Neuchatel	429	276	140.8	215.2		
5	Lake Lucerne	434	214	157.7	113.9	AD 1601: 3–4 m (Cysat, 1969)	SAQMM (earthquake-triggered)
						AD 1687: >5 m (Hilbe and Anselmetti, 2014 and references therein)	SAQMM
						AD 1931: 3.15 m Alpnachersee (Huber, 1982)	SAEMM
						AD 1982: 2–3 m Kehrsiten (Huber, 1982)	SAEMM
						AD 1982: 3–4 m Gersau (Huber, 1982)	SAEMM
						AD 1963: 4 m Obermatt (Huber, 1982)	SAEMM
						AD 1964: 15 m Obermatt (Huber, 1982)	SAEMM
						AD 2007: 5–6 m Obermatt, 1–1.5 m Weggis (Fuchs and Boes, 2010)	SAEMM
6	Lake Zurich	406	136	136.8	88.9		
7	Lake Lugano	271	288	100.1	49.2		
8	Lake Thun	558	215	63.4	47.8		
9	Lake Biel	429	74	50.2	41.2		
10	Lake Zug	413	197	43.3	38.4		
11	Lake Brienz	564	260	37.5	29.8	AD 1996: "Small tsunami wave" (Girardclos et al., 2007)	SAQMM
12	Lake Walen	419	150	39.4	24.1	AD 1946: 5–6 m (Huber 1982)	SAEMM
						AD 1924: 8–9 m (Huber 1982)	SAEMM
13	Lake Murten	429	46	24.9	22.7		
14	Lake Sempach	504	87	20.2	14.4		
15	Lake Hallwil	449	47	19.7	10.2		
16	Lake Joux	1,004	32	24.9	8.8		
17	Lake Greifen	435	34	17.3	8.3		
18	Lake Sarnen	468	52	17	7.4		
19	Lake Aegeri	724	82	16.1	7.3		
20	Lake Baldegg	463	66	13	5.2		
21	Lake Sils	1,797	71	14.8	4.1		
22	Lake Silvaplana	1,790	77	13.2	3.2		
23	Lake Kloental	844	45	12.5	3.1		
24	Lake Pfaeffikon	537	36	9.2	3.1		
25	Lake Lauerz	447	13	11.5	3	~15 m (Bussmann and Anselmetti, 2010 and references therein)	SAEMM triggered SAQMM (cascading effect)
26	Lake Lungern	688	68	10.5	2		
27	Lake Poschiavo	962	84	7.4	2		
28	Lake Oeschinen	1,578	56	5.5	1.2		

SAEMM, Subaerial mass movements; SAQMM, subaqueous mass movements.

[a]Only the outer shoreline from the SwissTLM3D (swisstopo) dataset (i.e., no shorelines of islands) are considered. This affects also the calculation of the lake area (i.e., land areas of islands not subtracted). Note: only documented mass-movements with wave height estimates are listed.

A well investigated example in Lake Lucerne with wave run-up heights of 3–4 m triggered by SAQMM is the 1601 event assigned to the Mw ~ 5.9 Unterwalden earthquake (Siegenthaler et al., 1987; Schnellmann et al., 2002; Monecke et al., 2004; Fäh et al., 2011). Another documented example is a tsunami (run-up > 5 m) triggered by a spontaneous river delta collapse in Lake Lucerne in 1687 (Siegenthaler and Sturm, 1991; Hilbe and Anselmetti, 2014; Hilbe and Anselmetti, 2015). A more recent event of a rockfall-triggered tsunami (also called impulse-wave) has been reported by Fuchs and Boes (2010): On July 20, 2007, a SAEMM with a total volume of 35,000 m^3 occurred in multiple phases at a closed quarry that is located directly at the shore. The resulting waves with observed heights between 1 and 1.5 m caused some damage at the opposite lake shore (~3.5 km away from the tsunami source). Fuchs and Boes (2010) estimated the maximum wave height close to the tsunami source to 5–6 m (**Table 1**). Shore collapses, mostly triggered by human activity in the past ~150 years, have also been responsible for triggering impulse waves on many Swiss lakes (Huber, 1980; Huber, 1982 and references therein). In addition to single mechanisms identified as tsunami triggers, cascading effects have also caused tsunamis, such as in the case of the "Rossberg" subaerial landslide that mobilized soft sediments on a swamp plane laterally, which, in turn caused a tsunami with an estimated wave height of ~15 m on Lake Lauerz in 1806 AD (Bussmann and Anselmetti, 2010). Similarly, in Lake Geneva, a subaerial rockfall is assumed to have triggered a partial collapse of the Rhone Delta, which led to the 563 AD tsunami with modeled wave heights of ~8 m arriving at the city of Geneva (Kremer et al., 2012).

Next to historically documented lacustrine tsunamis on Swiss lakes, geophysical (i.e., bathymetric and seismic reflection data) and sedimentological data (i.e., sediment cores retrieved at the bottom of several lakes) show evidence of large SAQMM and SAEMM that have occurred since de-glaciation, and many of them are assigned to earthquakes as triggers (e.g., Schnellmann et al., 2002; Monecke et al., 2004; Fanetti et al., 2008; Hilbe et al., 2011; Wirth et al., 2011; Strasser et al., 2013; Corella et al., 2014; Kremer et al., 2015; Reusch, 2015; Fabbri et al., 2017; Kremer et al., 2017; Strupler et al., 2018a).

Potential lake tsunamis resulting from mass-movements as well as the tsunami hazard to date can only be estimated with models. Case studies on tsunamis triggered by SAEMM and SAQMM exist for selected sites in specific lakes (Fuchs and Boes, 2010; Hilbe and Anselmetti, 2015; Strupler et al., 2018c). These studies indicate clearly that there is a potential for future tsunamis on Swiss perialpine lakes. As detailed assessments of the tsunami hazard caused by mass movements require the acquisition of vast amounts of high-resolution geophysical and geological data, it is important to make a preselection of the lakes to be investigated, before evaluating the tsunami potential on a specific lake in detail and with considerable costs. The main aim of this study is therefore to classify all Swiss lakes >1 km^2 (engineered reservoirs excluded) according to their relative tsunami potential caused by SAQMM and SAEMM. Results of such a rapid classification will be used to prioritize lakes for a detailed data acquisition and numerical modeling. Lakes with a relatively low tsunami potential can then be excluded from further analyses. In the following paragraphs, an overview about characteristics of tsunamis that are triggered by SAQMM and SAEMM is given. In the term "mass movements," we include both landslides and rockfalls.

Tsunami Generation by SAEMM

Due to the alpine and perialpine environment, several Swiss lakes are surrounded by steep slopes that may trigger SAEMM. Volumes of reported SAEMM in Swiss lakes have been mostly in the range between a few 1′000 to 1 million m^3 (Huber, 1980). Impulse waves generated by SAEMM have been extensively studied for decades with hydraulic scale-model experiments (Hager and Evers, 2020). Compared to field surveys in the aftermath of an event, where only maximum run-up heights may be tracked along the shores (Roberts et al., 2013), this approach allows for measuring wave characteristics under controlled laboratory conditions (Heller et al., 2008; Evers et al., 2019b). Among the experimental studies conducted in 2D wave channels, Heller and Hager (2010) covered the most extensive range of experimental parameters, including slide volume, slide density, slide thickness, slide porosity, slide impact velocity, slide impact angle, and still-water depth. The slide impact velocity, slide thickness, slide mass, and slide impact angle were found to be the governing 2D parameters: Generally, greater slide impact velocities and masses, i.e., slide volumes for constant slide density, as well as flat impact angles, lead to larger wave heights. Considering a simple block slide model as proposed by Körner (1976), the slide impact velocity is mainly controlled by the drop height, the slope angle, the dynamic bed friction angle, and the gravitational acceleration. A maximum wave height therefore requires an optimal balancing between impact velocity and impact angle when all other slide parameters are considered constant. Heller and Hager (2014) identified a slide impact angle of 51.6° to provide the best conditions for efficient wave generation on a constantly inclined slope. A vertical impact of a SAEMM leads to smaller waves compared to the optimal slide impact angle, due to a less efficient slide to wave energy transfer. Considering only the parameters imposed by the topography, large drop heights and steep slope angles induce high slide velocities. Based on experiments in a wave basin, Evers et al. (2019a) found the slide width to be an additional governing parameter for 3D wave generation and propagation: The wider a slide, the larger the wave.

Tsunami Generation by SAQMM

SAQMM include subaqueous landslides and delta collapses. The occurrence of SAQMM is mainly dependent on a favourable topography, a necessary amount of sediments, and a trigger mechanism (Nadim et al., 1996). Previous work on Swiss lakes has shown that most documented landslides occur on slopes with inclinations between ~10 and 25° (Schnellmann et al., 2006; Hilbe et al., 2011;

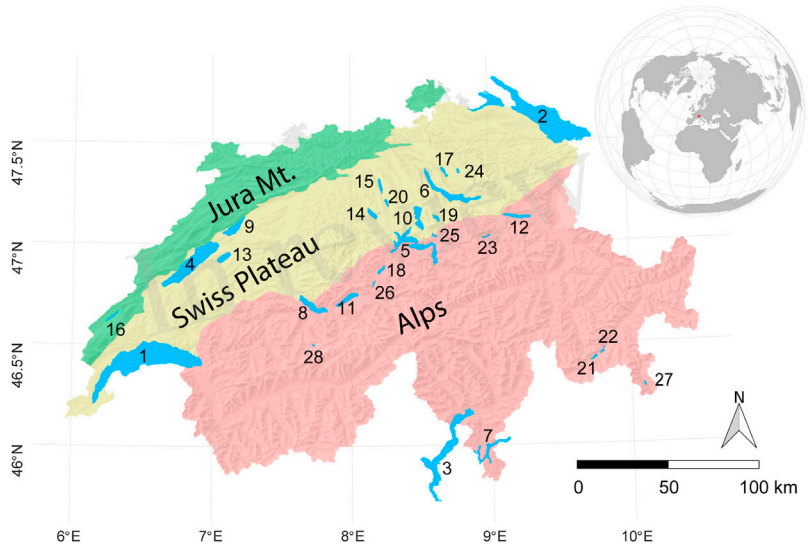

FIGURE 1 | Location of the Swiss (non-reservoir) lakes with surface areas <1 km. Labels refer to **Table 1**. Geodata used with permission from swisstopo.

Strasser et al., 2011; Strupler et al., 2018b). Many of these slides are initiated within a weak layer at the transition from Late Glacial to Holocene sediments (e.g., Strasser et al., 2007; Strasser et al., 2011; Strupler et al., 2017). To date, the yet unfailed lateral slopes of the investigated lakes are covered with a ~3–10 m of potentially mobile, Holocene sediment drape.

Important properties of SAQMM to estimate the characteristic amplitude of resulting waves (i.e., directly above the landslide source area) are the landslide volume, the landslide acceleration, and the submergence depth of the centroid of the landslide below lake level (Watts et al., 2005; Tappin et al., 2008). Generally, a larger slide volume leads to larger wave amplitudes, and a greater central submergence depth of a landslide leads to smaller wave amplitudes.

The basin depth can have an influence on the wave amplitude during generation, as the amplitude is also dependent on the Froude number *Fr* [i.e., ratio between landslide velocity *u* and the shallow-water wave celerity *c* (Løvholt et al., 2015; Glimsdal et al., 2016, **Eq. 1**)],

$$Fr = \frac{u}{c}. \tag{1}$$

Slides that move at velocities close to the shallow-water wave celerity (i.e., $Fr \approx 1$) will generally increase the wave amplitudes (Ward, 2001).

Tsunami propagation and Inundation

After its generation, the wave will propagate across the basin. Dispersion (i.e., the spreading of energy due to different wave celerities for waves with different wavelengths) can cause wave trains that change their shape with distance from the tsunami source and the geometry of the water body (e.g., Glimsdal et al., 2013; Evers et al., 2019b).

In zones where the wave amplitudes are much smaller and the wavelengths are much larger than the stillwater depth *h*, the tsunami propagation velocity *c* can be modeled with the linear shallow water theory:

$$c = \sqrt{gh}. \tag{2}$$

In very narrow valleys, the wave cannot spread radially. During propagation into shallow areas in proximity of shores, the wave develops an increased surface elevation (due to shoaling) and can have devastating effects onshore (e.g., Hafsteinsson et al., 2017).

Existing Approaches for Comparing Tsunami Hazard

Different approaches for comparing the tsunami hazard on multiple lakes and fjords exist. Romstad et al. (2009) conducted a geospatial assessment of the relative rockslide-induced tsunami hazard for Norwegian lakes larger than 0.1 km^2 by calculating a (tsunami-generating) topographic rock slide potential for 18,976 lakes. They assume that all subaerial cells with slope inclinations larger than 30° are potential landslide-release cells, and that only landslides with volumes >5,000 m^3 entering a lake causes a tsunami, based on empirical knowledge and numerical simulations. The volumes of the potential landslides possibly reaching the lake are estimated from an empirical relationship involving the required mobility of each cell, which is represented by a head to horizontal distance of a travel path ratio. Hermanns et al. (2012, 2013) propose a hazard and risk classification system for large unstable rock slopes, which includes structural site investigations and analysis of the activity of the slopes. Based on this classification methodology, Hermanns et al. (2016) classify 22 mapped rock slopes and do i) a volume computation, ii) run-out assessments, iii) assessment of possible wave propagation and run-up if a rockfall enters a water body, and iv) an estimation of people exposed to rock avalanches and rockfall-induced tsunami waves. The results of these studies build on multiple years of systematical mapping of unstable rock-slopes and are to be used as support tool for risk management.

In contrast to these studies, our goal is to estimate the relative tsunami potential on peri-alpine lakes that is caused both by

TABLE 2 | Overview of the input parameters used for the classification of the tsunami potential (before normalization).

Input parameter	Represented by	Main assumption
IP1: Potential for subaerial mass-movements	Ratio of Fahrböschung >30° to total watershed area for each lake	Ratio of area within watershed with Fahrböschung >30° to total watershed area is an indicator of subaerial mass-movement caused tsunami potential, as subaerial rocks tend to mobilize for Fahrböschung >30°
IP2: Potential for subaqueous mass-movements	Ratio of slope area within 10–25° to total slope area. Slope area is defined as all zones with inclinations >5°	Most sublacustrine mass movements occur on slopes with inclinations between 10 and 25°
IP3: Potential for seismicity	Expected SA(0.3s) for earthquakes with an exceedance probability of 10% in 50 years from Wiemer et al. (2016) for each lake center point	Lakes located in zones with greater seismic activity are expected to experience more earthquake-triggered subaerial and subaqueous mass movements
IP4: Inverse SDR	1/"SDR" (Aronow, 1982): Inverse of the actual shoreline length divided by a hypothetical shoreline length for a perfect circle with the actual lake area	The more complex a lake shape (i.e., the larger the ratio between the actual shoreline and the hypothetical shoreline length for a perfect circle), the lower the general tsunami potential on the whole lake. This is assumed as for complex lakes with many basins only a few basins may be affected
IP5: Potential for inundation	Low-lying shore zones. Ratio of zones below lake level up to <5 m above mean lake level within 1,000 m shore-strip around shoreline to total area of 1,000 m shore-strip	Lakes surrounded by a greater percentage of low-lying areas can be affected by larger inundated areas

SDR, shoreline development ratio.

SAEMM and SAQMM. In this study, we do not aim at including site-specific field measurements. Rather, we conduct a desktop analysis of the tsunami potential and the related consequences, based on parameters that are derived mainly from previous studies on peri-alpine lakes. In contrast to the workflow of Strupler et al. (2019), that estimates the location and characteristics of potential SAQMM within a specific peri-alpine lake basin, the methodology presented uses a country-level scale, comparing the tsunami potential on various lakes.

Regional Setting

In Switzerland, a total of 28 lakes with surface areas greater than 1 km^2 (engineered reservoirs excluded) exist (**Figure 1**; **Table 1**). Of these lakes, Lake Geneva has the largest surface area (~580 km^2), while Lake Maggiore has the greatest water depth (372 m). Four of the lakes share borders with neighboring countries, i.e., France (Lake Geneva), Germany, and Austria (Lake Constance), and Italy (Lakes Maggiore and Lugano). Of the investigated lakes, 14 are located in the Alps, 13 on the Swiss Plateau, and one in the Jura Mountains. The origin of these lakes is related to subglacial erosion as they represent glacial overdeepenings. Since de-glaciation after the Last Glacial Maximum, deposition of sediments has been ongoing in the lake-basins.

The lakes with the largest surface area are found in the "Swiss Plateau" region, which is geologically formed by sediments from the Molasse basin and which is characterized by a relatively smooth topography. The "Swiss Plateau" is the region in Switzerland with the highest population density (e.g., Henriod et al., 2016).

Geologically, the Central and Southern Alps consist mainly of crystalline rocks, the Northern Alps of limestones and marls, and the Molasse basin consists mainly of conglomerates and sandstones. The Jura mountains are rich in limestones.

It is estimated that earthquakes with a magnitude 6 or greater are expected to occur every 50–150 years in Switzerland (Wiemer et al., 2016). The highest earthquake hazard can be found in the regions Valais, Basel, and Grisons. Earthquakes in these regions are generally a result of the collision between the European and African plates.

METHODOLOGY AND DATA

General Methodology and Data

In the following, a methodology for the classification of the tsunami potential is presented and applied to Swiss lakes with surface areas greater than 1 km^2 (engineered reservoirs excluded). The automated workflow is implemented in R (R Core Team 2018). Geospatial operations are either conducted directly in R or calculated in ArcGIS, which can be steered from within R using the package "RPyGeo" (Brenning et al., 2018).

First, five input parameters (IP1–IP5; **Table 2**) contributing to the tsunami potential are calculated for each lake. These parameters are discussed in detail in *Parametrization* below. After their calculation, the parameters are normalized by their range (*Normalization of the Input Parameters*). In general, a larger input value means a larger contribution to the tsunami potential. Next, a classification of investigated lakes, according to

their potential for SAEMM (IP1) and SAQMM (IP2) is conducted. Shorelines used in the workflow are taken from SwissTLM3D (swisstopo). Only the outer shorelines are considered, shorelines of islands in lakes are not considered. As topographic elevation model, SRTM (Shuttle Radar Topography Mission) data is used (Jarvis et al., 2008). The dataset has a spatial resolution of 90 m and is used due to the data availability also alongshore border lakes in non-Swiss territory. For a large part of the investigated lakes, high-resolution digital bathymetric datasets SwissBATHY3D (swisstopo) are available. For various lakes, however, bathymetric data has to be interpolated from isobaths (SwissMap Vector 10/25 data; swisstopo). For comparability reasons, both datasets are resampled to a grid resolution of 20 m.

Parametrization

Five different input parameters ("IP1"–"IP5") are identified as crucial for the estimation of the tsunami potential (**Table 2**). As we ultimately aim at (de)selecting lakes for further investigations, depending on the potential for tsunami generation and the potential for consequences of tsunamis, we include both these aspects in the term "tsunami potential." "IP1"–"IP3" focus on the tsunami-generating potential, while "IP4" and "IP5" focus on the tsunami consequences. The five parameters are selected to represent the first-order tsunami potential derived from basic topographical, bathymetrical, and seismological input parameters, due to their simplicity.

IP1: Potential for SAEMM

For the parameterization of the potential for tsunamis generated by SAEMM for each lake, it is important to assess i) the potential for SAEMM that enter the water, and ii) their potential to generate a tsunami. To answer ii), estimations of expected volumes entering the water are crucial. Making statements about likely locations of mass failures requires an understanding of factors and processes relevant for slope instabilities as well as their spatial variability (Fischer et al., 2012). Without knowing the local site conditions, topography is often used as a proxy for potential mass movements (e.g., Coe et al., 2004; Fernandes et al., 2004; Cauzzi et al., 2018). The Fahrböschung (Heim 1932) is defined as

$$\tan \alpha = \frac{H}{L} \tag{3}$$

where H equals the fall height and L the horizontal runout distance. The Fahrböschung can thus be interpreted as the slope angle from the top of a slide to its runout.

Equation 3 is often used to estimate the travel distance of a mass movement, depending on its volume. As the volumes of such potential SAEMM alongshore the investigated lakes are unknown, our model is based on a very simple assumption: Rocks tend to mobilize for Fahrböschung >30° (Gerber, 1994; Heinimann et al., 1998), therefore we calculate the Fahrböschung for each pixel of the SRTM DEM down to its closest point on the shoreline. These calculations are made for each pixel within the watershed around each lake, which we limit to a buffer zone of 5 km around each lake's shoreline (in order not to get very large watersheds in the relatively flat zones of the Swiss Plateau). This value of 5 km corresponds also to the runout distance of the Rossberg landslide, one of the major historic landslides in Switzerland (volume: ~40 Million m^3; Thuro et al., 2006). The input parameter representing the relative tsunami potential posed by SAEMM for each lake (IP1; before normalization) is then estimated by calculating the ratio of pixels with Fahrböschung >30° to the total amount of pixels in the watershed area. Hence, due to the lack of landslide-volume information, we assume here that any potential landslide entering the water may generate a tsunami (which is a conservative assumption). By calculating the Fahrböschung for each pixel of the DEM to the shoreline, potential landslide source zones with locally steep slope inclinations that are too far away from the shoreline (and thus getting a low Fahrböschung value) are not considered as sources of landslides that may reach the lake.

IP2: Potential for SAQMM

The parametrization of the potential for SAQMM is quite simple and straightforward: As subaqueous landslide source areas in Swiss perialpine lakes tend to occur on slopes with inclinations between 10 and 25° (Schnellmann et al., 2006; Hilbe et al., 2011; Strasser et al., 2011; Strupler et al., 2018b), the ratio between the amount of pixels with inclinations between 10 and 25° to the amount of pixels belonging to the lake's slopes (here defined as slope inclinations >5°) is used as input parameter representing the potential for SAQMM (IP2). For the lakes Lugano and Maggiore, which share boundaries with Italy, SwissMap Vector 10/25 data (swisstopo) to interpolate bathymetries is partly not available for the Italian territory (~12% and ~43% of the respective lake's area are not covered; see **Supplementary Table S1**; **Supplementary Figures S1** and **S2**). Therefore, potential SAQMM that may occur in these zones of missing bathymetry data are not considered. The omission of these zones is discussed in *Quality and Limitations of the Relative Tsunami-Potential Classification*.

IP3: Potential for Seismicity

The potential for seismicity at each lake site is given by the seismic hazard levels in terms of elastic 5%-damped Spectral Acceleration at vibration period T = 0.3s − SA(0.3s) for a mean exceedance probability of 10% in 50 years (SuiHaz2015; Wiemer et al., 2016) at each lake center point. The SA(0.3s) values at each lake center were obtained through interpolation of the data of the national Swiss hazard map using ordinary kriging. The seismic hazard values are valid for a reference rock with an average shear-wave velocity of the uppermost 30 m of the soil (Vs_{30}) of 1,100 m/sec. Potential site amplification due to the lake sediments was not considered, as models are still being developed. We did not use Peak Ground Acceleration due to its intrinsic strong saturation with magnitude and distance, that implies comparatively poorer representation of the earthquake sources dominating the hazard at a given location. Mid-to-long period spectral ordinates should be preferred as seismic shaking parameters for the exercise at hand; however, SuiHaz2015 results for T > 1s should be used with caution, as some of the ground motion models used for SuiHaz2015 are better constrained at short and mid periods

(due to the larger number of records used for calibration.) With this background, we finally opted for SA(0.3s), that has the additional advantage of showing a good correlation with macroseismic intensity shaking for damaging events in Switzerland (Panzera et al., under review).

IP4: Inverse Shoreline Development Ratio

It is assumed that for tsunamis occurring in lakes featuring complex shapes with multiple basins, geometric effects could limit the main damage to a single basin. The amount of wave energy transferred around bends also depends on the wave length relative to the lake width. For narrow lakes, long wavelengths can be transmitted without loss of energy (Harbitz, 1992). Oppikofer et al. (2019) state that numerical simulations of SAEMM-induced tsunamis show reductions in wave heights by 30% or more for perpendicular changes in wave direction, which is often the case for fjord-type lakes with multiple basins. To account for the complexity of a lake's shape, an input parameter calculating the inverse of the "shoreline development ratio (SDR)" (Aronow, 1982) is calculated for each lake (IP4). The SDR is calculated from the ratio of the shoreline length for a hypothetical, perfectly circular lake with the same surface area to the actual shoreline length. Higher values mean less complex lake shapes and thus higher potential damage for large parts of the lake shores.

IP5: Inundation Potential

The second parameter related to the tsunami-damage potential (**Table 2**), is called inundation potential (IP5). The assumption made here for parameterization is that low-lying areas (here defined as <5 m above mean lake level) are particularly prone to tsunami inundation. IP5 is obtained by calculating the ratio of the number of pixels that are located in the elevation range from below lake level up to 5 m above lake level to the total amount of pixels within a buffer zone of 1,000 m around the lakeshore. The 1,000 m buffer is arbitrarily chosen, based on modeled inundation distances caused by potential Lake Lucerne landslide-tsunamis (Hilbe and Anselmetti, 2015).

Normalization of the Input Parameters

In order to obtain similar ranges for each IP, each IP is normalized by the range of the values for all lakes (i.e., the minimum value of each IP equals 0 and the maximum value of each IP equals 1). For the IPs that represent ratios (i.e., all IPs except IP3), it is thus important to note that this normalization does not mean that a value of 1 corresponds to a calculated ratio of 100%. Non-normalized IP values can be found in the **Supplementary Table S2**.

Classification

Classification by Main Tsunami Sources

Classification by main tsunami sources (IP1 and IP2) is done with a k-means cluster analysis algorithm (Hartigan and Wong, 1979). The goal of this approach is to construct different lake classes that share common characteristics, i.e., similar combinations of IP1 and IP2 values.

TABLE 3 | Normalized input parameters for each lake.

Index	Name	IP1	IP2	IP3	IP4	IP5
1	L. Geneva	0.02	0.601	0.329	0.286	0.168
2	L. Constance	0.005	0.472	0.019	0.005	0.626
3	L. Maggiore	0.062	0.664	0	0.007	0.114
4	L. Neuchatel	0.002	0.41	0.265	0.282	0.726
5	L. Lucerne	0.207	0.773	0.463	0	0.215
6	L. Zurich	0.009	0.741	0.131	0.01	0.328
7	L. Lugano	0.221	0.651	0.011	0.018	0.052
8	L. Thun	0.072	0.796	0.538	0.319	0.268
9	L. Biel	0.007	0.305	0.223	0.464	0.511
10	L. Zug	0.068	0.819	0.252	0.582	0.288
11	L. Brienz	0.438	0.717	0.533	0.6	0.163
12	L. Walen	0.373	0.812	0.619	0.44	0.123
13	L. Murten	0.005	0.049	0.284	0.954	0.705
14	L. Sempach	0.002	0.226	0.07	0.928	0.549
15	L. Hallwil	0.01	0.681	0.036	0.73	0.36
16	L. Joux	0.018	0.257	0.106	0.397	0.167
17	L. Greifen	0.002	0.121	0.107	0.765	0.687
18	L. Sarnen	0.007	0.687	0.469	0.71	0.255
19	L. Aegeri	0.046	0.732	0.327	0.768	0.198
20	L. Baldegg	0.001	0.594	0.067	0.831	0.508
21	L. Sils	0.177	0.81	0.634	0.532	0.134
22	L. Silvaplana	0.064	0.884	0.686	0.528	0.112
23	L. Kloental	0.68	0.456	0.568	0.57	0
24	L. Pfaeffikon	0	0.227	0.121	0.959	1
25	L. Lauerz	0.053	0	0.447	0.642	0.411
26	L. Lungern	0.258	0.734	0.487	0.524	0.096
27	L. Poschiavo	0.466	0.791	0.59	0.944	0.176
28	L. Oeschinen	1	1	1	1	0.077

Prioritization by Additional Preconditioning Parameters (IP3–IP5)

The lakes in each class are further prioritized by the additional input parameters IP3–IP5. As the tsunami potential for each lake needs to be assessed with regard to a specific purpose, we do the prioritization for each class by sorting it according to IP3–IP5 separately (i.e., we do not aggregate IP3–IP5).

RESULTS

Input parameters for Each Lake

The input parameters for each lake are shown in **Table 3** and their spatial distribution are shown in **Figure 2**.

Table 3 and **Figure 2** show that:

- The highest values of IP1 (SAEMM) are found for alpine lakes Oeschinen, Kloental, Poschiavo, Brienz, and Walen, whereas the lowest values can be found for "Swiss Plateau" lakes Pfaeffikon, Baldegg, Sempach, and Greifen.
- The highest IP2 (SAQMM) values include lakes Oeschinen, Silvaplana, Zug, Walen, and Lake Sils. The lakes with the lowest potential for SAQMM are lakes Lauerz, Murten, Greifen, Sempach, and Pfaeffikon.
- The highest IP3 (seismicity) value is found in Lake Oeschinen, followed by lakes Silvaplana, Sils, Walen, and Poschiavo. The lowest values are found at Italy-bordering lakes Maggiore and Lugano, and at lakes Constance, and Hallwil.

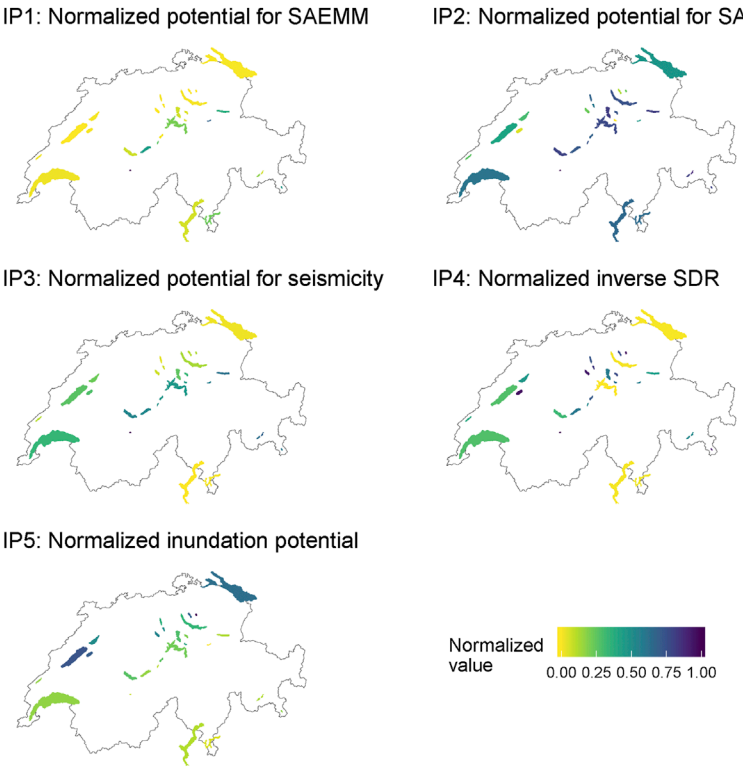

FIGURE 2 | Spatial distribution of the normalized input parameters.

- The highest IP4 (inverse SDR) values are found for lakes Oeschinen, Pfaeffikon, Murten, Poschiavo, and Sempach. All these lakes have simple circular or oval shapes. The lowest values of IP4 are assigned to lakes Lucerne, Constance, Maggiore, and Zurich. These lakes consist of multiple basins, and many of them are visually separated into different branches
- IP5 (inundation potential) is generally higher for alpine-distal lakes than for alpine-proximal lakes, with lake Pfaeffikon having the highest value, followed by lakes Neuchatel, Murten, Greifen, and Constance. The lowest IP5-values are found for lakes Kloental, Lugano, Oeschinen, and Lungern.

Classification Results

Main Tsunami Source Classes

Four different clusters have been created with the k-means clustering algorithm applied to IP1 and IP2 (**Figure 3**): One cluster with a low potential for both SAEMM (IP1) and SAQMM (IP2) ("**class I**," gray, amount (n) = 8), one cluster with a high potential for SAQMM (IP2) but low potential for SAEMM (IP1) ("**class II**," cyan, n = 11), one cluster with a medium potential for SAEMM (IP1) and high potential for SAQMM (IP2) ("**class III**," brown, n = 7), and one cluster with a very high potential for SAEMM (IP1) and high potential for SAQMM (IP2) ("**class IV**," purple, n = 2). No cluster exists for the combination of a high potential of SAEMM (IP1) but low potential of SAQMM (IP2) (**Figure 3**).

The spatial distribution of the lakes, colored according to the identified main tsunami potential classes, is shown in **Figure 4**. Lakes of class I only exist north of the Alps (Swiss Plateau and Jura Mountains). Lakes of class II predominate on the Swiss Plateau, but also occur in the Alps. All class III and IV lakes are located in the Alps.

Prioritization by IP3–IP5

Results of the prioritization of the lakes in classes I-IV (cf. **Figure 4**) according to IP3, IP4, and IP5, respectively (**Table 4**), are shown in the following:

DISCUSSION

The proposed workflow allows for a classification of lakes to be investigated more in depth with regard to the respective tsunami triggers. Although landslide-generated waves are complex hazards (e.g., Bullard et al., 2019), the simple parametrization of inputs contributing to SAEMM and SAQMM-induced tsunamis should facilitate identifying the relative tsunami potential for each lake.

Tsunami Potential on the Investigated Lakes

The definition of four different lake classes according to their main tsunami-source (i.e., SAEMM, SAQMM, or a combination of both) gives a first overview on what potential source to consider for each lake. In the Alps, class III [i.e., medium potential for SAEMM (IP1)

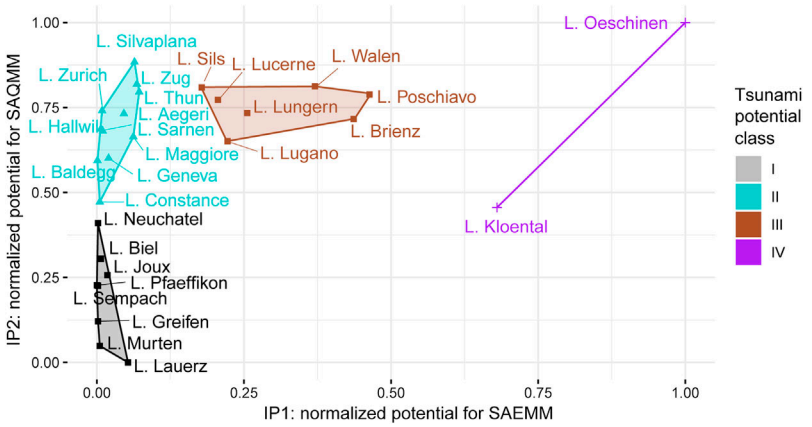

FIGURE 3 | Clusters of lakes according to IP1 and IP2 values, depicting the potential main tsunami potential classes.

and high potential for SAQMM (IP2)] and class IV [i.e., very high potential for SAEMM (IP1) and high potential for SAQMM (IP2)] lakes dominate (**Figures 1**, **4**). Both parameters IP1 and IP2 express the abundance of favourable topographic conditions for mass-movements (i.e., Fahrböschung > 30° for SAEMM and subaquatic slope ranges 10–25° for SAQMM, respectively). The high values of IP1 are related to the fact that many alpine lakes are surrounded by relatively steep slopes. For Lake Oeschinen (**Figure 5**), which is evaluated as having the greatest potential for SAEMM-induced tsunamis, traces of 11 rock-falls that have occurred during the last 2,500 years could be identified at the bottom of the lake (Knapp et al., 2018). The high mean recurrence rate of 200–300 years between the single events supports the high score in our simple model.

Also, the SAEMM-induced tsunamis described in Huber (1982) have occurred in Lake Walen and Lake Lucerne. Both lakes show a relatively high potential for SAEMM (IP1) according to our approach. The comparison of the evaluated potential for SAQMM with documented events show that traces of underwater landslides were found in most of the lakes with a high IP2 score. On the one hand, this can be interpreted as validation of the approach. On the other hand, relatively recent (i.e., younger than a few thousand years) mass movements have decreased the potential for SAQMM occurring in the near future at the same locations, as the slopes need to be re-charged with sediment to become unstable again. It is therefore important for a hazard assessment to further investigate if lakes with historically documented tsunamis that were triggered by SAQMM still have a high potential for such events to recur. However, for comparability reasons between all investigated lakes that build on different dataset qualities (e.g., high-resolution bathymetric and seismic data are not available for all investigated lakes), the history of SAQMM on the lateral slopes is not considered in our simple approach.

The observation that no class for lakes with a high potential for SAEMM but low potential for SAQMM exists, and that lakes closer to the Alps show a generally higher potential for SAQMM,

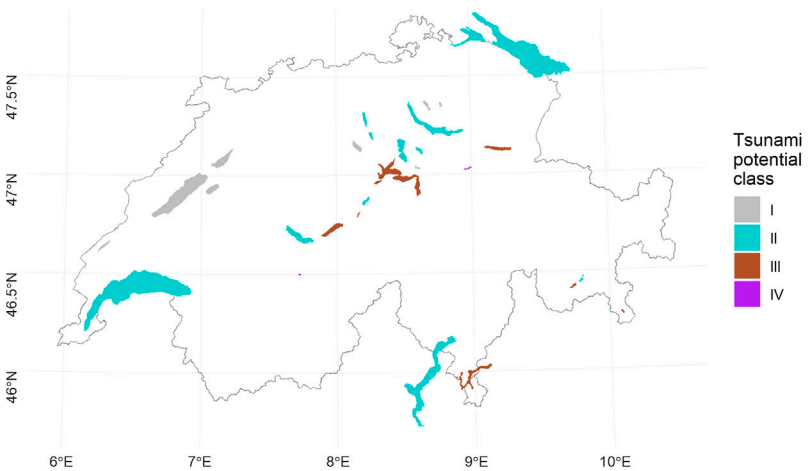

FIGURE 4 | Spatial distribution of the lakes colored according to the identified main tsunami source classes.

TABLE 4 | Prioritization according to IP3 (seismicity, left), IP4 (inverse SDR, middle), and IP5 (inundation potential, right), grouped by main tsunami source classes.

Class	Name	Normalized IP3 (seismicity)	Name	Normalized IP4 (inverse SDR)	Name	Normalized IP5 (inundation potential)
I	L. Lauerz	0.447	L. Pfaeffikon	0.959	L. Pfaeffikon	1.000
	L. Murten	0.284	L. Murten	0.954	L. Neuchatel	0.726
	L. Neuchatel	0.265	L. Sempach	0.928	L. Murten	0.705
	L. Biel	0.223	L. Greifen	0.765	L. Greifen	0.687
	L. Pfaeffikon	0.121	L. Lauerz	0.642	L. Sempach	0.549
	L. Greifen	0.107	L. Biel	0.464	L. Biel	0.511
	L. Joux	0.106	L. Joux	0.397	L. Lauerz	0.411
	L. Sempach	0.070	L. Neuchatel	0.282	L. Joux	0.167
II	L. Silvaplana	0.686	L. Baldegg	0.831	L. Constance	0.626
	L. Thun	0.538	L. Aegeri	0.768	L. Baldegg	0.508
	L. Sarnen	0.469	L. Hallwil	0.730	L. Hallwil	0.360
	L. Geneva	0.329	L. Sarnen	0.710	L. Zurich	0.328
	L. Aegeri	0.327	L. Zug	0.582	L. Zug	0.288
	L. Zug	0.252	L. Silvaplana	0.528	L. Thun	0.268
	L. Zurich	0.131	L. Thun	0.319	L. Sarnen	0.255
	L. Baldegg	0.067	L. Geneva	0.286	L. Aegeri	0.198
	L. Hallwil	0.036	L. Zurich	0.010	L. Geneva	0.168
	L. Constance	0.019	L. Maggiore	0.007	L. Maggiore	0.114
	L. Maggiore	0.000	L. Constance	0.005	L. Silvaplana	0.112
III	L. Sils	0.634	L. Poschiavo	0.944	L. Lucerne	0.215
	L. Walen	0.619	L. Brienz	0.600	L. Poschiavo	0.176
	L. Poschiavo	0.590	L. Sils	0.532	L. Brienz	0.163
	L. Brienz	0.533	L. Lungern	0.524	L. Sils	0.134
	L. Lungern	0.487	L. Walen	0.440	L. Walen	0.123
	L. Lucerne	0.463	L. Lugano	0.018	L. Lungern	0.096
	L. Lugano	0.011	L. Lucerne	0.000	L. Lugano	0.052
IV	L. Oeschinen	1.000	L. Oeschinen	1.000	L. Oeschinen	0.077
	L. Kloental	0.568	L. Kloental	0.570	L. Kloental	0.000

SDR, shoreline development ratio.

may be related to the topographic and geologic predisposition during the glacial excavation of the subsurface: In alpine valleys that are surrounded by steep rock walls, the ice masses were laterally confined and thus the glaciers were thick (Bini et al., 2009), exerting considerable pressure on the substratum, leading to a steep bedrock topography. In contrast, for lakes located on the Swiss Plateau, further from the Alps, the glaciers were able to spread laterally due to the absence of steep rockwalls, which resulted in thinner local ice thicknesses of piedmont-style glaciers, and probably smoother excavations of the bedrock. Certainly, the local geological and geotechnical variability (i.e., relatively soft rocks of the "Molasse" vs. mainly harder rocks of the "Alpine nappes") must have contributed as well to these differences.

FIGURE 5 | Visualization of Lake Oeschinen (Swissimage Orthophoto using base heights of SwissALTI3D: copyright Swisstopo).

On class III/IV lakes, detailed investigations on potential tsunamis generated by SAEMM and SAQMM are recommended. In lakes of class II the potential for SAQMM-generated tsunamis needs to be analyzed more in-depth. For lakes of class I, we do not see an urgent need for further tsunami investigations. Therefore, class I lakes are not considered further in this paper.

Whereas IP1 and IP2 indicate a general predisposition for SAEMM and SAQMM, which was used for the classification into four classes, IP3–IP5 can be used to prioritize between lakes within each class.

The purpose of this study is not to identify and decide on which specific lake should be investigated in more detail, but rather to indicate lakes with a high potential for tsunamis caused by different tsunami sources. The presented results are intended as a guideline for the selection of lakes for further studies, and prioritization of lakes should be based on additional parameters that include IP3–IP5 (**Table 4**), as well as practical considerations (e.g., acquisition time, funding, and inclusion of risk aspects, such as vulnerability and exposure).

- If we assume that most of the mass-movements are triggered seismically, then the prioritization could be made based on IP3 for each class. In this case, lakes that need to be investigated first are lakes Oeschinen, Sils, and Walen for class III and IV, and lakes Silvaplana, Thun, and Sarnen for class II.
- If we focus on whether a potential tsunami could mainly affect single basins and not necessarily entire lakes, then prioritization could be made based on IP4 for each class. In class III/IV, lakes that need to be investigated first in this case are lakes Oeschinen, Poschiavo, and Brienz. In class II, lakes Baldegg, Aegeri, Hallwil, and Sarnen would have priority for further investigations.
- If we focus on the consequences of potential tsunamis, here characterized by the potentially inundated fractions of each lake's shore zone (up to 1 km inland), then the prioritization could be based on IP5 for each class. No lake in class III, which indicates a high potential for SAEMM and SAQMM, has a high inundation potential (IP5). This makes sense, as for a high SAEMM potential (IP1) large parts of the lakeshore needs to be surrounded by a steep topography, which, in turn conflicts with a high inundation potential (IP5), which is parametrized by low-lying areas along the shore. However, lakes in class II (which are characterized by a high potential for SAQMM) that have a relatively high inundation potential are the lakes Constance, Baldegg, and Hallwil. Fortunately, the lakes with the highest inundation potential are the lakes of class I, which do not show a high tsunamigenic potential.

Quality and Limitations of the Relative Tsunami-potential Classification

Due to the limited amount of local site data available for each lake (e.g., no information about expected volumes of potential SAEMM), the nation-wide approach presented here is only based on basic topographical, bathymetrical, and seismological input parameters and thus gives only a broad overview of the relative tsunami potential and main expected triggers. For a full assessment, site-specific geological characteristics (such as acquired for potential SAEMM in Norway; Hermanns et al., 2016) are required. However, despite its simplicity, the method presented here is able to identify lakes with priority for further investigations. Nevertheless, the presented methodology to calculate the various input parameters certainly oversimplifies certain aspects:

- As the volumes of mass movements displacing the water are crucial for the estimation of potential tsunami wave-amplitudes, our simplified methodology is not able to estimate wave heights. At this scale of investigation and with the limited area-wide information available, it is out of scope to assess potential wave heights for each lake, considering the complex interplay between multiple landslide characteristics (see *Background*).
- Additionally, it would be difficult to compare estimated wave heights with the heights documented in historical sources, as, unfortunately, it is rarely documented where and how the waves or their run-up were measured. For assessing the impact at the shore, it is crucial to know whether the wave in the deep water, nearshore, or after shoaling has been described (e.g., Huber, 1980; Fuchs and Boes, 2010).
- Sensitivity analyses showed that the prioritization according to IP3 depends on the selected hazard parameter. If, for example, Peak Ground Acceleration instead of SA(0.3s) is chosen, a few lakes will slightly change positions in the ranking (**Supplementary Figure S60**). This however has no impact on the lakes tsunami classes discussed in the paper. Also, soft sediments, such as occurring on the lake bottom, may amplify seismic shaking considerably. These amplification effects have been neglected in the present study, as consolidated experimental results are not yet available. An ongoing project of the Swiss Seismological Service at Swiss Federal Institute of Technology Zurich is collecting amplification values at the subaqueous slopes and expects them to be remarkably different from those observed onshore.
- To calculate IP5, the ratio of zones lower than 5 m above lake level within the zone of 1 km inland along the shore is calculated. A downside of this approach is that it neglects the micro-topography, e.g., a moraine ridge around the lake may limit the potential inundation, and thus a low-lying area within this shore zone that is located behind such a micro-topographic elevation may contribute to the inundation potential of a lake, but in reality the moraine ridge would hinder the flow (unless overtopping occurred) (c.f. figures in Section 6 of **Supplementary Material**).
- The relatively coarse resolution of the topographic and bathymetric datasets used (SRTM data with 90 m grid resolution) and resampled SwissBathy3D/interpolation from SMV10/25 data (20 m grid resolution) are in our opinion sufficient for such a categorical analysis. Simple tests with a topographic elevation model of better resolution (DHM25) surrounding lakes where existing showed that the relative ranking of the lakes of IP1 did not change.
- The fact that small parts of the SMV 10/25 isobaths of Lakes Lugano and Maggiore are missing on the Italian territory (**Supplementary Figures S1 and S2**) is not expected to change the results of our classification, as the input parameter (IP2) is calculated by the ratio of the pixels with a slope inclination between 10–25° to the total slope area (defined as pixels with inclinations >5°). Both lakes Lugano and Maggiore have a high value of IP2. The missing parts are not likely to lower the IP values considerably, regarding the general morphology of the lakes (**Supplementary Figures S43 and S45**), and their Alpine setting on both the Swiss and Italian side.

The documented historical tsunami events in Swiss perialpine lakes can be used to validate our simplified classification approach. It is worth noting that the historical SAEMM- and SAQMM-tsunami events have occurred on lakes that are evaluated as lakes of classes II and III in our approach, indicating lakes with a high SAQMM- or combined SAEMM- and SAQMM-tsunami potential, with the exception of the

tsunami that occurred on Lake Lauerz (**Table 1**; Bussmann and Anselmetti, 2010 and references therein). According to our classification, Lake Lauerz shows a low tsunamigenic potential posed by SAEMM and SAQMM (and 4). However, the Rossberg landslide significantly changed the lake's shape and size; it has become much smaller with a center further away from the failed mountain slope (Bussmann and Anselmetti, 2010). It would be interesting to compare the tsunami potential for the pre-Rossberg-slide bathymetry to the bathymetry to date and to analyze if the tsunami potential has been reduced. Furthermore, Bussmann and Anselmetti (2010) interpret the tsunami originating from a cascading event, as the mass movement itself did not reach the lake. The subaerial landslide mobilized soft sediments on a swamp plane laterally, which, in turn formed an indenter into the lake causing a tsunami wave. Such cascading effects are not considered in our simplified classification. A cascading effect is also assumed to have caused the AD 563 Tsunami in Lake Geneva (Kremer et al., 2012).

CONCLUSIONS AND OUTLOOK

In this study, a simplified workflow for the classification of the tsunami potential, caused by SAEMM and SAQMM, respectively, in Swiss perialpine lakes, was presented. The results of this study may serve as a starting point for more detailed investigations (e.g., numerical modeling), also considering more field data. Findings show that lakes located within the Alps show generally a higher potential for SAEMM and SAQMM, due to the often steep surrounding rock-walls, and the fjord-type topography of the lake basins with large portions of the lateral slopes lying in the unstable range (i.e., ~10–25°). In contrast, the low lying topography along the shores of the lakes in the Swiss Plateau and Jura Mountains favor inundation caused by potential tsunamis on these lakes. Our results further indicate that all investigated lakes with high potential for SAEMM also have a high potential for SAQMM. The converse is not true, not all lakes with a high potential for SAQMM do have a high potential for SAEMM. We recommend that detailed investigations of the SAQMM-caused tsunami hazard should focus on lakes of classes II–IV (n = 20), and of the SAEMM-caused tsunami hazard on the classes III and IV (n = 9), prioritized by the additional input parameter (IP3–IP5) according to the main purpose of a potential study.

Due to its simplicity, this methodology could also be applied to other lakes worldwide. The minimum of required inputs include digital-elevation raster data, bathymetric raster data, shoreline vector data, and earthquake accelerations. The approach presented herein can be extended by adding further input parameters (e.g., considering cascading hazards). In the context of global warming and thawing of permafrost regions, the parametrization of the potential for subaerial mass-movement may include data extracted from permafrost maps. Furthermore, information about vulnerability and exposure (e.g., degree of building development and type of building) along the shores may be included, when prioritizing specific lakes for more in-depth investigations, especially when considering potential economic damage.

DATA AVAILABILITY STATEMENT

The data analyzed in this study is subject to the following licenses/restrictions: The swisstopo geodata that were used to extract the various Input parameters are copyrighted by swisstopo. However, they can be viewed by everyone for free on maps.geo.admin.ch, but not downloaded. Requests to access these datasets should be directed to the Swiss federal geoportal: maps.geo.admin.ch.

AUTHOR CONTRIBUTIONS

MS: formal analysis, methodology, visualization, and writing—original draft (lead); FE, KK, CC, PB, DV, RB, and DF,: review and editing. FA and SW: funding acquisition, review, and editing.

FUNDING

Funding was received by the Swiss Federal Office for the Environment (FOEN) (17.0092.PJ) and the Swiss National Science Foundation SNSF (171017).

ACKNOWLEDGMENTS

Geodata was used with permission from swisstopo. The authors would like to thank the editor and reviewers for their constructive and helpful comments on this article.

SUPPLEMENTARY MATERIAL

The Supplementary Material for this article can be found online at: https://www.frontiersin.org/articles/10.3389/feart.2020.564783/full#supplementary-material

REFERENCES

Aronow, S. (1982). "Shoreline development ratio," in *Beaches and coastal geology. Encyclopedia of Earth science* (Boston, MA: Springer US), 754–755. doi:10.1007/0-387-30843-1_417

Bini, A., Buoncristiani, J.-F., Couterrand, S., Ellwanger, D., Felber, M., Florineth, D., et al. (2009). *Die Schweiz während des letzteiszeitlichen Maximums (LGM). 1: 500,000*. Köniz, Switzerland: Bundesamt für Landestopografie Swisstopo Wabern.

Bussmann, F., and Anselmetti, F. S. (2010). Rossberg landslide history and flood chronology as recorded in Lake Lauerz sediments (Central Switzerland). *Swiss J. Geosci.* 103, 43–59. doi:10.1007/s00015-010-0001-9

Cauzzi, C., Fäh, D., Wald, D. J., Clinton, J., Losey, S., and Wiemer, S. (2018). ShakeMap-based prediction of earthquake-induced mass movements in Switzerland calibrated on historical observations. *Nat. Hazards* 92, 1211–1235. doi:10.1007/s11069-018-3248-5

Coe, J., Godt, J., Baum, R., Bucknam, R., and Michael, J. (2004). "Landslide susceptibility from topography in Guatemala," in *Landslides: evaluation and stabilization*. Editors W. A. Lacerda, M. M. Ehrlich, S. A. B. Fontura, and A. S. F. Sayão (London, UK: Taylor & Francis Group), 69–78. doi:10.1201/b16816-8

Corella, J. P., Arantegui, A., Loizeau, J. L., DelSontro, T., le Dantec, N., Stark, N., et al. (2014). Sediment dynamics in the subaquatic channel of the Rhone delta (Lake Geneva, France/Switzerland). *Aquat. Sci.* 76, 73–87. doi:10.1007/s00027-013-0309-4

Evers, F. M., Hager, W. H., and Boes, R. M. (2019a). Spatial impulse wave generation and propagation. *J. Waterw. Port Coast. Ocean Eng.* 145, 1–15. doi:10.1061/(ASCE)WW.1943-5460.0000514

Evers, F. M., Heller, V., Fuchs, H., Hager, W. H., and Boes, R. M. (2019b). *Landslide-generated impulse waves in reservoirs: basics and computation. VAW-Mitteilung*. Editor R. M. Boes (Zürich, Switzerland: Versuchsanstalt für Wasserbau, Hydrologie und Glaziologie (VAW), ETH Zürich).

Fabbri, S. C., Herwegh, M., Horstmeyer, H., Hilbe, M., Hübscher, C., Merz, K., et al. (2017). Combining amphibious geomorphology with subsurface geophysical and geological data: a neotectonic study at the front of the Alps (Bernese Alps, Switzerland). *Quat. Int.* 451, 101–113. doi:10.1016/j.quaint.2017.01.033

Fäh, D., Giardini, D., Kästli, P., Deichmann, N., Gisler, M., Schwarz-Zanetti, G., et al. (2011). ECOS-09 earthquake catalogue of Switzerland release 2011. Report and Database. Public catalogue, Zürich, Switzerland, April 17, 2011.

Fanetti, D., Anselmetti, F. S., Chapron, E., Sturm, M., and Vezzoli, L. (2008). Megaturbidite deposits in the Holocene basin fill of Lake Como (Southern Alps, Italy). *Palaeogeogr. Palaeoclimatol. Palaeoecol.* 259, 323–340. doi:10.1016/j.palaeo.2007.10.014

Fernandes, N. F., Guimarães, R. F., Gomes, R. A. T., Vieira, B. C., Montgomery, D. R., and Greenberg, H. (2004). Topographic controls of landslides in Rio de Janeiro: field evidence and modeling. *Catena* 55, 163–181. doi:10.1016/S0341-8162(03)00115-2

Fischer, L., Purves, R. S., Huggel, C., Noetzli, J., and Haeberli, W. (2012). On the influence of topographic, geological and cryospheric factors on rock avalanches and rockfalls in high-mountain areas. *Nat. Hazards Earth Syst. Sci.* 12, 241–254. doi:10.5194/nhess-12-241-2012

Fuchs, H., and Boes, R. (2010). Berechnung felsrutschinduzierter Impulswellen im Vierwaldstättersee. *Wasser Energ. Luft* 102 (3), 215–221. doi:10.3929/ethz-b-000256996

Gerber, W. (1994). "Beurteilung des Prozesses Steinschlag," in *Ganzheitliche Gefahrenbeurteilung. Kursunterlagen FAN-Kurs 1994*. Editors C. Rickli, A. Böll, and W. Gerber (Birmensdorf, Switzerland: Eidgenössische Forschungsanstalt für Wald, Schnee und Landschaft).

Girardclos, S., Schmidt, O. T., Sturm, M., Ariztegui, D., Pugin, A., and Anselmetti, F. S. (2007). The 1996 AD delta collapse and large turbidite in Lake Brienz. *Mar. Geol.* 241, 137–154. doi:10.1016/j.margeo.2007.03.011

Gisler, M., and Fäh, D. (2011). *Grundlagen des Makroseismischen Erdbebenkatalogs der Schweiz*. Zürich, Switzerland: Schweizerischer Erdbebendienst/VDF Hochschulverlag AG). doi:10.3218/3407-3

Glimsdal, S., L'Heureux, J.-S., Harbitz, C. B., and Løvholt, F. (2016). The 29th January 2014 submarine landslide at Statland, Norway-landslide dynamics, tsunami generation, and run-up. *Landslides* 13, 1435–1444. doi:10.1007/s10346-016-0758-7

Glimsdal, S., Pedersen, G. K., Harbitz, C. B., and Løvholt, F. (2013). Dispersion of tsunamis: does it really matter? *Nat. Hazards Earth Syst. Sci.* 13, 1507–1526. doi:10.5194/nhess-13-1507-2013

Hafsteinsson, H. J., Evers, F. M., and Hager, W. H. (2017). Solitary wave run-up: wave breaking and bore propagation. *J. Hydraul. Res.* 55, 787–798. doi:10.1080/00221686.2017.1356756

Hager, W. H., and Evers, F. M. (2020). Impulse waves in reservoirs: research up to 1990. *J. Hydraul. Eng.* 146, 1–13. doi:10.1061/(ASCE)HY.1943-7900.0001770

Harbitz, C. B. (1992). Tech. Rep. 6. Reflection-transmission of nonlinear waves in channel bends. Oslo, Norway: Institute of Mathematics, University of Oslo.

Hartigan, J. A., and Wong, M. A. (1979). Algorithm as 136: a K-means clustering algorithm. *J. Appl. Stat.* 28, 100. doi:10.2307/2346830

Heim, A. (1932). *Bergsturz und Menschenleben. Beiblatt zur Vierteljahrsschrift der Naturforschenden Gesellschaft in Zürich*. Zürich, Switzerland: Beer & Co. Vol. 77, Issue 20.

Heinimann, H. R., Hollenstein, K., Kienholz, H., Krummenacher, B., and Mani, P. (1998). *Methoden zur Analyse und Bewertung von Naturgefahren*. Bern, Switzerland: Bundesamt für Umwelt, Wald und Landschaft (BUWAL). Umwelt-Materialien Naturgefahren 85, 248.

Heller, V., and Hager, W. H. (2010). Impulse product parameter in landslide generated impulse waves. *J. Waterw. Port Coast. Ocean Eng.* 136, 145–155. doi:10.1061/(ASCE)WW.1943-5460.0000037

Heller, V., and Hager, W. (2014). A universal parameter to predict subaerial landslide tsunamis? *J. Marine. Sci. Eng.* 2, 400–412. doi:10.3390/jmse2020400

Heller, V., Hager, W. H., and Minor, H.-E. (2008). Scale effects in subaerial landslide generated impulse waves. *Exp. Fluid* 44, 691–703. doi:10.1007/s00348-007-0427-7

Henriod, S., Douard, R., Ullmann, D., and Humbel, R. (2016). *Statistik der Bevölkerung und Haushalte (STATPOP)*. BFS-Nummer: be-d-00.03-13-STATPOP-v16. Bern, Switzerland: Bundesamt für Statistik (BFS).

Hermanns, R. L., Oppikofer, T., Anda, E., Blikra, L. H., Böhme, M., and Bunkholt, H. (2012). NGU Rep. 2012.029, 49. Recommended hazard and risk classification system for large unstable rock slopes in Norway. Available at: http://www.ngu.no/no/hm/Publikasjoner/Rapporter/2012/2012-029/ (Accessed April 16, 2020).

Hermanns, R. L., Oppikofer, T., Anda, E., Blikra, L. H., Böhme, M., and Bunkholt, H. (2013). Hazard and risk classification for large unstable rock slopes in Norway. *Ital. J. Eng. Geol. Environ.* 6, 245–254. doi:10.4408/IJEGE.2013-06.B-22

Hermanns, R. L., Oppikofer, T., Böhme, M., Dehls, J., Molina, F., and Penna, I. (2016). Rock slope instabilities in Norway: first systematic hazard and risk classification of 22 unstable rock slopes from northern, western and southern Norway. *Landslides Eng. Slopes Exp. Theory Pract.* 2, 1107–1114. doi:10.1201/b21520-133

Hilbe, M., and Anselmetti, F. S. (2014). Signatures of slope failures and river-delta collapses in a perialpine lake (Lake Lucerne, Switzerland). *Sedimentology* 61, 1883–1907. doi:10.1111/sed.12120

Hilbe, M., and Anselmetti, F. S. (2015). Mass movement-induced tsunami hazard on perialpine Lake Lucerne (Switzerland): scenarios and numerical experiments. *Pure Appl. Geophys.* 172, 545–568. doi:10.1007/s00024-014-0907-7

Hilbe, M., Anselmetti, F. S., Eilertsen, R. S., Hansen, L., and Wildi, W. (2011). Subaqueous morphology of Lake Lucerne (Central Switzerland): implications for mass movements and glacial history. *Swiss J. Geosci.* 104, 425–443. doi:10.1007/s00015-011-0083-z

Huber, A. (1980). *Schwallwellen in seen als Folge von Felsstürzen. VAW-Mitteilung*. Editor D. Fischer (Zürich, Switzerland: Versuchsanstalt für Wasserbau, Hydrologie und Glaziologie, ETH Zürich).

Huber, A. (1982). Felsbewegungen und Uferabbrüche an Schweizer Seen, ihre Ursachen und Auswirkungen. *Eclogae Geol. Helv.* 75, 563–578. doi:10.5169/seals-165242

Jarvis, A., Reuter, H. I., Nelson, E. G., and Guevara, E. (2008). Hole-filled SRTM for the globe version 4, available from the CGIAR-CSI SRTM 90m database. Available at: http://srtm.csi.cgiar.org (Accessed March 16, 2020).

Knapp, S., Gilli, A., Anselmetti, F. S., Krautblatter, M., and Hajdas, I. (2018). Multistage rock-slope failures revealed in lake sediments in a seismically active Alpine region (Lake Oeschinen, Switzerland). *J. Geophys. Res. Earth Surf.* 123, 658–677. doi:10.1029/2017JF004455

Kremer, K., Hilbe, M., Simpson, G., Decrouy, L., Wildi, W., and Girardclos, S. (2015). Reconstructing 4,000 years of mass movement and tsunami history in a deep peri-Alpine lake (Lake Geneva, France-Switzerland). *Sedimentology* 62, 1305–1327. doi:10.1111/sed.12190

Kremer, K., Simpson, G., and Girardclos, S. (2012). Giant Lake Geneva tsunami in ad 563. *Nat. Geosci.* 5, 756–757. doi:10.1038/ngeo1618

Kremer, K., Wirth, S. B., Reusch, A., Fäh, D., Bellwald, B., Anselmetti, F. S., et al. (2017). Lake-sediment based paleoseismology: limitations and perspectives from the Swiss Alps. *Quat. Sci. Rev.* 168, 1–18. doi:10.1016/j.quascirev.2017.04.026

Løvholt, F., Pedersen, G., Harbitz, C. B., Glimsdal, S., and Kim, J. (2015). On the characteristics of landslide tsunamis. *Phil. Trans. R. Soc. A* 373, 20140376. doi:10.1098/rsta.2014.0376

Monecke, K., Anselmetti, F. S., Becker, A., Sturm, M., and Giardini, D. (2004). The record of historic earthquakes in lake sediments of Central Switzerland. *Tectonophysics* 394, 21–40. doi:10.1016/j.tecto.2004.07.053

Nadim, F., Kalsnes, B., and Eide, A. (1996). "Analysis of submarine slope stability under seismic action," in *Landslides*. Editor K. Senneset (Rotterdam, Netherlands: Balkema), 561–565.

Oppikofer, T., Hermanns, R. L., Roberts, N. J., and Böhme, M. (2019). SPLASH: semi-empirical prediction of landslide-generated displacement wave run-up heights. *Geol. Soc. Spec. Publ.* 477, 353–366. doi:10.1144/SP477.1

Reusch, A. (2015). Sublacustrine paleoseismology and fluid flow in the Western Swiss Molasse basin: new constraints from the sedimentary archive of Lake Neuchâtel. PhD Thesis. Zurich, Switzerland: ETH Zurich, Nr. 232131.

Roberts, N. J., McKillop, R. J., Lawrence, M. S., Psutka, J. F., Clague, J. J., and Brideau, M.-A. (2013). "Impacts of the 2007 landslide-generated tsunami in Chehalis Lake, Canada," in *Landslide science and practice*. Editors C. Margottini, P. Canuti, and K. Sassa (Berlin, Germany and Heidelberg, Germany: Springer), 133–140. doi:10.1007/978-3-642-31319-6_19

Romstad, B., Harbitz, C. B., and Domaas, U. (2009). A GIS method for assessment of rock slide tsunami hazard in all Norwegian lakes and reservoirs. *Nat. Hazards Earth Syst. Sci.* 9, 353–364. doi:10.5194/nhess-9-353-2009

Schnellmann, M., Anselmetti, F. S., Giardini, D., and McKenzie, J. A. (2006). 15,000 years of mass-movement history in Lake Lucerne: implications for seismic and tsunami hazards. *Eclogae Geol. Helv.* 99, 409–428. doi:10.1007/s00015-006-1196-7

Schnellmann, M., Anselmetti, F. S., Giardini, D., McKenzie, J. A., and Ward, S. N. (2002). Prehistoric earthquake history revealed by lacustrine slump deposits. *Geology* 30, 1131–1134. doi:10.1130/0091-7613(2002)030<1131:PEHRBL>2.0.CO;2

Siegenthaler, C., Finger, W., Kelts, K., and Wang, S. (1987). Earthquake and seiche deposits in Lake Lucerne, Switzerland. *Eclogae Geol. Helv.* 80, 241–260.

Siegenthaler, C., and Sturm, M. (1991). Slump induced surges and sediment transport in Lake Uri, Switzerland. *SIL Proc. 1922–2010* 24, 955–958. doi:10.1080/03680770.1989.11898889

Strasser, M., Hilbe, M., and Anselmetti, F. S. (2011). Mapping basin-wide subaquatic slope failure susceptibility as a tool to assess regional seismic and tsunami hazards. *Mar. Geophys. Res.* 32, 331–347. doi:10.1007/s11001-010-9100-2

Strasser, M., Monecke, K., Schnellmann, M., and Anselmetti, F. S. (2013). Lake sediments as natural seismographs: a compiled record of Late Quaternary earthquakes in Central Switzerland and its implication for Alpine deformation. *Sedimentology* 60, 319–341. doi:10.1111/sed.12003

Strasser, M., Stegmann, S., Bussmann, F., Anselmetti, F. S., Rick, B., and Kopf, A. (2007). Quantifying subaqueous slope stability during seismic shaking: Lake Lucerne as model for ocean margins. *Mar. Geol.* 240, 77–97. doi:10.1016/j.margeo.2007.02.016

Strupler, M., Anselmetti, F. S., Hilbe, M., Kremer, K., and Wiemer, S. (2020). A workflow for the rapid assessment of the landslide-tsunami hazard in peri-alpine lakes. *Geol. Soc. Spec. Publ.* 500, 81–95. doi:10.1144/SP500-2019-166

Strupler, M., Anselmetti, F. S., Hilbe, M., and Strasser, M. (2018a). Quantitative characterization of subaqueous landslides in Lake Zurich (Switzerland) based on a high-resolution bathymetric dataset. *Geol. Soc.Spec. Publ.* 477, 399–412. doi:10.1144/SP477.7

Strupler, M., Danciu, L., Hilbe, M., Kremer, K., Anselmetti, F. S., Strasser, M., et al. (2018b). A subaqueous hazard map for earthquake-triggered landslides in Lake Zurich, Switzerland. *Nat. Hazards* 90, 51–78. doi:10.1007/s11069-017-3032-y

Strupler, M., Hilbe, M., Anselmetti, F. S., Kopf, A. J., Fleischmann, T., and Strasser, M. (2017). Probabilistic stability evaluation and seismic triggering scenarios of submerged slopes in Lake Zurich (Switzerland). *Geo Mar. Lett.* 37, 241–258. doi:10.1007/s00367-017-0492-8

Strupler, M., Hilbe, M., Kremer, K., Danciu, L., Anselmetti, F. S., Strasser, M., et al. (2018c). Subaqueous landslide-triggered tsunami hazard for Lake Zurich, Switzerland. *Swiss J. Geosci.* 111, 353. doi:10.1007/s00015-018-0308-5

Tappin, D. R., Watts, P., and Grilli, S. T. (2008). The Papua New Guinea tsunami of 17 July 1998: anatomy of a catastrophic event. *Nat. Hazards Earth Syst. Sci.* 8, 243–266. doi:10.5194/nhess-8-243-2008

Thuro, K., Berner, C., and Eberhard, E. (2006). Der Bergsturz von Goldau 1806 - was wissen wir 200 Jahre nach der Katastrophe? *Bull. Angew. Geol.* 11, 13–24.

Ward, S. N. (2001). Landslide tsunami. *J. Geophys. Res.* 106, 11201–11215. doi:10.1029/2000jb900450

Watts, P., Grilli, S. T., Tappin, D. R., and Fryer, G. J. (2005). Tsunami generation by submarine mass failure. II: predictive equations and case studies. *J. Waterw. Port Coast. Ocean Eng.* 131, 298–310. doi:10.1061/(asce)0733-950x(2005)131:6(298)

Wiemer, S., Danciu, L., Edwards, B., Marti, M., Fäh, D., and Hiemer, S. (2016). Seismic hazard model 2015 for Switzerland. 1–163. doi:10.12686/a2

Wirth, S. B., Girardclos, S., Rellstab, C., and Anselmetti, F. S. (2011). The sedimentary response to a pioneer geo-engineering project: tracking the Kander River deviation in the sediments of Lake Thun (Switzerland). *Sedimentology* 58, 1737–1761. doi:10.1111/j.1365-3091.2011.01237.x

Conflict of Interest: The authors declare that the research was conducted in the absence of any commercial or financial relationships that could be construed as a potential conflict of interest.

frontiers in Earth Science

ORIGINAL RESEARCH
published: 21 October 2020
doi: 10.3389/feart.2020.591663

A Source Clustering Approach for Efficient Inundation Modeling and Regional Scale Probabilistic Tsunami Hazard Assessment

Amy L. Williamson[1], Donsub Rim[2], Loyce M. Adams[3], Randall J. LeVeque[3], Diego Melgar[1] and Frank I. González[4]*

[1]Department of Earth Sciences, University of Oregon, Eugene, OR, United States, [2]Courant Institute, New York University, New York, NY, United States, [3]Department of Applied Mathematics, University of Washington, Seattle, WA, United States, [4]Department of Earth and Space Sciences, University of Washington, Seattle, WA, United States

For coastal regions on the margin of a subduction zone, near-field megathrust earthquakes are the source of the most extreme tsunami hazards, and are important to handle properly as one aspect of any Probabilistic Tsunami Hazard Assessment. Typically, great variability in inundation depth at any point is possible due to the extreme variation in extent and pattern of slip over the fault surface. In this context, we present an approach to estimating inundation depth probabilities (in the form of hazard curves at a set of coastal locations) that consists of two components. The first component uses a Karhunen-Loève expansion to express the probability density function (PDF) for all possible events, with PDF parameters that are geophysically reasonable for the Cascadia Subduction Zone. It is then easy and computationally cheap to generate a large N number of samples from this PDF; doing so and performing a full tsunami inundation simulation for each provides a brute force approach to estimating probabilities of inundation. However, to obtain reasonable results, particularly for extreme flooding due to rare events, N would have to be so large as to make the tsunami simulations prohibitively expensive. The second component tackles this difficulty by using importance sampling techniques to adequately sample the tails of the distribution and properly re-weight the probability assigned to the resulting realizations, and by grouping the realizations into a small number of clusters that we believe will give similar inundation patterns in the region of interest. In this approach, only one fine-grid tsunami simulation need be computed from a representative member of each cluster. We discuss clustering based on proxy quantities that are cheap to compute over a large number of realizations, but that can identify a smaller number of clusters of realizations that will have similar inundation depths. The fine-grid simulations for each cluster representative can also be used to develop an improved strategy, in which these are combined with cheaper coarse-grid simulations of other members of the cluster. We illustrate the methodology by considering two coastal locations: Crescent City, CA and Westport, WA.

Keywords: probabilistic tsunami hazard assessment, clustering, stochastic earthquakes, Karhunen-Loève expansion, GeoClaw

OPEN ACCESS

Edited by:
Finn Løvholt, Norwegian Geotechnical Institute, Norway

Reviewed by:
Gareth Davies, Geoscience Australia, Australia
Ignacio Sepulveda, University of California, San Diego, United States

****Correspondence:***
Amy L. Williamson
awillia5@uoregon.edu

Specialty section:
This article was submitted to Geohazards and Georisks, a section of the journal Frontiers in Earth Science

Received: *05 August 2020*
Accepted: *11 September 2020*
Published: *21 October 2020*

Citation:
Williamson AL, Rim D, Adams LM, LeVeque RJ, Melgar D and González FI (2020) A Source Clustering Approach for Efficient Inundation Modeling and Regional Scale Probabilistic Tsunami Hazard Assessment. Front. Earth Sci. 8:591663. doi: 10.3389/feart.2020.591663

INTRODUCTION

The primary goal of this work is to present a general methodology for developing the hazard curve for a quantity of interest (e.g., maximum water depth) at a coastal location that may be inundated by tsunamis. An inundation hazard curve shows the annual probability that the flooding depth will exceed each value in a range of specified exceedance values. The same techniques could be applied to other quantities of interest (e.g., maximum flow speed or momentum flux) but here we concentrate on water depth h for illustration, and use $h_{\max}$ to represent the maximum value of h over the entire simulation (at some particular point of interest). Let $\widehat{h}$ denote some particular exceedance value. The hazard curve is then obtained by determining $P[h_{\max} > \widehat{h}]$, the annual probability that $h_{\max}$ exceeds $\widehat{h}$ at this particular location, as a function of $\widehat{h}$. The ultimate goal is to develop such a hazard curve at each point on a fine grid covering a community of interest, from which it is possible to then create *hazard maps* that show the spatial distribution of maximum water depth expected for a given annual probability, or the spatial distribution of annual probability for a given exceedance value, or potentially other products useful to emergency managers or community planners. We give some examples of how this can be done in **Section 6**.

A full probabilistic tsunami hazard assessment (PTHA) would have to include all potential sources of tsunamis, far-field as well as near-field, and also possibly tsunamis induced by landslides or other processes; a complete review of this can be found in Grezio and Babeyko (2017). Here we concentrate on one aspect of PTHA, assessing the probabilities in a coastal region due to a megathrust event on a nearby subduction zone. This is a difficult aspect of PTHA because variations in the spatial distribution of the slip can have a significant effect on the resulting tsunami (Goda et al., 2016; Melgar et al., 2019). In addition, some events may cause substantial subsidence or uplift of the coast around the location of interest, which can also greatly effect the inundation extent and depth of the resulting tsunami.

To perform PTHA it is necessary to first have some model for the probability density function (PDF) of all possible events. It is impossible to know the correct distribution due to the high degree of epistemic uncertainty in subduction zones with infrequent past megathrust events. However, recent studies have suggested ways to generate a geophysically reasonable distribution that can be easily sampled to generate large numbers of hypothetical events (LeVeque et al., 2016); accordingly, the approach we use is based on a Karhunen-Loève (K-L) expansion to generate slip patterns with correlation lengths that are thought to be "reasonable" from studies of past events, e.g., (Mai and Beroza, 2002; Goda et al., 2016; Melgar and Hayes, 2019; Crempien et al., 2020), as discussed further in **Section 2**. We stress, however, that we do not claim we have the "correct" distribution, or even the best possible based on available science, and so our focus is on a methodology that could also easily be applied to other choices of the PDF. We also suggest that any PTHA study intended as guidance for decision makers should include a sensitivity study that considers how robust the results are to changes in the assumed earthquake distribution, along with other approaches for assessing the effects of the epistemic uncertainty inherent in this problem, see, for example, Davies and Griffin (2020). In addition there is a need for further testing of random tsunami models comparing their statistical properties with historical tsunamis as is done in Davies (2019) for 18 recent events in the Pacific and Indian Oceans. Of course too few data points are available from the Cascadia Subduction Zone (CSZ) itself to allow a local validation of any PDF.

TABLE 1 | Table of the four magnitude classes used in this work, with the annual probability P_j for an event from each class, along with the corresponding return period $1/P_j$, based on the Gutenberg-Richter formula $p = 10^{6.279-M_w}$ for a magnitude M_w event.

Class j	M_w	Annual probability P_j	Return period (years)
1	7.5	0.06012	16.6
2	8.0	0.01901	52.6
3	8.5	0.00601	166.3
4	9.0	0.00190	526.0

In this paper we focus on how best to handle the aleatoric uncertainty, i.e., assuming that we have a probability distribution to use for the PTHA, how do we efficiently create hazard curves based on this distribution? The brute force approach would be to choose a very large number N of samples from the distribution, perform a numerical tsunami simulation with each, and then (for each location of interest and each exceedance value) determine the number $\widehat{N}$ of samples for which $h_{\max}$ exceeds $\widehat{h}$. Then the ratio $\widehat{N}/N$ is an estimate of a conditional probability that $h_{\max}$ exceeds $\widehat{h}$ given that some event from the set of all possible events occurs. If P_{total} is the annual probability that any event from the classes considered occurs, then $P_{\text{total}}\widehat{N}/N$ could be used as the annual probability of $h_{\max}$ exceeding $\widehat{h}$.

The primary difficulty we address is that N may need to be very large in order to get meaningful statistics, particular for the relatively unlikely but most dangerous higher values of $\widehat{h}$. Since a single tsunami simulation with a reasonable spatial resolution can take several minutes if not hours of computer time, this is problematic; and even more so if one also wants to do sensitivity studies and/or must consider many different communities over hundreds of miles of coastline.

A fundamental problem already arises when we ask for a reasonable value of P_{total} since it depends very much on what set of possible earthquakes to consider. Since earthquakes with magnitude less than Mw 7.5 rarely cause damaging tsunamis we could define P_{total} as the annual probability of any event with magnitude greater than this. In **Section 2** we discuss our choice of PDF for the distribution of earthquakes. Although not necessarily correct for large subduction zone events, the Gutenberg-Richter law is a reasonable starting point for choosing a distribution. According to this, a magnitude Mw 7.5 event is 10 times more likely than an 8.5 event and roughly 32 times more likely than Mw 9.0. Hence, for example, if we sample $N = 3,200$ events we would expect perhaps 100 to be Mw 9.0 or larger, a rather sparse sampling of these important and potentially quite diverse events. Moreover, most of the samples would be small events for which there is little or no inundation, a clear waste of computing resources.

We can address this by a simple application of importance sampling. We first split the space of all possible events of interest into a small number of classes. For illustration in this paper we use four classes based on magnitude: Mw 7.5, 8.0, 8.5, and 9.0, but this could easily be expanded. We then assign an annual probability to each class, call this P_j for class j ($j = 1, , 2, 3, 4$ for our case, for which we assign the probabilities shown in **Table 1**). We then take N_j samples from class j, compute the fraction $\widehat{N}_j$ that exceed $\widehat{h}$, and use $P_j\widehat{N}_j/N_j$ as an estimate of the annual probability of exceeding $\widehat{h}$ by an event from class j. These can then be combined to obtain the annual probability of exceeding $\widehat{h}$ by any event (see **Section 6**). The advantage of splitting into classes is that we can choose a large number of events in a class corresponding to high impact but low probability (Mw 9.0 in our case) and then the corresponding fraction $\widehat{N}_j/N_j$ is weighted by a smaller annual probability P_j when combining with the probabilities obtained from other classes. For illustration, we have chosen to take $N_j = 500$ for each of the four classes so that we only consider 2,000 events in total but 500 of them are in the Mw 9.0 class (In **Section 6** we discuss the rationale and implications of choosing this number of realizations.).

Next we tackle the problem that even 2,000 tsunami simulations may be excessively demanding, particularly when we expect that many of these events will give very similar inundation patterns and depths as other events, and so in principle it should be possible to estimate the hazard curve with fewer simulations of judiciously chosen representative tsunamis. We develop an approach for clustering that can be applied to the 2,000 events before doing any fine-scale tsunami modeling, in order to identify clusters of events that we expect to give very similar tsunami impact in the location of interest. We then do a fine-scale tsunami model of only one realization from each cluster (which we call the "cluster representative") and assign it a weight that is based on the collection of events in that cluster. Based on this we can estimate the contribution that this cluster should make to each hazard curve. This clustering is explained in much more detail in **Section 5**. Other studies have used clustering to achieve scenario reduction. For example, see Lorito et al. (2015) for hazard assessment, Gusman et al. (2014) for early warning and Volpe et al. (2019) for a study more closely related to this paper.

The clustering approach we illustrate in this paper is based on doing a coarse-grid tsunami simulation for each of the 2,000 realizations, with a grid resolution that allows much faster simulation, but is too coarse to properly represent the tsunami inundation over the communities of interest. However, we show that these coarse grid simulations give information in the form of proxy variables that can be used to very effectively cluster the events.

Moreover, the coarse-grid simulations can be greatly enhanced to provide "pseudo-fine" results that are at the resolution of the desired fine grid and that agree very well with the actual fine-grid simulations of the same realization, but are much cheaper to compute. This enhancement is performed in part using information about the difference between the coarse and fine grid simulations performed for the few realizations where both are available (the cluster representatives). This procedure is described in more detail in **Section 4**.

For illustration we consider two sample communities: Crescent City, CA, which is near the southern extent of the CSZ and Westport, WA, roughly 570 km north of Crescent City. These communities are both at high risk to CSZ tsunamis and have been the subject of past studies. They also have quite different topographic features as discussed further in **Section 3**. The same set of 2,000 CSZ realizations was used for each site, although the clustering algorithm is applied separately to each, since the set of realizations that give similar inundation patterns at one site may not form a suitable cluster at the second site. For illustration we show that selecting only 18 clusters (and hence performing only 18 fine-grid simulations for each site) gives hazard curves and maps that compare very well with those obtained if all 2,000 realizations are simulated on the fine grid, particularly after adding in additional information obtained from coarse-grid simulations of each realization. These results are presented in **Section 7**.

Some of the techniques presented in this paper were first developed as part of a project funded by Federal Emergency Management Agency Region IX, and presented in the project Final Report by Adams et al. (2017). Subsequently we have improved some of these techniques. We are also now using a probability distribution that is potentially more realistic than the original choice, and we consider two different target communities with quite different topography in order to better test the general applicability of these ideas. The original report and associated webpages (Adams et al., 2017) contain more discussion of some of these ideas, along with illustrations of some related approaches that are not reported in this paper. Research on PTHA using stochastic collections of sources goes back many years, see, for example, the early review Geist and Parsons (2006) and the more recent ones of Geist and Lynett (2014) and Grezio and Babeyko (2017) for many more references.

Recently, several researchers have adopted the use of a K-L expansion to generate large suites of realizations for PTHA studies of particular regions and/or to study sensitivities and uncertainty. For example, Gonzalez et al. (2020) generated 400 realizations for a hybrid deterministic/PTHA to Iquique, Chile, and Crempien et al. (2020) generated 10,000 realizations on a idealized fault and performed GeoClaw tsunami simulations of each on idealized topography to study the effect of spatial slip correlation on tsunami intensity. The techniques developed in this paper could help to accelerate such studies.

Research on reducing the work required to handle large sets of realizations has also been done by others. For example, Sepúlveda et al. (2017) used the K-L expansion together with a stochastic reduced order model to obtain better results than with a brute force Monte Carlo simulation, and Sepúlveda et al. (2019) used these techniques to do a PTHA analysis including a sensitivity study for Hong Kong and Taiwan locations due to earthquakes on the Manila Subduction Zone. These techniques reduced the number of simulations needed from 10,000 to 200 for each of 11 sets of earthquakes, followed by fine-grid simulations of the resulting 2,200 realizations. The reduction was based on seafloor deformation statistics at the earthquake sources. That paper also has a strong

emphasis on using sensitivity analysis to quantify errors in PTHA.

Even closer to the methodology presented in this paper is the source filtering approach developed recently by Volpe et al. (2019). They started with a suite of more than 1.7 million scenarios that affect their study region, and used a clustering algorithm based on cheaply obtained proxies to reduce this to a smaller set of 1,154. They then performed fine-grid simulations for one representative from each cluster. One significant difference in our approach is that we use coarse-grid simulations (using the full nonlinear tsunami model, including onshore inundation over the study region) and the associated pseudo-fine results, which allowed us to obtain PTHA results with fewer fine-grid simulations. On the other hand, we performed 2,000 coarse-grid simulations to obtain these, whereas Volpe et al. (2019) performed the clustering based on proxy data that was more cheaply obtained. A hybrid approach might be to apply our methodology to the 1,154 cluster representatives identified in Volpe et al. (2019), performing only coarse-grid inundation simulations of these, and then further clustering into a much smaller set for the fine-grid simulations.

The approach we use to create pseudo-fine results is also similar to the idea of multilevel or multifidelity Monte Carlo methods (Giles, 2015; Peherstorfer et al., 2018), in which results from two or more different resolution simulations are combined to reduce the computational load. This is often done in the context of creating a surrogate model or emulator that can be very cheaply evaluated for new parameter choices in order to do a more extensive Monte Carlo simulation. This approach has been used in connection with tsunami modeling by de Baar and Roberts (2017), and by Salmanidou et al. (2017) for underwater landslide and tsunami modeling. For a review of these types of statistical approaches, see Viana et al. (2017). Our approach is somewhat different in the way we use cluster representatives and the differences in the local topography at different resolutions in defining the corrections.

EARTHQUAKE PROBABILITY DENSITY AND REALIZATIONS

Probability distributions proposed for CSZ earthquake magnitudes have included both characteristic and Gutenberg–Richter (G-R) types. More generally, Parsons et al. (2012) noted that this is a long-standing controversy for many other fault zones. Consequently, they developed both types of distribution models for the Nankai Trough, based on data from many past events. The characteristic earthquake model was based on fixed rupture geometries and historical/palaeoseismic recurrence times, and the G-R model was based on fault-slip rates and an estimated distribution slope (b-value). They found that the G-R distribution, constrained with a spatially variable long-term slip rate, replicated much of the spatial distribution of observed segmented rupture rates along the Nankai, Tonankai, and Tokai subduction zones, although with some rate differences between the two methods in the Tokai zone. Thus, where supporting information exists (e.g., palaeoseismic and historical recurrence data), and fault segmentation observations are absent, they suggested that very simple earthquake rupture simulations based on empirical data and fundamental earthquake laws could be useful forecast tools in settings with sparse data from past events. Models using a G-R distribution but without the explicit guidance of a varying long-term slip rate have also been employed, both globally and specifically along the Cascadia margin (Rong et al., 2014). We thus view a G-R distribution of magnitudes as adequate for this study.

We generated 2,000 slip realizations over four magnitude classes: Mw 7.5, 8.0, 8.5, and 9.0 (with 500 of each). To determine the annual probabilities of earthquakes in each of the magnitude classes, we follow a G-R law using a b-value of 1, indicating "normal" seismic behavior. We also assume a yearly rate of occurrence of a Mw 9.0 along the CSZ as once every 526 years based on paleotsunami records from Goldfinger et al. (2012). This implies an a-value of 6.279 in the G-R relation and gives us annual probabilities P_j in **Table 1** for each of our magnitude classes. Incidentally, **Table 1** could also be extrapolated to show that the CSZ should have a M6.3 earthquake every year. However, this is not the case on the anomalously-quiet CSZ. Nonetheless, for the purposes of presenting a PTHA methodology, using a Gutenberg-Richter law is a starting point. In this study, we use 0.5 magnitude unit spacing between our classes. Other studies, such as Li et al. (2016) use much smaller spacing between classes. For a full PTHA analysis, a fine spacing that allows for the complete overlap of earthquake properties between different magnitudes would be preferred.

We limit our earthquake realizations to imitate a series of thrust events located on the megathrust interface along the CSZ. To introduce variability to each realization, we allow for geophysically reasonable variations in slip distribution, location, and rupture dimension. An example of a rupture from each magnitude class is shown in **Figure 1**. We employ a regional fault geometry that approximates the CSZ from McCrory et al. (2012). This is then discretized into triangular subfaults using the three-dimensional finite element mesh generator GMSH (Geuzaine and Remacle, 2009). A triangular mesh allows a variable strike and dip that can better approximate the McCrory et al. (2012) geometry than a rectangular discretization. Our area of interest extends along the entire CSZ margin and down to a depth of 30 km beyond which slip is not expected to continue (Frankel et al., 2015).

In order to introduce variability in ruptures of the same magnitude, as is observed from past earthquakes, the length and width of each realization is obtained from a probabilistic source dimension scaling law (Blaser et al., 2010). For each individual rupture we sample from a lognormal PDF such that

$$\begin{aligned} \log_{10} L &\sim \mathcal{N}(-2.37 + 0.57M_w, \sigma_L), \\ \log_{10} W &\sim \mathcal{N}(-1.86 + 0.46M_w, \sigma_W). \end{aligned} \tag{1}$$

where σ_L and σ_W depend on the faulting environment and for reverse faulting (subduction zones) are 0.18 and 0.17, respectively (Blaser et al., 2010). The rupture extent is then centered about a

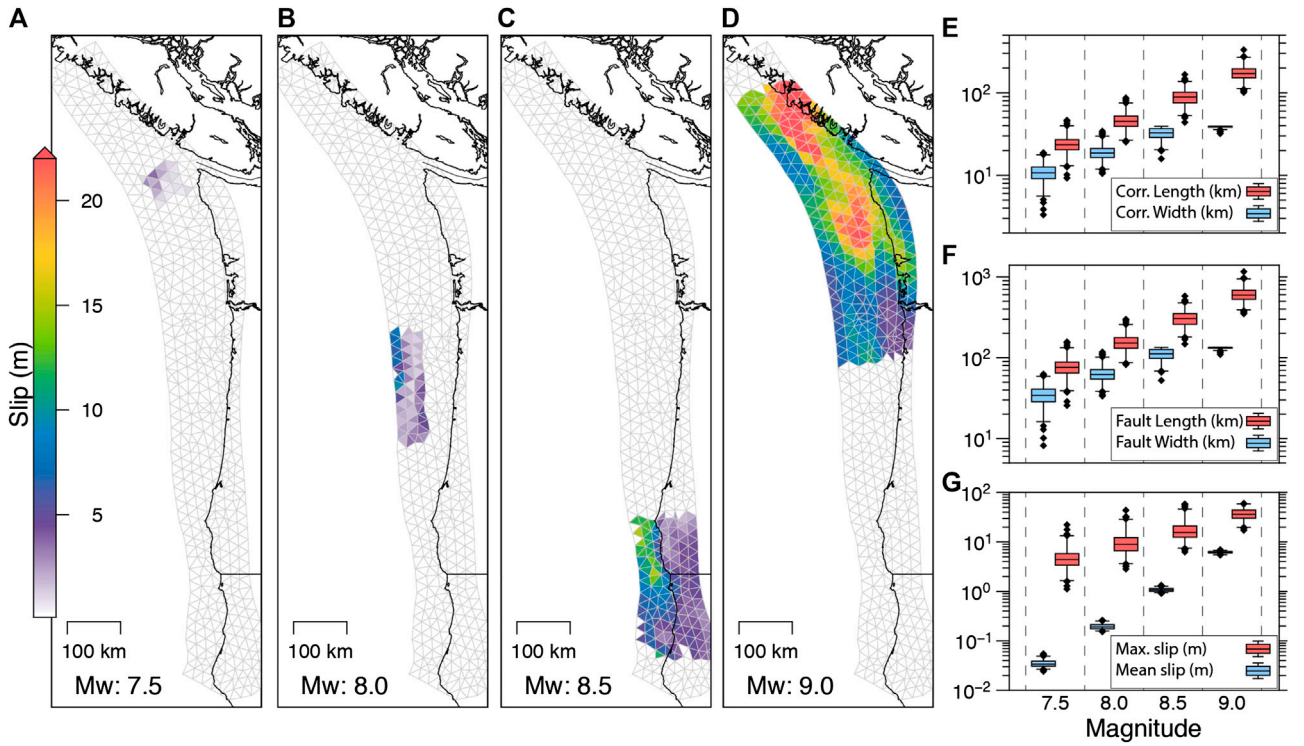

FIGURE 1 | (A–D) Example earthquake realizations for each magnitude class. **(E)** Variability in correlation length and width per each magnitude. **(F)** Variability in total fault length and width per magnitude class. **(G)** Variability in mean and maximum slip, in meters, for realizations in each magnitude class.

randomly chosen subfault within our CSZ mesh geometry. If the chosen subfault is located in such a place that the rupture extent exceeds the bounds of the rupture geometry, then it is moved up/down dip and/or along strike until it falls completely within the CSZ.

Once the bounds of the rupture area are established, we generate a stochastic slip distribution using an application of the Karhunen-Loève (K-L) expansion following LeVeque et al. (2016) and Melgar et al. (2016). Here, we assign slip over participating subfaults using a von Karman correlation function, $C(r)$, which replicates the statistics of slip distributions as observed from finite-fault solutions of past moderate sized earthquakes (Mai and Beroza, 2002). Here, the correlation between the sth and dth subfaults (in along strike and along dip directions) is

$$C_{sd}(r_{sd}) = \frac{G_H(r_{sd})}{G_0(r_{sd})}, \tag{2}$$

where

$$G_H(r_{sd}) = r_{sd}^H K_H(r_{sd}), \tag{3}$$

H is the Hurst exponent (set in this study as 0.75), K_H is the modified Bessel function of the second kind, and (r_{sd}) is a length measurement for sth and dth subfaults that depends on the distance between subfaults in the along strike (r_s) and along dip (r_d) directions as well as the correlation length along strike (a_s) and dip (a_d), written as

$$r_{sd} = \sqrt{\frac{r_s^2}{a_s} + \frac{r_d^2}{a_d}}. \tag{4}$$

The correlation length and width for each realization governs the size of asperities and uses a magnitude dependent scaling law from Melgar and Hayes (2019) where

$$\begin{aligned} a_s &= 17.7 + 0.35L_{\text{eff}}, \\ a_d &= 6.7 + 0.41W_{\text{eff}}. \end{aligned} \tag{5}$$

The variables L_{eff} and W_{eff} are based on the effective length and width scales (in kilometers) from **Eq. 1** and are determined from Mai and Beroza (2000). Using the defined correlation function the distribution of slip across the fault surface is treated as a spatially random field. The vector s containing the amount of slip at each subfault is then given by the Karhunen-Loève expansion as,

$$\mathrm{s} = \mu + \sum_{k=1}^{n_f} \mathrm{z}_k \sqrt{\lambda_k} v_k, \tag{6}$$

where μ is the mean slip over the entire fault, λ_k and v are the eigenvalues and eigenvectors of the chosen correlation function, and z_k are random numbers normally distributed with a mean of 0 and standard deviation of 1. After defining the correlation function we assume a marginal log-normal distribution as described by LeVeque et al. (2016) where we use a standard deviation of 0.45 of the mean slip in any given model. This value is

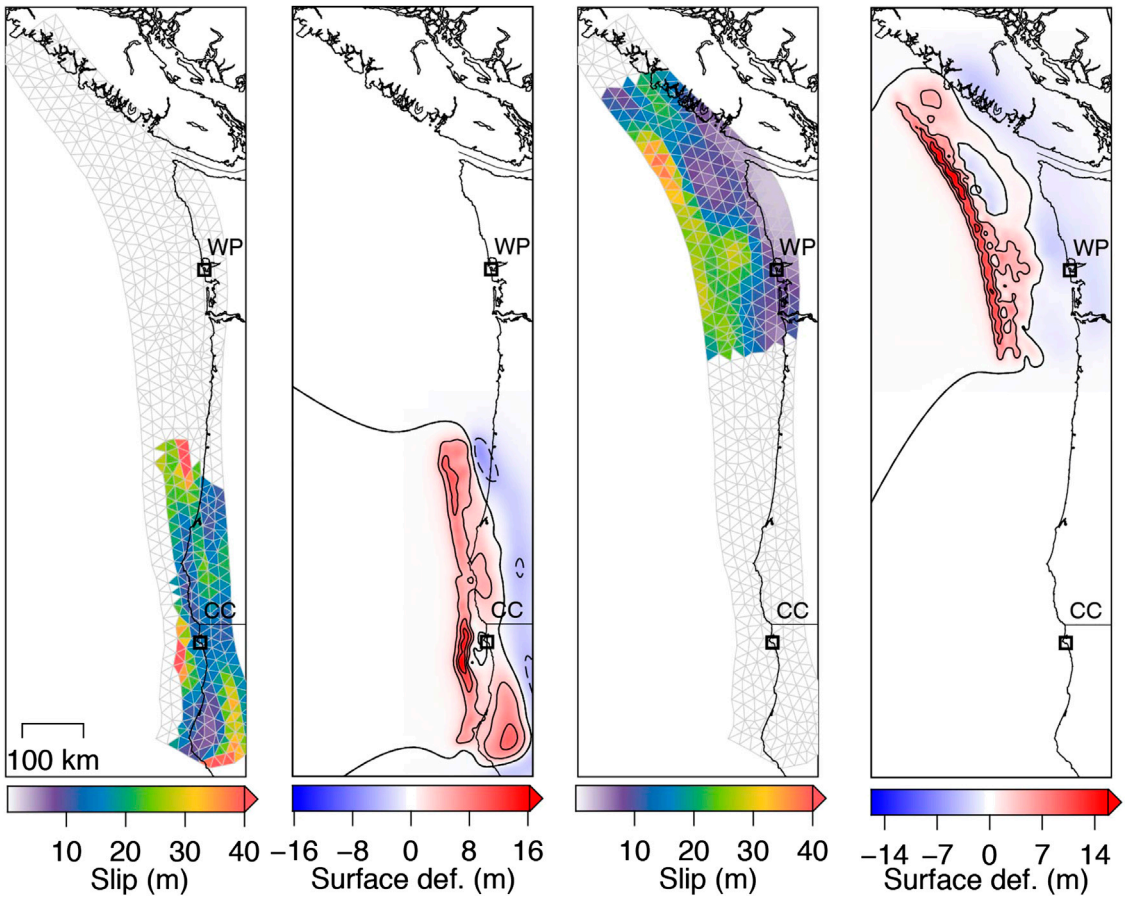

FIGURE 2 | Slip on our fault geometry and associated seafloor deformation for two sample realizations, numbered 1,665 and 1,999, shown in **Figures 5**, **8**. WP marks the location of Westport, WA. CC marks the location of Crescent City, CA.

obtained from an analysis of a database of slip models dating back to 1990 (Melgar and Hayes, 2019). It is important to note that there are as many eigenvectors or eigenmodes (n_f) as there are subfaults in the model geometry. **Equation 6** is a statement of how each eigenmode distributes slip away from the background mean model modulated by a random number z_k and thus achieving a stochastic realization of slip. For tsunami modeling because seafloor deformation is a relatively long period phenomena LeVeque et al. (2016) showed how high order modes contribute relatively little to tsunamigenesis so it is possible to truncate the sum to just a few tens or even hundreds of terms. Here we limit the number of contributing modes to no more than 200. Finally for the background mean model we assume enough homogeneously distributed slip to match the target magnitude given the chosen fault dimensions. It is also possible to make other choices for μ such as a known slip distribution or a geodetic locking model (Goldberg and Melgar, 2020).

We cap the upper level of slip possible for any realization in this study to 60 m, as was recommended in Melgar et al. (2016) and based on plate convergence rates from McCaffrey et al. (2007). We achieve this by rejecting and re-running any realization where any subfault in our mesh has an assigned slip that is greater than our maximum slip threshold. This cap is in place in order to limit the possibility of unrealistically large amounts of slip in any earthquake realization. It should be noted that this cap creates an upper limit in tsunami intensity that may be reflected in any final PTHA analysis. We do not enforce the target magnitudes in a strict sense. The resulting magnitude after the stochastic process can be slightly higher or lower than the requested values. We do not re-scale the slip in anyway to force the rupture to have the target magnitude exactly. This, and the maximum slip requirement, can introduce departures from the desired PDF (Sepúlveda et al., 2017) but this is generally an effect that is much smaller than the epistemic uncertainty.

We calculate the total seafloor deformation of each earthquake realization using angular dislocations for triangular subfaults in an elastic half space (Comninou and Dundurs, 1975). This method can be seen as a variant of the Okada equations, which focus on rectangular subfaults (Okada, 1985). We obtain the deformation over the entire CSZ study region with at a 30" spatial resolution. This is a fine enough spacing to ensure

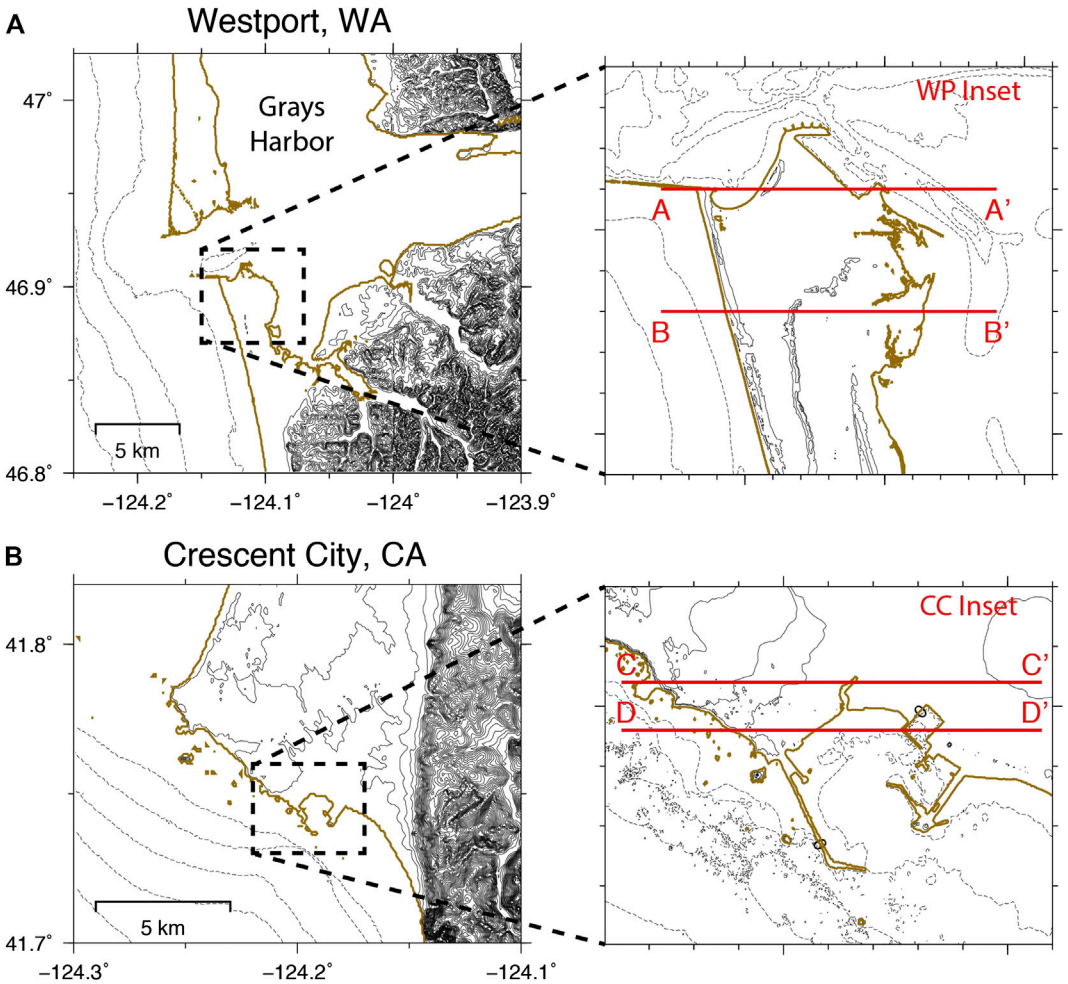

FIGURE 3 | Communities of interest in this study. **(A)** Regional and inset view of Westport, WA and two representative cross sections shown in **Section 7**. **(B)** Regional and inset view of Crescent City, CA with two representative cross sections. Both regional views have a bathymetric (dashed) and topographic (solid) contour interval of 10 m. Inset figures use a contour interval of 5 m. The coastline is differentiated with a bolded brown line.

that we recover slip features that may be present at our smallest magnitude class, including rupturing asperities at the smallest reported slip correlation length (see examples in **Figure 2**).

Seafloor deformation is directly translated to a disturbance at sea level by assuming an incompressible water column. While some large magnitude earthquakes can have rupture durations extending multiple minutes, this kinematic effect on the tsunami in the near-field is minimal (Satake, 1987; Williamson et al., 2019). Here, we simplify the rupture process by treating all seafloor deformation as instantaneous and occurring at the initial time step of our tsunami model. It is this initial disturbance that initializes the tsunami model, as discussed further in **Section 3**.

Figure 2 shows both slip on the fault and the resulting seafloor deformation for two of the magnitude 9.0 realizations. We use R_i to denote the ith realization and the figure shows the realizations $R_{1,655}$ and $R_{1,999}$ out of the $N = 2,000$ realizations, chosen because R_{1655} has slip concentrated on the southern margin of the fault while $R_{1,999}$ has it concentrated to the north, and hence they have very different effects in Westport and Crescent City, as discussed in the next section. This illustrates that even within a single magnitude class there are significant variations between the tsunamis generated.

COMMUNITIES OF INTEREST AND TSUNAMI MODELING

We consider two sample communities as shown in **Figure 3**. Crescent City, CA was used in previous work on this topic (Adams et al., 2017), and was the subject of a previous PTHA analysis by González et al. (2014) and Adams et al. (2015). Tsunamis tend to focus in Crescent City due to the offshore bathymetry and harbor (Horrillo et al., 2008), and the central business district is bounded by the harbor, the low-lying Elk River valley to the east, and higher hills to the north.

Westport, WA lies on a peninsula at the entrance to Grays Harbor. The topography is below roughly 10 m everywhere on

the peninsula, and a number of north-south running ridges protect some areas from the direct waves arriving from the west that may still be flooded from the east after the tsunami enters Grays Harbor. Westport is the site of the Ocosta Elementary School, recently rebuilt to include the first tsunami vertical evacuation structure constructed in the United States, for which tsunami modeling was presented by González et al. (2013). We selected these two communities to showcase the versatility clustering PTHA methodology. However, this methodology can be extended to any coastal community.

Tsunami simulations are performed using GeoClaw Version 5.7.0, distributed as part of the open source Clawpack software (Clawpack Development Team, 2020). This solves the two-dimensional depth-averaged non-linear shallow water equations using adaptive mesh refinement on rectangular grid patches (in longitude-latitude coordinates). GeoClaw allows each cell to be wet or dry and to change dynamically, so that the wet/dry boundary of the coastline evolves as the tsunami inundates the coastal site of interest.

For this study we simulated the tsunami from each of the 2,000 realizations in two separate simulations. The first set were the "fine-grid runs" where refinement down to 1 arcsecond (roughly 30 m in latitude, less in longitude) was enforced over both study sites. This provided the "ground truth model" hazard curves and maps to use for comparison purposes, i.e., we assume that our goal is to produce good approximations to these curves and maps with much less work than was required to run 2,000 fine-grid simulations. The second set of simulations were the "coarse-grid runs" in which the refinement only went down to 9," and hence a factor of 81 fewer grid points on the finest level than in the fine-grid runs. Moreover on these coarser grids it is also possible to take larger time steps [while still respecting the Courant-Friedrichs-Lewy condition required by the explicit finite volume method used in GeoClaw], potentially giving another factor of 9. However, since some of the computation takes place on coarser grids over the entire computational domain, the coarse grid simulations are on average 5 times faster than the fine grid simulations; see below. We also note that for a real PTHA we might want to use even finer grids, e.g., 1/3" is often used now used for hazard studies, and 1/9" topography is becoming available in many locations. In this case the relative speedup for coarse-grid simulations could be much more dramatic.

We use adaptive mesh refinement to optimize the computational cost of each tsunami simulation. All simulations used three levels of refinement in the open-ocean, with grid resolution 1″, 6″, and 3″, and with regridding every few time steps to follow the propagating waves (based on a tolerance on the sea surface elevation). On the continental shelf, refinement is allowed to the next Adaptive Mesh Refinement level at 90". An additional refinement level of 9" is enforced around both study sites. For the coarse-grid simulations only these five levels of Adaptive Mesh Refinement are used. For the fine-grid runs, two additional Adaptive Mesh Refinement levels are introduced at 3" and 1" resolutions, and the study areas are forced to be resolved at the finest 1" level. The ETOPO1 topography Digital Elevation Model at 1 arcminute resolution (Amante and Eakins, 2009) was used over the full computational domain. A subset of the Astoria, Oregon 1/3" Digital Elevation Model (NOAA NCEI, 2017) was used around Westport, and around Crescent City a version of the Crescent City, California 1/3" Digital Elevation Model (NOAA NCEI, 2012) was used that was modified to remove the pier in the harbor, since water flows under the pier, for an earlier PTHA study of this region by González et al. (2014).

In each simulation we monitor the maximum water depth h over a grid of points covering the study area (at the finest resolution of the simulation) over the duration of the simulation. For this study we ran each tsunami simulation to 4 h of simulated time after the instantaneous seafloor displacement. Examining the results we found that in a few cases there were still significant edge waves trapped along the coast that could have lead to slightly larger values of the maximum at some points, so a realistic PTHA should run some realizations out to later times. For the purposes of this study our reference solution uses the maximum h over the same time period as our approximations and so comparisons are still valid.

At each point where h is monitored, these maximum values (denoted by $h^f_{\max}$ for the fine-grid runs) are used to compute a reference hazard curve. The coarse-grid simulations produce their own set of $h^c_{\max}$ values on a coarser set of points (which can be extended to the fine grid by piecewise constant interpolation within each coarse grid cell). These coarse-grid values are used both in the clustering algorithm and in computing a pseudo-fine result from each coarse result, as explained in the sections below.

The reference hazard curve is affected by the spatial distribution and properties of the rupture realizations which act as our ground truth. Therefore, it is important to have enough realizations at each magnitude class to capture all tsunamigenic behavior that is possible given the seismic constraints we presented in **Section 2**. The total number of realizations per magnitude bin is based on the variability in the likelihood of exceeding a set of tsunami amplitudes in the harbors of both Crescent City, and Westport, as illustrated in **Figure 4**. Here, we calculate the likelihood that h exceeds a set of tsunami thresholds, ranging from 1 cm to 10 m at one particular point in each study region. As more realizations in a magnitude class are added, the variability in the probability of exceeding each tsunami threshold reduces. We can estimate that we have enough realizations to act as our ground truth when each probability curve has flattened out. Here, this occurs at about 400 realizations per magnitude.

The tsunami simulations were performed using the OpenMP feature of GeoClaw using 30 threads on a Linux server. The total Central Processing Unit time varied for each realization, depending on whether the initial deformation came from a small localized slip patch (requiring small regions of refinement in the ocean and possibly resulting in a negligible tsunami) or a larger rupture. Total Central Processing Unit time (summed over all threads and over all 2,000 simulations) was 49.2 h for the coarse-grid runs and 255.6 h for the fine-grid runs.

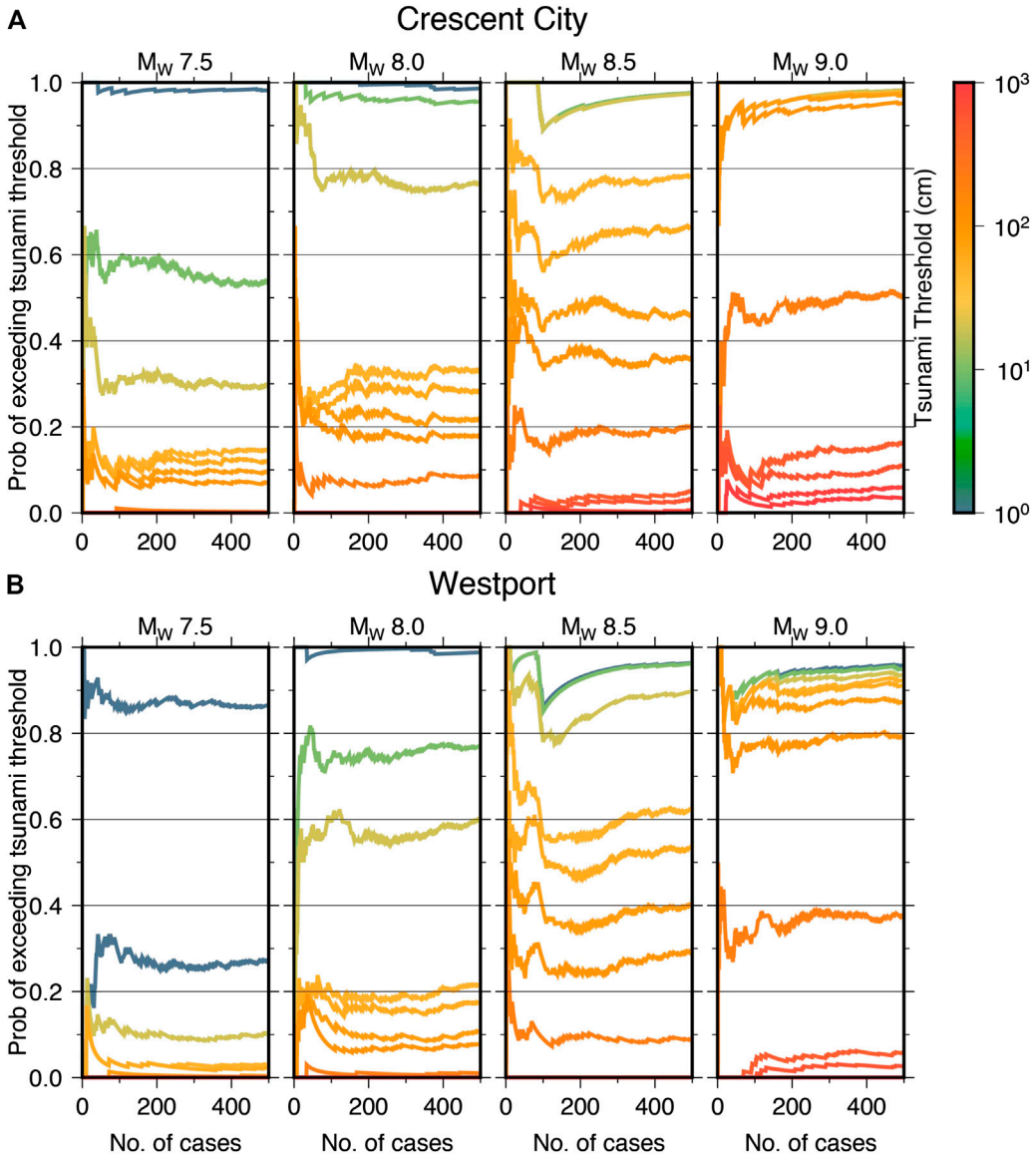

FIGURE 4 | The probability of exceeding a specified tsunami threshold as a function of the number of cases included for each magnitude class at particular points in **(A)** Crescent City and **(B)** Westport. Thresholds tested range from 1 cm to 10 m, with a separate curve for each, color-coded as indicated by the color bar.

Sample Realizations

Before proceeding, we first show $h_{\max}$ in each study region for the two sample $M_w = 9.0$ realizations shown in **Figure 2**. **Figures 5, 6** show $h_{\max}$ for $R_{1,665}$ at Westport and Crescent City, respectively, and similarly **Figures 7, 8** show $h_{\max}$ for $R_{1,999}$. In each case, panel A shows the fine-grid result $h^f_{\max}$ while B shows the coarse-grid result $h^c_{\max}$. Note that the 9" grid cell resolution is clearly visible in B and that this coarse grid cannot resolve all features of the flow, but that the general order of magnitude is correct. Panel C shows the difference between coarse and fine results, which are substantial in some regions.

The remaining panels of each figure show the result of enhancing the coarse-grid results using techniques developed in the next section, where these will be discussed in more detail.

COARSE-MOD AND PSEUDO-FINE ENHANCEMENTS

Our PTHA approach starts by sampling N realizations, which we denote by R_i (for $i = 1, 2, \ldots, N$). These may consist of N_j realizations from class j as described in **Section 1**, with $N = \sum_j N_j$. Performing coarse-grid simulations of each gives us $h^c_{\max}$ at each location on a coarse grid covering the study region. We wish to avoid doing fine-grid simulations of all realizations, and instead we will use a clustering approach, described in detail in below, to group these into K clusters and to choose one representative realization from each cluster. This "cluster representative" will be denoted by $\overline{R}_k$ for the particular realization from cluster $k = 1, 2, \ldots, K$.

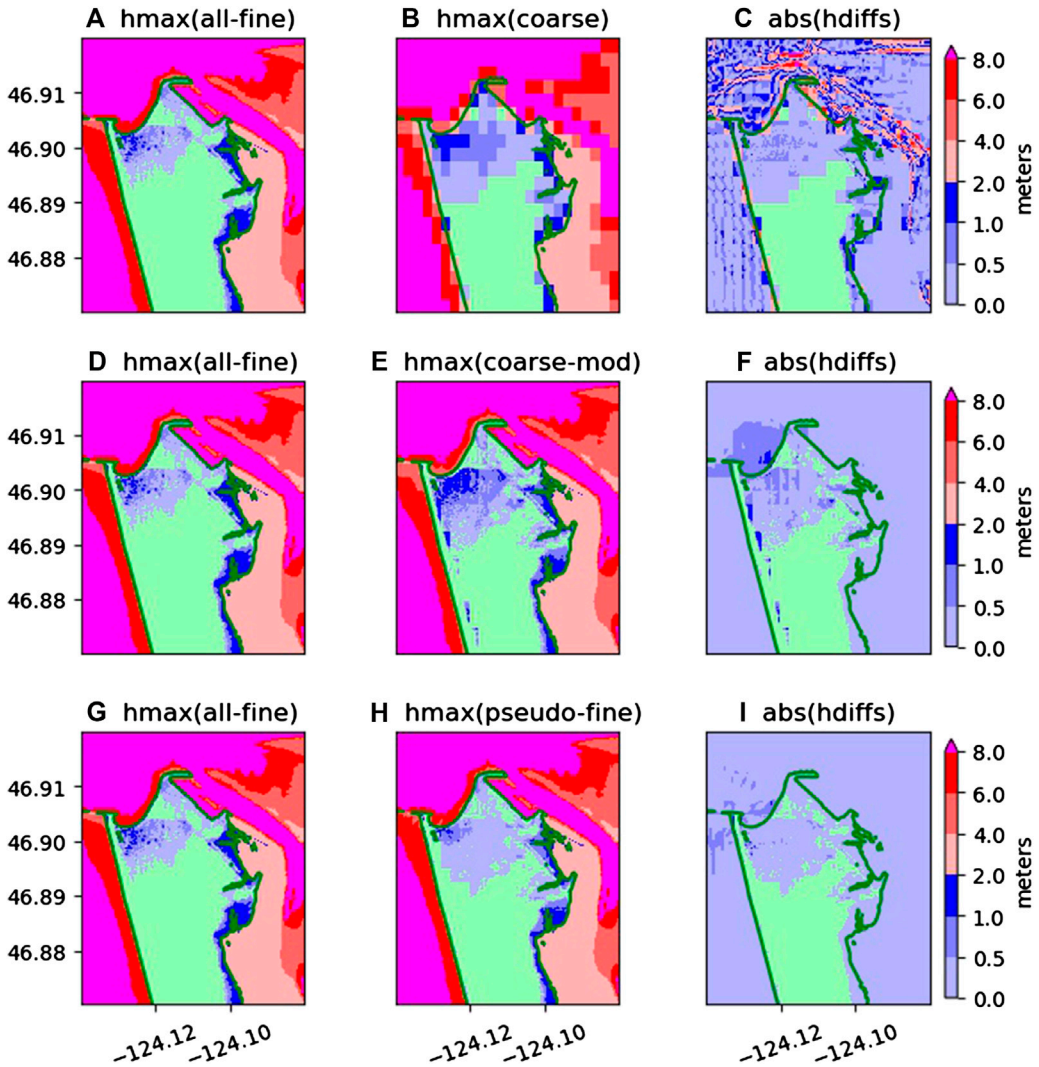

FIGURE 5 | Sample results for realization 1,665 at Westport, where the tsunami was small. **(A, D, G)** $h^f_{\max}$ **(B)** $h^c_{\max}$ **(E)** $h^c_{\max}$ after coarse-mod corrections. **(H)** $h^c_{\max}$ after pseudo-fine corrections. **(C, F, I)** Errors relative to $h^f_{\max}$. Purple is above 8 m and Green is land not inundated. See the text for more explanation.

One approach to approximating the hazard curves for N realizations using K clusters is to perform only one fine-grid simulation for each cluster (for a "cluster representative" realization selected from the cluster), and assign a weight to each that is the sum of the weights of all realizations in the cluster. We show results of this approach in **Section 7**. However, using only K events will give a hazard curve with only K jump discontinuities and cannot well approximate the true hazard curve if K is much smaller than N, particularly at the lower probabilities. In our example application, $N = 2,000$ and we will choose $K = 18$.

Much better results are obtained if we also make use of the remaining $N - K = 1,982$ coarse-grid simulations that were performed to do the clustering. The coarse grid results alone do not give sufficient resolution of $h_{\max}$ for use directly, but they can be enhanced to approximate the inundation that each would produce on a fine grid with much less work than required to do the fine-grid simulation. This is done as a two-stage process. In the first ("coarse-mod") step the coarse grid results are combined with the fine-grid topography to give estimates of the maximum depth on the fine topography. This is independent of the clustering and can be done immediately following each coarse grid simulation. The second ("pseudo-fine") step uses the clustering, and the idea that the difference between the coarse-mod and fine-grid simulations at the cluster representative (both of which are available) gives a good indication of how other coarse-mod results in the same cluster should be adjusted to better approximate the result of a fine-grid simulation. We describe each of these in turn.

Modified Coarse Grid Corrections

Each of the $N = 2,000$ coarse-grid runs provides an estimate of $h^c_{\max}$ at a set of coarse grid points covering the study region. These were computed using a coarse grid (with resolution nine" in our

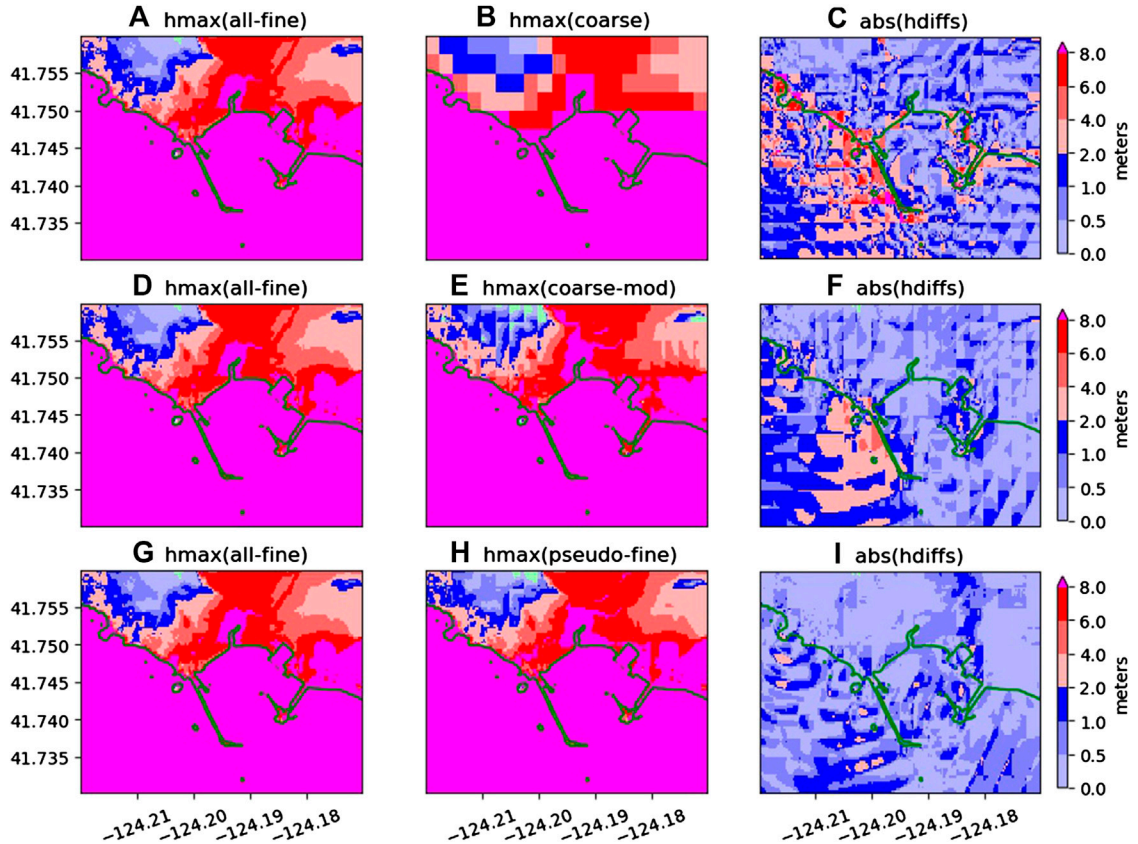

FIGURE 6 | Sample results for realization 1,665 at Crescent City, where the tsunami was large. Panels as described in **Figure 5**. Purple is above 8 m. and Green is land not inundated.

case), which is inadequate to represent the community of interest. For example, the top row of **Figures 5-8** shows $h_{\max}$ in each study region for two particular realizations, and the difference in resolution is apparent between the fine-grid simulation ($h^f_{\max}$ in Panel **A** of each figure) and the corresponding coarse-grid simulation ($h^c_{\max}$ in Panel **B**). Panel **C** of each figure shows the difference between the fine and coarse results, after the coarse-grid results are interpolated to the fine grid as a piecewise constant function over each coarse grid cell.

The coarse-mod corrections are based on the observation that the maximum water surface $\eta_{\max} = B + h_{\max}$ (where B is the pre-seismic topography) is often much more smoothly varying over a community than is the maximum water depth $h_{\max}$ (Note that even a constant $\eta_{\max}$ throughout the study region would still have large variations in $h_{\max} = \eta_{\max} - B$ due to the variations in topography B.). Hence at any point, if we assume $\eta_{\max}$ is roughly correct, we can get a better estimate of $h_{\max}$ by subtracting off the fine-grid topography at this point from the $\eta^c_{\max}$ value predicted by the coarse-grid simulation. As usual, we focus on values at a single grid point on the fine grid. Let B^f represent topography from the fine-grid simulation at this point and B^c the topography value from the coarse-grid simulation in the coarse cell containing this point. Then $\eta^c_{\max} = B^c + h^c_{\max}$. The correction we make defines a modified value $h^{cm}_{\max}$ at this point as

$$h^{cm}_{\max} = \eta^c_{\max} - B^f = B^c + h^c_{\max} - B^f = h^c_{\max} - \Delta B \tag{7}$$

where

$$\Delta B = B^f - B^c. \tag{8}$$

In other words, we simply adjust $h^c_{\max}$ at each fine grid point by ΔB, the difference between the fine and coarse topography at this point. This represents the most common situation where water reaches both the coarse and fine bathymetry levels and is given in the first two lines in **Eq. 9**.

However, there are a few special cases where we can not use (**7**). Clearly, if $\Delta B > h^c_{\max} > 0$, we can not allow $h^{cm}_{\max}$ to become negative (the water reaches the coarse bathymetry level but not the fine level), so $h^{cm}_{\max}$ is set to 0 in the third line in **Eq. 9**.

The last three lines in **Eq. 9** refer to the special case when water does not reach the coarse bathymetry level ($h^c_{\max} = 0$). In this case, water may or may not reach the fine bathymetry level. To determine if it does, we define an η threshold value, called η_T and now use η^c to denote the $\eta_{\max}$ value at a point of interest on the coarse grid. Over the four neighboring grid cells around the coarse cell containing the location of interest, we find η_T, the

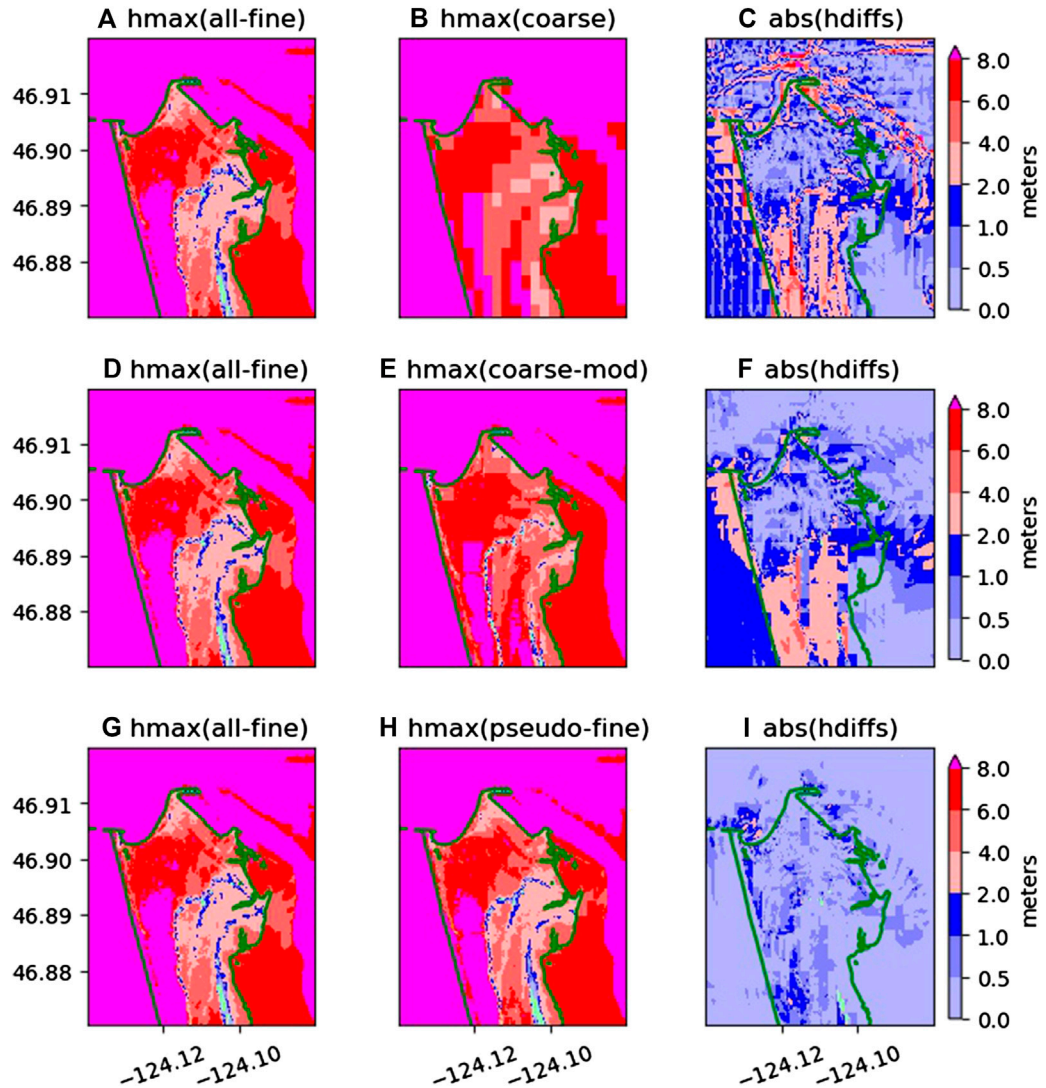

FIGURE 7 | Sample results for realization 1,999 at Westport, where the tsunami was large. Panels as described in **Figure 5**. Purple is above 8 m and Green is land not inundated.

maximum η^c value where $h^c_{\max} > 0$; that is, the threshold where we have seen flooding locally. Lines four and five in **Eq. 9** give $h^{cm}_{\max}$ when water can reach the fine bathymetry but not the coarse bathymetry level. In line four, the threshold is at least the fine bathymetry, but doesn't exceed the coarse bathymetry, so only $\eta_T - B^f$ meters of water can be placed above the fine bathymetry. In line five, the threshold η_T computed from including the four neighboring coarse cells is at least the coarse bathymetry level, but we do not allow $h^{cm}_{\max}$ to exceed the value of $B^c - B^f$ since no water appeared above B^c in the cell of interest. Lastly, the sixth line in **Eq. 9** gives the situation where water does not reach either the fine or coarse bathymetry levels since η_T did not exceed B^f. In all cases, $h^{cm}_{\max}$ will remain as $h^c_{\max}$ at locations where the fine and coarse bathymetries were equal ($\Delta B = 0$).

Based on the above discussion the modified coarse grid value is given by:

$$h^{cm}_{\max} = \begin{cases} h^c_{\max} - \Delta B & \text{if } 0 \le \Delta B < h^c_{\max} \\ h^c_{\max} - \Delta B & \text{if } \Delta B < 0 < h^c_{\max} \\ 0 & \text{if } 0 < h^c_{\max} \le \Delta B \\ \eta_T - B^f & \text{if } h^c_{max} = 0 \text{ and } B^f \le \eta_T \le B^c \\ B^c - B^f & \text{if } h^c_{\max} = 0 \text{ and } B^f \le B^c \le \eta_T \\ 0 & \text{if } h^c_{\max} = 0 \text{ and } \eta_T \le B^f \le B^c \end{cases} \quad (9)$$

The second row of **Figures 5-8** shows examples of the effect of this. Panel **D** is again the fine grid $h_{\max}$ but now Panel **E** shows the $h_{\max}$ estimated on the fine grid after applying these coarse-mod corrections. Panel **F** shows the resulting errors.

An earlier version of this coarse-mod strategy was used in (Adams et al., 2017), and more examples are given in the Appendix of that report showing how well the modified coarse data can compare to the original coarse data and the fine data. We have since improved this strategy by looking only locally for the

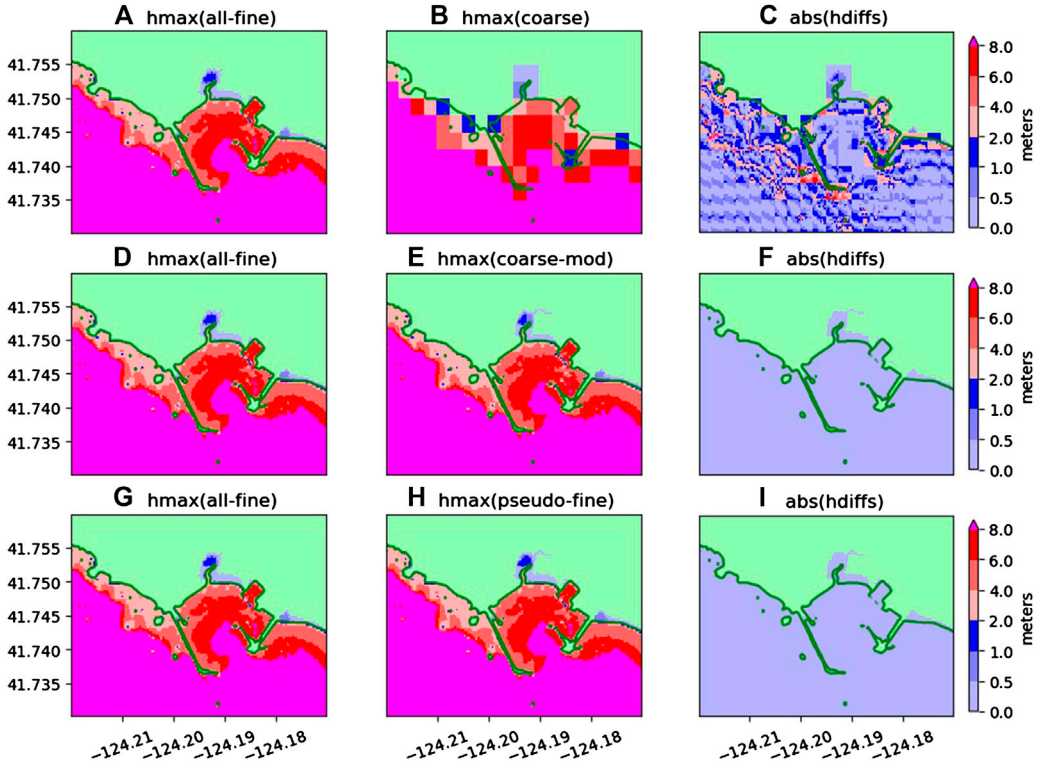

FIGURE 8 | Sample results for realization 1,999 at Crescent City, where the tsunami was small. Panels as described in **Figure 5**. Purple is above 8 m and Green is land not inundated.

threshold value η_T as opposed to across the entire community in the Federal Emergency Management Agency report, and have allowed this value to even be negative, which makes the strategy more applicable to locations near the shoreline that see little inundation during an uplift event. These improvements also result in a more effective pseudo-fine strategy as discussed below.

Pseudo Fine Grid Corrections

We now present an approach to further improve each of the coarse-mod results defined by **(9)** by also using the fine-grid runs performed for each cluster representative. We begin by clustering the N modified coarse grid runs (or the original N coarse grid runs) into a small number of non-overlapping clusters. For this paper, the clustering was done using the original $N = 2,000$ coarse grid runs, to produce $K = 18$ clusters, as described in **Section 5**. These clusters contain different numbers of runs. Each cluster has one run designated as its cluster representative, which we will denote by $\overline{R}_k$ for the particular realization from cluster $k = 1, 2, \ldots, K$.

After the clustering has been done, more information is available that can be used to further improve the coarse-mod approximations. Since we assume that the cluster representative $\overline{R}_k$ is somewhat typical of the pattern of flooding seen for all realizations in the cluster, and since we have both fine-grid and coarse-mod results available for this representative realization, we can use the difference between these as an estimate of what the difference between fine-grid and coarse-mod results would be for all realizations in the cluster. This is used to modify each coarse-mod result to get a better approximation to the expected fine-grid result. This is what we call the pseudo-fine result for each realization. We again use $h^{cm}_{\max}(R_i)$ to denote the $h_{\max}$ value obtained for a particular realization R_i from the coarse-grid simulation after applying the coarse-mod corrections, and similarly $h^{f}_{\max}(R_i)$ comes from the fine-grid simulation, as always focusing on a single spatial location. Then the pseudo-fine approximation at this location for each realization R_i in Cluster k is given by

$$h^{pf}_{\max}(R_i) = h^{cm}_{\max}(R_i) + \left(h^{f}_{\max}(\overline{R}_k) - h^{cm}_{\max}(\overline{R}_k)\right). \qquad (10)$$

Note in particular that the pseduo-fine result for the cluster representative itself (i.e, for $R_i = \overline{R}_k$) agrees exactly with the fine-grid result for that realization. For non-representative cluster members, the pseudo-fine results improve as the clustering improves, since differences between their coarse-mod and fine results become closer to the difference between the cluster representative's coarse-mod and fine results (the last two terms in **Eq. 10**). Increasing the number of clusters would increase the number of cluster representatives while reducing the number of non-representatives per cluster, and could improve the pseudo-fine results at the expense of additional fine grid simulations. We have not investigated these tradeoffs, as the pseudo-fine results reported in the next sections were quite good already for our two chosen communities of interest using a small number of clusters.

We also believe the modified-coarse results provide an excellent start in building the pseudo-fine results because the coarse grid GeoClaw simulations already contain information about the nonlinear flow dynamics on land. This is in contrast to cheaper coarse results that could have been obtained in deep water using the linearlized shallow water equations, such as the thousands used by Li et al. (2016), but this is an approximation we wished to avoid since our focus is the inundation on land.

The third row of **Figures 5-8** show examples of the effect of this. Panel G is again the fine grid $h_{\max}$ but now Panel H shows the $h_{\max}$ estimated on the fine grid after applying these pseudo-fine corrections. Panel I shows the resulting errors relative to the fine-grid result. Additional illustrations of this idea can be found in the Appendix to (Adams et al., 2017).

CLUSTERING

In this section we discuss how one can subdivide the individual events into a small number of clusters that are likely to have similar inundation patterns. The clustering will be based on proxy quantities for each event that can be computed solely from the coarse-grid (low-resolution) simulations, whose runtime is orders of magnitude smaller than the fine-grid (high-resolution) tsunami inundation simulations.

In our previous work (Adams et al., 2017), proxy variables based only on the seafloor deformation of each realization were also considered. These are much cheaper to compute than the coarse-grid simulation proxies, but did not do as good a job of clustering, even though in that work we only considered ruptures on the southern margin of CSZ and only one near-field study region, Crescent City. Given the wider range of events now being considered, where many events are localized far away from a study region, we believe that it may be harder to develop robust proxies based only on the seafloor deformations. However, due to the greater efficiency of that approach, this could be a fruitful area for future research. We also note that Volpe et al. (2019) used seafloor deformation near the study region, both to classify realizations into near-field and far-field, and also in clustering the near-field realizations.

In this work we use three proxy variables computed from the coarse-grid simulations for each realization. Each realization thus corresponds to a point in a three-dimensional space and various clustering methods can then be used to identify clusters. We consider variables that attempt to capture aspects of the spatial variation of the inundation patterns. For each realization, and each coastal location, we compute the value η^c from the coarse-grid tsunami simulation that measures the surface level at maximum inundation, defined by

$$\eta^c = B^c + h^c_{\max}, \tag{11}$$

where B^c represents the pre-event topography on the coarse grid. We consider the spatial variation of η^c over the onshore points that are flooded: the grid-cells in the simulation centered at (x_i, y_j) that satisfy both $B^c(x_i, y_j) \geq 0$ and $h^c_{\max}(x_i, y_j) > 0$. We will denote these values from the coarse-grid simulation by η^c_{ij}. The total number of flooded onshore points will be denoted by N_{flood}.

As the proxy variables, we will use the following statistics of η^c, where the sums are over all onshore flooded points (i, j):

$$\begin{aligned}
\eta^c_{\text{logsum}} &= \log\left(1 + \sum_{ij} \eta^c_{ij}\right), \\
\eta^c_{\text{mean}} &= \frac{1}{N_{\text{flood}}} \sum_{ij} \eta^c_{ij}, \\
\eta^c_{\text{sd}} &= \sqrt{\frac{1}{N_{\text{flood}}} \sum_{ij} \left(\eta^c_{ij} - \eta^c_{\text{mean}}\right)^2}.
\end{aligned} \tag{12}$$

The first variable η^c_{logsum} is a measure of the total extent and elevation of the flooding, while the second variable η^c_{mean} is the mean surface elevation. The third variable η^c_{sd} measures the spatial variation of surface elevation over the onshore flooded region. The first two variables summarize the severity of the flooding while the third variable summarizes the spatial variation of the flooding pattern.

Utilizing these quantities, the coarse-grid inundation from each individual realization can be mapped to a point in the three-dimensional space of proxy variables, which we will call "proxy-space," as shown in **Figure 9**. To perform clustering it is also necessary to define a metric that measures the distance between two points in this space, and here we simply use the Euclidean distance (the square root of the sum of squares of differences in each of the three proxy variables). We then use K-means clustering (Lloyd, 1982), as implemented in scipy. sklearn by Pedregosa et al. (2011) to cluster the 2,000 points in proxy-space into K clusters, with the property that each point belongs to the cluster with the closest centroid (as measured in the specified metric). Note that because η^c_{mean} typically has larger magnitudes than the other two proxy variables (see **Figure 9**), the use of the Euclidean distance effectively weights differences in η^c_{mean} more heavily than differences in the other proxy variables. We also tried first normalizing all proxy variables (equivalent to using a different weighted metric) and somewhat different clusters were generated but with very similar final results in the hazard curves. If using proxy variables with vastly different magnitudes, and/or where some variables are thought to be more important than others, some care should be used in choosing the metric.

This clustering is done independently for the two study regions, and the results are shown in the scatter plots in **Figure 9**. The plot also highlights which realization is closest to the centroid of each cluster, which we refer to as the cluster representative $\overline{R}_k$ for Cluster k. The number of clusters is determined by the user, and in this instance 18 clusters were used to subdivide the 2,000 events of varying magnitude. We also tried clustering with only 6 or 12 clusters but the results did not match the all-fine (ground truth model) as well, while using more than 18 clusters did not seem necessary for this particular data set. Volpe et al. (2019) use an iterative procedure to select the number of clusters by enforcing a maximum distance between cluster members and the centroid and this might be a good approach in general.

From **Figure 9** one observes that there is a general monotonic behavior with respect to all three variables. Higher magnitude

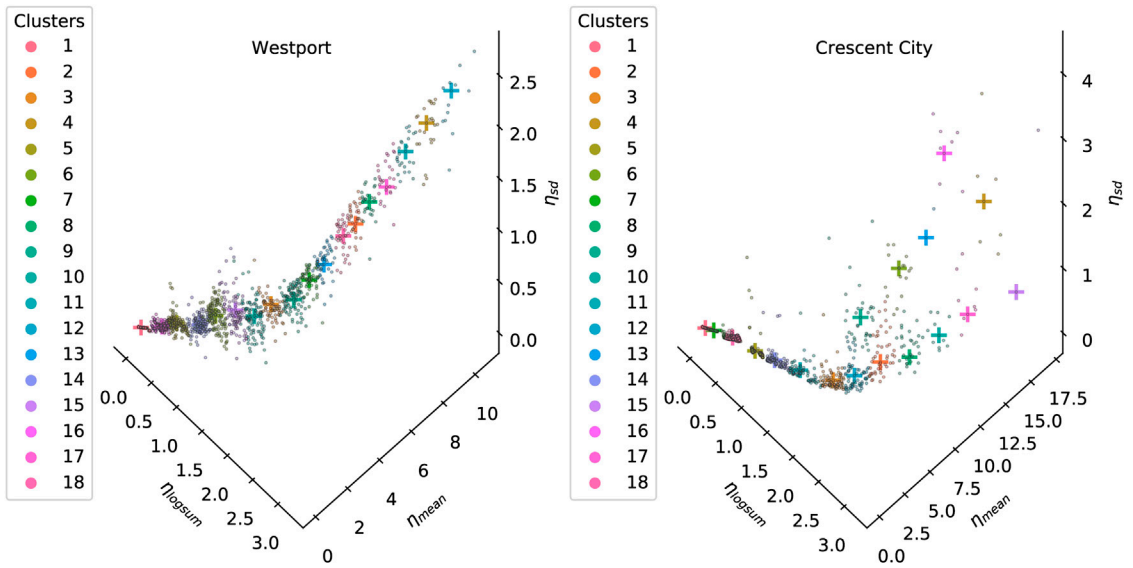

FIGURE 9 | Clustering results for the two study regions. In each case all 2,000 realizations are represented as a point in the three-dimensional proxy-space, and colored by cluster after with 18 clusters in each case. The crosses indicate the cluster representative, i.e., the realization closest to the centroid of each cluster.

events tend to have higher values for all three variables. But also note that the scatter plot for the two coastal communities show qualitatively different patterns. While the points in proxy space for Westport show a more predictable behavior with higher magnitude events more concentrated along a smooth, monotone increasing curve, there is much more variation in the proxy variable η_{sd}^c in Crescent City and consequently more scatter. This can be explained by the difference in topography. In Westport there are ridges in the north-south direction which roughly separates the onshore regions into zones that can flood independently, leading to more variation in η_{sd}^c for most realizations. However, for realizations with the most severe surface elevations, all zones are inundated, leading to smaller variation in η_{sd}^c. In Crescent City, most of the onshore region is facing the south-west direction and is rising more monotonically away from the coast, but there is a sharp gradient in the topography in the west shoreline, acting as a barrier. The variation of inundation along this barrier is significant for extreme realizations, causing more scatter in η_{sd}^c.

HAZARD CURVES AND MAPS

Finally we combine the techniques developed in the previous sections to produce approximate hazard curves with much less work than would be required to perform all N fine-grid simulations. We first summarize our notation and the definition of the hazard curves and these approximations. For other discussions of hazard curves, see, for example, (González et al., 2014; Adams et al., 2015), and also the review paper (Grezio and Babeyko, 2017). and associated Jupyter notebooks that illustrate these concepts interactively.

We assume that we have split all possible events into J classes indexed by $j = 1, 2, \ldots, J$ (in our case $J = 4$ and the classes are for Mw 7.5, 8.0, 8.5, and 9.0). We assume each class has an associated annual probability P_j. We also make the reasonable assumption that these probabilities are sufficiently small that the probability of two events happening in a year is negligible. More specifically, we assume that the annual probability of at least one earthquake (from the classes considered) is well approximated by the sum of the P_j. In fact if the different classes represent potentially independent events, then the probability of at least one of them occurring is given by

$$\begin{aligned} P_{\text{total}} &= 1 - \prod_{j=1}^{J} \left(1 - P_j\right) \\ &= \sum_{j=1}^{J} P_j - \sum_{i \neq j} P_i P_j + \text{higher order terms} \\ &\approx \sum_{j=1}^{J} P_j. \end{aligned} \tag{13}$$

As long as the probabilities are small, the final line of (13) is a good approximation to the true value. For the probabilities listed in **Table 1**, $P_{\text{total}} = 0.08527$ when calculated using the product formula in the first line of **(13)**, and is well approximated by the slightly larger value obtained using the sum $\sum P_j = 0.08704$.

We next chose N_j realizations from each class j, for a total of $N = \sum_j N_j$ realizations. We use R_i as shorthand for "Realization i", for $i = 1, 2, \ldots, N$ (enumerating all realizations from all of the classes). For each R_i we assign an associated *weight* w_i defined as $w_i = P_j/N_j$ if R_i is of class j.

Now consider a fixed location in the study region where we have computed $h_{\max}$, the maximum tsunami inundation depth, for each realization. The value computed on the fine grid for

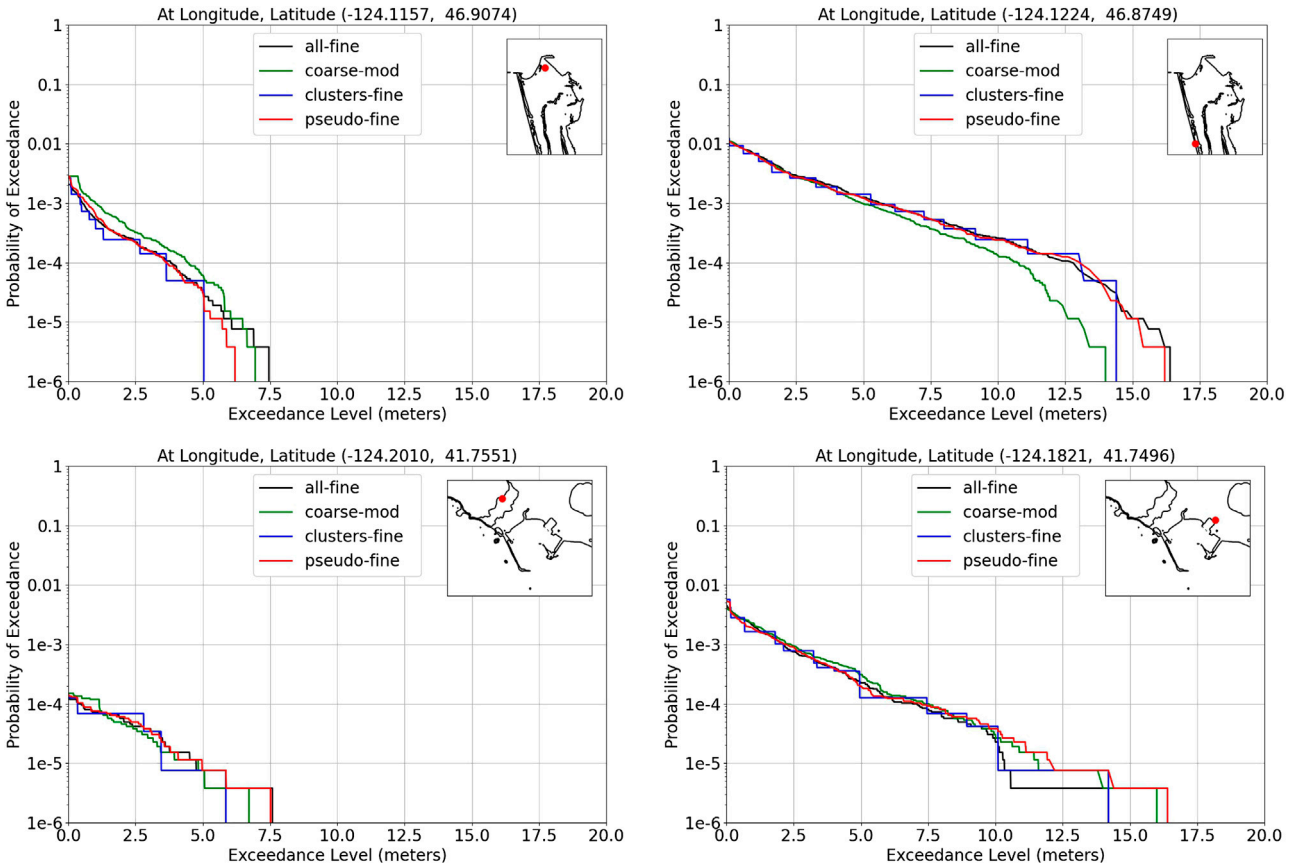

FIGURE 10 | Sample hazard curves at two locations in Westport **(top)** and two locations in Crescent City **(bottom)**, in each case indicated by the dots in the inset maps. The curves show the reference all-fine result $p^f(\widehat{h})$ and three approximate hazard curves $p^{cm}(\widehat{h})$, $p^{cf}(\widehat{h})$, and $p^{pf}(\widehat{h})$ as defined in **Section 6**.

realization R_i will be denoted by $h^f_{\max}(R_i)$. If we perform fine-grid simulations for all realizations, then we can define the ground truth model hazard curve (at this location) as follows. For any exceedance value $\widehat{h} \geq 0$ we might choose, let $\{i : h^f_{\max}(R_i) > \widehat{h}\}$ denote the indices of the set of realizations for which $h_{\max}$ computed on the fine grid exceeds this value. Then we define

$$P\left[h_{\max} > \widehat{h}\right] = p^f\left(\widehat{h}\right) \equiv \sum w_i \quad \text{summed over } \left\{i : h^f_{\max}(R_i) > \widehat{h}\right\}. \tag{14}$$

Plotting $p^f(\widehat{h})$ vs. $\widehat{h}$ gives the hazard curves, as shown, for example, in **Figure 10**. From the hazard curve at each point on a grid covering the study region, it is possible to extract the data needed to produce a hazard map; see **Section 7.2**.

Note that summing the weights w_i over all R_i for which $\widehat{h}$ is exceeded, as done in **(14)**, is equivalent to computing $\sum_{j=1}^{J}(\widehat{N}_j/N_j)P_j$, where $\widehat{N}_j$ is the number of realizations from Class j for which $h^f_{\max}(R_i) > \widehat{h}$ (Since each $w_i = P_j/N_j$ for some j and we add in one such contribution for each realization that exceeded $\widehat{h}$.). We refer to the w_i as weights rather than probabilities because we do not mean to imply that every realization in a class has the same probability of occurring, even though they each have the same weight. Some of the realizations may be outliers that are very unlikely to occur, while most of them will come from closer to the center of the distribution. But because we assume that we sampled the distribution within each class properly, the fraction $\widehat{N}_j/N_j$ is the proper frequency to modify the probability P_j, and our choice of weights accomplishes this *via* the definition **(14)**.

In **Section 5** we discussed an approach to clustering the R_i into clusters indexed by $k = 1, 2, \ldots, K$, for some number of clusters K that is much smaller than N. For each cluster we identified one realization $\overline{R}_k$ from the cluster that we will call the "cluster representative," with the hope that a single fine-grid simulation of the tsunami resulting from $\overline{R}_k$ will give a good indication of the flooding expected for all realizations in the cluster.

One simple strategy for approximating the hazard curve is then to assign a weight $\overline{w}_k$ to Cluster k, defined by

$$\overline{w}_k = \sum w_i \quad \text{summed over } \{i : R_i \text{ is in cluster } k\}, \tag{15}$$

and then approximate $P[h_{\max} > \widehat{h}]$ by a function we will denote $p^{cf}(\widehat{h})$ with the superscript standing for "cluster-fine":

$$p^{cf}(\widehat{h}) = \sum \overline{w}_k \quad \text{summed over } \{k : h^f_{\max}(\overline{R}_k) > \widehat{h}\}. \tag{16}$$

In other words, we assume that if the tsunami from the cluster representative $\overline{R}_k$ gives an $h_{\max}$ exceeding $\widehat{h}$ then all realizations in the cluster will, and we add in the cluster weight $\overline{w}_k$ in this case, which is just the sum of the weights w_i for all realizations in the cluster.

Another approximation, which requires no clustering, would be to approximate $P[h_{\max} > \widehat{h}]$ by

$$p^{c}(\widehat{h}) = \sum w_i \quad \text{summed over } \{i : h^c_{\max}(R_i) > \widehat{h}\} \tag{17}$$

where $h^c_{\max}(R_i)$ is the $h_{\max}$ value obtained with a coarse grid simulation of realization R_i. This uses information from all N realizations, but is presumably not a good approximation because, by definition, the coarse grid is not sufficiently fine to resolve the study region adequately.

Much better results can be obtained by using all of the coarse-grid results after enhancing them using the techniques presented in **Section 4**. Using only the coarse-mod corrections to each coarse-grid result would lead to the approximation

$$p^{cm}(\widehat{h}) = \sum w_i \quad \text{summed over } \{i : h^{cm}_{\max}(R_i) > \widehat{h}\} \tag{18}$$

while also using the clustering to produce the pseudo-fine corrections gives

$$p^{pf}(\widehat{h}) = \sum w_i \quad \text{summed over } \{i : h^{pf}_{\max}(R_i) > \widehat{h}\}. \tag{19}$$

In general using **Eq. 19** as an approximation to the all-fine grid (ground truth model) hazard curve defined by $p^f(\widehat{h})$ has been found to give very good results with much less work. Only K fine-grid simulations need to be performed, but the results are based on all N realizations, with pseudo-fine approximations that are often nearly as good as the all-fine grid results when incorporated into PTHA. Hazard curves, hazard plan view and transect maps, and a table of differences for comparing these models to the all-fine grid ground truth model are given in **Section 7** below.

PROBABILISTIC TSUNAMI HAZARD ASSESSMENT RESULTS

We now explore the results of performing PTHA using the clustering strategies developed in **Section 5**, either alone or in conjunction with additional coarse-mod or pseudo-fine results as developed in **Section 4**.

Recall that we have sampled $N = 2,000$ realizations of a CSZ event using the techniques described in **Section 2**, and for the purposes of this paper we assume that the hazard curves (and resulting maps) that are generated from a fine-grid tsunami simulation of each of these events is the correct reference solution, which we are trying to approximate more cheaply using the clustering and pseudo-fine grid techniques. To assess the accuracy of our approximations, we performed fine-grid simulations of all realizations in order to compute $p^f(\widehat{h})$, although in practice this is what we wish to avoid.

Hazard Curves

Recall from **Section 6** that a hazard curve is defined at each point in the study region where $h_{\max}$ values have been calculated over the entire simulation. **Figure 10** shows sample hazard curves at two locations in Westport, and two in Crescent City. At each location the figure shows the reference curve $p^f(\widehat{h})$ and three of the approximations discussed above, the clusters-fine, coarse-mod, and pseudo-fine strategies. The particular spatial points were chosen to illustrate typical hazard curves. Additional hazard curves can be found on the website Williamson et al. (2020).

Note that the all-fine, coarse-mod, and pseudo-fine hazard curves obtained using 2,000 realizations typically have 2,000 jump discontinuities, one at the location of $h_{\max}$ for each realization. The magnitude of the jump in probability at each discontinuity is equal to the weight w_i assigned to that realization. This is because this $h_{\max}$ value contributes w_i to the estimated annual probability for any smaller exceedance value, but not for any larger exceedance value. Also note that the smallest nonzero probability that can occur on any hazard curve is the weight we assign to M_w9 events, $w_4 = P_4/500 = 3.8 \times 10^{-6}$ where P_4 is from **Table 1**.

The hazard curve $p^{cf}(\widehat{h})$ for the cluster-fine strategy is computed using only the fine-grid results $h^f_{\max}(\overline{R}_k)$ for the 18 cluster representatives. As a result, it has only 18 jump discontinuities and the jump in annual probability at each discontinuity is the cluster weight $\overline{w}_k$. This generally gives a reasonable approximation to the true hazard curve within the constraint of a piecewise constant function with so few jumps. It may not agree well for the most extreme events (smallest probabilities) since it assigns 0 annual probability to any exceedance value $\widehat{h}$ greater than the maximum of $h^f_{\max}(\overline{R}_k)$ over the $k = 1, 2, \ldots, 18$, whereas the true hazard curve goes to 0 only above $\widehat{h} = \max_i h^f_{\max}(R_i)$ maximized over all 2,000 realizations. If the realization that maximizes this happens to be a cluster representative then the two hazard curves indicate the same maximum possible flooding, but in general this will not be the case. Similarly, for other very small values of p that correspond to inundation by only a few of the 2,000 realizations, the probability can not be properly represented when only using the 18 cluster representatives.

Using the coarse-mod enhancement of each coarse-grid result gives the hazard curve $p^{cm}(\widehat{h})$. Even though all N simulations are now used, this correction is not sufficient to give good results in general, and this hazard curve generally deviates significantly from the correct hazard curve $p^f(\widehat{h})$. However, using the pseudo-fine version of all N coarse-grid simulations gives much better results, as seen in **Figure 10** and also generally seen at other locations.

In evaluating the results shown in **Figure 10**, it is important to remember that we cannot expect very good agreement at the smallest annual probabilities, where the results depend entirely on the most extreme tsunamis out of the 2,000 selected. Of most interest in this study is the portion of the hazard curve above say $p = 10^{-4}$, which corresponds to a return time of $T = 10,000$ years. Developing an accurate hazard curve for lower probabilities would require more than 2,000 realizations, even considering only the aleatoric

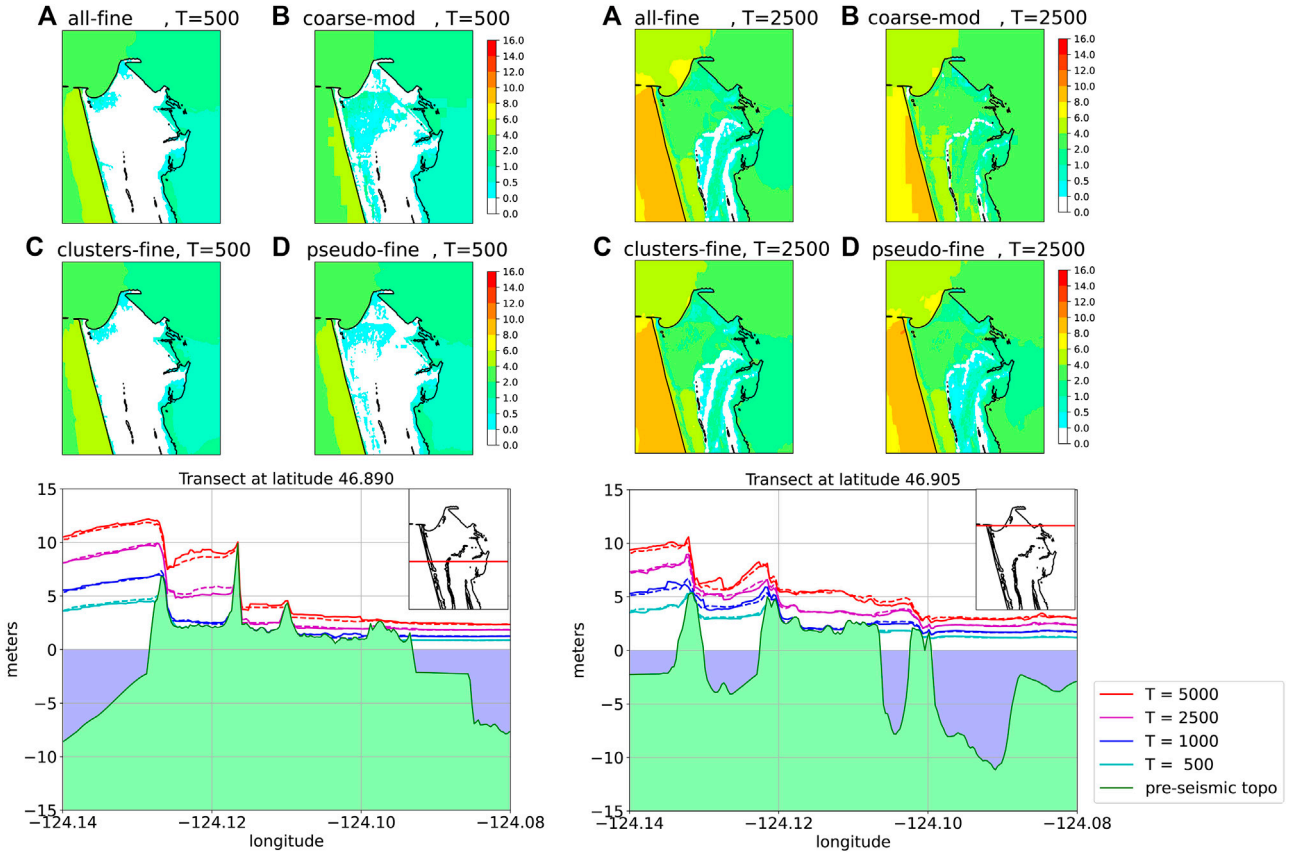

FIGURE 11 | Sample hazard maps and transects for select locations in Westport. The top panels show plan view plots for return times $T = 500$ years **(left)** and 2,500 years **(right)**, over the same spatial domain as shown in **Figure 3**. In each case panel **(A)** shows the reference all-fine hazard maps produced with the all-fine hazard curves $p^f(\widehat{h})$, **(B)** shows the map produced with the coarse-mod hazard curves $p^{cm}(\widehat{h})$, **(C)** shows the map produced with the clusters-fine hazard curves $p^{cf}(\widehat{h})$, **(D)** shows the map produced with the pseudo-fine hazard curves $p^{pf}(\widehat{h})$. The bottom figures show transects of the hazard maps for four different choices of annual probabilities p, corresponding to different return times $T = 1/p$ as indicated in the legend. In each case the dashed line is the all-fine reference solution, while the solid line is the approximation generated using 18 clusters and the pseudo-fine improvements of the other coarse-grid runs.

uncertainty. Moreover, the epistemic lack of knowledge of the proper probability distribution would also be a limiting factor.

Hazard Maps and Transects

The hazard curves $p^f(\widehat{h})$ at every point on the $h_{\max}$ grid can be combined to produce hazard maps, as follows. For a fixed annual probability $\widehat{p}$ we determine from each hazard curve the corresponding value of $\widehat{h}$ such that $p^f(\widehat{h}) = \widehat{p}$. After doing this at every grid point in the study region we can produce plan view plots of the expected inundation depth $\widehat{h}$ for this $\widehat{p}$. **Figures 11, 12** show such plots for two different probabilities, $p = 0.002$ (return time $T = 500$ years) and $p = 0.0004$ (return time $T = 2,500$ years). In each case we show the results for four of the strategies listed above. Again the all-fine strategy gives the reference result, and we compare this to the cluster-fine, coarse-mod, and pseudo-fine strategies. In general the pseudo-fine strategy gives the best approximation to the all-fine results.

Note that in these maps we show offshore points as well as onshore points, since $h_{\max}$ for both the fine-grid and coarse-grid simulations were obtained by monitoring the maximum water depth on rectangular grids also covering some offshore points. At these points $h_{\max}$ is always at least as great as the original pre-seismic water depth, so at these points we do not plot $h_{\max}$ itself but rather the quantity we call zeta, defined by $\zeta_{\max} = h_{\max} + B$, where B is the pre-seismic topography at the point. More generally we define

$$\zeta_{\max} = \begin{cases} h_{\max} & \text{if } B > 0, \\ h_{\max} + B & \text{if } B \le 0. \end{cases} \tag{20}$$

Then $\zeta_{\max}$ agrees with $h_{\max}$ onshore, is continuous at the shoreline, and offshore it indicates the maximum tsunami elevation relative to sealevel (We always use the pre-seismic topography in defining this, since each realization can have a different amount of uplift or subsidence.).

It is hard to quantitatively compare these hazard maps, and impossible to present results for more than one probability $\widehat{p}$ on the same map of this type. So in **Figures 11**, **12** we also show two selected transects in each study region (each at some fixed latitude). We then plot a cross section of the hazard map along this transect for four different values of $T = 1/p$ as

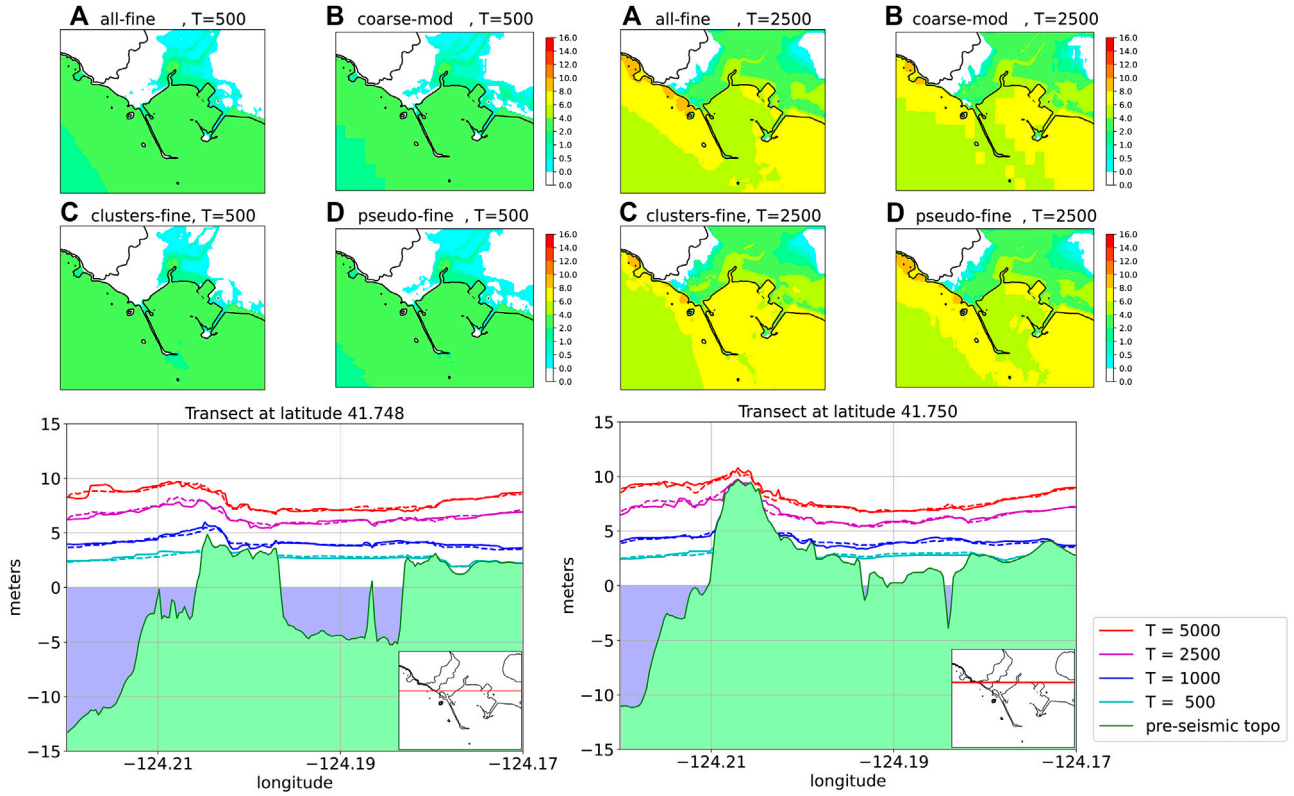

FIGURE 12 | Sample hazard maps and transects for Crescent City. As described in the caption to **Figure 11**.

TABLE 2 | The magnitude of ζ_{max} and differences between ζ_{max} as computed using the coarse-mod, clusters-fine, and all-pseudo strategies, compared to the reference all-fine strategy at both Westport and Crescent City (CC), for return times T = 2,500 and 500 years (p = 0.0004 and 0.002).

T	2,500 years				500 years			
	Max (Δ)	Max (ζ)	Mean (Δ)	Mean (ζ)	Max (Δ)	Max (ζ)	Mean (Δ)	Mean (ζ)
Westport								
All-fine	0.00	10.1	0.00	3.75	0.00	5.06	0.00	2.01
Coarse-mod	5.86	8.93	0.67	3.74	3.03	4.70	0.22	1.70
Clusters-fine	1.72	9.64	0.28	3.52	0.95	4.81	0.10	2.03
All-pseudo	1.19	10.1	0.13	3.62	0.75	4.87	0.07	1.88
CC								
All-fine	0.00	9.62	0.00	5.23	0.00	3.87	0.00	2.19
Coarse-mod	2.54	8.86	0.32	5.21	1.58	3.35	0.45	2.10
Clusters-fine	2.78	10.5	0.47	5.34	1.10	3.68	0.22	2.30
All-pseudo	1.61	9.87	0.14	5.18	0.64	3.88	0.11	2.14

All values are in meters. The columns labeled max (Δ) and mean (Δ) are the maximum and mean of the difference over all grid points (i,j), e.g., for the coarse-mod row, $\Delta = |\zeta^{cm}_{max} - \zeta^{f}_{max}|$. For comparison, the corresponding maximum and mean values of ζ_{max} across the community are also listed for each strategy, in the columns labeled max (ζ) and mean (ζ). Recall that ζ represents the maximum flooding depth on land, or the flooding depth added to the pre-seismic bathymetry for points offshore.

indicated in the legend. As T increases the expected flood level naturally increases. In these plots we also compare two strategies, the reference all-fine result as a dashed line and the pseudo-fine strategy as the solid line. These plots clearly show that the pseudo-fine strategy does a remarkably good job of estimating the all-fine (ground truth model) inundation for all four return times, at least along these particular transects. These are fairly typical of the results seen at other locations in the study regions, and additional plots are available on the webpage Williamson et al. (2020).

Finally, in **Table 2**, we give the maximum and mean differences between ζ_{max} over each study region for two different return times, for each of the three strategies illustrated above. Note that in each case, the pseudo-fine strategy has mean errors less than 15 cm, even though the mean value of ζ_{max} varied from 1.88 to 5.18 m in the four

cases shown ($T = 2,500$ and 500 years, at the two study regions). This indicates that our approach is capable of giving very small relative errors compared to the all-fine (ground truth model) in the maximum flooding depth of the tsunami, even for the longer return time shown.

CONCLUSIONS

We have presented a general approach to performing PTHA when given a) a set of classes of possible events with an annual probability or return time for each class, and b) a probability density within each class that can be sampled to obtain a sufficiently large number of sample realizations that hazard curves can be accurately approximated by performing fine grid tsunami simulations for each realization. The problem we considered is that the number of realizations needed may be too large to perform fine grid simulations of each, particularly if many coastal locations are of interest, and so the goal is to obtain good approximations to the hazard curves that would be generated by all the fine-grid simulations with much less work, employing only coarse-grid simulations, clustering, and correction procedures.

We considered a model problem where 2,000 fine-grid inundation simulations were performed in order to obtain a reference hazard curve to test our methodology, which we again summarize. We first performed coarse-grid inundation simulations for each realization, using a set of four magnitude classes and a K-L expansion to define the probability density within each class for illustrative purposes. We then clustered them into only 18 clusters and performed one fine-grid simulation for a single representative from each cluster. We also used these 18 simulations, with very little additional work, to enhance the remaining coarse-grid results. The resulting 2,000 pseudo-fine results were then used to produce approximate hazard curves that are much more accurate than those obtained using the cluster representatives alone.

Although we chose geophysically reasonable parameters, we do not claim that the results of our fine-grid hazard curves are correct, only that they are reasonable reference solutions against which to compare cheaper strategies. We have also ignored other magnitude events on the CSZ, other fault mechanisms such as splay faults, along with distant earthquakes and other tsunami sources, so the results in this paper should not be interpreted as providing realistic estimates of hazards in either Crescent City or Westport. Certainly any realistic PTHA meant to inform decision-making should also include sensitivity studies, particularly in light of the large epistemic uncertainty in the parameters that go into the probability densities (whether generated by K-L expansion or by any other technique). The techniques of this paper can be useful for such sensitivity studies since they can accelerate the PTHA for any set of realizations and thus allow testing more sets of realizations in order to investigate the resulting variation in hazard curves. Sets of realizations might be generated with different density parameters, or be of different sizes. Different random sets of realizations of the same size can also help to better explore the aleatoric uncertainty.

More work is needed to better understand and optimize the clustering method used in this paper. In particular there is a need to better quantify the number of clusters that should be used, and the best set of proxy variables to use in performing the clustering.

However, we note that we were generally able to achieve nearly the same hazard curves with our pseudo-fine results as when using all the fine-grid results, down to an annual probability of $p = 10^{-4}$ or less for each of our test communities. We therefore believe these techniques can be a useful component in a full probabilistic study of these sites, and many others. We also note that they can be applied to any other choice of classes and probability densities, and adapted to work with any tsunami modeling software.

DATA AVAILABILITY STATEMENT

The datasets presented in this study can be found in online repositories. The names of the repository/repositories and accession number(s) can be found below: http://depts.washington.edu/ptha/frontiers2020a/.

AUTHOR CONTRIBUTIONS

All authors contributed to the initial development and project goals of this study. AW and DM developed the earthquake realizations and performed the tsunami simulations. FG, RL, and DR developed the clustering methodology, and LA developed the coarse-mod and pseudo-fine techniques. All authors contributed to writing the text and producing the figures presented.

FUNDING

This research was supported in part by FEMA Region IX, Grant EMW-2014-CA-00218, and by NASA DISASTERS grant 80NSSC19K1104, AFOSR CoE FA9550-17-1–0195, AFOSR MURI FA9550-15-1-0038, NSF Hazard SEES grant EAR-1331412, and NSF CoPe-EAGER ICER-1940024.

REFERENCES

Adams, L. M., LeVeque, R. J., and González, F. I. (2015). The Pattern Method for incorporating tidal uncertainty into probabilistic tsunami hazard assessment (PTHA). *Nat. Hazards.* 76, 19–39. doi:10.1007/s11069-014-1482-z

Adams, L. M., LeVeque, R. J., Rim, D., and Gonzalez, F. I. (2017). Probabilistic source selection for the Cascadia Subduction Zone. Results from a study supported by FEMA region IX. Available at: http://depts.washington.edu/ptha/FEMA (Accessed March, 2017).

Amante, C., and Eakins, B. W. (2009). "ETOPO1 1 Arc-minute global relief model: procedures, data sources and analysis," in NOAA Technical Memorandum NESDIS NGDC-24. Boulder, CO. March 2009. Available

at: http://www.ngdc.noaa.gov/mgg/global/global.html (Accessed March, 2009).

Blaser, L., Krüger, F., Ohrnberger, M., and Scherbaum, F. (2010). Scaling relations of earthquake source parameter estimates with special focus on subduction environment. *Bull. Seismol. Soc. Am.* 100, 2914–2926. doi:10.1785/0120100111

Clawpack Development Team (2020). Data from: Clawpack software. Version 5.7.0. doi:10.5281/zenodo.3764278

Comninou, M., and Dundurs, J. (1975). The angular dislocation in a half space. *J. Elasticity.* 5, 203–216. doi:10.1007/bf00126985

Crempien, J. G., Urrutia, A., Benavente, R., and Cienfuegos, R. (2020). Effects of earthquake spatial slip correlation on variability of tsunami potential energy and intensities. *Sci. Rep.* 10, 1–10. doi:10.1038/s41598-020-65412-3

Davies, G. (2019). Tsunami variability from uncalibrated stochastic earthquake models: tests against deep ocean observations 2006–2016. *Geophys. J. Int.* 218, 1939–1960. doi:10.1093/gji/ggz260

Davies, G., and Griffin, J. (2020). Sensitivity of probabilistic tsunami hazard assessment to far-field earthquake slip complexity and rigidity depth-dependence: case study of Australia. *Pure Appl. Geophys.* 177, 1521–1548. doi:10.1007/s00024-019-02299-w

de Baar, J., and Roberts, S. (2017). Multifidelity sparse-grid-based uncertainity quantification for the Hokkaido Nansei-oki tsunami. *Pure Appl. Geophys.* 174, 3107–3121. doi:10.1007/s00024-017-1606-y

Frankel, A., Chen, R., Petersen, M., Moschetti, M., and Sherrod, B. (2015). 2014 update of the Pacific Northwest portion of the U.S. National seismic hazard maps. *Earthq. Spectra.* 31, S131–S148. doi:10.1193/111314eqs193m

Geist, E., and Lynett, P. (2014). Source processes for the probabilistic assessment of tsunami hazards. *Oceanography.* 27, 86–93. doi:10.5670/oceanog.2014.43

Geist, E. L., and Parsons, T. (2006). Probabilistic analysis of tsunami hazards. *Nat. Hazards.* 37, 277–314. doi:10.1007/s11069-005-4646-z

Geuzaine, C., and Remacle, J.-F. (2009). Gmsh: a 3-D finite element mesh generator with built-in pre- and post-processing facilities. *Int. J. Numer. Methods Eng.* 79, 1309–1331. doi:10.1002/nme.2579

Giles, M. B. (2015). Multilevel Monte Carlo methods. *Acta Numer.* 24, 259–328. doi:10.1017/S096249291500001X

Goda, K., Yasuda, T., Mori, N., and Maruyama, T. (2016). New scaling relationships of earthquake source parameters for stochastic tsunami simulation. *Coast Eng. J.* 58, 1650010–1650011. doi:10.1142/s0578563416500108

Goldberg, D. E., and Melgar, D. (2020). Generation and validation of broadband synthetic P waves in semistochastic models of large earthquakes. *Bull. Seismol. Soc. Am.* 110, 1982–1995. doi:10.1785/0120200049

Goldfinger, C., Nelson, C. H., Morey, A. E., Johnson, J. E., Patton, J. R., Karabanov, E. B., et al. (2012). Turbidite event history—methods and implications for Holocene paleoseismicity of the Cascadia subduction zone. *Tech. rep., US Geological Survey*, 170 pp. doi:10.3133/pp1661f

González, F., LeVeque, R., Adams, L., Goldfinger, C., Priest, G., and Wang, K. (2014). *Probabilistic tsunami hazard assessment (PTHA) for Crescent City, CA final report September 11, 2014.* Seattle, WA: University of Washington ResearchWorks Archive. Available at: http://hdl.handle.net/1773/25916 (Accessed September 11, 2014).

González, F. I., LeVeque, R. J., and Adams, L. M. (2013). *Tsunami hazard assessment of the Ocosta School site in Westport, WA.* Seattle, WA: University of Washington ResearchWorks Archive. . Available at: http://hdl.handle.net/1773/24054 (Accessed September 11, 2013).

González, J., González, G., Aránguiz, R., Melgar, D., Zamora, N., Shrivastava, M. N., et al. (2020). A hybrid deterministic and stochastic approach for tsunami hazard assessment in Iquique, Chile. *Nat. Hazards.* 100, 231–254. doi:10.1007/s11069-019-03809-8

Grezio, A., Babeyko, A., Baptista, M. A., Behrens, J., Costa, A., Davies, G., et al. (2017). Probabilistic tsunami hazard analysis: multiple sources and global applications. *Rev. Geophys.* 55, 1158–1198. doi:10.1002/2017rg000579

Gusman, A. R., Tanioka, Y., Macinnes, B. T., and Tsushima, H. (2014). A methodology for near-field tsunami inundation forecasting: application to the 2011 Tohoku tsunami. *J. Geophys. Res. Solid Earth.* 119, 8186–8206. doi:10.1002/2014JB010958

Horrillo, J., Knight, W., and Kowalik, Z. (2008). Kuril islands tsunami of November 2006: 2. Impact at Crescent City by local enhancement. *J. Geophys. Res. Oceans.* 113, C01021. doi:10.1029/2007jc004404

LeVeque, R. J., Waagan, K., Gonzalez, F. I., Rim, D., and Lin, G. (2016). Generating random earthquake events for probabilistic tsunami hazard assessment. *Pure Appl. Geophys.* 173, 3671–3692. doi:10.1007/s00024-016-1357-1

Li, L., Switzer, A. D., Chan, C.-H., Wang, Y., Weiss, R., and Qiu, Q. (2016). How heterogeneous coseismic slip affects regional probabilistic tsunami hazard assessment: a case study in the south China Sea. *J. Geophys. Res. Solid Earth.* 121, 6250–6272. doi:10.1002/2016jb013111

Lloyd, S. (1982). Least squares quantization in PCM. *IEEE Trans. Inf. Theor.* 28, 129–137. doi:10.1109/tit.1982.1056489

Lorito, S., Selva, J., Basili, R., Romano, F., Tiberti, M. M., and Piatanesi, A. (2015). Probabilistic hazard for seismically induced tsunamis: accuracy and feasibility of inundation maps. *Geophys. J. Int.* 200, 574–588. doi:10.1093/gji/ggu408

Mai, P. M., and Beroza, G. C. (2000). Source scaling properties from finite-fault-rupture models. *Bull. Seismol. Soc. Am.* 90, 604–615. doi:10.1785/0119990126

Mai, P. M., and Beroza, G. C. (2002). A spatial random field model to characterize complexity in earthquake slip. *J. Geophys. Res.* 107, 10–11. doi:10.1029/2001jb000588

McCaffrey, R., Qamar, A. I., King, R. W., Wells, R., Khazaradze, G., Williams, C. A., et al. (2007). Fault locking, block rotation and crustal deformation in the Pacific Northwest. *Geophys. J. Int.* 169, 1315–1340. doi:10.1111/j.1365-246x.2007.03371.x

McCrory, P. A., Blair, J. L., Waldhauser, F., and Oppenheimer, D. H. (2012). Juan de Fuca slab geometry and its relation to Wadati-Benioff zone seismicity. *J. Geophys. Res.* 117, B09306. doi:10.1029/2012jb009407

Melgar, D., and Hayes, G. P. (2019). The correlation lengths and hypocentral positions of great earthquakes. *Bull. Seismol. Soc. Am.* 109, 2582–2593. doi:10.1785/0120190164

Melgar, D., LeVeque, R. J., Dreger, D. S., and Allen, R. M. (2016). Kinematic rupture scenarios and synthetic displacement data: an example application to the Cascadia Subduction Zone. *J. Geophys. Res. Solid Earth.* 121, 6658–6674. doi:10.1002/2016jb013314

Melgar, D., Williamson, A. L., and Salazar-Monroy, E. F. (2019). Differences between heterogenous and homogenous slip in regional tsunami hazards modelling. *Geophys. J. Int.* 219, 553–562. doi:10.1093/gji/ggz299

NOAA NCEI (2012). Crescent city, California 1/3 Arc-second MHW coastal digital elevation model. Available at: https://www.ngdc.noaa.gov/metaview/page?xml=NOAA/NESDIS/NGDC/MGG/DEM/iso/xml/693.xml&view=getDataView&header=none (Accessed July 14, 2010).

NOAA NCEI (2017). Astoria, Oregon 1/3 Arc-second MHW Coastal Digital Elevation Model. Available at: https://www.ngdc.noaa.gov/metaview/page?xml=NOAA/NESDIS/NGDC/MGG/DEM/iso/xml/5490.xml&view=getDataView&header=none (Accessed June 18, 2016).

Okada, Y. (1985). Surface deformation due to shear and tensile faults in a half-space. *Bull. Seismol. Soc. Am.* 75, 1135–1154.

Parsons, T., Console, R., Falcone, G., Murru, M., and Yamashina, K. I. (2012). Comparison of characteristic and Gutenberg-Richter models for time-dependent M ≥ 7.9 earthquake probability in the Nankai-Tokai subduction zone, Japan. *Geophys. J. Int.* 190, 1673–1688. doi:10.1111/j.1365-246x.2012.05595.x

Pedregosa, F., Varoquaux, G., Gramfort, A., Michel, V., Thirion, B., Grisel, O., et al. (2011). Scikit-learn: machine learning in Python. *J. Mach. Learn. Res.* 12, 2825–2830.

Peherstorfer, B., Willcox, K., and Gunzburger, M. (2018). Survey of multifidelity methods in uncertainty propagation, inference, and optimization. *SIAM Rev.* 60, 550–591. doi:10.1137/16M1082469

Rong, Y., Jackson, D. D., Magistrale, H., and Goldfinger, C. (2014). Magnitude limits of subduction zone earthquakes. *Bull. Seismol. Soc. Am.* 104, 2359–2377. doi:10.1785/0120130287

Salmanidou, D. M., Guillas, S., Georgiopoulou, A., and Dias, F. (2017). Statistical emulation of landslide-induced tsunamis at the rockall bank, NE Atlantic. *Proc. R. Soc. A.* 473, 20170026. doi:10.1098/rspa.2017.0026

Satake, K. (1987). Inversion of tsunami waveforms for the estimation of a fault heterogeneity: method and numerical experiments. *J. Phys. Earth.* 35, 241–254. doi:10.4294/jpe1952.35.241

Sepúlveda, I., Liu, P. L. F., and Grigoriu, M. (2019). Probabilistic tsunami hazard assessment in South China Sea with consideration of uncertain earthquake characteristics. *J. Geophys. Res. Solid Earth.* 124, 658–688. doi:10.1029/2018jb016620

Sepúlveda, I., Liu, P. L.-F., Grigoriu, M., and Pritchard, M. (2017). Tsunami hazard assessments with consideration of uncertain earthquake slip distribution and location. *J. Geophys. Res. Solid Earth.* 122, 7252–7271. doi:10.1002/2017jb014430

Viana, F., Simpson, T., Balabanov, V., and Toropov, V. (2017). Metamodeling in multidisciplinary design optimization: how far have we really come? *AIAA J.* 52, 670–690. doi:10.2514/1.J052375

Volpe, M., Lorito, S., Selva, J., Tonini, R., Romano, F., and Brizuela, B. (2019). From regional to local SPTHA: efficient computation of probabilistic tsunami inundation maps addressing near-field sources. *Nat. Hazards Earth Syst. Sci.* 19, 455–469. doi:10.5194/nhess-19-455-2019

Williamson, A., Melgar, D., and Rim, D. (2019). The effect of earthquake kinematics on tsunami propagation. *J. Geophys. Res. Solid Earth.* 124, 11639–11650. doi:10.1029/2019jb017522

Williamson, A. L., Rim, D., Adams, L. M., LeVeque, R. J., Melgar, D., and Gonzaléz, F. I. (2020). A Source Clustering Approach for Efficient Inundation Modeling and Regional Scale PTHA. Frontiers in Earth Science, 2020 [Preprint]. Available at: http://depts.washington.edu/ptha/frontiers2020a/ (Accessed 2020).

Conflict of Interest: The authors declare that the research was conducted in the absence of any commercial or financial relationships that could be construed as a potential conflict of interest.

frontiers in Earth Science

ORIGINAL RESEARCH
published: 30 October 2020
doi: 10.3389/feart.2020.598235

Global Dissipation Models for Simulating Tsunamis at Far-Field Coasts up to 60 hours Post-Earthquake: Multi-Site Tests in Australia

Gareth Davies[1]*, *Fabrizio Romano*[2] *and Stefano Lorito*[2]

[1]Geoscience Australia, Canberra, ACT, Australia, [2]Istituto Nazionale di Geofisica e Vulcanologia, Roma, Italy

At far-field coasts the largest tsunami waves may occur many hours post-arrival, and hazardous waves may persist for more than 1 day. Such tsunamis are often simulated by nesting high-resolution nonlinear shallow water models (covering sites of interest) within low-resolution reduced-physics global-scale models (to efficiently simulate propagation). These global models often ignore friction and are mathematically energy conservative, so in theory the modeled tsunami will persist indefinitely. In contrast, real tsunamis exhibit slow dissipation at the global-scale with an energy e-folding time of approximately 1 day. How strongly do these global-scale approximations affect nearshore tsunamis simulated at far-field coasts? To investigate this we compare modeled and observed tsunamis at sixteen nearshore tide-gauges in Australia, generated by the following earthquakes: M_w9.5 Chile 1960; M_w9.2 Sumatra 2004; M_w8.8 Chile 2010; M_w9.1 Tohoku 2011; and M_w8.3 Chile 2015. Each tsunami is represented using multiple published source models, to prevent bias in any single source from dominating the results. Each tsunami is simulated for 60 h with a nested global-to-local model. On nearshore grids we solve the nonlinear shallow water equations with Manning-friction, while on the global grid we test three reduced-physics propagation models which combine the linear shallow water equations with alternative treatments of friction: 1) frictionless; 2) nonlinear Manning-friction; and 3) constant linear-friction. Compared with data, the frictionless global model well simulates nearshore tsunami maxima for $\simeq$8 h after tsunami arrival, and Manning-friction gives similar predictions in this period. Constant linear-friction underestimates the size of early arriving waves. As the simulation duration is increased from 36 to 60 h, the frictionless model increasingly overestimates observed wave heights, whereas models with global-scale friction work relatively well. The constant linear-friction model can be improved using delayed-linear-friction, where propagation is simulated with an initial frictionless period (12 h herein). This prevents systematic underestimation of early wave heights. While nonlinear Manning-friction offers comparably good performance, a practical advantage of the linear-friction models herein is that solutions can be computed, to high accuracy, via a simple transformation of frictionless solutions. This offers a pragmatic approach to improving unit-source based global tsunami simulations at late times.

OPEN ACCESS

Edited by:
Chong Xu,
National Institute of Natural Hazards, China

Reviewed by:
Alexander B. Rabinovich,
P.P. Shirshov Institute of Oceanology (RAS), Russia
Efim Pelinovsky,
Institute of Applied Physics (RAS), Russia

***Correspondence:**
Gareth Davies
gareth.davies@ga.gov.au

Specialty section:
This article was submitted to Geohazards and Georisks, a section of the journal Frontiers in Earth Science

Received: *24 August 2020*
Accepted: *02 October 2020*
Published: *30 October 2020*

Citation:
Davies G, Romano F and Lorito S (2020) Global Dissipation Models for Simulating Tsunamis at Far-Field Coasts up to 60 hours Post-Earthquake: Multi-Site Tests in Australia. Front. Earth Sci. 8:598235. doi: 10.3389/feart.2020.598235

Keywords: tsunamis, shallow water equations, friction, tsunami observations, numerical methods

1. INTRODUCTION

Large earthquake-tsunamis can be hazardous even at far-field coasts. For example the 1946 Aleutian earthquake-tsunami caused 159 deaths in Hawaii; the 1960 Chile earthquake-tsunami caused 142 deaths in Japan; the 2004 Sumatra earthquake-tsunami led to 300 deaths in Somalia (Fritz and Borrero, 2006; Okal, 2011). Smaller yet more-common tsunamis are also of interest for risk management because they can generate hazardous currents and minor inundation, with potential to harm people, damage assets, and disrupt economic activity at ports (e.g., Beccari, 2009; Borrero et al., 2015b). To mitigate the risk, early warning systems and hazard assessments are employed to guide emergency management and planning (Kânoğlu et al., 2015; Grezio et al., 2017; Davies and Griffin, 2018). They are underpinned by numerical models of tsunami propagation and inundation which exploit various approximations for computational tractability (e.g., Gica et al., 2008; Greenslade et al., 2011; Lorito et al., 2015; Setiyono et al., 2017; Volpe et al., 2019; Davies and Griffin, 2020). It is important to understand how well such models simulate key quantities of interest for applications (e.g., maximum wave heights and current speeds, their timing, and the duration of dangerous waves). Herein we focus on the tsunami wave size at far-field coasts in the period from 0-to-60 h post-earthquake. This is motivated by the fact that hazardous waves can persist for several days (Tang et al., 2012). Some historical tsunami observations in Australia and New Zealand exhibited wave maxima arriving 1-to-2 days post earthquake, long after the initial tsunami arrival (Pattiaratchi and Wijeratne, 2009; Borrero et al., 2015a).

For tsunami modeling applications at far-field sites, it is often advantageous to simulate global-scale propagation with linear models, noting nonlinearity should be small because ocean depths are generally much larger than tsunami amplitudes (Shuto, 1991). Linear models are typically faster to solve numerically (e.g., Liu et al., 2008; Baba et al., 2014), and if many scenarios are required then even greater speedups follow by constructing solutions $S(\mathbf{x}, t)$ as linear combinations "unit-source" solutions $U_i(\mathbf{x}, t)$.

$$S(\mathbf{x}, t) = \sum_{i \in \text{ set of unit-sources in database}} s_i U_i(\mathbf{x}, t) \qquad (1)$$

Here $\mathbf{x}, t$ denote space and time, while the s_i are constant coefficients defining the solution S (e.g., Gica et al., 2008; Miranda et al., 2014). For linear models S will be an exact solution, because the definition of linearity implies linear combinations of solutions are also solutions, and the calculation is very fast once a unit-source database is constructed (containing solutions U_i). For this reason the unit-source approach is very popular for large-scale probabilistic hazard assessment (e.g., Burbidge et al., 2008; Li et al., 2016; Molinari et al., 2016; Davies et al., 2017; Davies and Griffin, 2020; Zhang and Niu, 2020). Unit-sources also greatly simplify tsunami source-inversion algorithms, including for early-warning applications, because techniques from linear-regression can be combined with tsunami observations to solve for s_i (e.g., Tang et al., 2012; Fujii and Satake, 2013; Percival et al., 2014; Romano et al., 2016). Unit-source solutions U_i are sometimes computed with nonlinear hydrodynamic models (e.g., Yue et al., 2015; Molinari et al., 2016; Zhang and Niu, 2020) in which case **Eq. 1** does not produce an exact solution of the original model, but irrespective solutions derived from linear combinations of unit-sources are linear (by construction). In practice this approach works well if nonlinearity is small, which can be tested on a case-by-case basis (e.g., Yue et al., 2015; Molinari et al., 2016; Zhang and Niu, 2020). Linear models cannot simulate inundation and become unreliable if the wave amplitude is a significant fraction of the water depth, but are widely used to force nonlinear coastal inundation models using one-way or two-way nesting (e.g., Tang et al., 2009; Baba et al., 2014; Borrero et al., 2015a).

Tsunami propagation models at ocean-basin scales also often neglect friction, which has little effect on deep ocean tsunami simulations for a few hours post-arrival (Tang et al., 2012; Fujii and Satake, 2013; Allgeyer and Cummins, 2014; Baba et al., 2017; Heidarzadeh et al., 2018; Davies, 2019). However the frictionless shallow water equations are energy conservative, assuming smooth solutions, which mathematically implies the tsunami persists forever (Arakawa and Hsu, 1990; Fjordholm et al., 2011; Tang et al., 2012). In contrast real global-scale tsunamis eventually dissipate. Observations at coastal and deep-ocean gauges in the Pacific and Indian Oceans suggest an exponential time-decay of available potential energy, with an e-folding timescale about 1 ± 0.5 days following the initial diffusion of the tsunami energy throughout the ocean (Miller et al., 1962; Munk, 1963; van Dorn, 1984, van Dorn, 1987; Mofjeld et al., 2000; Rabinovich et al., 2011; Nyland and Huang, 2013; Rabinovich et al., 2013). The wave-amplitude e-folding timescale is twice as long, because available potential energy is proportional to the squared wave-amplitude. Empirically, the e-folding timescale depends on the tsunami spectral properties as well as the site and its distance from the source (Rabinovich et al., 2011; Rabinovich et al., 2013). Comparatively short energy e-folding timescales have been reported in small coastal seas ($\simeq 3 - 13$ hours; van Dorn, 1987; Oh and Rabinovich, 1994) which can be explained if tsunami dissipation mainly occurs in shallow shelf regions (van Dorn, 1987). Munk (1963) suggested that tsunami dissipation might additionally be affected by energy transfer to internal ocean waves. This was subsequently confirmed to be important for simulating tidal dissipation (Munk, 1997; Egbert and Ray, 2000; Llewellyn Smith and Young, 2002) and is typically represented in tidal models using spatially varying linear friction, in addition to standard quadratic bottom-friction (Buijsman et al., 2015; Kleermaeker et al., 2019), although the significance of this process for tsunami dissipation remains unclear.

Quadratic bottom friction (e.g., Manning or Chezy) is most common in tsunami models, but the solutions cannot be represented with unit-sources (**Eq. 1**) over timescales for

which the nonlinear dissipation is important. To represent global-scale tsunami dissipation within a linear hydrodynamic model, Fine et al. (2013) and Kulikov et al. (2014) combined the linear shallow water equations (LSWE) with a constant linear-friction term. Although not justified from hydrodynamic theory, this model implies an exponential time-decay of the tsunami's energy which is consistent with observational studies. The linear-friction coefficient may thus be estimated using observed tsunami decay timescales (Fine et al., 2013; Kulikov et al., 2014). The model was implemented using numerical methods that have good energy conservation to prevent numerical dissipation from dominating the results at late times, which was reportedly easier to achieve by modifying a linear model (Fine et al., 2013; Kulikov et al., 2014). Numerical dissipation is often significant for models solving the nonlinear shallow water equations (NSWE) and can even exceed the physical dissipation of global scale tsunamis at computationally practical resolutions (Popinet, 2011; Tang et al., 2012; Tolkova, 2014). This has been used to explain persistent under-estimation of late time tsunami wave heights in some nested nearshore models, even without any friction in the global propagation model (Tang et al., 2012; Tolkova, 2014). However, in the absence of significant numerical dissipation, friction is necessary to represent the late-time energy decay observed in global-scale tsunamis.

Modeled coastal tsunami wave heights are likely to be qualitatively affected at sufficiently late times by the treatment of global-scale dissipation. This has the potential to affect tsunami hazard assessments (e.g., runup maxima) and warnings (e.g., warning cancellation). Our study seeks to better understand the practical significance of this issue, focusing on the empirical performance of alternative models rather than the physics of tsunami dissipation. To this end we test several global-to-local scale nested-grid tsunami models by comparison with tsunami observations at tide-gauges in Australia, for the period 0–60 h post-earthquake. The alternative models differ only in their treatment of friction on the global-scale grid (where propagation is simulated with some variant of the LSWE); in all cases the tsunami at nearshore sites of interest is simulated on nested grids which solve the NSWE with Manning-friction. The tsunami initial conditions are derived from published earthquake-source inversions. We focus on relatively simple tsunami models which are computationally cheap and very practical in applications, while acknowledging that tsunami propagation may be simulated more accurately using computationally intensive approaches that include higher order physics such as dispersion, loading, seawater density stratification, and self-gravitation (Allgeyer and Cummins, 2014; Baba et al., 2017). Model improvements may also be sought through use of higher quality elevation data outside the primary area of interest, combined with higher model resolution, to better represent remote reflections (Kowalik et al., 2008; Geist, 2009). The practical benefit of very high-accuracy propagation modeling may be limited for hazard assessments, because plausible source variations can have an even greater effect on the simulated tsunami (Davies, 2019), although further study of this issue is warranted.

The paper is structured as follows. **Section 2.1** presents the earthquake-tsunami sources (initial water-surface perturbations) used to model each historic event. **Section 2.2** presents the tide-gauge data used to test each model. **Section 2.3** reviews the tsunami model setup. **Section 2.4** details the alternative reduced-physics hydrodynamic models that are tested. **Section 3.1** illustrates each model's performance using examples from three historic tsunamis. **Sections 3.2** and **3.3** compare the modeled and observed tsunami maxima for all sites and events. **Section 3.4** considers how the model errors are affected by the tsunami source.

2. MATERIALS AND METHODS

2.1. Earthquake Source Models for Historical Tsunamis

Five historic tsunamigenic earthquake events were analyzed in this study: M_w 9.5 Chile 1960, M_w9.2 Sumatra 2004, M_w8.8 Chile 2010, M_w9.1 Tohoku 2011, and M_w8.3 Chile 2015 (**Figure 1**). These events were chosen because they generated relatively large tsunamis and resulted in good quality tide-gauge observations in Australia. The earthquake sources were represented using twelve published finite-fault inversions (**Figure 2**) which represent an ad-hoc sample from the literature. The set of finite-fault inversions was not modified on the basis of our tsunami model performance because that could inadvertently compensate for any model biases which are of primary interest herein. Instead multiple inversions were used for each historic tsunami to prevent bias in a single source model from dominating the results.

Most tsunami initial conditions in **Figure 2** were derived by computing the vertical co-seismic deformation from the published fault-geometries and slip vectors, assuming instantaneous rupture in a homogeneous elastic half-space (Okada, 1985; Meade, 2007). The effect of horizontal deformation over a sloping seabed (Tanioka and Satake, 1996) was not included as this tends to add shorter waves to the source which may not be well simulated with our long-wave hydrodynamic model (Saito et al., 2014). However source R14 was taken directly from the finite-element model of Romano et al. (2014); this includes horizontal components so is rougher than our other sources (**Figure 2**). Source H19 was derived from water-surface unit-sources following Ho et al. (2019). A Kajiura filter (Kajiura, 1963; Glimsdal et al., 2013) was applied to all models except the water-surface inversion H19.

The studies on which our source models are based generally inverted the source using deep sea and/or coastal tsunami data, sometimes combined with geodetic data (GPS, InSAR, leveling) and occasionally teleseismic data. None made use of the Australian tide-gauge data studied herein. All inverted the source with linear combinations of earthquake and/or tsunami Green's functions, in some cases including regularization constraints (L11, Y14, R16, W17, Y18). Most simulated the co-seismic displacement assuming a homogeneous elastic half-space, although R14 used a 3D finite-element model to account for material heterogeneity. Tsunami Green's functions were

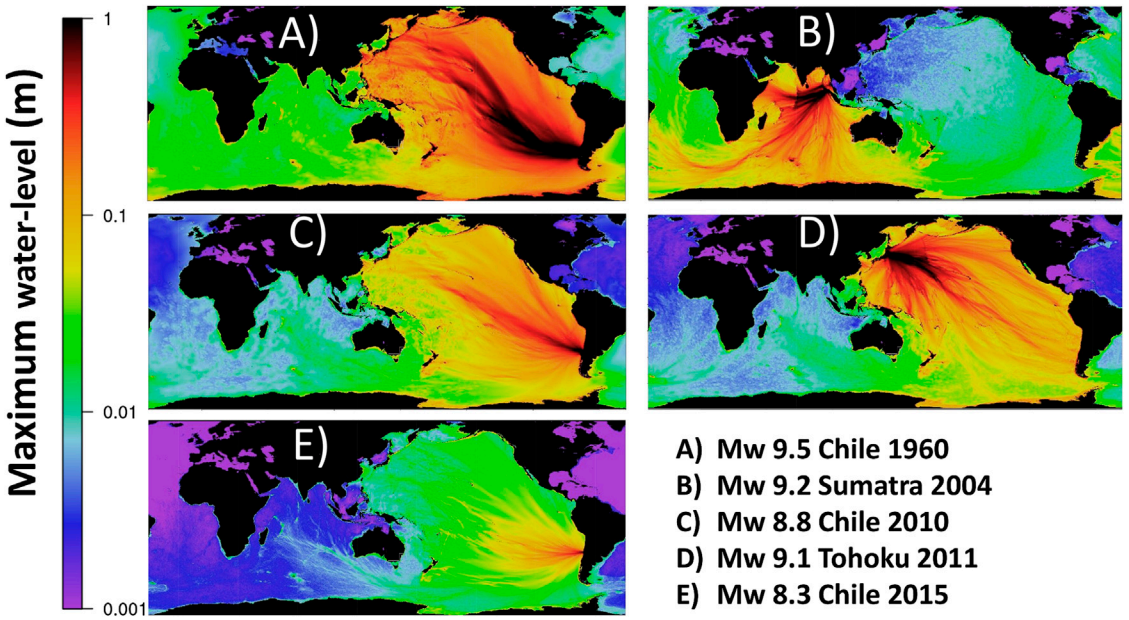

FIGURE 1 | Tsunami events considered in this study. The images are model outputs derived using the solver from **Section 2.4.3** on the global grid and a subset of the source models in **Figure 2** [**(A)**: H19, **(B)**: F07, **(C)**: L11, **(D)**: Y18, **(H)**: W17].

mostly modeled with shallow water schemes, although R14, R16 and Y18 employed a non-hydrostatic model. Some papers reported both a best-fitting source model and an average source model; in such cases we always used the former. Full details are available in the repository (see *Data Availability Statement*).

2.2. Test Sites and Data

The model is compared with data at 16 sites in Australia that have good bathymetry and relatively good quality tsunami observations at tide-gauges (**Figure 3**). Most gauges only record one of the modeled tsunami events, although Fort Denison in Sydney Harbor records all five (**Figure 3**). By using multiple sites with good quality data for each historic tsunami, we reduce the risk that site-specific factors limiting the model performance are mistakenly attributed to source/propagation model biases (e.g., undiagnosed errors in the bathymetry or tide-gauge records). No gauge observations were rejected on the basis of disagreement with our tsunami model, to avoid biasing the results.

Tide-gauge data was obtained from a range of sources (see *Acknowledgments*). To detide the observations we first subtracted tidal predictions, which were either provided with the tide-gauge data, or obtained from TPXO7.2 (Egbert and Erofeeva, 2002). Next a high pass filter was used to remove the residual long-period sea-level variations by applying a discrete Fourier transform and zeroing the amplitude of waves with period exceeding a threshold. At most sites the tides are semi-diurnal and the high pass filter threshold was 3 h. At our Western Australia sites the tides are diurnal and a longer threshold was used (6 h); the 3 h threshold led to non-stationary oscillations in the non-tsunami sea-level component at the time of the Sumatra 2004 tsunami, suggesting a longer threshold is appropriate. Irrespective this has little impact on the tsunami signal. In all cases the detided tsunami record might still be affected by other physical processes (e.g., seiching due to transient atmospheric forcings) or measurement errors (e.g., excess mechanical smoothing in the gauge, Satake et al., 1988); however it represents our best estimate of the tsunami signal.

Most gauges used herein have a sampling frequency of 1-min. For the Sumatra 2004 event, three of the four gauges used in Western Australia have 5-min sampling frequency (excepting Hillarys which has a 1-min frequency). For the 1960 Chile event only two gauges are available (Fort Denison and Cronulla), both of which were digitized at approximately 2-min sampling frequency from scans of the analogue tide-gauge records (the former by Wilson et al., 2018). Although in recent decades additional 15-min tide-gauge data is available at several sites, this was not used because it under-samples the tsunami making interpretation more difficult (Rabinovich et al., 2011). At Port Kembla the outer-harbour gauge is used; the inner-harbour gauge was not used based on advice from the data custodians (NSW Port Authority, personal communication 2020) and the issues noted in Allen and Greenslade (2016).

2.3. Tsunami Model

The tsunami is simulated from source to the tide-gauges using the open-source hydrodynamic model SWALS, which solves several variants of the shallow water equations in spherical or Cartesian coordinates and was used for the 2018 Australian Probabilistic Tsunami Hazard Assessment (Davies and Griffin, 2018). The source code includes a validation test-suite of more than 20

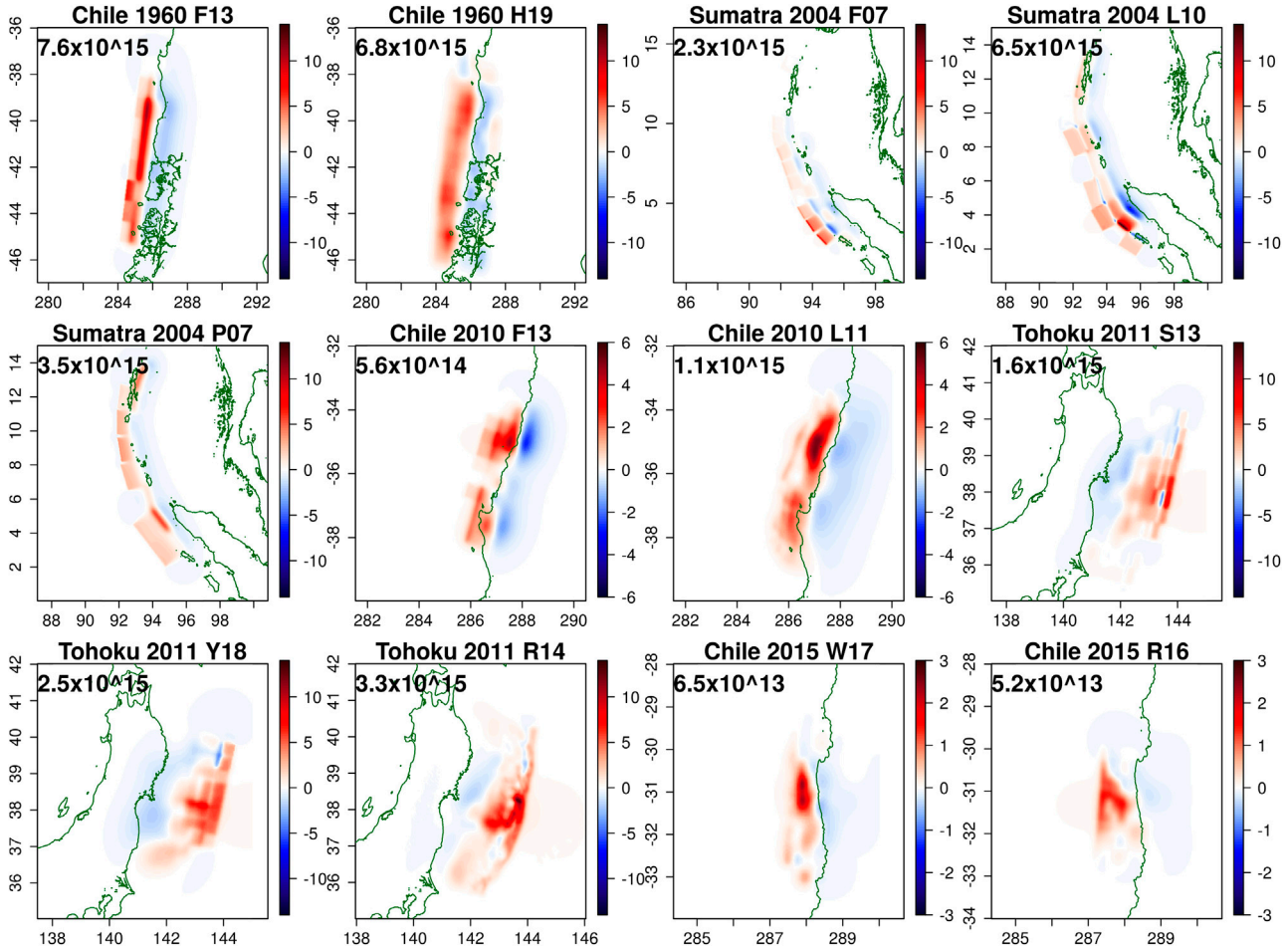

FIGURE 2 | The vertical co-seismic displacement for all source models. Text beneath the title gives the initial available potential energy of the ocean surface displacement (kg m^2/s^2, derived by integrating **Eq. 5** in space; there is no contribution from deformation on land). The sources are based on finite-fault inversions in the following publications: F13 (Fujii and Satake, 2013); H19 (Ho et al., 2019); F07 (Fujii and Satake, 2007); L10 (Lorito et al., 2010); P07 (Piatanesi and Lorito, 2007); L11 (Lorito et al., 2011); S13 (Satake et al., 2013); Y18 (Yamazaki et al., 2018); R14 (Romano et al., 2014); W17 (Williamson et al., 2017); R16 (Romano et al., 2016).

analytical, laboratory and field problems, including well-known tests such as those in NTHMP (2012) (excluding landslides) and two recent field-scale NTHMP problems (Macías et al., 2020). It uses structured grids with two-way nesting, and flux-correction to enforce conservation at nested grid boundaries. Different grids can employ different solvers simultaneously; this is used in the current study to test a range of reduced-physics solvers on the global grid (only) while solving the NSWE on refined grids.

The global scale tsunami propagation is simulated on a 1 arc-minute grid (**Figure 3A**) using bathymetry derived from GEBCO 2014 (Weatherall et al., 2015) and GA250 (Whiteway, 2009) (details in Davies and Griffin, 2018). East-West periodic boundary conditions are used. The southern boundary (79° S) is covered by land. At the northern boundary (68° N) a reflective wall is imposed; while artificial this closes the model and facilitates energy conservation calculations (as SWALS does not track energy fluxes through boundaries). Physically this is reasonable given little tsunami energy will radiate through either Bering strait (which is small) or north Atlantic (which is very far from our tsunami sources). The reduced-physics solvers used on this grid are described in **Sections 2.4.2–2.4.4**.

Nearshore regions containing good-quality tide-gauge observations are simulated on refined grids (1/7 and 1/49 arc-minutes, (**Figures 3C–E**), which are linked with the global grid and each other via two-way nesting. Good quality nearshore elevation data is used on the highest-resolution grids, mostly derived from LIDAR and gap-filled using available single-beam bathymetric surveys and gridded elevation from prior studies (see *Acknowledgments*; Allen and Greenslade, 2016; Wilson and Power, 2018). Breakwalls close to our tide-gauges were burned into the model's elevation to ensure they are represented irrespective of the grid resolution. On these nearshore grids the tsunami is simulated using the NSWE with Manning-friction (**Section 2.4.1**).

To check the numerical convergence of the model at the default resolution (1, 1/7 and 1/49 arc-minute nested grids),

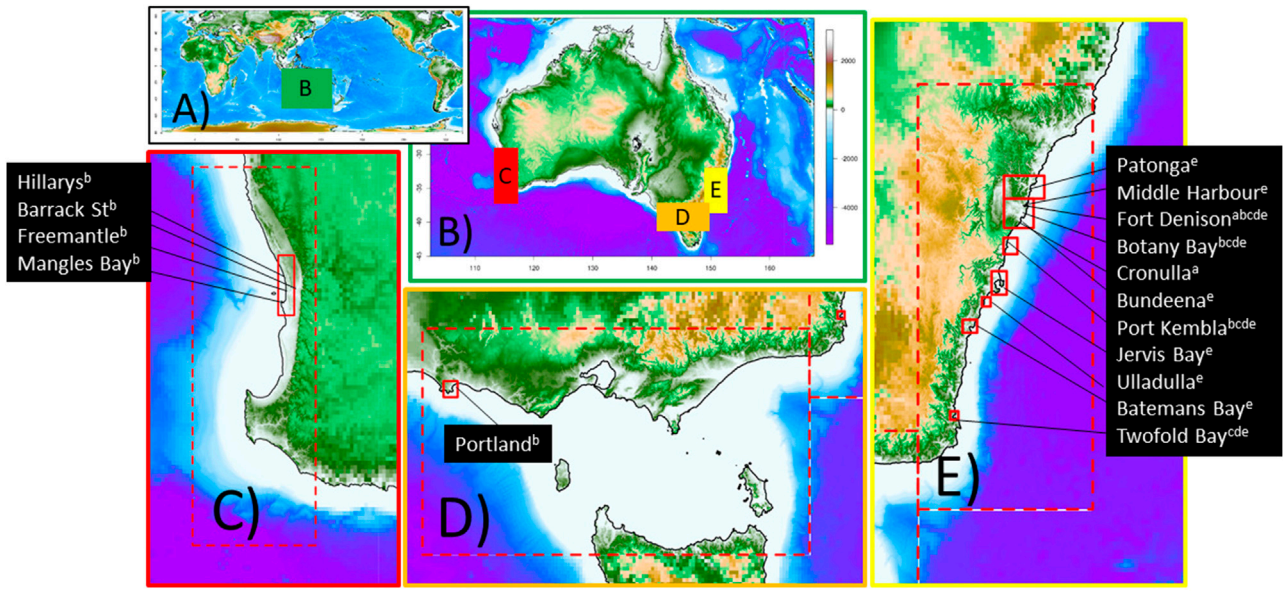

FIGURE 3 | The model extent and tide-gauge locations. Superscripts on tide-gauges (a,b,c,d,e) indicate the tsunamis for which we have data, corresponding to the 1960, 2004, 2010, 2011, 2015 events, respectively. **(A)** The global grid has a spatial resolution of 1-arc-minute and is modeled with reduced-physics approaches; **(B)** zoom near Australia which shows the three regions where refined grids are used and the NSWE are solved; **(C–E)** the refined grids around western and south-eastern Australia. Dashed boxes denote regions with 1/7-arc-minute spatial resolution (≃260 m), and solid boxes denote regions with 1/49-arc-minute resolution (≃ 37 m) which contain the tide-gauges.

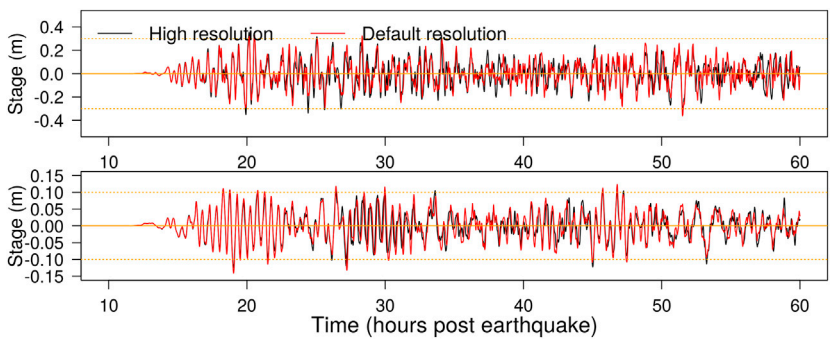

FIGURE 4 | Comparison of nearshore gauge results in two models; one with default resolution (1, 1/7, 1/49 arc-minute nested grids) and one with higher-resolution (1/2, 1/14, 1/98 arc-minute nested grids). Locations correspond to tide-gauges at Port Kembla **(top)** and Botany Bay **(bottom)**; results elsewhere were qualitatively similar. The simulation corresponds to the Tohoku 2011 Y18 source, using Manning-friction in the global model.

higher resolution simulations (1/2, 1/14, 1/98 arc-minute) were run for two of our sources (F07, Y18), using the reduced physics solver of **Section 2.4.3** on the coarsest grid. Results were compared with the default model at twelve sites with corresponding good-quality observations, as this is where the model results will be used. Waveforms were similar although not completely convergent, with tsunami maxima showing changes ranging from −12% to +21% with a median of 2% (typical examples in **Figure 4**). In general greater differences are anticipated between the models and data, so the default resolution was considered adequate for the current study.

2.4. Hydrodynamic Simplifications for Global Scale Tsunami Propagation

Several reduced-physics solvers are tested on the global grid, all based on the linear shallow water equations (LSWE) with alternative dissipation models:

(1) Frictionless (**Section 2.4.2**)
(2) Nonlinear Manning-friction (**Section 2.4.3**)
(3) Constant linear-friction (**Section 2.4.4**)

These represent computationally efficient alternatives to solving the full NSWE for global tsunami propagation.

The frictionless LSWE were tested because they are often used to simulate large-scale tsunami propagation (e.g., Choi et al., 2003; Burbidge et al., 2008; Thio, 2015; Li et al., 2016; Davies and Griffin, 2020) and arguably represent the simplest model of this kind. The Manning-friction approach was tested because it is closer to the full NSWE; however over timescales where dissipation is important, the nonlinearity will prevent a unit-source implementation. The constant linear-friction approach (Fine et al., 2013; Kulikov et al., 2014) was tested because it enables dissipation to be included in a linear framework, with all the associated efficiency benefits. Furthermore, although unit-sources are not employed in this study, below it is shown that solutions of the constant linear-friction model can be well approximated with a simple transformation of solutions of the frictionless LSWE, which is convenient because the latter are available in several existing tsunami propagation databases (e.g., Thio, 2015; Li et al., 2016; Davies and Griffin, 2018).

2.4.1. Nonlinear Shallow Water Equations

The 2D NSWE with friction are (e.g., Baba et al., 2015; Behrens and Dias, 2015):

$$\begin{aligned} &\frac{\partial \eta}{\partial t} + \nabla \cdot \mathbf{q} = 0 \\ &\frac{\partial \mathbf{q}}{\partial t} + \nabla \cdot \left(\mathbf{u} \otimes \mathbf{q}\right) + gh\nabla\eta + gh\mathbf{S_f} + \mathbf{\Omega} = 0 \end{aligned} \tag{2}$$

Here $\eta = h + z$ is the free surface elevation (m), h is the depth (m), z is the bed elevation (m), $\mathbf{q} = h\mathbf{u}$ is the 2D flux vector (m^2/s), $\mathbf{u} = (u, v)$ is the 2D velocity vector (m/s), g is gravity (m/s^2), $\mathbf{S_f} = n^2\mathbf{u}|\mathbf{u}|h^{-4/3}$ is the friction slope vector with Manning-friction coefficient n, and $\mathbf{\Omega} = \omega(-vh, uh)$ is the Coriolis force with latitude dependent Coriolis parameter ω.

If friction is neglected ($\mathbf{S_f} = 0$) then for smooth flows **Eq. 2** is energy conservative (Arakawa and Hsu, 1990):

$$\int_D \left(e_k + e_p\right) dA = E_0 \tag{3}$$

Here the depth-integrated energy density $(e_k + e_p)$ is integrated over a two-dimensional domain D with no inflow or outflow through boundaries, dA is an area element, E_0 is the constant total energy in D, e_k is the depth-integrated kinetic energy density:

$$e_k = \frac{\rho h}{2}\left(u^2 + v^2\right) \tag{4}$$

with water density ρ (kg/m^3), and e_p is the "depth-integrated available potential energy density":

$$e_p = \frac{\rho g}{2}\left(\eta^2 - z^2\right) + C_2 \tag{5}$$

By definition the integral of e_p in D is zero if the fluid mass is redistributed in D to make the free-surface constant (Lorenz, 1955); herein C_2 is a constant that satisfies this definition. If the vertical datum is the model's mean sea level, and there is no wetting and drying, then **Eq. 5** simplifies to $e_p = \frac{\rho g}{2}\eta^2$ in wet regions and zero in dry regions. The latter form is common in the tsunami literature (Tang et al., 2012; Saito et al., 2014; Tolkova, 2014) but does not generalize to flows with wetting and drying or other vertical datums.

On refined grids the model herein solves **Eq. 2** in flux-conservative form with a constant Manning-friction $n = 0.03$. The refined-grid n value might be improved with site-specific tuning, but that was not attempted herein. A second-order accurate finite-volume scheme is used based on the hydrostatic-reconstruction approach of Audusse et al. (2004). The details are similar to the ANUGA software's DE1 flow algorithm (Davies and Roberts, 2015), although the latter uses a triangular mesh while the solver herein uses structured grids with two-way nesting.

2.4.2. Linear Shallow Water Equations Without Friction

In the deep ocean even large earthquake tsunamis are of small amplitude relative to ocean depths and velocities are slight compared to the gravity wave speed. Under these conditions **Eq. 2** is well approximated with the frictionless LSWE:

$$\begin{aligned} &\frac{\partial \eta}{\partial t} + \nabla \cdot \mathbf{q} = 0 \\ &\frac{\partial \mathbf{q}}{\partial t} + gh_0\nabla\eta + gh_0\mathbf{S_{0f}} + \mathbf{\Omega} = 0 \end{aligned} \tag{6}$$

Here h_0 is the time-invariant depth below mean-sea-level, and the friction slope is zero

$$\mathbf{S_{0f}} = 0 \tag{7}$$

but is included in **Eq. 6** to facilitate extensions below. These equations are also energy conservative.

Herein the LSWE are solved numerically with the classical leap-frog scheme (Goto and Ogawa, 1997). Importantly this scheme has good numerical energy conservation; in our twelve simulations that used the frictionless LSWE on the global grid the numerically integrated energy (**Eq. 3**) varied within [−2.7%, 0.25%] over 60 h. Minor dissipation is expected in the full model because refined grids solve the NSWE with friction and employ a more dissipative finite-volume numerical scheme; minor energy increase can occur because the leap-frog scheme is not perfectly energy conservative. In comparison the literature suggests global tsunami propagation simulations often have much greater numerical dissipation; Tang et al. (2012) and Tolkova (2014) used several variants of the MOST and CLIFFS solvers to simulate the Tohoku tsunami globally without friction and found $\simeq$ 80–90% of the total energy was numerically dissipated in 24 h. Popinet (2011) reported substantial numerical dissipation when modeling the Sumatra 2004 tsunami from source with the Gerris finite-volume solver. Although the frictionless LSWE are energy conservative, physically some dissipation is expected. Considering the observed energy e-folding timescale of global tsunamis at late-times ($\simeq$1 day) these frictionless LSWE simulations should under-estimate the physical dissipation, but the numerical scheme offers a good basis for testing dissipation models because it adds negligible numerical dissipation.

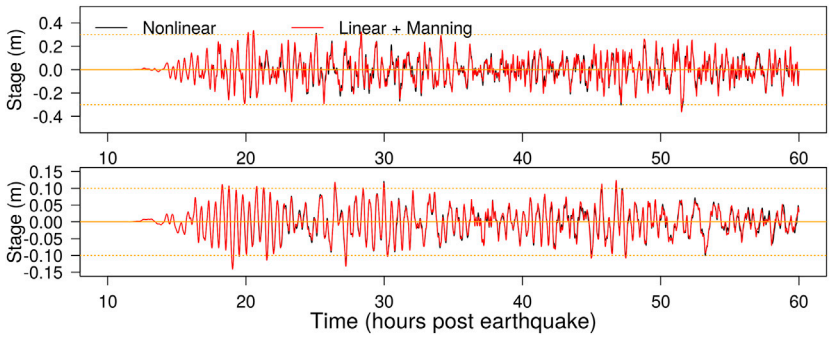

FIGURE 5 | Comparison of nearshore gauge results in two models which use different solvers on the global grid; one solves the full NSWE, the other solves the LSWE with a nonlinear Manning-friction term. In both cases the NSWE are solved on refined grids. The site locations and scenario details are the same as in **Figure 4**.

2.4.3. Linear Shallow Water Equations With Manning-Friction

To add dissipation to the global model it is natural to consider a Manning-friction closure in **Eq. 6**. For computational efficiency our approach exploits the approximation $h \simeq h_0$ inherited from the LSWE:

$$\mathbf{S}_{0f} = \mathbf{q}|\mathbf{q}|\left(n^2 h_0^{-10/3}\right) \tag{8}$$

where n is the Manning-friction coefficient, which was set to 0.035 on the global grid (slightly larger than our nearshore Manning coefficient of 0.03). Real tsunamis likely dissipate due to a mixture of nonlinear bottom friction in shallow regions, and other deep-ocean dissipation mechanisms which are important for simulating tides (Egbert and Ray, 2000; Buijsman et al., 2015; Kleermaeker et al., 2019). Our global model poorly resolves most shallow nearshore areas, neglects nonlinear tidal interactions, and ignores other dissipation mechanisms, so the Manning model is likely a strong simplification of reality. In preliminary simulations we also tried a smaller global Manning coefficient ($n = 0.02$) which did not perform as well; however further optimization of the global n may be possible.

Equation 8 is nonlinear so solutions cannot be constructed from unit-sources (at least not over timescales long enough for nonlinear dissipation to be important). However the term in large parenthesis is time-invariant which reduces the computational expense of our implementation. A semi-implicit discretization is used to include **Eq. 8** in the leap-frog scheme, with $|\mathbf{q}|$ evaluated explicitly and $\mathbf{q}$ evaluated implicitly. The total energy dissipation over 60 h varied between 63 and 96% in our twelve simulations using this model on the global grid, with the lowest percentage dissipation corresponding to the smallest tsunami (2015 Chile) as expected with quadratic friction.

For global tsunami propagation this model is relatively close to the NSWE with Manning-friction (**Eq. 2**). **Figure 5** compares solutions at some nearshore tide-gauges when using the above reduced-physics model on the global grid, vs. the full NSWE (the latter were solved with a leap-frog numerical scheme combined with an upwind treatment of nonlinear advection, for similarity with our reduced-physics solver, Goto and Ogawa, 1997; Liu et al., 1995). At our nearshore gauges of interest, which are inside the refined grids and thus simulated with the NSWE finite-volume scheme (**Section 2.4.1**), the difference between the two models is smaller than differences caused by grid refinement (compare **Figures 4** and **5**). However the full simulation ran three times faster when using the simpler model on the global grid (about 2 vs. 6 h for the 60 h simulation with all nested grids, using 8 CPU nodes of the Gadi supercomputer NCI, 2020), due purely to a factor-of-6.6 speedup in the global grid calculation.

2.4.4. Linear Shallow Water Equations With Constant Linear-Friction, and Approximation via Frictionless Solutions

To represent global-scale tsunami dissipation with a linear model, Fine et al. (2013) and Kulikov et al. (2014) appended constant linear-friction to the LSWE (**Eq. 6**) by replacing $\frac{\partial}{\partial t} \rightarrow \left(\frac{\partial}{\partial t} + f\right)$ in the momentum equations only, implying:

$$\mathbf{S}_{0f} = f\mathbf{q}/(gh_0) \tag{9}$$

where f is a constant linear drag coefficient. Fine et al. (2013) and Kulikov et al. (2014) show **Eqs 6** and **9** cause the globally integrated energy to decay exponentially in time with e-folding timescale of $1/f$, thus mimicking classical observations of tsunami energy time-decay at late times (Miller et al., 1962; Munk, 1963; van Dorn, 1984; van Dorn, 1987; Rabinovich et al., 2011; Rabinovich et al., 2013). On this basis they used $f = 1 \times 10^{-5}$ which corresponds to an energy e-folding time of 27.7 h. Herein an implicit discretization is used to include **Eq. 9** in the leap-frog scheme for **Eq. 6**. The total energy dissipation over 60 h was close to 88.5% for all twelve simulations using this model on the global grid, as expected theoretically.

Linear-friction is attractive, if it works well enough in practice, because the model retains all the practical benefits of linearity for simulating global propagation (e.g., unit-source solutions are exact). The use of a constant f is not essential to preserve linearity; often linear friction is implemented by linearizing a quadratic drag model about a reference depth and velocity (e.g., Tolkova, 2015). However the use of a

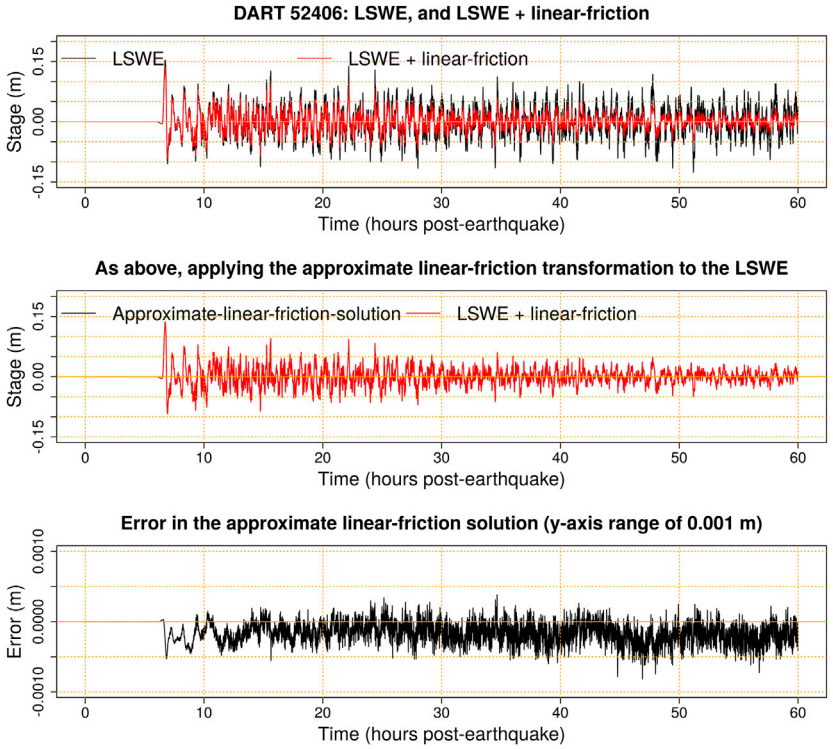

FIGURE 6 | Illustration of the approximate linear-friction solution at a deep ocean site (DART 52406), using the Y18 source. Top: Comparison of numerical solutions using the frictionless LSWE (**Section 2.4.2**) and the LSWE with constant linear-friction (**Section 2.4.4**). Middle panel: Comparison of the approximate linear-friction solution (derived with the LSWE solution via **Eq. 10**) and the LSWE with constant linear-friction. They are visually indistinguishable. Bottom: Difference between the two solutions in the middle panel, using a vertical scale of ± 0.001 m.

constant f has a practical advantage, above those noted in Fine et al. (2013) and Kulikov et al. (2014): it is possible to approximate solutions of the model with negligible error by using transformed solutions of the frictionless LSWE (**Eqs 6** and **7**). To illustrate this point, **Figure 6** compares a numerically derived solution to the constant linear-friction model **Eqs 6** and **9** with an "approximate linear-friction" solution defined as:

$$[\eta^a, uh^a, vh^a] = \exp\left(\frac{f}{2}t\right)[\eta^0, uh^0, vh^0] \tag{10}$$

Here the superscript a denotes the approximate linear-friction solution, and the superscript 0 denotes the frictionless LSWE solution which is prescribed the same initial conditions as the solution of interest.

Although **Eq. 10** does not produce an exact solution of the constant linear-friction model, the error is negligible in practice (**Figure 6**) for global-scale tsunamis and other waves having a period much smaller than the decay timescale $1/f$. This is justified mathematically below. Thus unit-source databases based on the frictionless LSWE can be used, without modification, as a convenient means to derive solutions with linear-friction using **Eq. 10**. This makes the model very easy to use in practice, via existing frictionless tsunami scenario databases, and motivates us to test it herein.

2.4.4.1 Justification of the Approximate Linear-Friction Solution (Eq. 10)

It is standard to convert the frictionless LSWE to a single wave equation for the free surface by applying $\frac{\partial}{\partial t}$ to the mass equation and $\nabla\cdot$ to the momentum equation in **Eq. 6**, and eliminating mixed derivatives of $\mathbf{q}$. Using the superscript 0 to denote solutions of the frictionless LSWE, this leads to:

$$\frac{\partial^2\eta^0}{\partial t^2} - \nabla\cdot\left(gh_0\nabla\eta^0\right) - \nabla\cdot\boldsymbol{\Omega}^0 = 0 \tag{11}$$

where $\boldsymbol{\Omega}^0 = \omega[-vh^0, uh^0]$. For solutions of the constant linear-friction model (denoted with superscript l) the same calculation yields an additional source-term on the RHS:

$$\frac{\partial^2\eta^l}{\partial t^2} - \nabla\cdot\left(gh_0\nabla\eta^l\right) - \nabla\cdot\boldsymbol{\Omega}^l = -f\frac{\partial\eta^l}{\partial t} \tag{12}$$

For the approximate linear-friction solution (**Eq. 10**), the analogous equation follows by substituting $[\eta^0, uh^0, vh^0] = \exp\left(\frac{f}{2}t\right)[\eta^a, uh^a, vh^a]$ into **Eq. 11**:

$$\frac{\partial^2\eta^a}{\partial t^2} - \nabla\cdot\left(gh_0\nabla\eta^a\right) - \nabla\cdot\boldsymbol{\Omega}^a = -f\frac{\partial\eta^a}{\partial t} - \eta^a\frac{f^2}{4} \tag{13}$$

Equation 13 is the same as **Eq. 12** except for the second RHS source term, which has magnitude $\simeq \alpha f^2/4$ where α is the wave

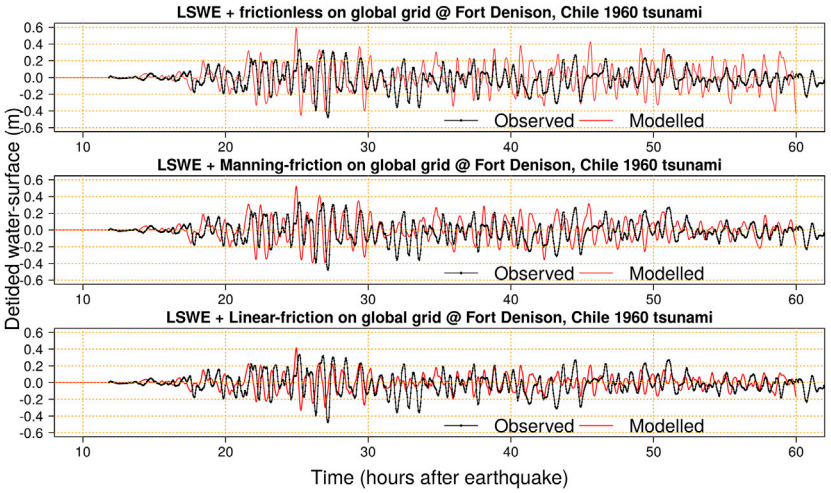

FIGURE 7 | Simulations and observations of the Chile 1960 tsunami at Fort Denison near Sydney. All simulations use the Chile 1960 H19 source model. Top: Using the frictionless LSWE on the global grid. Middle: Using LSWE with Manning-friction on the global grid. Bottom: Using LSWE with linear-friction on the global grid.

amplitude. If the wave has period T then the average absolute value of $\frac{\partial \eta^4}{\partial t}$ is $4\alpha/T$. Thus the first RHS source-term has magnitude $\simeq f\,(4\alpha/T)$, so is $\simeq 1000$ times larger than the second source term for a typical earthquake-generated tsunami in the deep ocean (period 30 min, $f \simeq 10^{-5}$). In this circumstance **Eq. 13** is a minor perturbation of **Eq. 12** and their solutions will be arbitrarily close if $fT/16$ is sufficiently small, which explains the excellent agreement in practice (**Figure 6**).

3. RESULTS

Section 3.1 provides examples to illustrate how the global dissipation models affect nearshore tsunami simulations in comparison with data. This gives context for a subsequent statistical analysis but necessarily represents a small sample of the results; figures comparing models and data at all sites are available via the repository (see *Data Availability Statement*). **Section 3.2** uses statistical techniques to evaluate each model by comparing all simulations and observations simultaneously, focusing on biases in the modeled tsunami maxima and their relation to the simulation duration. These results motivate tests of several modified linear-friction models on the global grid (**Section 3.3**). **Section 3.4** considers how the model performance varies among the source-inversions.

3.1. Effect of Global Dissipation at Nearshore Gauges: Examples

3.1.1. Fort Denison, Chile 1960, H19 Source Model

The 1960 Chile tsunami was observed widely on Australia's east-coast where it induced widespread marine hazards and minor inundation (Beccari, 2009). Based on our simulations, the tsunami reached the eastern Australian mainland $\simeq$ 14 h after the earthquake via waves which propagated south of New Zealand. Further waves arrived via the ocean north of New Zealand, including due to prominent scattering of the leading wave around bathymetry near French Polynesia ($\simeq$ 11 h post-earthquake, reaching eastern Australia $\simeq$22 h post-earthquake). This led to a steady growth in the nearshore tsunami energy on Australia's east coast (**Figure 7**). At Fort Denison the largest waves occurred around 25–29 h post-earthquake, while they were slightly earlier ($\simeq$22 – 25 h) at the Cronulla gauge which is 25 km south and closer to the open coast.

At Fort Denison the models with frictionless and Manning-friction global grid solvers give similar results prior to the observed maxima, with predicted waves slightly larger than observed (**Figure 7**). Linear-friction on the global grid produces slightly smaller initial waves. Constant linear-friction induces greater dissipation in the deep-ocean compared to Manning-friction which dissipates most energy in nearshore areas; at later times the cumulative effect of nearshore propagation leads to significant global energy dissipation with Manning-friction, but this has little influence on the early arrivals. All models well approximate the timing of the maximum wave but differ in its size (**Figure 7**). In this case linear-friction best represents the observed tsunami maxima, but at later times consistently under-predicts the tsunami size. Manning-friction better simulates the size of late arriving waves, while the frictionless global model leads to nearshore waves that are too large at late times.

The data has a phase-lag relative to all models (**Figure 7**). This is expected given our use of the LSWE on the global grid. The phase-lag should be better simulated by including additional terms in the global model related to loading, seawater density stratification, and self-gravitation (Watada et al., 2014; An and Liu, 2016), although this would be computationally expensive (Allgeyer and Cummins, 2014; Baba et al., 2017).

3.1.2. Hillarys, Sumatra 2004, F07 Source Model

The Sumatra 2004 tsunami induced significant marine hazards in Western Australia, including 35 ocean rescues, damages to boats

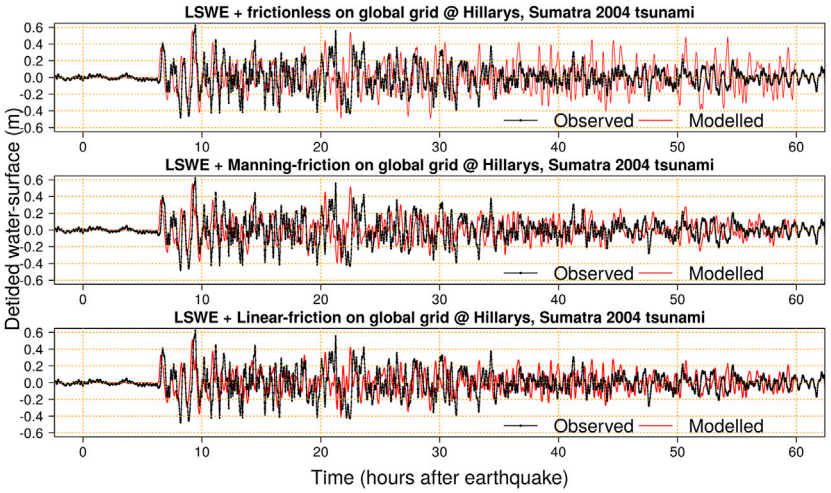

FIGURE 8 | Simulations and observations of the Sumatra 2004 tsunami at Hillarys in Western Australia. All simulations use the Sumatra 2004 F07 source model. Top: Using the frictionless LSWE on the global grid. Middle: Using LSWE with Manning-friction on the global grid. Bottom: Using LSWE with linear-friction on the global grid.

and marinas, and minor inundation at a number of coastal towns (Anderson, 2015). It took about 6 h to reach Hillarys in Western Australia (**Figure 8**), which is the shortest travel time among the tsunamis considered herein. The fourth wave was the largest at Hillarys and occurred a few hours after the tsunami arrival, although waves around 21 h post-earthquake were only slightly smaller (**Figure 8**). Pattiaratchi and Wijeratne (2009) noted these later waves were the largest observed at several other sites in Western Australian, and attributed them to tsunami energy reaching Australia via reflections off distant Indian Ocean topography.

At Hillarys the simulated leading waves are not strongly affected by the choice of global dissipation model (**Figure 8**). About 30 h post-earthquake the frictionless global model results in larger nearshore waves than simulations with friction, although initially it is not obvious that any model better agrees with data. However from about 36 h post-earthquake the frictionless global model consistently predicts larger nearshore waves than were observed, as seen in the previous Chile 1960 example, indicating a lack of global dissipation. At late times the models with global friction predict smaller waves and agree much better with data in the nearshore (**Figure 8**).

The data evidences some phase-lag relative to the model, as noted in the previous Chile 1960 example. For instance the modeled long-period wave around 20–23 h arrives slightly earlier than the observed wave (**Figure 8**), and a similar result is obtained with the P07 and L10 source models (see online repository). These phase-lags may be better modeled by accounting for loading, seawater density stratification, and self-gravitation (Baba et al., 2017). The neglect of wave dispersion is also likely to be significant for the Sumatra 2004 example, which shows much more short-period wave energy than the Chile 1960 example (e.g., compare **Figures 7** and **8**). Non-dispersive shallow-water wave theory will over-estimate the celerity of shorter period waves, as previously noted in the context of the 2004 Sumatra tsunami (Kulikov, 2006).

3.1.3. Twofold Bay, Tohoku 2011, S13 Source Model

The 2011 Tohoku tsunami was widely observed in eastern Australia (Hinwood and Mclean, 2013). The initial waves reached Australia's east-coast via straits around eastern Papua New Guinea, the Solomon Islands and Vanuatu, while at later times much of the wave energy arrived via the ocean north of New Zealand (Hinwood and Mclean, 2013). Our models suggest the leading wave reached South America around 20–22 h post-earthquake where it was prominently reflected into the Pacific Ocean, adding significantly to the late-time wave energy in the southwest Pacific Ocean. In eastern Australia the tide-gauges at Fort Denison and Twofold Bay exhibited late-time maxima (46–50 h post-earthquake, **Figure 9**) while gauges at Botany Bay and Port Kembla exhibited earlier maxima (18–20 h post-earthquake) but nonetheless showed relatively large late-time waves that we attribute to reflections from the eastern Pacific. This is similar to reports from New Zealand where Borrero et al. (2015a) found some sites (but not all) experienced late-time tsunami maxima up to 2 days post-earthquake.

At Twofold Bay the first few waves (up to 20 h post-earthquake) are similar in the models with frictionless and Manning-friction global grid solvers, and agree quite well with data (**Figure 9**). Linear-friction produces smaller initial waves than the Manning model, as noted for above for the Chile 1960 tsunami, which is attributed to its greater dissipation in the deep ocean. At late times the frictionless global model produces overly large waves in the nearshore compared to data (as in the previous examples). In this case the Manning and linear-friction models predict late-time waves smaller than were observed. These results again highlight the sensitivity of later waves to the global dissipation model.

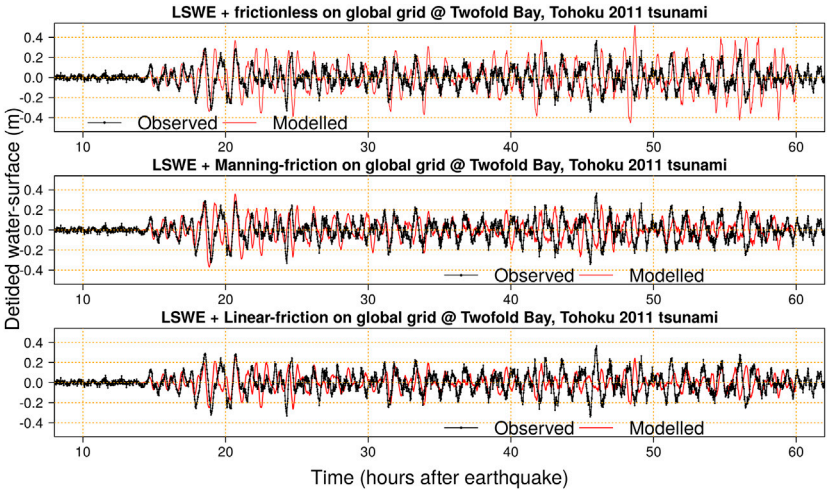

FIGURE 9 | Simulations and observations of the Tohoku 2011 tsunami at Twofold Bay. Note the observed late-time maxima 46 h post-earthquake. All simulations use the Tohoku 2011 S13 source model. Top: Using the frictionless LSWE on the global grid. Middle: Using LSWE with Manning-friction on the global grid. Bottom: Using LSWE with linear-friction on the global grid.

3.2. Effect of Global Dissipation at Nearshore Gauges: Tsunami Maxima Statistics

To compare the models and observations at all gauges simultaneously the tsunami maxima (i.e. detided water-level maxima) is used following Allen and Greenslade (2016) and Adams and LeVeque (2017). The results above suggest that model biases may be related to the simulation duration, and to assess this both simulations and data are truncated to various time-intervals (**Figure 10**):

(1) 0–8 h after the tsunami arrival. The arrival time is defined, for each model and gauge separately, as the time that the modeled stage absolute value exceeds 5×10^{-4} of its maximum, and is typically 12 h post-earthquake herein (range of 5.8–16.0 h).
(2) 0–36 h post-earthquake.
(3) 0–60 h post-earthquake.
(4) The last day of the 60 h simulation (i.e., 36–60 h post-earthquake).

All but one observed time-series extends for the full 60 h simulation; the 1960 Cronulla tide-gauge record is truncated at 29 h post-earthquake and dropped from comparison with longer simulations.

Statistics describing the model bias (G^m) and accuracy ($|G|^m$) are reported for each variation of the global model $m \in$ (Frictionless, Manning, Linear) (**Figure 10**). These emphasize the error as a fraction of the observation and deliberately weight each source inversion equally, even though they have different numbers of corresponding gauge observations, because biases in any one source-inversion will lead to correlated errors among its gauges (**Section 3.4**).

The bias statistic G^m summarizes the relative model bias (e.g., $G^m = -0.1$ suggests 10% under-estimation is typical). It is calculated as:

$$\begin{aligned} G^m &= \underset{i \in \text{source inversions}}{\text{Median}} \left(G_i^m\right) \\ G_i^m &= \underset{j \in \text{available gauge observations for source inversion } i}{\text{Median}} \left(\left(p_{i,j}^m - d_j\right)/d_j\right) \end{aligned} \quad (14)$$

Here G_i^m gives the median relative error for model m and source-inversion i ($i = 1 \ldots 12$) over all available tide-gauges j. The tide-gauges have observed tsunami maxima d_j and modeled tsunami maxima $p_{i,j}^m$.

The superscript"**" is appended to G^m values that show strong evidence of being significantly different from zero. It is applied when 10 or more of the 12 G_i^m values have the same sign. This criterion is heuristic but is motivated by the following argument: if the model m and source-inversions i have little bias on average then any G_i^m has an equal chance of being positive or negative. If all G_i^m are independent then the signs of the G_i^m behave like a binomial random variable, and with 12 source models the resulting binomial distribution (parameters $p = 0.5$, size = 12) implies a 96% chance that fewer than 10 have the same sign.

The accuracy statistic $|G|^m$ is similar to G^m, except the absolute value of the relative model error is used:

$$\begin{aligned} |G|^m &= \underset{i \in \text{source inversions}}{\text{Median}} \left(|G|_i^m\right) \\ |G|_i^m &= \underset{j \in \text{available gauge observations for source inversion } i}{\text{Median}} \left(\left|\left(p_{i,j}^m - d_j\right)/d_j\right|\right) \end{aligned} \quad (15)$$

Thus $|G|^m$ estimates the typical magnitude of the model error as a fraction of the data, irrespective of its sign.

Figure 10 highlights the interaction of the simulation duration and the model bias, most prominently for the frictionless global model. If simulations are restricted to 0–8 h following tsunami

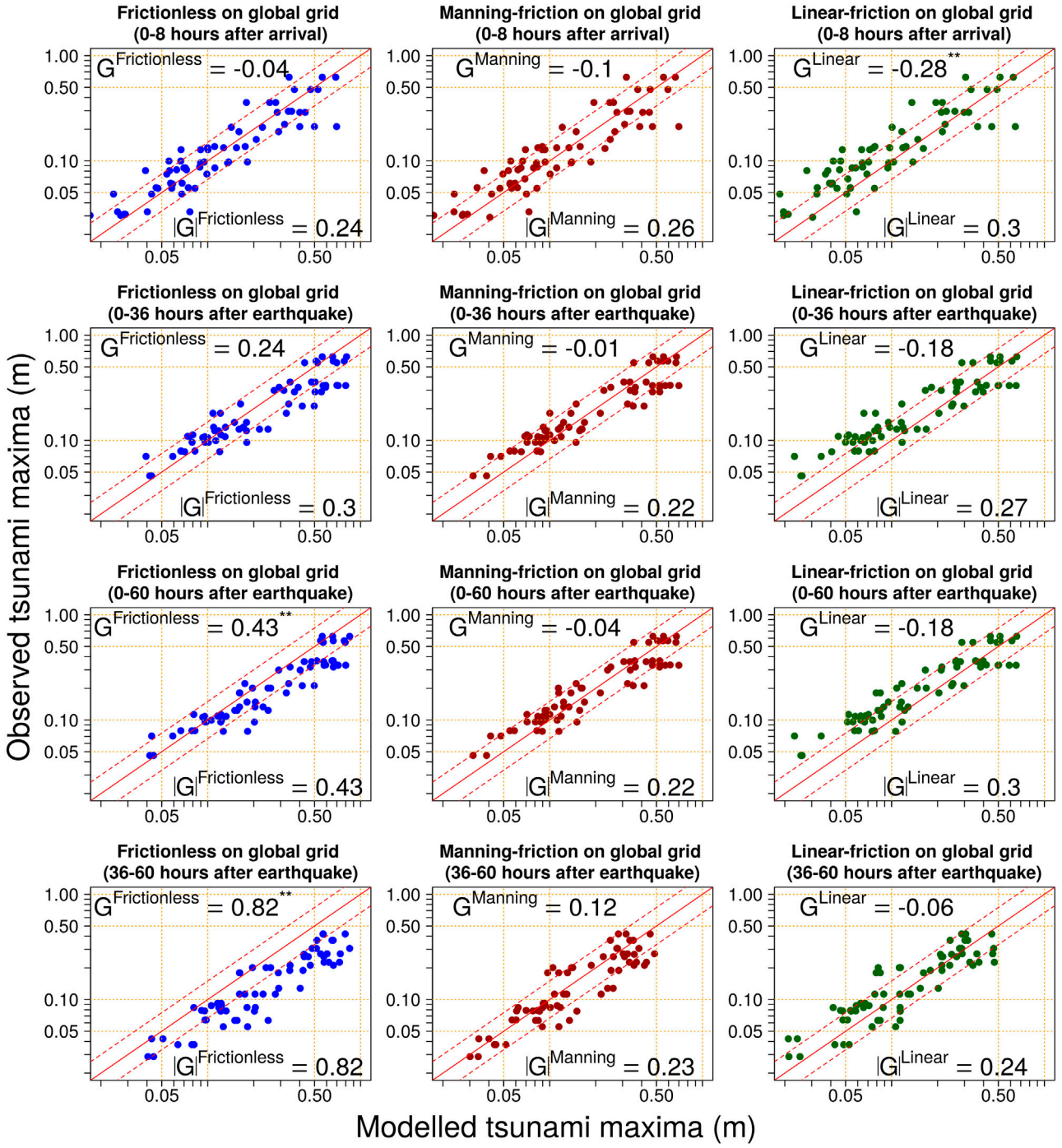

FIGURE 10 | Modelled-vs-observed tsunami maxima for different global model types (frictionless, Manning-friction, linear-friction), and different temporal subsets of the simulation (0–8 h after tsunami arrival; 0–36 h after earthquake; 0–60 h after earthquake, 36–60 h after earthquake). Diagonal solid line is $y = x$; diagonal dashed lines are $y = 1.5x$ and $y = x/1.5$. Where the G_m values are followed by **, there were 10 or more source-inversions having G_i^m values of the same sign.

arrival, this model exhibits small bias and a typical accuracy around 24% (top-left panel of **Figure 10**). For a 36 h simulation there is increasing positive bias (≃24%), which becomes pronounced in the 60 h simulation (≃43%). The frictionless model bias on the last day of 60 h simulation is very strong (≃82%), emphasizing that it consistently overestimates the size of late-arriving waves (**Section 3.1**).

Manning-friction in the global model leads to much better agreement with observed tsunami-maxima for long simulations (**Figure 10**). For short simulations (0–8 h post-arrival) it

performs similarly to the frictionless model, suggesting friction has limited influence on early arriving waves. But over long simulations the cumulative effect of nearshore dissipation at the global scale reduces the nearshore wave heights, in a manner broadly consistent with observations (**Figure 10**).

Linear-friction in the global model induces a moderate negative bias in the early (0–8 h post-arrival) nearshore tsunami maxima ($\simeq -28\%^{**}$, **Figure 10**). The constant linear-friction formulation induces greater deep-ocean dissipation than Manning-friction, and the results here suggest this dissipation is too large. However the bias weakens for longer simulations, and for the final 36–60 h post-earthquake the model performs as well as Manning-friction (**Figure 10**). Compared with the frictionless model, which shares the advantages of linearity, the constant linear-friction model is clearly superior at late times but inferior at short times (**Figure 10**).

To gauge the model accuracy it is useful to cross-reference the G^m and $|G|^m$ statistics in **Figure 10** with previous studies which compared modeled and observed tsunami maxima for multiple source-inversions. Allen and Greenslade (2016) modeled 9 historic tsunamis at Port Kembla outer-harbour with the MOST model, using source inversions based on the T2 database (Greenslade et al., 2011). From data in table 3 of Allen and Greenslade (2016) we computed $G^m = -0.1$ and $|G|^m = 0.36$. Their results at another inner-harbour site were less accurate but are not reported herein because the tide-gauge accuracy is doubtful (NSW Port Authority, personal communication 2020). Adams and LeVeque (2017) studied five source-inversions with 4–6 gauges each using two models (GEOCLAW and MOST). Using results tabulated in **Figure 3** of Adams and LeVeque (2017) we compute $G^m = -0.11,\ -0.01$ and $|G|^m = 0.375, 0.213$, respectively. Given the small number of source-inversions and gauges used in all studies, and their different methodologies, differences between these statistics are probably not meaningful. But they suggest model errors comparable to those obtained with our methodology using global-scale Manning-friction (at all times); using the global-scale frictionless model (at early times); and using global-scale linear-friction (at late times).

3.3. Alternative Linear-Friction Models With Reduced Bias for Earlier Waves

Because linear models have significant practical benefits (e.g., unit sources), herein two variations of the linear-friction model are tested. Both aim to reduce downward bias in nearshore waves 0–8 h after arrival, as compared with the constant linear-friction model, while retaining the benefits of friction for longer simulations. In addition, both models retain the convenient property that their solutions can be approximated from solutions of the frictionless model:

(1) Reduced-linear-friction. This model uses $f = 1/(36 \times 3600) \simeq 7.71 \times 10^{-6}$, corresponding to an artificially long tsunami energy e-folding timescale of 36 h (vs. 27.7 h in the original model). The 36 h decay-timescale will reduce energy loss but is *a-priori* expected to be too long, noting Rabinovich et al. (2013) empirically estimated energy-decay timescales less than 36 h (more typically 24 h) at all DART buoys which recorded the 2009 Samoa, 2010 Chile, and 2011 Tohoku tsunamis.

(2) Delayed-linear-friction. This model is frictionless for the first 12 h, and subsequently uses $f = 1 \times 10^{-5}$ as for the original linear-friction model. The heuristic motivation for an initial frictionless period is that early waves reach Australia predominantly via the deep-ocean, with few nearshore interactions, so the cumulative effect of bottom friction should initially be small. The 12 h time-period matches the median tsunami arrival time for the events studied herein (**Section 4** will consider alternative estimates of this time-period). In contrast to reduced-linear friction, this model's late-time energy-decay timescale remains broadly consistent with observations (Rabinovich et al., 2013). Solutions of this model can still be well approximated by frictionless solutions via straightforward modification of **Eq. 10**:

$$[\eta^a, uh^a, vh^a] = \exp\left(-\frac{f}{2}\mathrm{Max}\,(0, t - t_{12})\right)[\eta^0, uh^0, vh^0] \quad (16)$$

where t_{12} gives the number of seconds in 12 h. **Figure 11** compares the performance of these models and the original linear-friction model with data.

The reduced-linear-friction model continues to show downward bias for waves 0–8 h after arrival, even though its friction coefficient is *a-priori* too small (**Figure 11**). If constant linear-friction were a good approximation of dissipation for early-arriving waves, then the *a-priori* small friction coefficient should lead to overestimation of tsunami maxima, but this does not occur. That indicates weaknesses in the constant linear-friction parameterization of tsunami dissipation; friction is still too large in the deep ocean. However the model performs reasonably well for longer simulations (**Figure 11**).

In contrast, the delayed-linear-friction model performs better in the 0–8 h post-arrival period than any other linear model with friction (**Figure 11**). Furthermore, over longer simulations it continues to exhibit relatively low-bias in the tsunami maxima, with results comparable to the Manning-friction model (**Figure 10**). Among the linear models tested herein, this appears the most promising overall for simulating global-scale tsunami propagation.

3.4. Source-Inversion Effects on Modeled Tsunami Maxima

The previous section highlights that error in the modeled tsunami maxima varies from gauge-to-gauge and also depends on the simulation duration. However there is also a significant component related to the source-inversion itself (**Figure 12**). For simplicity **Figure 12** only depicts results using the Manning-friction and delayed-linear-friction global models, which exhibited the least overall bias above, although comparable variations between source-inversions exist for the other models.

For a given historical tsunami, inversions with a larger model/observed ratio in **Figure 12** tend to have greater available

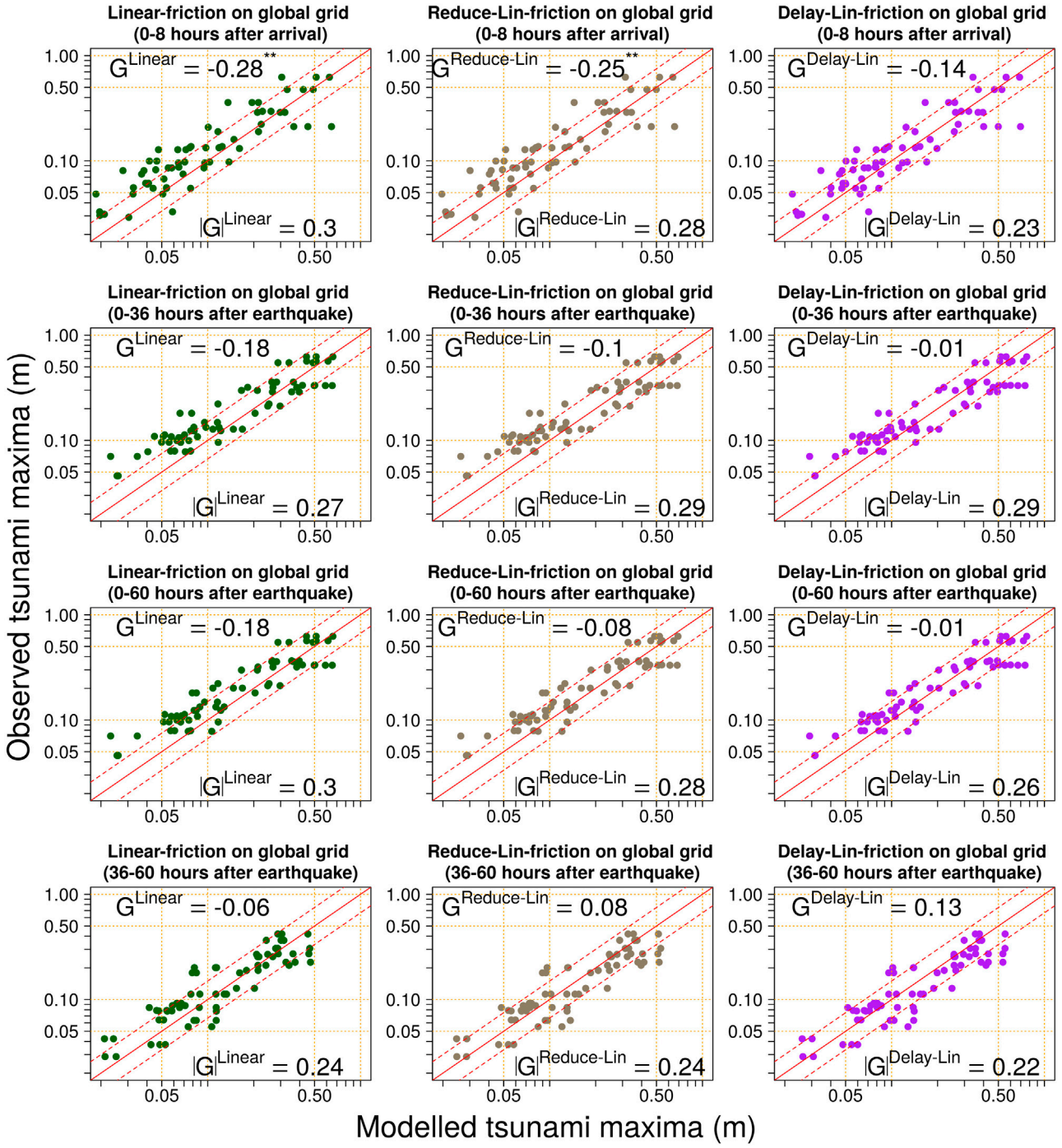

FIGURE 11 | Modelled-vs-observed tsunami maxima for different global model types (linear-friction, linear-friction with a lower friction factor, linear-friction with delayed onset of 12 h), and different temporal subsets of the simulation (0–8 h after tsunami arrival; 0–36 h after earthquake; 0–60 h after earthquake, 36–60 h after earthquake). Diagonal solid line is $y = x$; diagonal dashed lines are $y = 1.5x$ and $y = x/1.5$. The LHS column is the same as in **Figure 10**.

potential energy in their ocean-displacement (reported in **Figure 2**). For example consider the Chile 2010 tsunami; the L11 inversion produces higher model/obs ratios than the F13 inversion, while the former also exhibits greater available potential energy (**Figures 2**, **12**). For the Chile 2015 tsunami the W17 inversion exhibits greater model/obs than the R16 inversion, and has greater initial available potential energy (**Figures 2**, **12**). Other cases behave similarly with one

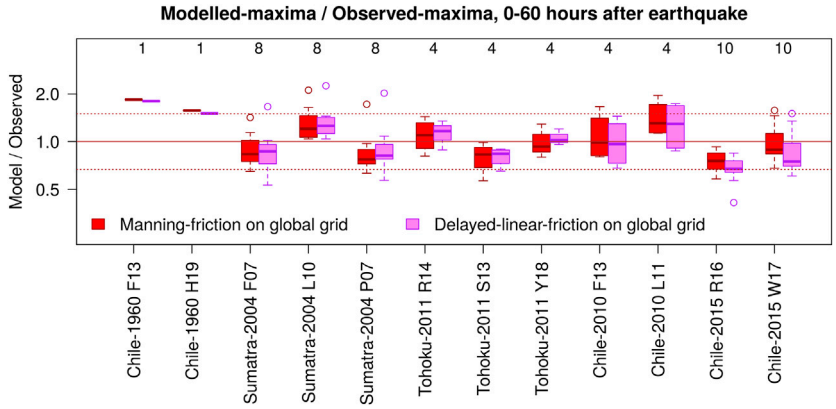

FIGURE 12 | Per-inversions boxplots of ratio between modeled and observed tsunami maxima at all gauges, for simulations of 60 h, and two model types. The integers above the boxes count the tide-gauge observations. Dotted horizontal lines are $y = 1.5$ and $y = 1/1.5$. Definition of the boxplots: The box defines the inter-quartile range with the central line defining the median. The "whiskers" extend from the box for at most 1.5 inter-quartile ranges, or up to the range of the data. Points not covered by whiskers are plotted directly. The Chile 1960 sources only have one gauge record that covers the 0–60 h simulation (**Figure 7**), so the boxplot reduces to a horizontal line.

exception; for Sumatra 2004 the P07 inversion has slightly smaller model/observed than the F07 inversion (**Figure 12**), despite having a slightly larger available potential energy (**Figure 2**). This may reflect that compared to F07, the P07 inversion has greater co-seismic displacement toward the north of the rupture area (**Figure 2**), which may have less effect on Australia than deformation in the southeast due to tsunami dynamics in the Bay of Bengal. In any case this result is consistent with the suggestion of Titov et al. (2016) that far-field tsunamis are sensitive to the location and energy of the initial ocean-surface displacement, with other source details having a secondary role.

4. DISCUSSION

Linear models provide a very convenient basis for global-scale tsunami scenario databases, and these are often implemented without friction (Burbidge et al., 2008; Li et al., 2016; Davies and Griffin, 2020). Our results suggest this approach is adequate for simulating tsunami maxima up to 8 h following tsunami arrival, when combined with nearshore models based on the NSWE with Manning-friction. Herein 8 h post-arrival corresponds to a median of 20 h post-earthquake; for hazard applications this duration would typically include the most significant waves for the most hazardous scenarios, where sites of interest are well exposed to the tsunami's leading wave. However, tsunamis may remain dangerous for a considerably longer duration. Over longer simulations the lack of global model dissipation leads to slow divergence of the frictionless model wave heights, as compared to both data and models with friction. It is difficult to estimate a "threshold" duration after which the frictionless model biases become important. In comparison to observed tsunami maxima, our results for 36 h simulations suggest bias $\simeq$24% in the frictionless model, but considering variations among the source-inversions this is not strong enough to be conclusive. However the biases are very clear in frictionless simulations of 60 h duration, especially if the model-data comparison is restricted to final 36–60 h post-earthquake.

The late-time model biases are largely removed using nonlinear Manning-friction in the global propagation model with $n = 0.035$. For simulations of 24 h duration the resulting tsunami maxima are often $\simeq$ 10% smaller than with the frictionless model, but the difference grows for longer simulations (top row of **Figure 13**). Because Manning-friction is nonlinear this approach cannot be applied using unit-sources (at least not over timescales long enough for nonlinear-dissipation to be important), but it is a good option if one can simulate the tsunami from source. From a physical perspective this model remains over-simplified; it neglects tides which will interact nonlinearly with the tsunami, and furthermore, the tidal literature suggests about one-third of tidal-dissipation occurs in the deep ocean due to mechanisms that are not represented with shallow-water bottom friction (Egbert and Ray, 2000; Buijsman et al., 2015). However we focus on pragmatic methodologies for applications, and by this standard Manning-friction is a good choice for late-time global-propagation simulation, assuming it is viable to model tsunami propagation from source.

In some instances unit-source based treatments of global tsunami propagation are essential; for example if many tsunami scenarios must be simulated for a small nearshore area, global propagation modeling may be computationally prohibitive. In such circumstances the delayed-linear friction model is worth considering, particularly for long simulation durations where biases in the frictionless model are anticipated. While not motivated from hydrodynamic theory, this model addresses the early-time bias of constant linear-

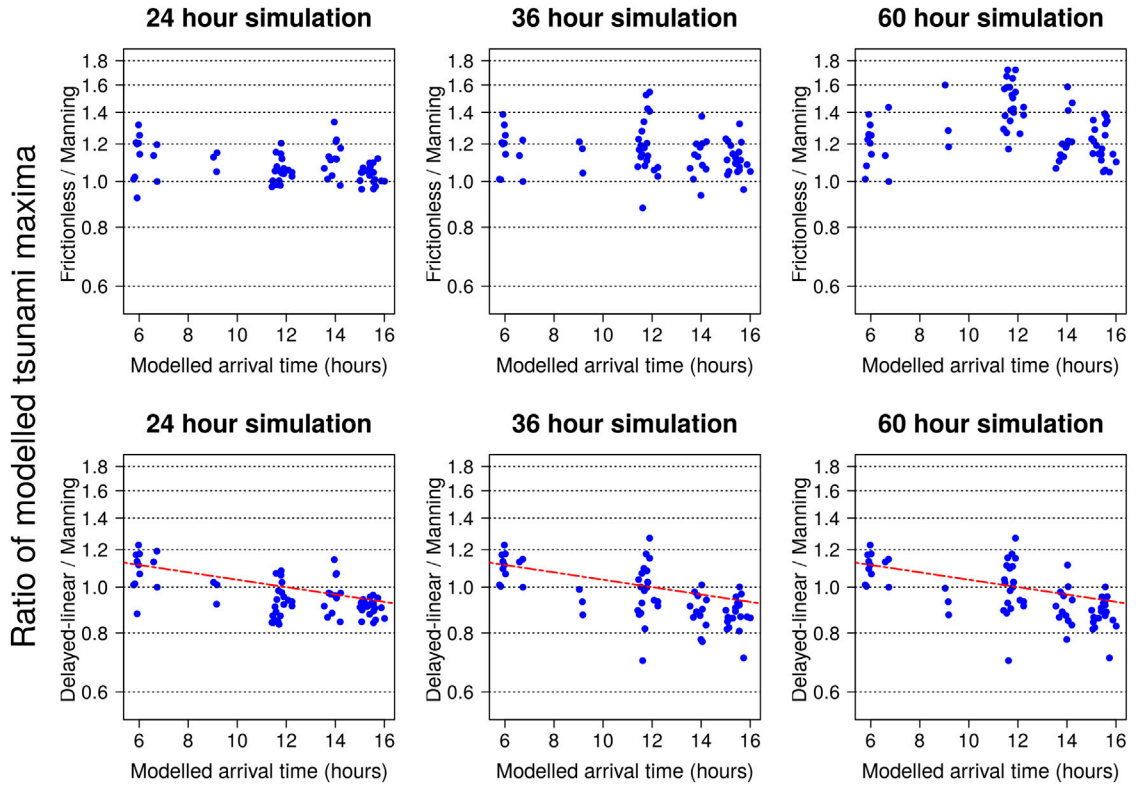

FIGURE 13 | Ratios of modeled tsunami maxima, at nearshore sites with tide-gauge data, using different offshore friction treatments: *Top row* frictionless/Manning; *Bottom row* Delayed-linear-friction/Manning-friction. In the bottom row the dashed line is $y = 1/\exp(-f\,(t_{12} - t_a)/2)$ where t_a is the modeled gauge-specific tsunami arrival time and t_{12} is the number of seconds in 12 h; this is a linear approximation of the proportionate reduction in the delayed-linear-friction tsunami maxima if the initial frictionless period was t_a instead of t_{12} (under various assumptions appropriate for our sites, as discussed in the text).

friction, which was found to underestimate observed tsunami maxima 0–8 h post-arrival. A key result of this study is that the model can be implemented, to high-accuracy, via a trivial transformation of frictionless solutions (**Eq. 16**). Thus the model is very easy to implement with existing unit-source databases based on the frictionless LSWE (e.g., Thio, 2015; Davies and Griffin, 2020).

Herein delayed-linear-friction was applied with a 12 h frictionless period (t_{12}), and it is natural to ask if this duration is optimal. **Figure 13** (bottom row) shows that while delayed-linear-friction generally predicts tsunami maxima similar to the Manning-friction model, there is a negative correlation between the modeled tsunami arrival time and the ratio of the two models (**Figure 13**). This result is expected if the Manning-friction model is better approximated using the gauge-specific arrival time t_a to define the frictionless period in **Eq. 16** rather than t_{12}, i.e.:

$$[\eta^a, uh^a, vh^a] = \exp\left(-\frac{f}{2}\mathrm{Max}\,(0, t - t_a)\right)[\eta^0, uh^0, vh^0] \quad (17)$$

One may estimate the relative change r in the tsunami maxima that would result from this approach, vs. the use of t_{12} herein, by assuming the modeled maxima responds linearly to the incoming wave. In this case r is equal to the ratio of **Eqs 16** and **17**:

$$r = \frac{\exp\left(-\frac{f}{2}\mathrm{Max}\,(0, t_M - t_a)\right)}{\exp\left(-\frac{f}{2}\mathrm{Max}\,(0, t_M - t_{12})\right)} = \exp\left(-\frac{f}{2}(t_{12} - t_a)\right) \quad \text{if} \quad t_M > t_{12} \quad \text{and} \quad t_M > t_a \quad (18)$$

where t_M indicates the timing of the offshore waves controlling the tsunami maxima. The inequality constraints in **Eq. 18** should hold for almost all of our delayed-linear-friction modeled gauge-records; only 2/68 modeled time-series in **Figure 13** have tsunami maxima arriving before 14 h post-earthquake, or less than 3 h post-tsunami-arrival; only one observed gauge maxima occurs before 18 h post-earthquake (Hillarys for Sumatra 2004; **Figure 8**). The fact that $1/r$ reasonably approximates the tsunami maxima ratio in **Figure 13** suggests that, for site-specific studies, the Manning-friction results may be better approximated with delayed-linear-friction using a "local" initial frictionless period defined by t_a. This "local" approach was not implemented herein because a wide range of sites were modeled simultaneously, each having their own t_a (**Figure 3**). However it would be straightforward to apply in site-specific studies, and merits further testing.

Finally we emphasize limitations of this study and directions for further work. All results are based on global-scale propagation models with little numerical dissipation. Clearly these techniques should not be applied to models where numerical dissipation is already comparable to or greater than the required physical dissipation, as this could exaggerate any under-estimation of late arriving waves. Our models neglect various physical processes which can affect tsunami propagation (dispersion, loading, self-gravitation, density stratification), and we make no attempt to resolve coastal inundation outside our areas of interest in Australia although this may affect remote wave reflections; future work should consider the influence of these approximations on modeled waves at the coast. Following previous work (Allen and Greenslade, 2016; Adams and LeVeque, 2017) we used the tsunami-maxima statistic to quantify model biases, and while this is useful, there is much more information available in the full time-series that may be extracted using other statistics and provide new insights into the model performance. The tests herein consider only five historic tsunamis using sources derived from 12 finite-fault inversions, with a total of 28 tide-gauge records. The testing should be extended to consider more historic events and sites, and other types of data (e.g., inundation footprints and depths; tsunami currents). Of particular interest is the global-record of historical tsunami energy-decay timescales (e.g., van Dorn, 1987; Rabinovich et al., 2011, 2013); further insights into dissipation models would likely be obtained by simulating these observations with alternative models. The tests should also be extended to consider tsunami scenarios derived for hazard assessment (Davies, 2019), including characterization of the nearshore performance of random hazard scenarios.

5. CONCLUSION

When modeling far-field tsunamis in the nearshore it is often convenient to nest high-resolution nonlinear shallow water models (which cover coastal regions of interest) within reduced-physics global-scale models (which efficiently simulate tsunami propagation). In this context we evaluated the performance of several reduced-physics global propagation models which combine the LSWE with alternative treatments of friction. Nearshore tsunamis were simulated with a nested nonlinear model and compared with coastal tide-gauge observations in Australia. Tsunami initial conditions were derived from published source-models. Our results suggest the commonly used frictionless global-scale model is adequate for simulating far-field coastal tsunamis for 0–8 h following arrival. However for sufficiently long simulations the frictionless model overestimates coastal wave heights because it is mathematically energy conservative (which is well approximated with our numerical methods) and thus does not represent global-scale tsunami dissipation. In our simulations this bias was clear from comparison with data 36–60 h post-earthquake; it is difficult to define a precise time at which the bias becomes significant. Better estimates of late-time wave heights can be obtained by appending Manning-friction to the global model, although this renders the model nonlinear. For unit-source based implementations it is preferable work with linear models, and so variants of linear-friction were tested; these are not derived from hydrodynamic theory yet can mimic observed tsunami energy decay rates. Among these, delayed-linear-friction most accurately simulated tsunami maxima at nearshore gauges. Solutions of this model can be conveniently derived by transforming frictionless LSWE solutions with **Eq. 16**, making it easy to implement via existing unit-source databases that are derived with the frictionless LSWE (e.g., Davies and Griffin, 2020). These results may facilitate improved simulation of late-time tsunami wave heights for hazard and early warning applications in the far-field.

DATA AVAILABILITY STATEMENT

The datasets presented in this study can be found in online repositories. The names of the repository/repositories and accession number(s) can be found below: https://github.com/GeoscienceAustralia/ptha/tree/master/misc/nearshore_testing_2020.

AUTHOR CONTRIBUTIONS

GD led the study design and implementation and wrote the first draft manuscript, with guidance from FR and SL. FR provided code and data to construct the sources R14 and R16. All authors contributed to the final manuscript.

ACKNOWLEDGMENTS

This paper was published with the permission of the CEO, Geoscience Australia, and was undertaken with the assistance of resources and services from the National Computational Infrastructure (NCI), which is supported by the Australian Government. Discussions with Jon Hinwood and reviews by Kaya Wilson, Phil Cummins, Alexander Rabinovich and Efim Pelinovsky improved the work. Tide-gauge data was provided by the NSW Department of Planning, Industry and Environment, Manly Hydraulics Laboratory, the NSW Port Authority, the WA Department of Transport, and the Australian Bureau of Meteorology. The elevation data was based on a range of elevation products available from ELVIS http://elevation.fsdf.org.au/, The Australian Oceans Data Network https://portal.aodn.org.au/, Ausseabed http://www.ausseabed.gov.au/data, and the WA Department of Transport https://catalogue.data.wa.gov.au/dataset/composite-surfaces-multibeam-lidar-laser.

REFERENCES

Adams, L. M., and LeVeque, R. J. (2017). Technical Report. GeoClaw model tsunamis Compared to tide gauge results, final report. University of Washington (Accessed November 3, 2017).

Allen, S. C. R., and Greenslade, D. J. M. (2016). A pilot tsunami inundation forecast system for Australia. *Pure Appl. Geophys.* 173, 3955–3971. doi:10.1007/s00024-016-1392-y

Allgeyer, S., and Cummins, P. (2014). Numerical tsunami simulation including elastic loading and seawater density stratification. *Geophys. Res. Lett.* 41, 2368–2375. doi:10.1002/2014GL059348

An, C., and Liu, P. L.-F. (2016). Analytical solutions for estimating tsunami propagation speeds. *Coastal Engg.* 117, 44–56. doi:10.1016/j.coastaleng.2016.07.006

Anderson, S. (2015). Tsunami: the ultimate guide. *Aust. J. Emerg. Manag.* 30, 24–41.

Arakawa, A., and Hsu, Y. G. (1990). Energy conserving and potential-enstrophy dissipating schemes for the shallow water equations. *Mon. Weather Rev.* 118, 1960–1969. doi:10.1175/1520-0493(1990)118<1960:ECAPED>2.0.CO;2

Audusse, E., Bouchut, F., Bristeau, M.-O., Klein, R., and Perthame, B. (2004). A fast and stable well-balanced scheme with hydrostatic reconstruction for shallow water flows. *SIAM J. Sci. Comput.* 25, 2050–2065. doi:10.1137/s1064827503431090

Baba, T., Allgeyer, S., Hossen, J., Cummins, P. R., Tsushima, H., Imai, K., et al. (2017). Accurate numerical simulation of the far-field tsunami caused by the 2011 Tohoku earthquake, including the effects of Boussinesq dispersion, seawater density stratification, elastic loading, and gravitational potential change. *Ocean Model.* 111, 46–54. doi:10.1016/j.ocemod.2017.01.002

Baba, T., Takahashi, N., Kaneda, Y., Ando, K., Matsuoka, D., and Kato, T. (2015). Parallel implementation of dispersive tsunami wave modeling with a nesting algorithm for the 2011 tohoku tsunami. *Pure Appl. Geophys.* 172, 3455–3472. doi:10.1007/s00024-015-1049-2

Baba, T., Takahashi, N., Kaneda, Y., Inazawa, Y., and Kikkojin, M. (2014). "Tsunami inundation modeling of the 2011 tohoku earthquake using three-dimensional building data for Sendai, Miyagi prefecture, Japan," in *Tsunami events and lessons learned*. Editors Y. A. Kontar, T. Takahashi, and V. Santiago-Fandino (Amsterdam: Springer).

Beccari, B. (2009). Technical Report. Measurements and impacts of the Chilean tsunami of may 1960 in new south wales, Australia. NSW State Emergency Service.

Behrens, J., and Dias, F. (2015). New computational methods in tsunami science. *Philos. Trans. R. Soc. London A* 373, 20140382. doi:10.1098/rsta.2014.0382

Borrero, J. C., Goring, D. G., Greer, S. D., and Power, W. L. (2015a). Far-field tsunami hazard in New Zealand ports. *Pure Appl. Geophys.* 172, 731–756. doi:10.1007/s00024-014-0987-4

Borrero, J. C., Lynett, P. J., and Kalligeris, N. (2015b). Tsunami currents in ports. *Phil. Trans. Math. Phys. Eng. Sci.* 373, 20140372. doi:10.1098/rsta.2014.0372

Buijsman, M., Arbic, B., Green, J., Helber, R., Richman, J., Shriver, J., et al. (2015). Optimizing internal wave drag in a forward barotropic model with semidiurnal tides. *Ocean Model.* 85, 42–55. doi:10.1016/j.ocemod.2014.11.003

Burbidge, D., Cummins, P., Mleczko, R., and Thio, H. (2008). A probabilistic tsunami hazard assessment for western Australia. *Pure Appl. Geophys.* 165, 2059–2088. doi:10.1007/s00024-008-0421-x

Choi, B. H., Pelinovsky, E., Kim, K. O., and Lee, J. S. (2003). Simulation of the trans-oceanic tsunami propagation due to the 1883 krakatau volcanic eruption. *Nat. Hazards Earth Syst. Sci.* 3, 321–332. doi:10.5194/nhess-3-321-2003

Davies, G., Griffin, J., Løvholt, F., Glimsdal, S., Harbitz, C., Thio, H. K., et al. (2017). A global probabilistic tsunami hazard assessment from earthquake sources. *Geol. Soc. London Spec. Publ.* 456, 219–244. doi:10.1144/sp456.5

Davies, G., and Griffin, J. (2018). Technical Report, Geoscience Australia Record 2018/41. The 2018 Australian probabilistic tsunami hazard assessment: hazards from earthquake generated tsunamis. doi:10.11636/Record.2018.041

Davies, G., and Griffin, J. (2020). Sensitivity of probabilistic tsunami hazard assessment to far-field earthquake slip complexity and rigidity depth-dependence: case study of Australia. *Pure Appl. Geophys.* 177, 1521–1548. doi:10.1007/s00024-019-02299-w

Davies, G., and Roberts, S. (2015). Open source flood simulation with a 2D discontinuous-elevation hydrodynamic model. *Proc. of MODSIM 2015, GoldCoast.* doi:10.36334/modsim.2015.l5.davies.

Davies, G. (2019). Tsunami variability from uncalibrated stochastic earthquake models: tests against deep ocean observations 2006-2016. *Geophys. J. Int.* 218, 1939–1960. doi:10.1093/gji/ggz260

Egbert, G. D., and Erofeeva, S. Y. (2002). Efficient inverse modeling of barotropic ocean tides. *J. Atmos. Ocean. Technol.* 19, 183–204. doi:10.1175/1520-0426(2002)019〈0183:EIMOBO〉2.0.CO;2

Egbert, G. D., and Ray, R. D. (2000). Significant dissipation of tidal energy in the deep ocean inferred from satellite altimeter data. *Nature* 405, 775–778. doi:10.1038/35015531

Fine, I. V., Kulikov, E. A., and Cherniawsky, J. Y. (2013). Japans 2011 tsunami: characteristics of wave propagation from observations and numerical modelling. *Pure Appl. Geophys.* 170, 1295–1307. doi:10.1007/s00024-012-0555-8

Fjordholm, U. S., Mishra, S., and Tadmor, E. (2011). Well-balanced and energy stable schemes for the shallow water equations with discontinuous topography. *J. Comput. Phys.* 230, 5587–5609. doi:10.1016/j.jcp.2011.03.042

Fritz, H. M., and Borrero, J. C. (2006). Somalia field survey after the december 2004 Indian ocean tsunami. *Earthq. Spectra.* 22, 219–233. doi:10.1193/1.2201972

Fujii, Y., and Satake, K. (2007). Tsunami source of the 2004 sumatra-andaman earthquake inferred from tide gauge and satellite data. *Bull. Seismol. Soc. Am.* 97, S192. doi:10.1785/0120050613

Fujii, Y., and Satake, K. (2013). Slip distribution and seismic moment of the 2010 and 1960 Chilean earthquakes inferred from tsunami waveforms and coastal geodetic data. *Pure Appl. Geophys.* 170, 1493–1509. doi:10.1007/s00024-012-0524-2

Geist, E. (2009). Phenomenology of tsunamis: statistical properties from generation to runup. *Adv. Geophys.* 51, 107–169. doi:10.1016/S0065-2687(09)05108-5

Gica, E., Spillane, M. C., Titov, V. V., Chamberlin, C. D., and Newman, J. C. (2008). Technical Report No. 139. Development of the forecast propagation database for NOAA's short-term inundation forecast for tsunamis (SIFT). NOAA Technical Memorandum OAR PMEL, Seattle, WA.

Glimsdal, S., Pedersen, G., Harbitz, C., and Løvholt, F. (2013). Dispersion of tsunamis: does it really matter? *Nat. Hazards Earth Syst. Sci.* 13, 1507–1526. doi:10.5194/nhess-13-1507-2013

Goto, C., and Ogawa, Y. (1997). Technical Report No. 35. Numerical method of tsunami simulation with the leap-frog scheme. IUGG/IOC Time Project.

Greenslade, D. J. M., Allen, S. C. R., and Simanjuntak, M. A. (2011). An evaluation of tsunami forecasts from the T2 scenario database. *Pure Appl. Geophys.* 168, 1137–1151. doi:10.1007/s00024-010-0229-3

Grezio, A., Babeyko, A., Baptista, M. A., Behrens, J., Costa, A., Davies, G., et al. (2017). Probabilistic tsunami hazard analysis: multiple sources and global applications. *Rev. Geophys.* 55, 1158–1198. doi:10.1002/2017RG000579.2017RG000579

Heidarzadeh, M., Satake, K., Takagawa, T., Rabinovich, A., and Kusumoto, S. (2018). A comparative study of far-field tsunami amplitudes and ocean-wide propagation properties: insight from major trans-Pacific tsunamis of 2010-2015. *Geophys. J. Int.* 215, 22–36. doi:10.1093/gji/ggy265

Hinwood, J. B., and Mclean, E. J. (2013). Effects of the march 2011 Japanese tsunami in bays and estuaries of SE Australia. *Pure Appl. Geophys.* 170, 1207–1227. doi:10.1007/s00024-012-0561-x

Ho, T.-C., Satake, K., Watada, S., and Fujii, Y. (2019). Source estimate for the 1960 Chile earthquake from joint inversion of geodetic and transoceanic tsunami data. *J. Geophys. Res. Solid Earth.* 124, 2812–2828. doi:10.1029/2018JB016996

Kânoğlu, U., Titov, V., Bernard, E., and Synolakis, C. (2015). Tsunamis: bridging science, engineering and society. *Philos. Trans. R. Soc. London.* 373, 20140369. doi:10.1098/rsta.2014.0369

Kajiura, K. (1963). The leading wave of a tsunami. *Bull. Earthq. Res. Inst.* 41, 535–571.

Kleermaeker, S. D., Apecechea, M. I., Verlaan, M., Mortlock, T., and Rego, J. L. (2019). "Global-to-local scale storm surge modelling: operational forecasting and model sensitivities," in Australasian coasts & ports 2019 conference, Hobart, September 10–13, 2019.

Kowalik, Z., Horrillo, J., Knight, W., and Logan, T. (2008). Kuril Islands tsunami of november 2006: 1. Impact at crescent city by distant scattering. *J. Geophys. Res.* 113, C01020. doi:10.1029/2007JC004402

Kulikov, E. A., Fine, I. V., and Yakovenko, O. I. (2014). Numerical modeling of the long surface waves scattering for the 2011 Japan tsunami: case study. *Izvestiya Atmos. Ocean. Phys.* 50, 498–507. doi:10.1134/S0001433814050053

Kulikov, E. (2006). Dispersion of the Sumatra Tsunami waves in the Indian Ocean detected by satellite altimetry. *Russ. J. Earth Sci.* 8, 1–5. doi:10.2205/2006es000214

Li, L., Switzer, A. D., Chan, C.-H., Wang, Y., Weiss, R., and Qiu, Q. (2016). How heterogeneous coseismic slip affects regional probabilistic tsunami hazard assessment: a case study in the South China Sea. *J. Geophys. Res. Solid Earth.* 121, 6250–6272. doi:10.1002/2016JB013111. 2016JB013111

Liu, P. L. F., Cho, Y.-S., Briggs, M. J., Kanoglu, U., and Synolakis, C. E. (1995). Runup of solitary waves on a circular island. *J. Fluid Mech.* 302, 259–285. doi:10.1017/S0022112095004095

Liu, Y., Shi, Y., Yuen, D. A., Sevre, E. O. D., Yuan, X., and Xing, H. L. (2008). Comparison of linear and nonlinear shallow wave water equations applied to tsunami waves over the China sea. *Acta Geotechnica.* 4, 129–137. doi:10.1007/s11440-008-0073-0

Llewellyn Smith, S. G., and Young, W. R. (2002). Conversion of the barotropic tide. *J. Phys. Oceanogr.* 32, 1554–1566. doi:10.1175/1520-0485(2002)032⟨1554:COTBT⟩2.0.CO;2

Lorenz, E. N. (1955). Available potential energy and the maintenance of the general circulation. *Tellus* 7, 157–167. doi:10.1111/j.2153-3490.1955.tb01148.x

Lorito, S., Piatanesi, A., Cannelli, V., Romano, F., and Melini, D. (2010). Kinematics and source zone properties of the 2004 Sumatra-Andaman earthquake and tsunami: nonlinear joint inversion of tide gauge, satellite altimetry, and GPS data. *J. Geophys. Res.* 115, B02304. doi:10.1029/2008jb005974

Lorito, S., Romano, F., Atzori, S., Tong, X., Avallone, A., McCloskey, J., et al. (2011). Limited overlap between the seismic gap and coseismic slip of the great 2010 Chile earthquake. *Nat. Geosci.* 4, 173–177. doi:10.1038/ngeo1073

Lorito, S., Selva, J., Basili, R., Romano, F., Tiberti, M., and Piatanesi, A. (2015). Probabilistic hazard for seismically induced tsunamis: accuracy and feasibility of inundation maps. *Geophys. J. Int.* 200, 574–588. doi:10.1093/gji/ggu408

Macías, J., Castro, M. J., Ortega, S., and González-Vida, J. M. (2020). Performance assessment of Tsunami-HySEA model for NTHMP tsunami currents benchmarking. Field cases. *Ocean Model.* 152, 101645. doi:10.1016/j.ocemod.2020.101645

Meade, B. J. (2007). Algorithms for the calculation of exact displacements, strains, and stresses for triangular dislocation elements in a uniform elastic half space. *Comput. Geosci.* 33, 1064–1075. doi:10.1016/j.cageo.2006.12.003

Miller, G. R., Munk, W. H., and Snodgrass, F. E. (1962). Long-period waves over California's continental borderland part ii. tsunamis. *J. Mar. Res.* 20, 31–41.

Miranda, J. M., Baptista, M. A., and Omira, R. (2014). On the use of Green's summation for tsunami waveform estimation: a case study. *Geophys. J. Int.* 199, 459–464. doi:10.1093/gji/ggu266

Mofjeld, H. O., González, F. I., Bernard, E. N., and Newman, J. C. (2000). Forecasting the heights of later waves in pacific-wide tsunamis. *Nat. Hazards.* 22, 71–89. doi:10.1023/A:1008198901542

Molinari, I., Tonini, R., Lorito, S., Piatanesi, A., Romano, F., Melini, D., et al. (2016). Fast evaluation of tsunami scenarios: uncertainty assessment for a Mediterranean Sea database. *Nat. Hazards Earth Syst. Sci.* 16, 2593–2602. doi:10.5194/nhess-16-2593-2016

Munk, W. (1963). "Some comments regarding diffusion and absorption of tsunamis," in Proceedings Tsunami Meetings, Tenth Pacific Science Congress, Honolulu (IUGG Monograph), Vol. 24, 53–72.

Munk, W. (1997). Once again: once again—tidal friction. *Prog. Oceanogr.* 40, 7–35. doi:10.1016/S0079-6611(97)00021-9

NCI (2020). [Dataset] National computational infrastructure hpc systems. Available at:https://nci.org.au/our-systems/hpc-systems.

NTHMP(2012). Technical Report. Proceedings and results of the 2011 NTHMP model benchmarking workshop. National Tsunami Hazard Mitigation Program, NOAA Special Report.

Nyland, D., and Huang, P. (2013). Forecasting wave amplitudes after the arrival of a tsunami. *Pure Appl. Geophys.* 171, 3501–3513. doi:10.1007/s00024-013-0703-9

Oh, I., and Rabinovich, A. (1994). Manifestation of hokkaido southwest (okushiri) tsunami 12 July, 1993, at the coast of korea. *Sci. Tsunami Hazards.* 12, 93–116.

Okada, Y. (1985). Surface deformation due to shear and tensile faults in a half-space. *Bull. Seismol. Soc. Am.* 75, 1135–1154.

Okal, E. A. (2011). Tsunamigenic earthquakes: past and present milestones. *Pure Appl. Geophys.* 168, 969–995. doi:10.1007/s00024-010-0215-9

Pattiaratchi, C., and Wijeratne, E. M. S. (2009). Tide gauge observations of 2004-2007 Indian Ocean tsunamis from Sri Lanka and Western Australia. *Pure Appl. Geophys.* 166, 233–258. doi:10.1007/s00024-008-0434-5

Percival, D. M., Percival, D. B., Denbo, D. W., Gica, E., Huang, P. Y., Mofjeld, H. O., et al. (2014). Automated tsunami source modeling using the sweeping window positive elastic net. *J. Am. Stat. Assoc.* 109, 491–499. doi:10.1080/01621459.2013.879062

Piatanesi, A., and Lorito, S. (2007). Rupture process of the 2004 sumatra–andaman earthquake from tsunami waveform inversion. *Bull. Seismol. Soc. Am.* 97, S223–S231. doi:10.1785/0120050627

Popinet, S. (2011). Quadtree-adaptive tsunami modelling. *Ocean Dynam.* 61, 1261–1285. doi:10.1007/s10236-011-0438-z

Rabinovich, A. B., Candella, R. N., and Thomson, R. E. (2011). Energy decay of the 2004 Sumatra tsunami in the world ocean. *Pure Appl. Geophys.* 168, 1919–1950. doi:10.1007/s00024-011-0279-1

Rabinovich, A. B., Candella, R. N., and Thomson, R. E. (2013). The open ocean energy decay of three recent trans-pacific tsunamis. *Geophys. Res. Lett.* 40, 3157–3162. doi:10.1002/grl.50625

Romano, F., Piatanesi, A., Lorito, S., Tolomei, C., Atzori, S., and Murphy, S. (2016). Optimal time alignment of tide-gauge tsunami waveforms in nonlinear inversions: application to the 2015 Illapel (Chile) earthquake. *Geophys. Res. Lett.* 43, 11226–11235. doi:10.1002/2016GL071310. 2016GL071310

Romano, F., Trasatti, E., Lorito, S., Piromallo, C., Piatanesi, A., Ito, Y., et al. (2014). Structural control on the Tohoku earthquake rupture process investigated by 3D FEM, tsunami and geodetic data. *Sci. Rep.* 4, 5631. doi:10.1038/srep05631

Saito, T., Inazu, D., Miyoshi, T., and Hino, R. (2014). Dispersion and nonlinear effects in the 2011 Tohoku-oki earthquake tsunami. *J. Geophys. Res. Oceans.* 119, 5160–5180. doi:10.1002/2014jc009971

Satake, K., Fujii, Y., Harada, T., and Namegaya, Y. (2013). Time and space distribution of coseismic slip of the 2011 tohoku earthquake as inferred from tsunami waveform data. *Bull. Seismol. Soc. Am.* 103, 1473–1492. doi:10.1785/0120120122

Satake, K., Okada, M., and Abe, K. (1988). Tide gauge response to tsunamis: measurements at 40 tide gauge stations in Japan. *J. Mar. Res.* 46, 557–571. doi:10.1357/002224088785113504

Setiyono, U., Gusman, A. R., Satake, K., and Fujii, Y. (2017). Pre-computed tsunami inundation database and forecast simulation in Pelabuhan Ratu, Indonesia. *Pure Appl. Geophys.* 174, 3219–3235. doi:10.1007/s00024-017-1633-8

Shuto, N. (1991). Numerical simulation of tsunamis—its present and near future. *Nat. Hazards.* 4, 171–191. doi:10.1007/BF00162786

Tang, L., Titov, V. V., Bernard, E. N., Wei, Y., Chamberlin, C. D., Newman, J. C., et al. (2012). Direct energy estimation of the 2011 Japan tsunami using deep-ocean pressure measurements. *J. Geophys. Res.: Oceans.* 117, C08008. doi:10.1029/2011JC007635

Tang, L., Titov, V. V., and Chamberlin, C. D. (2009). Development, testing, and applications of site-specific tsunami inundation models for real-time forecasting. *J. Geophys. Res.* 114, C12025. doi:10.1029/2009JC005476

Tanioka, Y., and Satake, K. (1996). Tsunami generation by horizontal displacement of ocean bottom. *Geophys. Res. Lett.* 23, 861–864. doi:10.1029/96GL00736

Thio, H. (2015). "Tsunami hazards of the pacific rim," in Proceedings of the 10th pacific conference on earthquake engineering, Sydney, November 6–8, 2015

Titov, V., Song, Y. T., Tang, L., Bernard, E. N., Bar-Sever, Y., and Wei, Y. (2016). Consistent estimates of tsunami energy show promise for improved early warning. *Pure Appl. Geophys.* 173, 3863–3880. doi:10.1007/s00024-016-1312-1

Tolkova, E. (2014). Land-water boundary treatment for a tsunami model with dimensional splitting. *Pure Appl. Geophys.* 171, 2289–2314. doi:10.1007/s00024-014-0825-8

Tolkova, E. (2015). Tsunami penetration in tidal rivers, with observations of the Chile 2015 tsunami in rivers in Japan. *Pure Appl. Geophys.* 173, 389–409. doi:10.1007/s00024-015-1229-0

van Dorn, W. G. (1984). Some tsunami characteristics deducible from tide records. *J. Phys. Oceanogr.* 14, 353–363. doi:10.1175/1520-0485(1984)014⟨0353:STCDFT⟩2.0.CO;2

van Dorn, W. G. (1987). Tide gauge response to tsunamis. part 2: other oceans and smaller seas. *J. Phys. Oceanogr.* 17, 1507–1516. doi:10.1175/1520-0485(1987)017<1507:TGRTTP>2.0.CO;2

Volpe, M., Lorito, S., Selva, J., Tonini, R., Romano, F., and Brizuela, B. (2019). From regional to local SPTHA: efficient computation of probabilistic tsunami inundation maps addressing near-field sources. *Nat. Hazards Earth Syst. Sci.* 19, 455–469. doi:10.5194/nhess-19-455-2019

Watada, S., Kusumoto, S., and Satake, K. (2014). Traveltime delay and initial phase reversal of distant tsunamis coupled with the self-gravitating elastic earth. *J. Geophys. Res. Solid Earth.* 119, 4287–4310. doi:10.1002/2013jb010841

Weatherall, P., Marks, K. M., Jakobsson, M., Schmitt, T., Tani, S., Arndt, J. E., et al. (2015). A new digital bathymetric model of the world's oceans. *Earth Space Sci.* 2, 331–345. doi:10.1002/2015EA000107

Whiteway, T. (2009). Technical Report, Geoscience Australia Record 2009/21. Australian bathymetry and topography grid, June 2009.

Williamson, A., Newman, A., and Cummins, P. (2017). Reconstruction of coseismic slip from the 2015 Illapel earthquake using combined geodetic and tsunami waveform data. *J. Geophys. Res.* 122, 2119–2130. doi:10.1002/2016JB013883

Wilson, K. M., Allen, S. C. R., and Power, H. E. (2018). The tsunami threat to Sydney Harbour, Australia: modelling potential and historic events. *Sci. Rep.* 8, 15045. doi:10.1038/s41598-018-33156-w

Wilson, K. M., and Power, H. E. (2018). Seamless bathymetry and topography datasets for new south wales, Australia. *Scientific Data.* 5, 180115. doi:10.1038/sdata.2018.115

Yamazaki, Y., Cheung, K. F., and Lay, T. (2018). A self-consistent fault slip model for the 2011 tohoku earthquake and tsunami. *J. Geophys. Res. Solid Earth.* 123, 1435–1458. doi:10.1002/2017JB014749

Yue, H., Lay, T., Li, L., Yamazaki, Y., Cheung, K. F., Rivera, L., et al. (2015). Validation of linearity assumptions for using tsunami waveforms in joint inversion of kinematic rupture models: application to the 2010 MentawaiMw7.8 tsunami earthquake. *J. Geophys. Res. Solid Earth.* 120, 1728–1747. doi:10.1002/2014jb011721

Zhang, X., and Niu, X. (2020). Probabilistic tsunami hazard assessment and its application to southeast coast of Hainan Island from Manila Trench. *Coastal Engg.* 155, 103596. doi:10.1016/j.coastaleng.2019.103596

Conflict of Interest: The authors declare that the research was conducted in the absence of any commercial or financial relationships that could be construed as a potential conflict of interest.

frontiers in Earth Science

ORIGINAL RESEARCH
published: 09 November 2020
doi: 10.3389/feart.2020.592444

Multi-Hazard Portfolio Loss Estimation for Time-Dependent Shaking and Tsunami Hazards

Katsuichiro Goda[1,2]*

[1]Department of Earth Sciences, Western University, London, ON, Canada, [2]Department of Statistical and Actuarial Sciences, Western University, London, ON, Canada

Megathrust subduction earthquakes generate intense ground shaking and massive tsunami waves, posing major threat to coastal communities. The occurrence of such devastating seismic events is uncertain and depends on their recurrence characteristics (e.g., inter-arrival time distribution and parameters) as well as elapsed time since the last major event. Current standard probabilistic loss models for earthquakes and tsunamis are based on a time-independent Poisson process and uniform earthquake slip distribution. Thereby, considerations of more realistic time-dependent earthquake occurrence and heterogeneous earthquake slip distribution are necessary. This study presents an innovative computational framework for conducting a time-dependent multi-hazard loss estimation of a building portfolio subjected to megathrust subduction earthquakes and tsunamis. The earthquake occurrence is represented by a set of multiple renewal models, which are implemented using a logic-tree approach, whereas earthquake rupture characterization is based on stochastic source models with variable fault geometry and heterogeneous slip distribution. By integrating these hazard components with seismic and tsunami fragility functions, multi-hazard loss potential for a coastal community can be evaluated quantitatively by considering different possibilities of earthquake recurrence and rupture characteristics. To demonstrate the implementation of the developed time-dependent multi-hazard loss model, the Tohoku region of Japan is considered.

Keywords: strong shaking, tsunami, building portfolio, multi-hazard loss estimation, megathrust subduction earthquake, time-dependent earthquake occurrence

OPEN ACCESS

Edited by:
Finn Løvholt,
Norwegian Geotechnical Institute, Norway

Reviewed by:
Qi Yao,
China Earthquake Networks Center, China
Mario Andres Salgado-Gálvez, International Center for Numerical Methods in Engineering, Spain

***Correspondence:**
Katsuichiro Goda
kgoda2@uwo.ca

Specialty section:
This article was submitted to Geohazards and Georisks, a section of the journal Frontiers in Earth Science

Received: *07 August 2020*
Accepted: *09 October 2020*
Published: *09 November 2020*

Citation:
Goda K (2020) Multi-Hazard Portfolio Loss Estimation for Time-Dependent Shaking and Tsunami Hazards. Front. Earth Sci. 8:592444. doi: 10.3389/feart.2020.592444

INTRODUCTION

Quantitative multi-hazard loss estimation against major earthquakes and tsunamis is essential to make effective risk management decisions in seismic regions where risk potential due to megathrust subduction earthquakes is significant. Buildings and infrastructures located in coastal areas are exposed to a sequence of shaking-tsunami hazards (Maeda et al., 2013; Selva et al., 2016). As a result, catastrophic damage and loss may be caused (Kajitani et al., 2013; Daniell et al., 2017). Shaking damage occurs widely in space, while tsunami damage is localized in coastal areas (Goda and De Risi, 2018; Park et al., 2019). For quantifying financial risks, it is important to consider the multi-hazard loss generation process because the damage patterns for shaking and tsunami are different.

Earthquake occurrence is one of the most influential components in probabilistic seismic hazard analysis (PSHA) and probabilistic tsunami hazard analysis (PTHA) (Parsons and Geist, 2008; Field

and Jordan, 2015; Grezio et al., 2017). It is common to shaking and tsunami hazards and thus impacts both assessments simultaneously. A standard model for earthquake occurrence is a homogeneous Poisson process, which is typically combined with a Gutenberg-Richter (G-R) magnitude recurrence relationship in PSHA and PTHA. In recent years, applying non-Poissonian and quasi-periodic earthquake occurrence models to well-defined fault systems and subduction earthquakes has become more popular (Ogata, 1999; Ceferino et al., 2020). In particular, a renewal process is capable of characterizing the evolution of occurrence probability with time in terms of inter-arrival time distribution of earthquakes and is suitable to conduct time-dependent hazard and risk assessments (Goda and Hong, 2006). Popular inter-arrival time distributions include the lognormal distribution, Brownian Passage Time (BPT) distribution (Matthews et al., 2002), and Weibull distribution (Abaimov et al., 2008), whereas a homogeneous Poisson process corresponds to the exponential distribution with a constant occurrence rate. Typically, the inter-arrival time distribution is characterized by three parameters: mean recurrence time, coefficient of variation (CoV) of occurrence time (also referred to as aperiodicity), and elapsed time since the previous event. These models can be used to calculate the occurrence probabilities of major earthquakes over a period of interest.

Moreover, earthquake source characterization has major influence on both shaking and tsunami hazard assessments. In the context of empirical ground motion modeling, variable geometry and location of an earthquake rupture plane affect the calculation of source-to-site distances significantly when the earthquake size is large (Goda and Atkinson, 2014). On the other hand, realistic modeling of heterogeneous earthquake slips (asperities) has significant impact on ground motion simulations (Pitarka et al., 2017; Frankel et al., 2018) and tsunami hazard assessments (Mueller et al., 2015; Li et al., 2016; Melgar et al., 2019). Stochastic source modeling methods (Goda et al., 2014), combined with probabilistic earthquake source scaling relationships (Goda et al., 2016), have major advantages over uniform slip methods with fixed fault geometry by capturing the effects of earthquake source uncertainties.

With regard to the earthquake occurrence and source modeling approaches, Goda (2019) combined the renewal model with the stochastic source modeling method to conduct a time-dependent PTHA for a single location in the Tohoku region of Japan. On the other hand, Goda and De Risi (2018) extended probabilistic seismic-tsunami hazard analysis to multi-hazard seismic-tsunami loss estimation for a building portfolio, but their modeling was based on a time-independent Poisson process. To enable quantitative multi-hazard risk assessments of coastal communities that face time-dependent seismic-tsunami hazards, time-dependent earthquake occurrence, variable earthquake source, and multi-hazard loss to properties in coastal areas need to be integrated into a consistent numerical modeling framework.

This study addresses the above-mentioned research gap by developing a novel multi-hazard earthquake-tsunami catastrophe model of residential houses in a coastal community subject to time-dependent occurrence of megathrust subduction earthquakes. The main objective of this study is to investigate the effects of considering different renewal and magnitude models, in comparison with the conventional time-dependent models. For this purpose, an earthquake occurrence model, consisting of temporal renewal and magnitude recurrence models, is considered, whereas stochastic source models with variable geometry and heterogeneous slip distribution are incorporated to quantify the uncertainty associated with earthquake rupture characteristics. Multiple earthquake occurrence models are considered by implementing them using a logic tree (Fukutani et al., 2015; Marzocchi et al., 2015), enabling more comprehensive characterization of epistemic uncertainties for shaking and tsunami hazards. Subsequently, ground motion intensities and tsunami inundations in coastal areas are evaluated *via* Monte Carlo simulations by propagating uncertain earthquake occurrence and source effects into multi-hazard damage assessment and loss estimation. The final outputs from the developed tool include single-hazard as well as multi-hazard loss exceedance probability curves and related risk metrics (e.g., annual expected loss and value at risk). To demonstrate the effects of different earthquake occurrence and slip models on multi-hazard loss curves, a case study for residential wooden houses in Miyagi Prefecture, Japan is set up. This case study is relevant because the *M*9.0 Tohoku earthquake and tsunami occurred in 2011. One may consider that the accumulated earthquake stress/strain over the past years prior to 2011 were released and thus renewal-type earthquake occurrence models may be more applicable to the current situation than Poisson-type models.

The paper is organized as follows. *Multi-Hazard Portfolio Loss Model for Time-dependent Shaking and Tsunami Hazards* presents a computational methodology to carry out time-dependent earthquake-tsunami loss estimation using stochastic rupture sources. An overall computational framework is introduced in *Computational Framework*, followed by more detailed descriptions of the earthquake occurrence model and the conditional loss distribution in *Earthquake Occurrence Model* and *Conditional Multi-Hazard Loss Distribution*, respectively. Subsequently, numerical cases are set up in *Numerical Calculation Set-Up*. Results for time-independent loss estimation are discussed in *Time-independent Multi-Hazard Loss Estimation*. Sensitivity of multi-hazard loss estimation results to the occurrence model components and earthquake slip characterization is investigated in *Sensitivity Analysis of Time-Dependent Multi-Hazard Loss Estimation*, whereas in *Logic-Tree Analysis of Time-Dependent Multi-Hazard Loss Estimation*, multiple occurrence models are implemented in a logic tree to quantify some of major epistemic uncertainties associated with the loss estimation.

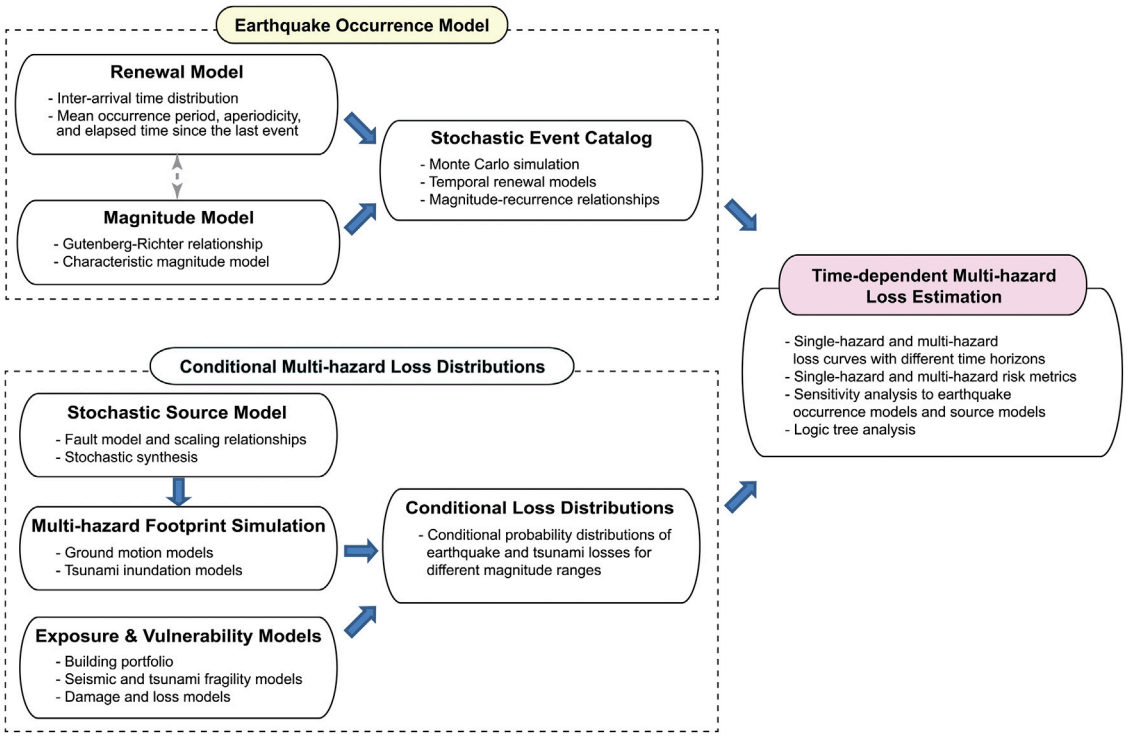

FIGURE 1 | Multi-hazard portfolio loss model framework.

MULTI-HAZARD PORTFOLIO LOSS MODEL FOR TIME-DEPENDENT SHAKING AND TSUNAMI HAZARDS

Computational Framework

To develop a multi-hazard portfolio loss model for time-dependent shaking and tsunami hazards due to megathrust subduction earthquakes, the computational framework for multi-hazard loss estimation developed by Goda and De Risi (2018), which was formulated based on a conventional Poisson process, is extended by incorporating the earthquake occurrence component that is based on a renewal process (Goda, 2019). An overview of the computational procedure is illustrated in **Figure 1**, whereas the model components that are implemented for the Tohoku region of Japan are summarized in **Table 1**. The numerical evaluation is based on Monte Carlo simulations. Since formulations and descriptions of the multi-hazard loss model and the renewal-process-based tsunami hazard model are available in Goda and De Risi (2018) and Goda (2019), respectively, detailed explanations are not repeated. Instead, the following subsections provide a concise summary of the key model components and focus upon how different models are integrated to enable the time-dependent multi-hazard loss estimation. The limitations of the implemented model will also be mentioned to encompass the future extensions/improvements of the developed loss model.

The first major building block of the portfolio loss model is the generation of stochastic event sets for a specified duration of interest from a set of earthquake occurrence models. The occurrence of major tsunamigenic seismic events is modeled by a renewal process, which captures quasi-periodic characteristics of major tsunamigenic earthquakes (e.g., evens having *M*7.5 or above) *via* non-exponential inter-arrival time distributions and the last occurrence of such an event. The magnitude of these major events is characterized by a set of magnitude recurrence models. Popular magnitude models include the truncated exponential model (i.e., G-R relationship) and the characteristic model. The outputs from this model component are numerous stochastic event catalogs of major earthquakes that occur within the specified temporal window (e.g., 1 million catalogs over a 1-year period). In the current model set-up, a physical relationship between the earthquake occurrence and the magnitude is not explicitly captured. In other words, the future earthquake size does not depend on the waiting time (or accumulated stress/strain) since the last event (note: these events still have large magnitudes). More descriptions for the earthquake occurrence model are given in *Earthquake Occurrence Model*.

The second major building block of the portfolio loss model is the conditional multi-hazard loss distribution. In developing such conditional loss distributions, a magnitude range of interest for the major tsunamigenic events that is considered in the earthquake occurrence model above is discretized into several bins. Subsequently, a stochastic method for earthquake source modeling is used to generate a number of stochastic earthquake rupture models with variable geometry and location and with

TABLE 1 | Components of the time-dependent multi-hazard portfolio loss model for the Tohoku region of Japan.

Model component	Details
Renewal model	Inter-arrival time distributions are based on the exponential distribution, lognormal distribution, BPT distribution, and Weibull distribution. Due to the very small probability of major earthquakes for the lognormal and BPT distributions when the elapsed time is set to 10 years and the duration is set to 1 year, the Weibull distribution is mainly focused upon for the renewal earthquake occurrence process.
Magnitude model	The truncated exponential model with upper and lower bounds of *M*7.5 and *M*9.1 (with 0.2 interval) is considered with the mean recurrence period of 12.5 years for >*M*7.5 events. The characteristic earthquake models with upper and lower bounds of *M*8.3 and *M*9.1, *M*8.7 and *M*9.1, and *M*8.9 and *M*9.1, are considered with the mean recurrence periods of 105, 168, and 225 years for >*M*8.3, >*M*8.7, and >*M*8.9 events, respectively. The moment release rate is conserved for different magnitude models.
Earthquake source model	Fault geometry and earthquake slip distributions are characterized by using the stochastic synthesis method by Goda et al. (2014) and the statistical scaling relationships by Goda et al. (2016). 500 stochastic source models are generated for each of the magnitude ranges having 0.2-unit interval between *M*7.5 and *M*9.1 (i.e., 4,000 source models).
Ground motion model	The PGV model by Morikawa and Fujiwara (2013) is considered. Average shear wave velocity is obtained from J-SHIS (250-m grids). The intra-event spatial correlation model of Goda and Atkinson (2010) is implemented.
Tsunami inundation model	The TUNAMI code by Goto et al. (1997) is used to evaluate nonlinear shallow water equations with run-up. Initial dislocation profiles are computed using Okada (1985) equations and Tanioka and Satake (1996) equations. A nested grid system of 1350-m, 450-m, 150-m, and 50-m is obtained from the Miyagi Prefectural Government. The coastal defense structures and Manning's roughness coefficients are taken into account.
Seismic fragility functions	The empirical PGV-based models by Yamaguchi and Yamazaki (2001), Midorikawa et al. (2011), and Wu et al. (2016) are considered with equal weighting of the three functions. The underlying shaking damage data are from the 1995 Kobe earthquake, seven crustal earthquakes that occurred between 2003 and 2008, and the 2011 Tohoku earthquake, respectively. The damage-loss functions are based on Kusaka et al. (2015).
Tsunami fragility functions	The empirical inundation-depth-based model by De Risi et al. (2017) is considered. The underlying tsunami damage data are from the 2011 Tohoku tsunami. The damage states are defined based on the MLIT tsunami damage database for the 2011 Tohoku event, and the corresponding damage-loss functions are adopted.
Building exposure model	The building data are obtained from the MLIT tsunami damage database for the 2011 Tohoku event. The regional building cost information is obtained from the MLIT statistics of regional construction data (http://www.mlit.go.jp/toukeijouhou/chojou/stat-e.htm) and from Construction Research Institute (2011).

heterogeneous earthquake slip distribution. To evaluate the hazard footprint of the synthesized stochastic events in terms of shaking intensity and tsunami inundation at building locations of interest, Monte Carlo ground motion and tsunami inundation simulations are implemented for different magnitude ranges. After applying seismic as well as tsunami fragility functions to the building portfolio of interest and relevant damage-loss functions, shaking and tsunami damage severities can be evaluated for both individual buildings and aggregated building portfolio. Eventually, the probability distribution functions of single-hazard and multi-hazard loss metrics can be obtained for different magnitude ranges. More descriptions of the conditional multi-hazard loss distribution are given in *Conditional Multi-Hazard Loss Distribution*.

To combine the outputs from the first and second major components, for each event in the stochastic event catalogs, the single-hazard and multi-hazard loss values are sampled from the conditional loss distribution that corresponds to the event's magnitude. For instance, for a seismic event with representative magnitude of 8.6, loss values are sampled from the empirical loss distribution of the 500 stochastic source events that have earthquake magnitudes between *M*8.5 and *M*8.7. In this sampling, the dependency of the loss event is maintained, and thus information on the earthquake event characteristics, such as rupture geometry and slip distribution, becomes accessible (Goda and De Risi, 2018). By repeating this loss sampling, the stochastic event catalog can be expanded to include information on the single-hazard and multi-hazard building portfolio loss (i.e., event loss table). Subsequently, statistical analysis can be performed on the event loss table to derive the loss exceedance curves as well as related risk metrics for the building portfolio (Mitchell-Wallace et al., 2017). It is important to emphasize that the time dependency of the shaking and tsunami hazards is retained in the stochastic event sets and thus in the event loss table.

The computational efficiency of the multi-hazard portfolio loss estimation method that is outlined above can be attributed to the decoupling of the earthquake occurrence model and the conditional loss distribution. Simulations of the former component are fast. In contrast, the latter requires significant computations based on a large number of stochastic source models for megathrust subduction events. When the earthquake occurrence model is altered (e.g., different renewal and magnitude models are considered) or extended (e.g., multiple combinations of renewal and magnitude models are considered in a logic tree), the conditional loss distributions do not need to be changed. Moreover, it is noteworthy that instead of resampling the loss quantities from the finite number of stochastic source models, an analytical loss distribution (e.g., Pareto distribution) can be fitted to the simulated conditional loss data. When such analytical models are considered, the direct connection between the loss value and the event characteristics (e.g., earthquake slip distribution) will be lost. Therefore, suitable approaches should be employed depending on the purposes of the developed multi-hazard loss model.

Earthquake Occurrence Model

A stochastic renewal process is adopted for characterizing earthquake occurrence, where the inter-arrival time between successive earthquakes is modeled by some suitable

probabilistic model (Ogata, 1999). In this study, four distribution types are considered: i) the exponential distribution is most popular and corresponds to a memory-less Poisson process; ii) the lognormal distribution is often adopted for practical reasons; iii) the BPT distribution can be related to physical phenomena of loading and unloading processes of stress along fault rupture planes (Matthews et al., 2002); and iv) the Weibull distribution is often used for modeling failure times of engineering products and is suitable for representing a process having the increasing hazard function since the last failure (Abaimov et al., 2008). The details of the mathematical formula for these distributions can be found in standard statistical textbooks (see also Goda, 2019).

Three model parameters define the inter-arrival time distribution: the mean recurrence time μ, the aperiodicity ν, and the elapsed time since the last event T_E. The mean recurrence time is typically estimated based on historical earthquake records and geological records (e.g., Ogata, 1999; Ceferino et al., 2020). The ν parameter determines the periodicity of earthquake occurrence. Suitable ν values for large subduction events can be in the range of 0.5 ± 0.2 (Sykes and Menke, 2006). When ν is small (e.g., less than 0.2) the process becomes more periodic, whereas when ν is large the process becomes more random and clustering of the events tends to occur more frequently. The probability distribution of inter-arrival time needs to be modified when T_E is not equal to zero to account for the fact that no major events have occurred to date.

Evaluation of the renewal process can be facilitated through Monte Carlo simulations. In the simulation-based approach, random numbers from a specified inter-arrival time distribution are generated using an inverse transformation method or a rejection method. For the renewal process, a special attention is necessary to distinguish the first event and subsequent events (i.e., $T_E \neq 0$ vs. $T_E = 0$). This is illustrated in **Figure 2A**. For simulating the occurrence time of the first event, the modified inter-arrival time distribution should be used by taking into account T_E. When the simulated time t_{IAT} is less than the duration for the hazard assessment T_D, the simulated event should be registered as $t_1 = t_{IAT}$ in a stochastic event catalog and proceed to the second event; otherwise the simulation process is stopped for this catalog realization. For the second event, the elapsed time is reset to 0 and an inter-arrival time t_{IAT} is sampled from the original distribution and the occurrence time is updated as $t_2 = t_1 + t_{IAT}$. If t_2 is less than T_D, the second event is registered in the stochastic event catalog; otherwise the simulation ends for this catalog realization. This process should be continued until the updated time of the most recent event exceeds T_D. By repeating the simulations of event occurrence S times, a set of S stochastic event catalogs, each with the duration T_D, can be obtained.

The magnitude recurrence distribution characterizes the uncertainty of earthquake magnitude when a major event occurs. A popular model is of G-R type, where the overall occurrence rate for major events and the relative distribution of earthquake magnitude (i.e., b-value) are determined from statistical analysis of regional seismicity. Other types of the magnitude model include the characteristic magnitude models with uniform or truncated normal distributions. **Figure 2B** shows two examples of the magnitude models, namely a G-R model that is defined over a magnitude range between $M7.5$ and $M9.1$, whereas a characteristic-uniform model that is defined over a magnitude range between $M8.3$ and $M9.1$. It is important to emphasize that the magnitude models should be consistent with regional seismotectonic conditions. As such, the occurrence frequency of major events (i.e., mean recurrence time of the renewal model) needs to be adjusted based on regional seismic moment release constraints, which can be determined from the regional G-R analysis and/or the regional plate movements. For the case of the Tohoku region, the regional G-R analysis indicates the annual occurrence frequency of 0.08 for $M7.5$ and above events (with $b = 0.9$; Goda and De Risi, 2018). When the characteristic-uniform model shown in **Figure 2B** is considered, the annual occurrence frequency is decreased to 0.01.

By simulating the stochastic occurrence process of large subduction events, numerous stochastic event catalogs are obtained. This is illustrated in **Figure 2C**. Each catalog contains N_i events, $i = 1,\ldots,S$, and is characterized by the paired information of occurrence time t_{ij} and magnitude m_{ij}, $j = 1,\ldots,N_i$. These simulated earthquake sequences are used in the multi-hazard portfolio loss model. It is noted that when multiple combinations of the renewal and magnitude models are implemented in a logic tree, sampling of the renewal and magnitude model parameters is performed first and then based on the realized parameters, the stochastic event information t and m over a T_D-year period is generated. For a different catalog, the renewal and magnitude model parameters need to be resampled prior to the stochastic event generation.

Conditional Multi-Hazard Loss Distribution

The multi-hazard shaking-tsunami loss for a magnitude range is estimated by integrating five modules: a) stochastic source model, b) shaking-tsunami footprint simulations, c) building exposure model, d) seismic-tsunami vulnerability model, and e) conditional multi-hazard loss estimation. A computational procedure of the conditional multi-hazard loss distributions is illustrated in **Figure 3**. Brief descriptions of the modules are given below.

Stochastic Source Model

The stochastic source model captures the spatial uncertainty of earthquake rupture for a given earthquake magnitude (**Figure 3A**). The model for the Tohoku region of Japan covers an offshore area of 650 by 250 km. The source uncertainty is characterized by probabilistic models of earthquake source parameters and stochastic synthesis of earthquake slip (Goda and De Risi, 2018). For a magnitude value, eight source parameters, i.e., fault width, fault length, mean slip, maximum slip, Box-Cox power parameter, correlation length along dip, correlation length along strike, and Hurst number, are generated using empirical prediction equations based on 226 finite-fault models of the past earthquakes. Once the geometry and position of a stochastic source model are determined, a random heterogeneous slip distribution is generated using a Fourier integral method, where amplitude spectrum is represented by von Kármán spectra and random phase (Mai and Beroza, 2002). To

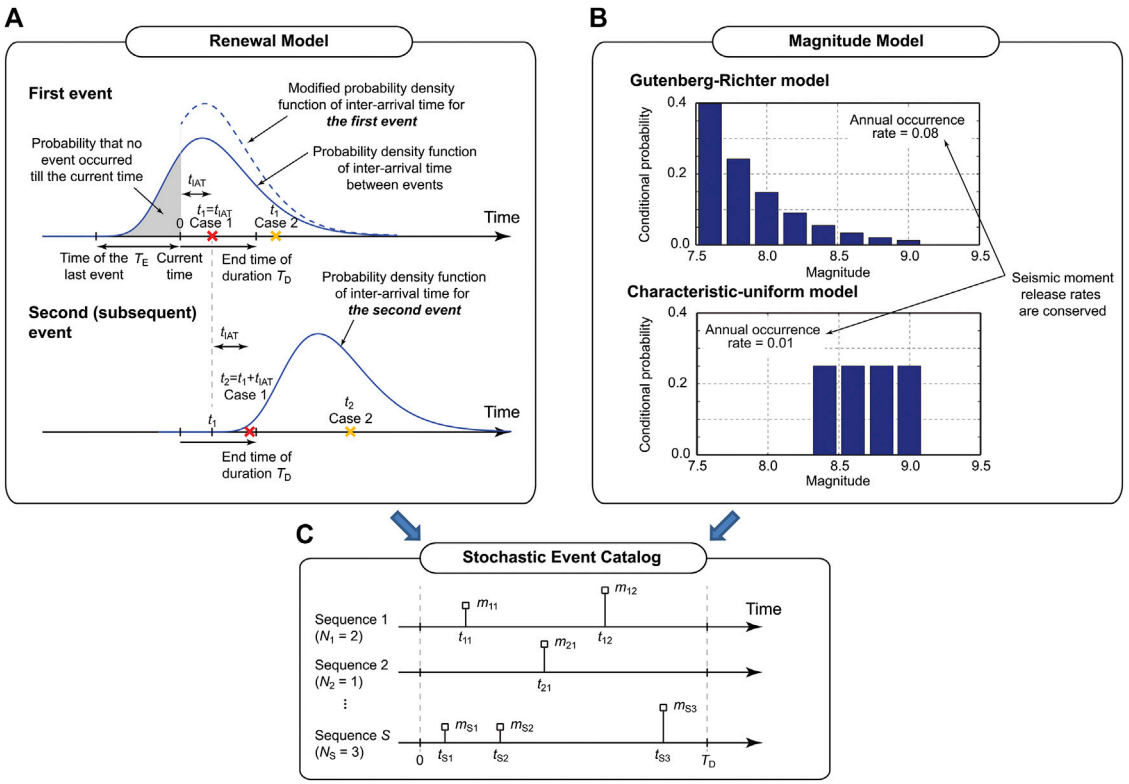

FIGURE 2 | Evaluation of earthquake occurrence processes. **(A)** Renewal model, **(B)** Magnitude model, **(C)** Stochastic event catalog.

generate a slip distribution with realistic right-heavy tail features, the synthesized slip distribution is converted *via* Box-Cox power transformation. The transformed slip distribution is then adjusted to achieve the suitable slip characteristics, such as mean slip and maximum slip. In this study, 500 stochastic source models are generated for eight magnitude ranges with 0.2 bin width spanning from *M*7.5 and *M*9.1 (i.e., 4,000 models in total). The synthesized earthquake source models reflect possible variability of tsunamigenic earthquakes in terms of geometry, fault location, and slip distribution.

Multi-Hazard Footprint Simulations

For a given earthquake source model, shaking and tsunami hazard intensities at building locations are evaluated by using a ground motion model and by solving non-linear shallow water equations for initial boundary conditions of sea surface caused by an earthquake rupture, respectively (**Figure 3B**). In this study, the peak ground velocity (PGV) is selected for shaking and the maximum inundation depth is adopted for tsunami. The choice of PGV as seismic hazard measure is due to its compatibility with empirical seismic fragility functions in Japan (see **Table 2**). The local site conditions are based on the J-SHIS average shear-wave velocity database (http://www.j-shis.bosai.go.jp/en/; 250-m grids). The PGV ground motion model by Morikawa and Fujiwara (2013) together with the intra-event spatial correlation model of Goda and Atkinson (2010) is used to generate spatially correlated ground motion fields for all 4,000 stochastic sources. On the other hand, tsunami inundation and run-up simulations are performed using a well-tested TUNAMI computer code by Goto et al. (1997). The computational domains are nested with 1,350, 450, 150, and 50-m resolution grids. The maximum inundation depths at the building locations are determined by subtracting land elevations from the maximum inundation heights. It is noted that inundation depth does not capture the tsunami flow effects on buildings directly; for such purposes, flow velocity-based tsunami fragility functions can be adopted (De Risi et al., 2017). Tsunami simulations are conducted for all 4,000 stochastic sources by considering duration of 2 h.

Building Exposure Model

Using a building dataset that was compiled by the Japanese Ministry of Land Infrastructure and Transportation (MLIT) for the post-2011-Tohoku tsunami damage assessment, an exposure model is developed for Iwanuma City and Onagawa Town (**Figure 3C**). Building types that are considered in this study are low-rise wooden structures (up to 4-story buildings; the majority of the buildings are 1 story or 2 stories), for which well-calibrated seismic and tsunami fragility models are available. The numbers of wooden structures in Iwanuma and Onagawa are 6,152 and 1,706, respectively. To obtain estimates of the building costs for the wooden buildings in Iwanuma and Onagawa, two sources of information are utilized. Using the Japanese building cost information handbook published by the Construction Research Institute (2011) and MLIT building stock database,

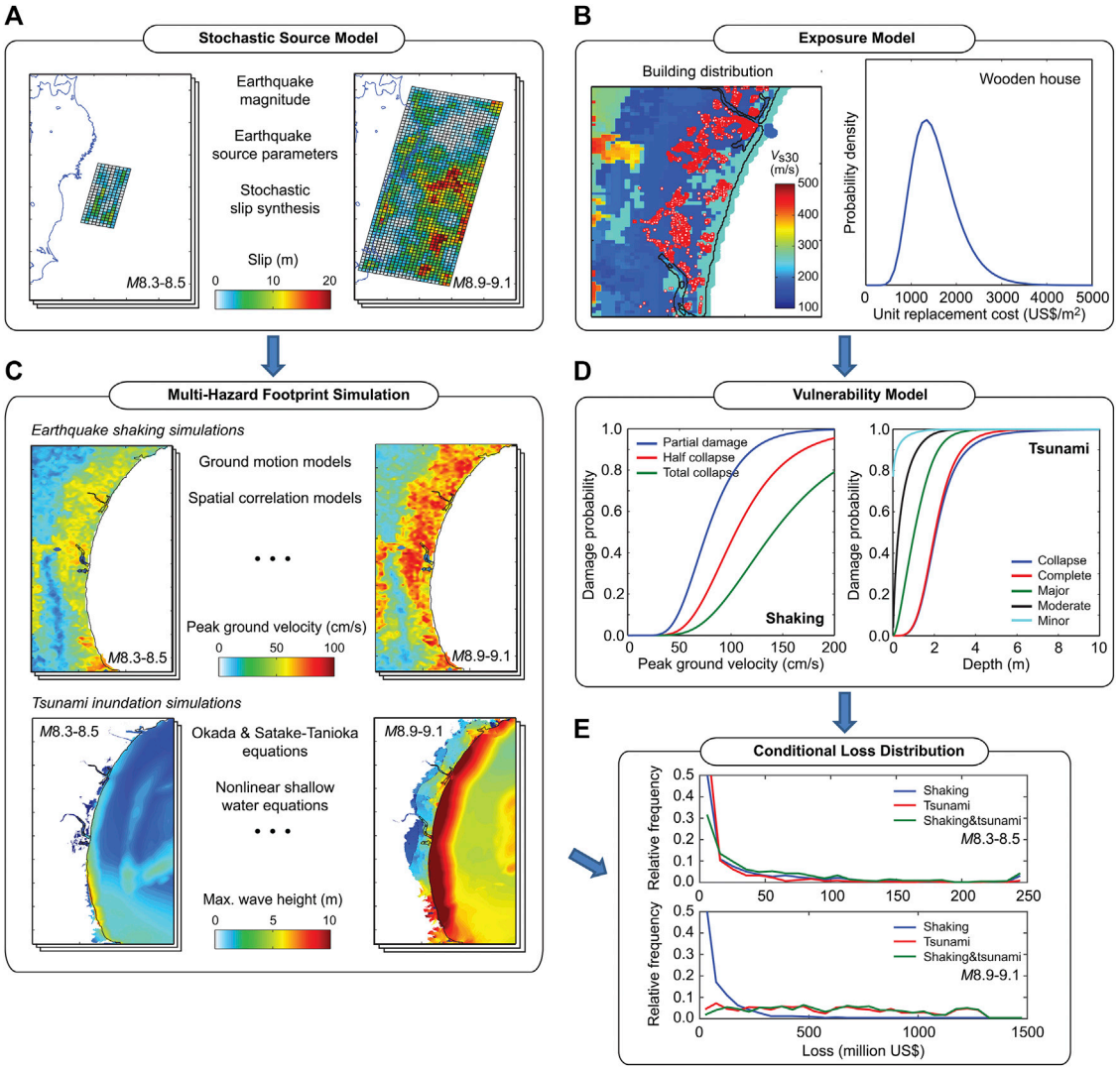

FIGURE 3 | Evaluation of conditional shaking-tsunami loss distributions. **(A)** Stochastic source model, **(B)** Exposure model, **(C)** Multi-hazard footprint simulation, **(D)** Vulnerability model, **(E)** Conditional loss distribution.

the mean and CoV of the unit replacement cost for wooden buildings are obtained as 1,600 US$/m2 and 0.33, respectively (assuming 1 US$ = 100 yen), whereas the mean and CoV of typical floor areas of wooden houses are determined as 130 m^2 and 0.33, respectively. Both unit cost and floor area are modeled by the lognormal distribution. Based on the above building cost information, the expected total costs of the 6,152 buildings in Iwanuma and the 1,706 buildings in Onagawa are 1,280 million US$ and 355 million US$, respectively.

Vulnerability Model

Damage ratios for shaking and tsunami are estimated by applying seismic and tsunami fragility functions (**Figure 3D**). The seismic fragility models are based on three empirical functions for low-rise wooden buildings in Japan (Yamaguchi and Yamazaki, 2001; Midorikawa et al., 2011; Wu et al., 2016), whereas the tsunami fragility model is based on the tsunami damage data from the 2011 Tohoku earthquake and tsunami (De Risi et al., 2017). The damage states for shaking are defined as: partial damage, half collapse, and complete collapse, and the corresponding damage ratios are assigned as 0.03–0.2, 0.2–0.5, and 0.5–1.0, respectively (Kusaka et al., 2015). For tsunami damage, the following five damage states are considered: minor, moderate, extensive, complete, and collapse, together with the damage ratios of 0.03–0.1, 0.1–0.3, 0.3–0.5, 0.5–1.0, and 1.0, respectively (MLIT, http://www.mlit.go.jp/toshi/toshi-hukkou-arkaibu.html). Subsequently, for each building, a greater of the estimated shaking and tsunami damage ratios is adopted as the final damage ratio of the building. A multi-hazard loss value is calculated by sampling a value of the building replacement cost from the lognormal distribution and then by multiplying it by the final damage ratio. The above-mentioned method of calculating the combined shaking-tsunami damage ratio does not account for interaction between shaking and

TABLE 2 | Numerical calculation cases.

Case	Inter-arrival time distribution	Elapsed time T_E	Magnitude model	Duration T_D	Figure
1	Exponential with μ = 12.5	N/A	G-R with *M*7.5 to *M*9.1	1 year	7
2	Exponential with μ = 105	N/A	Characteristic with *M*8.3 to *M*9.1	1 year	8
3	Exponential with μ = 168	N/A	Characteristic with *M*8.7 to *M*9.1	1 year	8
4	Exponential with μ = 225	N/A	Characteristic with *M*8.9 to *M*9.1	1 year	8
5	Weibull with μ = 105 and ν = 0.3	10 years	Characteristic with *M*8.3 to *M*9.1	1 year	9
6	Weibull with μ = 105 and ν = 0.5	10 years	Characteristic with *M*8.3 to *M*9.1	1 year	9
7	Weibull with μ = 105 and ν = 0.7	10 years	Characteristic with *M*8.3 to *M*9.1	1 year	9
8	Weibull with μ = 105 and ν = 0.5	50 years	Characteristic with *M*8.3 to *M*9.1	1 year	10
9	Weibull with μ = 105 and ν = 0.5	100 years	Characteristic with *M*8.3 to *M*9.1	1 year	10
10	Weibull with μ = 105 and ν = 0.3	10 years	Characteristic with *M*8.3 to *M*9.1	30 years	11
11	Weibull with μ = 105 and ν = 0.5	10 years	Characteristic with *M*8.3 to *M*9.1	30 years	11
12	Weibull with μ = 105 and ν = 0.7	10 years	Characteristic with *M*8.3 to *M*9.1	30 years	11
13	Weibull with μ = 105 and ν = 0.3	100 years	Characteristic with *M*8.3 to *M*9.1	30 years	11
14	Weibull with μ = 105 and ν = 0.5	100 years	Characteristic with *M*8.3 to *M*9.1	30 years	11
15	Weibull with μ = 105 and ν = 0.7	100 years	Characteristic with *M*8.3 to *M*9.1	30 years	11
16	Exponential with μ = 105	N/A	Characteristic with *M*8.3 to *M*9.1	30 years	12
17	Lognormal with μ = 105 and ν = 0.5	10 years	Characteristic with *M*8.3 to *M*9.1	30 years	12
18	BPT with μ = 105 and ν = 0.5	10 years	Characteristic with *M*8.3 to *M*9.1	30 years	12
19	Lognormal with μ = 105 and ν = 0.5	100 years	Characteristic with *M*8.3 to *M*9.1	30 years	12
20	BPT with μ = 105 and ν = 0.5	100 years	Characteristic with *M*8.3 to *M*9.1	30 years	12

tsunami damage explicitly. For the current model of the Tohoku region, this limitation is alleviated because the tsunami fragility model by De Risi et al. (2017) is based on tsunami damage data from the 2011 Tohoku event that include the effects due to shaking damage.

Conditional Multi-Hazard Loss Estimation

A numerical procedure of integrating the hazard and risk model components is implemented using Monte Carlo simulations (Goda and De Risi, 2018; **Figure 3E**). At the end of the simulation, loss samples for all buildings are obtained for the 4,000 stochastic source models. These loss samples can be used to construct the conditional distribution functions of the total portfolio loss for different magnitude ranges.

One of the notable features of the developed multi-hazard shaking-tsunami loss estimation is the consideration of variable fault geometry and heterogeneous earthquake slip distribution. The latter is particularly influential on tsunami hazard predictions (Goda et al., 2016). To illustrate this effect on tsunami loss, cumulative probability distributions of tsunami loss for Iwanuma and Onagawa are shown in **Figure 4** by considering heterogeneous slip distributions and uniform slip distributions. The cumulative probability distributions are developed for the eight magnitude ranges to better distinguish the loss results in terms of earthquake magnitude (i.e., conditional tsunami loss distribution). The heterogeneous slip distributions take into account variability in both fault geometry and spatial slip distribution, whereas the uniform slip distributions reflect variability of fault geometry only but with average slip across the fault plane (note: for a given earthquake source model, the earthquake magnitude is identical for the heterogeneous and uniform slip cases). **Figure 4** clearly shows the effects of spatial slip distribution and the consideration of realistic heterogeneous slip distributions results in significantly greater and more variable conditional tsunami loss distributions than uniform slip distributions. This is in agreement with the previous studies (Mueller et al., 2015; Li et al., 2016; Melgar et al., 2019). For instance, for the building portfolio in Iwanuma (**Figures 4A,B**), probability that the tsunami loss exceeds 600 million US$ is circa 0.5 for the heterogeneous slip case, whereas that probability for the uniform slip case is approximately 0.1.

As mentioned in *Computational Framework*, the computational efficiency of the proposed multi-hazard loss estimation procedure depends on the stability of the conditional loss distributions for the magnitude ranges. In other words, the sample size of stochastic source models per magnitude bin should be sufficiently large. To examine whether such stable loss distributions are achieved for the case studies that are discussed in *Results*, the five percentiles (2.5th, 16th, 50th, 84th, and 97.5th) of shaking loss, tsunami loss (with heterogeneous or uniform slip distributions), and combined loss (with heterogeneous or uniform slip distributions) for Iwanuma and Onagawa are displayed as a function of the number of stochastic source models. For illustration, the magnitude range between *M*8.3 and *M*8.5 is considered in **Figure 5**. It can be observed that with 300 or more source models, the conditional loss distributions become stable for this magnitude bin. Similar stabilizing trends are observed for different magnitude bins (not reported in the paper). It is important to note that the stability of the conditional loss distributions depends on the target metric that is adopted for the investigation. When a portfolio-aggregated loss is concerned (as in this study), the sum of losses of individual buildings fluctuate less, compared to a loss of a particular building. Therefore, for the latter case, it may require more stochastic source models to achieve such stability.

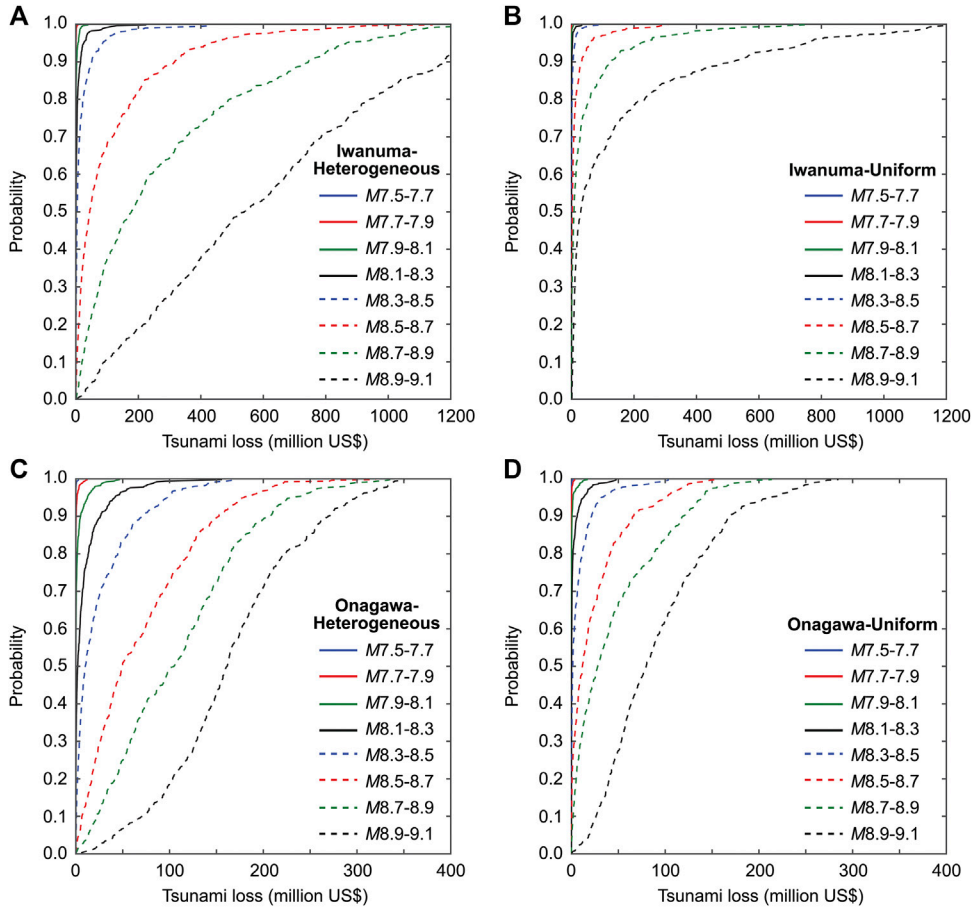

FIGURE 4 | Cumulative probability distributions of tsunami loss for the building portfolios in Iwanuma **(A,B)** and Onagawa **(C,D)** by considering heterogeneous distributions **(A,C)** and uniform distributions **(B,D)** of earthquake slip.

Model Limitations

The multi-hazard portfolio loss estimation framework for time-dependent shaking and tsunami hazards presented in this section has limitations and is specific to the case study region in Japan. The region-specific modules include applicable earthquake occurrence models, earthquake source characteristics (overall fault geometry and source parameters), ground motion models for seismic intensity parameters, regional and local factors that affect tsunami inundation (e.g., bathymetry and elevation), seismic and tsunami fragility functions, and exposure databases (e.g., building cost and design information). Some of the model choices are constrained by other modules (for example, the use of PGV in ground motion modeling is prescribed by seismic hazard measures used in seismic fragility functions, whereas unavailability of seismic fragility functions for non-wooden building typologies leads to exclusion of non-wooden buildings in the exposure model).

Some of the limitations of the developed multi-hazard loss model are listed in the following. These are not the complete list of the limitations and each of these is worthy of future investigations.

- In modeling interaction between spatiotemporal earthquake occurrence and magnitude, a simple renewal process is adopted in this work. Time-predictable and slip-predictable models by Shimazaki and Nakata (1980) and Kiremidjian and Anagnos (1984), respectively, can capture causal relationships between the inter-arrival time and magnitude. When the subduction zone is divided into several distinct segments, the space- and time-interaction model by Ceferino et al. (2020) can be implemented.
- The framework only considers a single source region (i.e., offshore Tohoku region), while other sources that could cause major destruction to the building portfolio can be incorporated. Such additional sources include crustal and inslab seismic sources for shaking damage and far-field tsunami sources for tsunami damage (e.g., Cascadia and Chile subduction zones for the Tohoku region).

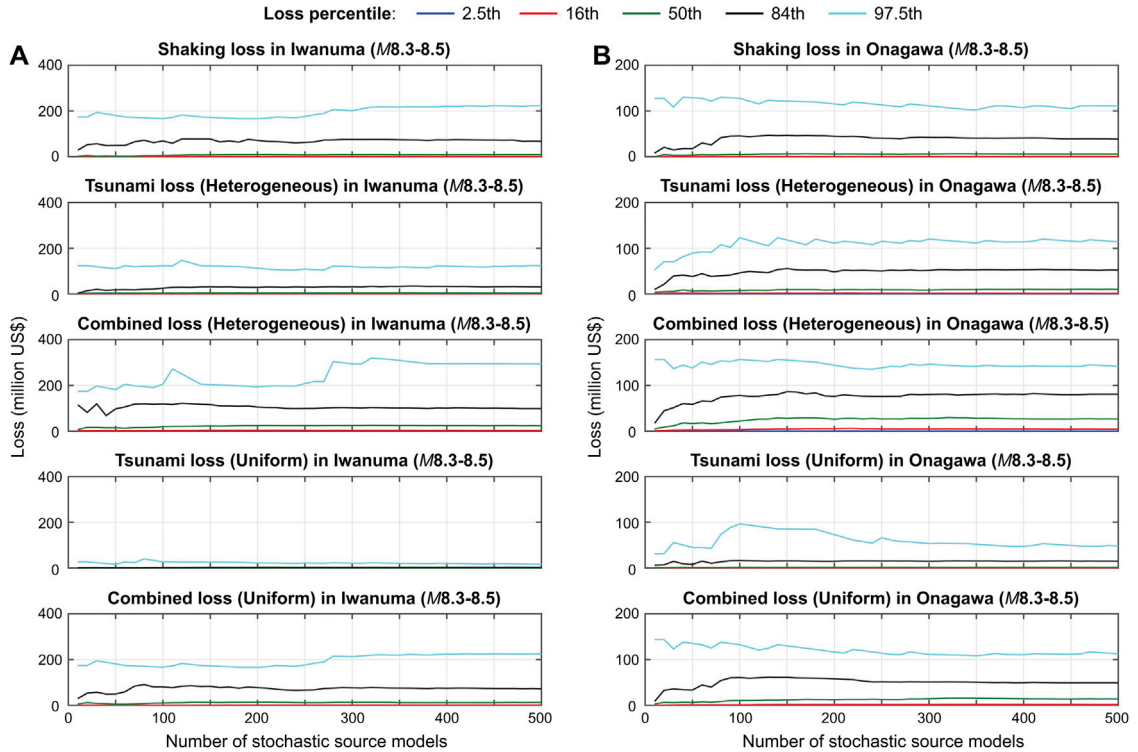

FIGURE 5 | Stability of conditional loss distributions for the building portfolios in Iwanuma **(A)** and Onagawa **(B)** due to stochastic source models with magnitudes between *M*8.3 and *M*8.5.

- Although the tsunami footprint simulation is performed by solving the nonlinear shallow water equations, ground motion simulation is based on empirical statistical model of ground motion intensity. When a high-resolution 3D crustal velocity model is available and more computational resources are dispensable, hybrid ground motion simulations (Pitarka et al., 2017; Frankel et al., 2018) can be implemented to incorporate more physical features in the evaluation of ground shaking intensity.
- In assessing the damage extent of a building subjected to a sequence of shaking and tsunami hazards, the damage accumulation of the cascading hazards becomes an important factor. Such a damage accumulation model can be developed based on reliable numerical models of structures by subjecting these models to a sequence of shaking-tsunami loads (Park et al., 2012).

RESULTS

Numerical Calculation Set-Up

Two case study locations are considered for the exposure model. Iwanuma is located on the Sendai plain, whereas Onagawa is located along the Sanriku ria coast. Both locations were devastated during the 2011 Tohoku earthquake and tsunami (Fraser et al., 2013). **Figures 6A,B** show the spatial distributions of buildings in Iwanuma and Onagawa, respectively. The markers shown in the figure are color-coded with actual building damage states assigned by the MLIT after the 2011 Tohoku event. In addition, histograms of the damage for Iwanuma and Onagawa are shown in **Figures 6C,D**, respectively. Different spatial patterns of building damage, which essentially reflect the tsunami inundation extents at these two locations, can be observed. With the increase of distance from the coastal line, the damage states in Iwanuma become less severe as the inundation depths become smaller. In contrast, the collapse damage states in Onagawa are prevalent across nearly all buildings that are located in the valley because of the very high inundation heights exceeding 18 m (Fraser et al., 2013). By applying the same damage-loss functions introduced in *Conditional Multi-Hazard Loss Distribution*, the total damage costs for the buildings in Iwanuma and Onagawa are calculated as 743 million US$ and 337 million US$, respectively, which are equal to the average loss ratio of 58 and 95% for the 2011 Tohoku event. These empirical results indicate that the occurrence of catastrophic loss is for real for these two locations.

The main aim of this paper is to investigate the effects of considering different renewal and magnitude models, in comparison with the conventional time-dependent counterpart. To facilitate such comparisons of the results, the baseline result is set to the case of the time-independent multi-hazard loss estimation (Goda and De Risi, 2018; *Time-Independent Multi-Hazard Loss Estimation*), which adopts the

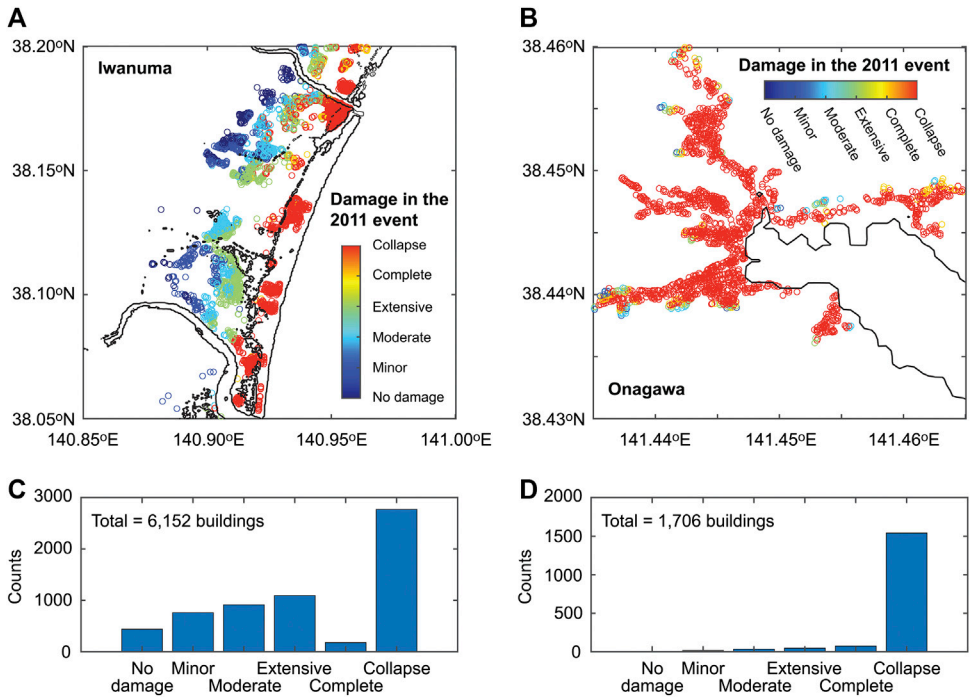

FIGURE 6 | Building portfolios in Iwanuma **(A)** and Onagawa **(B)**. The colors represent the MLIT damage survey results after the 2011 Tohoku earthquake and tsunami. Histograms of damage states of the considered buildings after the 2011 Tohoku earthquake and tsunami for Iwanuma and Onagawa are shown in **(C)** and **(D)**, respectively.

Poisson process and the G-R magnitude model (Case 1). Several variations for the magnitude models are considered by keeping the time-independent occurrence model (Cases 2 to 4). Subsequently, results for the time-dependent cases are discussed to conduct sensitivity analyses for time-dependent multi-hazard loss estimation (*Sensitivity Analysis of Time-Dependent Multi-Hazard Loss Estimation*). Cases 5 to 7 consider Weibull-based renewal models with different ν values. Cases 8 and 9 adopt different elapsed times since the last major event (T_E = 10, 50, and 100 years; note that T_E = 10 years corresponds to the current situation since the 2011 event). For Cases 1 to 9, the duration of the multi-hazard loss estimation is set to T_D = 1 year. In contrast, a longer time horizon of T_D = 30 years is considered for Cases 10 to 15 by varying both values of T_E and ν. Moreover, Cases 16 to 20 are set up to investigate the effects of using different inter-arrival time distributions (Weibull, lognormal, and BPT) for T_D = 30 years. These calculation cases are summarized in **Table 2**. For each case, 10 million T_D-year stochastic event catalogs are generated, and the maximum combined loss event in each T_D-year catalog is adopted as a loss metric in developing the single-hazard and multi-hazard loss curves.

Time-independent Multi-Hazard Loss Estimation

Figure 7 shows single-hazard and multi-hazard loss curves for Iwanuma and Onagawa based on the time-independent earthquake occurrence model (Case 1). The consideration of different earthquake slip representations (i.e., heterogeneous vs. uniform) results in significantly different tsunami loss curves as well as combined loss curves (see also **Figure 4**). The shaking loss is not affected by the differences of the earthquake slip representation because in the context of ground motion modeling, the fault geometry only affects the predicted ground motion intensities. At higher annual exceedance probability levels (shorter return periods), shaking loss contributes more to the combined loss, whereas at lower annual exceedance probability levels (longer return periods), tsunami loss dominates the combined loss. The changeover of the loss-origin dominance depends significantly on the earthquake slip representation. This difference can be explained by different hazard characteristics for ground shaking and tsunami. Ground motion intensity at a specific location tends to be saturated in terms of earthquake magnitude (Morikawa and Fujiwara, 2013), although areas that experience intense shaking increase rapidly due to the expanding rupture size). On the other hand, tsunami inundation height and spatial extent increase rapidly with earthquake magnitude; devastating inundations of coastal plain areas like Iwanuma happen very rarely (as seen during the 2011 Tohoku event; Fraser et al., 2013). In short, the coastal topography (plain vs. ria) is one of the crucial factors that determine how frequent and how severe the tsunami damage and loss will turn out to be.

For very large earthquakes, different magnitude models may be more applicable. To investigate the effects of different

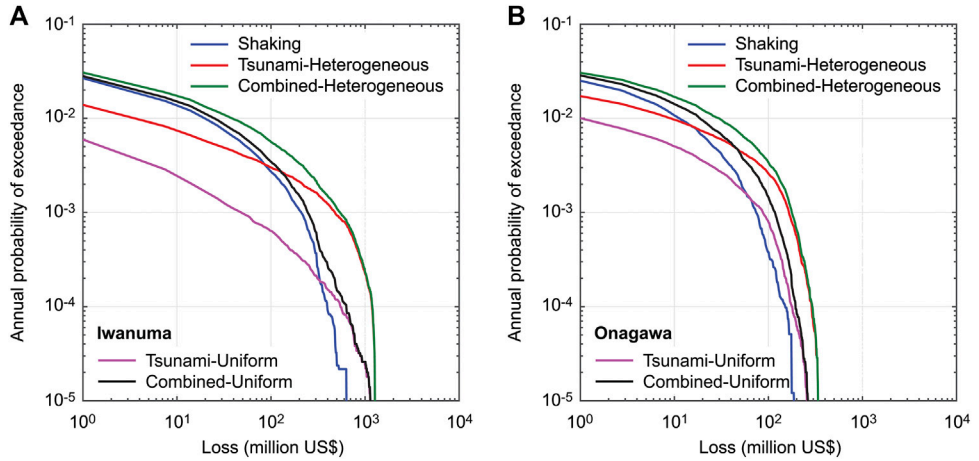

FIGURE 7 | Single-hazard and multi-hazard loss curves for Iwanuma **(A)** and Onagawa **(B)** based on the time-independent earthquake occurrence model (Case 1).

magnitude models on the single-hazard and multi-hazard loss curves, three characteristic magnitude models with uniform distribution are considered by varying the lower-bound magnitudes from *M*8.3 to *M*8.9. Accordingly, the mean recurrence period of major earthquakes is changed from 105 to 225 years by conserving the seismic moment release from the specified source region based on the regional G-R model (see **Table 2**).

Figure 8 shows single-hazard and multi-hazard loss curves for Iwanuma and Onagawa by considering different magnitude models (Cases 1 to 4); to facilitate the inspection of the results, shaking, tsunami, and combined loss curves are presented in separate figure panels. With the consideration of more characteristic behavior of the magnitude distribution, shorter return-period portions of the shaking loss curves are shifted down from the annual probability of exceedance of 0.02 to 0.004 due to longer mean recurrence periods of major events (**Figures 8A,B**). Longer return-period portions of the shaking loss curves are not affected by the different magnitude models because of the fixed upper magnitude limit at *M*9.1 and the magnitude saturation in the ground motion model.

The tsunami loss curves (**Figures 8C,D**) show the influence of the magnitude model at both ends of the loss curves. The shorter return-period portions of the tsunami loss curves are affected by the mean recurrence periods of major events (the same reason for the shaking loss curves). On the other hand, severe tsunami loss curves are resulted from the consideration of more characteristic behavior of the magnitude model. The effects of the earthquake slip distribution are noticeable for different magnitude models, especially remarkable for Iwanuma.

The multi-hazard loss curves (**Figures 8E,F**) exhibit combined effects from the shaking loss curves and tsunami loss curves, as discussed above. The consideration of the characteristic magnitude model results in more severe combined loss curves at annual exceedance probability levels lower than 0.01. These increased levels of the multi-hazard loss for the building stock in Iwanuma and Onagawa indicate the importance of considering a range of magnitude models for disaster risk management purposes. In *Sensitivity Analysis of Time-dependent Multi-Hazard Loss Estimation*, the characteristic magnitude model with uniform distribution between *M*8.3 and *M*9.1 is adopted to further investigate the effects of adopting different earthquake occurrence models on the multi-hazard loss estimation.

Sensitivity Analysis of Time-dependent Multi-Hazard Loss Estimation

Effects of different earthquake occurrence models are investigated in this section. More specifically, the effects of aperiodicity parameter are examined in *Sensitivity to Aperiodicity Parameter* by adopting the Weibull inter-arrival time distribution for T_E = 10 years (current situation) and T_D = 1 year. Note that for T_E = 10 years and T_D = 1 year, when the lognormal and BPT distributions are considered, the loss estimation results are nearly zero due to very small probabilities of earthquake occurrence within the specified time window; for this reason, the Weibull distribution is mainly focused upon. Subsequently, the effects of the elapsed time since the last major event are evaluated in *Sensitivity to Elapsed Time Since the Last Major Event* by considering hypothetical future situations of T_E = 50 and 100 years (T_D = 1 year). In *Sensitivity to Time Window Length*, the impact of considering a longer time window for the loss estimation is investigated by considering T_D = 30 years. The time window length of 30 years is often considered in Japan for long-term earthquake disaster risk mitigation purposes (e.g., national seismic hazard maps). Lastly, the effects of different inter-arrival time distributions are examined in *Sensitivity to Inter-Arrival Time Distribution* by considering the time horizon of T_D = 30 years.

Sensitivity to Aperiodicity Parameter

Figure 9 compares single-hazard and multi-hazard loss curves for Iwanuma and Onagawa by considering Weibull-based renewal models with different aperiodicity values of ν = 0.3,

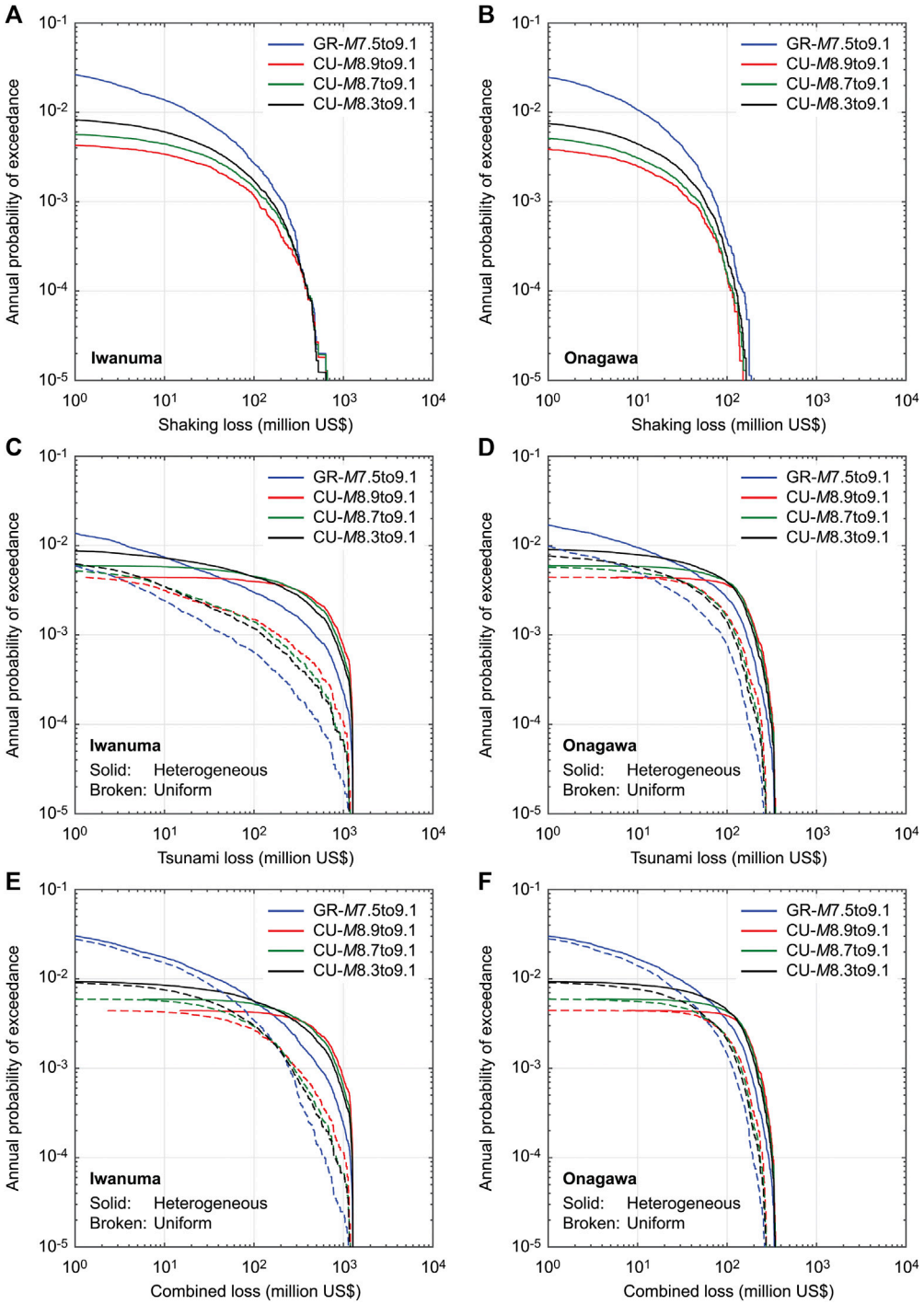

FIGURE 8 | Single-hazard and multi-hazard loss curves for Iwanuma **(A,C,E)** and Onagawa **(B,D,F)** by considering different characteristic-uniform (CU) magnitude models (Cases 1 to 4).

0.5, and 0.7 (Cases 5 to 7), which fall within the empirical estimates of this parameter for global subduction zones (Sykes and Menke, 2006). The inter-arrival time distribution is based on the Weibull model with mean recurrence period of 105 years (for M8.3 to M9.1 events) and T_E is set to 10 years. For the baseline comparison, the loss curves for Case 1 are included. The effects of the time-dependent hazards are paramount, changing the positions of the loss curves by a factor of 100 times in terms of annual probability of exceedance (from $\nu = 0.3$ to $\nu = 0.7$).

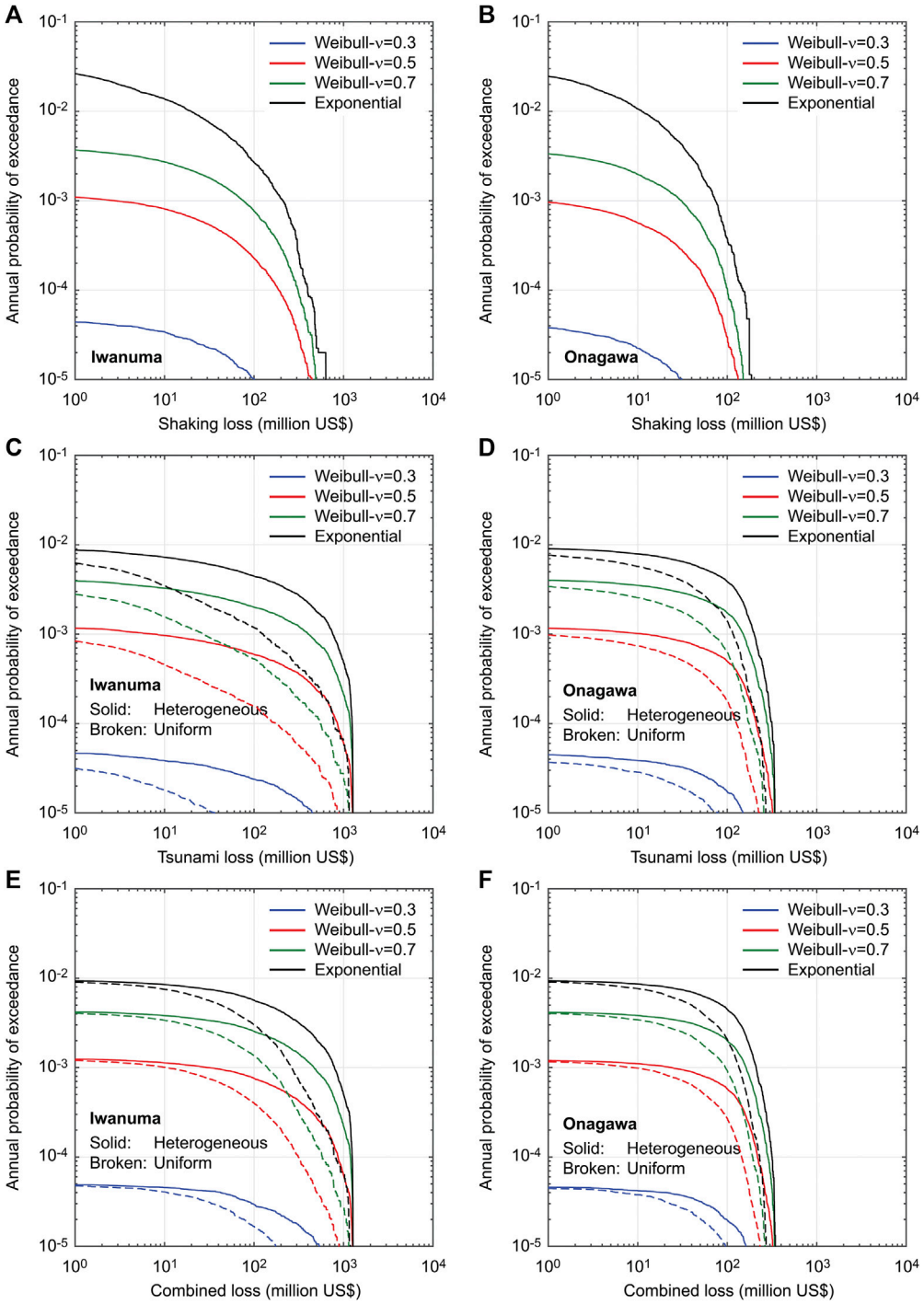

FIGURE 9 | Single-hazard and multi-hazard loss curves for Iwanuma **(A,C,E)** and Onagawa **(B,D,F)** by considering Weibull-based renewal models with different ν values (Cases 2, 5, 6, and 7).

Results for the shaking loss curves (**Figures 9A,B**) show that the loss curves for the time-dependent occurrence models are less risky than those for the time-independent occurrence model and with the increase in ν, the loss curves for the time-dependent occurrence models approach that of the time-independent occurrence model. This can be explained by the fact that the current time instance (T_E = 10 years) is shorter than the mean recurrence period (μ = 105 years) and is still in the early phase of stress accumulation process of major subduction events. Therefore, the less periodic earthquake occurrence behavior

(i.e., larger ν values) results in greater occurrence probability of major events within a time window of 1 year.

The same observations are applicable to the tsunami loss curves and combined loss curves shown in **Figures 9C–F**). Essentially, respective loss curves are shifted down according to the occurrence probabilities of major events. Overall, the effects of aperiodicity parameter (i.e., steepness of the inter-arrival time distribution around mean) are significant, especially for the early phase of the renewal process. Since the effects of the time-dependent occurrence model are qualitatively identical to shaking, tsunami, and combined loss curves (for the same magnitude model), the multi-hazard loss curves are mainly discussed in the following.

Sensitivity to Elapsed Time Since the Last Major Event

Different temporal phases within a renewal process lead to different risk estimates of the time-dependent hazards. To investigate this aspect, hypothetical values of T_E = 50 and 100 years (Cases 8 and 9) are considered and their combined loss curves for Iwanuma and Onagawa are compared in **Figure 10** with the time-independent occurrence case (Case 2) and the time-dependent occurrence case for the current situation (Case 5). The time window length is 1 year and the ν value for the time-dependent cases is set to 0.5. Considering a longer elapsed time since the last major event results in significant increase of the multi-hazard loss by changing the positions of the loss curves by a factor of 10 times or more in terms of annual probability of exceedance.

The results shown in **Figure 10** indicate that when the intermediate temporal phase is reached (T_E = 50 years), the combined loss curves for the time-dependent (red) and time-independent (black) cases become similar. When major events are overdue (T_E = 100 years), the time-dependent loss curves exceed the time-independent counterparts. It is important to note that the observations made for **Figure 10** are specific to the numerical set-up of the models considered. In other words, they should not be generalized since the results depend other parameters, such as mean recurrence period (i.e., magnitude model) and aperiodicity parameter.

Sensitivity to Time Window Length

The time horizon of the multi-hazard loss estimation depends on the purposes of such quantitative risk assessments as well as the types of disaster risk mitigation planning and actions. As such, a longer time window of T_D = 30 years is chosen. To examine the effects of aperiodicity parameter in tandem with different elapsed times since the last major event, multi-hazard loss curves for Iwanuma and Onagawa are compared in **Figure 11** by considering Weibull-based renewal models with ν = 0.3, 0.5, and 0.7 (Cases 10 to 15). **Figures 11A,B** are based on T_E = 10 years (current), whereas **Figures 11C,D** are based on T_E = 100 years (hypothetical). Note that the vertical axis of the loss curves in **Figure 11** corresponds to 30-year probability of exceedance, and thus the direct comparisons with other previous figures are not possible.

When T_E is set to 10 years (**Figures 11A,B**), qualitatively, the observations made for **Figure 9** are applicable. Because the longer time window is considered, the differences of occurrence probability of major events are less dramatic (approximately increase by a factor of 10 in terms of annual probability of exceedance from ν = 0.3 to ν = 0.7), thereby the loss curves are more similar. The order of the loss curves in terms of ν is the same as that shown in **Figure 9**, i.e., loss curves become greater with the increase in ν.

When the cases with T_E = 100 years are inspected (**Figures 11C,D**), the loss curves are increased with respect to those for T_E = 10 years and the differences of the loss curves due to different ν values become relatively less noticeable (by a factor of 2), in comparison with the cases with T_E = 10 years. It is also important to note that the order of the loss curves in terms of ν is now reversed with respect to that for T_E = 10 years. This happens because with the smaller ν value (i.e., more periodic behavior) and the overdue situation of the renewal process ($T_E \approx \mu$), the probability of major events within the considered time window becomes greater.

Sensitivity to Inter-arrival Time Distribution

The last crucial model component of a renewal process is the inter-arrival time distribution. This component is varied by considering T_D = 30 years. Four inter-arrival time distributions are considered: exponential (i.e., time-independent, case 16), Weibull (this model is used as a reference inter-arrival time distribution in the previous cases, Cases 12 and 14), lognormal (Cases 17 and 19), and BPT (Cases 18 and 20). The ν value is set to 0.5 for all time-dependent occurrence models but T_E is changed to either 10 years (current) or 100 years (hypothetical). The results of these cases are compared in **Figure 12**.

The results for the cases with T_E = 10 years (**Figures 12A,B**) show that the time-dependent loss estimation for the current situation leads to overestimation of the multi-hazard loss (by a factor of nearly 10). The same situation is demonstrated in **Figure 10** for T_D = 1 year. It can be observed that the loss curves based on the lognormal and BPT models lead to smaller loss curves compared to those based on the Weibull model (being consistent with the remarks made above for T_D = 1 year). When a hypothetical future situation of T_E = 100 years is considered, the loss curves for the time-dependent cases exceed that for the time-independent case, which is also observed in **Figure 10** for T_D = 1 year. Importantly, the order of the loss curves is changed from BPT ≈ lognormal < Weibull < exponential for the case of T_E = 10 years to exponential < Weibull ≈ lognormal < BPT for the case of T_E = 100 years. The differences of the loss curves for different inter-arrival time distributions are noticeable.

Logic-Tree Analysis of Time-dependent Multi-Hazard Loss Estimation

Overall, the results and observations discussed previously in relation to **Figures 8–12** clearly indicate that all individual model components (i.e., mean recurrence period, aperiodicity, elapsed time since the last major event, time horizon window, and inter-arrival time distribution) can have major influence on the occurrence probability of major events. In addition, interaction between different components also plays an important role in

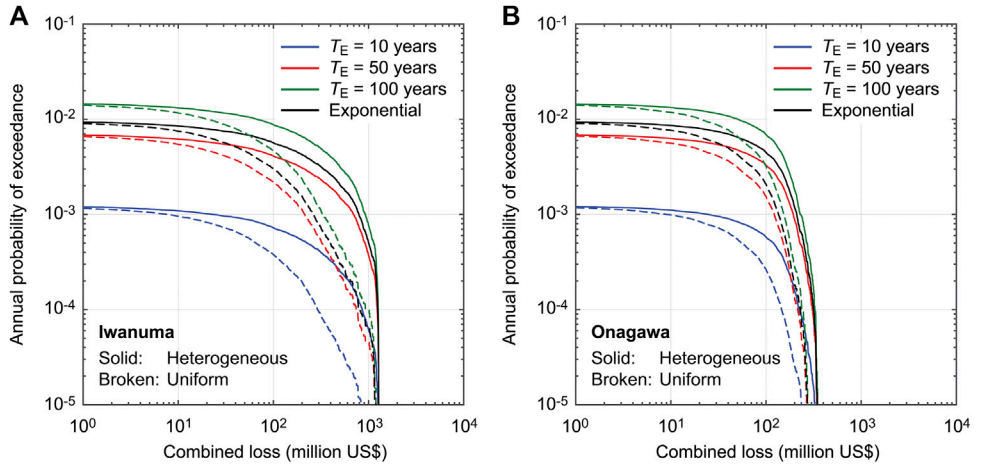

FIGURE 10 | Multi-hazard loss curves for Iwanuma **(A)** and Onagawa **(B)** by considering Weibull-based renewal models with different T_E values (Cases 2, 5, 8, and 9).

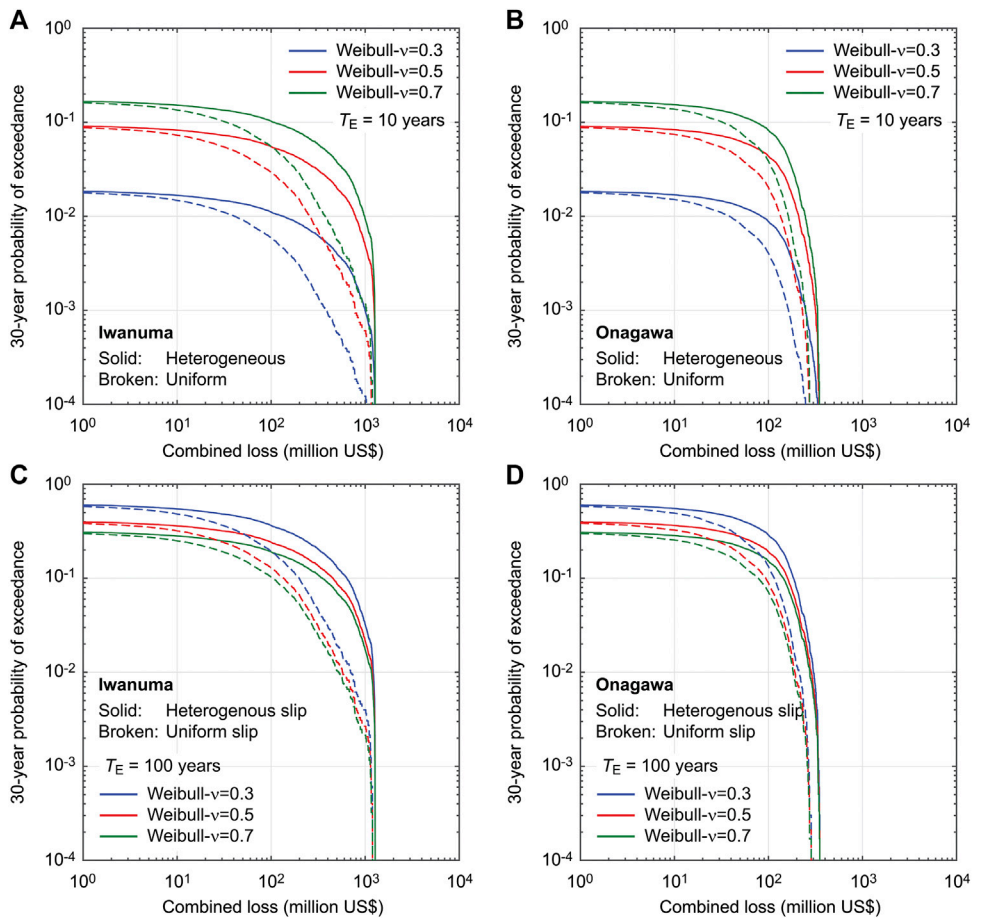

FIGURE 11 | Multi-hazard loss curves for Iwanuma **(A,C)** and Onagawa **(B,D)** by considering Weibull-based renewal models with different T_E and ν values (Cases 10 to 15). The duration of the stochastic event catalogs is set to T_D = 30 years.

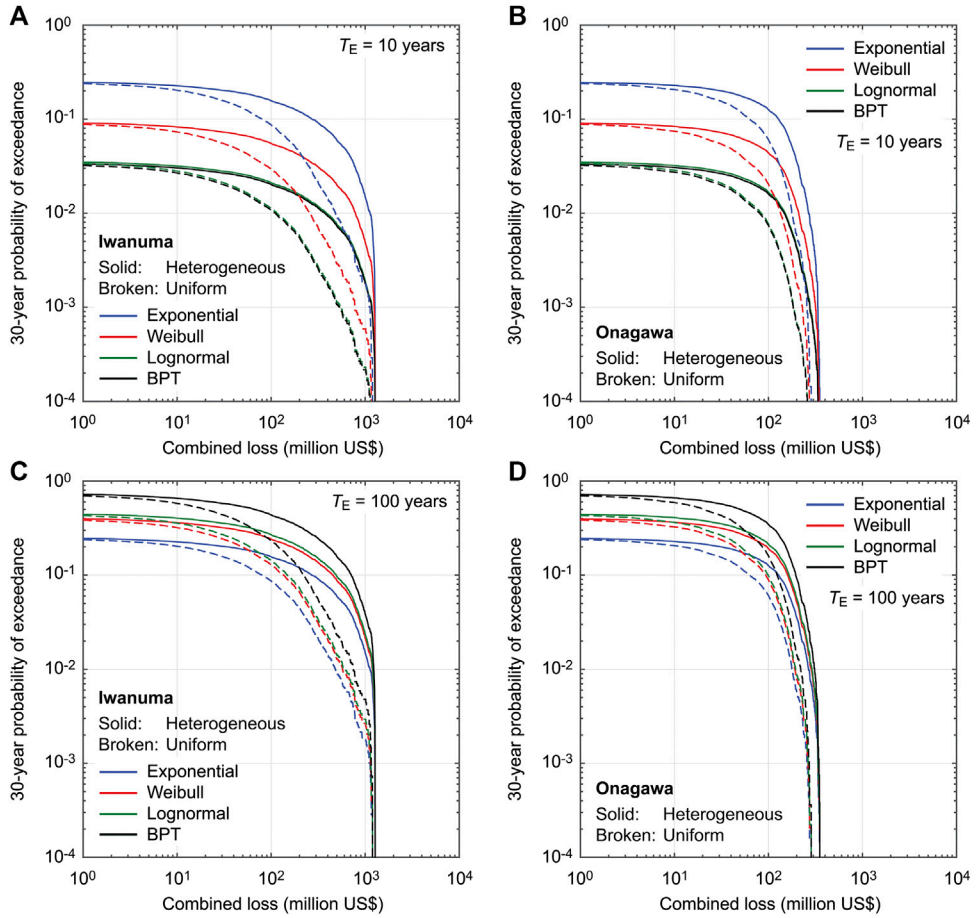

FIGURE 12 | Multi-hazard loss curves for Iwanuma **(A,C)** and Onagawa **(B,D)** by considering different inter-arrival time distributions with T_E = 10 and 100 years and ν = 0.5 (Cases 12, 14, and 16 to 20). The duration of the stochastic event catalogs is set to T_D = 30 years.

calculating such probabilities. Given that some of these model parameters are difficult to constrain based on regional seismicity data alone, it is essential to capture a range of plausible earthquake occurrence models when time-dependent multi-hazard loss estimation is conducted, in light of available data and state of the art knowledge.

To explore the extent of epistemic uncertainty associated with the time-dependent earthquake occurrence model, three characteristic magnitude models considered in Cases 2 to 4, three ν values considered in Cases 5 to 7, and two earthquake slip representations of heterogeneous and uniform slips are implemented in a logic tree (i.e., 18 cases). The inter-arrival time distribution is set to the Weibull model and the time window length is fixed at T_D = 1 year, whereas the elapsed time since the last major event is varied: T_E = 10, 50, and 100 years (as considered in Cases 8 and 9). The weights assigned to the characteristic magnitude models with the lower limits of M8.3, M8.7, and M8.9 are 0.4, 0.3, and 0.3, respectively. The weights for the ν values of 0.3, 0.5, and 0.7 are assigned as 0.3, 0.4, and 0.3, respectively. Equal weighting of the heterogenous and uniform slip distributions is considered. It is noted that the selection of models and parameter sets is limited and the assigned logic-tree weights are chosen arbitrarily for demonstration only. In actual shaking-tsunami hazard and risk assessments, a wider range of logic-tree branches should be considered and their weights need to be scrutinized. This is beyond the scope of this study.

Figure 13 shows multi-hazard loss curves for Iwanuma and Onagawa by considering the above-mentioned logic tree with different T_E values of 10, 50, and 100 years. The individual loss curves are shown with gray color, while the mean, median, and 16th/84th percentile loss curves are shown with solid-red, solid-blue, and broken-blue lines, respectively. For benchmarking purpose, the corresponding loss curves for the heterogenous and uniform slip distributions are also included in the figures (solid/broken-magenta lines). It is noted that for the case of T_E = 10 years (**Figures 13A,B**), the 16th percentile curves lie outside of the graph area and thus are not shown.

The results for T_E = 10 years (**Figures 13A,B**) show a wide variation of individual curves, all of which are below the time-independent loss curves. The minimum and maximum of the individual curves differ by a factor of 100 or more in terms of annual probability of exceedance (depending on the loss levels). The significant range of the results reflects the sensitivity of the

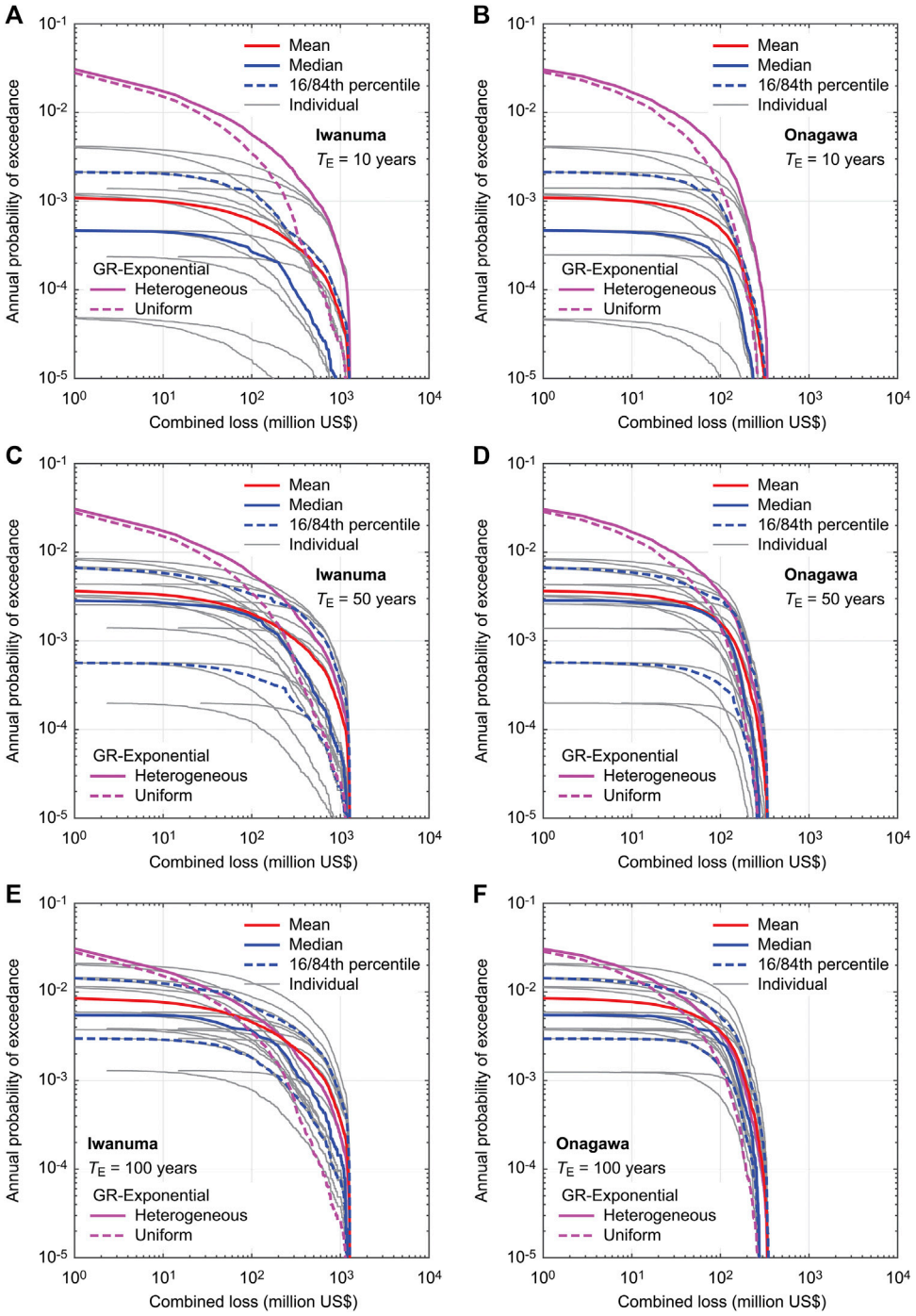

FIGURE 13 | Multi-hazard loss curves for Iwanuma **(A,C,E)** and Onagawa **(B,D,F)** by considering a logic tree with different T_E values of 10, 50, and 100 years.

time-dependent multi-hazard loss curves to the characteristics of the renewal processes considered (e.g., mean recurrence period and aperiodicity), especially in the early phase of the renewal process. With the longer elapsed time of T_E = 50 years (**Figures 13C,D**), the individual loss curves are all shifted upwards and their mean and median curves become more consistent with the time-independent loss curves in a broad sense. Notably, the variation of the individual loss curves is significantly reduced (a factor of circa 20 in terms of annual probability of exceedance), compared with the case of T_E = 10 years. The above-mentioned tendency of the decreased variation of the individual loss curves becomes more obvious

for the case of T_E = 100 years (**Figures 13E,F**), although many of individual cases tend to exceed the corresponding time-independent loss curves, except for annual exceedance probability levels higher than 0.01. An important observation from **Figure 13** is that the extent of epistemic uncertainty associated with time-dependent earthquake occurrence model depends on the elapsed time since the last major event, which is more fundamentally related to the corresponding phase of the temporal occurrence process.

CONCLUSIONS

Shaking and tsunami hazards caused by megathrust subduction earthquakes are time-dependent. Thereby, a suitable modeling framework is needed when multi-hazard risks to coastal communities are concerned. This study developed a novel catastrophe model for time-dependent seismic and tsunami hazards by adopting a renewal process for the earthquake occurrence model. The developed multi-hazard loss model was applied to the two case study locations in Miyagi Prefecture, Japan, having different topographical features. A series of sensitivity analyses was performed by altering the key elements of the renewal process, including mean recurrence period (*via* different magnitude models), aperiodicity parameter, elapsed time since the last major event, time window, and inter-arrival time distribution. The sensitivity analysis results highlight not only the significant influences of individual model components but also the impact of their interaction. The results indicate that the time-dependent earthquake occurrence model should be specified carefully and should account for a range of parameter combinations in a logic tree. Another important observation from the numerical results was that the degree of epistemic uncertainty associated with temporal earthquake occurrence changes with time. Noteworthily, the developed multi-hazard modeling approach for time-dependent shaking and tsunami hazards will enable new applications for evaluating financial risks due to subduction earthquakes and tsunamis at community and regional scales and can be further improved by overcoming the current limitations of the methods.

DATA AVAILABILITY STATEMENT

The raw data supporting the conclusions of this article will be made available by the authors, without undue reservation.

AUTHOR CONTRIBUTIONS

The author confirms being the sole contributor of this work and has approved it for publication.

FUNDING

The work was supported by the Canada Research Chair program (950-232015) and the NSERC Discovery Grant (RGPIN-2019-05898).

REFERENCES

Abaimov, S. G., Turcotte, D. L., Shcherbakov, R., Rundle, J. B., Yakovlev, G., Goltz, C., et al. (2008). Earthquakes: recurrence and interoccurrence times. *Pure Appl. Geophys.* 165, 777–795. doi:10.1007/s00024-008-0331-y

Ceferino, L., Kiremidjian, A., and Deierlein, G. (2020). Probabilistic space- and time-interaction modeling of mainshock earthquake rupture occurrence. *Bull. Seismol. Soc. Am.* 110, 2498–2518. doi:10.1785/0120180220

Construction Research Institute (2011). Japan Building Cost Information 2011. Tokyo, Japan, 547.

Daniell, J. E., Schaefer, A. M., and Wenzel, F. (2017). Losses associated with secondary effects in earthquakes. *Front. Built Environ.* 3, 30. doi:10.3389/fbuil.2017.00030

De Risi, R., Goda, K., Yasuda, T., and Mori, N. (2017). Is flow velocity important in tsunami empirical fragility modeling? *Earth Sci. Rev.* 166, 64–82. doi:10.1016/j.earscirev.2016.12.015

Field, E. H., and Jordan, T. H. (2015). Time-dependent renewal-model probabilities when date of last earthquake is unknown. *Bull. Seismol. Soc. Am.* 105, 459–463. doi:10.1785/0120140096

Frankel, A., Wirth, E., Marafi, N., Vidale, J., and Stephenson, W. (2018). Broadband synthetic seismograms for magnitude 9 earthquakes on the Cascadia megathrust based on 3D simulations and stochastic synthetics, Part 1: methodology and overall results. *Bull. Seismol. Soc. Am.* 108, 2347–2369. doi:10.1785/0120180034

Fraser, S., Raby, A., Pomonis, A., Goda, K., Chian, S. C., Macabuag, J., et al. (2013). Tsunami damage to coastal defences and buildings in the March 11th 2011 Mw 9.0 Great East Japan earthquake and tsunami. *Bull. Earthq. Eng.* 11, 205–239. doi:10.1007/s10518-012-9348-9

Fukutani, Y., Suppasri, A., and Imamura, F. (2015). Stochastic analysis and uncertainty assessment of tsunami wave height using a random source parameter model that targets a Tohoku-type earthquake fault. *Stoch. Environ. Res. Risk Assess.* 29, 1763–1779. doi:10.1007/s00477-014-0966-4

Goda, K., and Atkinson, G. M. (2010). Intraevent spatial correlation of ground-motion parameters using SK-net data. *Bull. Seismol. Soc. Am.* 100, 3055–3067. doi:10.1785/0120100031

Goda, K., and Atkinson, G. M. (2014). Variation of source-to-site distance for megathrust subduction earthquakes: effects on ground motion prediction equations. *Earthq. Spectra.* 30, 845–866. doi:10.1193/080512eqs254m

Goda, K., and De Risi, R. (2018). Multi-hazard loss estimation for shaking and tsunami using stochastic rupture sources. *Int. J. Disaster Risk Reduct.* 28, 539–554. doi:10.1016/j.ijdrr.2018.01.002

Goda, K., and Hong, H. P. (2006). Optimal seismic design for limited planning time horizon with detailed seismic hazard information. *Struct. Saf.* 28, 247–260. doi:10.1016/j.strusafe.2005.08.001

Goda, K., Mai, P. M., Yasuda, T., and Mori, N. (2014). Sensitivity of tsunami wave profiles and inundation simulations to earthquake slip and fault geometry for the 2011 Tohoku earthquake. *Earth Planets Space.* 66, 105. doi:10.1186/1880-5981-66-105

Goda, K. (2019). Time-dependent probabilistic tsunami hazard analysis using stochastic rupture sources. *Stoch. Environ. Res. Risk Assess.* 33, 341–358. doi:10.1007/s00477-018-1634-x

Goda, K., Yasuda, T., Mori, N., and Maruyama, T. (2016). New scaling relationships of earthquake source parameters for stochastic tsunami simulation. *Coast Eng. J.* 58, 1650010. doi:10.1142/s0578563416500108

Goto, C., Ogawa, Y., Shuto, N., and Imamura, F. (1997). Numerical method of tsunami simulation with the leap-frog scheme. IOC Manual, Paris, France: UNESCO, Technical No. 35.

Grezio, A., Babeyko, A., Baptista, M. A., Behrens, J., Costa, A., Davies, G., et al. (2017). Probabilistic tsunami hazard analysis: multiple sources and global applications. *Rev. Geophys.* 55, 1158, doi:10.1002/2017RG000579

Kajitani, Y., Chang, S. E., and Tatano, H. (2013). Economic impacts of the 2011 Tohoku-Oki earthquake and tsunami. *Earthq. Spectra.* 29, S457–S478. doi:10.1193/1.4000108

Kiremidjian, A. S., and Anagnos, T. (1984). Stochastic slip-predictable model for earthquake occurrences. *Bull. Seismol. Soc. Am.* 74, 739–755.

Kusaka, A., Ishida, H., Torisawa, K., Doi, H., and Yamada, K. (2015). Vulnerability functions in terms of ground motion characteristics for wooden houses evaluated by use of earthquake insurance experience. *AIJ J. Technol. Des.* 21, 527–532. doi:10.3130/aijt.21.527

Li, L., Switzer, A. D., Chan, C.-H., Wang, Y., Weiss, R., and Qiu, Q. (2016). How heterogeneous coseismic slip affects regional probabilistic tsunami hazard assessment: a case study in the South China Sea. *J. Geophys. Res. Solid Earth.* 121, 6250–6272. doi:10.1002/2016jb013111

Maeda, T., Furumura, T., Noguchi, S., Takemura, S., Sakai, S., Shinohara, M., et al. (2013). Seismic- and tsunami-wave propagation of the 2011 off the Pacific coast of Tohoku earthquake as inferred from the tsunami-coupled finite-difference simulation. *Bull. Seismol. Soc. Am.* 103, 1411–1428. doi:10.1785/0120120118

Mai, P. M., and Beroza, G. C. (2002). A spatial random field model to characterize complexity in earthquake slip. *J. Geophys. Res.: Solid Earth.* 107, 2308. doi:10.1029/2001jb000588

Marzocchi, W., Taroni, M., and Selva, J. (2015). Accounting for epistemic uncertainty in PSHA: logic tree and ensemble modeling. *Bull. Seismol. Soc. Am.* 105, 2151–2159. doi:10.1785/0120140131

Matthews, M. V., Ellsworth, W. L., and Reasenberg, P. A. (2002). A Brownian model for recurrent earthquakes. *Bull. Seismol. Soc. Am.* 92, 2233–2250. doi:10.1785/0120010267

Melgar, D., Williamson, A. L., and Salazar-Monroy, E. F. (2019). Differences between heterogeneous and homogenous slip in regional tsunami hazards modelling. *Geophys. J. Int.* 219, 553–562

Midorikawa, S., Ito, Y., and Miura, H. (2011). Vulnerability functions of buildings based on damage survey data of earthquakes after the 1995 Kobe earthquake. *J. Japan Assoc. Earthq. Eng.*, 11, 34–37. doi:10.5610/jaee.11.4_34

Mitchell-Wallace, K., Jones, M., Hillier, J., and Foote, M. (2017). *Natural catastrophe risk management and modelling: a practitioner's guide*. Wiley-Blackwell, 536

Morikawa, N., and Fujiwara, H. (2013). A new ground motion prediction equation for Japan applicable up to M9 mega-earthquake. *J. Disaster Res.* 8, 878–888. doi:10.20965/jdr.2013.p0878

Mueller, C., Power, W., Fraser, S., and Wang, X. (2015). Effects of rupture complexity on local tsunami inundation: implications for probabilistic tsunami hazard assessment by example. *J. Geophys. Res. Solid Earth.* 120, 488–502. doi:10.1002/2014jb011301

Ogata, Y. (1999). Estimating the hazard of rupture using uncertain occurrence times of paleoearthquakes. *J. Geophys. Res.* 104, 17995–18014. doi:10.1029/1999jb900115

Okada, Y. (1985). Surface deformation due to shear and tensile faults in a half-space. *Bull. Seismol. Soc. Am.* 75, 1135–1154

Park, H., Alam, M. S., Cox, D. T., Barbosa, A. R., and van de Lindt, J. W. (2019). Probabilistic seismic and tsunami damage analysis (PSTDA) of the Cascadia Subduction Zone applied to Seaside, Oregon. *Int. J. Disaster Risk Reduct.* 35, 101076. doi:10.1016/j.ijdrr.2019.101076

Park, S., van de Lindt, J. W., Cox, D., Gupta, R., and Aguiniga, F. (2012). Successive earthquake-tsunami analysis to develop collapse fragilities. *J. Earthq. Eng.* 16, 851–863. doi:10.1080/13632469.2012.685209

Parsons, T., and Geist, E. L. (2008). Tsunami probability in the Caribbean region. *Pure Appl. Geophys.* 168, 2089–2116. doi:10.1007/s00024-008-0416-7

Pitarka, A., Graves, R., Irikura, K., Miyake, H., and Rodgers, A. (2017). Performance of Irikura recipe rupture model generator in earthquake ground motion simulations with Graves and Pitarka hybrid approach. *Pure Appl. Geophys.* 174, 3537–3555. doi:10.1007/s00024-017-1504-3

Selva, J., Tonini, R., Molinari, I., Tiberti, M. M., Romano, F., Grezio, A., et al. (2016). Quantification of source uncertainties in seismic probabilistic tsunami hazard analysis (SPTHA). *Geophys. J. Int.* 205, 1780–1803. doi:10.1093/gji/ggw107

Shimazaki, K., and Nakata, T. (1980). Time-predictable recurrence model for large earthquakes. *Geophys. Res. Lett.* 7, 279–282. doi:10.1029/gl007i004p00279

Sykes, L. R., and Menke, W. (2006). Repeat times of large earthquakes: implications for earthquake mechanics and long-term prediction. *Bull. Seismol. Soc. Am.* 96, 1569–1596. doi:10.1785/0120050083

Tanioka, Y., and Satake, K. (1996). Tsunami generation by horizontal displacement of ocean bottom. *Geophys. Res. Lett.* 23, 861–864. doi:10.1029/96gl00736

Wu, H., Masaki, K., Irikura, K., and Kurahashi, S. 2016). Empirical fragility curves of buildings in northern Miyagi Prefecture during the 2011 off the Pacific coast of Tohoku earthquake. *J. Disaster Res.* 11, 1253–1270. doi:10.20965/jdr.2016.p1253

Yamaguchi, N., and Yamazaki, F. (2001). Estimation of strong motion distribution in the 1995 Kobe earthquake based on building damage data. *Earthq. Eng. Struct. Dynam.* 30, 787–801. doi:10.1002/eqe.33

Conflict of Interest: The authors declare that the research was conducted in the absence of any commercial or financial relationships that could be construed as a potential conflict of interest.

frontiers in Earth Science

ORIGINAL RESEARCH
published: 11 December 2020
doi: 10.3389/feart.2020.591549

Probabilistic Tsunami Hazard Analysis: High Performance Computing for Massive Scale Inundation Simulations

Steven J. Gibbons[1], Stefano Lorito[2], Jorge Macías[3], Finn Løvholt[1], Jacopo Selva[4], Manuela Volpe[2], Carlos Sánchez-Linares[3], Andrey Babeyko[5], Beatriz Brizuela[2], Antonella Cirella[2], Manuel J. Castro[3], Marc de la Asunción[3], Piero Lanucara[6], Sylfest Glimsdal[1], Maria Concetta Lorenzino[2], Massimo Nazaria[2], Luca Pizzimenti[2], Fabrizio Romano[2], Antonio Scala[7], Roberto Tonini[2], José Manuel González Vida[3] and Malte Vöge[1]*

[1]The Norwegian Geotechnical Institute (NGI), Oslo, Norway, [2]Istituto Nazionale di Geofisica e Vulcanologia (INGV), Rome, Italy, [3]Departamento de Análisis Matemático, Estadística e Investigacíon Operativa y Matemática Aplicada, Facultad de Ciencias, Universidad de Málaga, Málaga, Spain, [4]Istituto Nazionale di Geofisica e Vulcanologia (INGV), Bologna, Italy, [5]GFZ German Research Centre for Geosciences, Potsdam, Germany, [6]CINECA SuperComputing Applications and Innovation, Rome, Italy, [7]Department of Physics "Ettore Pancini", University of Naples "Federico II", Naples, Italy

OPEN ACCESS

Edited by:
Joanna Faure Walker, University College London, United Kingdom

Reviewed by:
Alberto Armigliato, University of Bologna, Italy
Hyoungsu Park, University of Hawaii at Manoa, United States

***Correspondence:**
Steven J. Gibbons
steven.gibbons@ngi.no

Specialty section:
This article was submitted to Geohazards and Georisks, a section of the journal Frontiers in Earth Science

Received: *04 August 2020*
Accepted: *17 November 2020*
Published: *11 December 2020*

Citation:
Gibbons SJ, Lorito S, Macías J, Løvholt F, Selva J, Volpe M, Sánchez-Linares C, Babeyko A, Brizuela B, Cirella A, Castro MJ, de la Asunción M, Lanucara P, Glimsdal S, Lorenzino MC, Nazaria M, Pizzimenti L, Romano F, Scala A, Tonini R, Manuel González Vida J and Vöge M (2020) Probabilistic Tsunami Hazard Analysis: High Performance Computing for Massive Scale Inundation Simulations. Front. Earth Sci. 8:591549. doi: 10.3389/feart.2020.591549

Probabilistic Tsunami Hazard Analysis (PTHA) quantifies the probability of exceeding a specified inundation intensity at a given location within a given time interval. PTHA provides scientific guidance for tsunami risk analysis and risk management, including coastal planning and early warning. Explicit computation of site-specific PTHA, with an adequate discretization of source scenarios combined with high-resolution numerical inundation modelling, has been out of reach with existing models and computing capabilities, with tens to hundreds of thousands of moderately intensive numerical simulations being required for exhaustive uncertainty quantification. In recent years, more efficient GPU-based High-Performance Computing (HPC) facilities, together with efficient GPU-optimized shallow water type models for simulating tsunami inundation, have now made local long-term hazard assessment feasible. A workflow has been developed with three main stages: 1) Site-specific source selection and discretization, 2) Efficient numerical inundation simulation for each scenario using the GPU-based Tsunami-HySEA numerical tsunami propagation and inundation model using a system of nested topo-bathymetric grids, and 3) Hazard aggregation. We apply this site-specific PTHA workflow here to Catania, Sicily, for tsunamigenic earthquake sources in the Mediterranean. We illustrate the workflows of the PTHA as implemented for High-Performance Computing applications, including preliminary simulations carried out on intermediate scale GPU clusters. We show how the local hazard analysis conducted here produces a more fine-grained assessment than is possible with a regional assessment. However, the new local PTHA indicates somewhat lower probabilities of exceedance for higher maximum inundation heights than the available regional PTHA. The local hazard analysis takes into account small-scale tsunami inundation features and non-linearity which the regional-scale assessment does not incorporate. However, the deterministic inundation simulations neglect some uncertainties stemming from the simplified source

treatment and tsunami modelling that are embedded in the regional stochastic approach to inundation height estimation. Further research is needed to quantify the uncertainty associated with numerical inundation modelling and to properly propagate it onto the hazard results, to fully exploit the potential of site-specific hazard assessment based on massive simulations.

Keywords: tsunami, hazard, probabilistic tsunami hazard analysis, high-performance computing, gpu, inundation, earthquakes

INTRODUCTION

Tsunamis are infrequent hazards that can potentially lead to devastating consequences. Earthquakes are the most common source of tsunamis (about 80% of tsunamis worldwide, see e.g. the NCEI global tsunami database: https://www.ngdc.noaa.gov/hazard/tsu_db.shtml) and we restrict the analysis here to seismic sources (coined seismic PTHA or S-PTHA, see e.g., Lorito et al., 2015). Their induced tsunamis pose a risk toward the global coastal population, both related to human casualties (Løvholt et al., 2012), direct economic losses (e.g., Løvholt et al., 2015), to critical infrastructures useful for crisis management (e.g., harbors: Argyroudis et al., 2020), or through secondary cascading events such as in the Fukushima event (e.g., Synolakis and Kânoğlu, 2015). The uncertainty in tsunami hazard models is great, resulting from the infrequency of events (and consequent relatively small datasets of past events), from the vast number of potential sources and tsunami-generating mechanisms (e.g., Grezio et al., 2017; Davies et al., 2018), from the accuracy of high resolution topo-bathymetry and friction models for inundation calculations (e.g., Park et al., 2014; Bricker et al., 2015; Griffin et al., 2015; Sepúlveda et al., 2020), and from the approximations of numerical simulations (e.g., Behrens and Dias, 2015). Among these, the hazard is largely controlled by the source probability of occurrence which is highly uncertain, in particular for large events like megathrust subduction earthquakes of the scale of the 2004 Indian Ocean and 2011 Tohoku event (Lay et al., 2005; Kagan and Jackson, 2013) or large crustal events (Basili et al., 2013). Furthermore, the hazard and related uncertainty stem from the complexity and variety of the various types of earthquake mechanisms such as tsunami earthquakes (e.g., Newman et al., 2011), outer rise events (e.g., the 2009 Samoa tsunami: Fritz et al., 2011), other significant unknown or only partially known crustal sources (Basili et al., 2013; Selva et al., 2016), variable slip (e.g., Geist, 2002; Scala et al., 2020), or generally due to unexpected source mechanisms such as revealed for the Palu tsunami in 2018 (Ulrich et al., 2019). Moreover, tsunamis often happen simultaneously with other hazards, and may interact with them (e.g. earthquakes, landslides, or volcanoes) in a complex manner (e.g., Goda and De Risi, 2018; Pitilakis et al., 2019; Argyroudis et al., 2020). This was demonstrated by the 2018 Palu earthquake and tsunami, where the earthquake (Bao et al., 2019), liquefaction (Cummins, 2019) and tsunami (e.g., Omira et al., 2019; Ulrich et al., 2019) impacted almost simultaneously. Clearly, it is important to have well established methods that can capture these complexities to represent the hazard.

In recent years, Probabilistic Tsunami Hazard Analysis (PTHA: Geist and Parsons, 2006; Grezio et al., 2017) has become the standard way of estimating this complex tsunami hazard. PTHA estimates the probability of exceeding a specified tsunami metric (e.g. flow depth, tsunami height, or momentum flux) at a given location within a given time interval, such as the probability of exceeding a specified inundation height within the next 50 years. Tsunami observations are usually not sufficient for constraining a PTHA. Computation-based PTHA considers a discretization of the total hazard into many potential source scenarios, together with the estimated probability of occurrence of each scenario, for as many scenarios as necessary to represent the expected natural variability in a probabilistic source model. To resolve tsunami source uncertainty adequately, many thousands or sometimes even millions of scenarios need to be simulated (e.g., Selva et al., 2016). To be feasible, PTHA applications have therefore often resorted to estimating the hazard offshore and extrapolating it onshore, and sometimes applying stochastic inundation modeling (e.g. Power et al., 2007; Burbidge et al., 2008; Horspool et al., 2014; Davies et al., 2018; Glimsdal et al., 2019). It has so far not been possible to conduct tsunami hazard analysis running this broad range of scenarios without renouncing some details needed for practical applications. For instance, the first widely accepted probabilistic tsunami hazard map for Europe was developed within the TSUMAPS-NEAM project (http://www.tsumaps-neam.eu/), which covers the hazard in the North-eastern Atlantic, the Mediterranean and connected seas (NEAM). This so-called NEAMTHM18 assessment (Basili et al., 2018; Basili et al., 2019) includes millions of sources, but estimates inundation probability at regional scales based on offshore analysis of tsunami simulations (Glimsdal et al., 2019), and so lacks the high-resolution inundation simulation typical of site-specific PTHA.

Local scale applications to date have needed to reduce the number of simulations dramatically in order to be feasible. González et al. (2009) provided the first local PTHA, generating inundation maps for a location in Oregon using the MOST simulation software (Titov and Gonzalez, 1997) on a system of nested grids. However, this study was limited to a small number of megathrust earthquake scenarios deemed to dominate the hazard at the target region. Lorito et al. (2015) address the feasibility of inundation maps for Seismic PTHA (S-PTHA) for the Mediterranean region, with strategies for reducing the number of simulations required to optimize accuracy in the hazard. This work was taken further by Volpe et al. (2019) who

emphasized the need to differentiate between near-field and far-field sources due to the alteration of the coastal height as a consequence of co-seismic displacement. However, to date, there exists no available benchmark that covers the source variability sufficiently, which can be used to test the degree to which the above simplifications are viable. A necessary element that has been lacking moving forward on this aspect, is the availability of computation resources and related workflows that allow effective use of PTHA on the major computational facilities, namely Tier-0 High Performance Computing (HPC) systems (Løvholt et al., 2019).

We here attempt to bridge the gap between regional-scale PTHA and scenario-specific local inundation simulation, by developing and prototyping a new workflow for site-specific high-resolution PTHA using HPC. This local PTHA workflow is a so-called pilot demonstrator of the H2020 funded ChEESE Center of Excellence (https://cheese-coe.eu/) for addressing geophysical problems related to solid earth processes using (future) pre-Exascale and Exascale supercomputers. A comprehensive PTHA with high resolution inundation calculations at local scale is a problem that is only tractable given such computational resources. In this paper, we used as a starting point for our site-specific analysis the existing regional-scale NEAMTHM18 tsunami hazard assessment (Basili et al., 2019). Hence, we will not assess source probabilities from scratch here, but rather use those probabilities derived by Basili et al. (2019) as input to our analysis. Our primary objective is to extend this regional analysis to local hazard combining high resolution topo-bathymetric data with nonlinear shallow water (NLSW) inundation modeling using the multi-GPU finite volumes Tsunami-HySEA model (de la Asunción et al., 2013; Macías et al., 2017; Macías et al., 2020a; Macías et al., 2020b), restricting the simulations to the sources deemed relevant by NEAMTHM18 at the specific site considered. To this end, we present a new workflow embedding Tsunami-HySEA into PTHA and demonstrate the suitability for HPC usage. We also present comparison with the previous NEAMTHM18 analysis for the offshore tsunami hazard, as well as new inundation hazard curves and maps.

This paper is organized as follows: In *The Seismic Probabilistic Tsunami Hazard Assessment in the Mediterranean Region: The Regional Model NEAMTHM18*, we describe briefly the NEAMTHM18 analysis relevant for creating the input to the local hazard. In *Implementation of a High-Performance Computing Oriented Seismic Probabilistic Tsunami Hazard Analysis Workflow*, the PTHA workflow is described, including the source disaggregation from NEAMTHM18 and the inundation simulations with Tsunami-HySEA on Tier-0 GPU clusters. The setup for the example case presented here, Catania harbor, is described in *Setup for Hazard Analysis Toward the City of Catania*. In *Results*, the inundation calculations and hazard aggregation are discussed in the context of previous results (*Setup for Hazard Analysis Toward the City of Catania*). We finally provide future perspectives.

THE SEISMIC PROBABILISTIC TSUNAMI HAZARD ASSESSMENT IN THE MEDITERRANEAN REGION: THE REGIONAL MODEL NEAMTHM18

The NEAMTHM18 tsunami hazard model provided a rigorous analysis of the annual rates of possible earthquake events and of the tsunami hazard curves for the coastlines of the NEAM region using many millions of scenarios. It is also the first community and consensus based regional tsunami hazard assessment in the NEAM, where the quantification of epistemic uncertainties was heavily based on expert opinion distilled through formal elicitation processes. For details related to the establishment of the source probabilities, we refer to Basili et al. (2019).

The NEAMTHM18 PTHA considered two types of earthquake sources (Selva et al., 2016), coined Predominant Seismicity (PS) and Background Seismicity (BS). PS consists of earthquakes associated with subduction interfaces and major fault systems, where the fault geometries and mechanisms are relatively well understood. The second (BS) class comprises (crustal) seismicity associated with other fault systems, the knowledge and geometry of which may be more incomplete. The BS earthquakes can, in principle, occur anywhere. This distinction was adopted for the sources established in TSUMAPS-NEAM and Basili et al. (2019) provide a comprehensive description of the employed source discretization. In the Mediterranean, PS comprises three main subduction interfaces: the Calabrian, Hellenic and Cyprian arcs. Here, PS scenarios are defined by a specified slip on each element of triangular meshes, modelling 3D fault geometries. BS scenarios are defined over a regular grid covering the entire Mediterranean Sea and nearby lands, with sea-bottom deformations modelled by considering uniform slip on rectangular faults (Okada, 1992). The set of tsunamigenic scenarios is defined by systematic discretizations of the earthquake parameters describing these two classes of seismicity.

The NEAMTHM18 tsunami scenarios were produced by linear combinations of previously simulated elementary Gaussian sources (Molinari et al., 2016). These simulations involved approximately 200,000 Tsunami-HySEA simulations carried out offshore for the entire NEAM region. This was possible since the offshore tsunami simulations were linear, and linear combinations could be employed to provide a much higher number of scenarios. Amplification factors translated the offshore wave characteristics to inundation height depending on the local bathymetry, and on the polarity and dominant period of the incident wave (Glimsdal et al., 2019). Amplification factors simplify the assessment for a regional hazard quantification. However, they do not capture the nonlinearity, nor include the detailed dynamics of inundation on local topography. This quantification is associated with very large uncertainties, mainly epistemic. These uncertainties are quantified by hundreds of NLSW inundation simulations carried out at different sites, and stem largely from the topographic variability onshore. These uncertainties are then treated by means of conditional probabilities as a function of

the amplified inundation heights (Glimsdal et al., 2019). However, these conditional probabilities are not site-specific, as they were estimated by aggregating inundation simulations from a variety of different coastal sites. The application of local high-resolution topography and inundation simulations here is mainly to try to reduce this epistemic uncertainty.

The number of scenarios considered in NEAMTHM18, restricted to the Mediterranean area only, is in the order of 10^6 (Basili et al., 2019). Even with massive Tier-0 HPC resources available, the number of source scenarios in NEAMTHM18 must be dramatically trimmed down to be feasible for local tsunami hazard computation. For this purpose, the most important sources can be determined through hazard disaggregation (e.g., Bazzurro et al., 1999; for tsunamis: Selva et al., 2016; Power et al., 2018). In the next section, we explain the entire workflow for the local PTHA, including details of the disaggregation in the context of NEAMTHM18.

IMPLEMENTATION OF A HIGH-PERFORMANCE COMPUTING ORIENTED SEISMIC PROBABILISTIC TSUNAMI HAZARD ANALYSIS WORKFLOW

Overview of the local Probabilistic Tsunami Hazard Analysis Workflow

The local PTHA workflow consists of the following main components, shown in **Figure 1**, all elaborated in separate subsections below:

- Provision of user specifications, including: definition of hazard metrics, thresholds for the specified metrics, availability of computational resources, and physical input parameters for the hydrodynamic simulations (e.g., topo-bathymetric grids, Manning friction coefficient, CFL number, dry land threshold value, etc.).
- Source selection of scenarios, here using the NEAMTHM18 disaggregation as input (*Disaggregation and Source Selection*). In this step, it is also possible to refine the sources (to provide more sources to cover more broadly the source variability, for example by more finely sampling location and slip distribution of local sources). This source refinement is not used in the example studies provided herein.
- A micro-workflow for HPC inundation simulation (*High-Performance Computing Inundation Simulations and Workflow*), using the NLSW model Tsunami-HySEA as the computational engine for the inundation simulations, capable of managing large ensembles of hundreds of thousands multi-GPU simulations;
- A hazard aggregation step, combining the different model runs to provide hazard curves and maps for potentially inundated areas (*Hazard Aggregation*). This step also manages the epistemic uncertainty by considering the alternative modelling and/or parametrizations for the seismic sources, their recurrence rates, and amplification models, providing the hazard's uncertainty statistics (returning a mean and percentiles). This quantification of epistemic uncertainty is not implemented here, and only the mean hazard curves and inundation maps are presented for the sake of conciseness.

Disaggregation and Source Selection

Local tsunami hazard analysis utilizes non-linear models. Hence it cannot exploit superposition of unit sources as in conventional regional-scale PTHA (Burbidge et al., 2008; Basili et al., 2019). As explained above, it may not be feasible to simulate millions of scenario simulations for local inundation analysis. However, for a specific site, only a limited set of these sources contributes significantly to the hazard. To identify the most significant scenarios, a disaggregation analysis is carried out on the regional hazard estimated in NEAMTHM18 as the first step of the local PTHA workflow. The disaggregation algorithm first ranks all the scenarios contributing to the target site (i.e. to one or more offshore points close to the target site) for a given intensity, or intensity interval, according to their relative importance for the site of interest, measured as their relative contribution to the local offshore hazard curve in terms of mean annual rates. Then, a desired "degree of accuracy" to which the local hazard should be approximated can be defined in terms of the resemblance of the original offshore hazard curves and of the ones calculated only with the selected scenarios, corresponding to the given intensity value or interval. This degree of accuracy formally corresponds to the probability that the occurrence of the target event (a tsunami in the selected interval) is caused by one of the selected sources, as computed from standard disaggregation (e.g., Bazzurro and Cornell, 1999). An example of an application of this procedure using the 1–4 m interval is given in *Scenario Selection and Representation of Probabilities*. The degree of accuracy controls the number of simulations required, and it should be selected based on the available resources and the computational cost, which mainly depends on the size and the spatial resolution of the computational grids.

The input parameters to the disaggregation procedure applied here consist of 1) the selection of the offshore Points of Interest (PoIs) to consider (should be in the vicinity of one or more sites for modelling inundation), 2) the mean annual rate of the set of scenarios retrieved from regional hazard, and 3) a specified value or range of values of interest, provided in terms of Maximum Inundation Height (MIH). We here define the MIH as the largest inundation height above mean sea level at any onshore point in the computational domain. However, when MIH is derived from the regional assessment using amplification factors, it represents a larger area, and must hence be interpreted as a stochastic quantity inheriting the spatial variability of the local MIH.

From NEAMTHM18, we obtain a first order source discretization and corresponding probabilities. The disaggregation of the TSUMAPS-NEAM assessment provides, for a predefined PoI, a list of those earthquake scenarios which dominate the tsunami hazard locally as estimated from offshore simulation results. When the available computational resources allow, we can subsequently perform a refinement of sources and corresponding splitting of probability, to improve the existing

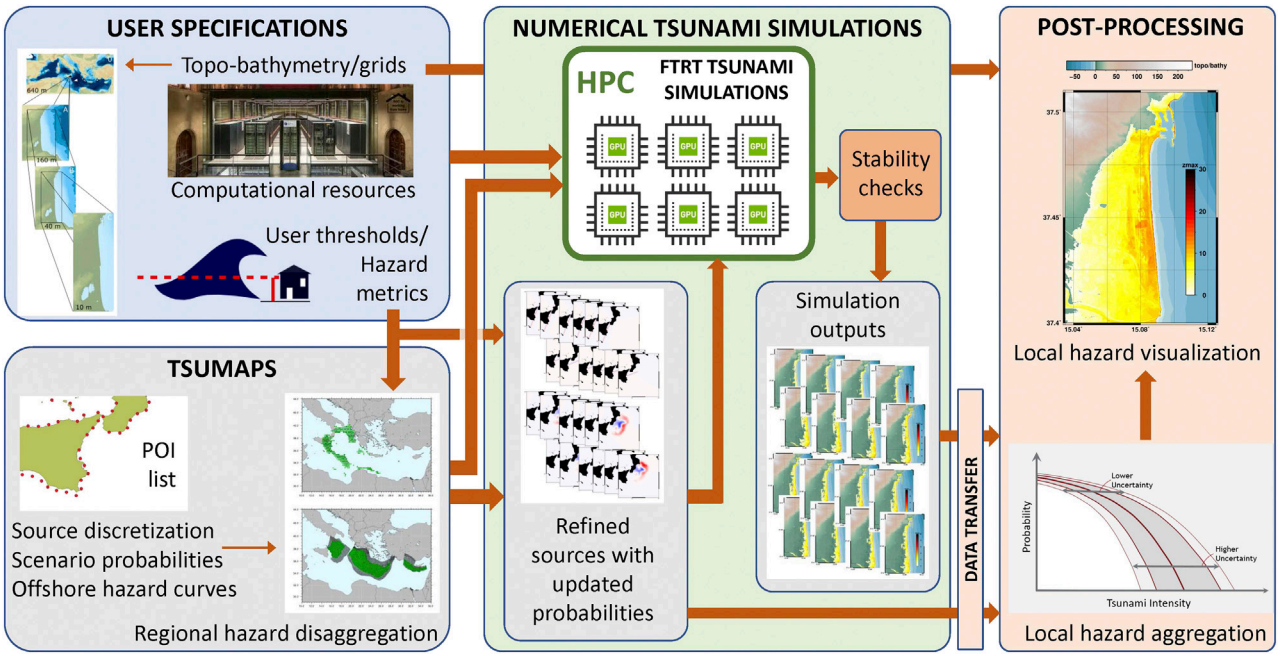

FIGURE 1 | Overview of the Probabilistic Tsunami Hazard Analysis (PTHA) workflow. The step involving HPC resources is shown in the green box. Preprocessing and hazard aggregation is performed outside the HPC system. As large amounts of data can be produced, attention is paid to continuous data transfer during the entire HPC project.

source discretization for the local hazard. We stress that this source splitting step is not carried out in the example cases presented in this paper, but it nevertheless is an essential element of the local PTHA workflow.

The source refinement procedure depends on the source type and, in this case, should be closely tied to the PS and BS source definition in NEAMTHM18. The PS sources may take larger Moment Magnitudes (M_w) that are represented by stochastic fields of heterogeneous slip, embedding the possibility of shallow slip amplification controlled by rigidity and coupling variations with depth (Scala et al., 2020). For the largest magnitudes, the PS sources were modeled by five different stochastic realizations for each given source region. In the local PTHA workflow, the source refinement may allow the user to extend this to an arbitrary increase of heterogeneous slip realizations (to e.g., 20, 30, 40 etc.) depending on computational resources available. Similarly, each individual BS source can be refined with greater resolution in location, fault orientation, and focal mechanism variability. For both the PS and the BS sources, source probabilities from NEAMTHM18 are split from the "parent" scenarios to the "children" scenarios which constitute the refinement of the parent sources, redistributing the total mean annual rates of parent scenarios.

This procedure, with or without refinements, ends with the definition of a list of scenarios to be modelled through HPC. To ensure the feasibility of PTHA, an iterative step in addition to the disaggregation and source refinement procedures is required. This step considers the computational resources available for the tsunami simulations and assesses how many scenarios can be simulated with these constraints. If necessary, a lower disaggregation level is selected, and the scenario list is consequently reduced. Similarly, a reduction of refinement level can be considered.

High-Performance Computing Inundation Simulations and Workflow

Tsunami-HySEA (de la Asunción et al., 2013) is an NLSW model implemented in CUDA for NVIDIA GPU computations and parallelized with MPI for running in multi-GPU architectures. Tsunami-HySEA models both open-ocean tsunami propagation and nested grid inundation using progressively finer grid resolution of the coastal areas in a single code. The code has undergone an intensive process of model validation and verification following, in particular, the benchmarking standards of the NTHMP, the National Tsunami Hazard and Mitigation Program, USA (Macías et al., 2017; Macías et al., 2020a; Macías et al., 2020b). The nested grid meshes are fixed with an arbitrary number of levels satisfying power-of-two refinement ratios. The nested grid algorithm updates the nested grids at coarser grid levels through spatial projection of the mesh values at the finer grids levels. In addition, values at nodes of the coarser grids along the boundaries of each finer grid level are used to drive the simulation on the finer grid. In this way, a two-way update between the fields on each grid level is performed. A new nested grid algorithm has been implemented for the PTHA simulations and adopted thereafter. Specifically, in the new algorithm, the values of the

free surface and water height are projected on the coarse grids and the bathymetry on the coarse grids is modified accordingly to preserve the consistency in the relation h (x,t) = H (x,t)+ŋ(x,t), where H is the bathymetry, h the total water depth, and ŋ the sea surface elevation (from a fixed reference level based on the bathymetric depth value).

The Tsunami-HySEA code is formulated using Finite Volumes and is implemented for multi-GPUs utilizing 2D domain decomposition with load balancing. The efficient use of GPUs makes it one of the most efficient NLSW models available (Løvholt et al., 2019). It includes methods for conveying seabed deformations into tsunami generation based on full potential hydrodynamic theory (Kajiura, 1963; Nosov and Kolesov, 2007). For treating the overland flow, a quadratic Manning friction term is implemented. Moreover, a minimum dry land threshold depth h_m is adopted for stability purposes.

The Tsunami-HySEA code has recently been optimized for improved HPC efficiency. The output is written into NetCDF files that are generated synchronously, or asynchronously using C++11 threads for efficient input-output. The output, one file for each of the two finest sub-meshes and one for storing time series, consists of data that has been compressed using the algorithm described in Tolkova (2007) to further reduce the size of the output files. Tsunami-HySEA has been tested on four Tier-0 supercomputers: the CTE-POWER cluster in the Barcelona Supercomputing Center (BSC), where it has already been used intensively, the DAVIDE cluster and the new MARCONI100 machine at the CINECA consortium in Italy, and Piz-Daint GPU at the Swiss National Supercomputer Center. Relevant to the present application is the synchronous simulations of many independent Tsunami-HySEA simulations in parallel, naturally achieving perfect parallelism (sometimes coined "embarrassing parallelism"). To this end, Tsunami-HySEA provides good so-called weak scalability on the different architectures it has been tested on, meaning that the computational speed is only marginally reduced when many simulations are run synchronously using embarrassing parallelism. For example, the weak scalability obtained for the present set of scenarios was 99.94% when using four GPUs and 98.96% for 64 GPUs on the Marconi-100 supercomputer. Hence, Tsunami-HySEA is well placed to utilize Tier-0 resources to conduct the high number of scenario simulations necessary for PTHA.

Tsunami-HySEA is the engine of the inner PTHA workflow that is carried out within the HPC Tier-0 environment, shown as the green box in **Figure 1**. This inner workflow consists of Faster Than Real Time (FTRT) numerical simulations for each of the selected earthquake scenarios from the disaggregation step on the provided system of nested grids. The nested grids allow for high resolution inundation calculations at the coastal region of interest while keeping a coarser spatial resolution for the open sea wave-propagation, appropriate for the temporal and spatial scale of the wave. It is the system of nested grids, and in particular the grids with the finest resolution, which dominates the simulation time. A more detailed look at the inner-workflow for the HPC resources is provided in **Figure 2**. This provides a closer look at the nested grid structure and illustrates the calculation of inundation maps exemplified for Catania for four example scenarios derived from the disaggregation and source splitting step explained above: two of the BS class, crustal seismicity, and two of the PS class, subduction earthquakes. Moreover, the inner-workflow also includes procedures for filtering spurious simulation results. In the cases where such simulations are discovered, scenarios can be removed from the assessment, and all other probabilities can be normalized. In the analysis presented here, such spurious simulations were not detected, and the renormalization option was not invoked.

Hazard Aggregation

The results from all the simulations are combined in the hazard aggregation step. This consists also of the post-processing and visualization that are performed outside of the HPC resources since these tasks do not require the same level of performance as the simulation calculations themselves. In the aggregation step, the different inundation simulation results are combined to provide hazard curves (probability of exceeding a given MIH during a given exposure time). For a local inundation site, a large number (typically hundreds of thousands) of such curves will be available, with one curve for each inundated point.

These curves are obtained in the following way (for a more complete description we refer to Basili et al., 2019); the individual scenario list and related mean annual rates are derived from the disaggregation and source refinement step, representing the most relevant sources for the local site of interest. For each of these scenarios, we can have different estimates of the mean annual rates and, consequently, of probabilities in the reference exposure time, depending on the epistemic uncertainty. In the aggregation, we assume a time-independent Poisson process implying that the exceedance probabilities can be computed using:

$$P(I > I_C, \Delta T) = 1 - e^{-\sum \lambda(I > I_C).\Delta T}$$

where $P(I > I_C \Delta T)$ represents the probability of the tsunami metric I exceeding a threshold value I_C during an exposure time period ΔT. $\lambda(I > I_C)$ represents the mean annual rates for an individual source giving rise to the tsunami exceeding the given impact metric. Due to their independence, all these rates are summed for deriving the probability of at least one exceedance (PoE) in ΔT for a given threshold I_C.

In this study, for simplicity, we assume that $\lambda(I>I_C)$ can be evaluated, for each individual source, as the product of the mean annual rate of the source and of an identity function which equals 1 if the simulated tsunami exceeds I_C, and 0 otherwise (e.g., Grezio et al., 2017). This procedure neglects the potential uncertainty stemming from the tsunami generation, propagation and inundation model, as well as the one due to the oversimplifications of the source model (Choi et al., 2002). Since this study has the main purpose of illustrating the new workflow, rather than an assessment for operational purposes, we considered our approach sufficiently elaborated. For a specific application, uncertainties can be applied in the form of a conditional probability (Glimsdal et al., 2019) but starting from inundation simulations rather than from offshore results.

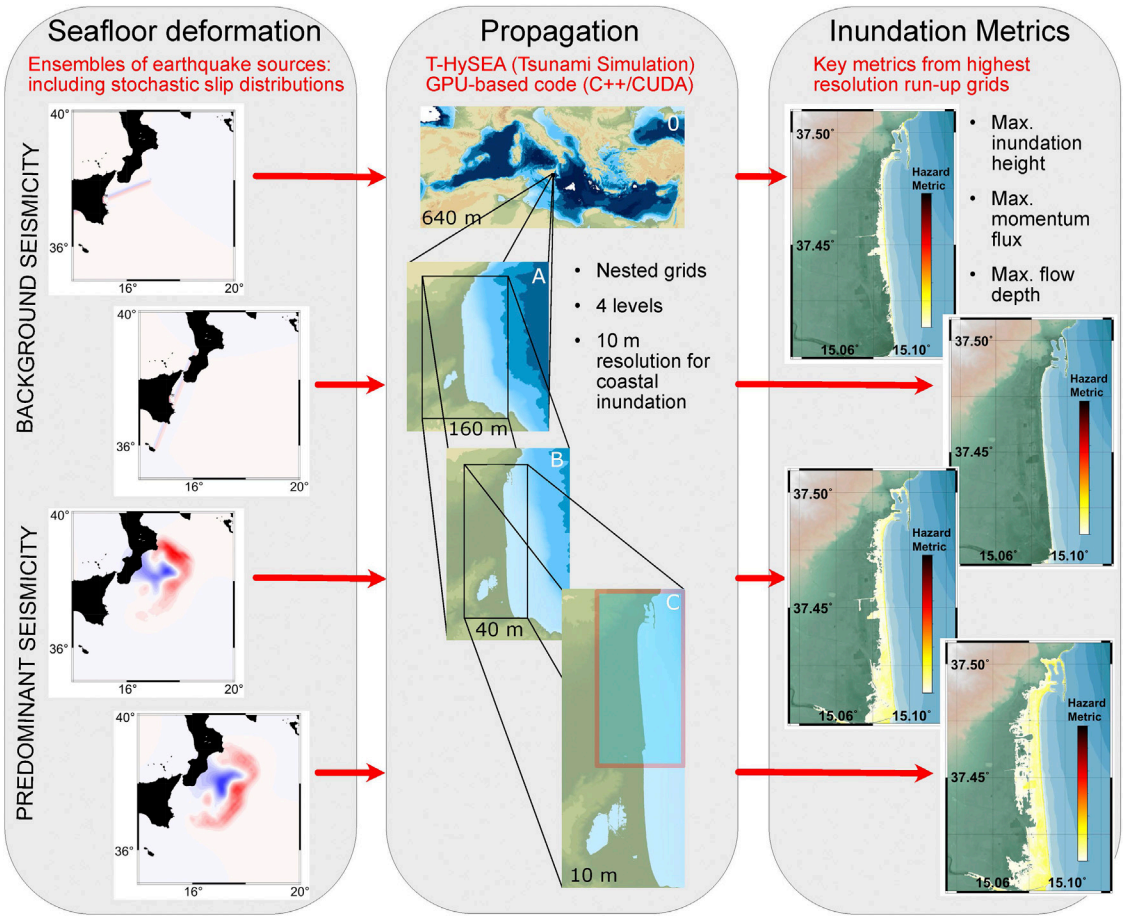

FIGURE 2 | Overview of simulation process, from source models and seafloor displacements **(left)** for BS and PS sources, the nested grid procedure **(center)**, and tsunami inundation **(right)** for different scenarios. The Tsunami-HySEA code simulates the flow depth on the co-seismically deformed bathymetry which is different from scenario to scenario. The aggregated hazard takes this into account. See Scala et al. (2020) for a detailed description of the stochastic slip distributions for the Predominant Seismicity sources.

Ideally, the parameters of the distributions (usually assumed log-normal, Glimsdal et al., 2019 and reference therein) should be calibrated with run-up observations.

Because we based all the present results on a subset of the potential sources selected through disaggregation, the mean annual rates are finally normalized by the degree of accuracy chosen in the disaggregation step. Assuming that the subset can be considered an unbiased sample of all the sources that may generate local tsunamis, we may compensate the removal of potentially impacting sources by re-normalizing the mean annual rates of the selected sources. For example, for a 99% disaggregation level, $\lambda(I>I_C)$ can be simply multiplied with a normalization factor 1/0.99. The PoE can also be converted into average return periods T through the expression $T = \Delta T/\text{abs}(\ln(1 - P(I > I_C \Delta T))$. In the application presented herein, we compute PoEs assuming a ΔT = 50-years exposure time. For example, a 2% PoE in 50 years then yields T ≈ 2,475 years, and a 10% PoE in 50 years yields T ≈ 475 years.

In this paper, we consider the following impact metrics, the MIH, the maximum flow depth H_m, and the maximum depth averaged momentum flux defined as the maximum of the instantaneous product of the square velocity and flow depth $(U^2H)_m$.

When multiple models for source probabilities and/or for tsunami generation, propagation and inundation are implemented, the results are represented as a family of different hazard curves, where each curve represents one realization of the epistemic uncertainty (Grezio et al., 2017). The epistemic uncertainty in annual rates may be inherited from the regional hazard model (here, NEAMTHM18). The epistemic uncertainty in tsunami generation, propagation, and inundation should be evaluated by analyzing the impact of source simplifications and limitations of the numerical tsunami simulations. However, in this paper, only the average of the epistemic uncertainty from the source model is presented: the weighted average of the alternative mean annual rates from NEAMTHM18. The alternatives are weighted according to the relative credibility assigned to the different considered source models in NEAMTHM18.

SETUP FOR HAZARD ANALYSIS TOWARD THE CITY OF CATANIA

Computational Grids and Hydrodynamic Parameters

The Tsunami-HySEA simulations use three levels of nested local grids, as well as one global 0-grid for the open ocean propagation covering the Mediterranean Sea. The finest grid resolution is 10 m, and a spatial refinement ratio of four is used here. Hence, the other grids have resolutions 40 m, 160 m, and 640 m respectively. Their extents are displayed in **Figure 2**. The grid with the coarsest resolution (640 m) uses the open GEBCO topo-bathymetry model (https://www.gebco.net/), which was resampled. Regarding the finest grid, a 10 m DEM model was built interpolating the following datasets:

- LiDAR inland points with 2 m resolution. The Geology and Geotechnologies Laboratory (INGV, http://istituto.ingv.it/it/36-laboratori/1656-laboratorio-geologia-e-geotecnologie.html) provided the LiDAR dataset in the framework of an agreement with the Ministry of the Environment, Earth and Sea (http://www.pcn.minambiente.it) - Italian National Geoportal, owner of the data).
- EMODnet Digital Bathymetry (DTM from EMODnet Bathymetry Consortium (2018) http://doi.org/10.12770/18ff0d48-b203-4a65-94a9-5fd8b0ec35f6, which has a resolution of nearly 112 m.
- EU-DEM, EU-DEM-4258: 1 arcsec - five arcsec, EU-DEM-3035: 25 m, Color shaded DEM derived from the EU-DEM-3035: 25 m "Produced using Copernicus data and information funded by the European Union - EU-DEM layers."
- MaGIC data, foglio 32 e foglio 33, data from the MaGIC project, Dipartimento della Protezione Civile (http://dati.protezionecivile.it/geoportalDPC/catalog/main/home.page).

The coarser intermediate grids (40 m and 160 m) were derived from the 10 m grid by using a bilinear resampling algorithm to assure depth compatibility among all the nesting involved in the simulations. To ensure stability, Tsunami-HySEA simulations use a threshold for water height at inundation (here set to 0.001 m), and a maximum allowed current velocity as a simulation stopping criteria (here set to 40 m/s). A uniform Manning coefficient n = 0.03 is employed for representation of the bed friction. A CFL number of 0.5 is used for the time stepping.

Scenario Selection and Representation of Probabilities

We carried out the disaggregation analysis for PoIs close to the East coast of Sicily, Italy, offshore Catania, based on the NEAMTHM18 regional hazard assessment. To make use of an example of potential practical interest, in this specific application, we selected the interval of MIH derived from the regional assessment between 1 m and 4 m. This should allow the inclusion, up to the 98th percentile, all the scenarios which

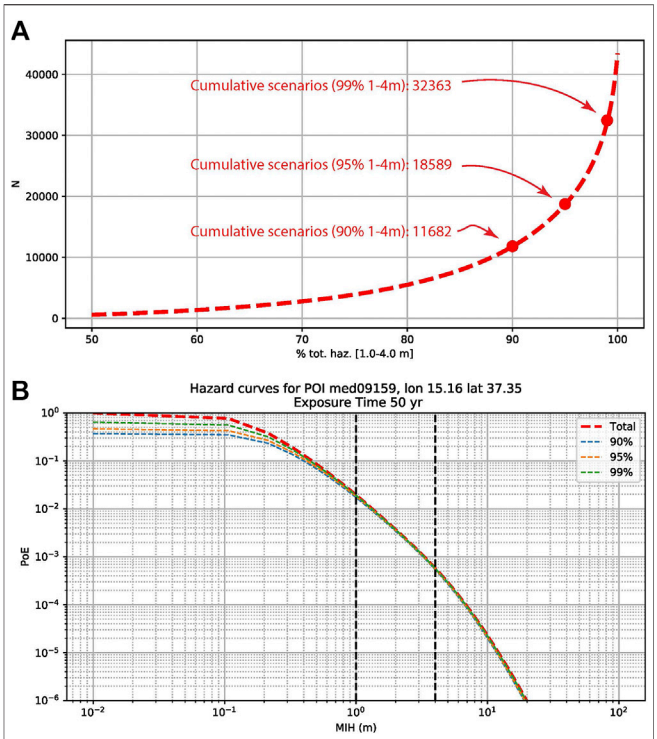

FIGURE 3 | Overview of the hazard disaggregation/scenario selection procedure **(A)** trade-off curve between number of scenarios contributing to the hazard at the site and percentage of hazard reproduction for the 1–4 m interval. The scenarios are ranked such that those contributing the most come first **(B)** The 1–4 m interval hazard curve reproduced with the selected scenarios as well as the complete one.

may generate a run-up comparable to the design value used for the construction of the tsunami evacuation maps in the Catania plain (Dipartimento della Protezione Civile, 2018; Basili et al., 2019). Locally, in fact, the design MIH value used for the subsequent preparation of the evacuation maps is 1.2 m. Since the disaggregation procedure (*Disaggregation and Source Selection*) attempts to approximate the total hazard by ranking the most probable scenarios, and since these highest ranked scenarios generate a smaller MIH in the considered interval, the scenarios in proximity of 1.2 m are almost surely included in the selection when using the 1–4 m interval. Note that the corresponding run-up design value is chosen as three times the design MIH. Based on the reanalysis by Basili et al. (2019) of the simulations performed by Glimsdal et al. (2019), the 98% of the run-up values in the vicinity of the POI where the MIH is estimated would not exceed three times the design value.

Figure 3 (panel A) displays a trade-off curve of the number of scenarios required to quantify the hazard at the Catania PoI as a function of the level of approximation of the total hazard in the 1–4 m interval. In this study, we chose to disaggregate to retain those sources that collectively have a 99% probability of causing hazards in the target interval. Adding up their individual contributions allows the reproduction of 99% of the total hazard. We indicate the number of scenarios required to reproduce 90, 95, and 99% of the hazard. We performed a

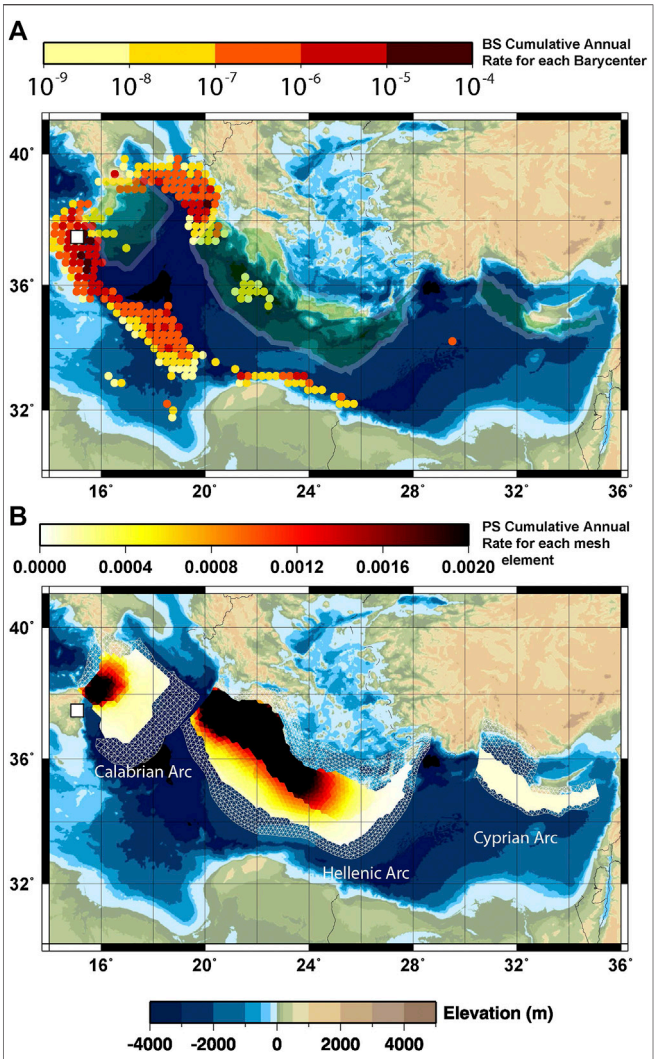

FIGURE 4 | Cumulative annual rates in NEAMTHM18 source discretization resulting in a maximum inundation height (MIH) in the range 1–4 m for Catania (white square) based upon the offshore tsunami simulation result, displayed together with topo-bathymetry of the Mediterranean. The outlines of the PS-source meshes are displayed in Panel **(A)**, demonstrating how crustal (BS) sources are also defined in the same locations as PS sources. "Remote" BS sources, geographically separated from the contiguous source clusters, may appear in the disaggregation given eg marginally more efficient tsunami wave propagation. However, their contribution to the total hazard at Catania is likely to be small given the total number of scenarios considered.

number of disaggregations over different and broader intervals and note that very few additional scenarios result from extending the upper limit of the interval, for example, from 4 m to 8 m. The scenarios that result in the highest inundations are associated with exceptionally low probabilities and few of these scenarios contribute to the PTHA for the time-intervals of interest. This is confirmed in panel B) where the hazard curves calculated from the full NEAMTHM18 model and approximated at the 99% level are nearly the same, providing confidence that neglected scenarios do not contribute significantly in the considered MIH interval.

Altogether 32,363 scenarios were obtained from the disaggregation. Of these scenarios, 11,120 were of type BS and 21,243 were of type PS. We display these scenarios in **Figure 4**, with BS and PS sources covered in panels (A) and (B) respectively. The colors indicate the cumulative rates of the sources, with the darker symbols and shapes indicating a higher probability of seismic slip at the location indicated within the relevant time interval. Both panels display simplifications of the earthquake generated tsunami sources. It can be qualitatively assessed that the hazard is driven by subduction earthquakes and by local crustal sources, consistently with the findings of Selva et al. (2016). For each symbol in panel (A), many earthquake scenarios defined by Okada source parameters have their hypocenter within the region indicated. The scenarios vary in all the other parameters: depth, rupture width, rupture length, slip, and the angles of strike, dip, and rake. The lateral dimensions of the rupture for any one earthquake scenario may exceed significantly the size of the pixel displayed. Similarly, for the PS sources in panel (B), each scenario consists of a slip distribution represented across many elements of a triangular mesh. Since variation in the slip distribution can have significant consequences for inundation, NEAMTHM18 therefore considered several stochastic realizations of slip for a given fault geometry (see Scala et al., 2020). The color of each triangular cell in panel (b) indicates the number of PS scenarios which have a non-zero slip on that particular cell.

For epistemic uncertainty quantification, we adopt the ensemble of mean annual rates describing the epistemic uncertainties on seismic rates in NEAMTHM18. This implies that each scenario simulation is associated with 1,000 alternative estimates of the mean annual rates λ to represent the epistemic uncertainty, that are sampled from the epistemic uncertainty alternative tree (Selva et al., 2016). These epistemic uncertainties represent uncertainty related to the seismicity models such as the Magnitude Frequency Distributions (MFDs), scaling relation used for the earthquake scenario, crustal rigidity model etc., as well as to the simplified inundation model (Glimsdal et al., 2019). All these uncertainties have been unraveled in NEAMTHM18 through a thorough expert elicitation process. As mentioned above, we here present only results based only on averaging the epistemic uncertainty.

RESULTS

Comparison of Offshore Hazard Curves

Before assessing onshore hazard curves, we first verify that the offshore tsunami hazard obtained with the new simulations is consistent with the regional scale hazard estimated in the NEAMTHM18 assessment. This is a general consistency test. Even if all parts of the study are implemented correctly, differences may arise because of several specific reasons. Firstly, we use here only the subset of sources selected after disaggregation and we renormalize the source mean annual rates accordingly to better approximate the hazard curves, even if we

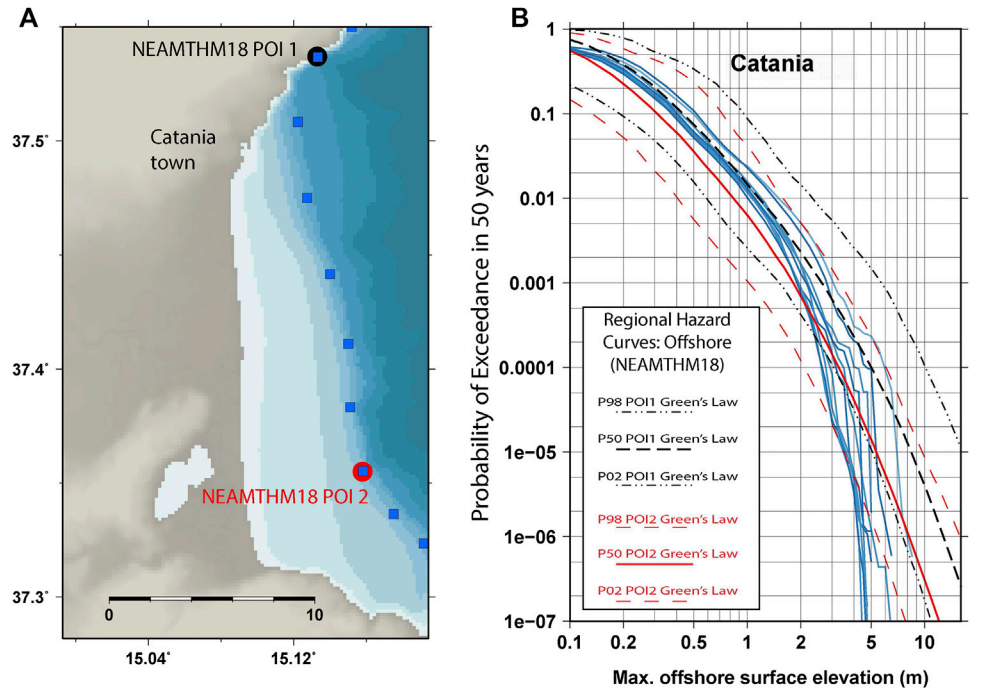

FIGURE 5 | Locations of PoIs offshore Catania **(A)** from the current study (blue squares, with 2 km spacing) and NEAMTHM18 (the red and black circles only, with 20 km spacing). Comparison of Probability of Exceedance curves **(B)** for the PoIs indicated on the map. The blue lines in panel **(B)** are the aggregated hazard curves from the new simulations at each of the PoIs marked with blue squares in panel **(A)**. The red and black curves in panel **(B)** are offshore PoE derived from the corresponding NEAMTHM18 hazard curves with the offshore height calculated from the MIH using Green's Law. The PoIs labeled POI1 (black) and POI2 (red) have geographical coordinates 37.537°N 15.133°E and 37.355°N 15.158°E respectively.

have seen in the previous section that this factor should not be very important. Secondly, a linear combination of elementary sources was used for NEAMTHM18 (Molinari et al., 2016), while in the current study we use direct simulations for each scenario considered. The third reason is that the bathymetric and topographic data and applied grid resolution within the system of nested grids are very different. It should be noted that the NEAMTHM18 hazard curves include log-normal uncertainty (Glimsdal et al., 2019). This treatment is meant to be a pragmatic approach for dealing with uncertainty stemming from potentially inaccurate source and inundation modeling, including DEM inaccuracy. This uncertainty treatment tends to increase the hazard relative to the point-value hazard curves which would be obtained without it, because both a bias and a dispersion are taken into account (see also Davies et al., 2018, their equation 15). We note that a similar observation is found for probabilistic seismic hazard, when the sigma of the ground motion prediction equation is increased (e.g., Bommer and Abrahamson, 2006).

Figure 5A shows the locations of the two offshore Points of Interest (PoIs) from the NEAMTHM18 assessment closest to the town of Catania. Separated by approximately 20 km along the 50 m depth isobath, the two PoIs have very different locations with respect to the coastline. The northernmost point (black), located on steep seafloor, is less than 1 km from the shoreline. The southernmost point (red) is approximately 6 km offshore on a gentler slope facing the coastline. The topo-bathymetric contrast between these two sites alone provides motivation to improve the resolution of the hazard assessment. The curves in **Figure 5B** display offshore maximum elevation Probability of Exceedance (PoE) for a 50-years interval. The red and black curves display the NEAMTHM18 model uncertainty where the 2nd, 50th, and 98th percentiles are estimated for 50 m water depth from the onshore MIH curves using Green's Law. Consistently higher offshore surface elevations are obtained for the northernmost PoI than for the southernmost PoI.

From the HySEA simulations carried out here, we stored time-series of wave height at each of the blue squared points indicated in **Figure 5A**, which are spaced at 2 km intervals along the 50 m isobath. The blue lines in **Figure 5B** show PoE curves for this refined set of PoIs. The new offshore PoE curves lie within the uncertainties estimated from NEAMTHM18 MIH curves up to a maximum offshore wave height of approximately 4 m. Above this level, the newly estimated PoE curves lie below the NEAMTHM18 estimates yet partly within the second percentile of the hazard corresponding to PoI 2. We stress that the (blue) hazard curves in **Figure 5B**, obtained from the local analysis, are not subject to the same uncertainty as the (red and black) curves derived from normalized NEAMTHM18 MIH percentiles. From this comparison, it is evident that the difference grows with growing intensity, as expected from the log-normal uncertainty. We then suggest that the divergence of the local hazard curves is strongly controlled by the uncertainty treatment.

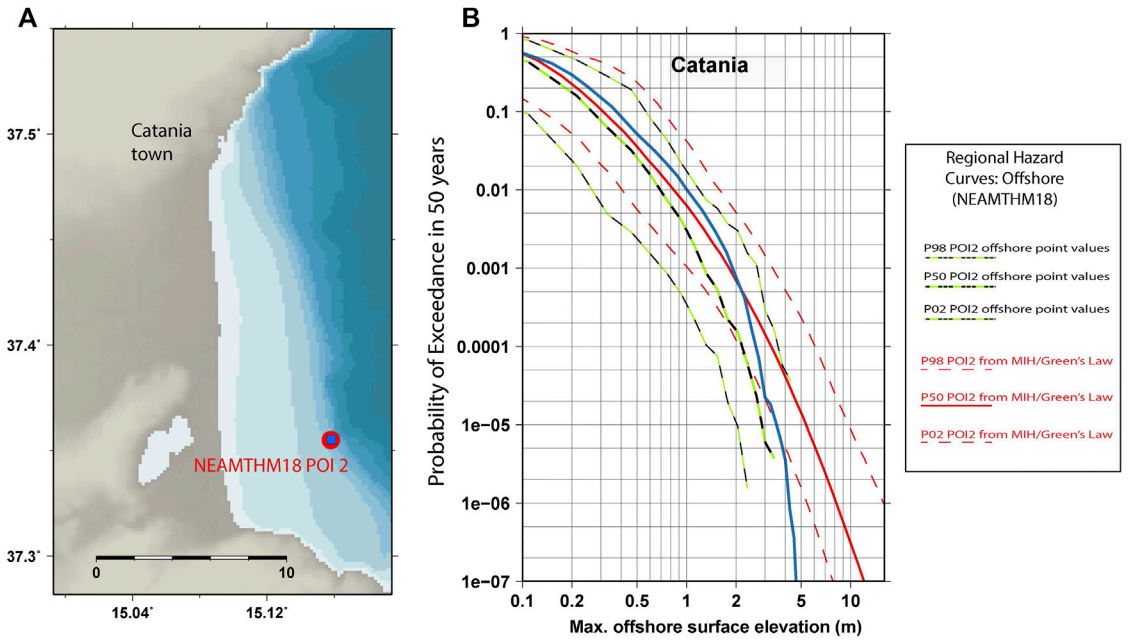

FIGURE 6 | Comparison of offshore PoE curves for the location 37.355°N 15.158°E (50 m depth). Panel **(A)** shows the location of this PoI with respect to the coastline and panel **(B)** displays the new mean offshore hazard curve (blue), the second, 50th, and 98th percentiles of offshore hazard estimated from the NEAMTHM18 MIH curves using Green's Law (red), and the corresponding offshore PoE curves calculated from the offshore point values (black/green).

To better address our claim, we provide a more direct comparison, limited to the single PoI indicated in **Figure 6**. Here, the single mean local hazard curve (blue) is displayed together with both the NEAMTHM18 curves derived from the onshore amplified MIH (red) and NEAMTHM18 percentiles based on offshore point values (black/green). These point-value curves do use the NEAMTHM18 sources and linear combinations, but do not use the amplification factors and associated uncertainty treatment. Whereas the red and the blue curves diverge for the higher tsunami surface elevations (lower probabilities), with the NEAMTHM18 hazard curves indicating a higher PoE for higher offshore surface elevations, the local hazard curve and the point-value NEAMTHM18 curves follow the same trend. We conclude that the NEAMTHM18 model and the local hazard analysis are relatively consistent, despite clear discrepancies on the mean curve that can possibly stem from differences in bathymetric data and spatial resolution as well as the linear combination vs. distinct specification of sources.

While the uncertainty in MIH curves from the amplification factors is neglected, the use of NLSW models reduces the overall uncertainty. However, a significant uncertainty remains due to factors such as NLSW approximations, uncertainties associated with topo-bathymetric data, assumptions in friction modeling, etc. This uncertainty likely has a big impact in the tail of the distribution but, to the best of our knowledge, a method for treating it consistently has not been yet developed. This goes beyond the goals of this paper. However, if site-specific hazard for higher intensities is required, for example due to the presence of a critical infrastructure, then an extended analysis of this uncertainty would be required, as clearly demonstrated in **Figure 5B**.

Inundation and Coastal Zone Hazard Results

Figure 7 displays, as an example, the MIH for a single simulation out of the many considered for the full hazard assessment, for the entire region of the inner grid (left panel). In addition, close-up views for near Catania harbor and on the plains south of the city are also shown (right panels). Clearly, the 10 m grid in the simulation resolves the distribution of inundation heights at a scale of detail of relevance to onshore infrastructures. For each scenario, Tsunami-HySEA stores the maximum inundation height over the co-seismically deformed topography achieved at each grid location. Additional metrics such as maximum current velocities and momentum fluxes, the latter measuring the maximum of the instantaneous products of H and U, are also stored. In the simulations conducted here, it took about 25 min to run a single simulation. However, up to 1,024 simulations could be run synchronously in the Tier-0 system Marconi-100, which meant that we were able to produce more than 2000 scenario simulations during just 1 h.

Figures 8–10 shows the aggregated probability maps using the local PTHA workflow for the city of Catania using three different metrics, namely the flow depth, maximum surface elevation, and the maximum instantaneous momentum flux. These give a first rough overview of the hazard products that can be obtained using the workflow. In each probability map, we assume a 50-years exposure time, and the average hazard with respect to epistemic

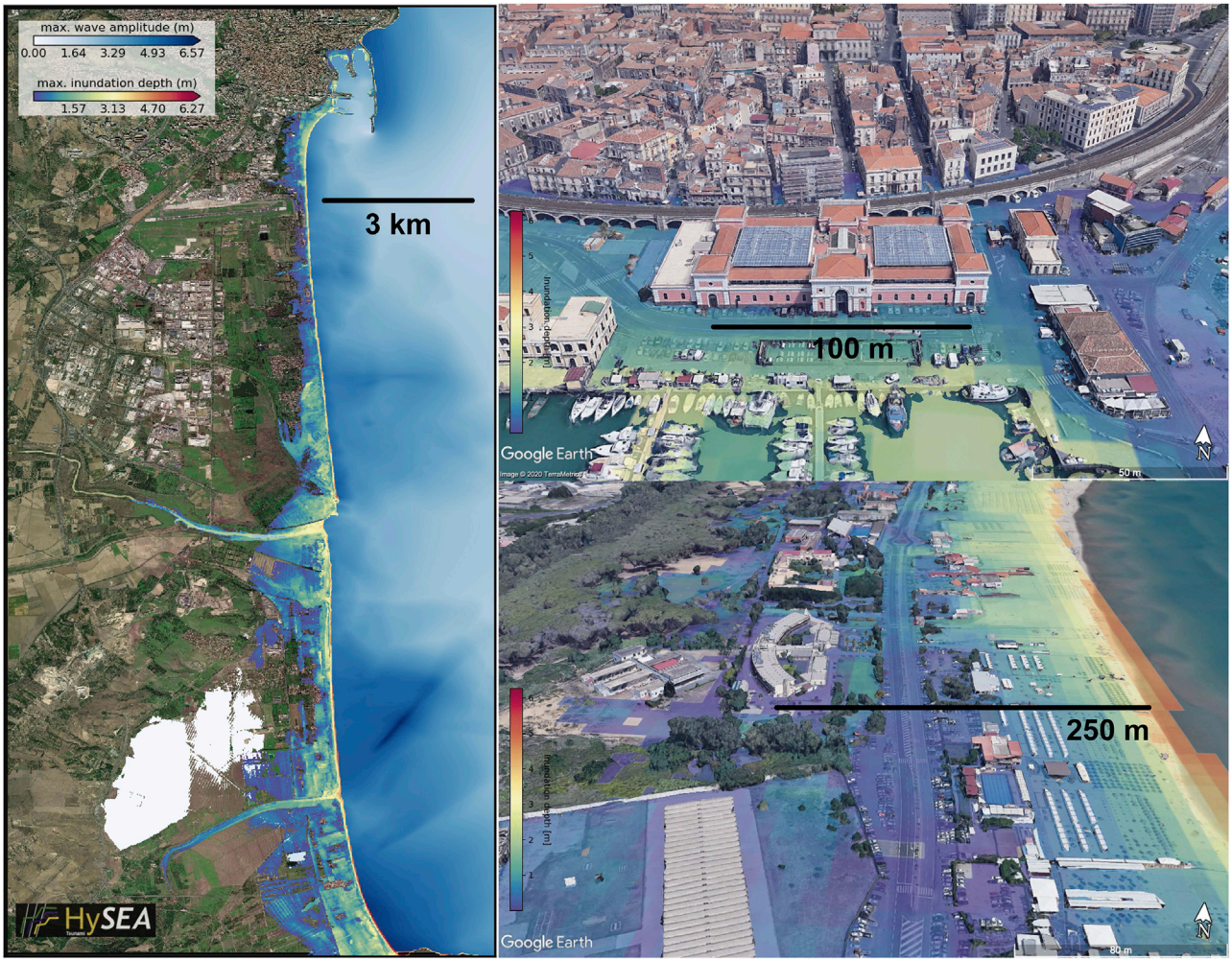

FIGURE 7 | Inundation visualizations at different scales at and close to Catania, Sicily, for a single scenario HySEA simulation to display flow depth in relation to infrastructure and communication routes. The maximum wave height and flow depth are displayed offshore and onshore, respectively. All imagery from and available via Google Earth.

uncertainty (percentile values are presented in a companion paper). Evidently, there is a significant local variability in the flow depth pattern, a clear indication that the local-scale hazard assessment adds much more information, more fine-grained through the utilization of details in the topography, than any regional assessment (using just the two offshore points displayed in **Figure 5** to present the overall hazard). The maps not only clearly differentiate between the more hazardous areas close to the shoreline, and the less hazardous areas located inland, but also resolve interesting differences along the shoreline.

We show the probability of exceeding flow depths of 1 cm, 1 m, 3 m, and 5 m in **Figure 8**. In the south, the PoE-50-years map for 1 m flow depth covers a rather large area extending up to 3–4 km inland, which is largely due to a rather flat and low-lying topography. The inner points have the smallest mapped PoE-50-years of the order of 10^{-5}, corresponding to an average return period T of about half a million years. If dealing with critical infrastructures, the need for looking at even longer return periods may arise.

For evacuation mapping design purposes, a flow depth below 1 m should be considered, given that a flow only a few tens of centimeters deep is considered sufficient in certain circumstances for dragging people away (Takagi et al., 2016). In the north, the flow depths do not extend as far inland due to steeper topography. PoE-50-years values exceeding 0.01 ($T \sim 5000$ years) are mostly confined within 500–1,000 m distances from the shoreline. Moreover, we see clearly that the highest likelihood of exceeding 3 m flow depth is confined to a small strip along the coastline. Note that the flow depth displayed in **Figure 8** is evaluated at locations for which the deformed topography is greater than zero. Hence, co-seismic displacement was dominantly positive, that is an uplift with respect to the pre-event coastline, likely caused by near-field sources which limited the inundation. Such an effect could not be appreciated by the

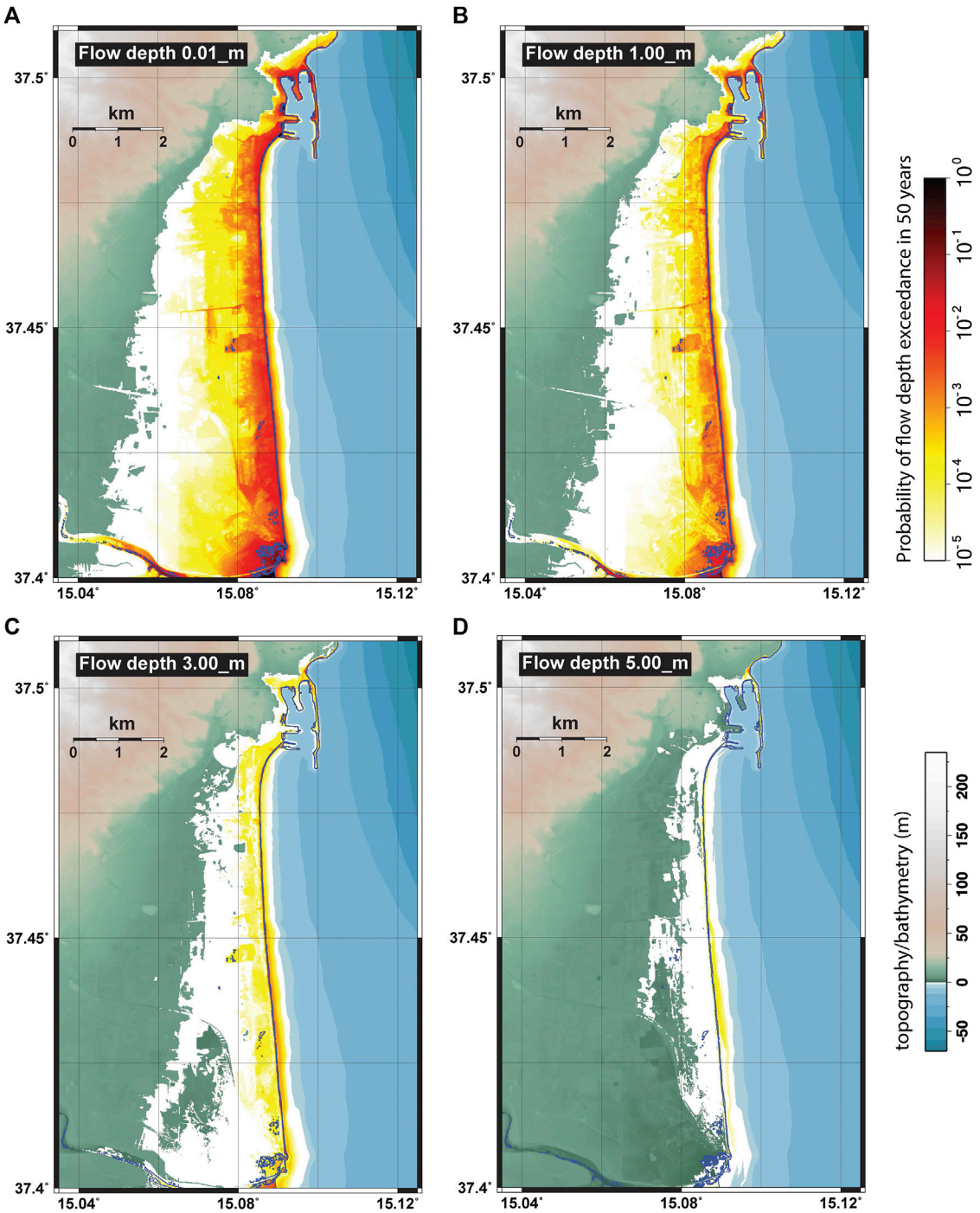

FIGURE 8 | Probability of exceedance within 50 years of flow depth of **(A)** 1 cm **(B)** 1 m **(C)** 3 m, and **(D)** 5 m, for Catania and neighboring areas. The zero-elevation contour line for the undeformed topography is shown in blue.

regional assessment not involving local scale inundation simulations for each considered seismic scenario.

In **Figure 9**, we zoom in on the Catania harbor area, and display PoE-50-years maps for exceeding maximum elevations of 1 m, 3 m, and 5 m, including both the maximum surface elevations (offshore) and the MIH (onshore). The different panels show again the relatively large heterogeneity in PoE depending on the location. Interesting results are obtained for the harbor and its vicinity. By taking a closer look to the panels of **Figure 9**, we note that the spatial distribution of the hazard depends, to first order, on the intensity threshold considered. The hazard is higher inside the harbor and lower outside it for the

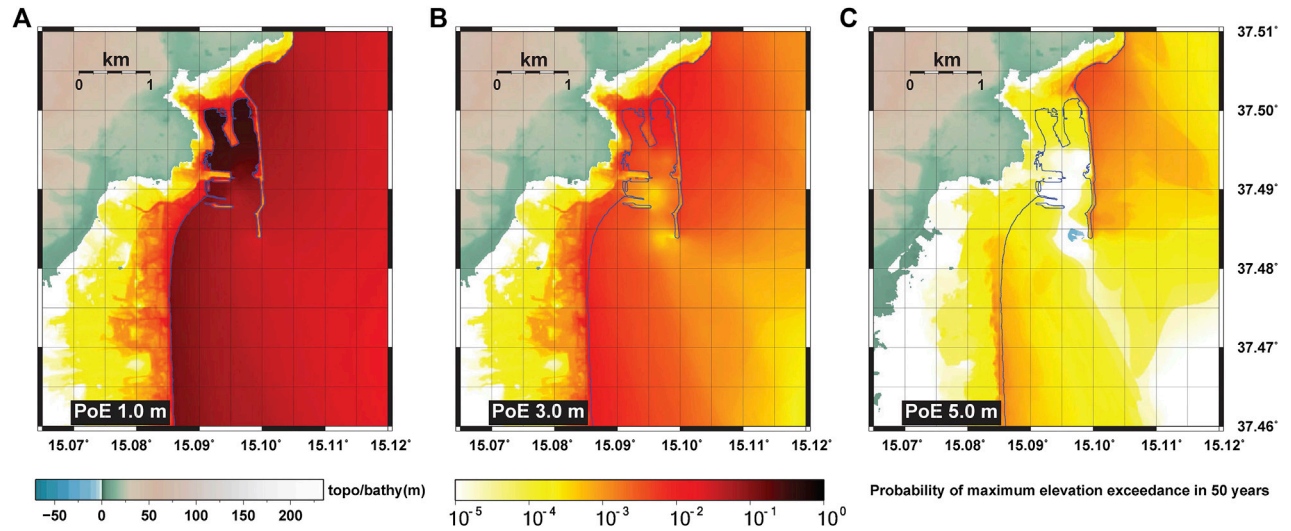

FIGURE 9 | Probability of exceedance within 50 years of maximum surface elevation (offshore) and MIH (onshore) of **(A)** 1 m **(B)** 3 m, and **(C)** 5 m, for Catania and neighboring areas. The zero-elevation contour line for the undeformed topography is shown in blue.

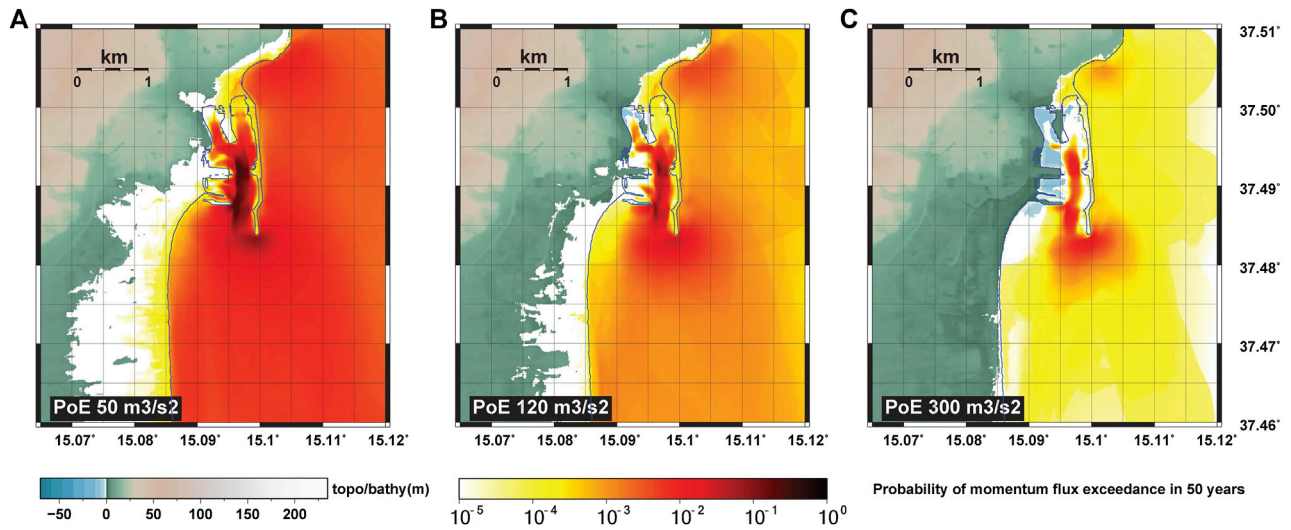

FIGURE 10 | Probability of exceedance within 50 years of maximum momentum flux of **(A)** 50 m^3/s^2 **(B)** 120 m^3/s^2, and **(C)** 300 m^3/s^2, for Catania and neighboring areas. The zero-elevation contour line for the undeformed topography is shown in blue.

lowest threshold considered of 1 m (**Figure 9A**). This might be an indication of harbor resonance under the forcing of tsunami oscillations related to relatively small magnitude and likely local earthquake sources, characterized in turn by relatively small characteristic periods. Conversely, for the largest intensity of 5 m (**Figure 9C**), the largest hazard is found offshore and north of the breakwaters, and south of the breakwaters. The breakwater and harbor orientation likely have in this case a clear positive effect in reducing the hazard inside the harbor, as PoEs are smaller here relative to the surrounding areas. Local extrema close to breakwater tips may be the indication of a tendency for the creation of horizontal eddies (e.g., Volpe et al., 2019). An intermediate more homogeneous situation is observed for intermediate intensity (**Figure 9B**).

The PoE-50-years map for the maximum momentum flux is shown in **Figure 10**. This impact metric is more sensitive to the position than the two other metrics displayed as it involves the current speed non-linearly. It seems to differ with respect to the spatial distribution too, having higher values in the northern part of the study region. Moreover, we see that the momentum fluxes have larger values inside the harbor, which may have implications for boats and other offshore objects.

To better investigate the differences between the present local-scale and the previous NEAMTHM18 regional-scale

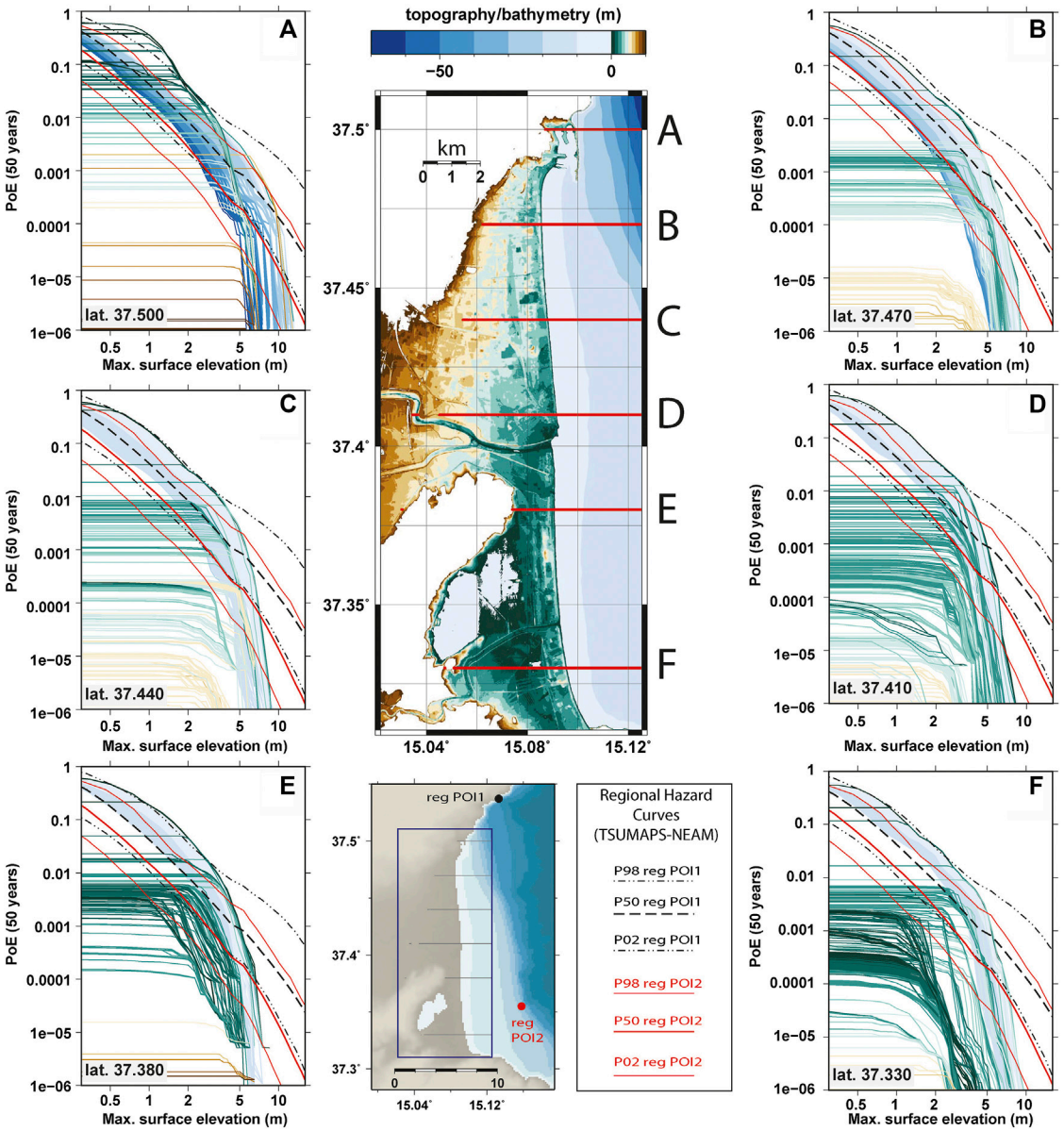

FIGURE 11 | Comparison of surface elevation (MIH onshore) between local and regional assessments. The red and black lines indicate percentiles as indicated for MIH estimated from offshore heights using amplification factors (Glimsdal et al., 2019) and the local hazard curves are displayed for every grid node along the transects indicated. Colors indicate the topographic elevation of the point as indicated: blue lines are offshore, green lines are low elevation onshore, and brown lines indicate higher elevations. Since we display maximum surface elevation (relative to the baseline sea level), and not flow depth, the hazard curve is flat until it reaches the local topographic height and only starts to be meaningful at values greater than this. Further details are provided in the text.

assessment, and to highlight the improvement in the spatial representation allowed by the site-specific analysis, **Figure 11** compares the hazard curves obtained from the two analyses. **Figure 11** displays the mean PoE-50-years hazard curves for MIH and offshore surface elevations at all the grid points along six different transects (A–F) in the innermost computational domain, compared with the NEAMTHM18 hazard curves derived using MIH values (related to the red curves in **Figures 5** and **6**) at the two PoI closest to Catania (coined PoI1 and PoI2, see also **Figure 5**). For both of these PoIs, we show the mean hazard curves as well as their 2nd and 98th percentile values. The local hazard curves are colored according to their topographic and bathymetric elevation/depth values. The regional hazard curves for PoI1 are displayed using red curves, with the thick solid line representing the mean value and the thin lines the percentiles. For PoI2, the black dashed curve shows the mean value and the dash-dotted curves the percentiles. By investigating the different transects, we see that it may be possible to separate the results roughly into families of curves:

the northern ones (A), the ones in the central part of the domain (B–D), and the southern ones (E,F).

Transect A intersects the harbor and hence the curves have rather different characteristics than the other transects. Up to at least 5 m, the nearshore hazard values (blue lines) resemble the mean value of PoI1, while they are clearly larger than for PoI2. For the largest MIHs (above 5–10 m), the local hazard curves drop much faster than in the regional assessment, as already commented above. The distribution of offshore maximum surface elevation gives a narrower height distribution than the regional 98th and 2nd percentile values. Onshore (green to brown lines), however, the variability is much larger. The probability for high inundation heights in the vicinity of the harbor infrastructure is also seen in **Figure 9**, with (dark green) onshore curves sometimes exceeding the 98th percentile. **Figure 10** illustrates the high momentum flux into the harbor; the resulting influx of water is trapped by the harbor wall and inundates the town. Such an effect would not be predicted in the regional assessment. The sensitivity of the hazard as a function of location, in relation to topographic details and coastal infrastructure, is only resolved in the local assessment. On the other hand, the regional hazard is averaged over coastal features, and so exceedances in few critical points are expected.

For transects B–D, we see that the nearshore hazard curves follow the same trend as for the transect A curves, closely following the mean value for PoI1 from NEAMTHM18 up to 5 m height (MIH or maximum surface elevation). Along these transects, the MIH hazard curves for the onshore points close to the shore do not exceed the offshore values, but rather seem to be in the same order of magnitude (the onshore curves are plotted on top of the offshore ones). For the largest MIHs, the discrepancies between the regional and local hazard curves are even larger than for transect A, with no MIH value exceeding 10 m even for the smallest PoE-50-years investigated (10^{-6}). However, based on the comparisons shown in **Figure 6**, this discrepancy is expected, as the uncertainty based NEAMTHM18 hazard curves provide larger probabilities at the highest intensities also for the offshore values. As we move southwards where the topography flattens, we see that the offshore curves are distributed over a larger probability range, and the probability depends mainly on the distance from the shoreline.

For curves E,F, we see a similar trend as for curves B–D, but here the offshore hazard curves are clearly higher than the mean hazard curves from NEAMTHM18 up to 3–5 m. In fact, the largest mean hazard curves from the local assessment along these transects correspond to the 98th percentile. However, there seems to be an opposite tendency onshore, where the tsunami hazard in the tail of the curves (low probability/high intensity) seems to be clearly lower than in the regional assessment. Again, we stress that this is expected due to offsets in the offshore hazard curves shown in **Figure 6**.

In summary, there is clear spatial variability in the hazard. Moreover, the local hazard seems to provide lower hazard estimates than regional assessment for the highest hazard intensities. We interpret the higher hazard for the highest intensities in the regional analysis as being due to the inclusion of uncertainties, which are not included in the local analysis. The spatial representation in the local hazard curves is superior to that in the regional assessment. This is both due to the spatial variability induced by applying a proper inundation model over realistic topo-bathymetric data, but also due to the more sophisticated model used to simulate the inundation, which includes in this case the co-seismic displacement associated with each scenario. The latter may compound the uncertainty treatment to increase the differences between the regional and site-specific assessments. The comparison with the NEAMTHM18 hazard curves show that the hazard can be locally even higher than the 98th percentiles of the regional assessment. This is not unexpected, as the amplification factors developed for NEAMTHM18 averaged the uncertainty treatment over a wide range of inundation sites within the NEAM region. Hence, very localized characteristics for a single site could not be resolved.

Topographic effects and friction have dramatic effects on the local inundation and overlooking the uncertainty on modelling them may reduce the hazard dramatically onshore. This is underpinned by the fact that the trend in the offshore hazard is opposite in the local analysis (with larger offshore hazard towards the south) than the NEAMTHM18 PoIs with larger hazard for PoI1 than for PoI2. The areas in the southern part of the domain have a gentler slope, which should exaggerate shoaling and hence increase the local hazard. On the other hand, the friction may act to reduce the tsunami amplitude during inundation, which may explain why the hazard for the inundated points are clearly lower for the largest MIH (and smallest probabilities). A second explanation for this discrepancy is the already observed prevalence of the coseismic uplift from local sources. Altogether, more sensitivity studies would be necessary to quantify the most influential factors of inundation variability.

CONCLUDING REMARKS

We have designed and implemented a workflow for site-specific Probabilistic Tsunami Hazard Assessment (PTHA) using High Performance Computing (HPC) to conduct tens of thousands of numerical tsunami simulations. To the best of our knowledge, this is the first occasion on which a PTHA has been performed for both a comprehensive discretization of seismic sources and high-resolution inundation calculations. To limit the number of scenarios calculated to a manageable number, we used the NEAMTHM18 source discretization and regional offshore PTHA (part of the TSUMAPS-NEAM project: Basili et al., 2019). A hazard disaggregation was performed and selecting those sources expected to constitute 99% of the total hazard for generating a maximum inundation height in the range 1–4 m for Catania, Sicily, resulted in a total of 32,363 scenarios. This range was selected as that of most likely relevance to evacuation planning. We used the Tsunami-HySEA program to model tsunamigenesis, open sea propagation, and coastal inundation using a system of nested grids with 10 m-spacing at the finest resolution. A complete Tsunami-HySEA tsunami simulation for Catania with the grid system presented here took approximately

25 min on the MARCONI-100 supercomputer at CINECA, meaning that approximately 13,600 GPU hours are required to complete the set of scenarios selected. With 1,024 simulations able to run in parallel, around 14 h of clock-time are needed to perform these calculations.

We compare directly offshore maximum surface elevation in the new calculations with the regional NEAMTHM18 assessment and find that the Probability of Exceedance curves for multiple locations offshore Catania fall comfortably within the uncertainty range indicated in the regional assessment for maximum inundation heights up to about 5 m. Above 5 m, the PoE curves are clearly lower than the NEAMTHM18 curves, likely related to the fact that the regional hazard methodology inherits uncertainties that are not present in our local analysis. This leads to increased probabilities for the highest MIH values in the regional assessment in comparison with the local hazard model presented here. However, existing uncertainty in the local analysis is neglected, preventing an effective evaluation of the robustness of this drop in the hazard tails. Therefore, to better interpret this drop, future studies should be focused on the development of methods to efficiently treat the uncertainty in tsunami generation, propagation and inundation also in local studies.

We display hazard maps for flow depth, maximum inundation height, and momentum flux for the Catania region, illustrating the higher resolution possible in the local PTHA. We find the local hazard curves, aggregated from the Tsunami-HySEA inundation maps, to correspond well with the uncertainty range indicated by the offshore based NEAMTHM18 hazard curves. However, the details in the local PTHA are far better resolved than in the regional PTHA and there are noteworthy deviations from the uncertainties predicted from the regional analysis. For many parts of the low-lying coastal region, the PoE curves are lower than the NEAMTHM18 curves, likely due to the more advanced inundation model. In the vicinity of the harbor and downtown Catania, the local hazard curves significantly exceed the regional curves, due to the presence of the harbor wall: effects that could not be resolved in the regional assessment.

This study has provided a comprehensive demonstration of a local PTHA workflow and analysis for a single coastal region with simulation of the vast number of scenarios made possible through parallel GPU computations on the pre-exascale MARCONI-100 machine. Improved accuracy in the tsunami hazard can be achieved both with regards to the inundation modeling and the discretization of sources. Increasing the resolution and/or dimensions at either end will increase the computational demands.

With regards to inundation, the Tsunami-HySEA program can handle arbitrarily many systems of nested grids in the same simulation. For example, we have run calculations with the nested grid system displayed here for Catania together with a corresponding system of nested grids for Siracusa (Sicily), further down the coast. To constitute 99% of the hazard for Catania for the selected hazard thresholds then 32,363 scenarios are deemed. A similar analysis for Siracusa found 32,514 scenarios which were deemed to constitute 99% of the hazard for that region. However, many of these scenarios are common to the hazard at both sites, and a total of 42,720 scenarios are needed to cover this specification of the hazard for both locations. However, were a third, fourth, or fifth site, further afield, to be added to the PTHA target region, the overlap of scenarios would likely be smaller and there is likely a trade-off in the efficiency of covering multiple stretches of coastline in the same simulations (the open sea tsunami propagation accounts for a small fraction of the total simulation time; the greatest part is spent calculating the inundation).

With regard to the accuracy of inundation, we stress that uncertainty in the inundation simulation is not accounted for here. Significant uncertainty may arise from the topo-bathymetric model, the spatially uniform approach to model friction, as well as from the nonlinear shallow water approximation. These uncertainty sources may significantly affect the entire hazard curve.

Regarding the accuracy of the hazard with regards to the source discretization, we can refine the source specifications of both the so-called PS and BS seismic scenarios. The BS scenarios have discrete sets of strike, dip, and rake angles, in addition to the hypocenter fault dimensions, and slip. This is a high-dimensional parameter space with a refinement factor in each parameter combining multiplicatively to the total number of BS scenarios required. We see that the vast majority of the BS scenarios dominating the local hazard are very concentrated close to the shore where the inundation is considered. For the PS scenarios, with the significance attached to the pattern of heterogeneous slip, five slip realizations were employed for each geometrical earthquake hypothesis. Would 10, or 25, or 50 provide a useful refinement of the source discretization? A sensitivity analysis would be required to assess the effect of all changes in the source.

A truly comprehensive PTHA for a given site would also need to consider other source mechanisms for tsunamis, including landslide and meteorological sources, together with realistic estimates of source probabilities. For non-seismic sources, e.g., landslides, volcanoes and meteotsunamis, PTHA is still in its infancy with just a handful of applications. Examples include for instance Grezio et al. (2012), Geist and Lynett (2014), SipkinBeck et al. (2016), Løvholt et al. (2020) (landslides), Paris et al. (2019) (volcanoes), Geist et al. (2014) (meteotsunamis), and Grezio et al. (2020) (multiple hazards). The methods applied for these sources lack the methodological complexity that earthquake PTHA has, and often diversity and lack of source frequency data make estimation of annual probability more uncertain and less constrained. Nevertheless, models for landslide tsunamis exist, including models such as BingClaw (Løvholt et al., 2017; Kim et al., 2019). Moreover, two codes of the HySEA family, Landslide-HySEA and Multilayer-HySEA (Macías et al., 2015; González-Vida et al., 2019, Macías et al., 2020c, 2020d), are also available. Related to HySEA, the numerical simulation of meteotsunamis will require the implementation of the pressure term that takes into account the key generating mechanism for these events.

This study is a demonstration of a workflow and is not an operational hazard assessment. The necessity of further investigating uncertainty quantification related to numerical modelling has been clearly highlighted. Nevertheless, we have

first and foremost demonstrated that PTHA with high resolution inundation calculations is now within reach using modern HPC resources.

DATA AVAILIABILITY STATEMENT

The original contributions presented in the study are included in the article/supplementary material, further inquiries can be directed to the corresponding author.

AUTHOR CONTRIBUTIONS

SG prepared the manuscript, assisted with the experiment design, performed analysis of the results, and generated illustrations and plots. SL contributed to conceiving the workflow, to design the experiment, to the post-processing of the simulation results, and to the interpretation of the hazard results. JM contributed to the workflow and in particular to the tsunami code development, to the numerical simulations and to code improvements for PTHA applications. FL contributed to the experiment design, analysis and interpretation of the results, and preparation of the manuscript. JS contributed to conceiving the workflow, to design the source selection, the post-processing, and the hazard aggregation, as well as to design of the case study and to the interpretation of the hazard results. MVol contributed to conceiving and implementing the workflow, performed the disaggregation, contributed to the tsunami numerical simulations setup, to the numerical simulations, to the post-processing of the simulation results and to the hazard aggregation calculations. CL performed the numerical simulations and sanity checks, 3D visualization and data management. AB contributed with code development for tsunami generation. MC contributed to the development of the tsunami code, the implementation of the new nested mesh algorithm and output compression. MA contributed to the development of the tsunami code, and to the implementation of the new nested mesh algorithm and output compression. FR contributed the tsunami numerical simulations setup, to the post-processing of the simulation results and to the hazard aggregation calculations. SGl and MVög prepared codes and tested performance and implementation of the HPC workflow. AC and AS contributed to the slip distribution simulation setup and computation for the PS scenarios. RT contributed to implement the workflow and to conceive the disaggregation step. ML and MN contributed to implementation of the workflow. BB and LP prepared the Digital Elevation Model and numerical grids used for numerical modeling. All the authors contributed to the article and approved the submitted version.

FUNDING

This work is partially funded by the European Union's Horizon 2020 Research and Innovation Program under grant agreement No 823844 (ChEESE Center of Excellence, www.cheese-coe.eu). Computing resources at the Barcelona Supercomputer Center (BSC), Spain, were used under grant AECT-2020-1-0009. Optimization and testing of the Tsunami-HySEA computational engine was partly performed at Piz Daint at CSCS (The Swiss National Computer Center) under the PRACE preparatory access N. 2010PA4869. Some of the authors also benefited from the financial support from the project "Assessment of Cascading Events triggered by the Interaction of Natural Hazards and Technological Scenarios involving the release of Hazardous Substances", funded by the Italian Ministry MIUR PRIN (Progetti di Ricerca di Rilevante Interesse Nazionale) 2017 – Grant 2017CEYPS8. Initial tests done in common with PD8 for the PRACE award 2019215169 TSU-CAST. Additional prototyping and testing was performed on resources provided by UNINETT Sigma2 - the National Infrastructure for High Performance Computing and Data Storage in Norway.

ACKNOWLEDGMENTS

We are grateful for assistance from BSC (Spain), CINECA (Italy), CSCS (Switzerland), and UNINETT Sigma2 (Norway), in implementing and executing the workflows and codes on the different HPC resources. Many of the figures in this paper are generated using GMT software (Wessel et al., 2019).

REFERENCES

Argyroudis, S. A., Fotopoulou, S., Karafagka, S., Pitilakis, K., Selva, J., Salzano, E., et al. (2020). A risk-based multi-level stress test methodology: application to six critical non-nuclear infrastructures in Europe. *Nat. Hazards* 100, 595–633. doi:10.1007/s11069-019-03828-5

Bao, H., Ampuero, J.-P., Meng, L., Fielding, E. J., Liang, C., Milliner, C. W. D., et al. (2019). Early and persistent supershear rupture of the 2018 magnitude 7.5 Palu earthquake. *Nat. Geosci.* 12, 200–205. doi:10.1038/s41561-018-0297-z

Basili, R., Brizuela, B., Herrero, A., Iqbal, S., Lorito, S., Maesano, F. E., et al. (2018). NEAM Tsunami Hazard Model 2018 (NEAMTHM18): online data of the Probabilistic Tsunami Hazard Model for the NEAM Region from the TSUMAPS-NEAM project. Istituto Nazionale di Geofisica e Vulcanologia (INGV). Available at: http://doi.org/10.13127/tsunami/neamthm18

Basili, R., Brizuela, B., Herrero, A., Iqbal, S., Lorito, S., Maesano, F. E., et al. (2019). NEAMTHM18 documentation: the making of the TSUMAPS-NEAM tsunami hazard model 2018. Istituto Nazionale di Geofisica e Vulcanologia (INGV). doi:10.5281/ZENODO.3406625

Basili, R., Tiberti, M. M., Kastelic, V., Romano, F., Piatanesi, A., Selva, J., et al. (2013). Integrating geologic fault data into tsunami hazard studies. *Nat. Hazards Earth Syst. Sci.* 13, 1025–1050. doi:10.5194/nhess-13-1025-2013

Bazzurro, P., and Cornell, C. A. (1999). Disaggregation of seismic hazard. *Bull. Seismol. Soc. Am.* 89, 501–520.

Behrens, J., and Dias, F. (2015). New computational methods in tsunami science. *Philos Trans A Math Phys Eng. Sci.* 373, 20140382. doi:10.1098/rsta.2014.0382

Bommer, J. J., and Abrahamson, N. A. (2006). Why do modern probabilistic seismic-hazard analyses often lead to increased hazard estimates?. *Bull. Seismol. Soc. Am.* 96, 1967–1977. doi:10.1785/0120060043

Bricker, J. D., Gibson, S., Takagi, H., and Imamura, F. (2015). On the need for larger Manning's roughness coefficients in depth-integrated tsunami inundation models. *Coast Eng. J.* 57, 1550005–1–1550005–13. doi:10.1142/S0578563415500059

Burbidge, D., Cummins, P. R., Mleczko, R., and Thio, H. K. (2008). "A probabilistic tsunami hazard assessment for western australia," in *tsunami science four Years after the 2004 Indian ocean tsunami*. basel: birkhäuser basel, 2059–2088. doi:10.1007/978-3-0346-0057-6

Choi, B. H., Pelinovsky, E., Ryabov, I., and Hong, J. S. (2002). Distribution functions of Tsunami wave heights. *Nat. Hazards*. 25, 1–21. doi:10.1023/A:1013379705323

Cummins, P. R. (2019). Irrigation and the Palu landslides. *Nat. Geosci.* 12, 881–882. doi:10.1038/s41561-019-0467-7

Davies, G., Griffin, J., Løvholt, F., Glimsdal, S., Harbitz, C., Thio, H. K., et al. (2018). A global probabilistic tsunami hazard assessment from earthquake sources. *Geol. Soc. London, Spec. Publ.* 456, 219–244. doi:10.1144/SP456.5

de la Asunción, M., Castro, M. J., Fernández-Nieto, E. D., Mantas, J. M., Acosta, S. O., and González-Vida, J. M. (2013). Efficient GPU implementation of a two waves TVD-WAF method for the two-dimensional one layer shallow water system on structured meshes. *Comput. Fluids* 80, 441–452. doi:10.1016/j.compfluid.2012.01.012

Dipartimento della Protezione Civile (2018). "Presidenza del Consiglio dei Ministri - Dipartimento della Protezione Civile - decreto 2 ottobre 2018alle Strutture operative del Servizio nazionale di protezione civile per l'aggiornamento delle pianificazioni di protezione civile per il rischio maremoto, (18A07309) (GU Serie Generale n.266 del 15-11-2018)". Available at: http://www.protezionecivile.gov.it/amministrazione-trasparente/provvedimenti/dettaglio/-/asset_publisher/default/content/indicazioni-alle-componenti-ed-alle-strutture-operative-del-servizio-nazionale-di-protezione-civile-per-l-aggiornamento-delle-pianificazioni-di-prot-1

Fritz, H. M., Borrero, J. C., Synolakis, C. E., Okal, E. A., Weiss, R., Titov, V. V., et al. (2011). Insights on the 2009 South Pacific tsunami in Samoa and Tonga from field surveys and numerical simulations. *Earth Sci. Rev.* 107, 66–75. doi:10.1016/j.earscirev.2011.03.004

Geist, E. L. (2002). Complex earthquake rupture and local tsunamis. *J. Geophys. Res.* 107, 2086. doi:10.1029/2000JB000139

Geist, E. L., and Parsons, T. (2006). Probabilistic analysis of tsunami hazards. Nat. *Hazards* 37, 277–314. doi:10.1007/s11069-005-4646-z

Geist, E. L., ten Brink, U. S., and Gove, M. (2014). A framework for the probabilistic analysis of meteotsunamis. *Nat. Hazards* 74 (1), 123–142. doi:10.1007/s11069-014-1294-1

Geist, E., and Lynett, P. (2014). Source processes for the probabilistic assessment of tsunami hazards. *Oceanography* 27 (2), 86–93. doi:10.5670/oceanog.2014.43

Glimsdal, S., Løvholt, F., Harbitz, C. B., Romano, F., Lorito, S., Orefice, S., et al. (2019). A new approximate method for quantifying tsunami maximum inundation height probability. *Pure Appl. Geophys.* 176, 3227–3246. doi:10.1007/s00024-019-02091-w

Goda, K., and De Risi, R. (2018). Multi-hazard loss estimation for shaking and tsunami using stochastic rupture sources. *Int. J. Disaster Risk Reduction.* 28, 539–554. doi:10.1016/j.ijdrr.2018.01.002

González, F. I., Geist, E. L., Jaffe, B., Kânoğlu, U., Mofjeld, H., Synolakis, C. E., et al. (2009). Probabilistic tsunami hazard assessment at Seaside, Oregon, for near- and far-field seismic sources. *J. Geophys. Res.* 114, C11023. doi:10.1029/2008JC005132

González-Vida, J. M., Macías, J., Castro, M. J., Sánchez-Linares, C., de la Asunción, M., Ortega, S., et al. (2019). The Lituya Bay landslide-generated mega-tsunami. Numerical simulation and sensitivity analysis,. *Nat. Hazards Earth Syst. Sci.* 19, 369–388. doi:10.5194/nhess-19-369-2019

Grezio, A., Babeyko, A., Baptista, M. A., Behrens, J., Costa, A., Davies, G., et al. (2017). Probabilistic tsunami hazard analysis: multiple sources and global applications. *Rev. Geophys.* 55, 1158–1198. doi:10.1002/2017RG000579

Grezio, A., Cinti, F. R., Costa, A., Faenza, L., Perfetti, P., Pierdominici, S., et al. (2020). Multisource bayesian probabilistic tsunami hazard analysis for the gulf of naples (Italy). *J. Geophys. Res. Oceans* 125 (2), e2019JC015373. doi:10.1029/2019JC015373

Grezio, A., Sandri, L., Marzocchi, W., Argnani, A., Gasparini, P., and Selva, J. (2012). "Probabilistic tsunami hazard assessment for Messina Strait area (Sicily, Italy)". *Nat. Hazards* 64 (1), 329–358. doi:10.1007/s11069-012-0246-x

Griffin, J., Latief, H., Kongko, W., Harig, S., Horspool, N., Hanung, R., et al. (2015). An evaluation of onshore digital elevation models for modeling tsunami inundation zones. *Front. Earth Sci.* 3, 32. doi:10.3389/feart.2015.00032

Horspool, N., Pranantyo, I., Griffin, J., Latief, H., Natawidjaja, D. H., Kongko, W., et al. (2014). A probabilistic tsunami hazard assessment for Indonesia. *Nat. Hazards Earth Syst. Sci.* 14, 3105–3122. doi:10.5194/nhess-14-3105-2014

Kagan, Y. Y., and Jackson, D. D. (2013). Tohoku earthquake: a surprise?. *Bull. Seismol. Soc. Am.* 103, 1181–1194. doi:10.1785/0120120110

Kajiura, K. (1963). The leading wave of a tsunami. *Bull. Earthq. Res. Inst.* 41, 535–571.

Kim, J., Løvholt, F., Issler, D., and Forsberg, C. F. (2019). Landslide material control on tsunami genesis—the Storegga Slide and tsunami (8,100 years BP). *J. Geophys. Res. Oceans* 124 (6), 3607–3627. doi:10.1029/2018JC014893

Lay, T., Kanamori, H., Ammon, C. J., Nettles, M., Ward, S. N., Aster, R. C., et al. (2005). The great sumatra-andaman earthquake of 26 december 2004. *Science.* 308, 1127–1133. doi:10.1126/science.1112250

Lorito, S., Selva, J., Basili, R., Romano, F., Tiberti, M. M., and Piatanesi, A. (2015). Probabilistic hazard for seismically induced tsunamis: accuracy and feasibility of inundation maps. *Geophys. J. Int.* 200, 574–588. doi:10.1093/gji/ggu408

Løvholt, F., Bondevik, S., Laberg, J. S., Kim, J., and Boylan, N. (2017). Some giant submarine landslides do not produce large tsunamis. *Geophys. Res. Lett.* 44 (16), 8463–8472. doi:10.1002/2017GL074062

Løvholt, F., Glimsdal, S., and Harbitz, C. B. (2020). On the landslide tsunami uncertainty and hazard. *Landslides* 17, 2301–2315. doi:10.1007/s10346-020-01429-z

Løvholt, F., Glimsdal, S., Harbitz, C. B., Zamora, N., Nadim, F., Peduzzi, P., et al. (2012). Tsunami hazard and exposure on the global scale. *Earth Sci. Rev.* 110, 58–73. doi:10.1016/j.earscirev.2011.10.002

Løvholt, F., Griffin, J., and Salgado-Gálvez, M. A. (2015). "Tsunami hazard and risk assessment on the global scale," in *Encyclopedia of Complexity and systems science*. Berlin, Heidelberg: Springer, 1–34. doi:10.1007/978-3-642-27737-5_642-1

Løvholt, F., Lorito, S., Macias, J., Volpe, M., Selva, J., and Gibbons, S. (2019). "Urgent tsunami computing" in IEEE/ACM HPC for urgent decision making (UrgentHPC) Denver, CO, November 17, 2019 (IEEE), 45–50. doi:10.1109/UrgentHPC49580.2019.00011

Macías, J., Castro, M. J., and Escalante, C. (2020a). Performance assessment of the Tsunami-HySEA model for NTHMP tsunami currents benchmarking Laboratory data. *Coast. Eng.* 158, 103667. doi:10.1016/j.coastaleng.2020.103667

Macías, J., Castro, M. J., Ortega, S., and González-Vida, J. M. (2020b). Performance assessment of Tsunami-HySEA model for NTHMP tsunami currents benchmarking. Field cases. *Ocean Model.* 152, 101645. doi:10.1016/j.ocemod.2020.101645

Macías, J., Escalante, C., and Castro, M. J. (2020c). "Multilayer-HySEA model validation for landslide generated tsunamis. Part I Rigid slides" Development of efficient hydrodynamic and morphodynamic simulators for risk assessment and forecasting (SIMURISK), May 22–August 27, 2000. doi:10.5194/nhess-2020-171

Macías, J., Escalante, C., and Castro, M. J. (2020d). Multilayer-HySEA model validation for landslide generated tsunamis Part II Granular slides. *Nat. Hazards Earth Syst. Sci.* doi:10.5194/nhess-2020-172

Macías, J., Castro, M. J., Ortega, S., Escalante, C., and González-Vida, J. M. (2017). Performance benchmarking of tsunami-HySEA model for NTHMP's inundation mapping activities. *Pure Appl. Geophys.* 174, 3147–3183. doi:10.1007/s00024-017-1583-1

Macías, J., Vázquez, J. T., Fernández-Salas, L. M., González-Vida, J. M., Bárcenas, P., Castro, M. J., et al. (2015). The Al-Boraní submarine landslide and associated tsunami. A modelling approach. *Mar. Geol.* 361, 79–95. doi:10.1016/j.margeo.2014.12.006

Molinari, I., Tonini, R., Lorito, S., Piatanesi, A., Romano, F., Melini, D., et al. (2016). Fast evaluation of tsunami scenarios: uncertainty assessment for a Mediterranean Sea database. *Nat. Hazards Earth Syst. Sci.* 16, 2593–2602. doi:10.5194/nhess-16-2593-2016

Newman, A. V., Hayes, G., Wei, Y., and Convers, J. (2011). The 25 October 2010 Mentawai tsunami earthquake, from real-time discriminants, finite-fault rupture, and tsunami excitation.*Geophys. Res. Lett.* 38, L05302. doi:10.1029/2010GL046498

Nosov, M. A., and Kolesov, S. V. (2007). Elastic oscillations of water column in the 2003 Tokachi-oki tsunami source: *in-situ* measurements and 3-D numerical modelling. *Nat. Hazards Earth Syst. Sci.* 7, 243–249. doi:10.5194/nhess-7-243-2007

Okada, Y. (1992). Internal deformation due to shear and tensile faults in a half-space. *Bull. Seismol. Soc. Am.* 82, 1018–1040.

Omira, R., Dogan, G. G., Hidayat, R., Husrin, S., Prasetya, G., Annunziato, A., et al. (2019). The september 28th, 2018, tsunami in palu-sulawesi, Indonesia: a post-event field survey. *Pure Appl. Geophys.* 176, 1379–1395. doi:10.1007/s00024-019-02145-z

Paris, R., Ulvrova, M., Selva, J., Brizuela, B., Costa, A., Grezio, A., et al. (2019). Probabilistic hazard analysis for tsunamis generated by subaqueous volcanic explosions in the Campi Flegrei caldera Italy. *J. Volc. Geothermal Res.* 379, 106–116. doi:10.1016/j.jvolgeores.2019.05.010

Park, H., Wiebe, D. M., Cox, D. T., and Cox, K. (2014). Tsunami inundation modeling: sensitivity of velocity and momentum flux to bottom friction with application to building damage at seaside. *Oregon. Coast. Eng. Proc.* 1, 1. doi:10.9753/icce.v34.currents.1

Pitilakis, K., Argyroudis, S., Fotopoulou, S., Karafagka, S., Kakderi, K., and Selva, J. (2019). Application of stress test concepts for port infrastructures against natural hazards. The case of Thessaloniki port in Greece. Reliab. Eng. Syst. *Saf. Now.* 184, 240–257. doi:10.1016/j.ress.2018.07.005

Power, W., Downes, G., and Stirling, M. (2007). "Estimation of tsunami hazard in New Zealand due to south American earthquakes," in *Tsunami and its Hazards in the Indian and pacific oceans*. basel: birkhäuser basel, 547–564. doi:10.1007/978-3-7643-8364-0-15

Power, W., Wang, X., Wallace, L., Clark, K., and Mueller, C. (2018). The New Zealand Probabilistic Tsunami Hazard Model: development and implementation of a methodology for estimating tsunami hazard nationwide. *Geol. Soc. London, Spec. Publ.* 456, 199–217. doi:10.1144/SP456.6

Scala, A., Lorito, S., Romano, F., Murphy, S., Selva, J., Basili, R., et al. (2020). Effect of shallow slip amplification uncertainty on probabilistic tsunami hazard analysis in subduction zones: use of long-term balanced stochastic slip models. *Pure Appl. Geophys.* 177, 1497–1520. doi:10.1007/s00024-019-02260-x

Selva, J., Tonini, R., Molinari, I., Tiberti, M. M., Romano, F., Grezio, A., et al. (2016). Quantification of source uncertainties in seismic probabilistic tsunami hazard analysis (SPTHA). *Geophys. J. Int.* 205, 1780–1803. doi:10.1093/gji/ggw107

Sepúlveda, I., Tozer, B., Haase, J. S., Liu, P. L. F., and Grigoriu, M. (2020). Modeling uncertainties of bathymetry predicted with satellite altimetry data and application to tsunami hazard assessments. *J. Geophys. Res. Solid Earth* 125, 1–25. doi:10.1029/2020JB019735

SipkinBeck, E. M., Mountjoy, J. J., Power, W. L., and Mueller, C. (2016). "Probabilistic hazard of tsunamis generated by submarine landslides in the cook strait canyon (New Zealand)" in *Global tsunami science: past and future, volume I. Pageoph topical volumes*. Editors E. L. Geist, H. M. Fritz, A. B. Rabinovich, and Y. Tanioka (Cham: Birkhäuser). doi:10.1007/978-3-319-55480-8_6

Synolakis, C., and Kânoğlu, U. (2015). The Fukushima accident was preventable. *Philos. Trans. A Math. Phys. Eng. Sci.* 373, 20140379. doi:10.1098/rsta.2014.0379

Takagi, H., Mikami, T., Fujii, D., Esteban, M., and Kurobe, S. (2016). Mangrove forest against dyke-break-induced tsunami on rapidly subsiding coasts. *Nat. Hazards Earth Syst. Sci.* 16, 1629–1638. doi:10.5194/nhess-16-1629-2016

Titov, V. V., and Gonzalez, F. I. (1997). Implementation and testing of the method of splitting tsunami (MOST) model. NOAA technical memorandum. Available at: https://repository.library.noaa.gov/view/noaa/10979/noaa_10979_DS1.pdf

Tolkova, E. (2007). Compression of MOST propagation database (NOAA technical memorandum OAR PMEL-134). Available at: https://repository.library.noaa.gov/view/noaa/13838/noaa_13838_DS1.pdf

Ulrich, T., Vater, S., Madden, E. H., Behrens, J., van Dinther, Y., van Zelst, I., et al. (2019). Coupled, physics-based modeling reveals earthquake displacements are critical to the 2018 Palu, sulawesi tsunami. *Pure Appl. Geophys.* 176, 4069–4109. doi:10.1007/s00024-019-02290-5

Volpe, M., Lorito, S., Selva, J., Tonini, R., Romano, F., and Brizuela, B. (2019). From regional to local SPTHA: efficient computation of probabilistic tsunami inundation maps addressing near-field sources. *Nat. Hazards Earth Syst. Sci.* 19, 455–469. doi:10.5194/nhess-19-455-2019

Wessel, P., Luis, J. F., Uieda, L., Scharroo, R., Wobbe, F., Smith, W. H. F., et al. (2019). The generic mapping tools version 6. *Geochem. Geophys. Geosystems* 20, 5556–5564. doi:10.1029/2019GC008515

Conflict of Interest: The authors declare that the research was conducted in the absence of any commercial or financial relationships that could be construed as a potential conflict of interest.

The reviewer (AA) declared a past co-authorship with several of the authors (SL, FR, MV) to the handling editor.

frontiers in Earth Science

ORIGINAL RESEARCH
published: 11 January 2021
doi: 10.3389/feart.2020.598839

New High-Resolution Modeling of the 2018 Palu Tsunami, Based on Supershear Earthquake Mechanisms and Mapped Coastal Landslides, Supports a Dual Source

Lauren Schambach[1], *Stephan T. Grilli*[1]* *and David R. Tappin*[2,3]

[1]Department of Ocean Engineering, University of Rhode Island, Narragansett, RI, United States, [2]British Geological Survey, Nottingham, United Kingdom, [3]Department of Earth Sciences, University College London, London, United Kingdom

OPEN ACCESS

Edited by:
Finn Løvholt, Norwegian Geotechnical Institute, Norway

Reviewed by:
Anawat Suppasri, Tohoku University, Japan
Phil Cummins, Australian National University, Australia

***Correspondence:**
Stéphan T. Grilli
grilli@uri.edu

Specialty section:
This article was submitted to Geohazards and Georisks, a section of the journal Frontiers in Earth Science

Received: *25 August 2020*
Accepted: *18 November 2020*
Published: *11 January 2021*

Citation:
Schambach L, Grilli ST and Tappin DR (2021) New High-Resolution Modeling of the 2018 Palu Tsunami, Based on Supershear Earthquake Mechanisms and Mapped Coastal Landslides, Supports a Dual Source. Front. Earth Sci. 8:598839. doi: 10.3389/feart.2020.598839

The Mw 7.5 earthquake that struck Central Sulawesi, Indonesia, on September 28, 2018, was rapidly followed by coastal landslides and destructive tsunami waves within Palu Bay. Here, we present new tsunami modeling that supports a dual source mechanism from the supershear strike-slip earthquake and coastal landslides. Up until now the tsunami mechanism: earthquake, coastal landslides, or a combination of both, has remained controversial, because published research has been inconclusive; with some studies explaining most observations from the earthquake and others the landslides. Major challenges are the numerous different earthquake source models used in tsunami modeling, and that landslide mechanisms have been hypothetical. Here, we simulate tsunami generation using three published earthquake models, alone and in combination with seven coastal landslides identified in earlier work and confirmed by field and bathymetric evidence which, from video evidence, produced significant waves. To generate and propagate the tsunamis, we use a combination of two wave models, the 3D non-hydrostatic model NHWAVE and the 2D Boussinesq model FUNWAVE-TVD. Both models are nonlinear and address the physics of wave frequency dispersion critical in modeling tsunamis from landslides, which here, in NHWAVE are modeled as granular material. Our combined, earthquake and coastal landslide, simulations recreate all observed tsunami runups, except those in the southeast of Palu Bay where they were most elevated (10.5 m), as well as observations made in video recordings and at the Pantoloan Port tide gauge located within Palu Bay. With regard to the timing of tsunami impact on the coast, results from the dual landslide/earthquake sources, particularly those using the supershear earthquake models are in good agreement with reconstructed time series at most locations. Our new work shows that an additional tsunami mechanism is also necessary to explain the elevated tsunami observations in the southeast of Palu Bay. Using partial information from bathymetric surveys in this area we show that an additional, submarine landslide here, when simulated with the

other coastal slides, and the supershear earthquake mechanism better explains the observations. This supports the need for future marine geology work in this area.

Keywords: tsunami hazard, coseismic tsunami, landslide tsunami, coastal landslides, numerical tsunami model

1 INTRODUCTION

On September 28, 2018 at 6:02:45 PM local time (10:02:45 AM UTC), a Mw 7.5 magnitude earthquake struck Central Sulawesi, Indonesia, with the epicenter located approximately 70 km north of the city of Palu (USGS, 2018) (**Figure 1**). The earthquake ruptured the Palu-Koro fault system, a predominantly strike-slip left-lateral fault (e.g., Socquet et al., 2019), along which large magnitude earthquakes have occurred in the past (Watkinson and Hall, 2017), two of which caused tsunamis in Palu Bay within the last century, in 1927 and 1968 (Prasetya et al., 2001). The 2018 rupture was supershear (Bao et al., 2019; Socquet et al., 2019; Fang et al., 2019) (i.e., it propagated faster along the fault than the local shear wave velocity), and the resulting ground motions caused widespread damage throughout the western Central Sulawesi region. Inland, the earthquake triggered landslides and induced considerable liquefaction that resulted in major destruction and numerous fatalities (Bradley et al., 2019; Watkinson and Hall, 2019; Miyajima et al., 2019). From eyewitness accounts and video evidence (Sassa and Takagawa, 2019), almost immediately after the earthquake, numerous coastal areas along Palu Bay experienced landslides (see locations of main ones marked LS- in **Figure 1B**), which were rapidly followed by destructive tsunami waves (Arikawa et al., 2018; Carvajal et al., 2019). The earthquake, ground liquefaction, landslides, and tsunamis resulted in 4,340 fatalities and approximately 68,500 buildings were damaged or destroyed (BNPB, 2019).

Tsunami elevation time series were measured at two tide gauges, in the far-field at Mamuju (−2.66° N, on W Sulawesi) and the near-field in Pantoloan Port (P in **Figure 1B**) (BIG, 2018). In the months following the event, international research teams conducted field surveys, recording earthquake and tsunami damage, landslides, and tsunami runup and inundation. Red dots in **Figure 1B** mark locations of runups collected by Mikami et al. (2019); Omira et al. (2019); Pribadi et al. (2018); Putra et al. (2019); Widiyanto et al. (2019) (note only data labeled as runup in these references was used). Earthquake shaking, tsunami generation (particularly by coastal landslides; e.g., **Figure 2**), and various tsunami impacts were recorded in many amateur videos posted on social media, that were collected and analyzed (e.g., Carvajal et al., 2019), providing critical information on the timing and sequence of events. From the field and marine surveys, videos, and survivor accounts, it is clear that the earthquake, coastal landslides, and tsunamis closely followed each other, with major tsunami impact often taking place within minutes of the first shaking. Runups were highest in the south of the bay, reaching up to 10.5 m in the SE (**Figure 3**). At many locations where the coast was low lying, inundation only penetrated a short distance inland, which was interpreted as evidence of a landslide rather than an earthquake as the main tsunami generation mechanism (e.g., Muhari et al., 2018).

The only analogous recent events to 2018 Palu were Flores Island in 1992 and Gulf of Izmit in 1999. The Flores Island event was a shallow dipping thrust which triggered a coastal slide (Imamura et al., 1995), but there is no marine mapping to validate the slide size or volume. The Gulf of Izmit event is similar to Palu, with a strike-slip earthquake along the very active North Anatolian Fault, which triggered coastal landslides (Altinok et al., 2001). But again these landslides have not been mapped. This makes Palu an important event in that, for the first time, we have numerous tsunami data, including a comprehensive video data set, not only to fully investigate tsunami generation and coastal impact, but also to discriminate between the two, very different, source mechanisms, earthquake and landslide, and their contributions to tsunami hazard; and for the latter to confirm the importance of including dispersive effects in tsunami modeling. The improved understanding and modeling of the Palu event in this work can help identify, model, and more fully assess tsunami coastal hazards resulting from other similar tectonic environments.

Although there are now many tsunami simulations of the 2018 Palu event (e.g., Heidarzadeh et al., 2019; Takagi et al., 2019; Carvajal et al., 2019; Pakoksung et al., 2019; Gusman et al., 2019; Jamelot et al., 2019; Ulrich et al., 2019; Goda et al., 2019; Nakata et al., 2020; Sepúlveda et al., 2020; Liu et al., 2020, see summary of studies characteristics in **Table 1**), the tsunami mechanism, earthquake, coastal landslides, or both in combination, is still uncertain. In addition, whereas many published models simulate some, or even most, recorded runups around the Bay, the mechanisms are often *ad hoc* and do not reproduce the timing of tsunami waves from eyewitness accounts or the video evidence. Most coseismic tsunami sources (e.g., USGS, 2018; Socquet et al., 2019; Jamelot et al., 2019; Yolsal-Çevikbilen and Taymaz, 2019), are based on a primarily horizontal strike-slip earthquake mechanism, with limited vertical seabed motion (1–2 m). Theoretically, this should not be strongly tsunamigenic and should not, therefore, generate the elevated tsunami runups recorded from the south of the bay. There are many different interpretations of where the rupture is located under Palu Bay. In some earthquake models, the rupture crosses the bay as a simple, north-south, trending, connection (e.g., Socquet et al., 2019; Ulrich et al., 2019) (**Figure 1B**). In others, there is a change in direction under the bay (e.g., Jamelot et al., 2019) (**Figure 1B**), and some locate the rupture along the west coast (e.g., Song et al., 2019). When we completed our work, there was no resolution to these alternatives from the multibeam bathymetric data acquired by Frederik et al. (2019) in the deeper waters of the bay, because no seabed features had been identified as a possible rupture.

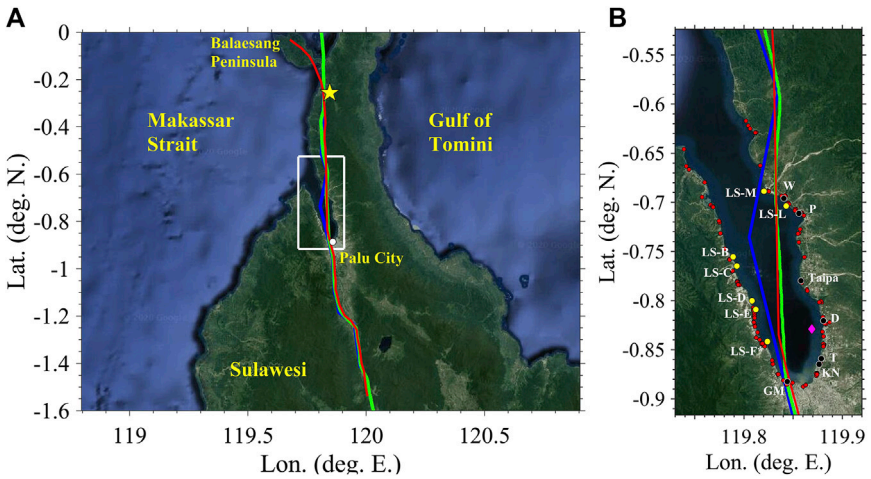

FIGURE 1 | (A) Study area with *base model grid* (BG) over Palu Bay (white box), epicenter location (USGS, 2018, yellow star), and traces of local faults used in earthquake source models by: (blue) Jamelot et al. (2019), (red) Socquet et al. (2019), and (green) Ulrich et al. (2019); **(B)** Footprint of BG with locations of (red dots) measured runups (Pribadi et al., 2018; Mikami et al., 2019; Omira et al., 2019; Putra et al., 2019; Widiyanto et al., 2019) (black dots) surface elevation time series inferred from shore-based videos (Carvajal et al., 2019, GM, grand mall; KN, KN Hotel; T, Talise; D, Dupa; P, Pantoloan; W, Wani) (yellow dots) observed landslides, (diamond) location of aircraft at 10:04:33 UTC, that filmed coastal landslides (**Figure 2**).

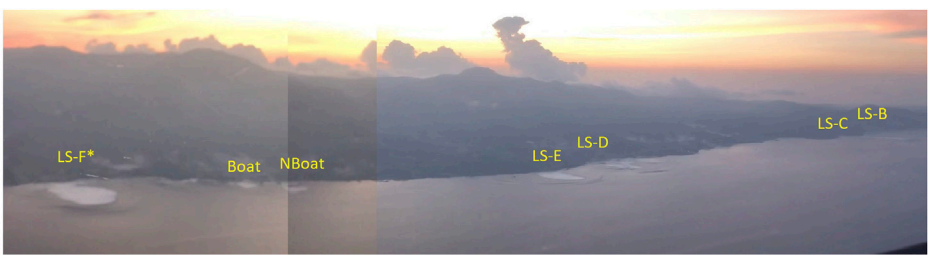

FIGURE 2 | Composite picture created from aircraft pilot video (Mafella, **Supplementary Video S38** in Carvajal et al., 2019), showing waves generated by coastal landslides LS-B,C,D,E and F* (**Figure 1B**), at $t \simeq 108$ s into the event (aircraft location in **Figure 1B**). "Boat" and "NBoat" mark where waves were also recorded on a small boat, as well as active subaerial slides (**Supplementary Video S39** in Carvajal et al., 2019).

Hence, to quantify the effect on tsunami impact of this epistemic uncertainty in earthquake rupture, we simulated three representative coseismic sources: 1) Jamelot et al. (2019) and 2) Socquet et al. (2019) who inferred parameters for 9 and 294 sub-faults, respectively, by assimilating remotely-sensed observations of ground motion, and 3) Ulrich et al. (2019), who modeled the supershear seabed deformation as a function of space and time. Note that the latter more advanced study predicted a 1.5 m maximum vertical seabed motion.

Other coseismic mechanisms, derived from geodetic observations, yield larger vertical seabed motions and, therefore, could be more tsunamigenic (e.g., ~ 3 m just south of the Balaesang Peninsula, **Figure 1A**, Song et al., 2019; Fang et al., 2019; He et al., 2019). These, however, are not within Palu Bay but farther north and, hence, cannot explain the tsunami here, particularly the fast arrival of large waves that impacted Palu City (the timing of events and waves will be detailed later).

Some have also argued (e.g., Ulrich et al., 2019) that the horizontal fault movement along the steep slope margins of Palu Bay resulted in an increased vertical water displacement causing elevated runups, in the manner proposed by Tanioka and Satake (1996). Hence, in our simulations of the three selected coseismic sources, we included this additional effect of enhanced vertical displacement as a function of the predicted horizontal fault movement.

The main challenge here, however, with the single earthquake mechanism, is that it cannot explain the timing of the tsunami impacts along the Bay from the coastal landslides reported in the survivor accounts and seen in video evidence, on land and in that captured by aircraft pilot Mafella flying over the bay shortly after the earthquake happened (**Figure 2**).

With regard to the landslide tsunami mechanisms published so far for 2018 Palu (**Table 1**), Takagi et al. (2019) used a simplified numerical model of a dual earthquake/landslide source, with a single landslide located in the southwest of Palu Bay, mapped by high-resolution multibeam echosounder (MBES), whose tsunami was identified in the aircraft pilot video (**Figure 2**). Their model suggested that

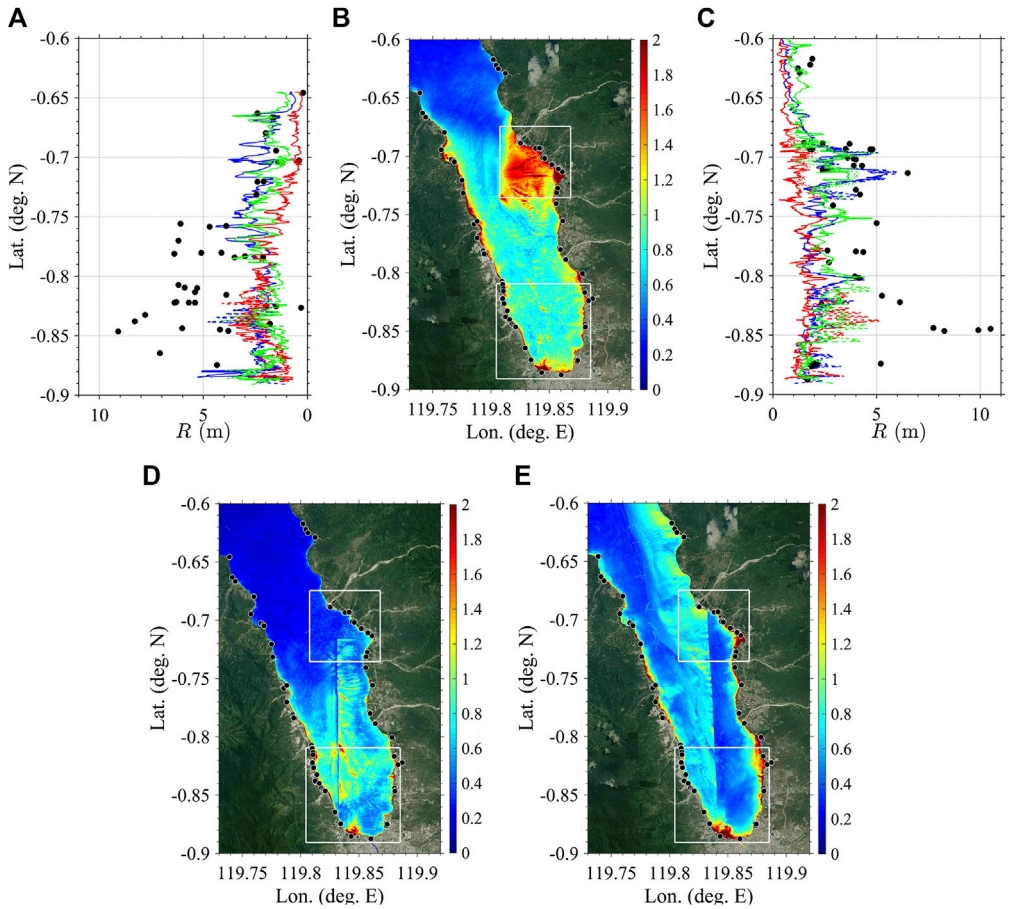

FIGURE 3 | (A,C) Runups *R* (black dots) measured in Palu Bay by international teams (Pribadi et al., 2018; Mikami et al., 2019; Omira et al., 2019; Putra et al., 2019; Widiyanto et al., 2019) (black dots in **(B,D,E)**). Lines in **(A,C)** are runups simulated with FUNWAVE for three coseismic sources: (blue) Jamelot et al. (2019), (red) Socquet et al. (2019), and (green) Ulrich et al. (2019), in (−-) 30 m resolution BG, and (—) 7.5 m resolution EG/SG grids (white footprints in figures **(B,D,E)**). Maximum surface elevations computed with each source are color scales in: **(B,D,E)**, respectively.

shorter period waves generated by the coastal landslide were followed by longer period waves from the earthquake. Pakoksung et al. (2019), Nakata et al. (2020), and Sepúlveda et al. (2020) identified and modeled landslides as the most important, if not the principal, contributors to the tsunami. Their landslide parameters and corresponding wave generation, however, were hypothetical and selected to match observations. To date, only Liu et al. (2020) modeled landslide tsunamis from mapped landslide locations, but they: 1) did not model the tsunami generation from the landslides directly, using instead semi-empirical sources, and 2) did not simulate an additional earthquake mechanism. Finally all the landslide modeling studies to date simulated tsunami propagation with a non-dispersive model, which, as we will show, affected results.

Here, for the first time, we demonstrate that to explain the tsunami observations in Palu Bay requires simultaneously modeling both coseismic and landslide sources. We simulate the three coseismic sources discussed above (Jamelot et al., 2019; Socquet et al., 2019; Ulrich et al., 2019), the mapped (rather than hypothetical) landslides (Liu et al., 2020; Takagi et al., 2019), and dual source combinations of these, using numerical models that include frequency dispersion effects (Shi et al., 2012; Ma et al., 2012). We show that dispersion affects the shorter wavelength landslide tsunamis propagating into the deeper waters in the center of Palu Bay. We simulate the landslides as deforming granular material, with their tsunami generation, using the 3D physics-based numerical model of Ma et al. (2015). We use finer model grids and higher resolution bathymetric and topographic data in Palu Bay (**Figure 1**) than in earlier work. We compare the results to a more comprehensive database of post-tsunami field survey results, including runups, tsunami elevations at the Pantoloan Port tide gauge together with those inferred at other locations from a novel analysis of the tsunami videos (Carvajal et al., 2019). From tsunami timing information in the aircraft pilot and other videos, we infer that there was a short delay in the triggering of the landslides by the earthquake, that

TABLE 1 | Overview of main characteristics of earlier studies of the 2018 Palu event and tsunami modeling.

Study/Paper	Numerical model	Bathymetry grid	EQ source	Landslide source
Heidarzadeh et al. (2019)	COMCOT	5 arc-sec (~ 150 m) resolution in palu bay, derived from GEBCO	USGS (2018), using Okada (1985) plus Tanioka and Satake (1996) for seafloor displacement	None, conclude landslides may contribute
Socquet et al. (2019)	No tsunami modeling	Fault trace from 2017 multi beam bathymetry	Their own based on 294 (42 × 7) subfaults with parameters inverted from satellite data, using Okada (1985)	None
Takagi et al. (2019)	Delft 3D flow, hydrostatic NLSWE mode	20 m resolution, derived from BIG14	None	LS-F*, assume initial surface depression equal to volume lost based on survey
Carvajal et al. (2019)	COMCOT	23 m resolution, derived from BIG14	Socquet et al. (2019) and USGS (2018), using Okada (1985) and Tanioka and Satake (1996) for seafloor displacement	None, conclude landslides may contribute
Pakoksung et al. (2019)	Two-layer model solving NLSWE for fluids of different density	30 m resolution, derived from DEMNAS and BATNAS	None	six landslides located in areas with reported subsidence, four hypothesized, modeled as a dense fluid
Gusman et al. (2019)	COMCOT	0.48 arc-sec (~ 14 m), topography derived from 2011 LiDAR and inSAR, bathymetry derived from BIG14 and BATNAS	Joint inversion method of SAR vertical displacement measurements and pantoloan tide gauge waveform data	three coastal landslides located off palu city modeled as solid blocks based off equations of Enet and Grilli (2007)
Jamelot et al. (2019)	NLSWE (Heinrich et al. (1998) and Hebert et al. (2001))	200 m resolution grid with two nested 10 m grids in palu city and pantoloan, derived from DEMNAS and BATNAS	USGS (2018) and their own (hybrid source with nine subfaults parameterized from satellite data), using Okada (1985) and Tanioka and Satake (1996) for seafloor displacement	None
Ulrich et al. (2019)	Coupled EQ + tsunami model, seisol + StormFlash2D	Triangular grid with maximum resolution 80 m in palu bay, derived from BATNAS	Their own, modeled with seisol and coupled to the wave model, use Tanioka and Satake (1996) to account for steep slopes	None, conclude that landslides are most likely secondary contributors to the overall tsunami
Goda et al. (2019)	NLSWE (Goto et al. (1997))	Nested to 10 m, derived from DEMNAS and BATNAS	USGS (2018) considering different spatial slip distribution and rake angles	None, conclude that landslides may contribute
Sepúlveda et al. (2020)	COMCOT	~ 45 m, Derived from BIG14 and DEMNAS	USGS (2018); Socquet et al. (2019) and their own 12 sources	Use Carvajal et al. (2019) time series estimates to invert for initial elevations at suspected slide locations, not modeled together with EQ sources
Nakata et al. (2020)	JAGURS	10 m, derived from DEMNAS and BATNAS	USGS (2018) and Jamelot et al. (2019)	Modeled six hypothetical slides as granular material with Titan2D
Liu et al. (2020)	COMCOT	0.012 arc-min (~ 20 m) derived from BIG14	None	seven coastal landslides evident in their bathymetric survey, modeled using semi-empirical equations

we use in modeling and show that this improves the agreement with observations.

In **Section 2**, we detail and analyze tsunami observations, present the modeling methodology and data used to define tsunami sources and bathymetry/topography in model grids. In **Section 3**, we present model results for coseismic, landslide, and combined earthquake/landslide tsunami simulations. Finally, in **Section 4** we discuss the results and offer conclusions and perspectives for future work.

2 MATERIALS AND METHODS

2.1 Tsunami Observations

In the following, we define $t = 0$ as the start of the 2018 Palu event (10:02:45 AM UTC), i.e., the time the earthquake rupture begins at the epicenter (yellow star in **Figure 1A**).

2.1.1 Tide Gauge Data

Two operational tide gauges recorded apparent tsunami signals for the 2018 Palu event: 1) in Mamuju (−2.66 ◦ N, 118.89 ◦ E), in the Makassar Strait, on western Sulawesi about 250 km SSW from Palu Bay, a maximum trough-to-crest wave height of ~ 0.25 m was recorded at $t = 19$ min; and 2) in Pantoloan, within Palu Bay (−0.71157 ◦ N, 119.85731 ◦ E; site P in **Figure 1B**), a maximum trough-to-crest wave height of ~ 3.8 m was recorded at $t = 5 - 6$ min (BIG, 2018, **Figure 4B**). As noted in previous publications (e.g., Heidarzadeh et al., 2019), a tsunami wave traveling from the approximate location of the earthquake epicenter, north of Palu Bay (**Figure 1A**) should take ~ 45 min to arrive to the Mamuju tide gauge location, indicating either a clock error or that the signal here was caused by some other local source. In this work, as we focus on tsunami waves within Palu Bay, we do not use the

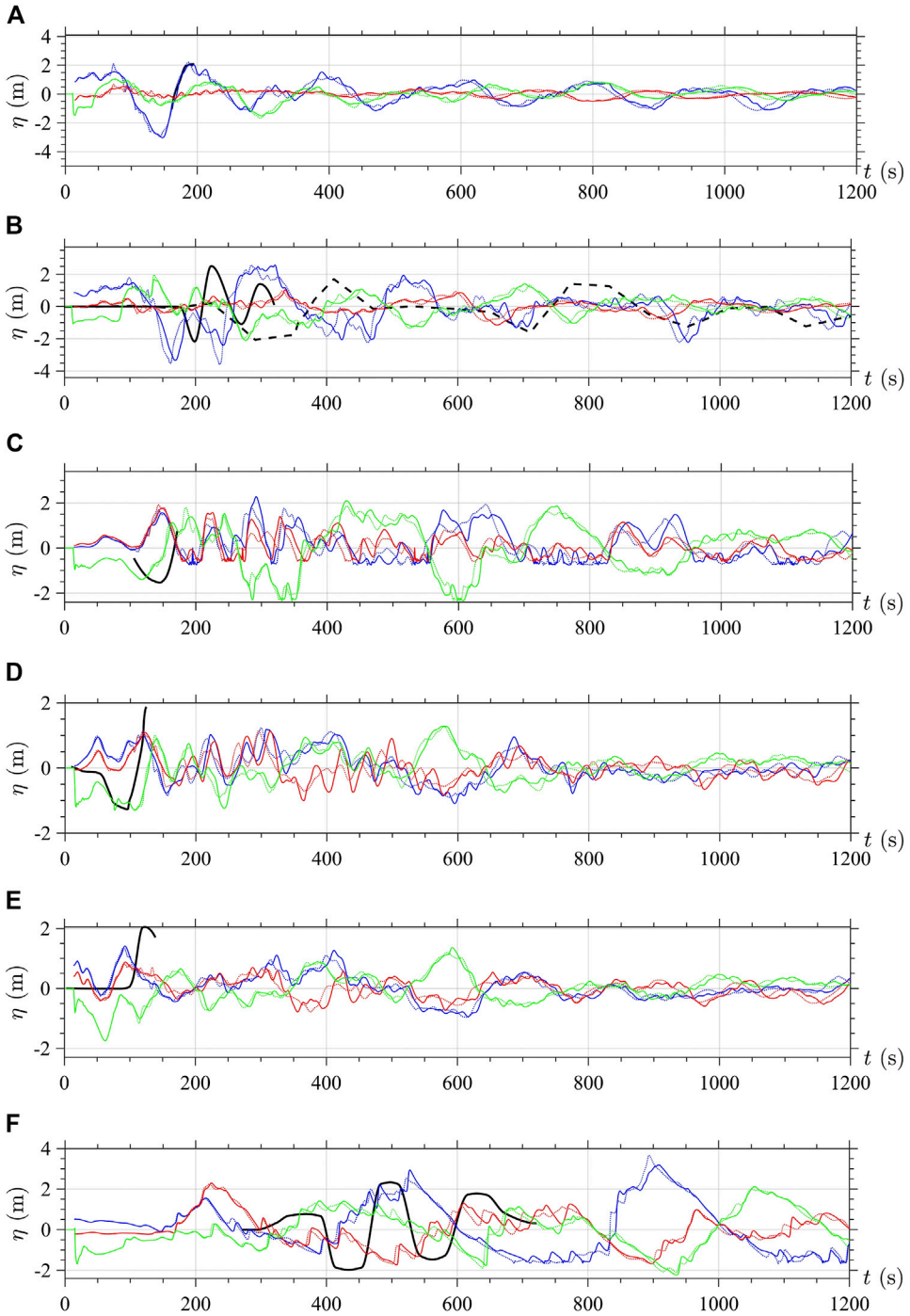

FIGURE 4 | Time series of surface elevation for 2018 Palu tsunami (—-) inferred from shore-based videos (Carvajal et al., 2019) at: **(A)** Wani dock (–0.6933◦ N, 119.8418◦ E) **(B)** Pantoloan Port dock near tide gauge (–0.7106◦ N, 119.8552◦ E) **(C)** Dupa (–0.8204 ◦ N, 119.8811◦E) **(D)** Talise (–0.8589◦ N, 119.8789◦ E) **(E)** KN Hotel (–0.8650◦ N, 119.8775◦ E), and **(F)** Grand Mall (–0.8836◦ N, 119.8437◦ E); and **(B)** (—) measured at the Pantoloan tide gauge (see **Figure 1B** for locations), compared to our tsunami simulations of three coseismic sources by: (blue) Jamelot et al. (2019), (red) Socquet et al. (2019), and (green) Ulrich et al. (2019). Time *t* is measured from the start of the Palu earthquake event, on September 28, 2018 at 6:02:45 PM local time (10:02:45 AM UTC). Solid/dashed colored lines are FUNWAVE results (NHWAVE for first 60 s with Ulrich et al. (2019)'s source) with dispersion turned on/off.

Mamuju data nor try to explain this discrepancy. At Pantoloan, the pre- and post-tsunami tide gauge record shows that the earthquake did not cause measurable permanent changes in mean sea level (MSL) (Sepúlveda et al., 2020). Here, as noted by Carvajal et al. (2019), Sepúlveda et al. (2020), and Liu et al. (2020), the tide gauge is located in shallow water inside a harbor

basin protected by a slotted seawall/dock (see **Supplementary Figure S1** in supplementary material), which is not represented in the available bathymetric data nor in our model grids. While not affecting tide measurements, harbor structures may cause seiching and affect tsunami wave dynamics by modifying their elevation through reflection or dissipation; later in time (> 650 s), the record may have been affected by waves reflected from the other side of the bay. The 1 Hz tide gauge measurements were averaged over 30 s and provided only every minute (BIG, 2018; Sepúlveda et al., 2020), yielding the fairly coarse time series plotted in **Figure 4B**. For this reason, while the gauge accurately measured long period waves, shorter waves, such as from landslides, were not recorded. This probably explains the difference in arrival time from the tide gauge data and closed circuit television (CCTV) video recording, overlooking the docks at Pantoloan Port (**Supplementary Video S11** in Carvajal et al. (2019)), showing a train of shorter period waves arriving 2–3 min before the tide gauge registers any tsunami wave activity. In the following, the Pantoloan tide gauge data is compared to model results with these observations in mind.

2.1.2 Video Analysis Overview

Carvajal et al. (2019) compiled and analyzed 41 amateur (taken with mobile phones) and CCTV videos that were taken around the bay during the earthquake and tsunami inundation. Based on the shore-based videos, they estimated surface elevation time series at six locations (**Figures 4A–F**): Wani, Pantoloan, Dupa, Talise, the KN Hotel, and the Palu Grand Mall, all marked in **Figure 1B**. They discuss uncertainties in time series reconstructed from the CCTV videos and point out that while these are larger on surface elevation, due to the time stamp in the videos, phase information is quite good at all locations. This large video archive provided overwhelming evidence of tsunamis generated by coastal landslides (see https://agsweb.ucsd.edu/tsunami/2018-09-28_palu/carvajal_2019_videos_palu/). Most notably, a video of landslide tsunami generation on the western side of the bay was taken by Batik Airways pilot Ricoseta Mafella, at approximately 10:04:33 UTC, i.e.,t = 108 s (**Supplementary Video S38** in the archive, aircraft location marked by a magenta diamond in **Figure 1B**, at −0.829 ∘ N, 119.869 ∘ E; Mafella, personal communication), a composite picture of which is shown in **Figure 2**. The video shows multiple tsunamis generated as sets of concentric waves, offshore of the locations of coastal landslides LS-B, -C, -D, -E and -F* (**Figure 1B**). Two of the smaller sets of waves at locations marked "Boat" and "NBoat" are consistent with a video made from a small boat at location "Boat" (**Supplementary Video S39** in the archive); this video also shows the failure of a subaerial coastal landslide. Furthermore, a video taken from a ship docked at Taipa, on the southeast coast of the bay (marked in **Figure 1B**; **Supplementary Video S31** in the archive) showed at least one other landslide failure to the north (potentially at location marked by LS-L or -M in **Figure 1B**).

Sunny et al. (2019) analyzed the waves generated on the western side of the bay at locations LS-D, -E, and -F* (**Figure 1B**), seen in the pilot **Supplementary Video S38**, using Google Earth to match camera viewing angles, and compared the observed wave measurements to dimensions of known objects. They estimated the widths of the sharp crescent waves to be 343 and 461 m, and the elevations (trough-to-crest) to be 24.1 m and 28.9 m at locations LS-D and -E, respectively (**Figure 1B**). Based on the boat **Supplementary Video S39**, they estimated that at location -F*, the splash of the outgoing wave was 28.4 m high, and the elevation of the unbroken outgoing wave traveling toward the Boat location was 8.2 m. These estimated wave heights are all much greater than the initial values, on the order of 2–10 m, predicted by Liu et al. (2020) using semi-empirical methods for the landslide tsunami waves generated at these locations.

2.1.3 Timing and Wave Sequence Analyses Based on Videos and Supershear Velocities

The combination of video evidence and supershear earthquake travel time can be used to estimate the time after rupture initiation that ground shaking began at various locations around Palu Bay.

CCTV footage at a house in Wani, in the northern section of the bay (**Supplementary Videos S7,S8** in Carvajal et al. (2019); −0.6935 ∘ N, 119.8417 ∘ E; W in **Figure 1B**) shows a timestamp of 10:02:54 UTC, or t = 9 s, when the ground begins shaking. Combining the supershear rupture speed of 4.81 km/s (Bao et al., 2019) and a distance of ∼ 50 km from the epicenter, shaking should have started at $t \simeq 10.4$ s in Wani, which is consistent with the camera time stamp. In Ulrich et al. (2019)'s simulations of the earthquake, horizontal and vertical deformations begin at Wani at t = 11 s, which is also in agreement with the video evidence.

From Pilot Ricoseta Mafella's flight log (personal communication), his aircraft, a large size passenger jet, began taking off at 10:02:40 UTC on the 2,500 m long runway 33 of Mutiara SIS Al-Jufrie Airport (PLW), located southeast of Palu Bay. In a social media post, the pilot wrote: "I felt something wrong on the runway during takeoff roll." The airport is ∼ 73.5 km from the epicenter, yielding an estimated start time for ground motion of t = 15.3 s based on supershear travel time; in Ulrich et al. (2019)'s simulations horizontal and vertical deformation at the airport start at t = 15.5 s. The aircraft reached 1,000 ft altitude at 10:02:59 UTC or t = 14 s, at −0.904 ∘ N, 119.903 ∘ E, just beyond the runway. Seismic travel time estimates are thus consistent with the aircraft flight log, within a few seconds.

Based on the consistent travel times and modeling estimates for the beginning of ground motion, we conclude that all locations within the bay most likely started shaking at t = 9 − 15.5 s, which allows to constrain the tsunami wave arrival times from the videos that also show the start of earthquake shaking. At Wani and Pantoloan, therefore, we included a 9 s delay, to allow for seismic waves to reach this area, and in the southern sites of Dupa, Talise, KN Hotel, and Grand Mall, a 14 s delay. As mentioned above, at 10:04:33 UTC, or t = 108 s, Pilot Mafella and his aircraft were located at −0.829 ∘ N, 119.869 ∘ E (near the eastern side of the Bay; **Figure 1B**), the approximate location where he started recording **Supplementary Video S38**, showing widespread evidence of

landslide tsunami generation on the west side of the bay (**Figure 2**).

Observations made by Carvajal et al. (2019) on their archived videos are analyzed in the following, and their time series of surface elevation estimated at various locations are plotted in **Figure 4**:

- **Supplementary Videos S7,S8** show a positive elevation wave striking the house in Wani at t = 223 s; Carvajal et al. (2019) estimated a 5 m/s on-land inundation speed for this wave, which, with the house located 150 m from the water, places the arrival time at the shoreline at $t \simeq 193$ s. **Figure 4A** shows the short time series of surface elevation they estimated at the Wani dock (−0.6933∘N, 119.8418∘E), with an elevation wave cresting at 2 m. Crew members on the Sabuk Nusantara vessel, docked at Wani, reported that immediately after the shaking there was a ∼7 m withdrawal of the water, followed 3–5 min (180–300 s) later by a ∼15 m height wave cresting at ∼8 m (VOA-News, 2018). Although this estimated crest elevation is larger than based on the videos at the house, its timing is consistent with that of Carvajal et al.'s; additionally, the ship observation confirms there was a large depression wave (trough) preceding the crest.
- **Supplementary Video S11**, taken in nearby Pantoloan Port by a CCTV camera looking toward a crane on the dock (−0.7106∘N, 119.8552∘E), captured the initial tsunami waves at this location. Assuming that the video footage begins at the time of shaking, the trough of the initial shoreline withdrawal occurs at t = 189 s, followed by a large positive wave at t = 215 s. **Figure 4B** shows the time series of surface elevation estimated at this location (solid black line), with a −2 m trough followed by a 2.5 m elevation wave. This is consistent with waves inferred from the video recorded in Wani, but at the Pantoloan tide gauge, those shorter and higher waves were filtered out by the gauge (dashed black line).
- In **Supplementary Videos S29–S31**, taken in Taipa (−0.7794∘N, 119.8580∘E; **Figure 1B**), the timing of the videos is unknown and the time series of surface elevation could not be estimated. However, in **Supplementary Video S29**, Carvajal et al. (2019) note that there is a wave to the north that appears similar to other landslide generated waves located in other parts of the bay, which could potentially be attributed to sites LS-L or M (**Figure 1B**).
- **Supplementary Video S14**, at Dupa (−0.8204∘N, 119.8811∘E; D in **Figure 1B**) begins some time after the earthquake shaking. Carvajal et al. (2019) estimated that the sea withdrawal started at t = 105 s and **Figure 4C** shows the short time series of surface elevation estimated here, with a ∼ −1.5 m trough.
- In **Supplementary Video S13**, at Talise (−0.8589∘N, 119.8789∘E; T in **Figure 1B**), the water begins to withdraw at t = 39 s, followed by a large wave striking the shore at $t \simeq 39$ s, as confirmed by the people transitioning from walking to running away from the coast. **Figure 4D** shows the short time series of surface elevation estimated here, with a −1.3 m trough followed by a ∼2 m crest.
- Six CCTV cameras were operated at the KN Hotel (−0.8650∘N, 119.8775∘E; KN in **Figure 1B**), ∼750 m south of Talise. The camera timestamps were adjusted to the time shaking started, at t = 106 s based on Ulrich et al. (2019). A sea withdrawal is not seen, but tsunami inundation from a northerly direction begins at t = 106 s. In Carvajal et al. (2019)'s **Supplementary Video S3**, the camera angle from the KN Hotel points across the bay in the direction of the LS-F* landslide. In **Figure 5**, showing video frames, a disturbance becomes visible at t = 52 s (video time 38 s) in the upper right corner behind a tree. This could potentially be the wave generated by the LS-F* landslide. **Figure 4E** shows the short time series of surface elevation estimated here, with a ∼2 m crest.
- Finally, many videos were made from various floors of a parking structure in Palu Grand Mall (−0.8836∘N, 119.8437∘E; GM in **Figure 1B**), which were combined into a 11′20″ video

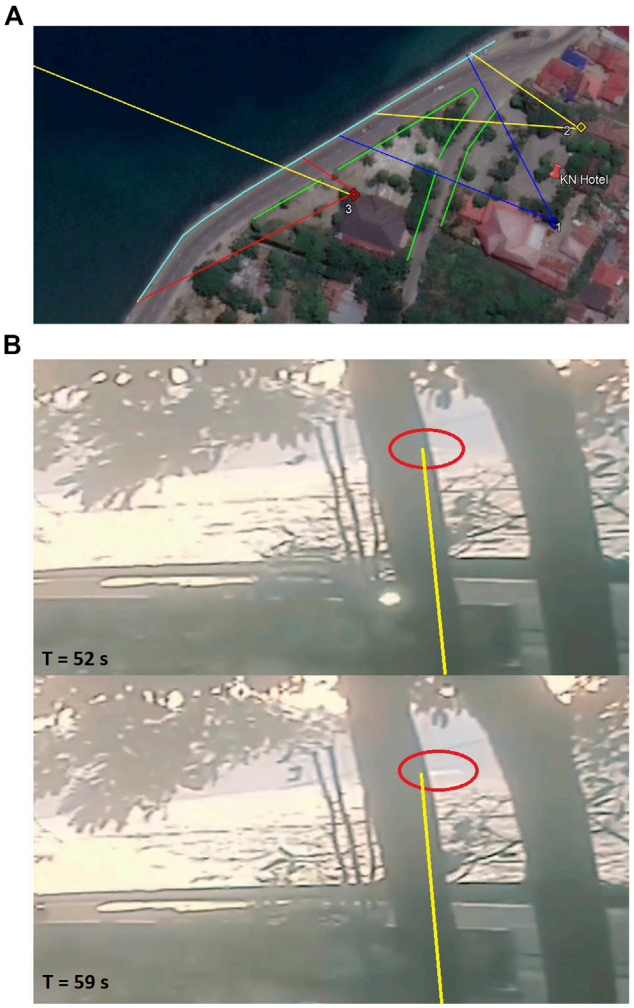

FIGURE 5 | Locations and video frames taken during tsunami impact by CCTV cameras at the KN Hotel (KN in (**Figure 1B**)). **(A)** Trace of three camera view angles corresponding to Carvajal et al. (2019)'s videos (blue) 1, (yellow) 2, and (red) 3. Cyan line marks seawall location, other green lines mark location of knee to chest high wall visible in videos. Yellow line pointing away from camera three corresponds to view shown in **(B)**. **(B)** Images from **Supplementary Video S3** at t = 52 and 59 s. Yellow line corresponds to that marked in **(A)**. Red ellipses encircle a growing free surface disturbance across the bay in landslide LS-F* area (**Figure 1B**).

referenced to the time of **Supplementary Video S43** by Carvajal et al. (2019), who could not infer the exact start time but estimated that the major impacts occurred 4–6 min after the main shock (t = 240–360 s). However, Takagi et al. (2019) analyzed other time-stamped videos from eyewitnesses here (see their **Figure 5**) and indicated that the second positive wave estimated by Carvajal et al. (2019) hit Palu Grand Mall at 10:10:49 UTC, or t = 484 s. To reconcile this disagreement, we shifted Carvajal et al. (2019)'s time series forward by 150 s. **Figure 4F** shows the short time series of surface elevation estimated here, with two waves with a −2.0 and 2.5 m largest trough and crest, respectively.

2.1.4 Post-tsunami Surveys

Bathymetry: Bathymetries acquired after the 2018 event were published by Takagi et al. (2019), Frederik et al. (2019), and Liu et al. (2020), who compared them to various pre-event data (see details in references). Takagi et al. (2019) surveyed a few square kilometers offshore of the Buluri landslide site LS-F* (**Figures 1B**, 2; see http://www.ide.titech.ac.jp/ takagi/file/2014_bathymetry_**Figure 3A**_in_paper_Landslides.dat and http://www.ide.titech.ac.jp/ takagi/file/2018_bathymetry_**Figure 3B**_in_paper_Landslides.dat; urls in their paper wrongly included a period or space after the word "Fig"). They estimated an approximate landslide volume of V_S = 3.2 10 m. Frederik et al. (2019) surveyed areas deeper than 200 m within Palu Bay, as well as outside of it, southwest of the Balaesang Peninsula. Within the bay, they could not find any clear sign in the bathymetry of a fault trace at seabed, nor any evidence that large deeper water submarine mass failures (SMF) occurred. Liu et al. (2020) surveyed the shallow coastal waters of Palu Bay and identified 14 locations where recent coastal landslides occurred. They estimated slide parameters based on differences between their new and the Badan Informasi Geospasial's (BIG; Geospatial Information Agency, Indonesia) pre-earthquake bathymetric contours. In a study published after our work was completed, Natawidjaja et al. (2020) reanalyzed the published bathymetries (Frederik et al., 2019; Liu et al., 2020) and interpreted the margins of the deep central channel in Palu Bay to be faults that were activated during the 2018 earthquake. They proposed several meters of vertical displacement for these, although this movement is within the m resolution of the data. These authors also suggested that the faulting triggered "massive" landslides in the southeast of the Bay, although comparisons of pre- and post-event data in this region by Liu et al. (2020) suggest that only the southern landslide was re-activated at this time.

In this work, we studied and modeled a subset of the coastal landslides clearly identified by Liu et al. (2020), labeled LS-B,-C,-D,-E,-F*,-L, and -M in **Figure 1B** (**Table 2**), for which video evidence confirmed that wave generation occurred, using dimensions and volumes adapted from Liu et al. (2020). For this reason, with the exception of landslide F*, for which we used data provided by Takagi et al. (2019), we used the same labeling scheme as in Liu et al. (2020).

Tsunami Coastal Impact: Post-tsunami surveys were conducted by various international teams, in which flow depth and runup (**Figure 1B**) were measured around Palu Bay. **Figure 3** shows runup values by: 1) Pribadi et al. (2018), 26 runups corrected to MSL, measured September 29–October 6, 2018 and October 10–17, 2018; 2) Putra et al. (2019), six runups referenced to MSL, measured October 8–18, 2018; 3) Widiyanto et al. (2019), 28 runups corrected to MSL, measured October 11–19, 2018; 4) Mikami et al. (2019), six runups corrected to tide level during earthquake (+1 m MSL), measured October 27–31, 2018; and 5) Omira et al. (2019), 55 runups corrected to tide level during earthquake, measured November 7–11, 2018. Here, we only compare simulation results to the measured runups, however, flow depth measurements were also reported by Arikawa et al. (2018), Cipta et al. (2018), Paulik et al. (2019), and Syamsidik et al. (2019). Runups referenced to MSL were transformed to MSL +1 m, to account for the tide elevation at the time of the tsunami.

TABLE 2 | Parameters used to model coastal landslides in NHWAVE at their estimated unfailed location (**Figure 1B**): azimuth angle θ (from N), down-slope length b, cross-slope width w, and maximum thickness T (assuming an elliptical footprint b by w and a quasi-Gaussian shape for the slide), volume . Lat./Lon. define slide center of mass initial location (See Schambach et al. (2019)'s appendix for parameter definition and sketch.) Data was adapted from Liu et al. (2020), except LS-F* for which actual landslide geometry was used in model based on Takagi et al. (2019)'s survey (TA). For the dual sources, these SMFs are modeled with NHWAVE, and then FUNWAVE, in combination with each of three coseismic sources by Jamelot et al. (2019), Socquet et al. (2019), and Ulrich et al. (2019) (**Figure 8**).

Label	Lon (°E)	Lat (°N)	θ (°)	b (m)	w (m)	T (m)	V_S ($10^6 m^3$)
LS-B	119.7890	−0.7554	0	340	380	32	1.44
LS-C	119.7927	−0.7647	345	405	440	36	2.26
LS-D	119.8082	−0.8002	0	410	1,220	18	3.07
LS-E	119.8121	−0.8090	0	175	335	18	0.37
LS-F*	119.8240	−0.8411	TA	TA	TA	40	3.2
LS-L	119.8430	−0.7038	225	830	515	44	6.66
LS-M	119.8204	−0.6887	200	800	350	35	3.44

2.2 Materials and Methods

We numerically simulate the 2018 Palu tsunami generation and propagation from earthquake or landslide sources, and the two in combination. We follow a methodology similar to that used in recent work by the authors and collaborators for other dual earthquake/landslide mechanisms (e.g., Tappin et al., 2014; Grilli et al., 2015; Grilli et al., 2017; Grilli et al., 2019; Schambach et al., 2019; Schambach et al., 2020). Using the best available bathymetric/topographic data, together with higher resolution computational grids than used in previous studies, we apply two state-of-the-art dispersive wave models: 1) the 3D non-hydrostatic wave model NHWAVE (Ma et al., 2012), with an underlying slide layer (Ma et al., 2015; Kirby et al., 2016), to simulate both the landslide motion and related tsunami generation, and 2) the 2D fully nonlinear Boussinesq wave model FUNWAVE-TVD (Shi et al., 2012) to simulate the propagation to the far-field and the coast of the superposition of landslide and coseismic tsunamis (or each individually), in nested grids of increasing resolution toward the shore. The grid data and modeling methodology are detailed next.

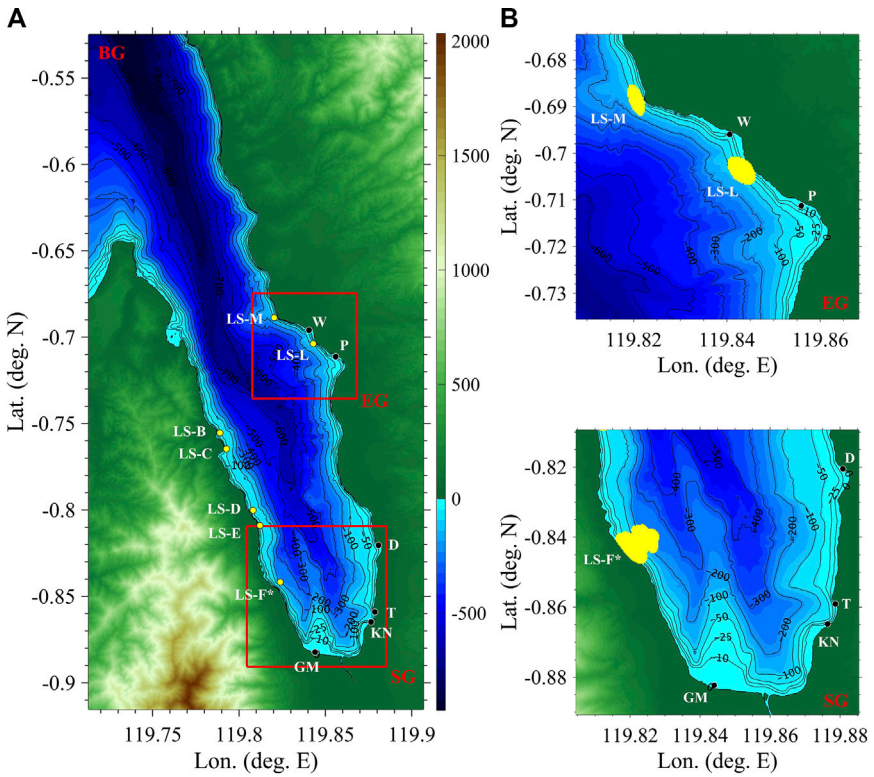

FIGURE 6 | (A) base computational grid (BG; 30 m resolution Cartesian, center at (–0.720∘N,119.810∘E); **Figure 1**) with two higher-resolution nested grids (red boxes, EG and SG; 7.5 m resolution Cartesian, center at (–0.705∘N,119.838∘E) and (–0.850∘N,119.845∘E), respectively) used in tsunami simulations. **(B)** Footprints of grids EG0020and SG. Color scale and contours indicates topography (> 0)/bathymetry (< 0) in meter. Various labels are defined in **Figure 1B**. Yellowed areas indicate failed slide areas estimated from field surveys (Takagi et al., 2019; Liu et al., 2020).

2.2.1 Study Area, Computational Grids, and Bathymetric/Topographic Data

The study area encompasses Palu Bay (**Figure 1**), which is approximately 30 km long by 7.25 km wide with depths reaching up to ~ 830 m (**Figure 6**). Analyses of pre- and post-earthquake satellite images show either N-S or NNE-SSW strike-slip ground motion north of Wani, and NNW-SSE motion south of the Palu Grand Mall (e.g., Valkaniotis et al., 2018; Socquet et al., 2019), indicating that the rupture trace changed direction somewhere in the bay. However, as mentioned above, the initial interpretations of the high-resolution deeper water bathymetric data of Frederik et al. (2019), and the separate high resolution bathymetric survey by Liu et al. (2020) did not show any evidence of a clear rupture trace in the bay. In their recent interpretation of this data, Natawidjaja et al. (2020), in contrast, suggest several meters of vertical fault movement. Notwithstanding these new interpretations and, as noted by Liu et al. (2020), since the Palu-Koro fault was not previously mapped underwater, the existing earthquake models have adopted various assumptions regarding where the fault trace is located. **Figure 1** shows fault traces from Jamelot et al. (2019), Socquet et al. (2019), and Ulrich et al. (2019), corresponding to their earthquake sources that are simulated in this work.

Three Cartesian computational grids are used in tsunami simulations (**Figure 6**; listed grid center coordinates are used as Mercator transverse geographic projection origin). The 30 m resolution base grid BG covers Palu Bay (**Figure 1**) and is used in FUNWAVE and NHWAVE simulations; the NHWAVE BG grid also includes five boundary fitted, equally-spaced, layers in the vertical direction (from ocean surface to seabed). Two 7.5 m resolution grids are nested within BG, and used in FUNWAVE to more accurately model tsunami coastal impact in two areas of particular interest: 1) in the south of the bay, south grid SG includes the observation points of Grand Mall, KN Hotel, Taipa and Dupa; and 2) near and around Pantoloan, east grid EG includes the observation points of Wani and Pantoloan (**Figure 1B**).

A variety of bathymetric and topographic data sets have been used in earlier modeling studies of this event. Here we similarly combine and interpolate onto our grids the best available bathymetric and topographic data to date for our study area. The resulting bathymetry and topography are shown in **Figure 6**. As an overall coarser data set, the earlier study of Heidarzadeh et al. (2019) used the General Bathymetric Chart of the Oceans 2014 (GEBCO14; Weatherall et al., 2015), which has a horizontal resolution of 30 arc-sec (~ 900 m), referenced to the local MSL.

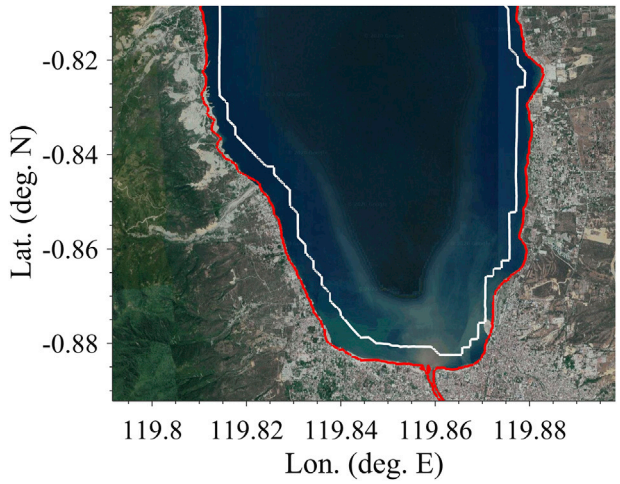

FIGURE 7 | Indonesian Geospatial Information Agency (BIG) six arc-sec bathymetric BATNAS dataset coastline (white line) plotted in the area of grid SG, with overlaid georeferenced satellite image from Google Earth™, showing the discrepancy between the BATNAS coastline and the actual coastline. Red line shows the coastline inferred from the combination of the DEMNAS and BIG14 datasets, in good agreement with the actual coastline.

GEBCO data, however, gives a maximum depth of ~ 300 m in the center of Palu Bay, which is largely in error as this depth is greater than 800 m in more accurate data sets (**Figure 6**); hence using GEBCO data may have caused errors in this earlier modeling study. The Indonesian Geospatial Information Agency (BIG) provides a national bathymetric dataset, referred to as BATNAS, which has a horizontal resolution of six arc-sec (~ 180 m) and is referenced to MSL. When comparing BATNAS to geo-referenced satellite images from Google Earth™, however, the coastline was not accurately located (**Figure 7**). BIG also provides bathymetric contours measured in Palu Bay during 2014, 2015, and 2017 surveys (referred to as BIG14, BIG15, and BIG17), all referenced to the lowest astronomical tide. These data sets are shown and discussed in detail by Liu et al. (2020), who point out that BIG17 is the most detailed, but only covers a small portion of the northern section of the bay. They also note that BIG15 is lower resolution and has a few anomalies compared to BIG14, concluding that BIG14 should be used to cover the areas of the bay not covered by BIG17. We proceeded similarly in this work. Regarding topographic data, BIG's national topographic digital elevation model, referred to as DEMNAS, has a horizontal resolution of 0.27 arc-sec (~ 8.3 m) and a vertical datum EGM2008. In contrast to the BATNAS data set, the DEMNAS topography data set is fully consistent with the BIG14 bathymetric contours and satellite images, with both agreeing well at the coast (**Figure 7**). Finally, as discussed earlier, three post-tsunami bathymetric surveys were reported by Takagi et al. (2019), Frederik et al. (2019), and Liu et al. (2020). In this work, we had access to and used the surveys of Takagi et al. (2019) and Frederik et al. (2019), whose reference vertical datum was MSL.

Thus, in our computational grids, we interpolated the deepwater bathymetry of Frederik et al. (2019) with the shallow water bathymetry from the BIG14 contours, and the topography from DEMNAS, after referencing them all to the same MSL +1 m vertical datum. To avoid numerical instabilities caused by slight discontinuities in bathymetry from combining different datasets, we applied a 2D Gaussian smoothing filter with a standard deviation of 1. The resulting bathymetry and topography are shown in **Figure 6**.

2.2.2 Numerical Models and Tsunami Modeling Methodology

Landslide tsunamis The 3D non-hydrostatic model NHWAVE is used to simulate initial wave generation and propagation for deforming submarine/subaerial slides, represented by a bottom layer of granular material (debris flow) (Ma et al., 2012; Ma et al., 2015), which was supported by various observations in Palu (e.g. Liu et al., 2020). Euler equations are solved in the water, in a horizontal Cartesian grid (x, y) with boundary fitted σ-layers in the vertical direction and, in the slide layer, conservation equations are depth-integrated. These equations are coupled along the slide-water interface through kinematic and dynamic conditions. One σ-layer achieves the same level of dispersive properties as a 2D Boussinesq model, but more layers allow accurately modeling wave dispersion in larger depth to wavelength ratios. Here we use five layers, which was shown to be adequate for simulating tsunamis from coastal landslides (e.g., Grilli et al., 2015; Schambach et al., 2019). As Palu Bay has steep shores, we use the latest implementation of NHWAVE, in which effects of vertical acceleration are included in the slide layer (Zhang et al., 2021a; Zhang et al., 2021b); these were found important on steep slopes (Grilli et al., 2019). In the absence of site-specific information, we used the same granular density and internal friction values for the slide material as in Nakata et al. (2020), and a basal friction value at the lower end of their tested range (2–6 deg); this was also the value Grilli et al. (2019) used to model the 2018 Anak Krakatau flank collapse. Hence we have,$\rho_S = 2,050$ kg/m for granular material density, with a 60% solid volume fraction, $\rho_w = 1,025$ kg/m for water density, internal friction angle $\phi_i = 30$ deg, and basal friction angle $\phi_b = 2$ deg. We did not perform a sensitivity study to basal friction, as we did not expect large effects of a small change in friction due to the short distances of slide motion and the rapidly increasing water depth across Palu Bay.

NHWAVE was extensively validated for a variety of tsunami benchmarks (Zhang et al., 2017), including laboratory experiments for slides made of glass beads performed by some of the authors (Grilli et al., 2017). The model was also used to simulate historical case studies, for which tsunami coastal impact had been measured (Tappin et al., 2014; Grilli et al., 2019; Schambach et al., 2020). In the latter cases, the initial unfailed landslide geometry is first recreated by moving the failed landslide material upslope. The model then simulates both the down-slope motion of the failing slide, coupled to that of the overlying water. For all benchmarks or actual events, NHWAVE was found to perform well and to adequately reproduce the reference data, provided the discretization was sufficient.

In the present simulations, except for slide LS-F* for which we use the actual mapped slide geometry, as in earlier work

(e.g., Enet and Grilli, 2007; Grilli et al., 2015; Schambach et al., 2019), the initial slide geometry is modeled at its unfailed location as a sediment mound of quasi-Gaussian cross-sections, with maximum thickness T, and an elliptical footprint of down-slope length b and cross-slope width w; with these definitions, the slide volume is calculated as, $V_S = 0.3508\, bwT$ (see Appendix in Schambach et al. (2019), for details). **Table 2** gives the geometric parameters and initial location estimated for each modeled landslide, based on Liu et al. (2020) (LS-B,C,D,E,L,M) or Takagi et al. (2019) (LS-F*) (**Figure 1B**). In simulations, the initial geometry of each landslide is carved out of the pre-failed bathymetry BIG14, gridded in NHWAVE's 30 m grid BG, at each slide estimated initial location (**Table 2**; **Figure 6**). Since the post-failure coastal bathymetry did not show clear slide deposits, no material was removed from the downslope bathymetry prior to simulations.

Based on the shear wave travel time from the earthquake epicenter to Palu Bay discussed above (on the order of 10–15 s), all the landslides should have been affected by ground shaking within seconds of each other; hence, they are all assumed to fail at the same time in the model. However, there was a delay between the first instance of ground shaking due to seismic waves and the actual landslide initiation of motion, likely because complete failure required a sufficient built-up of excess pore pressure (and perhaps some liquefaction) in the submerged toe of the slide material (e.g., Tappin et al., 2008). This delay was estimated to $t_S \simeq 75$ s based on the aircraft pilot video and using NHWAVE simulations to compute how much time was required to achieve the observed wave generation. **Figure 2** shows the state of wave generation at $t = 108$ s and, modeling the largest slides (in particular LS-F*), we find that it takes 30–35 s of wave generation to qualitatively achieve the same stage as observed in the video, hence on average $t_S \simeq 108 - 33 = 75$ s.

On this basis, the generation of landslide tsunamis and their initial propagation up to $t = t_f = 150$ s were simulated in grid BG with NHWAVE, simultaneously for all the considered slides (**Table 2**; an animation of this simulation *video4.mp4* is provided in supplementary material). Results show that, at time t_f, slides are no longer tsunamigenic and maximum landslide tsunami runups have occurred onshore of each slide location. For $t > t_f$, simulations are continued in FUNWAVE for landslide tsunamis alone or in combination with coseismic tsunamis, based on NHWAVE results for surface elevation and horizontal velocity (interpolated at 0.531 times the local depth for consistency with FUNWAVE). This is detailed next.

Coseismic or dual landslide/coseismic tsunamis Three different coseismic tsunami sources are simulated in grid BG for the 2018 Palu event. Two are modeled for $t \geq 0$ (Jamelot et al., 2019; Socquet et al., 2019) with the 2D fully nonlinear and dispersive Boussinesq model FUNWAVE (Wei et al., 1995; Shi et al., 2012), initialized with a static surface elevation equal to the maximum seafloor deformation, and one (Ulrich et al., 2019) using NHWAVE for $t \leq 60$ s based on directly specifying the bottom deformation in time and space, and then with FUNWAVE for $t > 60$ s (see details of coseismic sources later). For the dual earthquake/landslide sources, NHWAVE results are linearly superimposed at $t = t_f$ with those of FUNWAVE for the simulation of each coseismic source (i.e., surface elevation and horizontal velocity). Simulations of the combined tsunamis are then continued in FUNWAVE for $t > t_f$.

FUNWAVE has been extensively validated in various wave propagation and coastal inundation studies (e.g., Shi et al., 2012), including for tsunami inundation/runup and coastal velocity benchmarks (Horrillo et al., 2015; Lynett et al., 2017), and applied to tsunami case studies, both historical and hypothetical (e.g. Tappin et al., 2014; Grilli et al., 2015; Grilli et al., 2019; Schambach et al., 2019; Schambach et al., 2020).

For all cases simulated here, landslide or coseismic tsunamis alone, or dual sources, FUNWAVE simulations are performed by one-way coupling in the 2-level nested Cartesian grids (**Figure 6**) BG (30 m resolution) and EG/SG (7.5 m resolution; see the earlier studies for details). To prevent reflection at open boundaries, 1800/4,200 m wide sponge layers are specified along the western/northern boundaries of grid BG. Inundation and runup are modeled along coastal boundaries by way of a moving shoreline algorithm, with dissipation by wave breaking and bottom friction being simulated in FUNWAVE (Shi et al., 2012); here, a bottom friction coefficient $C_d = 0.0025$ is used, which corresponds to coarse sand (also used in NHWAVE).

As discussed in the introduction, all published studies of 2018 Palu to date used non-dispersive tsunami propagation models (**Table 1**). However, earlier work has shown the importance of frequency dispersion when modeling landslide tsunami generation and propagation, particularly when the initial slide footprint, and hence initial wavelength, are small compared to depth (e.g., Ma et al., 2012; Schambach et al., 2019). Here, we use dispersive models (NHWAVE and FUNWAVE) and, to assess the importance of dispersive effects, we run some simulations by turning off dispersion terms in the models (results are detailed later). In Palu Bay, while landslide tsunami waves generated in very shallow water may not initially be significantly dispersive, dispersion would become larger once waves propagated into the much deeper water of the center of the bay. Dispersion affects both phase speed and wave-wave interactions during propagation and, ultimately, tsunami coastal impact. Additionally, close to shore, dispersion may create undular bores (a.k.a. dispersive shock waves) near the crest and trough of longer shoaling tsunami waves, enhancing coastal impact (e.g., Madsen et al., 2008). This was demonstrated by Schambach et al. (2019) who also showed that higher resolution nearshore grids must be used to capture undular bores in FUNWAVE, which is one of the reasons here for using the 7.5 m grids EG and SG, even though the bathymetric data was not available at that level of detail; but, wave physics may call for it.

2.2.3 Earthquake Source Models

As there is no consensus on the 2018 Palu earthquake parameters, which fault(s) was(were) responsible, and how the rupture proceeded, to assess the source-related epistemic uncertainty in tsunami simulations, we modeled three representative earthquake sources, whose main characteristics are summarized in **Table 1**.

The first two sources use multiple subfaults whose parameters (depth, dimension, angles) were optimized, using Okada (1985)'s

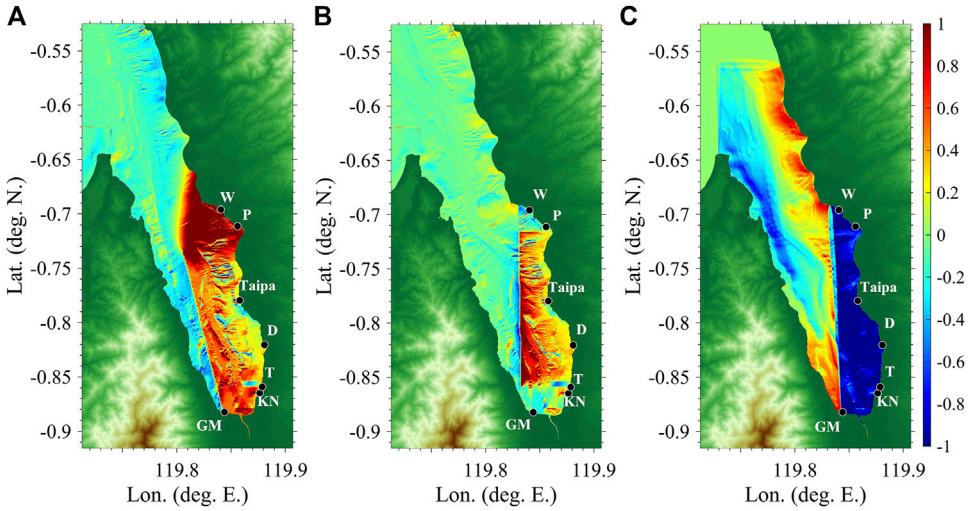

FIGURE 8 | Maximum seabed uplift/subsidence computed for 2018 Palu Mw 7.5 coseismic sources, **(A,B)** with Okada (1985)'s method or **(C)** from instantaneous deformation computed through space-time modeling, all corrected to include horizontal motion effects for steep bottom slopes (Tanioka and Satake, 1996): **(A)** Jamelot et al. (2019), **(B)** Socquet et al. (2019), and **(C)** Ulrich et al. (2019). For sources **(A,B)**, seabed motions are specified in FUNWAVE as static surface elevations at t = 15 s, while for source **(C)**, simulations are performed with NHWAVE up to t = 60 s, before continuing in FUNWAVE; for comparison with other sources, **(C)** shows the solution at t = 15 s. See **Figure 1B** for definition of location labels.

method, to best match observed onland displacements inferred from pre- and post-earthquake satellite observations, while satisfying the M7.5 centroid moment tensor. Jamelot et al. (2019) thus define nine subfaults with specified length and strike, and use displacements derived from Sentinel-2 satellite images to optimize other parameters. Socquet et al. (2019) use 294 subfaults (42 in the strike direction and seven in the dip direction), and displacements inferred from Sentinel-2 and Landsat-8 satellite images, as well as SAR interferograms from ALOS-2 satellite data to optimize fault parameters. For these two sources, we computed the maximum seafloor deformation with Okada (1985)'s model and used it as initial surface elevation in FUNWAVE (with no initial velocity). As some studies indicated that effects of steep shores might have been important (Carvajal et al., 2019; Heidarzadeh et al., 2019; Jamelot et al., 2019; Ulrich et al., 2019), we computed the additional vertical displacements due to horizontal displacements using Tanioka and Satake (1996)'s method. Assuming a supershear rupture, we specified the initial time for these surface elevations in FUNWAVE to t = 15 s into the event. **Figures 8A,B** show the initial elevations computed for these sources, which clearly are aligned along different fault traces (**Figure 1**), but both predict a positive initial elevation (seafloor uplift) on the east side of the bay and a negative initial elevation (seabed subsidence) on the west side. Jamelot et al. (2019)'s source was designed by the authors to cause larger elevations in the area of the Pantoloan tide gauge and Wani to the north of the bay, and in the area of Grand Mall and the KN Hotel to the south in Palu City, where large tsunami impact was observed. This is clearly reflected in **Figure 8A**, by the larger initial elevations for this source in those areas.

The third source by Ulrich et al. (2019) was developed from physics-based modeling of the earthquake failure in space and time using Seisol, which solves elastodynamic wave equations for spontaneous dynamic ruptures and seismic wave propagation (Dumbser and Käser, 2006; Pelties et al., 2014; Uphoff et al., 2017). Model inputs included geometry and frictional strength of the fault, tectonic stress state, and regional lithological structure, which were determined from datasets specific to the Palu region. Based on the authors' results for the horizontal and vertical ground motions (provided every 0.5 s for 50 s over a dense grid), we created time-series of seabed motion, which were used as bottom boundary conditions over grid BG in NHWAVE. As with the other sources, contributions to vertical displacement due to the horizontal movement of steep slopes were included. Simulations of tsunami generation/propagation were done in 3D with NHWAVE up to t = 60 s and then in 2D with FUNWAVE for t > 60 s. To compare results with the other two sources, the surface elevation computed with NHWAVE is plotted at t = 15 s in **Figure 8C**, where, we see that, while the deformation is aligned along a fault trace similar to that of Socquet et al. (2019), likely due to their very physics-based modeling, very different from that of the other two sources, the polarity of deformation is opposite, i.e., there are large negative elevations (subsidence) on the east and large positive elevations to the SW and NE, of the bay.

3 RESULTS

Simulations were performed with NHWAVE and FUNWAVE following the methodology detailed above, by considering first each of the three coseismic sources (**Figure 8**), then the seven parameterized landslide sources (**Table 2**), and finally for dual earthquake/landslide sources combining each coseismic source with all the landslide sources. Simulations for earthquake or

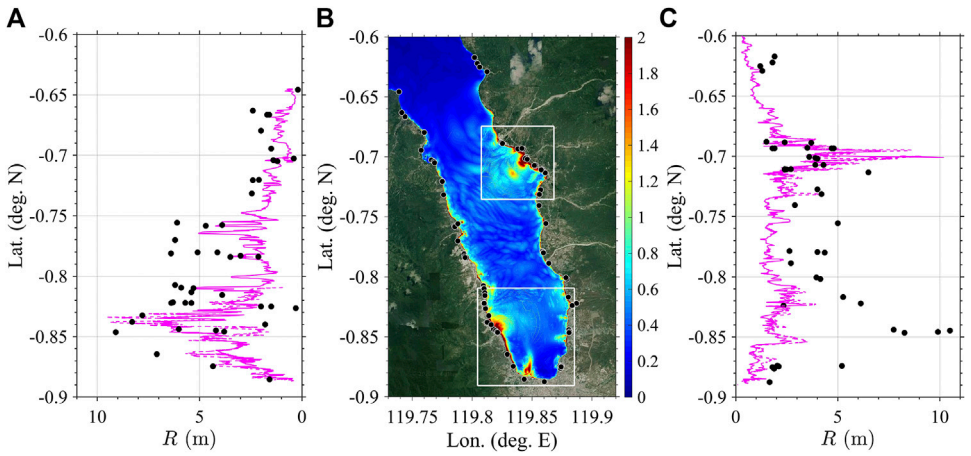

FIGURE 9 | (A,C) Runups R simulated with NHWAVE/FUNWAVE for landslide sources only (**Table 2**), compared with field measurements (see **Figure 3** for definitions). Landslide tsunami generation is first simulated with NHWAVE in grid BG (figure footprint) up to t_f = 150s, assuming all slides are triggered at t_S = 75 s. At this time, NHWAVE results (surface elevation and horizontal velocity a 0.531 times the local depth) are passed onto FUNWAVE to continue simulations for $t > t_f$, in grid BG and then in nested grids EG/SG (white footprints in figure **(B)**). Solid lines indicate results in 30 m grid BG and dashed lines in 7.5 m grids EG/SG. **(B)** Maximum surface elevations computed during landslide tsunami simulations.

landslide sources alone were performed with or without dispersive effects in the models. All simulations were performed up to $t = 1,200$ s, which was determined to be long enough for maximum runup to be achieved along the Palu Bay shores.

Similar results were computed for each type of simulation: 1) the envelope of maximum surface elevations over the study area and runups along the Palu Bay coastline, to be compared with measurements from field surveys (Pribadi et al., 2018; Mikami et al., 2019; Omira et al., 2019; Putra et al., 2019; Widiyanto et al., 2019), in **Figures 3,9,11**, for the coseismic, landslide, and dual sources, respectively (runups computed in both the coarser BG and finer SG/EG grids are provided, whereas envelopes are computed using the finer resolution results, wherever available); and 2) time series of surface elevations computed at locations where various observations or measurements were made or inferred, i.e., Wani, Pantoloan, Dupa, Talise, KN Hotel, and Grand Mall (**Figure 1B**), in **Figures 4,10,12**, respectively.

Animations of tsunami propagation simulations for: 1) coseismic sources alone (*video2.mp4*, *video5.mp4*, and *video6.mp4*); 2) landslide sources alone (*video4.mp4*); and 3) dual coseismic/landslide sources for the Ulrich case (*video1.mp4*) are given in supplementary material, together with an animation of the slide LS-F* and its corresponding wave generation (*video3.mp4*).

First, regarding the effects of grid resolution, **Figures 3,9,11** show that for all types of sources the largest runups simulated in the finer grids (EG/SG) are larger than in the coarser grid (BG), which justifies using nested grids in FUNWAVE. Then, regarding dispersion, for coseismic tsunamis, time series of surface elevation in **Figure 4** show that dispersion causes only small absolute changes in wave elevation (mostly near the crests), at most times and locations, compared to non-dispersive simulations. This is expected for the longer coseismic tsunami waves; nevertheless, relative differences between the two simulations can be 25–35% at some times/locations. In contrast, for landslide tsunamis, **Figure 10** shows that dispersion causes much larger absolute or relative differences in surface elevations, and larger phase shifts. This is also expected, based on earlier work (e.g., Glimsdal et al., 2013; Schambach et al., 2019), for shorter landslide tsunami waves, particularly considering the large depth of the bay. These results justify using dispersive wave models in this work.

For coseismic sources alone, **Figure 3** shows a similar trend for runups predicted around Palu Bay, but with large absolute differences; in particular runups are in general lower for the Socquet et al. (2019) source. All three sources, however, significantly underpredict runups observed in the southern part of the bay (south of $\sim -0.75°$N), with a maximum of 5 m whereas observed runups reached up to 10.5 m. In contrast, runups are relatively well predicted in the northern part of the Bay by Jamelot et al. (2019)'s and Ulrich et al. (2019)'s coseismic sources, with a slight advantage for the latter. This agrees with conclusions of earlier studies that coseismic sources alone cannot explain the tsunami coastal impact, particularly in the south (e.g., Nakata et al., 2020; Sepúlveda et al., 2020). Consistent with these results, **Figure 4** shows that measured or inferred time series of surface elevation are not well reproduced, particularly in the southern part of the bay. Exceptions are Wani, the northern location (**Figure 1B**), where results of the Jamelot et al. (2019)'s source agree well with the partial reconstruction based on a video recording, and Talise in the SE where results for Ulrich et al. (2019)'s source partly agree with the reconstructed surface elevation. It should be noted that runup distributions shown in **Figure 3** differ from those published by the sources' authors or others who used these. Reasons for these differences are multiple: 1) we use higher resolution model grids based on higher-resolution bathymetric data than in the earlier studies, hence

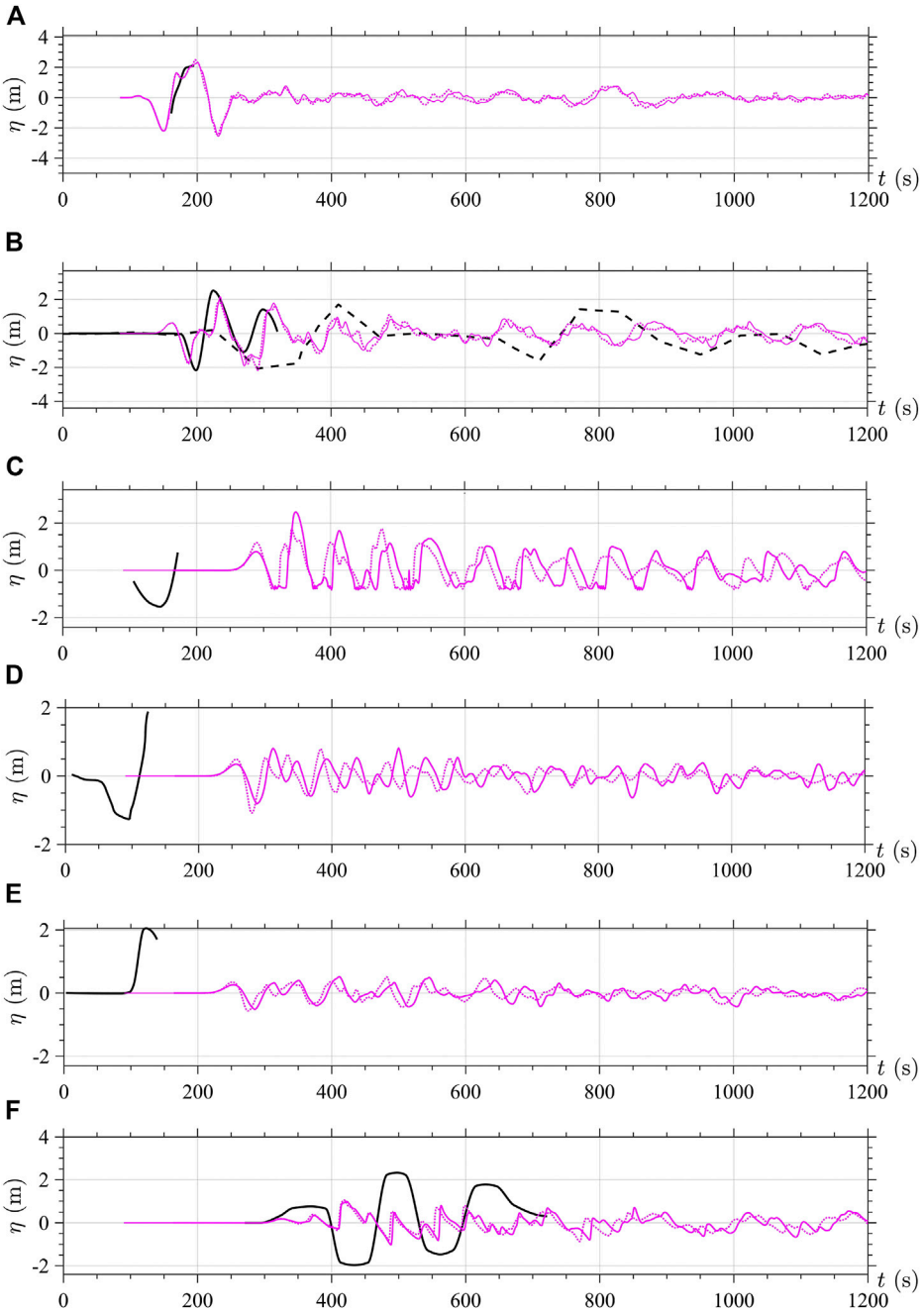

FIGURE 10 | (A-F) Similar results as in **Figure 4** (same vertical scale kept in figures for comparison), but for simulations with NHWAVE/FUNWAVE of landslide sources only (**Table 2**). Simulation results include a landslide trigger delay of t = 75 s. Solid/dashed colored lines are results with dispersion turned on/off.

both wave physics and runup are more accurately simulated; 2) unlike earlier studies, we use dispersive wave models in which wave-wave interactions differ, even for coseismic sources; 3) for Ulrich et al. (2019)'s source, we generate the tsunami dynamically for 60 s in a 3D model, whereas they used a 2D NSWE model; and 4) finally FUNWAVE has a particularly accurate moving shoreline algorithm to capture runup on steep slopes, which may not be the case for all models.

For the landslide sources alone, **Figure 9** shows that observed runups are well predicted in the SW part of Palu Bay, particularly in the area of the largest landslide sources (LS-E, LS-F*). However, a few of the largest observed runups are still underpredicted in the area of Dupa on the SE of the Bay (around −0.85° N). In the northern part of the bay, on the western side, observed runups are nearly as well predicted as for coseismic sources, but because of the timing of the event,

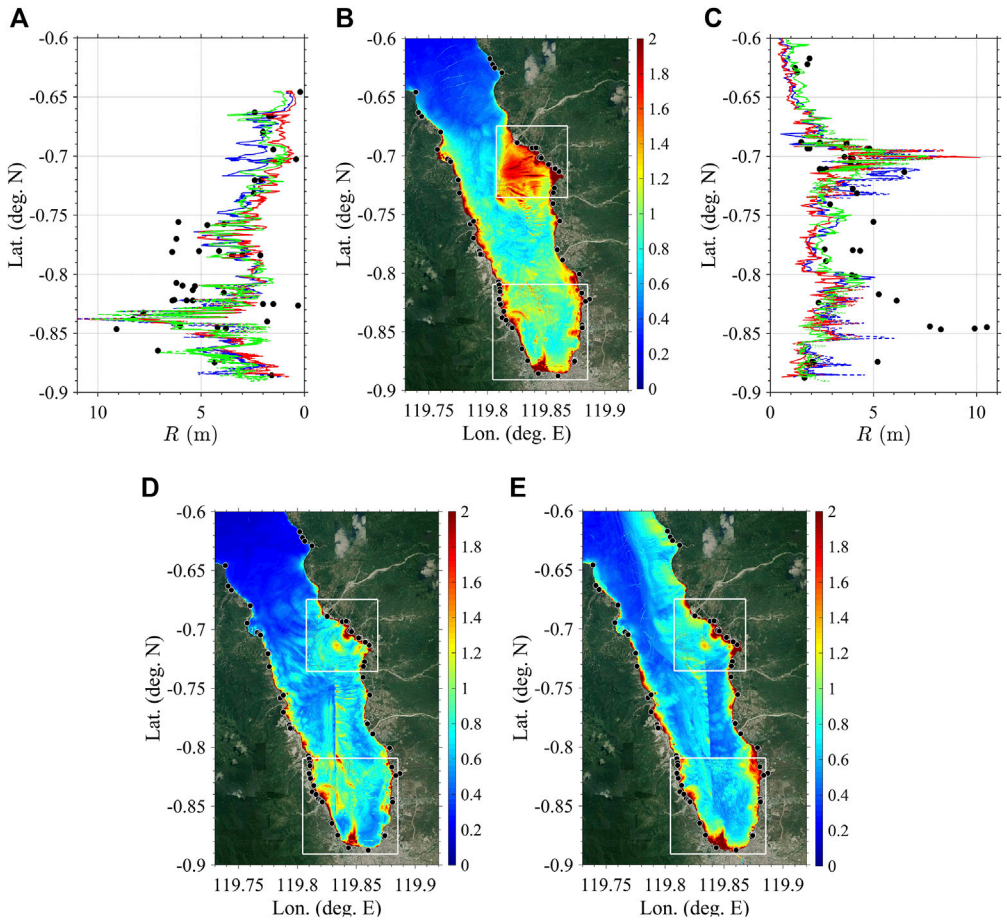

FIGURE 11 | (A,C) Runups R simulated with NHWAVE/FUNWAVE for dual earthquake/landslide (**Table 2**) sources, compared with field measurements (see **Figure 3** for definitions of data, three coseismic sources, line colors and types). Landslide tsunami generation is first simulated with NHWAVE in grid BG (figure footprint) up to t_f = 150s. At this time, NHWAVE results are linearly combined (surface elevation and velocity at 0.531 times the local depth) with those computed with FUNWAVE in grid BG for each of the three coseismic sources. Simulations are then continued with FUNWAVE for $t > t_f$, in grid BG and then nested EG/SG grids (white footprints in figures **(B,D,E)**).

maximum runups caused by coseismic or landslide sources would have likely occurred at different times here (see animations of model results). Hence, it is difficult to identify their primary source, which may explain the mitigated conclusions or even confusion in some earlier studies. On the NE side of the bay, around Wani and Pantoloan, the landslide tsunami impact is predicted to be quite large and explains the large runups observed better than for coseismic sources. This is confirmed in time series of surface elevation (**Figure 10**), where there is a much better agreement in Wani and Pantaloan of model results with the reconstituted time series than for the coseismic sources. In the SE of the bay, however, consistent with the underpredicted runups, the landslide tsunami simulations do not explain well the time series reconstructed in Dupa, Talise, and KN Hotel. Finally, at Grand Mall in the south, while the shorter period landslide tsunami waves agree better in timing with those of the reconstructed time series, their amplitude is still underpredicted, despite using a very fine model grid that could have enhanced wave shoaling.

Results of the dual earthquake/landslide source simulations (**Figure 11**) are consistent with the above observations. In all cases, but particularly for the combination of Ulrich et al. (2019)'s with the landslide sources, the observed runups on the entire west side of the bay are well simulated at most locations, and this is also the case on the east side of the bay, except for the area around Dupa where another local source of waves is required, perhaps from another landslide not yet identified in this region, as pointed out in some other studies (e.g., Liu et al., 2020). In the time series results of **Figure 12**, we see a good agreement between the dual source simulations with the reconstructed time series at Wani and Pantoloan, particularly when using Ulrich et al. (2019)'s or Socquet et al. (2019)'s source together with the landslides. A reasonable agreement is also found in the SE of the bay, in Dupa and Talise, when combining the landslides and Ulrich et al. (2019)'s source. At the KN Hotel, however, in the same area, none of the simulations agree well with the short reconstructed time series. Finally, at Grand Mall, in view of the uncertainty (and fairly arbitrary manner) of reconstructing the observed time series,

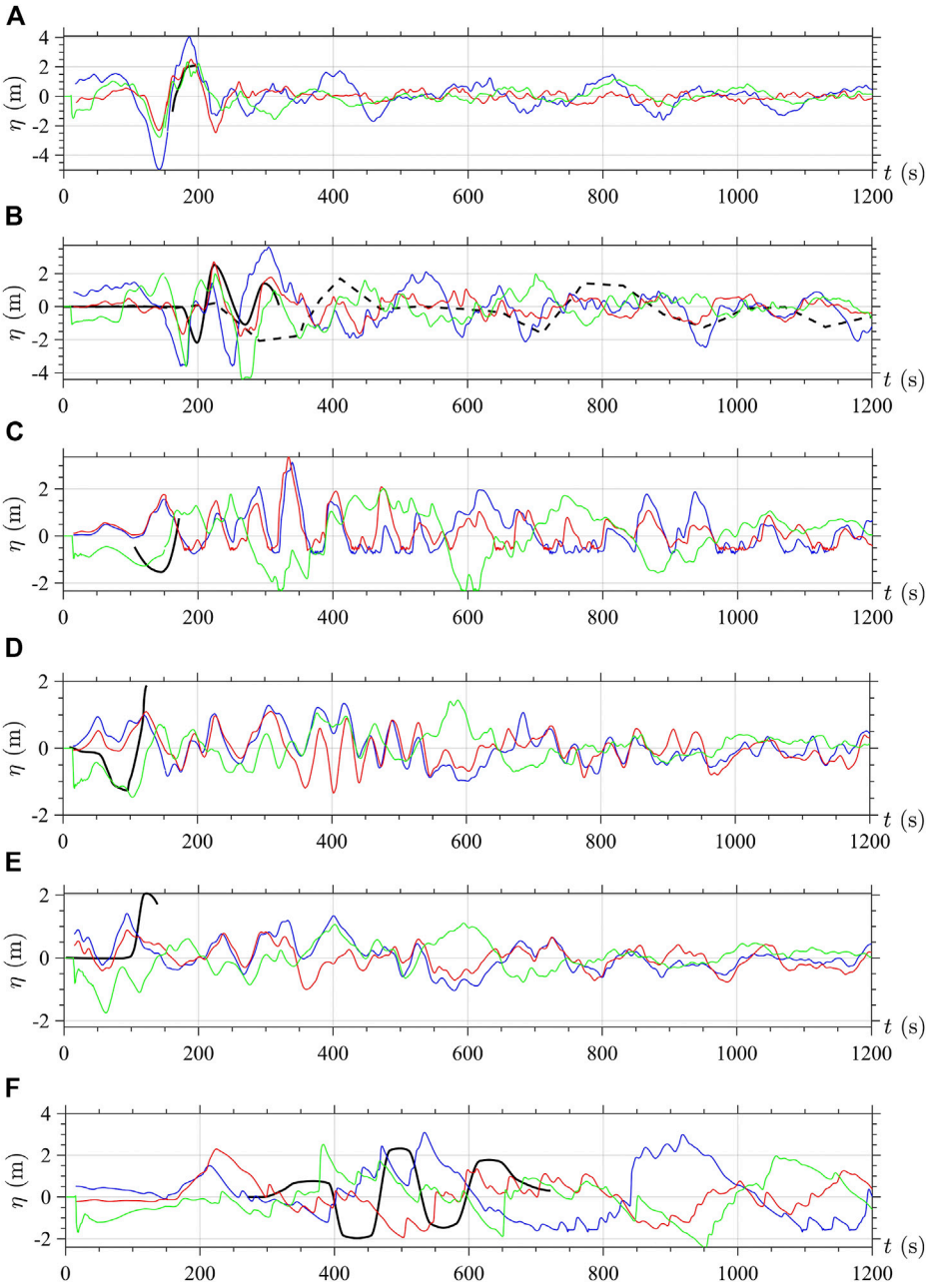

FIGURE 12 | (A-F) Similar results as in **Figures 4, 10** (same vertical scale kept in figures for comparison), for simulations with NHWAVE/FUNWAVE of combined (dual) coseismic/landslide (**Table 2**) sources. See **Figure 4** caption for definition of coseismic sources. All results are computed here with dispersion turned on.

one could argue that combining the landslide sources with Ulrich et al. (2019)'s coseismic source also provides a reasonable agreement with observations, at least in amplitude and, more or less, in phase.

4 DISCUSSION

Our work here shows that for the 2018 Palu event, a combination of earthquake and coastal landslides generated the tsunami. We also show that mapped (rather than hypothetical) landslides were critical in achieving this result. Video evidence was also instrumental in differentiating between the two possible mechanisms, especially at Pantoloan, where the tide gauge data used to validate previously published numerical models, was found to be partly misleading because it filtered out the high frequency landslide tsunami waves. To confirm this, we applied to the model results of **Figure 12B** a 30 s moving average and 1 min downsampling similar to that of the tide gauge

(Sepúlveda et al., 2020). **Supplementary Figure S2** (in supplementary Data Sheet 1) shows that this eliminates shorter waves from the time series, such as caused by the landslides or seen in the video recording near Pantoloan dock. Additionally, the filtered results based on Ulrich et al. (2019)'s dual source agree well with the first few waves in the tide gauge record, although amplitudes are smaller.

Our simulations of published earthquake sources (Jamelot et al., 2019; Socquet et al., 2019; Ulrich et al., 2019) show the epistemic uncertainty associated with modeling the coseismic tsunami. While the initial surface elevation from each coseismic source is quite different (**Figure 8**), the generated tsunamis all reproduce the runups observed in the northern section of the bay, but underpredict the larger runups in the south. Without a comparison of pre- and post- earthquake leveling data, it is not clear which, if any, of the earthquake models is most appropriate. The recent work by Natawidjaja et al. (2020), published too late to include for consideration here, re-interpreted Frederik et al. (2019)'s multibeam bathymetry and identified the major, meandering, submarine channel in the center of Palu Bay, as the seabed expression of the 2018 movement of the strike-slip fault. Based on this study, the fault could be considered to be more effective in tsunami generation than previously proposed. Several aspects of their model, however, lead us to conclude that further justification is required before it can be accepted as a viable alternative to those already published: 1) it is so very different to previously published interpretations based on the same datasets (Frederik et al., 2019; Liu et al., 2020); 2) interpretations of several meters of vertical seabed movement in the context of the resolution of Frederik et al. (2019)'s bathymetry (± 5 m) is questionable, as is the identification of recent (2018) seabed movement; and 3) the suggestion that the earthquake triggered "massive" SMFs to account for the tsunamis is contradicted by the available bathymetric evidence (Frederik et al., 2019; Liu et al., 2020).

In the southwest, the large runups observed just onshore of confirmed coastal landslides stress the importance of simulating landslide tsunamis. In this context, using a dispersive numerical tsunami model was particularly important for accurately propagating the shorter wavelength landslide tsunami waves. Here, Liu et al. (2020)'s shallow water bathymetric survey was critical in parameterizing the numerous coastal landslides. The detailed surveying of slide LS-F* by Takagi et al. (2019), where large wave generation was observed (see **Figure 2**), provided additional information. These authors were the first to identify these landslide tsunami mechanisms upon which we built our more complex and comprehensive model. The videos were instrumental in allowing us to identify a landslide trigger delay of 75 s, with the pilot video and time series of surface elevation at Wani and Pantoloan (**Figures 10A,B**) providing key evidence. The mapped landslildes we used in our modeling are found to be capable of generating runups on the same order as those observed onshore of their locations and their reconstructed time series impact, with good agreement at most locations. One exception is in the southeast of the bay, where runups are still underpredicted in the Dupa area (simulated 2–4 m, vs observed 8–10.5 m). At the Grand Mall, wave arrival matches that observed, however, the amplitudes are not as large.

To explain the large runups observed in the SE of the bay, Nakata et al. (2020) modeled a large 700 $\times 10^6$ m hypothetical SMF off of Talise and obtained a good agreement with observations near this location. There is no indication on the seafloor for such a large recent failure, although Liu et al. (2020) suggest that there are several large SMFs south of this location, but these do not appear to be recent. Our simulations suggest that an additional SMF off of Talise could explain both the large runups observed between Dupa and Talise, and improve the agreement of simulations with the time series inferred at Talise and the KN Hotel. However, as our stated goal was to only model proven landslide sources, we did not consider such a hypothetical SMF in our earlier dual sources.

Nevertheless, to test this hypothesis, we modeled a SMF at Nakata et al. (2020)'s location (i.e., 119.8675° Lon. E, −0.8540° Lat. N), where Liu et al. (2020) identify recent seabed movement, albeit with a much smaller volume. This SMF's elliptical footprint is marked in **Figure 13A**, with dimensions b = 500 m by w = 1,000 m; given a maximum thickness T = 150 m, the SMF volume is, V_s = 26.3 $\times 10^6$ m. As with the other landslides, the tsunami was first simulated with NHWAVE without a coseismic source, and then propagated with FUNWAVE in grids BG and SG. **Figures 13A,C** show that the landslide tsunami focuses on two areas onshore of the SMF: 1) just south of the KN Hotel (−0.866° N) causing a 3 m runup, consistent with measurements; and 2) north of Talise (−0.876° N) causing a ~6 m runup near where the largest 8–10.5 m runups were measured. **Figures 13B,C** also show results for a dual source combining the hypothetical SMF with Ulrich et al. (2019)'s earthquake source and the seven slides in **Table 2**. Some wave interferences slightly reduce the runup south of the KN Hotel, but north of Talise, the combined runup is still nearly 6 m, whereas without the SMF it was only 3 m (**Figure 11C**). Finally, **Figures 13E,F** show time series of surface elevations computed at Talise, KN Hotel, and Grand Mall, respectively. Compared to earlier results in **Figure 12**, the new dual source simulations improve the overall agreement with reconstructed time series. At the KN Hotel, in particular, only the inclusion of the SE SMF can explain the leading elevation wave observed at t = 125 s (underestimated but arriving at the correct time).

The 2018 Palu tsunami was unusual, and complicated, with a strike-slip earthquake mechanism which triggered coastal landslides. Previous publications show how difficult it has been to identify the tsunami generation mechanism(s). Our work here, however, demonstrates that, for most of Palu Bay, the earthquake and the mapped coastal landslides were equal contributors to the large runups measured around the bay, except in the southeast where an additional (although partly hypothetical) SMF is required. We show the importance of modeling dual earthquake/landslide sources, and of considering all available information to identify how the tsunami waves were generated including, for the first time, time series of tsunami impact reconstructed from video evidence, in addition to the (normally used) runup

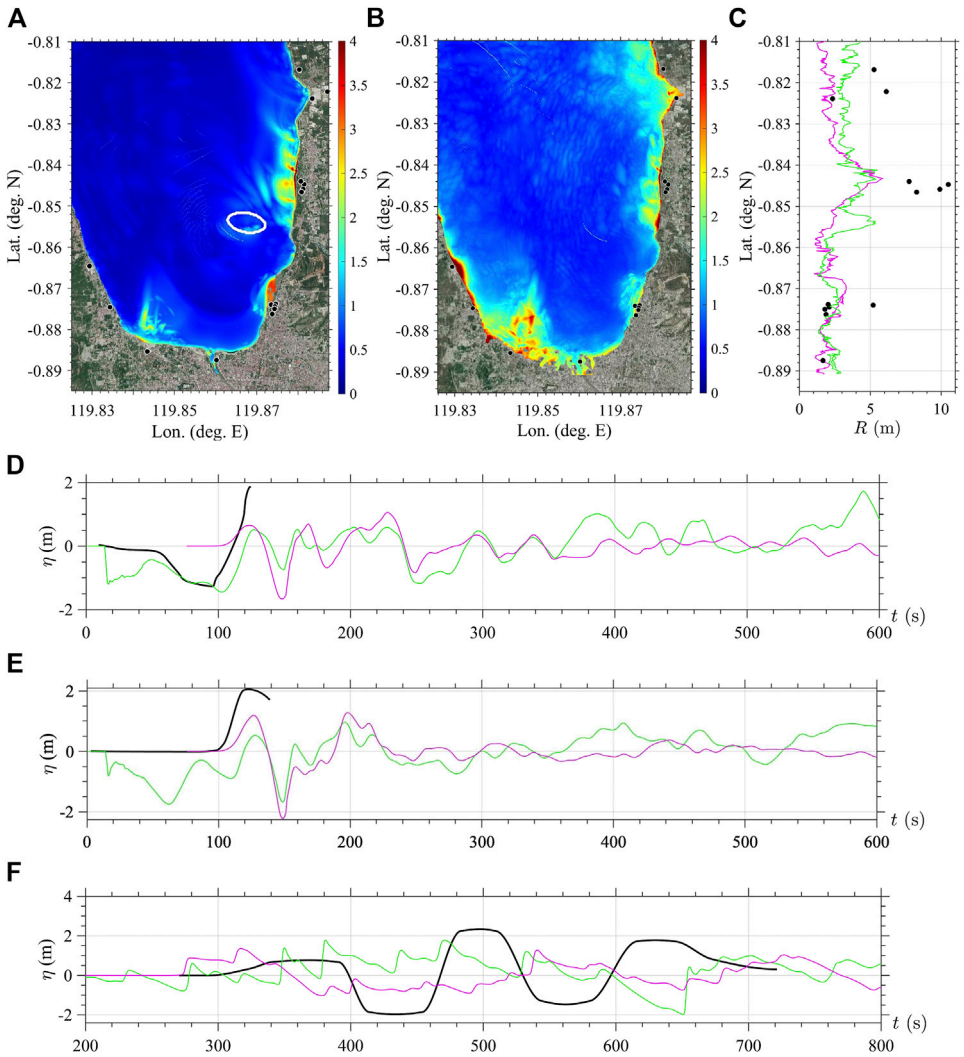

FIGURE 13 | (A,B) Maximum surface elevation and **(C)** Runups simulated for (**A** and magenta in **C**) hypothetical SE SMF with footprint marked as white ellipse in **(A)**, and (**B** and green in **C**) dual source combining the SMF with Ulrich et al. (2019)'s earthquake source and the seven slides in **Table 2**, compared with field measurements (black bullets). **(D–F)** Time series of surface elevation computed for each case (same color coding), compared to reconstructed time series at: **(D)** Talise, **(E)** KN Hotel, **(F)** Grand Mall (See **Figure 4** for definitions). Results are from 7.5 m resolution grid SG.

evidence from field surveys, tide gauge data, and survivor accounts.

A proper understanding and modeling of such destructive dual source tsunami events can help mitigate tsunami coastal hazard resulting from future similar events, here or in other tsunami-prone areas.

DATA AVAILABILITY STATEMENT

The datasets presented in this study can be found in online repositories. The names of the repository/repositories and accession number(s) can be found below: https://drive.google.com/drive/folders/1kPUnYcenRFa0KLhzhyZgJG9eya5CfC8D?usp=sharing.

AUTHOR CONTRIBUTIONS

LS performed all of the tsunami simulations, including post-processing, and worked on the manuscript. SG supervised all aspects of the work and worked on the manuscript. DT provided insight into the marine geology and worked on the manuscript.

FUNDING

Support was provided to the University of Rhode Island authors from Grant CMMI-15-35568 from the Engineering for Natural Hazards Program, National Science Foundation. Numerical simulations reported in this work used HPC

resources, as part of the Extreme Science and Engineering Discovery Environment (XSEDE) (project BCS-170006), which is supported by the National Science Foundation (NSF) grant number ACI-1548562.

ACKNOWLEDGMENTS

Special thanks to Anne Socquet for providing their earthquake slip distribution model, and to Thomas Ulrich for providing the time series of horizontal and vertical ground motion from their earthquake model. DT publishes with the permission of the CEO of the British Geological Survey United Kingdom Research and Innovation. Boma Kresning is acknowledged for helping to navigate and translate Indonesian data sources. The Pantoloan tide gauge records and related informations were obtained from the Agency for Geo-spatial Information, Indonesia (BIG) (http://tides.big.go.id).

SUPPLEMENTARY MATERIAL

The Supplementary Material for this article can be found online at: https://www.frontiersin.org/articles/10.3389/feart.2020.598839/full#supplementary-material.

REFERENCES

Altinok, Y., Tinti, S., Alpar, B., Yalciner, A., Ersoy, Ş., Bortolucci, E., et al. (2001). The tsunami of August 17, 1999 in Izmit Bay, Turkey. *Nat. Hazards* 24, 133–146. doi:10.1023/A:1011863610289

Arikawa, T., Muhari, A., Okumura, Y., Dohi, Y., Afriyanto, B., Sujatmiko, K. A., et al. (2018). Coastal subsidence induced several tsunamis during the 2018 Sulawesi earthquake. *J. Disaster Res.* 13,sc20181201. doi:10.20965/jdr.2018.sc20181201

Bao, H., Ampuero, J.-P., Meng, L., Fielding, E. J., Liang, C., Milliner, C. W., et al. (2019). Early and persistent supershear rupture of the 2018 magnitude 7.5 Palu earthquake. *Nat. Geosci.* 12, 200–205. doi:10.1038/s41561-018-0297-z

BIG (2018). Real time tidal observation/ pengamatan pasang surut real time. Available at: tides.big.go.id (Accessed April 30 2020) [Dataset].

BNPB (2019). Gempabumi dan tsunami sulawesi tengah. Available at: https://bnpb.go.id/infografis/infografis-gempabumi-m74-tsunami-sulawesi-tengah (Accessed May 5 2020) [Dataset].

Bradley, K., Mallick, R., Andikagumi, H., Hubbard, J., Meilianda, E., Switzer, A., et al. (2019). Earthquake-triggered 2018 Palu valley landslides enabled by wet rice cultivation. *Nat. Geosci.* 12, 935–939. doi:10.1038/s41561-019-0444-1

Carvajal, M., Araya-Cornejo, C., Sepúlveda, I., Melnick, D., and Haase, J. S. (2019). Nearly instantaneous tsunamis following the Mw 7.5 2018 Palu earthquake. *Geophys. Res. Lett.* 46, 5117–5126. doi:10.1029/2019gl082578

Cipta, A., Omang, A., Supartoyo, P. A., Solilkhin, A., Falah, F. N., et al. (2018). "Anomali perilaku gelombang tsunami (Geological Agency, Ministry of Energy and Mineral Resources) Anomaly of tsunami wave behavior," in Di balik pesona Palu. Badan Geologi, Kementerian Energi dan Sumber Daya Mineral (Geological Agency, Ministry of Energy and Mineral Resources), 133–141.

Dumbser, M., and Käser, M. (2006). An arbitrary high-order discontinuous galerkin method for elastic waves on unstructured meshes—ii. the three-dimensional isotropic case. *Geophys. J. Int.* 167, 319–336. doi:10.1111/j.1365-246x.2006.03120.x

Enet, F., and Grilli, S. T. (2007). Experimental study of tsunami generation by three-dimensional rigid underwater landslides. *J. Waterw. Port Coast. Ocean Eng.* 133 (6), 442–454. doi:10.1061/(asce)0733-950x(2007)133:6(442)

Fang, J., Xu, C., Wen, Y., Wang, S., Xu, G., Zhao, Y., et al. (2019). The 2018 Mw 7.5 Palu earthquake: a supershear rupture event constrained by insar and broadband regional seismograms. *Rem. Sens.* 11, 1330. doi:10.3390/rs11111330

Frederik, M. C., Adhitama, R., Hananto, N. D., Sahabuddin, S., Irfan, M., Moefti, O., et al. (2019). First results of a bathymetric survey of Palu Bay, central Sulawesi, Indonesia following the tsunamigenic earthquake of 28 September 2018. *Pure Appl. Geophys.* 176, 3277–3290. doi:10.1007/s00024-019-02280-7

Glimsdal, S., Pedersen, G. K., Harbitz, C. B., and Løvholt, F. (2013). Dispersion of tsunamis: does it really matter?. *Nat. Hazards Earth Syst. Sci.* 13 (6), 1507–1526. doi:10.5194/nhess-13-1507-2013

Goda, K., Mori, N., Yasuda, T., Prasetyo, A., Muhammad, A., and Tsujio, D. (2019). Cascading geological hazards and risks of the 2018 Sulawesi Indonesia earthquake and sensitivity analysis of tsunami inundation simulations. *Front. Earth Sci.* 7, 261. doi:10.3389/feart.2019.00261

Goto, C., Ogawa, Y., Shuto, N., and Imamura, F. (1997). Numerical method of tsunami simulation with the leap-frog scheme. *Intergovernmental Oceanogr. Comm. UNESCO Man. Guides* 35, 126.

Grilli, S. T., Tappin, D. R., Carey, S., Watt, S. F. L., Ward, S. N., Grilli, A. R., et al. (2019). Modelling of the tsunami from the December 22, 2018 lateral collapse of Anak Krakatau volcano in the Sunda Straits, Indonesia. *Sci. Rep.* 9, 11946–12013. doi:10.1038/s41598-019-48327-6

Grilli, S. T., O'Reilly, C., Harris, J. C., Bakhsh, T. T., Tehranirad, B., Banihashemi, S., et al. (2015). Modeling of SMF tsunami hazard along the upper East coast: detailed impact around Ocean City, MD. *Nat. Hazards* 76, 705–746. doi:10.1007/s11069-014-1522-8

Grilli, S. T., Shelby, M., Kimmoun, O., Dupont, G., Nicolsky, D., Ma, G., et al. (2017). Modeling coastal tsunami hazard from submarine mass failures: effect of slide rheology, experimental validation, and case studies off the East coast. *Nat. Hazards* 86, 353–391. doi:10.1007/s11069-016-2692-3

Gusman, A. R., Supendi, P., Nugraha, A. D., Power, W., Latief, H., Sunendar, H., et al. (2019). Source model for the tsunami inside Palu Bay following the 2018 Palu earthquake, Indonesia. *Geophys. Res. Lett.* 46, 8721–8730. doi:10.1029/2019gl082717

He, L., Feng, G., Li, Z., Feng, Z., Gao, H., and Wu, X. (2019). Source parameters and slip distribution of the 2018 Mw 7.5 Palu, Indonesia earthquake estimated from space-based geodesy. *Tectonophysics* 772, 228216. doi:10.1016/j.tecto.2019.228216

Hébert, H., Heinrich, P., Schindelé, F., and Piatanesi, A. (2001). Far-field simulation of tsunami propagation in the Pacific Ocean: impact on the Marquesas Islands (French Polynesia). *J. Geophys. Res. Oceans* 106, 9161–9177. doi:10.1029/2000jc000552

Heidarzadeh, M., Muhari, A., and Wijanarto, A. B. (2019). Insights on the source of the 28 September 2018 Sulawesi tsunami, Indonesia based on spectral analyses and numerical simulations. *Pure Appl. Geophys.* 176, 25–43. doi:10.1007/s00024-018-2065-9

Heinrich, P., Schindele, F., Guibourg, S., and Ihmlé, P. F. (1998). Modeling of the February 1996 Peruvian tsunami. *Geophys. Res. Lett.* 25, 2687–2690. doi:10.1029/98gl01780

Horrillo, J., Grilli, S. T., Nicolsky, D., Roeber, V., and Zhang, J. (2015). Performance benchmarking tsunami models for nthmp's inundation mapping activities. *Pure Appl. Geophys.* 172, 869–884. doi:10.1007/s00024-014-0891-y

Imamura, F., Gica, E., Takahashi, T., and Shuto, N. (1995). Numerical simulation of the 1992 Flores tsunami: interpretation of tsunami phenomena in northeastern Flores island and damage at Babi Island. *Pure Appl. Geophys.* 144, 555–568. doi:10.1007/bf00874383

Jamelot, A., Gailler, A., Heinrich, P., Vallage, A., and Champenois, J. (2019). Tsunami simulations of the Sulawesi Mw 7.5 event: comparison of seismic sources issued from a tsunami warning context versus post-event finite source. *Pure Appl. Geophys.* 176, 3351–3376. doi:10.1007/s00024-019-02274-5

Kirby, J. T., Shi, F., Nicolsky, D., and Misra, S. (2016). The 27 April 1975 Kitimat, British Columbia, submarine landslide tsunami: a comparison of modeling approaches. *Landslides* 13, 1421–1434. doi:10.1007/s10346-016-0682-x

Liu, P.-F., Higuera, P., Husrin, S., Prasetya, G., Prihantono, J., Diastomo, H., et al. (2020). Coastal landslides in Palu Bay during 2018 Sulawesi earthquake and tsunami. *Landslides* 17 (9), 2085–2098. doi:10.1007/s10346-020-01417-3

Lynett, P. J., Gately, K., Wilson, R., Montoya, L., Arcas, D., Aytore, B., et al. (2017). Inter-model analysis of tsunami-induced coastal currents. *Ocean Model.* 114, 14–32. doi:10.1016/j.ocemod.2017.04.003

Ma, G., Shi, F., and Kirby, J. T. (2012). Shock-capturing non-hydrostatic model for fully dispersive surface wave processes. *Ocean Model.* 43, 22–35. doi:10.1016/j.ocemod.2011.12.002

Ma, G., Kirby, J. T., Hsu, T.-J., and Shi, F. (2015). A two-layer granular landslide model for tsunami wave generation: theory and computation. *Ocean Model.* 93, 40–55. doi:10.1016/j.ocemod.2015.07.012

Madsen, P., Fuhrman, D., and Schaffer, H. (2008). On the solitary wave paradigm for tsunamis. *J. Geophys. Res.* 113, C12012. doi:10.1029/2008jc004932

Mikami, T., Shibayama, T., Esteban, M., Takabatake, T., Nakamura, R., Nishida, Y., et al. (2019). Field survey of the 2018 Sulawesi tsunami: Inundation and run-up heights and damage to coastal communities. *Pure Appl. Geophys.* 176, 3291–3304. doi:10.1007/s00024-019-02258-5

Miyajima, M., Setiawan, H., Yoshida, M., Ono, Y., Kosa, K., Oktaviana, I. S., et al. (2019). Geotechnical damage in the 2018 Sulawesi earthquake, Indonesia. *Geoenviron. Disasters* 6, 1–8. doi:10.1186/s40677-019-0121-0

Muhari, A., Imamura, F., Arikawa, T., Hakim, A. R., and Afriyanto, B. (2018). Solving the puzzle of the September 2018 Palu, Indonesia, tsunami mystery: clues from the tsunami waveform and the initial field survey data. *J. Disaster Res.* 13, sc20181108. doi:10.20965/jdr.2018.sc20181108

Nakata, K., Katsumata, A., and Muhari, A. (2020). Submarine landslide source models consistent with multiple tsunami records of the 2018 Palu tsunami, Sulawesi, Indonesia. *Earth Planets Space* 72, 1–16. doi:10.1186/s40623-020-01169-3

Natawidjaja, D., Daryono, M., Prasetya, G., Udrekh, U., Liu, P.-F., Hananto, N., et al. (2020). The 2018 Mw7.5 Palu supershear earthquake ruptures geological fault's multi-segment separated by large bends: results from integrating field measurements, lidar, swath bathymetry, and seismic-reflection data. *Geophys. J. Int.* [Epub ahead of print]. doi:10.1093/gji/ggaa498

Okada, Y. (1985). Surface deformation due to shear and tensile faults in a half-space. *Bull. Seismol. Soc. Am.* 75, 1135–1154. doi:10.1016/0148-9062(86)90674-1

Omira, R., Dogan, G., Hidayat, R., Husrin, S., Prasetya, G., Annunziato, A., et al. (2019). The september 28th, 2018, tsunami in Palu-Sulawesi, Indonesia: a post-event field survey. *Pure Appl. Geophys.* 176, 1379–1395. doi:10.1007/s00024-019-02145-z

Pakoksung, K., Suppasri, A., Imamura, F., Athanasius, C., Omang, A., and Muhari, A. (2019). Simulation of the submarine landslide tsunami on 28 September 2018 in Palu Bay, Sulawesi Island, Indonesia, using a two-layer model. *Pure Appl. Geophys.* 176, 3323–3350. doi:10.1007/s00024-019-02235-y

Paulik, R., Gusman, A., Williams, J. H., Pratama, G. M., Lin, S.-l., Prawirabhakti, A., et al. (2019). Tsunami hazard and built environment damage observations from Palu city after the September 28 2018 Sulawesi earthquake and tsunami. *Pure Appl. Geophys.* 176, 3305–3321. doi:10.1007/s00024-019-02254-9

Pelties, C., Gabriel, A.-A., and Ampuero, J.-P. (2014). Verification of an Ader-DG method for complex dynamic rupture problems. *Geosci. Model Dev.* 7, 847–866. doi:10.5194/gmd-7-847-2014

Prasetya, G., De Lange, W., and Healy, T. (2001). The Makassar Strait tsunamigenic region, Indonesia. *Nat. Hazards* 24, 295–307. doi:10.1023/A:1012297413280

Pribadi, S., Gunawan, I., Nugraha, J., Haryono, T., Ermawan, C., et al. (2018). *Survey tsunami teluk Palu 2018. Basri* [Dataset, see data repository].

Putra, P. S., Aswan, A., Maryunani, K. A., Yulianto, E., and Kongko, W. (2019). Field survey of the 2018 Sulawesi tsunami deposits. *Pure Appl. Geophys.* 176, 2203–2213. doi:10.1007/s00024-019-02181-9

Sassa, S., and Takagawa, T. (2019). Liquefied gravity flow-induced tsunami: first evidence and comparison from the 2018 Indonesia Sulawesi earthquake and tsunami disasters. *Landslides* 16, 195–200. doi:10.1007/s10346-018-1114-x

Schambach, L., Grilli, S., Tappin, D., Gangemi, M., and Barbaro, G. (2020). New simulations and understanding of the 1908 Messina tsunami for a dual seismic and deep submarine mass failure source. *Mar. Geol.* 421, 106093. doi:10.1016/j.margeo.2019.106093

Schambach, L., Grilli, S. T., Kirby, J. T., and Shi, F. (2019). Landslide tsunami hazard along the upper US east coast: effects of slide deformation, bottom friction, and frequency dispersion. *Pure Appl. Geophys.* 176, 3059–3098. doi:10.1007/s00024-018-1978-7

Sepúlveda, I., Haase, J. S., Carvajal, M., Xu, X., and Liu, P. L.-F. (2020). Modeling the sources of the 2018 Palu, Indonesia, tsunami using videos from social media. *J. Geophys. Res. Solid Earth* 125 (3), e2019JB018675. doi:10.1029/2019jb018675

Shi, F., Kirby, J. T., Harris, J. C., Geiman, J. D., and Grilli, S. T. (2012). A high-order adaptive time-stepping TVD solver for Boussinesq modeling of breaking waves and coastal inundation. *Ocean Model.* 43, 36–51. doi:10.1016/j.ocemod.2011.12.004

Socquet, A., Hollingsworth, J., Pathier, E., and Bouchon, M. (2019). Evidence of supershear during the 2018 magnitude 7.5 Palu earthquake from space geodesy. *Nat. Geosci.* 12, 192–199. doi:10.1038/s41561-018-0296-0

Song, X., Zhang, Y., Shan, X., Liu, Y., Gong, W., and Qu, C. (2019). Geodetic observations of the 2018 Mw 7.5 Sulawesi earthquake and its implications for the kinematics of the Palu fault. *Geophys. Res. Lett.* 46, 4212–4220. doi:10.1029/2019gl082045

Sunny, R. C., Cheng, W., and Horrillo, J. (2019). Video content analysis of the 2018 Sulawesi tsunami, Indonesia: impact at Palu Bay. *Pure Appl. Geophys.* 176, 4127–4138. doi:10.1029/2019gl082045

Syamsidik, B., Umar, M., Margaglio, G., and Fitrayansyah, A. (2019). Post-tsunami survey of the 28 September 2018 tsunami near Palu Bay in central sulawesi, Indonesia: impacts and challenges to coastal communities. *Int. J. Disaster Risk Reduct.* 38, 101229. doi:10.1016/j.ijdrr.2019.101229

Takagi, H., Pratama, M. B., Kurobe, S., Esteban, M., Aránguiz, R., and Ke, B. (2019). Analysis of generation and arrival time of landslide tsunami to Palu city due to the 2018 Sulawesi earthquake. *Landslides* 16, 983–991. doi:10.1007/s10346-019-01166-y

Tanioka, Y., and Satake, K. (1996). Tsunami generation by horizontal displacement of ocean bottom. *Geophys. Res. Lett.* 23, 861–864. doi:10.1029/96gl00736

Tappin, D. R., Grilli, S. T., Harris, J. C., Geller, R. J., Masterlark, T., Kirby, J. T., et al. (2014). Did a submarine landslide contribute to the 2011 Tohoku tsunami?. *Mar. Geol.* 357, 344–361. doi:10.1016/j.margeo.2014.09.043

Tappin, D., Watts, P., and Grilli, S. T. (2008). The Papua New Guinea tsunami of 17 July 1998: anatomy of a catastrophic event. *Nat. Hazards Earth Syst. Sci.* 8, 243–266. doi:10.5194/nhess-8-243-2008

Ulrich, T., Vater, S., Madden, E. H., Behrens, J., van Dinther, Y., Van Zelst, I., et al. (2019). Coupled, physics-based modeling reveals earthquake displacements are critical to the 2018 Palu, Sulawesi tsunami. *Pure Appl. Geophys.* 176, 4069–4109. doi:10.1007/s00024-019-02290-5

Uphoff, C., Rettenberger, S., Bader, M., Madden, E. H., Ulrich, T., Wollherr, S., et al. (2017). "Extreme scale multi-physics simulations of the tsunamigenic 2004 Sumatra megathrust earthquake," in Proceedings of the international conference for high performance computing, networking, storage and analysis, SC'17, November 2017, Denver, CO, 1–16.

USGS (2018). M 7.5 - 70 km N of Palu, Indonesia. Available at: https://earthquake.usgs.gov/earthquakes/eventpage/us1000h3p4/executive (Accessed April 30 2020).

Valkaniotis, S., Ganas, A., Tsironi, V., and Barberopoulou, A. (2018). A preliminary report on the M7.5 Palu 2018 earthquake co-seismic ruptures and landslides using image correlation techniques on optical satellite data. Report to EMSC on 19 October 2018 12:00 UTC. doi:10.5281/zenodo.1467128

VOA-News (2018). Crew recounts riding tsunami that dumped ferry in village. https://www.voanews.com/east-asia-pacific/crew-recounts-riding-tsunami-dumped-ferry-village (Accessed June 30 2020).

Watkinson, I. M., and Hall, R. (2017). Fault systems of the eastern Indonesian triple junction: evaluation of quaternary activity and implications for seismic hazards. *Geol. Soc. London Spec. Publ.* 441, 71–120. doi:10.1144/sp441.8

Watkinson, I. M., and Hall, R. (2019). Impact of communal irrigation on the 2018 Palu earthquake-triggered landslides. *Nat. Geosci.* 12, 940–945. doi:10.1038/s41561-019-0448-x

Weatherall, P., Marks, K. M., Jakobsson, M., Schmitt, T., Tani, S., Arndt, J. E., et al. (2015). A new digital bathymetric model of the world's oceans. *Earth Space Sci.* 2, 331–345. doi:10.1002/2015ea000107

Wei, G., Kirby, J. T., Grilli, S. T., and Subramanya, R. (1995). A fully nonlinear Boussinesq model for surface waves. Part 1. Highly nonlinear unsteady waves. *J. Fluid Mech.* 294, 71–92. doi:10.1017/s0022112095002813

Widiyanto, W., Santoso, P. B., Hsiao, S.-C., and Imananta, R. T. (2019). Post-event field survey of 28 september 2018 Sulawesi earthquake and tsunami. *Nat. Hazards Earth Syst. Sci.* 19 (12), 2781–2794. doi:10.5194/nhess-19-2781-2019

Yolsal-Çevikbilen, S., and Taymaz, T. (2019). Source characteristics of the 28 September 2018 Mw 7.5 Palu-Sulawesi, Indonesia (SE Asia) earthquake based on inversion of teleseismic bodywaves. *Pure Appl. Geophys.* 176, 4111–4126. doi:10.1007/s00024-019-02294-1

Zhang, C., Kirby, J. T., Shi, F., Ma, G., and Grilli, S. T. (2021a). A two-layer non-hydrostatic landslide model for tsunami generation on irregular bathymetry. 1. Theoretical basis. *Ocean Model.* 101749, https://doi.org/10.1016/j.ocemod.2020.101749

Zhang, C., Kirby, J. T., Shi, F., Ma, G., and Grilli, S. T. (2021b). A two-layer non-hydrostatic landslide model for tsunami generation on irregular bathymetry. 2. Numerical discretization and model validation. *Ocean Model.* (to appear)

Zhang, C., Tehranirad, B., Kirby, J. T., Derakhti, M., Nemati, F., Grilli, S. T., et al. (2017). *Tsunami benchmark results for the non-hydrostatic wave model NHWAVE, version 2.0.* Delaware: University of Delaware.

Conflict of Interest: The authors declare that the research was conducted in the absence of any commercial or financial relationships that could be construed as a potential conflict of interest.

frontiers in Earth Science

ORIGINAL RESEARCH
published: 14 January 2021
doi: 10.3389/feart.2020.597865

Faster Than Real Time Tsunami Warning with Associated Hazard Uncertainties

Daniel Giles[1]*, *Devaraj Gopinathan*[2], *Serge Guillas*[2] and *Frédéric Dias*[1]

[1]School of Mathematics and Statistics, University College Dublin, Dublin, Ireland, [2]Department of Statistical Science, University College London, London, United Kingdom

Tsunamis are unpredictable events and catastrophic in their potential for destruction of human lives and economy. The unpredictability of their occurrence poses a challenge to the tsunami community, as it is difficult to obtain from the tsunamigenic records estimates of recurrence rates and severity. Accurate and efficient mathematical/computational modeling is thus called upon to provide tsunami forecasts and hazard assessments. Compounding this challenge for warning centres is the physical nature of tsunamis, which can travel at extremely high speeds in the open ocean or be generated close to the shoreline. Thus, tsunami forecasts must be not only accurate but also delivered under severe time constraints. In the immediate aftermath of a tsunamigenic earthquake event, there are uncertainties in the source such as location, rupture geometry, depth, magnitude. Ideally, these uncertainties should be represented in a tsunami warning. However in practice, quantifying the uncertainties in the hazard intensity (*i.e.,* maximum tsunami amplitude) due to the uncertainties in the source is not feasible, since it requires a large number of high resolution simulations. We approximate the functionally complex and computationally expensive high resolution tsunami simulations with a simple and cheap statistical emulator. A workflow integrating the entire chain of components from the tsunami source to quantification of hazard uncertainties is developed here - quantification of uncertainties in tsunamigenic earthquake sources, high resolution simulation of tsunami scenarios using the GPU version of Volna-OP2 on a non-uniform mesh for an ensemble of sources, construction of an emulator using the simulations as training data, and prediction of hazard intensities with associated uncertainties using the emulator. Thus, using the massively parallelized finite volume tsunami code Volna-OP2 as the heart of the workflow, we use statistical emulation to compute uncertainties in hazard intensity at locations of interest. Such an integration also balances the trade-off between computationally expensive simulations and desired accuracy of uncertainties, within given time constraints. The developed workflow is fully generic and independent of the source (1945 Makran earthquake) studied here.

Keywords: faster than real time simulation, tsunami ensemble, Volna-OP2, Makran subduction zone, GPGPU computing, statistical emulation, probabilistic hazard, tsunami warning

OPEN ACCESS

Edited by:
Jörn Behrens,
University of Hamburg, Germany

Reviewed by:
Joern Lauterjung,
Helmholtz Centre Potsdam, Germany
José Pedro Matos,
Stucky SA, Switzerland

***Correspondence:**
Daniel Giles
daniel.giles@ucdconnect.ie

Specialty section:
This article was submitted to Geohazards and Georisks, a section of the journal Frontiers in Earth Science

Received: *22 August 2020*
Accepted: *27 October 2020*
Published: *14 January 2021*

Citation:
Giles D, Gopinathan D, Guillas S and Dias F (2021) Faster Than Real Time Tsunami Warning with Associated Hazard Uncertainties. Front. Earth Sci. 8:597865. doi: 10.3389/feart.2020.597865

1 INTRODUCTION

The 2004 Indian Ocean tsunami was the worst tsunami disaster in the world's history (Satake, 2014). It was responsible for massive destruction and loss of life along the coastlines of the Eastern Indian Ocean. In the aftermath of this event there was a concerted effort by the scientific community to mitigate the damage posed by these geophysical events (Bernard et al., 2006; Satake, 2014; Bernard and Titov, 2015). Scientific work was focused on developing tsunami warning centres, deploying tsunami wave gauges and increasing public awareness (Synolakis and Bernard, 2006). International collaborations were formed with tsunami early warning centres being set up across all the major oceans (Bernard et al., 2010). The responsibilities of tsunami early warning centres include detecting tsunamigenic sources, deducing the level of threat posed, deciding on the areas most at risk and then notifying the relevant authorities. As tsunami waves can propagate at extremely high speeds, arrival times on the coastline can be in the order of minutes. Therefore, severe time constraints compound the difficulties faced by tsunami early warning centres in providing accurate tsunami wave forecasts.

Tsunamis are long waves that can be generated from a variety of geophysical sources such as earthquakes, landslides and volcanic explosions. As stated, tsunami early warning centres are responsible for detecting tsunamigenic sources and in this paper we focus on tsunamis triggered by earthquakes. The detection and inversion of the seismic signal to constrain the earthquake's origin, magnitude and physical features is the first stage of a warning centre's workflow. Tsunami warning centres currently use a variety of techniques in this inversion stage (Melgar and Bock, 2013; Clément and Reymond, 2015; Inazu et al., 2016). After the seismic signal has been constrained, the second stage focuses on deducing the level of threat posed by the tsunamigenic event. The most simplistic approach is a decision matrix, which gives a crude hazard map based on a specified earthquake magnitude, location and depth (Gailler et al., 2013). A more involved approach incorporates the large databases of pre-computed tsunami simulations from identified sources that most tsunami warning centres possess for their respective regions. In the event of a seismic signal being detected, these pre-computed databases are queried for sources similar to the signal source. The resultant database simulation results are then combined to inform a warning decision (Reymond et al., 2012; Gailler et al., 2013). A different approach exploits independent multi-sensor measurements to minimize the uncertainty in the tsunami hazard for 'near-field' events, whilst also reducing the number of plausible representative scenarios from a pre-computed database (Behrens et al., 2010). Further, building on these extensive pre-computed database approaches, some centres utilize 'on the fly' tsunami simulations to constrain the associated hazard (Jamelot and Reymond, 2015). Real-time tsunami wave observations, where available, can also play an extremely important role (Behrens et al., 2010; Angove et al., 2019).

In the immediate aftermath of an earthquake event there is always some uncertainty associated with the characteristic features of the seismic source. At present, these uncertainties are not fully accounted for in traditional tsunami early warning approaches. Accurately assessing the uncertainties on the tsunami hazard from the uncertainties on the source requires a large number of tsunami simulations. The authors show here that by utilizing a statistical surrogate model (emulator) in conjunction with an efficient tsunami code, one can massively augment the number of source realisations sampled with minimal added runtime and computing resources. Statistical surrogate models approximate the functional of more expensive deterministic models. They have been utilized successfully in a large variety of fields such as biological systems (Oyebamiji et al., 2017), climate models (Castruccio et al., 2014), atmospheric dispersion (Girard et al., 2016), or building energy models (Kristensen et al., 2017), but pertaining to this work they have been leveraged to carry out tsunami sensitivity studies and uncertainty quantification (Salmanidou et al., 2017; Guillas et al., 2018; Gopinathan et al., 2020).

By utilizing the latest high performance computing architectures and efficient tsunami codes, it has become feasible to run regional tsunami simulations in a faster than real time setting (Løvholt et al., 2019). The massively parallelized Volna-OP2 is an example of one such capable code. It solves the nonlinear shallow water equations using a finite volume discretization (Dutykh et al., 2011). It has been successfully used to simulate faster than real time ensembles for a North East Atlantic tsunami (Giles et al., 2020b). Leveraging Volna-OP2's computational efficiency is a key component of this paper's workflow. However, in order to fully capture the uncertainty on a tsunami source, thousands of potential sources need to be investigated in a faster than real time setting. Even with the performance capabilities of Volna-OP2, carrying out thousands of tsunami simulations would require an unrealistic amount of computing resources. The functionality of this 'expensive' deterministic model can be captured by a 'cheap' emulator, which is trained on the resultant outputs of the deterministic simulations. The incorporation of the emulator balances the trade-off between expensive simulations and desired level of accuracy on uncertainties. The authors note that there have been substantial efforts made in developing tsunami codes which are capable of faster than real time simulations. Tsunami-HySEA is another code that has been shown to be capable in this respect (Macías et al., 2017).

The emulator is shown here to capture the tsunami hazard, *i.e.* maximum wave heights, and associated uncertainties in three different manners. Maximum wave height percentiles at output locations which are positioned at a fixed depth are produced along with local and regional maximum wave height and standard deviation maps. These three different products utilize the same method of constructing the emulators from input/output pairs. The general workflow introduced here is independent of the test case studied, the 1945 Makran earthquake and the specified areas of interest (Karachi, Chabahar and Muscat). Further, the authors would like to point out that the statistical surrogate framework introduced here in the context of early warning systems is a proof-of-concept and is not a fully fledged early warning system, for that more computing resources and efforts on parallelized workflow would be required. As each individual source realization and simulation is independent, the whole workflow lends itself to parallelization. The runtime for each step of the workflow is given in terms of one

source realization or total number of predictions at one output location. Therefore with adequate computing resources, this whole process could lead to a faster than real time setting.

The paper is structured as follows. **Section 2** outlines the proposed workflow for a tsunami early warning centre for providing relevant uncertainties of tsunami hazard (maximum tsunami wave heights). **Section 3** introduces the test case chosen here, the 1945 Makran earthquake and tsunami. As this is a historical source, we have chosen to centre the tsunami realisations in the vicinity of the source mechanism proposed by (Okal et al., 2015). **Section 4** highlights the tsunami modeling aspect of the study, which as stated utilizes the massively parallelized tsunami code Volna-OP2. The non-uniform unstructured meshes, refined around the areas of interest (Karachi, Chabahar and Muscat), are presented here. The construction, training and prediction procedures of the statistical emulator are explored in **section 5**. The results section (**section 6**) presents the two different outputs from the workflow presented below (**Figure 1**). The first type of outputs are produced directly by the deterministic Volna-OP2 simulations – regional maximum wave heights and time series plots. The second type involves the maximum tsunami wave heights with associated uncertainties generated using the emulator. These are presented for various output locations – points along a coastline at a fixed depth, localized maps and regional maps. Finally, the paper is wrapped up with concluding remarks and future work (**section 7**).

2 TSUNAMI WARNING WORKFLOW

The workflow (**Figure 1**) is launched with an input of a range of estimated location (latitude, longitude), magnitude and associated distribution of an earthquake source. A number of possible earthquake sources n_D in this space are then sampled using a Latin Hypercube design. The number of output locations n_G and prediction scenarios n_P are selected ahead of time. The output locations can be gauge points at a fixed depth, points within a localized region or points which provide coverage of the global region. The uplift of the earthquake sources is computed using the Okada model (Okada, 1985) by first extracting the remaining earthquake parameters, length and width from scaling relations and local geometry such as rake and dip. In this application an added plug in for the effect of sediment amplification on the slip is carried out. More details are provided in **section 3**. The displacement is then used as the initial condition in the Volna-OP2 simulations. The maximum runtime for generating the initial displacements using a Matlab code running on a *Xeon E5-2620V3 2.4 GHz × 12* workstation is 120s per scenario. This runtime could be reduced by generating the initial displacements on a dedicated cluster instead of a workstation, where faster and more CPUs could be incorporated. Each source realization is independent, thus the initial displacement calculation lends itself to parallelization. The non-uniform unstructured mesh required for the Volna-OP2 simulations is generated ahead of time, with refinement around the areas of interest. For this study these areas are Karachi, Chabahar and Muscat. The n_D simulations are carried out using Volna-OP2 on a *Nvidia Tesla V100 GPU* with a runtime of 136s per scenario. Regional maximum wave heights and selected time series plots from the n_D simulations are produced. The emulators $\mathcal{M}_i$ are constructed for each output location (with $i = 1$ to n_G and $\mathcal{M}$ being the set of $\mathcal{M}_i$ emulators) from the n_D extracted maximum wave heights and associated earthquake source parameters. Finally, the tsunami hazard (maximum wave height - η_{max}) and associated uncertainties at the n_G output locations are obtained by the n_P prediction scenarios using the emulators $\mathcal{M}_i$. If the estimated location or distribution of the earthquake source is updated, which is often the case in the aftermath of a seismic event, new predictions can be rapidly carried out with the updated information, again using the same emulator. Emphasis is placed on the nature of the runtimes quoted in this workflow. These are serial runtimes of time per scenario (n_D), time for construction of emulators per output location or time of n_P predictions per output location. Further, the time taken to post-process and visualize the data is not incorporated.

3 EARTHQUAKE SOURCE

The eastern section of the Makran subduction zone (MSZ) (**Figure 2**) is modeled by 559 (n_F) finite fault (FF) segments arranged in a 43 × 13 grid. The dimensions of each segment are approximately 10 km × 10 km. The entire fault model spans a rectangle of 420 km × 129 km. The analytical equations in Okada (1985) are used to generate the vertical displacement U from the slips and other geometric parameters that define the fault. The dip angles and depths of the fault (d_f) are taken from Slab2 (Hayes et al., 2018; Hayes, 2018), while the rake and strike are uniformly kept at 90° and 270° respectively. The seismic moment M_w is defined as (Kanamori, 1977; Hanks and Kanamori, 1979)

$$M_w = (2/3)\left(\log_{10} M_0 - 9.1\right), \quad M_0 = \sum_{i=1}^{n_F} \mu l_i w_i S_i, \tag{1}$$

where M_0 is the seismic moment, $\mu = 3 \times 10^{10}$ N/m^2 is the rigidity modulus, and l_i, w_i, and S_i are the length, width and slip on the ith fault segment. The slip profile for the entire fault or rupture is modeled as a smooth function that has a maximum near the origin of rupture, whose coordinates are denoted by (X_o,Y_o).

Amplification of U due to the presence of sediment layers in the MSZ is modeled via the sediment amplification curve in (Dutykh and Dias, 2010). The main component in arriving at the sediment amplification factor (S_a^i) on a segment is the relative depth (d_r^i) of the ith segment. d_r^i is defined as the ratio of the sediment thickness (d_s^i) and the down-dip fault depth (d_f^i) of the ith segment. d_s^i is sourced from GlobSed[1] (Straume, 2019), while d_f^i is interpolated from Slab2 (Hayes et al., 2018). The sediment amplification factor corresponding to d_r^i amplifies S_i to an effective slip S_i^e as

$$S_i^e = S_i\left(1 + S_a^i\right) \tag{2}$$

[1]available at *ngdc.noaa.gov/mgg/sedthick/*.

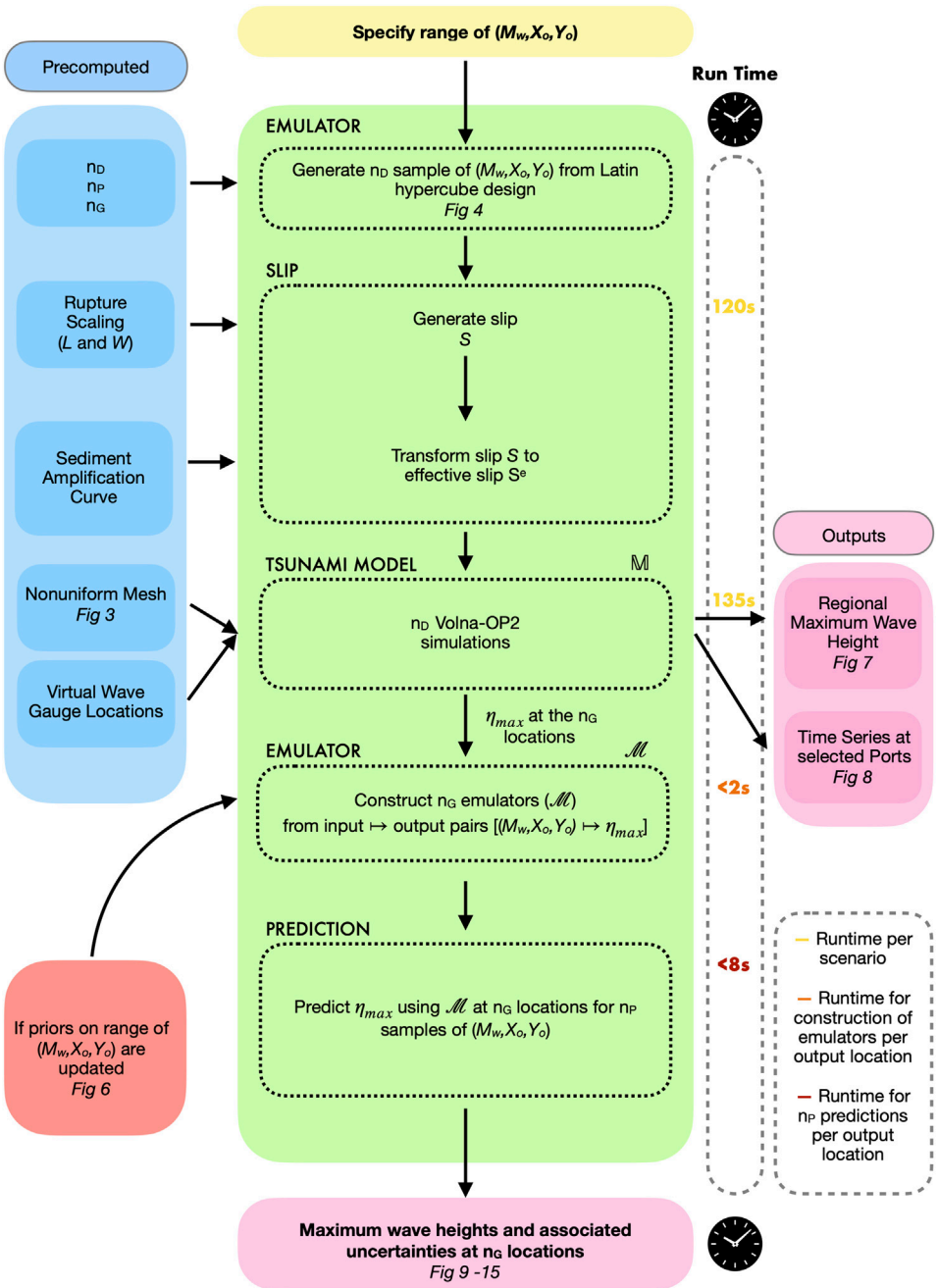

FIGURE 1 | Flowchart of the proposed workflow. n_D is the number of sample earthquake sources (training set), n_P is the number of prediction scenarios and n_G is the number of output locations where the emulators are constructed. The runtimes quoted in this workflow are time per source, time for construction of emulators per output location or time per predictions at an output location. η_{max} is defined as maximum wave height. The outputs in the right column come directly from the Volna-OP2 simulations, while the outputs at the bottom are obtained using the emulator.

The effective deformation due to S^e is generated by the Okada equations and denoted by U^e. The Okada equations are implemented based on the dMODELS[2] code (Battaglia et al., 2012; Battaglia et al., 2013). More details on the implementation of the slip profile and sediment amplification may be found in Gopinathan et al. (2020).

A major earthquake in the eastern MSZ generated a devastating tsunami on November 27, 1945 (Byrne et al., 1992). It is the strongest recorded tsunami in the MSZ. Seismic waveform inversion resulted in a magnitude range of M_w 8.0–8.24, with an average value of M_w 8.1 (Byrne et al., 1992). Another seismic

[2]v1.0 available from *pubs.usgs.gov/tm/13/b1/*.

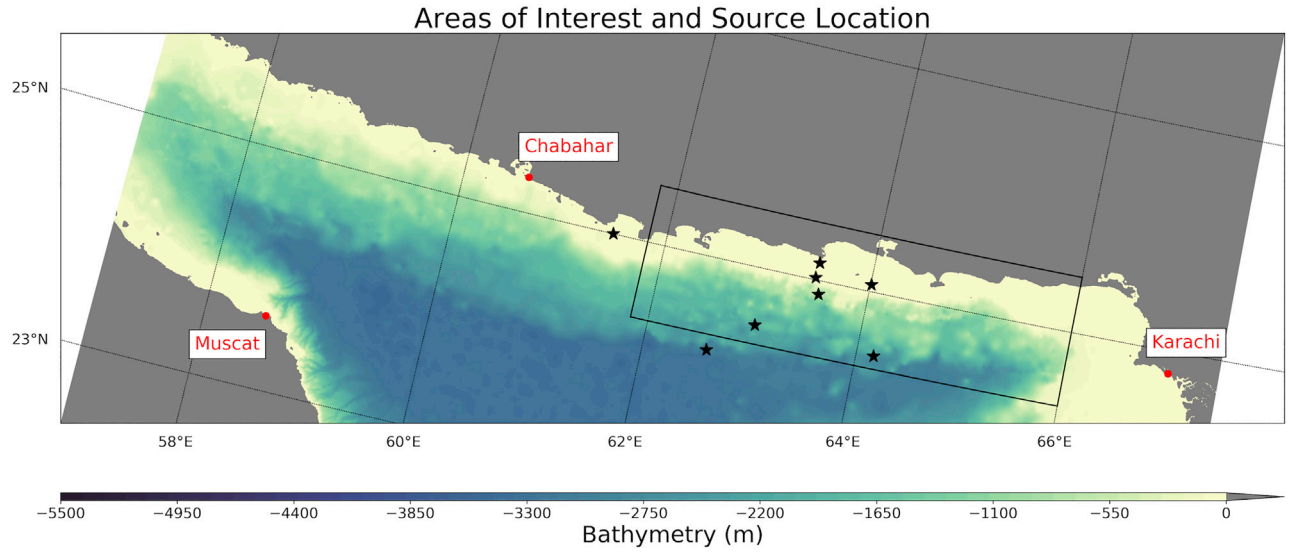

FIGURE 2 | Bathymetry of the Makran region, with the areas of interest: Chabahar, Muscat and Karachi ports, highlighted by the red dots. The locations of the 1945 earthquake sources from the literature are marked with the black stars. The eastern section of the Makran subduction zone (MSZ) considered in this study is bounded by the black box

inversion adjusted the location of the source and estimated the magnitude at M_w 8.2. Thus, an approximate range would be M_w 8.0–8.3 (Heidarzadeh and Satake, 2015). **Table 1** lists the various sources for the 1945 tsunami reported in the literature and the locations of these sources can be seen in **Figure 2**.

4 TSUNAMI MODELLING

Tsunamis exhibit small wave heights and long wavelengths when compared to depth whilst propagating across open oceans. This physical feature allows modellers to drastically simplify the

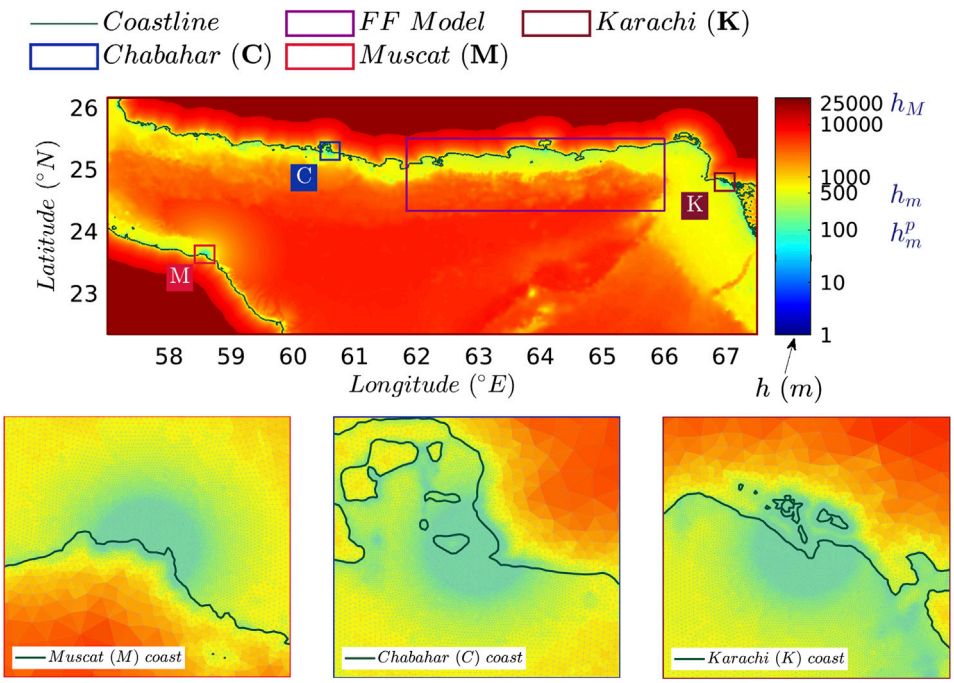

FIGURE 3 | Localized non-uniform unstructured mesh. **Top:** Mesh sizing function *(h)* supplied to Gmsh for the whole domain. The location of the three ports under consideration and the extent of the finite fault (FF) model for the eastern MSZ are also shown. The color scale marks the maximum mesh size h_M = 25 km on land, the mesh size at the coast h_m = 500 m, and the refined mesh size h_m^p = 100 m for the ports. **Bottom:** Zoom in of the locally refined meshes (of size h_m^p) at a scale of 32 km × 32 km for the three ports, Muscat **(left)**, Chabahar **(middle)** and Karachi **(right)**.

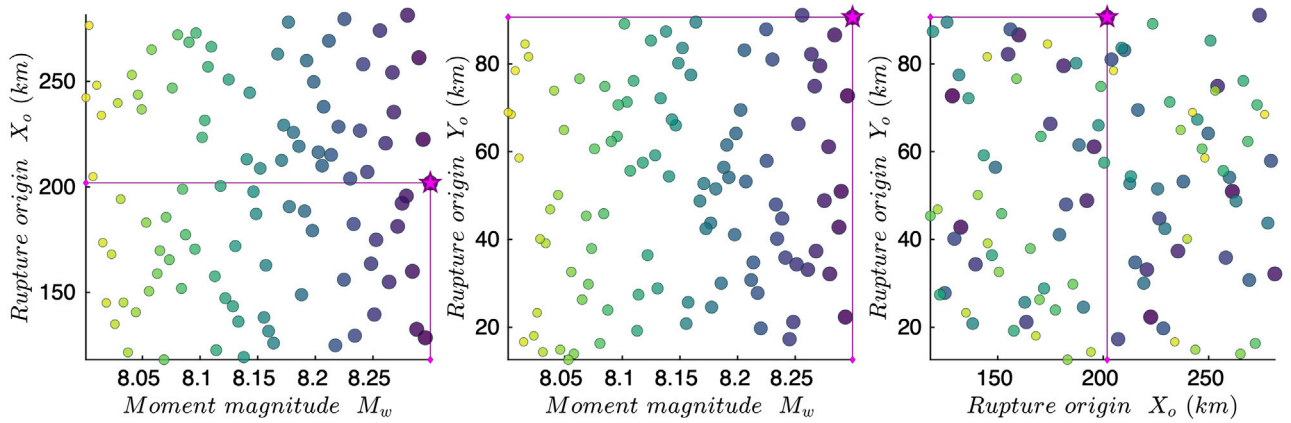

FIGURE 4 | The input parameters (M_ω, X_o, Y_o) for the 100 scenarios used to train the emulator generated by Latin Hypercube Design. The input parameters projected on M_ω–X_o plane **(left)**, M_ω–Y_o plane **(middle)**, and X_o–Y_o plane **(right)**. The dot color corresponds to moment magnitude (M_ω). Sample no. 1 is marked with a star.

TABLE 1 | Sources from the literature for the 1945 Makran earthquake and tsunami.

1945 source	Lon (°E)	Lat (°N)	Magnitude	Comment
Okal et al. (2015)	63.53	24.88	M_w 8.2	Seismic waveform inversion
Engdahl and Villseñor (2002)	63.00	24.50	M_w 8.0	Centennial catalog
Byrne et al. (1992)	63.48	25.15	M_w 8.0 – 8.24	Seismic waveform inversion
Quittmeyer and Jacob (1979)	63.48	25.15	M_w 8.0	Surface wave magnitude
Heidarzadeh and Satake (2015)	—	—	M_w 8.3	Tsunami wave inversion
Heidarzadeh et al. (2008)	64.01	25.06	M_w 8.4	Southeast corner of fault plane
Heidarzadeh et al. (2009)	64.17	24.45	M_w 8.1	Southeast corner of fault plane
Heck (1947)	61.50	25.00	—	List of tsunamis
Pendse (1946)	62.60	24.20	—	—
Ambraseys and Melville (1982)	63.47	25.02	—	—

governing system of equations. Due to this long wave nature, the linear shallow water equations have been shown to be effective in capturing tsunami dynamics across open oceans. However, as a tsunami propagates closer to the shoreline, the nonlinear behavior of the wave becomes important. As it is computational advantageous to solve only one set of equations, the nonlinear shallow water equations (NLSW) have become a popular choice for modellers. Examples of tsunami codes which solve the NLSW include NOAA's MOST (Titov and Gonzalez, 1997), COMCOT (Liu et al., 1998) and TsunAWI (Harig et al., 2008). However, physical dispersion can also play an important role in the ensuing tsunami dynamics (Glimsdal et al., 2013). In order to capture this, the dispersion terms must be included, which results in variants of the Boussinesq equations. Examples of tsunami codes which can capture this physical dispersion and therefore solve a variant of the Boussinesq equations include FUNWAVE (Kennedy et al., 2000), COULWAVE (Lynett et al., 2002) and Celerais (Tavakkol and Lynett, 2017).

4.1 Volna-OP2

Volna-OP2 is a finite volume nonlinear shallow water solver which is capable of harnessing the latest high performance computing architectures: CPUs, GPUs and Xeon-Phis. It captures the complete life-cycle of a tsunami, generation, propagation and inundation (Dutykh et al., 2011). The code has been carefully validated against the various benchmark tests and the performance scalability across various architectures has been explored (Reguly et al., 2018). An extensive error analysis of the code has also recently been carried out (Giles et al., 2020a). Owing to its computational efficiency it has been used extensively by the tsunami modeling community, in particular for tasks which require a large number of runs, such as sensitivity analyses or uncertainty quantification studies (Salmanidou et al., 2017; Gopinathan et al., 2020). The capabilities of the GPU version of the code at performing faster than real time simulations have also been recently highlighted (Giles et al., 2020b).

4.2 Non-Uniform Meshes

In order to capture localized effects on the tsunami dynamics, Volna-OP2 utilizes unstructured non-uniform meshes, which are refined around areas of interest. A customized mesh sizing function and the Gmsh software (Geuzaine and Remacle, 2009) are used to generate the non-uniform meshes. The customized mesh sizing procedure splits the domain into three

TABLE 2 | Runtimes using one Nvidia Tesla V100 GPU for the 6 h simulations with various mesh configurations. Text highlighted in bold refers to the chosen mesh set up used for this study (**Figure 5**).

Refined areas of interest	Minimum mesh size h_m^P [m]	No. of cells [$\times 10^6$]	Runtime [min]
Karachi, Chabahar and Muscat	200 **100** 50 25	0.715 **0.834** 1.030 1.670	1.2 **2.3** 5.3 16.3
Karachi	200 100 50 25	0.699 0.784 0.868 1.115	0.4 0.8 1.7 4.20
Chabahar	200 100 50 25	0.701 0.785 0.863 1.081	0.8 2.0 4.5 11.1
Muscat	200 100 50 25	0.704 0.787 0.855 1.041	1.2 1.8 4.1 9.40

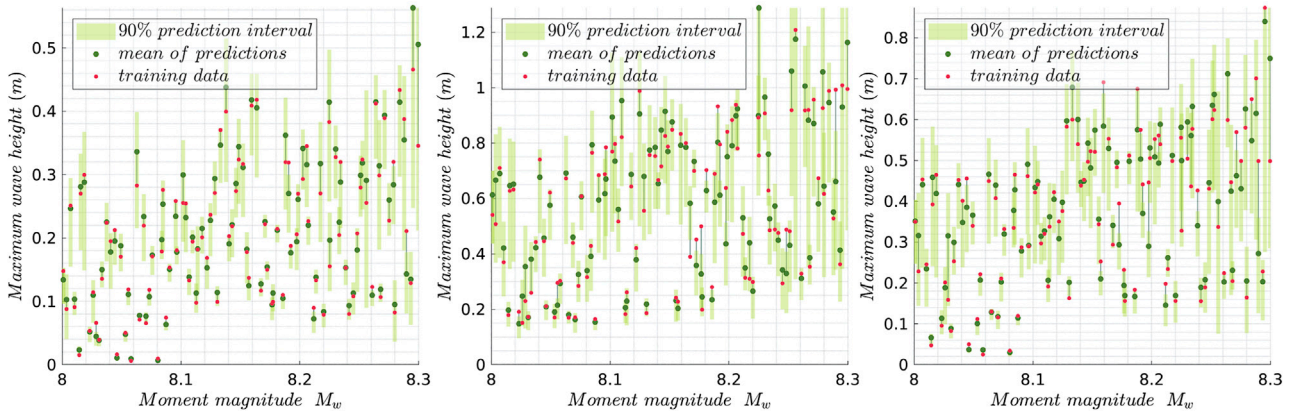

FIGURE 5 | Leave-One-Out diagnostics for a gauge in Muscat **(left)**, Karachi **(middle)**, and Chabahar **(right)**. The discrepancies between the training set and the predictions are shown by the vertical line segments

distinct regions - onshore, offshore and area of interest. In the onshore region cell sizes are based on distance from the coastline. For the offshore region the cell size is dependent on the bathymetry, while in the area of interest a fixed cell size is used. Full details on the customized mesh sizing procedure can be found in Gopinathan et al. (2020). For a consistent numerical method (Giles et al., 2020a), the numerical error decreases with increasing mesh resolution. One would therefore ideally use the finest mesh resolution available. However, as is the case with all numerical simulations there is a trade-off between minimum mesh resolution and runtime. This trade-off is acutely apparent here, where there is an added severe time constraint imposed by the early warning requirements. Numerous mesh size configurations (**Table 2**) were trialled and a minimum resolution of 100 m at the areas of interest was chosen for this work, as it provides results in an acceptable runtime.

Another key component for providing accurate tsunami forecasts is the bathymetry/topography data used. In this study the data is solely taken from GEBCO (GEBCO Bathymetric Compilation Group, 2020) (resolution ~400 m). However, it is noted that the meshing procedure and every stage of the workflow work with higher resolution data and ideally should be incorporated in the future. Problems with the GEBCO data can be seen in the zoomed in plot of the mesh around Chabahar (**Figure 3**), where artificial coastlines in Chabahar Bay are visible.

4.3 Performance Scaling

As stated various mesh configurations were trailed in this work. The associated runtimes for 6 h simulated time using one Nvidia Tesla V100 GPU are included in **Table 2**. The first column of the table refers to what areas of interest are included in the local refinement. Naturally, if all three ports are included (Karachi, Chabahar and Muscat) the number of cells is the greatest at a given minimum mesh size. The runtime for the chosen mesh setup (100 m minimum mesh resolution) on one GPU is 135 s (2.25 min). If the user has more time/greater computational resources available a higher resolution mesh could be chosen. Further, if the user is only interested in one area, faster runtimes can be achieved by using a mesh setup which is only refined around that area.

5 EMULATOR

In the setting of fast warnings, the need to quickly compute a range of predictions precludes the simulation of a large number of tsunami scenarios. Our paper only illustrates a proof-of-concept idea with a small number of parameters, and so the dimension of the input space describing the source is small. In more realistic settings, large dimensions of the source (e.g. uncertainties about the geometry of the source) would create a greater need for a large range of scenarios. The Gaussian Process (GP) emulator is a statistical surrogate ($\mathcal{M}$) that mimics the input-output

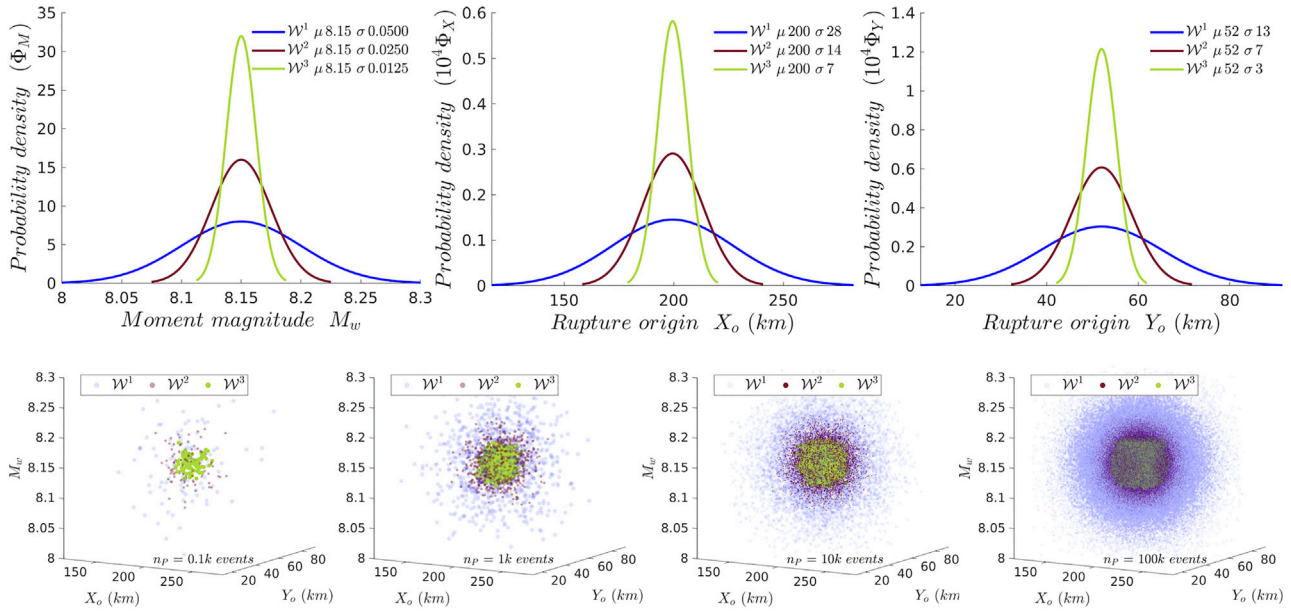

FIGURE 6 | The three stages of tsunami warning. **Top row:** The probability distributions of the input parameters - magnitude M_w **(left)**, rupture origin coordinates X_o **(middle)** and Y_o **(right)**. The standard deviation of the Gaussian distributions decreases by a factor of 2 as warning stages progress. **Bottom row:** The samples drawn from these three distributions, successively increasing in order from n_P = 0.1k in the left to n_P = 100k in the right.

relationship of the tsunami simulator (M). It is trained over a small set of input points, called a design, whose size (n_D) is much reduced compared to the number of predictions. The sources (or points in the space of input parameters) for training are chosen with the specific purpose of capturing the input-output relationship. Here, this is done via the Latin Hypercube Design (LHD), which maximizes the minimum distance between the training points resulting in a nearly uniform cover of the input space, i.e. a space-filling cover instead of a random scatter. **Table 1** gives some of the different earthquake sources that we have used to determine the ranges for the LHD, as shown in **Figure 4**. The geographical boundaries of the sources used in the design are rectangular, bounded by the axes limits of the X_o–Y_o plane in **Figure 4**. By providing an approximation of the simulator, along with uncertainties in its approximation to validate quality, the GP emulator allows for gains of orders of magnitude in computational costs. Tsunami GP emulation has supplied ranges of prediction for tsunamis generated by earthquakes and landslides over the North Atlantic, the Western Indian Ocean and Cascadia (Salmanidou et al., 2017; Guillas et al., 2018; Salmanidou et al., 2019; Gopinathan et al., 2020). We choose the GP emulator due to its versatility and our efficiently parallelized Multiple-Output Gaussian Process emulator (MOGP)[3] code. Alternative approaches could also be used, e.g. polynomial chaos (2010 Chile event (Giraldi et al., 2017)) and sparse-grid interpolation (1993 Hokkaido Nansei-oki tsunami (de Baar and Roberts, 2017)). A comparison of GP and polynomial chaos based surrogate methods may be found in Owen et al. (2017). An important ingredient in the construction of the GP emulator is the covariance function (or kernel). Here, we employ the Matern 5/2 kernel. This kernel is smooth enough to avoid the GP becoming too rough whilst not being excessively smooth, which is appropriate for modeling physical relationships. Examples of other kernels are exponential, squared exponential, rational quadratic, and piecewise polynomial (Rasmussen and Williams, 2005). The kernels have parameters (also called length scales) that are solved along with other hyperparameters via non-linear optimization in a maximum likelihood estimation (MLE) scheme (other approaches such as a Bayesian procedure are possible in MoGP). MOGP is flexible in its prescription of the optimization algorithm. In this work we employ the L-BFGS-B algorithm.

We fit an emulator to the tsunami maximum height η_{max} at each output location using a LHD of size 100 for 3 input parameters (M_w,X_o,Y_o) (**Figure 4**). This is well over the required number for a good approximation over an input space of dimension 3 and with small variations due to a narrow width that comes from the fact that seismic inversion restricts the values of these parameters compared to a wider risk assessment (Gopinathan et al., 2020), even more so for stages $\mathcal{W}^2$ and $\mathcal{W}^3$ compared to the initial stage $\mathcal{W}^1$ of seismic inversion/earthquake source updation. As a result, we can predict the whole distribution of tsunami heights at all output locations using these emulators.

We also show a quick validation of the quality of fit using Leave-one-out (L-O-O) diagnostics in **Figure 5**, where the match between predictions and removed runs provides confidence in the ability of the emulator to approximate the simulator. The mean of predictions

[3]v0.2.0 from *github.com/alan-turing-institute/mogp_emulator*.

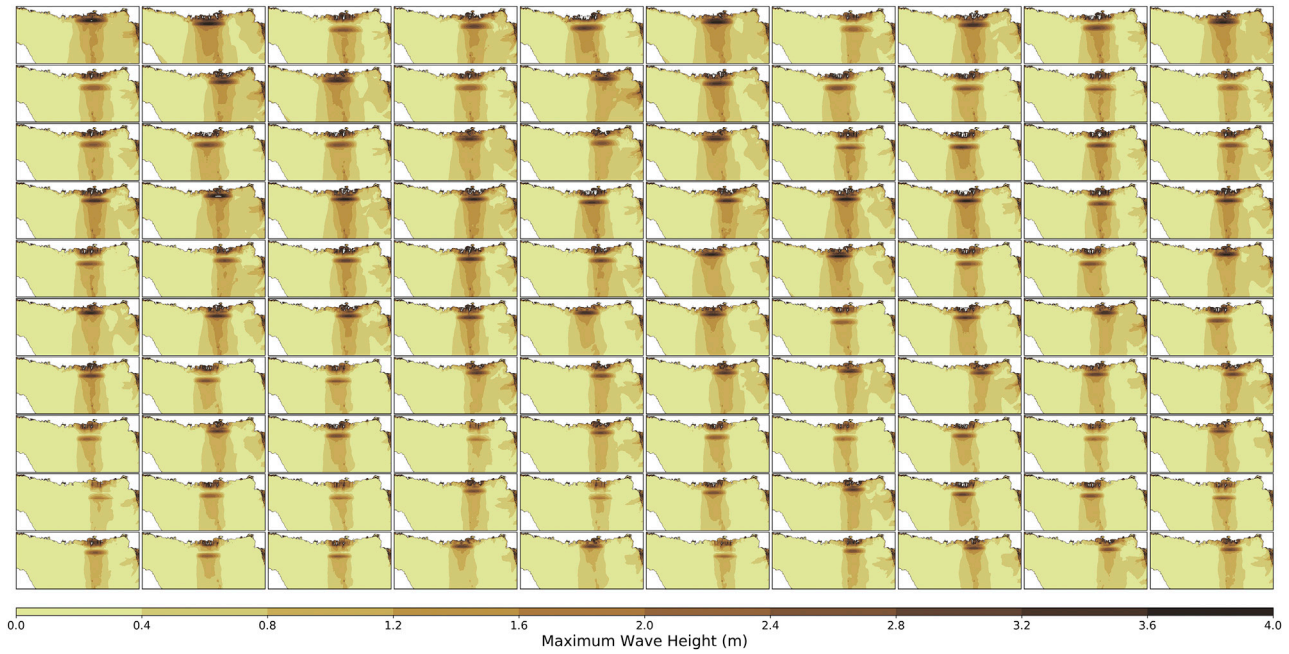

FIGURE 7 | Maximum wave heights (η_{max}) resulting from Volna-OP2 simulations corresponding to the 100 training source deformations shown in **Figure 4**.

is connected by a line segment to the corresponding training value, and is a visual indicator of the fit between them. The green bars show the 90% prediction intervals around the mean of predictions, and depict the measure of uncertainty in the prediction at that point. Importantly, around 90% of the training data lies within these bars, evidencing a good confidence in the fit. Note that the GP emulator is typically unable to extrapolate. The GP approximation (or prediction) outside or near the boundary of the convex hull spanned by points in the LHD contains more uncertainty. In our case, these regions include low and high values of M_w, and similarly locations of rupture origin at the corners or boundaries of the design. This limitation also crops up in the L-O-O diagnostics, hence higher uncertainties and lack of fit are expected at certain design locations. A denser design (i.e. increase in n_D) and focusing on the interpolation only (i.e. within the convex hull) would improve the predictions, and may be tailored depending on the requirements of the warning system. The L-O-O is nevertheless a good validation in the interior of the convex hull away from the boundaries.

In this work, the range of input parameters corresponds to the various source descriptions of the 1945 earthquake (**Table 1**). With current advances in seismic inversion, the uncertainties in the magnitude (M_w) and rupture origin (X_o, Y_o) in a seismic inversion may be very different from the ranges assumed here. For example, **Table 1** contains source descriptions from not only seismic inversions, but also tsunami wave inversion and forward modeling studies. For the sake of demonstration, we assume the first stage of earthquake warning $\mathcal{W}^1$ to be derived from the values in **Table 1**, the ranges informing the sampling limits in the Latin Hypercube samples shown in **Figure 4**. The emulator is trained using these 100 samples, *i.e.* no information on the probability distribution of the parameters is made use of. Once the emulator is constructed, it can be employed to predict the maximum wave height at the output locations rapidly. At the first stage of warning $\mathcal{W}^1$, the probability distributions of the input (or source) parameters are used to sample scenarios, which are subsequently propagated via the emulator to generate distributions of predicted η_{max}. We expect the uncertainties in the source parameters to decrease (here, successively by a factor of 2 in **Figure 6**) as the warning progresses to stages $\mathcal{W}^2$ and $\mathcal{W}^3$. This is an attempt to mimic the behavior of a realistic update in a seismic inversion. As soon as updated uncertainties in (and distributions of) source parameters from seismic inversion are available, new emulator predictions enable rapid updating of the output quantity. The number of stages of warning is limited to three for the sake of illustrating the methodology. The emulator can be used to predict for many more stages of warnings, as predictions form the cheapest computational component in the entire workflow (t^P in **Table 3**). Although we use Gaussian distributions to characterize the priors, the samples for predictions may be drawn from any kind of distribution (or Monte Carlo ensembles) depending on the outputs from the seismic inversion routines. Indeed, it requires only a set of points where the emulator needs to be evaluated.

6 RESULTS

There are two types of outputs from the proposed workflow (**Figure 1**). The first type of output relates directly to the n_D Volna-OP2 simulation results, regional maps (**Figure 7**) and wave gauge time series (**Figure 8**). The second type of output

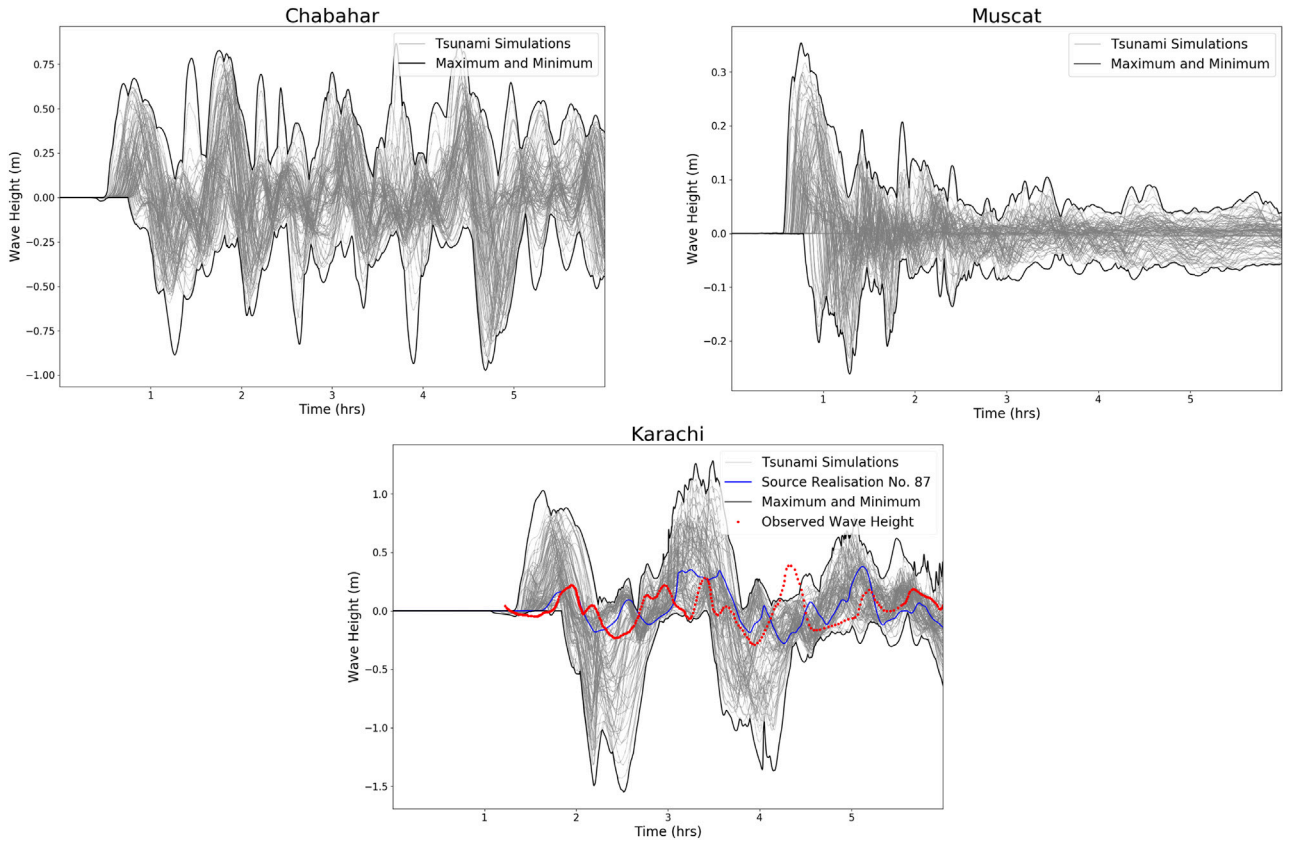

FIGURE 8 | Wave height time series plots at Chabahar, Muscat and Karachi from the 100 Volna-OP2 simulations. The output from each simulation is plotted in grey while the maximum and minimum wave heights at each point in time is plotted in black. The closest match (blue) to the observed wave gauge measurement from the 1945 event at Karachi is plotted along with the gauge signal (red dots).

TABLE 3 | Computational times in seconds per output location for emulation construction and prediction using MOGP on a *Xeon E5-2620V3 2.4 GHz × 12* workstation.

	$\frac{t^T}{n_G}$ [s]	$\frac{t^P}{n_G}$ [s]	$\frac{t^T+t^P}{n_G}$ [s]
Locations at fixed depth (**Figure 9**; **Supplementary Figures S1-S2**)	1.18	8.09	9.27
Local maps (**Figure 10**; **Supplementary Figures S3-S4**)	1.25	0.07	1.31
Regional map (**Figure 11**)	1.12	0.07	1.19

t^T *is the training time and* t^P *is the time to carry out* n_P *predictions.*

captures the uncertainty on the tsunami hazard (maximum wave height) by utilizing the emulator. These include maximum wave heights and associated variance at localized points at a fixed depth, over a localized area and regional maps (**Figures 9**–**11** and **Supplementary Figures S1**–**S4**).

6.1 Volna-OP2 – Regional Maps

Figure 7 highlights the maximum wave heights obtained over the whole domain during each of the n_D (100) 6 h simulations. This figure shows that despite the variation in the initial displacement there is a consistency in the directionality of the resultant tsunami wave. Most of the tsunami energy is propagated directly south. The figure provides valuable information on the sections of coastline most at risk, with the maximum wave heights focused along the local Pakistani and Iranian coastlines. A map like this provides information to a warning system on the areas most at risk. However, to completely capture the hazard and associated uncertainty for the three stages of warning over the whole the domain the emulator is leveraged to produce **Figure 11**.

6.2 Volna-OP2 – Time Series

Virtual wave gauges can be prescribed in the Volna-OP2 simulations, where the wave height as a function of time is outputted. For this work, virtual gauges are positioned within each of the refined port areas; Muscat, Chabahar and Karachi. The time series outputs from each of the n_D (100) simulations are plotted with the maximum and minimum wave heights at each point in time highlighted (**Figure 8**). These time series present the dynamics of the tsunami wave in each of the localized areas. This information can be extremely beneficial for a warning center, i.e. the

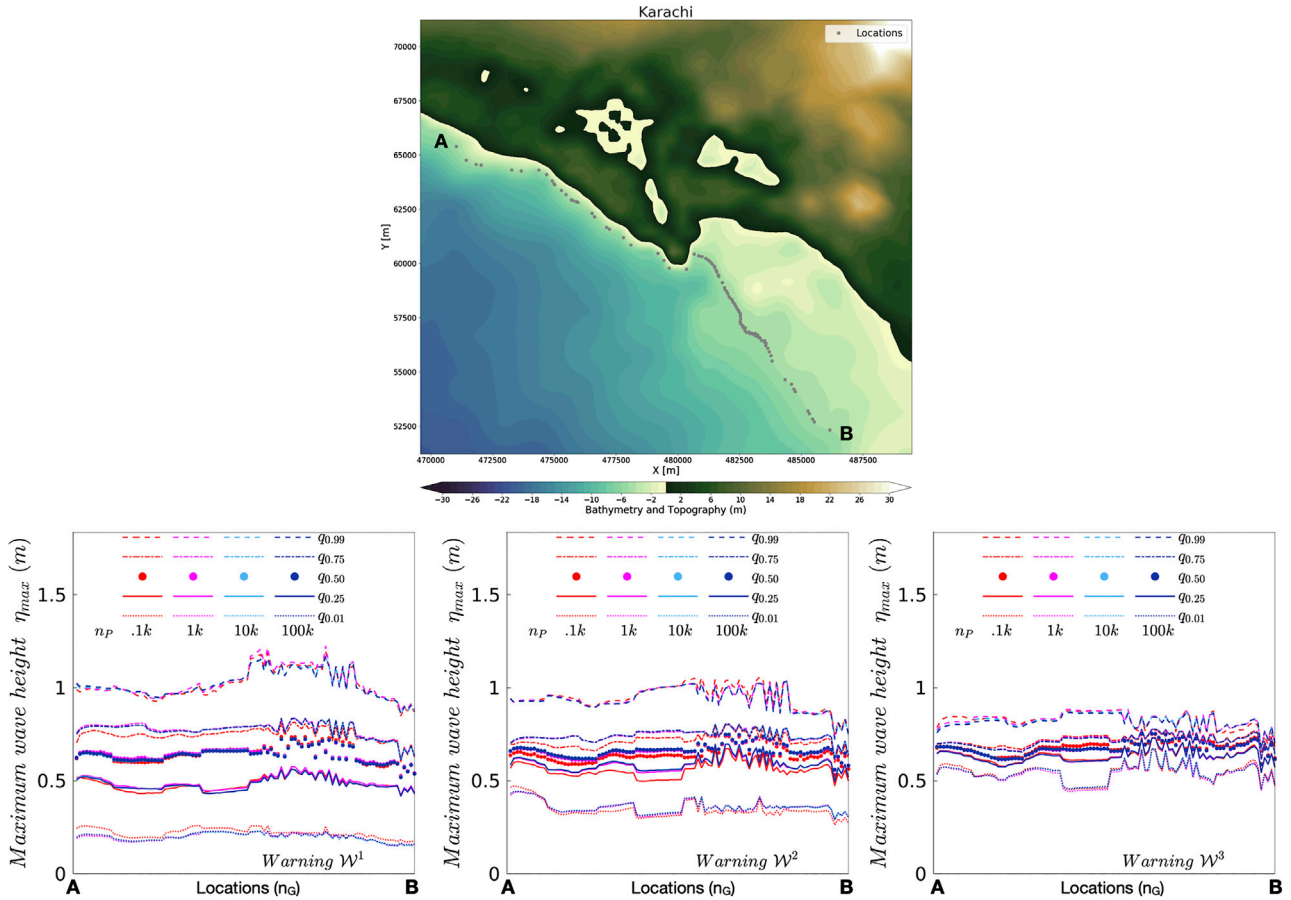

FIGURE 9 | Uncertainty at gauges along the coastline of Karachi. **Top row:** Location of 100 gauges ordered from A to B. **Bottom row:** Box plots for the maximum wave height η_{max} at the 100 gauges, for first **(left)**, second **(middle)** and third **(right)** warning stages. A boxplot for a gauge portrays the distribution of predicted η_{max} using the emulator via the quantiles for probabilities of 1, 25, 50, 75, and 99%. Superimposed on each plot are the distributions of the predicted η_{max} for four sets of samples from the priors (see **Figure 6**, Bottom row), i.e., for n_P = 0.1*k*, 1*k*, 10*k*, and 100*k*.

maximum wave at Karachi is not the initial wave. However, we would need to emulate the whole time series at each gauge (Guillas et al., 2018) to be able to present warnings at this level of precision. Furthermore, as pointed out elsewhere, higher resolution bathymetry data would be recommended for future work. The minimum mesh size in the areas of interest is ~100 m but the underlying bathymetry is sourced directly from GEBCO and thus has a resolution of ~400 m.

As there was a working wave gauge at Karachi port in 1945, the de-tided signal from the event is also plotted (Heidarzadeh and Satake, 2015). **Figure 8** shows the waveform of the 1945 tsunami superimposed over the 100 Volna-OP2 simulation results. The uncertainties on the tsunami wave from the design (**Figure 4**) are displayed, where none of these 100 runs is constructed to match the 1945 event exactly. Instead, this initial design has wide ranges spanned nearly uniformly by the LHD, consisting of 100 runs (slips) with the specific purpose of building the emulator.

However, the closest match to the 1945 Makran signal has been highlighted in **Figure 8**. In order to justly compare the signals, the following should be noted: the location of the virtual wave gauge in the simulations is different to the gauge's location in 1945 and this earthquake event is associated with a triggered submarine landslide (Okal et al., 2015), which is not considered in this work. The location of the 1945 wave gauge is located 'on-land' in the coarse GEBCO data, therefore a nearby offshore point had to be chosen. Despite all the problems outlined, the highlighted signal marked in blue matches closely the observed signal for this initial wave. Note that a good match from the curves in the design is not expected as these are only drawn to cover the space and create the emulator, in order to capture variability. Hence some runs of the emulator should match even better the actual measurements.

6.3 Emulator – Maximum Wave Heights at a Fixed Depth

An emulator $\mathcal{M}_i$ is constructed for each output location (n_G = 100, 95, and 100 for Karachi, Chabahar and Muscat respectively). The locations are selected to be at a fixed depth off the coastline. To construct the emulator, the maximum wave heights η_{max} at these

locations are extracted from the deterministic, *i.e.* Volna-OP2, simulations of the 100 training scenarios. Then, the emulator is employed to predict η_{max} at each location using the n_P samples from the priors for each warning (**Figure 6**). This results in a distribution of n_P η_{max} predictions at each location. The distribution of η_{max} at each location is portrayed as a box plot (see **Figure 9**; **Supplementary Figures S1, S2** for Karachi, Chabahar and Muscat respectively). Each box plot is asymmetric (non-Gaussian) and depicted by its quantiles at probabilities of 1, 25, 50 (median), 75, and 99%. This not only gives a sense of the spread of the distribution at the location but also gives a clear indication of the maximum wave height that is of interest to the warning centre. The plots show four boxplots for each location, corresponding to increasing numbers of samples from the priors, i.e., n_P = 100, 1000, 10,000, and 100,000. The distributions of η_{max} with 10,000 and 100,000 predictions are almost identical, since these large numbers of samples thoroughly interrogate the priors. Appreciable differences are noted when quantiles for 100 and 10,000 samples are compared – 75% quantiles for Karachi warning stage $\mathcal{W}^1$ (**Figure 9**), 75, 50, and 25% quantiles for Karachi warning stage $\mathcal{W}^2$ (**Figure 9**), 99% quantiles for all warning stages at Chabahar (**Supplementary Figure S1**), 99% and 75% quantiles for Muscat warning stage $\mathcal{W}^1$ (**Supplementary Figure S2**), and 75, 50, and 25% quantiles for Muscat warning stage $\mathcal{W}^2$ (**Supplementary Figure S2**). Note that slight differences in maximum wave height for high quantiles can establish with confidence whether or not there will be over-topping of defences, so are important to the warning process. The plots also show the restriction of the distributions as the warning stages proceed, resulting in tighter uncertainties in stage $\mathcal{W}^3$.

6.4 Emulator – Local Maps

The fixed depth locations in the previous section provide a good representation of the hazard and associated uncertainties along the coastline of interest. However, localized maps can be beneficial for highlighting the areas that could be exposed to the greatest hazard. Thus, in this section, the output locations are selected to be the barycenters of the mesh within the areas of interest (n_G = 19,749, 10,766, and 9,355 for Karachi, Chabahar and Muscat respectively). The procedure for emulator construction and predictions is similar to that described in the last section. The local maps for Karachi, Chabahar and Muscat depicting the mean and uncertainty in η_{max} are in **Figure 10**; **Supplementary Figures S3, S4** respectively. For each stage of warning, the maps are generated using n_P = 1000 samples for predictions. As observed in the plots for the locations in the previous section, the uncertainty in the predictions decreases as the warning progresses.

6.5 Emulator – Regional Maps

A regional understanding of the tsunami hazard and associated uncertainties can be extremely beneficial to a warning centre. However, to construct an emulator for each of the barycenters in the mesh is not feasible (~0.8 M points). Therefore, in this case the maximum wave heights (**Figure 7**) were interpolated onto a 2.5 km × 2.5 km grid and the offshore points of this grid were selected as the output locations (n_P ~ 50,000). Similar to the local maps, the uncertainties become tighter as the warning advances.

7 CONCLUSION AND DISCUSSION

In this paper we showcase the first possible combinations of tsunami simulation and emulation in order to reach faster than real time predictions of tsunami heights near shore, using synthetic teleseismic inversions to constrain the earthquake source. We are also able to provide uncertainties in the warning, as these can be very large, especially in the initial period following the earthquake. These uncertainties are essential toward accurate and wise disaster management.

Our study is a proof-of-concept investigation. Indeed, to demonstrate the appropriateness, we employed a safe margin in terms of the number of runs (100 for 3 parameters). The rule of thumb in emulation is to provide a minimum of around 10 runs per input parameter, the number of runs increasing with increasing complexity of the input-output relationship. Hence, for narrow intervals where the influence of inputs on outputs is typically smooth and monotonic, it may be possible to reduce the number of runs to around 30 (for three parameters considered here). The emulator construction can also be aided by using an informed mean function for the GP. These features can be exploited especially for stages of seismic inversions that progressively restrict the input space to small variations across the outputs, resulting in gains for warning time and computing resources.

Another attractive extension would be to retrain the emulator for each wave of seismic inversion, using a design that is focused on the seismic inversion region, and thus improve the fit. However the addition of the design of experiments would be costly in time compared to our first shot of runs. Furthermore, to be even more realistic, other parameters that could add uncertainty to this problem could be included. These include the uncertainties in geometry of the fault, in the rigidity, in the sediment amplification factor, in the near-shore bathymetry (Liu and Guillas, 2017), in case warnings were to be explicit in terms of inundations to make them more useful for subsequent action. To sample from a larger input space requires great care and emulation is the only available option since even thousands of runs would not suffice to cover the spread of uncertainties. Possible approaches include dimension reduction (Liu and Guillas, 2017), and sequential design of experiments (Beck and Guillas, 2016) but with some tailored tuning as the sequential nature would add time to the whole design sequence, albeit with large gains in efficiency in the approximation.

The workflow presented in this study is fully generic and could, with some additional resources/efforts, be applied by any tsunami warning centre. The emulator is used to obtain the level of tsunami hazard and uncertainty at selected points of interest. These points can cover a localized section of coastline, a regional area or fixed depths off the coastline of interest. The different types of warnings that the emulator produces could aid in a

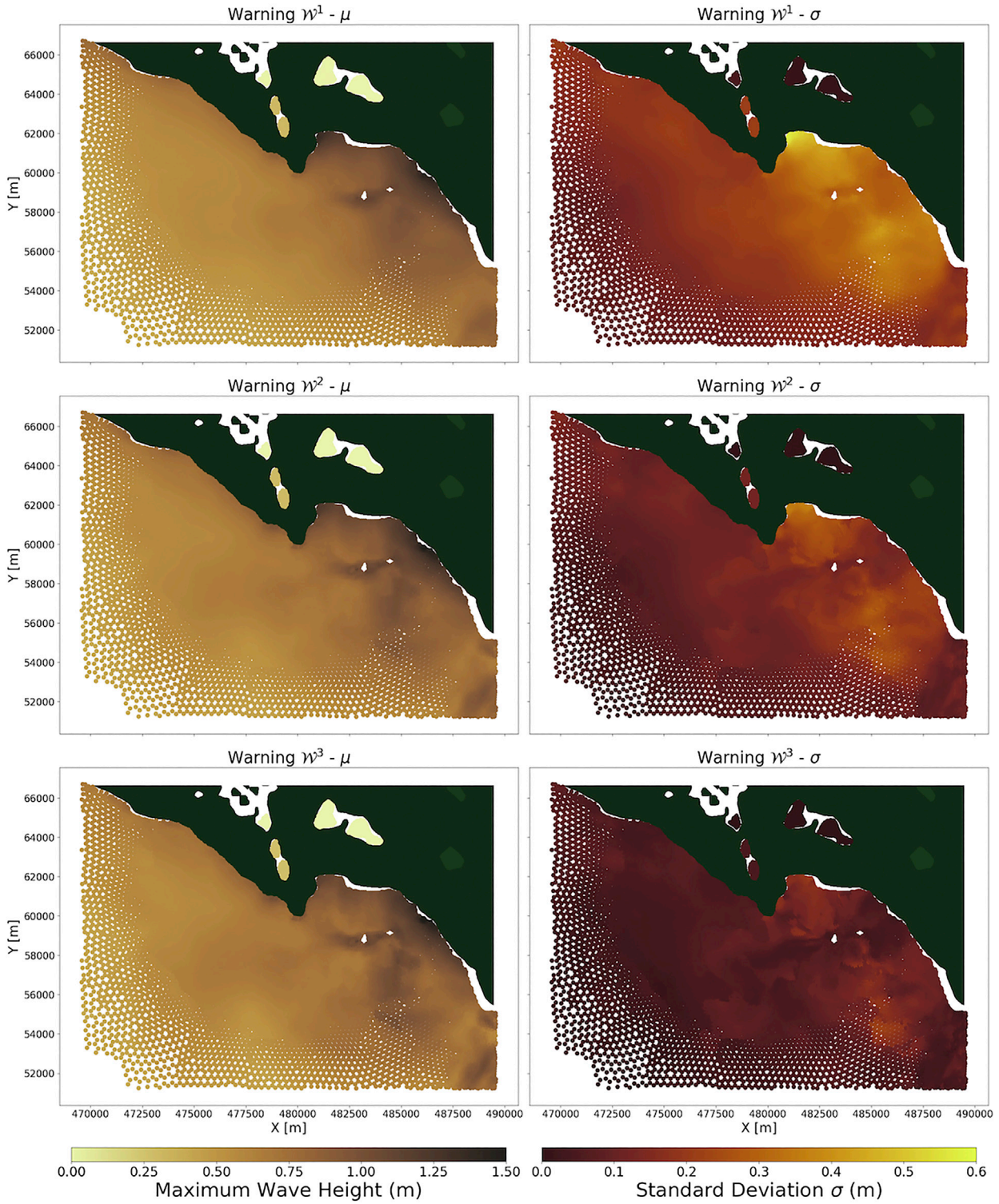

FIGURE 10 | Local map of uncertainties generated from emulator predictions of η_{max} at 19,749 gauges (barycentres of mesh triangles) near Karachi, for first **(top)**, second **(middle)** and third **(bottom)** stages of warning. Each warning stage depicts the mean of the predicted η_{max} **(left)** and associated standard deviation **(right)** using $n_P = 1k$ samples for prediction (**Figure 6**, Bottom row).

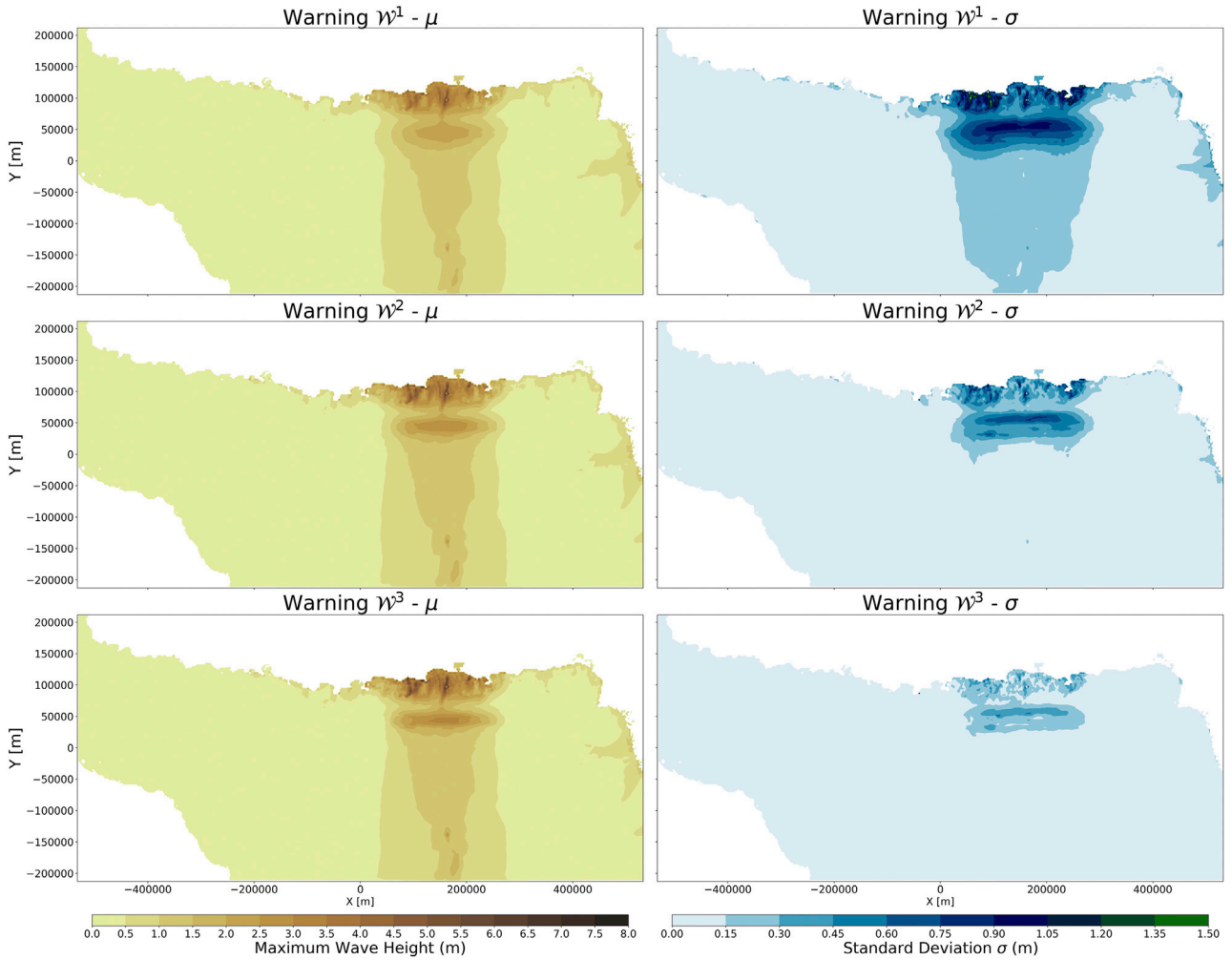

FIGURE 11 | Regional map of uncertainties generated from emulator predictions of η_{max} at 50,983 locations picked from a rectangular grid, for first **(top)**, second **(middle)** and third **(bottom)** stages of warning. Each warning stage depicts the mean of the predicted η_{max} **(left)** and associated standard deviation **(right)** using $n_P = 1k$ samples for prediction (**Figure 6**, Bottom row).

warning centre's ability for providing accurate warning recommendations. Further, the direct results from the deterministic model are extremely beneficial for providing an insight into the tsunami dynamics.

As stated, this is a proof-of-concept paper and the authors recognize that there are many outstanding issues that need to be addressed before the workflow presented here can be implemented by a warning centre. The main issues include a greater number of computational resources, a faster Okada solver and a fully parallelised/automated workflow. More computing resources, namely GPUs, would allow for the Volna-OP2 simulations to be carried out in parallel, ideally a GPU for each source realization being simulated. A faster Okada solver running on a cluster would reduce the runtime of the initialization steps. The runtimes presented are given in relation to time per scenario or time for predictions at a gauge. As these are fully independent the whole system lends itself to parallelization, but effort is required in this respect to carry out these tasks in parallel. Finally, another aspect that needs to be considered is the optimization of the post processing and displaying (plotting) of the results, runtimes which a warning centre would need to incorporate. However, with the outstanding issues addressed and greater computing capacities the total runtime is safely within the time frame afforded to warning centres in the aftermath of a tsunamigenic event.

DATA AVAILABILITY STATEMENT

The raw data supporting the conclusions of this article will be made available by the authors, without undue reservation.

AUTHOR CONTRIBUTIONS

DaG and DeG coordinated the scientific effort and performed all the numerical simulations. All authors contributed to the conceptualization and methodology of the study. DaG, DeG, and SG participated in the writing of the initial draft. All authors participated in the interpretation of results. The overall supervision was provided by FD and SG. All authors contributed to manuscript revision, read, and approved the submitted version.

FUNDING

DaG is supported by a Government of Ireland Postgraduate Scholarship from the Irish Research Council (GOIPG/2017/68).

ACKNOWLEDGMENTS

The authors wish to acknowledge the DJEI/DES/SFI/HEA Irish Centre for High-End Computing (ICHEC) for the provision of computational resources. SG and DeG acknowledge support from the Alan Turing Institute project "Uncertainty Quantification of multi-scale and multiphysics computer models: applications to hazard and climate models" as part of the grant EP/N510129/1 made to the Alan Turing Institute by EPSRC.

SUPPLEMENTARY MATERIAL

The Supplementary Material for this article can be found online at: https://www.frontiersin.org/articles/10.3389/feart.2020.597865/full#supplementary-material

REFERENCES

Ambraseys, N. N., and Melville, C. P. (1982). *A history of Persian earthquakes*. Cambridge, MA: Cambridge University Press.

Angove, M., Arcas, D., Bailey, R., Carrasco, P., Coetzee, D., Fry, B., et al. (2019). Ocean observations required to minimize uncertainty in global tsunami forecasts, warnings, and emergency response. *Front. Marine Sci.* 6, 350. doi:10.3389/fmars.2019.00350

Battaglia, M., Cervelli, P., and Murra-Muraleda, J. (2012). "Modeling crustal deformation: A catalog of deformation models and modeling approaches," in *U.S. Geological Survey Techniques and Methods*, 37–85.

Battaglia, M., Cervelli, P. F., and Murray, J. R. (2013). dMODELS: a MATLAB software package for modeling crustal deformation near active faults and volcanic centers. *J. Volcanol. Geoth. Res.* 254, 1–4. doi:10.1016/j.jvolgeores.2012.12.018

Beck, J., and Guillas, S. (2016). Sequential design with mutual information for computer experiments (MICE): emulation of a tsunami model. *SIAM/ASA J. Uncertain. Quantif.* 4 739–766. doi:10.1137/140989613

Behrens, J., Androsov, A., Babeyko, A. Y., Harig, S., Klaschka, F., and Mentrup, L. (2010). A new multi-sensor approach to simulation assisted tsunami early warning. *Nat. Hazards Earth Syst. Sci.* 10, 1085–1100. doi:10.5194/nhess-10-1085-2010

Bernard, E. N., and Titov, V. (2015). Evolution of tsunami warning systems and products. *Phil. Trans. R. Soc. A* 373, 20140371. doi:10.1098/rsta.2014.0371

Bernard, E. N., Meinig, C., Titov, V. V., O'Neil, K., Lawson, R., Jarrott, K., et al. (2010). "Tsunami resilient communities," in *Proceedings of the 'OceanObs'09: sustained ocean observations and information for society' conference*. Editors J. Hall, D. E. Harrison, and D. Stammer (Venice, Italy), Vol. 1, 21–25. doi:10.5270/oceanobs09.pp.04

Bernard, E. N., Mofjeld, H. O., Titov, V., Synolakis, C. E., and González, F. I. (2006). Tsunami: scientific frontiers, mitigation, forecasting and policy implications. *Phil. Trans. R. Soc. A* 364, 1989–2007. doi:10.1098/rsta.2006.1809

Byrne, D. E., Sykes, L. R., and Davis, D. M. (1992). Great thrust earthquakes and aseismic slip along the plate boundary of the Makran Subduction Zone. *J. Geophys. Res.: Solid Earth* 97, 449–478. doi:10.1029/91JB02165

Castruccio, S., McInerney, D. J., Stein, M. L., Liu Crouch, F., Jacob, R. L., and Moyer, E. J. (2014). Statistical emulation of climate model projections based on precomputed GCM runs. *J. Clim.* 27 1829–1844. doi:10.1175/JCLI-D-13-00099.1

Clément, J., and Reymond, D. (2015). New tsunami forecast tools for the French Polynesia tsunami warning system: Part I: moment tensor, slowness and seismic source inversion. *Pure Appl. Geophys.* 172, 791–804. doi:10.1007/s00024-014-0888-6

de Baar, J. H. S., and Roberts, S. G. (2017). Multifidelity sparse-grid-based uncertainty quantification for the Hokkaido Nansei-oki tsunami. *Pure Appl. Geophys.* 174, 3107–3121. doi:10.1007/s00024-017-1606-y

Dutykh, D., and Dias, F. (2010). Influence of sedimentary layering on tsunami generation. *Comput. Methods Appl. Mech. Eng.* 199, 1268–1275. doi:10.1016/j.cma.2009.07.011

Dutykh, D., Poncet, R., and Dias, F. (2011). The VOLNA code for the numerical modeling of tsunami waves: generation, propagation and inundation. *Eur. J. Mech. B Fluid* 30, 598–615. doi:10.1016/j.euromechflu.2011.05.005

Engdahl, E., and Villseñor, A. (2002). "Global seismicity: 1900–1999," in *International Handbook of Earthquake and Engineering Seismology*. Editor W. H. K. Lee, H. Kanamori, P. C. Jennings, and C. Kisslinger (Academic Press), 665–690.

Gailler, A., Hébert, H., Loevenbruck, A., and Hernandez, B. (2013). Simulation systems for tsunami wave propagation forecasting within the French tsunami warning center. *Nat. Hazards Earth Syst. Sci.* 13, 2465–2482. doi:10.5194/nhess-13-2465-2013

GEBCO Bathymetric Compilation Group (2020). The GEBCO_2020 Grid – a continuous terrain model of the global oceans and land. doi:10.5285/a29c5465-b138-234d-e053-6c86abc040b9

Geuzaine, C., and Remacle, J. F. (2009). Gmsh: a 3-D finite element mesh generator with built-in pre- and post-processing facilities. *Int. J. Numer. Methods Eng.* 79, 1309–1331. doi:10.1002/nme.2579

Giles, D., Kashdan, E., Salmanidou, D. M., Guillas, S., and Dias, F. (2020a). Performance analysis of Volna-OP2 – massively parallel code for tsunami modelling. *Comput. Fluids* 209, 104649. doi:10.1016/j.compfluid.2020.104649

Giles, D., McConnell, B., and Dias, F. (2020b). Modelling with Volna-OP2—towards tsunami threat reduction for the Irish coastline. *Geosciences* 10, 226. doi:10.3390/geosciences10060226

Giraldi, L., Le Maître, O. P., Mandli, K. T., Dawson, C. N., Hoteit, I., and Knio, O. M. (2017). Bayesian inference of earthquake parameters from buoy data using a polynomial chaos-based surrogate. *Comput. Geosci.* 21, 683–699. doi:10.1007/s10596-017-9646-z

Girard, S., Mallet, V., Korsakissok, I., and Mathieu, A. (2016). Emulation and Sobol' sensitivity analysis of an atmospheric dispersion model applied to the Fukushima nuclear accident. *J. Geophys. Res.: Atmos.* 121, 3484–3496. doi:10.1002/2015JD023993

Glimsdal, S., Pedersen, G. K., Harbitz, C. B., and Løvholt, F. (2013). Dispersion of tsunamis: does it really matter? *Nat. Hazards Earth Syst. Sci.* 13, 1507–1526. doi:10.5194/nhess-13-1507-2013

Gopinathan, D., Heidarzadeh, M., and Guillas, S. (2020). Probabilistic quantification of tsunami currents in Karachi Port, Makran subduction Zone, using statistical emulation. *Earth Space Sci. Open Archive* 38. doi:10.1002/essoar.10502534.2

Guillas, S., Sarri, A., Day, S. J., Liu, X., and Dias, F. (2018). Functional emulation of high resolution tsunami modelling over Cascadia. *Ann. Appl. Stat.* 12 2023–2053. 10.1214/18-AOAS1142

Hanks, T. C., and Kanamori, H. (1979). A moment magnitude scale. *J. Geophys. Res.: Solid Earth* 84, 2348–2350. doi:10.1029/JB084iB05p02348

Harig, S. C., Pranowo, W. S., and Behrens, J. (2008). Tsunami simulations on several scales. *Ocean Dynam.* 58, 429–440. doi:10.1007/s10236-008-0162-5

Hayes, G. P. (2018). Dataset: *Slab2 – a comprehensive subduction zone geometry model*. U.S. Geological Survey data release. doi:10.5066/F7PV6JNV

Hayes, G. P., Moore, G. L., Portner, D. E., Hearne, M., Flamme, H., Furtney, M., et al. (2018). Slab2, a comprehensive subduction zone geometry model. *Science* 362, 58–61. doi:10.1126/science.aat4723

Heck, N. H. (1947). List of seismic sea waves. *Bull. Seismol. Soc. Am* 37, 269–286.

Heidarzadeh, M., and Satake, K. (2015). New insights into the source of the Makran tsunami of 27 November 1945 from tsunami waveforms and coastal deformation data. *Pure Appl. Geophys.* 172, 621–640. doi:10.1007/s00024-014-0948-y

Heidarzadeh, M., Pirooz, M. D., Zaker, N. H., Yalciner, A. C., Mokhtari, M., and Esmaeily, A. (2008). Historical tsunami in the Makran Subduction Zone off the southern coasts of Iran and Pakistan and results of numerical modeling. *Ocean Eng.* 35, 774–786. doi:https://doi.org/10.1016/j.oceaneng.2008.01.017

Heidarzadeh, M., Pirooz, M. D., Zaker, N. H., and Yalciner, A. C. (2009). Preliminary estimation of the tsunami hazards associated with the Makran subduction zone at the northwestern Indian Ocean. *Nat. Hazards* 48, 229–243. doi:10.1007/s11069-008-9259-x

Inazu, D., Pulido, N., Fukuyama, E., Saito, T., Senda, J., and Kumagai, H. (2016). Near-field tsunami forecast system based on near real-time seismic moment tensor estimation in the regions of Indonesia, the Philippines, and Chile. *Earth Planets Space* 68, 73. doi:10.1186/s40623-016-0445-x

Jamelot, A., and Reymond, D. (2015). New tsunami forecast tools for the French Polynesia tsunami warning system Part II: numerical modelling and tsunami height estimation. *Pure Appl. Geophys.* 172, 805–819. doi:10.1007/s00024-014-0997-2

Kanamori, H. (1977). The energy release in great earthquakes. *J. Geophys. Res. (1896-1977)* 82, 2981–2987. doi:10.1029/JB082i020p02981

Kennedy, A. B., Chen, Q., Kirby, J. T., and Dalrymple, R. A. (2000). Boussinesq modeling of wave transformation, breaking, and runup. I: 1D. *J. Waterw. Port, Coast. Ocean Eng* 126 39–47. doi:10.1061/(ASCE)0733-950X(2000)126:1(39)

Kristensen, M. H., Choudhary, R., and Petersen, S. (2017). Bayesian calibration of building energy models: comparison of predictive accuracy using metered utility data of different temporal resolution. *Energy Procedia* 122, 77–282. doi:10.1016/j.egypro.2017.07.322

Liu, X., and Guillas, S. (2017). Dimension reduction for Gaussian process emulation: an application to the influence of bathymetry on tsunami heights. *SIAM/ASA J. Uncertain. Quantification* 5, 787–812. doi:10.1137/16M109064

Liu, P. L., Woo, S. B., and Cho, Y. S. (1998). *Computer programs for tsunami propagation and inundation. Tech. rep*, Ithaca, NY, USA: Cornell University Press.

Løvholt, F., Lorito, S., Macías, J., Volpe, M., Selva, J., and Gibbons, S. (2019). "Urgent tsunami computing," in Proceedings of UrgentHPC 2019: 1st international workshop on HPC for urgent decision making – held in conjunction with SC 2019: the International Conference for High Performance Computing, Networking, Storage and Analysis, Vol. 823–844, 45–50. doi:10.1109/UrgentHPC49580.2019.00011

Lynett, P. J., Wu, T. R., and Liu, P. L. F. (2002). Modeling wave runup with depth-integrated equations. *Coastal Eng.* 46, 89–107. doi:10.1016/S0378-3839(02)00043-1

Macías, J., Castro, M. J., Ortega, S., Escalante, C., and González-Vida, J. M. (2017). Performance benchmarking of tsunami-HySEA model for NTHMP's inundation mapping activities. *Pure Appl. Geophys.* 174, 3147–3183. doi:10.1007/s00024-017-1583-1

Melgar, D., and Bock, Y. (2013). Near-field tsunami models with rapid earthquake source inversions from land- and ocean-based observations: the potential for forecast and warning. *J. Geophys. Res.: Solid Earth* 118, 5939–5955. doi:10.1002/2013JB010506

Okada, B. (1985). Surface deformation due to shear and tensile faults in a half-space. *Bull. Seismol. Soc. Am.* 75, 1135–1154.

Okal, E. A., Fritz, H. M., Hamzeh, M. A., and Ghasemzadeh, J. (2015). Field survey of the 1945 Makran and 2004 Indian ocean tsunamis in Baluchistan, Iran. *Pure Appl. Geophys.* 172, 3343–3356. doi:10.1007/s00024-015-1157-z

Owen, N. E., Challenor, P., Menon, P. P., and Bennani, S. (2017). Comparison of surrogate-based uncertainty quantification methods for computationally expensive simulators. *SIAM/ASA J. Uncertain. Quantif.* 5, 403–435. doi:10.1137/15M1046812

Oyebamiji, O., Wilkinson, D. J., Jayathilake, P., Curtis, T. P., Rushton, S., Li, B., et al. (2017). Gaussian process emulation of an individual-based model simulation of microbial communities. *J. Comput. Sci.* 22, 69–84. doi:10.1016/j.jocs.2017.08.006

Pendse, C. (1946). The Mekran earthquake of the 28th November 1945. *India Meteorol. Dep. Sci. Not.* 10, 141–145.

Quittmeyer, R. C., and Jacob, K. H. (1979). Historical and modern seismicity of Pakistan, Afghanistan, northwestern India, and southeastern Iran. *Bull. Seismol. Soc. Am.* 69, 773–823.

Rasmussen, C. E., and Williams, C. K. (2005). *Covariance functions. Gaussian processes for machine learning*. Cambridge, MA: The MIT Press.

Reguly, I. Z., Giles, D., Gopinathan, D., Quivy, L., Beck, J. H., Giles, M. B., et al. (2018). The VOLNA-OP2 tsunami code (version 1.5). *Geosci. Model Dev. (GMD)* 11, 4621–4635. doi:10.5194/gmd-11-4621-2018

Reymond, D., Okal, E. A., Hébert, H., and Bourdet, M. (2012). Rapid forecast of tsunami wave heights from a database of pre-computed simulations, and application during the 2011 Tohoku tsunami in French Polynesia. *Geophys. Res. Lett.* 39, 1–6. doi:10.1029/2012GL051640

Salmanidou, D. M., Guillas, S., Georgiopoulou, A., and Dias, F. (2017). Statistical emulation of landslide-induced tsunamis at the Rockall Bank, NE Atlantic. *Proc. Math. Phys. Eng. Sci.* 473, 20170026. doi:10.1098/rspa.2017.0026

Salmanidou, D. M., Heidarzadeh, M., and Guillas, S. (2019). Probabilistic landslide-generated tsunamis in the Indus Canyon, NW Indian ocean, using statistical emulation. *Pure Appl. Geophys.* 176, 3099–3114. doi:10.1007/s00024-019-02187-3

Satake, K. (2014). Advances in earthquake and tsunami sciences and disaster risk reduction since the 2004 Indian ocean tsunami. *Geosci. Lett.* 1, 1–13. doi:10.1186/s40562-014-0015-7

Straume, E. O., Gaina, C., Medvedev, S., Hochmuth, K., Gohl, K., Whittaker, J. M., et al. (2019). Globsed: updated total sediment thickness in the world's oceans. *G-cubed* 20, 1756–1772. doi:10.1029/2018GC008115

Synolakis, C. E., and Bernard, E. N. (2006). Tsunami science before and beyond Boxing Day 2004. *Phil. Trans. R. Soc. A* 364, 2231–2265. doi:10.1098/rsta.2006.1824

Tavakkol, S., and Lynett, P. (2017). Celeris: a GPU-accelerated open source software with a Boussinesq-type wave solver for real-time interactive simulation and visualization. *Comput. Phys. Commun.* 217 117–127. doi:10.1016/j.cpc.2017.03.002

Titov, V. V., and Gonzalez, F. I. (1997). Implementation and testing of the method of splitting tsunami (MOST) model. Tech. Report, NOAA Technical Memorandum ERL PMEL, Vol. 112, 11, 1997 UNIDATA.

Conflict of Interest: The authors declare that the research was conducted in the absence of any commercial or financial relationships that could be construed as a potential conflict of interest.

The handling editor declared a past co-authorship with one of the authors (FD).

frontiers in Earth Science

ORIGINAL RESEARCH
published: 20 January 2021
doi: 10.3389/feart.2020.602171

Tsunamis From Submarine Collapses Along the Eastern Slope of the Gela Basin (Strait of Sicily)

Filippo Zaniboni[1,2], Gianluca Pagnoni[1], Maria Ausilia Paparo[1], Tugdual Gauchery[3,4], Marzia Rovere[3], Andrea Argnani[3], Alberto Armigliato[1] and Stefano Tinti[1]*

[1]*Department of Physics and Astronomy "Augusto Righi", University of Bologna, Bologna, Italy,* [2]*National Institute of Geophysics and Volcanology, Bologna, Italy,* [3]*Institute of Marine Sciences, National Research Council, Bologna, Italy,* [4]*Department of Civil, Chemical, Environmental and Materials Engineering, University of Bologna, Bologna, Italy*

Geophysical surveys in the eastern slope of the Gela Basin (Strait of Sicily, central Mediterranean) contributed to the identification of several episodes of sediment mass transport, recorded by scars and deposits of various dimensions within the Pleistocene succession. In addition to a huge failure called Gela Slide with volume exceeding 600 km^3, the most studied events show volumes estimated between 0.5 and 1.5 km^3, which is common to many other submarine landslide deposits in this region and that can therefore be considered as a characteristic value. In this work, the tsunamigenic potential of two of such landslides, the so-called Northern Twin Slide and South Gela Basin Slide located about 50 km apart along the eastern slope of the Gela Basin, are investigated using numerical codes that describe the onset and motion of the slide, as well as the ensuing tsunami generation and propagation. The results provide the wave height of these tsunami events on the coast of southern Sicily and Malta and can be taken as representative of the tsunamigenic potential of typical landslides occurring along the slope of the Gela Basin.

Keywords: margin instability, landslide dynamics, tsunami, numerical simulation, geo-marine hazard

OPEN ACCESS

Edited by:
Jörn Behrens,
University of Hamburg, Germany

Reviewed by:
Roger Urgeles,
Consejo Superior de Investigaciones Científicas (CSIC), Spain
Juan Horrillo,
Texas A&M University College Station, United States

****Correspondence:***
Filippo Zaniboni
filippo.zaniboni@unibo.it

Specialty section:
This article was submitted to Geohazards and Georisks, a section of the journal Frontiers in Earth Science

Received: *02 September 2020*
Accepted: *20 November 2020*
Published: *20 January 2021*

Citation:
Zaniboni F, Pagnoni G, Paparo MA, Gauchery T, Rovere M, Argnani A, Armigliato A and Tinti S (2021) Tsunamis From Submarine Collapses Along the Eastern Slope of the Gela Basin (Strait of Sicily). Front. Earth Sci. 8:602171. doi: 10.3389/feart.2020.602171

INTRODUCTION

Continental margins are one of the most favorable environments for the generation of relevant landslide-tsunamis (Masson et al., 2006; Tappin, 2010; Kawamura et al., 2014), due to many factors. Amongst these, one very relevant is the continuous supply of unconsolidated sediments from rivers, which may be activated in a submarine landslide by both seismic shaking and gravitational load. When the collapse starts from relatively shallow water the tsunami generation is particularly efficient: the perturbation is more easily transmitted to the whole water column, and the sliding mass soon attains high velocities, due to the steep slope typical of such environments, that can exceed 10°.

The most adopted approach in the description of mass transport deposits (MTD) along submarine slopes considers the size distribution and their frequency, providing in this way an assessment of the potential hazard connected to these occurrences. This has been repeatedly applied for the hazard analysis in several margins around the world, mainly in North America: the United States Atlantic margin (Chaytor et al., 2009; ten Brink et al., 2014); the United States Pacific coast (McAdoo et al., 2000; Greene et al., 2006); the Puerto Rico northern platform (ten Brink et al., 2006); the Gulf of Mexico (Pampell-Manis et al., 2016; Fan et al., 2020); Alaska (Sawyer et al., 2017). The Norway margin (North-East Atlantic Ocean) as well, has been object of investigation from this point of view (Solheim et al., 2005).

TABLE 1 | List of submarine landslides with volumes comparable to the NTS and the SGBS whose tsunamigenic potential has been explored in literature.

Name	Location	Headwall depth (m)	Deposit depth (m)	Initial volume (km^3)	Deposit volume (km^3)	References
Thasos slide	Aegean sea	~375		1.85	3.8	Janin et al. (2019)
	Papua New Guinea	1,420			6.4	Tappin et al. (2008)
	Alboran sea	700–800		0.5	2.2–5.6	Rodriguez et al. (2017)
Al-Borani	Alboran sea	70	800		1	Macias et al. (2015)
	Atsumi escarpment near Namkai Trough, Japan				1.26	Harbitz et al. (2014)
Assi slide	Offshore southern Calabria				1.85	Ceramicola et al. (2014)
	Southern Adriatic	560	700		0.03	Argnani et al. (2011)
Gaviota mudflow	Santa Barbara channel, Southern California	380	500		0.2	Fisher et al. (2005)

In the Mediterranean Sea, the tsunami hazard connected to continental slopes is still poorly constrained. The comprehensive study by Urgeles and Camerlenghi (2013) represents the first step toward the characterization of MTDs in the whole basin. In total, 696 events have been mapped and described, spanning wide area and volume ranges, $(10^{-3} \div 10^{5}\ km^2)$ and $(10^{-4} \div 10^{4}\ km^3)$ respectively. Among these, 28 events are reported to have generated tsunamis, both by direct observations and by deposits characterization. While it is not surprising the presence in this subset of huge masses (9 events in the volume range 10÷100 km^3, 3 exceeding 100 km^3), it is significant the incidence in terms of tsunami generation of smaller occurrences: 9 between 1 and 10 km^3, and 7 below 1 km^3. Such typology of MTD is scarcely considered in the study of non-seismic tsunami hazard, since in general they generate considerable waves only when occurring in shallow water and in proximity of the coast.

One of the main characteristics of the Mediterranean Sea is the high recurrence of the combination of these two elements: mass wasting features (scars, headwalls, canyons) are recognizable along several margins close to populated coastal communities. Some of them are here recalled:

- The Balearic Sea, where one of the most impressive underwater sliding bodies has been found along the Ebro margin, the so-called BIG'95 (Lastras et al., 2005; Lastras et al., 2007), whose tsunamigenic potential has been explored through numerical modeling (Iglesias et al., 2012; Zaniboni et al., 2014a; Løvholt et al., 2014).
- The margin of the Ligurian Sea (French-Italian Riviera), with very steep slopes and relatively frequent seismicity that can mobilize sediments (Ioualalen et al., 2014), such as the case of the 1979 Nice tsunami (Assier-Rzadkiewicz et al., 2000).
- The Tyrrhenian and Ionian margins, where many mass wasting processes covering different spatial scales have been mapped in the framework of the Italian project MaGIC (Chiocci and Ridente, 2011; Casalbore et al., 2014; Rovere et al., 2014; Casalbore et al., 2019). Among the many potential occurrences, numerical simulations for the study of the generated tsunamis have been performed for the 1977 Gioia Tauro event (Zaniboni et al., 2014b), on the Tyrrhenian Calabrian side, with an estimated volume of approximately 0.005 km^3 volume. On the Ionian side of Calabria, the Assi landslide (Ceramicola et al., 2014), has been object of investigation (see **Table 1** for details). Also, the area of Crotone, Calabria, is worth of mention, with the (indeed still questioned) homonymous potential mega-landslide involving a very thick sedimentary sequence (Zecchin et al., 2018).
- The southern Adriatic Margin, where structures favoring mass transport such as the Bari Canyon (Trincardi et al., 2007) are found and pieces of evidence of vast movements exist, such as the large Gondola slide, a complex of events mobilizing deposits in the order of tens of km^3 (Ridente et al., 2008). The tsunamigenic potential of small landslides on the eastern margin has been investigated as well (see **Table 1**; Argnani et al., 2011).
- The Hyblean-Malta Escarpment (Ionian coast of Sicily), where many canyons and scars are evident (Micallef et al., 2014), and the potential for tsunami generation has been examined (Paparo et al., 2017). To mention also that the possibility of a 5 km^3 submarine landslide occurring in the occasion of the 1,693 earthquake, that might have enhanced considerably the effects of the earthquake-tsunami at a local scale (Argnani et al., 2012).
- The margins close to the coasts of Crete and Cyprus (Papadopoulos et al., 2007b; Papadopoulos et al., 2014) and along the Corinth Gulf, where on 1963 a coastal slump generated relevant waves (Papadopoulos et al., 2007a; Tinti et al., 2007).
- The African coast of the Mediterranean, that is still scarcely investigated. Some indications of collapses have been reported in Loncke et al. (2009), describing mass wasting processes covering a large volume range (from 1 km3 to around 500 km^3) along the Nile river submarine fan, offshore the town of Alexandria (Egypt).
- The Levantine Basin is a place of large mass transport complexes, ranging from 35 to 94 km^3, occurring along the continental margin off Israel and Lebanon (see Eruteya et al., 2016, and references therein).

The above list constitutes only a subset of the potential margins that are prone to sliding in the Mediterranean Sea and can potentially generate tsunamis. In this paper, we consider the Gela Basin eastern slope (GBES from now on) that is found in the northern part of the Strait of Sicily and extends from the shelf-edge at relatively shallow water (~200 m) rapidly deepening to about 900 m depth. Studies based on

morpho-bathymetric data show that the GBES has been extensively affected by submarine mass wasting during the Late Quaternary, involving volumes of sediments in the order of magnitude of 1 km^3 (e.g., Minisini et al., 2007; Kuhlmann et al., 2017).

Among the recorded landslide events, we select two as representative of potential scenarios along the GBES. To evaluate their tsunamigenic potential, a comprehensive investigation through numerical codes is performed, mainly consisting into three phases: the simulation of the landslide dynamics; the computation of the tsunamigenic impulse, that is time-dependent; the simulation of wave propagation, with the assessment of the tsunami hazard for the neighboring coasts of Sicily and Malta. The analysis is limited to the effects of the tsunami on a regional scale, leaving the study of inland flooding for future publications.

The study of these two landslide scenarios along the GBES has been performed in the framework of the Italian project SPOT (Sismicità Potenzialmente innescabile Offshore e Tsunami; Antoncecchi et al., 2020), aiming at assessing the tsunamigenic potential of earthquakes and landslides possibly triggered by hydrocarbon production offshore the Italian coasts.

THE GELA BASIN EASTERN SLOPE

Geological Setting

The Gela Basin is a bathymetric depression of limited water depth (up to 936 m) located south of central Sicily. It represents the foreland basin of the Maghrebian thrust belt of Sicily (Argnani et al., 1987; Lickorish et al., 1999), and is filled by up to 2000 m of turbidites and pelagic sediments of Pliocene-Quaternary age. The sedimentation rate from Pliocene to Middle Pleistocene (800 ka) was 150 m/Myr and reached 900 m/Myr in the last 800 kyr (Gauchery et al., 2021). The upper part of the sedimentary fill is characterized by abundant mass transport deposits. The northern margin of the basin is partly shaped by the arcuate front of the Gela Nappe (Argnani, 1987), which represents the most recent Maghrebian thrust front (**Figure 1**). A sedimentary prograding set, fed from the north, developed on top of the Gela Nappe. This prograding set extends eastward, away from the thrust front, fringing the Hyblean Plateau. The most recent clinoform of this prograding set represents the northern and eastern bathymetric slope of the Gela Basin.

The eastern slope, denoted as GBES here, has been the site of several mass transport events, as evidenced by the abundant slide scars which are visible on the morpho-bathymetry map (see **Figures 1B,C**), and as reported in detailed studies of selected sectors (e.g., Minisini et al., 2007). The morphological evidence indicates that complex and recurrent sediment failures affected the GBES during the Late Quaternary.

Mass Failures Along the GBES

Mass transport events characterize the whole extent of the GBES, and in some cases, the reconstruction of the sliding mechanism and sequence is quite difficult, due to the superposition of different occurrences.

Starting from the north, the first occurrence is the Gela Slide (GS, see **Figure 1A**), a 630 km^3 landslide affecting an area of more than 1,500 km^2, characterized by a few km downslope movement and occurred presumably in the Late Pleistocene. First described in the geological work by Trincardi and Argnani (1990), this collapse has been taken as one of the scenarios in the study of tsunami hazard on the coasts of the Malta archipelago by Mueller et al. (2020). According to their tsunami simulations, the flow depth exceeded 10 m on the island of Gozo, which was hit around 18 min after onset of the landslide.

Moving to the east of the GS, several other landslides have been recognized by Trincardi and Argnani (1990) and in more recent investigations (Minisini and Trincardi, 2009; Kuhlmann et al., 2017). The most interesting cases are the so-called Twin Slides located about 30 km far from the GS (see **Figure 1B**). These collapses, that occurred probably simultaneously in Late Holocene, are characterized by well-defined scars (see the headwalls, **Figure 1B**), deepening from 200 to 500 m water depth with well-recognizable deposits of comparable size at the toe (enclosed within the dashed-red and dashed-green boundaries respectively), down to 700 m b.s.l. The estimated volume is slightly less than 0.5 km^3 for both slides. The Northern and Southern Twin Slides (NTS and STS) have been interpreted as the final stage of a very complex sliding sequence, tentatively reconstructed in Kuhlmann et al. (2017), that started with a larger "Father Slide" (black line in **Figure 1B**) 87 ka ago and that repeats periodically about every 10 kyr.

Another submarine slide is placed southward, about 40 km north of the Malta archipelago (**Figure 1C**). In this work, it is named South Gela Basin Slide (SGBS) according to Gauchery et al. (2021). Pieces of evidence of collapse are very clear: a large scar at the shelf-edge, more than 5 km long (blue line in **Figure 1C**), with a 5° average slope from 200 to 500 m water depth; a large deposit, easily recognizable at the toe of the slope (350–550 m water depth), covering an area of more than 50 km^2 (delimited by the dashed-blue contour in **Figure 1C**).

In this paper, we have opted to compute the tsunamis produced by two slides out of the many that have been identified along the GBES, namely the NTS and the SGBS. Although there is not any direct piece of evidence of the occurrence and the effects of such tsunamis, nonetheless exploring these scenarios is important mainly because 1) the involved volumes are the most frequently observed in the Mediterranean Sea (see the frequency distribution in Urgeles and Camerlenghi, 2013) and 2) landslides with comparable volumes are known to produce relevant (though local) waves, which stresses the need to systematically include also such sources in tsunami hazard evaluation. Some interesting examples of tsunami studies from this kind of landslides are listed in **Table 1**.

NUMERICAL METHODS

The study of the tsunamis associated with submarine mass movements along the GBES is performed through a well-

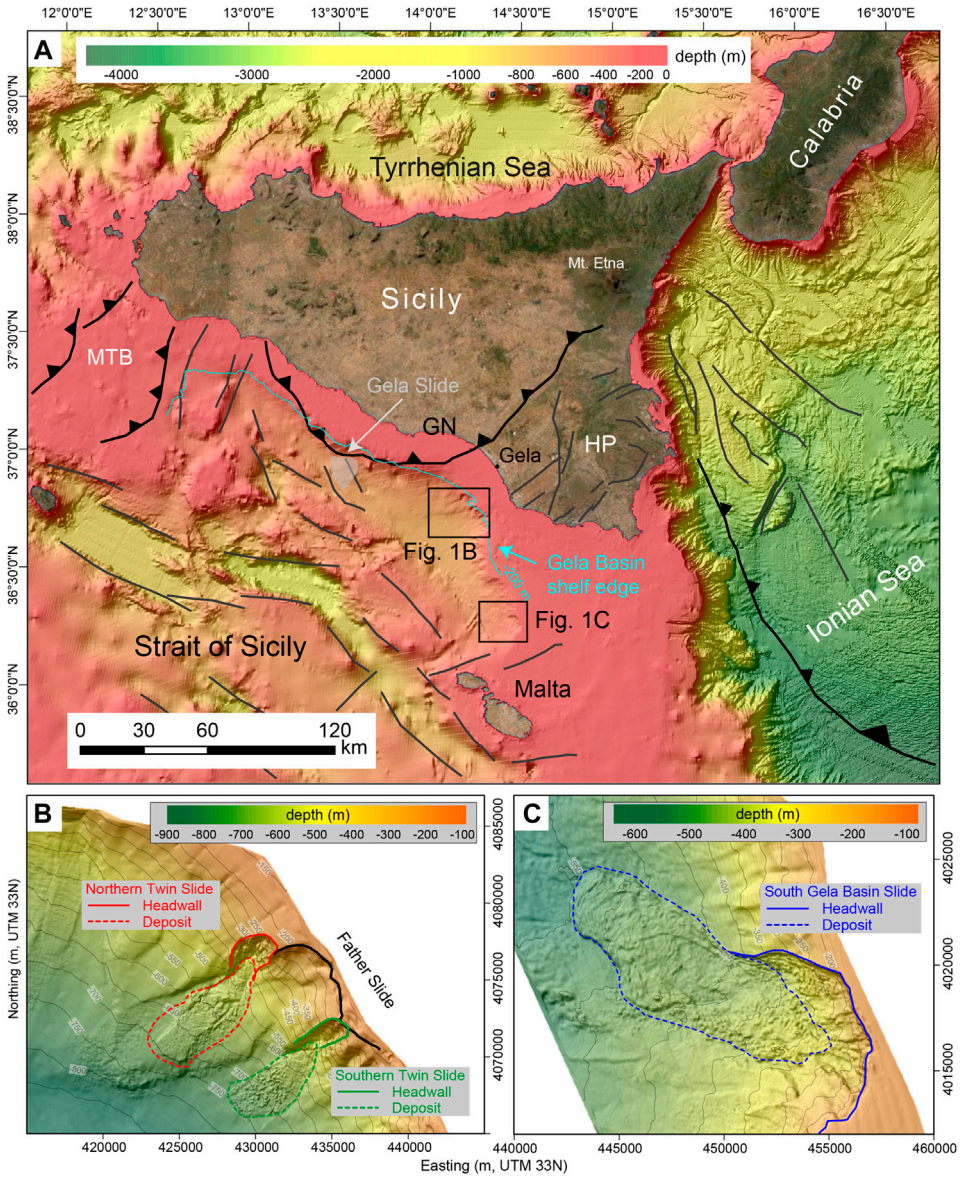

FIGURE 1 | (A) Simplified structural sketch of the Strait of Sicily and adjacent regions with the shelf-edge of the Gela Basin eastern slope (GBES) highlighted by the 200 m isobath (in light blue). Structural elements adapted from various sources (mainly Argnani et al., 1987; Argnani et al., 2012). Bathymetric data are from EMODnet (EMODnet Bathymetry Consortium, 2018). MTB = Maghrebian Thrust Belt, GN = Gela Nappe, HP = Hyblean Plateau. **(B)** Zoom on the north-eastern sector of the GBES, highlighting the Twin Slides complex and the different slide features. The black line marks the "Father Slide" headwall, the red and green ones are for the subsequent NTS and STS headwalls, respectively. At the toe of the scarps, the deposits of the two slides are shown with the red-dashed and green-dashed lines, respectively. **(C)** Zoom on the southern sector of the GBES. The blue line marks the SBGS headwall, at about 200 m depth, while the dashed-blue line delimits the slide deposit, at the toe of the slope.

tested numerical procedure that has been developed in-house and applied to several cases of landslide-generated tsunamis (Zaniboni et al., 2014b; Ceramicola et al., 2014; Zaniboni and Tinti, 2014; Zaniboni et al., 2016; Zaniboni et al., 2019; Gallotti et al., 2020; Triantafyllou et al., 2020). Under the assumption that the submarine slope will fail, the simulation sequence covers the whole process including 1) the dynamics of the sliding motion, 2) the tsunamigenic impulse caused by the movement of the mass along the sea bottom, and 3) the propagation of the tsunami over the computational domain.

Landslide Dynamics

When the sliding body reaches instability conditions, it starts moving along the slope. The dynamics of such motion is computed through the code UBO-BLOCK1, which implements a Lagrangian approach. The sliding body is partitioned into a set of interacting blocks, whose centers of mass (CoMs) motion is determined by the interaction with the surrounding environment, i. e., by the body forces (gravity, buoyancy), the surface stresses (basal friction, water drag on the exposed surfaces), and the internal interactions between blocks. The blocks conserve their

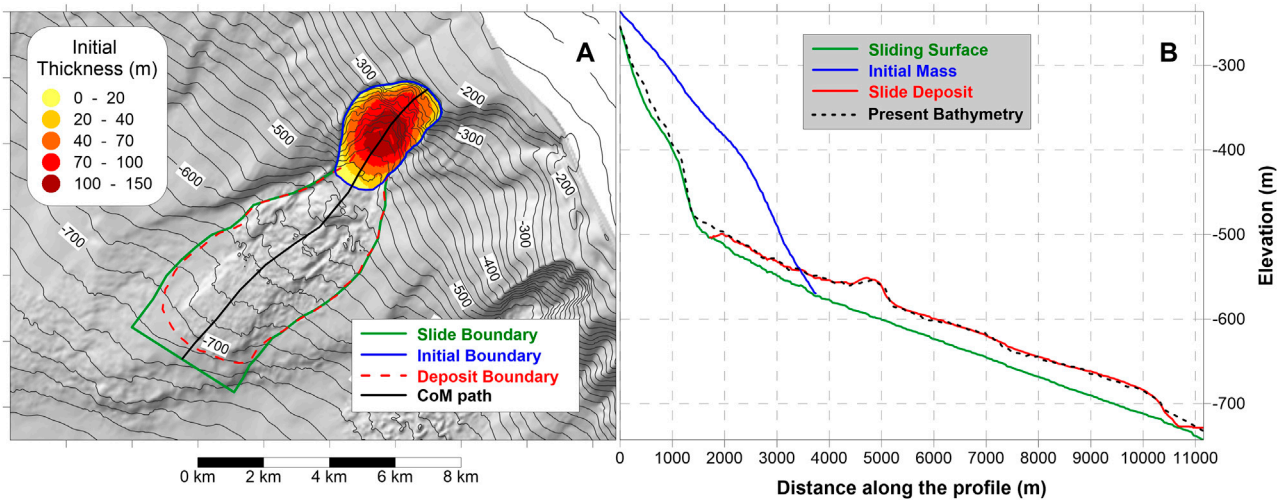

FIGURE 2 | (A) Bathymetric map of the NTS scenario. The blue contour marks the initial slide boundary, the dashed-red one delimits the observed slide deposit. The green line denotes the whole slide boundary, one of the code inputs. The black line describes the predefined trajectory of the blocks' CoM. The initial thickness is shown via the yellow-red-brown color scale. **(B)** Landslide profile cut along the CoM path. The blue, red, and green lines mark the initialmass, the deposit, and the gliding surface profiles, respectively. The black-dashed line is for the present morphology.

mass and cannot penetrate nor superimpose with each other. This approach allows one to quantify how much the slide changes its shape during its descent, a crucial factor in tsunami generation. The simulation is stopped when the mass exits the computational domain, or when the mean velocity lowers a predefined threshold.

The application of UBO-BLOCK1 requires as input:

i. The undisturbed sliding surface;
ii. The upper surface of the initial sliding mass;
iii. The predefined CoM trajectory;
iv. The lateral boundaries of the sliding surface.

Further details on the code can be found in Tinti et al. (1997).

Tsunami Generation and Propagation

The motion of the sliding body on the sea bottom changes the sea depth and mobilizes the whole water column, generating a perturbation that propagates throughout the water body. The tsunami impulse provided by the slide is not instantaneous, since the time scale of the two phenomena (landslide motion – wave propagation) is comparable, in contrast to the process of earthquake-generated waves, where the source can be considered instantaneous.

The tsunamigenic impulse is computed as the time history of the seabed change due to the passage of the mass, over each node of the tsunami computational grid. This perturbation is filtered with the water depth through a function cutting higher frequencies. These tasks are performed by a specific code, named UBO-TSUIMP, which is described in full detail in Tinti et al. (2006).

The wave propagation is modeled by the application of the classic non-linear shallow-water equations (SWE), that are solved by a finite difference approach (leap-frog numerical scheme) implementing the staggered grids technique. When the computational grid boundary is the open sea, a pure transparency condition is imposed, while the interaction with the coast is handled in two possible ways: in case of land inundation, the model implements the moving boundary technique, considering the flooded inland cells as part of the bathymetry; when the no-inundation condition is selected, the coast is considered as a vertical wall and the wave is reflected seaward. The choice between the two approaches depends on the aims of the investigation. If one wants to evaluate the tsunami hazard at a regional scale over a wide domain, the second is preferable. If the interest is on the effect on coastal communities and buildings, one should select the first option. The two alternatives usually require domains with different characteristics: high resolution to compute inundation, low resolution to simulate propagation in oceanic regions. The code, named UBO-TSUFD, includes also the possibility to manage domains with different spatial steps implementing the nested-grid technique, useful if a heterogeneous resolution is convenient for the simulation.

The input datasets needed to run the code are:

i. The tsunami computational grid, or set of grids;
ii. The tsunami initial condition.

This code is more extensively described in Tinti and Tonini (2013). Its applications are reported in the same references cited in the previous section. Besides, one can find an application to a case of an earthquake-tsunami in Loreto et al. (2017).

BUILDING THE LANDSLIDE SCENARIOS AND THE TSUNAMI COMPUTATIONAL GRID

In this paper we study the NTS and the SGBS since we consider their volume as typical of tsunamigenic mass movements in this region, and, more in general, because events of this size require

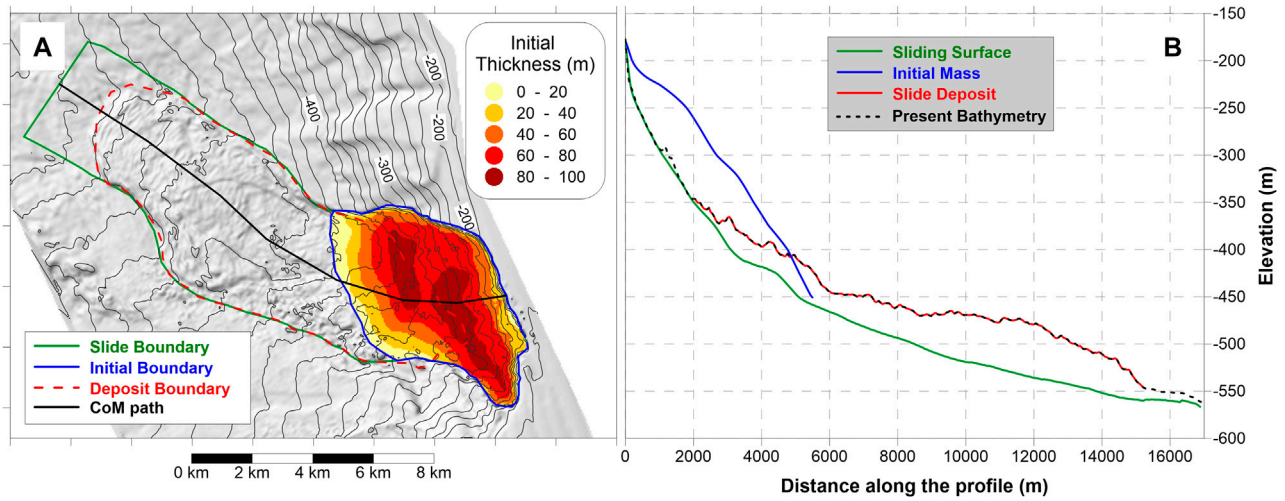

FIGURE 3 | (A) Bathymetric map of the SGBS scenario, with the initial mass boundary marked in blue and observed deposit in dashed-red. The resulting initial slide thickness is marked by the yellow-red-brown color scale. The other input for the simulation code, the lateral slide boundaries, and the CoM predefined trajectory, are reported in green and black respectively. **(B)** Morphological slice along the CoM path. In blue the initial slide profile, in red the observed deposit. The green line marks the undisturbed gliding surface, the black-dashed line the present bathymetry.

more attention and investigations. The tsunamis from NTS and SGBS are expected to be relevant for the coasts of southern Sicily and the Malta archipelago, and this consideration has guided us in building the grids for tsunami simulations.

Landslide Scenario for NTS

The simulation of the landslide motion requires the definition of the four elements listed in *Landslide Dynamics* Section. These have been devised mainly on morphological considerations, starting from the present seabed bathymetry given in **Figure 2**. In the NTS scenario, the sliding surface (green line in **Figure 2B**) coincides with the slide scar in the steeper part of the margin, uncovered after the sliding event down to 500 m depth. The remaining portion, now hidden by the slide deposit, has been inferred by extending the outer isobaths inside the sliding boundary (green boundary, **Figure 2A**) since these are supposed to represent the undisturbed surface under the slide deposit. After the sliding surface has been reconstructed, it is straightforward to obtain the sliding deposit, simply by difference with the present bathymetry (red line, **Figure 2B**). Though not essential for the simulation itself, the observed final distribution of the mass is very useful as a constraint for the parameters governing the sliding model. The initial mass has been obtained simply by filling the scar, again extending the isobaths inside the initial landslide contour (blue line, **Figure 2A**). The result is a body with volume of 0.46 km^3, consistent with the deposit at the toe of the slope, covering an area of almost 7 km^2. The initial slide mass distribution, obtained as the difference with the gliding surface, evidences a thicker central part, reaching 150 m (**Figure 2A**). The CoM path follows the direction of local maximum steepness, while the slide lateral boundaries (**Figure 2A**, in green) follow the observed slide deposit (red line, **Figure 2A**).

Landslide Scenario for SGBS

The second landslide scenario selected is placed around 50 km south of the NTS, closer to the Malta archipelago. The same procedure followed for the NTS has been used for the preparation of the SGBS simulation input. The sliding surface follows the uncovered steeper part of the slope and under the present deposit, is inferred by continuity with the outer isobaths (green profile in **Figure 3B**). The initial mass is obtained by filling the scar inside the respective boundary (blue boundary in **Figure 3A**), providing an initial sediment body with a volume of 1.48 km^3 (three times bigger than NTS), over an area of more than 26 km^2 (four times larger than NTS), implying a smaller thickness (maximum less than 100 m, **Figure 3A**). The final deposit is obtained by the difference between the present morphology and the sliding surface. As in the previous case, the obtained volume has been used as a further constraint on the reconstruction of the initial mass, since the two amounts have to be compatible.

Tsunami Computational Grids

The simulations of the landslide-generated tsunamis require a regularly spaced computational grid. The investigated area is shown in **Figure 4**: the larger grid (G1, in green) covers the southern corner of Sicily, more specifically the SE coast watered by the Strait of Sicily to the south and by the Ionian Sea to the east. This grid has been built with a spatial step of 250 m. The source data come from the EMODnet public database, covering this area with a resolution of about 115 m.

Due to the limited extent of the tsunami sources, that would have been described by too few nodes with the resolution of grid G1, it was necessary to make use of finer domains, covering the two tsunami generation areas. Grid G2, marked in blue in **Figure 4**, accounts for the SGBS scenario and includes the Malta archipelago as well; grid G3 (in red) covers the NTS case and the coast of the Gulf of Gela. Both computational

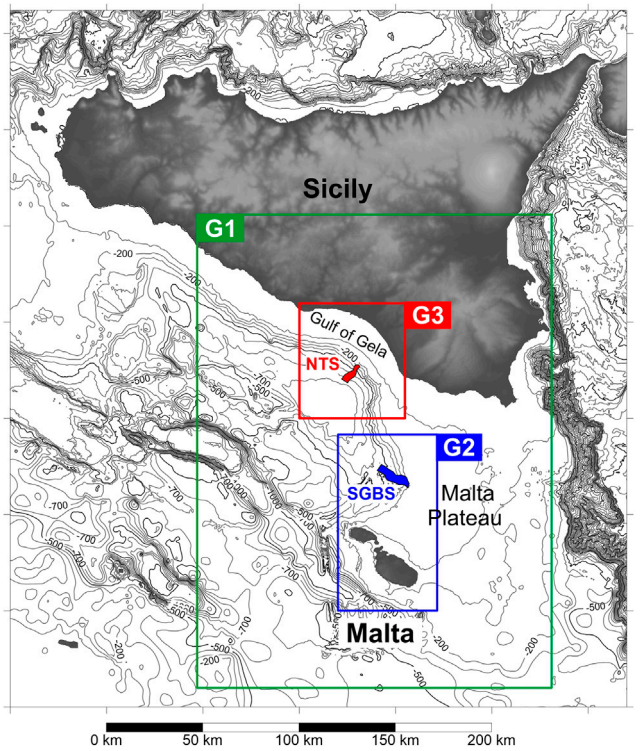

FIGURE 4 | Tsunami computational grids: the larger (G1) is characterized by a 250-m step, while the smaller ones (G2 and G3) have higher resolution (50-m spaced nodes) and are focused on the SGBS and NTS areas, respectively. The propagation of the tsunami over domains with different spatial intervals is possible through the nested-grids technique.

grids have been built with a 50 m spatial step by combining a swath bathymetry dataset acquired with 30–100 kHz multibeam systems and an overall 50 m resolution along the slope (Gauchery et al., 2021), with the already cited EMODnet bathymetry used to fill the data gaps.

This grids configuration (a larger 250-m mesh, G1, and two smaller 50-m domains, G2 and G3) allows an acceptable and detailed reconstruction of the landslide dynamics and their tsunamigenic impulse in the source areas, and sufficient coverage of the tsunami propagation in the Strait of Sicily. The simulation with this grid set is possible through the nested-grid technique implemented in the model UBO-TSUFD, allowing to account for the passage of the tsunami wave across boundaries of contiguous computational domains with different resolutions.

LANDSLIDES SIMULATIONS

The code UBO-BLOCK1 provides the complete time-history of the motion of each block composing the landslide mass. As a consequence, the simulation accounts for the mass shape variation during the descent, a factor that deeply influences the perturbation produced on the water column, necessary to evaluate the time-dependent tsunamigenic impulses associated with the mass moving along the seabed.

The comparison with the observed deposit provides important constraints on the simulation parameters governing the slide motion. Concerning the friction coefficient, a value of 0.03 provided the best fit: this is a typical value for submarine landslides. The drag coefficients have been selected basing on values coming from previous applications, simulating similar failures. For the superficial stress, the value chosen for the drag parameter is C_d = 0.02; as for the frontal drag, C_f = 0.5 (for a more detailed description of these coefficients and of their range of values, refer to Tinti et al., 1997). Both sliding bodies are affected by a considerable elongation, as inferable also from the profiles of **Figures 2,3**: NTS passes from 4 km to more than 8 km at the end of the motion; SGBS from 6 km to more than 12 km. The values adopted for the internal interaction parameters, governing the mass deformation, have been tuned to account for this behavior.

Figure 5 reports some of the motion features of the two scenarios. Panels A and B report the velocity evolution with time: it can be noticed that the two curves are similar, with an initial abrupt acceleration phase followed by a slower deceleration, typical of masses moving along steep margins, and then reaching the flat area at their toe. The NTS reaches the mean velocity peak (15 m/s) after around 100 s, while for SGBS the peak is slightly smaller, and attained at around 200 s. The black dots mark the individual CoM velocity record: notice that there is a generalized spread around the mean values (continuous line, red for NTS, and blue for SGBS), which is a natural consequence of the mass elongation during the descent. The mass comes to rest after almost 700 s for NTS and more than 850 s for SGBS, but it can be noticed that some blocks stop much earlier (already after 300 s for NTS; at 500 s for SGBS), while other have still residual velocity when the simulation is stopped.

The block thickness evolution is represented in Panels C and D of **Figure 5**: reflecting the elongation and spreading at the end of the motion, the sliding mass gets thinner, passing from an average of 75 m to around 20 m for NTS, and from 58 m to 31 m for SGBS. It is noticeable that in correspondence with the velocity peak, the block thickness increases considerably, especially for the NTS where some blocks reach height values of more than 120 m, with obvious influence on tsunami generation.

A typical indicator of the tsunamigenic efficiency is the Froude number, *Fr*. This is computed as the ratio between the horizontal component of the slide velocity and the wave phase speed ($\sqrt{gh}$, with g gravity acceleration and h local sea depth). When the two quantities are equal, the energy transfer from the slide to the water is maximum, and the resonance condition is attained (Fr = 1). For values lower than 1 (subcritical condition, typical of deep slides) the wave moves faster than the slide; for $Fr > 1$ (supercritical condition, typical of fast subaerial slides entering the water, usually occurring close to the generation area) the mass runs away from the generated wave. In the present cases, one can notice that the motion is always subcritical (panels E and F, **Figure 5**). The maximum

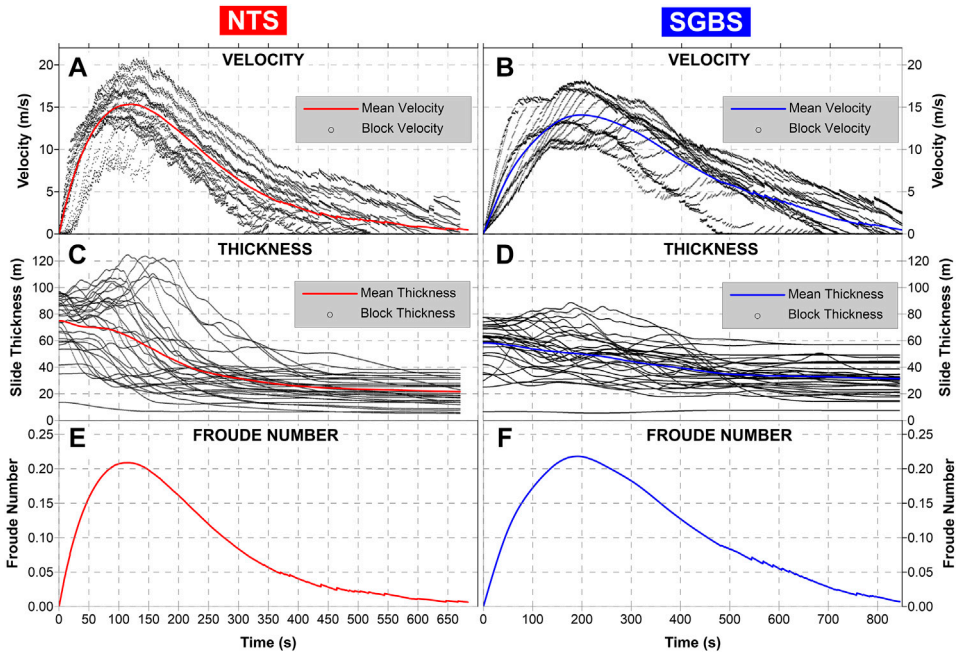

FIGURE 5 | Landslide dynamics for NTS **(left)** and SGBS **(right)**. **(A)** Mean velocity (red line) and individual CoM velocity (black dots) vs. time for the NTS scenario. **(B)** Analogous quantities for the SGBS scenario. **(C)** Mean thickness (red line) and individual block thickness (black dots) time history for the NTS case. **(D)** SGBS mean thickness (blue line) and block thickness (black dots). **(E)** Froude number vs. time for the NTS case. **(F)** Froude number vs. time for the SGBS scenario.

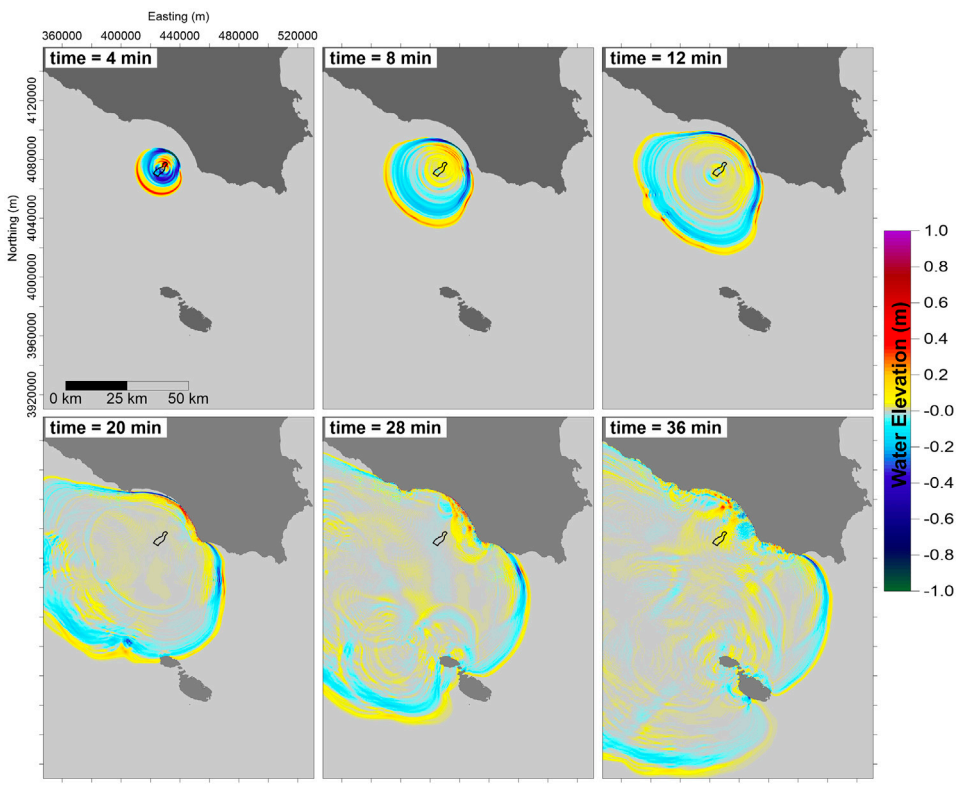

FIGURE 6 | Propagation sketches for the NTS-generated tsunami. The color scale is saturated for values higher than 1 m and lower than −1 m for graphical reasons. The black contour marks the area swept by the slide.

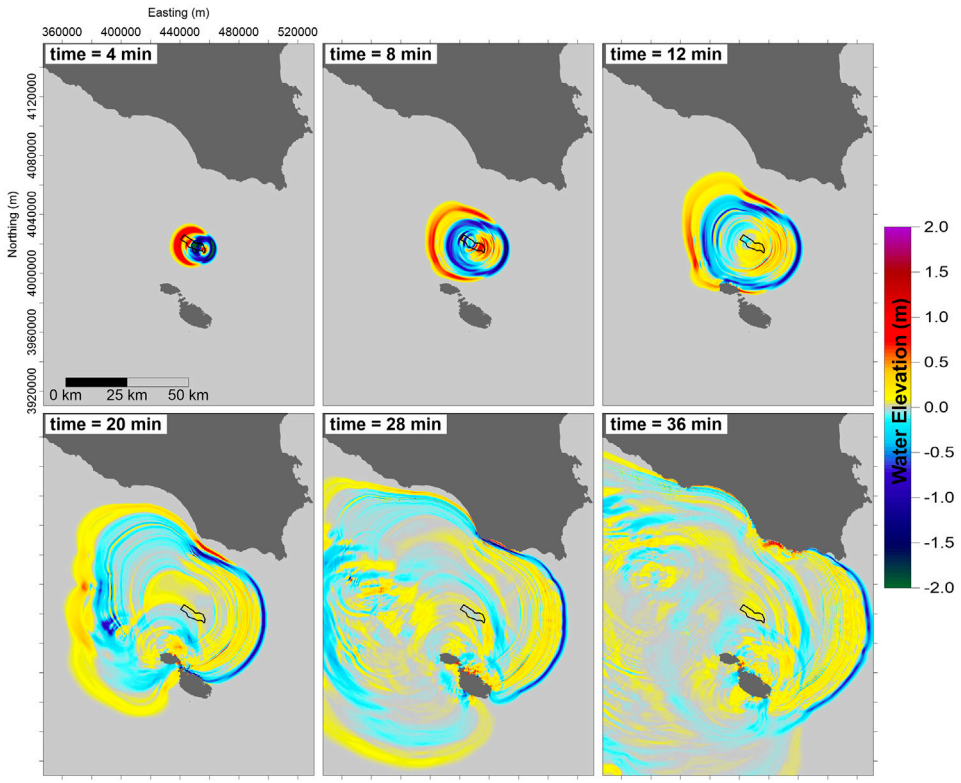

FIGURE 7 | Propagation frames for the SGBS-generated tsunami. The color scale spans the interval [−2;2] m and is saturated for values out of this range. The black contour delimits the SGBS slide area.

value of *Fr* (0.2) is attained in correspondence with the velocity peak for both slides.

TSUNAMI PROPAGATION

Tsunami simulations have been run with the linear version of the code UBO-TSUFD, without considering land inundation. Concerning the Malta archipelago where coasts have complex morphology, this task would require more refined grids, to describe better the many small gulfs and inlets characterizing especially the northern coast.

The propagation of the NTS-generated tsunami is shown in **Figure 6**. In the first frames (4 and 8 min) the typical circular radiation of landslide-tsunamis can be noticed, with a positive front propagating in the same direction as the slide motion (offshore, toward south-west) and a negative signal on the opposite side. This entails that the tsunami firstly manifests with a sea withdrawal at the Sicily coast, a factor that can be important in terms of alert management. The wave hits the coasts after about 12 min, with the negative front, which is soon followed by a positive wave, meaning sea-level increase. Within 20 min the whole Gulf of Gela (see **Figure 2** for geographic location) is affected by the wave, the same happens for Gozo (the north-westernmost island of the Malta archipelago), that in contrast to Sicily is hit by a positive wavefront. Notice that the travel time is very similar to the one obtained in Mueller et al. (2020) for a much bigger mass, the Gela Slide. The 36-min sketch shows that at this time almost the entire Malta islands are affected by the tsunami. Finally, notice the strong deceleration effect of the Malta Plateau, the shallow-water area between Sicily and Malta (whose location is shown in **Figure 4** as well), on the wave propagation due to bathymetry and shoaling mechanisms.

The SGBS-tsunami propagation sketches (**Figure 7**) show some similarities with the NTS case, especially in the first frames, i. e., the circular radiation from the source and the polarity of the wavefront (positive westward, negative eastward). Conversely, the SGBS tsunami is generally higher than the NTS one. Gozo island is attacked by a positive front between 8 and 12 min, and the whole Malta archipelago within 28 min. Considering the Sicily coasts, one can notice that already at the 12 min frame the wavefront tends to deform, due to the interaction with the bathymetry. The first affected coastal stretch is the southern extreme of the Gulf of Gela, between 20 and 28 min. At this time a positive signal reaches the coast. Here the tsunami signal deceleration in the Malta Plateau area is evident as well, with the negative front (in blue) taking several minutes to cross this sea region.

Interesting insights on the tsunami characteristics come from **Figure 8**, representing the maximum sea surface elevation computed for each node of the tsunami grid, during the whole

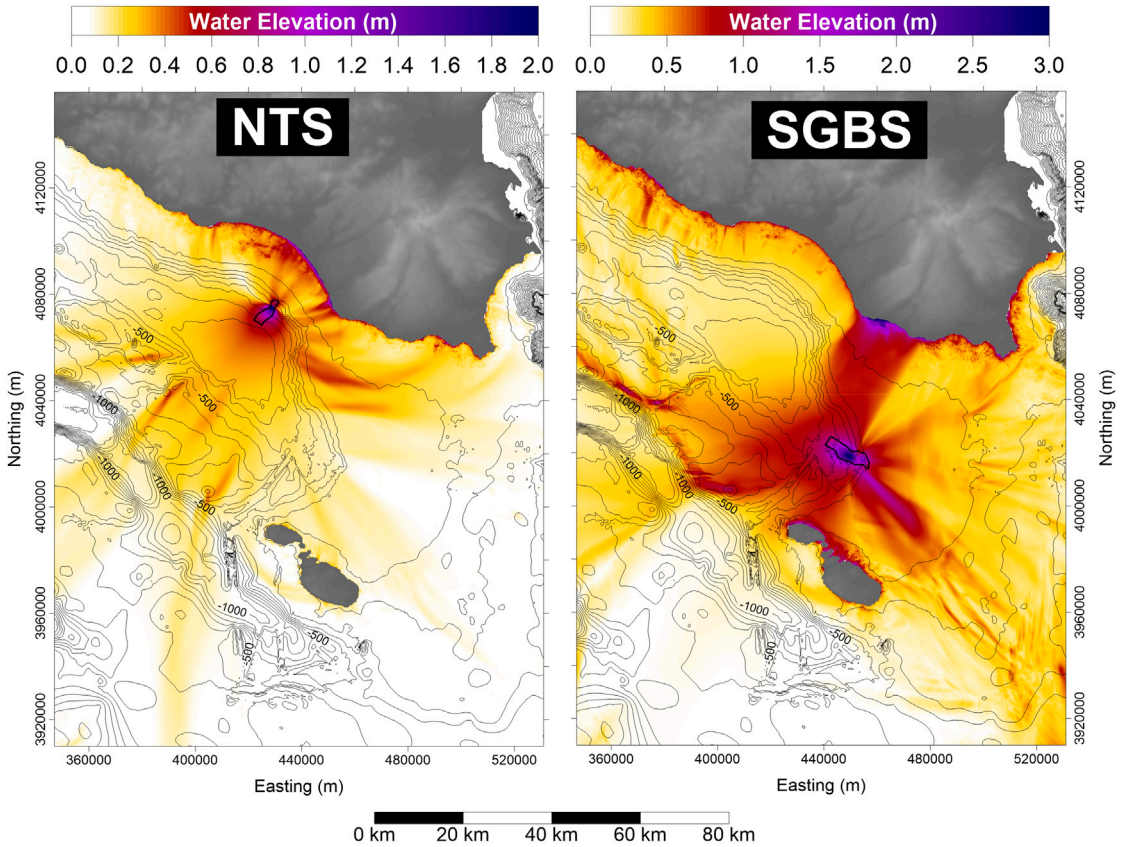

FIGURE 8 | Maximum water elevation for the two landslide scenarios, NTS **(left)** and SGBS **(right)**. The black boundaries mark the area swept by the landslide motion. Notice that the color scales cover different intervals for the two plots.

tsunami propagation history. This plot provides a useful glance at the spatial distribution of the tsunami energy.

One can notice that most of the tsunami energy in the NTS scenario is captured within the Gulf of Gela. Some tsunami beams are visible, evidencing preferential directions for water maximum elevation. Noticeable are two rays hitting the central part of the gulf, two more affecting its eastern end, and another one moving south-eastward. The Malta archipelago coasts seem scarcely affected by waves generated from the NTS scenario.

Concerning the SGBS (**Figure 8** – right panel), the pattern is quite different. The Malta islands are hit by relevant maximum waves, reaching also 2 m. A strong beam heads towards the Malta Plateau, south-east, but the most noticeable feature is the high concentration of energy directing towards the coast of Sicily, east of the Gulf of Gela. Here the water elevation exceeds 3 m. Conversely, the coasts of the gulf itself are moderately protected, since most of the tsunami energy is attracted to the east. The SGBS scenario, though more distant, produces more relevant and diffused effects on the Sicily coasts than the NTS scenario.

These observations are confirmed by **Figure 9**, representing the maximum water elevation along the coast of Sicily. The water height is computed along the 5-m isobath since the linear version of the simulation code with fixed coastal boundary has been run and no inundation has been computed. Therefore, the results described here can be considered as underestimations of the effective run-up heights in terms of hazard, also considering that non-linear terms would amplify the waves when approaching the coast.

Figure 9 confirms that the NTS tsunami is mainly confined within the Gela Gulf (between points #1 and #4), where a maximum of 3 m is reached close to Marina di Acate (node #3) and another 2 m peak can be observed around node #4 (Santa Croce Camerina). Out of this coastal stretch, about 80 km long, the wave height rapidly drops below 1 m and is almost negligible west of Licata (#1) and beyond Capo Passero (point #6).

The curve representing SGBS coastal water height, on the other hand, shows the maximum elevations reached between points #4 and #5, i. e., the area towards which the tsunami beam mentioned above (**Figure 9**) is directed. Here waves reach 3.5 m and remain higher than 2 m for at least 30 km along the coast. Within the Gulf of Gela, the water elevation oscillates around the value of 1.5 m, comparable then to the NTS case. West of Licata (#1) the wave height remains in the range of 1–1.5 m for almost the entire coast. On the east, similar behavior is observed, with oscillations exceeding 1.5 m towards Capo Passero (node #6) and also farther, along the eastern coast of Sicily. In general, the SGBS affects the coast of Sicily with waves exceeding 1 m for almost the whole coastal stretch covered by the simulation, 300 km long, dropping down to 1 m elevation only at the plot borders.

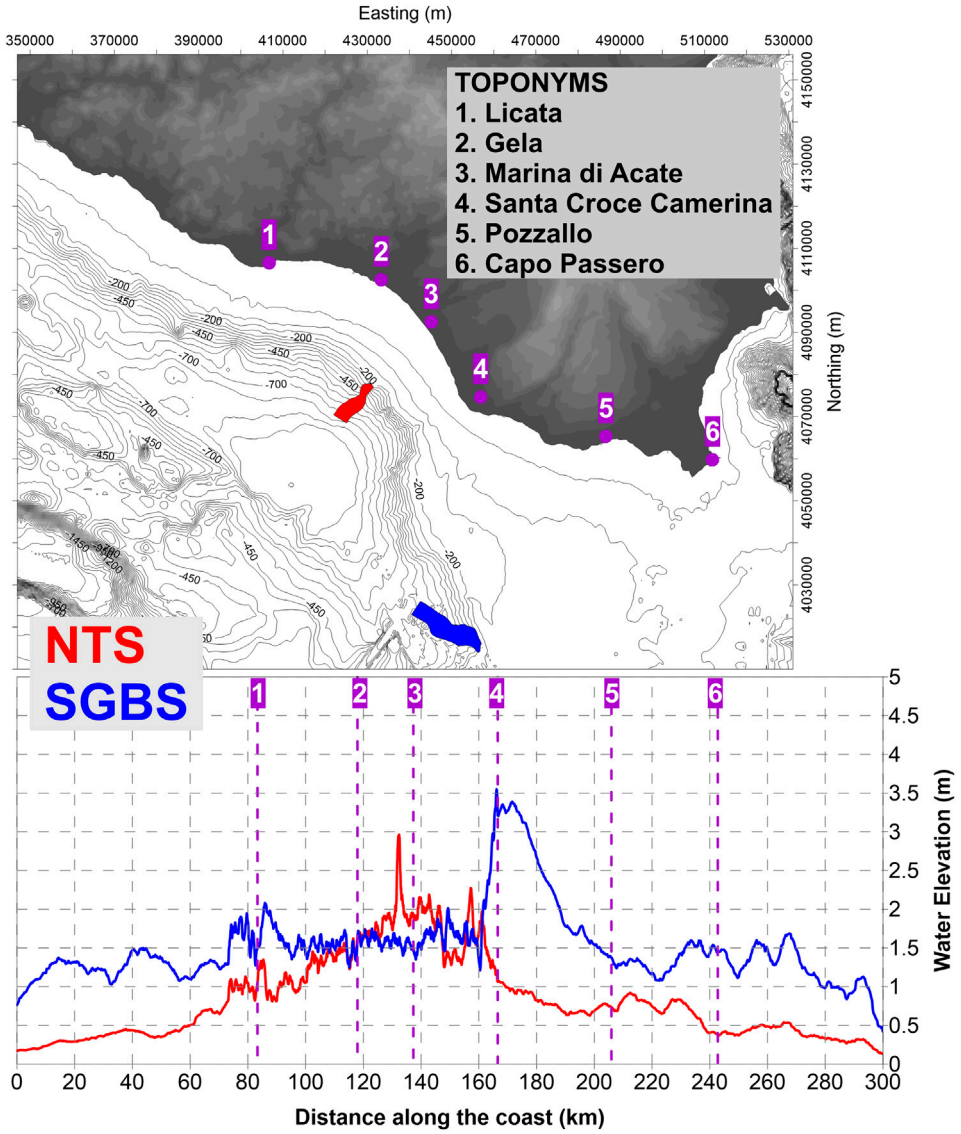

FIGURE 9 | (Upper panel) Map of the Sicily coast, with relevant coastal cities. The red and blue spots represent the NTS and SGBS, respectively. **(Lower panel)** Maximum water height associated with the two tsunami scenarios (NTS and SGBS, in red and blue respectively) along the coast of Sicily from west to east. The numbers and the dashed-purple lines refer to the toponyms reported in the upper panel.

Focusing the attention on the Malta archipelago, we consider the maximum water elevation along the 20-m isobath rather than along the 5-m isoline (**Figure 10**). This choice is motivated by the fact that the bathymetry in the shallow coastal zone here is quite complex, being characterized by numberless small inlets, bays, promontories that could be well described only by high-resolution grids, which in turn would require heavier computational costs. The results we will show on the 20-m isoline are expected to be underestimates of the maximum tsunami waves since they do not account for possible resonance amplification nor tsunami energy focusing. Nonetheless, they provide a good basis to evaluate the overall impact of the tsunami on the Malta islands.

The NTS tsunami produces limited effects, mainly on the northern part of the Gozo island, where 0.4 m height is reached. The inlets along the northern coasts are affected by waves at most of some tens of centimeters, that can be considered negligible in terms of human hazard but can be amplified by resonance effects, producing heavy damage on boats and harbor facilities.

The SGBS source area is closer to the Malta archipelago, producing relevant effects especially along the northern coasts. Gozo island is the most affected, with the north-western coast hit by waves exceeding 2 m. Also, the northern half of the main Malta island is impacted by a wave at least 1.5 m high, with relevant waves entering St. Paul's Bay (point #1 in **Figure 10**), the most populated town of the island, with a substantial increase of population in the tourist season. Also, the inlet of La Valletta (point #2 in **Figure 10**) is affected by waves higher than 1 m. All

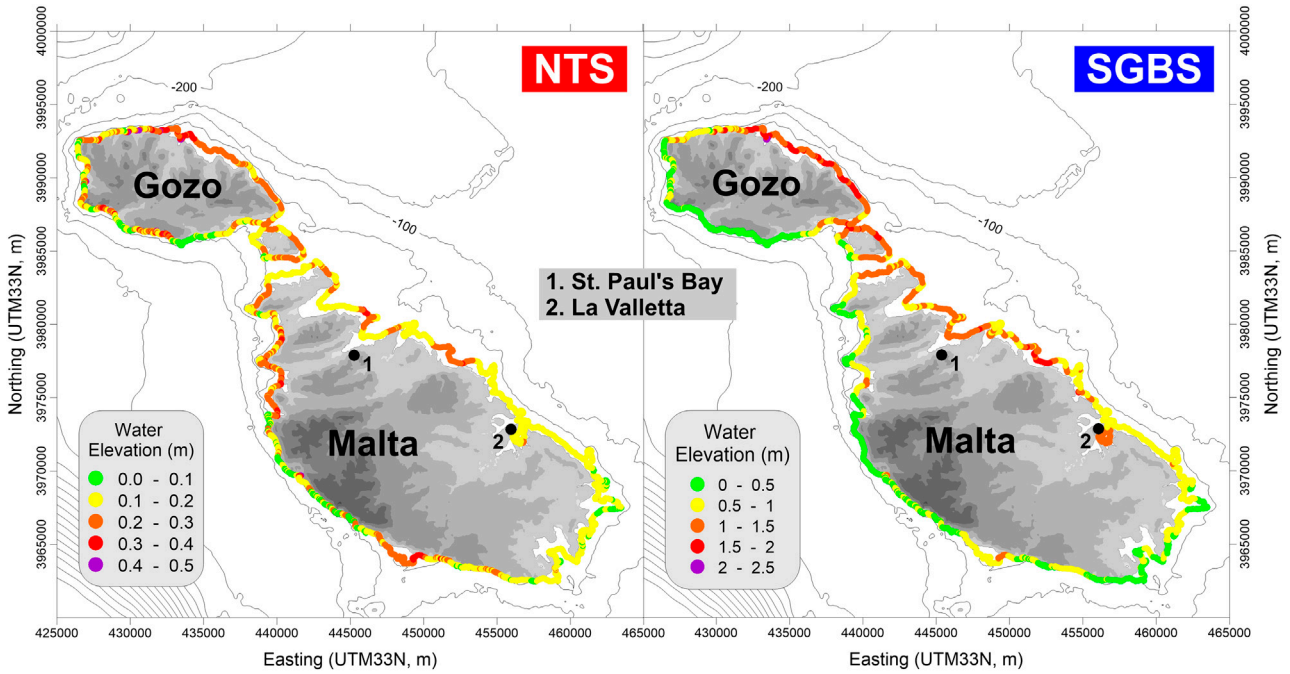

FIGURE 10 | Maximum water elevation along the coast of the Malta archipelago, taken on the 20-m isobath, for the two tsunami scenarios: NTS on the left, SGBS on the right. The numbered dots mark the main toponyms. Notice the different range of the color scales used for the two cases.

the southern coast, on the contrary, seems protected with maximum waves barely reaching half a meter.

CONCLUSIONS

In this paper, we have studied two cases of tsunamis produced by mass failures along the GBES, selected mainly for two reasons. First, high-quality seafloor geomorphological data are available, accurately describing the scar and the slide deposit, which allows a suitable reconstruction of the landslide sources and provides useful constraints for the simulation model. Moreover, these slides can be considered representative of typical failure episodes along the slope.

In the framework of the SPOT project, aimed at assessing the influence of local earthquakes on tsunami generation and mobilization of sediments, the stability analysis of the two landslide scenarios have been performed (see results in **Supplementary Appendix A**). They showed that failures in the northern sector of the GBES, where the NTS is located, can be activated with a return period of few thousands of years. More in the south, farther away from the seismic faults, at least according to the present knowledge of the offshore tectonics, failures like the SGBS cannot be explained by invoking seismic load, and other destabilizing causes have to be found, which implies further research efforts.

Mass movements along the GBES require particular attention since they occur in relatively shallow water. Moreover, in the initial stage, they soon attain large velocity, due to the high steepness of the continental slope (5°–10°). The combination of these two elements (large velocity and shallow water) enhances the tsunamigenic potential in a considerable way.

The tsunami simulations show that masses such as the NTS and the SGBS can produce relevant waves impacting coastal stretches from tens to hundreds of km long. For the NTS, the arrival of the tsunami on the Sicily coasts manifests as a sea withdrawal. In this case, a useful precursor could be the earthquake, destabilizing the underwater body since it anticipates the tsunami arrival by some tens of minutes. This latter kind of phenomenon sometimes called "surprise tsunami" (Ward, 2001) needs increasing attention and continental margins should therefore be more extensively mapped, investigated and possibly monitored, especially off those coasts of the Mediterranean Sea that are densely populated. The continuous supply of sediments by rivers, the diffused seismicity in the whole basin, the presence of other destabilizing phenomena (such as strong submarine bottom currents and volcanoclastic material) are elements contributing to increasing the potential hazard.

Further Improvements and Perspectives

The GBES is particularly interesting for many reasons. First of all, it is placed in relatively shallow water, connecting a wide shelf at 200 m depth to the deeper sea (800–900 m). This permits the characterization of the morphology in detail, both for the reconstruction of past events and for the recognition of possible future occurrences. Many submarine landslide events can be mapped by high-resolution bathymetric data and described with sufficient accuracy, covering a large spectrum of volumes and return periods, making it possible to apply probabilistic approaches.

The study of the tsunami effects on the coast should also consider land inundation and the impact on coastal communities. This issue was the scope of the Italian project SPOT (Antoncecchi et al., 2020) for the coast of Sicily, but not for the Malta archipelago. It was addressed by employing empirical laws for tsunami flow over coastal 1D transects and the results are left to further publications. As regards the Malta coasts, the inlets along the northern coasts, in particular, favor wave amplifications that should be investigated through more detailed computational grids. The two scenarios explored in this work, together with the ones reported in Mueller et al. (2020), could be integrated into a more comprehensive study of tsunami hazard of the Malta archipelago.

An exhaustive study of the tsunami hazard related to collapses along the GBES would require more scenarios, covering a larger spectrum of volumes, also using a probabilistic approach. Nonetheless, the authors are convinced that the two cases presented here provide interesting insights for the evaluation of the tsunami hazard along the coast of Sicily and Malta and that will stimulate the interest on these phenomena, which should require increasing consideration.

Validation of results from numerical simulations can come from the analysis of tsunami deposits in the sedimentary sequences on land and also offshore. This was the case, for example, of the geological investigations by Pantosti et al. (2008), De Martini et al. (2012) and Smedile et al. (2020), that were able to associate sediment layers found in trenches or cores in eastern Sicily to historical- as well as paleo-tsunami cases. The GBES morphology suggests that mass collapses along the slope repeat cyclically, and the generated tsunami can reach the coasts of Sicily and Malta with potentially relevant waves. The events investigated here are prehistorical. Finding their coastal signature is a hard, but not an impossible task and future research by tsunami geologists could fill this gap.

DATA AVAILABILITY STATEMENT

The raw data supporting the conclusions of this article will be made available by the authors, without undue reservation.

AUTHOR CONTRIBUTIONS

FZ realized the datasets describing the landslide scenarios; contributed to develop and maintain the landslide simulation code; performed the landslide dynamics simulations; wrote the first draft of the paper; produced most of the figures in the paper; collected and harmonized all the contributions from coauthors; managed the manuscript progress. GP contributed to develop and maintain the tsunami simulation code; built the tsunami computational grids; run the simulations of the tsunami propagation. MAP contributed to the definition of the landslide scenarios; contributed to develop and maintain the stability analysis code; performed the slope stability analysis. TG contributed to the definition of the SGBS scenario and the discussion of the collapse triggering factors; performed the literature review on landslide-tsunamis; revised the paper. MR provided bathymetric data for landslide scenarios and tsunami computational grids; contributed to the definition of the landslide scenarios; supervised the geological part of the work; produced **Figure 1**; contributed to the manuscript revision. AArg: contributed to the definition of the landslide scenarios; supervised the geological part of the work; contributed to the manuscript revision; produced **Figure 1**. AArm contributed to develop and maintain the tsunami simulation code; supervised the modeling part of the work; revised the paper. ST developed the stability, landslide, and tsunami numerical codes; supervised the whole work; revised the paper.

ACKNOWLEDGMENTS

The bathymetric metadata and Digital Terrain Model data products have been derived from the EMODnet Bathymetry portal - http://www.emodnet-bathymetry.eu. The *PGA*s in the landslide areas originated by the selected faults were provided by Barbara Borzi and her research team (Eucentre), in the framework of the SPOT project. The SPOT project was funded by the Italian Ministry of Economic Development, Directorate General for Safety—National Mining Office for Hydrocarbons and Georesources (DGS–UNMIG) under the umbrella of the Offshore safety network "Clypea," which is in force since 2014, and was established with bilateral agreements between the Ministry and Research Centres, Governmental Bodies and Universities to increase the safety, also in terms of environmental protection, of offshore plants operations. The Ph.D. of Tugdual Gauchery is funded by the European Union's Horizon 2020 research and innovation program under the Marie-Skłodowska-Curie grant via project ITN SLATE (Grant Agreement No 721403). The authors are indebted to the editor and the reviewers, Roger Urgeles and Juan Horrillo, whose comments and suggestions contributed to considerably improve the manuscript.

SUPPLEMENTARY MATERIAL

The Supplementary Material for this article can be found online at: https://www.frontiersin.org/articles/10.3389/feart.2020.602171/full#supplementary-material.

REFERENCES

Ai, F., Kuhlmann, J., Huhn, K., Strasser, M., and Kopf, A. (2014). Submarine slope stability assessment of the central Mediterranean continental margin: the Gela Basin," in *Submarine mass movements and their consequences. Advances in natural and technological hazards research*. Editors S. Krastel, et al. (Cham: Springer), Vol. 37. doi:10.1007/978-3-319-00972-8_20

Antoncecchi, I., Ciccone, F., Dialuce, G., Grandi, S., Terlizzese, F., Di Bucci, D., et al. (2020). *Progetto SPOT – Sismicità Potenzialmente innescabile Offshore e Tsunami. Report integrato di fine progetto*, ISBN 9788894366945 (in Italian). doi:10.5281/zenodo.3732887

Argnani, A. (1987). The Gela Nappe: evidence of accretionary melange in the Maghrebian foredeep of Sicily. *Mem. Società Geol. Italiana* 38, 419–428.

Argnani, A., Armigliato, A., Pagnoni, G., Zaniboni, F., Tinti, S., and Bonazzi, C. (2012). Active tectonics along the submarine slope of south-eastern Sicily and the source of the 11 January 1693 earthquake and tsunami. *Nat. Hazards Earth Syst. Sci.* 12, 1311–1319. doi:10.5194/nhess-12-1311-2012

Argnani, A., Cornini, S., Tortelli, L., and Zitellini, N. (1987). Diachronous foredeep system in the neogene-quaternary of the strait of sicily. Memorie Società Geologica Italiana. 38, 407–417.

Argnani, A., Tinti, S., Zaniboni, F., Pagnoni, G., Armigliato, A., Panetta, D., et al. (2011). The eastern slope of the southern Adriatic basin: a case study of submarine landslide characterization and tsunamigenic potential assessment, *Mar. Geophys. Res.* 32, 299–311. doi:10.1007/s11001-011-9131-3

Assier-Rzadkiewicz, S., Heinrich, P., Sabatier, P. C., Savoye, B., and Bourillet, J. F. (2000). Numerical modelling of a landslide-generated tsunami: the 1979 nice event. *Pure Appl. Geophys.* 157, 1707–1727. doi:10.1007/PL00001057

Casalbore, D., Bosman, A., Ridente, D., and Chiocci, F. L. (2014). "Coastal and submarine landslides in the tectonically-active tyrrhenian calabrian margin (southern Italy): examples and geohazard implications," in *Submarine mass movements and their consequences. Advances in natural and technological hazards research*. Editors S. Krastel, et al. (Cham, Springer), Vol. 37. doi:10.1007/978-3-319-00972-8_23

Casalbore, D., Martorelli, E., Bosman, A., Morelli, E., and Chiocci, F. L. (2019). Failure dynamics of landslide scars on the lower continental slope of the Tyrrhenian Calabrian margin: insights from an integrated morpho-bathymetric and seismic analysis. *Geol. Soc., London, Spec. Publ.* 477, 389–397. doi:10.1144/SP477.16

Ceramicola, S., Tinti, S., Zaniboni, F., Praeg, D., Planinsek, P., Pagnoni, G., et al. (2014). "Reconstruction and tsunami modeling of a submarine landslide on the Ionian margin of Calabria (Mediterranean Sea)," in *Landslide science for a safer geoenvironment*. Editors K. Sassa, P. Canuti, and Y. Yin (Cham: Springer International Publishing Switzerland), Vol. 3, 557–562. doi:10.1007/978-3-319-04996-0_85

Chaytor, J. D., ten Brink, U. S., Solow, A. R., and Andrews, B. D. (2009). Size distribution of submarine landslides along the U.S. Atlantic margin. *Mar. Geol.* 264, 16–27. doi:10.1016/j.margeo.2008.08.007

Chiocci, F. L., and Ridente, D. (2011). Regional-scale seafloor mapping and geohazard assessment. The experience from the Italian project MaGIC (Marine Geohazards along the Italian Coasts). *Mar. Geophys. Res.* 32, 13–23. doi:10.1007/s11001-011-9120-6

De Martini, P. M., Barbano, M. S., Pantosti, D., Smedile, A., Pirrotta, C., Del Carlo, P., et al. (2012). Geological evidence for paleotsunami along eastern Sicily (Italy): an overview. *Nat. Hazards Earth Syst. Sci.* 12, 2569–2580. doi:10.5194/nhess-12-2569-2012

EMODnet Bathymetry Consortium (2018). *EMODnet digital bathymetry (DTM)*. Brussels: The European Marine Observation and Data Network, European Maritime and Fisheries Fund. http://doi.org/10.12770/18ff0d48-b203-4a65-94a9-5fd8b0ec35f6

Eruteya, O. E., Safadi, M., Waldmann, N., Makovsky, Y., and Ben-Avraham, Z. (2016). "Seismic geomorphology of the Israel slump complex in the levant basin (SE Mediterranean)," in *Submarine mass movements and their consequences. Advances in natural and technological hazards research*. Editor G. Lamarche, et al. (Cham: Springer), Vol. 41. doi:10.1007/978-3-319-20979-1_4

Fan, W., McGuire, J. J., and Shearer, P. M. (2020). Abundant Spontaneous and dynamically triggered submarine landslides in the gulf of Mexico. *Geophys. Res. Lett.* 47, e2020GL087213. doi:10.1029/2020GL087213

Fisher, M., Normark, W. R., Gary Greene, H., Lee, H. L., and Sliter, R. W. (2005). Geology and tsunamigenic potential of submarine landslides in Santa Barbara channel, southern California. *Mar. Geol.* 224, 1–22. doi:10.1016/j.margeo.2005.07.012

Gallotti, G., Passaro, S., Armigliato, A., Zaniboni, F., Pagnoni, G., Wang, L., et al. (2020). Potential mass movements on the Palinuro volcanic chain (southern Tyrrhenian Sea, Italy) and consequent tsunami generation. *J. Volcanol. Geoth. Res.* 404, 107025. doi:10.1016/j.jvolgeores.2020.107025

Gauchery, T., Rovere, M., Pellegrini, C., Cattaneo, A., Campiani, E., and Trincardi, F. (2021). Factors controlling margin instability during the plio-quaternary in the Gela Basin (Strait of Sicily, Mediterranean Sea). *Mar. Petrol. Geol.*, 123, 104767. doi:10.1016/j.marpetgeo.2020.104767

Greene, H. G., Murai, L. Y., Watts, P., Maher, N. A., Fisher, M. A., Paull, C. E., et al. (2006). Submarine landslides in the Santa Barbara channel as potential tsunami sources. *Nat. Hazards Earth Syst. Sci.* 6, 63–88. doi:10.5194/nhess-6-63-2006

Harbitz, C. B., Lovholt, F., and Bungum, H. (2014). Submarine landslide tsunamis: how extreme and how likely? *Nat. Hazards* 72, 1341–1374. doi:10.1007/s11069-013-0681-3

Iglesias, O., Lastras, G., Canals, M., Olabarrieta, M., Gonzalez, M., Aniel-Quiroga, I., et al. (2012). The BIG'95 submarine landslide-generated tsunami: a numerical simulation. *J. Geol.* 120 (1), 31–48. doi:10.1086/662718

Ioualalen, M., Larroque, C., Scotti, O., and Daubord, C. (2014). Tsunami mapping related to local earthquakes on the French–Italian Riviera (Western Mediterranean). *Pure Appl. Geophys.* 171, 1423–1443. doi:10.1007/s00024-013-0699-1

Janin, A., Rodriguez, M., Sakellariou, D., Lykousis, V., and Gorini, C. (2019). Tsunamigenic potential of a Holocene submarine landslide along the North Anatolian Fault (northern Aegean Sea, off Thasos island): insights from numerical modelling, *Nat. Hazards Earth Syst. Sci.* 19, 121–136. doi:10.5194/nhess-19-121-2019

Kawamura, K., Laberg, J. S., and Kanamatsu, T. (2014). Potential tsunamigenic submarine landslides in active margins. *Mar. Geol.* 356, 44–49. doi:10.1016/j.margeo.2014.03.007

Kuhlmann, J., Asioli, A., Trincardi, F., Klügel, A., and Huhn, K. (2015). Sedimentary response to Milankovitch-type climatic oscillations and formation of sediment undulations: evidence from a shallow-shelf setting at Gela Basin on the Sicilian continental margin. *Quat. Sci. Rev.* 108, 76–94. doi:10.1016/J.QUASCIREV.2014.10.030

Kuhlmann, J., Asioli, A., Trincardi, F., Klügel, A., and Huhn, K. (2017). Landslide frequency and failure mechanisms at NE Gela Basin (Strait of Sicily). *J. Geophys. Res.: Earth Surf.* 122, 2223–2243. doi:10.1002/2017JF004251

Lastras, G., Canals, M., Amblas, D., Frigola, J., Urgeles, R., Calafat, A. M., et al. (2007). Slope instability along the northeastern Iberian and Balearic continental margins. *Geol. Acta.* 5, 35–47. doi:10.1344/105.000000308

Lastras, G., De Blasio, F. V., Canals, M., and Elverhøi, A. (2005). Conceptual and numerical modeling of the BIG'95 debris flow, Western Mediterranean Sea. *J. Sediment. Res.* 75, 784–797. doi:10.2110/jsr.2005.063

Lickorish, W. H., Grasso, M., Butler, R. W. H., Argnani, A., and Maniscalco, R. (1999). Structural styles and regional tectonic setting of the Gela Nappe (SE Sicily). *Tectonics* 18, 655–668. doi:10.1029/1999TC900013

Loncke, L., Gaullier, V., Droz, L., Ducassou, E., Migeon, S., and Mascle, J. (2009). Multi-scale slope instabilities along the Nile deep-sea fan, Egyptian margin: a general overview. *Mar. Petrol. Geol.* 26: 633–646. doi:10.1016/j.marpetgeo.2008.03.010

Loreto, M. F., Pagnoni, G., Pettenati, F., Armigliato, A., Tinti, S., Sandron, D., et al. (2017). Reconstructed seismic and tsunami scenarios of the 1905 Calabria earthquake (SE Tyrrhenian sea) as a tool for geohazard assessment. *Eng. Geol.* 224, 1–14. doi:10.1016/j.enggeo.2017.04.018

Løvholt, F., Harbitz, C. B., Vanneste, M., De Blasio, F. V., Urgeles, R., Iglesias, O., et al. (2014). Modeling potential tsunami generation by the BIG'95 landslide," in *Submarine mass movement and their consequences, Advances in natural and technological hazards research*. Editors S. Krastel, J.-H. Behrmann, D. Völker, M. Stipp, C. Berndt, R. Urgeles, et al. (Dordrecht, The The Netherlands: Springer), Vol. 37, 507–515. doi:10.1007/978-3-319-00972-8_45

Macías, J., Vázquez, J. T., Fernández-Salas, L. M., González-Vida, J. M., Bárcenas, P., Castroa, M. J., et al. (2015). The Al-Borani submarine landslide and associated tsunami. A modelling approach. *Mar. Geol.* 361, 79–95. doi:10.1016/j.margeo.2014.12.006

Masson, D. G., Harbitz, C. B., Wynn, R. B., Pedersen, G., and Løvholt, F. (2006). Submarine landslides: processes, triggers and hazard prediction. *Phil. Trans. R Soc. A* 364, 2009–2039. doi:10.1098/rsta.2006.1810

McAdoo, B. G., Pratson, L. F., and Orange, D. L. (2000). Submarine landslide geomorphology, US continental slope. *Mar. Geol.* 169, 103–136. doi:10.1016/S0025-3227(00)00050-5

Meletti, C., and Montaldo, V. (2007). Stime di pericolosità sismica per diverse probabilità di superamento in 50 anni: valori di ag. Progetto DPC-INGV S1, Deliverable D2, http://esse1.mi.ingv.it/d2.html (Accessed June, 2018).

Micallef, A., Georgiopoulou, A., Le Bas, T., Mountjoy, J. J., Huvenne, V., and Lo Iacono, C. (2014). "The Malta-Sicily Escarpment: mass movement dynamics in a sediment-undersupplied margin," in *Submarine mass movements and their consequences. Advances in natural and technological hazards research*. Editors S. Krastel, et al. (Cham: Springer), Vol. 37. doi:10.1007/978-3-319-00972-8_28

Minisini, D., and Trincardi, F. (2009). Frequent failure of the continental slope: the Gela Basin (Sicily channel), *J. Geophys. Res.* 114, F03014. doi:10.1029/2008JF001037

Minisini, D., Trincardi, F., Asioli, A., Canu, M., and Foglini, F. (2007). Morphologic variability of exposed mass-transport deposits on the eastern slope of Gela Basin (Sicily channel). *Basin Res.* 19 (2), 217–240. doi:10.1111/j.1365-2117.2007.00324.x

Miramontes, E., Garziglia, S., Sultan, N., Jouet, G., and Cattaneo, A. (2018). Morphological control of slope instability in contourites: a geotechnical approach. *Landslides* 15, 1085–1095. doi:10.1007/s10346-018-0956-6

Mueller, C., Micallef, A., Spatola, D., and Wang, X. (2020). The tsunami inundation hazard of the Maltese islands (central Mediterranean Sea): a submarine landslide and earthquake tsunami scenario study. *Pure Appl. Geophys.* 177, 1617–1638. doi:10.1007/s00024-019-02388-w

Pampell-Manis, A., Horrillo, J., Shigihara, Y., and Parambath, L. (2016). Probabilistic assessment of landslide tsunami hazard for the northern Gulf of Mexico. *J. Geophys. Res.: Oceans.* 121, 1009–1027. doi:10.1002/2015JC011261

Pantosti, D., Barbano, M. S., Smedile, A., De Martini, P. M., and Tigano, G. (2008). Geological evidence of paleotsunamis at Torre degli Inglesi (northeast Sicily), *Geophys. Res. Lett.* 35, L05311. doi:10.1029/2007GL032935

Papadopoulos, G. A., Daskalaki, E., and Fokaefs, A. (2007b). Tsunamis generated by coastal and submarine landslides in the Mediterranean Sea." in *Submarine mass movements and their consequences. Advances in natural and technological hazards research*. Editors V. Lykousis, D. Sakellariou, and J. Locat (Dordrecht: Springer), Vol. 27. doi:10.1007/978-1-4020-6512-5_43

Papadopoulos, G. A., Gràcia, E., Urgeles, R., Sallares, V., De Martini, P. M., Pantosti, D., et al. (2014). Historical and pre-historical tsunamis in the Mediterranean and its connected seas: geological signatures, generation mechanisms and coastal impacts. *Mar. Geol.* 354, 81–109. doi:10.1016/j.margeo.2014.04.014

Papadopoulos, G. A., Lobkovsky, L. I., Mazova, R. Kh., Garagash, I. A., Karastathis, V., Kataeva, L. Yu., et al. (2007a). Numerical modeling of sediment mass sliding and tsunami generation: the case of February 7, 1963, in Corinth Gulf, Greece. *Mar. Geodes.* 30, 315–331. doi:10.1080/01490410701568541

Paparo, M. A., and Tinti, S. (2017). Analysis of seismic-driven instability of Mt. Nuovo in the Ischia Island, Italy. *Bull. Seismol. Soc. Am.* 107 (2), 750–759. doi:10.1785/0120160139

Paparo, M. A., Armigliato, A., Pagnoni, G., Zaniboni, F., and Tinti, S. (2017). Earthquake-triggered landslides along the Hyblean-Malta Escarpment (off Augusta, eastern Sicily, Italy) – assessment of the related tsunamigenic potential. *Adv. Geosci.* 44, 1–8. doi:10.5194/adgeo-44-1-2017

Ridente, D., Fracassi, U., Di Bucci, D., Trincardi, F., and Valensise, G. (2008). Middle Pleistocene to Holocene activity of the Gondola fault zone (Southern Adriatic Foreland): deformation of a regional shear zone and seismotectonic implications. *Tectonophysics* 453, 110–121. doi:10.1016/j.tecto.2007.05.009

Rodriguez, M., Maleuvre, C., Jollivet-Castelot, M., d'Acremont, E., Rabaute, Al., Lafosse, M., et al. (2017). Tsunamigenic submarine landslides along the Xauen–Tofiño banks in the Alboran Sea (WesternMediterranean Sea). *Geophys. J. Int.* 209, 266–281. doi:10.1093/gji/ggx028

Rovere, M., Gamberi, F., Mercorella, A., and Leidi, E. (2014). Geomorphometry of a submarine mass-transport complex and relationships with active faults in a rapidly uplifting margin (Gioia Basin, NE Sicily margin). *Mar. Geol.* 356, 31–43. doi:10.1016/j.margeo.2013.06.003

Sawyer, D. E., Reece, R. S., Gulick, S. P. S., and Lenz, B. L. (2017). Submarine landslide and tsunami hazards offshore southern Alaska: seismic strengthening versus rapid sedimentation, *Geophys. Res. Lett.* 44, 8435–8442. doi:10.1002/2017GL074537

Shipboard Scientific Party (1996). "Site 963," in Proceedings of the ocean drilling program, initial reports, Editor K.-C. Emeis, Robertson A. H. F., Richter C., M.-M. Blanc-Valleron, I. Bouloubassi, H.-J Brumsac, et al. (Houston, TX: Texas A&M University), 160, 55–84. doi:10.2973/odp.proc.ir.160.104.1996

Smedile, A., Molisso, F., Chagué, C., Iorio, M., De Martini, P. M., Pinzi, S., et al. (2020). New coring study in Augusta Bay expands understanding of offshore tsunami deposits (Eastern Sicily, Italy). *Sedimentology* 67, 1553–1576. doi:10.1111/sed.12581

Solheim, A., Bryn, P., Sejrup, H. P., Mienert, J., and Berg, K. (2005). Ormen Lange—an integrated study for the safe development of a deep-water gas field within the Storegga slide complex, NE Atlantic continental margin; executive summary. *Mar. Petrol. Geol.* 22, 1–9. doi:10.1016/j.marpetgeo.2004.10.01

Tappin, D. R. (2010). "Mass transport events and their tsunami hazard." in *Submarine mass movements and their consequences. Advances in natural and technological hazards research*. Editors D. C. Mosher, et al. (Dordrecht: Springer), Vol. 28. doi:10.1007/978-90-481-3071-9_54

Tappin, D. R., Watts, P., and Grilli, S. T. (2008). The Papua New Guinea tsunami of 17 July 1998: anatomy of a catastrophic event. *Nat. Hazards Earth Syst. Sci.* 8, 243–266. doi:10.5194/nhess-8-243-2008

ten Brink, U. S., Chaytor, J. D., Geist, E. L., Brothers, D. S., and Andrews, B. D. (2014). Assessment of tsunami hazard to the U.S. Atlantic margin. *Mar. Geol.* 353, 31–54. doi:10.1016/j.margeo.2014.02.011

ten Brink, U. S., Giest, E. L., and Andrews, B. D. (2006). Size distribution of submarine landslides and its implication to tsunami hazard in Puerto Rico. *Geophys. Res. Lett.* 33, L11307. doi:10.1029/2006GL026125

Tinti, S., and Manucci, A. (2008). A new computational method based on the minimum lithostatic deviation (MLD) principle to analyse slope stability in the frame of the 2D limit-equilibrium theory. *Nat. Hazards Earth Syst. Sci.* 8, 671–683. doi:10.5194/nhess-8-671-2008

Tinti, S., and Manucci, A. (2006). Gravitational stability through the limit equilibrium method revisited. *Geophys. J. Int.* 164, 1–14. doi:10.1111/j.1365-246X.2005.02796.x

Tinti, S., and Tonini, R. (2013). The UBO-TSUFD tsunami inundation model: validation and application to a tsunami case study focused on the city of Catania, *Italy. Nat. Hazards Earth Syst. Sci.* 13, 1795–1816. doi:10.5194/nhess-13-1795-2013

Tinti, S., Bortolucci, E., and Vannini, C. (1997). A block-based theoretical model suited to gravitational sliding. *Nat. Hazards* 16, 1–28. doi:10.1023/A:1007934804464

Tinti, S., Pagnoni, G., and Zaniboni, F. (2006). The landslides and tsunamis of 30th December 2002 in Stromboli analysed through numerical simulations, *Bull. Volcanol.* 68, 462–479. doi:10.1007/s00445-005-0022-9

Tinti, S., Zaniboni, F., Armigliato, A., Pagnoni, G., Gallazzi, S., Manucci, A., et al. (2007). "Tsunamigenic landslides in the western Corinth gulf: numerical scenarios," in *Submarine mass movements and their consequences III. Advances in natural and technological hazards research*. Editors V. Lykousis, D. Sakellariou, and J. Locat (Springer), Vol. 27, 405–414.

Triantafyllou, I., Zaniboni, F., Armigliato, A., Tinti, S., and Papadopoulos, G. A. (2020). The large earthquake (* M7) and its associated tsunami of 8 november 1905 in Mt. Athos, Northern Greece. *Pure Appl. Geophys.* 117, 1267–1293. doi:10.1007/s00024-019-02363-5

Trincardi, F., and Argnani, A. (1990). Gela submarine slide: a major basin-wide event in the plio-quaternary foredeep of Sicily. *Geo Mar. Lett.* 10, 13–21. doi:10.1007/BF02431017

Trincardi, F., Foglini, F., Verdicchio, G., Asioli, A., Correggiari, A., Minisini, D., et al. (2007). The impact of cascading currents on the Bari canyon system, SW-Adriatic margin (Central Mediterranean). *Mar. Geol.* 246, 208–230. doi:10.1016/j.margeo.2007.01.013

Urgeles, R., and Camerlenghi, A. (2013). Submarine landslides of the Mediterranean Sea: trigger mechanisms, dynamics, and frequency-magnitude distribution. *J. Geophys. Res.: Earth Surf.* 118, 2600–2618. doi:10.1002/2013JF002720

Urlaub, M., Talling, P. J., and Masson, D. G. (2013). Timing and frequency of large submarine landslides: implications for understanding triggers and future geohazard. *Quat. Sci. Rev.* 72, 63–82. doi:10.1016/j.quascirev.2013.04.020

Ward, S. N. (2001). Landslide tsunami. *J. Geophys. Res.* 106, 11201–11215. doi:10.1029/2000JB900450

Zaniboni, F., and Tinti, S. (2014). Numerical simulations of the 1963 Vajont landslide, Italy: application of 1D Lagrangian modelling. *Nat. Hazards* 70, 567–592. doi:10.1007/s11069-013-0828-2

Zaniboni, F., Armigliato, A., Pagnoni, G., and Tinti, S. (2014b). Continental margins as a source of tsunami hazard: the 1977 Gioia Tauro (Italy) landslide-tsunami investigated through numerical modelling. *Mar. Geol.* 357 (2014), 210–217. doi:10.1016/j.margeo.2014.08.011

Zaniboni, F., Armigliato, A., and Tinti, S. (2016). A numerical investigation of the 1783 landslide-induced catastrophic tsunami in Scilla, Italy. *Nat. Hazards* 84, 455–470. doi:10.1007/s11069-016-2461-3

Zaniboni, F., Pagnoni, G., Armigliato, A., Tinti, S., Iglesias, O., and Canals, M. (2014a). "Numerical simulation of the BIG'95 debris flow and of the generated tsunami," in *Engineering geology for society and territory – Volume 4*. Editors G. Lollino, A. Manconi, J. Locat, Y. Huang, and M. Canals Ardilas (Springer International Publishing Switzerland). doi:10.1007/978-3-319-08660-6_19

Zaniboni, F., Pagnoni, G., Gallotti, G., Paparo, M. A., Armigliato, A., and Tinti, S. (2019). Assessment of the 1783 Scilla landslide–tsunami's effects on the Calabrian and Sicilian coasts through numerical modelling. *Nat. Hazards Earth Syst. Sci.* 19, 1585–1600. doi:10.5194/nhess-19-1585-2019

Zecchin, M., Accaino, F., Ceramicola, S., Civile, D., Critelli, S., Da Lio, C., et al. (2018). The Crotone Megalandslide, southern Italy: Architecture, timing and tectonic control. *Sci. Rep.* 8, 7778. doi:10.1038/s41598-018-26266-y

Conflict of Interest: The authors declare that the research was conducted in the absence of any commercial or financial relationships that could be construed as a potential conflict of interest.

The reviewer RU declared a past co-authorship with one of the authors MR to the handling editor.

frontiers in Earth Science

ORIGINAL RESEARCH
published: 28 January 2021
doi: 10.3389/feart.2020.602462

Tsunami Hazard Evaluation for the Head of the Gulf of Elat–Aqaba, Northeastern Red Sea

Amos Salamon[1], Eran Frucht[1,2], Steven N. Ward[3], Erez Gal[2], Marina Grigorovitch[2], Rachamim Shem-Tov[4], Ran Calvo[1] and Hanan Ginat[4]*

[1]Geological Survey of Israel, Jerusalem, Israel, [2]Structural Engineering Department, Faculty of Engineering Sciences, Ben-Gurion University of the Negev, Beer Sheva, Israel, [3]Institute of Geophysics and Planetary Physics, University of California, Santa Cruz, CA, United States, [4]The Dead Sea-Arava Science Center, Mount Masada, Israel

Unique geological and seismotectonic settings may trigger a multicascading hazard and should be identified beforehand. Such is the head of the Gulf of Elat–Aqaba (HGEA) at the northeastern end of the Red Sea where its geology, tectonics, bathymetry, and earthquake and tsunami history exhibit clear potential for earthquake and submarine-landslide tsunami generation. We thus investigated the possible tsunamigenic sources in the gulf and evaluated the resulting hazard at the HGEA. First, we assembled a bathymetric grid and adopted GeoClaw software to simulate most of the earthquake-tsunami scenarios. Next, we resolved the scheme of the largest possible tsunamigenic earthquakes along the deep basins of the Gulf of Elat (GEA) and the associated Dead Sea rift valley, as well as the potential tsunamigenic submarine landslides in the HGEA. The use of GeoClaw was verified against the 1995 tsunami generated by the Nuweiba Mw 7.2 earthquake, and then operated to simulate a suite of earthquake scenarios. Results showed that the marginal faults of Elat Basin pose the highest tsunami hazard to the Israeli part of the HGEA. To better assess that hazard, we screened the geology and seismotectonics of the HGEA and found that the Elat normal fault presents the worst-case scenario for Elat city. It is capable of generating a multicascading threat of earthquake and submarine-landslide tsunami, local subsidence that can increase inundation, and above all, destructive ground motion. Scenarios of a tsunami caused by the worst-case earthquake on the Elat fault simulated by GeoClaw and Ward's (Tsunami, The encyclopedia of solid earth geophysics. 2011, 1473–1493) approach, and submarine landslide in the HGEA simulated by Wang et al.'s (Geophys. J. Int., 2015, 201, 1534–1544) 'Tsunami Squares' approach, demonstrated waves as high as 4 m along these coasts. Accordingly, we constructed a map of the evacuation zone. We also show that strong ground-shaking and retreat of the sea at the HGEA should be considered a tsunami warning, although false alarms are inevitable. Furthermore, tsunami hazard exists all along the gulf and further assessments are needed to quantify this hazard and increase awareness among the area's population.

Keywords: earthquake-tsunami, Gulf of Elat (Aqaba), landslide-tsunami, multi-hazard, tsunami evacuation zone, worst-case scenario

OPEN ACCESS

Edited by:
Jacopo Selva, Istituto Nazionale di Geofisica e Vulcanologia (INGV), Italy

Reviewed by:
Mathilde Sørensen, University of Bergen, Norway
Anita Grezio, Istituto Nazionale di Geofisica e Vulcanologia (INGV), Italy

****Correspondence:***
Amos Salamon
salamon@gsi.gov.il

Specialty section:
This article was submitted to Geohazards and Georisks, a section of the journal Frontiers in Earth Science

Received: *03 September 2020*
Accepted: *17 December 2020*
Published: *28 January 2021*

Citation:
Salamon A, Frucht E, Ward SN, Gal E, Grigorovitch M, Shem-Tov R, Calvo R and Ginat H (2021) Tsunami Hazard Evaluation for the Head of the Gulf of Elat–Aqaba, Northeastern Red Sea. Front. Earth Sci. 8:602462. doi: 10.3389/feart.2020.602462

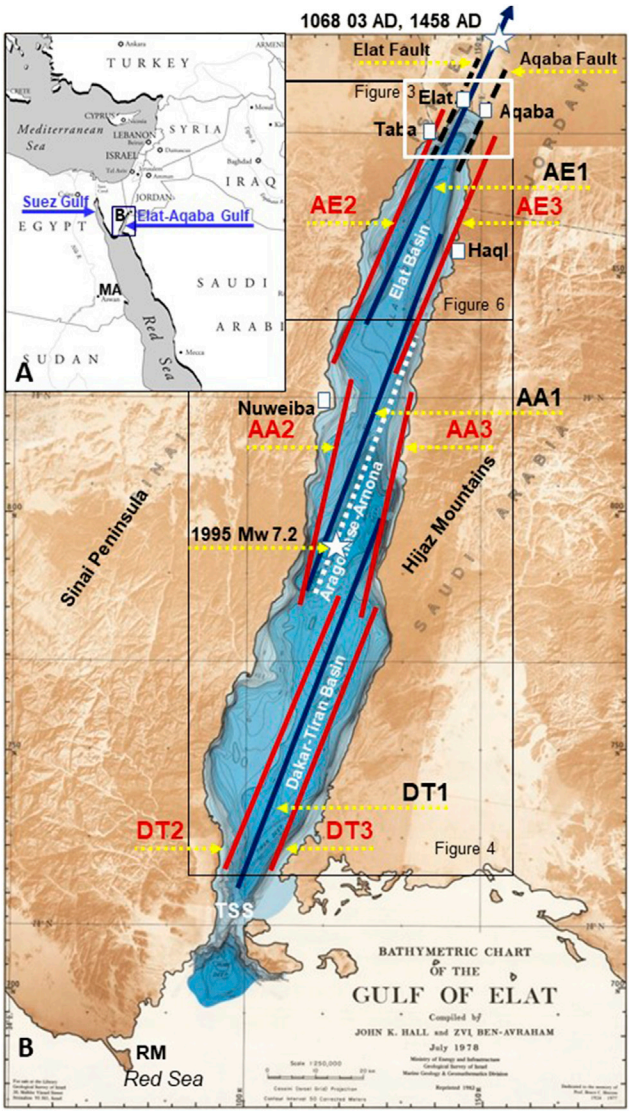

FIGURE 1 | Location maps of the study area. The white rectangle marks the Head of the Gulf of Elat-Aqaba (HGEA). **(A)** General setting (modified from https://www.freeusandworldmaps.com/index.html). MA, Marsa Alam. **(B)** Tectonic scheme of the potential tsunamigenic structures of the Gulf of Elat–Aqaba superimposed on the geography and bathymetry map (modified from Hall and Ben-Avraham, 1978). Black lines, schematic trace of the Dead Sea Transform by segments: Elat-Aqaba (AE1), Aragonese-Arnona (AA1) and Dakar-Tiran (DT1). Dark red lines, assumed western (AE2, AA2, DT2) and eastern (AE3, AA3, DT3) marginal faults of the basins. Dashed black lines, Elat and Aqaba faults. White dashed line, 1995 Nuweiba earthquake rupture (from Baer et al., 2008). Stars, epicenter of strong earthquakes; RM, Ras Muhammad; TSS, Tiran-Sharm El Sheikh Straits. The rectangles delimit the location of **Figures 3**, **4**, and **6**.

INTRODUCTION

Some recent catastrophic tsunamis have occurred in unexpected settings that were misinterpreted or overlooked by existing early warning procedures and surprised the population. Such were, for example, the sudden 1998 Papua New Guinea tsunami that followed a nearby seismogenic submarine landslide (Synolakis et al., 2002), the multiple cascading earthquake and tsunami hazards triggered by the 2018 Sulawesi strike-slip earthquake that severely affected Palu Bay (Goda et al., 2019), and the tsunamigenic collapse of the Anak Krakatoa emerging volcano (Walter et al., 2019). The high toll of casualties and the unique geological, seismotectonic and geographical setting of such events have attracted comprehensive reviews (e.g., Okal, 2015) and investigations dedicated to understanding unconventional mechanisms and configurations of tsunami generation: for example, tsunami earthquakes (Polet and Kanamori, 2016), the frequent appearance of tsunamis generated by seismogenic submarine landslides (Salamon and Di Manna, 2019), and tsunamis associated with strike-slip earthquakes (e.g., Imamura et al., 1995; Frucht et al., 2019).

Moreover, remote and pastoral coasts with short documented history may seem to be safe from tsunamis, but if they are in

active seismotectonic regions, tsunami hazard should not be overlooked. Such is the Gulf of Elat–Aqaba (GEA) at the northeastern end of the Red Sea (**Figure 1**), which is the focus of this research. The GEA is a deep water body that stretches along the southern segments of the Dead Sea Transform (DST) fault and rift system (e.g., Bartov et al., 1980; Garfunkel, 1981; Ben-Avraham et al., 2008; Ben-Avraham et al., 2012), between the Arabian plate to the east and the Sinai subplate to the west. Since the DST has already produced strong and destructive earthquakes (e.g., Salamon et al., 1996; Salamon et al., 2003, and references therein), it should also be considered capable of generating tsunamis in the GEA. Indeed, the Nuweiba Mw 7.2 earthquake in 1995—the strongest event recorded along the DST in modern times—did produce a tsunami in the GEA (Frucht et al., 2019, and references therein). Today, the head of the GEA (HGEA), which is occupied by Egypt, Israel, Jordan and Saudi Arabia, is undergoing intensive development of residential districts, infrastructure facilities, and international tourist resorts with inner lagoons and large hotels. Realizing that this is a unique setting of a transform in a marine environment with the potential of generating both earthquake and submarine-landslide tsunamis, we initiated a tsunami hazard evaluation for the HGEA to characterize the hazard and assess its potential severity.

The characterization of earthquake source parameters for tsunami modeling is associated with large unknowns, complexities and uncertainties, especially in areas where the geology and seismotectonics are not fully known or understood (e.g., Selva et al., 2016; Geist et al., 2019). Although location, geometry and tectonic deformation are necessary for tsunami simulation, they need to be simplified where data are limited (e.g., Basili et al., 2013). Furthermore, rupture properties of magnitude and slip for a given fault for which there are no data on past earthquake activity have to rely on empirical scaling relations from elsewhere (e.g., Wells and Coppersmith, 1994; Thingbaijam et al., 2017). Above all, mechanical properties, rupture dynamics, complexities and heterogeneities that are necessary for realistic modeling of sea floor coseismic deformation, are associated with large uncertainties (e.g., Geist and Oglesby, 2014) and require large modeling resources.

Landslide-tsunami modeling is no less difficult. Although it is common to assume that the volume of a slide is the most influential factor (Ward, 2001), Løvholt et al. (2017) showed that under certain circumstances, smaller landslides can generate larger tsunamis than those generated by larger landslides. It is thus important to know beforehand the mechanical properties of the sliding materials that control landslide kinematics for realistic modeling (e.g., Harbitz et al., 2014; Kim et al., 2019), but these are largely unknown. Recent comprehensive reviews (e.g., Huhn et al., 2019; Løvholt et al., 2020) discuss the need for a probabilistic framework to consider both aleatory and epistemic uncertainties in tsunami hazard analysis.

The scope of this work, however, is limited to a preliminary investigation based on the available data and expert judgment where needed, with the understanding of the need for a complementary probabilistic assessment in the future.

The Gulf of Elat–Aqaba

Topography, Bathymetry and Geography

The GEA is 180 km long and 15–25 km wide, extending NNE from the northern end of the Red Sea at its junction with the Gulf of Suez (**Figure 1**). The water depth in this narrow and elongated gulf is about 900 m, reaching 1,850 m in some places. The marginal slopes of the GEA are steep, both offshore in the gulf and on land, where the nearby mountains of Sinai to the west and Hijaz to the east rise steeply to about 1,000 m above sea level (masl). The southernmost point of the GEA connects with the Red Sea through the Tiran-Sharm El Sheikh Straits and with the Gulf of Suez near Sharm El Sheikh at the southernmost tip of the Sinai Peninsula. The northern end of the bay is the HGEA, which is the focus of this work; it is about 5–8 km wide and 8–10 km long, altogether ~50 km^2 (Tibor et al., 2010). The bathymetry of the HGEA consists of a narrow, 100-m wide shelf in the north, a much narrower shelf in the west, and almost no shelf in the east. Toward the central Elat (Eilat) Basin, the narrow shelves change abruptly into steep slopes and impressive submarine canyons of about 700 m depth (Ben-Avraham and Tibor, 1993; Sade et al., 2008). The slopes are spotted with fresh scars and collapsed materials (Tibor et al., 2010), implying submarine landslides, which may be tsunamigenic. Based on underwater drill cores, Kanari et al. (2014) and Ash-Mor et al. (2017) suggested correlating such landslides with the strong 1068 AD and 1458 AD earthquakes along the DST.

The northwestern and northeastern coasts of the HGEA are densely populated, with the Israeli city of Elat and the Jordanian city of Aqaba. The cities of Taba (Egypt) and Haql (Saudi Arabia) are located on the western and eastern HGEA coasts, respectively.

Geology and Seismotectonics

The GEA is a fault-controlled depression that consists of a series of three deep basins that have formed along the southern part of the DST since the Early Miocene (Ben-Avraham et al., 1979; Ben-Avraham, 1985; Ben-Avraham and Tibor, 1993; Ben-Avraham et al., 2012). The basins follow left-wize segmentation of the left-lateral DST in the form of a leaky transform (Garfunkel, 1981) that has reached a total offset of about 105 km (Quennell, 1959; Freund et al., 1968; Garfunkel, 2014; and others) and that opens as wide as 20 km in the south (Bartov et al., 1980; Garfunkel, 1981; and others). Southward, the DST meets the Red Sea and Suez Gulf rifts at a triple junction that connects the plates of Africa and Arabia with the Sinai subplate.

The long-term geological activity along the southern DST has resulted in a left lateral motion of 5 mm/year and an extension of about 0.5 mm/year (Garfunkel, 2014). Geodesy measurements show that the short-term rate of motion is consistent with its long-term rate (Hamiel et al., 2018), but emphasize the enigmatic deficit of seismic moment release that is reflected in historic and modern earthquake activity (Garfunkel, 1981; Salamon et al., 1996). The HGEA at the northernmost part of the Elat Basin is bounded by the Elat normal fault on the west, the Aqaba normal fault on the east, and several secondary faults in between (Hartman et al., 2014). The other basins, Aragonese-Arnona in the center of the gulf and the southernmost Dakar-Tiran,

are also bounded by a series of normal faults on their margins (Figure 11 in Ben-Avraham et al., 1979). Such an active seismotectonic configuration associated with a deep water body should clearly be considered tsunamigenic.

Seismicity along the GEA has been well documented since the 1980s, including several intensive swarms and the strong Mw 7.2 earthquake (**Figure 1B**) on November 22, 1995 (Hofstetter et al., 2014). Shapira and Hofstetter (1993, 2002) estimated that the return period of $M \geq 6$ earthquakes at the HGEA and along the Aragonese fault is about 460 years each, and about 300 years along the Arnona fault. Amit et al. (1999) estimated a minimal return period of $M > 6.5$ earthquakes along the Dead Sea fault across the Avrona (Evrona) Playa of about 2,000 years.

Pre-instrumental activity is known from historical events—the March 1,068, 1,212 and 1,458 AD earthquakes (Zohar et al., 2016, and references therein)—and these were verified by paleoseismic evidence to have ruptured the DST on land in the southern Arava Valley (Amit et al., 1999; Zilberman et al., 2005; Klinger et al., 2015). Based on paleoseismology, Klinger et al. (2015) and Lefevre et al. (2018) suggested that the 114 and 363 AD historical events also ruptured the surface there (in their opinion, another 363 AD event occurred in the north, along the Jordan Valley), as well as two other events unknown to history, in the fourth century BC and the eighth century AD. Paleoliquefaction evidence near Elat and Aila (a historic city, where Aqaba now sits) (Al-Homoud and Tal, 1998; Kanari et al., 2014) supports the presence of such activity. The long-term Holocene activity along the Evrona strike-slip fault (the DST segment in the southern Arava Valley) is estimated by Hartman et al. (2014) to be 2.3–3.4 mm/year. In their opinion, the rate of motion along the Elat fault (EF) is 1 and 0.4 mm/year along the Aqaba fault, both in a normal sense of motion.

Late Pleistocene events, 80K–20 K years BP, are known from paleoseismology to have occurred along the western margins of the DST rift (Amit et al., 2002). The findings show surface offsets of 1–1.5 m that imply M 6.7–7 events, and return periods of ~2,800 years (deviation 700 years). Over the last 20 K years, the offsets have become smaller—0.2–1.3 m, indicating weaker events in the range of M 5.9–6.7, while the return period has increased to ~1,200 years (deviation of 300 years).

Tsunami Reports and Evidence

The record of tsunamis in the HGEA is limited to a few events, some of them equivocal. Shaked et al. (2004) suggested that a sediment outcrop that is ~2,300 years old near Elat is a tsunamite. Goodman-Tchernov et al. (2016) interpreted evidence from two cores offshore of the HGEA as a record of a major paleotsunami that also occurred ~2,300 years ago. It is not clear whether the two findings relate to the same event. The historical accounts of a tsunami associated with the 1068 AD earthquakes are debated. Guidoboni and Comastri (2005) suggested that the tsunami occurred in the Mediterranean Sea in association with the earthquake of May 1,068 in central Israel, whereas Ambraseys (2009) argues that the available information does not allow pinpointing the exact location of the tsunami. In modern times, Ben-Menahem (1991) mentioned that the "*Sea at Eilat Gulf became stormy*" after the Shadwan M_L 6.8 earthquake that occurred where the Red Sea meets the Gulf of Suez, outside the GEA. The 1995 tsunami, however, was the first to have been recorded in the GEA (Wust, 1997; Frucht et al., 2019). The last report regards a 5-cm wave that was observed in Elat after the December 2004 Indian Ocean tsunami (Eng. S.D. Rosen, personal communication, 2017).

Indirect evidence of past tsunamis might be the finding of submarine mass-transport deposits in two different marine boreholes at the HGEA (Kanari et al., 2014; Ash-Mor et al., 2017). The two studies suggest a correlation between the submarine landslides and paleo and historic (1068 AD and 1458 AD) earthquakes. It is reasonable to assume that these slumps were tsunamigenic. Another study by Salem (2009) proposes some deposits near the city of Marsa Alem along the Egyptian coast of the Red Sea as evidence of a paleo tsunami.

METHODOLOGY

To achieve the goal of this research—understanding the potential of tsunami generation and the resulting hazard in the HGEA—we established the phases of our study as follows (**Figure 2**):

I Study the area and collect data: geography, geology, seismotectonics and bathymetry of the GEA, and a literature search for past tsunami evidence. This part was described in the introduction; Identify the potential tsunamigenic sources in the GEA, mainly earthquakes and submarine landslides, characterize their areal spread, geometry and magnitudes, and estimate the repeat times (*Potential Tsunamigenic Sources in the Gulf of Elat–Aqaba*); Formulate the potential tsunamigenic earthquakes and submarine landslides (*Potential Tsunamigenic Sources in the Gulf of Elat–Aqaba*).

II Build tsunami-propagation-modeling capacity, construct topographic and bathymetric grids for simulation (*Building Modeling Capability*).

III validate suitability of the adopted simulation platform against the real case of the 1995 M 7.2 Nuweiba earthquake and tsunami (*Testing the Modeling Capacity–The 1995 Nuweiba Tsunami*).

IV Simulate the potential earthquake scenarios, retrieve hazard parameters, such as arrival times and wave heights and identify the actual worst case scenario (*Tsunami Scenarios*).

V Evaluate the hazard and assess maximal wave heights, potential inundation, repeat times, construct map of evacuation zone, warning signals etc., (*Discussion*)

VI Conclude and recommend implementation of the outcomes, in terms of maximal wave height at the coast, return period of the worst-case scenario (WCS), evacuation zone, and early warning principles (*Conclusions and Recommendations*).

A similar methodology was found applicable and useful for tsunami hazard evaluation along the Mediterranean coast of Israel (Salamon et al., 2007; Salamon et al., 2010; Salamon, 2011), based on which Israel formulated its policy for warning principles and frame of preparedness (Salamon et al., 2014). The present evaluation is in line with this policy.

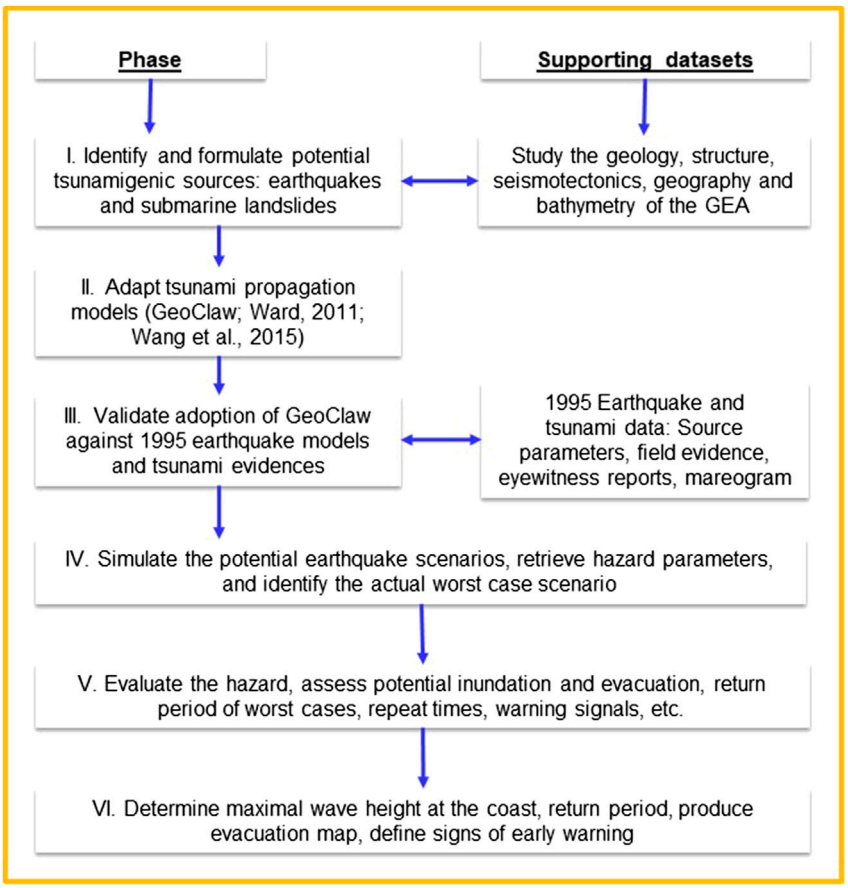

FIGURE 2 | Work plan and phases of the research. The hazard assessment focused on the Israeli coast of the head of the Gulf of Elat–Aqaba (HGEA).

Building Modeling Capability

Modeling capability was based on the adoption of a tsunami wave-propagation platform, construction of a topographic and bathymetric grid of the area of interest, and benchmark validation.

Tsunami Wave Propagation

The GeoClaw tsunami-modeling platform, which is part of the Clawpack Package (LeVeque, 2006; Clawpack Development Team, 2017), was selected to conduct most of the numerical simulations of earthquake-tsunami scenarios in the GEA. The GeoClaw is an open-source model that has already been validated worldwide and applied in numerous peer-reviewed publications (http://www.clawpack.org/geoclaw.html). The US Federal Emergency Management Agency (FEMA) has recognized GeoClaw as a suitable open-source alternative for its existing tsunami risk software platform (FEMA, 2017). In Israel, the Oceanographic and Limnological Research Institute (IOLR) and the Geological Survey of Israel (GSI) have adopted GeoClaw to conduct several projects (e.g., Galanti and Salamon, 2017).

GeoClaw solves the shallow water equations, a nonlinear system of hyperbolic conservation laws for depth and momentum, for two lateral space dimensions (**Eqs 1–3**) using finite-volume methods.

$$h_t + (hu)_x + (hv)_y = 0 \tag{1}$$

$$(hu)_t + \left(hu^2 + \frac{1}{2}gh^2\right)_x + (huv)_y = -ghB_x - Du \tag{2}$$

$$(hv)_t + \left(hv^2 + \frac{1}{2}gh^2\right)_y + (huv)_x = -ghB_y - Dv \tag{3}$$

$$D(h,u,v) = \frac{gM^2}{h^{5/3}}\sqrt{u^2+v^2} \tag{4}$$

where $h\ (x, y, t)$ is the fluid depth/thickness, and the two depth-averaged horizontal velocity components are $u\ (x, y, t)$ (eastward) and $v\ (x, y, t)$ (northward). $B\ (x, y, t)$ represents the varying topography (also referred to as bathymetry), g is the gravitational constant and $D\ (h, u, v)$ is the drag coefficient (**Eq. 4**), given by Berger et al. (2011). M is the Manning coefficient, taken as 0.0025 (Te Chow, 1959).

The coseismic deformation that displaces the water and initiates the tsunami waves was modeled according to Okada's (1985, 1992) approach which is now part of GeoClaw.

GeoClaw computation uses Adaptive Mesh Refinement (AMR), which is an efficient way to achieve high accuracy in

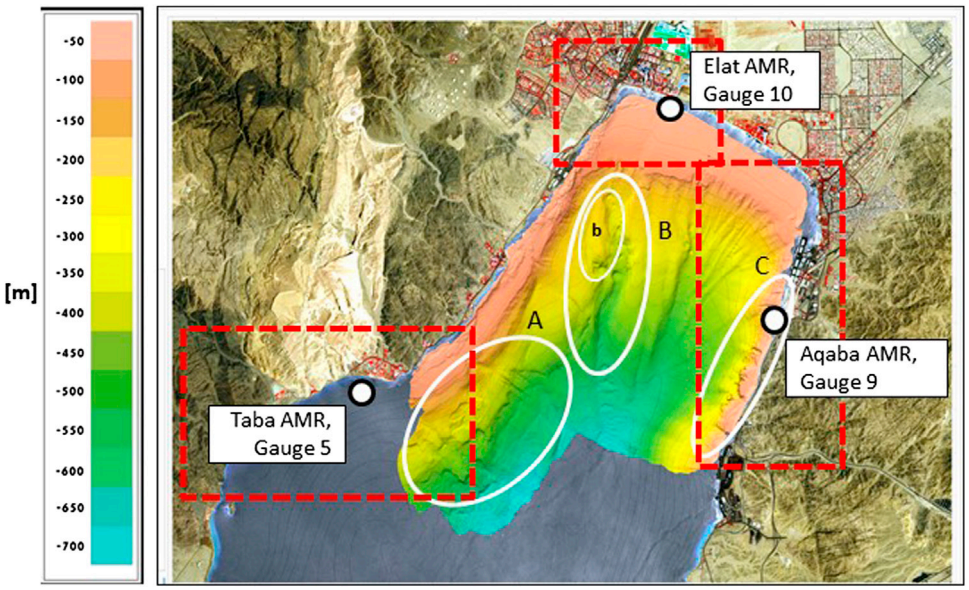

FIGURE 3 | Zones of past submarine slope failure projected on the multibeam bathymetric map of the head of the Gulf of Elat–Aqaba (HGEA) (after Sade et al., 2008). Note the three zones of submarine slope failure—**(A)**–**(C)**—and the potential area of the largest slide—b. Note also the location of the three artificial tide gauges used to record the waveforms presented in **Figure 5**. See **Figure 1** for the location of this map.

areas of interest if computation resources and time are limited. For our purposes, we constructed three AMR domains that were derived from the main GEA grid (**Figure 3**). The resolution level of the main grid is 1,539.2 m cells and the local, finest AMRs of Taba, Elat and Aqaba domains are 48.1 m cells. In addition, the run time of each scenario was limited to simulate the first 100 min of the event.

Elat Fault scenario was simulated also by the 'Tsunami Squares' approach (background and detailed formulation in Ward, 2011, Wang et al., 2015, and Xiao et al., 2015) which is a variant of the "Tsunami Balls" (Ward and Day, 2008). This method is capable of simulating propagation of tsunami waves, overland floods, inundation, dam breaks, lava flows, and more. In 'Tsunami Squares', the computational space is divided into a set of N square cells with chosen dimension. At time t each cell holds water with mean horizontal velocity and mean horizontal acceleration. The wave propagation is calculated by updating those conditions to time $t + dt$. The generation mechanism of the tsunami can be obtained by the No Momentum Transfer (NMT) approach (Xiao et al., 2015). This method is useful for simulating earthquake-tsunami or long run out submarine landslides. In NMT, seabed topography becomes time dependent and the water in each cell are vertically lifted up or dropped down accordingly. Gravity acts on the disturbed water surface, but no momentum is transferred in the lifting itself.

The landslide-tsunami was also simulated by the 'Tsunami Squares' approach that is able to simulates generation, propagation and resting of flow-like landslides. The sliding material is represented by squares that are accelerated downward by gravity and decelerated by basal and dynamic friction. While sliding, the squares are displaced and fractured into new squares again and again, but conserve the initial volume and linear momentum of the collapsed material. This procedure "takes into account of solid/fluid mechanics and particle interactions by updating velocities through the slope of the top or bottom surfaces of the flow" and "it incorporates entrainment and deposition into landslide modeling" (Wang et al., 2015).

In all methods, we regarded the GEA as a closed water body and thus saved, for simplicity, the need to calculate the incoming and outgoing waves through the southern narrow straits of Tiran-Sharm El Sheikh.

Bathymtric Grid of the Gulf of Elat–Aqaba

The GEA topographic and bathymetric grid was based on NASA's 30 m digital elevation model (DEM) (https://gdex.cr.usgs.gov/gdex/, last accessed 2017, now retired) of the land and sea areas. A 200 m DEM of the HGEA (Sade et al., 2008) was also used, along with many seagrass elevation measurements (5–15 m apart; Winters et al., 2017). The various nets were assembled and restructured into a 30 m cell-size grid, converted into the WGS84 geographical coordinate system, and then unified. The coseismic deformation calculated by the Okada model was based on a 460 m^2 cell grid.

Testing the Modeling Capacity–The 1995 Nuweiba Tsunami

The wealth of data available on the tsunami that followed the Nuweiba, Mw 7.2 strike-slip earthquake in 1995 (**Figure 1B**) allowed us to test our adopted GeoClaw computational platform. We examined which of the 1995 Nuweiba seismological and InSAR earthquake models was able to replicate and better match

the existing eyewitness accounts of an up to 1 m wave rise and drop along Elat coast, minor inundation that flooded local nomad dwellings and left some driftwood and beach waste along several coasts, limited damage in Nuweiba and Aqaba ports, and the analog mareogram recorded in Elat Port. Overall, the simulations correlated reasonably well with the existing reports, field evidence, and the arrival time, amplitude and wave period recorded by the mareogram. Thus, we were able to validate the computational platform, assumptions and approximations, verify that they do not bias the results, and consider our simulations reliable. A detailed description of this process appears in Frucht et al. (2019).

POTENTIAL TSUNAMIGENIC SOURCES IN THE GULF OF ELAT–AQABA

Aside from the source of the 1995 Nuweiba earthquake and the other segments of the DST, all of the largest active seismotectonic elements within the GEA that are capable of generating $M > 6$ earthquakes are potentially tsunamigenic due to the coseismic deformation that they can induce inside the water body. The steep bathymetric slopes in the HGEA that are dotted with numerous scars are also suspected of releasing tsunamigenic failures.

Earthquakes

While the structural scheme of the GEA's three basins is fairly well-known (Ben-Avraham et al., 1979; Hartman et al., 2014), the seismotectonic framework of its margins is not sufficiently recognized. The most significant shortcoming is the lack of information regarding the faults that form the rift valley and rise of the Sinai and Hijaz mountains on its margins. Whereas Reches et al. (1987) and Hartman et al. (2014) delineated the Elat and Aqaba faults along the western and eastern HGEA margins, there is no information on equivalent structures along the central and southern parts of the GEA. These tectonic elements are necessary to complement the pattern of potential tsunamigenic earthquake sources. To overcome this gap of knowledge and within the given scope of this work, we generalized the tectonic framework of the GEA and reduced it to three large basins (**Figure 1B**: Elat, Aragonese-Arnona, and Dakar-Tiran), with each basin associated with a main segment of the DST and two normal faults along its margins, one on the west and the other on the east. The marginal faults represent the tectonics of both the deep basins within the GEA and the shoulders of the rift valley. As such, they represent the largest possible earthquakes along the GEA margins (the DST can generate even stronger events) and are suitable for the largest earthquake-tsunami scenarios. Secondary faults are smaller and less effective in generating significant coseismic deformation and strong ground motion, and thus can be examined at later stages.

The pattern of the potential tsunamigenic sources in the HGEA region is better known. It is based on previous geological and tectonic field and marine work and maps (e.g., Ben-Avraham et al., 1979), on extrapolation of the trace of the main faults from land into the sea (Tibor et al., 2010; Hartman et al., 2014), and on the location of the steep bathymetric slopes along the basin margins (**Figures 1B**, **3**).

The Modeled Earthquakes

Following the conceptual structure of the GEA and the associated rift valley, we considered three basins and ascribed to each of them its relevant DST segment and two marginal faults on its western and eastern boundaries. All in all, we modeled nine tsunamigenic sources and assigned their seismogenic parameters on the basis of existing field evidence and research findings as follows (**Table 1**, **Figure 1B**):

- The basins are, from north to south, Elat (abbreviated AE), Aragonese-Arnona (AA) and Dakar-Tiran (DT).
- The three DST segments are annotated '1' (AE1, AA1 and DT1); their mechanism is left-lateral strike slip (LL, rake is 0). Regarding the dip, we followed Baer et al. (2008) who determined the source parameters of the 1995 Nuweiba earthquake that ruptured AA1, and Ben-Avraham (1985), who studied the structural framework of the GEA. Overall, AE1 was assigned 65°E, AA1 65°W, and DT1 65°E.
- The western marginal faults are annotated '2' (AE2, AA2 and DT2), located west of the DST segments inside the gulf; their mechanism is normal (*N*) and the dip is 60° which is typical of normal faults, to the east (E).
- The eastern marginal faults are annotated '3' (AE3, AA3 and DT3), located east of the DST segments inside the gulf; they are normal (N) and dip 60°W.
- The length of the marginal faults accord with the length of the basins, 60 km for AE and DT and 50 km for the shorter AA basin. The DST segments extend outside the basins toward the nearby structure and thus are longer. AE1 is 80 km, extending northwards to the Arava Valley, AA1, which connects with Elat Basin, is also 80 km, and DT1, which connects to Tiran-Sharm El Sheikh straits, is 85 km.
- The width of the faults in AE was set to 25 km, in accordance with the depth of the seismogenic zone in the nearby Arava Valley (Hofstetter et al., 2014). The width of the faults in the other basins (AA, DT) was set to 30 km, in accordance with the Nuweiba earthquake source parameters (Baer et al., 2008).
- The strike of the DST segments is N25E, whereas the strike of the marginal faults trends more or less NNE, in parallel with the geography of the GEA basins and coasts.
- The slip was adopted from the 'surface rupture length–maximum displacement' empirical relationships of Wells and Coppersmith (1994).
- The Mw magnitude was determined according to the length, width and slip.
- The rate of motion of the DST segments, 0.5 cm/year, reflects the relative motion of the DST. The rates of the western and eastern marginal faults follow Hartman et al. (2014), who determined 0.1 and 0.04 cm/year for the Elat and Aqaba faults, respectively.
- The Return Period was the maximal slip divided by the rate of motion.

TABLE 1 | Inventory of potential worst-case Gulf of Elat–Aqaba (GEA) earthquake scenarios used for our tsunami simulation. See *Earthquakes* for detailed explanation regarding the origin and rationale of the source parameters.

Scenario	Tectonics	Center point (Lat/Long)	Length (km)	Depth/ width (km)	Strike (deg.)	Dip (deg.) (E)	Mechanism (rake, deg.)	Slip (m)	Mw	Motion rate (cm/ year)	Return period (years)
AE1: Elat basin 1	Main transform	N 29.483; E 34.916	80	25	N25E	65	0 (LL)	5	7.6	0.5	1,000
AE2: Elat basin 2	Western margins	N 29.30; E 34.80	60	25	N25E	60	90 (N)	3	7.4	0.1	3,000
EF: Elat fault[a]	Western margin	N 29.5038; E 34.9362	20	20	N25E	75	90 (N)	3.5	7.1	0.1	3,500
AE3: Elat basin 3	Eastern margins	N 29.267; E 34.9	60	25	N20E	60	90 (N)	3	7.4	0.04	7,500
AA1: Aragonese-Arnona 1	Main transform	N 28.97; E 34.75	80	30	N25E	65	0 (LL)	5	7.7	0.5	1,000
1995 Nuweiba earthquake[b]	Main transform	N 28.97 E 34.75	58.5	30	N17.5E	67	−4 (LL)	3	7.2		
AA2: Aragonese-Arnona 2	Western margins	N 28.783; E 34.667	50	30	N10E	60	90 (N)	2	7.3	0.1	2,000
AA3: Aragonese-Arnona 3	Eastern margins	N 28.8; E 34.783	50	30	N10E	60	90 (N)	2	7.3	0.04	5,000
DT1: Dakar-Tiran 1	Main transform	N 28.5; E 34.667	85	30	N25E	65	0 (LL)	5	7.7	0.5	1,000
DT2: Dakar-Tiran 2	Western margins	N 28.4; E 34.583	60	30	N25E	60	90 (N)	3	7.4	0.1	3,000
DT3: Dakar-Tiran 3	Eastern margins	N 28.367; E 34.683	60	30	N25E	60	90 (N)	3	7.4	0.1	3,000

[a]*Realistic scenario, parameters derived from Hartman et al. (2014) and Beyth et al. (2018).*
[b]*Parameters from Baer et al. (2008).*

The modeled scenarios of the nine faults are discussed in *Tsunamigenic Earthquakes* and **Figures 4**, **5**.

Submarine Landslides

Although there is no direct evidence of a tsunami resulting from a submarine landslide in the GEA, the presence of numerous fresh scars and collapsed material along the HGEA bathymetric slopes clearly indicates such a potential (Makovsky et al., 2008; Sade et al., 2008; Tibor et al., 2010). Kanari et al. (2014) and Ash-Mor et al. (2017) identified four mass-transport deposits occurring in the past ~2,500 years in a core drilled in the submarine Elat canyon, and correlated the age of the last ones with the historical earthquakes of 1068 AD and 1458 AD. It is thus reasonable to assume that strong earthquakes in the region are capable of generating mass-transport deposits, and that future landslides may occur along unstable zones where failure has already occurred in the past. Furthermore, the GEA is located in an arid region, and the supply of sediments into the gulf is limited. Therefore, the given frequency of strong earthquakes in this region (*Return Period*) may suffice to release any load of accumulated sediment before it reaches metastable conditions and is released spontaneously. Extrapolating from the Mediterranean region and elsewhere around the world (Salamon and Di Manna, 2019), the threshold earthquake magnitude for the release of a tsunamigenic submarine landslide would be somewhat below M ~ 6 with a low probability, but the likelihood increases with the magnitude (Salamon et al., 2007).

The HGEA bathymetry shows several characteristics (Tibor et al., 2010):

- the shelf dips 3°–5°, is about 1 km wide in the north, several hundred meters in the west and minimal on the east
- the continental slope is much steeper and reaches 13°
- typical scars along the slope are several tens of meters wide and several tens to hundreds of meters long
- scar height is up to 20 m
- several scars are made up of combined curves, which hints at the occurrence of a complex failure or multiple events
- the failed materials are deposited below the scars and at the bottom of the slopes, to a distance of several hundred meters and even several kilometers along the Elat submarine canyon.

Following Reches et al. (1987) and Tibor et al. (2010), we recognized three main zones of slope instability in the HGEA (**Figure 3**):

- along the western slopes, below the city of Taba, at a water depth of ~200–~650 m below sea level (mbsl) ('A' in **Figure 3**)
- along the Elat submarine canyon in the northwestern corner of the HGEA, at a water depth of ~100–~700 mbsl ('B' in **Figure 3**). The largest slide in the area appears along the western bank of that canyon ('b' in **Figure 3**). The age and failure mechanism of that slide is not clear, whether by creep, fault controlled or collapse. The presence of fresh scars superimposed on top of it and the collapsed earth materials below, suggests that this mechanism has been active in recent times. Nonetheless, further investigation is needed to evaluate whether the large slide can also be activated in the future.

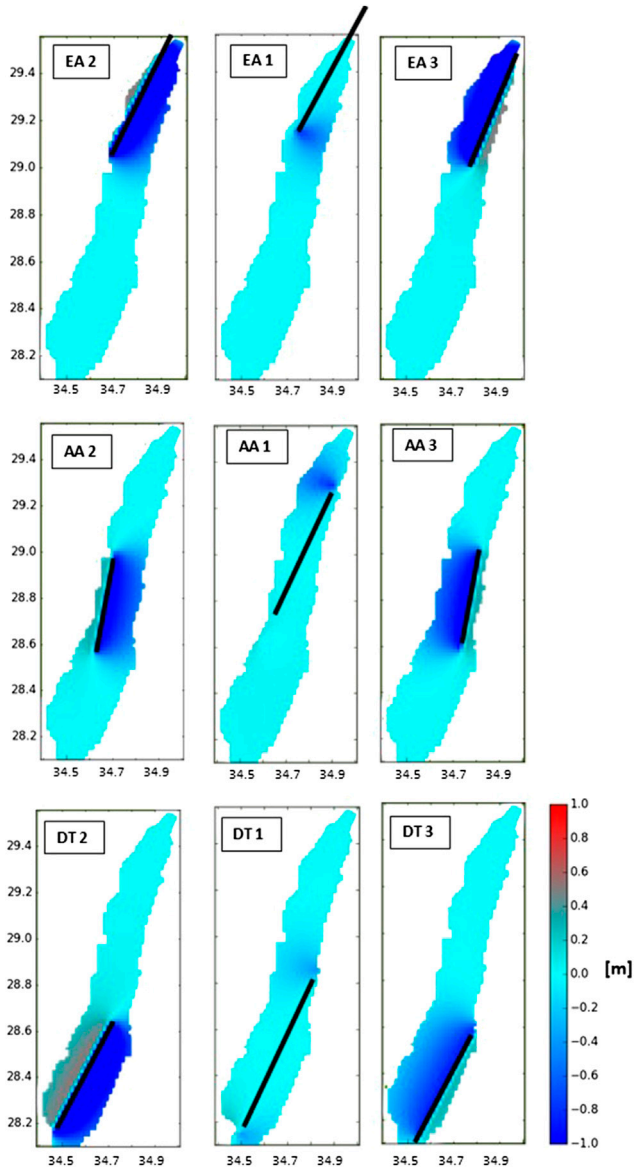

FIGURE 4 | Snapshots of the simulated scenarios that were taken 1 s into the event represent the shape of the water surface induced by the coseismic deformation at the initial stage of the tsunami. See *Earthquakes* for detailed explanation and **Table 1** for earthquake source parameters. Black lines denote the simulated faults; EA, Elat-Aqaba Basin; AA, Aragonese-Arnona Basin; DT, Dakar-Tiran Basin. Annotations 1, 2, and 3 refer to the main segment of the transform, and the western and eastern margin faults of the given basin, respectively. See **Figure 1** for the locations of these maps.

- along the eastern slopes and below the city of Aqaba ('C' in **Figure 3**). This is a very steep cliff-like slope. It continues from land into the sea with a minimal shelf. Slope failures are of the rock-fall type rather than slumps, and with smaller volume than elsewhere in the HGEA.

Table 2 summarizes the main parameters of the potential tsunamigenic submarine landslides.

The Modeled Submarine Landslide

To simplify the landslide-tsunami simulation and overcome the many unknowns in the geometrical, mechanical and hydrodynamic properties of submarine landslides that dominate the magnitude of the resulting tsunami (e.g., Ward, 2001; Løvholt et al., 2015), we focused on the largest recognizable slump in the HGEA as representing the worst case of landslide-tsunamis (**Table 2**, case 'b'). This, of course, does not exclude the need for future investigation of the complete spectrum of possible landslides along the HGEA submarine slopes.

The other missing parameters were inferred from the actual HGEA bathymetric profile, and the geometry and water depth at the initial and terminal track of the existing mass-transport deposits. Slide velocity and other mechanical properties were adopted from Ward (2001) and from Løvholt et al. (2015).

Other Tsunamigenic Sources

Other tsunamigenic sources that might affect the HGEA are considered of secondary importance. The steep topography of the Sinai and Hijaz mountains around the GEA may release subaerial tsunamigenic landslides in the manner of the Lituya Bay, Alaska event (Miller, 1960). However, preliminary screening of the on-land slopes did not reveal any mountain flanks that were vulnerable to failure with a considerable volume.

Tsunamis from afar, such as from the 1969 Shadwan earthquake in the Gulf of Suez and the 2004 Sumatra earthquake in the Indian Ocean, may have penetrated the GEA but had no significant effect (*Tsunami Reports and Evidence*). The narrow Tiran-Sharm El Sheikh straits at the southern end of the GEA seem to attenuate incoming waves. Nevertheless, further investigation is certainly needed to verify the actual contribution of subaerial landslides and remote sources to tsunami generation and propagation in the GEA.

TSUNAMI SCENARIOS

Tsunamigenic Earthquakes

The nine conceptual earthquake-tsunami scenarios originated in the three basins were simulated by the GeoClaw platform. Representative snapshots of the simulations that were taken 1 s into the event (**Figure 4**) portray the shape of the water surface induced by the coseismic deformation at the initial stage of the tsunami. The waveforms of the first 100 min (6,000 s) that were generated in Elat, Aragonese-Arnona and Dakar-Tiran basins, were recorded by three artificial tide gauges along the HGEA coasts (Taba, Elat and Aqaba, **Table 3**) and are presented in **Figure 5**. Here we briefly discuss the main outcomes of the simulations.

Dead Sea Transform Earthquake-Tsunamis

The left lateral rupture of the DST segments (AE1, AA1, DT1) in the range of Mw 7.6–7.7 causes slight subsidence at the far ends of the faults that drags the water such that the first wave spreads with a negative phase followed by a positive one. This is echoed in the HGEA gauges (**Figure 5**) by the negative phase of the first arrivals of about half a meter in Taba and Aqaba and 1 m at the most in

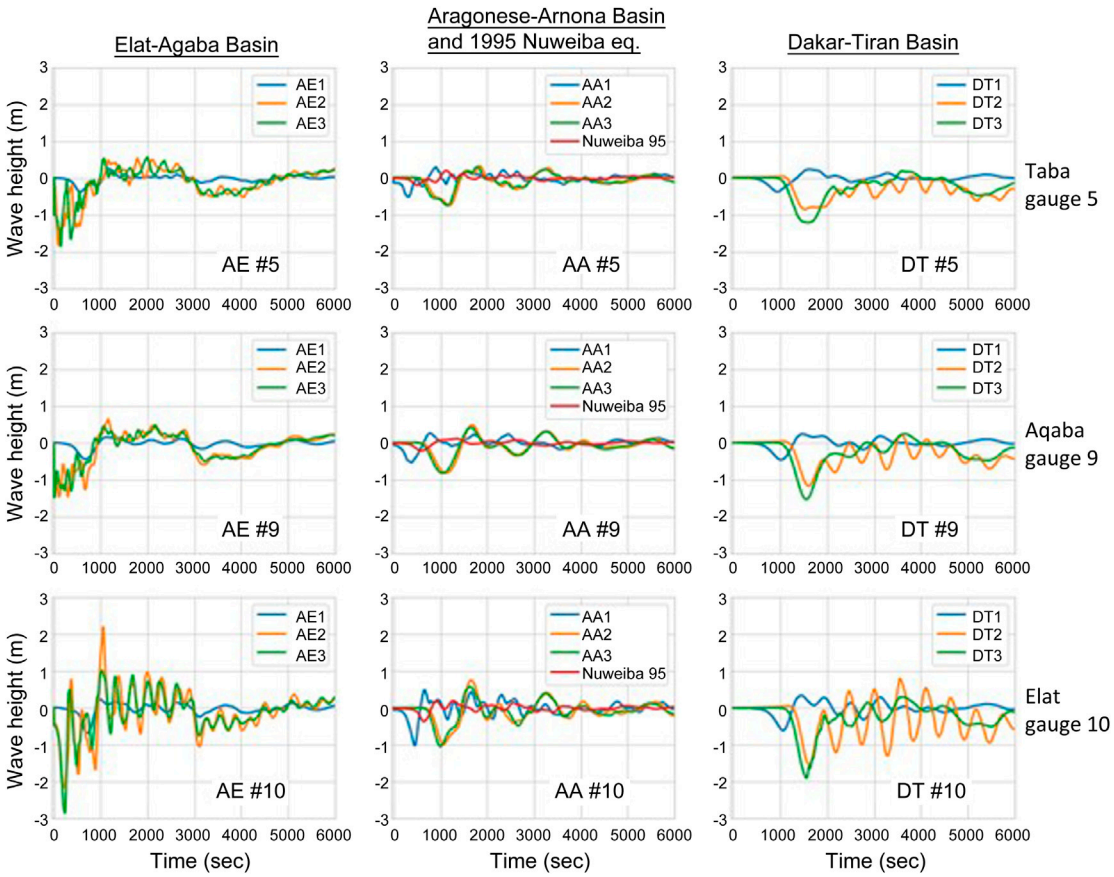

FIGURE 5 | Waveforms of the simulated tsunami scenarios recorded by artificial tide gauges in the head of the Gulf of Elat–Aqaba (HGEA) region. Each diagram presents waveforms of three scenarios simulated in the given basin (ordered by columns) as recorded by the given tide gauge (ordered by rows). The left column presents scenario waveforms propagated from Elat-Aqaba Basin (denoted AE), the central column shows waveforms generated in Aragonese-Arnona Basin (AA) and calculated waveform of the 1995 Nuweiba M 7.2 tsunami, the right column waves arriving from Dakar-Tiran Basin (DT). The rows arranged by waveforms recorded in the given gauge: upper row for Taba (#5), central for Aqaba (#9) and lower for Elat (#10).

TABLE 2 | Characteristics of potential tsunamigenic submarine landslides in the head of the Gulf of Elat–Aqaba (HGEA).

Bathymetric region	Location (Lat/ Long)		Water depth (m)	Length (m)	Width (m)	Thickness (m)	Volume (km^3)
	N	E					
Western slopes, below Taba ('A' in **Figure 3**)	29.47	34.91	250–400	500	150	20	0.0015
Elat submarine canyon ('B' in **Figure 3**)	29.52	34.96	250	250	200	20	0.001
The big slide ('b' in **Figure 3**)	29.52	34.95	200	1,600	500	40+	0.32
Eastern slopes, below Aqaba ('C' in **Figure 3**)	29.49	34.98	50	100	50	50	0.00025

Elat. The maximal amplitude of the following rise does not get larger than the first drop, and then the waves fade away slowly.

It is reasonable to assume that the AE1 scenario resembles the 1068 AD historic event that ruptured the northern part of this segment in the Arava Valley (Amit et al., 1999; Zilberman et al., 2005). In this case, the tsunamigenic trigger is the coseismic drop at the southeastern end of the segment which is located in the GEA (**Figure 5**). The waves hit Elat coast immediately after the earthquake with a drop of 70 cm and then a rise of 25 cm above the original sea level.

The southern part of the AA1 segment ruptured in 1995 (e.g., Baer et al., 2008) and generated a tsunami (Frucht et al., 2019). Therefore, the likelihood that it will rupture again in the near future is very low (**Figure 5**). The first arrivals to the HGEA start with a negative phase of about half a meter in Taba and Aqaba and of 1 m in Elat, and these are followed by a rise of about half these values within 11 min after the earthquake. The reason for the small amplitudes, even when compared to the 1995 scenario (**Figure 5**, central column) which was based on a smaller fault with a lower magnitude, is that the AA1 scenario is a pure strike-

TABLE 3 | Waveform characteristics of Elat fault scenario recorded by the three artificial tide gauges located in the head of the Gulf of Elat–Aqaba (HGEA).

Parameter					First arrival		Minima		Maxima	
G. #	Coast	Lat	Long	Depth (m)	Polarity '+' up '−' down	Emer. Time (s)	Time (s)	Amp. (cm)	Time (s)	Amp. (cm)
5	Taba	29.4848	34.8901	8	+	0	155	393	60	92
9	Aqaba	29.5005	34.9907	22	–	0	185	239	300	270
10	Elat	29.5458	34.9651	3.6	–	0	60	175	460	123

G., gauge; Emer., emergence; Amp., amplitude.

slip fault) with no vertical component (rake = 0). Nevertheless, some vertical deformation still occurs around the edges of the fault, and this is sufficient to produce some tsunami waves. The southernmost tip of the fault is close to the western GEA shores and thus most of the coseismic deformation disturbs on-land areas. The DT1 waves that are generated further south in the GEA arrive about 12 min after the earthquake (**Figure 5**) and reach an amplitude of a few tens of centimeters, mostly in the receding phase.

Marginal Basin Earthquake Scenarios

Scenarios of the marginal faults, Mw 7.3–7.4, show much higher coseismic subsidence than the DST segments at the center of the GEA (**Figure 5**). The subsidence drags the water and release higher waves with negative phase first. In each of the basins, the western marginal faults (AE2, AA2, DT2) mirror the eastern ones (AE3, AA3, DT3, respectively) in their location along the margins, strike, dip, rake and magnitude. Due to this symmetry, each pair generates about the same coseismic subsidence at the center of the GEA, and thus the waves propagating along the GEA are also almost similar in their first phase, amplitude and period. This is evidenced in the waveforms recorded by the HGEA gauges (**Figure 5**).

In the Elat gauge, the AE2 and AE3 scenarios induce instantaneous coseismic subsidence of about half a meter, associated with a sharp drop of sea level for an additional 1.5 and 2 m, respectively. The maxima arrive after several waves and reach about 2 and 1 m asl respectively, about 17 min after the earthquake. The next waves attenuate slowly with a period of ~5 min.

The first AA2 and AA3 arrivals to the HGEA gauges occur about 10 min after the earthquake, with a drop of ~1 m in Elat and ~80 cm in Taba and in Aqaba. This is followed by a rise of up to ~70 cm in Elat, and then the oscillations decrease. The average period is 13 min.

The DT2 tsunami waves reach the HGEA after 20 min with a drop in sea level of 1.2, 1.9 and 1.5 m in Taba, Elat and Aqaba, respectively. The waves continue to oscillate in a 9-min period, reach their highest level after 1 h, and then attenuate slowly. The DT3 waves arrive at the HGEA about 3 min earlier with slightly larger amplitude and longer period compared to the DT2 case (**Figure 5**), and then attenuate with time.

The Worst of the Tsunamigenic Earthquake Scenarios

The resulting waveforms of the nine earthquake scenarios (**Table 4** and **Figure 5**) show that all of the simulated waves reach the HGEA with a drop in sea level, which means a retreat of the sea. This is due to the transtensional tectonics of the GEA (leaky transform) where normal faults and strike slips induce coseismic subsidence. In all cases except for AE2, the subsequent rise does not achieve maxima larger than the preceding minima. In general, the strike-slip scenarios generate lower waves. Waves generated by the marginal faults of Elat Basin impact the HGEA immediately after the earthquake, while the first waves from the central and southern basins arrive 10 and 20 min later, respectively (**Table 4**).

Overall, the AE2 scenario produced the largest maxima in Elat (**Figure 5** and **Table 4**), more than 2 m. Furthermore, the AE2 and AE3 scenarios caused subsidence of the northernmost HGEA coasts, which, in turn, is expected to intensify the inundation. Even worse, high accelerations from AE1–3 quakes may trigger tsunamigenic submarine slope failure in the HGEA region that will add to the tsunami that has already been triggered by the earthquake. In these scenarios, however, the ground-shaking may be the dominant hazard to the northern HGEA cities, leaving the tsunami as a secondary contributor to the overall risk (see further discussion on this issue in *Elat Fault–The Worst-Case Scenario*). Therefore, we find the AE2 scenario to be the worst-case scenario for Elat city (**Table 4**) and AE3 the worst one for Aqaba city. A similar cascading suite of hazards was triggered by the 2018 Sulawesi, Indonesia, Mw 7.5 strike-slip earthquake (Goda et al., 2019), which had devastating consequences for Palu Bay. We thus searched for a comparable realistic occurrence in the HGEA region and identified the EF that stretches along the western margins of the southern Arava Valley and continues into the sea (**Figure 1B**).

Realistic Elat Fault Tsunami Scenario

Following the understanding that the EF is the actual worst-case scenario for Elat city due to its potential for generating the highest ground accelerations and the largest coseismic subsidence, we simulated the resulting earthquake tsunami as well as submarine-landslide tsunami. The EF has been mapped on land (geological map of Beyth et al., 2018, scale of 1:50,000), and in the sea (Reches et al., 1987; Hartman et al., 2014). Paleoseismic evidence show that this fault ruptured Late Pleistocene–Holocene erosion fans that descend from the Elat mountains toward the rift valley (Amit et al., 2002).

To simulate the potential impact of a tsunami generated by the EF, we determined its source parameters as follows: the length was taken from the geological and bathymetric maps (Beyth et al., (2018); Hartman et al., (2014), respectively) as 20 km. The 20-km depth to the seismogenic zone (width of the fault) was adopted

TABLE 4 | Characteristics of the resulting waveforms of the nine worst-case scenarios as recorded by the Elat artificial tide gauge (#10, **Figure 5**, lower row).

Parameter	First arrival		Minima		Maxima		Average wave length
Scenario	Polarity: '+' up '–' down	Emergence time (sec)	Time (sec)	Amp. (cm)	Time (sec)	Amp. (cm)	(sec)
AE1: Elat basin 1	–	0	700	70	980	25	~ 750
AE2: Elat basin 2	–	0	200	215	1,050	214	320
AE3: Elat basin 3	–	0	240	282	1,030	100	320
AA1: Aragonese-Arnona 1	–	100	450	100	655	50	677
AA2: Aragonese-Arnona 2	–	630	1,050	100	1,650	76	785
AA3: Aragonese-Arnona 3	–	620	990	105	1,630	57	770
DT1: Dakar-Tiran 1	–	500	1,020	50	1,440	13	700
DT2: Dakar-Tiran 2	–	1,200	1,620	170	3,560	81	547
DT3: Dakar-Tiran 3	–	1,000	1,550	190	3,600	30	767

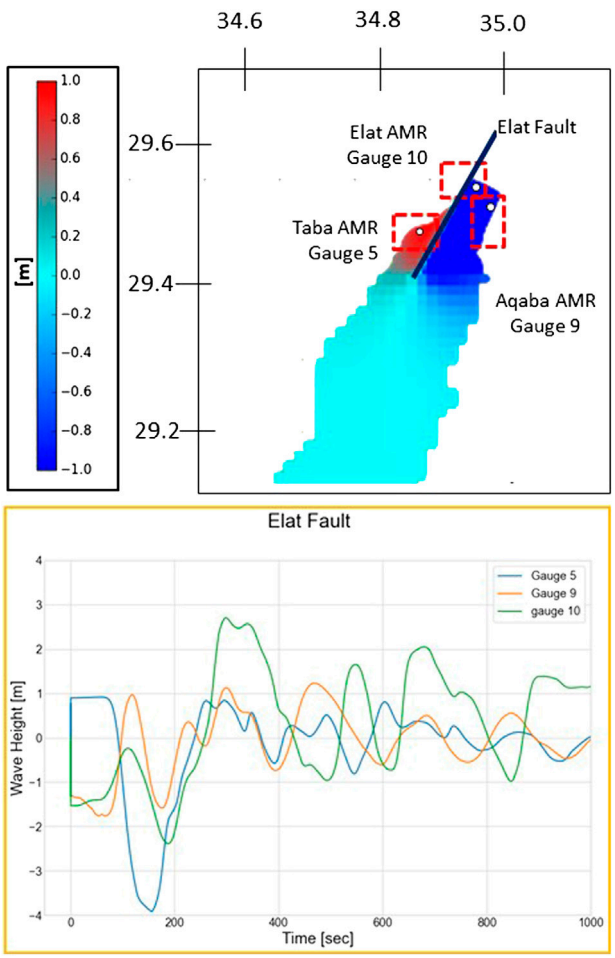

FIGURE 6 | Elat fault (EF, black line) tsunami scenario simulated by GeoClaw. See *Realistic Elat Fault Tsunami Scenario* for detailed explanation and **Figure 1** for the location. The upper figure shows a snapshot of the water surface taken 1 s after the start of the simulated event, and the lower diagram presents waveforms of the first 1,000 s as recorded by the artificial tide gauges of Taba (gauge #5), Elat (10#) and Aqaba (#9). Note the coseismic deformation effect on the tide gauges at the start of the event (time = 0): Taba (#5) goes up and Elat (#10) and Aqaba (9#) goes down. AMR locations are marked by red, dashed line squares.

from Aldersons and Ben-Avraham (2014). Hofstetter et al. (2014) proposed a 25-km depth but this is related to the DST plate border, whereas the EF is a marginal fault. The worst rupture was set to a vertical offset of 3.5 m, to reflect simultaneous rupture of several nearby parallel segments, such as was found by Amit et al. (2002). Such an offset indicates a maximal magnitude of Mw = 7.1 that satisfies the empirical relationships of maximum surface displacement with moment magnitude (Wells and Coppersmith, 1994). Given the average 1 mm/year slip rate of the EF (Hartman et al., 2014), the repeat time of the modeled scenario would be 3,500 years. The actual dip of the EF in the subsurface is not known. Consequently, we set it to 75°E to account for the worst subsidence of a normal fault.

The EF scenario was enacted using two different approaches. The first was with GeoClaw, similar to the previous scenarios. A snapshot of the first second shows a sharp drop of water east of the fault against a rise west of the fault (**Figure 6**), which is driven by the coseismic deformation. This is also reflected by the Elat gauge which shows a fast drop of about 2.5 m within 3 min after the earthquake and then an immediate rise to 2.7 masl (**Figure 6** and **Table 3**). The Taba gauge experiences a 1 m rise from the earthquake deformation and then a sharp drop to four mbsl within 2.5 min. The Aqaba gauge encounters waves that fluctuate between -1 and +1 m in the first 10 min, and then a slow attenuation.

The second approach followed Ward's (2011) methodology. At 11 min and 12 s, the waves reach 3 and 5 m along several sections of the western and eastern sides of the HGEA, respectively (**Figure 7**, red and blue lines on the right side diagram, respectively). In general, at that time, the waves along the Aqaba coast are about 2 m higher than in Elat. In Elat, the maximal wave height reaches around 4 m and the maximal current speed reaches about 2 m/s (**Figure 7**).

Overall, the GeoClaw scenario shows a maximum wave height of 2.7 m along the northern HGEA coast (Elat gauge), whereas Ward's (2011) approach results in ~4 m there. Considering that the GeoClaw wave height refers to the initial sea level datum, there is a need to add the coseismic drop of 1.5 m to get the actual wave height above ground at that gauge (**Figure 6**) That brings the GeoClaw wave height to 4.2 m, not much different from Ward's (2011) 4 m inundation at the coast.

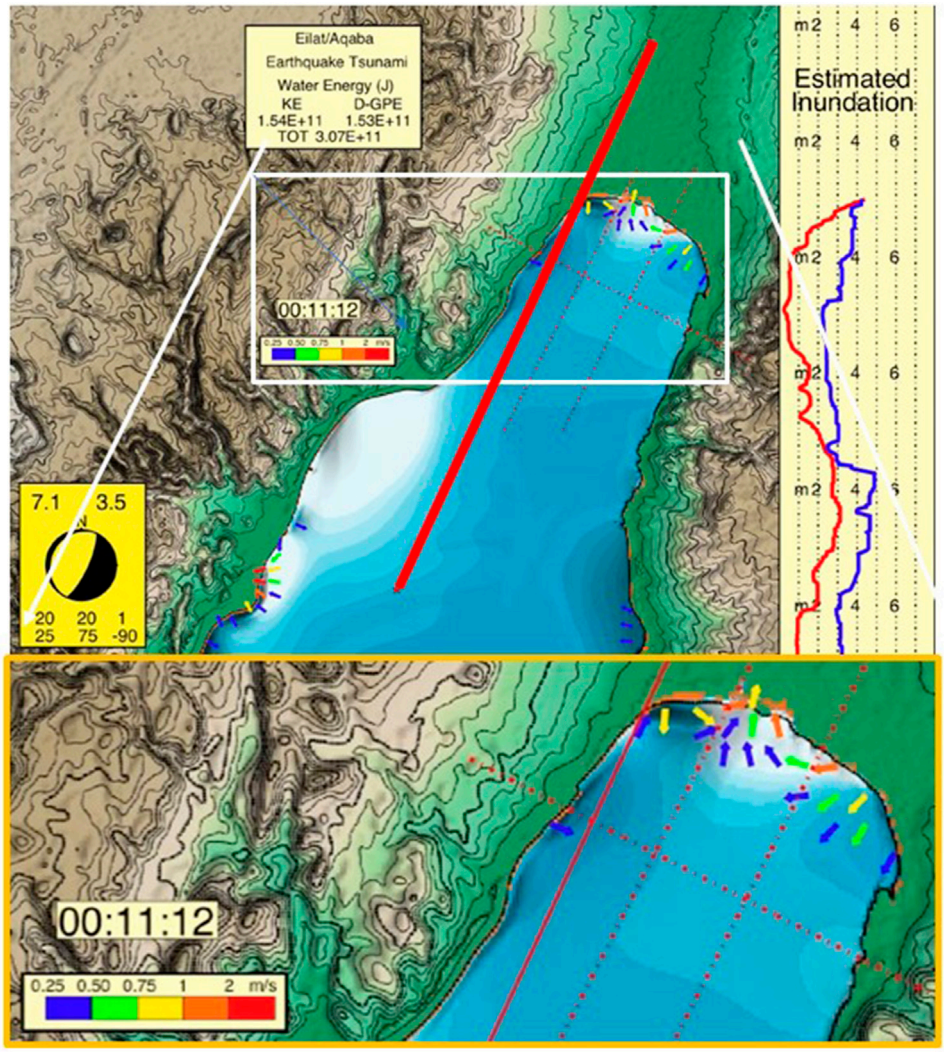

FIGURE 7 | Snapshot of the Elat fault (EF; red line) scenario at 11 min and 12 s after the start. Note the maximal wave heights achieved so far in this run along the western and eastern coasts (red and blue lines, respectively, on the right-side diagram). Flow velocities and directions along the coasts at this stage of the simulation are represented by small color coded arrows (enlarged map at the bottom).

Submarine-Landslide Scenario

Of the various submarine-landslide areas described in **Table 2** and **Figure 3**, the 'big slide' along the western slopes of the submarine Elat canyon ('b' in **Figure 3**) has the potential to generate the worst tsunami, due to its largest volume. Such a scenario was run with the Tsunami Square approach (Wang et al., 2015). The simulation shows that the maximal wave height at the eastern HGEA shores arrives within 2 min and reaches ~8 m (**Figure 8**). The reason is that the slide moves eastward and most of its energy is transferred to the waves in this direction. In Elat, the waves reach ~3 m and along the western HGEA coast, ~4 m. The slumps on the eastern side of the HGEA (**Figure 3** and **Table 2**) are much smaller than those on the western side (A and B in **Figure 3** and **Table 2**) and therefore are not expected to generate waves higher than those obtained in the current scenario.

DISCUSSION

Elat Fault–The Worst-Case Scenario

The modeled earthquake tsunamis along the western and eastern HGEA margins, especially AE2, are able to generate the largest tsunami waves from coseismic deformation (**Table 4**). They can also induce tsunamis from seismogenic submarine landslides. Even worse, the local subsidence can intensify the inundation along the HGEA coastal cities. It is reasonable to assume that the most serious effect, however, is the severe shaking from the earthquake that can spread destruction across the cities. In this case, the damage from a tsunami that is limited to the narrow coastal areas will not be the main concern. The Sulawesi, Indonesia, 2018 sequence of earthquake and then tsunami in Palu Bay shows that such a cascading scenario is feasible (Goda et al., 2019).

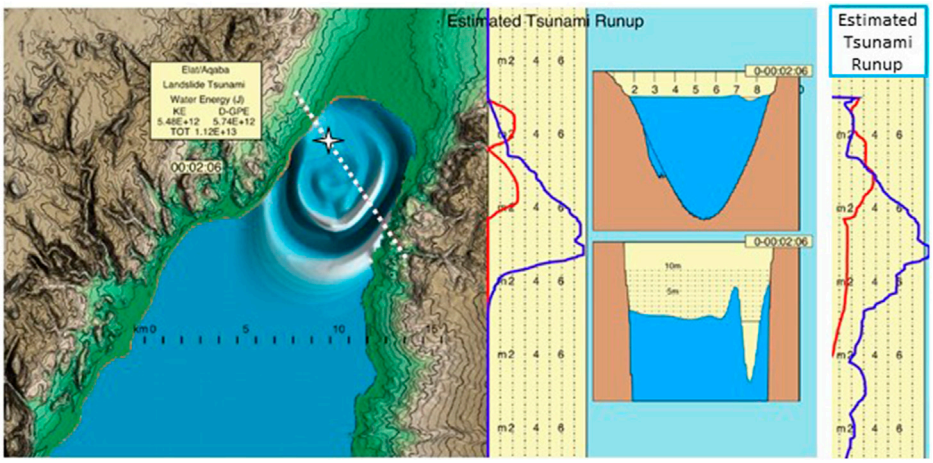

FIGURE 8 | Snapshot of the submarine-landslide tsunami at the head of the Gulf of Elat–Aqaba (HGEA) 2 min and 6 s after the start. The simulation followed the 'Tsunami Squares' approach (Wang et al., 2015). Maximal wave heights achieved until this moment along the western and eastern coasts are presented on the central diagram (red and blue lines, respectively). NW–SE cross sections (along the white dashed line on the map) on the right show the propagation of the waves. Note the location of the landslide on the map (white star) and the scar on the bathymetry in the upper cross section. The lower section zooms in on the vertical dimension and shows the shape and height of the advancing wave. Diagram on the right shows maximal wave heights achieved 10.5 min after the start.

Turning from conceptual modeling to the actual geology and seismotectonics of the HGEA region, the EF was found to pose the most severe threat to Elat city. While the Israeli design provisions for earthquake resistance of residential structures (Israel Standard, 2012) points to planning with a peak ground acceleration (PGA) of 0.21 g (10% @ 50 years) in Elat city, ground motion from a Mw 7.1 earthquake on the EF can reach at least >0.3 g in the city, much above the Israeli Standard. Levi et al. (2015) examined expected losses from a Mw seven earthquake in Elat city and showed that "...more than 60% of residential buildings are expected to be 'extensively and completely damaged', whereas more than 20% of the commercial buildings are expected to be extensively or completely damaged, highlighting the relatively high vulnerability of residential construction ... and the number of estimated fatalities range between a few and up to hundreds." Although a tsunami damage assessment has not yet been done for Elat city, the zone vulnerable to tsunami inundation along the coast is not expected to affect the residential district, and thus we expect that earthquake damage will be higher than tsunami damage. In the following, we discuss the tsunami hazard posed by the EF on Elat city.

Maximal Wave Height

Focusing on the northernmost HGEA coast and particularly on Elat, the maximal wave height of a tsunami following an earthquake in the EF scenario reaches 4.2 m by GeoClaw (*Realistic Elat Fault Tsunami Scenario* and **Figure 6**) and 4 m by Ward's (2011) approach (**Figure 7**). The landslide-tsunami scenario shows a 3 m wave height in Elat and 4 m along the western coast of the HGEA (**Figure 8**). Overall, it is suggested that 4 m maximal tsunami wave height along these coasts be considered a provisional value until probabilistic investigation is performed. Such an investigation will need to consider the uncertainties and unknowns (*Limitations and Uncertainties*), including the effect of a combined earthquake- and landslide-tsunami scenario on maximal wave height, which is not trivial at all. The interference between the two different tsunamis depends on many factors such as the time delay of the submarine landslide in relation to the earthquake, the evolution and kinematics of the landslide, and more.

Evacuation Zone

In light of the given uncertainties and limitations, the present outcomes are suitable for delineating a tsunami evacuation zone rather than an inundation map. Here we followed the Attenuation Model proposed by the New Zealand Ministry of Civil Defense and Emergency Management (Figure 38 in MCDEM, 2016). This model was tested against data from the 2011 Japan tsunami (Fraser and Power, 2013) and was found to be conservative and reliable. We thus constructed the map of an evacuation zone relevant to the Israeli HGEA coast (**Figure 9**) on the base of the 25 m DEM of Israel (Hall, 1993; Hall, 1997). First, we doubled the recommended wave height along the coast from 4 to 8 m, and then extrapolated this line landward in a descending slope of 1:200 until it meets with the nearest topography. The resulting map shows that on the northernmost coast, the evacuation zone covers the southern hotel district of Elat, but does not reach the residential district (**Figure 9**). On the west, it encircles the local port and coastal infrastructure facilities. We further examined how sensitive the delineated evacuation zone is to the maximal wave height at the coast, and introduced the values of 2 and 6 m (**Figure 9**). While the map shows a slight change on the western coast where the topography is steep, the evacuation zone along the northern, gentle slopes decreases or increases, respectively. Future assessment is certainly needed to verify the maximal wave height in order to delimit the zones that are vulnerable to inundation and construct the evacuation map.

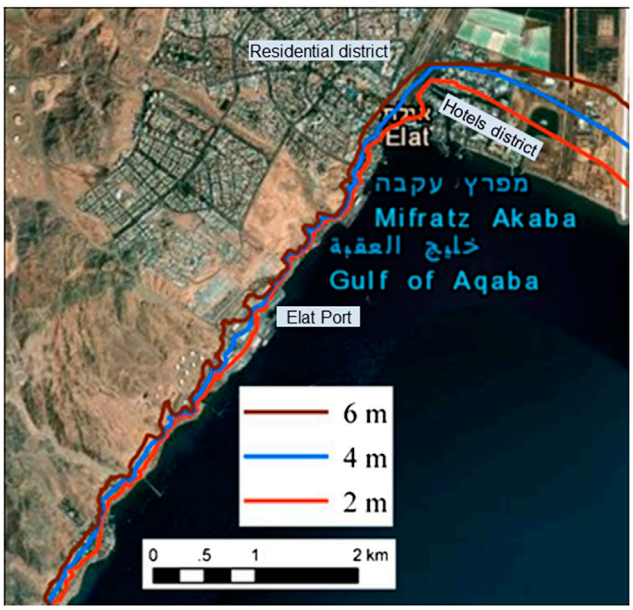

FIGURE 9 | Proposed evacuation zone along the Israeli HGEA coast. The blue line delimits the evacuation zone constructed according to the Attenuation Model (MCDEM, 2016), on the basis of 4-m wave height along the coast. For comparison, the red and brown lines delineate evacuation zones for wave heights of 2 and 6 m along the coast, respectively. See *Evacuation Zone* for detailed explanation. Background map from Google Earth: © 2020 Google, US Dept of State Geographer, Image © 2020 Maxar Technologies, © 2020 ORION-ME.

Return Period

Because earthquakes cannot be predicted, neither can the tsunamis that follow earthquakes or seismogenic submarine slides. Nevertheless, there are several approaches that may hint at the average repeat time of strong earthquakes, although experience shows that it varies a great deal with time.

Recorded seismicity, which shows earthquake frequency with time (Gutenberg–Richter relationship), can be extrapolated to high magnitudes to figure out the expected repeat times. This has already been done for Israeli Building Code SI-413 (Shapira and Hofstetter, 2002) for the three GEA basins, as well as for the Arava Valley north of the HGEA (**Table 5**). It appears that M > 6 earthquakes may affect the GEA once in a century and M > 7 earthquakes, once in a millennium.

Long-term seismicity: A comprehensive evaluation that combines recorded and historical seismicity, as well as paleoseismic evidence from the past 60,000 years along the southern Arava Valley (Hamiel et al., 2009), shows a repeat time of 500 years for Mw ~ 6 events and 5,000 years for Mw ~ 7 events. These are longer return periods than those given by present-day seismicity in the Arava Valley (**Table 5**, first row).

Seismotectonic considerations: As we were interested in the return period of the faults that pose the highest tsunami hazard to the HGEA, either directly by earthquake or by submarine failure, we focused on the marginal faults of the Elat Basin (scenarios AE2 and AE3) and the main transform (scenario AE1). The estimated repeat times of these structures are 3,000, 7,500 and 1,000 years, respectively (**Table 1**), and 700 years if combined. This estimate includes the return period of the EF, which in fact, is the realization of the AE2 scenario (*Realistic Elat Fault Tsunami Scenario*), despite its slightly longer period (3,500 years).

It appears that the maximal magnitude according to seismotectonic considerations is higher than that inferred from modern and long-term seismicity, and the repeat times of strong earthquakes is shorter. The differences may originate from the gap between the actual plate tectonic rate of motion and the lower rate inferred from the actual historic and recorded seismicity (e.g. Garfunkel, 1981; Salamon et al., 1996). A possible explanation is that the analysis of modern and long-term seismicity is based on G-R (Gutenberg–Richter) relationships while the seismotectonic analysis is based on characteristic earthquake behavior. It is also possible that the tectonic motion includes some fraction of a seismic slip that is not present in the earthquake catalogs.

Overall, it can be assumed that the return period of a tsunami in the HGEA, either by an earthquake or via seismogenic submarine landslide, will be longer than the actual seismicity, i.e., Mw > 6 earthquakes once in a century and Mw > 7 once in a millennium. The return time of tsunamis generated by a maximal magnitude earthquake on the main faults modeled in Elat Basin (AE1–3) will not be shorter than 700 years, as inferred from seismotectonic considerations. The return period of the worst-case EF scenario is once in ~3,500 years.

Limitations and Uncertainties

The limited scope of this preliminary investigation was associated with several unknowns, limitations and uncertainties. First and foremost, identifying the tsunamigenic sources relied on limited geological, seismotectonic and bathymetric data. While the structure of the GEA deep basins is sufficiently recognized (Ben Avraham, 1985), the tectonic elements that form the rift valley had to be presumed and their geometrical dimensions and source parameters had to be inferred from the areal plate tectonics, local geology and bathymetry, and where missing, by expert judgment (**Table 1**). Indeed, we validated the suitability of our modeling platform on the base of the specific 1995 Nuweiba earthquake and tsunami (Frucht et al., 2019), but examined the other earthquake and landslide scenarios on the base of a conceptual tectonic frame of the GEA. Only after evaluating the resulting scenarios (**Table 4**) were we able to single out EF and Elat submarine canyon as the real worst-case tsunamigenic sources that threaten Elat city, the focus of this research.

TABLE 5 | Repeat time (by magnitude in years) of strong earthquakes in the southern Arava Valley and Gulf of Elat–Aqaba (GEA) basins according to Building Code SI-413 (data and terminology after Shapira and Hofstetter, 2002).

Zones	M > 5 (years)	M > 6 (years)	M > 7 (years)
Arava valley	30	280	3,800
Elat basin	50	460	6,000
Aragonese	50	460	6,000
Arnona (Dakar) Basin[a]	30	300	4,000

[a]*Shapira and Hofstetter (2002) denote Dakar Basin as Arnona Basin.*

Earthquake-tsunamis by the EF were calculated by two different approaches (Ward, 2011), which gave comparable maximal wave heights of ~4 m at the coast. However, computational capacity limited us to determining the evacuation zone only, rather than the actual inundation zone. We found that the evacuation zone along the western HGEA coast is not very sensitive to the exact wave height value, whereas the gentle slopes of the northern coast are highly vulnerable and further research is needed to determine the exact runup limits.

Despite these shortcomings, the apparent potential of such a multicascading hazard in the GEA is clear. Nonetheless, concrete modeling is required for a comprehensive understanding of wave heights and extent of inundation in such scenarios, especially in the combined earthquake and landslide scenario.

CONCLUSION AND RECOMMENDATIONS

Seismotectonic considerations, and earthquake and tsunami history show that the GEA is vulnerable to tsunami generation. The worst case that might affect the HGEA is a strong earthquake along the margins of Elat Basin that can generate a combined tsunami due to coseismic deformation and submarine landslide. The associated subsidence may intensify the inundation along the northern HGEA coast. Such an earthquake may occur once in a millennium or so (*Return Period*), and the WCS once in ~3,500 years if on the EF. The main concern of such a cascading event, however, is the strong shaking across local urban areas. Palu Bay, following the 2018 Sulawesi, Indonesia Mw 7.5 earthquake (Goda et al., 2019), showed that this is a probable sequence.

A maximal wave height of 4 m along the Israeli portion of the HGEA coast calls for tsunami hazard considerations. We further drafted a map of the evacuation zone for this region (**Figure 9**), with an understanding of the need to complement the zones of expected inundation, as well as the evacuation map, in a future study. Nevertheless, the outcomes of this research can promote public awareness and education on tsunami hazard, enable preliminary planning of evacuation routes, and support civil protection activities, mong others.

The simulations indicate that tsunami waves generated by earthquakes in Elat Basin hit the HGEA coasts immediately after the earthquake. The events start with immediate retreat of the sea and are followed by high waves within 15 min (**Figure 5** and **Table 4**). Landslide-tsunamis however, bring the high waves to Elat coast within 3 min. Travel time of tsunamis originating from the Aragonese-Arnona and Dakar-Tiran basins in the south are short and arrive at the HGEA in about 10 and 20 min, respectively (**Table 4**). Thus, strong shaking and retreat of the sea at the HGEA should be considered warnings of a tsunami.

Currently, there is no tsunami warning system in the GEA, and the nearby NEAMTWS system does not monitor this area (http://neamtic.ioc-unesco.org/). It is therefore important to communicate to the public that under the current state of knowledge, strong shaking and retreat of the sea are the main and only tsunami warnings. However, since moderate earthquakes that can feel like strong shaking are not necessarily tsunamigenic, the public should be educated about the inevitability of false alarms, and that these are not a reason to mistrust the notion that strong shaking is a tsunami warning.

Consequently, each country around the GEA needs to rely on its own seismic and tide gauge networks. It is recommended, however, that they all share their data and welcome supporting information from elsewhere. Tsunamis from afar, outside the GEA, seem to pose no significant hazard to the HGEA, but further studies are needed to verify this notion.

This research focused on the HGEA and in particular, on the city of Elat. However, the examined scenarios indicate that tsunami hazard exists, albeit infrequently, all along the GEA coasts and needs to be quantified. It is hoped that this work will raise awareness among those who are part of the GEA and advance focused assessment of the expected hazard and extent of potential risk.

DATA AVAILABILITY STATEMENT

The original contributions presented in the study are included in the article, further inquiries can be directed to the corresponding author/s.

AUTHOR CONTRIBUTIONS

AS and HG conceived the present idea and coordinated the project. AS planned the project, defined the earthquake and submarines landslide scenarios, and took the lead in writing the manuscript and editing the tables and figures. HG summarized the geology and tectonics of the study area. EG supervised the adoption, preparation and configuration of the GeoClaw numerical model. EF and MG carried out the implementation and brought the GeoClaw to operation. EF performed the GeoClaw computations, interpreted the results and prepared the scenario and waveforms figures. SNW supervised all the tsunami scenarios and simulated tsunamis from the worst-case Elat Fault earthquake and Elat canyon submarine landslide. RS-T assembled and restructured the bathymetry grid. RC prepared the evacuation map. All authors discussed the results and contributed to the final manuscript.

FUNDING

This work was funded by the Israel Ministry of National Infrastructures, Energy and Water Resources (now Israel Ministry of Energy), Contract No. 213-17-010.

ACKNOWLEDGMENTS

We thank Mathilde Sørensen and Anita Grezio for thorough reading and detailed comments and suggestions which helped us improve the manuscript. Their effort is very much appreciated. The Editor, Jacopo Selva is acknowledged for handling our submission.

REFERENCES

Aldersons, F., and Ben-Avraham, Z. (2014). "The seismogenic thickness in the Dead Sea area," in *Dead Sea transform fault system: reviews, modern approaches in solid earth sciences*. Editors Z. Garfunkel, Z. Ben-Avraham, and E. Kagan (Dordrecht, Netherlands: Springer), 53–89.

Al-Homoud, A. S., and Tal, A. B. (1998). Geotechnical study for evaluating stability and restoration work at the 1000 year old archaeological site of Ayla, Gulf of Aqaba, Kingdom of Jordan. *Environ. Eng. Geosci.* 4 (1), 103–114. doi:10.2113/gseegeosci.IV.1.103

Ambraseys, N. N. (2009). *Earthquakes in the mediterranean and Middle East. A multidisciplinary study of seismicity up to 1900*. New York, NY: Cambridge University Press.

Amit, R., Zilberman, E., Enzel, Y., and Porat, N. (2002). Paleoseismic evidence for time dependency of seismic response on a fault system in the southern Arava Valley, Dead Sea rift, Israel. *Geol. Soc. Am. Bull.* 114, 192–206. doi:10.1130/0016-7606(2002)114<0192:PEFTDO>2.0.CO;2

Amit, R., Zilberman, E., Porat, M., and Enzel, Y. (1999). Relief inversion in the Avrona playa as evidence of large-magnitude historic earthquakes, southern Arava valley, dead sea rift. *Quat. Res.* 52, 76–91. doi:10.1006/qres.1999.2050

Ash-Mor, A., Bookman, R., Kanari, M., Ben-Avraham, Z., and Almogi-Labin, A. (2017). Micropaleontological and taphonomic characteristics of mass transport deposits in the northern Gulf of Eilat/Aqaba, Red Sea. *Mar. Geol.* 391, 36–47. doi:10.1016/j.margeo.2017.07.009

Baer, G., Funning, G. J., Shamir, G., and Wright, T. J. (2008). The 1995 November 22, Mw 7.2 gulf of Elat earthquake cycle revisited. *Geophys. J. Int.* 175, 1040–1054. doi:10.1111/j.1365-246X.2008.03901.x

Bartov, Y., Steinitz, G., Eyal, M., and Eyal, Y. (1980). Sinistral movement along the gulf of aqaba—its age and relation to the opening of the Red Sea. *Nature.* 285, 220–221. doi:10.1038/285220a0

Basili, R., Tiberti, M. M., Kastelic, V., Romano, F., Piatanesi, A., Selva, J., et al. (2013). Integrating geologic fault data into tsunami hazard studies. *Nat. Hazards Earth Syst. Sci.* 13, 1025–1050. doi:10.5194/nhess-13-1025-2013

Ben-Avraham, Z. (1985). Structural framework of the gulf of Elat (AQABA), northern Red Sea. *J. Geophys. Res. Solid Earth* 90, 703–726. doi:10.1029/JB090iB01p00703

Ben-Avraham, Z., Almagor, G., and Garfunkel, Z. (1979). Sediments and structure of the gulf of Elat (Aqaba)—northern Red Sea. *Sediment. Geol.* 23, 239–267. doi:10.1016/0037-0738(79)90016-2

Ben-Avraham, Z., Garfunkel, Z., and Lazar, M. (2008). Geology and evolution of the southern dead sea fault with emphasis on subsurface structure. *Annu. Rev. Earth Planet Sci.* 36, 357–387. doi:10.1146/annurev.earth.36.031207.124201

Ben-Avraham, Z., Lazar, M., Garfunkel, Z., Reshef, M., Ginzburg, A., Rotstein, Y., et al. (2012). "Structural styles along the Dead Sea fault," in *Regional geology and tectonics: phanerozoic passive margins, cratonic basins and global tectonic maps*. Editors D. G. Roberts and A. W. Bally (Burlington, MA: Elsevier), 617–634.

Ben-Avraham, Z., and Tibor, G. (1993). The northern edge of the Gulf of Eilat. *Tectonophysics* 226, 319–331. doi:10.1016/0040-1951(93)90125-4

Ben-Menahem, A. (1991). Four thousand years of seismicity along the Dead Sea rift. *J. Geophys. Res.* 91, 20195–20216. doi:10.1029/91JB01936

Berger, M. J., George, D. L., LeVeque, R. J., and Mandli, K. T. (2011). The GeoClaw software for depth-averaged flows with adaptive refinement. *Adv. Water Resour.* 34 (9), 1195–1206. doi:10.1016/j.advwatres.2011.02.016

Beyth, M., Eyal, Y., and Garfunkel, Z. (2018). Geological map of Israel 1:50,000, elat sheet 26-I,II. Available at: https://www.gov.il/he/departments/general/eilat-map (Accessed August 27, 2020).

Clawpack Development Team (2017). Clawpack version 5.4.0. Available at: http://www.clawpack.orghttp://www.bosai.go.jp/study/application/dc3d/DC3Dhtml_E.html (Accessed August 27, 2020).

FEMA (2017). *Hazus tsunami model user guidance*. Washington DC, United States: Federal Emergency Management Agency.

Fraser, S. A., and Power, W. L. (2013). Validation of a GIS-based attenuation rule for indicative tsunami evacuation zone mapping. Report 2013/02.

Freund, R., Zak, I., and Garfunkel, Z. (1968). Age and rate of the sinistral movement along the Dead Sea rift. *Nature.* 220, 253–255. doi:10.1038/220253a0

Frucht, E., Salamon, A., Gal, E., Ginat, H., Grigorovitch, M., Shem Tov, R., et al. (2019). A fresh view of the tsunami generated by the Dead Sea transform, 1995 Mw 7.2 Nuweiba EARTHQUAKE, along the Gulf of Elat-Aqaba. *Seismol Res. Lett.* 90 (4), 1483–1493. doi:10.1785/0220190004

Galanti, B., and Salamon, A. (2017). Simulation of tsunami scenarios along the mediterranean coast of Israel, final report. Israel oceanographic and limnological research LTD report H48/2015. Geological Survey of Israel. Rep. GSI/26/2017.

Garfunkel, Z. (1981). Internal structure of the Dead Sea leaky transform (rift) in relation to plate kinematics. *Tectonophysics* 80, 81–108. doi:10.1016/0040-1951(81)90143-8

Garfunkel, Z. (2014). "Lateral motion and deformation along the Dead Sea transform," in *Dead Sea transform system reviews*. Editors Z. Garfunkel, Z. Ben-Avraham, and A. Kagan (Dordrecht, Netherlands: Springer), 109–151.

Geist, E. L., and Oglesby, D. D. (2014). "Earthquake mechanism and seafloor deformation for tsunami generation," in *Encyclopedia of earthquake engineering*. Editors M. Beer, I. A. Kougioumtzoglou, E. Patelli, and I. S.-K. Au (Berlin, Heidelberg: Springer), 1–17.

Geist, E. L., Oglesby, D. D., and Ryan, K. J. (2019). "Tsunamis: stochastic models of occurrence and generation mechanisms," in *Encyclopedia of complexity and systems science*. Editor R. A. Meyers (Berlin, Heidelberg: Springer), 1–30.

Goda, K., Mori, N., Yasuda, T., Prasetyo, A., Muhammad, A., and Tsujio, D. (2019). Cascading geological hazards and risks of the 2018 Sulawesi Indonesia earthquake and sensitivity analysis of tsunami inundation simulations. *Front. Earth Sci.* 7, 261. doi:10.3389/feart.2019.00261

Goodman-Tchernov, B., Katz, T., Shaked, Y., Qupty, N., Kanari, M., Neimi, T., et al. (2016). Offshore evidence for an undocumented tsunami event in the 'low risk' Gulf of Aqaba-Eilat, Northern Red Sea. *PloS One* 11 (1), 1–14. doi:10.1371/journal.pone.0145802

Guidoboni, E., and Comastri, A. (2005). *Catalogue of earthquakes and tsunamis in the mediterranean area from the 11th to the 15th century*. Bologna, Italy: INGV-SGA.

Hall, J. K. (1997). *Landform of Israel and adjacent areas, 1:500,000 scale*. Jerusalem, Israel: Geological Survey of Israel.

Hall, J. K. (1993). The GSI digital terrain model (DTM) project completed. *Geol. Surv. Isr. Curr. Res.* 8, 47–50.

Hall, J. K., and Ben-Avraham, Z. (1978). *Bathymetric chart of the gulf of Elat, scale 1:250,000*. Jerusalem, Israel: Geological Survey of Israel.

Hamiel, Y., Amit, R., Begin, Z. B., Marco, S., Katz, O., Salamon, A., et al. (2009). The seismicity along the Dead Sea Fault during the last 60,000 years. *Bull. Seismol. Soc. Am.* 99, 2020–2026. doi:10.1785/0120080218

Hamiel, Y., Masson, F., Piatibratova, O., and Mizrahi, Y. (2018). GPS measurements of crustal deformation across the southern Arava Valley section of the Dead Sea Fault and implications to regional seismic hazard assessment. *Tectonophysics* 724–725, 171–178. doi:10.1016/j.tecto.2018.01.016

Harbitz, C. B., Løvholt, F., and Bungum, H. (2014). Submarine landslide tsunamis: how extreme and how likely? *Nat. Hazards.* 72 (3), 1341–1374. doi:10.1007/s11069-013-0681-3

Hartman, G., Niemi, T. M., Tibor, G., Ben-Avraham, Z., Al-Zoubi, A., Makovsky, Y., et al. (2014). Quaternary tectonic evolution of the northern gulf of elat/aqaba along the Dead Sea transform. *J. Geophys. Res. Solid Earth* 119, 1–23. doi:10.1002/2013JB010879

Hofstetter, A., Dorbath, C., and Dorbath, L. (2014). "Instrumental data on the seismic activity along the Dead Sea transform," in *Dead Sea transform fault system: reviews*, *Modern approaches in solid earth sciences*. Editors Z. Garfunkel, Z. Ben-Avraham, and E. Kagan (Dordrecht, Netherlands: Springer), 263–278.

Huhn, K., Arroyo, M., Cattaneo, A., Clare, M. A., Gràcia, E., Harbitz, C. B., et al. (2019). "Modern submarine landslide complexes: a short review," in *Submarine landslides: subaqueous mass transport deposits from outcrops to seismic profiles*. Editors K. Ogata, A. Festa, and G. A. Pini (Washington D.C., United States: American Geophysical Union), 181–200.

Imamura, F., Gica, E., Takahashi, T., and Shuto, N. (1995). Numerical simulation of the 1992 flores tsunami: interpretation of tsunami phenomena in northeastern flores island and damage at babi island. *Pure Appl. Geophys.* 144, 555–568. doi:10.1007/BF00874383

Israel Standard (2012). Israel Standard, SI, 413, 1995/2004, amendment No. 5, 2012 Design provisions for earthquake resistance of structures. Tel-Aviv, Israel: The Standards Institution of Israel. . Available at: https://ibr.sii.org.il/ibr/#/about.

Kanari, M., Ben-Avraham, Z., Tibor, G., Bookman, R., Goddman-Tchernov, B. N., Neimi, T. M., et al. (2014). "On-land and offshore evidence for Holocene

earthquakes in the northern gulf of aqaba-elat, Israel/Jordan," in 6th international INQUA Meeting on paleoseismology, active tectonic and archeoseismology, Pescina, Italy, 19–24 April, 2015. Roma, Italy: Miscellanea INGV, 240–243.

Kim, J., Løvholt, F., Issler, D., and Forsberg, C. F. (2019). Landslide material control on tsunami genesis—the Storegga Slide and tsunami (8,100 years BP). *J. Geophys. Res. Oceans* 124 (6), 3607–3627. doi:10.1029/2018JC014893

Klinger, Y., Le Béon, M., and Al-Qaryouti, M. (2015). 5000 yr of paleoseismicity along the southern Dead Sea fault. *Geophys. J. Int.* 202, 313–327. doi:10.1093/gji/ggv134

Lefevre, M., Klinger, Y., Al-Qaryouti, M., Le Béon, M., and Moumani, K. (2018). Slip deficit and temporal clustering along the Dead Sea fault from paleoseismological investigations. *Sci. Rep.* 8, 4511. doi:10.1038/s41598-018-22627-9

LeVeque, R. J. (2006). Clawpack software. Available at: http://www.clawpack.org (Accessed August 27, 2020). [

Levi, T., Bausch, D., Katz, O., Rozelle, J., and Salamon, A. (2015). Insights from hazus loss estimations in Israel for Dead Sea transform earthquakes. *Nat. Hazards* 75, 365–388. doi:10.1007/s11069-014-1325-y

Løvholt, F., Bondevik, S., Laberg, J. S., Kim, J., and Boylan, N. (2017). Some giant submarine landslides do not produce large tsunamis. *Geophys. Res. Lett.* 44 (16), 8463–8472. doi:10.1002/2017GL074062

Løvholt, F., Glimsdal, S., and Harbitz, C. B. (2020). On the landslide tsunami uncertainty and hazard. *Landslides* 17, 2301–2315. doi:10.1007/s10346-020-01429-z

Løvholt, F., Pedersen, G., Harbitz, C. B., Glimsdal, S., and Kim, J. (2015). On the characteristics of landslide tsunamis. *Phil. Trans. R. Soc. A.* 373, 20140376. doi:10.1098/rsta.2014.0376

Makovsky, Y., Wunch, A., Ariely, R., Shaked, Y., Rivlin, A., Shemesh, A., et al. (2008). Quaternary transform kinematics constrained by sequence stratigraphy and submerged coastline features: the Gulf of Aqaba. *Earth Planet Sci. Lett.* 271, 109–122. doi:10.1016/j.epsl.2008.03.057

MCDEM (2016). Tsunami evacuation zones, director's guideline for civil defence emergency management groups. Available at: http://www.civildefence.govt.nz/assets/Uploads/publications/dgl-08-16-Tsunami-Evacuation-Zones.pdf (Accessed August 27, 2020).

Miller, D. J. (1960). *Giant waves in Lituya bay, Alaska*. U.S. Geological Survey. Professional Paper 354-C.

Okada, Y. (1992). Internal deformation due to shear and tensile faults in a half space. *Bull. Seismol. Soc. Am.* 82, 1018–1040.

Okada, Y. (1985). Surface deformation due to shear and tensile faults in a half-space. *Bull. Seismol. Soc. Am.* 75, 1135–1154.

Okal, E. A. (2015). The quest for wisdom: lessons from 17 tsunamis, 2004–2014. *Phil. Trans. Math. Phys. Eng. Sci.* 373, 20140370. doi:10.1098/rsta.2014.0370

Polet, J., and Kanamori, H. (2016). "Tsunami earthquakes," in *Encyclopedia of Complexity and systems science*. Editor R. A. Meyers (Berlin, Germany: Springer), 1–22.

Quennell, A. M. (1959). The structural and geomorphic evolution of the Dead Sea Rift. *Quart. J. Geol. Soc.* 144, 1–24. doi:10.1144/gsjgs.114.1.0001

Reches, Z., Erez, J., and Garfunkel, Z. (1987). Sedimentary and tectonic features in the northwestern Gulf of Elat, Israel. *Tectonophysics* 141, 169–180. doi:10.1016/0040-1951(87)90183-1

Sade, A. R., Hall, J. K., Tibor, G., Neimi, T. M., Ben-Avraham, Z., Al-Zoubi, A., et al. (2008). Multibeam bathymetry of the northern gulf of 'aqaba/elat. GSI Rep. GSI/03/2008, IOLR Rep. IOLR/08/2008, MDSRC Rep. MDSRC/02/2008.

Salamon, A., and Di Manna, P. (2019). Empirical constraints on magnitude-distance relationships for seismically induced submarine tsunamigenic landslides. *Earth Sci. Rev.* 191, 66–92. doi:10.1016/j.earscirev.2019.02.001

Salamon, A., Hofstetter, A., Garfunkel, Z., and Ron, H. (1996). Seismicity of the eastern Mediterranean region: perspective from the Sinai subplate. *Tectonophysics* 263, 293–305. doi:10.1016/S0040-1951(96)00030-3

Salamon, A., Hofstetter, A., Garfunkel, Z., and Ron, H. (2003). Seismotectonics of the Sinai subplate – the eastern Mediterranean region. *Geophys. J. Int.* 155, 149–173. doi:10.1046/j.1365-246X.2003.02017.x

Salamon, A. (2011). "Potential tsunamigenic sources in the eastern Mediterranean and a decision matrix for a tsunami early warning system," in *Marine Geo-Hazards in the Mediterranean, Workshop Monographs, Rapports et Procés-Verbaux des Réunions de la Commission Internationale pour l'Exploration Scientifique de la Mer Méditeranée (CIESM)*. Editor F. Briand (Monaco, United Kingdom: CIESM), 35–42.

Salamon, A., Rockwell, T., Guidoboni, E., and Comastri, A. (2010). A critical evaluation of tsunami records reported for the Levant coast from the second millennium BCE to the present, Israel. *Isr. J. Earth Sci.* 58 (3-4), 327–354. doi:10.1560/IJES.58.2-3.327

Salamon, A., Rockwell, T., Ward, S. N., Guidoboni, E., and Comastri, A. (2007). Tsunami hazard evaluation of the eastern Mediterranean: historical analysis and selected modeling. *Bull. Seismol. Soc. Am.* 97 (3), 705–724. doi:10.1785/0120060147

Salamon, A., Rosen, D. S., Gitterman, Y., Yahav, A., Ben-Arieh, S., Debutton, Y., et al. (2014). Recommendations on the policy, warning principles and frame of preparedness for tsunamis in Israel. The scientific committee for formulating policy of early warning principles for tsunami hazards in Israel. Geological survey of Israel report GSI/16/2014. Geophysical Institute of Israel. Rep. 30/797/14.

Salem, E. M. (2009). Paleo-tsunami deposits on the Red Sea beach, Egypt, arabian. *J. Geosci.* 2, 185–197. doi:10.1007/s12517-008-0027-8

Selva, J., Tonini, R., Molinari, I., Tiberti, M. M., Romano, F., Grezio, A., et al. (2016). Quantification of source uncertainties in seismic probabilistic tsunami hazard analysis (SPTHA). *Geophys. J. Int.* 205, 1780–1803. doi:10.1093/gji/ggw107

Shaked, Y., Agnon, A., Lazar, B., Marco, S., Avner, U., and Stein, M. (2004). Large earthquakes kill coral reefs at the north-west Gulf of Aqaba. *Terra. Nova.* 6, 133–138. doi:10.1111/j.1365-3121.2004.00541.x

Shapira, A., and Hofstetter, A. (2002). Seismic parameters of seismogenic zones. Appendix C in: Shapira A. 2002. An updated map of peak ground accelerations for Israel Standard 413. GII Rep. 592/230/02, 74 pp.

Shapira, A., and Hofstetter, A. (1993). Source parameters and scaling relationships of earthquakes in Israel. *Tectonophysics* 217, 217–229. doi:10.1016/0040-1951(93)90005-5

Synolakis, C. E., Bardet, J.-P., Borrero, J., Davies, H., Okal, E., Silver, E., et al. (2002). The slump origin of the 1998 Papua New Guinea tsunami. *Proc. R. Soc. Lond. Ser. A.* 458, 763–789. doi:10.1098/rspa.2001.0915

Te Chow, V. (1959). *Open-channel hydraulics*, Vol. 1. New York, NY: McGraw-Hill.

Thingbaijam, K. K. S., Mai, P. M., and Goda, K. (2017). New empirical earthquake source-scaling laws. *Bull. Seismol. Soc. Am.* 107, 2225–2246. doi:10.1785/0120170017

Tibor, G., Neimi, T., and Ben-Avraham, Z. (2010). Active tectonic morphology and submarine deformation of the northern Gulf of Eilat/Aqaba from analyses of multibeam data. *Geo Mar. Lett.* 30, 561–573. doi:10.1007/s00367-010-0194-y

Walter, T. R., Haghshenas Haghighi, M., Schneider, F. M., Coppola, D., Motagh, M., Saul, J., et al. (2019). Complex hazard cascade culminating in the Anak Krakatau sector collapse. *Nat. Commun.* 10, 4339. doi:10.1038/s41467-019-12284-5

Wang, J., Ward, S., and Xiao, L. (2015). Numerical modelling of rapid, flow-like landslides across 3-D terrains: a Tsunami Squares approach to El Picacho landslide, El Salvador, September 19, 1982. *Geophys. J. Int.* 201, 1534–1544. doi:10.1093/gji/ggv095

Ward, S. N. (2001). Landslide tsunami. *J. Geophys. Res.* 106, 11201–11216. doi:10.1029/2000JB900450

Ward, S. N. (2011). "Tsunami," in *The encyclopedia of solid earth geophysics*. Editor H. Gupta (Dordrecht, Netherlands: Springer Press), 1473–1493.

Ward, S. N., and Day, S. (2008). Tsunami balls: a granular approach to tsunami runup and inundation. *Commun. Comput. Phys.* 3 (1), 222–249.

Wells, D. L., and Coppersmith, K. J. (1994). New empirical relationships among magnitude, rupture length, rupture width, rupture area, and surface displacement. *Bull. Seismol. Soc. Am.* 84 (4), 974–1002.

Winters, G., Edelist, D., Shem-Tov, R., Beer, S., and Rilov, G. (2017). A low-cost field-survey method for mapping seagrasses and their potential threats: an example from the northern Gulf of Aqaba, Red Sea. *Aquat. Conserv. Mar. Freshw. Ecosyst.* 27, 324–339. doi:10.1002/aqc.2688

Wust, H.. (1997). The November 22, 1995, Nuweiba earthquake, Gulf of Elat (Aqaba), Post-seismic analysis of failure features and seismic hazard implications. Geological Survey of Israel Rep. GSI/3/97.

Xiao, L., Ward, S. N., and Wang, J. (2015). Tsunami squares approach to landslide-generated waves: application to gongjiafang landslide, three gorges reservoir, China. *Pure Appl. Geophys.* 172, 3639–3654. doi:10.1007/s00024-015-1045-6

Zilberman, E., Amit, R., Porat, N., Enzel, Y., and Avner, U. (2005). Surface ruptures induced by the devastating 1068 AD earthquake in the southern Arava valley, Dead Sea Rift, Israel. *Tectonophysics* 408, 79–99. doi:10.1016/j.tecto.2005.05.030

Zohar, M., Salamon, A., and Rubin, R. (2016). Reappraised list of historical earthquakes that affected Israel and its close surroundings. *J. Seismol.* 20 (3), 971–985. doi:10.1007/s10950-016-9575-7

Conflict of Interest: The authors declare that the research was conducted in the absence of any commercial or financial relationships that could be construed as a potential conflict of interest.

frontiers in Earth Science

ORIGINAL RESEARCH
published: 05 March 2021
doi: 10.3389/feart.2020.616594

The Making of the NEAM Tsunami Hazard Model 2018 (NEAMTHM18)

Roberto Basili[1], Beatriz Brizuela[1], André Herrero[1], Sarfraz Iqbal[2], Stefano Lorito[1], Francesco Emanuele Maesano[1], Shane Murphy[3], Paolo Perfetti[2], Fabrizio Romano[1], Antonio Scala[1,4], Jacopo Selva[2], Matteo Taroni[1], Mara Monica Tiberti[1], Hong Kie Thio[5], Roberto Tonini[1], Manuela Volpe[1], Sylfest Glimsdal[6], Carl Bonnevie Harbitz[6], Finn Løvholt[6], Maria Ana Baptista[7], Fernando Carrilho[8], Luis Manuel Matias[9], Rachid Omira[9], Andrey Babeyko[10], Andreas Hoechner[10,11], Mücahit Gürbüz[12], Onur Pekcan[12], Ahmet Yalçıner[12], Miquel Canals[13], Galderic Lastras[13], Apostolos Agalos[14], Gerassimos Papadopoulos[15], Ioanna Triantafyllou[16], Sabah Benchekroun[17], Hedi Agrebi Jaouadi[18], Samir Ben Abdallah[18], Atef Bouallegue[18], Hassene Hamdi[18], Foued Oueslati[18], Alessandro Amato[1], Alberto Armigliato[19], Jörn Behrens[20], Gareth Davies[21], Daniela Di Bucci[22], Mauro Dolce[22,23], Eric Geist[24], Jose Manuel Gonzalez Vida[25], Mauricio González[26], Jorge Macías Sánchez[25], Carlo Meletti[27], Ceren Ozer Sozdinler[28], Marco Pagani[29], Tom Parsons[24], Jascha Polet[30], William Power[31], Mathilde Sørensen[32] and Andrey Zaytsev[33]*

[1]*Istituto Nazionale Di Geofisica e Vulcanologia, Roma, Italy,* [2]*Istituto Nazionale Di Geofisica e Vulcanologia, Bologna, Italy,* [3]*Institut Francais De Recherche Pour l'Exploitation De La Mer, Plouzane, France,* [4]*Department of Physics "Ettore Pancini" University of Naples, Naples, Italy,* [5]*AECOM Technical Services, Los Angeles, CA, United States,* [6]*Norwegian Geotechnical Institute, Oslo, Norway,* [7]*Instituto Superior de Engenharia de Lisboa, Instituto Politécnico de Lisboa, Lisboa, Portugal,* [8]*Instituto Português Do Mar e da Atmosfera, Lisboa, Portugal,* [9]*Instituto Dom Luiz, Faculdade De Ciências Da Universidade De Lisboa, Lisboa, Portugal,* [10]*GFZ German Research Centre for Geosciences, Potsdam, Germany,* [11]*Gempa GmbH, Potsdam, Germany,* [12]*Department of Civil Engineering, Middle East Technical University, Ankara, Turkey,* [13]*CRG Marine Geosciences, Department of Earth and Ocean Dynamics, Faculty of Earth Sciences, University of Barcelona, Barcelona, Spain,* [14]*National Observatory of Athens, Athens, Greece,* [15]*International Society for the Prevention and Mitigation of Natural Hazards, Athens, Greece,* [16]*Department of Geology and Geoenvironment, National and Kapodistrian University of Athens, Athens, Greece,* [17]*Ecole Normale Supérieure De Rabat, Université Mohammed V, Rabat, Morocco,* [18]*National Institute of Meteorology, Tunis, Tunisia,* [19]*Dipartimento di Fisica e Astronomia, Università Degli Studi Di Bologna, Bologna, Italy,* [20]*Department of Mathematics, Universität Hamburg, Hamburg, Germany,* [21]*Geoscience Australia, Symonston, Australia,* [22]*Presidenza Del Consiglio Dei Ministri, Dipartimento Della Protezione Civile Rome, Rome, Italy,* [23]*Department of Structures for Engineering and Architecture, Università Degli Studi Di Napoli Federico II, Napoli, Italy,* [24]*US Geological Survey, Moffett Field, CA, United States,* [25]*Departamento de Análisis Matemático, Estadística e Investigacíon Operativa y Matemática Aplicada, Universidad de Malaga, Málaga, Spain,* [26]*Environmental Hydraulics Institute "IHCantabria", Universidad de Cantabria, Santander, Spain,* [27]*Istituto Nazionale Di Geofisica e Vulcanologia, Pisa, Italy,* [28]*Institute of Education, Research and Regional Cooperation for Crisis Management Shikoku Kagawa University, Takamatsu, Japan,* [29]*Fondazione GEM, Pavia, Italy,* [30]*Department of Geological Sciences, California State Polytechnic University, Pomona, CA, United States,* [31]*GNS Science, Lower Hutt, New Zealand,* [32]*Department of Earth Science, University of Bergen, Bergen, Norway,* [33]*Special Research Bureau for Automation of Marine Researches, Far Eastern Branch of Russian Academy of Sciences, Yuzhno-Sakhalinsk, Russia*

The NEAM Tsunami Hazard Model 2018 (NEAMTHM18) is a probabilistic hazard model for tsunamis generated by earthquakes. It covers the coastlines of the North-eastern Atlantic, the Mediterranean, and connected seas (NEAM). NEAMTHM18 was designed as a three-phase project. The first two phases were dedicated to the model development and hazard calculations, following a formalized decision-making process based on a multiple-expert protocol. The third phase was dedicated to documentation and dissemination. The hazard assessment workflow was structured in Steps and Levels. There are four Steps: Step-1) probabilistic earthquake model; Step-2) tsunami generation and modeling in deep water; Step-3) shoaling and inundation; Step-4) hazard aggregation and uncertainty

OPEN ACCESS

Edited by:
Victoria Miller, The University of the West Indies St. Augustine, Trinidad and Tobago

Reviewed by:
Nobuhito Mori, Kyoto University, Japan
Hyoungsu Park, University of Hawaii at Manoa, United States

***Correspondence:**
Roberto Basili
roberto.basili@ingv.it

Specialty section:
This article was submitted to Geohazards and Georisks, a section of the journal Frontiers in Earth Science

Received: *12 October 2020*
Accepted: *29 December 2020*
Published: *05 March 2021*

Citation:
Basili R, Brizuela B, Herrero A, Iqbal S, Lorito S, Maesano FE, Murphy S, Perfetti P, Romano F, Scala A, Selva J, Taroni M, Tiberti MM, Thio HK, Tonini R, Volpe M, Glimsdal S, Harbitz CB, Løvholt F, Baptista MA, Carrilho F, Matias LM, Omira R, Babeyko A, Hoechner A, Gürbüz M, Pekcan O, Yalçıner A, Canals M, Lastras G, Agalos A, Papadopoulos G, Triantafyllou I, Benchekroun S, Agrebi Jaouadi H, Ben Abdallah S, Bouallegue A, Hamdi H, Oueslati F, Amato A, Armigliato A, Behrens J, Davies G, Di Bucci D, Dolce M, Geist E, Gonzalez Vida JM, González M, Macías Sánchez J, Meletti C, Ozer Sozdinler C, Pagani M, Parsons T, Polet J, Power W, Sørensen M and Zaytsev A (2021) The Making of the NEAM Tsunami Hazard Model 2018 (NEAMTHM18). Front. Earth Sci. 8:616594. doi: 10.3389/feart.2020.616594

quantification. Each Step includes a different number of Levels. Level-0 always describes the input data; the other Levels describe the intermediate results needed to proceed from one Step to another. Alternative datasets and models were considered in the implementation. The epistemic hazard uncertainty was quantified through an ensemble modeling technique accounting for alternative models' weights and yielding a distribution of hazard curves represented by the mean and various percentiles. Hazard curves were calculated at 2,343 Points of Interest (POI) distributed at an average spacing of ~20 km. Precalculated probability maps for five maximum inundation heights (MIH) and hazard intensity maps for five average return periods (ARP) were produced from hazard curves. In the entire NEAM Region, MIHs of several meters are rare but not impossible. Considering a 2% probability of exceedance in 50 years (ARP≈2,475 years), the POIs with MIH >5 m are fewer than 1% and are all in the Mediterranean on Libya, Egypt, Cyprus, and Greece coasts. In the North-East Atlantic, POIs with MIH >3 m are on the coasts of Mauritania and Gulf of Cadiz. Overall, 30% of the POIs have MIH >1 m. NEAMTHM18 results and documentation are available through the TSUMAPS-NEAM project website (http://www.tsumaps-neam.eu/), featuring an interactive web mapper. Although the NEAMTHM18 cannot substitute in-depth analyses at local scales, it represents the first action to start local and more detailed hazard and risk assessments and contributes to designing evacuation maps for tsunami early warning.

Keywords: probabilistic tsunami hazard assessment, earthquake-generated tsunami, hazard uncertainty analysis, ensemble modeling, maximum inundation height, NEAM

INTRODUCTION

Tsunamis can be triggered by earthquakes, landslides, volcanic processes, meteorological events, and asteroid impacts. Earthquakes, and especially megathrust earthquakes in subduction zones, are the primary cause of the largest tsunamis. PTHA (all acronyms and abbreviations used herein are listed in **Table 1**) aims at evaluating the probability that a given tsunami hazard "intensity measure," such as the MIH or run-up, exceeds a predetermined threshold in a certain period. In the last 10–15 years, the techniques for computation-based PTHA, which is based on multiple tsunami numerical simulations starting from a probabilistic source model, have progressively evolved after the seminal works by Lin and Tung (1982) and Rikitake and Aida (1988). These authors extended the methods introduced at the end of the 60s for PSHA (Esteva, 1967; Cornell, 1968), recently reviewed by McGuire (2008) and Gerstenberger et al. (2020), to tsunamis (Geist and Parsons, 2006; Geist and Lynett, 2014; Grezio et al., 2017; Mori et al., 2018). The availability of modern HPC has made computational tsunami hazard assessment feasible at a global scale while retaining relatively high-resolution and extensive exploration of source uncertainty (Davies et al., 2018; Davies and Griffin, 2020).

The ICG/NEAMTWS was established in response to the Indian Ocean tsunami of December 26, 2004. NEAMTWS operates under IOC/UNESCO's umbrella and is currently based on five national monitoring centers in France, Greece, Italy, Portugal, and Turkey that act as TSPs. Other ICGs support the development and maintenance of TWS in other oceans of the world (**Figure 1**). Tsunami risk assessment and warning systems need PTHA as input and reference to achieve effective risk reduction (IOC, 2017). Before 2004, it was already well-known that several destructive tsunamis had occurred in the NEAM region, such as the tsunamis caused by the caldera collapse in the Santorini Island in the Minoan Era, the Mw~8 Crete earthquake in 365 CE and the Lisbon earthquake in 1755, and the Mw~7 Messina and Reggio Calabria earthquake in 1908 whose associated tsunami was possibly enhanced by a seismically-induced submarine landslide (Maramai et al., 2014; Papadopoulos et al., 2014). Some of these events are among the most destructive tsunamis in history. Nonetheless, hazard analysis efforts for the NEAM Region started being pursued only in the wake of the 2004 disaster in the Indian Ocean. Often, they are high-resolution studies focusing on specific sub-domains (Tinti et al., 2005; Papadopoulos et al., 2010; Tonini et al., 2011; Álvarez-Gómez et al., 2011; Grezio et al., 2012; Sørensen et al., 2012; Omira et al., 2015), or are included in global assessments with a relatively limited spatial resolution (Løvholt et al., 2012; Løvholt et al., 2015; Davies et al., 2018). Others are methodological analyses that considered case studies in the NEAM Region (Grezio et al., 2010; Grezio et al., 2015; Lorito et al., 2015; Selva et al., 2016).

During 2016 and 2017, the EU project TSUMAPS-NEAM developed the first long-term PTHA from earthquake-induced tsunamis for the NEAM Region (**Figure 1**), and in 2018 released the NEAM Tsunami Hazard Model 2018 (NEAMTHM18) (Basili et al., 2018). A large community of scientists and decision-makers were actively involved. The effort was funded by the EU DG-ECHO and formally supported by several potential end-users.

TABLE 1 | List of Acronyms, abbreviations, and relevant websites.

AGITHAR	Accelerating Global science In Tsunami HAzard and Risk analysis (https://www.agithar.uni-hamburg.de/)
AHP	Analytical hierarchical process
ARP	Average return period
ASTARTE	Assessment, STrategy and risk reduction for tsunamis in europe (http://www.astarte-project.eu/)
BS | SBS	Background seismicity | special BS
ChEESE	Center of excellence in solid earth (https://cheese-coe.eu/)
Cubit	CUBIT geometry and mesh generation toolkit (http://cubit.sandia.gov)
DG-ECHO	Directorate-general for european civil protection and humanitarian aid operations
FMD	Frequency-magnitude distribution
GAR15	Global assessment Report 2015 (https://reliefweb.int/report/world/global-assessment-report-disaster-risk-reduction-2015-gar15-making-development)
GPU	Graphics processing unit
GTM	Global tsunami model (http://globaltsunamimodel.org/)
HPC	High-performance computing
ICG/NEAMTWS	Intergovernmental coordination group for the tsunami early warning and mitigation system in the NEAM
IOC/UNESCO	Intergovernmental oceanographic commission (http://www.ioc-tsunami.org/) of the united nations educational, scientific and cultural organization (https://en.unesco.org/)
IR	Internal reviewers
MIH	Maximum inundation height
NEAM	North-eastern atlantic, the mediterranean, and connected seas
NEAMTHM18	NEAM tsunami hazard Model 2018 (http://www.tsumaps-neam.eu/neamthm18/)
NLSW	Non-linear shallow water
NTHMP	National tsunami hazard mitigation program (https://nws.weather.gov/nthmp/)
PDF	Probability density function
PDT	Project development team
PE	Pool of experts
PoE	Probability of exceedance
POI	Point of interest
PS | SPS	Predominant seismicity | special PS
PTHA	Probabilistic tsunami hazard assessment
SHARE	Seismic hazard harmonization in europe (http://www.share-eu.org/)
SiAM	National alert system for tsunami wave generated by earthquakes in the mediterranean sea (http://www.ingv.it/cat/en/the-italian-alert-system/the-siam-directive)
SRTM	Shuttle radar topography mission
STREST	Harmonized approach to stress tests for critical infrastructures against natural hazards (http://www.strest-eu.org/)
TRANSFER	Tsunami risk and strategies for the european region (https://cordis.europa.eu/project/id/37058)
TSP	Tsunami service provider
TSUMAPS-NEAM	Probabilistic TSUnami hazard MAPS for the NEAM region (http://www.tsumaps-neam.eu/; https://ec.europa.eu/echo/funding-evaluations/financing-civil-protection-europe/selected-projects/probabilistic-tsunami-hazard_en)
UNDRR	United nations focal point for disaster risk reduction (formerly UNISDR) (https://www.undrr.org/)

TSUMAPS-NEAM built its strategy upon previous and ongoing projects, such as the EU projects ASTARTE and SHARE, the UNDRR GAR15, and national projects or initiatives supporting PTHA efforts like the NTHMP (United States) and SiAM (Italy) (**Table 1**). TSUMAPS-NEAM also considered the PTHA effort to promote an informed process of outreach, the definition of guidelines, and capacity-building initiatives for Europe and neighboring countries under the auspices of the DG-ECHO. Such actions could also strengthen the connection between TSPs, Civil Protection Authorities, and other national authorities, thereby reinforcing the NEAMTWS effectiveness, including awareness-raising actions for improving tsunami risk perception (e.g., Cerase et al., 2019). The PTHA at the entire NEAM Region scale is also meant to become a baseline for PTHA efforts toward a consistent approach to risk assessment and long-term risk mitigation and planning at national and regional levels. Therefore, the PTHA devised by TSUMAPS-NEAM relied on a shared understanding of the best viable practices and sought compliance with European scientific and policy standards for hazard and risk assessment. The NEAMTHM18 has already been taken as the reference model by Civil Protection Authorities in Italy (DCDPC, 2018). In analogy with the well-established practice for defining seismic building codes, a homogeneous hazard level from NEAMTHM18 was chosen to define the inundation zone. The definition of evacuation zones and long-term coastal planning are both based on these inundation zones. Similar approaches are being followed in New Zealand (MCDEM, 2016) and the United States (American Society of Civil Engineers, 2017), based on the local PTHA. The region-wide NEAMTHM18 is also being taken as a reference for higher-resolution site-specific PTHAs (Gibbons et al., 2020) and applications dealing with critical infrastructures at risk (e.g., Argyroudis et al., 2020). The development of standardized PTHA products (hazard curves, hazard and probability maps, exhaustive and transparent documentation, web tools for dissemination and analysis) is the first step to include tsunamis in multi-hazard risk assessment and mitigation.

In this paper, we describe the NEAMTHM18 as the main result of the TSUMAPS-NEAM project. NEAMTHM18 is a Poissonian time-independent hazard model dealing with

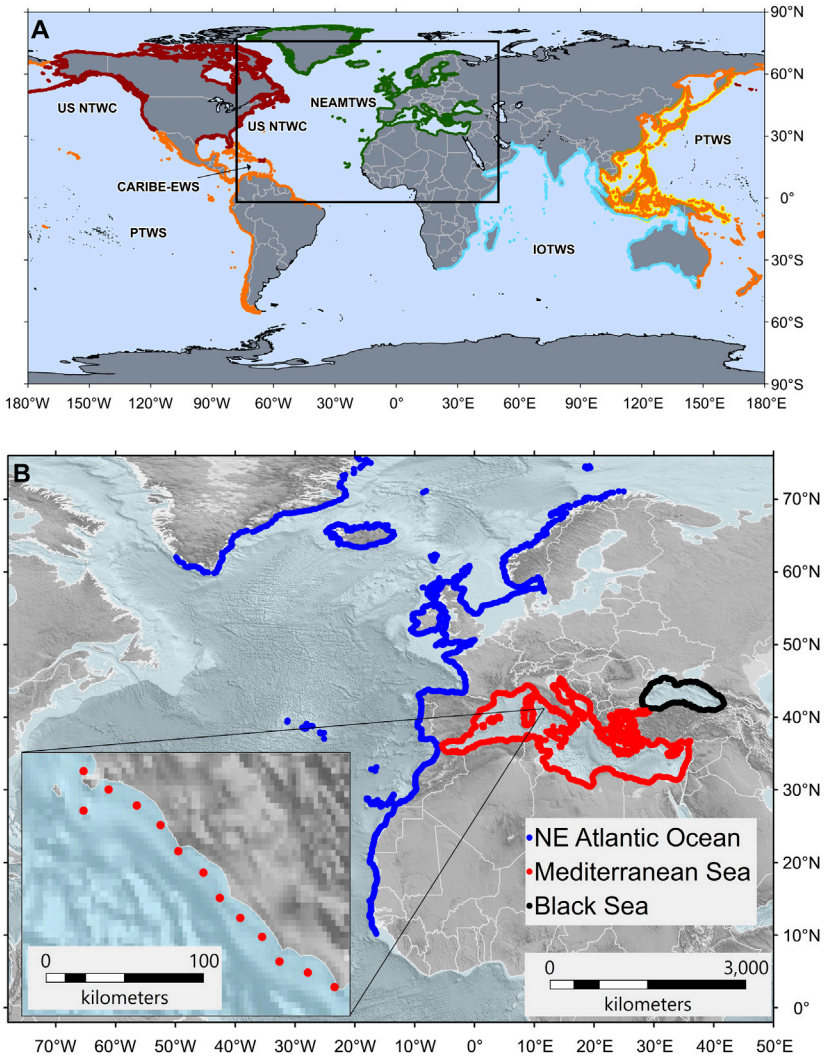

FIGURE 1 | (A) ICGs global area of coverage map of TWS (IOC, 2015). The black rectangle shows the location of the map in the lower panel covering a large part of the NEAMTWS (**Table 1**). US NTWC, US national tsunami warning center **(brownish red)**; IOTWS, indian ocean tsunami warning and mitigation system **(turquoise)**; PTWC, pacific tsunami warning center **(orange)**; CARIBE-EWS: interim of PTWC and US NTWC; PTWS: Northwest Pacific Tsunami Advisory Center/Japan Meteorological Agency **(yellow)**, PTWC, and US NTWC. **(B)** Distribution of the Points of Interest (POIs) where the NEAMTHM18 hazard is calculated. The inset shows a close-up view of the POIs to appreciate their spacing and offshore location. Topo-bathymetry is from the ETOPO1 Global Relief Model (NOAA, 2009; Amante and Eakins, 2009).

tsunamis generated by earthquakes. The primary hazard intensity measure is MIH (Glimsdal et al., 2019). The hazard results are provided by hazard curves, calculated at 2,343 POIs distributed at an average spacing of ~20 km along the NEAM coastlines, expressing the PoE in 50 years for different MIH thresholds.

The main challenges faced in the making of NEAMTHM18 were related to the diversity of tectonic environments hosting the potential seismic sources, the interconnections of large and small basins typical of the NEAM Region, the necessity to treat both near and distant seismic sources appropriately, and the vastness of the tsunami propagation domain requiring an intensive computational effort.

The hazard projects mentioned earlier undertook innovative approaches, followed by those specifically developed and implemented within TSUMAPS-NEAM. The first is the inclusion of sufficiently constrained 3D geometries for seismic sources (Selva et al., 2016; Tonini et al., 2020). The second is the potential of shallow slip amplification, as observed in recent tsunamigenic earthquakes (Romano et al., 2015a; Romano et al., 2020; Lorito et al., 2016) schematized as the effect of depth-dependent coupling and rigidity (Murphy et al., 2016; Murphy et al., 2018; Herrero and Murphy, 2018; Scala et al., 2019; Scala et al., 2020; Murphy and Herrero, 2020). The third is the massive use of HPC simulations with the multi-GPU Tsunami-HySEA benchmarked code (de la Asunción et al., 2013; Macías et al., 2017). The fourth is the approach to the tsunami reconstruction from precalculated elementary sources (Molinari et al., 2016), combined into the uncertainty

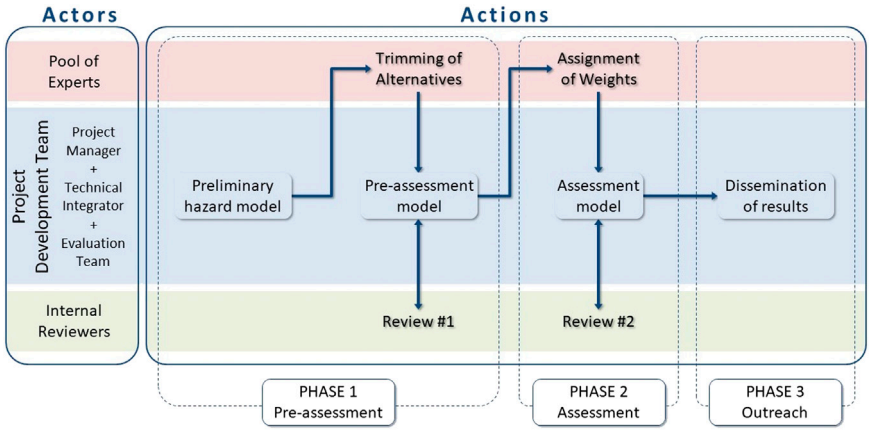

FIGURE 2 | Schematic illustration of the project's actors and correlative actions subdivided into three PHASES **(Supplementary Data Sheet S1.1)**. Notice that both phase 1 and phase 2 include an elicitation experiment and a revision stage each. PHASE 3 includes the NEAMTHM18 Documentation (Basili et al., 2019) of the two preceding PHASES, a web mapper to access the main results of the hazard assessment, scientific publications, and some materials for illustrating the results to the general public (e.g., Layman's Report).

propagation within a stochastic approach to inundation modeling (Glimsdal et al., 2019). Finally, the fifth is the quantification of uncertainty, combining ensemble modeling (Selva et al., 2016) with a multi-expert protocol for the management of subjective choices.

This paper provides a comprehensive overview of data, methods, and procedures adopted throughout the making of NEAMTHM18. It also illustrates the main results and discusses the model's implications, limitations, and possible future developments. More details about the NEAMTHM18 can be found in the TSUMAPS-NEAM project website, which provides access to the model-specific documentation, from now on referred to as NEAMTHM18 Documentation (Basili et al., 2019), and also allows for navigating the NEAMTHM18 in a web mapper, consult hazard curves, and download model data.

METHODOLOGY AND DATA

NEAMTHM18 was designed as a three-phase project (**Figure 2**; **Supplementary Data Sheet S1.1**) involving three main teams: PDT, PE, and IR. The PDT interacted with the PE and the IR during the first two phases of the project. The interactions between the PDT and the PE followed the prescriptions of a formalized decision-making process based on a multiple-expert protocol. This protocol, which was inspired by similar protocols developed for seismic hazard (USNRC, 1997; USNRC, 2012; USNRC, 2018), was developed and applied in the EU project STREST (2013–2016) (Argyroudis et al., 2020; Esposito et al., 2020), and subsequently adapted to the TSUMAPS-NEAM project needs. The TSUMAPS-NEAM implementation of the protocol included two elicitation experiments of the PE to identify the model alternatives to be implemented and assign proper weights to the selected alternatives (**Figure 2**). Managing

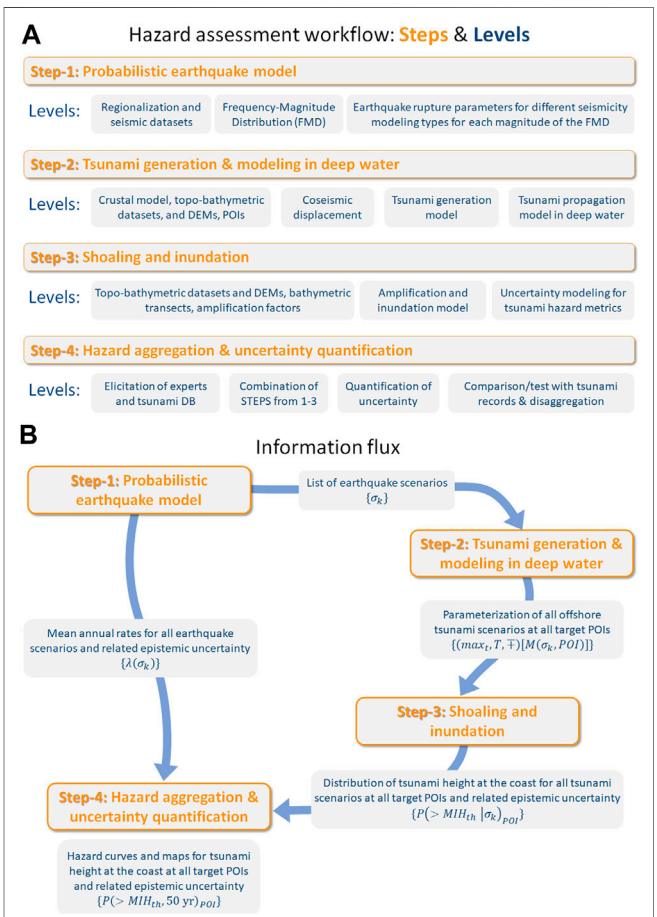

FIGURE 3 | (A) Sketch of the NEAMTHM18 workflow. **(B)** Sketch of the information flux to build the hazard model. This procedure is repeated for each considered alternative model.

the subjectivity of choosing among alternatives in a structured way is necessary because a hazard model is never completely constrained by observations, nor is the physics of the hazardous phenomenon totally understood. Different scientifically acceptable alternative models and relevant datasets may thus be used, thereby reflecting the inherent uncertainty. The different alternative models may have different degrees of credibility within the reference scientific community. In principle, the model credibility should coincide with the accuracy of its output, but this is not always quantifiable because of the general lack of independent data for rare phenomena such as tsunamis. The basis of the conceptual elicitation model and its implementation are presented in detail in Selva et al. (2015) and the NEAMTHM18 Documentation (Basili et al., 2019). The interaction between the PDT and the IR took place in two review rounds, leading to extensive project documentation, which was initially shared only with the IR and made publicly available through the project website after incorporating the IR's feedback.

The hazard assessment workflow is structured in "Steps" and "Levels" (**Figure 3A**), and the flux of information among the Steps proceeds along the paths illustrated in **Figure 3B**. There are four Steps, and each of them includes three to four Levels. Level-0 is common to all Steps and contains the definition of the used datasets. The other Levels constitute the finer grain of the hazard analysis within each Step, inside which the variables are treated as aleatory (for the aleatory variables in Step-1, see **Supplementary Figure S1** for a detailed scheme). At each Level within each Step, several alternative approaches, datasets, and models are implemented to explore the epistemic uncertainty. A relatively high number of alternatives was initially presented to the PE. The first elicitation experiment, held during phase 1 (pre-assessment), served to select only the alternative models deemed to be the most important uncertainty drivers **(Supplementary Table S1)**. The second elicitation experiment, held during phase 2 (assessment), served to establish the ranking of these alternatives by assigning weights to them **(Supplementary Table S2)**. Below we first introduce the Steps and Levels and then summarize their rankings according to the second elicitation experiment results. Ensemble modeling for hazard aggregation and model uncertainty quantification will be presented in the description of Step-4. Further details on the implemented alternative models describing their epistemic uncertainty, selection, and weighing procedure using the elicitation experiments are given in the NEAMTHM18 Documentation (Basili et al., 2019).

Step-1 concerns the Probabilistic Earthquake Model. It provides scenarios of all potential earthquakes in all considered seismic source regions, denoted as $\{\sigma_k\}$, and their mean annual rates $\{\lambda(\sigma_k)\}$, according to their FMDs and the scenario parameters (earthquake magnitude, fault rupture position, strike, dip, rake, rupture size, and rupture slip). It also provides alternative modeling schemes of the above scenarios and their mean annual rates.

Step-2 concerns the Tsunami Generation and Modeling in Deepwater. It provides the deterministic numerical simulations of the seafloor displacement fields corresponding to the earthquake scenarios defined at Step-1. It also provides the deterministic numerical simulations of the tsunami generation from these seafloor displacement fields and their propagation from the source to each offshore POI, resulting in synthetic mareograms, defined as $[M(\sigma_k, POI)]$, and parametric lookup tables of maxima ($\max_t$), periods (T), and polarities ($\mp$) for all mareograms, defined as $\{[\max_t, T, \mp][M(\sigma_k, POI)]\}$.

Step-3 concerns Shoaling and Inundation. It provides both stochastic and deterministic models of the tsunami impact at all POIs defined in Step-2 for all the scenarios defined in Step-1. The tsunami generated by each seismic scenario is expressed by two metrics: the probability distribution for the MIH calculated by applying local amplification factor to the offshore results, such as $AF(T, \mp, POI)$, and the single-valued impact obtained through the application of Green's law. Step-3 also provides the assessment of the alongshore tsunami variability as conditional hazard curves of the PoE of an MIH threshold value (MIH_{th}), denoted as $P(>MIH_{th}|\sigma_k)_{POI}$, and the assessment of the associated uncertainties, including those originating from linear combinations at Step-2.

Step-4 concerns the Hazard Aggregation and Uncertainty Quantification. It provides the probabilistic hazard model of the tsunami impact on NEAM coastlines expressed as the PoE in 50 years for different MIH thresholds $[P(>MIH_{th}, 50\,\mathrm{yr})_{POI}]$. The model is obtained by aggregating all annual scenario rates from Step-1 with the conditional PoE from Step-3. The model uncertainties are expressed through distributions of hazard curves of the PoE and their statistics. It also provides the preparation and display of hazard and probability maps, disaggregation products, sanity checks, and other by-products presented in the NEAMTHM18 Documentation (Basili et al., 2019).

Step-1: Probabilistic Earthquake Model

The basic principle applied here is that knowledge of the potential earthquake sources is always limited, and we then acknowledge that earthquakes are possible everywhere. The level of knowledge of some seismic sources can be higher than for others (e.g., Basili et al., 2013b). It is advisable to deal with this heterogeneous uncertainty while maximizing the use of all the available information. We thus subdivided the seismicity into different modeling types, each adopting a different approach for one or more parameters, depending on the level of knowledge of the underlying data (Field et al., 2014; Woessner et al., 2015; Selva et al., 2016).

The seismicity modeling types are defined by the different modeling and parameterization approaches. Our approach depends on how well the various parameters are constrained relative to each other for any given seismic source in its context. To apply this concept, we defined two main seismicity types: predominant seismicity (PS) and background seismicity (BS) (Selva et al., 2016). The PS type captures the larger earthquakes generated by well-known major faults, such as plate boundaries and subduction interfaces. This approach to tsunamigenic seismicity is common in PTHA (e.g., González et al., 2009; Power et al., 2013), rooted in the assumption that

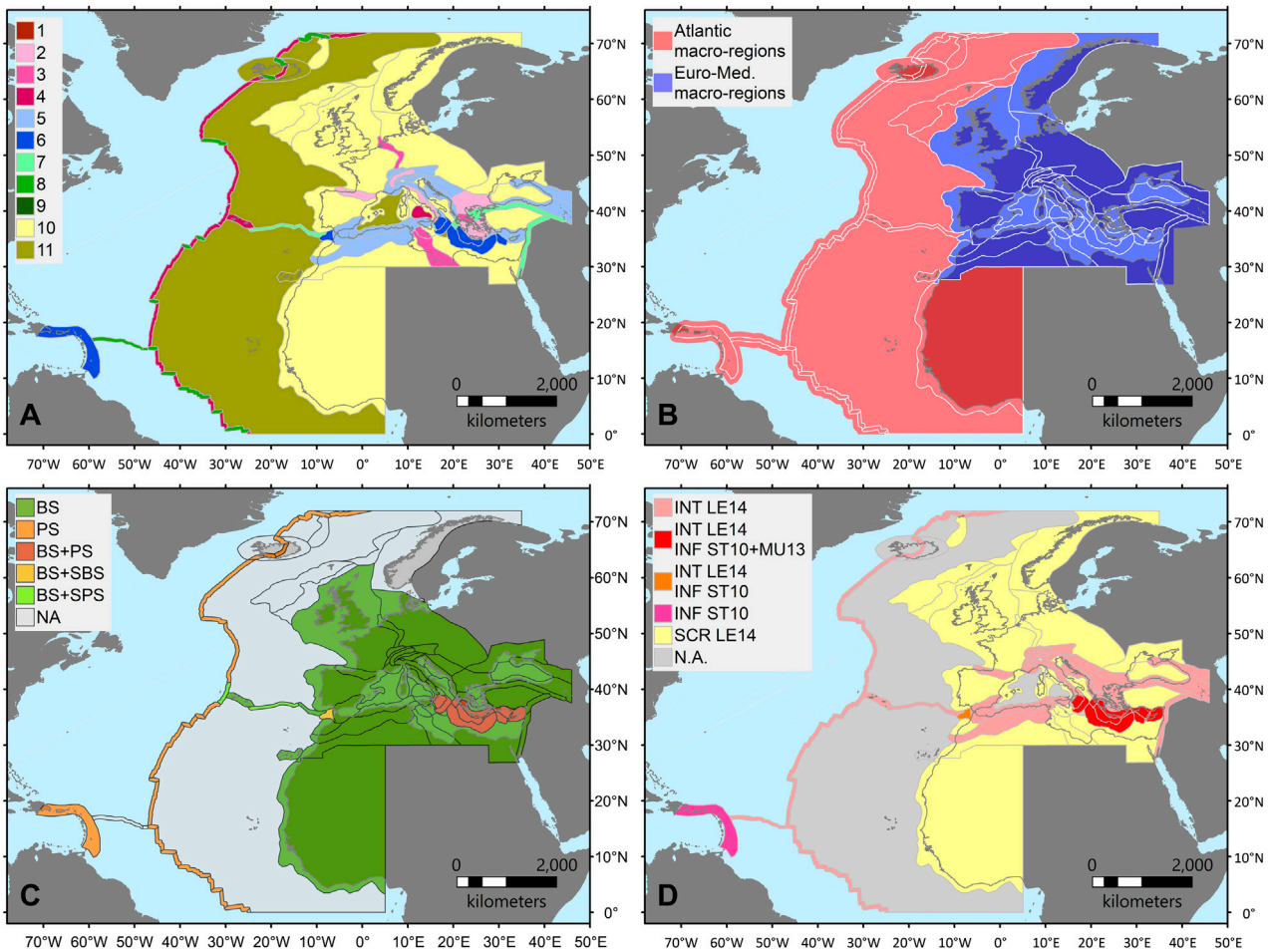

FIGURE 4 | (A) Map of the regions, color-coded depending on the tectonic setting and dominant deformation style, covering the whole source area. 1) Active volcano; 2) Back-arc and orogenic collapse; 3) Continental rift; 4) Oceanic rift; 5) Contractional wedge; 6) Accretionary wedge; 7) Conservative plate boundary (mainly major transcurrent faults); 8) Transform fault s.s.; 9) Shield; 10) Stable continental region; 11) Stable oceanic region. **(B)** Map showing the macro-regions used to analyze the completeness of the adopted earthquake catalogs **(Supplementary Figure S2)**. **(C)** Map showing the distribution of the seismicity model types assigned to each region of the tectonic regionalization. BS, background seismicity; PS, predominant seismicity; SPS, special PS; SBS, special BS; NA, not applied. **(D)** Map distribution of the adopted rupture scaling relations in the different tectonic settings. INT, interplate, crustal earthquakes; SCR, stable continental region, crustal earthquakes; INF, subduction interface. LE14 (Leonard, 2014); ST10 (Strasser et al., 2010); MU13 (Murotani et al., 2013); N.A, Not Applied.

relatively large earthquakes on known major faults dominate the tsunami hazard. Seismic sources of the PS type are then characterized by variability limited by the existing knowledge about them (e.g., fault geometry). The BS type captures all the diffuse seismicity in a tectonically-defined region. Therefore, sources of the BS type are characterized by the largest variability because of their lower level of knowledge, especially at the lower end of the earthquake magnitude values of interest. The BS type is less constrained by existing data and resembles seismic sources commonly adopted for seismic hazard analysis (Cornell, 1968), which have already been applied to tsunami hazard analysis (Sørensen et al., 2012). The above seismicity types may be modified to deal with specific situations considering the distance between the seismic source and the closest target coasts. In this respect, we defined two additional types: special PS (SPS) and special BS (SBS). While PS and BS types are two "end-members" featuring the maximum and the minimum number of fixed parameters, respectively, SBS and SPS types are intermediate cases in which the number of fixed and variable parameters is modulated case by case, also considering the necessary computational resources. These special cases are exclusive alternatives to each other and to the PS type, meaning that they are never considered together in the same source region.

Level-0: Input Data

Level-0 deals with the main input data that are used to build the probabilistic earthquake model. During phase 1 of the project (**Figure 2**), the possible alternatives to these input datasets were initially collected and analyzed. These potential alternatives were then reduced after the results of the elicitation experiment. Here we describe only the datasets retained for the actual hazard model implementation.

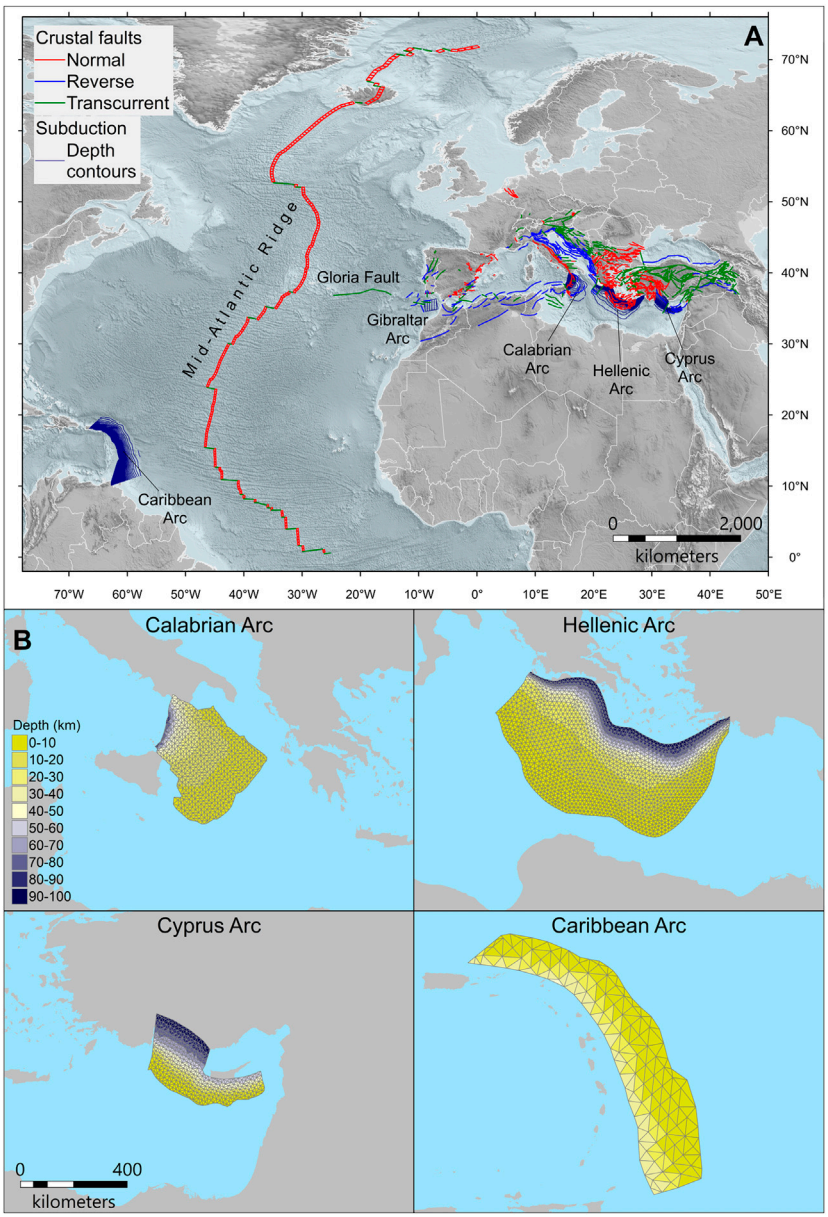

FIGURE 5 | (A) Map of the fault datasets. The primary sources of information for the fault geometry and kinematics are as follows: the European database of Seismogenic Faults (EDSF) (Basili et al., 2013a; Woessner et al., 2015); the database of Individual Seismogenic Sources, DISS version 3.2.1 (DISS Working Group, 2018), used to replace EDSF in the central Mediterranean; the global plate boundary model (Bird, 2003) as a reference for the Mid-Atlantic Ridge and the Gloria fault. All crustal faults are color-coded based on their mechanism. The geometry of the three Mediterranean slabs was initially derived from the European database of Seismogenic Faults (EDSF) (Basili et al., 2013a; Woessner et al., 2015) and then modified according to newer data where available. In particular, the Calabrian Arc was entirely replaced by a recent model (Maesano et al., 2017) derived from the interpretation of a dense network of seismic reflection profiles integrated with the analysis of the seismicity distribution at depth. The Hellenic Arc is the same as that in EDSF, but we verified its consistency with recent works (Sodoudi et al., 2015; Sachpazi et al., 2016). The Cyprus Arc was slightly modified in consideration of results from recent works (Bakırcı et al., 2012; Salaün et al., 2012; Sellier et al., 2013a; Sellier et al., 2013b; Howell et al., 2017) that are based on seismic reflection profiles and tomographic and seismological data and constrain the geometry of the western part of the slab. The geometry of the Caribbean slab was entirely derived from an early version of the Slab two model (Hayes et al., 2018), provided as a courtesy by G. Hayes. All slab geometries are represented with depth contours, except for the Gibraltar Arc, which is represented by a sketch to show its location only. Topo-bathymetry is from the ETOPO1 Global Relief Model (NOAA, 2009; Amante and Eakins, 2009). **(B)** Map views of the meshes used to discretize the subduction interfaces with color-coded depths. The locations of these slabs are shown in panel **(A)**. The meshes are built with element size set at ~15 km for the three subduction interfaces in the Mediterranean Sea, and ~50 km for the subduction interface of the Caribbean Arc, using the Cubit mesh generator (Casarotti et al., 2008). For all subduction interfaces, strike and dip are imposed by the discretization. Pure thrust faulting mechanism (rake 90°) is assumed for the Cyprus Arc because of the relatively small variability of the direction of plate convergence roughly normal to strike (Reilinger et al., 2006; Wdowinski et al., 2006), and the Caribbean Arc, according to other PSHA studies (e.g., Bozzoni et al., 2011). Variable rakes are used for the Calabrian Arc and Hellenic Arc in agreement with the direction of plate convergence.

Tectonic Regionalization

The tectonic regionalization is a subdivision of the entire domain of potential seismic sources into discrete regions internally as homogeneous as possible based on the dominant tectonic processes. The adopted regionalization (**Figure 4A**) was built following basic plate tectonics principles and by refining or adapting the regionalization of the European seismic hazard model (Delavaud et al., 2012; Woessner et al., 2015). This regionalization is only a two-dimensional subdivision of the crustal volume. In subduction zones, one must consider the three-dimensional geometry of slabs.

Seismic Datasets

The seismic datasets are used to determine the rates of seismicity. To this end, earthquake catalogs need to geographically cover all the potential seismic sources during the longest possible time and be as homogeneous as possible in terms of parameterization. We thus employed two different datasets: 1) the ISC catalog (ISC, 2016) for the area within the Atlantic Ocean (period 1900–2015) and the SHEEC-EMEC catalog (Grünthal and Wahlström, 2012; Stucchi et al., 2013) for the Mediterranean region (period 1000–2006). Their respective areas of application are shown in **Figure 4B**, which were produced by merging regions from the tectonic regionalization (**Figure 4A**) into four macro-regions in the Atlantic Ocean and six macro-regions in the Euro-Mediterranean area. For these two earthquake catalogs, we performed statistical completeness analyses (Wiemer, 2001; Woessner and Wiemer, 2005) separately for each macro-region **(Supplementary Table S3)** and adopted the Gardner and Knopoff (1974) method for the declustering **(Supplementary Figure S2)**. The non-declustered catalog is used to quantify annual earthquake rates and most other cases. The declustered catalog is used only to quantify the spatial distribution of BS-type sources through smoothed-seismicity (Level-2b).

Fault Datasets

The fault datasets aim to determine the orientation and sense of movement of future earthquake ruptures and, for a selection of them, the activity rate. To this end, we compiled two different datasets: focal mechanisms and geological faults. As with the earthquake catalogs, we favored geographic coverage over detail.

Regarding focal mechanisms, we considered the same macro-regions of the earthquake catalogs (**Figure 4B**). We adopted the global centroid moment tensors (Dziewonski et al., 1981; Ekström et al., 2012) for the North-East Atlantic and the regional centroid moment tensors (Pondrelli and Salimbeni, 2015) for the Euro-Mediterranean region **(Supplementary Figure S3)**.

Regarding the geological faults, we retrieved data from large public fault databases, plus some original additions or revisions of specific cases (**Figure 5**). In this collection, we separated crustal faults from subduction systems. For crustal faults, we considered faults deemed capable of generating earthquakes of magnitude ≥5.5 both inland and offshore. For subduction systems, we considered three subduction interfaces in the Mediterranean Sea (Calabrian Arc, Hellenic Arc, Cyprus Arc) and two in the western Atlantic Sea (Gibraltar Arc and Caribbean Arc). Additional information about the Gloria fault and the Gibraltar Arc was derived from the ASTARTE project, deliverables D3.16 and D3.40. The rate of activity of a selection of these faults is based on the tectonic parameters (**Supplementary Table S4**) derived from Christophersen et al. (2015) and Davies et al. (2018). It is worth noting, though, that the rates and coupling coefficients in the three Mediterranean subduction zones are highly debated and variable (Laigle et al., 2004; Ganas and Parsons, 2009; Tiberti et al., 2014; Vernant et al., 2014; Carafa et al., 2018; Nijholt et al., 2018).

Assignment of Seismicity Modeling Types to Different Seismic Sources

The four seismicity modeling types (BS, PS, SPS, SBS) are assigned to the regions resulting from the tectonic regionalization (**Figure 4A**) and are linked to relevant tectonic structures (**Figure 4C**). A maximum of two seismicity modeling types occurs in each region because the special cases (SPS and SBS) are alternative one to another. Faults shown in **Figure 5A** are geographically related to the regions of **Figure 4A** in this assignment.

The PS type is used in the Mediterranean area for the subduction interfaces of the Calabrian Arc, Hellenic Arc, and Cyprus Arc, and in the Atlantic area for the subduction interface of the Caribbean Arc and the crustal faults of the Mid-Atlantic Ridge far away from the Azores Islands (**Figure 5A**). The BS type is used everywhere in the Mediterranean area (**Figure 4C**), including regions overlaying the subduction interfaces (**Figure 5A**). In the Atlantic Ocean, the BS type is used for seismic sources near most coastlines (**Figure 4C**) but is neglected for seismic sources distant enough from some coastlines. One exception is the region around Iceland, where only PS is used. Possible seismic sources in the stable oceanic regions (**Figure 4A**) are ignored because seismicity rates seem to be too low to significantly contribute to tsunami hazards, according to global rates in this tectonic domain (Kagan et al., 2010). The SPS type is used for the Gloria Fault and a portion of the Mid-Atlantic Ridge near the Azores Islands (**Figure 5A**). SPS coexists with BS in all cases. The SBS type is used in the Gulf of Cadiz to model the Gibraltar Arc subduction interface (Gutscher et al., 2002; Duarte et al., 2013; Civiero et al., 2020), where the available geometric model (ASTARTE project deliverable D3.16) is a rather crude planar approximation. These choices are mainly due to the lack of computational resources to calculate elementary tsunami sources (Step-2), and therefore could change in future updates of the model.

Rupture Scaling Relations

Rupture scaling relations are used to determine the size of the earthquake ruptures and the geometrical discretization of the seismic sources. We initially reviewed the literature on fault scaling relations, analyzed the differences of their predictions, and tested their applicability to our modeling scheme. We adopted the scaling relations from Strasser et al. (2010) and Murotani et al. (2013) for the subduction interface earthquakes and those by Leonard (2014) for all crustal earthquakes. Although each scaling relation is subject to statistical uncertainty, we use only parameters from the best-

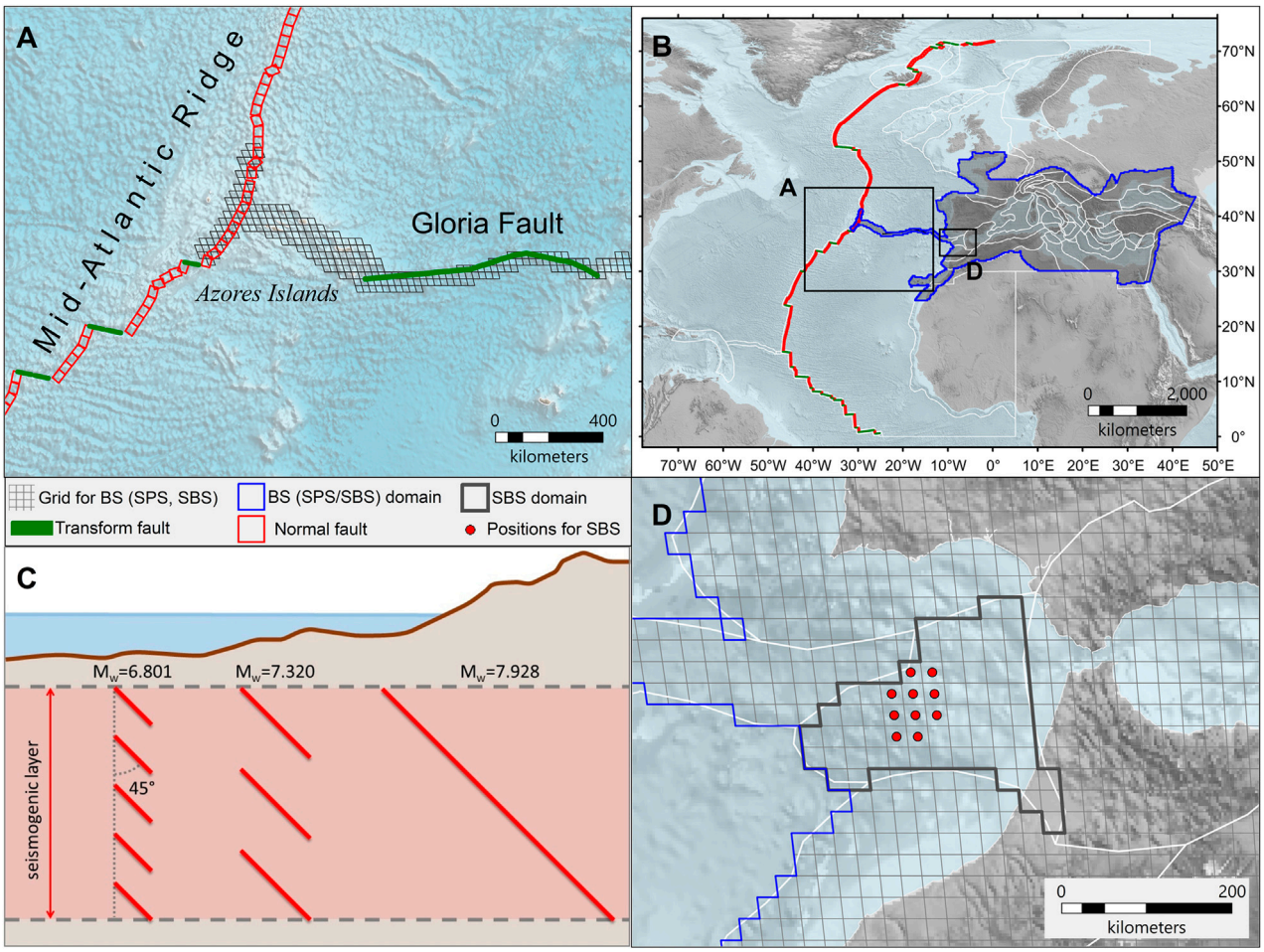

FIGURE 6 | (A) Close-up view of the Predominant Seismicity modeling type (PS) discretization in subfaults of the Mid-Atlantic Ridge and the Gloria Fault near the Azores Islands. Location of this map in panel **(A)**. There are in total 270 rectangular subfaults; 214 normal faults with a constant dip angle of 45° and size of 40 × 45 km; 57 strike-slip (transform) faults with a constant dip angle of 90° and size of 55 × 20 km. See **Supplementary Table S6** for the combinations of subfaults to make up large ruptures. The grid for the BS and SPS in this zone is also shown. **(B)** Regular grid (grey quadrangles, see the zoomed-in inset) composed of non-conformal equal-area cells of 25 × 25 km with the origin at 24°N–3°E for the discretization of the background seismicity modeling type (BS). Note that cell sides depart from right angles with increasing distance from the origin in this projection. The red outline marks the calculation domain, outside which only the predominant seismicity modeling type (PS) is modeled. The white outline of the tectonic regionalization (**Figure 4A**) is shown for reference. **(C)** Schematic of depth discretization for BS and SPS types due to the magnitude of earthquake ruptures applied to the center of each cell of the grid. For the SBS type, the magnitude range is extended to Mw = 9.026, and the depth limit of the crustal model is ignored. All magnitudes are always modeled for the shallowest depth position, irrespective of the crustal thickness being exceeded or not. Where the crust is very thin, some of the deeper positions are not occupied if the rupture crosses the base of the crust. **(D)** Cells of the grid (spatial discretization) in the Cadiz region showing the positions (center of 10 grid cells) occupied by the SBS type of the Gibraltar Arc subduction interface. Location of this map in panel **(A)**. Topo-bathymetry is from the ETOPO1 Global Relief Model (NOAA, 2009; Amante and Eakins, 2009).

fitting relations. **Figure 4D** shows the geographic distribution of their application in different tectonic regions.

Magnitude Discretization and Range

To improve the characterization of the FMD at higher magnitudes, we adopted a magnitude sampling that (roughly) becomes roughly exponentially finer as earthquake magnitude increases (**Supplementary Table S5**). This approach should allow for a more even sampling of the corresponding increase of the tsunami height, which seems nearly linear (Geist, 2012). The overall range of magnitude values modeled for each seismic source depends on different factors, such as fault size and discretization, seismogenic depth interval for subduction interfaces, crustal thickness, rupture scaling relations, and the distance between the seismic source and the target coastline. We adopted a lower threshold of Mw = 6 for seismic sources of seismicity model types (PS, BS, SBS, and SPS), except for seismic sources located far away from all target coastlines and modeled as PS type only, in which case we adopted a threshold of Mw = 7.3. The rationale for these limits is based on the FMD of globally analogous regions (Kagan et al., 2010). As not all possible earthquake magnitudes could be modeled, we tested the impact of unmodeled earthquakes at both ends of the considered magnitude range onto the hazard. The results of these tests are reported in the NEAMTHM18 Documentation (Basili et al., 2019).

Discretization and Parameterization of the Seismic Sources

A 3D geometry characterizes the subduction interfaces treated as PS type. Although 3D reconstructions yield more accurate representations of earthquake ruptures (Tonini et al., 2020), they are not available everywhere. Where available, their discretization must reflect the resolution of the data and constraints imposed by the modeling strategy. Starting from the slab geometries, we built 3D meshes (**Figure 5B**) with triangular elementary sources (subfaults) for setting the coseismic slip, which determines the seafloor displacement applied as a tsunami initial condition. The size of subfaults constrains the minimum modeled earthquake magnitude, considering the adopted scaling relations and the allowed maximum wave numbers of the slip spatial distribution. The crustal faults treated as PS types are the transcurrent (transform) and normal faults of the Mid-Atlantic Ridge and the Gloria Fault. They were discretized into rectangular subfaults (**Figure 6A**). As subfaults must be combined to form individual ruptures for different magnitudes, their size was determined to minimize deviations from the adopted scaling relations. Details of these parameters are provided in **Supplementary Table S6**. A summary of the implemented earthquake magnitude and depth ranges for all seismic sources modeled as PS type is provided in **Supplementary Tables S7, S8**.

The domain of the BS and SBS types is uniformly discretized into a grid (**Figure 6B**) trimmed where seismic sources are close to the target coastlines. At each grid cell, the earthquake ruptures can occur within the entire crustal thickness derived from the 1D global crustal model CRUST 1.0 (Laske et al., 2013) depending on the rupture width at the modeled earthquake magnitude (**Figure 6C**).

The rupture mechanisms may differ in each grid cell based on the available information from focal mechanisms and known faults. The discretization of the faulting mechanisms is made separately for each strike, dip, and rake by applying a reversible transformation (Selva and Marzocchi, 2004) from the standard convention (Aki and Richards, 1980). Considering four intervals for the strike, nine for the dip, and four for the rake yields 144 combinations. The Gibraltar Arc, modeled as SBS type, adopts a strategy like the BS type, but with more limited variability of rupture positions and faulting mechanism while allowing for larger magnitudes and depth range (**Figure 6D**).

Seismicity Separation in Catalogs

Once the regionalization is set (**Figure 4**) and all the tectonic sources are assigned to the four seismicity modeling types with their parameters defined, we need to separate the earthquakes assigned to individual faults of the PS/SPS from the earthquakes that remain within the BS/SBS. This separation is done by using two alternative cut-off distances of 5 km and 10 km. That is, assigning the seismicity within the cut-off distance to the PS and the remaining seismicity to the BS. We did not apply this procedure to the SBS (i.e., the Gibraltar Arc) because of its uncertainty in position and geometry. This hard-bound cut-off method is preferred over more sophisticated softer cut-offs (e.g., Bird and Kagan, 2004) because the Boolean separation provides two distinct catalogs of PS/SPS and BS/SBS events, which facilitates the implementation of the subsequent Levels.

Level-1: Frequency-Magnitude Distributions

The annual earthquake rates are based on the available seismicity data and tectonic data (convergence rates or slip rates) for selected PS as provided at Level-0. The earthquake rate determinations are also influenced by the assumption that larger earthquakes are increasingly likely to occur on major faults, possibly treated as PS/SBS/SPS types.

We implemented a set of Bayesian alternatives for quantifying the earthquake FMDs and their associated epistemic uncertainty, especially on annual rates and FMD tails. These alternatives concern the joint or separate quantification of earthquake rates for each seismic source, which allows for considering earthquake rate estimations derived from seismicity or tectonic rates, and functional forms (shape) of the FMDs and their parameters.

For the joint PS/BS quantification, the FMD is calculated in two stages (Selva et al., 2016; Taroni and Selva, 2020) first evaluating a global FMD distribution in each region and then separating this global FMD into PS/SPS/SBS and BS contributions, in regions where PS/SPS/SBS types are present. Both stages are based on a Bayesian formulation, with data coming from the non-declustered complete seismic catalog. This choice, also supported by the IR team, was made to avoid the significant underestimation of the real hazard that the declustering procedure may produce (Boyd, 2012; Iervolino et al., 2012; Marzocchi and Taroni, 2014). As shown by Kagan (2017), the Poisson distribution can also be used for non-declustered seismic catalogs if one is interested in modeling strong events (Mw > 6.5). Regarding the functional forms, we implemented both truncated and tapered Pareto formulations (Kagan, 2002a; Kagan, 2002b). Truncation and tapering are both applied to the probability density functions (PDFs). The parameters to be set are the rate for the smallest considered magnitude, the corner or the maximum magnitude (Mc or Mmax, for tapered and truncated distributions, respectively), and the scale parameter β (2/3 of the Gutenberg-Richter b-value). We set Mw = 5.0 as the minimum magnitude for assessing the rates, which is smaller than the minimum magnitude considered by the earthquake scenario (**Supplementary Table S5**) but allows for more robust rate estimations. The prior distributions are set as non-informative for the rates and the Mc (tapered Pareto). The Mmax for the truncated Pareto is set as discussed in Level-0, considering all known constraints (e.g., maximum magnitude observed in the region).

Two alternatives are implemented for estimating the parameter β. The first alternative is to compute the *b*-value from data by setting a weakly informative Gamma prior distribution centered on the worldwide tectonic analogs from Kagan et al. (2010) with variance corresponding to an equivalent sample size of 10. If there is a large dataset (>>10 samples), β is entirely controlled by the data, while in the case of very few data, the distribution is pushed toward the worldwide value. The second alternative is to force the *b*-value to be equal to one regardless of the observed seismicity in the region. As regards to the separation, we assumed a sigmoidal polynomial function that assigns a smooth transition between a high-magnitude regime

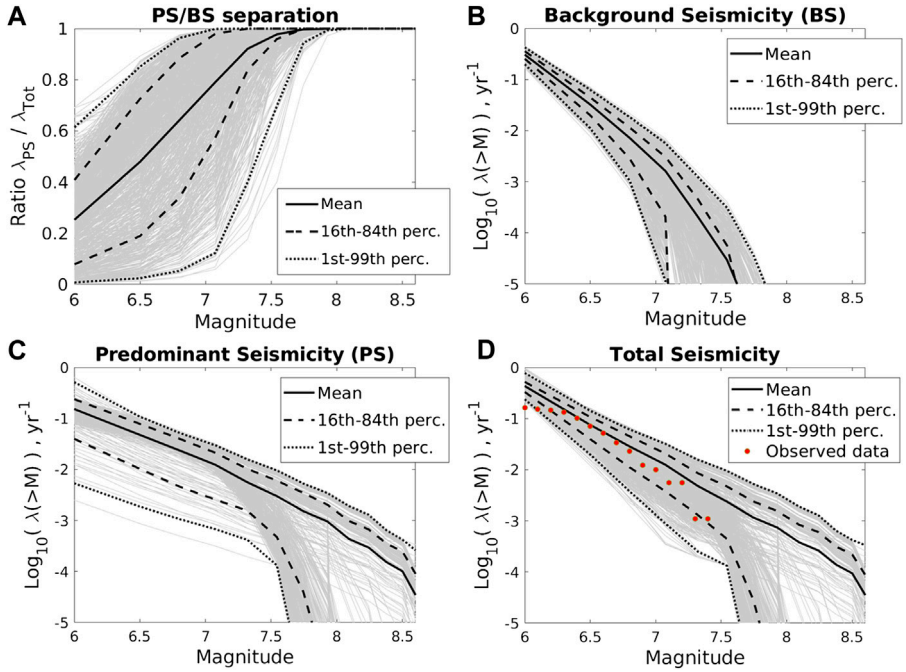

FIGURE 7 | Example of frequency-magnitude distributions for the Kefalonia-Lefkada, Greece, region. **(A)** Ratio between seismicity assigned to the PS type and total seismicity, evaluated with the Bayesian separation model. **(B)** BS seismicity type computed for all the alternative models (1,000 samples) and statistics of the epistemic uncertainty. **(C)** Same as panel **(B)**, but for PS seismicity. **(D)** Total seismicity, obtained by summing the BS and PS contributions, compared with the observed data from the relevant seismicity catalog. Grey lines in all panels represent the distribution samples.

where all earthquakes are supposed to be of PS/SPS/SBS type, a low-magnitude regime with a constant ratio between BS and PS/SPS/SBS, and an intermediate-magnitude regime where the ratio smoothly increases up to one (**Figure 7A**). Uncertainty on the three parameters of the separation (two magnitude thresholds separating high-, intermediate-, and low-magnitude regimes, and the ratio between BS and PS/SPS/SBS in the low-magnitude regime) is considered, with 1) uniform distribution for the lower threshold between magnitude five and six; 2) a uniform distribution for the higher threshold between magnitude six and seven in crustal BS and between magnitude seven and eight in subduction interfaces; and 3) a non-informative prior (uniform between 0 and 1) updated by likelihood functions based on the observed fraction between the PS/SPS and the BS earthquakes. Both alternative separation procedures are adopted, yielding two alternative separation models. These choices produce a total of $2 \times 4 = 8$ Bayesian alternative implementations for the joint PS-BS quantification of the FMD, with two alternative functional forms (tapered vs. truncated Pareto), two b-values (from data or set to 1), and two seismicity datasets from the two cut-off distances from PS. All of them are Bayesian alternatives; hence they automatically include the epistemic uncertainty emerging from parameter estimations. To propagate this uncertainty to the hazard results, we resampled these models 1,000 times, thereby providing 1,000 alternative realizations of the Bayesian model.

Further alternative FMDs for PS are set from Christophersen et al. (2015) and Davies et al. (2018), starting from tectonic convergence or slip rates (**Supplementary Table S4**). Conversely, the FMD for BS could not be quantified with a similar strategy due to the lack of resources. Therefore, each FMD for PS is complemented by randomly sampling one FMD for BS from the two-stage PS/BS quantification. In this way, the two quantifications are independent since they are based on different input data.

To derive the FMDs for PS from tectonic data, we adopt two functional forms, the characteristic and the truncated Pareto (Kagan, 2002a; Kagan, 2002b) (**Supplementary Table S2**), considering three alternative maximum magnitudes, three alternative b-values, three alternative estimations for the seismic coupling (**Supplementary Table S4**), we obtain $3 \times 3 \times 3 \times 2 = 54$ alternatives.

In **Figures 7B–D**, we provide an example implementation in the Kefalonia-Lefkada region (Ionian Islands, Greece) of the four -BS/PS Bayesian FMDs models and the 54 models of BS/PS separated seismicity (separated into two groups, one for truncated Pareto and another for characteristic G-R). This region includes part of the Hellenic Arc, i.e., both PS and BS. The resulting modeled total FMDs (sum of BS and PS contributions) are compared with data. The results for the remaining four Bayesian models, relative to the 10 km-wide cut-off, are equivalent.

Level-2: Earthquake Rupture Variability

The variability of earthquake ruptures for PS/SPS types (Level-2a) is analyzed in terms of rupture position and area on the hosting

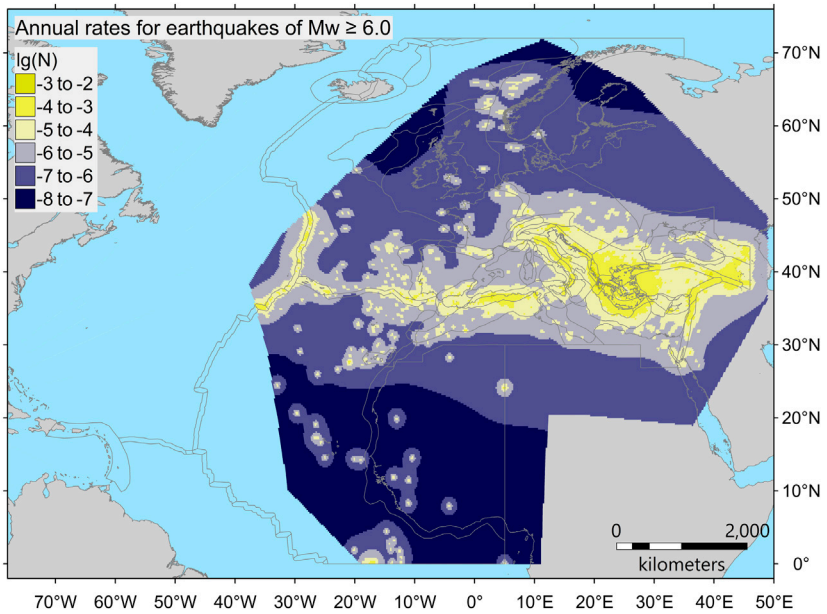

FIGURE 8 | Map showing the geographic distribution of annual earthquake rates (common logarithm scale) for Mw ≥ 6.0 for the BS/SBS seismicity model types, adopting the cut-off distance of 5 km for the seismicity separation between PS and BS. This separation is done by assigning the earthquakes located within the given cut-off distance from the PS sources (**Figures 4**, **5**) to the PS/SPS types and the remaining earthquakes to the BS/SBS types. The hazard model also includes the distribution of annual earthquake rates calculated with the cut-off distance of 10 km.

structures and, importantly, slip distribution. The position and size of the rupture area are treated simultaneously. Earthquake positions on each hosting fault are discretized by defining a set of coordinate pairs representing the rupture center on the fault geometry. The assessment consists of quantifying the joint probability of a rupture center, a rupture area, and slip for an earthquake of a given magnitude in the region. Earthquake magnitude, rupture area, and slip are derived from rupture scaling relations without considering their uncertainty. For PS and SPS in the Atlantic region (distant seismic sources), we use only the rupture scaling relation of Strasser et al. (2010) for earthquakes in the Caribbean subduction and that of Leonard (2014) for crustal earthquakes (**Figures 4C,D**). For the Mediterranean PS subduction interfaces, we adopted the scaling relations from Strasser et al. (2010) and Murotani et al. (2013). Murotani et al. (2013) predict larger areas and smaller average slips at larger magnitudes than Strasser et al. (2010). These scaling relations provide only the average slip in the rupture area. Here, we also model the aleatory variability of the heterogeneous slip distribution for the larger earthquakes on the Mediterranean subduction interfaces because they are close to target areas (**Figure 5**). We use the classic k^{-2} stochastic slip distributions on a non-planar surface, applying a technique that has been previously validated (Herrero and Murphy, 2018). Two alternative models have been considered: one considers depth-independent rigidity, the other considers shallow slip amplification controlled by depth-dependent rigidity variations (Bilek and Lay, 1999) while preventing systematic slip excess at shallow depths over one or more seismic cycles (Scala et al., 2020) (**Supplementary Figure S4**). For all the other structures assigned to PS and SPS, the slip is assumed to be uniform according to the average value resulting from the adopted scaling relation.

The earthquake ruptures variability of the BS/SBS types (Level-2b) is analyzed in terms of spatial distribution, depth distribution, and faulting mechanism. The variability associated with the rupture area and slip is not explored because only one rupture scaling relation is adopted for BS and SBS cases (**Figures 4C,D**). We use the smoothed seismicity approach (Frankel, 1995) to compute the spatial seismicity distribution and introduce a correction to account for the variability of the completeness magnitude in the spatial smoothing (Hiemer et al., 2014) to increase the number of seismic events considered. This approach enables longer intervals of the catalog, adopting an increasing magnitude of completeness while exploring older seismicity. The analysis is based on the complete part of the declustered catalog considering the two alternative cut-off distances (**Figure 8**).

Regarding the focal depth, all possible depths of the discretization shown in **Figure 6** are considered equally probable. In each cell of the spatial domain, various faulting mechanisms are possible for the modeled earthquake ruptures. The probabilities of these mechanisms are not uniform, and their expected PDF is derived through a Bayesian method according to centroid moment tensors of observed seismicity and data on known faults (Selva et al., 2016). The likelihood is modeled as a multinomial distribution based on the non-declustered entire (without considering completeness) catalogs of focal mechanism (**Supplementary Figure S3**), considering the two alternative cut-off distances (BS type only) and both nodal planes of each focal mechanism (Selva and Sandri, 2013). If faults occur in a grid cell,

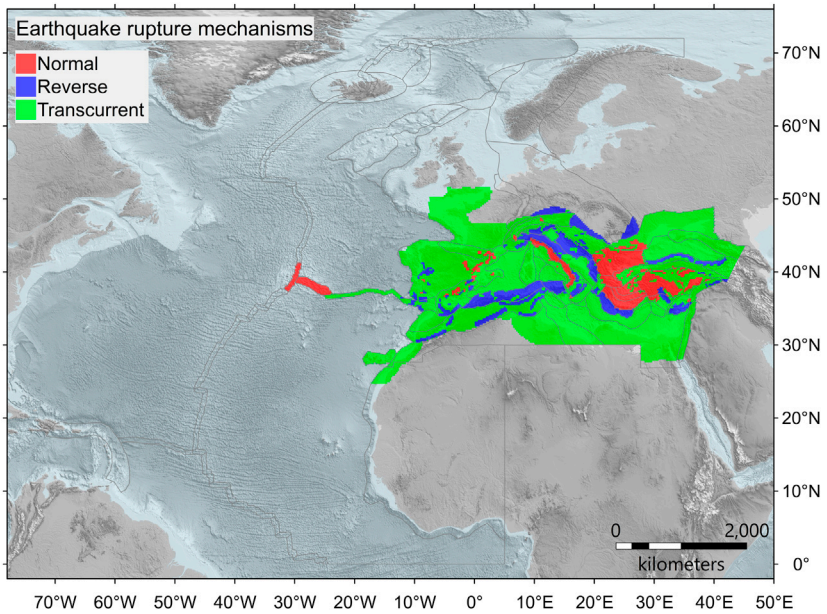

FIGURE 9 | Geographic distribution of crustal earthquake rupture mechanisms within the calculation domain for the BS/SPS type. Only the most probable mechanism in each grid cell is shown for simplicity. The complete distribution consists of strike discretization at four intervals of 45° starting from 22.5° clockwise from North, and dip discretization at nine intervals of 20° within the 0°–180° range. The rake discretization is at four intervals of 90°, corresponding to normal, reverse, left-lateral strike-slip, and right-lateral strike-slip. Altogether, this makes a total of 4 × 9 × 4 = 144 combinations of the strike, dip, and rake values. For the SBS type (**Figure 6D**), the variability of the mechanism is limited to four combinations (strike of 22.5° and 337.5°; dip at 10° and 30°, and rake fixed at 90°). Topo-bathymetry is from the ETOPO1 Global Relief Model (NOAA, 2009; Amante and Eakins, 2009).

a Dirichlet distribution is set by forcing an average equal to the fault strike, dip, and rake of the fault fraction intersected by the cell, weighting this information ten times as much as that from the focal mechanisms. When multiple faults are present in one cell, their mechanisms are weighted by their respective moment rate. **Figure 9** shows the geographic distribution of the resulting mechanisms classified as normal, reverse, and transcurrent. For simplicity, only the faulting mechanism with the highest probability (mode) is represented in each cell.

Step-2: Tsunami Generation and Modeling in Deepwater

In PTHA, it is common to use nonlinear shallow water (NLSW) models with wetting and drying to compute inundation and runup. As of today, NLSW simulations of coastal inundation are not yet affordable in the case of region-wide PTHA requiring millions of seismic scenarios. Moreover, sufficiently high-resolution bathymetry and topography models are not always available, which may discourage precise deterministic simulations. Conversely, simulations in deep waters may be conducted with reasonable accuracy by numerical integration of shallow water equations using relatively low-resolution bathymetric models available in the public domain. We thus separate tsunami modeling into two stages, one at Step-2 for generation and propagation in deep waters, and one at Step-3 for the coastal processes, characterized by larger uncertainty.

In Step-2, we assume linearity between the size of the tsunami and the coseismic displacement at the source. This approach makes Step-2 affordable from the computational viewpoint. Step-2 then provides the input to Step-3, which consists of synthetic tsunami mareograms and their parameters at offshore POIs.

Hence, Step-2 can be further divided into three main goals. The first is the deterministic numerical simulation of seafloor displacement corresponding to the individual earthquake scenarios defined at Step-1. The second is the deterministic numerical simulations of the tsunami generation and propagation from each source to any offshore POI. The third is the analysis of the mareograms to extract wave amplitude maxima, wave periods, and polarities for later use in Step-3.

Level-0: Input Data

The adopted crustal model for coseismic displacement calculations is an infinite half-space with the properties of an elastically homogeneous Poisson solid (e.g., Okada, 1992).

The topo-bathymetry model generally employed is SRTM30+ (Becker et al., 2009), which has a grid spacing of 30 arc seconds (~900 m), improved with local data in the Gulf of Cadiz (Zitellini et al., 2009). In the Black Sea, SRTM15+ (Tozer et al., 2019) resampled to 30 arc seconds is used.

The POIs are the locus of tsunami simulation outputs, and subsequent tsunami hazard quantities are derived from the topo-bathymetric models around them. We set our POIs to nominally lie along the 50-m isobath with a spacing of roughly 20 km from each other (**Figure 1**). The POI depths have some variability

related to the approximations made during the extraction of the 50 m-depth contour from the regularly gridded data with the GMT algorithms (Wessel et al., 2013) forced to remain within 40–100 m. The POIs outside this range are discarded. Hence, the distance between two adjacent POIs can be occasionally larger than 20 km, typically in areas with very steep slopes.

The spacing of POIs is a compromise between coastline coverage, computational cost, and storage containment. Similarly, the POI depth range is a compromise between preserving the linearity of the tsunami propagation and the need to be as close as possible to the target coastline. In principle, linearity should be guaranteed by ensuring the tsunami amplitude remains much smaller than the water depth. Linearity is needed to cope with the huge number (~50 million) of seismic scenarios, coupled with the geographical scale of the investigated region through a linear superposition of pre-computed virtual POI tsunami time-series from elementary sources (Molinari et al., 2016).

It must be noted, though, that there are also locations where a POI cannot be realistically associated with the coast behind it because it is too distant. This circumstance occurs, for example, in the southern part of the North Sea, in the northern Adriatic Sea, and on the eastern coast of Tunisia. In all such cases, special care should be adopted if using the results at the local scale.

Level-1: Coseismic Displacement Model

Level-1 concerns the coseismic seafloor displacement for each earthquake scenario defined at Step-1. Each earthquake scenario corresponds to a single fault rupture characterized by a set of parameters, including location, geometry (fault size and orientation), and rake-parallel slip vector. The coseismic seafloor displacement is modeled using Volterra's formulation of elastic dislocation theory applied to faults buried in an infinite elastic half-space. To this end, we used the analytical model by Okada (1992) in the case where fault ruptures consist of single or multiple planar quadrangles, and the code by Meade (2007) in the case of 3D triangular meshes, as defined in Step-1. Slip vectors are always constant for planar faults, whereas they can be either constant or variable for non-planar faults, as described in Step-1, Level-2a. The total seafloor deformation is computed as a linear superposition of contributions from the individual patches that describe the fault. The vertical component of the seafloor displacement, sampled on a regular 30 arc-second grid roughly centered automatically on the rupture, is used as input for Level-2, where the tsunami generation is treated. Since the fault elastic dislocation in an infinite elastic half-space solution produces very long "tails" of low-amplitude surface displacement, for practical reasons, we restricted the deformation area to vertical displacements larger than 1 cm.

Level-2: Tsunami Generation Model

Level-2 deals with the initial tsunami conditions at the surface derived from the seafloor vertical deformation obtained at Level-1. To account for the attenuation of the short wavelengths through the water column, we applied a two-dimensional filter of the form $1/\cosh(kH)$ (Kajiura, 1963) to the static vertical seafloor deformation field calculated at Level-1. Here k is the wavenumber, and H is the effective water depth taken as the average above the fault. This filter is performed through forward and backward fast Fourier transforms with the high-pass filtering applied to the Fourier image in between. Because of the constant water depth requirement, this approach has a drawback in the case of large ruptures stretching over highly variable bathymetry. The Kajiura (1963) filtering was not applied to all sources treated as rectangular subfaults, including all the relatively shallow but mostly distant sources of the Gloria Fault, the Mid-Atlantic Ridge, and the Caribbean Arc.

Level-3: Tsunami Propagation Model in Deepwater

Level-3 concerns the simulation of tsunami mareograms at the offshore POIs (**Figure 1**), according to the initial conditions evaluated at Level-2 for all the considered earthquake scenarios. These offshore time-series are also further analyzed to derive the principal wave characteristics, such as the maximum amplitude, period, and polarity, that are necessary inputs for the subsequent processing at Step-3.

The mareograms are obtained as linear combinations of Green's functions to save computational resources. The coefficients of the linear combinations (i.e., weights of the Green's functions) reflect the initial displacement computed at the previous Levels in this Step. Two types of tsunami Green's functions are used. The first is the type associated with Gaussian-shaped sea-level elevation unit sources. The second is the more usual type considering unit slip at elementary subfaults. This choice was made for practical reasons because the Gaussian tsunami database for the Mediterranean Sea already existed, and it was then extended farther to the Black Sea and part of the Atlantic Ocean. In some other cases, it was less expensive computationally to adopt the subfault approach, e.g., in the case of distant sources not requiring modeling of low earthquake magnitudes. More details are found in the NEAMTHM18 Documentation (Basili et al., 2019).

Green's functions were simulated with the Tsunami-HySEA NLSW GPU-optimized code (de la Asunción et al., 2013). The code has been benchmarked at NTHMP benchmarking workshops (Lynett et al., 2017; Macías et al., 2017; Macías et al., 2020a, Macías et al., 2020b). The open boundary at the coast is used as boundary conditions. The spatial resolution of the simulation grid is 30 arc seconds. Tsunami-HySEA automatically adapts the time-step to match the Courant–Friedrichs–Lewy stability condition for the deepest point in the simulation grid. The simulated time was 4 h in the Black Sea, 8 h in the Mediterranean Sea, and up to 16 h in the Atlantic Ocean. More details are found in the NEAMTHM18 Documentation (Basili et al., 2019). Simple linear combinations according to local slip values were performed for the elementary tsunamis generated by the subfaults. Conversely, for the Gaussians, we use an algorithm for sea level displacement reconstruction and unit sources linear combination coefficient determination starting from an arbitrary fault (Molinari et al., 2016).

The last activity within Level-3 of Step-2 is the post-processing of the mareograms obtained *via* linear combinations. The post-processing phase is necessary to obtain the main wave

characteristics needed for applying the amplification factors at Step-3. These are stored as matrices providing the amplitude, leading wave polarity, and dominant wave period at each POI for each considered scenario in the seismic model. The post-processing algorithm is described in the NEAMTHM18 Documentation (Basili et al., 2019) and in the study that deals with the local amplification factors and the uncertainty propagation procedure (Glimsdal et al., 2019).

Step-3: Shoaling and Inundation

Step-3 aims to evaluate the tsunami height at the coast, starting from the synthetic mareograms and their parameters computed offshore at each POI in Step-2. Our main metric to express tsunami size on the coast is the MIH measured relative to the mean sea level (**Supplementary Figure S5**) for the entire event duration.

Level-0: Input Data

As for Step-2, the SRTM15+ bathymetric model (Tozer et al., 2019), which has a grid spacing of 15 arc seconds (~450 m), was used for extracting the profiles in the Mediterranean Sea and the Black Sea. For the North-East Atlantic, we used the SRTM30+ (Becker et al., 2009), which has a grid spacing of 30 arc seconds (~900 m), improved with local data in the Gulf of Cadiz (Zitellini et al., 2009). The latter is the same already used in Step-2, Level-0.

This Level also provides 1D amplification factors that transform the incident wave amplitude into an MIH value based on local bathymetric profiles. The basic principles of the 1D method are described by Løvholt et al. (2012) and Løvholt et al. (2015). Here, we employ an improved version of this amplification method, which was partly developed within the ASTARTE project (deliverable D8.39) and then further developed and completed by Glimsdal et al. (2019). The latter describes how the amplification factors, which depend on the period and polarity of the incident wave and the local bathymetric profile, were calculated. For this, we used incident waves with leading peak (positive polarity) and leading trough (negative polarity), and wave periods of 120–3600 s. These amplification factors are provided as lookup tables providing the amplification factor value for each specific location as a function of the period and polarity.

The procedure to acquire the bathymetric profiles (**Supplementary Figure S5**) begins with extracting offshore POIs along a 50 m depth contour with an initial separation distance of ~20 km. The nearest-neighbor algorithm is then used to identify the nearest coastal point. These designated coastline points, also separated by roughly 20 km, were then applied to define a piecewise linear shoreline contour. A set of 40 transects, spaced at about 1 km and perpendicular to this contour line, were then created (i.e., 20 km to each side of the onshore hazard points). All profiles that intersected islands were deleted to avoid positive values (i.e., land). Profiles with anomalous orientation relative to the shoreline in areas characterized by complex non-planar coastlines or regions with many islands (e.g., Aegean and Croatian islands), deep and narrow bays (e.g., fjords) were identified, and transect positions were drawn manually. Further details can be found in Glimsdal et al. (2019).

The approach developed by Glimsdal et al. (2019) also addresses stochastic inundation modeling to consider the 2D character of the inundation process and its uncertainties. It also allows for propagating the uncertainty stemming from the previous Steps. Another dataset is the relative error distribution related to the approximation of the deep-sea tsunami propagation as a linear combination, introduced at Step-2. This modeling uncertainty distribution is one of those provided by Molinari et al. (2016). Moreover, to quantify the epistemic uncertainty related to the simplification made with the 1D amplification factors, we compared the obtained MIHs with the results of local high-resolution 2D NLSW numerical inundation models in six test sites where high-resolution bathymetric and topographic models were available from the ASTARTE project. One site is in the Atlantic Ocean at Sines, Portugal, whereas the other five sites are in the Mediterranean Sea, at Colonia Sant Jordi, Mallorca Island and SE Iberia (Spain), Siracusa and Catania (Italy), and Heraklion (Greece). In this way, we obtained the distributions of the bias and the variability of the inundation. The details of the applied methodology and the obtained uncertainty distributions can be found in Glimsdal et al. (2019). We recall that the numerical simulations are done in the 2D vertically-averaged NLSW, which is still approximate. For example, 3D free-surface Navier-Stokes models would be, in principle, more accurate. However, numerical simulations cannot replace observations, and tsunami run-up data generally do not suffice for hazard calculation purposes.

Level-1: Amplification and Inundation Model

The local coastal tsunami impact is here expressed by one primary and one alternative hazard intensity metric. Our primary metric is the MIH. An alternative metric is obtained *via* amplification through Green's law (e.g., Kamigaichi, 2011).

At this Level, the amplified MIH values corresponding to all the different tsunamis generated by the individual seismic sources at each POI are obtained by applying the lookup tables from Level-0 to the matrices of tsunami parameters provided by Step-2. Also, the simplest form of Green's law is applied. This relation defines the ratio between the offshore value H_D at a given depth D and the amplified value H_d after shoaling to a certain reference depth d, that is $H_d = H_D \sqrt[4]{D/d}$. We fix as customary this reference depth d to 1 m. D is the depth of the POIs. In this way, if a POI lies at a depth of 50 m, the amplification obtained *via* Green's law is, for example, ~2.66 times the maximum elevation provided by the mareogram.

Note that using Green's law is not an alternative model. It estimates a different tsunami hazard intensity metric, not an alternative approach to estimating the same metric. However, this allowed us to define a sanity check on NEAMTHM18 results, comparing them with what we would have obtained adopting an alternative amplification scheme. These sanity check results are presented in the NEAMTHM18 Documentation (Basili et al., 2019). The application of MIH from the amplification factors and Green's law does not require large computational efforts or very-high grid resolution for the offshore input simulations.

Level-2: Uncertainty Modeling

At Level-2, we quantify and sample the distributions describing the aleatory and epistemic uncertainty associated with tsunami modeling. The epistemic uncertainty related to the probability of exceeding a certain threshold MIH should account for the uncertainty inherent in the amplification factor method and uncertainties that may arise at the previous Steps due to different model approximations and non-modeled effects (Davies et al., 2018). These uncertainties are expressed with a conditional PoE, and the relative uncertainty is subsequently used at Step-4 combined with source probabilities for hazard assessment.

To start with, the probability of exceeding different values of threshold MIH given a certain MIH input value, as obtained by the deterministic amplification factors, is calculated using further lookup tables expressing conditional probabilities. This conditional probability describes the statistical variability of MIH along the shore, modeled as a log-normal distribution (Glimsdal et al., 2019). The resulting distribution describes the variability of MIH values across coastal transects approximately perpendicular to the coastline behind the POI, related to one single scenario. It is found that the MIH obtained with the amplification factor derived at Level-0 approximates the median value of the log-normal distribution of MIH values caused by any tsunami scenario, with small bias. From now on, this statistical variability of the MIH along the shore is treated as an aleatory uncertainty. This probability can be interpreted as the hazard curve at one randomly selected point within the stretch of coastline near the target POI, conditional to the occurrence of the specific tsunamigenic seismic scenario. This probability distribution and its parameters hence depend on the scenario, through the characteristics of the incident wave and on the bathymetric slope in front of the specific POI, and through the local amplification factor. The uncertainty on the parameters of the distribution is treated as epistemic uncertainty, including the uncertainty stemming from the linear combinations performed at Step-2, assuming that this uncertainty is not correlated with the uncertainty at the POI. We then sample both uncertainty sources within a Monte-Carlo type simulation scheme, using 1,000 samples, hence obtaining 1,000 alternative conditional hazard curves for each scenario at each POI. The variability of the results in this distribution of curves represents the sampled epistemic uncertainty in the conditional hazard curves for each tsunami scenario and each POI. The details of this methodology and the obtained uncertainty distributions can be found in Glimsdal et al. (2019) and the NEAMTHM18 Documentation (Basili et al., 2019). A potential step forward in assessing the uncertainty introduced by simplified source modeling, which was not feasible with the project resources, can be made with an approach based on run-up data (Davies et al., 2018), and treating the uncertainty from generation to inundation altogether (Davies, 2019; Scala et al., 2020). Nonetheless, it must be recalled that run-ups observed at a single location are generally incomplete samples of past tsunami variability.

Step-4: Hazard Aggregation and Uncertainty Quantification

The goal of Step-4 is the quantification of the hazard, including uncertainty, expressed by hazard curves at all POIs. The hazard curves provide the PoE within a given time window, here fixed at 50 years, for different MIH thresholds at any given POI, which is here expressed with the notation $P(>MIH_{th}, 50\,yr)_{POI}$.

This probability is obtained by aggregating the conditional PoE $P(>MIH_{th}|\sigma_k)_{POI}$ (from Step-3) with the mean annual rates $\lambda(\sigma_k)$ of each scenario σ_k (from Step-1). The uncertainty of the hazard is quantified through an ensemble modeling technique (Marzocchi et al., 2015; Selva et al., 2016), which accounts for the weighted alternative models from previous Steps to propagate uncertainty, and yields a family of hazard curves and their statistics (mean and percentiles). Alternatives are assumed to represent an unbiased sample of the epistemic uncertainty, in which weights simply measure their representativeness or credibility. The implication is that the alternatives at all Steps and Levels do not need to be mutually exclusive and collectively exhaustive (MECE). Step-4 also includes the post-processing of hazard curves, including the production of hazard and probability maps, hazard disaggregation, comparisons with observational data, and sanity checks. These post-processing results are part of Step-4 and can be found in the NEAMTHM18 Documentation (Basili et al., 2019).

Level-0: Input Data

The main input consists of the weight assessment resulting from the elicitation experiment held during phase #2 that provided the weights to the implemented alternatives (**Supplementary Table S2**). Specifically, we adopted the weighted mean of the scores obtained from two alternative implementations of an AHP (Saaty, 1980) as weights at each Step and each Level of the hazard model. Both AHP processes adopt two distinct criteria for comparing the alternative models: one is the experts' personal preference of a model, and the other is the most used model in the community according to experts' best knowledge. Following the AHP, these two criteria are not equally considered, but the same PE prioritizes them by answering a specific question. The AHP scores are finally evaluated as the weighted geometric mean of the different members of the PE (Forman and Peniwati, 1998), where experts have different weights. The two alternative AHP implementations emerge from two alternative weighting schemes for the experts: performance-based weights and acknowledgment-based weights (see the NEAMTHM18 Documentation (Basili et al., 2019) for details). These two alternative implementations of the AHP are then weighted according to experts' opinions, evaluated by adopting equal weights for the experts. The merged weights for each Step and Level are reported in **Supplementary Table S2**.

Another dataset required at Step-4 is the catalog of past tsunamis for comparing observations with the hazard results. To this end, a relevant dataset is provided by the Euro-Mediterranean Tsunami Catalogue (Maramai et al., 2014). Although this comparison is beyond the scope of this paper,

the outcomes of tests and checks on intermediate and final results are available from the NEAMTHM18 Documentation (Basili et al., 2019).

Level-1: Combination of Step-1, Step-2, and Step-3

The contributions to the hazard at each POI are aggregated by considering the mean annual rate of each seismic source (Step-1), the generation and propagation in the deepwater of the consequent tsunami (Step-2), and its inundation (Step-3). The assessment consists of quantifying the hazard curves in terms of PoE within the considered exposure time of 50 years and different hazard intensity thresholds MIH_{th}.

The hazard curve is first expressed in terms of the mean annual rate of exceedance of MIH_{th} at each POI, for a predefined set of MIH_{th} values. This curve is computed combining the mean annual rates $\lambda(\sigma_k)$ of each potential seismic scenario σ_k and the probability that this scenario leads to exceeding a given MIH_{th}, that is:

$$\lambda(>MIH_{th})_{POI} = \sum_i \lambda(\sigma_i)\, P(>MIH_{th}|\sigma_i)_{POI} = \sum_j \sum_k \lambda\left(\sigma_k^{(Type_j)}\right) P\left(>MIH_{th}\middle|\sigma_k^{(Type_j)}\right)_{POI}$$

where $Type_j$ covers all seismicity types described in Step-1 and the term $P(>MIH_{th}\left|\sigma_k^{(Type_j)}\right.)_{POI}$ is the PoE at one POI, conditioned to the kth scenario sampled from the epistemic uncertainty on the log-normal parameters, as described in Step-3, Level-2 (**Figure 3B**).

Each curve expressed as an annual rate of exceedance vs. different thresholds MIH_{th}, can be converted into a hazard curve (PoE vs. MIH_{th}) considering the exposure time and assuming that the tsunamigenic earthquakes follow a stationary (Poissonian) arrival time process (Kagan, 2017). Hence, the probability of observing at a given POI at least one exceedance of the tsunami threshold MIH_{th} in 50 years can be written as:

$$P(>MIH_{th}, 50\ \mathrm{yr})_{POI} = 1 - \exp\left(-\lambda(>MIH_{th})_{POI} \cdot 50\right)$$

The quantification of $\lambda(>MIH_{th})_{POI}$ and hence of $P(>MIH_{th}, 50\ \mathrm{yr})_{POI}$ is performed over a pre-defined set of 50 MIH_{th}.

It might be convenient to consider that the PoE in a given exposure time ΔT can be converted into ARP using the formula $ARP = \Delta T/\mathrm{abs}\{\ln[1 - P(>MIH_{th}, \Delta T)_{POI}]\}$. For example, a PoE = 2% in 50 years gives ARP≈2,475 years, whereas a PoE = 10% in 50 years gives ARP≈475 years. ARP≈2,475 years has been used in coastal planning against tsunamis (MCDEM, 2016), while ARP≈475 years is often used for civil seismic building code definition (NTC, 2018).

In theory, these quantities could be computed for all combinations of alternative models of all Steps and Levels and all possible realizations of the Bayesian model parameters at Step-1 Level-1 and Level-2b. We thus adopted a Monte Carlo sampling procedure to contain the computational effort (Selva et al., 2016). At each Step and Level, potential alternatives are sampled proportionally to their weights (the higher the weight, the higher the chance to sample the corresponding model). Once a complete chain of models is sampled from all potential alternatives at all Steps and Levels, one realization of $\lambda(>MIH_{th})_{POI}$ is computed. A total of 1,000 chains of models are sampled according to the model weights, obtaining a sample of 1,000 alternative $\lambda(>MIH_{th})_{POI}$, subsequently converted into a sample of 1,000 alternative hazard curves $P(>MIH_{th}, 50\ \mathrm{yr})_{POI}$ at each POI.

Level-2: Uncertainty Quantification

All the alternative implementations at Level-1 are used as input to the ensemble modeling procedure to produce, for each target POI, an ensemble distribution that quantifies both aleatory and epistemic uncertainty. The set of 1,000 alternative $P(>MIH_{th}, 50\ \mathrm{yr})_{POI}$ is treated as an unbiased sample of epistemically alternative hazard curves. The corresponding parent distribution represents the ensemble distribution quantifying simultaneously aleatory and epistemic uncertainties (Marzocchi et al., 2015). This distribution coincides with the community distribution for hazard curves (USNRC, 1997; Bommer, 2012).

Given the relatively large size of the sample of alternative models, we produced the ensemble distribution as an empirical distribution emerging from the sample itself, that is, without fitting any predefined parametric distribution. So, at Level-2, we derive statistics from the sampled empirical distributions of hazard curves, which is the simplest possible choice (Marzocchi et al., 2015). Given the relatively large sample size and considering that we provide both mean and median curves and restrict the epistemic statistics to the 98th and the 2nd percentiles, we argue that this approach should not have important practical implications.

Level-3: Post-processing

The post-processing of hazard results includes a series of analyses: sanity checks to verify if intermediate and final results are consistent with the input data and minimize the possibility of implementation bugs; sensitivity analyses to explicitly test the consequences of some methodological choices, especially the innovative ones; hazard disaggregation to deepen into the hazard results, unveiling "what is due to what"; checks against past tsunamis to compare the available recorded observations with the hazard results.

More specifically, the disaggregation was computed as in Selva et al. (2016). For example, the disaggregation for seismicity classes is made by evaluating the probability that a given seismicity class causes the exceedance of a given MIH threshold at the site through the Bayes' rule, that is

$$P(PS|>MIH_{th})_{POI} = \frac{\sum_{\sigma_i \in PS} \lambda(\sigma_i) P(>MIH_{th}|\sigma_i)_{POI}}{\sum_{\forall \sigma_i} \lambda(\sigma_i) P(>MIH_{th}|\sigma_i)_{POI}}$$

Epistemic uncertainty is evaluated by repeating this quantification for each alternative in the sample. The NEAMTHM18 Documentation (Basili et al., 2019) includes disaggregation results for seismicity class, tectonic region, magnitude, and fault location for a predefined set of 42 POIs in the NEAM Region.

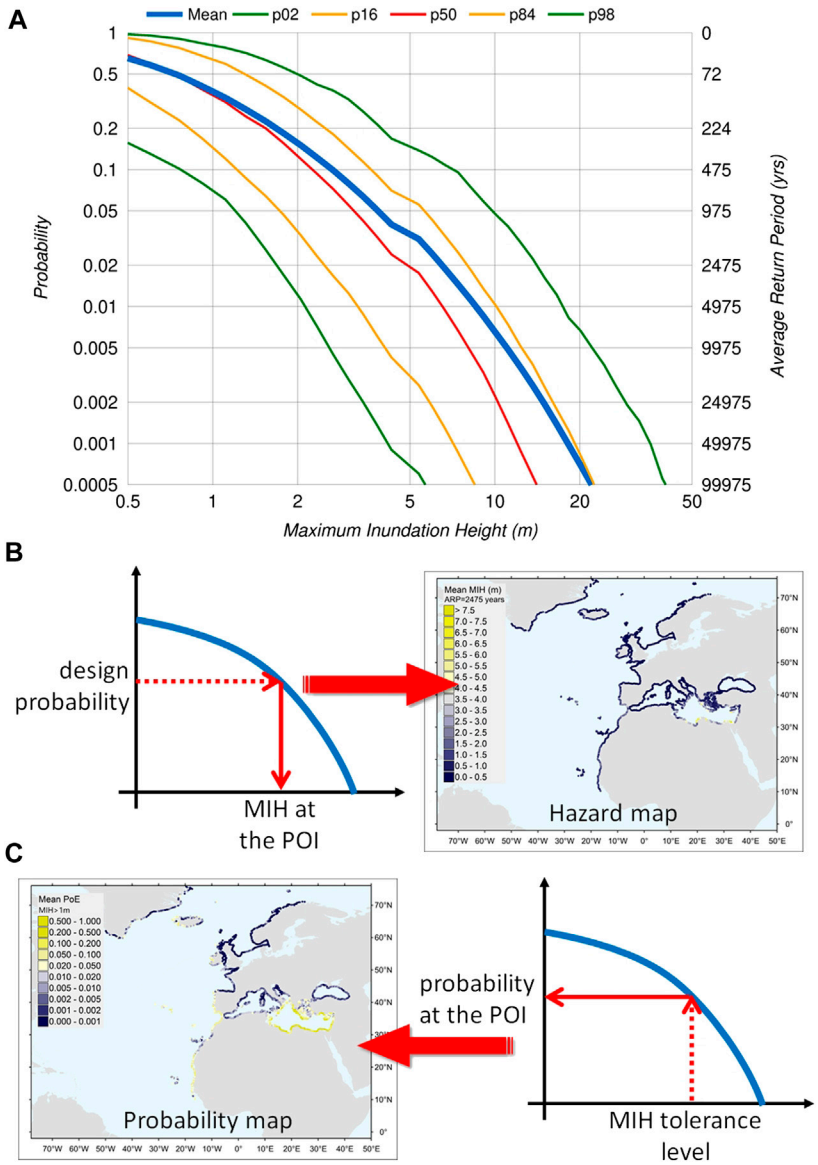

FIGURE 10 | (A) Example of an ensemble of hazard curves calculated for a point of interest. Each curve represents a different percentile of all the models spanning the epistemic uncertainty. **(B)** Hazard map (**Figure 11A**) produced to show the values of the maximum inundation height (MIH, in meters) at any point of interest (POI), obtained by cutting hazard curves at a given design probability of exceedance in 50 years. **(C)** Probability map (**Figure 11A**) produced to show the probability of exceedance in 50 years at any point of interest, obtained by cutting hazard curves at a given tolerance level of the maximum inundation height.

Statistical testing to compare hazard results with the record of past tsunami is complicated by the non-statistical independence of the records in the different POIs, the difficulty in translating qualitative tsunami intensity values in hydrodynamic quantities, and the general lack of significant datasets of complete records in any single POI. Besides, standard historical catalogs, such as the Euro-Mediterranean Tsunami Catalogue (Maramai et al., 2014), are organized per source rather than per site, reporting only the tsunami intensity in the Sieberg-Ambraseys scale (Ambraseys, 1962) for each event, thereby limiting the possibility of extensive testing.

Considering these limitations, we made two examples of possible comparisons. In the first test, we compared the hazard curves in a relatively small and closed basin such as the Marmara Sea, where all records may be assumed as being correlated. The test consists of checking the consistency of the provided hazard curves (specifically the probability for MIH > 0.5 m) with the number of large tsunamis (with intensity 4 or 5) observed in the past (five events in the past 1,500 years). In the second test, we compared a reference hazard map for an ARP = 2,500 years at the 84th percentile, which are the values adopted as a reference in New Zealand and Italy (MCDEM, 2016; DCDPC,

2018), with the maximum quantitative observations to verify if the exceedances are relatively rare. The test is performed along the Italian coasts, which may experience tsunamis from most of the seismic sources of both the eastern and western Mediterranean Sea. Both tests revealed general compatibility of the hazard results with the observations. However, we consider these tests only preliminary and that future research should be dedicated to developing improved and standardized techniques to enforce more extended testing between long-term PTHA results and past tsunami records. More details on all post-processing results can be found in the NEAMTHM18 Documentation (Basili et al., 2019).

HAZARD RESULTS

We recall that the NEAMTHM18 deals with earthquake-generated tsunamis and that it is a time-independent hazard model, as the earthquake occurrence is modeled as a Poisson process. As the output of Step-4, the model is constituted by a collection of hazard curves, one set per POI, and hazard and probability maps derived from these curves. The whole model is distributed online through the NEAMTHM18 webpage with a specially designed interactive tool (**Supplementary Figure S6**). There are also by-products, constituted by intermediate results obtained in the hazard calculation process, which were described, and briefly commented, within the presentation of the four Steps, which available for verification and reproducibility of NEAMTHM18 (**Supplementary Data Sheet S1.2**).

We calculated hazard curves at 2,343 POIs (North-East Atlantic: 1,076; Mediterranean Sea: 1,130; Black Sea: 137). The hazard curves represent the main result of all the calculations (**Figure 10A**). All other results are either intermediate results used to calculate hazard curves or are derived from hazard curves (e.g., hazard maps). The hazard curves express the PoE vs. different values of the MIH, our hazard intensity threshold, during a given exposure time.

Probability and frequency are linked together so that each PoE value corresponds to an ARP, which is the average time between two consecutive events of the same intensity. The adopted exposure time is 50 years, whereas the adopted hazard intensity measure (or metric) is the tsunami MIH evaluated at a POI, representing the coastal stretch behind the POI itself. A single MIH value at a single POI represents an estimate of the mean value along the coast because the actual MIH values vary laterally along the coast behind the POI. Based on our methodological analysis, local maxima of the actual MIH (and maximum run-up) values along the coast are expected not to exceed three-to-four times the mean MIH estimated at the POI. More details on MIH and its lateral variability can be found in Glimsdal et al. (2019).

Six hazard curves are shown in a single plot to represent the model uncertainty. Each curve corresponds to a different statistics of the model uncertainty represented by the hazard curve distribution (**Figure 10A**). The hazard curves are reported for the mean, and the 2nd, 16th, 50th, 84th, and 98th percentiles of the model ensemble. PoE can be considered robust in the range 10^{-3}–10^{0} (ARP<~50,000 years). Results for PoE < 5×10^{-4} (ARP >~100,000 years) are not considered sufficiently well constrained, for example, due to the period covered by the seismic catalogs. Consequently, they are omitted from the results.

Hazard (intensity) and probability maps are derived from hazard curves in which each POI is assigned a value according to the hazard intensity or PoE, respectively (**Figures 10B,C**). To make a hazard map, we extract the MIH corresponding to a chosen design PoE, or, equivalently, to a given ARP for each POI. To make a probability map, we extract the PoE in 50 years, corresponding to a chosen MIH value for each POI. In either case, map values are calculated by linear interpolation between the two closest points in the hazard curves. Based on this scheme, we put together a portfolio of probability maps for MIH of 1, 2, 5, 10, and 20 m, and hazard intensity maps for ARP of 500, 1,000, 2,500, 5,000, and 10,000 years, that can be navigated in the NEAMTHM18 web interactive tool (**Supplementary Figure S6**). Different views can be obtained for each map considering the mean or any of the percentiles of the epistemic uncertainty stored in the hazard curves. **Figure 11** shows two examples of such maps.

DISCUSSION

Tsunami waves can travel long distances without dispersing much energy. Therefore, a relatively high hazard can affect places far from the earthquake source that generated the tsunami. The Caribbean subduction is one of these cases that contributes to the tsunami hazard of European and African coastlines in the Atlantic Ocean. Within the Mediterranean Sea, seismic sources are always much closer to most coastlines than in the Atlantic Ocean. Nonetheless, tsunami hazards can also be high in zones known for not hosting significant seismic sources. For example, although Libya and Egypt do not have hazardous seismic sources, probability maps show that their coastlines are more likely to be affected by significant tsunamis than the coastlines of southern Italy, Greece, Turkey, and Cyprus–all regions located much closer to the subduction zones (**Figures 5**, **11A**). In other words, unlike other types of earthquake-related hazards, both local and distant seismic sources contribute to earthquake-generated tsunami hazards. Although the closeness to seismic sources is undoubtedly a good proxy for a relatively high tsunami hazard, the distance from seismic sources is not necessarily a proxy for a very low tsunami hazard.

An added value of a region-wide hazard computed in a consistent manner is that the hazard of different and very distant places, or even separate basins, can be compared at a glance, without having to worry about how much the hazard depends on the different input datasets or different methods adopted for the calculations. Although regional-scale models cannot replace in-depth analyses at sub-regional (national) and local levels, they can provide a common reference for performing local hazard quantifications focused on different areas (e.g., Bacchi et al., 2020). They also enable using unsupervised filters of seismic sources for more detailed local

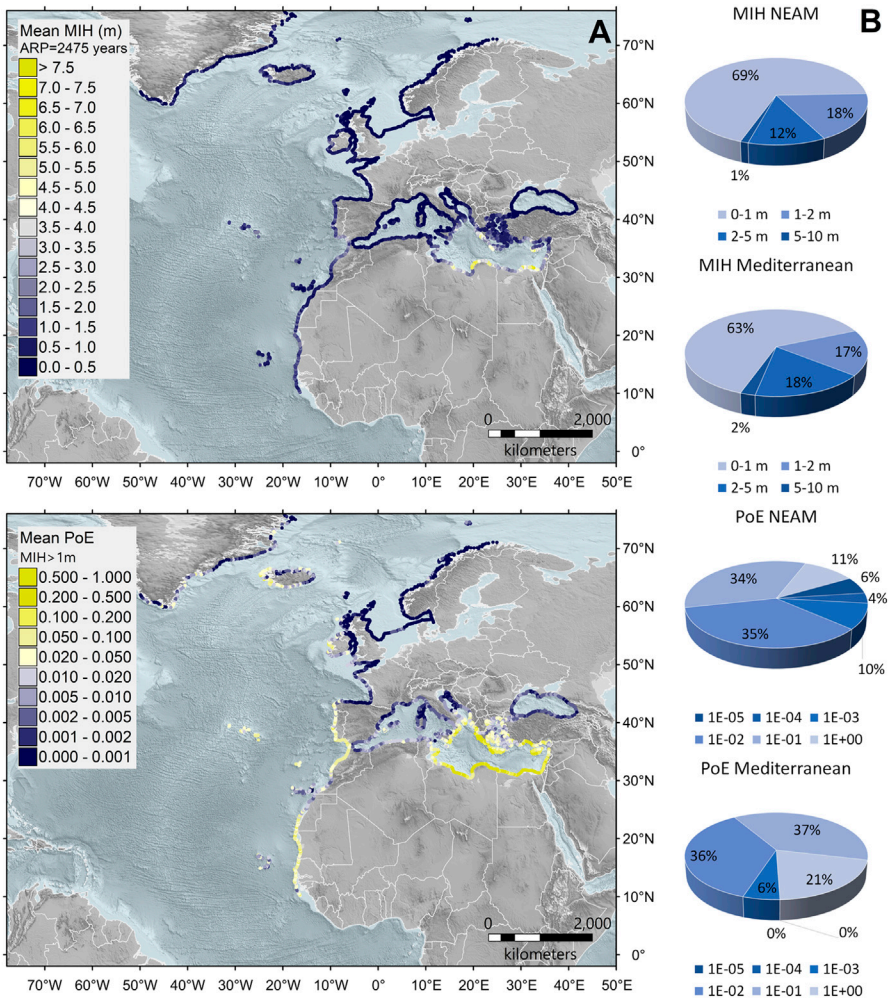

FIGURE 11 | (A) NEAMTHM18 hazard map for the probability of exceedance of 2% in 50 years, equivalent to an average return period of 2,475 years **(upper)** and NEAMTHM18 probability map for maximum inundation height larger than 1 m **(lower)**. Topo-bathymetry is from the ETOPO1 Global Relief Model (NOAA, 2009; Amante and Eakins, 2009). **(B)** Pie charts showing the percentage of points of interest in the NEAM and Mediterranean coastlines that correspond to different maximum inundation heights for an average return period of 2,475 years **(two upper charts)** and to different probabilities of exceedance of a maximum inundation height of 1 m **(two lower charts)**. Notice the increasing proportion of points of interest with higher hazard in the Mediterranean region relative to the entire NEAM Region.

analyses (Lorito et al., 2015; Volpe et al., 2019) (**Supplementary Data Sheet 1.3**).

Concerning the mean model for the ARP = 2,475 years, the number of POIs with MIH > 5 m remains within 1% of the entire NEAM Region. Over 30% of the POIs, however, correspond to an MIH > 1 m (**Figure 11B**), which with local fluctuations may lead to run-ups three times higher (Glimsdal et al., 2019). The NEAM Region is very large and includes coasts facing zones of relatively low seismicity. If we repeat the analysis only for the Mediterranean Sea, we find a larger incidence of potentially destructive events. Similar reasoning can be repeated for the PoE for a given MIH. MIH > 5 m is found only in the Mediterranean Sea. Specifically, in Cyrenaica (Libya), the Nile Delta (Egypt), Cyprus, and the Peloponnese (Greece). In the North-East Atlantic, the highest MIHs are generally lower than those in the Mediterranean Sea. MIH > 3 m is found only in a few locations, such as the Dakhlet Nouadhibou Bay (Mauritania), likely because of the Arguin Spur in the near offshore, and the Gulf of Cadiz (**Figure 12**).

When comparing hazard values in different localities, one should always consider uncertainty. Even if two places have the same mean hazard, the actual hazard can differ for different epistemic uncertainty levels. The spreading of the hazard curves at every POI conveys information about the uncertainty that affects these estimates. This fact can be expressed by the relative uncertainty of the MIH or PoE values corresponding to a given percentile around the mean. **Figure 13A** shows the geographic distributions of an example of the relative uncertainty calculated as the proportion of the 84th percentile with respect to the mean. In other words, this quantifies how much the mean values in the maps of

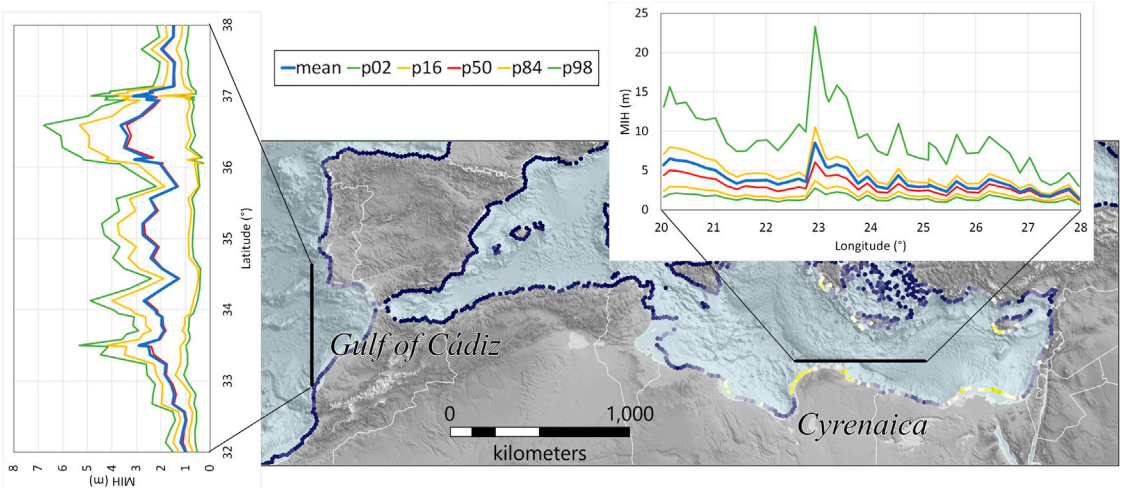

FIGURE 12 | Example profiles of the maximum inundation height (MIH; mean and the epistemic uncertainty represented by the 2nd, 16th, 50th, 84th, and 98th percentiles) along coastlines among those with the highest hazard of the NEAM Region. The two profiles span coast of the Gulf of Cadiz (N–S) and the Cyrenaica (E–W). Both profiles are with reference to the hazard model with the 2% probability of exceedance in 50 years (average return period of 2,475 years). The color scale in the map is as in **Figure 11**. Topo-bathymetry is from the ETOPO1 Global Relief Model (NOAA, 2009; Amante and Eakins, 2009).

Figure 11A can be overtaken if the 84th percentile of the epistemic uncertainty occurs. Geographically, the impact of the epistemic uncertainty varies significantly. For example, the existing uncertainty on the Gibraltar Arc subduction interface (modeled as SBS type in Step-1) is reflected by significantly distant hazard curves in the Gulf of Cadiz. **Figure 13B** shows that for most POIs (~67%), MIH values up to 40% larger than the mean can occur if alternative, though scientifically acceptable, interpretations are considered. The same reasoning applies to the relative uncertainty of the probability associated with specific MIH values.

In the entire NEAM Region, catastrophic events, such as those that can produce MIHs larger than several meters, are rare but not impossible. The highest tsunami hazard of the NEAM Region is found in the central-eastern Mediterranean, where long stretches of the coastline can exceed an MIH of 5 m with significant probability, and with lower probability in the region of the Gulf of Cadiz. In the latter, much of the hazard is likely driven by the Gibraltar Arc subduction interface. As discussed above, the epistemic uncertainty in this region can be reduced by improving the subduction interface characterization.

In NEAMTHM18, the model uncertainties have been addressed together with the PE through two elicitation experiments (**Figure 1**). The first elicitation experiment was devoted to identifying and prioritizing the possible alternative model implementations at all Steps and Levels (**Supplementary Table S1**). However, the list of specific aspects of each alternative could even be much longer than reported and possibly include cases of alternatives that became available after the first elicitation experiment but could not be implemented in the timeframe of the project. Some of these alternatives were also specifically suggested by the IR during the review phases (**Figure 1**), but their implementation was not feasible with the available data and resources.

At Step-1, for example, the SLAB two model (Hayes et al., 2018) represents a possible alternative for the geometry of subduction interfaces (PS type). Likewise, large crustal faults with sufficient information (3D geometry and tectonic rates) could be addressed in the PS type rather than the BS type. Using tectonic rates for the BS type would increase the FMD model alternatives, contributing to better addressing the long recurrence intervals of major crustal earthquakes as done for the PS type. As regards the earthquake ruptures, the modeling could explore the use of recent rupture scaling relations, such as those by Goda et al. (2016), Allen and Hayes (2017), and Thingbaijam et al. (2017), in addition to those used here. The coseismic slip distribution on such ruptures could also better reflect the open discussion on how best to describe the slip spectra (Herrero and Bernard, 1994; Somerville et al., 1999; Mai and Beroza, 2002; Goda et al., 2016). Our choice of a self-similar slip distribution was based on its consistency with the use of a stress drop that does not scale with the seismic moment, a feature that has been observed over a large range of magnitudes (Cocco et al., 2016). It may also be noted that we used heterogeneous slip distributions only for the largest earthquakes on subduction interfaces. Since slip heterogeneity may affect tsunami hazard even at large distances from the fault (e.g., Li et al., 2016), future model updates might consider developing heterogeneous slip distributions not only for large subduction interface earthquakes but also for smaller earthquakes and at least for the largest crustal sources. At Step-2, other possible improvements in modeling different aspects of the seismic sources would improve the tsunamigenic efficiency characterization of each considered earthquake scenario. Examples of such improvements are the description of the Earth's model in which the source is embedded (Masterlark, 2003; Romano et al., 2015b), the consideration of time-dependent ruptures, and of the mechanism of transmission of the coseismic seafloor displacement to the water column (e.g., Tanioka and

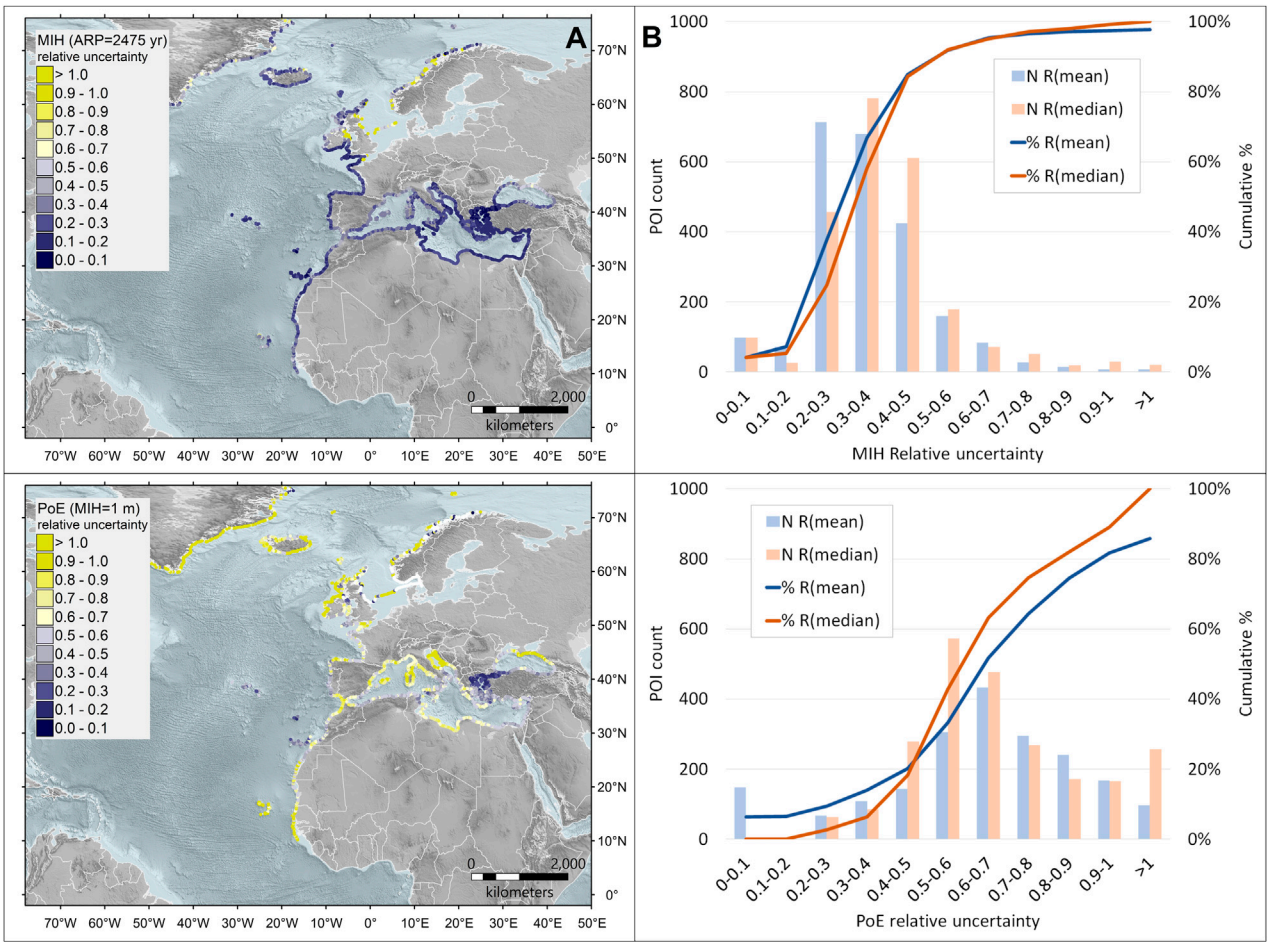

FIGURE 13 | (A) Geographic distributions of the maximum inundation height (MIH) relative uncertainty, defined as the ratio $R=(MIH_{p84}-MIH_{mean})/MIH_{mean}$, for the 2% probability of exceedance in 50 years, equivalent to an average return period of 2,475 years **(upper)**, and of the probability of exceedance relative uncertainty, defined as the ratio $R=(PoE_{p84}-PoE_{mean})/PoE_{mean}$, for the maximum inundation height of 1 m **(lower)**. Topo-bathymetry is from the ETOPO1 Global Relief Model (NOAA, 2009; Amante and Eakins, 2009). **(B)** Incremental and cumulative distribution of the relative uncertainty as defined in panel **(A)** for MIH **(upper)** and PoE **(lower)**. For comparison, both diagrams also show the relative uncertainty with respect to the median.

Satake, 1996; Nosov and Kolesov, 2011; Polet and Kanamori, 2015; Geist et al., 2019). It is also worth noting that further uncertainties also affect Step-2 and Step-3 due to the limited accuracy of the topo-bathymetric model and the numerical simulations with the Tsunami-HySEA code solving the NLSW equations. These additional uncertainties, and some of the above-mentioned uncertainties on tsunami generation, have been implicitly embedded in the amplification factors. Although rather roughly, they contribute to the log-normal distribution combined to the deterministic output of each single tsunami simulation as described for Step-3 and Step-4, based on the calibration made by Glimsdal et al. (2019) by means of numerical simulations. A similar approach, though based on tsunami observations, was previously adopted by Davies et al. (2018).

A probabilistic hazard model attempts to forecast future hazards at a location, but this prediction will never be an exact representation of the reality or precisely anticipate the occurrence of a specific hazardous event. The inherent uncertainty of such predictions is rooted in the limited understanding of natural phenomena and the lack of data to build models, as recalled above. In general, the longer the ARP, the scarcer the observations for building and testing the model. The large uncertainty of tsunami hazard models is strongly related to the fact that tsunamis are rather low-frequency but potentially high-impact events. Therefore, in comparison with hazard models for more frequent phenomena, tsunami hazard models have typically even scarcer observations that can be used for their calibration, perhaps except for the Pacific Ocean (Geist and Parsons, 2016). Accordingly, and following common practices (Geist and Lynett, 2014; Grezio et al., 2017), the NEAMTHM18 was built by modeling earthquake probability and tsunami generation and impact from these earthquakes, rather than building it directly from available tsunami observations, which is an almost impossible task for tsunamis. NEAMTHM18 also considers potential unknown events whose

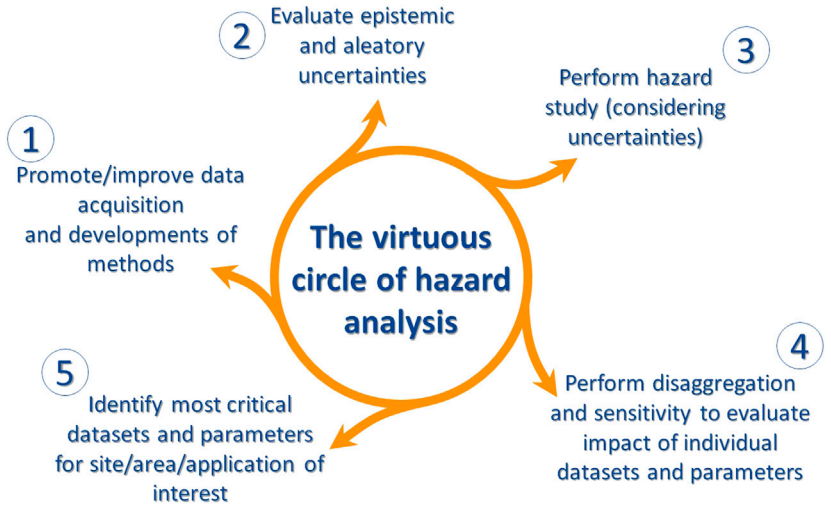

FIGURE 14 | The virtuous circle of hazard analysis.

occurrence cannot be ruled out for the future. Tsunami data, such as long records of a measured run-up at a specific coastal site, are even scarcer in the NEAM Region than in other regions characterized by more frequent (large) earthquakes, as may be the case for Chile. All the circumstances mentioned above suggest caution when using hazard results for practical applications, particularly for long ARPs.

Building on the legacy of recent European research projects dedicated to developing data and methods for tsunami hazard analysis and other hazards, the TSUMAPS-NEAM (2016–2017) project has brought about NEAMTHM18, the first long-term tsunami hazard assessment for the NEAM Region. Scientific and technical advancements are required to perform effective hazard analyses. This work is carried out by specialists of different disciplines and is never finalized. It is instead a never-ending process, as schematically illustrated in **Figure 14**. One full round of this circle may take several years to be completed. At each new round, hazard maps can be better. NEAMTHM18 represents the body of results in point 3 of **Figure 14**. The preceding points 1 and 2 (**Figure 14**) were completed in the framework of the TSUMAPS-NEAM project but started well before in other projects that were not necessarily dedicated to tsunami hazard alone, such as TRANSFER (2006–2009), SHARE (2009–2012), STREST (2013–2016), and ASTARTE (2013–2017) (**Table 1**), each of which contributed with the preparation of relevant datasets, with the development of methods, and, most importantly, with the building of a large community. Only a few actions are now needed to complete the first round of this circle. Disaggregation and sensitivity analyses have already been performed and are part of the NEAMTHM18 Documentation (Basili et al., 2019). Expanding and exploiting those analyses will eventually lead to a new round of improvements to the tsunami hazard model. Discussions aimed at establishing best practices in this respect are in progress within the GTM scientific network and its related AGITHAR COST Action. Successive hazard projects will use better data and newer methods. They will also exploit technological advancements and innovations, such as the enhanced performances of computer systems that will allow more complex approaches to be explored, like in the ongoing ChEESE project, thereby improving the capability to develop appropriate protection and resilience measures against tsunamis.

DATA AVAILABILITY STATEMENT

The datasets presented in this study can be found in online repositories. The names of the repository/repositories and accession number(s) can be found below: NEAM Tsunami Hazard Model 2018 (NEAMTHM18): online data of the Probabilistic Tsunami Hazard Model for the NEAM Region from the TSUMAPS-NEAM project, http://doi.org/10.13127/tsunami/neamthm18; NEAMTHM18 Documentation: the making of the TSUMAPS-NEAM Tsunami Hazard Model 2018, http://doi.org/10.5281/zenodo.3406625.

AUTHOR CONTRIBUTIONS

AAg, ABa, ABo, AHe, AHo, AS, AY, BB, CBH, FC, FEM, FL, FO, FR, GL, GP, HAJ, HH, HKT, IT, JS, LMM, MAB, MC, MGu, MMT, MT, MV, OP, PP, RB, RO, RT, SB, SBA, SG, SI, SL, and SM contributed to developing NEAMTHM18 as members of the Project Development Team. RB coordinated the TSUMAPS-NEAM project. SL led the project management and reporting, assisted by BB. JS and RO led the hazard assessment task. ABa and GP led the review and sanity check task. OP led the dissemination task. OP and MGu developed the interactive hazard curve tool. JMGV and JMS provided support with the use of the Tsunami-HySEA code. FR, RO, FL, ABa, AY, GP, MC, ABo, AAr, MS, COS, GD, WP, JP, and

CM were members of the Pool of Experts. JB, DDB, MD, MP, AAm, AZ, MGo, JMGV, EG, JMS, and TP were members of the panel of Internal Reviewers. All authors participated in one or more project meetings, in person or remotely, to contribute to or discuss various aspects of the NEAMTHM18. RB, SL, and JS prepared the first draft of the manuscript. All authors read and variably contributed to revising the manuscript.

FUNDING

The NEAMTHM18 was prepared in the framework of the European Project TSUMAPS-NEAM (http://www.tsumaps-neam.eu/) funded by the mechanism of the European Civil Protection and Humanitarian Aid Operations with grant no. ECHO/SUB/2015/718568/PREV26 (https://ec.europa.eu/echo/funding-evaluations/financing-civil-protection-europe/selected-projects/probabilistic-tsunami-hazard_en). The work by INGV authors also benefitted from funding by the INGV-DPC Agreement 2012-2021 (Annex B2).

ACKNOWLEDGMENTS

We acknowledge the valuable contributions of all the scientists, end-users, and stakeholders who actively participated in the TSUMAPS-NEAM project meetings. We also acknowledge the constructive comments made by the reviewers, which contributed to significantly improve the quality of the paper. Tsunami modeling was done with the HPC support by EDANYA Group (https://www.uma.es/edanya), Universidad de Málaga, Spain, that made the Tsunami-HySEA code available, and by CINECA Consortium (https://www.cineca.it/en) that provided access to their facilities.

SUPPLEMENTARY MATERIAL

The Supplementary Material for this article can be found online at: https://www.frontiersin.org/articles/10.3389/feart.2020.616594/full#supplementary-material.

REFERENCES

Aki, K., and Richards, P. G. (1980). *Quantitative seismology: theory and methods*. San Francisco, CA: Freeman.

Allen, T. I., and Hayes, G. P. (2017). Alternative rupture-scaling relationships for subduction interface and other offshore environments. *Bull. Seismol. Soc. Am.* 107, 1240–1253. doi:10.1785/0120160255

Álvarez-Gómez, J. A., Aniel-Quiroga, Í., González, M., and Otero, L. (2011). Tsunami hazard at the Western Mediterranean Spanish coast from seismic sources. *Nat. Hazards Earth Syst. Sci.* 11, 227–240. doi:10.5194/nhess-11-227-2011

Amante, C., and Eakins, B. W. (2009). ETOPO1 1 arc-minute global relief model: procedures, data sources and analysis. NOAA technical memorandum NESDIS NGDC-24. National Geophysical Data Center, NOAA. doi:10.7289/V5C8276M (Accessed December 5, 2020).

Ambraseys, N. N. (1962). Data for the investigation of the seismic sea-waves in the Eastern Mediterranean. *Bull. Seismol. Soc. Am.* 52, 895–913.

American Society of Civil Engineers (2017). *Minimum design loads and associated criteria for buildings and other structures*. 7th Edn. Reston, VA: American Society of Civil Engineers.

Argyroudis, S. A., Fotopoulou, S., Karafagka, S., Pitilakis, K., Selva, J., Salzano, E., et al. (2020). A risk-based multi-level stress test methodology: application to six critical non-nuclear infrastructures in Europe. *Nat. Hazards* 100, 595–633. doi:10.1007/s11069-019-03828-5

Bacchi, V., Jomard, H., Scotti, O., Antoshchenkova, E., Bardet, L., Duluc, C.-M., et al. (2020). Using meta-models for tsunami hazard analysis: an example of application for the French atlantic coast. *Front. Earth Sci.* 8, 41. doi:10.3389/feart.2020.00041

Bakırcı, T., Yoshizawa, K., and Özer, M. F. (2012). Three-dimensional S-wave structure of the upper mantle beneath Turkey from surface wave tomography: 3-D upper-mantle structure beneath Turkey. *Geophys. J. Int.* 190, 1058–1076. doi:10.1111/j.1365-246X.2012.05526.x

Basili, R., Brizuela, B., Herrero, A., Iqbal, S., Lorito, S., Maesano, F. E., et al. (2018). NEAM tsunami hazard model 2018 (NEAMTHM18): online data of the probabilistic tsunami hazard model for the NEAM region from the TSUMAPS-NEAM project. Roma: Istituto Nazionale di Geofisica e Vulcanologia (INGV). doi:10.13127/tsunami/neamthm18

Basili, R., Brizuela, B., Herrero, A., Iqbal, S., Lorito, S., Maesano, F. E., et al. (2019). NEAMTHM18 documentation: the making of the TSUMAPS-NEAM tsunami hazard model 2018. Roma: Istituto Nazionale di Geofisica e Vulcanologia (INGV), 352. doi:10.5281/Q20zenodo.3406625

Basili, R., Kastelic, V., Demircioglu, M. B., Garcia Moreno, D., Nemser, E. S., Petricca, P., et al. (2013a). The European database of seismogenic faults (EDSF) compiled in the framework of the project SHARE. Roma: Istituto nazionale di geofisica e vulcanologia (INGV). doi:10.6092/INGV.IT-SHARE-EDSF Available at: http://diss.rm.ingv.it/share-edsf/ (Accessed July 14, 2020).

Basili, R., Tiberti, M. M., Kastelic, V., Romano, F., Piatanesi, A., Selva, J., et al. (2013b). Integrating geologic fault data into tsunami hazard studies. *Nat. Hazards Earth Syst. Sci.* 13, 1025–1050. doi:10.5194/nhess-13-1025-2013

Becker, J. J., Sandwell, D. T., Smith, W. H. F., Braud, J., Binder, B., Depner, J., et al. (2009). Global bathymetry and elevation data at 30 arc seconds resolution: SRTM30_PLUS. *Mar. Geodes.* 32, 355–371. doi:10.1080/01490410903297766

Bilek, S. L., and Lay, T. (1999). Rigidity variations with depth along interplate megathrust faults in subduction zones. *Nature* 400, 443–446. doi:10.1038/22739

Bird, P. (2003). An updated digital model of plate boundaries. *Geochem. Geophys. Geosyst.* 4 (3), 1027. doi:10.1029/2001GC000252

Bird, P., and Kagan, Y. Y. (2004). Plate-tectonic analysis of shallow seismicity: apparent boundary width, beta, corner magnitude, coupled lithosphere thickness, and coupling in seven tectonic settings. *Bull. Seismol. Soc. Am.* 94, 2380–2399. doi:10.1785/0120030107

Bommer, J. J. (2012). Challenges of building logic trees for probabilistic seismic hazard analysis. *Earthq. Spectra.* 28, 1723–1735. doi:10.1193/1.4000079

Boyd, O. S. (2012). Including foreshocks and aftershocks in time-independent probabilistic seismic-hazard analyses. *Bull. Seismol. Soc. Am.* 102, 909–917. doi:10.1785/0120110008

Bozzoni, F., Corigliano, M., Lai, C. G., Salazar, W., Scandella, L., Zuccolo, E., et al. (2011). Probabilistic seismic hazard assessment at the eastern caribbean islands. *Bull. Seismol. Soc. Am.* 101, 2499–2521. doi:10.1785/0120100208

Carafa, M. M. C., Kastelic, V., Bird, P., Maesano, F. E., and Valensise, G. (2018). A "geodetic gap" in the Calabrian Arc: evidence for a locked subduction megathrust?. *Geophys. Res. Lett.* 45, 1794–1804. doi:10.1002/2017gl076554

Casarotti, E., Stupazzini, M., Lee, S. J., Komatitsch, D., Piersanti, A., and Tromp, J. (2008). "CUBIT and seismic wave propagation based upon the spectral-element method: an advanced unstructured mesher for complex 3D geological media," in *Proceedings of the 16th international meshing roundtable*. Editors M. L. Brewer and D. Marcum (Berlin, Heidelberg: Springer Berlin Heidelberg), 579–597.

Cerase, A., Crescimbene, M., La Longa, F., and Amato, A. (2019). Tsunami risk perception in southern Italy: first evidence from a sample survey. *Nat. Hazards Earth Syst. Sci.* 19, 2887–2904. doi:10.5194/nhess-19-2887-2019

Christophersen, A., Berryman, K., and Litchfield, N. (2015). The GEM faulted Earth project, version 1.0, April 2015, GEM faulted Earth project, GEM Foundation, Pavia. doi:10.13117/GEM.GEGD.TR2015.02

Civiero, C., Custódio, S., Duarte, J. C., Mendes, V. B., and Faccenna, C. (2020). Dynamics of the Gibraltar arc system: a complex interaction between plate convergence, slab pull, and mantle flow. *J. Geophys. Res. Solid Earth* 125, e2019JB018873. doi:10.1029/2019JB018873

Cocco, M., Tinti, E., and Cirella, A. (2016). On the scale dependence of earthquake stress drop. *J. Seismol.* 20, 1151–1170. doi:10.1007/s10950-016-9594-4

Cornell, C. A. (1968). Engineering seismic risk analysis. *Bull. Seismol. Soc. Am.* 58, 1583–1606.

Davies, G. (2019). Tsunami variability from uncalibrated stochastic earthquake models: tests against deep ocean observations 2006-2016. *Geophys. J. Int.* 218, 1939–1960. doi:10.1093/gji/ggz260

Davies, G., Griffin, J., Løvholt, F., Glimsdal, S., Harbitz, C., Thio, H. K., et al. (2018). A global probabilistic tsunami hazard assessment from earthquake sources. *Geological Society, London, Special Publications* 456, 219–244. doi:10.1144/sp456.5

Davies, G., and Griffin, J. (2020). Sensitivity of probabilistic tsunami hazard assessment to far-field earthquake slip complexity and rigidity depth-dependence: case study of Australia. *Pure Appl. Geophys.* 177, 1521. doi:10.1007/s00024-019-02299-w

DCDPC (2018). Indicazioni alla componenti ed alle strutture operative del Servizio nazionale di protezione civile per l'aggiornamento delle pianificazioni di protezione civile per il rischio maremoto. GU serie generale n.266. del 15–11–2018 (in Italian). Presidenza del consiglio dei ministri—dipartimento della protezione civile. Available at: http://www.protezionecivile.gov.it/amministrazione-trasparente/provvedimenti/dettaglio/-/asset_publisher/default/content/indicazioni-alle-componenti-ed-alle-strutture-operative-del-servizio-nazionale-di-protezione-civile-per-l-aggiornamento-delle-pianificazioni-di-prot-1 (Accessed December 16, 2020).

de la Asunción, M., Castro, M. J., Fernández-Nieto, E. D., Mantas, J. M., Acosta, S. O., and González-Vida, J. M. (2013). Efficient GPU implementation of a two waves TVD-WAF method for the two-dimensional one layer shallow water system on structured meshes. *Comput. Fluids* 80, 441–452. doi:10.1016/j.compfluid.2012.01.012

Delavaud, E., Cotton, F., Akkar, S., Scherbaum, F., Danciu, L., Beauval, C., et al. (2012). Toward a ground-motion logic tree for probabilistic seismic hazard assessment in Europe. *J. Seismol.* 16, 451–473. doi:10.1007/s10950-012-9281-z

DISS Working Group (2018). Database of individual seismogenic sources (DISS), version 3.2.1. Istituto nazionale di geofisica e vulcanologia (INGV). Available at: http://diss.rm.ingv.it/diss/ (Accessed July 14, 2020). doi:10.6092/INGV.IT-DISS3.2.1

Duarte, J. C., Rosas, F. M., Terrinha, P., Schellart, W. P., Boutelier, D., Gutscher, M.-A., et al. (2013). Are subduction zones invading the Atlantic? Evidence from the southwest Iberia margin. *Geology* 41, 839–842. doi:10.1130/G34100.1

Dziewonski, A. M., Chou, T.-A., and Woodhouse, J. H. (1981). Determination of earthquake source parameters from waveform data for studies of global and regional seismicity. *J. Geophys. Res.* 86, 2825–2852. doi:10.1029/JB086iB04p02825

Ekström, G., Nettles, M., and Dziewoński, A. M. (2012). The global CMT project 2004-2010: centroid-moment tensors for 13,017 earthquakes. *Phys. Earth Planet. In.* 200-201, 1–9. doi:10.1016/j.pepi.2012.04.002

Esposito, S., Stojadinović, B., Babič, A., Dolšek, M., Iqbal, S., Selva, J., et al. (2020). Risk-based multilevel methodology to stress test critical infrastructure systems. *J. Infrastruct. Syst.* 26, 04019035. doi:10.1061/(ASCE)IS.1943-555X.0000520

Esteva, L. (1967). "Criteria for the construction of spectra for seismic design," in *Third panamerican symposium on structures* (Venezuela: Caracas).

Field, E. H., Arrowsmith, R. J., Biasi, G. P., Bird, P., Dawson, T. E., Felzer, K. R., et al. (2014). Uniform California earthquake rupture forecast, version 3 (UCERF3)--The time-independent model. *Bull. Seismol. Soc. Am.* 104, 1122–1180. doi:10.1785/0120130164

Forman, E., and Peniwati, K. (1998). Aggregating individual judgments and priorities with the analytic hierarchy process. *Eur. J. Oper. Res.* 108, 165–169. doi:10.1016/S0377-2217(97)00244-0

Frankel, A. (1995). Mapping seismic hazard in the central and eastern United States. *Seismol Res. Lett.* 66, 8–21. doi:10.1785/gssrl.66.4.8

Ganas, A., and Parsons, T. (2009). Three-dimensional model of Hellenic Arc deformation and origin of the Cretan uplift. *J. Geophys. Res.* 114, B06404. doi:10.1029/2008JB005599

Gardner, J. K., and Knopoff, L. (1974). Is the sequence of earthquakes in Southern California, with aftershocks removed, Poissonian?. *Bull. Seismol. Soc. Am.* 64, 1363–1367.

Geist, E. L. (2012). Phenomenology of tsunamis II. *Adv.Geophys.* 53, 35–92. doi:10.1016/B978-0-12-380938-4.00002-1

Geist, E. L., Oglesby, D. D., and Ryan, K. J. (2019). "Tsunamis: stochastic models of occurrence and generation mechanisms," in *Encyclopedia of complexity and systems science*. Editor R. A. Meyers (Berlin, Heidelberg: Springer Berlin Heidelberg), 1–30.

Geist, E. L., and Parsons, T. (2006). Probabilistic analysis of tsunami hazards*. *Nat. Hazards* 37, 277–314. doi:10.1007/s11069-005-4646-z

Geist, E. L., and Parsons, T. (2016). Reconstruction of far-field tsunami amplitude distributions from earthquake sources. *Pure Appl. Geophys.* 173, 3703–3717. doi:10.1007/s00024-016-1288-x

Geist, E., and Lynett, P. (2014). Source processes for the probabilistic assessment of tsunami hazards. *Oceanog.* 27, 86–93. doi:10.5670/oceanog.2014.43

Gerstenberger, M. C., Marzocchi, W., Allen, T., Pagani, M., Adams, J., Danciu, L., et al. (2020). Probabilistic seismic hazard analysis at regional and national scales: state of the art and future challenges. *Rev. Geophys.* 58. doi:10.1029/2019RG000653

Gibbons, S. J., Lorito, S., Macías, J., Løvholt, F., Selva, J., Volpe, M., et al. (2020). Probabilistic tsunami hazard analysis: high performance computing for massive scale inundation simulations. *Front. Earth Sci.* 8, 623. doi:10.3389/feart.2020.591549

Glimsdal, S., Løvholt, F., Harbitz, C. B., Romano, F., Lorito, S., Orefice, S., et al. (2019). A new approximate method for quantifying tsunami maximum inundation height probability. *Pure Appl. Geophys.* 176, 3227–3246. doi:10.1007/s00024-019-02091-w

Goda, K., Yasuda, T., Mori, N., and Maruyama, T. (2016). New scaling relationships of earthquake source parameters for stochastic tsunami simulation. *Coast Eng. J.* 58, 1650010–1650011. doi:10.1142/S0578563416500108

González, F. I., Geist, E. L., Jaffe, B., Kânoğlu, U., Mofjeld, H., Synolakis, C. E., et al. (2009). Probabilistic tsunami hazard assessment at Seaside, Oregon, for near- and far-field seismic sources. *J. Geophys. Res.* 114, C11023. doi:10.1029/2008JC005132

Grezio, A., Marzocchi, W., Sandri, L., and Gasparini, P. (2010). A bayesian procedure for probabilistic tsunami hazard assessment. *Nat. Hazards* 53, 159–174. doi:10.1007/s11069-009-9418-8

Grezio, A., Sandri, L., Marzocchi, W., Argnani, A., Gasparini, P., and Selva, J. (2012). Probabilistic tsunami hazard assessment for Messina strait area (sicily, Italy). *Nat. Hazards* 64, 329–358. doi:10.1007/s11069-012-0246-x

Grezio, A., Roberto, T., Sandri, L., Pierdominici, S., and Selva, J. (2015). A methodology for a comprehensive probabilistic tsunami hazard assessment: multiple sources and short-term interactions. *J. Mar. Sci. Eng.* 3, 23–51. doi:10.3390/jmse3010023

Grezio, A., Babeyko, A., Baptista, M. A., Behrens, J., Costa, A., Davies, G., et al. (2017). Probabilistic tsunami hazard analysis: multiple sources and global applications. *Rev. Geophys.* 55, 1158–1198. doi:10.1002/2017rg000579

Grünthal, G., and Wahlström, R. (2012). The European-Mediterranean Earthquake Catalogue (EMEC) for the last millennium. *J. Seismol.* 16, 535–570. doi:10.1007/s10950-012-9302-y

Gutscher, M.-A., Malod, J., Rehault, J.-P., Contrucci, I., Klingelhoefer, F., Mendes-Victor, L., et al. (2002). Evidence for active subduction beneath Gibraltar. *Geol.* 30, 1071–1074. doi:10.1130/0091-7613(2002)030<1071:EFASBG>2.0.CO;2

Hayes, G. P., Moore, G. L., Portner, D. E., Hearne, M., Flamme, H., Furtney, M., et al. (2018). Slab2, a comprehensive subduction zone geometry model. *Science* 362, 58–61. doi:10.1126/science.aat4723

Herrero, A., and Bernard, P. (1994). A kinematic self-similar rupture process for earthquakes. *Bull. Seismol. Soc. Am.* 84, 1216–1228.

Herrero, A., and Murphy, S. (2018). Self-similar slip distributions on irregular shaped faults. *Geophys. J. Int.* 213, 2060–2070. doi:10.1093/gji/ggy104

Hiemer, S., Woessner, J., Basili, R., Danciu, L., Giardini, D., and Wiemer, S. (2014). A smoothed stochastic earthquake rate model considering seismicity and fault moment release for Europe. *Geophys. J. Int.* 198, 1159–1172. doi:10.1093/gji/ggu186

Howell, A., Jackson, J., Copley, A., McKenzie, D., and Nissen, E. (2017). Subduction and vertical coastal motions in the eastern Mediterranean. *Geophys. J. Int.* 211, 593–620. doi:10.1093/gji/ggx307

Iervolino, I., Giorgio, M., and Polidoro, B. (2012). Paper No. 66. "Probabilistic seismic hazard analysis for seismic sequences," in VEESD 2013, Vienna congress on recent advances in earthquake engineering and structural dynamics 2013, Vienna, Austria, August 28-30, 2013. Editors C. Adam, R. Heuer, W. Lenhardt, and C. Schranz (Vienna, Austria: OGE Vienna University of Technology). Available at: https://veesd2013.conf.tuwien.ac.at/about.html

IOC (2015). Working Group on Tsunamis and Other Hazards Related to Sea-Level Warning and Mitigation Systems (TOWS-WG), prepared by the Intergovernmental Oceanographic Commission, Reports of Meetings of Experts and Equivalent Bodies, Eighth Meeting,Morioka, Japan, Morioka, Japan. Available at: https://unesdoc.unesco.org/ark:/48223/pf0000234722?posInSet=1&queryId=N-EXPLORE-2afb4d13-21d9-4c6d-9276-c3de8073f23d (Accessed March 12–13, 2015).

IOC (2017). *Plans and procedures for tsunami warning and emergency management*. Paris: Intergovernmental Oceanographic Commission of UNESCO.

ISC (2016). On-line bulletin. International seismological centre. Available at: http://www.isc.ac.uk. (Accessed November 3, 2018).

Kagan, Y. Y. (2017). Earthquake number forecasts testing. *Geophys. J. Int.* 211, 335–345. doi:10.1093/gji/ggx300

Kagan, Y. Y. (2002a). Seismic moment distribution revisited: I. Statistical results. *J. Intell.* 148, 520–541. doi:10.1046/j.1365-246x.2002.01594.x

Kagan, Y. Y. (2002b). Seismic moment distribution revisited: II. Moment conservation principle. *Geophys. J. Int.* 149, 731–754. doi:10.1046/j.1365-246X.2002.01671.x

Kagan, Y. Y., Bird, P., and Jackson, D. D. (2010). Earthquake patterns in diverse tectonic zones of the globe. *Pure Appl. Geophys.* 167, 721–741. doi:10.1007/s00024-010-0075-3

Kajiura, K. (1963). The leading wave of a tsunami. *Bull. Earthq. Res. Inst. Univ. Tokyo* 41, 535–571.

Kamigaichi, O. (2011). "Tsunami forecasting and warning," in *Extreme environmental events*. Editor R. A. Meyers (New York, NY: Springer New York), 982–1007.

Laigle, M., Sachpazi, M., and Hirn, A. (2004). Variation of seismic coupling with slab detachment and upper plate structure along the western Hellenic subduction zone. *Tectonophysics* 391, 85–95. doi:10.1016/j.tecto.2004.07.009

Laske, G., Masters, G., Ma, Z., and Pasyanos, M. (2013). Update on CRUST1.0—a 1-degree global model of Earth's crust. *Geophys. Res. Abstr.* 15, EGU2013–2658.

Leonard, M. (2014). Self-consistent earthquake fault-scaling relations: update and extension to stable continental strike-slip faults. *Bull. Seismol. Soc. Am.* 104, 2953–2965. doi:10.1785/0120140087

Li, L., Switzer, A. D., Chan, C.-H., Wang, Y., Weiss, R., and Qiu, Q. (2016). How heterogeneous coseismic slip affects regional probabilistic tsunami hazard assessment: a case study in the South China Sea. *J. Geophys. Res. Solid Earth* 121, 6250–6272. doi:10.1002/2016JB013111

Lin, I.-C., and Tung, C. C. (1982). A preliminary investigation of tsunami hazard. *Bull. Seismol. Soc. Am.* 72, 2323–2337.

Lorito, S., Selva, J., Basili, R., Romano, F., Tiberti, M. M., and Piatanesi, A. (2015). Probabilistic hazard for seismically induced tsunamis: accuracy and feasibility of inundation maps. *Geophys. J. Int.* 200, 574–588. doi:10.1093/gji/ggu408

Lorito, S., Romano, F., and Lay, T. (2016). "Tsunamigenic major and great earthquakes (2004–2013): source processes inverted from seismic, geodetic, and sea-level data," in *Encyclopedia of complexity and systems science*. Editor R. A. Meyers (Berlin, Heidelberg: Springer Berlin Heidelberg), 1–52.

Løvholt, F., Glimsdal, S., Harbitz, C. B., Zamora, N., Nadim, F., Peduzzi, P., et al. (2012). Tsunami hazard and exposure on the global scale. *Earth Sci. Rev.* 110, 58–73. doi:10.1016/j.earscirev.2011.10.002

Løvholt, F., Griffin, J., and Salgado-Gálvez, M. A. (2015). "Tsunami hazard and risk assessment on the global scale," in *Encyclopedia of Complexity and systems science*. Editor R. A. Meyers (Berlin, Heidelberg: Springer), 1–34.

Lynett, P. J., Gately, K., Wilson, R., Montoya, L., Arcas, D., Aytore, B., et al. (2017). Inter-model analysis of tsunami-induced coastal currents. *Ocean Model.* 114, 14–32. doi:10.1016/j.ocemod.2017.04.003

Macías, J., Castro, M. J., and Escalante, C. (2020a). Performance assessment of the Tsunami-HySEA model for NTHMP tsunami currents benchmarking. Laboratory data. *Coast Eng.* 158, 103667. doi:10.1016/j.coastaleng.2020.103667

Macías, J., Castro, M. J., Ortega, S., and González-Vida, J. M. (2020b). Performance assessment of Tsunami-HySEA model for NTHMP tsunami currents benchmarking. Field cases. *Ocean Model.* 152, 101645. doi:10.1016/j.ocemod.2020.101645

Macías, J., Castro, M. J., Ortega, S., Escalante, C., and González-Vida, J. M. (2017). Performance benchmarking of tsunami-HySEA model for NTHMP's inundation mapping activities. *Pure Appl. Geophys.* 174, 3147–3183. doi:10.1007/s00024-017-1583-1

Maesano, F. E., Tiberti, M. M., and Basili, R. (2017). The calabrian arc: three-dimensional modelling of the subduction interface. *Sci. Rep.* 7, 8887. doi:10.1038/s41598-017-09074-8

Mai, P. M., and Beroza, G. C. (2002). A spatial random field model to characterize complexity in earthquake slip. *J. Geophys. Res.* 107 (B11), 10. doi:10.1029/2001JB000588

Maramai, A., Brizuela, B., and Graziani, L. (2014). The Euro-Mediterranean Tsunami catalogue. *Ann. Geophys.* 57(4), S0435. doi:10.4401/ag-6437

Marzocchi, W., Taroni, M., and Selva, J. (2015). Accounting for epistemic uncertainty in PSHA: logic tree and ensemble modeling. *Bull. Seismol. Soc. Am.* 105, 2151–2159. doi:10.1785/0120140131

Marzocchi, W., and Taroni, M. (2014). Some thoughts on declustering in probabilistic seismic-hazard analysis. *Bull. Seismol. Soc. Am.* 104, 1838–1845. doi:10.1785/0120130300

Masterlark, T. (2003). Finite element model predictions of static deformation from dislocation sources in a subduction zone: sensitivities to homogeneous, isotropic, Poisson-solid, and half-space assumptions. *J. Geophys. Res.* 108, 2540. doi:10.1029/2002JB002296

MCDEM (2016). *Tsunami evacuation zones—director's guideline for civil defence emergency management groups*. New Zealand: Ministry of Civil Defence and Emergency Management.

McGuire, R. K. (2008). Probabilistic seismic hazard analysis: early history. *Earthq. Eng. Struct. Dynam.* 37, 329–338. doi:10.1002/eqe.765

Meade, B. J. (2007). Algorithms for the calculation of exact displacements, strains, and stresses for triangular dislocation elements in a uniform elastic half space. *Comput. Geosci.* 33, 1064–1075. doi:10.1016/j.cageo.2006.12.003

Molinari, I., Tonini, R., Lorito, S., Piatanesi, A., Romano, F., Melini, D., et al. (2016). Fast evaluation of tsunami scenarios: uncertainty assessment for a Mediterranean Sea database. *Nat. Hazards Earth Syst. Sci.* 16, 2593–2602. doi:10.5194/nhess-16-2593-2016

Mori, N., Goda, K., and Cox, D. (2018). "Recent process in probabilistic tsunami hazard analysis (PTHA) for mega thrust subduction earthquakes," in The 2011 Japan Earthquake and tsunami: Reconstruction and restoration *advances in natural and technological hazards research*. Editors V. Santiago-Fandiño, S. Sato, N. Maki, and K. Iuchi (Cham: Springer International Publishing), 469–485.

Munson, C., Stamatakos, J., Juckett, M., Coppersmith, K., and Bommer, J.USNRC (2018). Updated implementation guidelines for SSHAC hazard studies, prepared by JP ake NUREG-2213. Available at: https://www.nrc.gov/reading-rm/doc-collections/nuregs/staff/sr2213/.

Murotani, S., Satake, K., and Fujii, Y. (2013). Scaling relations of seismic moment, rupture area, average slip, and asperity size for M ~9 subduction-zone earthquakes. *Geophys. Res. Lett.* 40, 5070–5074. doi:10.1002/grl.50976

Murphy, S., Di Toro, G., Romano, F., Scala, A., Lorito, S., Spagnuolo, E., et al. (2018). Tsunamigenic earthquake simulations using experimentally derived friction laws. *Earth Planet Sci. Lett.* 486, 155–165. doi:10.1016/j.epsl.2018.01.011

Murphy, S., and Herrero, A. (2020). Surface rupture in stochastic slip models. *Geophys. J. Int.* 221, 1081–1089. doi:10.1093/gji/ggaa055

Murphy, S., Scala, A., Herrero, A., Lorito, S., Festa, G., Trasatti, E., et al. (2016). Shallow slip amplification and enhanced tsunami hazard unravelled by dynamic simulations of mega-thrust earthquakes. *Sci. Rep.* 6, 35007. doi:10.1038/srep35007

Nijholt, N., Govers, R., and Wortel, R. (2018). On the forces that drive and resist deformation of the south-central Mediterranean: a mechanical model study. *Geophys. J. Int.* 214, 876–894. doi:10.1093/gji/ggy144

NOAA National Geophysical Data Center (2009). ETOPO1 1 arc-minute global relief model. NOAA National Centers for Environmental Information. Available at: https://www.ngdc.noaa.gov/mgg/global/. (Accessed December 5, 2020).

Nosov, M. A., and Kolesov, S. V. (2011). Optimal initial conditions for simulation of seismotectonic tsunamis. *Pure Appl. Geophys.* 168, 1223–1237. doi:10.1007/s00024-010-0226-6

NTC (2018). Norme Tecniche per le Costruzioni 2018. Aggiornamento delle "Norme tecniche per le costruzioni". Gazzetta Ufficiale Serie Generale n.42 del 2002-2018–suppl. Ordinario n. 8. Italian Building Code (in Italian). Available at: https://www.gazzettaufficiale.it/eli/id/2018/02/20/18A00716/sg (Accessed December 16, 2020).

Okada, Y. (1992). Internal deformation due to shear and tensile faults in a half-space. *Bull. Seismol. Soc. Am.* 82, 1018–1040.

Omira, R., Baptista, M. A., and Matias, L. (2015). Probabilistic tsunami hazard in the northeast atlantic from near- and far-field tectonic sources. *Pure Appl. Geophys.* 172, 901–920. doi:10.1007/s00024-014-0949-x

Papadopoulos, G. A., Daskalaki, E., Fokaefs, A., and Giraleas, N. (2010). Tsunami hazard in the eastern Mediterranean Sea: strong earthquakes and tsunamis in the west Hellenic Arc and trench system. *J. Earthquake Tsunami* 4, 145–179. doi:10.1142/S1793431110000856

Papadopoulos, G. A., Gràcia, E., Urgeles, R., Sallares, V., De Martini, P. M., Pantosti, D., et al. (2014). Historical and pre-historical tsunamis in the Mediterranean and its connected seas: geological signatures, generation mechanisms and coastal impacts. *Mar. Geol.* 354, 81–109. doi:10.1016/j.margeo.2014.04.014

Polet, J., and Kanamori, H. (2015). "Tsunami earthquakes," in *Encyclopedia of complexity and systems science*. Editor R. A. Meyers (Berlin, Heidelberg: Springer Berlin Heidelberg), 1–22.

Pondrelli, S., and Salimbeni, S. (2015). "Regional moment tensor review: An example from the european–mediterranean region," in *Encyclopedia of Earthquake Engineering*. Editors M. Beer, I. A. Kougioumtzoglou, E. Patelli, and I. S.-K. Au (Berlin, Heidelberg: Springer Berlin Heidelberg), 1–15.

Power, W., Wang, X., Lane, E., and Gillibrand, P. (2013). A probabilistic tsunami hazard study of the auckland region, Part I: propagation modelling and tsunami hazard assessment at the shoreline. *Pure Appl. Geophys.* 170, 1621–1634. doi:10.1007/s00024-012-0543-z

Reilinger, R., McClusky, S., Vernant, P., Lawrence, S., Ergintav, S., Cakmak, R., et al. (2006). GPS constraints on continental deformation in the Africa-Arabia-Eurasia continental collision zone and implications for the dynamics of plate interactions. *J. Geophys. Res. Solid Earth* 111, B01405. doi:10.1029/2005JB004051

Rikitake, T., and Aida, I. (1988). Tsunami hazard probability in Japan. *Bull. Seismol. Soc. Am.* 78, 1268–1278.

Romano, F., Lorito, S., Piatanesi, A., and Lay, T. (2020). Fifteen years of (major to great) tsunamigenic earthquakes. *Ref. Module Earth Syst. Environ. Sci.* 13. doi:10.1016/B978-0-12-409548-9.11767-1

Romano, F., Molinari, I., Lorito, S., and Piatanesi, A. (2015a). Source of the 6 february 2013 Mw = 8.0 santa cruz islands tsunami. *Nat. Hazards Earth Syst. Sci.* 15, 1371–1379. doi:10.5194/nhess-15-1371-2015

Romano, F., Trasatti, E., Lorito, S., Piromallo, C., Piatanesi, A., Ito, Y., et al. (2015b). Structural control on the Tohoku earthquake rupture process investigated by 3D FEM, tsunami and geodetic data. *Sci. Rep.* 4, 5631. doi:10.1038/srep05631

Sørensen, M. B., Spada, M., Babeyko, A., Wiemer, S., and Grünthal, G. (2012). Probabilistic tsunami hazard in the Mediterranean Sea. *J. Geophys. Res. Solid Earth* 117, B01305. doi:10.1029/2010JB008169

Saaty, T. L. (1980). *The analytic hierarchy process: planning, priority setting, resource allocation*. New York; London: McGraw-Hill International Book Co.

Sachpazi, M., Laigle, M., Charalampakis, M., Diaz, J., Kissling, E., Gesret, A., et al. (2016). Segmented Hellenic slab rollback driving Aegean deformation and seismicity. *Geophys. Res. Lett.* 43, 651–658. doi:10.1002/2015GL066818

Salaün, G., Pedersen, H. A., Paul, A., Farra, V., Karabulut, H., Hatzfeld, D., et al. (2012). High-resolution surface wave tomography beneath the Aegean-Anatolia region: constraints on upper-mantle structure: tomography of Aegea-Anatolia upper mantle. *Geophys. J. Int.* 190, 406–420. doi:10.1111/j.1365-246X.2012.05483.x

Scala, A., Festa, G., Vilotte, J.-P., Lorito, S., and Romano, F. (2019). Wave interaction of reverse-fault rupture with free surface: numerical analysis of the dynamic effects and fault opening induced by symmetry breaking. *J. Geophys. Res. Solid Earth* 124, 1743–1758. doi:10.1029/2018jb016512

Scala, A., Lorito, S., Romano, F., Murphy, S., Selva, J., Basili, R., et al. (2020). Effect of shallow slip amplification uncertainty on probabilistic tsunami hazard analysis in subduction zones: use of long-term balanced stochastic slip models. *Pure Appl. Geophys.* 177, 1497–1520. doi:10.1007/s00024-019-02260-x

Sellier, N. C., Loncke, L., Vendeville, B. C., Mascle, J., Zitter, T., Woodside, J., et al. (2013a). Post-messinian evolution of the florence ridge area (western Cyprus arc), Part I: morphostructural analysis. *Tectonophysics* 591, 131–142. doi:10.1016/j.tecto.2012.04.001

Sellier, N. C., Vendeville, B. C., and Loncke, L. (2013b). Post-messinian evolution of the florence rise area (western Cyprus arc) Part II: experimental modeling. *Tectonophysics* 591, 143–151. doi:10.1016/j.tecto.2011.07.003

Selva, J., Iqbal, S., Taroni, M., Marzocchi, W., Cotton, F., Courage, W., et al. (2015). Deliverable D3.1: Report on the effects of epistemic uncertainties on the definition of LP-HC events. INGV. Available at: http://strest.ethz.ch/opencms/export/sites/default/.content/STREST_public/STREST_D3.1_updated_151001.pdf (Accessed September 26, 2020).

Selva, J., and Marzocchi, W. (2004). Focal parameters, depth estimation, and plane selection of the worldwide shallow seismicity with Ms ≥ 7.0 for the period 1900-1976. *Geochem. Geophys. Geosystems* 5, Q05005. doi:10.1029/2003GC000669

Selva, J., and Sandri, L. (2013). Probabilistic seismic hazard assessment: combining cornell-like approaches and data at sites through bayesian inference. *Bull. Seismol. Soc. Am.* 103, 1709–1722. doi:10.1785/0120120091

Selva, J., Tonini, R., Molinari, I., Tiberti, M. M., Romano, F., Grezio, A., et al. (2016). Quantification of source uncertainties in seismic probabilistic tsunami hazard analysis (SPTHA). *Geophys. J. Int.* 205, 1780–1803. doi:10.1093/gji/ggw107

Sodoudi, F., Brüstle, A., Meier, T., Kind, R., Friederich, W., and EGELADOS working group (2015). Receiver function images of the Hellenic subduction zone and comparison to microseismicity. *Solid Earth* 6, 135–151. doi:10.5194/se-6-135-2015

Somerville, P., Irikura, K., Graves, R., Sawada, S., Wald, D., Abrahamson, N., et al. (1999). Characterizing crustal earthquake slip models for the prediction of strong ground motion. *Seismol Res. Lett.* 70, 59–80. doi:10.1785/gssrl.70.1.59

Strasser, F. O., Arango, M. C., and Bommer, J. J. (2010). Scaling of the source dimensions of interface and intraslab subduction-zone earthquakes with moment magnitude. *Seismol Res. Lett.* 81, 941–950. doi:10.1785/gssrl.81.6.941

Stucchi, M., Rovida, A., Gomez Capera, A. A., Alexandre, P., Camelbeeck, T., Demircioglu, M. B., et al. (2013). The SHARE European earthquake Catalogue (SHEEC) 1000–1899. *J. Seismol.* 17, 523–544. doi:10.1007/s10950-012-9335-2

Tanioka, Y., and Satake, K. (1996). Tsunami generation by horizontal displacement of ocean bottom. *Geophys. Res. Lett.* 23, 861–864. doi:10.1029/96GL00736

Taroni, M., and Selva, J. (in press 2020). GR_EST: an OCTAVE/MATLAB toolbox to estimate Gutenberg-Richter law parameters and their uncertainties. *Seismol Res. Lett.*

Thingbaijam, K. K. S., Martin Mai, P., and Goda, K. (2017). New empirical earthquake source-scaling laws. *Bull. Seismol. Soc. Am.* 107, 2225–2246. doi:10.1785/0120170017

Tiberti, M. M., Basili, R., and Vannoli, P. (2014). Ups and downs in western Crete (Hellenic subduction zone). *Sci. Rep.* 4, 5677. doi:10.1038/srep05677

Tinti, S., Armigliato, A., Tonini, R., Maramai, A., and Graziani, L. (2005). Assessing the hazard related to tsunamis of tectonic origin: a hybrid statistical-deterministic method applied to southern Italy coasts. *ISET J. Earthq. Technol.* 42, 189–201.

Tonini, R., Basili, R., Maesano, F. E., Tiberti, M. M., Lorito, S., Romano, F., et al. (2020). Importance of earthquake rupture geometry on tsunami modelling: the Calabrian Arc subduction interface (Italy) case study. *Geophys. J. Int.* 223, 1805–1819. doi:10.1093/gji/ggaa409

Tonini, R., Armigliato, A., Pagnoni, G., Zaniboni, F., and Tinti, S. (2011). Tsunami hazard for the city of Catania, eastern sicily, Italy, assessed by means of worst-case credible tsunami scenario analysis (WCTSA). *Nat. Hazards Earth Syst. Sci.* 11, 1217–1232. doi:10.5194/nhess-11-1217-2011

Tozer, B., Sandwell, D. T., Smith, W. H. F., Olson, C., Beale, J. R., and Wessel, P. (2019). Global bathymetry and topography at 15 arc sec: SRTM15+. *Earth Space Sci.* 6, 1847–1864. doi:10.1029/2019EA000658

USNRC (1997). Recommendations for probabilistic seismic hazard analysis: guidance on uncertainty and use of experts, prepared by the SSHAC (senior seismic hazard analysis committee - R.J. Budnitz (chairman), G. Apostolakis, D.M. Boore, L.S. Cluff, K.J. Coppersmith, C.A. Cornell, PA. Morris) NUREG/CR-6372. Available at: https://www.nrc.gov/reading-rm/doc-collections/nuregs/contract/cr6372/vol1/index.html (Accessed September 30, 2020).

USNRC (2012). Practical implementation guidelines for SSHAC level 3 and 4 hazard studies, prepared by A.M. Kammerer and J.P. Ake, NRC project manager: R. Rivera-Lugo NUREG-2117. Available at: https://www.nrc.gov/reading-rm/doccollections/nuregs/staff/sr2117/ (Accessed September 30, 2020).

USRNC (2018). Updated implementation guidelines for SSHAC hazard studies, prepared by J. Ake, C. Munson, J. Stamatakos, M. Juckett, K. Coppersmith, and J. Bommer NUREG-2213. Available at: https://www.nrc.gov/reading-rm/doc-collections/nuregs/staff/sr2213/ (Accessed September 30, 2020).

Vernant, P., Reilinger, R., and McClusky, S. (2014). Geodetic evidence for low coupling on the Hellenic subduction plate interface. *Earth Planet Sci. Lett.* 385, 122–129. doi:10.1016/j.epsl.2013.10.018

Volpe, M., Lorito, S., Selva, J., Tonini, R., Romano, F., and Brizuela, B. (2019). From regional to local SPTHA: efficient computation of probabilistic tsunami inundation maps addressing near-field sources. *Nat. Hazards Earth Syst. Sci.* 19, 455–469. doi:10.5194/nhess-19-455-2019

Wdowinski, S., Ben-Avraham, Z., Arvidsson, R., and Ekström, G. (2006). Seismotectonics of the cyprian arc. *Geophys. J. Int.* 164, 176–181. doi:10.1111/j.1365-246X.2005.02737.x

Wessel, P., Smith, W. H. F., Scharroo, R., Luis, J., and Wobbe, F. (2013). Generic mapping tools: improved version released. *Eos Trans. Am. Geophys. Union* 94, 409–410. doi:10.1002/2013EO450001

Wiemer, S. (2001). A software package to analyze seismicity: ZMAP. *Seismol Res. Lett.* 72, 373–382. doi:10.1785/gssrl.72.3.373

Woessner, J., Laurentiu, D., Giardini, D., Crowley, H., Cotton, F., Grünthal, G., et al. (2015). The 2013 European Seismic Hazard Model: key components and results. *Bull. Earthq. Eng.* 13, 3553–3596. doi:10.1007/s10518-015-9795-1

Woessner, J., and Wiemer, S. (2005). Assessing the quality of earthquake catalogues: estimating the magnitude of completeness and its uncertainty. *Bull. Seismol. Soc. Am.* 95, 684–698. doi:10.1785/0120040007

Zitellini, N., Gràcia, E., Matias, L., Terrinha, P., Abreu, M. A., DeAlteriis, G., et al. (2009). The quest for the Africa–Eurasia plate boundary west of the Strait of Gibraltar. *Earth Planet Sci. Lett.* 280, 13–50. doi:10.1016/j.epsl.2008.12.005

Conflict of Interest: Author HKT is employed by AECOM Technical Services, United States; author AHo is now employed at Gempa GmbH, Potsdam, Germany, but was employed at GFZ German Research Centre for Geosciences, Potsdam, Germany, while working on the project.

The remaining authors declare that the research was conducted in the absence of any commercial or financial relationships that could be construed as a potential conflict of interest.

frontiers in Earth Science

ORIGINAL RESEARCH
published: 11 March 2021
doi: 10.3389/feart.2021.628061

Testing Tsunami Inundation Maps for Evacuation Planning in Italy

Roberto Tonini[1], Pio Di Manna[2], Stefano Lorito[1], Jacopo Selva[3], Manuela Volpe[1], Fabrizio Romano[1], Roberto Basili[1], Beatriz Brizuela[1], Manuel J. Castro[4], Marc de la Asunción[4], Daniela Di Bucci[5], Mauro Dolce[5], Alexander Garcia[3], Steven J. Gibbons[6], Sylfest Glimsdal[6], José M. González-Vida[7], Finn Løvholt[6], Jorge Macías[4], Alessio Piatanesi[1], Luca Pizzimenti[1], Carlos Sánchez-Linares[4] and Eutizio Vittori[2]*

[1]Istituto Nazionale di Geofisica e Vulcanologia, Sezione di Roma 1, Roma, Italy, [2]Istituto Superiore per la Protezione e la Ricerca Ambientale, Roma, Italy, [3]Istituto Nazionale di Geofisica e Vulcanologia, Sezione di Bologna, Bologna, Italy, [4]Dpto. de Análisis Matemático, Estadística e Investigación Operativa y Matemática Aplicada, Facultad de Ciencias, Universidad de Málaga, Málaga, Spain, [5]Dipartimento della Protezione Civile, Rome, Italy, [6]Norwegian Geotechnical Institute, Oslo, Norway, [7]Dpto. de Matemática Aplicada, ETSII, Universidad de Málaga, Málaga, Spain

OPEN ACCESS

Edited by:
Clara Armaroli, University Institute of Higher Studies in Pavia, Italy

Reviewed by:
Marcello Di Risio, University of L'Aquila, Italy
Giuseppe Bilotta, National Institute of Geophysics and Volcanology, Italy

***Correspondence:**
Roberto Tonini
roberto.tonini@ingv.it

Specialty section:
This article was submitted to Geohazards and Georisks, a section of the journal Frontiers in Earth Science

Received: *10 November 2020*
Accepted: *02 February 2021*
Published: *11 March 2021*

Citation:
Tonini R, Di Manna P, Lorito S, Selva J, Volpe M, Romano F, Basili R, Brizuela B, Castro MJ, de la Asunción M, Di Bucci D, Dolce M, Garcia A, Gibbons SJ, Glimsdal S, González-Vida JM, Løvholt F, Macías J, Piatanesi A, Pizzimenti L, Sánchez-Linares C and Vittori E (2021) Testing Tsunami Inundation Maps for Evacuation Planning in Italy. Front. Earth Sci. 9:628061. doi: 10.3389/feart.2021.628061

Inundation maps are a fundamental tool for coastal risk management and in particular for designing evacuation maps and evacuation planning. These in turn are a necessary component of the tsunami warning systems' last-mile. In Italy inundation maps are informed by a probabilistic tsunami hazard model. Based on a given level of acceptable risk, Italian authorities in charge for this task recommended to consider, as design hazard intensity, the average return period of 2500 years and the 84th percentile of the hazard model uncertainty. An available, regional-scale tsunami hazard model was used that covers the entire Italian coastline. Safety factors based on analysis of run-up variability and an empirical coastal dissipation law on a digital terrain model (DTM) were applied to convert the regional hazard into the design run-up and the corresponding evacuation maps with a GIS-based approach. Since the regional hazard cannot fully capture the local-scale variability, this simplified and conservative approach is considered a viable and feasible practice to inform local coastal risk management in the absence of high-resolution hazard models. The present work is a first attempt to quantify the uncertainty stemming from such procedure. We compare the GIS-based inundation maps informed by a regional model with those obtained from a local high-resolution hazard model. Two locations on the coast of eastern Sicily were considered, and the local hazard was addressed with the same seismic model as the regional one, but using a higher-resolution DTM and massive numerical inundation calculations with the GPU-based Tsunami-HySEA nonlinear shallow water code. This study shows that the GIS-based inundation maps used for planning deal conservatively with potential hazard underestimation at the local scale, stemming from typically unmodeled uncertainties in the numerical source and tsunami evolution models. The GIS-based maps used for planning fall within the estimated "error-bar" due to such uncertainties. The analysis also demonstrates the need to develop local assessments to serve very specific risk mitigation actions to reduce the uncertainty. More in general, the presented case-studies highlight the importance to explore ways of dealing with uncertainty hidden within the high-resolution numerical inundation models, e.g., related to the crude parameterization of the bottom friction, or the inaccuracy of the DTM.

Keywords: tsunamis, inundation maps, early warning, probabilistic hazard, numerical modeling, Italy

INTRODUCTION

Tsunami early warning systems (TEWS) play a significant role in protecting coastal areas from the tsunami threat. The first TEWS was developed for the Pacific Ocean after the tsunami following the Mw 8.6 Aleutian Islands earthquake on the April 1, 1946. Since then, the development of increasingly accurate and reliable TEWS was strongly fostered under the lead of United Nations international agencies, in collaboration with the Member States, in particular after the devastating December 26, 2004 Indian Ocean tsunami. These political efforts, together with rapid technological developments during recent decades, increased the number of TEWS worldwide and their monitoring capabilities, extending the coverage of tsunami monitoring activities to virtually all the oceans worldwide (Bernard and Titov, 2015; Angove et al., 2019; Mulia and Satake, 2020).

Within the framework of the Intergovernmental Coordination Group for the Tsunami Early Warning and Mitigation System in the North-eastern Atlantic, the Mediterranean and connected seas (ICG/NEAMTWS), the Italian Tsunami Alert Center at the Istituto Nazionale di Geofisica e Vulcanologia (CAT-INGV) started operating 24/7 from October 1, 2014 as Candidate Tsunami Service Providers (TSPs) for the NEAM region (North-eastern Atlantic, the Mediterranean and connected seas, Bernardi et al., 2015; Amato, 2020). CAT-INGV is the upstream component of the Italian Tsunami Warning System (SiAM; see also the national implementing decrees of SiAM directive, DPCM, 2017; Dipartimento della Protezione Civile, 2018), constituted also by the Italian Civil Protection Department (DPC) and the Italian Institute for Environmental Protection and Research (ISPRA). As the other NEAM TSPs (CENALT, France; NOA, Greece; KOERI, Turkey; IPMA, Portugal), CAT-INGV is committed to deliver messages for potential earthquake-generated tsunamis, containing the alert levels and the estimated time of arrival at preselected forecast points along the coasts. The two alert levels established by the ICG/NEAMTWS agency are advisory/orange (tsunami runup ≤ 1 m) and watch/red (tsunami runup >1 m). Once an alert message has been generated, it is disseminated by CAT-INGV to the IOC/UNESCO subscriber Member States, and by DPC over Italian territory. DPC also carries out specific actions related to the forecasted alert levels (Dipartimento della Protezione Civile, 2018).

An upper limit for the expected runup is not specified by the NEAMTWS protocols and alert messages, which only forecast a state of significant inundation with runup >1 m. Coastal risk managers must then define this limit by identifying the inundation-prone areas with evacuation maps. Since it is impossible to define a deterministic maximum inundation, an upper boundary must be set as the evacuation distance which has a certain probability of being exceeded in a given time frame, in principle corresponding to a given risk reduction level for the same vulnerability and exposure levels. The probabilistic hazard frameworks are ideal in this respect, as they provide estimates of the exceedance probability for given intensity measures and for specific time frames. Such an approach, which we can refer to as a "uniform hazard", is commonly adopted for seismic building codes. For example, the design seismic action is often set as the one having a probability of being exceeded of 0.1 (10%) or 0.02 (2%) in 50 years (corresponding respectively to 475 and 2,475 years Average Return Period, hereinafter ARP), mostly within a "multi-tier" approach related to different performance levels, e.g., ranging from life-safety to building collapse as a target (ASCE/SEI 7-16, 2017; NTC, 2018). The use of a homogeneous risk target is sometimes advocated: it would be more consistent with the final use of seismic design maps to adopt a "uniform risk" assumption, in which the design ground motions are defined to provide the same level of risk everywhere, e.g., the annual probability of collapse (e.g., Luco et al., 2007). More recently, an approach based on probabilistic tsunami hazard analysis has been adopted in tsunami building codes, considering different performance levels, similarly to what is done for seismic design, and assuming a design probability of 0.02 (2%) in 50 years corresponding to the longer ARP of 2,475 years for the collapse prevention performance level (Chock et al., 2016). Authorities and stakeholders can use the same principles for land-use design (e.g., Geist and Lynett, 2014).

A specific difficulty with Probabilistic Tsunami Hazard Analysis (PTHA) is that representing the seismic source variability can require up to millions of scenarios, especially in areas where the crustal intermediate-magnitude seismicity provides a relevant contribution (Selva et al., 2016). Although the use of numerical simulations is by far the most accredited tool to model tsunami propagation and inundation (Behrens and Dias, 2015), a massive use of tsunami simulations on high-resolution topo-bathymetric grids still represents a challenge in several practical applications because of the computational cost. Inundation simulations are also subject to the availability of very accurate and detailed DTMs both on- and off-shore of the sites of interest which, even when available, may represent an important uncertainty source (e.g., Griffin et al., 2015; Song and Goda, 2019), also related to the choice of appropriate roughness values (e.g., Kaiser et al., 2011; Griffin et al., 2015). Therefore, the combination of numerical simulations offshore and rapid approximated methods onshore is a common practice as alternative to explicit numerical inundation simulations (Grezio et al., 2017, Grezio et al., 2020).

The method proposed by the Italian DPC to local authorities to define evacuation maps (Dipartimento della Protezione Civile, 2018) embodies this philosophy: 1) the design probability for the watch/red alert is fixed through the selection of the 2,500 years ARP and 84th percentile of the epistemic uncertainty from a regional and relatively coarse-scale Seismic PTHA (SPTHA, in the current implementation is the NEAMTHM18, NEAM Tsunami Hazard Model 2018; Basili et al., 2018; Basili et al., 2019; Basili et al., 2021), evaluated off-shore and amplified to the coast; 2) the extension of the evacuation area is the outcome of a chain of simplified and conservative approximations, including some "safety factors". The details of the procedure are subsequently provided in this paper. Very

similar approaches that inspired the Italian authorities have been adopted by New Zealand (Leonard et al., 2008; Fraser and Power, 2013; MCDEM, 2016) and Samoa (Wright et al., 2011). Defining inundation maps is not only important for the population to know where people have to evacuate in case of a tsunami alert, but it is also important for the local contingency planning, e.g., to identify tsunami-safe emergency management locations (local emergency centers and areas), further than for coastal planning in general.

The aim of the present work is to evaluate the performance of the Italian evacuation maps, as defined at the national level, in comparison with two more detailed case-studies at local scale. Starting from the same seismic model defined in the regional NEAMTHM18, a site-specific SPTHA, including massive high-resolution numerical inundation simulations (Gibbons et al., 2020), is here used to obtain the inundation maps for several different design levels, for two selected target sites in South-Eastern Sicily, Italy. These sites are the coastal zones in the vicinity and around the cities of Catania and Siracusa, two touristic, commercial and industrial urbanized areas, comprising harbour infrastructures and heterogeneous morphological terrain features (e.g., flat beaches, cliffs, jagged inlets), representing a test for a broad range of different coastal settings. This area has experienced destructive tsunamis in the past, as documented by both historical (Maramai et al., 2014; Maramai et al., 2019) and geological (De Martini et al., 2012; Polonia et al., 2017) evidence, with a rich and still open scientific debate on the causative sources of the most important events, in particular regarding the earthquakes occurred in 1693 and 1908 (Piatanesi and Tinti, 1998; Gutscher et al., 2006; Gerardi et al., 2008; Favalli et al., 2009; Pino et al., 2009; Billi et al., 2010; Tonini et al., 2011; Aloisi et al., 2013; Convertito and Pino, 2014; Ridente et al., 2014; Meschis et al., 2019).

The local SPTHA quantifies the exceedance probability as a function of the inland tsunami intensity (here, the maximum inundation height) on a regular grid of points at the simulation resolution (here, 10 m at the two target sites). This allows the extraction of high-resolution inundation lines corresponding to different ARPs and epistemic uncertainty percentiles, including the ones recommended for planning by the Italian DPC, for comparison with the evacuation maps derived from the simplified method. Uncertainties not explicitly modeled in the local SPTHA are also subsequently considered and estimated to first order. To discriminate between different uncertainty sources, the procedure used for the official inundation zones, originally applied to all the Italian coasts using a coarser DTM, is here applied to the same high-resolution DTM used for the numerical inundation simulations, yet based on the same hazard input. This updated version of the inundation maps can be compared with those obtained through local SPTHA to deal with the method approximations, and with the official maps to directly address the impact of DTM uncertainties.

DEVELOPMENT OF INUNDATION MAPS

In this section, the basic elements defining the inundation maps are introduced. We describe the procedure developed to design the maps adopted for tsunami risk-management in Italy from regional SPTHA, as well as the methodology for developing inundation maps starting from site-specific high-resolution SPTHA. In the following, for convenience, any quantity derived from the Italian authorities' indications to define the inundation maps (i.e., the 2,500 years ARP and the 84th percentile) are labeled as "design" quantities.

The Tsunami Hazard Regional Model

The indications issued by the Italian DPC for evacuation maps (Dipartimento della Protezione Civile, 2018) are based on a regional SPTHA model. In their current implementation, the reference SPTHA is the NEAMTHM18 (Basili et al., 2018). The NEAMTHM18 was produced in the frame of the TSUMAPS-NEAM project (http://www.tsumaps-neam.eu/; Basili et al., 2019). The model is the first long-term SPTHA for the entire NEAM region, covering a very high number of seismic sources and estimating inundation probability at a relatively coarse regional scale.

In NEAMTHM18, well-constrained seismic sources (as subduction interfaces or major fault systems) and diffuse crustal seismicity are treated separately and the epistemic uncertainty is estimated using an ensemble modeling technique (Selva et al., 2016; Basili et al., 2021). Offshore sea surface elevations are obtained by linear combinations of pre-computed elementary source scenarios (Molinari et al., 2016), which are propagated with the 2D shallow-water tsunami numerical code Tsunami-HySEA (de la Asunción et al., 2013), up to water depths of 50 m along a set of points of interest (POIs) spaced at about 20 km from each other (a subset of these points in the Mediterranean Sea is shown in **Figure 1A**). Offshore sea surface elevations are then transformed into maximum inundation height (*MIH*) through a simplified amplification factor (AF) method accounting for amplitudes, periods and polarities of the incident waves (Glimsdal et al., 2019).

The final results consist of a set of hazard curves (probability of exceedance in 50 years vs. *MIH*) at each POI. This set describes the epistemic uncertainty on the hazard, and it is summarized through the mean, median, and different percentiles (**Figures 1B,C**). NEAMTHM18 includes several sources of uncertainty, among which those related to the seismic recurrence modeling, to the simplified modeling of the seismic source, as well as to the tsunami modeling (generation, propagation and inundation). Noteworthy, several rather strong approximations exist, which can be considered appropriate for a regional-scale SPTHA. Full details can be found in Basili et al. (2021), in the TSUMAPS-NEAM project documentation (Basili et al., 2019), and in several studies dealing with specific aspects of the SPTHA methodology used therein (e.g., Molinari et al., 2016; Selva et al., 2016; Davies et al., 2017; Glimsdal et al., 2019; Scala et al., 2020; Taroni and Selva, 2020; Tonini et al., 2020).

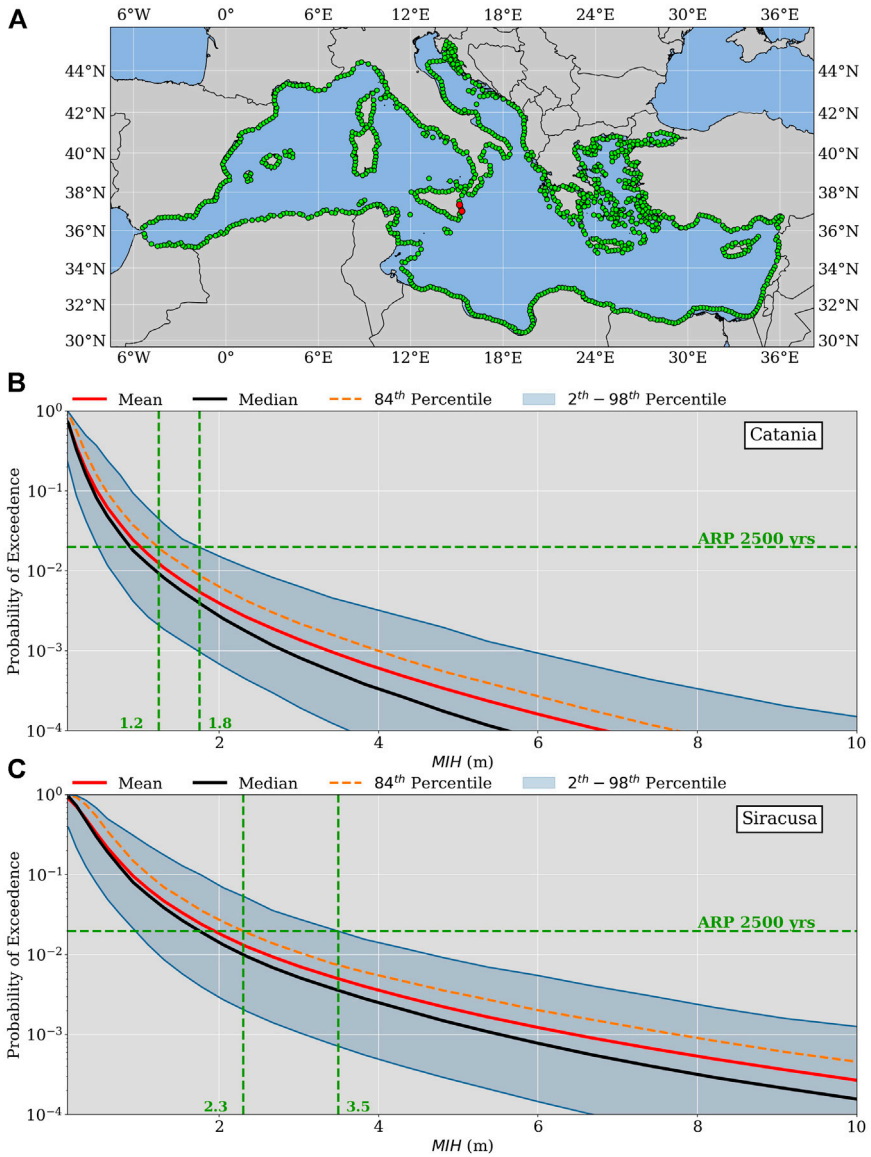

FIGURE 1 | Location of the points of interest (POIs, green dots) in the NEAMTHM18 tsunami hazard model for the Mediterranean area only [panel **(A)**]: the two POIs in front of Catania and Siracusa, used for the present case-study, are highlighted (red dots); the corresponding hazard curves [Catania, panel **(B)**, and Siracusa, panel **(C)**, respectively] are shown for different quantities: the mean (red line), the median (black line), the 84th percentile (orange line) and the interval 2nd–98th percentiles (blue area). For both POIs, *MIH* never exceeds 4 m for an average return period of 2,500 years (green lines). The curves can be downloaded from the NEAMTHM18 interactive hazard curve tool (http://www.tsumaps-neam.eu/neamthm18/).

Design of Italian Inundation Maps

Inundation maps in Italy feature two zones, corresponding to the advisory/orange and watch/red alert levels, respectively (Dipartimento della Protezione Civile, 2018). All the inundation maps are available through the Tsunami Map Viewer (http://sgi2.isprambiente.it/tsunamimap).

The extent of the advisory/orange zone is nominally set to 1 m elevation everywhere, to be consistent with the definition of advisory alert level (runup ≤1 m). Currently, to conservatively accommodate uncertainties of the DTM, the boundary of the advisory inundation zone is fixed where the DTM features a topography of 2 m above the average sea level.

The watch/red zone should define the inland extension of the potentially inundated area after an alert message forecasting a runup >1 m. To define an upper limit for the inundation distance the following procedure is adopted:

1. From NEAMTHM18, the *MIH* with the 2,500 years ARP at the 84th percentile of the epistemic uncertainty distribution is selected for each POI along the Italian coasts (among those in **Figure 1A**).

2. A design MIH_d value is associated with each point of the coastline point dataset (https://www.istat.it/it/archivio/137341) provided by the Istituto Nazionale di Statistica (ISTAT). These points have a spacing along the coastline on the order of hundreds of meters. Since the average inter-POI distance in NEAMTHM18 is about 20 km, a search radius of 40 km defines a circle around each of the coastline points and the design MIH_d for that point on the coast is the maximum among all the POIs falling in the circle. The result of the searching algorithm is shown in **Figure 2**. There are several exceptions to this algorithm, described in the Annexes to the "Indicazioni" (Dipartimento della Protezione Civile, 2018), due to specific local geomorphological features: the very shallow waters in the northern Adriatic Sea where no POI lies within 40 km from the coast; the need to avoid associating POIs offshore the opposite coasts of the narrow peninsula of southern Calabria; the need to associate more than one POI to small islands, for which a search radius of 80 km is chosen, to better characterize SPTHA variability.
3. The design MIH_d value is then converted into a design maximum run-up value $R_d^* = 3{*}MIH_d$. This factor of three is based on the analysis of the ratio between the maximum simulated runup and the mean of the simulated *MIH* at six different coastal locations in the Mediterranean Sea, including a variety of coastal morphologies (Glimsdal et al., 2019). The inundation simulations were carried out taking into account tsunamis generated at different distances by earthquakes having different fault orientations and various magnitudes. **Figure 3** shows that the 98% of such ratios are smaller than 3.
4. The design runup R_d defines the design inundation distance with the function $D_d(R_d)$ as the distance from the coast where the topography height over the sea level is R_d (**Figure 4A**). An exception is made when the coast is relatively flat (e.g., a coastal plain), which would result in a too large inundation given the dissipative character of inland propagation. An empirical dissipation factor is introduced to limit the maximum inundation distance (e.g., Leonard et al., 2008; Løvholt et al., 2012; Davies et al., 2017). The dissipation factor is derived from observed data collected during post tsunami field surveys (Fraser and Power, 2013, and references therein): an empirical rule featuring a 1 m reduction of the R_d every 200 m away from the coastline (1 m every 400 m along and surrounding a river mouth) is suggested. This rule is applied to the expected resulting maximum inundation distance D_d from the coast, which cannot exceed $D_d^{MAX} = 200{*}R_d$ (**Figure 4B**). D_d^{MAX} is obtained using a GIS-based approach to convert R_d into inundation lines over a DTM, through following a landward oblique line tilted down of an angle α defined by the attenuation coefficient as $tg(\alpha) = 1/200$ or $1/400$ (**Figure 4**). Summarizing, the actual design distance D_d^* is chosen as $D_d^* = \min(D_d, D_d^{MAX})$.
5. The local inundation zone is obtained for $R_d^* \geq R_d + 1$ m. One meter is added for taking into account the uncertainty on the DTMs and the variability in the accuracy of the coast line mapping, both of which may be difficult to quantify.
6. To find the inundation zone corresponding to R_d^*, a discrete set of possible inundation zones along the Italian coasts is first defined according to the classes $D_d^* = D_d^*\{R_i\}$, that is by constructing with the GIS-based procedure described above the inundation lines corresponding to the set of discrete input run-up values $R_d = \{2, 5, 10, 15, 20, 25\}$ expressed in meters. Then, the R_d^* is rounded to the closest $R_i \geq R_d^*$. This defines the inundation zone.

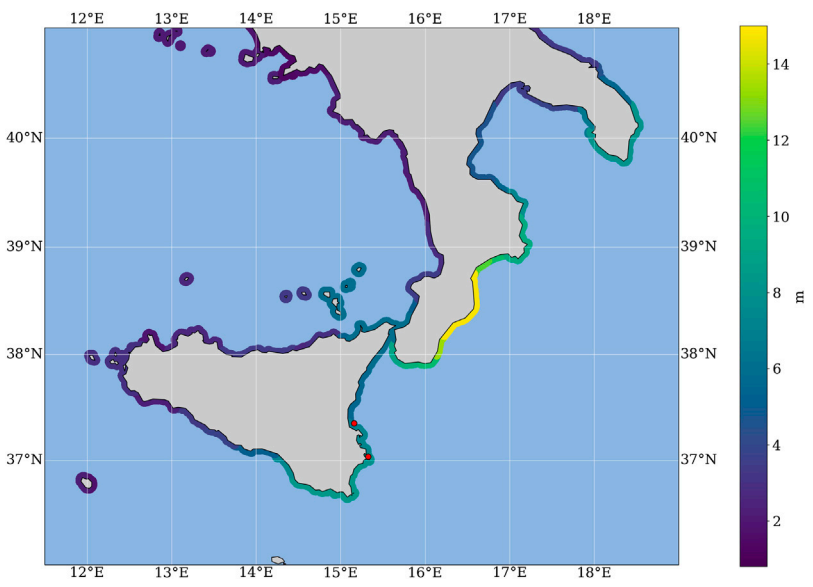

FIGURE 2 | Map showing the results of the searching radius algorithm described in *Design of Italian Inundation Maps* section. Each coastline point is associated to a value of R_d which is used to select the discrete runup class (among 2, 5, 10, 15, 20 and 25 m) and draw the inundation line. The segments of coast in front of the two POIs in Catania and Siracusa (red dots) have R_d higher than 5 m.

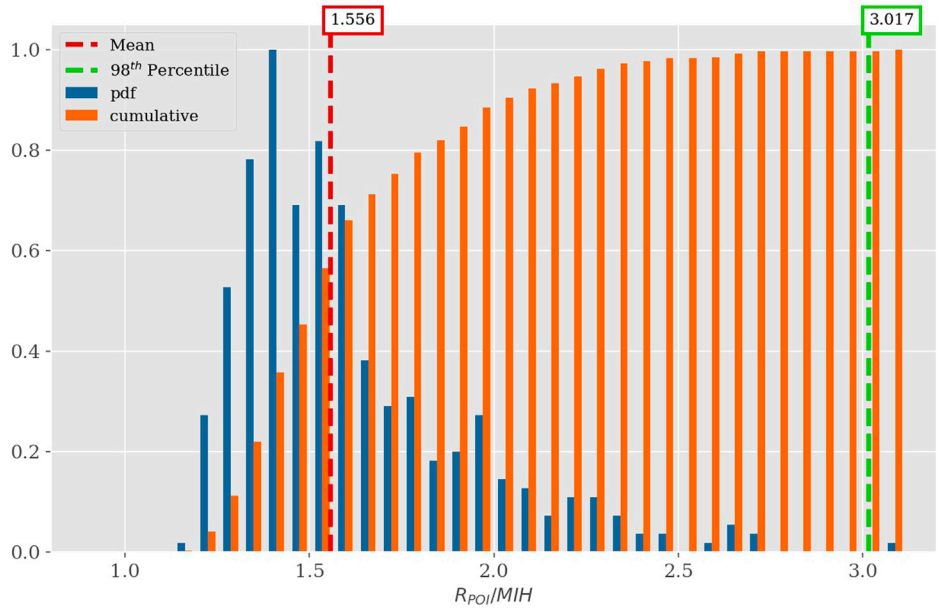

FIGURE 3 | Empirical probability density function (EPDF, blue bars) and empirical cumulative density function (ECDF, orange bars) of the ratio between the maximum Run-up (R_d) and the mean of the maximum inundation height (*MIH*) at each POI.

This first generation of the Italian tsunami inundation maps for emergency planning was elaborated using a composite DTM combining elevation data from different sources. High-resolution LIDAR data (1 m and 2 m resolution with a vertical accuracy as good as 25 cm), provided by MATTM (Ministry of the Environment) for the coastal zone only, have been integrated with the best available mid-resolution DTMs (2, 5, 10 m), provided by single administrative Regions of Italy, in order to

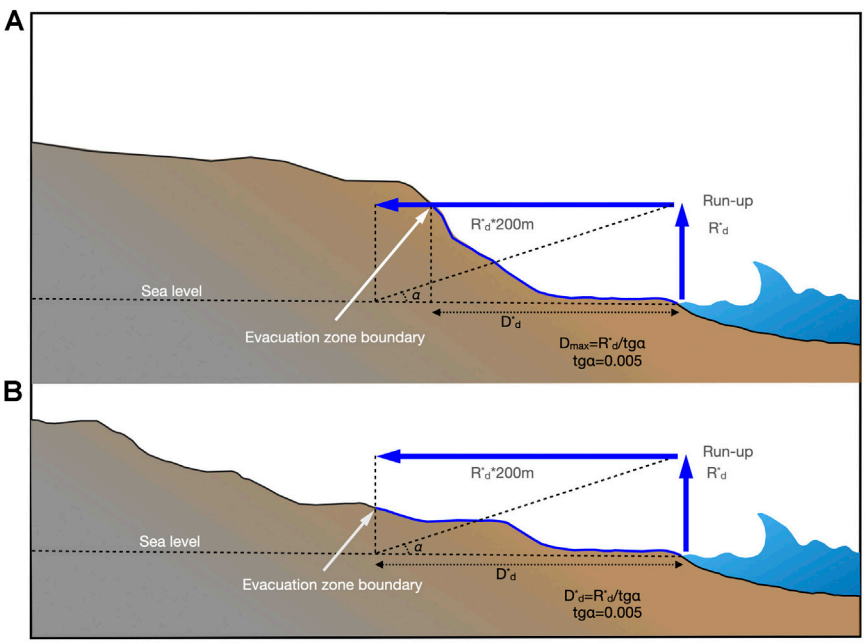

FIGURE 4 | Sketch of the method used to drawn inundation maps: R_d^* is the maximum estimated run-up value for a given stretch of coast, D_d^* is the inundation distance and, in the example, the dissipation factor is tgα = 0.005 (no rivers). The cartoon illustrates the two different behaviours when R_d^* crosses the topography before than the projected ray on the sea level (panel **A**) or vice versa (panel **B**).

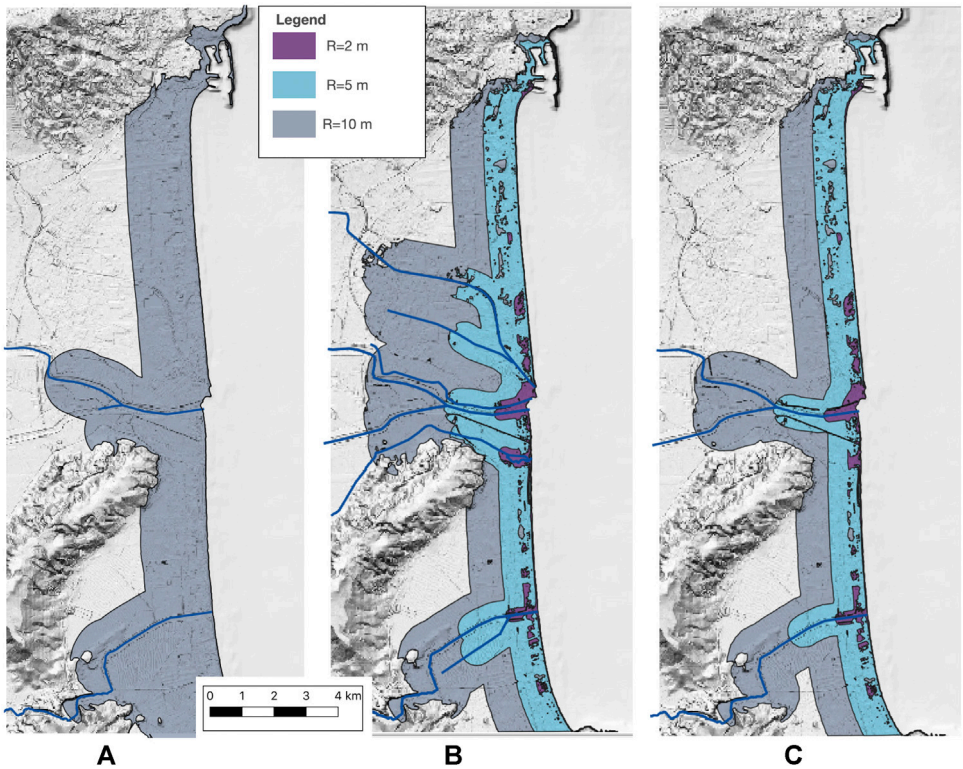

FIGURE 5 | The first generation inundation map of Catania [panel **(A)**] is compared with the GIS-based version inundation maps calculated for this work, using the more detailed DTM described in *Inundation Maps for the Case-Studies in South-Eastern Sicily* section, for different values of R_d^* and considering [panel **(B)**] or not [panel **(C)**] additional secondary river beds.

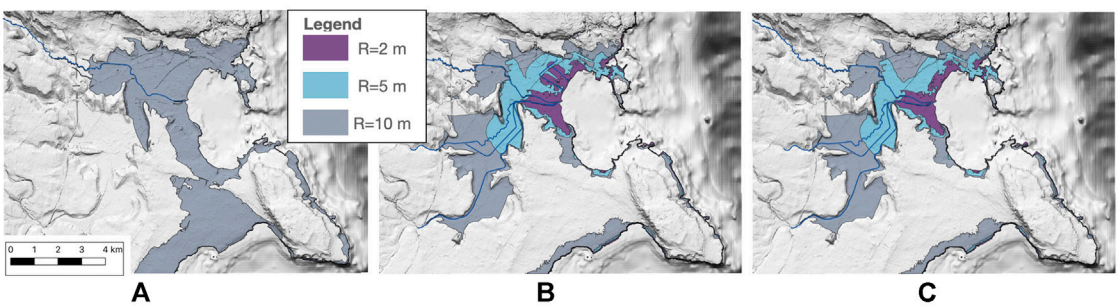

FIGURE 6 | Same as **Figure 5**, but for Siracusa.

obtain the complete coverage of the potential inundation areas. Other input data are the trace of the main waterways (scale 1: 10.000) as an update of the national river networks of ISPRA-SINAnet (http://www.sinanet.isprambiente.it/it/sia-ispra/download-mais/reticolo-idrografico/view), and the coast line derived from satellite and aerial images analysis available for the year 2009 at the Geoportale Nazionale (http://www.pcn.minambiente.it/mattm/), used only when applying the GIS-based procedure to achieve greater precision (item 6. above), while it was not deemed necessary to replace the less precise ISTAT coastline of (item 2.), since the latter is used in conjunction with search radii of 40 km. For both the segments of coast here considered as case-studies in south-eastern Sicily we used the hazard curves of the two nearest POIs to the locations (**Figure 1**) and the run-up design value approximated for excess to the next discrete values is $R_d^* = 10$ m.

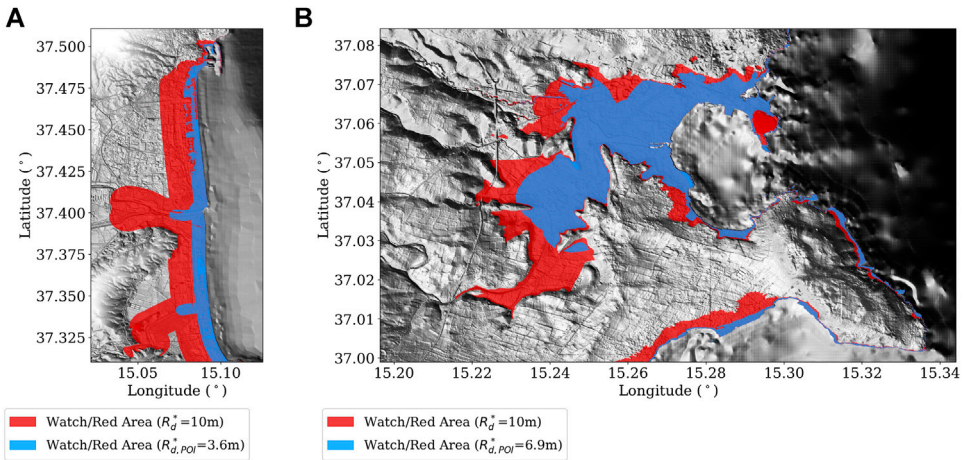

FIGURE 7 | Comparison between the Watch/Red areas designed for R_d^* = 10 m (the gray area in **Figures 5C, 6C**) and the inundation maps obtained using the values obtained from the POIs in front of Catania [panel **(A)**] and Siracusa [panel **(B)**].

Inundation Maps for the Case-Studies in South-Eastern Sicily

To test the performance of the method described in the previous section, in this study we produce several new inundation map versions.

A first version, coined GIS-based version, is obtained by repeating the procedure described in *Design of Italian Inundation Maps* section, but adopting a more accurate local DTM. More specifically, we used the same high-resolution DTM (10 m) implemented in the tsunami simulations to compute local SPTHA (see next section and also Gibbons et al., 2020). This DTM was produced by mosaicking rasters with different horizontal cell resolutions and then resampling them to a 10 m horizontal cell. For the land portion the used datasets were a 1 m cell resolution raster near the coastal zone (The Geology and Geotechnologies Laboratory, INGV, http://www.ingv.it/it/monitoraggio-e-infrastrutture-per-la-ricerca/laboratori/laboratorio-geologia-e-geotecnologia, provided the LiDAR dataset in the framework of an agreement with the Ministry of the Environment, Earth and Sea, http://www.pcn.minambiente.it - Italian National Geoportal, owner of the data) with the 25 m horizontal cell resolution EU-DEM Digital Elevation Model over Europe (EU-DEM-4258: 1 arcsec - 5 arcsec, EU-DEM-3035: 25 m, color shaded DEM derived from the EU-DEM-3035: 25m, produced using Copernicus data and information funded by the European Union - EU-DEM layers); for the offshore portion the DTM was obtained by interpolating the data available from the MaGIC project (foglio 32 e foglio 33, data from the MaGIC project, Dipartimento della Protezione Civile, http://dati.protezionecivile.it/) and then mosaicking the result to the EMODnet Digital Bathymetry raster (EMODnet Bathymetry Consortium, 2018). For both case-studies, we used the R_d^* values of 2, 5, 10 m, as defined for the current national administrative classification. The comparison between the inundation zones obtained with this DTM and the official ones shows some discrepancies resulting from the different characteristics of the DTM (resolution; ground filtering; different datasets used in the mosaic; different sources and data processing techniques for building the DTM from raw data) and from the different number and extension of the rivers considered in the analysis. While differences in the DTMs are responsible for relatively minor changes in the inundation maps, neglecting or including one or more rivers can impact significantly on the shape and the extent of the inundation line, since the assumed dissipation rate is halved in the presence of a river (**Figure 5** and **Figure 6**).

A second version of inundation maps is estimated adopting the same procedure, but using specific values of R_d^*, derived in this study from the NEAMTHM18 hazard curves for the two closest target POIs (**Figure 1**), and without approximating for excess to the next bigger discrete value. The obtained values are $R_{d,POI}^*$ = 3.6 m and $R_{d,POI}^*$ = 6.9 m, respectively for Catania and Siracusa (**Figure 7**).

We anticipate that a third version is obtained for the values of R_d^* resulting by considering a rough quantification of the tsunami intensity uncertainty superposed onto the Non Linear Shallow Water (NLSW) results, for which a hybrid version of the inundation maps will be coined. We obtain $R_{d,LOC}^*$ = 13.2 m and $R_{d,LOC}^*$ = 15.1 m for Catania and Siracusa respectively, as explained in *Results* section.

Inundation Maps From Local High-Resolution NLSW-Based SPTHA for Catania and Siracusa

Another version of inundation maps, coined SPTHA-based inundation maps, is obtained using a classical approach (e.g., González et al., 2009) directly from the local SPTHA, based on explicit, high-resolution (NLSW) modeling of the tsunami inundation (Gibbons et al., 2020).

The use of a regional SPTHA as input for a higher-resolution local SPTHA allows for a pre-screening of the full variability of seismic sources, selecting only those which contribute significantly to the hazard at the site of interest. Reducing the number, or the computational cost, of high-resolution tsunami

inundation simulations is often essential. In this respect, techniques based on cluster analysis (Lorito et al., 2015; Volpe et al., 2019; Williamson et al., 2020) or statistical emulators (Sarri et al., 2012) have been proposed. In the present work, given the availability of massive High-Performance Computing resources, a significant reduction of simulations is obtained with a hazard disaggregation approach (Gibbons et al., 2020).

The number of scenarios defined in NEAMTHM18 for the Mediterranean basin is of the order of 10^7, making the computational task potentially extremely demanding. However, the tsunamis from many of these scenarios are negligible at the sites of interest. A first significant reduction is obtained by selecting only the scenarios which produce a tsunami elevation greater than 0.01 m at the selected target POIs (red dots in **Figure 8**), resulting in little more than 10^6 scenarios, most of which in common between Catania and Siracusa, see **Table 1**. Then, hazard disaggregation is performed to select only the scenarios which reproduce a prescribed fraction of the total hazard (99%) simultaneously at the two POIs in the MIH interval between 1 m and 4 m (**Figure 9**). The reason for choosing this interval is that it should guarantee the inclusion of the scenarios which significantly contribute to the hazard curves around the design 2,500 years ARP and 84th percentile of the model uncertainty selected for planning, (**Figures 1B,C**). This is exactly the same approach followed by Gibbons et al. (2020), and most of the numerical simulations are the same as well. As already discussed by Gibbons et al. (2020), given that the selection and the hazard reproduction are operated at two offshore locations, we cannot

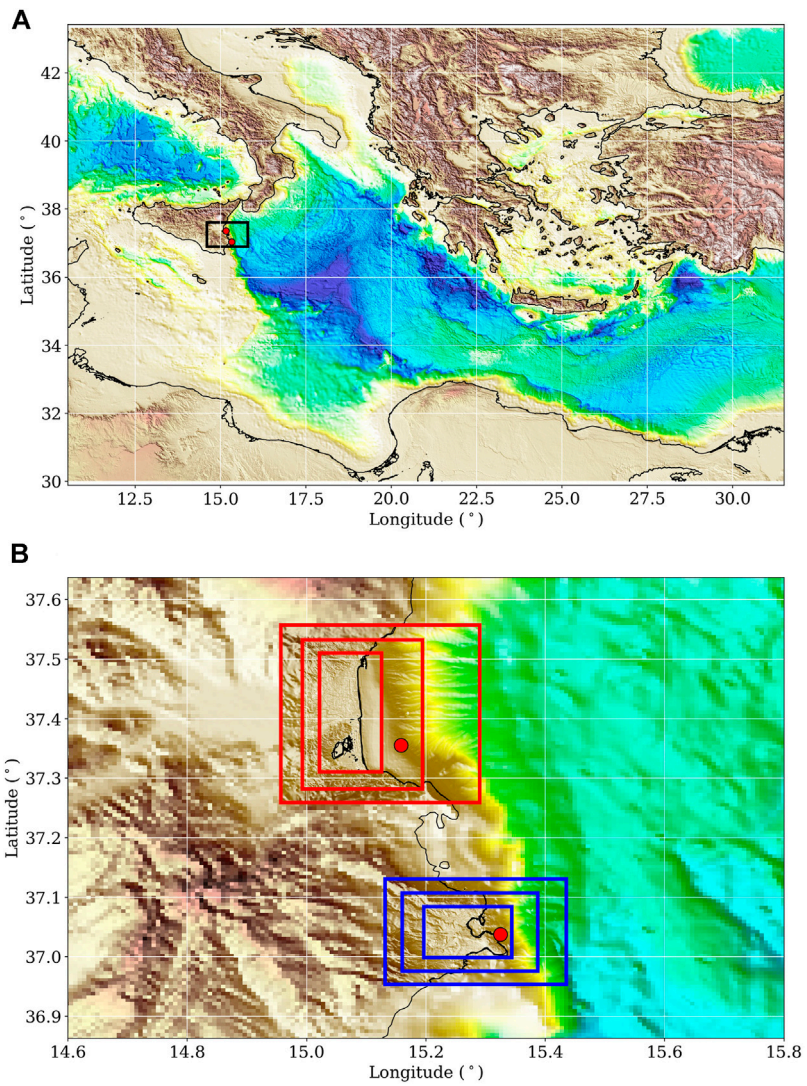

FIGURE 8 | Extension of the computational domain [panel **(A)**] showing the selected POIs used to perform the disaggregation analysis (red dots, as in **Figure 1**); the target area [black rectangle in the panel **(A)**] is zoomed to illustrate the inner levels (2nd, 3rd and 4th) of the nested grids [panel **(B)**] for inundation modeling in Catania (red rectangles) and Siracusa (blue rectangles). Grid resolution is 640 m for the larger domain in the top panel and 160, 40 and 10 m for the inner levels shown in the bottom panel.

TABLE 1 | Number of scenarios resulting from the disaggregation procedure representing the 99% of the hazard for both Catania and Siracusa in their respective *MIH* intervals. The number of required simulations with respect to the total number of scenarios representing the hazard in the same interval of *MIH* is strongly reduced by about 96%.

	99% of total hazard (#)	Total hazard (#)	Reduction (%)
Catania	32,443	923,924	96.5
Siracusa	39,714	902,334	95.6
Total[a]	45,827	1,039,551	95.6

[a]*Total is calculated excluding scenarios whose simulation should be repeated due to the vicinity of the two target areas.*

expect to perfectly reproduce the hazard everywhere onshore, because the difference between two tsunami waveforms may change during inundation: for example, this can be due to non-linear effects such as wave breaking, energy dissipation during inundation, or because of co-seismic coastal uplift or subsidence. It is also worth noting that the regional hazard curve for Siracusa is significantly higher than that for Catania for the considered ARP (**Figure 1**). For this reason, while the MIH range between 1 and 4 m turns out to be suitable to produce the onshore hazard curves for Catania (Gibbons et al., 2020), to better reproduce the hazard for Siracusa, we also modeled the scenarios obtained from the disaggregation in the interval 4–8 m, in addition to the 1–4 m range. We may conclude that the disaggregation procedure and applied ranges turned out to be quite accurate while remaining remarkably efficient, since the scenarios to be modeled were reduced, in total, to about 46,000 (i.e., the amount of scenarios is reduced by ~96%, see **Table 1**).

For the sake of completeness, we recall that the tsunami scenarios are simulated with Tsunami-HySEA, a non-linear hydrostatic shallow-water multi-GPU code (GPU, Graphics Processing Unit; de la Asunción et al., 2013; Macías et al., 2017), exploiting a nested grid algorithm. Tsunami-HySEA models in a single code tsunami generation, open-ocean propagation and nested grid inundation using progressively finer grid resolution of the coastal areas (Macías et al., 2016). The code has undergone an intensive process of model validation and verification following, in particular, the benchmarking standards of the NTHMP, the National Tsunami Hazard and Mitigation Program, United States (Macías et al., 2017; Macías et al., 2020a; Macías et al., 2020b). Four-level nested topo-bathymetric grids were used here (**Figure 8**). Three of them are local grids with progressively higher resolution (160, 40, and 10 m) and one is a global grid with the coarsest resolution (640 m), ensuring the analysis of the source-to-target propagation in the open sea. The 640 m grid was derived from the GEBCO topo-bathymetry model. The finest local 10 m grid is the same presented in the previous section for the construction of the inundation maps. To guarantee depth compatibility between all the nested local grids, a bilinear resampling algorithm was then applied to the 10 m grid, producing the local intermediate grids with 40 m and 160 m cell resolution (Gibbons et al., 2020). Bottom friction is treated with a Manning's coefficient of 0.03. The initial sea-level anomaly is obtained for each modeled seismic scenario through an elastic instantaneous dislocation model (Okada, 1992). The single-scenario Tsunami-HySEA simulation takes approximately 25 min on the MARCONI-100 supercomputer at CINECA, meaning that approximately

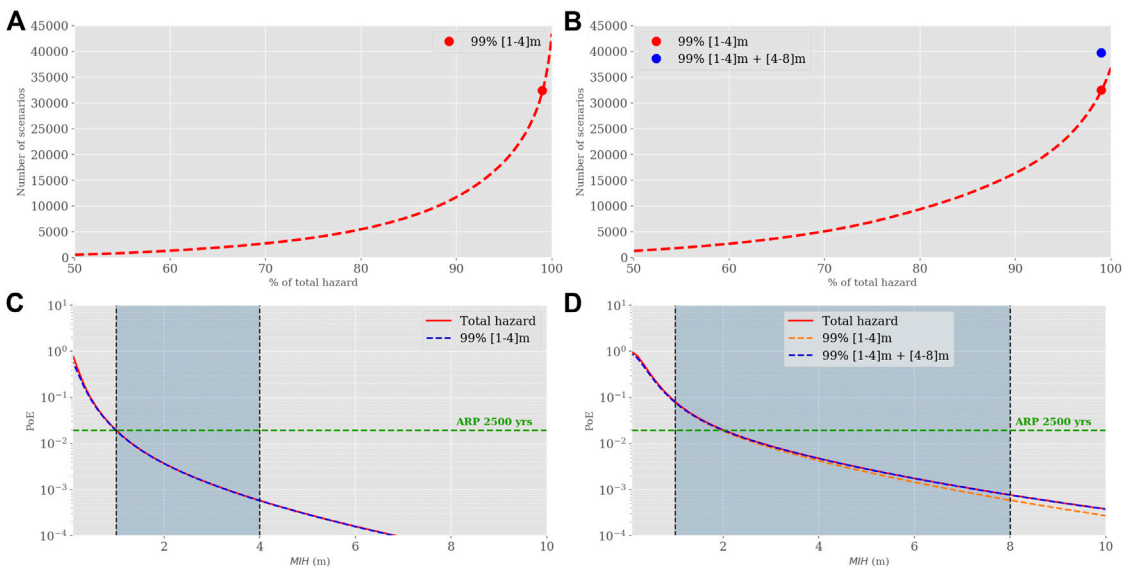

FIGURE 9 | Number of scenarios needed to represent the 99% (**Table 1**) of the total hazard for both target sites [Catania, in panels **(A)** and Siracusa, in panel **(B)**] in the selected interval of tsunami intensity (range [1–4] m for Catania and ranges [1–4] and [4–8] m for Siracusa). The corresponding hazard curves [panels **(C)** and **(D)** for Catania and Siracusa, respectively] in the respective *MIH* ranges are overlapped with the ones representing the total hazard. For Siracusa results without the [4–8]m range are shown to illustrate the discrepancy with respect the total hazard curve [orange line in panel **(D)**] and the number of additional scenarios [blue dot in panel **(B)**] needed to well represent the total hazard.

19,000 GPU hours were required to complete the set of selected scenarios. With 1024 simulations able to run in parallel, around 18 h of clock-time are needed to perform these calculations.

The simulation results obtained in the highest-resolution innermost grids at the two locations are then aggregated to calculate the hazard curves in each grid cell on land if reached by a minimum threshold of water (here, 0.01 m). Specifically, the hazard curves are obtained in each point x as

$$P(I > h; x, dT) = 1 - \exp\left[- \sum_i \lambda(s_i) H_{I(s_i,x) > h} dT \right] = 1 - \exp(-\lambda_{I>h} dT) \quad (1)$$

where dT is the exposure time (50 years as in NEAMTHM18), h is the threshold inundation height, s_i are individual scenarios with mean annual rate $\lambda(s_i)$, $H_{I(s_i,x)>h}$ is an indicator function (sometimes called Heaviside step function) that is 1 if the intensity $I(s_i, x)$ computed by NLSW simulations for the scenario s_i in x is $> h$, and 0 otherwise, and λ_h is the overall mean annual rate of exceedances of h. $P(I > h; x, 50yr)$ represents the Probability of Exceedance (hereinafter PoE), that is the probability that h has been exceeded at least once during the time $dT = 50$ years. The use of indicator functions implies that no uncertainty is modeled into the propagation factor of the hazard, that includes the tsunami generation, propagation and inundation process (Selva et al., 2016; Grezio et al., 2017).

The same seismic model $[s_i, \lambda(s_i)]$ used to create NEAMTHM18, which is at the base of the inundation maps described in *Design of Italian Inundation Maps* and *Inundation Maps for the Case-Studies in South-Eastern Sicily* sections, is also considered for calculating this local SPTHA. This source model includes epistemic uncertainty (Basili et al., 2021), represented through an ensemble of 1000 equally plausible models with alternative definitions of the scenarios and of their rates of occurrence. Collectively, this ensemble represents the seismic source variability as a function of many alternative but scientifically acceptable modeling choices (Selva et al., 2016; Basili et al., 2021). This epistemic variability propagates to hazard curves. Ideally, it should be combined with the epistemic uncertainty in the propagation factor (not modeled here). The resulting ensemble of hazard curves describes the epistemic uncertainty on the hazard model through different statistics such as mean or percentiles.

Inundation maps are then derived by selecting the tsunami intensity corresponding to a given value of the ARP, which is the reciprocal of the mean annual rate λ_h in **Eq. 1** and thus can be evaluated as a function of the PoE. Graphically, this means to intersect the hazard curves, at each grid point, with an horizontal plane having a constant PoE, corresponding to the selected ARP, and to draw a contour line corresponding to the wet area (maximum flow depth greater than 0.01 m, since this is the first threshold for which we calculated SPTHA; the tolerance for simulations with Tsunami-HySEA was instead set at 0.001 m). If needed, it is possible to draw different inundation maps for different ARPs, in the time span defined in the frame of the NEAMTHM18 model (up to about 100,000 years). Inundation maps can be obtained either from the mean hazard curve, or from any other hazard curve calculated for a different percentile.

Finally, it is important to remark that some uncertainties associated with the tsunami source (e.g., heterogeneous material properties, variability of fault dimensions, time-dependence, non-hydrostaticity), or with the tsunami propagation and inundation modeling (e.g., limits of the NLSW model, uniform Manning coefficient, wave dispersion, details of coastal morphology) are not quantitatively addressed in the present study. Neither is addressed the impact associated with potentially inaccurate bathymetry and topography models.

RESULTS

The main goal of our analysis was to compare the current strategy to define inundation maps, used to draw the evacuation areas for the Italian coasts and based on the regional hazard NEAMTHM18, with the hazard results obtained from local SPTHA models, hence evaluating the whole chain of adopted assumptions and approximations described in *Design of Italian Inundation Maps* section. This analysis was carried out in the two target areas of Catania and Siracusa.

We recall that the GIS-based inundation maps and those from the local SPTHA based on numerical simulations, which are compared to each other in this section, were obtained using the same DTM. In *Inundation Maps for the Case-Studies in South-Eastern Sicily* section, we have also qualitatively addressed the impact of using a different DTM and different treatments for the rivers onto the design of the inundation maps; we have observed that the latter is more influential than the differences between the DTMs (**Figures 5**, **6**).

As described in *Design of Italian Inundation Maps* section, for national planning the R_d^* design value was selected by searching the maximum tsunami intensity in an area containing several POIs (at distances up to 40 km), leading to a value greater than 5 m for both locations (**Figure 2**). Given the rough discretization of the inundation lines in the GIS-based method, such a value is eventually rounded up to the 10 m and the corresponding contour line is used. On the one hand, it could be argued that the value of R_d^*, corresponding to the specific POI located in front of each site of interest, could be a more calibrated solution to estimate the local inundation. On the other hand, the use of a regional assessment can be inappropriate for specific land use actions, since the tsunami behaviour in the near-field depends strongly on non-linear effects and detailed terrain morphology not explicitly treated at regional level. Moreover, the local sources may not be sufficiently finely discretized nor investigated closely enough. As a matter of fact, the closest POIs in front of Catania and Siracusa (**Figure 8B**) provide the two values $R_{d,POI}^*$ (as defined in *Inundation Maps for the Case-Studies in South-Eastern Sicily* section) equal to 3.6 m and 6.9 m, respectively. The first one is smaller than the value used for planning, which confirms that local effects are relevant, and not homogeneous from site to site. The inundation lines which correspond to these local values are shown in **Figure 7** for both Catania and Siracusa, and compared to the line corresponding to $R_d^* = 10$ m used for planning.

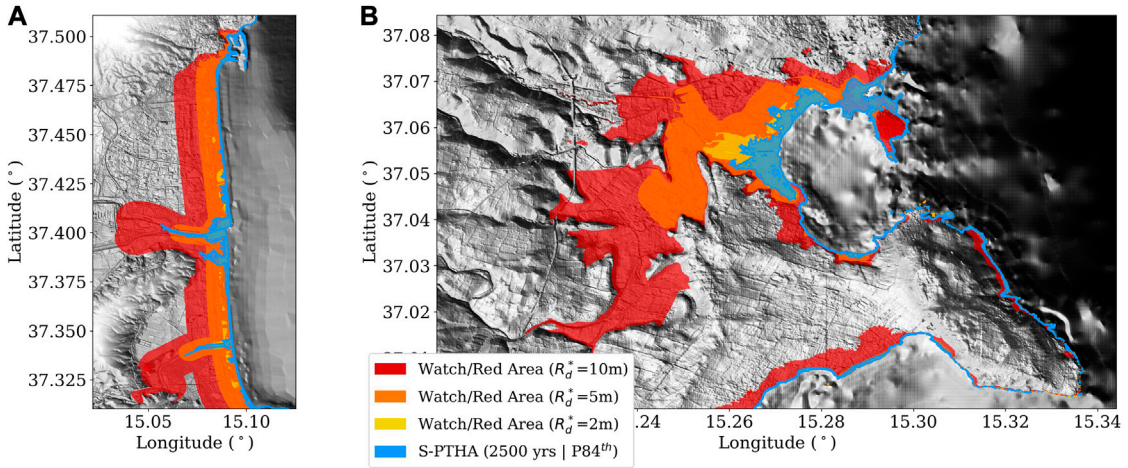

FIGURE 10 | Watch/Red areas designed for different values of R_d^* (2, 5 and 10 m, in red, orange, yellow and blue, respectively) compared to the local SPTHA inundation corresponding to 2,500 years ARP and the 84th percentile (blue) in Catania [panel **(A)**] and Siracusa [panel **(B)**].

A first and direct comparison between the inundation maps from the local SPTHA at 2,500 years ARP for the 84th percentile (*Inundation Maps From Local High-Resolution NLSW-Based SPTHA for Catania and Siracusa* section) and the GIS-based inundation maps (*Inundation Maps for the Case-Studies in South-Eastern Sicily* section; the first version, with the same design values as for the national planning) has been performed (**Figure 10**). The choice of $R_d^* = 10$ m for the national planning appears largely conservative, since the extension of the watch/red area exceeds greatly the inundation line calculated with local SPTHA for the same ARP and percentile. On a second glance, by comparing the inundation maps in **Figure 10** to those of **Figure 7**, it appears immediately clear that the local SPTHA predicts an inundation even much more limited than that associated with the POIs at both locations.

Selecting different ARPs and/or different percentiles, we can quantify the extent of this discrepancy. Firstly, we compare the impact of the epistemic uncertainty modeled on the local SPTHA by using different percentiles while keeping the ARP of 2,500 years fixed (**Figures 11A,B**). As expected, the inundation zone for the 98th percentile extends farther than those for the 50th and the 84th percentiles. However, they remain well within the watch/red inundation area defined with $R_d^* = 10$ m for both Catania and Siracusa. This can either mean that the discrepancy is greater than it could be explained by the epistemic uncertainty on the 2,500 years ARP, hence the GIS-based method leads to a large overestimation, or that there is a fraction of unmodelled epistemic uncertainty. Secondly, when longer ARPs are considered, the tsunamis from larger but rarer earthquakes progressively gain more importance. **Figures 11C–F** displays the inundation maps produced for ARPs = 25,000 and 100,000 years, considering the 50th, 84th, and 98th percentiles of the epistemic uncertainty. In this case, the watch/red inundation zone still contains the inundation lines in Siracusa, but it is overtaken at some locations in the Catania plain. This could be due to the very different morphology of the coastal area, where the large plain in the south of the harbour could facilitate the water invasion beyond the forecast capability of the empirical rules used for the GIS-based inundation maps. As a result of this comparison, according to the local SPTHA inundation maps, in Catania, the GIS-based inundation maps would correspond to a design ARP between 2,500 and 100,000 years, while in Siracusa to a design ARP >100,000 years.

It is worthy to note that the effect of the epistemic uncertainty for the 100,000 years ARP is smaller than for shorter ARPs (**Figure 11**). The hazard curves for a single target point (**Figure 1**) show, as expected when dealing with relatively rare events, that the longer the ARP (smaller PoE), the larger the difference between the tsunami intensity obtained with different percentiles of the epistemic uncertainty. However, when we look at the inundation areas, we observe the opposite behaviour, with the uncertainty on the hazard intensity unexpectedly decreasing for longer ARPs. We then argue that this can be the result of an underestimation of the epistemic uncertainty of the local SPTHA, and that the discrepancy between GIS-based and SPTHA-based maps cannot be entirely due to an overestimation of the former. Indeed, we stress once again that the regional SPTHA includes the epistemic uncertainty associated with the source model (Basili et al., 2021), which is the same as in the GIS-based approach. This uncertainty relates to the earthquake mean annual rates, the difference between empirical scaling relations, the slip heterogeneity and depth-dependent features of subduction zones (Scala et al., 2020). Conversely, the local SPTHA does not include the further epistemic uncertainty treatment applied in NEAMTHM18 using amplification factors (Glimsdal et al., 2019), stemming from numerical modeling of the co-seismic displacement, tsunami generation, and tsunami evolution up to inundation. In our local SPTHA, this uncertainty is in principle reduced by the use of NLSW simulations in place of the stochastic inundation treatment included by the local amplification factors, provided that we are not introducing a bias. Several sources of epistemic uncertainty currently exist also when using numerical inundation simulations,

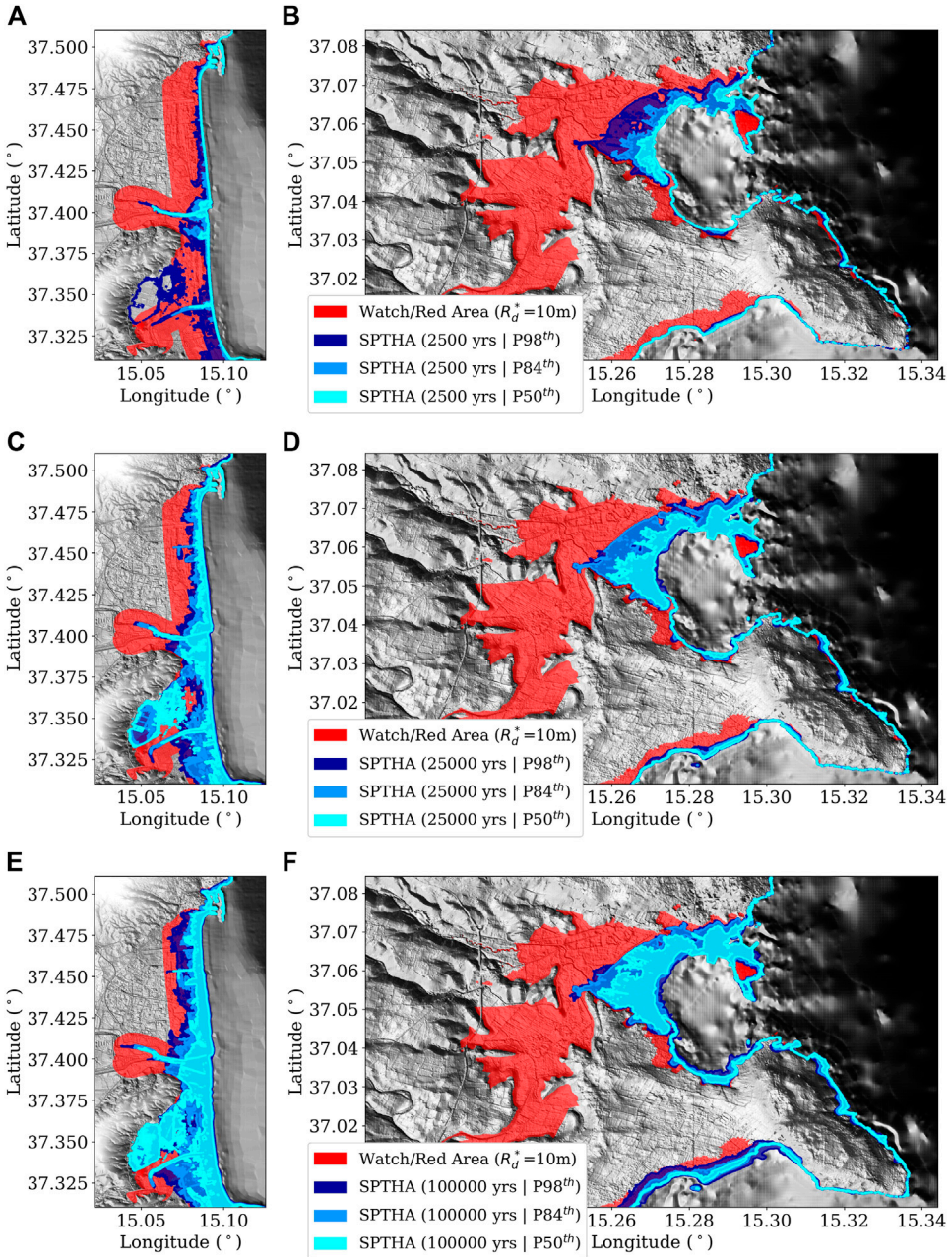

FIGURE 11 | Comparison between the Watch/Red areas designed for R_d^* = 10 m and inundation maps obtained for different SPTHA's percentiles (50th, 84th and 98th) and different ARPs (2,500, 25,000 and 100,000 years in both Catania [panels **(A, C, E)**] and Siracusa [panels **(B, D, F)**].

as discussed at the end of *Inundation Maps From Local High-Resolution NLSW-Based SPTHA for Catania and Siracusa* section. Nevertheless, the development of a robust inclusion of epistemic uncertainty into NLSW-based SPTHA is beyond the scope of this paper. As an alternative, one could also forbear from making detailed simulations, and perform a finer-scale version of the NEAMTHM18 PTHA, with more closely-spaced POIs, to better represent the MIH uncertainty through the higher-resolution amplification factors. Here, as anticipated at the end of *Inundation Maps for the Case-Studies in South-Eastern Sicily* section, and similarly to Scala et al. (2020), we roughly and probably much more conservatively quantify these uncertainties following Davies et al. (2017), such as:

$$P(h,x) = 1 - \Phi\left(\left\{\ln(h) - \left[I(s_i) + \beta\right]/\sigma\right\}\right) \quad (2)$$

where Φ is the cumulative distribution function of a log-normal distribution with mean $[I(s_i) + \beta]$ and standard deviation σ, $I(s_i)$ is the tsunami intensity modeled by the NLSW simulation for the scenario s_i, and β is a logarithmic bias. Based on the tables available in Davies et al. (2017) for four large tsunamis (1960 Chile, 1964 Alaska, 2004 Sumatra, and 2011 Tohoku earthquakes), we chose

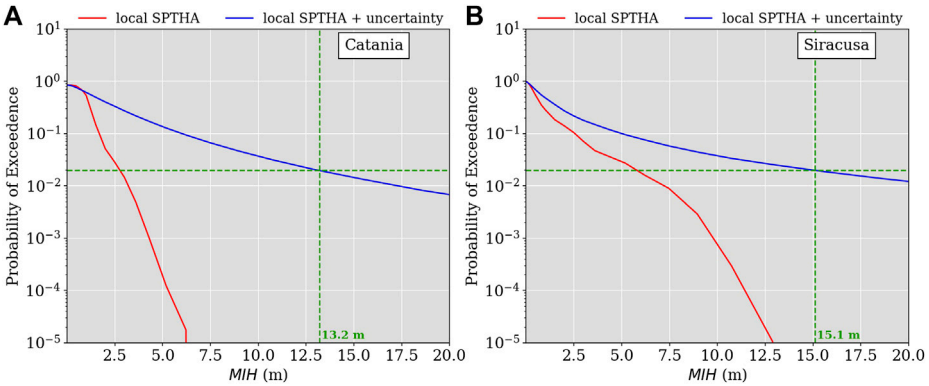

FIGURE 12 | Example of hazard curves calculated on land through the local SPTHA without (red lines) and with (blue lines) the epistemic uncertainty. The selected curves are the ones corresponding to the maximum intensity in Catania (panel **A**, 13.2 m) and Siracusa (panel **B**, 15.1 m) at the ARP equal to 2,500 years (green dashed lines).

conservative values for parameters $\beta = 0.2$ and $\sigma = 1$. This uncertainty has been originally set by comparing modeled intensity and run-up along large portions of coasts, thus it is possibly not ideal for the application to our local case-study; it may also include the contribution from landslide sources for the Alaska 1964 event. We speculate that, if locally calibrated, at least via numerical experiments considering uncertainty in the bathymetry and topography, and with variable bottom friction, the uncertainty on local NLSW simulations is expected to be smaller than that implied by **Eq. 2**. That being said, and in the absence of any other more specific method, we use this approach in the attempt to quantitatively set an upper bound to the model's uncertainty, hence to the extension of the inundation zone. To apply the uncertainty model, we replace the identity functions of **Eq. 1** with the expression in **Eq. 2**. We note that this correction does not affect the areas where each tsunami scenario did not propagate, being the log-normal distribution applicable only to strictly positive values, but it corrects the MIH estimations in the flooded area, for each scenario (**Figure 12**). In other words, adding the log-normal correction to the deterministic simulations cannot extend the inundated area. Thus, to evaluate the consequent inundation zones, we apply an approximated procedure mimicking the one described in *Design of Italian Inundation Maps* and *Inundation Maps for the Case-Studies in South-Eastern Sicily* sections for the determination of the maximum inundation distance, whose input is the design run-up R_d^*, corresponding to the maximum expected run-up in the area. We estimate the maximum calculated inundation heights for the 2,500 years ARP and 84th percentile over all the simulation domain, finding $R_{d,LOC}^* = 13.2$ m and $R_{d,LOC}^* = 15.1$ m in Catania and Siracusa, respectively. Such values occur relatively close to the coast, before coastal dissipation may become important, reflecting the fact that the maximum inundation height above the sea level is greater or equal than the maximum run-up. These numbers are much larger than the ones obtained from the regional SPTHA, that is 3.6 and 6.9 m, respectively, confirming that the overall effect of the uncertainty model is to increase the hazard, as well known in seismic hazard (e.g. Bommer and Abrahamson, 2006), and as already noted by Gibbons et al. (2020). The last version of the inundation maps is obtained from these values, using the simplified attenuation method described in *Design of Italian Inundation Maps* and *Inundation Maps for the Case-Studies in South-Eastern Sicily* sections (**Figure 13**). In a sense, this is a hybrid version, using both the results of the local SPTHA, with the addition of the log-normal uncertainty on each scenario, and the GIS-based attenuation method for the determination of the maximum inundation distance. We observe that the GIS-based inundation line used for planning (red zone in **Figure 13**) is now generally exceeded by the one we obtain with the newly proposed approach (orange zone in **Figure 13**). We argue that the hybrid version provides an upper bound to the uncertainty on the inundation distance, due the conservative parameters we have chosen here for the log-normal. The lower bound for the uncertainty is constituted by the maps obtained with the deterministic NLSW inundation scenarios.

We performed one last experiment, to check how inundation maps based on a worst-case scenario approach would compare with the GIS-based and the hybrid ones we have just introduced by adding uncertainty to the local SPTHA-based maps. We define the worst-case inundation scenario as a composite one from the envelope of all the wet grid points (with wave height >0.01 m), from all the scenarios modeled for the SPTHA, irrespective of the single scenario probability. Even though we have not traced back the scenarios contributing to the maximum inundation distance, we may argue that they are a limited number of relatively high magnitude earthquakes. Actually, such a worst-case corresponds to the SPTHA inundation map for an ARP tending to infinity, which includes all points where a non-identically-zero hazard curve exists (that is exceeding with non-zero probability the threshold of 0.01 m). This composite inundation distance from the envelope of all maximum inundation distances is shown in **Figure 14**, along with the other inundation maps. In the Catania plain, the worst-case inundation distance exceeds all the others with exception of limited zones along the rivers. In Siracusa, the comparison is more complex: in the northern area the worst-case inundation is similar to the extension of the $R_d^* = 10$ m inundation map (in red), whereas, in the middle and southern areas, its extension reaches and, occasionally, exceeds the inundation map corresponding to $R_{d,LOC}^* = 15.1$ m.

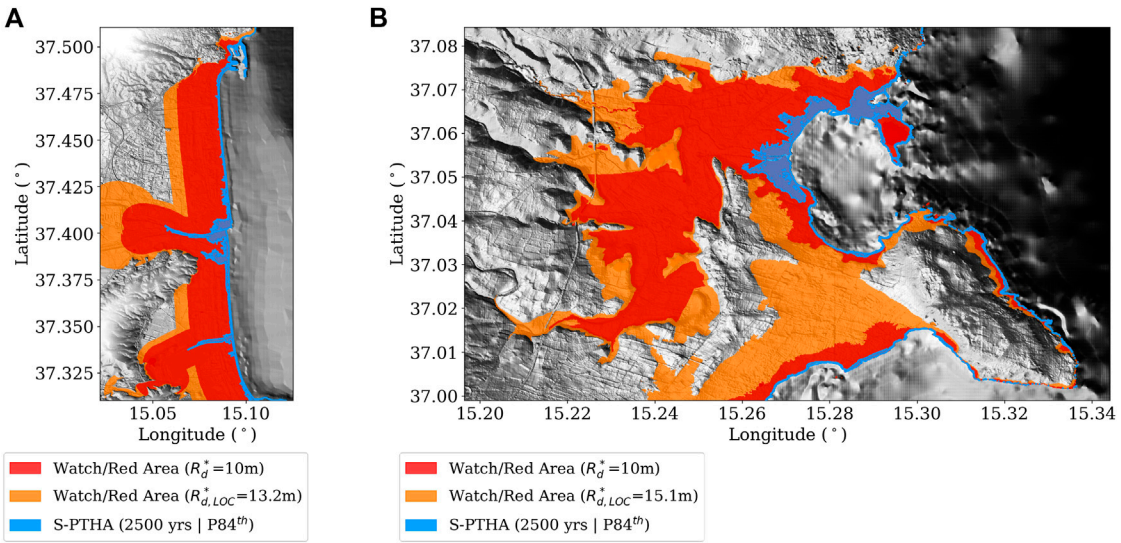

FIGURE 13 | For both Catania [panel **(A)**] and Siracusa [panel **(B)**], the watch/red alert areas designed using the values of R_d^* obtained from the local SPTHA increased with the 20% of uncertainty (orange areas) and the R_d^* = 10 m (red areas) compared to the local SPTHA inundation corresponding to 2,500 years ARP and the 84th percentile (blue areas).

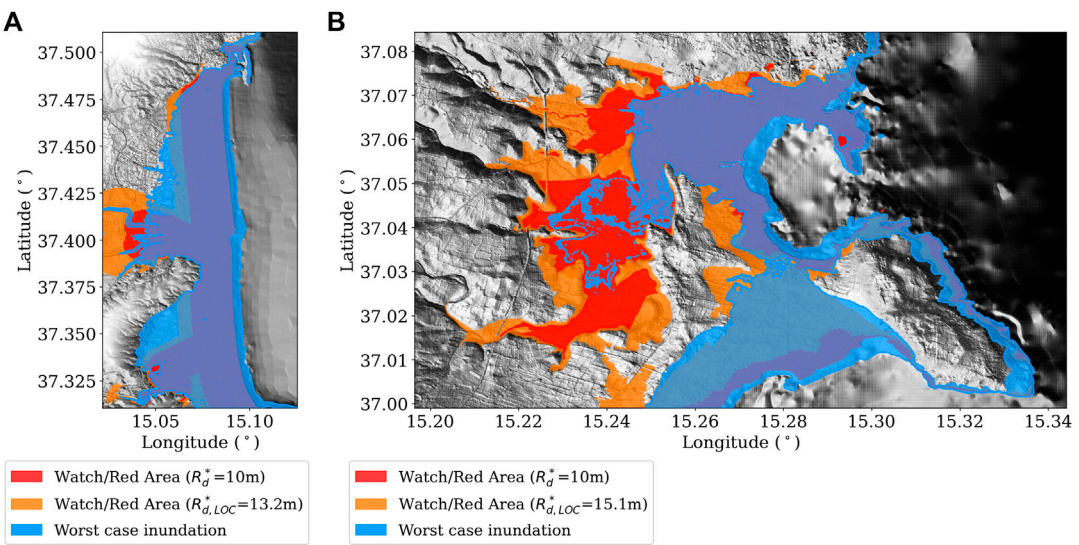

FIGURE 14 | Watch/Red areas designed for R_d^* = 10 m compared to the SPTHA-based inundation maps (with uncertainty) and the worst-case inundation scenario in both Catania [panel **(A)**] and Siracusa [panel **(B)**].

DISCUSSION

The method for designing tsunami evacuation maps for the Italian coasts has been analyzed to understand its limits and advantages, and for addressing to what extent it can be updated through local SPTHA studies. Our findings highlight several important points that should be taken into account for both local high-resolution SPTHA and tsunami coastal and evacuation planning.

The GIS-based method is severely affected by how many secondary riverbeds (depending on their sizes or flow rates) are assumed to be relevant, also when using the same DTM (**Figures 5**, **6**). The impact of less accurate DTM models had, at least in our case-study, a relatively smaller impact on the definition of inundation zones. However, the situation can be different in other cases depending on the extent of the discrepancies between the DTMs, so we cannot generalize this conclusion. It is noted that DTM uncertainty can be significant,

and the treatment can be imposed based on the setting. In PTHA for landslides in Norway for instance, evacuation zones occur on very steep slopes, and here 10 m horizontal distance is added as an additional buffer to the computed hazard zones (e.g., Løvholt et al., 2020). This equals the resolution of the local DTM, and due to the steep slopes, this can involve additional safety factors of the order of 1 m or more.

Regional-SPTHA-informed, GIS-based, inundation maps (defined in *Inundation Maps for the Case-Studies in South-Eastern Sicily* section) were compared with those derived from a local SPTHA using high resolution inundation simulation, in two specific target areas. Two SPTHA models have been used: one without considering epistemic uncertainty specifically associated with numerical inundation simulations (*Inundation Maps From Local High-Resolution NLSW-Based SPTHA for Catania and Siracusa* section), and one, dubbed as "hybrid", which includes a possible maximum estimate of this uncertainty (*Results* section). In a sense, we have defined an "error bar" for the inundation distance related to a given ARP and percentile from local SPTHA. In this way, we are preliminarily exploring the combination of deterministic tsunami modeling with the epistemic uncertainty in tsunami generation, propagation and inundation modeling. We recall that the superposition of uncertainty with deterministic simulations was already considered by some authors, yet in the context of a worst-case scenario approach (Tonini et al., 2011).

Our most important outcome is possibly that the inundation maps resulting from the GIS-based method used for national planning lie within the error bar bound by the NLWS-based model with and without uncertainty treatment. The GIS-based maps overestimated the extension of the inundation zone with respect to the maps obtained from local SPTHA with no uncertainty in the tsunami propagation model. Conversely, they underestimated the extension of the inundation zone when an upper bound of this uncertainty is considered in the hybrid approach.

Another significant outcome is that it results crucial to further characterize these uncertainties to reduce as much as possible this "error bar" or, in more classical terms, to reduce the epistemic uncertainty. Noteworthily, we find that ignoring the epistemic uncertainty of tsunami modeling may have a major impact on local hazard results, potentially producing severe underestimations. Thus, even if local SPTHA studies, in principle, reduce the uncertainty on the definition of local run-up maxima, disregarding completely the related uncertainty may be dangerous. We remark that the parametrization we used is a maximization of the epistemic uncertainty, derived from a global analysis. This highlights two main findings: 1) the important role played by the (usually neglected) uncertainty in tsunami modeling in hazard assessment and, consequently, in the definition of evacuation planning strategies and 2) the need of detailed local analyses based on local data to better calibrate the parametrization of the uncertainties. Nevertheless, it seems that in the absence of more detailed studies, the currently adopted choices for the national planning, which were the outcome of extensive discussions among the decision-makers and different scientific actors at the national level, remain fully justified.

Further considerations on such choices can be certainly made. The use of a regional SPTHA, as main input to determine the value of R_d^*, may be not ideal for local hazard quantifications. Indeed, results of the regional hazard are projected from the 50 m isobath to inland with mainly 1D assumptions and models; thus, any lateral effect (i.e., parallel to the coast) is difficult to be captured. This source of uncertainty was accounted for by using a multiplicative factor set equal to 3, as explained in *Design of Italian Inundation Maps* section. This choice maximizes the level of safety since it roughly represents the 98th percentile of the uncertainty estimated for the amplification factor, with the objective of dealing with local "extreme" run-up values, that is with locally maximum inundation height and maximum run-up variability around the average inundation height. The maximum inundation distance depends also on the local topography and the hydrodynamics, which are not always simply related to expected/design height. This is for example emphasized by the effect of the possible coseismic displacement altering the coastal elevation for near-source coasts, which is not modeled in the regional SPTHA (Volpe et al., 2019). A predominant uplift was in fact observed at least for the Catania use-case (Gibbons et al., 2020), which to some extent limits the inundation probability. Conversely, in case of subsidence in the target area, inundation would be facilitated, worsening the impact inland. Moreover, different slope steepness, for example ranging from cliffs to plains, or different terrain types or different land use in the coastal areas may determine the extent of nonlinearity and dissipation during the inundation. Here, we have only considered the main river streams to differentiate the attenuation rate of tsunami waves inland, and overlooked minor rivers and waterways. The two considered target areas are very different from one another: the target area in the south of Catania is a flat, straight and long plain mainly characterized by beaches, uncovered terrain and few buildings, which is very different from the steep and rocky coast featured with dense urban infrastructures of Siracusa. Better results could be derived by introducing different coastal dissipation factors as a function of the land use and by acquiring high resolution LIDAR data that completely cover the whole potential inundation area. However, the adopted empirical dissipation rule, in combination with the other choices, seems to be quite robust, according to the comparisons we have presented.

A final remark would be that, as a further experiment, a worst-case inundation scenario was produced and compared to the other approaches. This worst-case is based on maximizing the estimated impact, rather than using the biggest earthquake magnitude available. This is similar to the definition of the 2,500-years Tsunami Design Zone in the United States (Wei et al., 2017), based on the PTHA offshore tsunami amplitude at 100 m depth, in which a "super-scenario" is defined according to the maxima of the maxima of all the simulated tsunamis in front of the coast and, then, the corresponding inundation is numerically calculated. As a result of the huge range of scenarios

included in our seismic model, the variability for this SPTHA-based worst-case is more extensively explored than usually done for typical worst-case studies, based on a few earthquakes only. We argue that using such an approach may make sense for some critical infrastructures, yet complementing the worst-case effects by using some information from SPTHA about their ARPs. However, as for local-SPTHA, we note that the uncertainty associated with NLSW simulations is not considered also in the definition of this worst-case. On the other hand, if inundation uncertainty was introduced, the definition of worst-case would become even more difficult (e.g., log-normal are unbounded for large values), which challenges by itself the meaning of a worst-case approach not characterized by probability or ARP ranges. Without this, the meaning of the differences with an SPTHA-based approach may remain unclear.

CONCLUSION AND FUTURE DIRECTIONS

Tsunami evacuation maps designed for the Italian coasts have been evaluated and discussed using the results of a local SPTHA performed in the two target areas of Catania and Siracusa, Sicily, for which it was possible to run high resolution tsunami inundation simulations.

We demonstrated that, in lack of a local and detailed hazard analysis, the proposed procedure to define evacuation areas has a good degree of reliability, since the resulting maps are bound by the "error bar" defined by the outputs obtained from a local SPTHA performed with and without the estimation of its epistemic uncertainty.

The analysis underlines the importance to perform local studies using the proper level of data resolution, whenever available, to best serve specific risk mitigation actions, which may require a thorough site-specific uncertainty quantification. Nevertheless, strategies to improve the input regional assessment, such as using a higher density of POIs and/or a refinement of source parameters, would not only improve the regional analysis itself but also enhance the subsequent local analyses.

Awaiting for future site-specific PTHA studies, our results highlight the importance of quantifying the uncertainties that can affect numerical inundation modeling and are instead usually neglected. Not modeling these uncertainties can introduce important biases in the hazard evaluations. However, we have only scratched the surface here, and a specific definition of an uncertainty framework for tsunami inundation models and the calibration of site-specific SPTHA with local data is still required. A detailed local analysis, with massive simulations to explore the impact of the different assumptions and uncertainties is needed. The ongoing PRACE Project "Local Probabilistic Tsunami Hazard Assessment for HPC - TsuHazAP" (see https://prace-ri.eu/hpc-access/project-access/project-access-awarded-projects/projects-awarded-under-prace-project-access-call-21/) is providing us a framework to start dealing with the above identified issues, and in particular with the sensitivity to local seismic source mechanism discretization, the effects of uncertainty on bathymetry and topography, and treatment of onshore friction.

DATA AVAILABILITY STATEMENT

The raw data supporting the conclusions of this article will be made available by the authors, without undue reservation.

AUTHOR CONTRIBUTIONS

RT, PM, SL, JS, and MV conceived the experiment and prepared the first draft of the manuscript. All the authors contributed to the implementation of the analysis, to revising the article and approved the submitted version.

FUNDING

The work is funded by TSUMAPS-NEAM (grant agreement ECHO/SUB/2015/718568/PREV26), ChEESE Center of Excellence (grant agreement 823844) and benefited of the agreement between Istituto Nazionale di Geofisica e Vulcanologia and the Italian Presidenza del Consiglio dei Ministri, Dipartimento della Protezione Civile (DPC). Computing resources at the Barcelona Supercomputer Center (BSC), Spain, were used under grant AECT-2020-1-0009. Some of the authors benefited also of the project "Assessment of Cascading Events triggered by the Interaction of Natural Hazards and Technological Scenarios involving the release of Hazardous Substances," funded by the Italian Ministry MIUR PRIN (Progetti di Ricerca di Rilevante Interesse Nazionale) 2017—Grant 2017CEYPS8. Optimization and testing of the Tsunami-HySEA computational engine was partly performed using Piz Daint at CSCS (The Swiss National Computer Center) under the PRACE preparatory access N. 2010PA4869. We further acknowledge PRACE for awarding us access to Marconi100 based in Italy at Cineca (Italian National Computer Center) under the project Local Probabilistic Tsunami Hazard Assessment for HPC (TsuHazAP), PRACE award number 2020225386.

ACKNOWLEDGMENTS

This study has benefited from funding provided by the Italian Presidenza del Consiglio dei Ministri, Dipartimento della Protezione Civile (DPC). This paper does not necessarily represent DPC official opinion and policies. The research leading to these results has received funding from the European Union's Horizon 2020 research and innovation programme under the ChEESE project, grant agreement No. 823844. The authors would like to thank all the participants in the SiAM meetings for their insightful contribution to the discussion: Alessandro Amato, Giovanni Arena, Fabrizio Bernardi, Luigi D'Angelo, Maurizio Ferla, Francesco Lalli, Francesco Mariano Mele, Paola Pagliara, Eleonora Pannunzi, Stefano Pintore, Marzia Santini e Antonella Scalzo.

REFERENCES

Aloisi, M., Bruno, V., Cannavò, F., Ferranti, L., Mattia, M., Monaco, C., et al. (2013). Are the source models of the M 7.1 1908 Messina Straits earthquake reliable? Insights from a novel inversion and a sensitivity analysis of levelling data. *Geophys. J. Int.* 192, 1025–1041. doi:10.1093/gji/ggs062

Amato, A. (2020). Some reflections on tsunami Early Warning Systems and their impact, with a look at the NEAMTWS. *BGTA* 61, 403–420. doi:10.4430/bgta0329

Angove, M., Arcas, D., Bailey, R., Carrasco, P., Coetzee, D., Fry, B., et al. (2019). Ocean observations required to minimize uncertainty in global tsunami forecasts, warnings, and emergency response. *Front. Mar. Sci.* 6, 350. doi:10.3389/fmars.2019.00350

ASCE/SEI 7-16 (2017). *Minimum design loads and associated criteria for buildings and other structures*. Reston, Virginia: American Society of Civil Engineers.

Basili, R., Brizuela, B., Herrero, A., Iqbal, S., Lorito, S., Maesano, F. E., et al. (2018). *NEAM tsunami hazard model 2018 (NEAMTHM18): online data of the probabilistic tsunami hazard model for the NEAM region from the TSUMAPS-NEAM project*. Roma: Istituto Nazionale Di Geofisica E Vulcanologia.

Basili, R., Brizuela, B., Herrero, A., Iqbal, S., Lorito, S., Maesano, F. E., et al. (2019). NEAMTHM18 documentation: the making of the TSUMAPS-NEAM tsunami hazard model 2018. Roma: . Istituto Nazionale di Geofisica e Vulcanologia (INGV). doi:10.5281/Q20zenodo.3406625

Basili, R., Brizuela, B., Herrero, A., Iqbal, S., Lorito, S., Maesano, F. E., et al. (2021). The making of the NEAM tsunami hazard model 2018 (NEAMTHM18). *Front. Earth Sci.* 8, 616594. doi:10.3389/feart.2020.616594

Behrens, J., and Dias, F. (2015). New computational methods in tsunami science. *Phil. Trans. R. Soc. A* 373 (2053), 20140382

Bernard, E., and Titov, V. (2015). Evolution of tsunami warning systems and products. *Philos. Trans. R. Soc. Math. Phys. Eng. Sci.* 373, 20140371. doi:10.1098/rsta.2014.0371

Bernardi, F., Lomax, A., Michelini, A., Lauciani, V., Piatanesi, A., and Lorito, S. (2015). Appraising the early-est earthquake monitoring system for tsunami alerting at the Italian candidate tsunami service provider. *Nat. Hazards Earth Syst. Sci.* 15, 2019–2036. doi:10.5194/nhess-15-2019-2015

Billi, A., Minelli, L., Orecchio, B., and Presti, D. (2010). Constraints to the cause of three historical tsunamis (1908, 1783, and 1693) in the messina straits region, sicily, southern Italy. *Seismol. Res. Lett.* 81, 907–915. doi:10.1785/gssrl.81.6.907

Bommer, J. J., and Abrahamson, N. A. (2006). Why do modern probabilistic seismic-hazard analyses often lead to increased hazard estimates? *Bull. Seismol. Soc. Am.* 96, 1967–1977. doi:10.1785/0120060043

Chock, G., Yu, G., Thio, H. K., and Lynett, P. J. (2016). Target structural reliability analysis for tsunami hydrodynamic loads of the ASCE 7 standard. *J. Struct. Eng.* 142, 04016092. doi:10.1061/(ASCE)ST.1943-541X.0001499

Convertito, V., and Pino, N. A. (2014). Discriminating among distinct source models of the 1908 Messina Straits earthquake by modelling intensity data through full wavefield seismograms. *Geophys. J. Int.* 198, 164–173. doi:10.1093/gji/ggu128

Davies, G., Griffin, J., Løvholt, F., Glimsdal, S., Harbitz, C., Thio, H. K., et al. (2017). A global probabilistic tsunami hazard assessment from earthquake sources. *Geol. Soc. Lond. Spec. Publ.* 456, 219–244. doi:10.1144/SP456.5

de la Asunción, M., Castro, M. J., Fernández-Nieto, E. D., Mantas, J. M., Acosta, S. O., and González-Vida, J. M. (2013). Efficient GPU implementation of a two waves TVD-WAF method for the two-dimensional one layer shallow water system on structured meshes. *Comput. Fluids* 80, 441–452. doi:10.1016/j.compfluid.2012.01.012

De Martini, P. M., Barbano, M. S., Pantosti, D., Smedile, A., Pirrotta, C., Del Carlo, P., et al. (2012). Geological evidence for paleotsunamis along eastern Sicily (Italy): an overview. *Nat. Hazards Earth Syst. Sci.* 12, 2569–2580. doi:10.5194/nhess-12-2569-2012

Dipartimento della Protezione Civile (2018). Presidenza del Consiglio dei Ministri - Dipartimento della Protezione Civile - decreto 2 ottobre 2018. Indicazioni alle Componenti ed alle Strutture operative del Servizio nazionale di protezione civile per l'aggiornamento delle pianificazioni di protezione civile per il rischio maremoto, (18A07309) (GU Serie Generale n.266 del 15-11-2018). Available at: http://www.protezionecivile.gov.it/amministrazione-trasparente/provvedimenti/dettaglio/-/asset_publisher/default/content/indicazioni-alle-componenti-ed-alle-strutture-operative-del-servizio-nazionale-di-protezione-civile-per-l-aggiornamento-delle-pianificazioni-di-prot-1 (Accessed November 15, 2018).

DPCM (2017). Direttiva Del Presidente Del Consiglio Dei Ministri 17 febbraio 2017 Istituzione del Sistema d'Allertamento nazionale per i Maremoti generati da sisma - SiAM. (17A03755) (GU Serie Generale n.128 del 05-06-2017). Available at: http://www.gazzettaufficiale.it/atto/serie_generale/caricaDettaglioAtto/originario?atto.dataPubblicazioneGazzetta=2017-06-05&atto.codiceRedazionale=17A03755 (Accessed June 05, 2017).

EMODnet Bathymetry Consortium (2018). EMODnet digital bathymetry (DTM 2018). doi:10.12770/18FF0D48-B203-4A65-94A9-5FD8B0EC35F6

Favalli, M., Boschi, E., Mazzarini, F., and Pareschi, M. T. (2009). Seismic and landslide source of the 1908 straits of messina tsunami (sicily, Italy). *Geophys. Res. Lett.* 36, 16304. doi:10.1029/2009GL039135

Fraser, S., and Power, W. L. (2013). *Validation of a GIS-based attenuation rule for indicative tsunami evacuation zone mapping*. Lower Hutt, New Zealand: GNS Science Reports, 2.

Geist, E., and Lynett, P. (2014). Source processes for the probabilistic assessment of tsunami hazards. *Oceanography* 27, 86–93. doi:10.5670/oceanog.2014.43

Gerardi, F., Barbano, M. S., Martini, P. M. D., and Pantosti, D. (2008). Discrimination of tsunami sources (earthquake versus landslide) on the basis of historical data in eastern sicily and southern CalabriaDiscrimination of tsunami sources on the basis of historical data in eastern sicily/southern Calabria. *Bull. Seismol. Soc. Am.* 98, 2795–2805. doi:10.1785/0120070192

Gibbons, S. J., Lorito, S., Macías, J., Løvholt, F., Selva, J., Volpe, M., et al. (2020). Probabilistic tsunami hazard analysis: high performance computing for massive scale inundation simulations. *Front. Earth Sci.* 8, 591549. doi:10.3389/feart.2020.591549

Glimsdal, S., Løvholt, F., Harbitz, C. B., Romano, F., Lorito, S., Orefice, S., et al. (2019). A new approximate method for quantifying tsunami maximum inundation height probability. *Pure Appl. Geophys.* 176, 3227–3246. doi:10.1007/s00024-019-02091-w

González, F. I., Geist, E. L., Jaffe, B., Kânoğlu, U., Mofjeld, H., Synolakis, C. E., et al. (2009). Probabilistic tsunami hazard assessment at Seaside, Oregon, for near- and far-field seismic sources. *J. Geophys. Res.* 114, C11023. doi:10.1029/2008JC005132

Grezio, A., Babeyko, A., Baptista, M. A., Behrens, J., Costa, A., Davies, G., et al. (2017). Probabilistic tsunami hazard analysis: multiple sources and global applications. *Rev. Geophys.* 55, 1158–1198. doi:10.1002/2017RG000579

Grezio, A., Cinti, F. R., Costa, A., Faenza, L., Perfetti, P., Pierdominici, S., et al. (2020). Multisource bayesian probabilistic tsunami hazard analysis for the gulf of naples (Italy). *J. Geophys. Res. Oceans* 125, e2019JC015373. doi:10.1029/2019JC015373

Griffin, J., Latief, H., Kongko, W., Harig, S., Horspool, N., Hanung, R., et al. (2015). An evaluation of onshore digital elevation models for modeling tsunami inundation zones. *Front. Earth Sci.* 3, 32. doi:10.3389/feart.2015.00032

Gutscher, M.-A., Roger, J., Baptista, M. A., Miranda, J. M., and Tinti, S. (2006). Source of the 1693 Catania earthquake and tsunami (southern Italy): new evidence from tsunami modeling of a locked subduction fault plane. *Geophys. Res. Lett.* 33, L08309. doi:10.1029/2005GL025442

Kaiser, G., Scheele, L., Kortenhaus, A., Løvholt, F., Römer, H., and Leschka, S. (2011). The influence of land cover roughness on the results of high resolution tsunami inundation modeling. *Nat. Hazards Earth Syst. Sci.* 11, 2521–2540. doi:10.5194/nhess-11-2521-2011

Leonard, G. S., Power, W. L., Lukovic, B., Smith, W. D., Langridge, R. M., Johnston, D. M., et al. (2008). *Interim tsunami evacuation planning zone boundary mapping for the Wellington and Horizons regions defined by a GIS-calculated attenuation rule*. Lower Hutt, New Zealand: GNS Science Reports, 30.

Lorito, S., Selva, J., Basili, R., Romano, F., Tiberti, M. M., and Piatanesi, A. (2015). Probabilistic hazard for seismically induced tsunamis: accuracy and feasibility of inundation maps. *Geophys. J. Int.* 200, 574–588. doi:10.1093/gji/ggu408

Løvholt, F., Glimsdal, S., and Harbitz, C. B. (2020). On the landslide tsunami uncertainty and hazard. *Landslides* 17, 2301–2315. doi:10.1007/s10346-020-01429-z

Løvholt, F., Glimsdal, S., Harbitz, C. B., Zamora, N., Nadim, F., Peduzzi, P., et al. (2012). Tsunami hazard and exposure on the global scale. *Earth Sci. Rev.* 110, 58–73. doi:10.1016/j.earscirev.2011.10.002

Luco, N., Ellingwood, B. R., Hamburger, R. O., Hooper, J. D., Kimball, J. K., and Kircher, C. A. (2007). Risk-targeted versus current seismic design maps for the conterminous United States. Available at: https://pubs.er.usgs.gov/publication/70045059 (Accessed November 7, 2020).

Macías, J., Castro, M. J., and Escalante, C. (2020a). Performance assessment of the Tsunami-HySEA model for NTHMP tsunami currents benchmarking. Laboratory data. *Coast. Eng.* 158, 103667. doi:10.1016/j.coastaleng.2020.103667

Macías, J., Castro, M. J., Ortega, S., and González-Vida, J. M. (2020b). Performance assessment of Tsunami-HySEA model for NTHMP tsunami currents benchmarking. Field cases. *Ocean Model.* 152, 101645. doi:10.1016/j.ocemod.2020.101645

Macías, J., Castro, M. J., Ortega, S., Escalante, C., and González-Vida, J. M. (2017). Performance benchmarking of tsunami-HySEA model for NTHMP's inundation mapping activities. *Pure Appl. Geophys.* 174, 3147–3183. doi:10.1007/s00024-017-1583-1

Macías, J., Mercado, A., González-Vida, J. M., Ortega, S., and Castro, M. J. (2016). Comparison and computational performance of tsunami-HySEA and MOST models for LANTEX 2013 scenario: impact assessment on Puerto Rico coasts. *Pure Appl. Geophys.* 173, 3973–3997. doi:10.1007/s00024-016-1387-8

Maramai, A., Brizuela, B., and Graziani, L. (2014). The euro-mediterranean tsunami catalogue. *Ann. Geophys.* 57, 0435. doi:10.4401/ag-6437

Maramai, A., Graziani, L., and Brizuela Reyes, B. (2019). Italian Tsunami Effects Database (ITED): the first database of tsunami effects observed along the Italian coasts. Available at: https://ingv.maps.arcgis.com/apps/webappviewer/index.html?id=a14231712588470ea1c4454301b8294c&showLayers=ITED_Observation_Points_OP_ (Accessed September 30, 2020).

MCDEM (2016). *Tsunami evacuation zones. Director's guideline for Civil defence emergency management groups*. New Zealand: Published by the Ministry of Civil Defence & Emergency Management.

Meschis, M., Roberts, G. P., Mildon, Z. K., Robertson, J., Michetti, A. M., and Faure Walker, J. P. (2019). Slip on a mapped normal fault for the 28 th December 1908 Messina earthquake (Mw 7.1) in Italy. *Sci. Rep.* 9, 6481. doi:10.1038/s41598-019-42915-2

Molinari, I., Tonini, R., Lorito, S., Piatanesi, A., Romano, F., Melini, D., et al. (2016). Fast evaluation of tsunami scenarios: uncertainty assessment for a Mediterranean Sea database. *Nat. Hazards Earth Syst. Sci.* 16, 2593–2602. doi:10.5194/nhess-16-2593-2016

Mulia, I. E., and Satake, K. (2020). Developments of tsunami observing systems in Japan. *Front. Earth Sci.* 8, 145. doi:10.3389/feart.2020.00145

NTC (2018). Norme Tecniche per le Costruzioni 2018. Aggiornamento delle "Norme tecniche per le costruzioni". Gazzetta Ufficiale Serie Generale n.42 del 20-02-2018 - suppl. Ordinario n. 8. Italian Building Code (in Italian). Available at: https://www.gazzettaufficiale.it/eli/id/2018/2/20/18A00716/sg/pdf (Accessed September 30, 2020).

Okada, Y. (1992). Internal deformation due to shear and tensile faults in a half-space. *Bull. Seismol. Soc. Am.* 82, 1018–1040.

Piatanesi, A., and Tinti, S. (1998). A revision of the 1693 eastern Sicily earthquake and tsunami. *J. Geophys. Res. Solid Earth* 103, 2749–2758. doi:10.1029/97JB03403

Pino, N. A., Piatanesi, A., Valensise, G., and Boschi, E. (2009). The 28 december 1908 messina straits earthquake (MW 7.1): a great earthquake throughout a century of seismology. *Seismol. Res. Lett.* 80, 243–259. doi:10.1785/gssrl.80.2.243

Polonia, A., Nelson, C. H., Romano, S., Vaiani, S. C., Colizza, E., Gasparotto, G., et al. (2017). A depositional model for seismo-turbidites in confined basins based on Ionian Sea deposits. *Mar. Geol.* 384, 177–198. doi:10.1016/j.margeo.2016.05.010

Ridente, D., Martorelli, E., Bosman, A., and Chiocci, F. L. (2014). High-resolution morpho-bathymetric imaging of the Messina Strait (Southern Italy). New insights on the 1908 earthquake and tsunami. *Geomorphology* 208, 149–159. doi:10.1016/j.geomorph.2013.11.021

Sarri, A., Guillas, S., and Dias, F. (2012). Statistical emulation of a tsunami model for sensitivity analysis and uncertainty quantification. *Nat. Hazards Earth Syst. Sci.* 12, 2003–2018. doi:10.5194/nhess-12-2003-2012

Scala, A., Lorito, S., Romano, F., Murphy, S., Selva, J., Basili, R., et al. (2020). Effect of shallow slip amplification uncertainty on probabilistic tsunami hazard analysis in subduction zones: use of long-term balanced stochastic slip models. *Pure Appl. Geophys.* 177, 1497–1520. doi:10.1007/s00024-019-02260-x

Selva, J., Tonini, R., Molinari, I., Tiberti, M. M., Romano, F., Grezio, A., et al. (2016). Quantification of source uncertainties in seismic probabilistic tsunami hazard analysis (SPTHA). *Geophys. J. Int.* 205, 1780–1803. doi:10.1093/gji/ggw107

Song, J., and Goda, K. (2019). Influence of elevation data resolution on tsunami loss estimation and insurance rate-making. *Front. Earth Sci.* 7, 19. doi:10.3389/feart.2019.00246

Taroni, M., and Selva, J. (2020). GR_EST: an OCTAVE/MATLAB toolbox to estimate Gutenberg–Richter law parameters and their uncertainties. *Seismol. Res. Lett.* 92, 508–516. doi:10.1785/0220200028

Tonini, R., Armigliato, A., Pagnoni, G., Zaniboni, F., and Tinti, S. (2011). Tsunami hazard for the city of Catania, eastern sicily, Italy, assessed by means of worst-case credible tsunami scenario analysis (WCTSA). *Nat. Hazards Earth Syst. Sci.* 11, 1217–1232. doi:10.5194/nhess-11-1217-2011

Tonini, R., Basili, R., Maesano, F. E., Tiberti, M. M., Lorito, S., Romano, F., et al. (2020). Importance of earthquake rupture geometry on tsunami modelling: the Calabrian Arc subduction interface (Italy) case study. *Geophys. J. Int.* 223, 1805–1819. doi:10.1093/gji/ggaa409

Volpe, M., Lorito, S., Selva, J., Tonini, R., Romano, F., and Brizuela, B. (2019). From regional to local SPTHA: efficient computation of probabilistic tsunami inundation maps addressing near-field sources. *Nat. Hazards Earth Syst. Sci.* 19, 455–469. doi:10.5194/nhess-19-455-2019

Wei, Y., Thio, H. K., Titov, V., Chock, G., Zhou, H., Tang, L., et al. (2017). "Inundation modeling to create 2,500-year return period tsunami design zone maps for the asce 7-16 standard," in 16th World Conference on Earthquake Engineering, 16WCEE 2017, Santiago, CL, January 9–13, 2017, 10.

Williamson, A. L., Rim, D., Adams, L. M., LeVeque, R. J., Melgar, D., and González, F. I. (2020). A source clustering approach for efficient inundation modeling and regional scale probabilistic tsunami hazard assessment. *Front. Earth Sci.* 8, 591663. doi:10.3389/feart.2020.591663

Wright, K. C., Beavan, R. J., Daly, M. C., Gale, N. H., Leonard, G. S., Lukovic, B., et al. (2011). *Filling a critical gap in end-to-end tsunami warning in the Southwest Pacific: a pilot project in Samoa to create scientifically robust, community-based evacuation maps*. Lower Hutt, New Zealand: GNS Science. [GNS Science report. 2011/53 2 v]. CrossRef Full Text

Conflict of Interest: SG, SG and FL were employed by the company Norwegian Geotechnical Institute.

The remaining authors declare that the research was conducted in the absence of any commercial or financial relationships that could be construed as a potential conflict of interest.

frontiers in Earth Science

BRIEF RESEARCH REPORT
published: 18 March 2021
doi: 10.3389/feart.2021.596044

Italian Tsunami Effects Database (ITED): The First Database of Tsunami Effects Observed Along the Italian Coasts

Alessandra Maramai, Laura Graziani and Beatriz Brizuela*

Istituto Nazionale di Geofisica e Vulcanologia, Rome, Italy

Traditional tsunami catalogues are conceived as a collection of tsunamis classified by the generating cause, providing a general description of the effects observed for each tsunami. Those catalogues, even if they provide fundamental information, are not suitable for producing an exhaustive picture of the geographical distribution of the tsunami effects. In this paper we introduce the new Italian Tsunami Effects Database (ITED), a collection of evidence documenting the effects along the Italian coasts from historical times to present. The database comes forth the Euro-Mediterranean Tsunami Catalogue (EMTC) and focusses on the effects of tsunamis observed along the Italian coasts providing descriptive and quantitative information for each OP. The information reported in ITED does not only concern the effects produced by Italian tsunamis, but also those effects produced by tsunamis originated outside the Italian territory. ITED contains 318 OPs, related to 73 Italian tsunamis and to four tsunamis which occurred outside Italy. The database can be accessed through a WebApp that displays for each OP the description of effects, quantitative data (run-up, inundation, withdrawal, etc.) and tsunami intensity with the corresponding bibliographic references. The database also provides the tsunami intensity distribution along time (*tsunami-history*) for each site, allowing the end user to know how a place has been affected by tsunamis over the time. The information contained in ITED makes this database a useful tool to understand how tsunamis have affected the Italian territory and emphasizes the importance of studying the tsunami hazard along the Italian coasts.

Keywords: tsunami, tsunami effects, historical tsunami, Italian coasts, tsunami intensity, tsunami history, tsunami hazard

OPEN ACCESS

Edited by:
Tiziana Rossetto,
University College London,
United Kingdom

Reviewed by:
Raffaele De Risi,
University of Bristol, United Kingdom
Alison Raby,
University of Plymouth,
United Kingdom

****Correspondence:***
Alessandra Maramai
alessandra.maramai@ingv.it

Specialty section:
This article was submitted to Geohazards and Georisks, a section of the journal Frontiers in Earth Science

Received: *18 August 2020*
Accepted: *16 February 2021*
Published: *18 March 2021*

Citation:
Maramai A, Graziani L and Brizuela B (2021) Italian Tsunami Effects Database (ITED): The First Database of Tsunami Effects Observed Along the Italian Coasts. Front. Earth Sci. 9:596044. doi: 10.3389/feart.2021.596044

INTRODUCTION

Tsunami catalogues can contribute to identify the geographical areas that have experienced these kind of events, which can be a starting point for hazard and risk assessments. In addition, the data contained in such catalogues is also essential to validate those assessments. These catalogues can also help to increase public awareness contributing, in some ways, to reduce the impact of tsunamis. In the last decades, the growing interest in focusing on tsunami studies in the European region led to the compilation of the Euro-Mediterranean Tsunamis Catalogue (EMTC, Maramai et al., 2014), a collection of 290 tsunamis generated in the European and Mediterranean seas from 6150 B.C. to 2014, classified by the generating cause (earthquakes, volcanic activity, landslides) and providing parameters and information on the tsunamis as a whole.

According to EMTC, the Italian coast was struck by 71 tsunamis from 79 A.D. to 2002, placing Italy as one of the Euro-Mediterranean countries most prone to tsunami threat, as confirmed also by the probabilistic tsunami hazard assessment (PTHA) recently performed for the Euro-Mediterranean region (Basili et al., 2021). Regarding the triggering cause, the Italian tsunamis contained in EMTC are mostly generated by moderate magnitude earthquakes that occurred offshore or inland close to the coastline, nevertheless volcanic activity plays a significant role in tsunami generation, particularly Stromboli (Aeolian Islands) and Vesuvius volcanoes have triggered around ten tsunamis, mostly with local effects. The majority of the EMTC Italian tsunamis are ranked as high quality, being well documented. The quality of each event is given by the *reliability*, an index ranging from 0 (very improbable tsunami) to 4 (definite tsunami) (Tinti et al., 2004). According to the Sieberg-Ambraseys scale (Ambraseys, 1962), based on the effects observed along the coasts, most of the Italian tsunamis (about 75%) can be classified from low to rather strong intensity events, the rest caused severe damage and victims being assessed as high intensity events.

The existing tsunami catalogues currently available are based on the generating source (i.e., De Lange and Healy, 1986; Papadopoulos et al., 2000; Soloviev et al., 2000; Baptista and Miranda, 2009), listing its parameters and providing a general description of the effects observed. Even if they contain fundamental information, presenting this information only in a descriptive manner, do not allow an effective use of the data, as they do not provide a complete picture of the geographical distribution of the tsunami effects. In fact, the user can get a general overview of the effects produced by the tsunami but cannot easily get an idea of how the tsunami affected the different stretches of coast. Accurate information on the effects of tsunamis in terms of run-up and flooding values, could be a valuable resource for validating and tuning the inundation models used to assess tsunami risk (Kaiser et al., 2011). Considering the aforementioned gaps, based on the EMTC, a new database was compiled (ITED-Italian Tsunami Effects Database), starting from the general descriptions of the tsunamis that impacted Italy available in EMTC and focussing the attention on the sites interested by those tsunamis. ITED is an ancillary database and provides georeferred and detailed documented information on the effects (such as run-up, flooding, sea withdrawal, evidence of inundation, transport of sediment or objects on the coast, number of observed waves, tidal records, damage, casualties). The two databases, ITED and EMTC, are entirely interconnected and their information, available either as pop up display or tables, can be consulted and downloaded through a GIS WebApp (https://tsunamiarchive.ingv.it/ited.1.0/) that allows the user to switch from one database to another.

As described in Maramai et al. (2014), most of the data contained in EMTC has been assigned with high reliability value that was then transmitted to ITED. This characteristic makes ITED a tool that can provide a fundamental contribution to understand how tsunamis have affected the Italian territory and the importance of studying the tsunami hazard along the Italian coasts. Great effort has been made to extrapolate as much quantitative data as possible, arranging them in tabular form and allowing the user to easily download them.

MATERIALS

Italian Tsunami Effects Database (ITED) Characteristics and EMTC2.0

The Italian Tsunami Effect Database (ITED) has been compiled by selecting and analyzing the information already available in the portion of the EMTC dataset related to the Italian tsunamis, aiming to enhance the usability of the data.

Pointing to include on ITED new information on the effects observed at different locations an accurate research and analysis of the recent studies available in literature regarding Italian events was performed. Cross-checking with the recently published Catalogue of Strong Earthquakes in Italy (CFTI5Med, Guidoboni et al., 2018) was also carried out to produce a database as complete as possible.

The Italian tsunamis of seismic origin currently on ITED have been linked to the Parametric Catalogue of Italian Earthquakes (CPTI15, Rovida et al., 2016), adopted as the reference earthquake catalogue. This choice led to reappraise some Italian events that in EMTC had been classified with an unreliable seismic cause and to achieve the interoperability with CPTI15.

This process enabled to update also the Italian tsunamis in the EMTC, giving rise to the release of a new version, EMTC2.0. Compared to the old version, EMTC2.0 has undergone several changes. Additional information has enriched the knowledge on the tsunamis in the catalogue requiring leading to the revaluation of some parameters, such as reliability, intensity, generating cause, etc. Due to these relevant amendments, 63 Italian events were updated with respect to EMTC. The number of records has been increased since two events, not analysed in the first version, have been appended, namely the December 10, 1542 (Eastern Sicily) and the December 23, 1690 (Central Adriatic). The first one was triggered by a destructive earthquake (M = 6.7, Rovida et al., 2016) occurred during a seismic sequence in Southeastern Sicily, causing the destruction of some villages. Coeval sources referred that "*... after the shock the city of Augusta was almost submerged by the sea and many people were drowned*" (Guidoboni et al., 2018). As far as the 1690 event is concerned, a severe earthquake (M = 5.6, Rovida et al., 2016) hit the Central Adriatic region causing victims and severe damage at Ancona and in some neighboring villages. According to the coeval source Bonito (1691), "*in the beach of Ancona the boats touched the sea bottom and then they lifted up being shaken due to the sea water agitation.*"

ITED provides details on the effects of tsunamis observed/measured at several Observation Points (OP) that are geographically identifiable. When OPs cannot be exactly geo-localized, they are associated to toponymal coordinates of the nearest known locality, hereafter called Place Names (PNs),

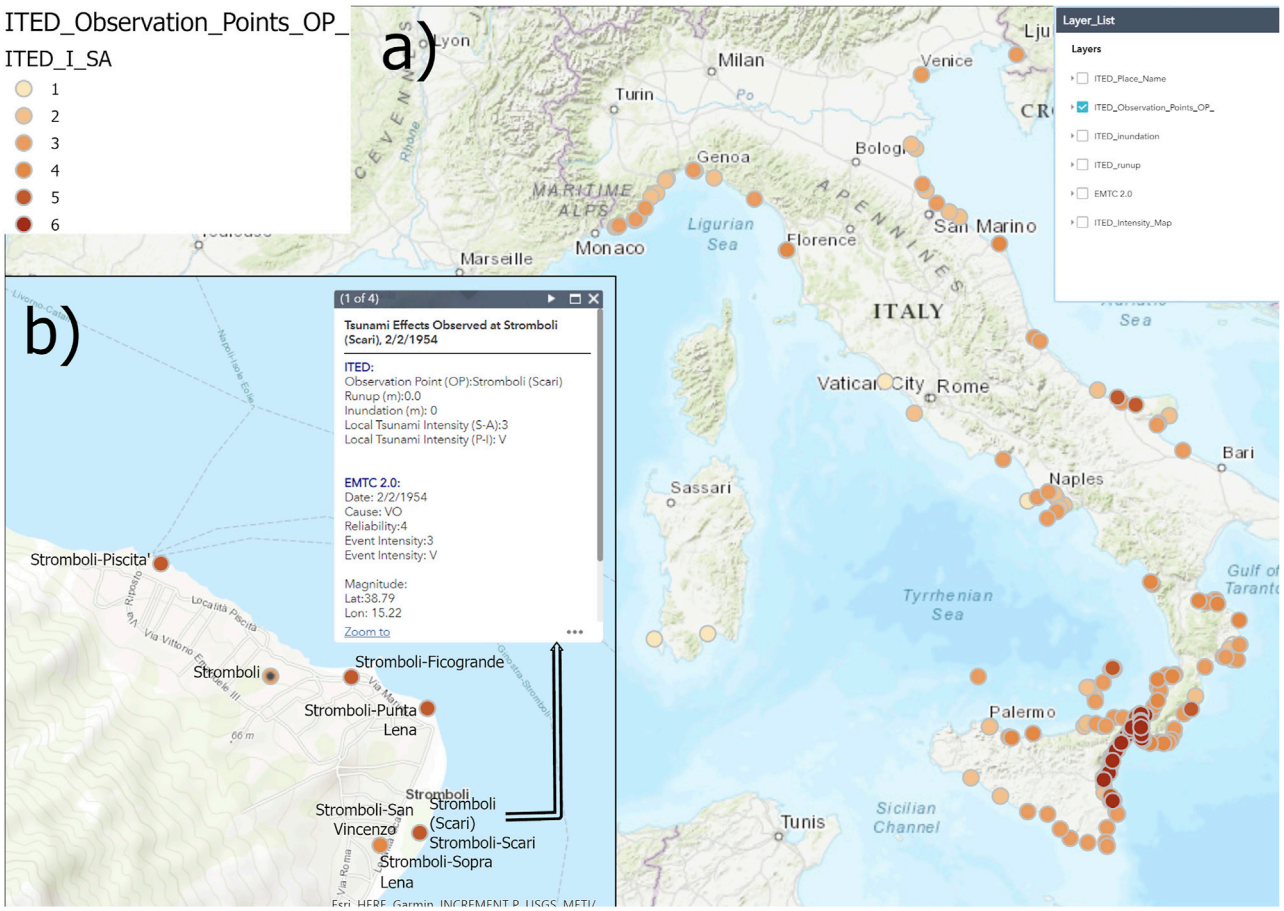

FIGURE 1 | (A) Screenshot of the WebApp layer ITED_Obervation_Point. The complete Layer list is also shown. **(B)** Stromboli Island: the black dot indicates the PN (Stromboli-San Vincenzo), whereas the brown dots indicate all the nearby OPs, colored according to local tsunami intensity. By clicking on the OP a pop-up allow the user to get details about the tsunami effects at that point (Service Layer Credits: sources: ©Esri, HERE, Garmin, Intermap, increment P Corp., GEBCO, USGS, FAO, NPS, NOAA, NRCAN, GeoBase, IGN, Kadaster NL, Ordnance Survey, Esri Japan, METI, NASA, Esri China (Hong Kong), ©swisstopo, ©OpenStreetMap contributors 2019. Distributed under a Creative Commons BY-SA License).

contained in the INGV internal Gazetteer, which is the unified geographical reference system for macroseismic observations of the Italian Macroseismic Database (DBMI, Locati et al., 2016). When the descriptions of effects were very detailed, it was possible to identify more observation points (OPs) related to the same PN. Currently, ITED contains 318 OPs at 189 PNs, providing quantitative and descriptive information.

For each OP the description of the tsunami effects found in literature, accompanied by the corresponding bibliographic references, can be accessed through a pop-up window, where quantitative data (run-up, inundation, withdrawal, etc. as shown in **Figure 1**) are also displayed. On the basis of the description, the estimated intensity of the phenomenon (local intensity) has been assigned to each point, assessed according to both the Sieberg-Ambraseys and the Papadopoulos-Imamura (Papadopoulos and Imamura, 2001) scales. These data populate an attribute table that can be retrieved by querying the database.

Figure 1A shows the main screen of the ITED WebApp, displaying the geographical distribution of the 318 OPs, coloured according to their local intensity value. In **Figure 1B** the example of Stromboli Island (Aeolian Islands) OPs are coloured according to the local intensity value while PN are represented by black dots.

ITED allows the user to view the intensity map for each tsunami, i.e., to view all the OPs related to a single tsunami event, with their local intensity. The December 28, 1908 Messina tsunami is by far the most documented event in Italy having 119 OPs along the Italian coasts. The information mostly comes from the reports of Platania (1909) and Baratta (1910) that soon after the event performed, independently, detailed surveys along Sicily and Calabria coasts. The 1908 tsunami spread over a few hundred kilometers reaching the island of Malta to the South (about 250 km away) with a sea level rise of more than 1 m causing slight damage. Northernmost, the event was recorded at the tide gauge of Civitavecchia, located about 450 km away. In **Figure 2A** the snapshot of ITED WebApp showing the intensity map for the 1908 Messina tsunami is visible.

As far as run-up values are concerned, in ITED there are 91 OPs for which a run-up value is specified: 7 OPs show values

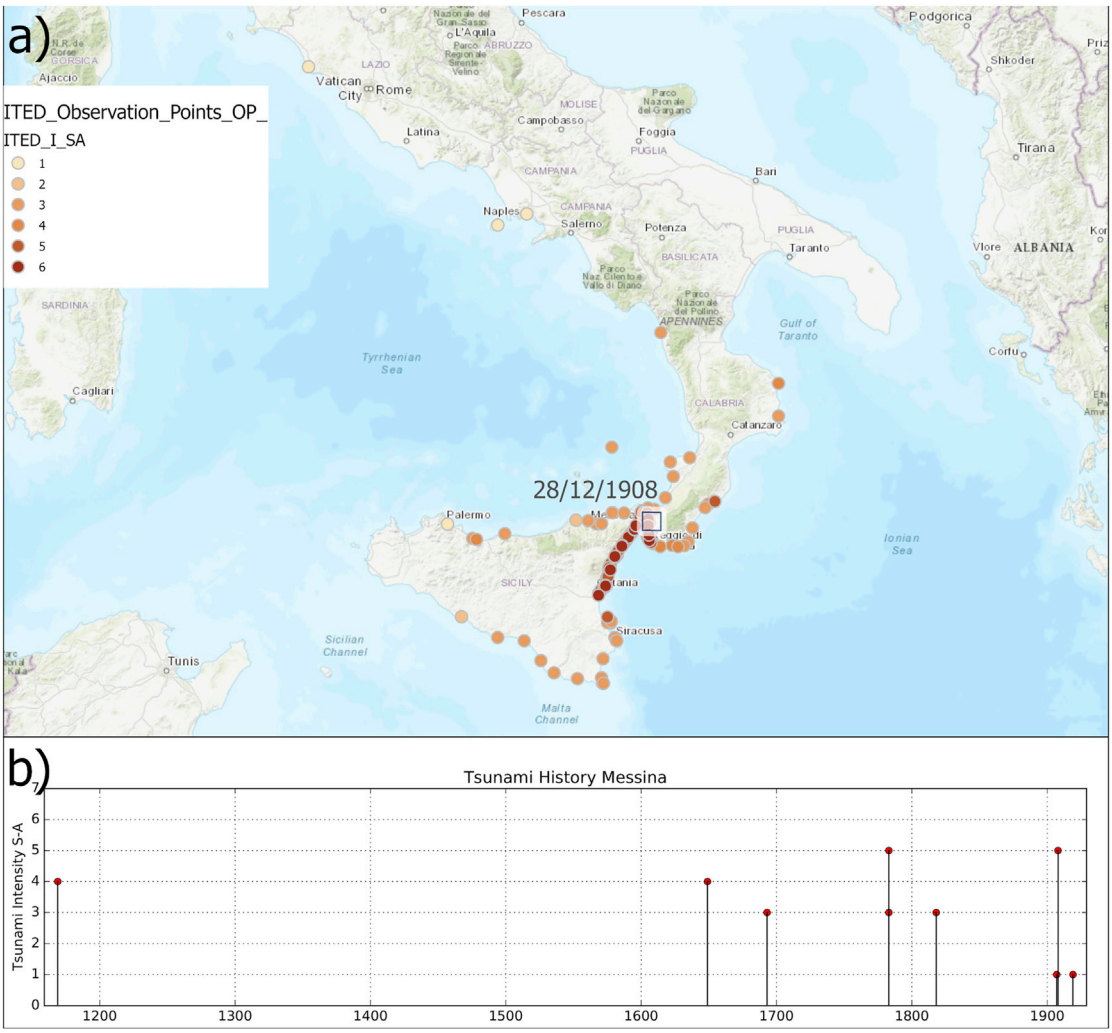

FIGURE 2 | (A) Snapshot of the OPs where the 1908 tsunami was observed, OPs symbols are colored according to the local tsunami intensity (Service Layer Credits: sources: ©Esri, HERE, Garmin, Intermap, increment P Corp., GEBCO, USGS, FAO, NOAA, NPS, NRCAN, GeoBase, IGN, Kadaster NL, Ordnance Survey, Esri Japan, METI, NASA, Esri China (Hong Kong), ©swisstopo, ©OpenStreetMap contributors 2019. Distributed under a Creative Commons BY-SA License). **(B)** Example of tsunami history contained in ITED: Messina.

higher than 10 m, all generated by the 1908 Messina and by the 2002 Stromboli (Aeolian Island) events. The 91 OPs for which run-up value is available count for four tsunamis of seismic origin, one event associated with a large landslide triggered by an earthquake (February 6, 1783) and of two events associated with the Stromboli volcano activity (1930 and 2002). The February 6, 1783 tsunami was generated by a $6 \times 106\ m^3$ landslide (Zaniboni et al., 2016; 2019) and caused more than 1,500 fatalities at Scilla (Tyrrhenian Calabria) where most of the people, frightened by the ongoing sequence of earthquakes, sought shelter on the beach close to the town and were surprised by the unexpected waves that reached the roofs of the buildings with a run-up of 9 m (Graziani et al., 2006). ITED also contains 70 OPs where inundation distances are specified, some of them are the same as those for which the run-up values are also available. For 32 OPs the inundation extent is greater or equal to 100 m. According to coeval sources, the maximum value was observed during the January 11, 1693 tsunami in Eastern Sicily where: *"At Mascali the sea flooded the shore for about one mile inland"* (Boccone, 1697).

The ITED WebApp allows the user to explore the tsunami intensity distribution along time (*tsunami history*) of all the PNs reported, and to know how many times a site has been hit by a tsunami in the past and how severe was the impact (**Figure 2B**). Among the 189 PNs included in the database, 51 experienced tsunami effects more than once. Details of each observation are supplied for every PN: the tsunami-history of the place is composed by a bar chart indicating the tsunami intensity vs the year of occurrence and by a table containing the detailed description of the observations. In **Figure 2B** the Messina tsunami history diagram is shown: as historical sources testify, Messina was hit by nine tsunamis, starting from the February 4,

1169 event that caused the flooding of the town. The February 5, 1783 and the December 28, 1908 were the strongest, reaching in Messina local tsunami intensity 5 according to Sieberg-Ambraseys scale.

Concerning the impact of the Italian tsunamis in terms of the geographical area involved, 14 tsunamis were observed at regional scale that indicates tsunami propagation for a distance greater than 100 km from the source. Besides the 1908 Messina tsunami, it is worth mentioning the January 11, 1693 Eastern Sicily event that was observed along the whole Ionian coasts of Sicily from Siracusa to Messina. Likewise, the February 23, 1887 Ligurian tsunami involved more than 200 km of coast, with run-up locally exceeding 1 m, and with remarkable sea withdrawals leaving boats stranded in many sites. All the regional events were generated by earthquakes, with the exception of the 2002 Stromboli Island tsunami, which was observed up to the coasts of Campania (about 140 km North). This event was triggered by a huge submarine ($20 \times 106\ m^3$) and sub-aerial ($4–9 \times 106\ m^3$) slides (Tinti et al., 2005) occurred during a relevant volcanic eruption on the Sciara del Fuoco, the steep flank of the Stromboli volcano. In the northern part of the island a maximum run-up of 10.90 m was measured (Tinti et al., 2006).

In order to have an exhaustive and complete collection of the tsunami effects observed along the Italian coasts, tsunamis generated outside the Italian territory have also been taken into account. As a result, two recent Greek events occurred in the Ionian Sea, respectively in November 2015 and October 2018 were appended to EMTC 2.0. The former was generated by a Mw = 6.4 earthquake near Lefkas Island and studied by (Ganas et al., 2015) and the latter occurred close to the island of Zakynthos, both were recorded at some Italian tide gauges (Papadopoulos et al., 2019). Other two events, already present in the EMTC, have produced effects on the Italian coast: the July 21, 365 tsunami, the most well-known and catastrophic event that has ever occurred in the Mediterranean, and the May 21, 2003 Boumerdès (Algeria) tsunami. In relation to the 365 event, the destructive tsunami was caused by a great catastrophic earthquake occurred in Crete, involving most of the Eastern and Central Mediterranean, reaching also the Southern Italy coasts and the Levantine coasts. Unfortunately, the information on the tsunami impact in Sicily is very little and too vague to consent the identification of the precise location where effects might have been observed. According to Putortì (1912), effects of the 365 tsunami in Reggio Calabria would have been documented by an inscription found during archaeological excavations. Finally, the tsunami generated by the May 2003 Algerian earthquake, causing damage in the Baleares, was recorded at some Italian tide gauges in the Tyrrhenian and Ligurian Seas.

ITED WebApp

The information contained in ITED has been made available to the public through the display of a web application that allows the users to visualize the georeferenced information on a map. The dedicated WebApp has been developed using the Esri ArcGIS online environment and can be freely accessed without the need of an Esri user account. The ITED WebApp (Maramai et al., 2019a), accessible through https://tsunamiarchive.ingv.it/ited.1.0/, hosts six layers containing the information available regarding all the tsunami effects observed at the Italian coasts. The layers loaded in the WebApp are listed in **Figure 1A**:

(1) ITED_Observation_Points_OP_, where the 318 OPs are visible and coloured according to the local tsunami intensity on the Sieberg Ambraseys scale;
(2) ITED_Place Name with the 189 PNs hit by tsunamis and their tsunami histories;
(3) ITED_inundation where the 70 OPs with reported inundation values are visible with symbols proportional to the extent of the metric;
(4) ITED_runup, where the 91 OPs with reported run-up values are visible with symbols proportional to the extent of the metric;
(5) EMTC 2.0 layer that hosts the new release of database of the tsunami events, including the two recently added events (November 2015 and October 2018);
(6) ITED_Intensity_Map layer, where it is possible to select an event of interest and show all the OPs related to it, with their local tsunami intensity (see **Figure 2A**).

Figure 3 shows the runup (ITED_runup, black bars) and inundation (ITED_inundation, blue halos) layers. Symbols refer to all values available in the database.

As said earlier, the ITED database is linked to the EMTC 2.0 catalogue, which is also displayed in ITEDWebApp as a point layer called EMTC 2.0 (*see* **Figure 1A**). Similarly to the previous version EMTC still available at (http://www.arcgis.com/apps/StorytellingTextLegend/index.html?appid=8329c2ad9b7f43c18562bdddc6c1ad26), EMTC 2.0 contains information such as date, time, reliability, cause, intensity, magnitude (if seismic), coordinates, macroseismic intensity and a detailed tsunami description including a list of the related bibliographical references that is reachable from the pop-up generated when clicking on each point of the layer.

The ITED WebApp allows the user to customize which kind of information to retrieve; through five widgets the user can choose the layers to be displayed (*Layer_List*), filter information (*Group Filter*), select the intensity map by entering the event data (Tsunami Intensity Map), query each of the available layers (*query*) and *print* a selected extent of the map. The tabular information contained in each layer of the WebApp can be exported in csv format by using several group filters (i.e., selecting data from the extent viewed, or by date, reliability, cause, site etc.; or by a combination of several of these parameters). The *print* widget allows the user to export and print maps with the results of their specific queries or a general view of the database. Data contained in ITED WebApp are freely accessible at the link https://tsunamiarchive.ingv.it/ited.1.0/

DATA ANALYSIS

ITED contains tsunami observations related to 77 tsunamis, 73 being originated within the Italian territory and four triggered by

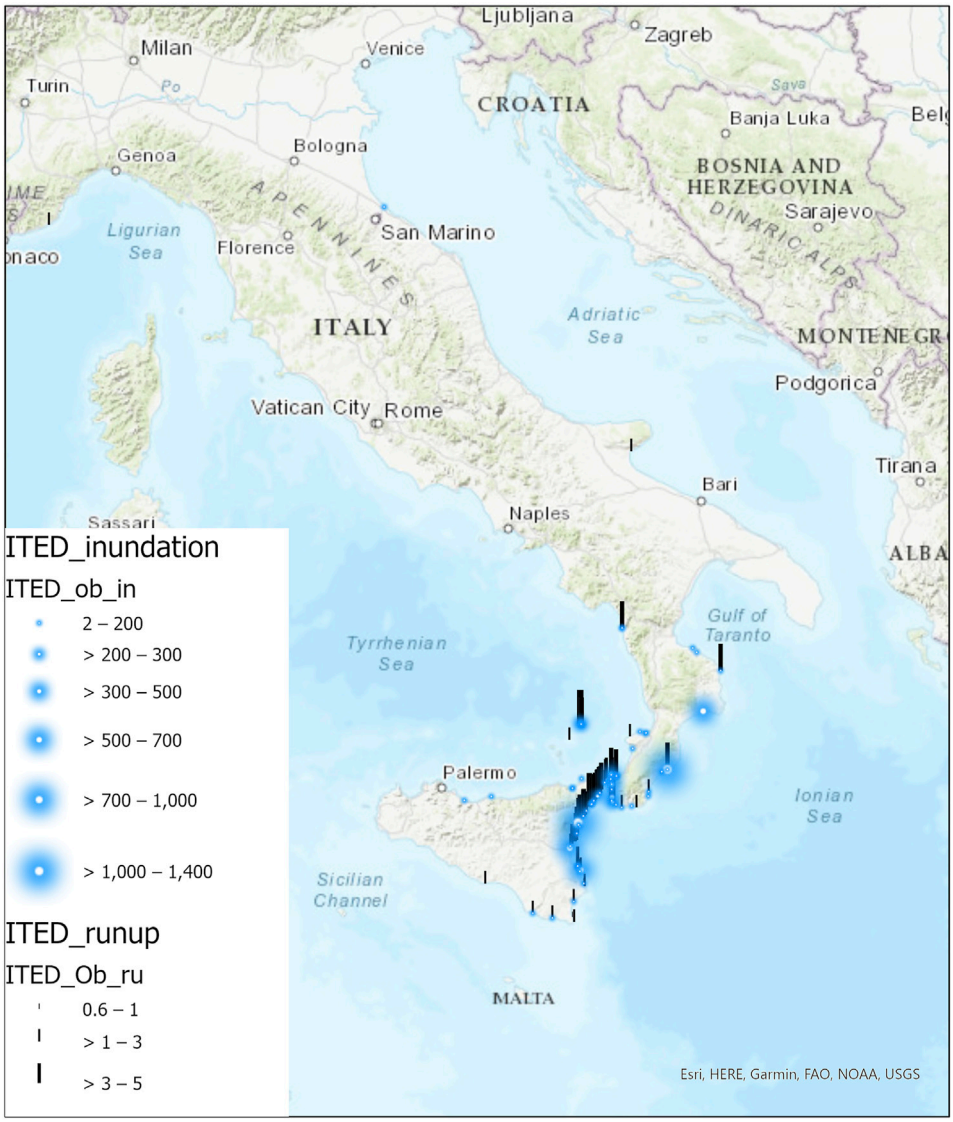

FIGURE 3 | Screenshot of the WebApp showing ITED_runup (black bars) and ITED_inundation (blue halos) layers; symbols are proportional to the measured values (Service Layer Credits: sources: ©Esri, HERE, Garmin, Intermap, increment P Corp., GEBCO, USGS, FAO, NPS, NRCAN, NOAA, GeoBase, IGN, Kadaster NL, Ordnance Survey, Esri Japan, METI, Esri China (Hong Kong), ©swisstopo, ©OpenStreetMap contributors 2019. Distributed under a Creative Commons BY-SA License).

sources located in neighboring Mediterranean countries causing slight effects on the Italian coasts. Following the pattern of the rest of the world, the majority of tsunamis observed or registered in Italy were caused by earthquakes (68%), see **Figure 4**. An important remark should be made regarding the activity of the Vesuvius and the Aeolian Islands volcanoes which has caused over the centuries a not negligible number of events (16%); in particular, the Stromboli volcano (Aeolian Islands) whose activity has generated the majority of the events of volcanic origin. On the basis of historical evidence and looking at the tsunami history, all these events have occurred since the 20th century, leaving open the possibility that the number could be even higher (**Figure 5**). Only two tsunamis were caused by mass failures due to mere gravity load events. Finally, for nine Italian events the reported description is typical of a tsunami but the generating mechanism has not been yet found, so that they are classified with an unknown cause, needing further investigation.

Following the same criteria established for EMTC, in the new version EMTC2.0 tsunamis are classified according to their quality by means of their *reliability* index, the value can be considered by the end user as an indicator of the trustworthiness of the data retrieved. Including low reliability index events, allows inserting in the database historical tsunamis for which scarce information is available. This on one hand, enables the possibility to report the information available for the event and on the other hand warns the end user that the

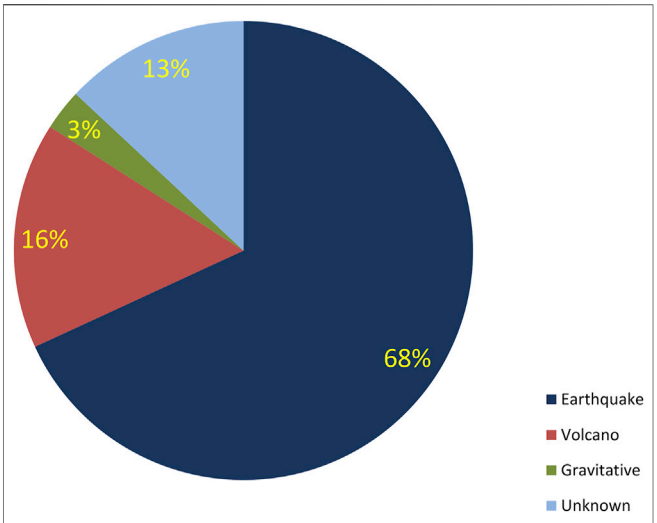

FIGURE 4 | Distribution of the tsunamis in ITED by generating cause, with the number of tsunamis indicated for each cause.

information related to that event is not as solid to be considered reliable. The number of unreliable tsunamis decreases over the years until the most recent time intervals in which almost exclusively reliable tsunamis are present, as shown in **Figure 6**. This is clearly an indication that data tends to be more abundant and more reliable in recent centuries and with the increasing use of sea-level instrumentation. The time period intervals in **Figure 6** are variable, being fixed to 50 years from 1700 a.D. to today. According to **Figure 6**, about half of the entries in the catalogue are classified as definite tsunamis, having been attributed reliability value of 4. There are only three entries prior to 1300 a.D. and five prior to 1600 a.D. while in later times the total number of entries per century is rather stable (on average 16 events). This provides information for estimating the possible completeness of the database from the 17th century onwards, even if it must be stressed that the number of events do not allow to perform a robust statistical analysis.

To have a picture of the severity of the Italian tsunamis and their impact along the coast, in **Figure 7** a bar chart of intensities per Italian region is shown. More than 50% of the tsunamis with origin within the Italian territory have been generated in the Calabria and Sicily regions: excluding the 1627 tsunami that occurred in Apulia, the most destructive tsunamis, with intensities 5 and 6, originated in these two regions.

Considering the local intensities assigned at the different OPs, the bar diagram in **Figure 8** shows the distribution of local intensity per Italian provinces. For the sake of reducing the information to the essentials, only provinces with at least three intensity values assigned were represented. Blue bars enclose the provinces of the Italian regions that have the highest number of OPs. On the left side of the graph provinces of the Liguria region are shown: local intensities in this region do not exceed intensity value 3 and most of the OPs are related to the 1887 tsunami. Calabria and Sicily are definitely the Italian regions most affected by tsunamis, not only in terms of numbers of observations but also in terms of severity of effects. Messina (ME) and Reggio Calabria (RC) are the provinces with the highest number of OPs with the most severe effects.

Finally, a further consideration on the impact of tsunamis generated by distant sources arises by looking at **Figure 9** that shows the OPs related to the 4 external tsunamis. It can be seen that the coasts of Sicily and Apulia are exposed to the tsunamis generated by the subduction zone of the Hellenic Arc, while the coasts of Sardinia and Liguria may be affected by the tsunamis generated by the Algerian thrust zone.

DISCUSSION

The ITED database comes forth from the information contained in Euro-Mediterranean Tsunami Catalogue (Maramai et al., 2014) related to effects of tsunamis observed or registered along the Italian coasts. ITED subdivides the general tsunami information contained on EMTC, geographically locating the specific information for each affected site and classifying the effects observed into intensity classes. The database is displayed through a WebApp, developed using the Esri ArcGIS online environment letting the user to retrieve information, to switch from ITED to EMTC 2.0 and vice versa, or consult them at the same time.

The ITED WebApp allows the user to query the database, export the data of interest, explore the tsunami history of all the main sites and print the information. The implementation of ITED also led to a new release of EMTC, called EMTC 2.0, that includes the updating of new information regarding some

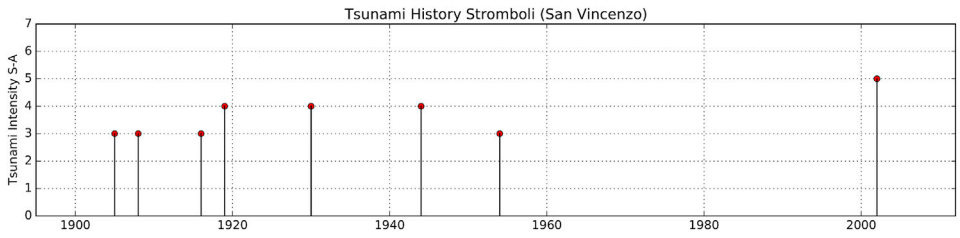

FIGURE 5 | Tsunami history of Stromboli.

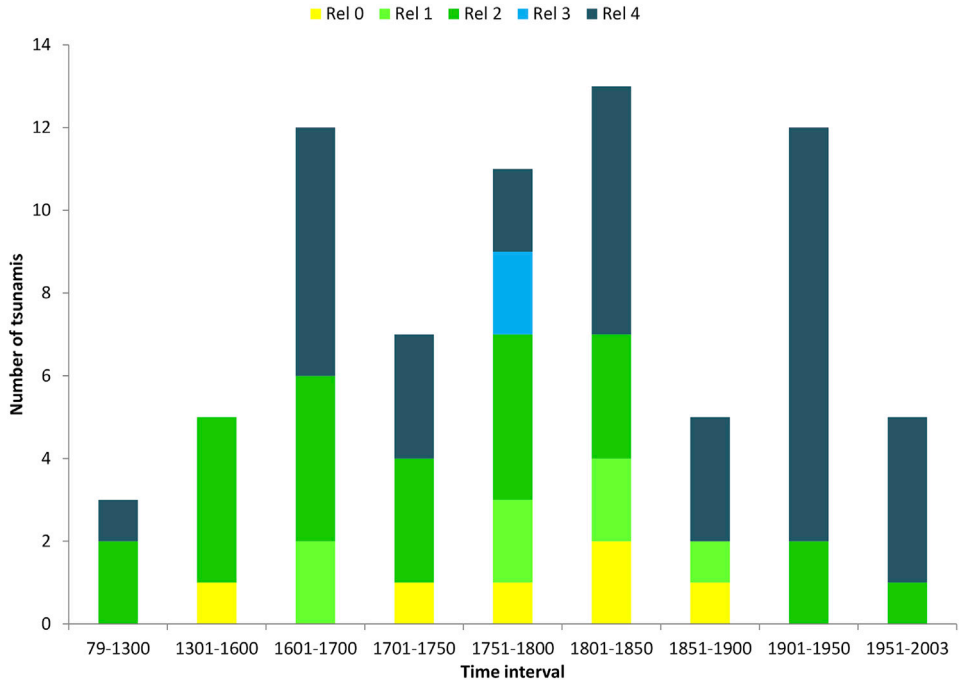

FIGURE 6 | Time distribution of the Italian tsunamis in EMTC2.0 per reliability classes, Rel 4: definite tsunami, Rel 3: probable tsunami, Rel 2: questionable tsunami, Rel 1: improbable tsunami, Rel 0: very improbable tsunami.

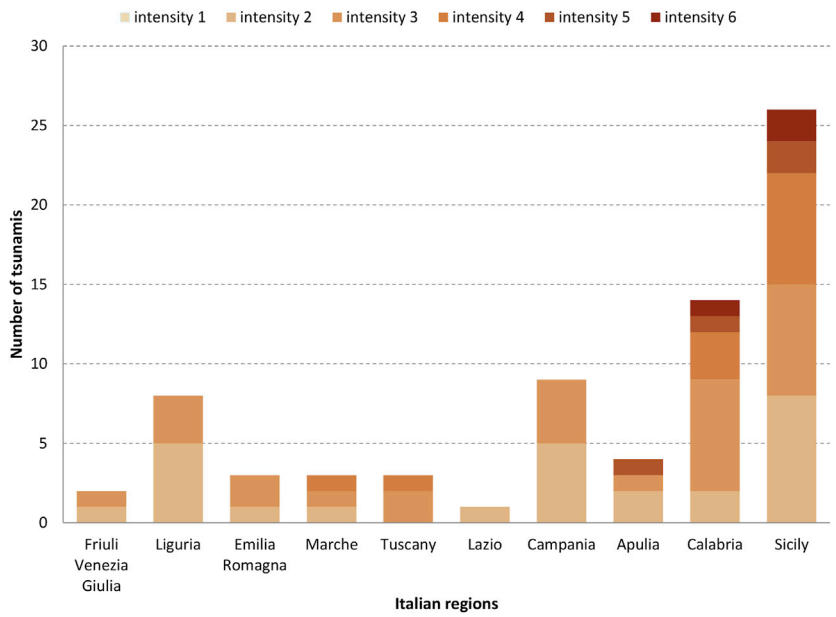

FIGURE 7 | Regional distribution of Italian tsunamis per intensity classes.

tsunami parameters, such as the reliability, intensity, generating cause, etc., as well as the appending of other two tsunamis, recently occurred within the Greek territory and whose effects were recorded along the Italian coasts. ITED was specifically built to meet the needs of the tsunami hazard community, thus providing useful information that can improve the knowledge of how much the Italian coasts are exposed to tsunamis. The database contains a great number of reliable data that can contribute to validate the models used for hazard assessment along the Italian coasts and can give useful

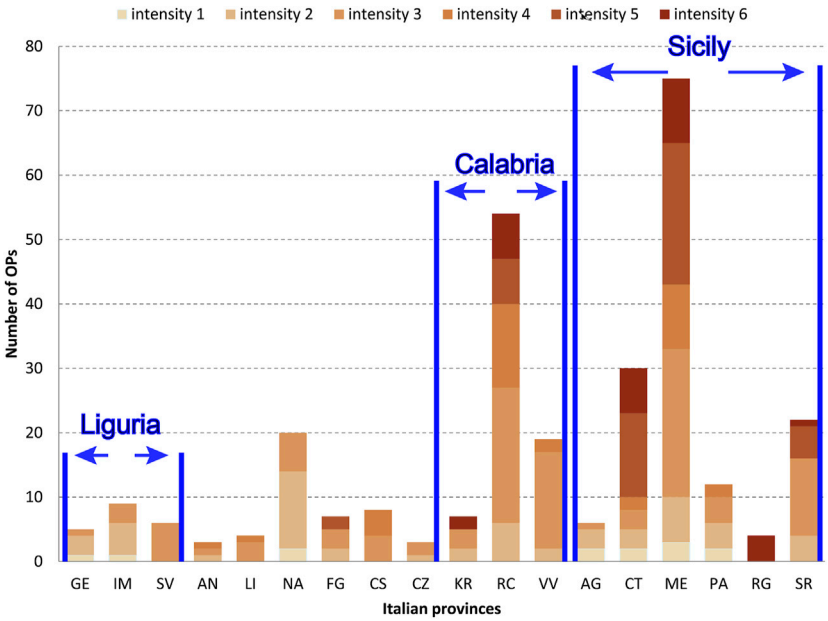

FIGURE 8 | Distribution of local intensities per Italian provinces with at least three Observation Points (OPs).

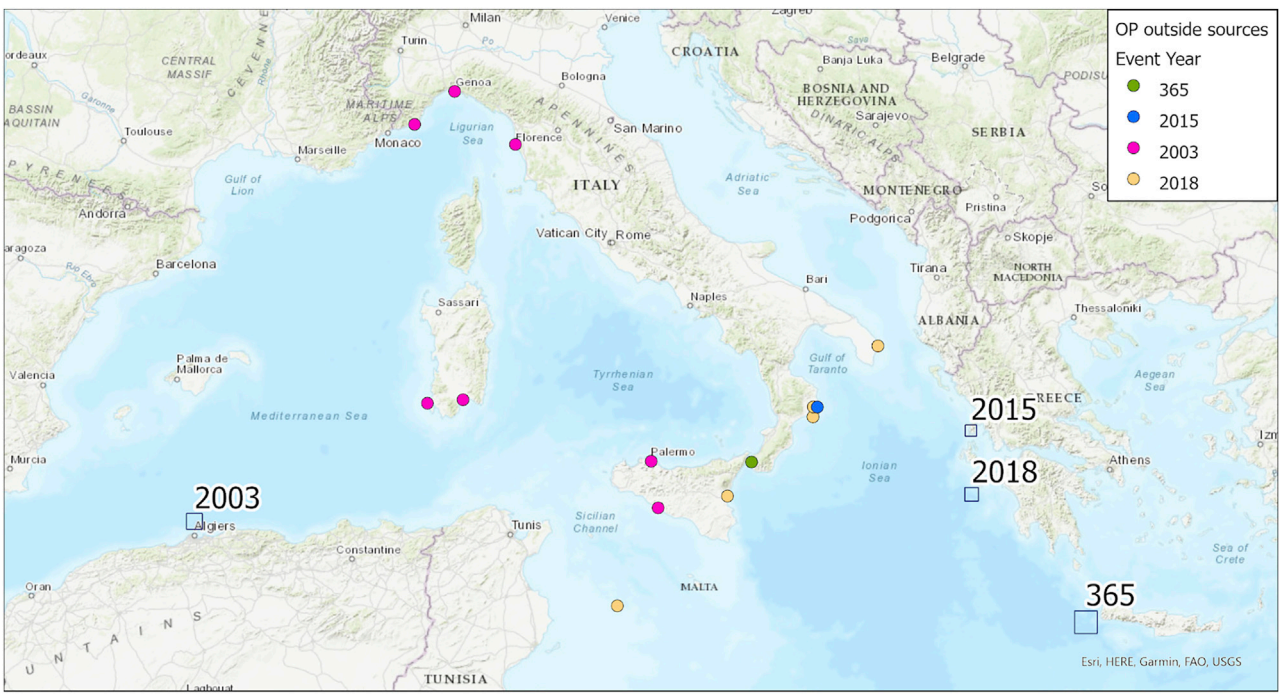

FIGURE 9 | Observation Points (OPs) related to the four tsunamis generated in the neighboring countries. Blue squares indicate the generating sources.

indications for the realization of inundation maps and emergency plans. ITED can also be used as a tool for increasing public awareness and, therefore, for reducing the risk of tsunamis.

DATA AVAILABILITY STATEMENT

The datasets presented in this study can be found in online repositories. The names of the repository/repositories and

accession number(s) can be found below: https://tsunamiarchive.ingv.it/ited.1.0/.

AUTHOR CONTRIBUTIONS

AM, LG, and BB equally contributed to the conception and design of the study. AM and LG have prepared, revised and organised in the suitable format the data included in the database. BB realized the dedicated WebApp in ArcGis. AM, LG, and BB wrote the manuscript. All authors contributed to manuscript revision, read, and approved the submitted version.

ACKNOWLEDGMENTS

Authors thank Dr. Mario Locati, (INGV, Milan) for the technical support during the realization of the ITED database and for contributing to link the ITED database to the INGV Gazetteer and to DBMI database. Authors wish to thank also Dr. Andrea Rovida and Dr. Andrea Antonucci (INGV, Milan) for their contribution. This manuscript has been released as a pre-print at [https://nhess.copernicus.org/preprints/nhess-2019-241/], (Maramai et al., 2019b). We also would like to thank the two anonymous referees for their comments and suggestions that helped to improve this paper.

REFERENCES

Ambraseys, N. (1962). Data for the investigation of the seismic sea-waves in the Eastern Mediterranean. *Bull. Seismol. Soc. Am.* 52, 895–913.

Baptista, M. A., and Miranda, J. M. (2009). Revision of the Portuguese catalog of tsunamis. *Nat. Hazards Earth Syst. Sci.* 9, 25–42. doi:10.5194/nhess-9-25-2009

Baratta, M. (1910). *La catastrofe sismica calabro messinese (28 dicembre 1908).* Roma: Relazione alla Società Geografica Italiana, Vol 2.[in Italian].

Basili, R., Brizuela, B., Herrero, A., Iqbal, S., Lorito, S., Maesano, F. E., et al. (2021). The making of the NEAM Tsunami Hazard Model 2018 (NEAMTHM18). *Front. Earth Sci.* 8, 616594. doi:10.3389/feart.2020.616594

Boccone, P. (1697). "Osservazione prima all'Illustrissimo et Eccellentissimo Sig. Francesco Uldarico intorno il terremoto della Sicilia seguito l'anno 1693," in *Museo di Fisica e di esperienze variato, e decorato di oservazioni naturali, e ragionamenti secondo i principiy de' moderni*. Editor G. B. Zuccato (Venezia), 4, 1–16. [in Italian].

Bonito, M. (1691). *Terra tremante, o vero continuatione de' terremoti dalla Creatione del Mondo fino al tempo presente*. Naples, Italy: Napoli, 822.[in Italian].

De Lange, W. P., and Healy, T. R. (1986). New Zealand tsunamis 1840-1982. *N. Z. J. Geol. Geophys.* 29 (1), 115–134. doi:10.1080/00288306.1986.10427527

Ganas, A., Briole, P., Papathanassiou, G., Bozionelos, G., Avallone, A., Melgar, D., et al. (2015). A preliminary report on the Nov 17, 2015 M=6.4 South lefkada earthquake, Ionian Sea, Greece. Available at: https://www.emsc-csem.org/Doc/Additional_Earthquake_Report/470390/Lefkada%2017%20Nov%202015%20earthquake%20report.pdf (Accessed December 4, 2015).

Graziani, L., Maramai, A., and Tinti, S. (2006). A revision of the 1783-1784 Calabrian (southern Italy) tsunamis. *Nat. Hazards Earth Syst. Sci.* 6, 1053–1060. doi:10.5194/nhess-6-1053-2006

Guidoboni, E., Ferrari, G., Mariotti, D., Comastri, A., Tarabusi, G., Sgattoni, G., et al. (2018). CFTI5Med, Catalogo dei Forti Terremoti in Italia (461 a.C.-1997) e nell'area Mediterranea (760 a.C.-1500). *Istituto Nazionale di Geofisica e Vulcanologia (INGV)*. doi:10.6092/ingv.it-cfti5

Kaiser, G., Scheele, L., Kortenhaus, A., Løvholt, F., Römer, H., and Leschka, S. (2011). The influence of land cover roughness on the results of high resolution tsunami inundation modeling. *Nat. Hazards Earth Syst. Sci.* 11, 2521–2540. doi:10.5194/nhess-11-2521-2011

Locati, M., Camassi, R., Rovida, A., Ercolani, E., Bernardini, F., Castelli, V., et al. (2016). DBMI15, the 2015 version of the Italian macroseismic database. *Ist. Naz. Geofis. Vulcanol.* doi:10.6092/INGV.IT-DBMI15

Maramai, A., Brizuela, B., and Graziani, L. (2014). The euro-mediterranean tsunami catalogue. *Ann. Geophys.* 57 (4), S0435. doi:10.4401/ag-6437

Maramai, A., Graziani, L., and Brizuela, B. (2019a). Italian tsunami effects database (ITED). *Ist. Naz. Geofis. Vulcanol. (INGV)*. doi:10.13127/tsunami/ited.1.0

Maramai, A., Graziani, L., and Brizuela, B. (2019b). Italian Tsunami Effects Database (ITED): the first database of tsunami effects observed along the Italian coasts. *Nat. Hazards Earth Syst. Sci. Discuss.* [preprint]. doi:10.5194/nhess-2019-241

Papadopoulos, G. A., Agalos, A., Annunziato, A., Bocchini, G. M., Charalampakis, M., Novikova, T., et al. (2019). "The South Ionian Sea earthquake (Mw6.8) of 25 october 2018 and its associated tsunami," in 21st EGU General Assembly, EGU2019, Proceedings from the conference, April7–12, 2019, Vienna, Austria. 21, 13705.

Papadopoulos, G. A., and Imamura, F. (2001). A proposal for a new tsunami intensity scale. Tsunami symposium 2001 Proc., Aug. 7-10, 2001, Seattle, Washington, 559–577.

Papadopoulos, G. A., Vassilopoulou, A., and Plessa, A. (2000). A new catalogue of historical earthquakes in the Corinth Rift, Central Greece: 480 B.C. - A.D. 1910. *Natl. Obs. Athens Inst. Geodyn. Publ. n 12 Athens*.

Platania, G. (1909). Il maremoto dello Stretto di Messina del 28 Dicembre 1908. *Boll. Soc. Sismol. Ital.* 13, 369–458.[in Italian].

Putortì, N. (1912). Di un titolo termale scoperto in Reggio Calabria. *Atti Accad. Naz. Lincei, RSM* 5 (21), 791–802.

A. Rovida, M. Locati, R. Camassi, B. Lolli, and P. Gasperini (Editors) (2016). *Catalogo Parametrico dei Terremoti Italiani (CPTI15). Istituto Nazionale di Geofisica e Vulcanologia (INGV)*. doi:10.6092/INGV.IT-CPTI15

Soloviev, S. L., Solovieva, O. N., Go, C. N., Kim, K. S., and Schetnikov, N. A. (2000). *Tsunamis in the Mediterranean sea 2000 B.C. - 2000 A.D*. New York: Kluwer Academic Publishers.

Tinti, S., Maramai, A., and Graziani, L. (2004). The new catalogue of Italian tsunamis. *Nat. Hazards* 33 (3), 439–465. doi:10.1023/B:NHAZ.0000048469.51059.65

Tinti, S., Armigliato, A., Manucci, A., Pagnoni, G., and Zaniboni, F. (2005). Landslides and tsunamis of December 30, 2002 at Stromboli, Italy: numerical simulations. *Boll. Geofis. Teorica Ed. Appl.* 46 (2-3), 153–168.

Tinti, S., Maramai, A., Armigliato, A., Graziani, L., Manucci, A., Pagnoni, G., et al. (2006). Observations of physical effects from tsunamis of December 30, 2002 at Stromboli volcano, southern Italy. *Bull. Volcanology* 68 (5), 450–461. doi:10.1007/s00445-005-0021-x

Zaniboni, F., Armigliato, A., and Tinti, S. (2016). A numerical investigation of the 1783 landslide-induced catastrophic tsunami in Scilla, Italy. *Nat. Hazards* 84, 455–470. doi:10.1007/s11069-016-2461-3

Zaniboni, F., Pagnoni, G., Gallotti, G., Paparo, M. A., Armigliato, A., and Tinti, S. (2019). Assessment of the 1783 Scilla landslide-tsunami's effects on the Calabrian and Sicilian coasts through numerical modeling. *Nat. Hazards Earth Syst. Sci.* 19, 1585–1600. doi:10.5194/nhess-19-1585-2019

Conflict of Interest: The authors declare that the research was conducted in the absence of any commercial or financial relationships that could be construed as a potential conflict of interest.

frontiers in Earth Science

ORIGINAL RESEARCH
published: 31 March 2021
doi: 10.3389/feart.2021.626809

A New Relative Risk Index for Hospitals Exposed to Tsunami

Marco Baiguera[1], Tiziana Rossetto[1], Juan Palomino[1], Priyan Dias[2], Susana Lopez-Querol[1], Chandana Siriwardana[2], Hashan Hasalanka[2], Ioanna Ioannou[1] and David Robinson[1]*

[1]EPICentre, Department of Civil, Environmental and Geomatic Engineering, University College London, London, United Kingdom, [2]Department of Civil Engineering, University of Moratuwa, Moratuwa, Sri Lanka

The failure of hospitals in recent tsunami have caused extensive social and economic losses. A simple but quantitative approach is required to assess the resilience of healthcare systems to tsunami, which relates not only to hospital building integrity, but also to maintaining hospital functionality. This paper proposes a new tsunami relative risk index (TRRI) that quantifies the impact of tsunami on critical units, (e.g. Intensive Care Unit, Maternity Ward, etc) in individual hospitals, as well as the impact on service provision across a network of hospitals. A survey form is specifically developed for collecting of field data on hospitals for the TRRI evaluation. In its current form TRRI is designed for hospital buildings of reinforced concrete construction, as these are the building types most commonly used worldwide for housing critical units. The TRRI is demonstrated through an application to three hospitals located along the southern coast of Sri Lanka. The TRRI is evaluated for three potential tsunami inundation events and is shown to be able to identify issues with both the building and functional aspects of hospital critical units. Three "what-if" intervention scenarios are presented and their effect on the TRRI is assessed. Through this exercise, it is shown that the TRRI can be used by decision makers to simply explore the effectiveness of individual and combined interventions in improving the tsunami resilience of healthcare provision across the hospital system.

Keywords: tsunami risk, relative risk index, hospitals, tsunami engineering, disaster risk reduction

OPEN ACCESS

Edited by:
Christina Robyn Magill, Macquarie University, Australia

Reviewed by:
Yo Fukutani, Kanto Gakuin University, Japan
Qi Yao, China Earthquake Networks Center, China

****Correspondence:***
Marco Baiguera
m.baiguera@ucl.ac.uk

Specialty section:
This article was submitted to Geohazards and Georisks, a section of the journal Frontiers in Earth Science

Received: *06 November 2020*
Accepted: *04 February 2021*
Published: *31 March 2021*

Citation:
Baiguera M, Rossetto T, Palomino J, Dias P, Lopez-Querol S, Siriwardana C, Hasalanka H, Ioannou I and Robinson D (2021) A New Relative Risk Index for Hospitals Exposed to Tsunami. Front. Earth Sci. 9:626809. doi: 10.3389/feart.2021.626809

INTRODUCTION

Hospitals and healthcare facilities are vital assets to communities and play a key role in recovery from natural disasters. During emergencies, hospital units must provide uninterrupted critical services such as emergency care to the injured, laboratories, blood banks, ambulances, pharmacies and immunization services to prevent outbreaks of diseases (WHO, 2010). In recognition of the critical role played by hospitals in disasters, the Hyogo Framework for Action (UNISDR, 2005) and subsequent Sendai Framework (UNDRR, 2015), have as one priority the achievement of safe and resilient hospitals through structural, non-structural and functional risk prevention. This has resulted in major global initiatives for hospital safety and several guidelines have been issued for the design, assessment and strengthening of hospital buildings for different hazards (FEMA, 1997; FEMA, 2003; FEMA, 2007; PAHO, 2008; WHO, 2015). However, it is only relatively recently that tsunami design codes have been issued, e.g., FEMA 55 (FEMA, 2005), MLIT 2570 (MLIT, 2011), ASCE 7–16 Standard (ASCE, 2017a). These have not been implemented in the design of most healthcare facilities worldwide, and failures of hospitals in recent tsunami have caused extensive

social and economic losses, (e.g. Kirsch et al., 2010; EEFIT, 2011). One means of disaster management for reducing life loss in tsunami is evacuation to sites outside the inundation zone or to upper levels in buildings considered strong enough to withstand the tsunami inundation (e.g. MHNI, 2015). Clearly, the vulnerable nature and reduced mobility of hospital patients makes evacuation difficult. Moreover, evacuation is only viable for locations that have tsunami warning systems in place and which are at a significant distance from the tsunami source.

Despite not being designed for tsunami, most hospitals are built to higher standards than normal residential buildings and present an enhanced resistance to natural hazards that may allow them to withstand small tsunami inundation without structural damage. However, hospital resilience relates not only to hospital building integrity, but also to maintaining hospital functionality. The latter depends heavily on the integrity of both non-structural elements and the lifelines supporting the hospital operation, such electricity, water and communications. The 2011 Tohoku tsunami presented several examples of hospitals that withstood the tsunami but had compromised functionality and ability to care for patients in the aftermath due to loss of lifelines and back-up systems in the tsunami inundation (EEFIT, 2011, EEFIT, 2013; ASCE, 2017b).

Hospitals can be considered as part of a network of healthcare provision, where only some parts of the network can be relied upon for the provision of any particular healthcare service, (e.g. not all hospitals have a trauma unit). As tsunami can affect large tracts of the coastline, they can damage several hospitals and/or supporting lifelines simultaneously. This not only disrupts the provision of healthcare locally but can result in the loss of particular healthcare services across large parts of the network, (e.g. if all hospitals with trauma units are affected over an extended region). Such scenarios result in affected people having to travel large distances and wait for excessive times to obtain specific treatments.

The inherent organisational complexity of hospitals, and the interactions and independencies of healthcare units makes the tsunami risk assessment of hospital services a challenging task. To date, several studies have investigated the performance of individual hospital buildings for different natural hazards using advanced engineering analysis, (e.g. Casarotti et al., 2009; Di Sarno et al., 2011). However, the use of advanced engineering analysis for the risk assessment of several hospitals is prohibitively expensive in terms of human and computational resources, as hospitals are typically composed of several buildings, built at different times and which do not follow a standard design. Furthermore, these studies rarely consider lifelines and back-up systems explicitly. As an alternative, several hospital safety indices (PAHO, 2008; WHO, 2015) and hospital safety checklists (WHO, 2008; WHO, 2010) have been proposed that offer rapid diagnostic tools for use by policy makers and hospital managers. These indices and checklists provide a qualitative estimate of the risk to hospitals from a set of hazards, i.e., natural and man-made hazards. The indicators can be applied to assess either single healthcare facilities or networks of hospitals, and generally account for the potential loss of critical infrastructure lifelines. These can be used to identify potential problem areas and for the prioritization of interventions to reduce the disaster risk to hospitals. However, these methods present two major shortcomings: 1) lack of quantitative approaches to support the assessment of the relative risk associated with the hospital facilities; and 2) little consideration of the nature of single hazards, (e.g. tsunami) and their interactions and interdependencies when impacting hospital infrastructure.

In order to improve both the safety and resilience of healthcare systems to tsunami, a simple but quantitative approach is required for assessing tsunami risk to healthcare services distributed across networks of hospitals. Such an approach needs to focus on healthcare service continuity, and go beyond hospital building integrity to consider the integrity of the lifelines and back-up systems that support the service provision and hospital functionality. This paper presents a new tsunami relative risk index (*TRRI*) developed to meet this need. Firstly, the components and calculation rationale for the *TRRI* are described. A survey form, specifically developed for collecting of field data on hospitals for the *TRRI* evaluation is also presented in the Appendix. In its current form *TRRI* is developed for hospital buildings of reinforced concrete construction, as these are the building types most commonly used worldwide for housing critical units, (e.g. Intensive Care Units). The *TRRI* is demonstrated through an application to 3 hospitals located along the southern coast of Sri Lanka (Galle, Matara and Hambantota Districts), which were surveyed by a team of researchers from UCL and University of Moratuwa. The *TRRI* is evaluated for three potential tsunami inundation events and is shown to be able to identify issues with both the buildings and functional aspects of hospital critical units. Three "what-if" intervention scenarios are selected and their effect on the *TRRI* is assessed. Through this exercise, it is shown that the *TRRI* can be used by decision makers to simply explore the effectiveness of individual and combined interventions in improving the tsunami resilience of healthcare provision across the hospital system.

Although the absence of numerical structural modeling to support the analysis can be seen as a limitation of this approach, the proposed relative risk index is based on objective engineering principles that are reflected in equations (and not merely expert opinions). The aim of using such an index is to be able to quickly assess a large portfolio of hospital facilities, identifying aspects of the facilities that require further detailed assessment, thus directing potential numerical modeling. For the case-study presented here, the inundation depths for the "what-if" intervention scenarios are based on limited onshore inundation scenarios based on the 2004 Indian Ocean Tsunami event, rather than on probabilistic data, since the latter is not available for Sri Lanka. Nevertheless, these scenarios give insight into the relative effectiveness of various mitigation measures that can be adopted by hospital administrators.

METHODOLOGY

The proposed Tsunami Relative Risk Index (*TRRI*) aims to quantify the influence of the tsunami inundation on critical

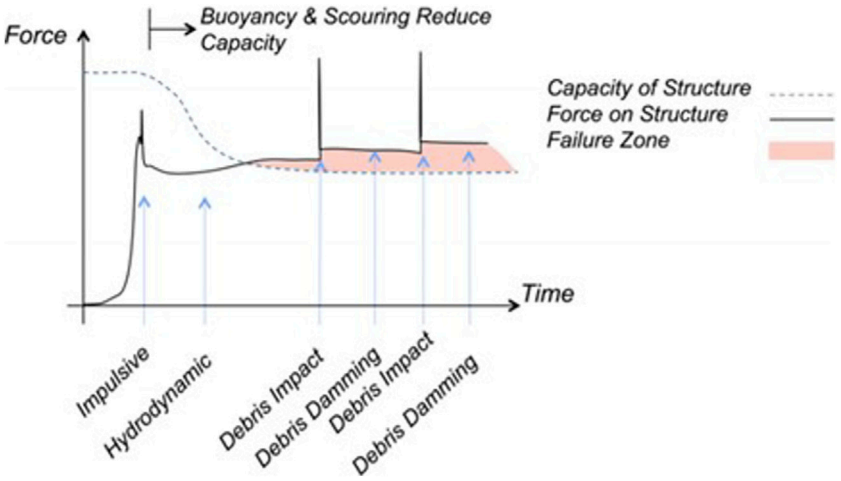

FIGURE 1 | Typical qualitative time series of loading on a building during tsunami inundation (Yeh et al., 2014).

units, (e.g. Intensive Care Unit, Maternity Ward, etc) in individual hospitals, as well as the impact on service provision across a network of hospitals. The objective is to identify some of the drivers of risk to the hospital unit functionality, such that these can be prioritized for further investigation and intervention.

The proposed *TRRI* considers both the structural and functional attributes of hospital critical units, e.g., Intensity Care Unit, Maternity Ward, etc. The ability of a hospital critical unit to function in the aftermath of a tsunami depends on: 1) the stability of the structure where the hospital critical unit is located; 2) the integrity of non-structural elements relevant to the critical units, particularly the medical equipment that is required to ensure unit functionality; and 3) the functioning of the critical lifeline systems supporting unit functionality e.g., electric power, water supply, telecommunications, etc. Therefore, the proposed *TRRI*, for a hospital unit is defined as:

$$TRRI = \max\left(RRI_{\text{bldg}},\ RRI_{\text{funct}},\ RRI_{\text{bcs}}\right), \tag{1}$$

where RRI_{bldg} considers the ability of the structural system to resist expected tsunami actions, RRI_{funct} represents whether the location of the critical unit within the building puts it at high risk of loss of functionality under the expected tsunami inundation, and RRI_{bcs} describes the risk of back-up critical systems to supporting lifelines being inundated. Each *RRI* component varies in value between 0 (no risk) and 1 (high risk). Each of these *RRI* components are further described in the following sections.

Building Relative Risk Index, RRI_{bldg}

Post-tsunami reconnaissance studies provide a spectrum of tsunami-induced damage mechanisms in buildings, that result from the actions of hydrodynamic forces, buoyancy, impact from floating debris and foundation scouring (EEFIT, 2006). **Figure 1** shows a typical load time series as a tsunami passes a building. Initially, as the front of the tsunami arrives and passes the building, there will be a sharp rise in force, which will then plateau and be maintained for several minutes, depending on the period of the wave and the proximity of the building to the shoreline. During this phase, there may be several short sharp spikes in loading from debris impacting with the building. The capacity of the building to withstand the tsunami loading will decrease during the course of inundation due to buoyancy forces reducing axial compression in vertical elements (Del Zoppo et al., 2020), and due to scour undermining the foundations. The impact of scour around the building can also have a considerable impact on the structural capacity of the building, by exposing the foundations and potentially leading to local collapse of vertical structural elements when local inundation levels increase, or under the return flow of the tsunami toward the sea.

The relative risk index associated with the integrity of the hospital building, indicated as RRI_{bldg}, looks to evaluate, in a simple way, the performance of a building subjected to the three main tsunami loading components, i.e., hydrodynamic loading, scouring and debris impact, as follows:

$$RRI_{\text{bldg}} = \max\left(RRI_{\text{struct}}, RRI_{\text{scour}},\ RRI_{\text{debris}}\right), \tag{2}$$

where $RRI_{\text{struct.}}$ represents the ability of the structural system to resist the overall tsunami hydrodynamic force (including debris damming), RRI_{scour} represents the ability of the building foundation system to resist scouring for the expected inundation, and RRI_{debris} represents the capacity and redundancy of the structure to resist debris impact from movable objects located within the hospital facility and in the surrounding areas. It is noted that each *RRI* component of RRI_{bldg} takes values between 0 (no risk) and 1 (high risk).

A main difference between RRI_{bldg} and other established tsunami building vulnerability indices for tsunami, is that RRI_{bldg} is based on a simplified assessment of the building failure and damage mechanisms, evaluated using physics and engineering based formulations. This is significantly different from, for example, the well-established PTVA relative

vulnerability index of Papathoma and Dominey-Howes. (2003) and Dall'Osso et al. (2016), which is constructed from a set of characteristics of the building that are thought to affect its tsunami resistance, combined through a weighting based on expert judgment.

Index for Structural Performance Under Hydrodynamic Loading RRI_{struct}

Tsunami hydrodynamic forces typically impact the lower floors of a building and generate large shear forces on the vertical elements of the structure, (i.e. the columns). Recent studies, (e.g. Alam et al., 2017; Petrone et al., 2017), have shown that in reinforced concrete (RC) structures this can lead to shear failure of columns at the ground storey, which precipitates global collapse if no strengthening measures are adopted. This failure mechanism is assumed in the development of the relative risk index for evaluating structural performance under hydrodynamic loading, RRI_{struct}, which is evaluated from a comparison between the overall lateral hydrodynamic force applied to the structure by the tsunami F_{TSU} and the shear strength of the ground floor columns Q_C as follows:

$$RRI_{struct} = \frac{F_{TSU}}{Q_C}. \tag{3}$$

The tsunami load on a structure F_{TSU} is estimated using the hydrodynamic drag equation in the ASCE 7–16 Standard (ASCE, 2017a), as:

$$F_{TSU} = \frac{1}{2}\rho_s C_d C_{cx} B\left(h_{TSU} u_{TSU}{}^2\right), \tag{4}$$

where ρ_S is the minimum fluid mass density, C_d is the drag coefficient, B is the building width perpendicular to the flow, h_{TSU} is the tsunami inundation depth, u_{TSU} is the tsunami flow velocity, and C_{cx} is the proportion of closure coefficient, (i.e. ratio of the closed facade to the total façade area), with a minimum value of 0.7, adopted in this study. The drag coefficient C_d varies based on the B/h ratio (ASCE, 2017a). The shear strength of the ground floor columns Q_C is estimated as the sum of the nominal design shear strength of the ground floor columns, Q_{CS}, as follows:

$$Q_C = N_{SC} * Q_{SC}, \tag{5}$$

where N_{SC} indicates the number of columns along the side of the building perpendicular to the tsunami flow. As this study focuses on RC structures, Q_{CS} is calculated for each column according to the formulae of ACI 318 (ACI, 2005) as follows:

$$Q_{CS} = \phi V_n = \phi\,(V_c + V_s), \tag{6}$$

$$V_c = 0.17\sqrt{f'_c}\, b_w\, d, \tag{7}$$

$$V_s = \frac{A_v f_{yt}\, d}{s}, \tag{8}$$

where V_n is the nominal shear strength, ϕ is the strength reduction factor, V_c and V_s are the concrete and transverse reinforcement components of shear strength, f'_c is the compressive strength of concrete, b_w is the section width, d is the effective depth, A_v is the area of transverse reinforcement, f_{yt} is the transverse reinforcement yield strength, and s is the hoop spacing.

Index for Structural Stability Under Scour, RRI_{scour}

In the aftermath of the 2004 Indian Ocean Tsunami in Sri Lanka, one of the main damage mechanisms observed for multi-story building was the undermining of foundations due to the scouring of sandy soils at the corners of buildings (Dias et al., 2006). This occurred for relatively low tsunami inundation depths, (i.e. 3 m) and resulted in the collapse of end bays of several RC buildings, such as schools. Such failure mechanisms have also been observed in several past events, with RC buildings composed of few frames and with shallow foundations being seen to be the most susceptible to this failure type (EEFIT, 2006; EEFIT, 2011; ASCE, 2017b).

Tsunami design guidelines (ASCE, 2017a) assume that foundations on rock or other non-erodible materials are at no risk of scour. For other types of soil, the scour depth d_{scour} is related to the tsunami inundation depth h_{TSU}, and is estimated from:

$$d_{scour} = \begin{cases} 1.2 * h_{TSU}; & h_{TSU} < 3.05\text{ m}, \\ 3.66\text{ m}; & h_{TSU} \geq 3.05\text{ m}. \end{cases} \tag{9}$$

Equation 9 provides a simple empirical prediction based on observations of local scour depths and estimated flow depths for different sediment types in the aftermath of the 2011 Tohoku tsunami (Tonkin et al., 2014). In ASCE 7–16 the extent (length) of the scour hole around corner foundations l_{scour} (see **Figure 2**) is dependent on the soil type and is calculated as follows:

$$l_{scour} = \begin{cases} d_{scour}, & \text{for cohesive soils}, \\ 3d_{scour}, & \text{for noncohesive soils}. \end{cases} \tag{10}$$

This approach requires soils to be classified as cohesive or non-cohesive. No indication is however provided in the ASCE 7–16 Standard or accompanying commentary, as to the procedure to be followed for this classification. For the RRI_{scour} it is proposed that a simple soil analysis, (i.e. particle size distribution analysis through sieving) be used as the basis for the classification, whereby: 1) *Non-cohesive or granular soils*, (e.g. gravels and sands), defined as those with less than 50% of fines content as per ASTM D2487–17 (USCS)–if the fines content is higher than 12% and less than 50%, then the soil is coarse grained though controlled by the fine soil nature, i.e., non-cohesive; 12% fines content is usually considered as a reference percentage below which soils are defined as purely granular; 2) *Cohesive soils*, (e.g. silts and clays), defined as those with more than 50% of fines content. If soil analysis data at the building site are not available, simple assumptions should be made to classify the soils based on local knowledge.

The calculation of d_{scour} and l_{scour} is instrumental for predicting how many of the building foundations are affected by scour and the corresponding loss of bearing capacity. The tsunami resistance of the foundations depends on the type of foundation, i.e., deep or shallow foundations, and the number of foundation elements affected. Empirical observations from past events indicate that deep pile foundations generally provide

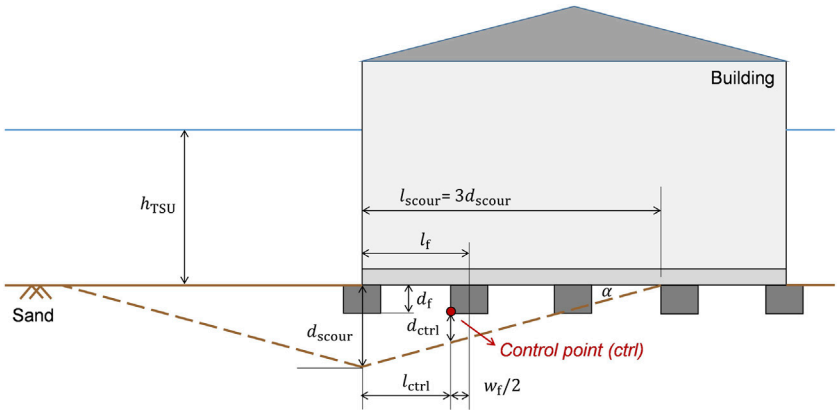

FIGURE 2 | Example sketch illustrating the effects around building with shallow foundations on noncohesive soils and the calculations for the second footing from the left corner.

adequate tsunami resistance, while buildings with shallow spread footings are likely to experience failure, especially at the building corners. Hence, in the development of *TRRI* a focus is placed on characterizing the impact of scour on shallow foundations. An approximate but quantitative procedure is proposed for calculating RRI_{scour} based on geotechnical engineering practice and is illustrated by the flowchart in **Figure 3**.

For simple pad foundations, the overall design load-bearing capacity of the system can be estimated by multiplying the ultimate bearing capacity of individual pad foundations q_f by the number of footings n_f:

$$Q_f = n_f * q_f = SF_d * W, \tag{11}$$

where W is the weight of the building plus loads and SF_d is the design safety factor. Typically, a large safety factor SF_d is adopted foundation design in order to account for the uncertainty related to the soil properties and behavior. For example, a common safety factor for shallow foundations is $SF_d = 2$. Using **Eq. 11**, the design load-bearing capacity of a pad foundation normalized to the building weight, q_f/W, can be estimated as:

$$\frac{q_f}{W} = \frac{SF_d}{n_f}, \tag{12}$$

when d_{scour} is larger than the foundation depth d_f, the foundations need to be checked for loss of bearing capacity. In this paper a minimum depth d_f of 1 m is considered for shallow foundations. Depending on the extent of the local scour l_{scour} along both sides of the building (x and y directions), a number of foundation supports $n_{f,scour}$ might be affected. Foundation pads are assumed to be placed at a distance l_f, which corresponds to the bay length. The depth d_{scour} is assumed to occur at the corner of the building. As shown in **Figure 2**, half of the scour hole length (l_{scour}) is assumed to extend from the point of maximum scour depth (in the corner). Due to the formulations used, the larger the value of d_{scour}, the larger the value of l_{scour} and greater the number of affected footings $n_{f,scour}$. A foundation is assumed to fail if, at the pad edges, the relevant scour hole depth equals or exceeds that of the foundation. This assumption considers the load bearing capacity of the soil beneath the foundation, (which is spreading the foundation loading outwards and downwards), to be compromised.

When subjected to scour, the load-bearing capacity of the foundation system is reduced and is estimated as that deriving solely from those foundations that have not been affected by scour, i.e.,:

$$\left(n_f - n_{f,scour}\right) * q_f = SF_{scour} * W. \tag{13}$$

In **Eq. 13**, SF_{scour} is the reduced design safety factor that accounts for the effects of local scour around the foundations, and can be determined as follows:

$$SF_{scour} = \frac{\left(n_f - n_{f,scour}\right) * q_f}{W} \quad \rightarrow \quad \frac{SF_{scour}}{SF_d} = \frac{n_f - n_{f,scour}}{n_f}. \tag{14}$$

Having evaluated the reduced design safety factor, RRI_{scour} can be determined following the flowchart presented in **Figure 3**, and from **Eq. 15**:

$$RRI_{scour} = \begin{cases} 1; & SF_{scour,min} \le 1, \\ 1 - \dfrac{SF_{scour,min}}{SF_d}; & SF_{scour,min} > 1. \end{cases} \tag{15}$$

where $SF_{scour,min}$ is the minimum value of SF_{scour} along both sides of the building. For $SF_{scour} \le 1$, the foundations are unlikely to be able to carry the gravity loads, i.e., $RRI_{scour} = 1$. This means that when the number of affected foundation supports, $n_{f,scour}$, along any side of the building is equal or greater than 50% of the total number of foundation supports n_f along that side of the building, the foundation system is considered at risk of failure, i.e., $RRI_{scour} = 1$.

Index for the Capacity and Redundancy of the Structure to Resist Debris Impact, RRI_{debris}

Generally, tsunamis transport a large volume of debris, including trees, cars, containers, utility poles and wood-frame houses. The perimeter structural components that are oriented perpendicular to the direction of the flow are at the greatest risk of impact. For

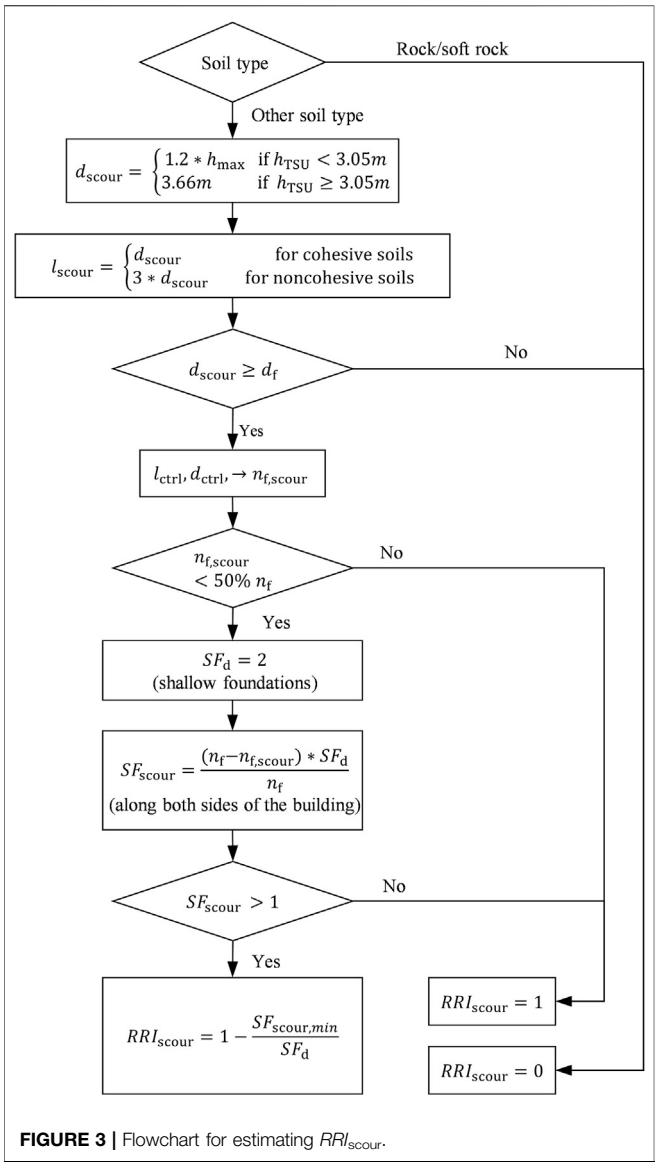

FIGURE 3 | Flowchart for estimating RRI_{scour}.

instance, the loss of a perimeter column may compromise the ability of a structure to support gravity loads. The ASCE 7–16 Standard (ASCE, 2017a) provides a framework for the calculation of the impact forces determined by debris. This includes the effects of the impact by floating wood poles, logs and vehicles, which should be taken into account when tsunami depths are larger than 0.9 m. RRI_{debris} is presented in this paper for the common case where debris consists mainly of logs (or similar). However, by changing the debris impact loads, RRI_{debris} can be modified to account for potential impacts from shipping containers, ships, barges and other large objects. Such sized debris should be considered if the hospital is in close proximity to a port or container yard.

In the RRI_{debris} evaluation, the maximum instantaneous debris impact force (F_{ni}) is first calculated using the impulse-momentum based formulation in the ASCE 7–16 Standard:

$$F_{ni} = C_0 u_{TSU} \sqrt{k m_d}, \tag{16}$$

where C_0 is the orientation coefficient (given as 0.65 by ASCE 7–16), u_{TSU} is the maximum tsunami flow velocity at the building site. k is the effective stiffness of the impacting debris and m_d is the mass of the debris. A minimum weight of 454 kg and minimum log stiffness of 61,300 kN/m are nominal values assumed in the ASCE 7–16 Standard.

The debris impact of a log is a dynamic event. However, an equivalent static approach can be used by multiplying the debris force in **Eq. 17** by a dynamic response factor R_{max}. The latter can be estimated based on the ratio of the impact duration to natural period of the impacted structural element. The impulse duration t_d is given in ASCE 7–16 as follows:

$$t_d = \frac{2 m_d u_{TSU}}{F_{ni}}. \tag{17}$$

Considering an exterior column of a RC building, the natural period of the column (T_{col}) can be estimated assuming fixed end boundary conditions:

$$T_{col} = 2\pi \left[\frac{L^2}{22.373} \right] \sqrt{\frac{\rho}{EI}}, \tag{18}$$

where L is the unbraced column length, ρ is the column mass per unit length, E is the modulus of elasticity of concrete and I is the second moment of area of the column section (Robertson, 2020). ASCE 7–16 *Table 6.11-1* gives the values of the dynamic response factor R_{max} based on the ratio t_d/T_{col}. The equivalent static load for debris impact F_i is calculated as:

$$F_i = R_{max} F_{ni}. \tag{19}$$

The force given by **Eq. 19** should not exceed the force from the alternative simplified impact load $F_{i,max}$, given in ASCE 7–16 Standard as:

$$F_{i,max} = 1,470 * C_0\,, \tag{20}$$

where C_0 is the orientation coefficient, taken as 0.65 (ASCE, 2017a). Furthermore, the value obtained in **Eq. 20** can be reduced by 50%, (i.e. 478 kN), if the site is not exposed to impact by containers, ships and barges. Therefore the debris impact force F_{debris} is estimated as:

$$F_{debris} = \min\left(F_i, F_{i,max}\right). \tag{21}$$

If F_{debris} exceeds the shear strength of the considered column, $Q_{SC,}$ (calculated using **Eq. 6**), then the structural system is at risk of local collapse and potential loss of stability, i.e., $RRI_{debris} > 0$.

The redundancy present in the structure can be beneficial to the stability of the building. In the context of RC structures, RRI_{debris} is calculated by taking the ratio between the number of impacted columns over the total number of columns present in the seaward side of the building. As the number of impacted columns cannot be predicted, it is assumed that two vertical columns (probably the corner columns) located within the seaward face of the building might fail due to debris impact. This assumption is based on observations that debris impact can be particularly common and severe for exposed corner columns

TABLE 1 | Fac-simile of the paired comparison questionnaire.

Which system is more critical in case of a tsunami?	System 1	System 2	System 3	...	System n
System 1		R	C	=	
System 2					
System 3					
...					
System n					

of frames (EEFIT, 2006). Therefore, RRI_{debris} is calculated as follows:

$$RRI_{\text{debris}} = \frac{2}{N_{\text{SC}}}. \tag{22}$$

Index Representing Risk to Critical Unit Functionality, RRI_{funct}

RRI_{funct} looks to represent the risk to continued function of a critical unit after a tsunami. The index is based on the location of the critical unit within the hospital complex with respect to the tsunami inundation. It is assumed that if the critical unit is inundated, the resulting damage to non-structural elements and medical equipment may prevent the unit from being fully operational in the aftermath of the event. RRI_{funct} is therefore binary, taking a value of zero if the critical unit lies outside the inundation zone or is located in a storey of the building above the local inundation depth, or 1 otherwise.

Index Representing Tsunami Risk to Lifeline Back-Up Systems, RRI_{bcs}

The loss of essential lifelines such as power, water, wastewater, natural gas, can severely limit the functionality of hospitals and their critical units. For instance, one of the case-study hospitals presented later in the report, i.e., the Mahamodara Teaching Hospital, suffered the failure of backup generator, water supply and sewer systems when it was inundated during the 2004 Indian Ocean Tsunami (Harlan, 2016).

From PAHO (2008) and WHO (2015) it is possible to identify eight main lifeline systems that are required to ensure the functionality of hospital critical units: Power (P), Air conditioning (HVAC), Telecommunications (TLC), Water Supply (WS), Fire Protection (FP), Waste Water (WW), Medical Gas (MG) and Fuel and Gas reserves (FG). Where national or regional lifelines are compromised, as can be the case in a large tsunami, the presence of back-up systems can provide immediate continuity in the aftermath of a disaster, for a few hours or even days. Hence, the proposed index RRI_{bcs} considers whether the back-up systems to lifelines needed for the functioning of critical units are 1) located within the hospital premises and 2) whether they are likely to be damaged under the expected inundation, as follows:

$$RRI_{\text{bcs}} = \frac{P\,w_{\text{P}} + HVAC\,w_{\text{HVAC}} + TLC\,w_{\text{TLC}} + WSw_{\text{WS}} + FP\,w_{\text{FP}} + WW\,w_{\text{WW}} + MG\,w_{\text{MG}} + FG\,w_{\text{FG}}}{w_{\text{P}} + w_{\text{HVAC}} + w_{\text{TLC}} + w_{\text{WS}} + w_{\text{FP}} + w_{\text{WW}} + w_{\text{MG}} + w_{FG}}. \tag{23}$$

where P, $HVAC$, etc. are the critical back-up systems and w_{p}, w_{HVAC}, etc. are the corresponding weights. As for the case of the critical unit functionality, the back-up systems are assumed non-functional if inundated by the tsunami. Hence, P, HVAC, etc., take a value of zero if the relevant back up system is located outside the inundation zone or is in a storey of the building above the local inundation depth, or 1 otherwise. An appropriate evaluation of the back-up system risk requires an understanding of these systems within the local context, and visual surveys play a key role in this. For example, in many hospital complexes the main HVAC systems may be complex mechanical systems with significant plant located within a hospital building, or housed in their own building. Alternatively, the HVAC system can be a distributed system across the hospital, as is seen in hospitals in Sri Lanka, where ventilation and air-conditioning equipment are distributed along the exterior walls of the hospital buildings and localized in each unit.

Evaluation of the back-up system weights also accounts for the local context. The weights are determined by from a ranking of the back-up systems in order of importance for the continued functioning of the critical unit being assessed. This ranking is determined from a structured expert elicitation technique termed *paired comparison*. The paired comparison method is well established, and although simple, it is reproducible, accountable and neutral. In this method, participants are invited to complete a ranking exercise individually without being influenced by an in-depth prior discussion of how critical each back-up system is. Participants are invited to compare every two back-up systems (one in a row and another in the column in the table) and using their judgment to identify which is the more important for the continued functioning of critical hospital units. If they believe the system in the row is more important than the one in the column, they enter "R" in the relevant box. If they believe the contrary is true then "C" is entered into the box. Else if they believe both the back-up systems are of equal importance, " = " is entered into the relevant box (**Table 1**).

The participants' opinions are treated with equal weights. Only the participants who are found to provide very inconsistent responses, such that they appear statistically random are excluded, (i.e. consistent answers are those for which if A > B and B > C then A > C is true). The paired comparison responses are then analyzed using the probabilistic inversion technique, as described in Kraan and Bedford (2005) and implemented in the free-software "UNIBALANCE" (Macutkiewicz and Cooke, 2006). This produces a mean score for each back-up system as well as the standard deviation around this mean score, which represents the level of disagreement within the expert group. These mean scores are adopted as the weights for the different back-up systems in the RRI_{bcs} calculation.

The level of agreement among the participants is examined in three different ways. Firstly, the degree of agreement is estimated by measuring how closely the pattern of the participants pairwise preferences match. Secondly, the degree of concordance is examined by measuring how similar the rank orders are among the group of participants. Thirdly, a chi-square test is used to check whether the group ranking preferences are made at random. Here, *p*-values below 0.05 indicate that the group ranking preferences have a structure and are not random. By contrast, *p*-values above 0.05 suggest a lack of consensus within the group regarding the ranking preferences.

TRRI RAPID VISUAL SURVEY (RVS) FORM

The *TRRI Rapid Visual Survey (TRRI-RVS)* form is developed to assist surveyors in assessing existing health facilities in terms of the integrity of hospital buildings, lifelines and back-up systems that support the service provision and hospital functionality. The *TRRI-RVS* form is presented in the Appendix (see **Supplementary Material**). The Rapid Visual Survey consists of two sections:

1) *Hospital Profile* ("*Form H*"). Through this form, surveyors collect general information about 1) the hospital location; 2) hospital type and hospital capacity, e.g., catchment population; 3) tsunami evacuation plans and disaster response plans; 4) hospital building locations within the healthcare facility; 5) location of critical hospital units within buildings, e.g., ICU, Labor Rooms, Maternity Wards, Pediatric Wards, Operating Theaters; and 6) presence and location of back-up supply systems.
2) *Building Structural and Non-Structural Assessment* ("*Form B*"). Through this form, surveyors gather information about: 1) the hospital building, e.g., number of storeys, year of construction, inter-storey height, and location of critical units; 2) the building surroundings, e.g., presence of containers, perimeter walls and vegetation; 3) building layout and elevation; 4) structural and non-structural systems; 5) The dimensions and structural details of the main structural elements, e.g., RC columns. The technical information is gathered using equipment such as rebar detector, laser distance meter, tape measure, and 3D cameras.

The *TRRI-RVS* form is specifically developed for collecting the attributes of hospital surroundings, buildings, critical units, lifeline and back-up systems required to evaluate *TRRI*. This form is used in the survey of Sri Lankan hospitals used to test the *TRRI* in this paper.

CASE-STUDY APPLICATION: HOSPITALS IN SRI LANKA SOUTHERN PROVINCE

Sri Lanka provides universal healthcare to its people through an established and robust healthcare system. Thanks to this, no major disease outbreaks occurred after the 2004 tsunami (Carballo et al., 2005), which hit two-thirds of the coastline affecting one million people. However, over 17% of all healthcare institutions were severely damaged, causing an estimated £40 M worth of losses (Komesaroff and Sundram, 2006). Over the last 15 years some of the affected health infrastructure of Sri Lanka has been re-built further inland, but some significant hospitals still lie within 2–3 km from the coast and are at potential threat from tsunami inundation. The Sri Lankan Ministry of Health (MoH) in collaboration with World Health Organization (WHO) has been working to strengthen the health sector for emergencies, through the development of a comprehensive national disaster management plan (WHO, 2015). However, this plan comprises capacity building in emergency management and health financing, and does not yet look at the structural, non-structural and functional performance of hospitals in natural hazards. Furthermore, as Sri Lanka is threatened by distal tsunami generated either at the Sunda trench or Makran Subduction zone, the main disaster management approach considered to date is the evacuation of hospitals (DPRD, 2015).

In this case study application, three hospitals in Galle, Matara and Hambantota Districts in Sri Lanka are selected for testing whether the *TRRI* can be used to 1) identify weaknesses in the systems supporting the functionality of critical units in individual hospitals, and 2) as a tool for use in prioritizing interventions for improved functional resilience across a series of hospitals.

The three hospitals selected are the District General Hospital (DGH) in Matara and the base Hospitals (BH) in Balapitiya and Tangalle. These are chosen as they are key hospitals for the Southern Province, geographically distributed across the Province (**Figure 4**) and all located within 400 m from the coast (base Hospitals) or a litte further (approx. 600 m) but near a waterway that discharges into the sea (DGH Matara). The case study application focuses on the five critical units that were indicated as the most important in the case of a disaster by the Disaster Preparedness and Response Division (DPRD) of the Sri Lankan Ministry of Health, Nutrition and Indigenous Medicine. These are: 1) Intensive Care Units (ICU); 2) Operating Theaters (OT); 3) Labor Rooms (LR); 4) Maternity Wards (MW); and 5) Pediatric Wards (PW). In the three hospitals, 19 buildings were found to house these critical units, and were surveyed by a joint team from UCL and University of Moratuwa in April 2019 using the form described in *TRRI Rapid Visual Survey (RVS) Form*.

Thirteen of the buildings are reinforced concrete moment resisting frame structures of 2–4 storeys. These house 85% of all the critical units in these three hospitals. The remaining six buildings are one-storey load-bearing unreinforced masonry (URM) structures (**Figure 5**). These structures are highly vulnerable to tsunami and would not be expected to be in an operational state following tsunami inundation. Hence, this assessment concentrates on the assessment of the 22 critical units housed in the RC buildings. The survey of these buildings highlighted that most of the critical units are located at the ground floor and are therefore at high risk from damage if the tsunami inundation reaches the building. The soil type at each

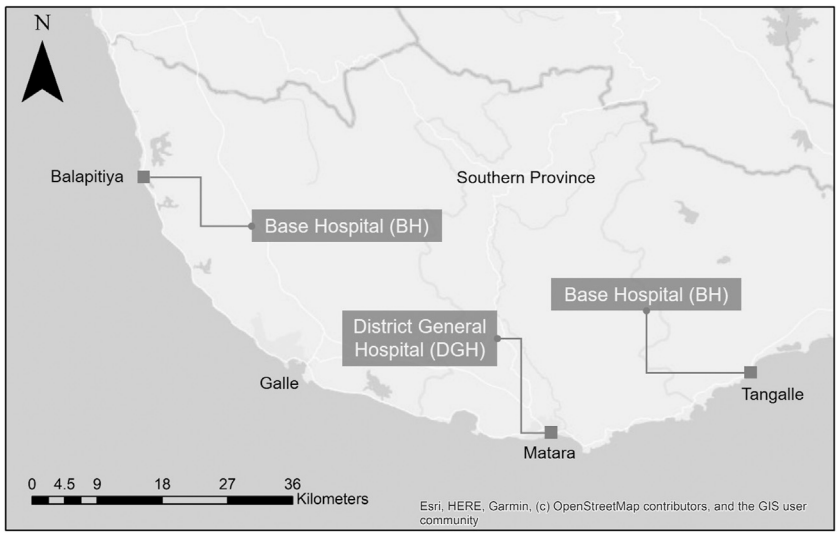

FIGURE 4 | Case-study hospitals in Southern Province, Sri Lanka.

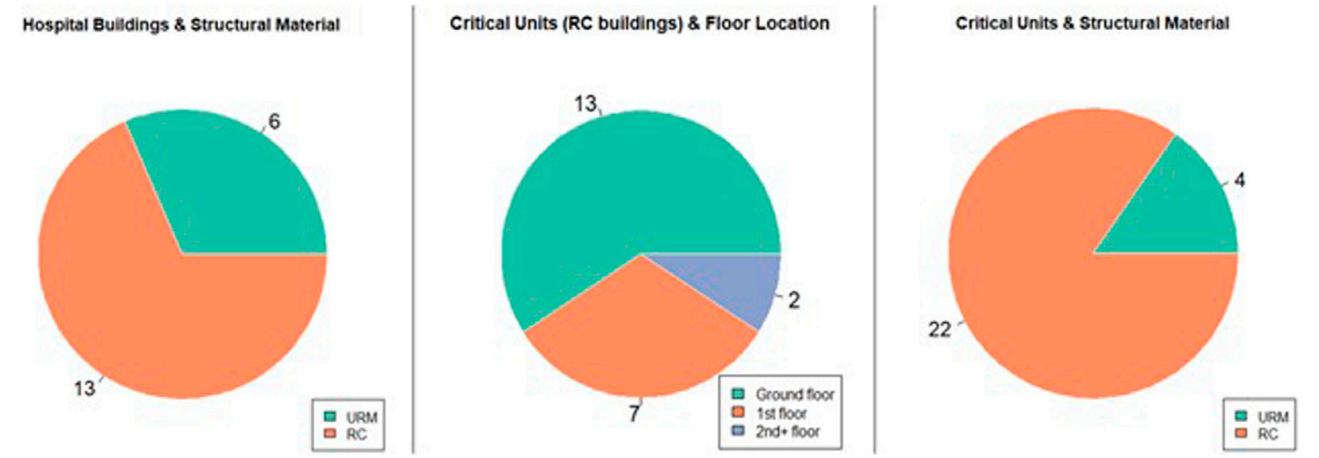

FIGURE 5 | Statistics of the hospital buildings and critical units.

hospital is determined as non-cohesive from observational and borehole data analysis. Hence all buildings are susceptible to scour in this case study application. None of the buildings assessed were located near ports and harbors, and are therefore not exposed to impact from containers, ships or barges. Consequently, the assumption of logs as debris is appropriate for this case study.

The surveys showed the HVAC to be a local system of air conditioning units attached to the walls of critical units. Hence, they will continue to function if the critical unit is not inundated. The location of TLC systems is assumed to be in the hospital administrative offices. This is because Hospital Directors and administrative staff typically have access to the emergency systems for communicating with the national and district-level healthcare networks. Where back-up systems were not recorded during the field survey it is assumed they are missing. As this is detrimental to functional resilience, these back-up systems are still included in the calculation of RRI_{bcs} and contribute to increasing its value. For example, no fire alarms, extinguishers or other fire protection systems were observed in any of the assessed buildings, hence a value of $FP = 1$ is applied for all buildings within the RRI_{bcs} calculation.

Hazard Scenarios

A probabilistic tsunami hazard analysis for the Indian Ocean by (Burbidge et al., 2009) shows that tsunami wave heights along the Sri Lankan coast could reach between 2.9–3.7 m for a return period of 2000 years, with the south-east coast being associated

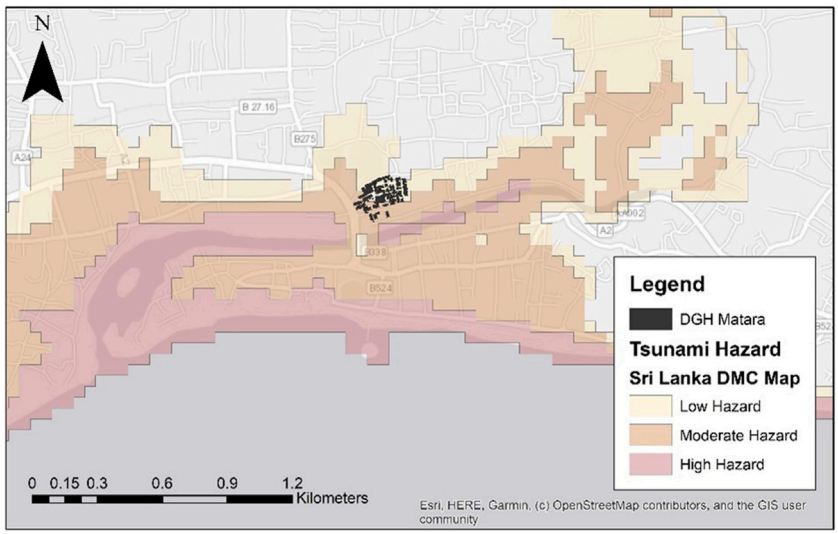

FIGURE 6 | Tsunami hazard map for the city of Matara (DMC, 2012).

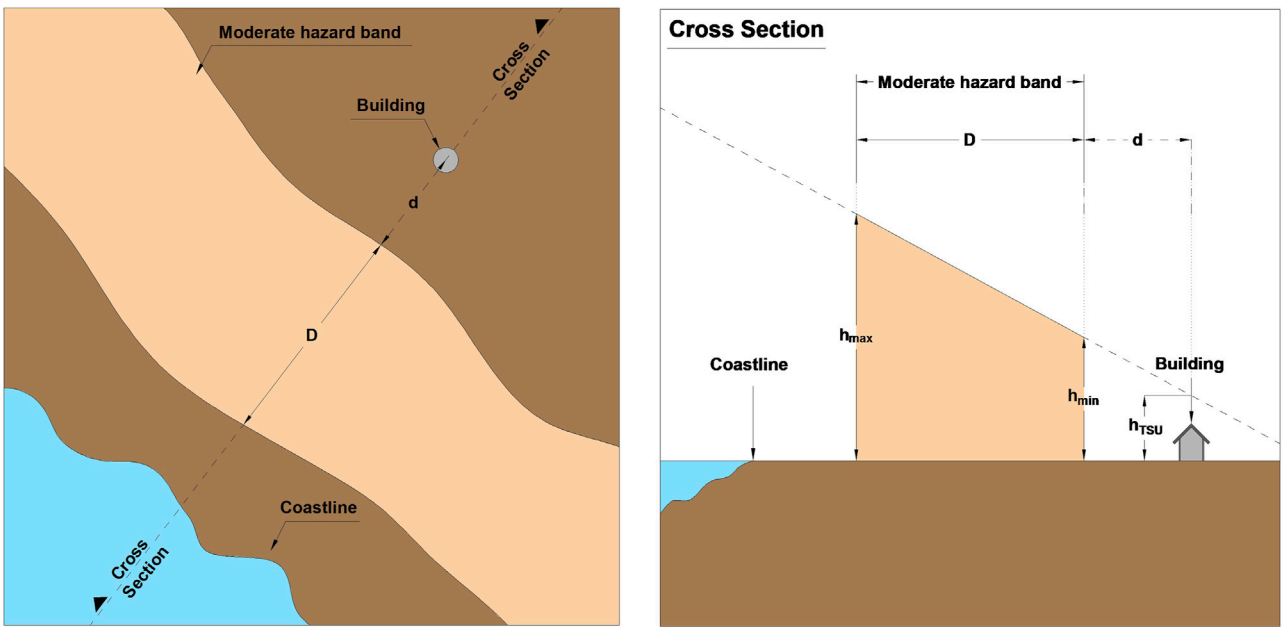

FIGURE 7 | Method for calculating the Hazard Levels.

with the highest hazard. However, this study does not provide the associated probabilistic tsunami onshore inundation depths (that would typically exceed the above) which would be what is required for the TRRI assessment.

A tsunami hazard map for Sri Lanka with associated inundation information was published by the Disaster Management Center (DMC, 2012), part of the Ministry of Public Administration and Disaster Management. This map is however not based on a probabilistic tsunami hazard assessment, but on deterministic inundations predicted by a numerical simulation of the 2004 Indian Ocean Tsunami by (Wijetunge, 2009). The DMC map identifies three distinct tsunami hazard zones along the Sri Lankan coast: 1) low hazard, where the inundation depth, $h_{TSU} < 0.5$ m, 2) moderate hazard, where $0.5\,\text{m} < h_{TSU} < 2\,\text{m}$, and 3) high hazard, where $h_{TSU} > 2$ m. **Figure 6** illustrates the tsunami hazard map for the city of Matara, where DGH Matara is located.

TABLE 2 | Hazard data for the surveyed hospital buildings.

Hospital	Building Id	Total no. of storeys	Critical unit	h_{TSU} (m)		
				Hazard level 1	Hazard level 2	Hazard level 3
Balapitiya	B7	4	ICU (x2)	0.00	0.00	1.37
	B6	3	LR	0.00	0.00	1.13
	B9	1	OT	0.00	0.00	1.05
	B10	3	ICU, OT	0.00	0.00	1.08
	B11	2	ICU, MW	0.00	0.00	1.18
Matara	M1	3	ICU (x2)	0.57	2.08	3.58
	M12	3	OT	0.43	1.93	3.43
	M15	3	ICU	0.43	1.93	3.43
	M27	2	ICU, LR, MW, OT	0.52	2.01	3.51
	M33	1	MW	0.00	0.87	2.37
Tangalle	T1	3	PW (x2)	0.00	0.00	0.35
	T4	2	ICU	0.00	0.00	0.67
	T9	2	MW (x2)	0.00	0.29	1.79

In the absence of probabilistic tsunami onshore inundation information and a detailed topographical map, this study employs a simplified approach for the development of three tsunami inundation scenarios to check the performance of TRRI for different hazard intensities. The first realization, indicated as Hazard Level 1, is derived directly from the DMC map and represents the 2004 Indian Ocean Tsunami. It should be noted that the DMC map only defines distinct inundation depths and geographical boundaries for the moderate tsunami hazard zone. Hence, this zone is adopted as a reference for estimating the inundation depth at the hospital building locations. This is done by first drawing a transect indicating the shortest distance between the coast and the building being assessed. A linear relationship is assumed to describe the change in inundation depth along the transect between the seaward and inland boundaries of the moderate hazard zone, as shown in **Figure 7**. The inundation depth at the building location h_{TSU} is then calculated from:

$$h_{TSU} = h_{min} - \frac{d}{D}(h_{max} - h_{min}), \quad (24)$$

where h_{max} and h_{min} are the Hazard Level-based tsunami inundation depths at the edges of the moderate hazard band, D is the width of the moderate hazard zone along the transect, and d is the distance along the transect of the building to the edge of the moderate hazard zone.

The second and third tsunami inundation scenarios, indicated as Hazard Levels 2 and 3, are derived by increasing the inundation depths defining the DMC moderate hazard zone by 1.5 m and 3 m, respectively. By so doing, more severe inundations are produced at the hospital sites in terms of depth and inland extent, helping to demonstrate the methodology. A limitation of such an approach is that the hazard levels do not reflect a specific probability of occurrence. **Table 2** lists the resulting tsunami inundation depths for each buildings.

Weighting of Back-Up Systems for RRI_{bcs}

A small pool of five hospital administrators (doctors) from Sri Lanka participated in the paired comparison of back-up systems for the evaluation of RRI_{bcs}. **Table 3** presents the resulting mean scores, standard deviation, overall ranking and weights for the back-up systems. The p-values of individual participants is found to be less than 0.05, indicating that no participant randomly ranked the back-up systems. The high values of coefficients of concordance (0.73) and agreement (0.47) suggest an overall agreement among the participants regarding the position of each back-up system in the ranking order. The p-value below 0.05 obtained for the chi-square test also indicates that the group ranking preferences have a structure and are not random. In particular, the water supply and electric power systems have the two highest best estimate ranking scores, while fire protection and air conditioning the lowest.

RESULTS OF THE ASSESSMENT OF CRITICAL UNITS FOR SRI LANKAN HOSPITALS

Table 4 presents the values of *TRRI* calculated for the five critical units of the three case-study hospitals, for the three hazard scenarios presented in *Hazard Scenarios*. Under Hazard Level 1, none of the buildings containing critical units in BH Balapitiya and BH Tangalle are subjected to tsunami inundation. Despite this, the RRI_{bcs} values for these hospitals are non-zero due to their both not having any fire protection system, and BH Tangalle missing power and water back-up systems. For DGH Matara, the values of RRI_{bldg} indicate that only building M15 would be likely to collapse due to scour ($RRI_{scour} = 1$, see **Table 5**), with the other buildings not suffering major damage, (i.e. $RRI_{bldg} \leq 0.5$). Despite

TABLE 3 | Summary of results for the performed rankings.

Back-up systems	Weight mean	Weight st. Dev
Electric power (EP)	0.81	0.11
Water supply (WS)	0.80	0.15
Telecommunications (TLC)	0.62	0.22
Medical gas (MG)	0.52	0.21
Fuel and gas services (FG)	0.37	0.26
Wastewater (WW)	0.36	0.20
Fire protection (FP)	0.25	0.21
Air conditioning (HVAC)	0.20	0.14

TABLE 4 | Summary of *TRRI* calculated for the critical units under three hazard levels.

Unit	Bldg id	Floor	Hazard level 1				Hazard level 2				Hazard level 3			
			Bldg	Funct	Bcs	*TRRI*	Bldg	Funct	Bcs	*TRRI*	Bldg	Funct	Bcs	*TRRI*
ICU	B11	GF	0.0	0.0	0.2	0.2	0.0	0.0	0.3	0.3	1.0	1.0	0.5	1.0
ICU	M15	GF	1.0	1.0	1.0	1.0	1.0	1.0	1.0	1.0	1.0	1.0	1.0	1.0
ICU	T4	GF	0.0	0.0	0.5	0.5	0.0	0.0	0.8	0.8	0.1	1.0	1.0	1.0
ICU	B10	GF	0.0	0.0	0.2	0.2	0.0	0.0	0.4	0.4	0.5	1.0	0.5	1.0
ICU	M27	GF	0.2	1.0	1.0	1.0	0.7	1.0	1.0	1.0	1.0	1.0	1.0	1.0
ICU	B7	1 F	0.0	0.0	0.2	0.2	0.0	0.0	0.4	0.4	1.0	0.0	0.5	1.0
ICU	M1	1 F	0.5	0.0	1.0	1.0	1.0	0.0	1.0	1.0	1.0	1.0	1.0	1.0
ICU	M1	1 F	0.5	0.0	1.0	1.0	1.0	0.0	1.0	1.0	1.0	1.0	1.0	1.0
ICU	B7	2 F	0.0	0.0	0.2	0.2	0.0	0.0	0.4	0.4	1.0	0.0	0.5	1.0
LR	B6	GF	0.0	0.0	0.2	0.2	0.0	0.0	0.4	0.4	0.3	1.0	0.5	1.0
LR	M27	GF	0.2	1.0	1.0	1.0	0.7	1.0	1.0	1.0	1.0	1.0	1.0	1.0
MW	M33	GF	0.0	1.0	1.0	1.0	1.0	1.0	1.0	1.0	1.0	1.0	1.0	1.0
MW	T9	GF	0.0	0.0	0.5	0.5	0.0	1.0	0.8	1.0	0.6	1.0	1.0	1.0
MW	M27	1 F	0.2	0.0	1.0	1.0	0.7	0.0	1.0	1.0	1.0	0.0	1.0	1.0
MW	T9	1 F	0.0	0.0	0.5	0.5	0.0	0.0	0.8	0.8	0.6	0.0	1.0	1.0
MW	B11	1 F	0.0	0.0	0.2	0.2	0.0	0.0	0.3	0.3	1.0	0.0	0.5	1.0
OT	B9	GF	0.0	0.0	0.2	0.2	0.0	0.0	0.3	0.3	0.3	1.0	0.4	1.0
OT	M27	GF	0.2	1.0	1.0	1.0	0.7	1.0	1.0	1.0	1.0	1.0	1.0	1.0
OT	B10	GF	0.0	0.0	0.2	0.2	0.0	0.0	0.4	0.4	0.5	1.0	0.5	1.0
OT	M12	2 F	0.2	0.0	1.0	1.0	0.6	0.0	1.0	1.0	1.0	0.0	1.0	1.0
PW	T1	GF	0.0	0.0	0.5	0.5	0.0	0.0	0.8	0.8	0.0	1.0	1.0	1.0
PW	T1	1 F	0.0	0.0	0.5	0.5	0.0	0.0	0.8	0.8	0.0	0.0	1.0	1.0

TABLE 5 | Summary of RRI_{bldg} calculated for the critical units under three hazard levels.

Unit	Bldg id	Floor	Hazard level 1				Hazard level 2				Hazard level 3			
			Struct	Debris	Scour	Bldg	Struct	Debris	Scour	Bldg	Struct	Debris	Scour	Bldg
ICU	B11	GF	0.0	0.0	0.0	0.0	0.0	0.0	0.0	0.0	0.3	1.0	1.0	1.0
ICU	M15	GF	0.0	0.0	1.0	1.0	0.4	0.2	1.0	1.0	1.0	0.2	1.0	1.0
ICU	T4	GF	0.0	0.0	0.0	0.0	0.0	0.0	0.0	0.0	0.1	0.0	0.0	0.1
ICU	B10	GF	0.0	0.0	0.0	0.0	0.0	0.0	0.0	0.0	0.3	0.3	0.5	0.5
ICU	M27	GF	0.1	0.0	0.2	0.2	0.7	0.2	0.4	0.7	1.0	0.2	1.0	1.0
ICU	B7	1 F	0.0	0.0	0.0	0.0	0.0	0.0	0.0	0.0	0.3	0.7	1.0	1.0
ICU	M1	1 F	0.1	0.2	0.5	0.5	0.8	0.2	1.0	1.0	1.0	0.2	1.0	1.0
ICU	M1	1 F	0.1	0.2	0.5	0.5	0.8	0.2	1.0	1.0	1.0	0.2	1.0	1.0
ICU	B7	2 F	0.0	0.0	0.0	0.0	0.0	0.0	0.0	0.0	0.3	0.7	1.0	1.0
LR	B6	GF	0.0	0.0	0.0	0.0	0.0	0.0	0.0	0.0	0.2	0.3	0.3	0.3
LR	M27	GF	0.1	0.0	0.2	0.2	0.7	0.2	0.4	0.7	1.0	0.2	1.0	1.0
MW	M33	GF	0.0	0.0	0.0	0.0	0.6	0.2	1.0	1.0	1.0	0.2	1.0	1.0
MW	T9	GF	0.0	0.0	0.0	0.0	0.0	0.0	0.0	0.0	0.6	0.3	0.3	0.6
MW	M27	1 F	0.1	0.0	0.2	0.2	0.7	0.2	0.4	0.7	1.0	0.2	1.0	1.0
MW	T9	1 F	0.0	0.0	0.0	0.0	0.0	0.0	0.0	0.0	0.6	0.3	0.3	0.6
MW	B11	1 F	0.0	0.0	0.0	0.0	0.0	0.0	0.0	0.0	0.3	1.0	1.0	1.0
OT	B9	GF	0.0	0.0	0.0	0.0	0.0	0.0	0.0	0.0	0.1	0.3	0.3	0.3
OT	M27	GF	0.1	0.0	0.2	0.2	0.7	0.2	0.4	0.7	1.0	0.2	1.0	1.0
OT	B10	GF	0.0	0.0	0.0	0.0	0.0	0.0	0.0	0.0	0.3	0.3	0.5	0.5
OT	M12	2 F	0.1	0.0	0.2	0.2	0.6	0.1	0.4	0.6	1.0	0.1	1.0	1.0
PW	T1	GF	0.0	0.0	0.0	0.0	0.0	0.0	0.0	0.0	0.0	0.0	0.0	0.0
PW	T1	1 F	0.0	0.0	0.0	0.0	0.0	0.0	0.0	0.0	0.0	0.0	0.0	0.0

the good building performance, five of the critical units would be directly inundated ($RRI_{funct} = 1$), and four more critical units would likely be non-functional due to compromised back-up systems ($RRI_{bcs} = 1$). The latter is due to the main back-up systems in this hospital being inundated. The consequence is that under this hazard scenario (and also for Hazard Levels 2 and 3), DGH Matara is predicted to lose functionality in all its critical units. Across the network of these three hospitals, this would mean a reduction of 40–45% in the number of ICU and MW units, and of 50% in the number of LR and OT units. Loss of critical unit functionality at DGH Matara would put particular stress on BH Tangalle, which is the closest hospital to it, and

TABLE 6 | Summary of *TRRI* for the critical units under three hazard levels: baseline scenario and three different What-If (WI) scenarios.

Unit	Bldg id	Floor	*TRRI*—hazard level 1				*TRRI*—hazard level 2				*TRRI*—hazard level 3			
			Base-line	WI1	WI2	WI3	Base-line	WI1	WI2	WI3	Base-line	WI1	WI2	WI3
ICU	B11	GF	0.2	0.1	0.2	0.1	0.3	0.1	0.3	0.1	1.0	1.0	1.0	1.0
ICU	M15	GF	1.0	1.0	1.0	0.1	1.0	1.0	1.0	1.0	1.0	1.0	1.0	1.0
ICU	T4	GF	0.5	0.1	0.5	0.1	0.8	0.1	0.8	0.1	1.0	1.0	1.0	0.1
ICU	B10	GF	0.2	0.1	0.2	0.1	0.4	0.1	0.4	0.1	1.0	1.0	0.5	0.5
ICU	M27	GF	1.0	1.0	1.0	0.1	1.0	1.0	1.0	0.7	1.0	1.0	1.0	1.0
ICU	B7	1 F	0.2	0.1	0.2	0.1	0.4	0.1	0.4	0.1	1.0	1.0	1.0	1.0
ICU	M1	1 F	1.0	0.5	1.0	0.5	1.0	1.0	1.0	1.0	1.0	1.0	1.0	1.0
ICU	M1	1 F	1.0	0.5	1.0	0.5	1.0	1.0	1.0	1.0	1.0	1.0	1.0	1.0
ICU	B7	2 F	0.2	0.1	0.2	0.1	0.4	0.1	0.4	0.1	1.0	1.0	1.0	1.0
LR	B6	GF	0.2	0.1	0.2	0.1	0.4	0.1	0.4	0.1	1.0	1.0	0.5	0.3
LR	M27	GF	1.0	1.0	1.0	0.1	1.0	1.0	1.0	0.7	1.0	1.0	1.0	1.0
MW	M33	GF	1.0	1.0	1.0	1.0	1.0	1.0	1.0	1.0	1.0	1.0	1.0	1.0
MW	T9	GF	0.5	0.1	0.5	0.1	1.0	1.0	0.8	0.1	1.0	1.0	1.0	0.6
MW	M27	1 F	1.0	0.1	1.0	0.1	1.0	0.7	1.0	0.7	1.0	1.0	1.0	1.0
MW	T9	1 F	0.5	0.1	0.5	0.1	0.8	0.1	0.8	0.1	1.0	0.6	1.0	0.6
MW	B11	1 F	0.2	0.1	0.2	0.1	0.3	0.1	0.3	0.1	1.0	1.0	1.0	1.0
OT	B9	GF	0.2	0.1	0.2	0.1	0.3	0.1	0.3	0.1	1.0	1.0	1.0	1.0
OT	M27	GF	1.0	1.0	1.0	0.1	1.0	1.0	1.0	0.7	1.0	1.0	1.0	1.0
OT	B10	GF	0.2	0.1	0.2	0.1	0.4	0.1	0.4	0.1	1.0	1.0	0.5	0.5
OT	M12	2 F	1.0	0.1	1.0	0.1	1.0	0.6	1.0	0.6	1.0	1.0	1.0	1.0
PW	T1	GF	0.5	0.1	0.5	0.1	0.8	0.1	0.8	0.1	1.0	1.0	1.0	0.1
PW	T1	1 F	0.5	0.1	0.5	0.1	0.8	0.1	0.8	0.1	1.0	0.1	1.0	0.1

which has only two ICU units overall (only one in an RC building) and no Operating Theater.

Under Hazard Level 2, BH Balapitiya remains outside the inundation zone, but building T9 of BH Tangalle is subjected to a small inundation of 0.29 m depth. This inundation is insufficient to cause structural damage in this building but does compromise the functionality of one of the Maternity Wards, as this is located at the ground floor of T9. Moreover, all other critical units in BH Tangalle are seen to be at significant risk of functionality loss from damaged back-up systems. Hazard Level 2 imposes a larger inundation depth at DGH Matara, which results in three predicted building collapses (RRI_{bldg} = 1.0). Through analysis of the components of RRI_{bldg} (see **Table 5**), the risk of structural failure from hydrodynamic loading is significantly higher than in Hazard Level 1, but overall building failures are dominated by the effects of scour around the foundations. With almost all the critical units in both BH Tangalle and DGH Matara predicted to be non-operational (see **Table 4**), Hazard Level 2 sees a reduction across the three hospitals of 55% in the number of ICU units, 50% in the number of LR and OT units, and 80% in number of MW units.

When subjected to Hazard Level 3, all critical hospital units would likely be non-operational. As listed in **Table 5**, all hospital units in DGH Matara are located within buildings at significant risk of structural damage and severe scouring at the foundations. At BH Balapitiya, although power, water supply and medical gases would continue to function (RRI_{bcs} = 0.5) (**Table 4**), two buildings (B7 and B11) would be at high risk of collapse due to effects of scour and debris impact (**Table 5**). This would make two ICUs and one MW non-operational, despite their being located on building storeys that would not be inundated by Hazard Level 3. For 64% of the units across the three hospitals RRI_{bcs} = 1, since the backup systems would be compromised. At BH Tangalle, the lack of power and water supply combined with damage to the rest of the back-up systems, results in RRI_{bcs} = 1 for all units. If this can be prevented, BH Tangalle would be able to operate 50% of its the Maternity and Pediatric Wards (since buildings T1 and T9 have RRI_{bldg} = 0 and 0.6, respectively, and their first floors have RRI_{funct} = 0 even for Hazard Level 3–see **Table 4**).

The results of the analysis of *TRRI* for the three hospitals and Hazard Levels shows a high vulnerability of back-up systems and critical units under low levels of tsunami inundation. This is caused by most being located on the ground floor of inundated buildings (see **Table 4**). These two components of *TRRI* are seen to dominate whether or not critical units will be operational after a "small to moderate" tsunami event (Hazard Levels 1 and 2). Note that *TRRI* = 1.0 for nearly half of the units (45% of the total) at Hazard Level 2, although RRI_{bldg} = 1.0 only for 18% of them. Hence, re-positioning critical units and back-up systems to higher floors within the surveyed buildings would improve the functional resilience of the hospitals. Building failure plays an increasing role in the critical unit operationality for "moderate to high" tsunami events (Hazard Levels 2 and 3). At Hazard Level 3, all 22 units have *TRRI* = 1.0, of which 13 units (59%) also have RRI_{bldg} = 1.0. In particular scour of foundations can precipitate building failure. Protection against scour would require the installation of piles or deeper foundations. This is more appropriate as a design improvement for future hospital buildings, since this can be disruptive and expensive as a retrofit intervention.

WHAT-IF SCENARIOS

Given the findings in *Results of the Assessment of Critical Units for Sri Lankan Hospitals*, this section presents a comparison of the

effectiveness of three possible interventions in reducing the immediate loss of operationality of critical units after a tsunami. The intervention effectiveness is examined by running "what-if" scenarios, wherein the intervention is applied to all buildings and *TRRI* is recalculated. The effectiveness of the intervention on each critical unit type is represented as the ratio between the number of functional units for the intervention and baseline scenarios (Note: the baseline is the no-intervention scenario). The "what-if" scenarios considered are:

- What-if 1 (WI1) consists in the relocation of back-up systems to places that are not affected by the tsunami inundation, e.g., by either relocating or elevating the system to be outside the inundation zone. Within this scenario, any missing back-up system, other than Fire Protection and HVAC (as these are co-located with the critical unit) are installed.
- What-if 2 (WI2) consists in the relocation of critical units one storey up from their current position in the building that houses them. Where the unit is already located in the uppermost floor of the building, it is assumed to remain in its current position.
- What-if 3 (WI3) combines the effects of adopting WI1 and WI2, i.e., both relocation of back-up systems and critical units. In this case Fire Protection and HVAC are also installed if missing, and are assumed to be co-located with the newly positioned critical units.

Table 6 presents the *TRRI* resulting from implementation of the three "what-if" scenarios and the baseline (no intervention) scenario for the three Hazard Levels. **Table 7** summarizes the effectiveness of each "what-if" scenario in increasing the number of operational critical units after a tsunami, as compared to the baseline scenario. In **Table 7**, the effectiveness of the "what-if" scenario, indicated as E_{WI}, is calculated for each critical unit type, as follows:

$$E_{WI} = \frac{n_{\mathrm{ou,\,WI}} - n_{\mathrm{ou,\,BL}}}{n_{\mathrm{u}}}, \tag{25}$$

where n_{u} is the total number of units (for each type), $n_{\mathrm{ou,WI}}$ is the number of operational units in the "what-if" scenario, and $n_{\mathrm{ou,BL}}$ is the number of operational units for the baseline scenario.

From **Tables 6** and **7** it is observed that moving the back-up systems to a safe location (WI1) significantly improves the number of operational MW, OT and PW available after tsunami for all Hazard Levels, but is not effective in improving the number of operational ICU and LR units with respect to the baseline for tsunami above Hazard Level 1. This is because many critical units remain vulnerable to direct tsunami inundation.

Implementation of WI2 provides no/little improvement over the baseline scenario for Hazard Levels 1 and 2, as the failure of back-up systems in DGH Matara and BH Tangalle compromise their critical unit operationality and BH Balapitiya is not inundated at these Hazard Levels. However, for Hazard Level 3, despite inundation of BH Balapitiya, some of the back-up systems are not compromised and by elevating the critical units their risk of direct inundation is reduced and their operationality maintained.

An increased effectiveness is observed for What-If scenario 3, as compared to either WI1 or WI2 individually. The combined intervention on back-up systems and critical units is more beneficial than the sum of their individual effects. This is because in WI3 any missing back-up systems are added to the hospital buildings, and the HVAC and Fire Protection systems are moved to upper levels with the critical units, thus joining the other back-up systems in being in a safe location. This results in RRI_{bcs} values close to zero, which when combined with the reduced risk of critical unit inundation, results in 95%, 82%, and 64% of all critical units being operational under Hazard Levels, 1, 2, and 3, respectively. It is highlighted that even in WI3, ICU and OT remain at significant risk from tsunami of Hazard Level 3, with only one quarter of the units predicted to remain operational. To further increase their tsunami resilience, interventions would be needed on the buildings that house these critical units, in order to improve their structural and foundation systems. The *TRRI* analysis prioritizes buildings M1, M15, and M27 in DGH Matara for such interventions, as these are predicted to suffer heavy damage and/or collapse under the tsunami hazard scenarios, even though the risk to back-up systems and critical units can be reduced through WI3.

The suggested interventions are not based on financial considerations or other constraints, and are applied to all three hospitals. However, it is clear that the *TRRI* and proposed efficiency measure (E_{WI}) can be adopted for other What-If scenarios that could apply more targeted or different interventions on single hospitals or buildings to optimize the cost-to-benefit. The advantage of the *TRRI* is that such interventions can be explored across single or multiple hospitals in a manner that is not computationally expensive and does not require high levels of technical expertise.

CONCLUSION

This paper presents a new tsunami relative risk index (*TRRI*) for the assessment of risk to critical units in hospitals exposed to tsunami inundation. The *TRRI* is a quantitative index that considers tsunami risk to 1) the hospital buildings housing critical units, with tsunami hydrodynamic loading, debris impact and scour considered, 2) the critical units themselves and 3) the critical back-up systems that support the functioning of critical units. Each component of tsunami risk is evaluated on a scale of 0 (no risk) to 1 (high risk), and the overall risk to the

TABLE 7 | Summary of the effectiveness of each What-If (WI) scenario.

Unit	E_{WI}—hazard level 1			E_{WI}—hazard level 2			E_{WI}—hazard level 3		
	WI1	WI2	WI3	WI1	WI2	WI3	WI1	WI2	WI3
ICU	0.22	0	0.44	0	0	0.11	0	0.11	0.22
LR	0	0	0.50	0	0	0.50	0	0.50	0.50
MW	0.20	0	0.20	0.20	0.20	0.40	0.20	0	0.40
OT	0.25	0	0.50	0.25	0	0.50	0	0.25	0.25
PW	0[a]	0[a]	0[a]	0[a]	0[a]	0[a]	0.50	0.50	1.0

[a]*indicates that all critical units were predicted as functional in the baseline scenario for the Hazard Level considered.*

critical unit is taken as the highest value from the three components. A methodology is provided for the simple evaluation of the tsunami risk indices for each component that draws upon engineering principles and practice, physical interpretation of tsunami risk and expert elicitation. The *TRRI* approach is tested for a case study of three hospitals in Sri Lanka, wherein the *TRRI* is used to assess the number of critical units (that are housed in reinforced concrete buildings) remaining operational after tsunami inundations of three intensities. It is demonstrated that the *TRRI* approach allows the identification of the drivers of loss of operationality of critical units under the different hazard scenarios. The *TRRI* analysis for the three hospitals show a high functional vulnerability of back-up systems and critical units under low levels of tsunami inundation. These findings can inform decisions to be made as to interventions for improving the operational resilience of critical units within a single hospital complex, as well as across a network of hospitals to ensure health service provision. The latter is demonstrated by conducting a series of "what-if" scenarios for different interventions on the case study hospital network and re-calculating the *TRRI* values for each critical unit. Comparison of the number of critical units predicted to be functional after a tsunami under the baseline scenario, (i.e. no intervention) and the different "what-if" scenarios, allows the identification of individual and combined interventions in improving the tsunami resilience of healthcare provision across the hospital system. For the three hospitals in Sri Lanka, relocating back-up systems and units to safe locations would be an effective intervention; however, under large tsunami events the hospital buildings and their foundations are predicted to suffer heavy damage and/or collapse.

DATA AVAILABILITY STATEMENT

The raw data supporting the conclusion of this article will be made available by the authors, without undue reservation.

AUTHOR CONTRIBUTIONS

TR, MB, and PD developed the aim, goals and scope of this study. MB, JP, DR, CS, and HH carried out the fieldwork activity in Sri Lanka. TR, MB, JP, PD, SLQ, and II developed the methodology. MB and JP developed the R script to perform the analysis. MB, TR, JP, and PD contributed to writing the text and producing the figures presented.

FUNDING

This work is part of the project titled "Hospital Engineering Assessment for Resilience to Tsunami and Storm surge—Sri Lanka" (HEARTS-SL), funded by Research England (Award 177,813) via Global Challenges Research Fund. The project grant was awarded to Prof Tiziana Rossetto.

ACKNOWLEDGMENTS

The authors acknowledge the support of Disaster Preparedness and Response Division (Ministry of Health, Nutrition and Indigenous Medicine, Sri Lanka) in providing valuable advice and assistance; and also the cooperation of the directors of the hospitals surveyed. Other members that are acknowledged for their support and help are Dr. Carmine Galasso and Prof Ian Eames from UCL, and Eng. Devmini Kularatne, Eng. Ishani Shehara, Mr. S. Harisuthan and Mr. Bahirathan Koneswaran from University of Moratuwa.

SUPPLEMENTARY MATERIAL

The Supplementary Material for this article can be found online at: https://www.frontiersin.org/articles/10.3389/feart.2021.626809/full#supplementary-material.

REFERENCES

ACI (2005). *Building code requirements for structural concrete (ACI 318-05) and commentary (ACI 318r-05)*. Farmington Hills, MI: ACI Committee 318, American Concrete Institute.

Alam, M. S., Barbosa, A. R., Scott, M. H., Cox, D. T., and van de Lindt, J. W. (2017). Development of physics-based tsunami fragility functions considering structural member failures. *ASCE J. Struct. Eng.* 144 (3), 04017221. doi:10.1061/(ASCE)ST.1943-541X.0001953

ASCE (2017a). *Minimum design loads and associated criteria for buildings and other structures*. Reston, VA, USA: ASCE/SEI 7-16.

ASCE (2017b). *Tohoku, Japan, earthquake and tsunami of 2011: lifeline performance*. Editor K. Alex Tang (Reston, VA, USA:Technical Council on Lifeline Earthquake Engineering).

Burbidge, D. R., SCummins, P. R., SLatief, H., SMleczko, R., SMokhtari, M., SNatawidjaja, D., et al. (2009). *A probabilistic tsunami hazard assessment of the Indian Ocean Nations*. Canberra, NSW, Australia: Geoscience Australia, Australian Government, Professional Opinion 2009/11.

Carballo, M., Heal, B., and Hernandez, M. (2005). Psychosocial aspects of the tsunami. *J. R. Soc. Med.* 98, 396. doi:10.1258/jrsm.98.9.396

Casarotti, C., Pavese, A., and Peloso, S. (2009). *"Seismic response of the san salvatore hospital of coppito (L'Aquila) during the 6th April 2009 earthquake", progettazione sismica*. Pescara, Italy: Special Abruzzo, 159–172.

Dall'Osso, F., Dominey-Howes, D., Tarbotton, C., Summerhayes, S., and Withycombe, G. (2016). "Revision and improvement of the PTVA-3 model for assessing tsunami building vulnerability using "international expert judgment": introducing the PTVA-4 model". *Nat. Hazards* 83, 1229–1256. doi:10.1007/s11069-016-2387-9

Del Zoppo, M., Rossetto, T., Di Ludovico, M., Prota, A., and Robertson, I. N. (2020). Structural response under tsunami-induced vertical loads, Proceedings of the 17th World Conference on Earthquake Engineering, Sendai, Japan, 13–18 September.

Di Sarno, L., Chioccarelli, E., and Cosenza, E. (2011). Seismic response analysis of an irregular Base isolated building. *Bull. Earthquake Eng.* 9 (5), 1673–1702. doi:10.1007/s10518-011-9267-1

Dias, P., Dissanayake, R., and Chandratilake, R. (2006). Lessons learned from tsunami damage in Sri Lanka. *Proc. Inst. Civil Eng.—Civil Eng.* 159, 74–81. doi:10.1680/cien.2006.159.2.74

DMC (2012). *Tsunami Hazard Map. Coastal Research Design, Coast Conservation and Resource Management Department with the assistance from Disaster Management Centre*. Srilanka. Available online at: http://www.dmc.gov.lk/images/hazard/hazard/Tsunami.html (Accessed March 22, 2021).

DPRD (2015). *"Standard operating procedures for tsunami warnings." disaster preparedness and response division, Ministry of health, nutrition and indigenous medicine*. Colombo, Srilanka: DPRD.

EEFIT (2006). *The Indian Ocean Tsunami of 26 december 2004: mission findings in Sri Lanka and Thailand Earthquake engineering field investigation team*. London, United Kingdom: Institution of Structural Engineers.

EEFIT (2011). *"The Mw9.0 tōhoku earthquake and tsunami of 11th march 2011. A field report by EEFIT." earthquake engineering field investigation team*. London, United Kingdom: Institution of Structural Engineers.

EEFIT (2013). *"Recovery two years after the 2011 Tōhoku earthquake and tsunami: a return mission report by EEFIT." Earthquake Engineering Field Investigation Team*. London, United Kingdom: Institution of Structural Engineers.

FEMA (1997). *"Commentary on the guidelines for the seismic rehabilitation of buildings". FEMA 274 NEHRP rehabilitation*. Washington, DC, United States: FEMA.

FEMA (2003). *Incremental seismic rehabilitation of hospital buildings*. Washington, DC, United States: FEMA, 396.

FEMA (2005). *Coastal construction manual*. 3rd edition. Washington, DC, United States: FEMA, 55.

FEMA (2007). *Design guide for improving hospital safety in earthquakes, floods, and high winds*. Washington, DC, United States: FEMA, 577.

Harlan, E. (2016). *After the tsunami, a Sri-Lanka hospital springs to life. A wave of compassion*. Evanston, IL: The Rotarian.

Kirsch, T., Mitrani-Reiser, J., Bissell, R., Sauer, L., Mahoney, M., Holmes, W., et al. (2010). Impact on hospital functions following the 2010 Chilean Earthquake. *Disaster Med. Public Health Prep.* 4, 122–128. doi:10.1001/dmphp.4.2.122

Komesaroff, P. A., and Sundram, S. (2006). Challenges of post-tsunami reconstruction in Sri Lanka: health care aid and the Health Alliance. *Med. J. Aust.* 184, 23–26. doi:10.5694/j.1326-5377.2006.tb00091.x1

Kraan, B., and Bedford, T. (2005). Probabilistic inversion of expert judgments in the quantification of model uncertainty. *Manag. Sci.* 51, 995–1006. doi:10.1287/mnsc.1050.0370

Macutkiewicz, M., and Cooke, R. M. (2006). *UNIBALANCE software*. Delft, Netherlands: TU Delft.

MHNI (2015). *Standard operating procedures (SOPs) for the health institutions to respond to tsunami warnings*. Colombo, Sri Lanka: Disaster Preparedness and Response Division, Ministry of Health, Nutrition & Indigenous Medicine.

MLIT (2011). *Further information concerning the design method of safe buildings that are structurally resistant to tsunamis—technical advice No. 2570*. Tokyo, Japan: Ministry of Land, Infrastructure, Transport and Tourism.

PAHO (2008). *Hospital safety index: guide for evaluators*. Geneva, Switzerland: Pan-American Health Organization (PAHO).

Papathoma, M., and Dominey-Howes, D. (2003). Tsunami vulnerability assessment and its implications for coastal hazard analysis and disaster management planning, Gulf of Corinth, Greece. *Nat. Hazards Earth Syst. Sci.* 3 (6), 733–747. doi:10.5194/nhess-3-733-2003

Petrone, C., Rossetto, T., and Goda, K. (2017). Fragility assessment of a RC structure under tsunami actions via nonlinear static and dynamic analyses. *Eng. Structures* 136, 36–53. doi:10.1016/j.engstruct.2017.01.013

Robertson, I. N. (2020). *Tsunami loads and effects: guide to the tsunami design provisions of ASCE 7-16*. Reston, VA: ASCE.

Tonkin, S. P., Francis, M., and Bricker, J. D. (2014). Limits on coastal scour depths due to tsunami. *Int. Efforts Lifeline Earthquake Eng.* 9780784413234 , 671–678.

UNDRR (2015). Sendai framework for disaster risk reduction 2015—2030, UN office for disaster risk reduction. Available online at: https://www.unisdr.org/files/43291_sendaiframeworkfordrren.pdf (Accessed November 4, 2020).

UNISDR (2005). Hyogo framework for action 2005-2015: building the resilience of nations and communities to disasters. World Conference on Disaster Reduction 18-22 January 2005, Kobe. Hyogo, Japan, 18–22 January, 2005. Available online at: https://www.unisdr.org/2005/wcdr/intergover/official-doc/L-docs/Hyogo-framework-for-action-english.pdf (Accessed November 6, 2020).

WHO (2008). *Hospitals should be safe from disasters: reduce risk, protect health facilities, save lives*. Manila, Philippines: WHO Regional Office for the Western Pacific.

WHO (2010). *Safe hospitals in emergencies and disasters: structural, non-structural and functional indicators*. Manila, Philippines: WHO Regional Office for the Western Pacific.

WHO (2015). *Hospital safety index: guide for evaluators*. 2nd ed.. Geneva, Switzerland: World Health Organization https://apps.who.int/iris/handle/10665/258966.

Wijetunge, J. J. (2009). Field measurements and numerical simulations of the 2004 tsunami impact on the south coast of Sri Lanka. *Ocean Eng.* 36 (12-13), 960–973. doi:10.1016/j.oceaneng.2009.06.002

Yeh, H., Barbosa, A. R., Ko, H., and Cawley, J. G. (2014). Tsunami loadings on structures: review and analysis. *Int. Conf. Coastal. Eng.* 1 (34), 4. doi:10.9753/icce.v34.currents.4

Conflict of Interest: The authors declare that the research was conducted in the absence of any commercial or financial relationships that could be construed as a potential conflict of interest.

frontiers in Earth Science

ORIGINAL RESEARCH
published: 01 April 2021
doi: 10.3389/feart.2020.591514

Microzoning Tsunami Hazard by Combining Flow Depths and Arrival Times

Natalia Zamora[1,2]*, *Patricio A. Catalán*[2,3,4], *Alejandra Gubler*[2,3] and *Matías Carvajal*[5,6†]

[1]Barcelona Supercomputing Center - Centro Nacional de Supercomputación, Barcelona, Spain, [2]Research Center for Integrated Disaster Risk Management (CIGIDEN), Santiago, Chile, [3]Departamento de Obras Civiles, Universidad Técnica Federico Santa María, Valparaíso, Chile, [4]Centro Científico Tecnológico de Valparaíso (CCTVal), Valparaíso, Chile, [5]Millennium Nucleus the Seismic Cycle Along Subduction Zones (CYCLO), Valdivia, Chile, [6]Programa de Doctorado en Ciencias Geológicas, Facultad de Ciencias Químicas, Universidad de Concepción, Concepción, Chile

Tsunami hazard is typically assessed from inundation flow depths estimated from one or many earthquake scenarios. However, information about the exact time when such inundation occurs is seldom considered, yet it is crucial for pedestrian evacuation planning. Here, we propose an approach to estimating tsunami hazard by combining tsunami flow depths and arrival times to produce a nine-level, qualitative hazard scale that is translated into a simple tsunami hazard map. To do this, one of the most populated regions of the coast of Chile is considered as the sample site, using a large set of 2,800 tsunamigenic sources from earthquakes with magnitudes in the range M_w 8.6 – 9.2, modeled from generation to inundation at high resolution. Main outcomes show great dependency of the hazard categorization on the tsunami time arrival, and less to the flow depths. Also, these results demonstrate that incorporating different sources of variability such as different earthquake magnitudes and locations as well as stochastic slip distributions is essential. Moreover, this proof-of-concept exercise clearly shows that the qualitative hybrid categorization of the tsunami hazard allows for its more effective understanding, which can be beneficial for designing mitigation strategies such as evacuation planning, and its management.

Keywords: Tsunami hazard, microzoning, arrival times, flow depths, evacuation, slip distributions, earthquakes, central Chile

OPEN ACCESS

Edited by:
Stefano Lorito, Istituto Nazionale di Geofisica e Vulcanologia (INGV), Italy

Reviewed by:
Katsuichiro Goda, Western University, Canada
Alberto Armigliato, University of Bologna, Italy
William Power, GNS Science, New Zealand

***Correspondence:**
Natalia Zamora
natalia.zamora@bsc.es

***Present address:**
Matías Carvajal, Instituto de Geografía, Pontificia Universidad Católica de Valparaíso, Valparaíso, Chile

Specialty section:
This article was submitted to Geohazards and Georisks, a section of the journal Frontiers in Earth Science

Received: *04 August 2020*
Accepted: *28 December 2020*
Published: *01 April 2021*

Citation:
Zamora N, Catalán PA, Gubler A and Carvajal M (2021) Microzoning Tsunami Hazard by Combining Flow Depths and Arrival Times. Front. Earth Sci. 8:591514. doi: 10.3389/feart.2020.591514

1 INTRODUCTION

Tsunamis are natural events that can have a range of disastrous consequences, such as loss of life (Doocy et al., 2013), damage to infrastructure (Charvet et al., 2017; UNISDR, 2018), and triggering morphological changes that can affect the sustainability of coastal environments and communities (Morton et al., 2011; Atwater et al., 2013; Catalán et al., 2015; Hoang et al., 2018; Imamura et al., 2019). Moreover, tsunamis can spread over large portions of the ocean basins where they occur, and their hydrodynamic behavior can vary significantly along the affected coasts. The triggering of a

Abbreviation: ALOS, Global Digital Surface Model "ALOS World 3D-30m (AW3D30)"; CENDHOC, Centro Nacional de Datos Hidrográficos y Oceanográficos de Chile; CIGIDEN, Research Center for Integrated Disaster Risk Management, ANID/FONDAP/15110017; CITSU, Cartas de Inundación por Tsunami; INE, Instituto Nacional de Estadísticas; ONEMI, Oficina Nacional de Emergencia del Ministerio del Interior; SHOA, Servicio Hidrográfico y Oceanográfico de la Armada de Chile.

tsunami can be due to several processes, some of which are not yet fully understood, and the capability to forecast the inundation following a known tsunami source is still undergoing active research.

Partially due to recent tsunami-related disasters, tsunamis have been increasingly recognized by coastal communities throughout the world as potential hazards that need to be accounted for to mitigate the associated risk. The safest approach to minimize risk would be to relocate outside the inundation zone, which would yield zero exposure, yet would be a costly measure and is thus, to some extent, unlikely. Since redesigning coastal settlements is not usually a feasible option, evacuation planning is necessary for risk and loss of life minimization. Indeed, it has been shown that evacuation is the most effective measure to reduce casualties during tsunami events (McAdoo et al., 2006; Makinoshima et al., 2020). As demonstrated by past tsunamis, wave heights, inundation flow depths and inland extent, and arrival times can vary substantially over horizontal spatial scales of a few hundred meters. This means that risk, as a result of exposure and other dependencies, likewise varies over short spatial scales, and should thus be assessed with the corresponding resolution.

To characterize risk, the required first step is to obtain an estimate of the tsunami hazard, both in terms of its magnitude and recurrence. Aided by progressively increasing computational capacities due to new hardware and software, as well as novel numerical implementations, state-of-the-art tsunami numerical models allow for a large number of computations in shorter time, even when the modeling considers tsunami generation, propagation and inundation (e.g. Yamazaki et al., 2009; LeVeque et al., 2011; Macías et al., 2017). As a result of the improved numerical performance, the once standard method of estimating the tsunami hazard based on single (or small number of) worst credible scenarios (Scenario-Based Tsunami Hazard Assessment SBTHA, Tinti et al., 2011; Harbitz et al., 2013) is being gradually superseded by Probabilistic Tsunami Hazard Assessments that considers multiple scenarios with stochastically defined slip distributions (PTHA, e.g. Geist and Parsons, 2006; LeVeque et al., 2016; Park and Cox, 2016; De Risi and Goda, 2017; Davies et al., 2017; Volpe et al., 2019). In the latter, different sources of uncertainty can be included, especially those regarding recurrence rates, source variability and complexity (Grezio et al., 2017; Mori et al., 2018; Sepúlveda et al., 2018).

Regardless of the procedure to generate data, the tsunami hazard assessment follows two steps. First, it is based mostly on tsunami intensity metrics such as the tsunami peak coastal amplitudes (offshore) or inland flow depths. Ideally, other quantities such as tsunami momentum fluxes or velocities should be included also. Second, these tsunami intensity metrics are treated independently, and the focus is set on extreme values. The reason for this is obvious, considering that amplitude and flow depth can be correlated with the damage potential of the event. In some countries like Chile, evacuation plans are derived only from the information available on the tsunami hazard maps, which typically depict the flow depth in meters as a measure of the hazard, which can be difficult to interpret (Cubelos et al., 2019). Moreover, in the Chilean case, these maps are often derived from single scenario modeling (SHOA, 2012), and therefore, they may not consider the unavoidable uncertainties of the tsunami sources.

While considering hydrodynamic quantities such as the flow depths has implications for structural design, it can be less relevant for evacuation purposes, where the tsunami arrival time is of great significance. Yet, arrival times are seldom accounted for in tsunami evacuation maps (Wood and Schmidtlein, 2013), which possibly stems from the notion that evacuation should be instantaneous. While large flow depths obviously can seriously hamper evacuation, it should be noted that evacuation can also be affected when amplitudes or flow depths are small. Even flows of a few decimeters high can block routes, alter the psychological behavior of people, and even hurt them if the flow comes with debris and large speeds. Therefore, it could be argued that arrival time should be the only quantity of interest. However, flow depths are also relevant for the purpose of evacuation planning. Spatial information of flow depths is important for the design process of evacuation routes, (e.g. orientation and routing), or placement and design of potential vertical evacuation shelters. However, despite having detailed information about flow depths, current hazard maps tend to treat it in a binary way, that is, as a proxy to identify whether it is required to evacuate or not (León et al., 2018; Cubelos et al., 2019). Having a high level of detail for flow depths does not necessarily lead to improved insights, as they do not provide sufficient information for the decision on when to evacuate nor provide an estimate of how long it is required to remain outside the inundated area.

To overcome these deficiencies, evacuation studies resort to using agent-based modeling coupled with detailed, phase resolving tsunami modeling (e.g., León et al., 2020, among others). The downside is that, due to the high computational burden, only a small number of scenarios is usually considered, and the results become scenario-dependent and decoupled from the hazard map. Relying on single scenarios for evacuation planning appears to be a step back from the benefits gained by carrying out probabilistic tsunami hazard assessments that accounts for uncertainties of the tsunami sources. For purposes such as integral risk management, it will be useful to incorporate the tsunami arrival time as an additional intensity measure (Park and Cox, 2016; Park et al., 2018). However, providing hazard probabilities may hinder the ability to convey these results in a straightforward manner, which may lead to a lack of awareness or understanding of local tsunami risk by the population, thus hampering tsunami evacuation preparedness.

Tsunami arrival times also vary between events in the same region. The tsunamigenic zone width in Chile (distance between the trench and the coastline) is among the smallest in the world, resulting in very short propagation times. A country-wide assessment by Williamson and Newman (2019) yields times of 15–20 min or less. This has been observed empirically: during the 2010 M_w 8.8 Maule event, the first arrival was reported to be of the order 20 min (Fritz et al., 2011), whereas during the 2014 M_w 8.2 Pisagua tsunami, a 15 min arrival was measured at the Pisagua tide gauge (Catalán et al., 2015). Finally, anecdotal

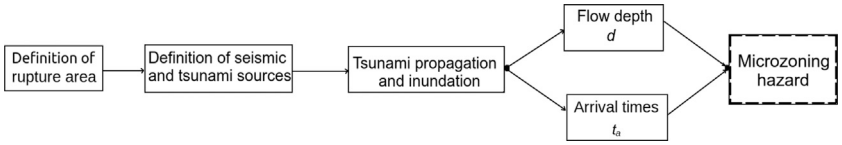

FIGURE 1 | Flowchart summarizing the overall procedure used in this study.

evidence indicates arrivals of about 8–12 min during the 2015 M_w 8.3 Illapel tsunami (Aránguiz et al., 2016). This highlights the importance of conveying the notion of arrival time to the public, but has also emphasized the inevitable limitations and challenges of existing early warning systems. The Chilean tsunami warning system requires a period of at least 3–4 min after the onset of the earthquake to be able to first determine the preliminary source characteristics, based on seismic data (Catalán et al., 2020). This could leave little time to trigger evacuation, and emphasizes the need to account for tsunami arrival times in the mitigation strategies. For example, it has been observed that some coastal communities are unlikely to achieve a complete horizontal evacuation before the tsunami inundation arrives or reaches its maximum level, which can be attributed to a combination of the long distance to higher ground, early tsunami arrival, and spatial conditions that can contribute to an inefficient evacuation (León et al., 2019a, León et al., 2020).

Such challenges have been identified along the central zone of Chile (Zamora et al., 2020), an area that hosts a large coastal population and is highly exposed to large earthquakes (Martínez et al., 2020). From this follows the need to account for standard tsunami intensity metrics (such as flow depth) as well as very short expected arrival times (e.g., Williamson and Newman, 2019). The goal of the present study is to evaluate the benefit of coupling these metrics as a way to improve tsunami hazard assessment and mapping. This is done within the context of a proof-of-concept case study based on some aspects of seismic probabilistic tsunami hazard analysis (SPTHA; Lorito et al., 2015) and a hybrid aggregated-scenario approach (e.g., González et al., 2020). In particular, the aim is to introduce an approach to microzone tsunami hazards based on the hybrid distribution of flow depth and arrival time in the populated coastal cities of Viña del Mar and Valparaíso. For illustration purposes, a set of 2,800 synthetic earthquake ruptures was generated and used as input for numerical simulations of tsunami inundation along the region.

The paper is structured as follows: In **Section 2**, the methods and data used to achieve the objectives are described. In **Section 3**, results of the source characterization used for tsunami modeling and the numerical tsunami flow depth and arrival time outcomes are explained. Finally, in **Sections 4** and **5**, the discussion of the main findings and the conclusions are given.

2 DATA AND METHODS

Tsunami hazard assessment relies on the proper characterization of the potential tsunamigenic sources (e.g., earthquakes, submarine or subaerial mass movements, etc.,). In this paper, only tsunamis triggered by seismic sources along the subduction megathrust are considered. While this could limit the scope of the tsunami hazard assessment performed, it is considered sufficient for illustrating the proposed approach. The overall procedure follows the workflow shown in **Figure 1**. First, an area of interest is identified where earthquakes are expected to occur. Next, the seismic source is characterized, leading to the generation of multiple scenarios considering a stochastic distribution of slip and an appropriate range of magnitudes. For each scenario, the initial sea-surface displacement is computed from regularly used elastic dislocation models. These displacements are treated as initial conditions for tsunami numerical modeling, from propagation to inundation, using high-resolution topographic and bathymetric computational grids. From these numerical simulations, the tsunami flow depths and arrival times are obtained. These tsunami intensity metrics are analyzed and integrated into an hybrid tsunami hazard microzoning map. The quantitative categorizations of each metric, microzoning map evaluated independently, are then combined to produce a qualitative characterization of the hazard. The details of these steps and their implications are discussed below.

2.1 Definition of Seismic and Tsunami Sources

A high tsunamigenic potential due to megathrust earthquakes exists offshore of the cities of Valparaíso and Viña del Mar, in Central Chile, where regions of high frictional strength have been identified (Sippl et al., 2020). The expected rupture zone roughly coincides with the most populated coastal zone of metropolitan Chile (**Figure 2**), including the cities of Viña del Mar and Valparaíso, which are home to about 40,000 people that live within the inundation zone. Their population increases significantly during the summer season, increasing risk (data available at http://siedu.ine.cl).

At least 11 earthquakes with magnitudes larger that M_w 8.0 have ruptured near the area of interest since the mid-16th century when written history began. The largest of these is the mega-earthquake that occurred in central Chile in 1730, with an estimated magnitude of M_w 9.1 – 9.3 (Carvajal et al., 2017a). Since then, at least three interplate earthquakes with magnitudes larger than M_w 8.0 took place, in 1822 ($M_w \sim 8.2$), 1906 ($M_w \sim 8.0 - 8.2$), and 1985 (M_w 8.0), whose rupture extent is shown in **Figure 2**. The 1822 and 1906 earthquakes only triggered small tsunamis, which caused no damage along the coast (Carvajal et al., 2017b; NGDC/WDS, 2018). Similarly, the 1985 earthquake (Barrientos, 1988) produced a small tsunami,

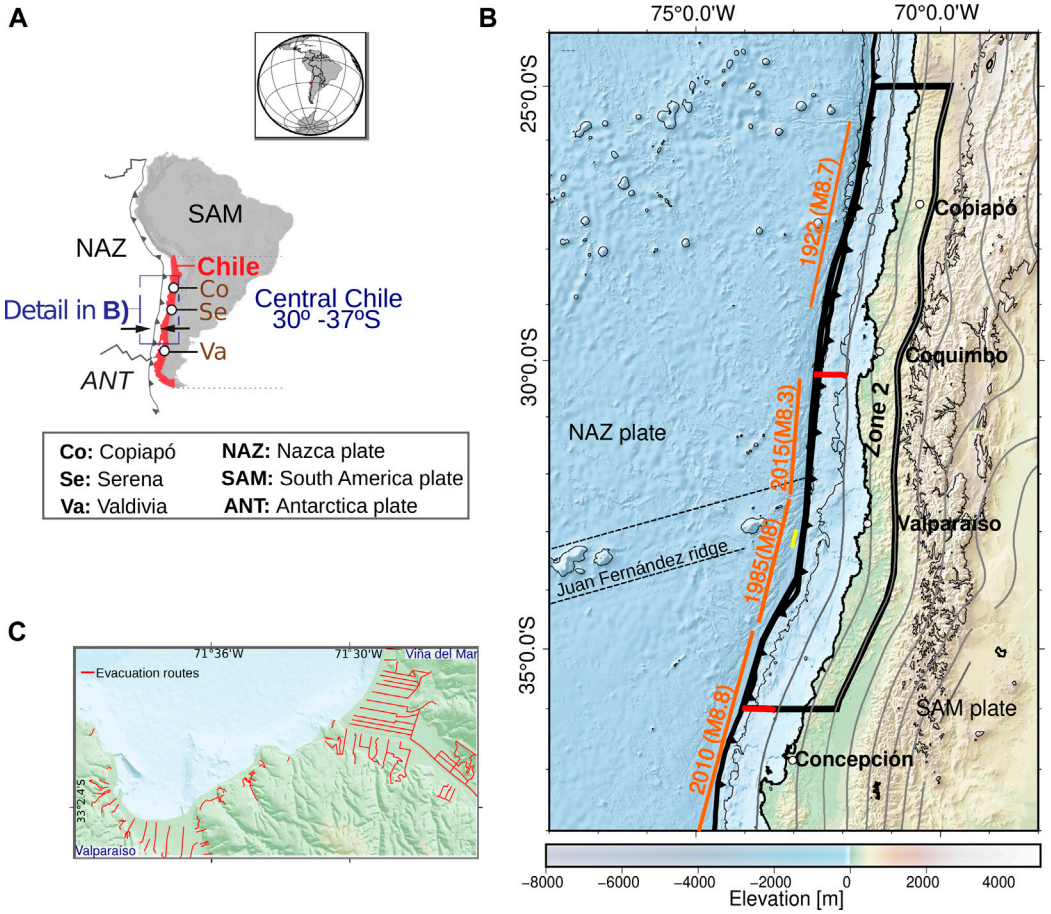

FIGURE 2 | Tectonic setting, seismic source zone and study area. **(A)** Regional map of South America showing the subduction zone formed between the Nazca and South America plates that converge at 6–7 cm/yr **(B)** Seismic source zone. The black polygon demarcates the Zone 2 from Poulos et al. (2019), where 2,800 seismic sources with stochastic slip distributions were generated. For reference, thin grey lines show Slab 1.0 depth contours every 20 km (Hayes et al., 2012). Orange lines show the along-strike extent of selected earthquake ruptures from 1900–2020, and the 1730 rupture estimated by Carvajal et al. (2017a) is shown in red **(C)** Digital elevation model of Valparaíso and Viña del Mar coastal cities. The red lines show the official tsunami evacuation routes.

with an amplitude of less than 2 m, as locally measured in the Valparaíso tide gauge (Nakamura, 1992). These observations in the 1822, 1906 and 1985 events have been explained by deeper than average ruptures (Carvajal et al., 2017b; Bravo et al., 2019), highlighting that tsunami characteristics can vary significantly among different megathrust earthquakes in this region. Consequently, it has been suggested that the shallow part of the megathrust offshore Valparaíso, which was ruptured in 1730 but not in those that followed in 1822, 1906 and 1985, is highly coupled, and thus may generate a large tsunamigenic earthquake in the near future. Further to the north, the 1922 M_w ~ 8.5 Vallenar (Copiapó) earthquake, whose rupture extended for about 300 km (Beck et al., 1998), generated a tsunami that was recorded in the far field (i.e., Japan and New Zealand), and affected coastal cities from Callao (Perú) to La Serena, Coquimbo and the San Felix island (80.04° W, 26.37° S, not shown in **Figure 2**), yet it did not produce a large tsunami in Valparaíso nor Viña del Mar. Neither did the 2015 Illapel earthquake. Events to the south, such as the 1960 Valdivia and the 2010 Maule earthquakes, produced large tsunamis that caused no damage in these cities. Hence, it appears that tsunamis in this region are related to earthquakes with ruptures closer to these cities, with large tsunami inundation events occurring on average every 500 years (Dura et al., 2015).

While a complete SPTHA in this region is required, a recent study has estimated the tsunami hazard in central Chile based on the potential rupture of only very large magnitude events (Becerra et al., 2020), by generating seismic scenarios over a rupture area similar to or larger than that of the 1730 Valparaíso earthquake (Carvajal et al., 2017a). A broader range of magnitudes will need to be considered, which includes also smaller magnitudes, and a full range of uncertainties. It should be noted that the goal of this study is not to conduct a full SPTHA, which essentially follows other goals and takes into account additional uncertainties. However, future SPTHA efforts could follow the same basic approach as presented here.

For the present study, an extensive rupture area is considered, over which great earthquakes of magnitudes ranging from M_w 8.6 to 9.2 may occur. In particular, the domain is based on the Zone 2 defined in the study of Poulos et al. (2019), which is shown by a black polygon in **Figure 2B**. Ruptures located further north or south of it are not considered due to their minimal effect in the study area, as observed in past tsunamis. The source geometry extends from latitude 25° S to about 36° S along-strike, roughly 1,100 km, and has a varying width of around 200 km down-dip (Poulos et al., 2019). Source parameters are based on the subduction zone model of Hayes et al. (2012). Over this source zone, a set of 2,800 rupture scenarios with varying slip in both dimensions of the fault are generated, considering 400 scenarios for each of seven magnitude bins between M_w 8.6 to 9.2, with 0.1 magnitude unit increments. Each scenario does not necessarily use the whole extent of this region, and their individual sizing follows the scaling laws proposed by Blaser et al. (2010).

To generate the set of scenarios, the fault region is discretized into 505 rectangular sub-faults with dimensions of 22 × 22 km along strike and downdip. The Karhoenen-Loeve expansion is used to generate aleatory slip distributions (LeVeque et al., 2016; Melgar et al., 2016). This is done to account for epistemic and aleatory uncertainties due to intra-event variability, i.e., the range of possible slip distributions for events of the same magnitude. The approach departs from SPTHA in the sense that the recurrence, or the probability of a target magnitude earthquake to occur in a given time window, is not considered, and all scenarios have the same weight. It is not intended to address the probability of occurrence for a certain flow depth or arrival time, but the focus is on evaluating what to do in case it occurs.

For each rupture scenario, a tsunami initial condition is obtained based on its respective coseismic seafloor displacement, which is modeled to be equivalent to the free sea-surface displacement, under the assumption of incompressible water and instantaneous rupture (Kajiura, 1970). Although this simplification may not completely hold in reality, this approach should be a reasonable first-order approximation. Seafloor and land deformation were computed with the analytical solutions of a rectangular source given by Okada (1985). The total sea-surface displacements, which were used as the initial conditions for tsunami modeling, were approximated by superposing the displacements of each subfault. Although the horizontal displacement of the inclined seafloor may contribute to the total sea-surface displacement (Tanioka and Satake, 1996), here only the vertical deformation of the upper plate is considered, since it has been suggested to control the tsunami generation in the study area (Bletery et al., 2015). For the purpose of retrieving accurate arrival times, the use of an instantaneous rupture can introduce an error owing to the finite rupture propagation velocity. For the size of the sources considered here, it was estimated that the error would be at most $\Delta t \sim 3 - 4$ min, for the worst-case situation of a unilateral rupture propagating from the northern end of the domain. Including this additional scenario uncertainty introduces several unconstrained parameters such as rupture origin, rupture propagation speed and direction. While future implementations of the methodology presented here could address these additional uncertainties, for instance through Monte Carlo schemes, here the non-kinematic rupture assumption is retained for simplicity and illustration. No sensitivity analysis was carried out on alternative sub-fault dimensions (Li et al., 2016).

2.2 Tsunami Numerical Modeling

For each tsunami source, the inland flow depths and arrival times are computed using the tsunami modeling software Tsunami-HySEA (Macías et al., 2017). Tsunami-HySEA solves the two-dimensional shallow-water equations (NLSWE) using a high-order path-conservative finite volume method. Values of instantaneous water depth h, and momentum fluxes q_x and q_y at each grid cell are estimated with mass preserving properties, where a high order is achieved by a non linear Total Variation Diminishing (TVD) reconstruction operator. During the reconstruction procedure, the positivity of the water depth is ensured. For wet-dry front discretization and tracking, Tsunami-HySEA implements a 1D Riemann solver used during the propagation step that takes into account the presence of a dry cell. This allows tracking the wave front and therefore a quantification of the arrival time, by registering the time when a land grid cell first changes from a dry to a wet state. More information on the numerical scheme can be found at https://edanya.uma.es/hysea/.

High-resolution bathymetric and topographic computational grids were produced. A topo-batyhmetric elevation model was created using data from the General Bathymetric Chart of the Oceans (GEBCO, 2019), nautical charts from the National Hydrographic and Oceanographic Service of the Chilean Navy (SHOA, by its Spanish acronym), local cartography and ALOS World 3D-30 m (AW3D30) elevation data (Tadono et al., 2014). The coordinate reference system was in geographical coordinates referenced to ellipsoid WGS84, and the vertical datum was set to the local mean sea level. Due to the 1.8 m microtidal range, the tide level is kept constant for simplicity, although it could be considered an additional source of uncertainty. The computational grids were generated using triangular irregular networks, and Delaunay triangulation was used to interpolate to a uniform grid among different sources. Four nested regular grids were generated, with resolutions of 30, 7.5, 1.875 and 0.234 arc seconds (~925, ~230, ~55 and ~10 m), respectively, as shown in **Figure 3**. The finest grid covers the urban area of the cities of Valparaíso and Viña del Mar. A constant Manning's roughness coefficient was set to $n = 0.025$. The simulation time was set to 4 h, using a variable time step to satisfy the Courant-Friedrichs-Lewy's (CFL) stability condition in each grid, with a common value of $CFL = 0.5$ for all of them.

2.3 Assessment of Tsunami Inundation Metrics

Time series of inundation flow depth $d^i(x, y, t)$ were obtained at each grid point (x, y), where the superscript i indicates a scenario,

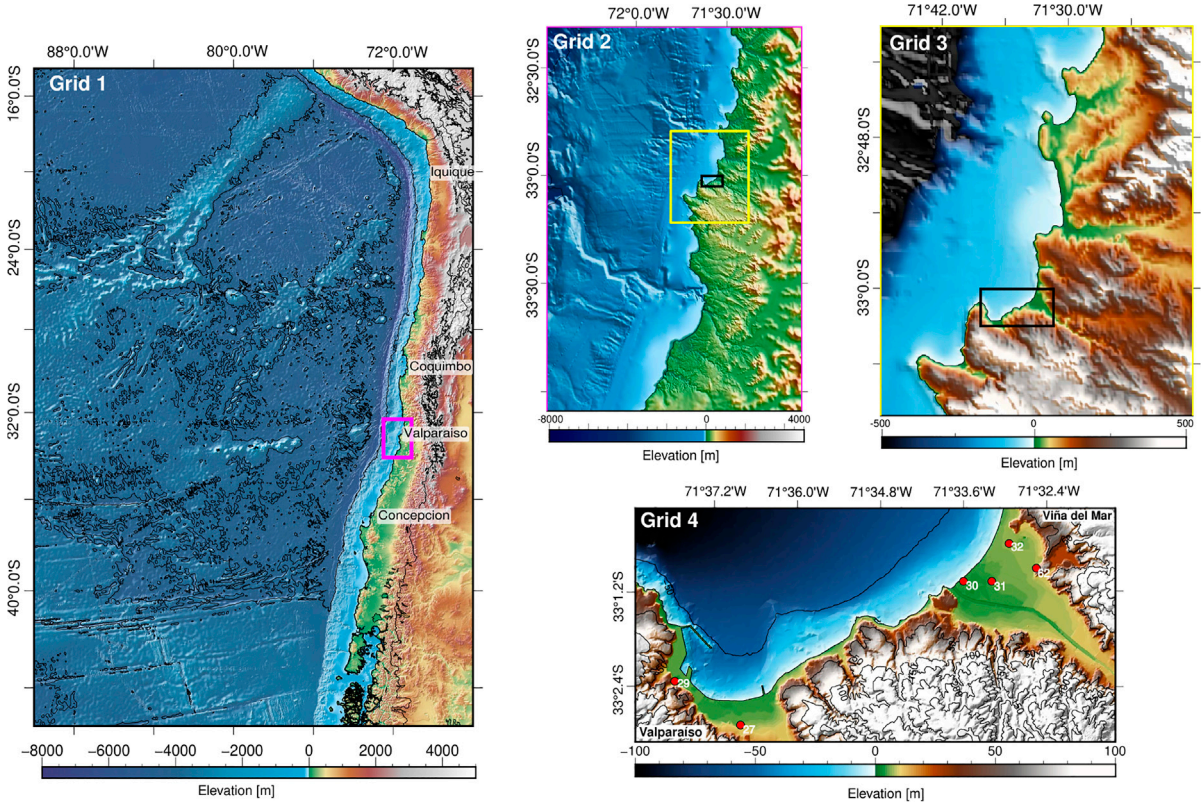

FIGURE 3 | Nested digital elevation models used in the numerical simulations. The colorbar stands for the terrain elevation with resolutions of 30 arcsec (grid 1), 7.5 arcsec (grid 2), 1.875 arcsec (grid 3) and 0.234 arcsec (grid 4). Red points show the points of interest where tsunami arrival times are analyzed.

$i = 1, \ldots, 2800$. The flow depth was computed as the instantaneous free surface water elevation computed by Tsunami HySEA $h^i(x, y, t)$ minus the terrain elevation $z^i(x, y)$ at the time of the tsunami arrival. The latter differs among scenarios because each scenario produces different seafloor and land coseismic deformation. Since the goal was to assess the likelihood of a land cell to be inundated, zero values meaning no inundation were retained in the analysis. In addition to this, the arrival time was retrieved from the model by recording the first time a grid cell was inundated, denoted $t_a^i(x, y)$. Instances of no inundation can be considered as an infinite arrival time. Since this could, however, negatively bias the results, they were removed for the analysis of arrival times. In defining the arrival time in this way, it becomes decoupled from the flow depth, and the two variables are considered independent.

This approach, at least initially, imposes constraints similar to simplified SPTHA methods that consider inundation (e.g., those of Lorito et al., 2015; Sepúlveda et al., 2018). But, unlike those, no subsampling to reduce the computational burden is applied because arrival times can be controlled by aspects such as relative orientation and relative distance to the slip patches. This may preclude clustering and linearization, and instead makes it necessary to perform inundation modeling with the complete catalog of synthetic scenarios.

The focus of the present study is to produce relevant information for evacuation planning. This goal definition controls the hierarchy among the variables, and also the rationale behind selecting a representative value among all scenarios and modeled quantities. For evacuation purposes, the earliest arrival at each cell among the set of scenarios is considered as the worst situation. Similarly, the worst case would be the maximum flow depth. Hence, each time series of flow depth $d^i(x, y, t)$ is reduced to its maximum, $d_m^i(x, y) = \max_{|t} d^i(x, y, t)$. Next, the extrema among all scenarios are computed, yielding the final set $d_m(x, y) = \max_{|i} d^i(x, y)$ and $t_a(x, y) = \min_{|i} t_a^i(x, y)$. At each cell, the shortest arrival time and the maximum flow depth do not necessarily correspond to the same scenario.

Tsunami hazard maps usually convey information about flow depth, measured discretely in length units, (e.g. meters) with some level of discretization. This can be counterintuitive and difficult to interpret as to its implications. In contrast, the approach used for some tsunami warning systems is to characterize the hazard based upon peak tsunami coastal amplitudes estimated closely offshore. The use of actual numerical values is discarded in favor of a categorization based on thresholds, as it is then possible to relate it univocally to an evacuation action to be performed by the

TABLE 1 | Classification of hazard levels.

Max. Flow depth (d_m) \ Arrival time (t_a)	Very short $t_a < 10$ min	Short $10 < t_a < 20$ min	Delayed $t_a > 20$ min
Small $d_m \leq 0.30$ m	C1	B1	A1
Medium $0.30 < d_m \leq 1.00$ m	C2	B2	A2
Large $d_m > 1.00$ m	C3	B3	A3

population. This is the case, for instance, of the tsunami warning system in Chile, where the tsunami hazard analysis identifies four hazard levels that are associated with three different evacuation actions (Catalán et al., 2020):

$$\max(\eta)\begin{cases} \leq 0.30\,m & : \text{Informative} \\ [0.30, 1.00]m & : \text{Advisory} \\ [1.00, 3.00]m & : \text{Watch} \\ > 3.00\,m & : \text{Warning} \end{cases} \quad (1)$$

where $\max(\eta)$ is estimated offshore, at a prescribed water depth. Of these hazard levels, both Watch and Warning prompt a complete evacuation of areas that are under the 30 m elevation contour, and the Advisory hazard level indicates evacuation of the closest 80 m (horizontally) to water bodies and the ocean. For the Informative hazard level, no action is required.

No equivalent metric or categorization exists for the inundation flow depth, as it has been implicitly assumed that any inundation level is hazardous enough to prompt evacuation. Moreover, no categorization exists for the arrival time either, as it has been assumed that evacuation needs to occur immediately, regardless of when the inundation takes place. Here it is hypothesized that coupling these parameters can produce relevant information for a more detailed analysis of evacuation strategies. Also, it could lead to maps that could be easier to interpret by the general public.

Therefore, as a first step, it is proposed to categorize the final set of flow depth and arrival time values, using a nine-level qualitative hazard scale, from A1 (least hazardous) to C3 (most hazardous), as shown in **Table 1**. These levels result from the combination of the hazard levels as established in the Informative, Advisory and Watch levels, defined in **Eq. 1**, now mapped as values 1, 2 and 3, respectively, with a new classification of the arrival time.

The temporal thresholds presented in **Table 1** were defined arbitrarily, and could be subject to modification depending on the location and/or objectives of the assessment. Here, we use as first reference the expected issuance of the first assessment by the Chilean Tsunami Warning System in Chile (about 8 min, which is rounded up to 10 min), and twice that time. These threshold values are consistent with arrivals observed during past tsunamis in Chile, and with observed and modeled evacuation times in the area (León et al., 2020). These are denoted by letters, from A to C (least to most hazardous). The applied hierarchy gives more relevance to the arrival time compared to flow depth. Hence, a very early arrival with small flow depth, (i.e. C1), is considered more hazardous for evacuation than an early arrival with large amplitude, (i.e. B2). This is based upon the consideration that even flow depths as low as 70 cm with 1.3 m/s flow speeds can already put under threat a pedestrian (Koshimura et al., 2006), and the tsunami fatality rate is highly increased when inundation depths exceeds 2 m according to fragility curves (Koshimura et al., 2009). While this hazard ranking is arbitrary, for the present goal it is proposed as a baseline scheme that could be further developed if deemed necessary. For completeness, alternative thresholds were tested and are shown in the (**Supplementary Table S1, S2**), which do not alter the main conclusions of this work.

3 RESULTS

3.1 Source Characterization and Tsunami Modeling

Before analyzing the resulting hazard maps, it is relevant to first evaluate the data that supports them. The statistics of the slip distributions used as initial conditions for the tsunami modeling are thus reviewed. In **Figure 4A**, a sample scenario is shown, where a relatively shallow and concentrated peak slip area is observed, with a maximum slip value that exceeds 15 m. This particular value is slightly lower than the 19 m estimate of offshore slip deficit accumulated since the last large earthquake in 1730 (Carvajal et al., 2017a), considering a convergence rate of about 6.5 cm/yr. This source does not feature slip in the entire considered seismogenic domain, which allows for the rupture size adjustment according to scaling laws (Blaser et al., 2010). This was the intended behavior of the scenario generation algorithm for producing earthquakes with different magnitudes.

The randomness and variability of slip across all scenarios are illustrated in other panels (**Figure 4B–D**). Since slip is always positive, data are not Gaussian distributed. Hence, non-Gaussian statistics will be used. All data at each cell are sorted and normalized, and the local cumulative distribution function, $P_{a,\alpha\%}$ is estimated as the value of the variable a below which α % of the data are ranked. The a can stand for slip, flow depth or arrival time. The expected value is estimated by the 50-percentile ($P_{a,50\%}$) while the range of variability is estimated by the difference $P_{a,95\%} - P_{a,5\%}$.

The spatial statistics for coseismic slip are shown in **Figures 4B–D**. The $P_{s,95\%}$ value is presented as a proxy for the maximum value. It yields a relatively uniform distribution, highlighting that the generation method does not include areas of preferential slip, as intended. Similarly, the variability range shows a similar structure, although there is slightly larger

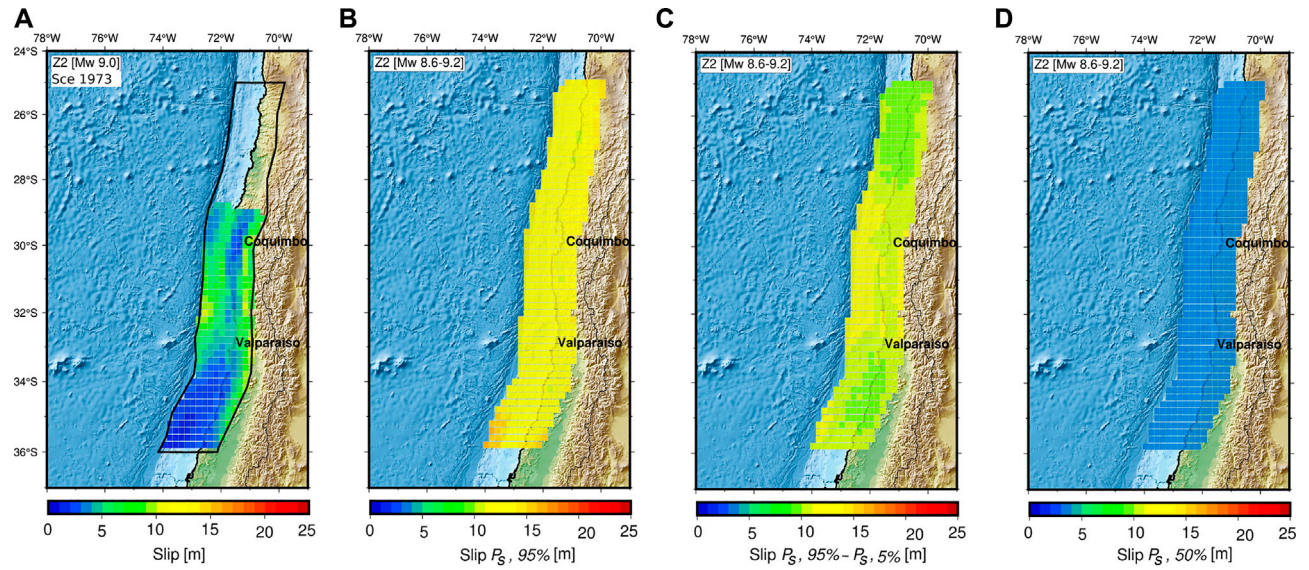

FIGURE 4 | Statistics of the slip distribution estimated at each cell including all seismic scenarios generated using the K-L expansion for the range M_w 8.6 to M_w 9.2 **(A)** One scenario (M_w 9.0) is shown as an example **(B)** $P_{s,95\%}$ slip values **(C)** $P_{s,95\%} - P_{s,5\%}$ slip values; and **(D)** $P_{s,50\%}$, median slip values.

variability close to the shoreline. The same structure is found for the median value, indicating that the source scenarios do not show a strong bias toward a certain subset of sources. Additional data and analysis can be found in the (**Supplementary Figure S1**).

Figure 5 shows the results of tsunami inundation at Viña del Mar and Valparaíso, in a way that aggregates information from all simulated scenarios. For instance, **Figure 5A** shows the envelope of maximum flow depths, $d_m(x, y)$. In Viña del Mar, maximum flow depth reaches up to $\approx d_m \approx$ 15–17 m over a very narrow band near the shoreline (dark red color), which decreases to $d_m \approx$ 10–15 m in almost the entire river floodplain area, with larger values in the vicinity of the river mouth and in the low elevation areas of the city. The largest tsunamis among the set can propagate up to 4.0 km inland. On the northern end of Viña del Mar and in the section between Viña del Mar and Valparaíso, hills very close to the coast control the flow, leading to a minimal inundation extent, although maximum inundation depths can reach up to 25–30 m. Results for Valparaíso show a similar pattern, where the maximum flow depths in the low-lying areas can reach about 10–15 m. However, the inundated area is smaller, owing to the typical steep topography of the city. These results are consistent with the tsunami inundation chart provided by SHOA (available at http://www.shoa.cl/php/citsu.php), which was elaborated using a few seismic sources based on previous estimates of the 1730 earthquake (M_w 8.8–9.1), slightly lower than the most recent M_w 9.1–9.3 assessment based on near-and far-field tsunami evidence (Carvajal et al., 2017a).

These results focus on the absolute maximum at each cell, which is usually the quantity of interest. **Figure 5B** shows the $P_{d_m,95\%}$ value. In general, there is a reduction of about 50% in the flow depth values between the maximum and $P_{d_m,95\%}$. This is indicative of a heavy tail in the distribution at each cell, and shows that a small number of scenarios may control the distribution. **Figure 5C** shows the fraction of scenarios that inundate each cell. Typically, less than 20% of the modeled scenarios are capable of inundating beyond the shoreline in Valparaíso. In Viña del Mar, typical values are 30% of the scenarios inundating parts of the floodplain, and a few more inundate the river bed and propagate upstream. These results highlight that a relatively low number of scenarios are capable of inundating large parts of the domain. As 2,800 scenarios were used in this study, 10% of them represent 280 scenarios, which is still a large number in absolute terms. These scenarios inundate the domain with a wide variety of flow depths and spatial extents of inundation. This could indicate a large sensitivity of the inundation characteristics to the details of the source, such as the distance between concentrations of high slip and the studied cities.

Figure 5D shows the spatial distribution of the envelope of the minimum arrival time, $t_a(x, y)$, in minutes. A smooth evolution of arrival times is apparent, which may imply that arrivals are uniform among different scenarios, or perhaps controlled by a single scenario. Arrival times are short, ranging between 5 and 35 min, with typical values less than 20 min for most of the inundated area, which would put significant stress on a timely evacuation effort. Results for Valparaíso and Viña del Mar are similar, with the latter having slightly longer times due to the larger extent of the inundation zone.

3.2 Hazard Microzoning

Based on these data, the categorization and thresholds presented in **Table 1** are applied to the ensemble of 2,800 scenarios. **Figure 6**, top row, shows the categorization (Cat.)

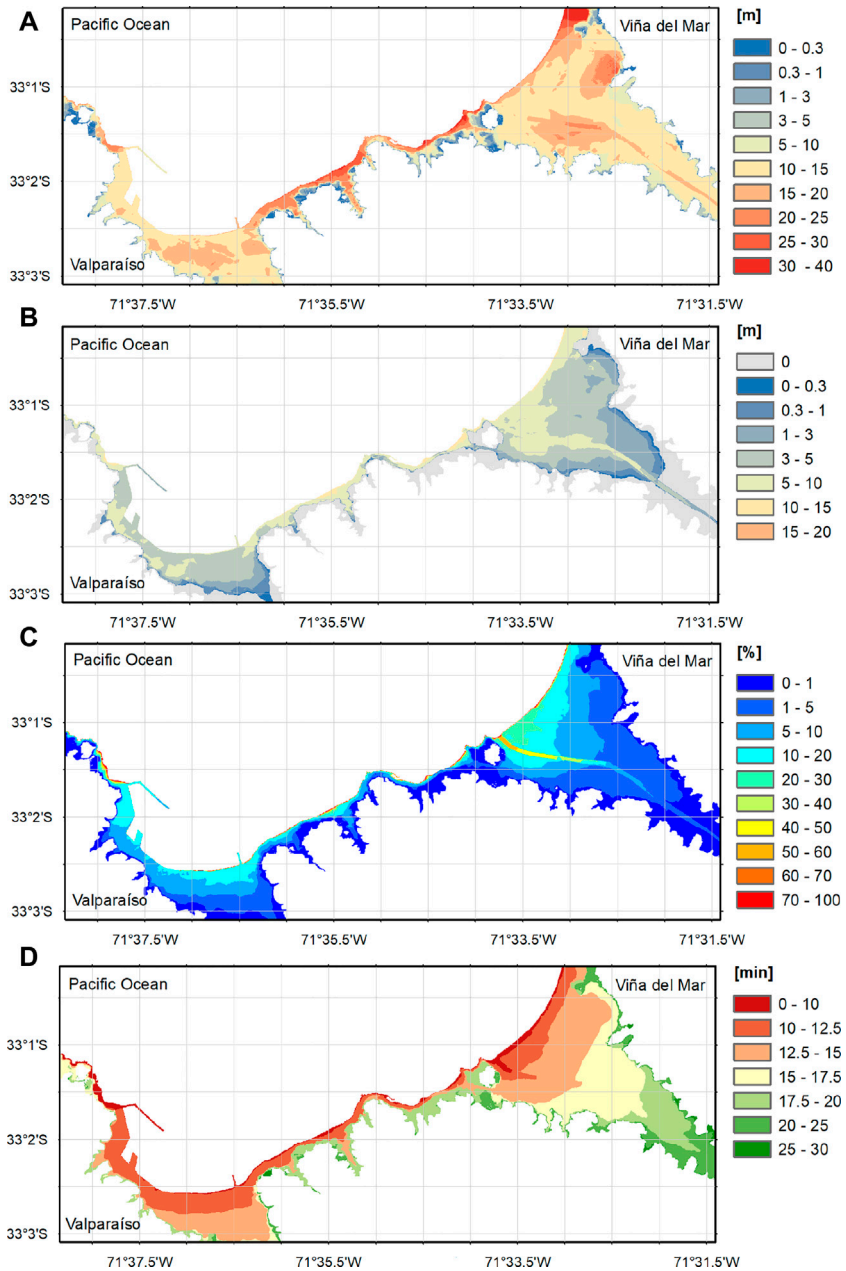

FIGURE 5 | Maps of inundation statistics at Valparaíso and Viña del Mar: integration of all scenarios between M_w 8.6–9.2 **(A)** Envelope of the maximum flow depth $d_m(x,y)$ **(B)** $P_{d_m,95\%}$ of the maximum flow depth of the set of scenarios **(C)** Fraction of events that inundate each cell; and **(D)** Minimum arrival time at each cell, $t_a(x,y)$. Values of flow depth are provided in meters, arrival time in minutes and the fraction in percentage. In the **Supplementary Figures S3–S9** similar maps are shown for each M_w.

based solely on the flow depth, where these flow values larger than 1 m (Cat. 3) cover most of the map, resulting in rather uniform maps. This may be taken to imply that the whole area should be treated equally, and that the same evacuation response should be triggered during an emergency. Hence, this map can be further simplified to a binary map for evacuation planning purposes. The use and categorization of arrival time leads to a similar result (middle panel), where most of the arrivals are Cat. B (between 10 and 20 min), again resulting in uniform maps. Just a small area near the river entrance in Viña del Mar, and west of the breakwater in Valparaíso, show very early arrivals (Cat. C, <10 min). Note that this breakwater is intended to protect the port from wind waves, and there were no tsunami considerations in its design. In fact, no coastal defenses that target tsunami mitigation exist in this area.

The hybrid categorization proposed in this work is presented in the bottom row of **Figure 6**. The extent is the

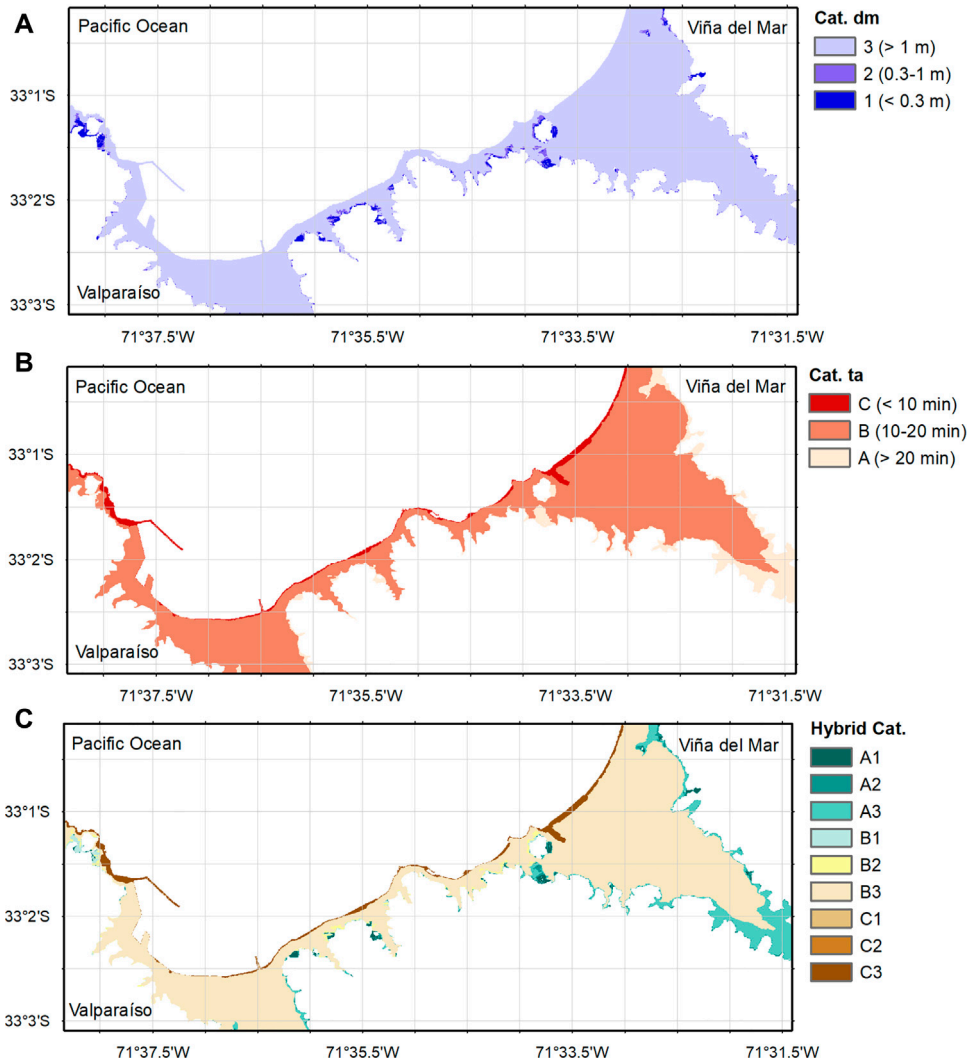

FIGURE 6 | Application of categorization thresholds to qualify hazard **(A)** Hazard levels based on tsunami flow depth **(B)** Hazard levels based on tsunami arrival time **(C)** Hybrid categorization hazard levels. Thresholds for each case are defined in **Table 1**. Refer to **Fig. S10** in the Supplementary Material where the fraction of events in each hazard level is shown, and **Figs. S11-S17** to see the categorization for each Mw.

same as in the other maps, adding no information as to which locations need to be evacuated. However, the combined use of both parameters adds an extra layer of detail that can provide significant information. For example, some small areas that yield large amplitudes have been classified as Cat. A3 (dark green), because of the large inundation depths (>1 m) and relatively late arrival inundation times (>20 min). Regions of extreme hazard are identified as Cat. C3 (dark brown) near the river entrance and northwest of the port. However, most areas are classified as level B3 (pale brown). At first glance, it may seem as if this categorization is not sufficiently informative compared to the original maps. The B3 level likewise suggests that the tsunami is not only large but will also arrive slightly later (between 10–20 min). In the following, the consequences of the proposed mapping are analyzed.

4 DISCUSSION

4.1 Implications for Evacuation Procedures

Typically, tsunami hazard maps are presented in terms of flow depth values, consistent with the notion that flow depth is the main driver of tsunami damage, at least to first order. Yet, within the context of evacuation, the relevant variable is the time difference between evacuation and arrival time, which needs to be maximized. The premise of evacuation studies is that a person is considered under threat once the tsunami arrives first, (i.e. before evacuation is completed), regardless of its flow depth. While this concept may be debated, it is notably decoupled from the parameter flow depth. Evacuation strategies, on the other had, usually attempt to promote instantaneous evacuation, ideally triggered by the earthquake itself (self-evacuation) or by alarms issued by authorities. Within the context, it is relevant to know the extent of the inundation zone,

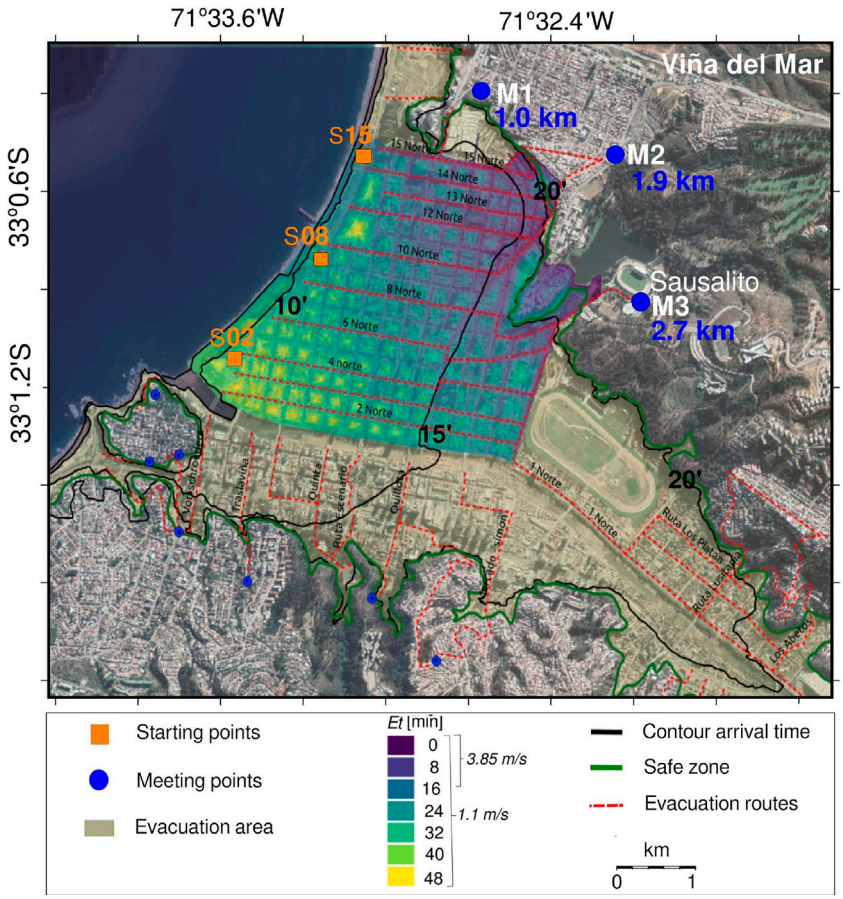

FIGURE 7 | Map comparing evacuation times (shown with the colored grid) and distances to tsunami arrival times for Viña del Mar. Black contours represent tsunami arrival time isolines. Orange squares show three example starting points (S02, S08, S15) for persons to be evacuated, for estimating their distances to the three corresponding meeting points M1, M2 and M3; *Et:* pedestrian evacuation times according to the shortest routes from León et al. (2019b). Evacuation route (red) locations have been retrieved from: https://www.onemi.gov.cl/mapas/region/valparaiso/.

and promote instantaneous evacuation inside it. A binary map could suffice for this.

Real-world evacuation processes, in contrast, cannot be accomplished instantaneously. Travel times to safe ground vary dramatically depending on several factors, such as topography, road connectivity, blockages, criteria to define "safe zones", and others. For the study area, León et al. (2019b) and León et al. (2020) noted that many areas of Viña del Mar are too far away to reach the high ground defined as "safe zones" (up to 48 min). This is shown in detail in **Figure 7**, where official evacuation routes and safe zones are presented. National guidelines indicate evacuation sites have to be located above the 30 m terrain contour, shown in green in **Figure 7**. This contour is generally located relatively far from the inundation zone, thus requiring long travel times for some residents. To illustrate this, tsunami arrival time and the expected behavior of the population to an alert, in case that people are located close to the beach area, is examined for three starting points within the C3 zone. These starting points are denoted by orange squares in **Figure 7**, where dashed red lines highlight the suggested evacuation routes according to the evacuation map. If a person departs from starting point S15, the route along 15 Norte should be followed for 1.0 km to arrive at the M1 safe zone. A second person, located in S08 would be required to walk 1.9 km before reaching the M2 safe zone as per the current evacuation recommendations. Critically, a person located in site S02 would have to walk about 2.7 km in order to arrive at the M3 evacuation site. As shown by the tsunami arrival time (shown in black contour lines), after 15–20 min, maximum flow depths of $d_m \approx$ 1.5 m can be expected. Flow depths of $d_m \approx$ 0.5 m can occur 1.5 km inland just 20–30 min after the earthquake. If a person walks at an average speed of 1.1 m/s (Fraser et al., 2014), it is clear that the tsunami front would catch evacuating pedestrians. Using agent-based models to assess multi-scale evacuation (León et al., 2018; León et al., 2020) found successful evacuation rates of about 61% of the people if the current "safe zones" are used. Their data are presented in the color scale in 7, depicting the time required to reach a safe zone depending on the starting location: a person starting around point S02 could take about 48 min to reach safety, whereas the tsunami could arrive as early as 10 min.

Including tsunami arrival times in hazard estimation is thus essential, but it does not suffice to drive evacuation

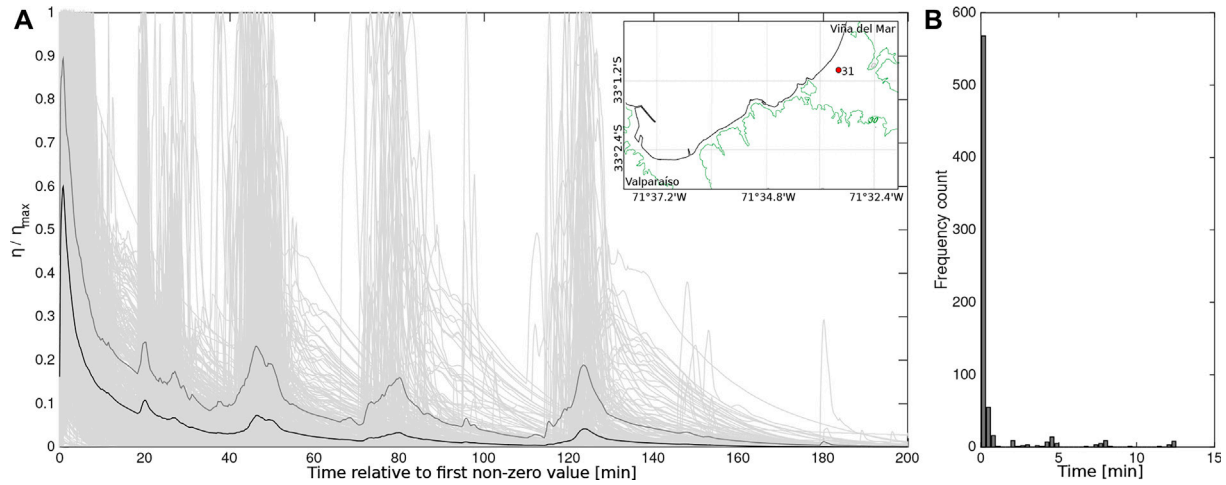

FIGURE 8 | Arrival times at point of interest (POI) ID 31 **(A)** Time series of the normalized flow depth of 2,800 scenarios recorded at POI 31 shown in the inset map. The assessment is done considering inland arrival with time relative to the first non-zero value. Black line shows the mean and darker grey shows the standard deviation **(B)** Frequency of the time difference between the maximum amplitude arrival and the first amplitude arrival at POI 31.

planning. Using time alone neglects the effect of the magnitude of the tsunami. When arrival times are combined with flow depths, as in the present proposal, a more detailed zoning arises. This allows for further analyzing the connectivity of evacuation routes, and even the placing of evacuation infrastructure (e.g., for vertical evacuation). In the example, some of the Cat. C3 areas are located near Cat. A1 or Cat. B1 areas. This is relevant, because it means that properly designed vertical evacuation infrastructure could be located in these Category. One zones. While these areas are still subject to inundation, it occurs with smaller flow depths and late arrivals, which could result in reduced pedestrian evacuation both in distance and time. Of course, this would require proper design of said infrastructure. Another alternative worth considering could be a shift of meeting points, with people traversing over zones not foreseen now. For instance, from the vicinity of point S02, to the nearby hill (see **Figure 7**), if the safeness of the evacuation route is previously guaranteed. These hybrid maps illuminate other viable options that may not be derived when only the flow depth is taken into account.

One apparent downside is that most of the area in the hybrid categorization map (**Figure 6C**) falls into a single category, B3. Although this is not ideal, it is also not a severe handicap. León et al. (2018) carried out an exercise where additional evacuation shelters were placed within the inundation zone, greatly improving safe evacuation. Their rationale for locating these additional vertical evacuation sites was based on structural and building type considerations. Based on our results shown in the hybrid map, additional vertical evacuation could have been carried out in locations close to the orange squares in **Figure 7**. For this purpose, it is not useful to locate additional evacuation sites in the A3 or B3 areas, but possibly in an A2 or B2 area, since there would be shorter pedestrian travel times, with less risk of damage due to the smaller flow depth. It is thus hypothesized that planning exercises can be greatly improved using this hybrid mapping approach, without the need to use costly single scenario models that do not cover all possibilities.

Note that the proposed map is not aimed to be used during an evacuation, but in advance of it. The design of the map is based upon considerations that need to be coordinated with decision and/or policy makers. The more clear the definition of thresholds of the hazard variables and time arrivals, based on elicitation with authorities, will ensure more practical use on decision making. Arrival times vary between locations, and early arrivals can be defined in accordance to local values and evacuation times. A second important aspect is the hierarchy that has been imposed on the data, with the proposed categorization giving precedence to arrival time over flow depth. The rationale for this is based on the understanding that even a small flow depth could hamper evacuation. Nevertheless, the matrix-style categorization used here may be rearranged upon further considerations and analysis, e.g., during a systematic process of elicitation with authorities. A sensitivity analysis on this regard was performed (refer to **Supplementary Figures S18, S19**), which results in changes to the map. Nevertheless, it was found that the usefulness of the presented methodological approach is not affected by these decisions.

Once thresholds and hierarchies are defined, the next step is to quantify the hydrodynamic variables. While the relevance and definition of maximum flow depth is well established and thus does not necessitate further analysis, time of arrival is a metric that has a relatively loose definition. For the present case, it was identified as the instance when a zero flow depth becomes non-zero for the first time,

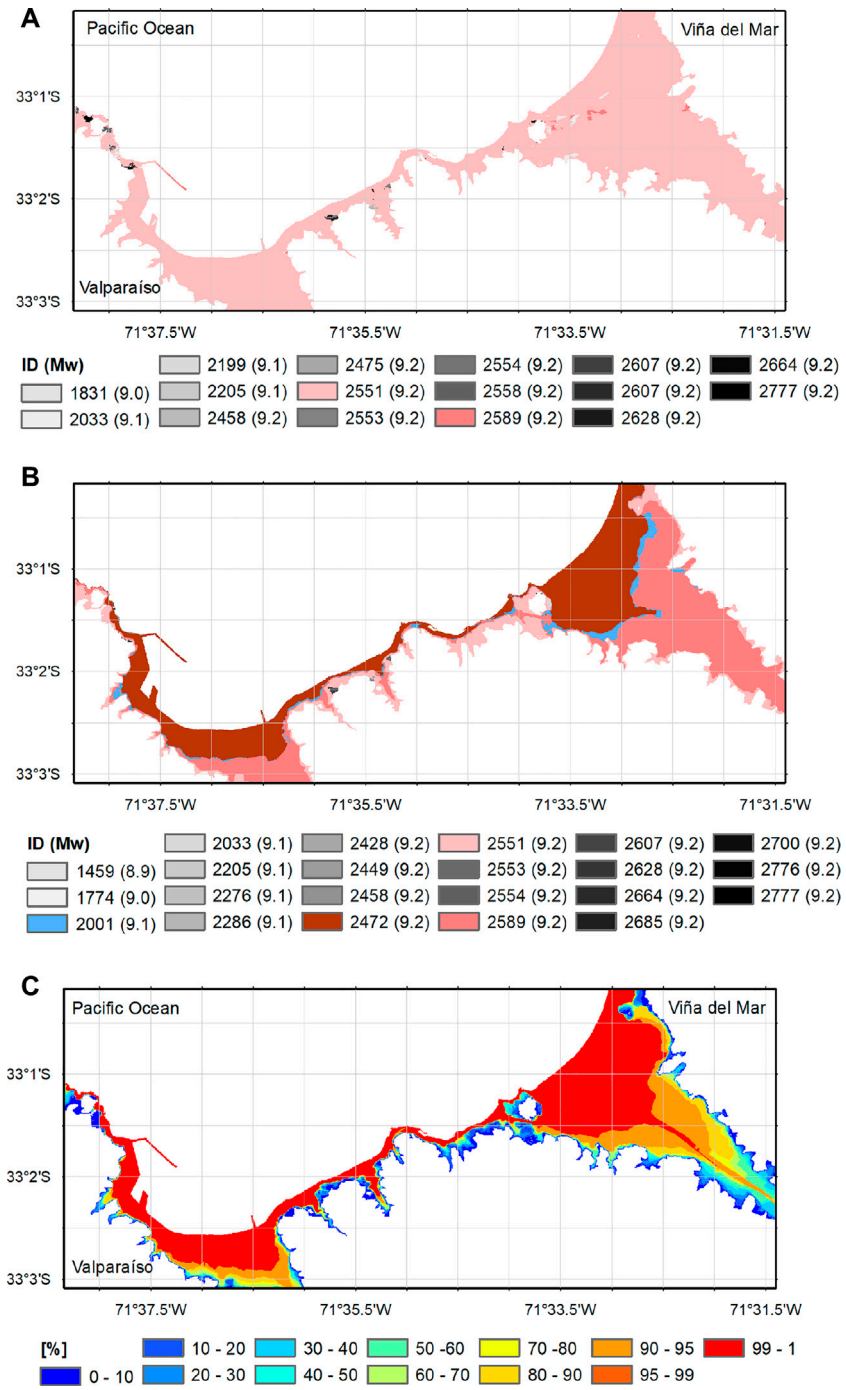

FIGURE 9 | Discrimination of extreme values among scenarios **(A)** Scenarios that contribute to the maximum flow depth. Left number shows the scenario Id and in parenthesis the corresponding moment magnitude **(B)** Scenarios that contributed to the arrival time **(C)** Fraction of those scenarios that inundate each pixel.

regardless of its amplitude. Other criteria could consider the first time a flow depth threshold is exceeded, or the timing of the maximum flow depth. To study the effect of these decisions, all 2,800 time series at a selected point in the region C3 are analyzed. **Figure 8A** shows individual flow depth time series normalized by their maxima, and their mean and standard deviation (after removing zero flow depth series). The time axis of each series has been shifted by subtracting the arrival time, so all series have a common time domain. The time series are characterized by sharp fronts once the wave first inundates the shoreline. Although the maximum does not necessarily occur during

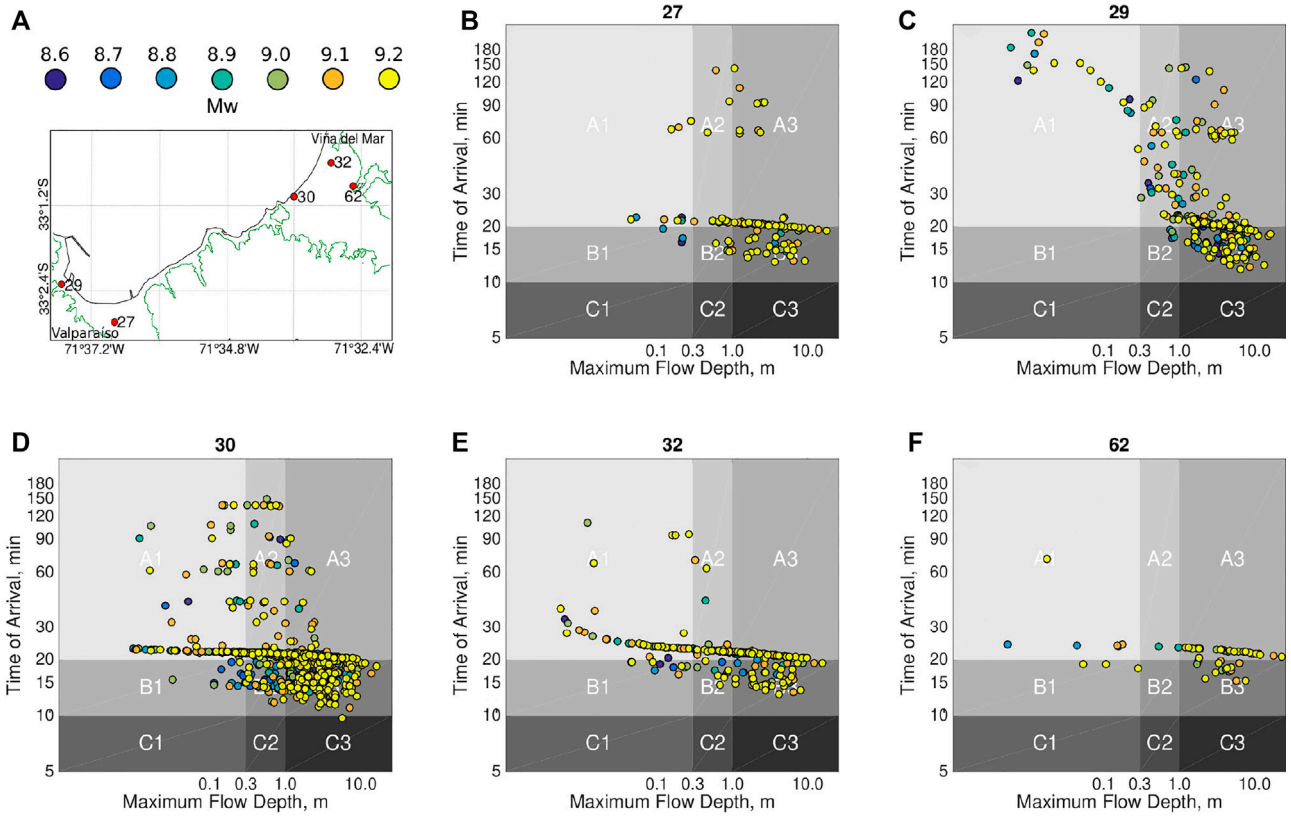

FIGURE 10 | Scatter plots of earliest arrival time against maximum flow depth, color coded by M_w from blue (M_w 8.6) to yellow (M_w 9.2)M_w **(A)** Location of selected points of interest shown in red. The black line is the coastline, and the green line stands for the 30 m a.s.l. contour. The background color indicates the categorization for five selected points of interest shown with red circles in the map **(B)** Point of interest ID 27 **(C)** Point of interest ID 29 **(D)** Point of interest ID 30 **(E)** Point of interest ID 32; and **(F)** Point of interest ID 62.

the first wave, the difference between the time of the maximum and the recorded arrival time is typically less than 3 min, as shown by the histogram in **Figure 8B**. Thus, for the present case, the definition of the threshold of inundation depths to determine the arrival time is not very important. However, choosing a lower amplitude threshold would make the method and the resulting map more conservative for evacuation planning, which is recommended.

4.2 Scenario Contributions to the Hazard Mapping

The presented approach to producing hazard maps departs from a deterministic, scenario based framework by considering a large number of different scenarios. It is also different from PTHA, because recurrence and probabilities are not considered. This is justified since saving lives ought to follow a low-probability, high consequences approach Muhari et al. (2015); Langenbruch et al. (2020). The planning must thus consider low probability events that cause high potential damage to the people, to minimize loss of life (Ranghieri and Ishiwatari, 2014). While it is desirable to ensure that evacuation routes and safe zones are designed in this way, other elements such as vertical evacuation structures could follow a different approach for their structural design.

An apparent feature of the performed modeling is that even though the scenario dataset considers a broad range of magnitudes and hundreds of slip realizations per magnitude bin, the final results and maps appear to be defined by just a small number of events. This is depicted by the fraction of events inundating the domain (**Figure 5C**). Whilst a large variability of tsunami inundation metrics was found, only few events in each magnitude bin were capable of inundating large swaths of the coast, while the majority were not able to inundate beyond the coastline. This is interpreted as an appropriate response from the modeling, since the set of scenarios incorporates shallower and deeper rupture depths, consistent with knowledge about past earthquakes in the area. For example, although smaller in magnitude than the present target scenario, the two last local events in 1985 (M_w 8.0 Barrientos, 1988) and 1906 (M_w 8.0 – 8.2 Carvajal et al., 2017b) triggered small tsunamis not perceived by the population, suggesting they occurred at deeper than average depths on the plate interface (Carvajal et al., 2017b).

The retrieved intra-event variability incorporates these uncertainties, which makes the assessment more realistic than in the case of using a maximum credible scenario. However, this could be interpreted as an unnecessary step of the procedure when evacuation and reducing loss of life are the driving objectives. A more cost-efficient approach could consider sub-sampling of the parameter space, for instance, by focusing on large magnitudes only.

To better understand this, the scenarios that produce the extreme value at each cell are identified (**Supplementary Figure S2**). **Figure 9A** shows that only 16 scenarios contributed to generate the maximum flow depth map. Two scenarios control most of the domain (IDs 2,551 and 2,558), but several others are relevant for the western end of the domain, west of the breakwater. This could indicate a large sensitivity to whether these scenarios are included in the analysis. However, when the percentage of events (among this set of 16) that inundate each grid cell is considered (**Figure 9C**), it can be seen that typically, 80% or more of these 16 events do inundate a large section of the domain. Hence, similar results would be obtained as long as any of those 16 events was included. Five of the above-mentioned events are capable of reaching the maximum inundation, and they significantly modify the overall extent of the inundation zone. This means that including intra-event variability is essential to account for all cases, and may preclude filtering or subsampling for extreme (but plausible) earthquakes beforehand. This is reinforced when arrival time is considered. **Figure 9B** shows scenarios that contribute to the minimum arrival time for each cell, resulting in a set of 32 scenarios (**Figure 9**). A less uniform distribution compared to inundation depths is observed, with two scenarios controlling the minimum arrival time (ID 2589 and 2,472). Notably, scenario ID 2472 was not part of the scenarios contributing to flow depth maxima. Again, this further shows not only the need to include a large number of scenarios, but also the importance to treat the inundation depth and arrival times independently, as proposed here.

This analysis may lead to the impression that only those large magnitude scenarios contribute to the presented results. To check this, a scatter plot of maximum flow depth and arrival time from all 2,800 scenarios was computed at five locations within the inundated area. Results are classified by magnitude, and the category thresholds are also shown in **Figure 10**. A large number of scenarios of different magnitude is observed to fall into the extreme category, and these are more frequent in the set than previously suggested, which can be observed in the cloud of scenarios that are classified as Cat. B3 at POI 29 (**Figure 10C**). The scenario of the maximum flow depth does not coincide with that of the minimum arrival time. Maximum flow depths appear to be more sensitive to scenario selection, with one or two scenarios having extreme flow depths. In contrast, arrival time usually has a larger number of events with similar values, as shown by a flatter distribution of data points at the shortest times. Some of the presented locations highlight the need to include different magnitudes and scenarios in the assessment. POI 62 (**Figure 10F**) shows that the largest events have late arrivals (Cat. A3), but there are several smaller events of different magnitude that arrive significantly earlier (Cat. B3). POI 30 (**Figure 10D**) shows that events of different magnitudes can yield a large range of flow depths, but all of them occurring within 10–20 min after the earthquake. Remarkably, this point (POI 30) is located near the river mouth, the area previously identified as the one having longer evacuation times. This reinforces the need to decouple arrival time and flow depth. **Figure 10** also highlights the sensitivity of the results to the choice of thresholds, especially those related to arrival time. At POI 30, a single event arrives in less than 10 min, which controls the C3 category. Had the threshold been chosen at 12 min, 3 scenarios would have been considered.

A by-product of the presented analysis is that it is possible to identify the latest arrival (uppermost points in the scatter plots). This means that after evacuation has been issued, no safe return to the inundated area should be allowed before approximately 180 min. This also implies that if no inundation has been observed after 180 min, or with some extra time added to be conservative, it would be reasonable to assume that no inundation will occur. The inclusion of arrival times hence not only defines the necessary promptness of evacuation, but could also be used to define the time of issuance of safe returns. To our understanding, this aspect has been largely missing from tsunami hazard assessments, yet it is a key aspect to be considered in areas where evacuations might be recurrent, as in Chile, and the system is at risk of a loss of confidence by the population due to perceived false alarms. A more detailed modeling exercise should also contain the effect of resonance and edge waves (Catalán et al., 2015; Cortés et al., 2017; Aránguiz et al., 2019), by modeling the domain for a sufficient time for them to occur. This could also necessitate an expansion of the analysis to seismogenic areas located further away from the area of interest.

These results show that it is relevant to include a wide range of scenarios and magnitudes, although the categorization may not be as sensitive to the inclusion of extreme events. This opens the possibility to implement post-processing methods (Sepúlveda et al., 2018; Davies, 2019) in order to omit some scenarios that can be contributing as outliers (or erroneous numerical artifacts), while also keeping the distribution of the starting configuration of stochastic realizations. This has not been implemented here, but could be part of a further refinement of the method.

5 CONCLUSION

In this work, the hybrid use of tsunami arrival times and flow depths in the elaboration of a hazard map has been evaluated. To this end, 2,800 stochastic sources and their respective tsunamis were modeled from generation to inundation in two cities of central Chile. Different ways of arranging the tsunami hazard categorization were tested, with the goal of producing a map that can be useful for decision making in evacuation planning and management, while being easy to understand.

The main findings show that a small number of scenarios generate large tsunami inundation, but with variable arrival times not necessarily associated to the same event. In contrast,

similar tsunami arrival times can be the result of multiple events of different magnitudes. This result stresses that when evacuation is considered, reliance on the maximum flow depth alone does not suffice, and the inclusion of multiple events and magnitudes is essential, highlighting the need to incorporate intra-and inter-event variability. In the present study, aspects such as recurrence were not included, and ought to be subject of subsequent research. The approach used herein used the hazard envelope, under a low probability, high consequence framework.

Combining these two intensity metrics into a 9-level categorization that gives more weight to arrival time while acknowledging the maximum hazard as presented by the tsunami flow depth, yields maps that allow a better understanding of the hazard, especially when having evacuation as its main purpose. The hazard scale is built on a priori decisions such as the definition of thresholds, which could affect the details of the final map, and could be defined locally with authorities.

It was found that the map conveys relevant information as intended. Among the benefits found is the capacity of providing support for improving evacuation routes and safe zone placement, based on a very simple representation of the hazard. In addition, the arrival time-based maps allow for introducing the notion of safe return time windows after an evacuation has been issued.

At the local level, assessing tsunami hazard due to future Chilean megathrust earthquakes (and in the far-field) must be a multidisciplinary and comprehensive approach based on the current knowledge of tsunami source specification, propagation and inundation, that should include arrival times as a key parameter.

This will help reducing tsunami risk along coastal communities with education and outreach programs based on the scientific knowledge especially in regions with a false notion of low tsunami hazard and risk (Bernard and Titov, 2015; Zamora et al., 2020). It is hypothesized that these simpler maps, even though considering more information, can be better interpreted by the general public and enhance people's awareness.

DATA AVAILABILITY STATEMENT

The datasets presented in this article are not readily available because part of the bathymetric and topographic datasets are restricted to the public, since it was shared by SHOA under an agreement. Requests to access the datasets should be directed to patricio.catalan@usm.cl.

AUTHOR CONTRIBUTIONS

NZ: Conceptualization. Data processing, writing manuscript and editing. PC: Conceptualization. Writing and editing the manuscript. AG: Data processing, writing and editing the manuscript. MC: Conceptualization, writing, and editing the manuscript.

ACKNOWLEDGMENTS

The authors acknowledge SHOA's support to this work, particularly making available nautical charts and coastal zone plans used to generate high resolution terrain models. PC, NZ and AG were partially funded by ANID through its grants ANID/FONDAP/15110017 (CIGIDEN), and ANID/FONDEF/ID19I10048. PAC also thanks ANID PIA/APOYO AFB180002. MC acknowledges the support from 'Millennium Nucleus CYCLO: The Seismic Cycle Along Subduction Zones' and Chile's Fondo Nacional de Desarrollo Científico y Tecnológico, FONDECYT Projects N°1190258 and N° 1181479. The authors also acknowledge C. Sippl for discussion about asperities offshore Valparaíso and corrections to the manuscript. The authors thankfully acknowledges the computer resources at CTE-POWER and the technical support provided by BSC (RES-AECT-2020-2-0001), and the EDANYA Group at Málaga university for providing the HySEA code. We acknowledge D. Melgar for making available the MudPy code at: https://github.com/dmelgarm/MudPy. J. León is acknowledge for sharing the evacuation results. We are very grateful to the editor S. Lorito and the comments of K. Goda, A. Armigliato and W. Power, for a thoughtful and insightful discussion that helped us to greatly improve this work. NZ has received funding from the STARS programme part of the Marie Skłodowska-Curie grant agreement H2020-MSCA-COFUND-2016-75443.

SUPPLEMENTARY MATERIAL

The Supplementary Material for this article can be found online at: https://www.frontiersin.org/articles/10.3389/feart.2020.591514/full#supplementary-material.

REFERENCES

Aránguiz, R., Catalán, P. A., Cecioni, C., Bellotti, G., Henriquez, P., and González, J. (2019). Tsunami resonance and spatial pattern of natural oscillation modes with multiple resonators. *J. Geophys. Res.: Oceans* 124, 7797–7816. doi:10.1029/2019JC015206

Aránguiz, R., González, G., González, J., Catalán, P. A., Cienfuegos, R., Yagi, Y., et al. (2016). The 16 september 2015 Chile tsunami from the post-tsunami survey and numerical modeling perspectives. *Pure Appl. Geophys.* 173, 333–348. doi:10.1007/s00024-015-1225-4

Atwater, B. F., Cisternas, M., Yulianto, E., Prendergast, A. L., Jankaew, K., Eipert, A. A., et al. (2013). El tsunami de 1960 en una planicie de cordones litorales cerca de Maullín, Chile: Descenso tierra adentro, surcos renovados, abanicos agradados, múltiples predecesores. *Andean Geol.* 40, 393–418. doi:10.5027/andgeoV40n3-a01

Barrientos, S. E. (1988). Slip distribution of the 1985 central Chile earthquake. *Tectonophysics* 145, 225–241. doi:10.1016/0040-1951(88)90197-7

Becerra, I., Aránguiz, R., González, J., and Benavente, R. (2020). An improvement of tsunami hazard analysis in central Chile based on stochastic rupture scenarios. *Coast Eng. J.* 62, 1–16. doi:10.1080/21664250.2020.1812943

Beck, S., Barrientos, S., Kausel, E., and Reyes, M. (1998). Source characteristics of historic earthquakes along the central Chile subduction zone. *J. S. Am. Earth Sci.* 11, 115–129. doi:10.1016/S0895-9811(98)00005-4

Bernard, E., and Titov, V. (2015). Evolution of tsunami warning systems and products. *Philos Trans A Math Phys Eng Sci.* 373, 20140–20371. doi:10.1098/rsta.2014.0371

Blaser, L., Kruger, F., Ohrnberger, M., and Scherbaum, F. (2010). Scaling relations of earthquake source parameter estimates with special focus on

subduction environment. *Bull. Seismol. Soc. Am.* 100, 2914–2926. doi:10.1785/0120100111

Bletery, Q., Sladen, A., Delouis, B., and Matteó, L. (2015). Quantification of tsunami bathymetry effect on finite fault slip inversion. *Pure Appl. Geophys.* 172, 3655–3670. doi:10.1007/s00024-015-1113-y

Bravo, F., Koch, P., Riquelme, S., Fuentes, M., and Campos, J. (2019). Slip distribution of the 1985 Valparaíso earthquake constrained with seismic and deformation data. *Seismol Res. Lett.* 90, 1792–1800. doi:10.1785/0220180396

Carvajal, M., Cisternas, M., and Catalán, P. A. (2017a). Source of the 1730 Chilean earthquake from historical records: implications for the future tsunami hazard on the coast of Metropolitan Chile. *J. Geophys. Res.: Solid Earth* 122, 3648–3660. doi:10.1002/2017JB014063

Carvajal, M., Cisternas, M., Gubler, A., Catalán, P., Winckler, P., and Wesson, R. (2017b). Reexamination of the magnitudes for the 1906 and 1922 Chilean earthquakes using Japanese tsunami amplitudes: implications for source depth constraints. *J. Geophys. Res.* 122, 4–17. doi:10.1002/2016JB013269

Catalán, P. A., Aránguiz, R., González, G., Tomita, T., Cienfuegos, R., González, J., et al. (2015). The 1 april 2014 Pisagua tsunami: observations and modeling. *Geophys. Res. Lett.* 42, 2918–2925. doi:10.1002/2015GL063333

Catalán, P. A., Gubler, A., Cañas, J., Zuñiga, C., Zelaya, C., Pizarro, L., et al. (2020). Design and operational implementation of the integrated tsunami forecast and warning system in Chile (SIPAT). *Coast Eng. J.* 62, 373–388. doi:10.1080/21664250.2020.1727402

Charvet, I., Macabuag, J., and Rossetto, T. (2017). Estimating tsunami-induced building damage through fragility functions: critical review and research needs. *Frontiers in Built Environment* 3, 36. doi:10.3389/fbuil.2017.00036

Cortés, P., Catalán, P. A., Aránguiz, R., and Bellotti, G. (2017). Tsunami and shelf resonance on northern Chile coast. *J. Geophys. Res.: Oceans* 122, 7364–7379. doi:10.1002/2017JC012922

Cubelos, C., Shyam Kularathna, A. H. T., Valenzuela, V. P. B., Iliopoulos, N., Quiroz, M., Yavar, R., et al. (2019). Understanding community-level flooding awareness in remote coastal towns in northern Chile through community mapping. *Geosciences* 9, 279. doi:10.3390/geosciences9070279

Davies, G., Griffin, J., Løvholt, F., Glimsdal, S., Harbitz, C., Thio, H. K., et al. (2017). A global probabilistic tsunami hazard assessment from earthquake sources. *Geological Society, London, Special Publications* 456, 219–244. doi:10.1144/SP456.5

Davies, G. (2019). Tsunami variability from uncalibrated stochastic earthquake models: tests against deep ocean observations 2006-2016. *Geophys. J. Int.* 218, 1939–1960. doi:10.1093/gji/ggz260

De Risi, R., and Goda, K. (2017). Simulation-based probabilistic tsunami hazard analysis: empirical and robust hazard predictions. *Pure Appl. Geophys.* 174, 3083–3106. doi:10.1007/s00024-017-1588-9

Doocy, S., Daniels, A., Packer, C., Dick, A., and Kirsch, T. D. (20132013). The human impact of earthquakes: a historical review of events 1980-2009 and systematic literature review. *PLoS Curr*, 5, 1–26. doi:10.1371/currents.dis.67bd14fe457f1db0b5433a8ee20fb833

Dura, T., Cisternas, M., Horton, B. P., Ely, L. L., Nelson, A. R., Wesson, R. L., et al. (2015). Coastal evidence for Holocene subduction-zone earthquakes and tsunamis in central Chile. *Quat. Sci. Rev.* 113, 93–111. doi:10.1016/j.quascirev.2014.10.015

Fraser, S. A., Wood, N. J., Johnston, D. M., Leonard, G. S., Greening, P. D., and Rossetto, T. (2014). Variable population exposure and distributed travel speeds in least-cost tsunami evacuation modelling. *Nat. Hazards Earth Syst. Sci.* 14, 2975–2991. doi:10.5194/nhess-14-2975-2014

Fritz, H. M., Petroff, C. M., Catalán, P. A., Cienfuegos, R., Winckler, P., Kalligeris, N., et al. (2011). Field survey of the 27 february 2010 Chile tsunami. *Pure Appl. Geophys.* 168, 1989–2010. doi:10.1007/s00024-011-0283-5

GEBCO (2019). *The GEBCO-2019 grid. a continuous terrain model of the global oceans and land. the british oceanographic data centre*., NERC, UK: national oceanography centre.

Geist, E. L., and Parsons, T. (2006). Probabilistic analysis of tsunami hazards. *Nat. Hazards* 37, 277–314. doi:10.1007/s11069-005-4646-z

González, J., González, G., Aránguiz, R., Melgar, D., Zamora, N., Shrivastava, M. N., et al. (2020). A hybrid deterministic and stochastic approach for tsunami hazard assessment in Iquique, Chile. *Nat. Hazards* 1, 231–254. doi:10.1007/s11069-019-03809-8

Grezio, A., Babeyko, A., Baptista, M. A., Behrens, J., Costa, A., Davies, G., et al. (2017). Probabilistic tsunami hazard analysis: multiple sources and global applications. *Rev. Geophys.* 55, 1158–1198. doi:10.1002/2017RG000579

Harbitz, C. B., Løvholt, F., and Bungum, H. (2013). Submarine landslide tsunamis: how extreme and how likely? *Nat. Hazards* 72, 1341–1374. doi:10.1007/s11069-013-0681-3

Hayes, G. P., Wald, D. J., and Johnson, R. L. (2012). Slab1.0: a three-dimensional model of global subduction zone geometries. *J. Geophys. Res.: Solid Earth* 117, B01. doi:10.1029/2011JB008524

Hoang, V. C., Tanaka, H., and Mitobe, Y. (2018). Estuarine morphology recovery after the 2011 great east Japan earthquake tsunami. *Mar. Geol.* 398, 112–125. doi:10.1016/j.margeo.2018.01.001

Imamura, F., Boret, S. P., Suppasri, A., and Muhari, A. (2019). Recent occurrences of serious tsunami damage and the future challenges of tsunami disaster risk reduction. *Progress in Disaster Science*, 1, 100 009. doi:10.1016/j.pdisas.2019.100009

Kajiura, K. (1970). Tsunami source, energy and the directivity of wave radiation. *Bull. Earthq. Res. Inst.* 48, 835–869. doi:10.1007/BF02109296

Koshimura, S., Katada, T., Mofjeld, H. O., and Kawata, Y. (2006). A method for estimating casualties due to the tsunami inundation flow. *Nat. Hazards* 39, 265–274. doi:10.1007/s11069-006-0027-5

Koshimura, S., Namegaya, Y., and Yanagisawa, H. (2009). Tsunami fragility: a new measure to identify tsunami damage. *J. Disaster Res.* 4, 479–488. doi:10.20965/jdr.2009.p0479

Langenbruch, C., Ellsworth, W. L., Woo, J.-U., and Wald, D. J. (2020). Value at induced risk: injection-induced seismic risk from low-probability, high-impact events. *Geophys. Res. Lett.* 47, e2019GL085. doi:10.1029/2019GL085878

León, J., Castro, S., Mokrani, C., and Gubler, A. (2020). Tsunami evacuation analysis in the urban built environment: a multi-scale perspective through two modeling approaches in viña del mar, Chile. *Coast Eng. J.* 62, 389–404. doi:10.1080/21664250.2020.1738073

León, J., Mokrani, C., Catalán, P., Cienfuegos, R., and Femenías, C. (2018). Examining the role of urban form in supporting rapid and safe tsunami evacuations: a multi-scalar analysis in Viña del Mar, Chile. *Procedia Engineering* 212, 629–636. doi:10.1016/j.proeng.2018.01.081

León, J., Mokrani, C., Catalán, P., Cienfuegos, R., and Femenías, C. (2019a). The role of built environment's physical urban form in supporting rapid tsunami evacuations: using computer-based models and real-world data as examination tools. *Frontiers in Built Environment* 4, 89. doi:10.3389/fbuil.2018.00089

León, J., Vicuña, M., and Gubler, A. (2019b). Increasing tsunami risk through intensive urban densification in metropolitan areas: a longitudinal analysis in viña del mar, Chile. *International Journal of Disaster Risk Reduction* 41, 101–312. doi:10.1016/j.ijdrr.2019.101312

LeVeque, R., George, D., and Berger, M. (2011). Tsunami modelling with adaptively refined finite volume methods. *Acta Numer.* 20, 211–289. doi:10.1017/S0962492911000043

LeVeque, R. J., Waagan, K., González, F. I., Rim, D., and Lin, G. (2016). Generating random earthquake events for probabilistic tsunami hazard assessment. *Pure Appl. Geophys.* 173, 3671–3692. doi:10.1007/s00024-016-1357-1

Li, L., Switzer, A. D., Chan, C.-H., Wang, Y., Weiss, R., and Qiu, Q. (2016). How heterogeneous coseismic slip affects regional probabilistic tsunami hazard assessment: a case study in the South China Sea. *J. Geophys. Res.: Solid Earth* 121, 6250–6272. doi:10.1002/2016JB013111

Lorito, S., Selva, J., Basili, R., Romano, F., Tiberti, M. M., and Piatanesi, A. (2015). Probabilistic hazard for seismically induced tsunamis: accuracy and feasibility of inundation maps. *Geophys. J. Int.* 200, 574–588. doi:10.1093/gji/ggu408

Macías, J., Castro, M. J., Ortega, S., Escalante, C., and González-Vida, J. M. (2017). Performance benchmarking of tsunami-HySEA model for NTHMP's inundation mapping activities. *Pure Appl. Geophys.* 174, 3147–3183. doi:10.1007/s00024-017-1583-1

Makinoshima, F., Imamura, F., and Oishi, Y. (2020). Tsunami evacuation processes based on human behaviour in past earthquakes and tsunamis: a literature review. *Progress in Disaster Science* 7, 100–113. doi:10.1016/j.pdisas.2020.100113

Martínez, C., Cienfuegos, R., Inzunza, S., Urrutia, A., and Guerrero, N. (2020). Worst-case tsunami scenario in cartagena bay, central Chile: challenges for coastal risk management. *Ocean Coast Manag.*, 185, 105060. doi:10.1016/j.ocecoaman.2019.105060

McAdoo, B. G., Dengler, L., Prasetya, G., and Titov, V. (2006). How an oral history saved thousands on Indonesia's simeulue island during the december 2004 and march 2005 tsunamis. *Earthq. Spectra* 22 (3), 661–669. doi:10.1193/1.2204966

Melgar, D., LeVeque, R. J., Dreger, D. S., and Allen, R. M. (2016). Kinematic rupture scenarios and synthetic displacement data: an example application to the cascadia subduction zone. *J. Geophys. Res.: Solid Earth* 121, 6658–6674. doi:10.1002/2016JB013314

Mori, N., Goda, K., and Cox, D. (2018). "Recent process in probabilistic tsunami hazard analysis (PTHA) for mega thrust subduction earthquakes," in *The 2011 Japan earthquake and tsunami: reconstruction and restoration. Advances in natural and technological hazards research*. Editors V. Santiago-Fandiño, S. Sato, N. Maki, and K. Iuchi, 47, 469–485. doi:10.1007/978-3-319-58691-5_27

Morton, R. A., Gelfenbaum, G., Buckley, M. L., and Richmond, B. M. (2011). Geological effects and implications of the 2010 tsunami along the central coast of Chile. *Sediment. Geol.* 242, 34–51. doi:10.1016/j.sedgeo.2011.09.004

Muhari, A., Imai, K., Sugawara, D., and Imamura, F. (2015). "A method to determine the level 1 and level 2 tsunami inundation areas for reconstruction in Eastern Japan and possible application in pre-disaster areas," in Post-tsunami hazard. Editors V. Santiago-Fandiño, Y. Kontar, and Y. Kaneda (Cham: Springer), 133–155. doi:10.1007/978-3-319-10202-3_10

Nakamura, S. (1992). An analysis of the 1985 Chilean tsunami. *Mar. Geodes* 15, 277–281. doi:10.1080/01490419209388064

NGDC/WDS (2018). National Geophysical Data Center, World Data Service. *Global historical tsunami database*. Washington, D.C, United States: National Geophysical Data Center.

Okada, Y. (1985). Surface deformation due to shear and tensile faults in a half-space. *Bull. Seismol. Soc. Am.* 75, 1135–1154.

Park, H., Cox, D. T., and Barbosa, A. R. (2018). Probabilistic Tsunami Hazard Assessment (PTHA) for resilience assessment of a coastal community. *Nat. Hazards* 94, 1117–1139. doi:10.1007/s11069-018-3460-3

Park, H., and Cox, D. T. (2016). Probabilistic assessment of near-field tsunami hazards: inundation depth, velocity, momentum flux, arrival time, and duration applied to Seaside, Oregon. *Coast Eng.* 117, 79–96. doi:10.1016/j.coastaleng.2016.07.011

Poulos, A., Monsalve, M., Zamora, N., and de la Llera, J. C. (2019). An updated recurrence model for Chilean subduction seismicity and statistical validation of its Poisson nature. *Bull. Seismol. Soc. Am.* 109, 66–74. doi:10.1785/0120170160

Ranghieri, F., and Ishiwatari, M. (2014). Chapter: strategies for managing low-probability, high-impact events. *Learning from megadisasters: lessons from the great east Japan earthquake*, 297–304. doi:10.1596/978-1-4648-0153-2ch32

Sepúlveda, I., Liu, P. L.-f., and Grigoriu, M. D. (2018). Probabilistic tsunami hazard assessment in south China sea with consideration of uncertain earthquake characteristics. *J. Geophys. Res.: Solid Earth* 124, 658–688. doi:10.1029/2018JB016620

SHOA (2012). *Carta de inundación por tsunami (CITSU) de Valparaíso y Viña del Mar.*, Valparaíso, Chile: Servicio Hidrográfico y Oceanográfico de la Armada de Chile. Available at: http://www.shoa.cl/php/citsu.php (Accessed January 15, 2021).

Sippl, C., Moreno, M., and Benavente, R. (2020). Microseismicity appears to outline highly coupled regions on the central Chile megathrust. *Preprint at EarthArXiv*. doi:10.31223/X56S3B

Tadono, T., Ishida, H., Oda, F., Naito, S., Minakawa, K., and Iwamoto, H. (2014). Precise global DEM generation by ALOS PRISM. *ISPRS. Annals* 4, 71–76. doi:10.5194/isprsannals-II-4-71-2014

Tanioka, Y., and Satake, K. (1996). Tsunami generation by horizontal displacement of ocean bottom. *Geophys Res Lett.* 23, 861–864. doi:10.1029/96GL00736

Tinti, S., Tonini, R., Bressan, L., Armigliato, A., Gardi, A., Guillande, R., et al. (2011). *Handbook of tsunami hazard and damage scenarios. EUR 24691 EN – joint research centre – institute for the protection and security of the citizen. Tech. rep* (Luxembourg: Publications Office of the European Union), 43.

UNISDR (2018). Economic losses, poverty & disasters 1998-2017. *Tech. Report*. Available at: https://www.undrr.org/publication/economic-losses-poverty-disasters-1998-2017

Volpe, M., Lorito, S., Selva, J., Tonini, R., Romano, F., and Brizuela, B. (2019). From regional to local SPTHA: efficient computation of probabilistic tsunami inundation maps addressing near-field sources. *Nat. Hazards Earth Syst. Sci.* 19, 455–469. doi:10.5194/nhess-19-455-2019

Williamson, A. L., and Newman, A. V. (2019). Suitability of open-ocean instrumentation for use in near-field tsunami early warning along seismically active subduction zones. *Pure Appl. Geophys.* 176, 3247–3262. doi:10.1007/s00024-018-1898-6

Wood, N. J., and Schmidtlein, M. C. (2013). Community variations in population exposure to near-field tsunami hazards as a function of pedestrian travel time to safety. *Nat. Hazards* 65, 1603–1628. doi:10.1007/s11069-012-0434-8

Yamazaki, Y., Kowalik, Z., and Cheung, K. F. (2009). Depth-integrated, non-hydrostatic model for wave breaking and run-up. *Int. J. Numer. Methods Fluid* 61, 473–497. doi:10.1002/fld.1952

Zamora, N., Gubler, A., Orellana, V., León, J., Urrutia, A., Carvajal, M., et al. (2020). The 1730 great metropolitan Chile earthquake and Tsunami commemoration: joint efforts to increase the country's awareness. *Geosciences* 10, 1–15. doi:10.3390/geosciences10060246

Conflict of Interest: The authors declare that the research was conducted in the absence of any commercial or financial relationships that could be construed as a potential conflict of interest.

frontiers in Earth Science

REVIEW
published: 29 April 2021
doi: 10.3389/feart.2021.628772

Probabilistic Tsunami Hazard and Risk Analysis: A Review of Research Gaps

Jörn Behrens[1], Finn Løvholt[2], Fatemeh Jalayer[3], Stefano Lorito[4], Mario A. Salgado-Gálvez[5,6], Mathilde Sørensen[7], Stephane Abadie[8], Ignacio Aguirre-Ayerbe[9], Iñigo Aniel-Quiroga[9], Andrey Babeyko[10], Marco Baiguera[11], Roberto Basili[4], Stefano Belliazzi[3], Anita Grezio[12], Kendra Johnson[13], Shane Murphy[14], Raphaël Paris[15], Irina Rafliana[16,17], Raffaele De Risi[18], Tiziana Rossetto[11], Jacopo Selva[12], Matteo Taroni[4], Marta Del Zoppo[3], Alberto Armigliato[19], Vladimír Bureš[20], Pavel Cech[20], Claudia Cecioni[21], Paul Christodoulides[22], Gareth Davies[23], Frédéric Dias[24], Hafize Başak Bayraktar[3], Mauricio González[9], Maria Gritsevich[25,26,27], Serge Guillas[11], Carl Bonnevie Harbitz[2], Utku Kânoğlu[28], Jorge Macías[29], Gerassimos A. Papadopoulos[30], Jascha Polet[31], Fabrizio Romano[4], Amos Salamon[32], Antonio Scala[3], Mislav Stepinac[33], David R. Tappin[11,34], Hong Kie Thio[35], Roberto Tonini[4], Ioanna Triantafyllou[36], Thomas Ulrich[37], Elisa Varini[38], Manuela Volpe[4] and Eduardo Vyhmeister[39]*

[1]Department of Mathematics/CEN, Universität Hamburg, Hamburg, Germany, [2]NGI - Norwegian Geotechnical Institute, Oslo, Norway, [3]University of Naples Federico II, Naples, Italy, [4]Istituto Nazionale di Geofisica e Vulcanologia, Rome, Italy, [5]ERN Internacional, Mexico City, Mexico, [6]Centre Internacional de Metodes Numerics en Enginyeria (CIMNE), Barcelona, Spain, [7]University of Bergen, Bergen, Norway, [8]Universite de Pau et des Pays de L'Adour, E2S UPPA, SIAME, France, [9]IHCantabria - Instituto de Hidráulica Ambiental de La Universidad de Cantabria, Santander, Spain, [10]Deutsches GeoForschungsZentrum GFZ, Potsdam, Germany, [11]University College London, London, United Kingdom, [12]Istituto Nazionale di Geofisica e Vulcanologia, Sezione di Bologna, Bologna, Italy, [13]GEM Foundation, Pavia, Italy, [14]Ifremer, Plouzané, France, [15]Laboratoire Magmas and Volcans, Aubière, France, [16]German Development Institute/Deutsches Institut für Entwicklungspolitik (DIE), Bonn, Germany, [17]Indonesian Institute of Sciences (LIPI), Jakarta, Indonesia, [18]University of Bristol, Bristol, United Kingdom, [19]Alma Mater Studiorum - University of Bologna, Bologna, Italy, [20]University of Hradec Kralove, Hradec Kralove, Czech Republic, [21]Università Degli Studi Roma Tre, Rome, Italy, [22]Cyprus University of Technology, Limassol, Cyprus, [23]Geoscience Australia, Canberra, ACT, Australia, [24]University College Dublin, Dublin, Ireland, [25]Finnish Geospatial Research Institute (FGI), Masala, Finland, [26]Department of Physics, University of Helsinki, Helsinki, Finland, [27]Institute of Physics and Technology, Ural Federal University, Ekaterinburg, Russian Federation, [28]Department of Engineering Sciences, Middle East Technical University, Ankara, Turkey, [29]Facultad de Ciencias, Universidad de Málaga, Málaga, Spain, [30]International Society for the Prevention and Mitigation of Natural Hazards, Athens, Greece, [31]Cal Poly Pomona, Pomona, CA, United States, [32]Geological Survey of Israel, Jerusalem, Israel, [33]University of Zagreb, Zagreb, Croatia, [34]British Geological Survey, Nottingham, United Kingdom, [35]AECOM, Los Angeles, CA, United States, [36]Department of Geology and Geoenvironment, National and Kapodistrian University of Athens, Athens, Greece, [37]Department of Earth and Environmental Sciences, Ludwig-Maximilians-Universität München, Munich, Germany, [38]C.N.R. - Institute for Applied Mathematics and Information Technologies, Milano, Italy, [39]Insight Research Centre, University College Cork, Cork, Ireland

Tsunamis are unpredictable and infrequent but potentially large impact natural disasters. To prepare, mitigate and prevent losses from tsunamis, probabilistic hazard and risk analysis methods have been developed and have proved useful. However, large gaps and uncertainties still exist and many steps in the assessment methods lack information, theoretical foundation, or commonly accepted methods. Moreover, applied methods have very different levels of maturity, from already advanced probabilistic tsunami hazard analysis for earthquake sources, to less mature probabilistic risk analysis. In this review we give an overview of the current state of probabilistic tsunami hazard and risk analysis. Identifying research gaps, we offer suggestions for future research directions. An extensive literature list allows for branching into diverse aspects of this scientific approach.

Keywords: tsunami, probabilistic method, hazard, risk, research gap

OPEN ACCESS

Edited by:
Victoria Miller, The University of the West Indies St. Augustine, Trinidad and Tobago

Reviewed by:
Eric Geist, United States Geological Survey (USGS), United States
Patricio Andres Catalan, Federico Santa María Technical University, Chile

****Correspondence:***
Jörn Behrens, joern.behrens@uni-hamburg.de

Specialty section:
This article was submitted to Geohazards and Georisks, a section of the journal Frontiers in Earth Science

Received: *12 November 2020*
Accepted: *10 February 2021*
Published: *29 April 2021*

Citation:
Behrens J, Løvholt F, Jalayer F, Lorito S, Salgado-Gálvez MA, Sørensen M, Abadie S, Aguirre-Ayerbe I, Aniel-Quiroga I, Babeyko A, Baiguera M, Basili R, Belliazzi S, Grezio A, Johnson K, Murphy S, Paris R, Rafliana I, De Risi R, Rossetto T, Selva J, Taroni M, Del Zoppo M, Armigliato A, Bureš V, Cech P, Cecioni C, Christodoulides P, Davies G, Dias F, Bayraktar HB, González M, Gritsevich M, Guillas S, Harbitz CB, Kânoğlu U, Macías J, Papadopoulos GA, Polet J, Romano F, Salamon A, Scala A, Stepinac M, Tappin DR, Thio HK, Tonini R, Triantafyllou I, Ulrich T, Varini E, Volpe M and Vyhmeister E (2021) Probabilistic Tsunami Hazard and Risk Analysis: A Review of Research Gaps. Front. Earth Sci. 9:628772. doi: 10.3389/feart.2021.628772

INTRODUCTION

Tsunamis are rare but potentially devastating natural hazards. With often limited available data, a coherent framework that incorporates data, physical assumptions (i.e., the general model of the system), and statistical methods for hazard and risk analysis is necessary to assess consequences affecting different layers of societies. To further develop, standardize and document such a framework is the underlying objective of COST Action AGITHAR (Accelerating Global Science in Tsunami Hazard and Risk Analysis; AGITHAR, 2020) and this article forms one outcome of the Action.

Probabilistic tsunami hazard and risk analyses (PTHA and PTRA, respectively) offer structured and rigorous procedures that allow for tracing and weighting the key elements in understanding the potential tsunami hazard and risk in globally distributed applications (e.g., Basili et al., 2021). Because of this, PTHA are becoming a standard basis for tsunami risk assessment around the world. Significant challenges in this analysis method are 1) the choice of hypothetical events and assigning "correct" probabilities, and ii) the impact of source regions distributed throughout an ocean basin and, conceivably, unifying distinct types of sources in a homogeneous probabilistic framework with a comprehensive treatment of uncertainty. The great importance of PTHA is due to its practical implications for society providing information for long-term planning and coastal management in areas where potential tsunamis may occur. Conversely, PTRA are still less abundant and standardized than PTHA, as elaborated in this review.

Few mega-tsunamis have been observed in the instrumental period, a timeframe spanning from approximately the 1960s to today. Thus, it is challenging to confidently assess the rate at which consequential tsunamis will occur. Predominantly seismically triggered tsunamis comprise about 80% of all tsunamis worldwide (e.g., Harbitz et al., 2014) with the remainder caused by landslides, volcanoes, or meteorological phenomena.

The sparsity of background data and requirements in engineering applications have driven the development of probabilistic methods for assessing tsunami hazard and risk aiming for unbiased comparisons of different hazards (natural and anthropogenic) as well as their uncertainty quantification. In recent years, the probabilistic framework has been increasingly applied. However, broadly accepted approaches are not yet defined, and potentially incompatible implementations of probabilistic methods are used in different regions across the world, and different tsunami source types are often treated separately and are rarely combined.

In this study, we have documented current gaps and open research questions related to PTHA and PTRA. We have organized this review into two main sections, one focused on tsunami hazard and the other on risk. We preface these topics with a brief introduction to the probabilistic framework underlying both PTHA and PTRA. Note that we grouped the gaps in numerical modeling in the hazard analysis related section, even though modeling may also be considered a cross-cutting topic. We believe, however, that the mentioned gaps are more related and addressed in a similar way as the other hazards related research gaps.

While PTHA and PTRA allow for including uncertainty in a consistent way, it is necessary to point out that it is not always simple to describe the knowledge gaps formally, for example through alternative models, and quantify their impact on hazard and risk models in terms of epistemic uncertainty (i.e., caused by lack of knowledge or data, Kiureghian and Ditlevsen, 2009). Overall, the research gaps identified in this study are "known unknowns" (e.g., Logan, 2009) and deserve more thorough research efforts, in order to determine their influence on the overall outcome of the PTHA or PTRA workflow.

This fact makes it hard to determine quantitatively the importance of each of the research gaps. Nevertheless, we tried to assess—in a qualitative way—the relative priority of research gaps and discuss this in the last section of this report.

PROBABILISTIC FRAMEWORK

In this section, we present a structure for probabilistic hazard and risk analyses. An overview is given in **Figure 1**. More in-depth reviews of identified gaps related to the individual probabilistic framework components are discussed in sections "*Probabilistic Tsunami Hazard Analysis*" and "*Probabilistic Tsunami Risk Assessment*".

The purpose of PTHA is to find the probability for a tsunami intensity measure (*IM*) to exceed a given threshold in a predefined time interval. Note that, in the PTHA framework, "Intensity Measure" is used with a meaning that differs from the "tsunami intensity scale" used, for instance, in tsunami catalogs to define the "size" of a tsunami or the effects it produces inland. In the PTHA context, an *IM* is a physical observable strictly connected to the physics of the process. Common *IM*s are wave amplitude, flow depth, current velocity, momentum flux, or maximum inundation height, depending on the problem setting (Grezio et al., 2017).

Different probabilistic framework alternatives for computational PTRA exist. One option, rooted in seismic risk analysis, is *performance-based* risk assessment, presented by PEER (Pacific Earthquake Engineering Center) in 2000. The term performance-based is often used in contraposition to traditional prescriptive assessment procedures for seismic-resistant building design (Fardis, 2009). The performance-based framework aims to provide a practical yet rigorous workflow and has also been used for risk assessment for hurricanes (e.g., van de Lindt and Dao, 2009; Barbato et al., 2013), floods (De Risi et al., 2013; Jalayer et al., 2016), and tsunamis (Chock et al., 2011; Chock, 2016; Attary et al., 2017). This framework can be organized in different modules; for example, *hazard* and *vulnerability* or *hazard*, *fragility* and *consequence*. Modules communicate with each other through intermediate variables and their conditional probabilities. Examples of intermediate variables are intensity measure (*IM*), damage measure (*DM*) and decision variable (*DV*). *IM* serves as an intermediate variable between hazard and vulnerability. *DM*

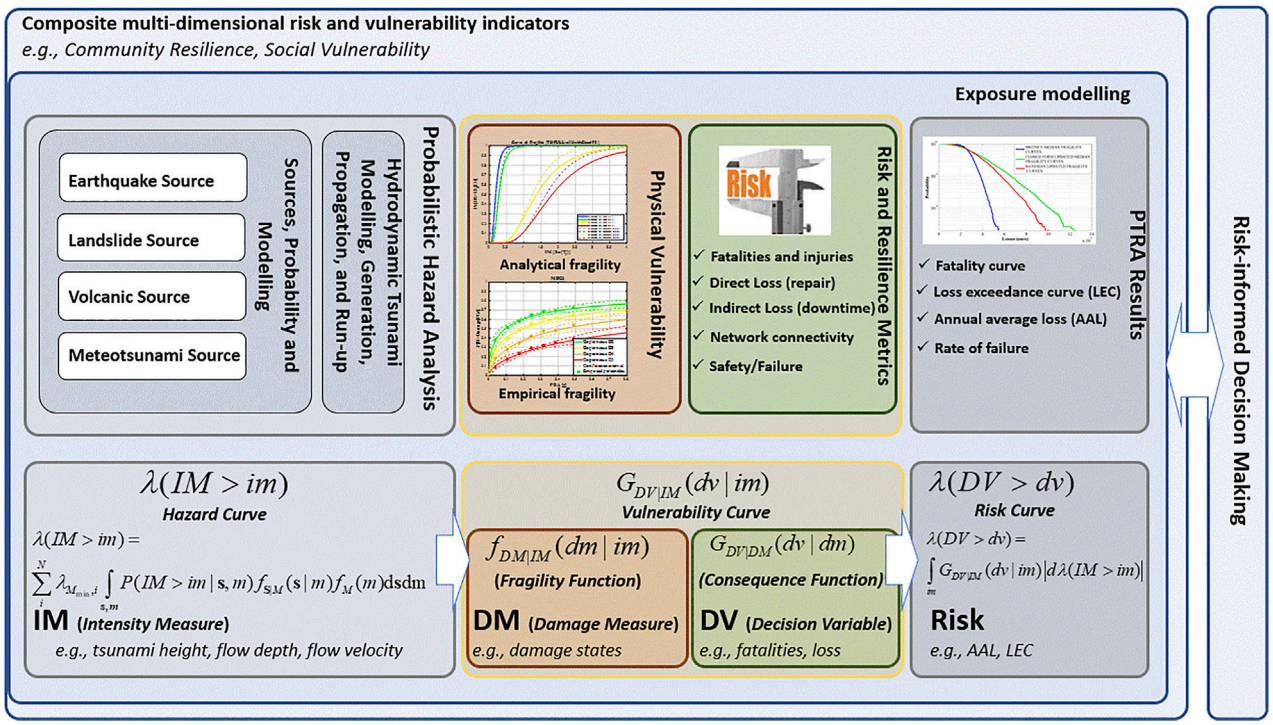

FIGURE 1 | Roadmap of PTHA and PTRA frameworks: The entire process of risk evaluation needs to interact with the (risk-informed) decision-making process. *Composite multi-dimensional risk and vulnerability indicators* ("*Probabilistic Tsunami Hazard Analysis*" section) are shown as defining the context for the complex tsunami risk evaluation. The *exposure modeling* ("*Probabilistic Tsunami Risk Assessment*" section) defines groups of individuals and assets at risk. The horizontal flowchart at the bottom of the figure shows the PEER-like workflow for risk assessment. *Probabilistic hazard analysis* ("*Probabilistic Tsunami Hazard Analysis*" section) discusses estimation of the mean annual frequency (rate) of exceedance of a given value (*im*) of an intensity measure (*IM*, **Eq. 1**) commonly visualized as a hazard curve. The *IM* can be a vector or a scalar that describes the intensity of a tsunami. Examples of IM's are flow depth, maximum tsunami inundation height, etc. *M* refers in a generic manner to the size of various tsunami sources (e.g., earthquake magnitude, landslide volume). The tsunami *sources, probability and modeling* (earthquake, landslide, volcanic and meteotsunami) are discussed in "*Probabilistic Tsunami Hazard Analysis*" section. **s** denotes the vector of source parameters. *N* denotes the number of tsunamigenic sources. $\lambda_{M_{\min,i}}$ denotes the mean annual frequency of tsunamigenic events exceeding $M_{\min}$ from source *i*. "*Gaps in Hydrodynamic Tsunami Modeling, Generation, Propagation, and Run-up*" section discusses *hydrodynamic tsunami modeling, generation, propagation and run-up*. The *physical vulnerability* ("*Gaps in Physical Vulnerability*" section) discusses the estimation of the probability distribution for a damage measure (DM, specific value *dm*) given *IM* (specific value *im*), known as the fragility function. The most common example of a DM is the physical damage state. The *risk and resilience metrics* section ("*Gaps in Risk and Resilience Metrics*" section) discusses the estimation of various decision variables (e.g., fatalities, repair costs, downtime) denoted as DV (specific value *dv*). More specifically, it discusses the probability distribution for DV given DM also known as the consequence function. The vulnerability function (**Eq. 3**) describes the (mean and standard deviation) of the probability distribution for DV given *IM* and is obtained by integrating over the entire domain of DM. One way to show the PTRA results is through visualizing the mean annual frequency of exceeding a specific value *dv* of DV (e.g., the loss exceedance curve (LEC) or the annual average loss (AAC)) shown in **Eq. 2**, referred to generically as the risk curve.

connects vulnerability with fragility and describes physical damage. *DV* connects fragility with consequences and reaches out to decision-makers with numbers of casualties, repair costs, or downtimes. Interestingly, several risk-informed decision-making processes related to tsunamis are based on PTHA information only (e.g., hazard-based evacuation zones, hazard-based land-use planning). As an example, the criterion "flow depth (*IM*) larger than a threshold (*im*)" can be used as a basis for decision-making (e.g., assigning evacuation zones). In other words, an *IM* can act as an intermediate variable (intensity measure) as well as a decision variable.

To illustrate the framework, suppose a finite set of *N* hypothetical tsunamigenic sources representing all possible tsunami events affecting the site of interest. Each event occurs randomly in time and independently of all others (i.e., as a Poisson process). The tsunami hazard curve–the main outcome of PTHA–describes the mean annual rate of a tsunami event affecting location *x* with an intensity measure *IM(x)* greater than some threshold *im*, denoted as $\lambda(IM(x) \geq im)$. This can be expressed as:

$$\lambda\left(IM\left(x\right) \geq im\right) = \sum_{i}^{N} \lambda_{M_{\min,i}} \int P\left(IM\left(x\right) \geq im | s, m\right) f_{S|M}\left(s|m\right) f_{M}\left(m\right) \mathrm{dsd}m \quad (1)$$

where $\lambda_{M_{\min,i}}$ is the mean annual rate of occurrence of tsunamigenic events from source *i* (e.g., earthquakes, landslides, etc.) having magnitudes *M* exceeding $M_{\min}$, f_M is the conditional probability density function for $M \geq M_{\min,i}$, and $f_{S|M}$ is the probability density function of the set of source parameters *S* given magnitude *M*. The aleatoric uncertainty associated with variable source characteristics can be represented by probabilistic prediction models of the source

parameters. Finally, $p(IM(x) \geq im|\boldsymbol{s},m)$ is the complementary cumulative distribution function of IM given $S = s$ and $M = m$, and can be evaluated through tsunami simulations. Note that **Eq. 1** can be used only if sources are independent; a counterexample being a landslide generated from the same earthquake that amplifies the ensuing tsunami's destruction.

Epistemic uncertainty in PTHA is often accounted for using logic trees or, more recently, ensemble modeling, which allow alternative hypotheses for uncertain parameters, each of which is assigned a weight reflecting confidence in the respective parameter value (e.g., Geist and Parsons, 2006; Selva et al., 2016; Grezio et al., 2017). **Equation 1** is computed for each logic tree 'end branch'.

Building on tsunami hazard, the tsunami loss curve at any location is calculated by convolving vulnerability and hazard over the entire span of IM:

$$\lambda(DV \geq \mathrm{d}v) = \int_{im} G_{DV|IM}(\mathrm{d}v|im)|\mathrm{d}\lambda(IM(x) \geq im)| \quad (2)$$

where $\lambda(DV \geq \mathrm{d}v)$ is the mean annual rate of occurrence of DV larger than a threshold $\mathrm{d}v$. Vulnerability is expressed through the complementary probability distribution function denoted as $G_{DV|IM}(\mathrm{d}v|im)$, for DV given IM, and is itself calculated by integrating fragility and consequence functions (see also **Figure 1**):

$$G_{DV|IM}(\mathrm{d}v|im) = \int_{\mathrm{d}m} G_{DV|DM}(dv|dm) f_{DM|IM}(dm|im) ddm, \quad (3)$$

with

- $f_{DM|IM}$, the *tsunami fragility function,* predicts the probability of incurring a particular value (dm) of damage measure DM (e.g., damage states) for a given $IM = im$;
- $G_{DV|DM}(\mathrm{d}v|\mathrm{d}m)$, the *tsunami consequence function* (e.g., the damage-loss function), expressed as the complementary cumulative distribution function of DV given DM.

Strictly speaking, **Eqs. 1** and **2** do not consider multi-hazard and multi-risk aspects such as cascading effects, combined damage due to tsunami loading and earthquake shaking. Assuming a Poisson process, the rate of exceedance λ is often transformed the first excursion of a specific value $\mathrm{d}v$ for a generic decision variable DV in the time Δt (e.g., 1 year, 50 years):

$$P(DV \geq \mathrm{d}v; \Delta t) = 1 - \exp(-\lambda(DV \geq \mathrm{d}v)\Delta t) \quad (4)$$

PROBABILISTIC TSUNAMI HAZARD ANALYSIS

This section discusses gaps in PTHA, focusing on those in tsunami sources and hydrodynamic modeling. Each subsection includes a summary of the present state-of-the-art, followed by an in-depth discussion of the gaps.

Gaps in Earthquake Source Representation

Existing Methods

Seminal Seismic PTHA (SPTHA) was performed using crude source and tsunami representations (Lin and Tung, 1982; Rikitake and Aida, 1988; Tinti, 1991). Since then, the methodology has evolved dramatically (Geist and Parsons., 2006; Annaka et al., 2007; Power et al., 2007; Thio et al., 2007; Burbidge et al., 2008; González et al., 2009; Sørensen et al., 2012; Hoechner et al., 2016; Miyashita et al., 2020), also in the framework of large programs (e.g., Horspool et al., 2014; Davies et al., 2018; Davies and Griffin, 2018; Basili et al., 2021).

SPTHA methodology for spatio-temporal and kinematic source treatment and the basic uncertainty framework were mostly transcribed from Probabilistic Seismic Hazard Analysis (PSHA, Esteva, 1967; Cornell, 1968; a historical perspective: McGuire, 2008). Due to tsunami data scarcity, it is challenging to derive hazard estimates directly from historical records (Geist and Parsons, 2006; Grezio et al., 2017). Consequently, numerical modeling is a distinctive characteristic of SPTHA where seafloor displacement and tsunami evolution from generation to inundation are simulated for each scenario (Geist and Parsons, 2006; Geist and Lynett, 2014). Source parameters can be inferred from past seismicity or from balancing the seismic moment across a fault zone, potentially constrained by geodetic strain rates (Grezio et al., 2017). Often only major subduction zones are considered in SPTHA, assuming that they are the main hazard drivers (e.g., González et al., 2009; Davies et al., 2018). In this case, spatial characterization provides geometrical and kinematic constraints, such as the fault geometry, preferential slip direction, and other source zone properties. Crustal and general seismicity from unconstrained or unknown faults is treated with a larger uncertainty (e.g., Selva et al., 2016; Basili et al., 2021). Earthquakes are usually simplified to having either uniform (e.g., Horspool et al., 2014) or heterogeneous instantaneous slip (e.g., De Risi and Goda, 2017). Seafloor deformation is predominantly computed analytically assuming an elastic homogeneous half-space (Mansinha and Smylie, 1971; Okada, 1992; Meade, 2007; Nikkhoo and Walter, 2015).

State-of-the-art seismic source representation for tsunami simulations is reviewed by Geist and Oglesby (2014) and Geist et al. (2019). Additionally, we note some innovative efforts for complex, yet computationally affordable, approaches to source simulation (Melgar et al., 2016; Murphy et al., 2016; Sepúlveda et al., 2017; Scala et al., 2020), and methods for handling source modeling uncertainties and sensitivity including temporal aspects and recurrence (Grezio et al., 2010; Basili et al., 2013; Lorito et al., 2015; Selva et al., 2016; Lotto et al., 2017; Davies, 2019; Goda, 2019; Davies and Griffin, 2020).

Identified Gaps

Limited Past Events and Data to Inform Hazard Models (S1)

Completeness and quality of historical earthquake data, needed to constrain seismic source parameters, varies greatly depending on the history of the investigated geographical region (Stucchi et al., 2004; Albini et al., 2014). Event catalogs are generally too short to account for the source frequency needed to model large average return periods in PTHA. The description of earthquake

recurrence and of the tail of the frequency-magnitude distribution is highly uncertain (Kagan, 2002; Geist and Parsons, 2014; Rong et al., 2014; Bommer and Stafford, 2016). In the attempt of constraining this uncertainty, seismic source parameters have been estimated globally using seismic or geodetic data or both (e.g., Bird and Kagan, 2004; Bird et al., 2015; Bird and Kreemer, 2015); however, these types of input data are not always considered by PTHAs. Moreover, a framework for constraining PTHA directly from tsunami observations exists (Geist and Parsons, 2006; Grezio et al., 2017), while treatment of incomplete catalogs is described by Smit et al. (2017). Where possible, other data types should also be considered. Paleo-seismic and paleo-tsunami catalogs may help constrain or validate at least large event recurrence (e.g., Priest et al., 2017; Paris et al., 2020), while GPS-constrained strain accumulation can indicate the total seismic moment rate (e.g., Hayes et al., 2018). Care should be taken of potential biases coming from overweighting evidence of large tsunamis in the past (Geist and Parsons, 2006).

Fault Identification, Fault and Source Zone Parameterization and Tsunamigenic Potential Characterization (S2)

Tsunami sources are often constrained from infrequent offshore geologic studies investigating very large areas. Therefore, geologic fault data are often incomplete, causing a wide range of source knowledge levels (Basili et al., 2013). Seismic source characterization for SPTHA generally refers to properties of pre-existing large faults, and often only to great subduction zone sources. All other–mostly crustal–faults are seldomly considered in PTHA, although non-subduction earthquakes may control tsunami hazard, especially when located near the target site (Selva et al., 2016). Despite overall good constraint of subduction interface geometries (e.g., Hayes et al., 2018), along-strike trench segmentation and its impact on rupture propagation remains uncertain, limiting rupture forecasts and hindering estimates of subduction earthquake maximum magnitude (e.g., Bilek, 2010; Kopp, 2013; Grezio et al., 2017). Whenever fault knowledge is incomplete, more randomized "background" seismicity modeling is needed, with less predictable geometry and seismic behavior compared to subduction interfaces (Sørensen et al., 2012; Selva et al., 2016). Fault slip rates can constrain seismicity recurrence parameters; these can vary both spatially (Zechar and Frankel, 2009) and temporally (e.g., Ota and Yamaguchi, 2004; Ramírez-Herrera et al., 2011; Tiberti et al., 2014) but usually only averages are considered due to a lack of information. Kagan and Jackson (2014) pointed out that more research would be needed for focal mechanism forecasting; identifying the prevailing faulting mechanism is a critical task particularly in tectonically complex environments. This is expected, in turn, to exert a strong influence on tsunami hazard.

Variety, Complexity, and Dynamics of Fault Mechanics (S3)

Source simplification represents a dominant uncertainty in SPTHA (Geist and Oglesby, 2014). Its effect on seafloor deformation needs to be investigated better, concerning deformation models that incorporate complex material properties, geometrical complexity, varying depth-dependent fault conditions, dynamic simulations including off-fault damage and near-surface amplification, which all may increase tsunami hazard (Masterlark, 2003; Ma, 2012; Kozdon and Dunham, 2013; Ryan et al., 2015; Murphy et al., 2016; Lotto et al., 2017; Murphy et al., 2018; Scala et al., 2019; Scala et al., 2020; Tonini et al., 2020). Secondary ruptures including splay faulting may happen as an independent source or as part of a large earthquake on the subduction interface (Wendt et al., 2009; Li et al., 2014; Hananto et al., 2020).

Tsunami earthquakes produce excessively large tsunami intensities compared to their moment magnitude (Polet and Kanamori, 2016), and their global and local frequency is unconstrained. A simplified characterization of *tsunami earthquakes*, which is sometimes adopted, assumes larger slip associated with less rigid materials at shallow depths to preserve the seismic moment (e.g., Bilek and Lay, 1999; Geist and Bilek, 2001). These and other very complex ruptures, potentially containing fault branching, rupture jumping, and mixed-mode slip (e.g., Ulrich et al., 2019a; Ulrich et al., 2019b), are not well represented in PTHA. On a larger scale, rupture area may be shared by more than one subduction interface, like in the case of triple junctions (e.g., Solomon event 2007, Lorito et al., 2016). Due to a lack of observations the likelihood of such events is uncertain and quantification of their relative contribution to SPTHA therefore difficult.

Due to all these uncertainties and the extreme computational demand for dynamic computation, numerical simulations are *de facto* replaced with heterogeneous stochastic slip modeling (e.g., Herrero and Bernard, 1994; Mai and Beroza, 2002; Davies et al., 2015; Sepúlveda et al., 2017), and less frequently with stochastic stress modeling (e.g., Wendt et al., 2009). Because source observations are relatively scarce, more statistical tests (Davies and Griffin, 2019) are needed for source model validation.

Empirical Scaling Relations (S4)

Several different empirical scaling relations are used to define earthquake rupture properties, such as length, width, average slip, and earthquake magnitude (e.g., Wells and Coppersmith, 1994; Murotani et al., 2008; Blaser et al., 2010; Strasser et al., 2010; Murotani et al., 2013; Goda et al., 2016; Skarlatoudis et al., 2016; Allen and Hayes, 2017; Thingbaijam et al., 2017). These relationships quantify appreciable uncertainties that are seldomly accounted for in SPTHA. These relations imply stress drop and time-dependent rupture characteristics and self-similarity of earthquakes across scales, but this is apparently violated in some cases. For example, the 2011 Tohoku earthquake released a huge amount of slip in a relatively small portion of the subduction interface compared to the Sumatra 2004 or Chile 1960 earthquakes (Okal, 2015); scaling relations are not directly applicable to abnormally slow and unusually large shallow slip occurring in low-rigidity zones during *tsunami earthquakes*.

Complex, Non-stationary Seismic Cycle (S5)

Even in the simplest subduction environment, the seismic cycle over co-seismic, inter-seismic and post-seismic phases is complex and non-stationary, for example due to visco-elastic rheology and

the role of fluids (Wang et al., 2012; Moreno et al., 2014; Melnick et al., 2017). Time-dependent models could potentially be used to estimate the stress transfer from one earthquake to the neighboring faults (King et al., 1994). Stress transfer from megathrust earthquakes triggering outer-rise ruptures or possibly even the opposite are such examples (e.g., Lorito et al., 2016). Based on seismic catalogs, it is possible to infer non-Poissonian earthquake recurrence, for example earthquake clustering (Kagan and Jackson, 1991). A time-dependent model, which could better describe the probability of earthquake occurrence for some specific applications or timeframes, is taken into account by only a few PTHAs (e.g., Goda et al., 2017; Goda, 2020).

Other Constraints (S6)

It is reasonable to assume that high seismic coupling correlates with future slip location. Under simplifying assumptions, along-strike geodetic coupling variation can be inferred from geodetic strain (Métois et al., 2012). Large uncertainty remains, particularly regarding the near-trench region (Loveless and Meade, 2011). Recent developments in seafloor geodesy and modeling techniques are offering improved constraints (e.g., increasing offshore coupling resolution, Bürgmann and Chadwell, 2014; Foster et al., 2020), and slow slip events and consequently the stress evolution on the fault (e.g., Araki et al., 2017). High seismic coupling combined with stress accumulation in areas of seismic inactivity is described as a seismic gap. The possibility of using seismic gaps to identify zones of enhanced seismic hazard has long been debated (e.g., Bilek and Lay, 2018). Attempts to obtain physically motivated constraints on the maximum magnitude utilizing convergence rate, age of the oceanic crust and sediment thickness have been rather unsuccessful (Okal, 2015). Ongoing research explores these and other controlling factors of subduction zone seismicity, including small- and large-scale roughness of the subduction interface, static friction coefficient, upper plate strain and rigidity, dip angle and curvature (e.g., Heuret et al., 2012; Bletery et al., 2016; Sallarès and Ranero, 2019; Rijsingen, et al., 2019; Muldashev and Sobolev, 2020). Additionally, rupture cycles and supercycles over multiple segments controlled by geological asperities have been proposed (Philibosian and Meltzner, 2020). Similar to some of the previously discussed items in this section, no consensus has been reached on the statistical meaning of such information and on how to frame it within SPTHA.

Gaps in Landslide Source Representation

Existing Methods

Landslide tsunami PTHA (LPTHA) was introduced less than a decade ago (Geist and Lynett, 2014). Its application is often similar to SPTHA (e.g., ten Brink et al., 2006; Lane et al., 2016), but can also be based on geotechnical interpretations with a strong emphasis on expert judgment (e.g., Grilli et al., 2009; Hermanns et al., 2013; Løvholt et al., 2020). Salamon and Di Manna (2019) derive empirical scaling relations for landslides triggered by onshore earthquakes. In LPTHA, the landslide volume is used analogously to the seismic moment in SPTHA as a rate of occurrence. The slide volume is generally also the most influential factor on tsunami genesis (Snelling et al., 2020). Landslide motion has a strong influence too (Løvholt et al., 2015b; Yavari-Ramshe and Ataie-Ashtiani, 2016). LPTHA source models are coupled to numerical tsunami models in Monte Carlo simulations. Methods for simulating both the landslide dynamics and tsunami generation range from block models (Harbitz, 1992; Tinti et al., 1997; Watts, 2000; Grilli and Watts, 2005; Tinti et al., 2006; Løvholt et al., 2015b), depth-averaged rheological models of viscoplastic or granular nature (e.g., Kelfoun and Druitt, 2005; Jop et al., 2006; Løvholt et al., 2017; Kim et al., 2019), to computational fluid dynamics (CFD) based approaches with different landslide complexity (e.g., Crosta et al., 2016; Abadie et al., 2020). Submarine landslide tsunamis are mainly characterized by the Froude number (landslide velocity over wave celerity) measuring the degree of critical landslide velocity, the landslide acceleration, and the rate of landslide mass mobilization (e.g., Ward, 2001; Løvholt et al., 2015b). Subaerial landslides are characterized by the landslide frontal area, along with the Froude number, landslide density, and slope angle (e.g., Fritz et al., 2003; Heller and Hager, 2010; Bullard et al., 2019).

Identified Gaps

Lack of Understanding and Likelihoods for Tsunamigenic Landslide Volumes (L1)

For submarine landslides, we refer to the reviews of Huhn et al. (2019) and Harbitz et al. (2014). The challenge can be attributed to several factors:

- Limited or insufficient mapping of past landslide occurrences. Their characteristics and lack of dating prevent constraining the age of the sediments without excessive uncertainty ranges (e.g., Geist et al., 2013). The new global landslide database initiative (Clare et al., 2019) is a good starting point for standardizing, but not yet complete enough for feeding LPTHA. Good data coverage exists for certain regions such as the Mediterranean (Urgeles and Camerlenghi, 2013), Gulf of Mexico (Pampell-Manis et al., 2016) and the US East Coast (Chaytor et al., 2009, Geist et al., 2014).
- Limited understanding of how past landslide recurrence can be projected into the future hazard, including time and geological context dependency. For example, we cannot yet generally link climatically driven trends to past landslide frequency (Urlaub et al., 2013). However, it is concluded that the last ice age affect present landslide probability offshore US (Lee, 2009) and Norway (Bryn et al., 2005).
- Limited available geological and geotechnical data inhibit identification of failure-prone sediments and discrimination from stable areas, including weak failure zones, pore pressure conditions or fractures, as well as obstacles or structures. When data exist, they may be proprietary, and a challenge is related to the need for covering very large geographical and heterogeneous regions. A methodological gap exists in bridging geotechnical data and slope stability models (e.g., Carlton et al., 2019) to volume-frequency relationships.

- Limited data and knowledge on triggers of landslides, such as meteorological or seismic events, impedes the quantitative assessment of potential landslide magnitude.

Difference of Onshore and Offshore Landslides (L2)
The specific character of subaerial and submarine landslides is often vastly different. Potential direct or indirect trigger mechanisms are sometimes not fully understood or difficult to embed into the probability of failure (e.g., precipitation-induced landslides, weak zones and fluid overpressure, range of failure propagation and cascading failure propagation spread). Understanding and estimating the annual probability of landslide failure in rock slopes with complex fracture patterns and stress conditions is associated with large uncertainty. Extensively monitored rock slopes in Norway (e.g., Blikra et al., 2005) show large motion over decades before failure takes place, rendering assessment of failure probability difficult. Matching expert judgment (e.g., Hermanns et al., 2013) to observed landslide magnitude frequency statistics (e.g., Nes, 2018) will help aggregate understanding of landslide frequencies and help link knowledge on failure-prone areas to probability. While epistemic uncertainties in the described situations are large, current LPTHA models do not incorporate them.

Limited Constraints on Landslide Dynamics and Material Behavior (L3)
The interplay of diverse tsunamigenic landslide parameters makes the generation complex, implying that much less voluminous landslides may be more effective tsunami generators than respectively larger ones. As an example, we note that the approximately 500 km^3 Trænadjupet Slide that occurred 4,500 years BP likely produced a moderate coastal impact possibly of just a few meters (e.g., Løvholt et al., 2017), while the 100 times less voluminous 1998 Papua New Guinea landslide induced more than 10 m run-up locally (e.g., Tappin et al., 2008). Because tsunami genesis is tightly linked to landslide acceleration as well as rate of mobilization of the landslide volume (e.g., Løvholt et al., 2005), quantifying the rate and nature of the slope failure is important. Just a few studies discuss the effect of initial failure rate on tsunami generation (e.g., Trapper et al., 2015; Germanovich et al., 2016; Puzrin et al., 2016) and related aspects such as remoulding and cascading failures on the landslide tsunami generation (e.g., Løvholt et al., 2017; Kim et al., 2019; Zengaffinen et al., 2020). How to include these factors and their associated probabilities in PTHA is not resolved. While advanced numerical models for landslide dynamics exist (e.g., Tinti et al., 1997; Jop et al., 2006; Savage et al., 2014; Si et al., 2018a; Si et al., 2018b; Kim et al., 2019; Wang et al., 2019; Gallotti and Tinti, 2020), their complexity and variety obfuscate understanding on which models are most suitable to be used. Furthermore, some models (e.g., Savage et al., 2014; Si et al., 2018a; Si et al., 2018b) are presently too comprehensive to be used in PTHA. Procedures for linking them to measured material properties and geological settings are not in place. Finally, fluid resistance forces (pressure drag, skin friction, and added mass) may be as important as the landslide properties, in particular for submarine landslides and further investigating physical understanding is necessary to constrain epistemic uncertainty.

Limited Availability of Benchmarks (L4)
Suitable benchmarks have recently been made available (e.g., Huang and Garcia, 1998; NTHMP, 2018; Kim et al., 2019), but are arguably less mature and fewer than their hydrodynamic modeling counterparts (e.g., Pedersen, 2008; Synolakis et al., 2008). A challenge is a transition from simplified laboratory tests to real-world landslide representation. Moreover, while numerous empirical lab experiments exist, they are significantly influenced by scale effects (Heller, 2011). Neither complex rheological behavior nor real-world complexity is covered in the benchmarks. Complex laboratory experiments (e.g., Rondon et al., 2011) can be used for validating CFD models, but CFD models are presently too computationally expensive for tsunami hazard analysis modeling.

Limited Past Events to Inform Hazard Models (L5)
Information about past landslides and tsunamis can be used to infer landslide dynamics uncertainty. This can be done using landslide run-out information alone (e.g., Salmanidou et al., 2017), which consequently yields broad epistemic uncertainties in LPTHA. By using tsunami information, such uncertainties can be drastically reduced (e.g., Gylfadóttir et al., 2017; Kim et al., 2019; Løvholt et al., 2020). In practice, however, very few landslide tsunami data are available.

Gaps in Volcano Source Representation

Existing Methods

Volcanic PTHA, coined VPTHA here, is even less developed than LPTHA (Grezio et al., 2017). Among the few examples are the VPTHA framework developed in Ulvrova et al. (2016) and Paris et al. (2019) for underwater explosions at Campi Flegrei, and Grezio et al. (2020) for pyroclastic flows of Vesuvius. Given that risk reduction measures at volcanoes are often related to the identification of precursory patterns preceding eruptions or to recognizing unrest episodes with increased volcanic activity, the volcanic hazard is often computed conditional to eruptions or unrest, and without an explicit quantification of long-term probability. For example, in Paris et al. (2019), the hazard analysis (Campi Flegrei, Naples, Italy) is confined to conditional tsunami intensity probabilities, due to probabilistic realizations of eruptions with different vent size and location.

Identified Gaps

Variety of Potential Volcanic Sources (V1)
Tsunamigenic volcanic events are diverse and they include both eruptive and non-eruptive triggering phenomena, such as underwater explosions, pyroclastic flows, lahars, slope failures, volcanic earthquakes, shock waves from large explosions, and caldera subsidence (Latter, 1981; Kienle et al., 1987; Begét et al., 2005; Day, 2015; Paris, 2015; Grezio et al., 2017). A large range of wave characteristics is typical for volcano tsunamis, even if most such sources are localized and generate mainly short-period waves with greater dispersion and limited far-field effects compared to earthquake-generated tsunamis (e.g., Yokoyama,

1987; Nomanbhoy and Satake, 1995; Le Méhauté and Wang, 1996; Choi et al., 2003; Watts and Waythomas, 2003; Bellotti et al., 2009; Maeno and Imamura, 2011; Ulvrova et al., 2016; Selva et al., 2019, 2020). However, tsunamis are among the farthest propagating volcanic perils, often generating regional impact (e.g., Krakatau, Stromboli, Ischia, etc., see for example Paris et al., 2014; Rosi et al., 2018; Selva et al., 2019; Gallotti et al., 2020). Notably, some of the tsunamigenic volcanic events overlap with those recorded for seismic and landslide tsunami: flank collapse, slope failure and even pyroclastic flows are related to landslides (Løvholt et al., 2015b; Paris, 2015); volcano-tectonic earthquakes occur with high frequency in volcanic areas (Paris, 2015). Such frequency information as well as understanding material properties and transformation during flow should draw upon volcanological expertise. It is often difficult to define a single generation phenomenon since different potentially tsunamigenic processes can occur during the same volcanic episode, especially during large caldera-forming eruptions (Paris, 2015).

Difficulties in Constraining Recurrence Rates (V2)

Since volcanic tsunami generation is so diverse, constraining recurrence rates for the different source types as eruptive phenomena (Walter et al., 2019), unrest episodes (Tinti et al., 1999; Selva et al., 2020), and triggered subaerial landslides (Selva et al., 2019) is difficult. The integration into a multi-source VPTHA is further complicated by the need for accounting for the complex interdependencies that may exist among the different source mechanisms. The hazard is often nonstationary through time (e.g., Bebbinghton, 2008; Bebbinghton, 2010), which represents another challenge.

Gaps in Modeling Tsunami Generation and Propagation (V3)

Extensive reviews on existing strategies to model volcanic sources are found in Paris, (2015), Grezio et al. (2017) and Paris et al. (2019). Given the complexity, an important part of the hazard analysis is oriented toward understanding the physical mechanism of generation, and how to represent this probabilistically. Similar to landslide generated tsunamis, volcano tsunami modeling suffers from the difficulty of coupling the complex dynamics of the generating event and its interaction with wave propagation. For example, pyroclastic flows are complex, multi-phase phenomena involving the interaction of high-temperature gases and volcanic clasts covering a very large range of granulometric dimensions (Freundt, 2003; Bougouin et al., 2020). This difficulty leads to simplified modeling schemes (e.g., Bevilacqua et al., 2017; Sandri et al., 2018). These simplified strategies may be too reduced for an effective constraint of their tsunami potential (Grezio et al., 2020). Some phenomena may be represented by empirical models (for submarine explosions, see Paris et al., 2019, and for caldera collapse, see Ulvrova et al., 2016). Experimental and numerical simulations coupled with field data increased understanding of the physics and main parameters of volcanic tsunamis (Grezio et al., 2017).

Lack of Data From the Geological Record (V4)

Tsunami is often not dealt with in the volcanological community, although it may be more fatal than other volcanic hazards such as lava flows or ash falls (Auker et al., 2013; Brown et al., 2017). Consequently, a systematic investigation of tsunami-related data in geological surveys at volcanoes is often missing. Because different volcanic phenomena may trigger tsunamis, even when tsunami data exist, attributing the observation to a specific mechanism is difficult (e.g., Krakatau 1883 eruption: Paris et al., 2014). Therefore, a systematic collection of available volcano-generated tsunami data and linking to potential volcanic generating processes is required. This will imply defining a strategy of tsunami-oriented monitoring around coastal volcanoes. It would be useful to combine such efforts with existing data collections such as the Global Volcanism Program (Global Volcanism Program, 2013).

Limited Availability of Well Recorded Past Events or Benchmark Studies (V5)

Only a few past events are well constrained in terms of both the source and of the subsequent tsunami (e.g., Unzen 1792, Karymskoye Lake 1996; Montserrat 1997 and 2003, Anak Krakatau 2018; Stromboli 2002 and 2019). The lack of consensus in modeling procedures for each type of tsunamigenic volcanic event, along with the tendency to consider all sources as "unique", complicates the task of defining benchmarks for volcano tsunamis.

Gaps in Meteorological Source Representation

Existing Methods

Meteotsunami PTHA, coined MPTHA here, was developed only recently (see Grezio et al., 2017). A framework for MPTHA development is proposed by Geist et al. (2014). The dynamics of meteotsunamis are fairly well-known (e.g., Monserrat et al., 2006; Sibley et al., 2020), related to unusually strong and rapid atmospheric pressure fluctuations and resonance effects causing strong waves closely associated with the behavior of tsunamis. The source mechanisms of meteotsunamis are also well understood (Monserrat et al., 2006; Pattiaratchi and Wijeratne, 2015) with a major driver a Proudman resonance (Proudman, 1929). Because meteotsunamis are strongly linked to (un)favorable combinations of pressure fluctuations, shallow (shelf) bathymetry, and directivity of the weather system, they take place more frequently in specific geographical areas, such as in the Adriatic Sea (Vilibić and Šepić, 2009), the Baltic Sea (Pellikka et al., 2020), and the East Coast of the United States (Pasquet et al., 2013). The main input data for meteotsunamis include meteorological pressure data, preferably with full spatial and temporal characteristics of the pressure field for given meteorological events. Such data can be used to provide synthetic probabilistic source scenarios as input to an MPTHA, where an example for the Northeast US coastline is given by Geist et al. (2014). While this field does

not share the data sparsity issues that are associated with volcanoes and landslides, large uncertainties persist, as briefly discussed below.

Identified Gaps

Lack of Understanding the Potential and Likelihood for Tsunamigenic Meteorological Patterns (M1)

A systematic assessment of potential source areas and exposed coastal regions is not available. Some regional studies can serve as a preliminary indication (e.g., Dusek et al., 2019; Šepić et al., 2012; Šepić et al., 2016), but a rigorous catalog is missing. Climatological information is likely available, but a systematic extraction of data concerning meteotsunami potential has not been performed. It is not clear whether the resolution of available climatological data (e.g., from reanalysis) is sufficiently fine to allow for the extraction of corresponding relevant meteotsunami source patterns.

High Sensitivity to Several Parameters and Lack of Understanding of Local Amplification Factors (M2)

Whitmore and Knight (2014) demonstrate the high sensitivity of typical tsunami impact to source parameters and hence a large gap in knowledge on relevant localized parameters. The size, speed, amplitude, directivity, and duration of an atmospheric disturbance resonating with the water column in a specific topographic setting need to be known to assess the hazard. Therefore, such parameters need to be derived for all tsunamigenic regions, then applied to available climatological data sets, and finally fed into corresponding models for assessment of hazard. An assessment of amplifying tidal conditions in each of such regions is also missing.

Limited Availability of Benchmark Studies (M3)

While there are many individual meteotsunami events described in the literature (e.g., Churchill et al., 1995; González et al., 2001; Pasquet et al., 2013; Vilibić et al., 2014), no truly validated benchmark data are available for meteotsunami benchmarking. In principle, a similar methodology as described in Synolakis et al. (2008) could be followed. However, only very little unification of source modeling has been achieved and except for preliminary simplified tests (as in Vilibić, 2008), there exists no widely accepted test suite. This applies in particular to verification and validation of the probabilistic workflow of MPTHA.

Limited Past Events and Data to Inform Hazard Models (M4)

There is no consistent catalog of occurrences, although regional studies have been performed (e.g., Haslett et al., 2009; Woodruff et al., 2018). As stated before, there are no unified parameterizations of meteotsunami sources, which could be entered into such a catalog. Even though many individual events are described in the literature (see subsection above), these are by no means representative or complete to be used in hazard models. More rigorous collection of data with the special focus on meteotsunamis–background climatology, meteorological situation, ocean state, topo-bathymetry–for the diverse areas of interest would be desirable.

Gaps in Hydrodynamic Tsunami Modeling, Generation, Propagation, and Run-up

Existing Methods

Hydrodynamic tsunami modeling includes numerical simulation of tsunami generation, propagation as well as coastal and onshore impact. It is an essential part of any PTHA or PTRA analysis. Reviews of commonly applied methods are available (e.g., Pedersen, 2008; Synolakis et al., 2008; Behrens and Dias, 2015). The pre-eminent challenge is the need to bridge a broad range of scales. First, in the probabilistic regime, a comprehensive PTRA must consider a very large number of scenarios to cover all relevant tsunamigenic sources, explore wave physics, and quantify uncertainties. Second, for each individual scenario source, large-scale propagation and coastal inundation modeling (optimally at scales of 1–10 m) need to be represented to quantify tsunami-related on-shore damages and losses. However, the fastest HPC simulation workflows (e.g., de la Asunción et al., 2013; Oishi et al., 2015; Macías et al., 2017; Musa et al., 2018) still require typically 10–60 min to simulate tsunami inundation at a scale of tens of meters, rendering them unsuitable for extensive PTRA studies with up to millions of scenarios (Basili et al., 2021). To overcome this "challenge of scales", modeling approximations are presently necessary for PTHA feasibility and can either involve 1) largely reducing the number of inundation scenarios (e.g., González et al., 2009; Lorito et al., 2015; Volpe et al., 2019; Williamson et al., 2020), 2) use of approximate models or statistics such as amplification factors (e.g., Løvholt et al., 2012; Kriebel et al., 2017; Gailler et al., 2018; Glimsdal et al., 2019), or 3) machine learning-based tsunami emulators (e.g., Sarri et al., 2012; Salmanidou et al., 2017; Giles et al., 2020).

Identified Gaps

PTHA Uncertainty Treatment for Tsunami Inundation Processes (H1)

At present, we lack well tested local PTHA benchmarks where the sources of uncertainties are effectively characterized, in a way that allows their formal propagation along the PTHA/PTRA assessment chain. Moreover, the effect of coseismic coastal displacement due to near field sources (e.g., Volpe et al., 2019), which affects tsunami inundation, should be investigated more deeply, especially when using techniques for reducing the number of scenarios. For this purpose, a large number of inundation scenarios are needed to quantify the epistemic uncertainty and bias caused by simplifications introduced through approximate methods. A local PTHA application using more than 40,000 earthquake sources (Gibbons et al., 2020) is only a start.

Tsunami Generation (H2)

Unit source models (Kajiura, 1963; Nosov and Kolesov, 2007; Molinari et al., 2016) of varying computational cost and complexity approximate the volumetric deep-water source displacements. While Lotto et al. (2019) clarified that the horizontal momentum does not effectively contribute to tsunami generation in deep-water sources, an extensive sensitivity analysis of how such simplifications affect PTHA

has not been carried out. Incorporating time-dependent and moving sources, be it earthquakes (e.g., Ulrich et al., 2019a), landslides (e.g., Løvholt et al., 2015b) or volcanoes, will involve much higher computational burden. How to limit the number of source time steps for time-dependent source modeling is sparsely studied (e.g., Zengaffinen et al., 2020). For landslide tsunamis, closed-form models (e.g., Watts et al., 2003; Cecioni and Bellotti, 2010) represent a simple alternative but can introduce biases when conveyed to real geographical settings, due to oversimplification or inadequacy for the real situation. Subaerial landslides and volcanoes are often simplified because the required consideration of full 3D hydrodynamics (e.g., Abadie et al., 2020) into PTHA poses too high computational demand. Hence, more research is needed for developing simplified time-dependent sources compatible with PTHA demands, while quantifying the epistemic uncertainty and bias caused by the simplification. New methods may facilitate more detailed characterization of past inundation scenarios and their sources (e.g., Chagué-Goff et al., 2012; Sugawara et al., 2014; Paris et al., 2020).

Uncertainty and Variability due to Numerical Model for Tsunami Propagation (H3)

Most non-linear shallow water (NLSW) simulation codes produce similar results in the propagation phase, in particular in controlled benchmark cases (e.g., Synolakis et al., 2008). However, clear model differences can appear due to varying components (applied numerical method, workflow, sources, setup etc.) in practical applications. Comparing different numerical forecast models in the Indian Ocean, Greenslade et al. (2014) found large variations, attributed to differences in the workflow and source representation rather than to the tsunami model itself. Testing how such kinds of uncertainty quantification relate to "heterogeneous modeling practices" has not been carried out systematically. Moreover, a rigorous investigation of the performance of far-field propagation is sparse (Dao and Tkalich, 2007; Davies and Griffin, 2020). Differences in numerical dissipation and discretization can also contribute to modeling deviations. As there is no standardized test case for far-field propagation that could reveal the differences in performance of different approaches, it is pressing to address these issues more systematically. Due to the computational burden, most PTHA applications today employ shallow water type models, neglecting frequency dispersion, which can lead to bias. Dispersion can be incorporated through conventional dispersive wave solvers (e.g., Bellotti et al., 2008; Løvholt et al., 2008; Kim et al., 2009; Shi et al., 2012), or through manipulating numerical schemes in NLSW codes (like MOST, e.g., Wei et al., 2008), although the general applicability of the latter is presently not clear. A systematic investigation quantifying the effect of dispersion (as in Glimsdal et al., 2013) on PTHA for practical source configurations would be desirable.

Nonlinearity and Resonances (H4)

Most tsunami simulations to date start from an ocean at rest and assume that interaction of currents with gravity waves is negligible. Androsov et al. (2011) demonstrated that significant alterations of the wave height can be attributed to tidal activity. A quantitative sensitivity analysis of this effect, its dependence on bathymetry, and its correlation to the choice of model (NLSW) is necessary. Huthnance (1975) described the phenomenon of trapped waves on continental shelves that may trigger edge waves and other amplified phenomena. Tsunami resonance effects in Chile and the Balearic Islands are studied in Aranguiz et al. (2019) and Vela et al. (2014). Pattiaratchi and Wijeratne (2015) describe the effect of such phenomena as amplifying factors for meteotsunamis. It is currently unclear how such amplifying phenomena can be represented in the numerical model, nor if the strength is captured adequately.

Quantifying the Influence of Modeling Assumptions and Scaling (H5)

A hierarchy of modeling approaches, from shallow water assumption, over dispersive long wave solvers, to Navier Stokes type models, can be used to numerically treat tsunami hazard analysis in varying complexity. Due to ever-increasing computational resources, a trend toward more involved model equations can be observed. However, a clear quantitative assessment of the difference has only partly been performed. Lynett et al. (2017) use extensive benchmarking to study and compare modeling approaches to currents induced by tsunami waves. While this study is enlightening and provides very good benchmarking tools, further assessment is necessary to quantify the influence of higher fidelity modeling techniques. Generally, we note that current benchmarking (e.g., Synolakis et al., 2008) stays behind current high-fidelity modeling capabilities. Additionally, some benchmarks based on laboratory experiments have issues with scaling (see Heller, 2011; Pedersen et al., 2013), and related bias and accuracy have not been investigated systematically.

Modeling Situations With Complex Tsunami Inundation (H6)

NLSW models are predominantly used to simulate tsunami inundation. However, real inundation situations involve features too complex for NLSW approximate modeling, such as urban structures, or damage and erosion due to debris transport. At present, these topics are only partly represented, often using heuristic model formulations. Examples include spatially variable friction mapping (e.g., Gayer et al., 2010; Kaiser et al., 2011), or porous body equivalent friction models representing buildings (e.g., Yamashita et al., 2018). Bottom friction parameterization is almost insensitive for offshore modeling (see Arcos and LeVeque, 2015). However, variable bottom friction parameterizations may pose a viable tool for simulating detailed inundation, but large uncertainties still prevail (e.g., Griffin et al., 2015; Macías et al., 2020). While small scale laboratory tests exist (Park et al., 2013), the heuristic nature of named models and the difficulty to perform controlled tests, implies potentially large epistemic uncertainties. Debris impact and transport are predominantly addressed through post-disaster surveys and experimental analysis of data so far (e.g., Nistor et al., 2017a; Nistor et al.,

2017b; Stolle et al., 2019), and is mostly embedded in only vulnerability analysis (see below), and not in hydrodynamic modeling or PTHA to our knowledge. Extending the modeling dimensions and physical complexity is desirable (e.g., Marras and Mandli, 2021). Open and related to this issue is the influence and potential bias of the accuracy of topo-bathymetric grids, including filtering of structures and vegetation, on the accuracy of inundation simulations (see Griffin et al., 2015; Goda and Song, 2019). Unphysical bias can also be introduced when coupling high resolution (nested) models to large-scale propagation models as shown in Harig et al. (2008).

PROBABILISTIC TSUNAMI RISK ASSESSMENT

This section discusses identified gaps in PTRA. We go through current state for exposure modeling, physical vulnerability, and risk and resilience metrics, as they naturally follow each other in a consequence-based risk workflow (**Figure 1**). Methods characterizing the complex social, organizational, and economic context in a tsunami risk assessment are discussed subsequently.

Gaps in Exposure Modeling

Existing Methods

Exposure data provide information about the characteristics and location of people and assets at risk. There are several techniques for the acquisition of exposure data, with different degrees of resolution and precision (Pittore et al., 2017). Data from governmental agencies are most commonly used, as they are open and available in most developed countries. These data often provide coverage for the entire building inventory (e.g., physical assets) and are regularly updated for asset management (e.g., national technical maps) and fiscal reasons (e.g., cadastral data). Different exposure databases exist. The Global Exposure Database—GED (De Bono and Mora, 2014; De Bono and Chatenoux, 2015) developed for GAR13 and updated later for GAR15 (UNISDR, 2013; 2015) provides a global dataset at 5 km grid resolution at inland and 1 km at coastal locations, including data for buildings, their use, and exposed value. The 2013 and 2015 versions of the GED served as the exposure databases for the global risk model by the United Nations Office for Disaster Risk Reduction, which considered earthquakes, hurricanes, tsunamis and riverine floods as hazards. The DRMKC Risk Data Hub WebGIS tool (Antofie et al., 2019) has been developed to provide access and sharing of EU-wide information relevant for disaster risk management. Initiatives such as the Open Exposure Data (OED) with roots in proprietary catastrophe modeling and reinsurance industry, provide the opportunity to generate exposure data, including those relevant to tsunami risk, with interoperability between different modeling tools. These databases mainly contain data from census or remote sensing. A recent interview-based approach, relying on local practicing engineers with knowledge of building features, has been adopted for the compilation of building inventories at regional scales (Polese et al., 2020). Careful validation needs to address possible heterogeneity in data. At present, the only guidelines and tools that exist for capturing and classifying exposure data for a tsunami are the multi-hazard exposure taxonomy, and associated tools, provided by GED4ALL (Silva et al., 2018b).

Identified Gaps

Lack of Detail (E1)

Most available exposure data have not been collected for the purpose of tsunami risk assessment and may be missing important information for modeling tsunami fragility or vulnerability. For instance, population cadastral data are often collected at the municipal, district or residential unit level, requiring extra assumptions to determine the geographical distribution. Tsunami hazard intensities can vary considerably between two nearby locations. Accurate geo-localization of the exposed assets and people is needed to obtain robust results, necessitating a minimum resolution level for the exposure databases. While main building construction characteristics are often known, tsunami relevant features (e.g., building lateral load resistance, foundation) are missing (Rivera et al., 2020). Exposure data for critical structures and infrastructure should include functionality information for the exposed asset. This would allow for proper modeling and hence assessment of community resilience, considering different services such as healthcare and education. In other cases, data gaps and uncertainties are associated with regulatory and privacy limitations or outdated sources.

Lack of Exposure Data (E2)

In many developing countries, where cities have rapid urbanization processes and long-term planning is not consistently enforced, exposure data are not always available or updated. Such data may be inferred from satellite and aerial imagery, from freeware data made available from international projects (e.g., NASA's EOSDIS), from volunteered geographic information systems (e.g., Huyck et al., 2011; Huyck and Eguchi, 2017; OpenStreetMap, 2020), or through intergovernmental organizations (e.g., JRC Risk Data Hub, 2020).

Lack of Tsunami Exposure Model and Taxonomy (E3)

Significant efforts have been made in the earthquake risk community to define a common exposure taxonomy (e.g., GED4GEM, Silva et al., 2018a; METEOR, Huyck et al., 2019). However, these taxonomies do not contain all the required structural attributes for estimating tsunami risk such as geomorphological, land use, and land cover datasets, or number and size of openings in buildings. A recent development is GED4ALL, a multi-hazard taxonomy (Silva et al., 2018b), which considers tsunami as a hazard. GED4ALL also discusses multiple asset types like buildings, people, infrastructure systems and crops. Common taxonomy and attributes are fundamental to avoid heterogeneity, especially when considering multiple asset types.

Spatio-Temporal Variability (E4)

Most exposure models are static in time and do not consider the spatio-temporal variability of exposure components. This aspect

is critical when modeling human exposure since there can be daily and seasonal variations. For example, coastal regions often attract tourists, visitors and seasonal workers, leading to significant seasonal fluctuations in the population (Fraser et al., 2014). Spatio-temporal variation in exposure heavily influences the tsunami risk.

Gaps in Physical Vulnerability

Existing Methods

As tsunami losses are closely connected to damages to buildings and infrastructure, the vulnerability component is often cut into two parts: a tsunami-to-damage fragility function, and a damage-to-loss consequence function (**Figure 1**). Advancements in tsunami vulnerability models have significantly lagged behind those of tsunami hazard, with almost no studies found to precede the 2004 Indian Ocean Tsunami (Charvet et al., 2017). However, with the recent devastating tsunamis providing a large quantity of observed damage and loss data to develop and validate fragility and vulnerability models, this field of study has rapidly grown. Several empirical fragility functions for the assessment of buildings (Koshimura et al., 2009; Mas et al., 2012; Suppasri et al., 2014; Charvet et al., 2015; Chock et al., 2016) and infrastructure (Eguchi et al., 2014; Hatayama, 2014) have been derived from observed damage in the 2004 Indian Ocean, 2009 Samoa, 2010 Chile, and 2011 Tohoku tsunamis. Recently, analytical fragility functions were derived from numerical simulations of building response under tsunami inundation (Petrone et al., 2017; Alam et al., 2018; Karafagka et al., 2018; Páez-Ramírez et al., 2020), and under sequential earthquake and tsunami impact (Park et al., 2012; Attary et al., 2019; Petrone et al., 2020). Only a few studies exist that move from fragility to vulnerability modeling (De Risi et al., 2017). There is a lack of consensus on many aspects of physical fragility and vulnerability modeling.

Identified Gaps

Limitation in Asset Types and Geographical Scope (P1)

The vast majority of existing tsunami fragility and vulnerability models relate to buildings, few exist for bridges, fuel tanks, or other types of infrastructure. The main reason is that most fragility functions are empirical, and few observational damage or loss data are available for infrastructure components. Even for buildings, the geographical scope of existing vulnerability and fragility models is limited. Most empirical fragility functions are based on data from the 2004 Indian Ocean and 2011 Tohoku events, and hence represent non-engineered buildings in countries surrounding the Indian Ocean and engineered buildings typical of Japan. With analytical fragility functions only covering a small number of building types, large portions of the world's exposure remain unrepresented by current studies.

Effect of Multiple Hazard on Empirical Tsunami Fragility Mode (P2)

Tsunamis are commonly triggered by large earthquakes. Near-source, observational data on asset damage and loss collected after the tsunami often include the combined effects of earthquake ground shaking and tsunami inundation. Hence, empirical fragility and vulnerability models derived from such data inherently comprise the effects of both hazards. Therefore, corresponding empirical fragility models may be regarded as inappropriate for use in a tsunami-only risk assessment. Pure tsunami damage data is rare and currently limited to non-engineered structures (Charvet et al., 2017).

Lack of Consensus Regarding Best Tsunami Intensity Measure (P3)

The intensity measure *IM* (**Figure 1**) links the hazard and vulnerability components within risk models. Traditionally, tsunami inundation maps are presented in terms of inundation depth. While the majority of fragility and vulnerability models adopt inundation depth as *IM*, other tsunami *IM* have also been used such as the flow velocity or momentum flux. The absence of inundation velocity measurements in field data requires running tsunami inundation simulations to use such *IM* (Koshimura et al., 2009; Song et al., 2017). More recently, force-based *IM* (e.g., flow velocity, momentum flux) were used in fragility functions for engineered buildings yielding better correlation to observed damage than inundation depth (Macabuag et al., 2016). However, no consensus on the most appropriate *IM* could be reached. As a consequence, mismatches between representations of hazard and vulnerability in risk modeling may exist.

Gaps in Building Analysis and Assessment for Use in Analytical Tsunami Fragility (P4)

Buildings are often used as vertical evacuation shelters and an assessment of their structural fragility is therefore an important information in the risk assessment workflow. Tsunami engineering being a younger discipline than earthquake engineering has adopted approaches from the latter community. This was supported by the physical similarity of both hazards applying predominantly horizontal loads to structures. However, there are fundamental differences in how earthquake and tsunami loads are applied to buildings. For example, tsunami loads affect the lower floors of a high-rise building, whereas seismic loads are inertial forces usually causing increasing magnitude for higher floors (Baiguera et al., 2019). Thus, earthquakes induce large bending moments in structural elements, whereas tsunamis typically induce large shear. Since typical structural modeling approaches tend to prioritize flexural effects, the bias in tsunami fragility assessment may be large. Furthermore, seismic loads are dynamic, whereas loads from tsunami inundation can be considered quasi-static, and Rossetto et al. (2018) have shown that building ductility is often not crucial in the tsunami response of structures. Although no consensus has been reached in this regard, more fragility functions based on static rather than time-dependent non-linear approaches are derived now (Petrone et al., 2017; Rossetto et al., 2019). As a tsunami applies direct pressures to a structure, non-structural components like infill walls (and their openings) are seen to play an important role in determining tsunami forces (Del Zoppo et al., 2021). Furthermore, buoyancy, foundation scour and debris impact, which significantly affect building damage from tsunami inundation are rarely modeled (Del Zoppo et al., 2019). These

effects are still to be investigated; therefore, published analytical tsunami fragility functions are subjected to large modeling uncertainties. Progress towards more comprehensive and reliable analytical fragility and vulnerability models is needed.

Gaps in Risk and Resilience Metrics

Existing Methods

Tsunami risk assessments typically reflect the impact on the exposed population and infrastructure. The most commonly used decision variables (or metrics) are the number of fatalities, injuries, affected people, besides the direct and indirect economic losses. Direct economic losses represent the repairing/replacement costs of damaged assets, whereas indirect losses reflect costs as down-time, partial loss of functionality of buildings and infrastructure, loss or reduction in network connectivity, flow and/or capacity. These metrics can be used in alternative approaches such as worst-case scenarios, scenario-based for a prescribed return-period, and fully probabilistic. A review of early methods for tsunami risk assessment can be found in Jelínek and Krausmann (2008).

Fully probabilistic risk assessments require the integration of hazard estimates (PTHA) with vulnerability functions (see **Figure 1**, Løvholt et al., 2015a; 2019). Since the results of PTHA are not always available, tsunami risk assessments are often performed considering selected (worst-case) scenarios as hazard input (e.g., Triantafyllou et al., 2019), which sometimes represent past disasters (e.g., Daniell et al., 2017). Having the results of PTHA available, tsunami risk assessment can also be performed for a limited number of scenarios (e.g., Nadim and Glade, 2006; Okumura et al., 2017). When the PTHA results are available in the form of stochastic event sets, a fully probabilistic tsunami risk assessment (PTRA) can be performed (Ordaz, 2000; Strunz et al., 2011; Salgado-Gálvez et al., 2014), although these types of analyses usually demand an extensive computational effort (e.g., Løvholt et al., 2015a; Jaimes et al., 2016; Goda and Song, 2019; Ordaz et al., 2019).

In a fully probabilistic tsunami risk assessment workflow, risk results are obtained in terms of exceedance frequencies for the above-mentioned metrics (**Figure 1**). For instance, loss exceedance curves (LEC) provide the relationship between loss values and their exceedance frequencies (Løvholt et al., 2015a; Jaimes et al., 2016; Attary et al., 2017; Ordaz et al., 2019). The area under the LEC corresponds to the average annual loss (AAL), a metric that provides a long-term overview of risk and accounts for the contribution of large and infrequent events as well as small and more frequent ones. From the LEC, loss values associated with a given return period can be obtained, such as loss values estimated by Løvholt et al. (2015a) at a global level representing direct losses. The Hazus tsunami loss estimation methodology provides state-of-the-art decision-support software for estimating potential losses from tsunami events (FEMA, 2017a; FEMA, 2017b).

Risk assessment is not necessarily limited to quantifying the direct and indirect impact on exposed populations and infrastructures. The evaluation of safety and reliability of physical systems is of interest too and for this, fragility functions ("*Gaps in Physical Vulnerability*" section) can be integrated with hazard to obtain the frequency of exceeding a given damage level (see **Figure 1**, e.g., Park et al., 2019; Fukutani et al., 2019). The risk metrics provide valuable data also for the assessment of quantitative resilience (also denoted as engineering resilience), which aims to estimate the resilience of a network, an infrastructure, or even an urban ecosystem to a specific natural hazard (see Mebarki et al., 2016 for industrial plants, Akiyama et al., 2020 for bridges). Quantitative resilience should not be confused with coastal community resilience which is discussed in detail in the following section.

Identified Gaps

Gaps Related to Characterization and Propagation of Uncertainties (R1)

Most existing PTRA models rely on a homogeneous Poisson process as the probabilistic backbone for the occurrence process (**Eq. 4**). The Poisson model, strictly speaking, should be used for propagating only those uncertainty sources that renew with the occurrence of each new event (Kiureghian, 2005). This means that propagation of other sources of uncertainties in a PTRA framework (i.e., those that lack renewal properties), such as the uncertainties in modeling, analysis method, and in general epistemic uncertainties, need more research (Goda and De Risi, 2018; Goda, 2020). One possible direction could point to Bayesian methods (Jalayer and Ebrahimian, 2020).

Challenges in Characterizing Vulnerability Functions (R2)

PTRA lacks a clear distinction and definition of the different loss components that are quantified through the vulnerability functions. On the one hand, direct economic losses can be estimated with a good degree of confidence using existing methodologies (Pagnoni et al., 2019). Long-term direct (e.g., cost of maintenance) and indirect losses (e.g., down-time and reduced functionality including business interruption) typically represent a significant component of the total economic loss (direct + indirect) yet require better quantitative approaches.

Lack of a Tsunami Consequences Database (R3)

There is a lack of tsunami-specific consequence databases accounting for casualties and losses (Yamao et al., 2015). These types of databases exist for disasters in general (e.g., EM-DAT) and more specifically for earthquakes (So et al., 2012; Cardona et al., 2018). They are useful not only to keep a consistent record of past events and the affected regions but to disaggregate the impacts of large events in terms of losses (direct and indirect) and casualties (fatalities and injured), besides assessing the consequences in particular sectors (e.g., road networks, heritage sites, etc.) at different resolution levels. The information included in the consequences databases provides valuable data to validate and calibrate different components of the models (e.g., fragility curves, vulnerability functions). Some data can be partially acquired from collections of documented eyewitness accounts (Santos and Koshimura, 2015), or other sources (e.g., ITIC, 2020).

General Lack of Risk Studies for Networks and Lifelines (R4)

Current implementations of PTRA are mainly focused on residential buildings and emergency planning activities such as

the definition of evacuation routes. However, the resilience of coastal areas relies on conventional and strategic infrastructures (Akiyama et al., 2013; Pitilakis et al., 2019). Conventional infrastructure such as roads, bridges, power, water, sanitation and communication networks, underpin economic and social activities in most urban areas (Salgado-Gálvez et al., 2018). Schools and hospitals support the provision of education and health services, which are essential to recovery. Critical infrastructures in coastal areas include harbors (nuclear) power plants, gas and oil storage, and early warning infrastructure, such as tidal buoys and offshore bottom pressure gauges (De Risi et al., 2018). Such infrastructures are complex, often interconnected and geographically distributed systems involving multiple sectors (Duenas-Osorio and Vemuru, 2009; Argyroudis et al., 2019), where further research is needed to quantify their resilience to tsunamis.

Assessing Tsunami Risk in a Multi-Hazard and Multi-Risk Framework (R5)

As triggered events, tsunamis fit naturally within a multi-hazard framework. Moreover, there can be several cascading consequences associated with the occurrence of tsunamis, such as technological disasters induced by natural hazards known as NATECH risks (e.g., the Fukushima Disaster), disruption to supply chains, and societal impacts. Therefore, management and decision-making for tsunami risk should be framed in a multi-risk context. To be able to make risk-informed decisions considering tsunamis, it is important to model the interaction of tsunamis with other phenomena at the level of hazards, vulnerabilities, and socio-economic consequences. An important gap related to risk assessment for tsunamis (and in general) is the lack of a streamlined and standard workflow for modeling the multi-hazard and multi-risk aspects. Currently, most studies consider the different hazards to be independent or "simultaneous" (e.g., earthquake and tsunami as independent events); whereas, few works consider interacting hazards such as coupled simulation of tsunami and earthquake (De Risi and Goda, 2016; Goda et al., 2017; Goda and De Risi, 2018; Ordaz et al., 2019; Park et al., 2019), the cumulation of tsunami and earthquake damages and losses (Ordaz, 2015; Attary et al., 2019; Park et al., 2019; Petrone et al., 2020), and interaction of tsunami and aging infrastructure (Akiyama et al., 2020).

Lack of Understanding and Quantification of Mortality (R6)

Strikingly, the 2004 tsunami with more than 226,000 dead and missing people (EM-DAT, 2020) caused an order of magnitude higher fatalities than the 2011 Tohoku tsunami with 19,846 (EM-DAT, 2020). Hence, past major disasters indicate that the vulnerability to tsunami mortality of a population is much more sensitive to demographic factors (Løvholt et al., 2014) than to physical vulnerabilities ("*Gaps in Physical Vulnerability*" section). Correlations of tsunami flow depth and number of fatalities following the 2004 Indian Ocean, 2006 Java and 2011 Tohoku tsunamis reveal much larger scatter than those observed in physical vulnerability functions, even when derived from the same events (Reese et al., 2007; Koshimura et al., 2009; Suppasri et al., 2016). As human behavior influences mortality strongly (Johnston et al., 2016; Blake et al., 2018), deriving simplified vulnerability charts based on single tsunami intensity measures may not be appropriate. Tsunami awareness and availability of tsunami early warning systems and infrastructure are important (Gregg et al., 2006; Fraser et al., 2014), as well as proximity to source areas. Our understanding and ability to quantify and assess the effect of all these factors on tsunami mortality is still very limited.

The Weakness of Capturing Multi-Faceted Aspects of Vulnerability (R7)

Quantitative risk assessments typically address several socio-economic parameters (e.g., safety, downtime, direct and indirect economic losses, and even human behavior and response) as dimensions of consequences to disruptive tsunami events. However, PTRA falls short in modeling some dimensions of vulnerability that are part of a given context and not directly caused by a disruptive event (e.g., governance-related issues, adaptation and coping capacities, societal inequalities). There are no established methodologies, within the context of the PTRA framework (**Equations 1–4**), for characterizing context-based impacts of tsunami on the social, political and economic dimensions, leaving it unclear how to address these dimensions. Integrated and heuristic approaches such as "MOVE" (Birkmann et al., 2013) or holistic approaches as those proposed by Carreño et al. (2007) or Aguirre-Ayerbe et al. (2018), have strived to address the context-based and multi-dimensional nature of vulnerability and risk and could be adapted to be used as physical risk indicators in the outcomes of PTRA.

Gaps in Social Vulnerability, Multi-Dimensional Vulnerability and Risk Indicators

Existing Methods

Although not directly addressing tsunami risk, Jasanoff (1993) pointed out the urge to bridge the two cultures of quantitative and qualitative risk assessment, stressing the importance to view risk in a larger context of social justice (*who* should we protect, from *which* harm, at *what* cost, and by foregoing *what* other opportunities). The societal factors impacting vulnerability and risk are mainly rooted in a complex and diverse aggregate, which varies over time and space. Qualitative vulnerability investigations use models and frameworks considering several dimensions (e.g., economic, demographic, psychological, political or physical), summarized by composite vulnerability and risk indices. These indicators can be distinguished from the risk and resilience metrics discussed in the previous section ("**Gaps in Risk and Resilience Metrics**" section) since some of them cannot be directly integrated into a computational PTRA procedure. Examples of existing multi-dimensional vulnerability and risk indicators are: The *community resilience* (e.g., Lam et al., 2016; Saja et al., 2019), *the urban disaster risk index* (Carreño et al., 2007; Salgado-Gálvez et al., 2016), the *social vulnerability index* (Cutter et al., 2003; Flanagan et al., 2011), the *Coastal vulnerability index* (McLaughlin and Cooper, 2010), *Metropolitan Tsunami Human Vulnerability Assessment* (Tufekci et al., 2018).

Identified Gaps

The Difficulty of "Quantifying" Social Vulnerability (I1)

Social vulnerability describes combinations of social, cultural, economic, political, and institutional processes that determine differentials in the experience of hazards and recovery from dangerous events (Spielman et al., 2020). Experts may construct meaningful indicators to include a social component in hazard planning, preparation, and response. Integrating social vulnerability research into emergency and disaster risk management is essential, but caution is required to assign quantitative elements. Integration of social factors may allow planners and decision-makers to better identify problems in case of destructive events and provide insights into addressing recovery solutions (Cardona, 2001; Chakraborty et al., 2005; Schmidtlein et al., 2008). Social Vulnerability Index (SoVI) is a single quantitative indicator which was developed through a review of hazard case studies by Cutter et al. (2003) examining the spatial patterns of social vulnerability to natural hazards at the county level in the United States. Because of the complex and multidimensional nature of factors contributing to vulnerability, no variable has yet been identified to fully validate SoVI. An alternative approach to assess its reliability is to identify how the changes in the SoVI algorithm construction may lead to the changes in the outcome. Schmidtlein et al. (2008) investigated the sensitivity of quantitative features of the SoVI such as the scale of application, the set of used variables, and various geographic contexts.

Ambiguities in Definition of Community Resilience (I2)

Resilience is a frequently used term to discuss the capacity of a society or ecosystem to recover quickly from a disaster. The United Nations Office for Disaster Risk Reduction has defined resilience as "*the capacity of a system, community or society potentially exposed to hazards to adapt, by resisting or changing in order to reach and maintain an acceptable level of functioning and structure. This is determined by the degree to which the social system is capable of organizing itself to increase this capacity for learning from past disasters for better future protection and to improve risk reduction measures*" (UNISDR, 2007). A comprehensive review of various definitions of resilience can be found in Davoudi et al. (2012) and Ayyub (2014). The definition of coastal resilience is hindered by varying definitions and non-unified terminology, difficulties in selecting and combining different resilience indicators, and lack of data for validation (Lam et al., 2016). In fact, resilience is still lacking rigorous measurement methods (Bozza et al., 2015), especially in the context of tsunami hazard (Genadt, 2019).

Lack of Tsunami Vulnerability Index (I3)

A specific tsunami Disaster Risk Index (TDRI), similarly to the Disaster Risk Index (DRI) developed by the UN Development Program to compare disaster risk between countries exposed to hazards (UNDP, 2004) or the Urban Seismic Risk Index by Carreño et al. (2007) should be developed.

Integrated Approaches to Consider the Multi-Dimensional Aspects of Tsunami Risk (I4)

Vulnerability and risk are multi-faceted concepts and encompass various assets, physical, organizational, and institutional dimensions (e.g., Herslund et al., 2016). Vulnerability and risk assessment considering these different facets often requires different scientific backgrounds and approaches (Hufschmidt et al., 2005). A consequence-based approach to risk assessment (e.g., the PEER framework, or computational PTRA in general) has its roots in engineering. The approach follows a logical flow from causes associated with a disruptive event toward quantifying its direct and indirect socio-economic consequences. This approach focuses on the physical dimension of vulnerability, acting as a "container" of functions and services and thereby invokes–directly or indirectly–other dimensions of vulnerability such as social, economic and organizational vulnerability. On the other hand, the context-based approach (e.g., approaches based on integrated indicators) has its roots in the humanities and social disciplines. This approach deals with the context and the interactions between different actors, the respective territory, the different drivers (climate, societal changes) and how decisions can affect the overall context and the complex interplay between actors and drivers. Needless to say, the two approaches complement each other and have to be taken into account in policymaking for DRR in an integrated manner (O'Brien et al., 2007).

Considering Community Response and Organizational Capacities (I5)

Recent tsunami events worldwide have highlighted the need to critically revisit how human behavior in tsunami evacuation, and more generally, the human dimension of preparedness for tsunamis is addressed within the risk assessments. The lessons from Japan 2011, Chile 2010 and Indonesia in 2010 and 2018 events highlight such needs. Questions arise on how and if the different and seemingly inconsistent human behavior can be addressed in tsunami risk assessments. Moreover, atypical events such as the Krakatoa, Indonesia 2018, do not allow for conventional prevention, warning and mitigation strategies. In most cases, aid and help arrive late due to limited organizational capacities, leaving the affected communities in even more vulnerable conditions, especially during the first critical hours and days after the event. Events with growing levels of complexity are likely to continue to occur in the future and this calls for a more in-depth consideration of how different communities respond and how those variations can be integrated within the risk assessment framework.

Incorporating Risk Perception in the Formulation and Analysis of Complex Risks (I6)

Perceptions are dynamic and socially constructed. Perceptions can change abruptly or gradually, depending on the context. Understanding evacuation behavior requires an understanding of risk perceptions. This can help explain why the response to tsunami drills may be different than when responding to a real event. It is quite challenging for risk methodologies to consider the dynamic, complex and subjective aspects of risk perception. Only by understanding the subjective meanings of perceived risks allows risk communication to be designed and applied more effectively.

CONCLUSIONS AND DIRECTIONS

In this review, we discuss a large number of research gaps in PTHA and PTRA. It becomes obvious that methods have substantially improved over the past decades, but also that open questions remain in the physical description, conceptualization, modeling, as well as the social and psychological dimensions of the topic.

The physics and geological complexity of tsunamigenic sources are still not captured nor understood adequately, leading to large uncertainties. For SPTHA, neither all earthquake faults nor their exact location, geometry, boundary and initial conditions (e.g., stress, friction) are fully constrained. Statistical models of recurrence constitute the largest uncertainties in large and rare events, including tsunami earthquakes. Uncertainty may become excessive for landslide tsunamis, where statistics on past events often are absent, and our understanding of slope failure probability is limited. The need for covering vast geographical scales, source diversity and related uncertainties, render LPTHA extremely challenging. For VPTHA additional difficulties arise due to the complexity of tsunamigenic volcano sources and triggers, but they are constrained spatially. MPTHA may benefit from a large meteorological data network allowing for (prototypical) forecasting as well as PTHA applications, but sensitivity to source parameters is still unconstrained.

While modeling and parameterization of individual phenomena are possible, they are often excessively computationally expensive or highly uncertain due to missing constraints on input parameters. The multiple scales involved in PTHA from far-field propagation over oceanic distances to the need to resolve small scale inundation features while capturing physics and resolving uncertainties still represent an open challenge. Yet, this solution is needed to convey PTHA information properly into risk analysis.

Even more challenging is the situation in PTRA, where gaps exist in the transformation of physical hazard to risk and quantifying the uncertainties in the assessment of risk and resilience. Key concepts, such as physical vulnerability and mortality and their related uncertainties, are less developed than the main PTHA elements. There are gaps regarding selection of IM, limited observed damage asset- and location-wise, and limited experimental validation.

Furthermore, tsunami science is immature concerning embedding issues with intrinsically multi-hazard and multi-risk aspects, such as the cascading events that are entangled with tsunami hazards. A weakly developed link between quantitative PTRA and the social sciences is a clear gap. At this point, it is worth noting that terms "vulnerability" and "resilience" are multi-dimensional concepts that are used both in the consequence-based–natural sciences inspired–as well as context-based approaches–motivated by social sciences. Therefore, they may have quite different interpretations depending on the analysis context.

The overarching issue is integrating all the above components and developing an overall consistent sensitivity and uncertainty quantification framework, to understand tsunami risk and identify risk drivers, from the probability of the sources causing hazards to the probability of their physical consequences and societal impact. This understanding must be developed and prioritized in future research.

To guide such efforts, we have performed an expert judgment exercise that we discuss in the following subsection. It may help to identify most pressing research needs as well as prioritize research efforts.

Prioritizing Research Gaps

A scientific sensitivity analysis of the impact of each research gap, as conducted for individual sources in Sepúlveda et al. (2017) or Davies and Griffin (2020), on the overall result of a PTHA or PTRA is certainly out of the scope of a single review paper. However, some guidance on prioritization of efforts is certainly desirable. Since we focused our description on research gaps, we suggest two important metrics for the prioritization: The susceptibility of PTHA and PTRA results on uncertainty due to the research gap (sensitivity) and the difficulty or amount of research effort needed to fill that respective gap (tractability).

In order to assess these two metrics, we conducted a first-pass expert judgment among the more than 50 co-authors of this article–all experts in one or more of the aspects of our review. A questionnaire was designed that asked three questions for each of the 47 research gap subsections that we have described before. The first two questions addressed the two metrics just mentioned. The third question asked if experts were of the opinion if the research gap existed because of a missing theoretical understanding, a lack of data, or both. While this somewhat ad hoc prioritization is not as solid as a rigorous expert elicitation (e.g., Cooke, 1991; Budnitz et al., 1997; Morgan, 2014; for tsunami hazard see an application in Basili et al., 2021, or the discussion in Grezio et al., 2017) and hence could be somehow biased, we believe it still provides a valuable starting point for future efforts. It is a qualitative broad-brush answer to the question, which research gap may be of highest importance. More details on this exercise are given in the **Supplementary Material**.

The result of this exercise is visualized in a priority matrix (**Figure 2**). It may appear natural to respond first to those research gaps that are located in the left upper quadrant of the matrix, since these gaps are considered less difficult to solve, while they are expected to influence the risk considerably. It can be noted that most of the research gaps are judged hard to solve but with a highly sensitive impact on the overall result. This seems natural, since high impact but simple problems would have been solved already.

Based on our qualitative assessment, we can therefore identify some overall trends. First, we see some common challenges related to establishing annualized source probability of occurrence, which tend to cluster in the upper right corner of **Figure 2**. This means that they are considered relatively most important, yet hardest to solve. Of these, obtaining landslide related annual source probabilities (L1) is considered both the largest yet most important obstacle, while a just slightly lower similar prioritization is evident for earthquake and volcano sources (S1 and V2). Another aspect that is considered important (and challenging) is the multi-hazard and cascading

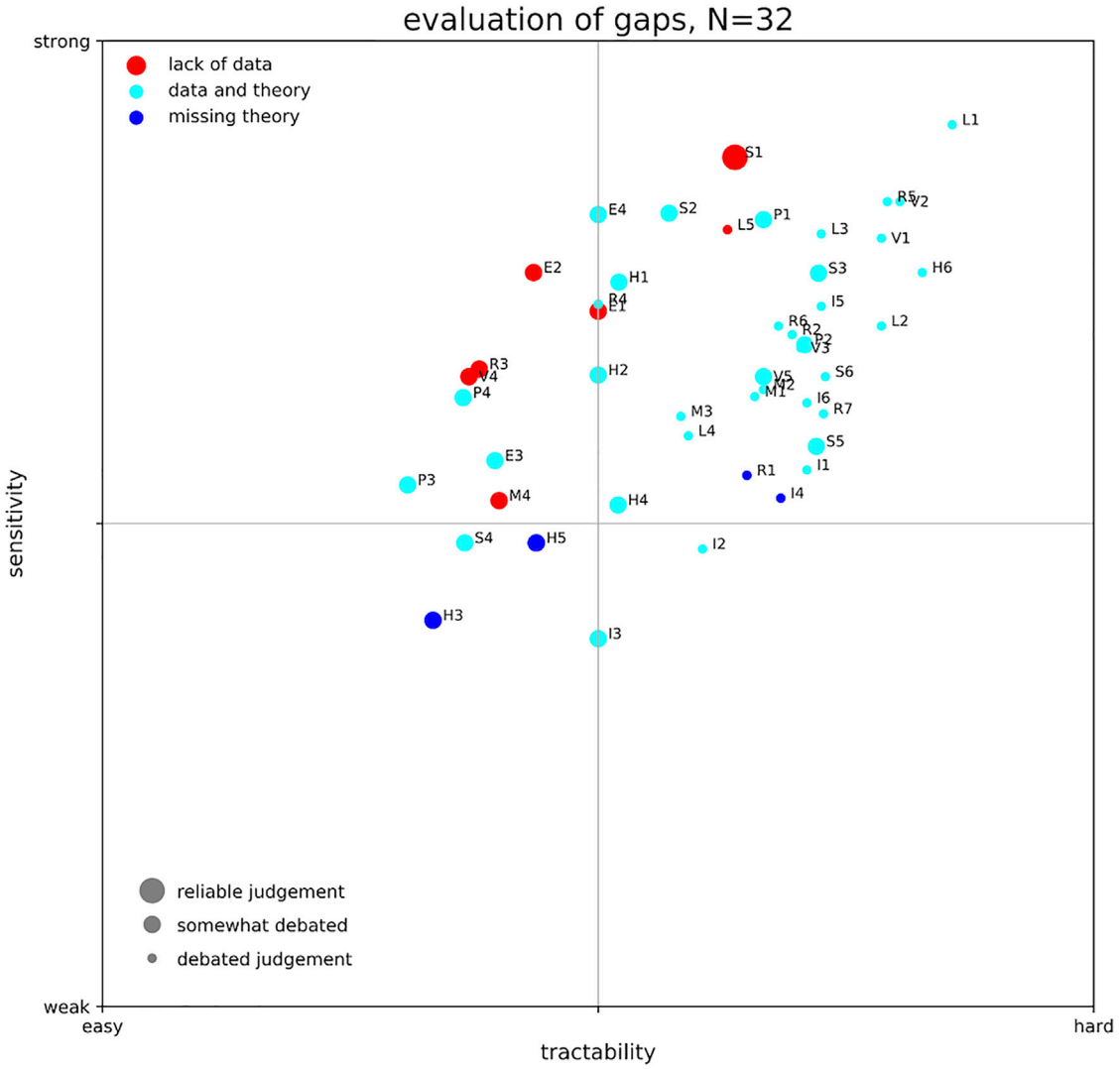

FIGURE 2 | Priority Matrix for all the 47 research gaps identified. Letters indicate seismic source gaps (S), landslide source gaps (L), volcanic source gaps (V), meteorological source gaps (M), hydrodynamical modeling gaps (H), exposure related gaps (E), physical vulnerability related gaps (P), resilience related gaps (R), social vulnerability and risk indicators related gaps (I). The size of each marker relates to the agreement of experts, larger marker size means less spread in the answers. Colors are used to indicate if the gap is caused by missing theoretical understanding (blue), a lack of data (red), or both (cyan).

hazard aspect (R5). On the other hand, the research gaps that appear to be least sensitive and also easy to be filled are related to the numerical modeling of wave propagation (H3), as well as lack of joint intensity measures (I3) and gaps related to earthquake scaling relations (S4). Finally, we also note **Figure 2** allows us to analyze several instances of components with similar sensitivity but with clearly different tractability. For instance, the lack of tsunami exposure data (E2) is considered as important as modeling complicated aspects of inundation (H6), but the former is assumed by the authors of this paper to be more easily achieved. Several other similar examples can be analyzed from **Figure 2**.

It is noteworthy that most of the research gaps that most experts find consensus on are highly sensitive in their impact (all located at the upper margin of the point cloud). It is also worth noting that most research gaps are considered to relate to data and theory gaps and that those that relate to only a missing theoretical understanding are considered of relatively low sensitivity. This may be related to the fact that when we don't understand a phenomenon, we cannot really judge whether it affects our results or not. In other words, this may be an "unknown". Whereas a data related research gap may already have proved to be sensitively influential by a specific example, but due to a lack of data cannot be involved concisely into the workflow.

This priority matrix is just a very first approach. Since tsunami research eventually aims at protecting life from natural hazard, one could also prioritize those research gaps with direct impact on this goal. These would be in particular those topics mentioned in sections "*Gaps in Physical Vulnerability*," "*Gaps in Risk and*

Resilience Metrics," and "*Gaps in Social Vulnerability, Multi-Dimensional Vulnerability and Risk Indicators*" (marked with P, R, and I; respectively).

Final Considerations

We have described and prioritized a comprehensive list of research gaps in PTHA and PTRA. While our approach to prioritization and the metric used to do so are to some extent subjective, it remains for the scientific community and further investigation as well as future incentives to decide, which directions to choose from. Nevertheless, our priority matrix will serve as a first impression on the weight of each of the identified research gaps.

An important part of the future puzzle will be exploring how uncertainties propagate to risk across disciplines. While uncertainties are more extensively explored in earthquake-related hazard analysis, non-seismic hazard, vulnerability, exposure and risk are lagging behind. On the other hand, different levels of maturity of methods and understanding will always exist. Hence, it is imperative to develop PTRA standards and guidelines to appropriately merge all risk analysis components considering their different uncertainty exploration and maturity level.

While validation of individual components has been addressed in several of the sections in our text, validating the PTHA and PTRA workflow as a whole is still ongoing research. Marzocchi and Jordan (2014) propose a methodology for a meaningful test of general probabilistic hazard models and an example of a successful application can be found in Meletti et al. (2021).

Certainly, research gaps exist also outside of the scope of PTHA and PTRA. New computational methods, like fuzzy methods, machine learning techniques and even advances in classical computational methods have to be considered. Rigorous, information theory inspired approaches to validation may also be explored.

Considering the goals of the Sendai Framework for Disaster Risk Reduction and acknowledging the vast number of challenges outlined in the sections before, a concerted interdisciplinary effort to close the most pressing gaps is required. Attempts to gather expertize, facilitate exchange and development, and coordinate community efforts are represented by the Global Tsunami Model (GTM, 2020) and the COST Action AGITHAR. A thorough consolidation of available sources of information in openly accessible databases, documentation of standard workflows, unification of terminology and metrics, as well as information hubs need to be established.

AUTHOR CONTRIBUTIONS

All Authors contributed in early stages of the manuscript by individual contributions from their respective research field. Major contributions are listed as follows: Early compilation of text: MS, FL, SL, JB, IA-Q, TR; Abstract and Conclusions: JB, FL, SL, JS; Introduction: FL, FJ, SL, JB, JS, MS-G; Probabilistic Framework: FJ, MS-G, IA-A; Earthquake Sources: SL, JS, FL, KJ, MV, SM; Landslide Sources: FL, RP, SA, AS; Volcano Sources: JS, FL, SA; Meteotsunami Sources: JB; Hydrodynamic Modeling: JB, FL, JM, IA-Q, AB; Exposure: FJ, TR, MS-G; Physical Vulnerability: TR, FJ, JS, MDZ; Risk/Resilience: IA-A, FJ; Social Vulnerability: FJ, IA-A, IR; substantial revisions: AG, KJ, SL, SM, RDR, MS, JS, RP, AB, RB, SA, MV, MDZ, AS, IA-Q, CC; internal review: all authors.

FUNDING

This article is based upon work from COST Action CA18109 AGITHAR, supported by COST (European Cooperation in Science and Technology). VB and PC obtained support through the VES20 Inter-Cost LTC 20020 project. MS-G obtained support through the Severo Ochoa Centers of Excellence Program (Ref. CEX 2018–000797-S). TU acknowledges funding from the European Union's Horizon 2020 research and innovation program (ChEESE project, Grant Agreement No. 823844).

ACKNOWLEDGMENTS

This work would not have been possible without the help of many researchers, who are too many to be named individually, but we thank all participants of COST Action AGITHAR for their valuable input in official or informal conversations, workshops and interactions. We would like to thank the reviewers and editor for very considerate and challenging suggestions that improved this manuscript substantially.

SUPPLEMENTARY MATERIAL

The Supplementary Material for this article can be found online at: https://www.frontiersin.org/articles/10.3389/feart.2021.628772/full#supplementary-material

REFERENCES

Abadie, S., Paris, A., Ata, R., Le Roy, S., Arnaud, G., Poupardin, A., et al. (2020). La Palma landslide tsunami: calibrated wave source and assessment of impact on French territories. *Nat. Hazards Earth Syst. Sci.* 20, 1–20. doi:10.5194/nhess-20-1-202010.5194/nhess-20-3019-2020

AGITHAR. (2020). Accelerating global science in tsunami hazard and risk analysis. Available at: https://www.agithar.uni-hamburg.de (Accessed November 5, 2020).

Aguirre-Ayerbe, I., Martínez Sánchez, J., Aniel-Quiroga, Í., González-Riancho, P., Merino, M., Al-Yahyai, S., et al. (2018). From tsunami risk assessment to disaster risk reduction—the case of Oman. *Nat. Hazards Earth Syst. Sci.* 18, 2241–2260. doi:10.5194/nhess-18-2241-2018

Akiyama, M., Frangopol, D. M., Arai, M., and Koshimura, S. (2013). Reliability of bridges under tsunami hazards: emphasis on the 2011 Tohoku-oki earthquake. *Earthq. Spectra* 29 (S1), S295–S314. doi:10.1193/1.4000112

Akiyama, M., Frangopol, D. M., and Ishibashi, H. (2020). Toward life-cycle reliability-, risk- and resilience-based design and assessment of bridges and bridge networks under independent and interacting hazards: emphasis on

earthquake, tsunami and corrosion. *Struct. Infrastruct. Eng.* 16 (1), 26–50. doi:10.1080/15732479.2019.1604770

Alam, M. S., Barbosa, A. R., Scott, M. H., Cox, D. T., and van de Lindt, J. W. (2018). Development of physics-based tsunami fragility functions considering structural member failures. *J. Struct. Eng.* 144 (3), 04017221. doi:10.1061/(ASCE)ST.1943-541X.0001953

Albini, P., Musson, R. M. W., Rovida, A., Locati, M., Gomez Capera, A. A., and Viganò, D. (2014). The global earthquake history. *Earthq. Spectra* 30 (2), 607. doi:10.1193/122013EQS297

Allen, T. I., and Hayes, G. P. (2017). Alternative rupture-scaling relationships for subduction interface and other offshore environments. *Bull. Seismol. Soc. Amer.* 107, 1240–1253. doi:10.1785/0120160255

Androsov, A., Behrens, J., and Danilov, S. (2011). "Tsunami modelling with unstructured grids Interaction between tides and tsunami waves," in,*Computational science and high performance computing IV*. Editors E. Krause, Y. Shokin, M. Resch, D. Kröner, and N. Shokina (Heidelberg: Springer Berlin), 115, 191–206. doi:10.1007/978-3-642-17770-5_15

Annaka, T., Satake, K., Sakakiyama, T., Yanagisawa, K., and Shuto, N. (2007). Logic-tree approach for probabilistic tsunami hazard analysis and its applications to the Japanese coasts. *Pure Appl. Geophys.* 164, 577–592. doi:10.1007/s00024-006-0174-3

Antofie, T., Luoni, S., Faiella, A., and Marin Ferrer, M. (2019). *Risk data hub—web platform to facilitate management of disaster risks*. Luxembourg: Publications Office of the European Union. doi:10.2760/68372

Araki, E., Saffer, D. M., Kopf, A. J., Wallace, L. M., Kimura, T., Machida, Y., et al. (2017). Recurring and triggered slow-slip events near the trench at the Nankai Troaugh subduction megathrust. *Science* 356 (6343), 1157–1160. doi:10.1126/science.aan3120

Aranguiz, R., Catalán, P. A., Cecioni, C., Bellotti, G., Henriquez, P., and González, J. (2019). Tsunami resonance and spatial pattern of natural oscillation modes with multiple resonators. *J. Geophys. Res. Oceans* 124 (11), 7797–7816. doi:10.1029/2019JC015206

Arcos, M. E. M., and LeVeque, R. J. (2015). Validating velocities in the GeoClaw tsunami model using observations near Hawaii from the 2011 Tohoku tsunami. *Pure Appl. Geophys.* 172, 849–867. doi:10.1007/s00024-014-0980-y

Argyroudis, S. A., MitoulisA., S., Winter, M. G., and Kaynia, A. M. (2019). Fragility of transport assets exposed to multiple hazards: state-of-the-art review toward infrastructural resilience. *Reliab. Eng. Syst. Saf.* 191. 106567. doi:10.1016/j.ress.2019.106567

Attary, N., Unnikrishnan, V. U., van de Lindt, J. W., Cox, D. T., and Barbosa, A. R. (2017). Performance-based tsunami engineering methodology for risk assessment of structures. *Eng. Struct.* 141, 676–686. doi:10.1016/j.engstruct.2017.03.071

Attary, N., Van De Lindt, J. W., Barbosa, A. R., Cox, D. T., and UnnikrisAhnan, V. U. (2019). Performance-based tsunami engineering for risk assessment of structures subjected to multi-hazards: tsunami following earthquake. *J. Earthq. Eng.* 7, 1–20. doi:10.1080/13632469.2019.1616335

Auker, M. R., Sparks, R. S. J., Siebert, L., Crosweller, H. S., and Ewert, J. (2013). A statistical analysis of the global historical volcanic fatalities record. *J. Appl. Volcanol.* 2, 2. doi:10.1186/2191-5040-2-2

Ayyub, B. M. (2014). Systems resilience for multihazard environments: definition, metrics, and valuation for decision making. *Risk Anal.* 34, 340–355. doi:10.1111/risa.12093

Baiguera, M., Rossetto, T., Robertson, I. N., and Petrone, C. (2019). "Towards a tsunami nonlinear static analysis procedure for the ASCE 7 standard," in 2nd International conference on natural hazards and infrastructure. Available at: https://discovery.ucl.ac.uk/id/eprint/10078809

Barbato, M., Petrini, F., Unnikrishnan, V. U., and Ciampoli, M. (2013). Performance-based hurricane engineering (PBHE) framework. *Struct. Saf.* 45, 24–35. doi:10.1016/j.strusafe.2013.07.002

Basili, R., Brizuela, B., Herrero, A., Iqbal, S., Lorito, S., Maesano, F. E., et al. (2021). , The making of the NEAM tsunami hazard model 2018 (NEAMTHM18). *Front. Earth Sci.* 8, 616594. doi:10.3389/feart.2020.616594

Basili, R., Tiberti, M. M., Kastelic, V., Romano, F., Piatanesi, A., Selva, J., et al. (2013). Integrating geologic fault data into tsunami hazard studies. *Nat. Hazards Earth Syst. Sci.* 13, 1025–1050. doi:10.5194/nhess-13-1025-2013

Beauval, C., Yepes, H., Audin, L., Alvarado, A., Nocquet, J.-M., Monelli, D., et al. (2014). Probabilistic seismic-hazard assessment in quito, estimates and uncertainties. *Seismol. Res. Lett.* 85 (6), 1316–1327. doi:10.1785/0220140036

Bebbington, M. (2010). Trends and clustering in the onsets of volcanic eruptions. *J Geophys. Res.* 115, B01203. doi:10.1029/2009jb006581

Bebbington, M. (2008). Incorporating the eruptive history in a stochastic model for volcanic eruptions. *J. Volcanol. Geothermal Res.* 175, 325–333. doi:10.1016/j.jvolgeores.2008.03.013

Begét, J. E., Cecioni, C., and Yepes, H. (2000). "Volcanic tsunamis," in *Encyclopedia of volcanoes*. Editor Sigurdsson, H. (London, UK: Academic Press), 1005–1013.

Behrens, J., and Dias, F. (2015). New computational methods in tsunami science. *Phil. Trans. R. Soc. A.* 373 (2053), 20140382. doi:10.1098/rsta.2014.0382

Bellotti, G., Cecioni, C., and de Girolamo, P. (2008). Simulation of small-amplitude frequency-dispersive transient waves by means of the mild-slope equation. *Coastal Eng.* 55, 447–458.

Bellotti, G., Di Risio, M., and De Girolamo, P. (2009). Feasibility of tsunami early warning systems for small volcanic islands. *Nat. Hazards Earth Syst. Sci.* 9, 1911–1919. doi:10.5194/nhess-9-1911-2009

Bevilacqua, A., Neri, A., Bisson, M., Esposti Ongaro, T., Flandoli, F., Isaia, R., et al. (2017). The effects of vent location, event scale, and time forecasts on pyroclastic density current hazard maps at Campi Flegrei caldera (Italy). *Front. Earth Sci.* 5, 112. doi:10.3389/feart.2017.00072

Bilek, S. L. (2010). Invited review paper: seismicity along the South American subduction zone: review of large earthquakes, tsunamis, and subduction zone complexity. *Tectonophysics* 495 (1–2), 2–14. doi:10.1016/j.tecto.2009.02.037

Bilek, S. L., and Lay, T. (1999). Rigidity variations with depth along interplate megathrust faults in subduction zones. *Nature* 400, 443–446. doi:10.1038/22739

Bilek, S. L., and Lay, T. (2018). Subduction zone megathrust earthquakes. *Geosphere* 14, 1468–1500. doi:10.1130/GES01608.1

Bird, P., Jackson, D. D., Kagan, Y. Y., Kreemer, C., and Stein, R. S. (2015). GEAR1: a global earthquake activity rate model constructed from geodetic strain rates and smoothed seismicity. *Bull. Seismol. Soc. Amer.* 105, 2538–2554. doi:10.1785/0120150058

Bird, P., and Kagan, Y. Y. (2004). Plate-tectonic analysis of shallow seismicity: apparent boundary width, beta, corner magnitude, coupled lithosphere thickness, and coupling in seven tectonic settings. *Bull. Seismol. Soc. Amer.* 94 (6), 2380–2399. doi:10.1785/0120030107

Bird, P., and Kreemer, C. (2015). Revised tectonic forecast of global shallow seismicity based on version 2.1 of the global strain rate map. *Bull. Seismol. Soc. Amer.* 105, 152–166. doi:10.1785/0120140129

Birkmann, J., Cardona, O. D., Carreño, M. L., Barbat, A. H., Pelling, M., Schneiderbauer, S., et al. (2013). Framing vulnerability, risk and societal responses: the MOVE framework. *Nat. Hazards* 67 (2), 193–211. doi:10.1007/s11069-013-0558-5

Blake, D., Johnston, D., Leonard, G., McLaren, L., and Becker, J. (2018). A citizen science initiative to understand community response to the kaikōura earthquake and tsunami warning in petone and eastbourne, wellington, aotearoa/New Zealand. *Bull. Seismol. Soc. Amer.* 108 (3B), 1807–1817. doi:10.1785/0120170292

Blaser, L., Krüger, F., Ohrnberger, M., and Scherbaum, F. (2010). Scaling relations of earthquake source parameter estimates with special focus on subduction environment. *Bull. Seismol. Soc. Amer.* 100, 2914–2926. doi:10.1785/0120100111

Bletery, Q., Thomas, A. M., Rempel, A. W., Karlstrom, L., Sladen, A., and De Barros, L. (2016). Mega-earthquakes rupture flat megathrusts. *Science* 354 (6315), 1027–1031. doi:10.1126/science.aag0482

Blikra, L. H., Longva, O., Harbitz, C., and Løvholt, F. (2005). Quantification of rock-avalanche and tsunami hazard in Storfjorden, western Norway. *Landslides Avalanches: ICFL Conf. Proc.* 12, 57–64. doi:10.1007/springerreference_5010

Bommer, J. J., and Stafford, P. J. (2016). *Seismic hazard and earthquake actions*, in *Seismic design of buildings to eurocode 8*. Editor A. Elghazouli (Boca Raton: CRC Press), 21–54. doi:10.1201/9781315368221-9

Bougouin, A., Paris, R., and Roche, O. (2020). Impact of fluidized granular flows into water: implications for tsunamis generated by pyroclastic flows. *J. Geophys. Res. Solid Earth* 7, e2019JB018954. doi:10.1002/asl2.471

Bozza, A., Asprone, D., and Manfredi, G. (2015). Developing an integrated framework to quantify resilience of urban systems against disasters. *Nat. Hazards* 78 (3), 1729–1748. doi:10.1007/s11069-015-1798-3

Brown, S. K., Jenkins, S. F., Sparks, R. S. J., Odbert, H., and Auker, M. R. (2017). Volcanic fatalities database: analysis of volcanic threat with distance and victim classification. *J. Appl. Volcanol.* 6, 15. doi:10.1186/s13617-017-0067-4

Bryn, P., Berg, K., Forsberg, C. F., Solheim, A., and Kvalstad, T. J. (2005). Explaining the storegga slide. *Mar. Pet. Geol.* 22 (1–2), 11–19. doi:10.1016/j.marpetgeo.2004.12.003

Budnitz, R. J., Apostolakis, G., and Boore, D. M. (1997). Nuclear regulatory commission, Washington: The Academy Press. Recommendations for probabilistic seismic hazard analysis: guidance on uncertainty and use of experts. Technical Report. doi:10.2172/479072

Bullard, G. K., Mulligan, R. P., Carreira, A., and Take, W. A. (2019). Experimental analysis of tsunamis generated by the impact of landslides with high mobility. *Coastal Eng.* 152, 103538. doi:10.1016/j.coastaleng.2019.103538

Burbidge, D., Cummins, P. R., Mleczko, R., and Thio, H. K. (2008). A probabilistic tsunami hazard assessment for western Australia. *Pure Appl. Geophys.* 165, 2059–2088. doi:10.1007/s00024-008-0421-x

Bürgmann, R., and Chadwell, D. (2014). Seafloor geodesy. *Annu. Rev. Earth Planet. Sci.* 42, 509–534. doi:10.1146/annurev-earth-060313-054953

Cardona, O. D. (2001). Estimación holística del riesgo sísmico utilizando sistemas dinámicos complejos. Ph.D. Thesis. Barcelona, Spain: Polytechnic University of Catalonia.

Cardona, O. D., Ordaz, M., Salgado-Gálvez, M. A., Barbat, A. H., and Carreño, M. L. (2018). Latin American and caribbean earthquakes in the GEM's earthquake consequences database (GEMECD). *Nat. Hazards* 93 (1), S113–S125. doi:10.1007/s11069-017-3087-9

Carlton, B., Vanneste, M., Forsberg, C. F., Knudsen, S., Løvholt, F., Kvalstad, T., et al. (2019). Geohazard assessment related to submarine instabilities in Bjørnafjorden, London. *Spec. Publ. Geol. Soc.* 477, 549–566. doi:10.1007/bf00305006

Carreño, M.-L., Cardona, O. D., and Barbat, A. H. (2007). Urban seismic risk evaluation: a holistic approach. *Nat. Hazards* 40 (1), 137–172. doi:10.1007/s11069-006-0008-8

Cecioni, C., and Bellotti, G. (2010). Inclusion of landslide tsunamis generation into a depth integrated wave model. *Nat. Hazards Earth Syst. Sci.* 10 (11), 2259–2268. doi:10.5194/nhess-10-2259-2010

Chagué-Goff, C., Andrew, A., Szczuciński, W., Goff, J., and Nishimura, Y. (2012). Geochemical signatures up to the maximum inundation of the 2011 Tohoku-oki tsunami—implications for the 869 AD Jogan and other palaeotsunamis. *Sediment. Geol.* 282, 65–77. doi:10.1016/j.sedgeo.2012.05.021

Chakraborty, J., Tobin, G. A., and Montz, B. E. (2005). Population evacuation: assessing spatial variability in geophysical risk and social vulnerability to natural hazards. *Nat. Hazards Rev.* 6 (1), 23–33. doi:10.1061/(asce)1527-6988(2005)6:1(23)

Charvet, I., Macabuag, J., and Rossetto, T. (2017). Estimating tsunami-induced building damage through fragility functions: critical review and research needs. *Front. Built Environ.* 3, 121. doi:10.3389/fbuil.2017.00036

Charvet, I., Suppasri, A., Kimura, H., Sugawara, D., and Imamura, F. (2015). A multivariate generalized linear tsunami fragility model for Kesennuma City based on maximum flow depths, velocities and debris impact, with evaluation of predictive accuracy. *Nat. Hazards* 79 (3), 2073–2099. doi:10.1007/s11069-015-1947-8

Chaytor, J. D., Uri, S., Solow, A. R., and Andrews, B. D. (2009). Size distribution of submarine landslides along the US Atlantic margin. *Mar. Geol.* 264 (1-2), 16–27. doi:10.1016/j.margeo.2008.08.007

Chock, G. (2016). Design for tsunami loads and effects in the ASCE 7-16 standard. *J. Struct. Eng.* 142 (11), 04016093. doi:10.1061/(ASCE)ST.1943-541X.0001565

Chock, G. Y., Robertson, I., and Riggs, H. R. (2011). "Tsunami structural design provisions for a new update of building codes and performance-based engineering," in *Solutions to coastal disasters 2011*, Editors Wallendorf, L.A., Jones, C., and Ewing, L. (London: ASCE) 423–435. doi:10.1061/41185(417)38

Chock, G., Yu, G., Thio, H. K., and Lynett, P. J. (2016). Target structural reliability analysis for tsunami hydrodynamic loads of the ASCE 7 standard. *J. Struct. Eng.* 142, 04016092–4016112. doi:10.1061/(ASCE)ST10.1061/(asce)st.1943-541x.0001499

Choi, B. H., Pelinovsky, E., Kim, K. O., and Lee, J. S. (2003). Simulation of the trans-oceanic tsunami propagation due to the 1883 Krakatau volcanic eruption. *Nat. Hazards Earth Syst. Sci.* 3, 321–332. doi:10.5194/nhess-3-321-2003

Churchill, D. D., Houston, S. H., and Bond, N. A. (1995). The daytona beach wave of 3-4 july 1992: a shallow-water gravity wave forced by a propagating squall line. *Bull. Amer. Meteorol. Soc.* 76 (1), 21–32. doi:10.1175/1520-0477(1995)076<0021:tdbwoj>2.0.co;2

Clare, M., Chaytor, J., Dabson, O., Gamboa, D., Georgiopoulou, A., Eady, H., et al. (2019). A consistent global approach for the morphometric characterization of subaqueous landslides. *Geol. Soc. Lond. Spec. Publ.* 477 (1), 455–477. doi:10.1144/sp477.15

Cooke, R. M. (1991). *Experts in uncertainty: opinion and subjective probability in science*. Oxford: Oxford University Press.

Cornell, C. A. (1968). Engineering seismic risk analysis. *Bull. Seismol. Soc. Amer.* 58, 1583–1606.

Crosta, G. B., Imposimato, S., and Roddeman, D. (2016). Landslide spreading, impulse water waves and modelling of the Vajont rockslide. *Rock Mech. Rock Eng.* 49 (6), 2413–2436. doi:10.1007/s00603-015-0769-z

Cutter, S. L., Boruff, B. J., and Shirley, W. L. (2003). Social vulnerability to environmental hazards*. *Soc. Sci. Q.* 84 (2), 242–261. doi:10.1111/1540-6237.8402002

Daniell, J. E., Schaefer, A. M., and Wenzel, F. (2017). Losses associated with secondary effects in earthquakes. *Front. Built Environ.* 3, 133. doi:10.3389/fbuil.2017.00030

Dao, M. H., and Tkalich, P. (2007). Tsunami propagation modelling—a sensitivity study. *Nat. Hazards Earth Syst. Sci.* 7, 741–754. doi:10.5194/nhess-7-741-2007

Davies, G., and Griffin, J. (2018). The 2018 Australian probabilistic tsunami hazard assessment *Record 2018/41*. Canberra: Geoscience Australia. doi:10.11636/Record

Davies, G., Griffin, J., Løvholt, F., Glimsdal, S., Harbitz, C., Thio, H. K., et al. (2018). A global probabilistic tsunami hazard assessment from earthquake sources. *Geol. Soc. Lond. Spec. Publ.* 456, 219–244. doi:10.1144/SP456.5

Davies, G., and Griffin, J. (2019). Sensitivity of probabilistic tsunami hazard assessment to far-field earthquake slip complexity and rigidity depth-dependence: case study of Australia. *Pure Appl. Geophys.* 177, 1521–1548. doi:10.1007/s00024-019-02299-w

Davies, G., and Griffin, J. (2020). Sensitivity of probabilistic tsunami hazard assessment to far-field earthquake slip complexity and rigidity depth-dependence: case study of Australia. *Pure Appl. Geophys.* 177, 1521–1548. doi:10.1007/s00024-019-02299-w

Davies, G., Horspool, N., and Miller, V. (2015). Tsunami inundation from heterogeneous earthquake slip distributions: evaluation of synthetic source models. *J. Geophys. Res. Solid Earth* 120, 6431–6451. doi:10.1002/2015JB012272

Davies, G. (2019). Tsunami variability from uncalibrated stochastic earthquake models: tests against deep ocean observations 2006-2016. *Geophys. J. Int.* 218, 1939–1960. doi:10.1093/gji/ggz260

Davoudi, S., Shaw, K., Haider, L. J., Quinlan, A. E., Peterson, G. D., Wilkinson, C., et al. (2012). Resilience: a bridging concept or a dead end? "Reframing" resilience: challenges for planning theory and practice interacting traps: resilience assessment of a pasture management system in northern Afghanistan urban resilience: what does it mean in planning practice? Resilience as a useful concept for climate change adaptation? The politics of resilience for planning: a cautionary note. *Plann. Theor. Pract.* 13 (2), 299–333. doi:10.1080/14649357.2012.677124

Day, S. J., et al. (2015). Volcanic tsunamis, in *Encyclopedia of volcanoes*. Editor Sigurdsson, H. (London, UK:Academic Press), 993–1009.

De Bono, A., and Chatenoux, B. (2015). A global exposure model for GAR 2015. UNEP-GRID, GAR.

De Bono, A., and Mora, M. G. (2014). A global exposure model for disaster risk assessment. *Int. J. Disaster Risk Reduct.* 10, 442–451. doi:10.1016/j.ijdrr.2014.05.008

de la Asunción, M., Castro, M. J., Fernández-Nieto, E. D., Mantas, J. M., Acosta, S. O., and González-Vida, J. M. (2013). Efficient GPU implementation of a two waves TVD-WAF method for the two-dimensional one layer shallow water system on structured meshes. *Comput. Fluids* 80, 441–452. doi:10.1016/j.compfluid.2012.01.012

De Risi, R., and Goda, K. (2016). Probabilistic earthquake–tsunami multi-hazard analysis: application to the Tohoku region. *Jpn. Front. Built Environ.* 2, 25. doi:10.3389/fbuil.2016.00025

De Risi, R., Goda, K., Mori, N., and Yasuda, T. (2017). Bayesian tsunami fragility modeling considering input data uncertainty. *Stoch. Environ. Res. Risk Assess.* 31, 1253–1269. doi:10.1007/s00477-016-1230-x

De Risi, R., and Goda, K. (2017). Simulation-based probabilistic tsunami hazard analysis: empirical and robust hazard predictions. *Pure Appl. Geophys.* 174, 3083–3106. doi:10.1007/s00024-017-1588-9

De Risi, R., Jalayer, F., De Paola, F., Iervolino, I., Giugni, M., Topa, M. E., et al. (2013). Flood risk assessment for informal settlements. *Nat. Hazards* 69 (1), 1003–1032. doi:10.1007/s11069-013-0749-0

De Risi, R., Muhammad, A., and Goda, K. (2018). *A way forward to resilient infrastructures against earthquake-tsunami multi-hazard* in *Routledge handbook of sustainable and resilient infrastructure*. Editor P. Gardoni (Oxon, U.K.: Routledge), 180–196.

Del Zoppo, M., Di Ludovico, M., and Prota, A. (2021). Methodology for assessing the performance of RC structures with breakaway infill walls under tsunami inundation. *J Struct Eng.* 147 (2), 04020330. doi:10.1016/b978-0-12-107180-6.50009-3

Del Zoppo, M., Rossetto, T., Di Ludovico, M., and Prota, A. (2019). "Assessing the effect of tsunami-induced vertical loads on RC frames," in Proceedings of the 1st fib Italy Symposium on Concrete and Concrete Structures. Parma, Italy.

Dueñas-Osorio, L., and Vemuru, S. M. (2009). Cascading failures in complex infrastructure systems. *Struct. Saf.* 31 (2), 157–167. doi:10.1016/j.strusafe.2008.06.007

Dusek, G., DiVeglio, C., Licate, L., Heilman, L., Kirk, K., Paternostro, C., et al. (2019). A meteotsunami climatology along the U.S. East coast. *Bull. Amer. Meteorol. Soc.* 100, 1329–1345. doi:10.1175/BAMS-D-18-0206.1

Global Volcanism Program. (2013). "Volcanoes of the world," Editor Venzke, E. (London: Smithsonian Institution) (Accessed Januray 5, 2021). doi:10.5479/si.GVP.VOTW4-2013

Eguchi, R. T., Eguchi, M. T., Bouabid, J., Koshimura, S., and Graf, W. P. (2014). "Benchmarking, validation and calibration of newly-developed HAZUS tsunami methodology." in 10th U.S. National conference on earthquake engineering: Frontiers of earthquake engineering. NCEE 2014. Anchorage: United States. doi:10.4231/D31834329

EM-DAT. (2020). The international disaster database CRED. Available at: https://www.emdat.be (Accessed November 4, 2020).

Esteva, L. (1967). "Criteria for the construction of spectra for seismic design," in Presented at third Panamerican symposium on structures. Caracas, Venezuela.

Fardis, M. N. (2009). *Seismic design, assessment and retrofitting of concrete buildings: based on EN-Eurocode 8*. Berlin: Springer. doi:10.1007/978-1-4020-9842-0

FEMA (2017b). Federal emergency management agency. Hazus tsunami model technical guidance. FEMA, fed. Emerg. Manag. Agency, Washingt. DC. Available at: https://www.fema.gov/media-library-data/1511284000276-4f18206fb0c7bab3c5ecbbbdf504b9fd/Hazus_40_Tsunami_Tech_Manual.pdf

FEMA (2017a). Federal emergency management agency. Hazus tsunami model user guidance. FEMA, fed. Emerg. Manag. Agency, Washingt. DC. Available at: https://www.fema.gov/media-library-data/1511284000292-4f18206fb0c7bab3c5ecbbbdf504b9fd/Hazus_40_Tsunami_User_Manual.pdf.

Flanagan, B. E., Gregory, E. W., Hallisey, E. J., Heitgerd, J. L., and Lewis, B. (2011). A social vulnerability index for disaster management. *J. Homeland Security Emerg. Manag.* 8 (1), 3. doi:10.2202/1547-7355.1792

Foster, J. H., Ericksen, T. L., and Bingham, B. (2020). Wave glider-enhanced vertical seafloor geodesy. *J. Atmos. Oceanic Technol.* 37, 417–427. doi:10.1175/JTECH-D-19-0095.1

Fraser, S. A., Wood, N. J., Johnston, D. M., Leonard, G. S., Greening, P. D., and Rossetto, T. (2014). Variable population exposure and distributed travel speeds in least-cost tsunami evacuation modelling. *Nat. Hazards Earth Syst. Sci.* 14 (11), 2975–2991. doi:10.5194/nhess-14-2975-2014

Freundt, A. (2003). Entrance of hot pyroclastic flows into the sea: experimental observations. *Bull. Volcanol.* 65 (2-3), 144–164. doi:10.1007/s00445-002-0250-1

Fritz, H. M., Hager, W. H., and Minor, H.-E. (2003). Landslide generated impulse waves. *Experiments in Fluids* 35 (6), 505–519. doi:10.1007/s00348-003-0659-0

Fukutani, Y., Moriguchi, S., Terada, K., Kotani, T., Otake, Y., and Kitano, T. (2019). Tsunami hazard and risk assessment for multiple buildings by considering the spatial correlation of wave height using copulas. *Nat. Hazards Earth Syst. Sci.* 19 (11), 2619–2634. doi:10.5194/nhess-19-2619-2019

Gailler, A., Hébert, H., Schindelé, F., and Reymond, D. (2018). Coastal amplification laws for the French tsunami warning center: numerical modeling and fast estimate of tsunami wave heights along the French riviera. *Pure Appl. Geophys.* 175 (4), 1429–1444. doi:10.1007/s00024-017-1713-9

Gallotti, G., Passaro, S., Armigliato, A., Zaniboni, F., Pagnoni, G., Wang, L., et al. (2020). Potential mass movements on the Palinuro volcanic chain (southern Tyrrhenian Sea, Italy) and consequent tsunami generation. *J. Volcanol. Geothermal Res.* 404, 107025. doi:10.1016/j.jvolgeores.2020.107025

Gallotti, G., and Tinti, S. (2020). A new approach for landslide modeling: application to the Scilla 1783 tsunamigenic landslide, South Italy. *Pure Appl. Geophys.* 177, 3563–3576. doi:10.1007/s00024-020-02546-5

Gayer, G., Leschka, S., Nöhren, I., Larsen, O., and Günther, H. (2010). Tsunami inundation modelling based on detailed roughness maps of densely populated areas. *Nat. Hazards Earth Syst. Sci.* 10 (8), 1679–1687. doi:10.5194/nhess-10-1679-2010

Geist, E. L., and Bilek, S. L. (2001). Effect of depth-dependent shear modulus on tsunami generation along subduction zones. *Geophys. Res. Lett.* 28, 1315–1318. doi:10.1029/2000GL012385

Geist, E. L., Brink, U. S., and Parsons, U. S. (2019). Offshore landslide hazard curves from mapped landslide size distributions. *J. Geophys. Res. Solid Earth* 124 (4), 3320–3334. doi:10.1029/2018jb017236

Geist, E. L., Chaytor, J. D., Parsons, T., and Brink, U. T. (2013). Estimation of submarine mass failure probability from a sequence of deposits with age dates. *Geosphere* 9 (2), 287–298. doi:10.1130/ges00829.1

Geist, E. L., and Oglesby, D. D. (2014). Earthquake mechanism and seafloor deformation for tsunami generation, in *Encyclopedia of earthquake engineering*. Editors M. Beer, I. A. Kougioumtzoglou, E. Patelli, and I. S.-K. Au (Berlin, Heidelberg: Springer), 1–17. doi:10.1007/978-3-642-36197-5_296-1

Geist, E. L., Oglesby, D. D., and Ryan, K. J. (2019). "Tsunamis: stochastic models of occurrence and generation mechanisms," in *Encyclopedia of complexity and systems science*," Editor R. A. Meyers (Berlin, Heidelberg: Springer), 1–30. doi:10.1007/978-3-642-27737-5_595-2

Geist, E. L., and Parsons, T. (2006). Probabilistic analysis of tsunami hazards*. *Nat. Hazards* 37, 277–314. doi:10.1007/s11069-005-4646-z

Geist, E. L., and Parsons, T. (2014). Undersampling power-law size distributions: effect on the assessment of extreme natural hazards. *Nat. Hazards* 72, 565–595. doi:10.1007/s11069-013-1024-0

Geist, E. L., ten Brink, U. S., and Gove, M. (2014). A framework for the probabilistic analysis of meteotsunamis. *Nat. Hazards* 74, 123–142. doi:10.1007/s11069-014-1294-1

Geist, E., and Lynett, P. (2014). Source processes for the probabilistic assessment of tsunami hazards. *Oceanog* 27 (2), 86–93. doi:10.5670/oceanog.2014.43

Genadt, A. (2019). Three lessons from Japan on architectural resilience. *Architectural Histories* 7 (1), 16. doi:10.5334/ah.393

Germanovich, L. N., Kim, S., and Puzrin, A. M. (2016). Dynamic growth of slip surfaces in catastrophic landslides. *Proc. R. Soc. A.* 472 (2185), 20150758. doi:10.1098/rspa.2015.0758

Gibbons, S. J., Lorito, S., Macías, J., Løvholt, F., Selva, J., Volpe, M., et al. (2020). Probabilistic tsunami hazard analysis: high performance computing for massive scale inundation simulations. *Front. Earth Sci.* 8, 623. doi:10.3389/feart.2020.591549

Giles, D., Gopinathan, D., Guillas, S., and Dias, F. (2020). Faster than real time tsunami warning with associated hazard uncertainties. *Front. Earth Sci.* 8, 66. doi:10.3389/feart.2020.597865

Glimsdal, S., Løvholt, F., Harbitz, C. B., Romano, F., Lorito, S., Orefice, S., et al. (2019). A new approximate method for quantifying tsunami maximum inundation height ProbabilityA new approximate method for quantifying tsunami maximum inundation height probability. Pure appl. *Pure Appl. Geophys.* 176, 3227–3246. doi:10.1007/s00024-019-02091-w

Glimsdal, S., Pedersen, G. K., Harbitz, C. B., and Løvholt, F. (2013). Dispersion of Tsunamis: does it really matter?. *Nat. Hazards Earth Syst. Sci.* 13, 1507–1526. doi:10.5194/nhess-13-1507-2013

Goda, K., and De Risi, R. (2018). Multi-hazard loss estimation for shaking and tsunami using stochastic rupture sources. *Int. J. Disaster Risk Reduct.* 28, 539–554. doi:10.1016/j.ijdrr.2018.01.002

Goda, K. (2020). Multi-hazard portfolio loss estimation for time-dependent shaking and tsunami hazards. *Front. Earth Sci.* 8, 512. doi:10.3389/feart.2020.592444

Goda, K., Petrone, C., De Risi, R., and Rossetto, T. (2017). Stochastic coupled simulation of strong motion and tsunami for the 2011 Tohoku, Japan earthquake. *Stoch. Environ. Res. Risk Assess.* 31 (9), 2337–2355. doi:10.1007/s00477-016-1352-1

Goda, K., and Song, J. (2019). Influence of elevation data resolution on tsunami loss estimation and insurance rate-making. *Front. Earth Sci.* 7, 246. doi:10.1016/b978-0-12-107180-6.50007-x

Goda, K. (2019). Time-dependent probabilistic tsunami hazard analysis using stochastic rupture sources. *Stoch. Environ. Res. Risk Assess.* 33, 341–358. doi:10.1007/s00477-018-1634-x

Goda, K., Yasuda, T., Mori, N., and Maruyama, T. (2016). New scaling relationships of earthquake source parameters for stochastic tsunami simulation. *Coastal Eng. J.* 58, 1650010–1650011. doi:10.1142/S0578563416500108

González, F. I., Geist, E. L., Jaffe, B., Kânoğlu, U., Mofjeld, H., Synolakis, C. E., et al. (2009). Probabilistic tsunami hazard assessment at Seaside, Oregon, for near- and far-field seismic sources. *J. Geophys. Res.* 114, 37. doi:10.1029/2008JC005132

González, J. I., Farreras, S. F., and Ochoa, J. (2001). Seismic and meteorological tsunami contributions in the Manzanillo and Cabo San Lucas Seiches of September 14, 1995. *Mar. Geodesy* 24 (4), 219–227. doi:10.1080/014904101753227860

Greenslade, D. J. M., Annunziato, A., Babeyko, A. Y., Burbidge, D. R., Ellguth, E., Horspool, N., et al. (2014). An assessment of the diversity in scenario-based tsunami forecasts for the Indian Ocean. *Continental Shelf Res.* 79, 36–45. doi:10.1016/j.csr.2013.06.001

Gregg, C. E., Houghton, B. F., Paton, D., Lachman, R., Lachman, J., Johnston, D. M., et al. (2006). Natural warning signs of tsunamis: human sensory experience and response to the 2004 great Sumatra earthquake and tsunami in Thailand. *Thai. Earthq. Spectra* 22 (S3), 671–691. doi:10.1193/1.2206791

Grezio, A., Babeyko, A., Baptista, M. A., Behrens, J., Costa, A., Davies, G., et al. (2017). Probabilistic tsunami hazard analysis: multiple sources and global applications. *Rev. Geophys.* 55, 1158–1198. doi:10.1002/2017RG000579

Grezio, A., Cinti, F. R., Costa, A., Faenza, L., Perfetti, P., Pierdominici, S., et al. (2020). Multisource bayesian probabilistic tsunami hazard analysis for the Gulf of Naples (Italy). *J. Geophys. Res. Oceans* 125, 12. doi:10.1029/2019JC015373

Grezio, A., Marzocchi, W., Sandri, L., and Gasparini, P. (2010). A bayesian procedure for probabilistic tsunami hazard assessment. *Nat. Hazards* 53, 159–174. doi:10.1007/s11069-009-9418-8

Griffin, J., Latief, H., Kongko, W., Harig, S., Horspool, N., Hanung, R., et al. (2015). An evaluation of onshore digital elevation models for modeling tsunami inundation zones. *Front. Earth Sci.* 3, 32. doi:10.3389/feart.2015.00032

Grilli, S. T., Taylor, O. D. S., Baxter, C. D., and Maretzki, S. (2009). A probabilistic approach for determining submarine landslide tsunami hazard along the upper east coast of the United States. *Mar. Geol.* 264 (1–2), 74–97. doi:10.1016/j.margeo.2009.02.010

Grilli, S. T., and Watts, P. (2005). Tsunami generation by submarine mass failure. I: modeling, experimental validation, and sensitivity analyses. *J. Waterway, Port, Coastal, Ocean Eng.* 131 (6), 283–297. doi:10.1061/(asce)0733-950x(2005)131:6(283)

GTM (2020). Global Tsunami Model. http://edanya.uma.es/gtm/ (Accessed November 12, 2020).

Gylfadóttir, S. S., Kim, J., Helgason, J. K., Brynjólfsson, S., Höskuldsson, Á., Jóhannesson, T., et al. (2017). The 2014 Lake Askja rockslide-induced tsunami: optimization of numerical tsunami model using observed data. *J. Geophys. Res. Oceans* 122 (5), 4110–4122. doi:10.1002/2016jc012496

Hananto, N. D., Leclerc, F., Li, L., Etchebes, M., Carton, H., Tapponnier, P., et al. (2020). Tsunami earthquakes: vertical pop-up expulsion at the forefront of subduction megathrust. *Earth Planet. Sci. Lett.* 538, 116197. doi:10.1016/j.epsl.2020.116197

Harbitz, C. B. (1992). Model simulations of tsunamis generated by the Storegga slides. *Mar. Geol.* 105 (1-4), 1–21. doi:10.1016/0025-3227(92)90178-k

Harbitz, C. B., Løvholt, F., and Bungum, H. (2014). Submarine landslide tsunamis: how extreme and how likely?. *Nat. Hazards* 72 (3), 1341–1374. doi:10.1007/s11069-013-0681-3

Harig, S., Chaeroni, Pranowo, W. S., and Behrens, J. (2008). Tsunami simulations on several scales. *Ocean Dyn.* 58, 429–440. doi:10.1007/s10236-008-0162-5

Haslett, S. K., Mellor, H. E., and Bryant, E. A. (2009). Meteo-tsunami hazard associated with summer thunderstorms in the United Kingdom. *Phys. Chem. Earth, Parts A/B/C* 34, 1016–1022. doi:10.1016/j.pce.2009.10.005

Hatayama, K. (2014). "Damage to oil storage tanks due to tsunami of the Mw9.0 2011 off the Pacific coast of Tohoku, Japan." in 10th U.S. National conference on earthquake engineering, frontiers of earthquake engineering. Anchorage, USA: Earthquake Engineering Research Institute. doi:10.4231/D3VX0639C

Hayes, G. P., Moore, G. L., Portner, D. E., Hearne, M., Flamme, H., Furtney, M., et al. (2018). Slab2, a comprehensive subduction zone geometry model. *Science* 362 (6410), 58–61. doi:10.1126/science.aat4723

Heller, V., and Hager, W. H. (2010). Impulse product parameter in landslide generated impulse waves. *J. Waterway, Port, Coastal, Ocean Eng.* 136 (3), 145–155. doi:10.1061/(asce)ww.1943-5460.0000037

Heller, V. (2011). Scale effects in physical hydraulic engineering models. *J. Hydraulic Res.* 49 (3), 293–306. doi:10.1080/00221686.2011.578914

Hermanns, R., Oppikofer, T., Anda, E., Blikra, L., Böhme, M., Bunkholt, H., et al. (2013). Hazard and risk classification for large unstable rock slopes in Norway. *It. J. Eng. Geol. Env.* 11, 28. doi:10.4408/IJEGE.2013-06.B-22

Herrero, A., and Bernard, P. (1994). A kinematic self-similar rupture process for earthquakes. *Bull. Seismol. Soc. Amer.* 84, 1216–1228.

Herslund, L. B., Jalayer, F., Jean-Baptiste, N., Jørgensen, G., Kabisch, S., Kombe, W., et al. (2016). A multi-dimensional assessment of urban vulnerability to climate change in Sub-Saharan Africa. *Nat. hazards* 82 (2), 149–172. doi:10.1007/s11069-015-1856-x

Heuret, A., Conrad, C. P., Funiciello, F., Lallemand, S., and Sandri, L. (2012). Relation between subduction megathrust earthquakes, trench sediment thickness and upper plate strain. *Geophys. Res. Lett.* 39, a. doi:10.1029/2011GL050712

Hoechner, A., Babeyko, A. Y., and Zamora, N. (2016). Probabilistic tsunami hazard assessment for the Makran region with focus on maximum magnitude assumption. *Nat. Hazards Earth Syst. Sci.* 16, 1339–1350. doi:10.5194/nhess-16-1339-2016

Horspool, N., Pranantyo, I., Griffin, J., Latief, H., Natawidjaja, D. H., Kongko, W., et al. (2014). A probabilistic tsunami hazard assessment for Indonesia. *Nat. Hazards Earth Syst. Sci.* 14, 3105–3122. doi:10.5194/nhess-14-3105-2014

Huang, X., and García, M. H. (1998). A Herschel-Bulkley model for mud flow down a slope. *J. Fluid Mech.* 374, 305–333. doi:10.1017/s0022112098002845

Hufschmidt, G., Crozier, M., and Glade, T. (2005). Evolution of natural risk: research framework and perspectives. *Nat. Hazards Earth Syst. Sci.* 5 (3), 375–387. doi:10.5194/nhess-5-375-2005

Huhn, K., Arroyo, M., Cattaneo, A., Clare, M. A., Gràcia, E., Harbitz, C. B., et al. (2019). "Modern submarine landslide complexes: a short review," in *Submarine. Landslides: Subaqueous mass transport deposits from outcrops to seismic profiles*. Editor Ogata, K. (Hoboken, NJ, USA:Wiley), 181–200.

Huthnance, J. M. (1975). On trapped waves over a continental shelf. *J. Fluid Mech.* 69 (4), 689–704. doi:10.1017/S0022112075001632

Huyck, C., Hu, Z., Amyx, P., Esquivias, M. H., Eguchi, M., Contributors, K., et al. (2019). METEOR: exposure data classification. *Metadata Popul. Confidence Assess. Rep. Number* 3, 2. doi:10.3403/30126912u

Huyck, C. K., and Eguchi, M. T. (2017). GFDRR africa disaster risk financing-result area 5 exposure development. Replace. Cost Refinements Expo. Data. Prepared for World Bank/GFDRR.

Huyck, C. K., Esquivias, G., Gamba, P., Hussain, M., Odhiambo, O., Jaiswal, K., et al. (2011). D2.2 survey of available input databases for GED, report produced in the context of the global exposure databases for the global earthquake model (IDCT). *Constraints Databases* 4, 139–161. doi:10.1007/978-1-4615-5515-5_7

ITIC (2020). International tsunami information center. Available at: http://itic.ioc-unesco.org/ (Accessed November 11, 2020).

Jaimes, M. A., Reinoso, E., Ordaz, M., Huerta, B., Silva, R., Mendoza, E., et al. (2016). A new approach to probabilistic earthquake-induced tsunami risk assessment. *Ocean Coastal Manage.* 119, 68–75. doi:10.1016/j.ocecoaman.2015.10.007

Jalayer, F., Carozza, S., De Risi, R., Manfredi, G., and Mbuya, E. (2016). Performance-based flood safety-checking for non-engineered masonry structures. *Eng. Struct.* 106, 109–123. doi:10.1016/j.engstruct.2015.10.007

Jalayer, F., and Ebrahimian, H. (2020). Seismic reliability assessment and the nonergodicity in the modelling parameter uncertainties. *Earthq. Eng. Struct. Dyn.* 49 (5), 434–457. doi:10.1002/eqe.3247

Jasanoff, S. (1993). Bridging the two cultures of risk Analysis1,2. *Risk Anal.* 13 (2), 123–129. doi:10.1111/j.1539-6924.1993.tb01057.x

Jelínek, R., and Krausmann, E. (2008). Approaches to tsunami risk assessment. *JRC Sci. Tech. Rep.* 48713, 112. doi:10.4324/9781351140843-3

Johnston, D., Tarrant, R., Tipler, K., Lambie, E., Crawford, M., Becker, J., et al. (2016). Towards tsunami-safer schools in the Wellington Region, New Zealand:

evaluating drills and awareness programmes. *Aust. J. Emerg. Manage.* 31, 59–66. doi:10.7717/peerj-cs.386/table-1

Jop, P., Forterre, Y., and Pouliquen, O. (2006). A constitutive law for dense granular flows. *Nature* 441 (7094), 727–730. doi:10.1038/nature04801

JRC Risk Data Hub (2020). Available at: https://ec.europa.eu/jrc/en (Accessed November 11, 2020).

Kagan, Y. Y., and Jackson, D. D. (1991). Long-term earthquake clustering. *Geophys. J. Int.* 104, 117–134. doi:10.1111/j.1365-246X.1991.tb02498.x

Kagan, Y. Y., and Jackson, D. D. (2014). Statistical earthquake focal mechanism forecasts. *Geophys. J. Int.* 197, 620–629. doi:10.1093/gji/ggu015

Kagan, Y. Y. (2002). Seismic moment distribution revisited: I. Statistical results. *Geophys. J. Int.* 148, 520–541. doi:10.1046/j.1365–246x.2002.01594.x

Kaiser, G., Scheele, L., Kortenhaus, A., Løvholt, F., Römer, H., and Leschka, S. (2011). The influence of land cover roughness on the results of high resolution tsunami inundation modeling. *Nat. Hazards Earth Syst. Sci.* 11 (9), 2521–2540. doi:10.5194/nhess-11-2521-2011

Kajiura, K. (1963). The leading wave of a tsunami. *B. Earthq. Res. Inst.* 41, 535–571.

Karafagka, S., Fotopoulou, S., and Pitilakis, K. (2018). Analytical tsunami fragility curves for seaport RC buildings and steel light frame warehouses. *Soil Dyn. Earthq. Eng.* 112, 118–137. doi:10.1016/j.soildyn.2018.04.037

Kelfoun, K., and Druitt, T. H. (2005). Numerical modeling of the emplacement of socompa rock avalanche, Chile. *J. Geophys Res: solid Earth.* 110 (B12), 113. doi:10.3133/ofr01383

Kienle, J., Kowalik, Z., and Murty, T. S. (1987). Tsunamis generated by eruptions from mount st. Augustine volcano, Alaska. *Science* 236, 1442–1447. doi:10.1126/science.236.4807.1442

Kim, D. H., Lynett, P. J., and Socolofsky, S. A. (2009). A depth-integrated model for weakly dispersive, turbulent, and rotational fluid flows. *Ocean Model.* 27 (3–4), 198–214. doi:10.1016/j.ocemod.2009.01.005

Kim, J., Løvholt, F., Issler, D., and Forsberg, C. F. (2019). Landslide material control on tsunami genesis-the storegga slide and tsunami (8,100 Years BP). *J. Geophys. Res. Oceans* 124 (6), 3607–3627. doi:10.1029/2018jc014893

King, G. C. P., Stein, R. S., and Lin, J. (1994). Static stress changes and the triggering of earthquakes. *Bull. Seismol. Soc. Am.* 84, 935–953.

Kiureghian, A. D., and Ditlevsen, O. (2009). Aleatory or epistemic? Does it matter? *Struct. Saf.* 31 (2), 105–112. doi:10.1016/j.strusafe.2008.06.020

Kiureghian, A. D. (2005). Non-ergodicity and PEER's framework formula. *Earthq. Eng. Struct. Dyn.* 34 (13), 1643–1652. doi:10.1002/eqe.504

Kopp, H. (2013). Invited review paper: the control of subduction zone structural complexity and geometry on margin segmentation and seismicity. *Tectonophysics* 589, 1–16.

Koshimura, S., Oie, T., Yanagisawa, H., and Imamura, F. (2009). Developing fragility functions for tsunami damage estimation using numerical model and post-tsunami data from Banda Aceh, Indonesia. *Coastal Eng. J.* 51 (3), 243–273. doi:10.1142/s0578563409002004

Kozdon, J. E., and Dunham, E. M. (2013). Rupture to the trench: dynamic rupture simulations of the 11 march 2011 Tohoku earthquake. *Bull. Seismol. Soc. Amer.* 103, 1275–1289. doi:10.1785/0120120136

Kriebel, D. L., Lynett, P. J., Cox, D. T., Petroff, C. M., Robertson, I. N., and Chock, G. Y. (2017). Energy method for approximating overland tsunami flows. *J. Waterway Port Coastal Ocean Eng.* 143 (5),04017014. doi:10.1061/(ASCE)WW.1943-5460.0000393

Lam, N. S., Reams, M., Li, K., Li, C., and Mata, L. P. (2016). Measuring community resilience to coastal hazards along the northern Gulf of Mexico. *Nat. Hazards Rev.* 17 (1), 113. doi:10.1061/(ASCE)NH.1527-6996.0000193

Lane, E. M., Mountjoy, J. J., Power, W. L., and Mueller, C. (2016). "Probabilistic hazard of tsunamis generated by submarine landslides in the cook strait canyon (New Zealand), in *Global tsunami science Past and Future*. Editor Geist, H. (Basel, Switzerland: birkhäuser), Vol. I, 3757–3774.

Latter, J. H. (1981). Tsunamis of volcanic origin: summary of causes, with particular reference to Krakatoa, 1883. *Bull. Volcanol* 44, 467–490. doi:10.1007/bf02600578

Lee, H. J. (2009). Timing of occurrence of large submarine landslides on the Atlantic Ocean margin. *Mar. Geol.* 264 (1-2), 53–64. doi:10.1016/j.margeo.2008.09.009

LeMéhauté, B. L., and Wang, S. (1996). *Water waves generated by underwater explosion. Advanced series on ocean engineering*. New Jersey: World Scientific.

Li, S., Moreno, M., Rosenau, M., Melnick, D., and Oncken, O. (2014). Splay fault triggering by great subduction earthquakes inferred from finite element models. *Geophys. Res. Lett.* 41, 385–391. doi:10.1002/2013GL058598

Lin, I.-C., and Tung, C. C. (1982). A preliminary investigation of tsunami hazard. *Bull. Seismol. Soc. Amer.* 72, 2323–2337.

Logan, D. C. (2009). Known knowns, known unknowns, unknown unknowns and the propagation of scientific enquiry. *J. Exp. Bot.* 60 (3), 712–714. doi:10.1093/jxb/erp043

Lorito, S., Romano, F., and Lay, T. (2016). "Tsunamigenic major and great earthquakes (2004–2013): source processes inverted from seismic, geodetic, and sea-level data," in *Encyclopedia of complexity and systems science*. Editor R. A. Meyers (Berlin, Heidelberg: Springer), 1–52. doi:10.1007/978-3-642-27737-5_641-1

Lorito, S., Selva, J., Basili, R., Romano, F., Tiberti, M. M., and Piatanesi, A. (2015). Probabilistic hazard for seismically induced tsunamis: accuracy and feasibility of inundation maps. *Geophys. J. Int.* 200 (1), 574–588. doi:10.1093/gji/ggu408

Lotto, G. C., Dunham, E. M., Jeppson, T. N., and Tobin, H. J. (2017). The effect of compliant prisms on subduction zone earthquakes and tsunamis. *Earth Planet. Sci. Lett.* 458, 213–222. doi:10.1016/j.epsl.2016.10.050

Lotto, G. C., Jeppson, T. N., and Dunham, E. M. (2019). Fully coupled simulations of megathrust earthquakes and tsunamis in the Japan trench, nankai trough, and cascadia subduction zone. *Pure Appl. Geophys.* 176, 4009–4041. doi:10.1007/s00024-018-1990-y

Loveless, J. P., and Meade, B. J. (2011). Spatial correlation of interseismic coupling and coseismic rupture extent of the 2011 MW= 9.0 Tohoku-oki earthquake. *Geophys. Res. Lett.* 38 (17), 39. doi:10.1029/2011GL048561

Løvholt, F., Bondevik, S., Laberg, J. S., Kim, J., and Boylan, N. (2017). Some giant submarine landslides do not produce large tsunamis. *Geophys. Res. Lett.* 44 (16), 8463–8472. doi:10.1002/2017GL074062

Løvholt, F., Fraser, S., Salgado-Galvez, M., Lorito, S., Selva, J., Romano, F., et al. (2019). Global trends in advancing tsunami science for improved hazard and risk understanding. Contributing Paper to GAR19, June. doi:10.1109/urgenthpc49580.2019.00011

Løvholt, F., Glimsdal, S., and Harbitz, C. B. (2020). On the landslide tsunami uncertainty and hazard. *Landslides* 17, 2301–2315. doi:10.1007/s10346-020-01429-z

Løvholt, F., Glimsdal, S., Harbitz, C. B., Zamora, N., Nadim, F., Peduzzi, P., et al. (2012). Tsunami hazard and exposure on the global scale. *Earth-Sci. Rev.* 110 (1–4), 58–73. doi:10.1007/978-3-642-27737-5_642-1

Løvholt, F., Griffin, J., and Salgado-Gálvez, M. (2015a). Tsunami hazard and risk assessment on the global scale, in *Encyclopedia of complexity and systems science*. Editor R. A. Meyers (Berlin, Heidelberg: Springer), 1–34. doi:10.1007/978-3-642-27737-5642-1

Løvholt, F., Harbitz, C. B., and Haugen, K. B. (2005). A parametric study of tsunamis generated by submarine slides in the Ormen Lange/Storegga area off western Norway. *Mar. Pet. Geol.* 22 (1–2), 219–231. doi:10.1016/b978-0-08-044694-3.50023-8

Løvholt, F., Pedersen, G., and Gisler, G. (2008). Oceanic propagation of a potential tsunami from the La palma island. *J Geophs Res: Oceans.* 113 (C9), 38. doi:10.1029/2007JC004603

Løvholt, F., Pedersen, G., Harbitz, C. B., Glimsdal, S., and Kim, J. (2015b). On the characteristics of landslide tsunamis. *Phil. Trans. R. Soc. A.* 373 (2053), 20140376. doi:10.1098/rsta.2014.0376

Løvholt, F., Setiadi, N. J., Birkmann, J., Harbitz, C. B., Bach, C., Fernando, N., et al. (2014). Tsunami risk reduction–are we better prepared today than in 2004? *Int. J. Disaster Risk reduction* 10, 127–142.

Lynett, P. J., Gately, K., Wilson, R., Montoya, L., Arcas, D., Aytore, B., et al. (2017). Inter-model analysis of tsunami-induced coastal currents. *Ocean Model.* 114, 14–32. doi:10.1016/j.ocemod.2017.04.003

Ma, S. (2012). A self-consistent mechanism for slow dynamic deformation and tsunami generation for earthquakes in the shallow subduction zone. *Geophys. Res. Lett.* 39 (11), 12. doi:10.1029/2012GL051854

Macabuag, J., Rossetto, T., Ioannou, I., Suppasri, A., Sugawara, D., Adriano, B., et al. (2016). A proposed methodology for deriving tsunami fragility functions for buildings using optimum intensity measures. *Nat. Hazards* 84 (2), 1257–1285. doi:10.1007/s11069-016-2485-8

Macías, J., Castro, M. J., and Escalante, C. (2020). Performance assessment of the Tsunami-HySEA model for NTHMP tsunami currents benchmarking.

Laboratory data. *Coastal Eng.* 158, 103667. doi:10.1016/j.coastaleng.2020.103667

Macías, J., Castro, M. J., Ortega, S., Escalante, C., and González-Vida, J. M. (2017). Performance benchmarking of tsunami-HySEA model for NTHMP's inundation mapping activities. *Pure Appl. Geophys.* 174, 3147–3183. doi:10.1007/s00024-017-1583-1

Maeno, F., and Imamura, F. (2011). Tsunami generation by a rapid entrance of pyroclastic flow into the sea during the 1883 Krakatau eruption, Indonesia. *J Geophys Res.* 116 (B09), 205. doi:10.1029/2011JB008253

Mai, P. M., and Beroza, G. C. (2002). A spatial random field model to characterize complexity in earthquake slip. *J. Geophys. Res.* 107, 10–11. doi:10.1029/2001JB000588

Mansinha, L., and Smylie, D. E. (1971). The displacement of the earthquake fault model. *Bull. Seismol. Soc. Amer.* 61, 1433–1440.

Marras, S., and Mandli, K. T. (2021). Modeling and simulation of tsunami impact: a short review of recent advances and future challenges. *Geosciences* 11 (1), 5. doi:10.3390/geosciences11010005

Marzocchi, W., and Jordan, T. H. (2014). Testing for ontological errors in probabilistic forecasting models of natural systems. *Proc. Natl. Acad. Sci.* 111 (33), 11973–11978. doi:10.1073/pnas.1410183111

Mas, E., Koshimura, S., Suppasri, A., Matsuoka, M., Matsuyama, M., Yoshii, T., et al. (2012). Developing Tsunami fragility curves using remote sensing and survey data of the 2010 Chilean Tsunami in Dichato. *Nat. Hazards Earth Syst. Sci.* 12, 2689–2697. doi:10.5194/nhess-12-2689-2012

Masterlark, T. (2003). Finite element model predictions of static deformation from dislocation sources in a subduction zone: sensitivities to homogeneous, isotropic, Poisson-solid, and half-space assumptions. *J. Geophys. Res.* 108, 12. doi:10.1029/2002JB002296

McGuire, R. K. (2008). Probabilistic seismic hazard analysis: early history. *Earthq. Eng. Struct. Dyn.* 37, 329–338. doi:10.1002/eqe.765

McLaughlin, S., and Cooper, J. A. G. (2010). A multi-scale coastal vulnerability index: a tool for coastal managers?. *Environ. Hazards* 9 (3), 233–248. doi:10.3763/ehaz.2010.0052

Meade, B. J. (2007). Algorithms for the calculation of exact displacements, strains, and stresses for triangular dislocation elements in a uniform elastic half space. *Comput. Geosci.* 33, 1064–1075. doi:10.1016/j.cageo.2006.12.003

Mebarki, A., Jerez, S., Prodhomme, G., and Reimeringer, M. (2016). Natural hazards, vulnerability and structural resilience: tsunamis and industrial tanks. *Geomat. Nat. Hazards Risk* 7 (Suppl. 1), 5–17. doi:10.1080/19475705.2016.1181458

Meletti, C., Marzocchi, W., D'Amico, V., Lanzano, G., Luzi, L., and Martinelli, F., et al.; MPS19 Working Group (2021). The new Italian seismic hazard model (MPS19). *Ann. Geophys.* 64 (1), SE112. doi:10.4401/ag-8579

Melgar, D., LeVeque, R. J., Dreger, D. S., and Allen, R. M. (2016). Kinematic rupture scenarios and synthetic displacement data: an example application to the Cascadia subduction zone. *J. Geophys. Res. Solid Earth* 121, 6658–6674. doi:10.1002/2016JB013314

Melnick, D., Moreno, M., Quinteros, J., Baez, J. C., Deng, Z., Li, S., et al. (2017). The super-interseismic phase of the megathrust earthquake cycle in Chile. *Geophys. Res. Lett.* 44, 784–791. doi:10.1002/2016GL071845

Métois, M., Socquet, A., and Vigny, C. (2012). Interseismic coupling, segmentation and mechanical behavior of the central Chile subduction zone. *J. Geophys. Res.* 117, 18. doi:10.1029/2011JB008736

Miyashita, T., Mori, N., and Goda, K. (2020). Uncertainty of probabilistic tsunami hazard assessment of Zihuatanejo (Mexico) due to the representation of tsunami variability. *Coastal Eng. J.* 62, 413–428. doi:10.1080/21664250.2020.1780676

Molinari, I., Tonini, R., Lorito, S., Piatanesi, A., Romano, F., Melini, D., et al. (2016). Fast evaluation of tsunami scenarios: uncertainty assessment for a Mediterranean Sea database. *Nat. Hazards Earth Syst. Sci.* 16 (12), 2593–2602. doi:10.5194/nhess-16-2593-2016

Monserrat, S., Vilibić, I., and Rabinovich, A. B. (2006). Meteotsunamis: atmospherically induced destructive ocean waves in the tsunami frequency band. *Nat. Hazards Earth Syst. Sci.* 6, 1035–1051. doi:10.5194/nhess-6-1035-2006

Moreno, M., Haberland, C., Oncken, O., Rietbrock, A., Angiboust, S., and Heidbach, O. (2014). Locking of the Chile subduction zone controlled by fluid pressure before the 2010 earthquake. *Nat. Geosci.* 7, 292–296. doi:10.1038/ngeo2102

Morgan, M. G. (2014). Use (and abuse) of expert elicitation in support of decision making for public policy. *Proc. Natl. Acad. Sci.* 111 (20), 7176–7184. doi:10.1073/pnas.1319946111

Muldashev, I. A., and Sobolev, S. V. (2020). What controls maximum magnitudes of giant subduction earthquakes?. *Geochem. Geophys. Geosyst.* 21, e2020GC009145. doi:10.1029/2020GC009145

Murotani, S., Miyake, H., and Koketsu, K. (2008). Scaling of characterized slip models for plate-boundary earthquakes. *Earth Planet. Sp* 60, 987–991. doi:10.1186/BF03352855

Murotani, S., Satake, K., and Fujii, Y. (2013). Scaling relations of seismic moment, rupture area, average slip, and asperity size for M ~9 subduction-zone earthquakes. *Geophys. Res. Lett.* 40, 5070–5074. doi:10.1002/grl.50976

Murphy, S., Di Toro, G., Romano, F., Scala, A., Lorito, S., Spagnuolo, E., et al. (2018). Tsunamigenic earthquake simulations using experimentally derived friction laws. *Earth Planet. Sci. Lett.* 486, 155–165. doi:10.1016/j.epsl.2018.01.011

Murphy, S., Scala, A., Herrero, A., Lorito, S., Festa, G., Trasatti, E., et al. (2016). Shallow slip amplification and enhanced tsunami hazard unravelled by dynamic simulations of mega-thrust earthquakes. *Sci. Rep.* 6, 35007. doi:10.1038/srep35007

Musa, A., Watanabe, O., Matsuoka, H., Hokari, H., Inoue, T., Murashima, Y., et al. (2018). Real-time tsunami inundation forecast system for tsunami disaster prevention and mitigation. *J. Supercomput.* 74, 3093–3113. doi:10.1007/s11227-018-2363-0

Nadim, F., and Glade, T. (2006). "On tsunami risk assessment for the west coast of Thailand," in *Geohazards*. Available at: https://dc.engconfintl.org/geohazards/28/

Nes, N. (2018). Past slope collapse and current unstable slopes along a cliff at Hyllestad Kommune. MSc thesis, Norway: Techical University Science.

Nikkhoo, M., and Walter, T. R. (2015). Triangular dislocation: an analytical, artefact-free solution. *Geophys. J. Int.* 201, 1119–1141. doi:10.1093/gji/ggv035

Nistor, I., Goseberg, N., and Stolle, J. (2017b). Tsunami-driven debris motion and loads: a critical review. Front. *Built Environ.* 3, 2. doi:10.3389/fbuil.2017.00002

Nistor, I., Goseberg, N., Stolle, J., Mikami, T., Shibayama, T., Nakamura, R., et al. (2017a). Experimental investigations of debris dynamics over a horizontal plane. *J. Waterway Port Coastal Ocean Eng.* 143, 04016022. doi:10.2139/ssrn.2277688

Nomanbhoy, N., and Satake, K. (1995). Generation mechanism of tsunamis from the 1883 Krakatau eruption. *Geophys. Res. Lett.* 22, 509–512. doi:10.1029/94gl03219

Nosov, M. A., and Kolesov, S. V. (2007). Elastic oscillations of water column in the 2003 Tokachi-oki tsunami source: *in-situ* measurements and 3-D numerical modelling. *Nat. Hazards Earth Syst. Sci.* 7, 243–249. doi:10.5194/nhess-7-243-2007

NTHMP. (2018). National tsunami hazard mitigation program Landslide tsunami modelling benchmark workshop—Benchmark problems. http://www1.udel.edu/kirby/landslide/problems.html

O'Brien, K., Eriksen, S., Nygaard, L. P., and Schjolden, A. (2007). Why different interpretations of vulnerability matter in climate change discourses. *Clim. Pol.* 7 (1), 73–88. doi:10.1080/14693062.2007.9685639

Oishi, Y., Imamura, F., and Sugawara, D. (2015). Near-field tsunami inundation forecast using the parallel TUNAMI-N2 model: application to the 2011 Tohoku-Oki earthquake combined with source inversions. *Geophys. Res. Lett.* 42, 1083–1091. doi:10.1002/2014GL062577

Okada, Y. (1992). Internal deformation due to shear and tensile faults in a half-space. *Bull. Seismol. Soc. Am.* 82, 1018–1040.

Okal, E. A. (2015). The quest for wisdom: lessons from 17 tsunamis, 2004-2014. *Phil. Trans. R. Soc. A.* 373 (2053), 20140370. doi:10.1098/rsta.2014.0370

Okumura, N., Jonkman, S. N., Esteban, M., Hofland, B., and Shibayama, T. (2017). A method for tsunami risk assessment: a case study for Kamakura, Japan. *Nat. Hazards* 88 (3), 1451–1472. doi:10.1007/s11069-017-2928-x

OpenStreetMap. (2020). Available at: https://www.openstreetmap.org/ (Accessed November 1, 2020).

Ordaz, M. (2000). Metodología para la evaluación del riesgo sísmico enfocada a la gerencia de seguros por terremoto. Universidad Nacional Autónoma de México. México DF.

Ordaz, M. (2015). A simple probabilistic model to combine losses arising from the simultaneous occurrence of several hazards. *Nat. Hazards* 76, 389–396. doi:10.1007/s11069-014-1495-7

Ordaz, M., Salgado-Gálvez, M. A., Huerta, B., Rodríguez, J. C., and Avelar, C. (2019). Considering the impacts of simultaneous perils. *Dpm* 28 (6), 823–837. doi:10.1108/DPM-09-2019-0295

Ota, Y., and Yamaguchi, M. (2004). Holocene coastal uplift in the western Pacific Rim in the context of late Quaternary uplift. *Quat. Int.* 120 (1), 105–117. doi:10.1016/j.quaint.2004.01.010

Páez-Ramírez, J., Lizarazo-Marriaga, J., Medina, S., Estrada, M., Mas, E., and Koshimura, S. (2020). A comparative study of empirical and analytical fragility functions for the assessment of tsunami building damage in Tumaco, Colombia. *Coastal Eng. J.* 62 (3), 362–372. doi:10.1080/21664250.2020.1726558

Pagnoni, G., Armigliato, A., and Tinti, S. (2019). *Estimation of human damage and economic loss of buildings related to tsunami inundation in the city of Augusta, Italy. Special publications, 501*. London: Geological Society.

Pampell-Manis, A., Horrillo, J., Shigihara, Y., and Parambath, L. (2016). Probabilistic assessment of landslide tsunami hazard for the northern Gulf of Mexico. *J. Geophys. Res. Oceans* 121 (1), 1009–1027. doi:10.1007/978-3-642-13296-4_8

Paris, R., Falvard, S., Chagué, C., Goff, J., Etienne, S., and Doumalin, P. (2020). Sedimentary fabric characterized by X-ray tomography: a case-study from tsunami deposits on the Marquesas Islands, French Polynesia. *Sedimentology* 67, 1207–1229. doi:10.1111/sed.12582

Paris, R. (2015). Source mechanisms of volcanic tsunamis. *Phil. Trans. R. Soc. A.* 373, 20140380. doi:10.1098/rsta.2014.0380

Paris, R., Switzer, A. D., Belousova, M., Belousov, A., Ontowirjo, B., Whelley, P. L., et al. (2014). Volcanic tsunami: a review of source mechanisms, past events and hazards in Southeast Asia (Indonesia, Philippines, Papua New Guinea). *Nat. Hazards* 70, 447–470. doi:10.1007/s11069-013-0822-8

Paris, R., Ulvrova, M., Selva, J., Brizuela, B., Costa, A., Grezio, A., et al. (2019). Probabilistic hazard analysis for tsunamis generated by subaqueous volcanic explosions in the Campi Flegrei caldera, Italy. *J. Volcanol. Geothermal Res.* 379, 106–116. doi:10.1016/j.jvolgeores.2019.05.010

Park, H., Alam, M. S., Cox, D. T., Barbosa, A. R., and van de Lindt, J. W. (2019). Probabilistic seismic and tsunami damage analysis (PSTDA) of the Cascadia Subduction Zone applied to Seaside, Oregon. *Int. J. Disaster Risk Reduct.* 35, 101076. doi:10.1016/j.ijdrr.2019.101076

Park, H., Cox, D. T., Lynett, P. J., Wiebe, D. M., and Shin, S. (2013). Tsunami inundation modeling in constructed environments: a physical and numerical comparison of free-surface elevation, velocity, and momentum flux. *Coastal Eng.* 79, 9–21. doi:10.1016/j.coastaleng.2013.04.002

Park, S., van de Lindt, J. W., Cox, D., Gupta, R., and Aguiniga, F. (2012). Successive earthquake-tsunami analysis to develop collapse fragilities. *J. Earthq. Eng.* 16 (6), 851–863. doi:10.1080/13632469.2012.685209

Pasquet, S., Vilibić, I., and Šepić, J. (2013). A survey of strong high-frequency sea level oscillations along the US East Coast between 2006 and 2011. *Nat. Hazards Earth Syst. Sci.* 13, 473–482. doi:10.5194/nhess-13-473-2013

Pattiaratchi, C. B., and Wijeratne, E. M. S. (2015). Are meteotsunamis an underrated hazard? *Phil. Trans. R. Soc. A.* 373, 20140377. doi:10.1098/rsta.2014.0377

Pedersen, G. (2008). *Advanced numerical models for simulating tsunami waves and runup. Modeling runup with depth integrated equation models*. Singapore: World Scientific, 3–41.

Pedersen, G. K., Lindstrøm, E., Bertelsen, A. F., Jensen, A., Laskovski, D., and Sælevik, G. (2013). Runup and boundary layers on sloping beaches. *Phys. Fluids.* 25 (1), 012102. doi:10.1063/1.4773327

Pellikka, H., Laurila, T. K., Boman, H., Karjalainen, A., Björkqvist, J.-V., and Kahma, K. K. (2020). Meteotsunami occurrence in the Gulf of Finland over the past century. *Nat. Hazards Earth Syst. Sci.* 20, 2535–2546. doi:10.5194/nhess-20-2535-2020

Petrone, C., Rossetto, T., Baiguera, M., la Barra Bustamante, C. D., and Ioannou, I. (2020). Fragility functions for a reinforced concrete structure subjected to earthquake and tsunami in sequence. *Eng. Struct.* 205, 110120. doi:10.1016/j.engstruct.2019.110120

Petrone, C., Rossetto, T., and Goda, K. (2017). Fragility assessment of a RC structure under tsunami actions via nonlinear static and dynamic analyses. *Eng. Struct.* 136, 36–53. doi:10.1016/j.engstruct.2017.01.013

Philibosian, B., and Meltzner, A. J. (2020). Segmentation and supercycles: a catalog of earthquake rupture patterns from the Sumatran Sunda Megathrust and other well-studied faults worldwide. *Quat. Sci. Rev.* 241, 106390. doi:10.1016/j.quascirev.2020.106390

Pitilakis, K., Argyroudis, S., Fotopoulou, S., Karafagka, S., Kakderi, K., and Selva, J. (2019). Application of stress test concepts for port infrastructures against natural hazards. The case of Thessaloniki port in Greece. *Reliab. Eng. Syst. Saf.* 184, 240–257. doi:10.1016/j.ress.2018.07.005

Pittore, M., Wieland, M., and Fleming, K. (2017). Perspectives on global dynamic exposure modelling for geo-risk assessment. *Nat. Hazards* 86 (1), 7–30. doi:10.1007/s11069-016-2437-3

Polese, M., Di Ludovico, M., Gaetani d'Aragona, M., Prota, A., and Manfredi, G. (2020). Regional vulnerability and risk assessment accounting for local building typologies. *Int. J. Disaster Risk Reduct.* 43, 101400. doi:10.1016/j.ijdrr.2019.101400

Polet, J., and Kanamori, H. (2016). "Tsunami earthquakes," in *Encyclopedia of complexity and systems science*. Editor R. A. Meyers (Berlin, Heidelberg: Springer), 1–22. doi:10.1007/978-3-642-27737-5567-2

Power, W., Downes, G., and Stirling, M. (2007). Estimation of tsunami hazard in New Zealand due to south American earthquakes. *Pure Appl. Geophys.* 164, 547–564. doi:10.1007/s00024-006-0166-3

Priest, G. R., Witter, R. C., Zhang, Y. J., Goldfinger, C., Wang, K., and Allan, J. C. (2017). New constraints on coseismic slip during southern Cascadia subduction zone earthquakes over the past 4600 years implied by tsunami deposits and marine turbidites. *Nat. Hazards* 88, 285–313. doi:10.1007/s11069-017-2864-9

Proudman, J. (1929). The effects on the sea of changes in atmospheric pressure. *International* 2, 197–209. doi:10.1111/j.1365-246x.1929.tb05408.x

Puzrin, A. M., Germanovich, L. N., and Friedli, B. (2016). Shear band propagation analysis of submarine slope stability. *Géotechnique* 66 (3), 188–201. doi:10.1680/jgeot.15.lm.002

Ramírez-Herrera, M. T., Kostoglodov, V., and Urrutia-Fucugauchi, J. (2011). Overview of recent coastal tectonic deformation in the Mexican subduction zone. *Pure Appl. Geophys.* 168, 1415–1433. doi:10.1007/s00024-010-0205-y

Reese, S., Cousins, W. J., Power, W. L., Palmer, N. G., Tejakusuma, I. G., and Nugrahadi, S. (2007). Tsunami vulnerability of buildings and people in South Java—field observations after the July 2006 Java tsunami. *Nat. Hazards Earth Syst. Sci.* 7, 573–589. doi:10.5194/nhess-7-573-2007

Rijsingen, E.V, Funiciello, F., Corbi, F., and Lallemand, S. (2019). Rough subducting seafloor reduces interseismic coupling and mega-earthquake occurrence: insights from analogue models. *Geophys. Res. Lett.* 46 (6), 3124–3132. doi:10.1029/2018GL081272

Rikitake, T., and Aida, I. (1988). Tsunami hazard probability in Japan. *Bull. Seismol. Soc. Amer.* 78, 1268–1278.

Rivera, F., Rossetto, T., and Twigg, J.(2020). An interdisciplinary study of the seismic exposure dynamics of Santiago de Chile. *Int. J. Disaster Risk Reduct.* 48, 101581. doi:10.1016/j.ijdrr.2020.101581

Rondon, L., Pouliquen, O., and Aussillous, P. (2011). Granular collapse in a fluid: role of the initial volume fraction. *Phys. Fluids* 23 (7), 073301. doi:10.1063/1.3594200

Rong, Y., Jackson, D. D., Magistrale, H., and Goldfinger, C. (2014). Magnitude limits of subduction zone earthquakes. *Bull. Seismol. Soc. Amer.* 104, 2359–2377. doi:10.1785/0120130287

Rosi, M., Di Traglia, F., Pistolesi, M., Esposti Ongaro, T., de' Michieli Vitturi, M., and Bonadonna, C. (2018). Dynamics of shallow hydrothermal eruptions: new insights from Vulcano's Breccia di Commenda eruption. *Bull. Volcanol.* 80, 83. doi:10.1007/s00445-018-1252-y

Rossetto, T., De la Barra, C., Petrone, C., De la Llera, J. C., Vásquez, J., and Baiguera, M. (2019). Comparative assessment of nonlinear static and dynamic methods for analysing building response under sequential earthquake and tsunami. *Earthq. Eng. Struct. Dyn.* 48, 867–887. doi:10.1002/eqe.3167

Rossetto, T., Petrone, C., Eames, I., De La Barra, C., Foster, A., and Macabuag, J. (2018). *Advances in the assessment of buildings subjected to earthquakes and tsunami. In European Conference on Earthquake Engineering Thessaloniki Greece* (Cham, Switzerland: Springer), 545–562.

Ryan, K. J., Geist, E. L., Barall, M., and Oglesby, D. D. (2015). Dynamic models of an earthquake and tsunami offshore Ventura, California. *Geophys. Res. Lett.* 42, 6599–6606. doi:10.1002/2015GL064507

Šepić, J., Vilibić, I., and Strelec Mahović, N. (2012). Northern Adriatic meteorological tsunamis: observations, link to the atmosphere, and predictability. *J. Geophys. Res.* 117, C02002. doi:10.1029/2011JC007608

Saja, A. M. A., Goonetilleke, A., Teo, M., and Ziyath, A. M. (2019). A critical review of social resilience assessment frameworks in disaster management. *Int. J. Disaster Risk Reduct.* 35, 101096. doi:10.1016/j.ijdrr.2019.101096

Salamon, A., and Di Manna, P. (2019). Empirical constraints on magnitude-distance relationships for seismically-induced submarine tsunamigenic landslides. *Earth-Sci. Rev.* 191, 66–92. doi:10.1016/j.earscirev.2019.02.001

Salgado-Gálvez, M. A., Zuloaga, D., Henao, S., Bernal, G. A., and Cardona, O. D. (2018). Probabilistic assessment of annual repair rates in pipelines and of direct economic losses in water and sewage networks. Application to Manizales, Colombia. *Nat. Hazards* 93 (1), S5–S24. doi:10.1007/s11069-017-2987-z

Salgado-Gálvez, M. A., Zuloaga Romero, D., Velásquez, C. A., Carreño, M. L., Cardona, O.-D., and Barbat, A. H. (2016). Urban seismic risk index for Medellín, Colombia, based on probabilistic loss and casualties estimations. *Nat. Hazards* 80 (3), 1995–2021. doi:10.1007/s11069-015-2056-4

Salgado-Gálvez, M. A., Zuloaga-Romero, D., Bernal, G. A., Mora, M. G., and Cardona, O.-D. (2014). Fully probabilistic seismic risk assessment considering local site effects for the portfolio of buildings in Medellín, Colombia. *Bull. Earthq. Eng.* 12 (2), 671–695. doi:10.1007/s10518-013-9550-4

Sallarès, V., and Ranero, C. R. (2019). Upper-plate rigidity determines depth-varying rupture behaviour of megathrust earthquakes. *Nature* 576, 96–101. doi:10.1038/s41586-019-1784-0

Salmanidou, D. M., Guillas, S., Georgiopoulou, A., and Dias, F. (2017). Statistical emulation of landslide-induced tsunamis at the rockall bank, NE atlantic. *Proc. R. Soc. A.* 473 (2200), 20170026. doi:10.1098/rspa.2017.0026

Sandri, L., Tierz, P., Costa, A., and Marzocchi, W. (2018). Probabilistic hazard from pyroclastic density currents in the Neapolitan area (Southern Italy). *J. Geophys. Res. Solid Earth* 123, 3474–3500. doi:10.1002/2017JB014890

Santos, A., and Koshimura, S. (2015). The historical review of the 1755 lisbon tsunami. *J. Geodesy Geomat. Eng.* 1, 38–52. doi:10.17265/2332-8223/2015.04.004

Sarri, A., Guillas, S., and Dias, F. (2012). Statistical emulation of a tsunami model for sensitivity analysis and uncertainty quantification. *Nat. Hazards Earth Syst. Sci.* 12 (6), 2003. doi:10.5194/nhess-12-2003-2012

Savage, S. B., Babaei, M. H., and Dabros, T. (2014). Modeling gravitational collapse of rectangular granular piles in air and water. *Mech. Res. Commun.* 56, 1–10. doi:10.1016/j.mechrescom.2013.11.001

Scala, A., Festa, G., Vilotte, J. P., Lorito, S., and Romano, F. (2019). Wave interaction of reverse-fault rupture with free surface: numerical analysis of the dynamic effects and fault opening induced by symmetry breaking. *J. Geophys. Res. Solid Earth* 124, 1743–1758. doi:10.1029/2018JB016512

Scala, A., Lorito, S., Romano, F., Murphy, S., Selva, J., Basili, R., et al. (2020). Effect of shallow slip amplification uncertainty on probabilistic tsunami hazard analysis in subduction zones: use of long-term balanced stochastic slip models. *Pure Appl. Geophys.* 177, 1497–1520. doi:10.1007/s00024-019-02260-x

Schmidtlein, M. C., Deutsch, R. C., Piegorsch, W. W., and Cutter, S. L. (2008). A sensitivity analysis of the social vulnerability index. *Int. J.* 28 (4), 1099–1114. doi:10.1111/j.1539-6924.2008.01072.x

Selva, J., Acocella, V., Bisson, M., Caliro, S., Costa, A., Della Seta, M., et al. (2019). Multiple natural hazards at volcanic islands: a review for the Ischia volcano (Italy). *J. Appl. Volcanol.* 8 (1), 5. doi:10.1186/s13617-019-0086-4

Selva, J., Bonadonna, C., Branca, S., De Astis, G., Gambino, S., Paonita, A., et al. (2020). Multiple hazards and paths to eruptions: a review of the volcanic system of Vulcano (Aeolian Islands, Italy). *Earth-Sci. Rev.* 207, 103186. doi:10.1016/j.earscirev.2020.103186

Selva, J., Tonini, R., Molinari, I., Tiberti, M. M., Romano, F., Grezio, A., et al. (2016). Quantification of source uncertainties in seismic probabilistic tsunami hazard analysis (SPTHA). *Geophys. J. Int.* 205, 1780–1803. doi:10.1093/gji/ggw107

Sepúlveda, I., Liu, P. L.-F., Grigoriu, M., and Pritchard, M. (2017). Tsunami hazard assessments with consideration of uncertain earthquake slip distribution and location. *J. Geophys. Res. Solid Earth* 122, 7252–7271. doi:10.1002/2017JB014430

Shi, F., Kirby, J. T., Harris, J. C., Geiman, J. D., and Grilli, S. T. (2012). A high-order adaptive time-stepping TVD solver for Boussinesq modeling of breaking waves and coastal inundation. *Ocean Model.* 43, 36–51. doi:10.1016/j.ocemod.2011.12.004

Si, P., Shi, H., and Yu, X. (2018b). A general numerical model for surface waves generated by granular material intruding into a water body. *Coastal Eng.* 142, 42–51. doi:10.1016/j.coastaleng.2018.09.001

Si, P., Shi, H., and Yu, X. (2018a). Development of a mathematical model for submarine granular flows. *Phys. Fluids* 30, 083302. doi:10.1063/1.5030349

Sibley, A. M., Cox, D., and Tappin, D. R. (2020). Convective rear-flank downdraft as driver for meteotsunami along English Channel and North Sea coasts 28-29 May 2017. *Nat. Hazards* 14, 114. doi:10.1007/s11069-020-04328-7

Silva, V., Amo-Oduro, D., Calderon, A., Dabbeek, J., Despotaki, V., Martins, L., et al. (2018a). *Global Earthquake Model (GEM) Seismic Risk Map (version 2018.1)*, Available at: https://maps.openquake.org/map/global-seismic-risk-map (Accessed November 10, 2020).

Silva, V., Yepes-Estrada, C., Dabbeek, J., Martins, L., and Brzev, S. (2018b). GED4ALL-Global exposure database for multi-hazard risk analysis–multi-hazard exposure taxonomy. GEM Technical Report 2018-01. Pavia: GEM Foundation.

Skarlatoudis, A. A., Somerville, P. G., and Thio, H. K. (2016). Source-scaling relations of interface subduction earthquakes for strong ground motion and tsunami simulation. *Bull. Seismol. Soc. Amer.* 106, 1652–1662. doi:10.1785/0120150320

Smit, A., Kijko, A., and Stein, A. (2017). Probabilistic tsunami hazard assessment from incomplete and uncertain historical catalogues with application to tsunamigenic regions in the pacific ocean. *Pure Appl. Geophys.* 174, 3065–3081. doi:10.1007/s00024-017-1564-4

Snelling, B., Neethling, S., Horsburgh, K., Collins, G., and Piggott, M. (2020). Uncertainty quantification of landslide generated waves using Gaussian process emulation and variance-based sensitivity analysis. *Water* 12 (2), 416. doi:10.3390/w12020416

So, E. K. M., Pomonis, A., Below, R., Cardona, O., King, A., Zulfikar, C., et al. (2012). "An introduction to the global earthquake consequences database (GEMECD)," in Proceedings of the 15th world conference on earthquake engineering. Lisbon: Springer.

Song, J., De Risi, R., and Goda, K. (2017). Influence of flow velocity on tsunami loss estimation. *Geosciences* 7 (4), 114. doi:10.3390/geosciences7040114

Sørensen, M. B., Spada, M., Babeyko, A., Wiemer, S., and Grünthal, G. (2012). Probabilistic tsunami hazard in the mediterranean sea. *J. Geophys. Res.* 117 (B1), 13. doi:10.1029/2010JB008169

Spielman, S. E., Tuccillo, J., Folch, D. C., Schweikert, A., Davies, R., Wood, N., et al. (2020). Evaluating social vulnerability indicators: criteria and their application to the Social Vulnerability Index. *Nat. Hazards* 100 (1), 417–436. doi:10.1007/s11069-019-03820-z

Stolle, J., Takabatake, T., Hamano, G., Ishii, H., Iimura, K., Shibayama, T., et al. (2019). Debris transport over a sloped surface in tsunami-like flow conditions. *Coastal Eng. J.* 61 (2), 241–255. doi:10.1080/21664250.2019.1586288

Strasser, F. O., Arango, M. C., and Bommer, J. J. (2010). Scaling of the source dimensions of interface and intraslab subduction-zone earthquakes with moment magnitude. *Seismol. Res. Lett.* 81, 941–950. doi:10.1785/gssrl.81.6.9410.1785/gssrl.81.6.941

Strunz, G., Post, J., Zosseder, K., Wegscheider, S., Mück, M., Riedlinger, T., et al. (2011). Tsunami risk assessment in Indonesia. *Nat. Hazards Earth Syst. Sci.* 11 (1), 67–82. doi:10.5194/nhess-11-67-2011

Stucchi, M., Albini, P., Mirto, M., and Rebez, A. (2004). Assessing the completeness of Italian historical earthquake data. *Ann. Geophys.* 47, 35. doi:10.4401/ag-3330

Sugawara, D., Goto, K., and Jaffe, B. E. (2014). Numerical models of tsunami sediment transport—current understanding and future directions. *Mar. Geol.* 352, 295–320. doi:10.1016/j.margeo.2014.02.007

Suppasri, A., Charvet, I., Imai, K., and Imamura, F. (2015). Fragility curves based on data from the 2011 tohoku-oki tsunami in ishinomaki city, with discussion of parameters influencing building damage. *Earthq. Spectra* 31, 841–868. doi:10.1193/053013EQS138M

Suppasri, A., Hasegawa, N., Makinoshima, F., Imamura, F., Latcharote, P., and Day, S. (2016). An analysis of fatality ratios and the factors that affected human fatalities in the 2011 Great East Japan tsunami. *Front. Built Environ.* 2, 32. doi:10.3389/fbuil.2016.00032

Synolakis, C. E., Bernard, E. N., Titov, V. V., Kânoğlu, U., and González, F. I. (2008). Validation and verification of tsunami numerical models. *Pure Appl. Geophys.* 165, 2197–2228. doi:10.1007/s00024-004-0427-y

Šepić, J., Vilibić, I., and Monserrat, S. (2016). Quantifying the probability of meteotsunami occurrence from synoptic atmospheric patterns. *Geophys. Res. Lett.* 43, 10377–10384. doi:10.1002/2016GL070754

Tappin, D. R., Watts, P., and Grilli, S. T. (2008). The Papua New Guinea tsunami of 17 July 1998: anatomy of a catastrophic event. *Nat. Hazards Earth Syst. Sci.* 8 (2), 243–266. doi:10.5194/nhess-8-243-2008

ten Brink, U., Geist, E. L., and Andrews, B. D. (2006). Size distribution of submarine landslides and its implication to tsunami hazard in Puerto Rico. *Geophys. Res. Lett.*. 33 (11), 23. doi:10.1142/9789812774613_0004

Thingbaijam, K. K. S., Martin Mai, P., and Goda, K. (2017). New empirical earthquake source-scaling laws. *Bull. Seismol. Soc. Am.* 107, 2225–2246. doi:10.1785/0120170017

Thio, H. K., Somerville, P., and Ichinose, G. (2007). Probabilistic analysis of strong ground motion and tsunami hazards in southeast asia. *J. Earthq. Tsunami* 01, 119–137. doi:10.1142/S1793431107000080

Tiberti, M. M., Basili, R., and Vannoli, P. (2014). Ups and downs in western Crete (Hellenic subduction zone). *Sci. Rep.* 4, 5677. doi:10.1038/srep05677

Tinti, S. (1991). Assessment of tsunami hazard in the Italian seas. *Nat. Hazards* 4, 267–283. doi:10.1007/bf00162792

Tinti, S., Bortolucci, E., and Armigliato, A. (1999). Numerical simulation of the landslide-induced tsunami of 1988 on Vulcano Island, Italy. *Bull. Volcanol.* 61 (1), 121–137. doi:10.1007/s004450050267

Tinti, S., Bortolucci, E., and Vannini, C. (1997). A block-based theoretical model suited to gravitational sliding. *Nat. Hazards* 16, 1–28. doi:10.1023/A10.1023/a:1007934804464

Tinti, S., Pagnoni, G., and Zaniboni, F. (2006). The landslides and tsunamis of the 30th of December 2002 in Stromboli analysed through numerical simulations. *Bull. Volcanol.* 68, 462–479. doi:10.1007/s00445-005-0022-9

Tonini, R., Basili, R., Maesano, F. E., Tiberti, M. M., Lorito, S., Romano, F., et al. (2020). Importance of earthquake rupture geometry on tsunami modelling: the Calabrian Arc subduction interface (Italy) case study. *Geophys. J. Int.* 223, 1805–1819. doi:10.1093/gji/ggaa409

Trapper, P. A., Puzrin, A. M., and Germanovich, L. N. (2015). Effects of shear band propagation on early waves generated by initial breakoff of tsunamigenic landslides. *Mar. Geol.* 370, 99–112. doi:10.1016/j.margeo.2015.10.014

Triantafyllou, I., Novikova, T., Charalampakis, M., Fokaefs, A., and Papadopoulos, G. A. (2019). Quantitative tsunami risk assessment in terms of building replacement cost based on tsunami modelling and GIS methods: the case of crete isl., hellenic arc. *Pure Appl. Geophys.* 176 (7), 3207–3225. doi:10.1007/s00024-018-1984-9

Tufekci, D., Suzen, M. L., Yalciner, A. C., and Zaytsev, A. (2018). Revised MeTHuVA method for assessment of tsunami human vulnerability of Bakirkoy district, Istanbul. *Nat. Hazards* 90 (2), 943–974. doi:10.1007/s11069-017-3082-1

Ulrich, T., Gabriel, A.-A., Ampuero, J.-P., and Xu, W. (2019a). Dynamic viability of the 2016 Mw 7.8 Kaikōura earthquake cascade on weak crustal faults. *Nat. Commun.* 10 (1), 1213. doi:10.1038/s41467-019-09125-w

Ulrich, T., Vater, S., Madden, E. H., Behrens, J., van Dinther, Y., van Zelst, I., et al. (2019b). Coupled, physics-based modeling reveals earthquake displacements are critical to the 2018 palu, sulawesi tsunami. *Pure Appl. Geophys.* 176, 4069–4109. doi:10.1007/s00024-019-02290-5

Ulvrova, M., Paris, R., Nomikou, P., Kelfoun, K., Leibrandt, S., Tappin, D. R., et al. (2016). Source of the tsunami generated by the 1650 AD eruption of Kolumbo submarine volcano (Aegean Sea, Greece). *J. Volcanol. Geothermal Res.* 321, 125–139. doi:10.1016/j.jvolgeores.2016.04.034

UNISDR. (2013). *United Nations international Office for disaster risk reduction. Global assessment report on disaster risk reduction 2013*. Geneva: Springer.

UNISDR. (2015). *United Nations international Office for disaster risk reduction. Global assessment report on disaster risk reduction 2015*. Geneva: Switzerland..

UNISDR. (2007). United Nations international Office for disaster risk reduction. Hyogo framework for action 2005–2015: building the resilience of Nations and communities to disasters. Geneva. Switzerland. Available at: https://www.unisdr.org/files/1037_hyogoframeworkforactionenglish.pdf (Accessed October 22, 2020).

Urgeles, R., and Camerlenghi, A. (2013). Submarine landslides of the Mediterranean Sea: trigger mechanisms, dynamics, and frequency-magnitude distribution. *J. Geophys. Res. Earth Surf.* 118 (4), 2600–2618. doi:10.1002/2013jf002720

Urlaub, M., Talling, P. J., and Masson, D. G. (2013). Timing and frequency of large submarine landslides: implications for understanding triggers and future geohazard. *Quat. Sci. Rev.* 72, 63–82. doi:10.1016/j.quascirev.2013.04.020

van de Lindt, J. W., and Dao, T. N. (2009). Performance-based wind engineering for wood-frame buildings. *J. Struct. Eng.* 135 (2), 169–177. doi:10.1061/(asce)0733-9445(2009)135:2(169)

Vela, J., Pérez, B., González, M., Otero, L., Olabarrieta, M., Canals, M., et al. (2014). Tsunami resonance in palma bay and harbor, majorca island, as induced by the 2003 western mediterranean earthquake. *J. Geol.* 122 (2), 165–182. doi:10.1086/675256

Vilibić, I. (2008). Numerical simulations of the Proudman resonance. *Continental Shelf Res.* 28 (4), 574–581. doi:10.1016/j.csr.2007.11.005

Vilibić, I., Horvath, K., Strelec Mahović, N., Monserrat, S., Marcos, M., Amores, A., et al. (2014). Atmospheric processes responsible for generation of the 2008 Boothbay meteotsunami. *Nat. Hazards* 74, 25–53. doi:10.1007/s11069-013-0811-y

Vilibić, I., and Šepić, J. (2009). Destructive meteotsunamis along the eastern adriatic coast: overview. Physics and chemistry of the Earth. *Parts A/B/C* 34 (17–18), 904–917. doi:10.1016/j.pce.2009.08.004

Volpe, M., Lorito, S., Selva, J., Tonini, R., Romano, F., and Brizuela, B. (2019). From regional to local SPTHA: efficient computation of probabilistic tsunami inundation maps addressing near-field sources. *Nat. Hazards Earth Syst. Sci.* 19, 455–469. doi:10.5194/nhess-19-455-2019

Walter, T. R., Haghshenas Haghighi, M., Schneider, F. M., Coppola, D., Motagh, M., Saul, J., et al. (2019). Complex hazard cascade culminating in the Anak Krakatau sector collapse. *Nat. Commun.* 10, 4339. doi:10.1038/s41467-019-12284-5

Wang, K., Hu, Y., and He, J. (2012). Deformation cycles of subduction earthquakes in a viscoelastic Earth. *Nature* 484, 327–332. doi:10.1038/nature11032

Wang, L., Zhang, X., and Tinti, S. (2019). Shallow landslides modeling using a particle finite element model with emphasis on landslide evolution. 11, 21. doi:10.5194/esurf-2019-17

Ward, S. N. (2001). Landslide tsunami. *J. Geophys. Res.* 106 (B6), 11201–11215. doi:10.1029/2000jb900450

Watts, P., Grilli, S. T., Kirby, J. T., Fryer, G. J., and Tappin, D. R. (2003). Landslide tsunami case studies using a Boussinesq model and a fully nonlinear tsunami generation model. *Nat. Hazards Earth Syst. Sci.* 3, 391–402. doi:10.5194/nhess-3-391-2003

Watts, P. (2000). Tsunami features of solid block underwater landslides. *J. Waterway Port Coastal Ocean Eng.* 126 (3), 144–152. doi:10.1061/(asce)0733-950x(2000)126:3(144)

Watts, P., and Waythomas, C. F. (2003). Theoretical analysis of tsunami generation by pyroclastic flows. *J. Geophys. Res.* 108 (B12), 2563. doi:10.1029/2002JB002265

Wei, Y., Bernard, E. N., Tang, L., Weiss, R., Titov, V. V., Moore, C., et al. (2008). Real-time experimental forecast of the Peruvian tsunami of August 2007 for U.S. coastlines. *Geophys. Res. Lett.* 35 (4), 67. doi:10.1029/2007GL032250

Wells, D. L., and Coppersmith, K. J. (1994). New empirical relationships among magnitude, rupture length, rupture width, rupture area, and surface displacement. *Bull. Seismol. Soc. Am.* 84, 974–1002.

Wendt, J., Oglesby, D. D., and Geist, E. L. (2009). Tsunamis and splay fault dynamics. *Geophys. Res. Lett.* 36 (15), 34. doi:10.1029/2009GL038295

Whitmore, P., and Knight, B. (2014). "Meteotsunami forecasting: sensitivities demonstrated by the 2008 Boothbay, Maine, event," in *Meteorological Tsunamis, U. S. The East Coast, and Other Coastal Regions*. Editors Vilibić, I., Monserrat, S., and Rabinovich, A. B. (Cham, Switzerland: Springer). doi:10.1007/978-3-319-12712-5_2

Williamson, A. L., Rim, D., Adams, L. M., LeVeque, R. J., Melgar, D., and González, F. I. (2020). A source clustering approach for efficient inundation modeling and regional scale probabilistic tsunami hazard assessment. *Front. Earth Sci.* 8, 442. doi:10.3389/feart.2020.591663

Woodruff, I., Kirby, J., Shi, F., and Grilli, S. (2018). Estimating meteo-tsunami occurrences for the US East coast. *Int. Conf. Coastal. Eng.* 1 (36) 66. doi:10.9753/icce.v36.currents.66

Yamao, S., Esteban, M., Yun, N. Y., Mikami, T., and Shibayama, T. (2015). "Estimation of the current risk to human damage life posed by future tsunamis in Japan," in *Handbook of coastal disaster mitigation for engineers and planners*. Editor Esteban, M. (Boston: Butterworth-Heinemann), 257–275.

Yamashita, K., Suppasri, A., Oishi, Y., and Imamura, F. (2018). Development of a tsunami inundation analysis model for urban areas using a porous body model. *Geosciences* 8 (1), 12. doi:10.3390/geosciences8010012

Yavari-Ramshe, S., and Ataie-Ashtiani, B. (2016). Numerical modeling of subaerial and submarine landslide-generated tsunami waves-recent advances and future challenges. *Landslides* 13 (6), 1325–1368. doi:10.1007/s10346-016-0734-2

Yokoyama, I. (1987). A scenario of the 1883 Krakatau tsunami. *J. Volcanol. Geothermal Res.* 34, 123–132. doi:10.1016/0377-0273(87)90097-7

Zechar, J. D., and Frankel, K. L. (2009). Incorporating and reporting uncertainties in fault slip rates. *J. Geophys. Res.* 114, 121. doi:10.1029/2009JB006325

Zengaffinen, T., Løvholt, F., Pedersen, G. K., and Harbitz, C. B. (2020). *Effects of rotational submarine slump dynamics on tsunami genesis: new insight from idealized models and the 1929 Grand Banks event Special publications*. London: Geological Society.

Conflict of Interest: HT was employed by AECOM.

The remaining authors declare that the research was conducted in the absence of any commercial or financial relationships that could be construed as a potential conflict of interest.

frontiers in Earth Science

ORIGINAL RESEARCH
published: 07 May 2021
doi: 10.3389/feart.2021.628652

Modeling Tsunamis Generated by Submarine Landslides at Stromboli Volcano (Aeolian Islands, Italy): A Numerical Benchmark Study

Tomaso Esposti Ongaro[1], Mattia de' Michieli Vitturi[1], Matteo Cerminara[1], Alessandro Fornaciai[1], Luca Nannipieri[1], Massimiliano Favalli[1], Benedetta Calusi[1], Jorge Macías[2], Manuel J. Castro[2], Sergio Ortega[2], José M. González-Vida[2] and Cipriano Escalante[2]*

[1] *Istituto Nazionale di Geofisica e Vulcanologia, Sezione di Pisa, Pisa, Italy,* [2] *EDANYA Group, Universidad de Málaga, Málaga, Spain*

OPEN ACCESS

Edited by:
Jörn Behrens,
Universität Hamburg, Germany

Reviewed by:
Paris Raphael,
UMR6524 Laboratoire Magmas et Volcans (LMV), France
Stephan Grilli,
University of Rhode Island, United States
Valentin Heller,
University of Nottingham, United Kingdom

****Correspondence:***
Tomaso Esposti Ongaro
tomaso.espostiongaro@ingv.it

Specialty section:
This article was submitted to Volcanology, a section of the journal Frontiers in Earth Science

Received: *12 November 2020*
Accepted: *30 March 2021*
Published: *07 May 2021*

Citation:
Esposti Ongaro T, de' Michieli Vitturi M, Cerminara M, Fornaciai A, Nannipieri L, Favalli M, Calusi B, Macías J, Castro MJ, Ortega S, González-Vida JM and Escalante C (2021) Modeling Tsunamis Generated by Submarine Landslides at Stromboli Volcano (Aeolian Islands, Italy): A Numerical Benchmark Study. Front. Earth Sci. 9:628652. doi: 10.3389/feart.2021.628652

We present a benchmark study aimed at identifying the most effective modeling approach for tsunami generation, propagation, and hazard in an active volcanic context, such as the island of Stromboli (Italy). We take as a reference scenario the 2002 landslide-generated tsunami event at Stromboli simulated to assess the relative sensitivity of numerical predictions to the landslide and the wave models, with our analysis limited to the submarine landslide case. Two numerical codes, at different levels of approximation, have been compared in this study: the NHWAVE three-dimensional non-hydrostatic model in sigma-coordinates and the Multilayer-HySEA model. In particular, different instances of Multilayer-HySEA with one or more vertical discretization layers, in hydrostatic and non-hydrostatic formulation and with different landslide models have been tested. Model results have been compared for the maximum runup along the shores of Stromboli village, and the waveform sampled at four proximal sites (two of them corresponding to the locations of the monitoring gauges, offshore the Sciara del Fuoco). Both rigid and deformable (granular) submarine landslide models, with volumes ranging from 7 to 25 million of cubic meters, have been used to trigger the water waves, with different physical descriptions of the mass movement. Close to the source, the maximum surface elevation and the resulting runup at the Stromboli village shores obtained with hydrostatic and non-hydrostatic models are similar. However, hydrostatic models overestimate (with respect to non-hydrostatic ones) the amplitude of the initial positive wave crest, whose height increases with the distance. Moreover, as expected, results indicate significant differences between the waveforms produced by the different models at proximal locations. The accurate modeling of near-field waveforms is particularly critical at Stromboli in the perspective of using the installed proximal sea-level gauges, together with numerical simulations, to characterize tsunami source in an early-warning system. We show that the use of non-hydrostatic models, coupled with a multilayer approach, allows a better description of the waveforms. However, the source description remains the most sensitive (and uncertain) aspect of the modeling. We finally show that non-hydrostatic models, such as Multilayer-HySEA, solved on accelerated

GPU architectures, exhibit the optimal trade-off between accuracy and computational requirements, at least for the envisaged problem size and for what concerns the proximal wave field of tsunamis generated by volcano landslides. Their application and future developments are opening new avenues to tsunami early warning at Stromboli.

Keywords: landslide, tsunami, volcano, Stromboli, numerical simulation, benchmark, hazard assessment

1. INTRODUCTION

The generation of large tsunamis is a relatively rare phenomenon at volcanic islands on a decadal scale (Latter, 1981; Béget, 2000; Tinti et al., 2003a), but it represents a remarkable risk, in reason of the catastrophic impact it may have along the nearby coasts (Auker et al., 2013; Paris et al., 2013; Paris, 2015). The most common phenomena capable to generate tsunami on volcanic islands are submarine and subaerial landslides (Harbitz et al., 2013; Løvholt et al., 2015; Yavari-Ramshe and Ataie-Ashtiani, 2016). Landslides are particularly frequent at active volcanoes during periods of intense eruptive activity, resulting in overloading and instability in both the submarine and subaerial portions of the volcano flanks (cf. Tibaldi, 2001; Pistolesi et al., 2020), especially on the parts of the edifice characterized by unconsolidated pyroclastic deposits and steep slopes (Bisson et al., 2007; Pistolesi et al., 2020). Rapid pyroclastic avalanches are a special type of subaerial mass flow composed of air and hot pyroclastic particles (ash, lapilli, and blocks produced during explosive eruptions). They are peculiar of volcanic settings and differ from other subaerial landslide by their generation mechanism, which can be associated with the collapse of eruptive jets and/or lava domes, or by the impulsive directional ejection of pyroclasts (Branney and Kokelaar, 2002). Moreover, they are characterized by an initially higher momentum, finer granulometry, and higher temperature, facilitating the built-up of pore pressure (Roche et al., 2011; Lube et al., 2020). For these features, the tsunamigenic capacity of pyroclastic avalanches is still only partially understood (De Lange et al., 2001; Freundt, 2003; Walder, 2003; Watts and Waythomas, 2003; Bougouin et al., 2020).

At Stromboli Island (Aeolian Islands, Southern Tyrrhenian Sea, Italy), the generation of tsunamis represents one among the several relevant hazards associated with ordinary and extraordinary volcanic activity (Rosi et al., 2013) for the shores of the island, for the nearby Aeolian Archipelago, and for the Southern Tyrrhenian Sea (**Figure 1**).

All known tsunami events at Stromboli were associated with intense explosive and/or effusive eruptions and subsequent landslides associated with gravitational instabilities of the Sciara del Fuoco (SdF) (Tinti et al., 2008; Casalbore et al., 2011; Pistolesi et al., 2020) (**Figure 2**). At least eight events of tsunami have been recognized since 1900 CE (Maramai et al., 2005b; Rosi et al., 2019; Pistolesi et al., 2020). The largest one was initiated on 30 December 2002 by two landslides (with total volume of the order of 10×10^6 m^3 Chiocci et al., 2008) that detached from the submarine and subaerial flanks of the SdF scar (Bonaccorso et al., 2003; Maramai et al., 2005a; Tinti et al., 2006; Marani et al., 2008). The 2002 event is presently taken as a reference for emergency planning by the Italian Civil Protection. Two smaller but more recent events were associated with the July 3rd and August 28th, 2019, paroxysmal events (i.e., eruptions with exceedingly high mass eruption rate, with respect to the ordinary Strombolian activity; Rosi et al., 2013; Giordano and De Astis, 2020; Giudicepietro et al., 2020). Both events generated pyroclastic avalanches along the SdF, whose entrance into the sea triggered two sequences of tsunamis (INGV, 2019; LGS, 2019a,b). Although they did not have significant impact on the island shores (with maximum surface elevation of a few centimeters), they provided first-hand evidence of the capability of relatively small rapid pyroclastic avalanches to trigger water waves (Freundt, 2003; Watts and Waythomas, 2003; Bougouin et al., 2020). The analysis of the witnessed cases of the 20th century suggests in any case a dominant submarine component of the tsunami source mechanism at Stromboli (Maramai et al., 2005b; Rosi et al., 2013). Although probability of occurrence of submarine/subaerial landslides at SdF is not rigorously established yet, in this work we preliminary address submarine landslides and leave the study of subaerial landslides and pyroclastic avalanches for a future work.

Modeling of tsunamis generated by submarine landslides entails different levels of complexity. Modeling of the tsunamigenic source requires description of the mechanisms of landslide triggering (Harbitz et al., 2006, 2013; Masson et al., 2006; Clare et al., 2018), propagation (Hungr et al., 2005; Pudasaini and Mergili, 2019), and deformation (Løvholt et al., 2015). These difficulties are common also for volcanic mass flows, whose capability to transfer energy to water waves, involving complex multiphase processes and dissipative phenomena, is still largely unknown (Tinti and Bortolucci, 2000; Ruff, 2003; Watts and Waythomas, 2003; Bougouin et al., 2020). For what concerns wave dynamics, volcanic tsunamis share some of the complexities that make the assumptions underlying the wave equations at the open sea fail: the source of the tsunami is almost always close to the shore, where non-linear shoaling effects are significant (cf. Guyenne and Grilli, 2003); the interaction with the coast and with a steep and rapidly varying bathymetry induces significant reflection and refraction effects (cf. Glimsdal et al., 2013); non-hydrostatic effects (i.e., frequency dispersion) are significant due to steep slopes and for the high-frequency component of generated waves on the shallow bathymetry (cf. Grilli and Watts, 2005). For these reasons, non-linear, non-hydrostatic wave dispersive models are recognized to be essential components to simulate landslide-generated tsunamis, including those at volcanic islands (Yavari-Ramshe and Ataie-Ashtiani, 2016).

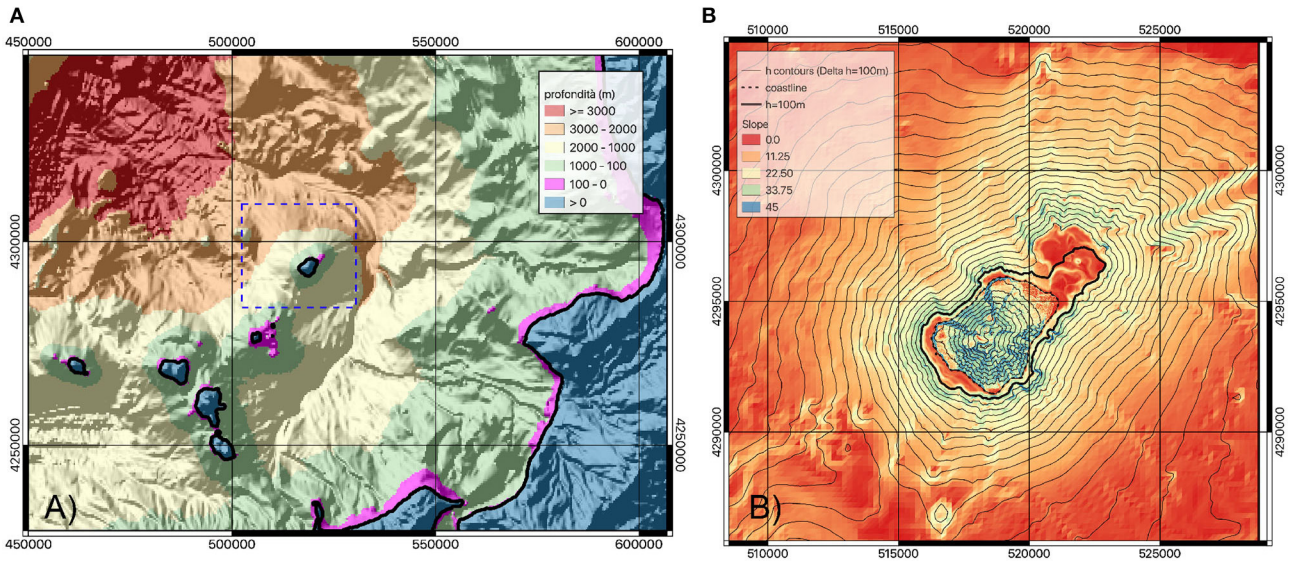

FIGURE 1 | (A) Topo-bathymetry of the Southern Tyrrhenian sea, with the Aeolian archipelago and the island of Stromboli (dashed inset frame). **(B)** Map of proximal topographic and bathymetric slopes of the Stromboli volcano.

At Stromboli, numerical modeling of tsunamis has been carried out and reported in a number of previous works, for the 2002 event (Tinti et al., 2006) and for potential scenarios generated outside the SdF area (Tinti et al., 2008), including considerations about extremely large volume landslides with tsunami (Tinti et al., 2000). These simulations have been carried out by means of a Lagrangian block model to compute the motion of the collapsing mass, and a finite-element, shallow water (hydrostatic) model to compute the propagation of the tsunami. The impact on Stromboli Island, on the Aeolian Archipelago and on the Southern Tyrrhenian Sea have been addressed (Tinti et al., 2003b) with a scenario approach based on the knowledge of past volcanic and tsunamigenic activity at Stromboli. However, the use of shallow-water models for landslide-generated tsunamis is nowadays known to suffer severe limitations, due to non-dispersive features and because of relevant three-dimensional effects associated with propagation along steep slopes (Yavari-Ramshe and Ataie-Ashtiani, 2016). For these reasons, Fornaciai et al. (2019) proposed a new numerical simulation work of the 2002 event at Stromboli, in which several landslide scenarios were studied by coupling a rigid landslide with a non-hydrostatic wave model to study the near-shore wave generation and propagation, including wave dispersion, shoaling and diffraction effects. To compute further wave propagation in the Southern Tyrrhenian Sea and the potential inundation, Fornaciai et al. (2019) have used a depth-averaged, dispersive Boussinesq wave model. That study allowed setting further constraints to the magnitude of either submarine and subaerial landslide phases for scenarios compatible with the 2002 event at Stromboli, and highlighted the importance of shoaling and diffraction phenomena which can increase the waves heights locally, with initial wave as large as 10 m and runups on the shores as high as 5–10 m. However, the high computational cost of the used three-dimensional solver (even when run on clusters of parallel processors) made its use for hazard assessment purposes problematic, limiting its use to single scenario analysis and to relatively small computational domains.

In the tsunami community there has been a continuous effort to identify criteria and appropriate validation experiments for the assessment of numerical model reliability. This was aimed especially to seismically induced tsunamis (Synolakis et al., 2007; Horrillo et al., 2015; Lynett et al., 2017), but the need of better understanding landslide-generated tsunamis recently stimulated a comparable effort. In this context, a set of experiments have been proposed as benchmarks for landslide-induced tsunami by Kirby et al. (2018). For conical islands, a specific benchmark based on laboratory experiments has been proposed by Romano et al. (2016), to be used for validation of numerical models (Montagna et al., 2011). Analysis of experimental data allowed Romano et al. (2013) and Bellotti and Romano (2017) to accurately characterize the physical properties of the wave generated by a subaerial, rigid landslide, the inundation mechanism (controlled by the trapped edge-wave) and the energy content of the radiating waves. However, it is still challenging to compare models against natural phenomena, due to the scarcity of the observations, the uncertainty on initial and boundary conditions and complex interactions between subsystems.

In this paper, we present a synthetic benchmark (or model inter-comparison) study aimed at quantifying the impact of different physical and numerical approximations on the resulting waveforms and tsunami inundation patterns at Stromboli, and identifying the most effective trade-off between computational cost and model accuracy. The Material and Methods section describes the landslide and wave models used for the benchmark and the simulation conditions. We take as a reference the 2002 scenario described by Fornaciai et al. (2019) and assess

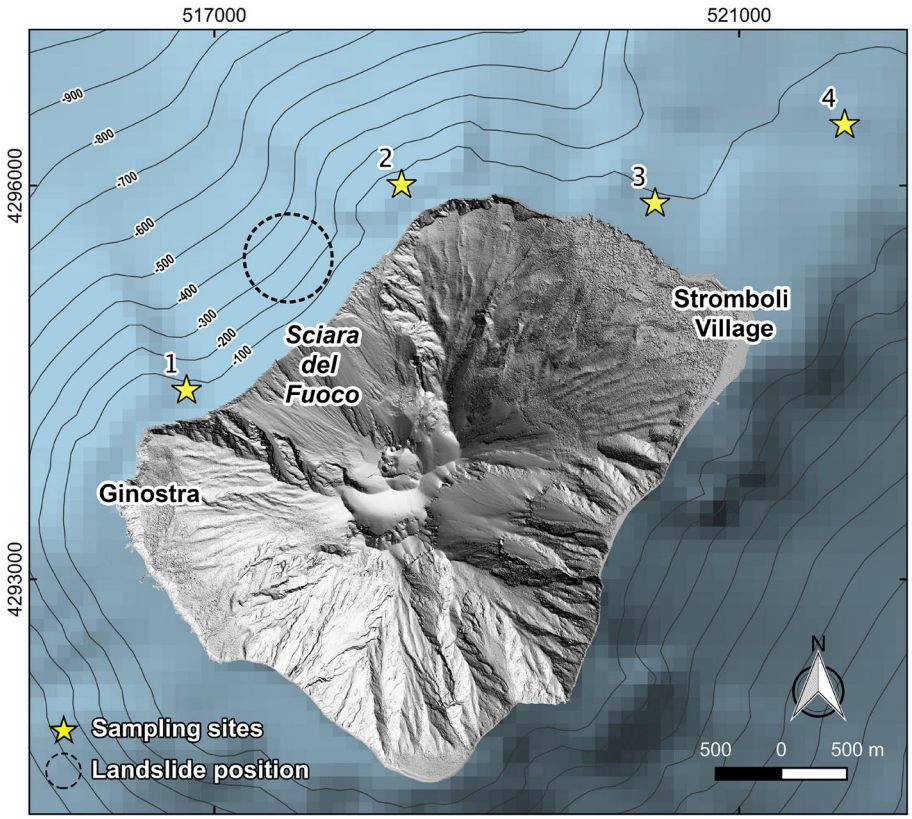

FIGURE 2 | Topography and bathymetry of the island of Stromboli. Stars indicate the positions of the actual (1 and 2) and virtual gauges (3 and 4), where simulated waves are sampled. The initial position of the 2002 submarine landslide identified by Fornaciai et al. (2019) is indicated by the circle.

the relative sensitivity of numerical predictions to the landslide and the wave models. In the Results section we present the model results, emphasizing the comparison among proximal waveforms, sampled at the same locations of the two elastic gauges recently installed by Università di Firenze and the Italian Department of Civil Protection near the shoreline of the SdF (http://lgs.geo.unifi.it/; Lacanna and Ripepe, 2020). We also discuss differences in the inundation patterns at Stromboli village, by comparing the maximum wave height on the shoreline with the field data collected after the 2002 event, for different landslide volumes and models. In the context of the development of an early warning system, it is of primary importance to provide a reliable and effective (from the point of view of accuracy and computational time) model able to interpret proximal wave signals, and to potentially assimilate them into a predictive wave propagation model. Such aspects are addressed in the Discussion section, where we also discuss our results in the framework of the recent scientific literature. Finally, in the Conclusion section, we provide a short summary of the main results and an outline of future work.

2. MATERIALS AND METHODS

The two models used in our study (named NHWAVE and Multilayer-HySEA) and shortly described below have been tested against validation laboratory experiments proposed by Kirby et al. (2018) during the Landslide Tsunami Model Benchmarking Workshop (LTMBW, 2017). Their formulation, implementation and validation are documented in the referenced literature. Both numerical codes include a wave generation mechanism describing the landslide and its interaction with the water (**Table 1**) and implement different approximations of the wave dynamics (**Table 2**). Their implementation is here described and summarized in **Table 3**.

2.1. Rigid Landslide Model

In most of the presented numerical results, we adopt a simple conceptualization of the landslides, which considers a rigid sliding mass whose center of mass has prescribed kinematics. The slide has a nearly elliptical footprint on the slope and vertical cross sections varying according to truncated hyperbolic secant functions in the two orthogonal directions (the analytical expression is reported in the **Supplementary Material**), and it is identified by its length, width and maximum thickness, defining its volume (Enet and Grilli, 2007; Fornaciai et al., 2019). The Rigid Landslide model (abbreviated by the acronym RL in **Tables 1**, **2**) considers the balanced effects of inertia, gravity, buoyancy, Coulomb friction, hydrodynamic friction, and drag forces. These are described by the equation of motion defined by Enet and Grilli (2007) and proposed by Kirby et al. (2018) at the Landslide Tsunami Model Benchmarking Workshop (LTMBW,

TABLE 1 | Different modeling approaches used in this work for the description of the landslide.

	Landslide Model	Dynamics	Coupling with wave model
RL	Rigid Landslide	The landslide volume and shape are constant, the kinematics of the center of mass are prescribed by a prognostic equation obtained by balancing the effects of inertia, gravity, buoyancy, Coulomb (bed) friction, hydrodynamic friction, and drag forces Enet and Grilli, 2007.	1. Bathymetric changes (one-way: the water wave does not affect the landslide). 2. Landslide-water considered in the kinematic law.
GL	Granular Landslide	The landslide is described by a depth-averaged model as an incompressible granular fluid, with an empirical rheology and basal friction model Savage and Hutter, 1989. The landslide volume is constant, but the shape and velocity depend on the water and granular fluid dynamics Fernández-Nieto et al., 2008.	1. Bathymetric changes. 2. Landslide-water friction. 3. Neglected fluctuations of granular fluid pressure due to the variations of the free-surface.

TABLE 2 | Acronym and hierarchy of the different approaches to the modeling of water waves, ordered from top to bottom by decreasing complexity.

	Description	Approximations	Described phenomena	Phenomena not described
NS	Navier-Stokes	Incompressible fluid with constant density (except in gravity terms treated with Boussinesq approximation).	Dispersive waves, dissipation, turbulence, non-linear wave propagation (e.g., solitons), vertical variations of pressure and velocity. Rapidly changing bathymetry and steep slopes	Compressible effects, surface tension.
sNH	Navier-Stokes in sigma coordinates, non-hydrostatic	Incompressible fluid, dispersive waves ($H/\lambda \sim 1$) (depending on the number of sigma-layers)	Same as NS.	Same as NS. Limited vertical resolution, but better free surface tracking, with respect to NS on fixed meshes.
mNH	Multi-layer non-hydrostatic	Incompressible fluid, dispersive waves ($H/\lambda \sim 1$) (depending on the number of layers).	Same as NS.	Same as sNH.
NH	Single-layer, non-hydrostatic	Incompressible fluid, long waves ($H/\lambda \ll 1$ at an order higher than one).	Dispersive waves, non-linear phenomena.	Vertical mass/momentum flows and stratification. Deep-water waves.
SW	Single-layer, hydrostatic (non-linear shallow water)	Incompressible fluid, long wavelengths (first order). Gentle bathymetric changes.	Topographic including shoaling effects.	Phase dispersion, wave breaking, steep, and complex bathymetry.

H is the water depth and λ is the tsunami wavelength.

2017). They have been adopted by Fornaciai et al. (2019) for the study of the 2002 scenario at Stromboli:

$$(\gamma + C_m)\ddot{s} = (\gamma - 1)(\sin\theta - C_n \cos\theta)g - \frac{1}{2} C_d \frac{A_b}{V_b} \dot{s}^2 \qquad (1)$$

where s is the spatial coordinate, θ is the slope angle, C_m is the added mass coefficient, $\gamma = \frac{\rho_L}{\rho_W}$ is the landslide over water density ratio, C_d is the global drag coefficient, C_n is the basal Coulomb friction coefficient, g is the gravity acceleration, A_b and V_b are the landslide cross section and volume, calculated from the analytical expression reported in the **Supplementary Material**. Analytical integration of this equation on a constant slope and for large times gives the semi-empirical prognostic equation proposed by Grilli and Watts (2005) and Enet and Grilli (2007),

$$s(t) = s_0 \ln\left(\cosh\frac{t}{t_0}\right) \qquad (2)$$

In this expression s_0 and t_0 are the characteristic distance and time, defined as $s_0 = \frac{u_t^2}{a_0}$, and $t_0 = \frac{u_t}{a_0}$, with u_t (terminal velocity for large slides) and a_0 (initial acceleration) defined as in Grilli and Watts (2005). On the 3D topography, we solve Equation (1) numerically by integrating the x and y components in time with a backward Euler scheme. With the RL model, coupling between landslide and water is essentially due to the transient modification of the bathymetry.

2.2. Granular Landslide Model

The Granular Landslide (GL) model (Savage and Hutter, 1989; Fernández-Nieto et al., 2008), describes the landslide as a deformable, incompressible granular medium with constant average density (i.e., constant porosity) which moves under the competing effect of gravity and frictional forces (Ma et al., 2013, 2015; Macías et al., 2015; Macías et al., 2020b; González-Vida et al., 2019). With the GL model, the landslide-wave coupling is two-way: the bottom landslide movement affects the water

column by changing the bathymetry, and the two fluids (the landslide and the water) are coupled through friction terms. On the contrary, the fluctuation of pressure due to the variations of the free-surface can be neglected in the momentum equation of the granular material, thus simplifying the system of equations (Macías et al., 2020b). The comparison between the RL and GL model is carried out by imposing that the granular volume has the same initial shape of the rigid slide and using friction coefficients and density contrast within a comparable range. The rheology of the granular landslide is the most difficult part of the model to calibrate. In this work, we only analyze the results of a granular landslide with one of the two codes, Multilayer-HySEA. The model assumes a Coulomb rheology, with the friction coefficient depending on the landslide Froude number (Pouliquen and Forterre, 2002; Macías et al., 2020b). The friction law is thus characterized by three parameters (three friction angles) μ_1, μ_2, μ_3. We set $\mu_1 = \mu_3$ and as a preliminary study we assessed the sensitivity of the results to variations of μ_1 (static friction) and μ_2 (reduced friction) in the ranges 0.02–0.18. The uncertainty of the resulting wave amplitude is always $<$10%. However, it is worth remarking that NHWAVE also includes the possibility of using a deformable granular model (Ma et al., 2013, 2015). Its most recent version (Zhang et al., 2021a,b) includes the possibility to simulate arbitrary bathymetry, viscous or granular slides, and also has non-hydrostatic pressure included in the slide layer.

2.3. Water Wave Models

In our study, we compare results of the two numerical solvers, run with the same initial and boundary conditions, to assess the influence of different physical and numerical approximations, for the specific natural case of Stromboli. Part of our analysis is dedicated to a comparison between hydrostatic and non-hydrostatic approximations. In the former, the condition of pressure being everywhere hydrostatic derives from the assumption of negligible vertical acceleration in the equation of vertical momentum. This is usually a good approximation for shallow-water (thin) flows (having horizontal wavelengths much larger than the flow thickness) and on mild slopes. It is nowadays recognized that non-linear, non-hydrostatic wave dispersive models are essential components to forecast landslide-generated tsunamis (Yavari-Ramshe and Ataie-Ashtiani, 2016), because their wavelengths are smaller and they are generated on steep slopes. However, legacy shallow-water models are still widely used by practitioners and researchers for assessing tsunami risk and impact (e.g., Liu et al., 2020). For this reason, we analyze the hydrostatic limit at Stromboli, in order to quantify the uncertainty associated with such an approximation.

NHWAVE is a 3D shock-capturing non-hydrostatic wave model developed by Ma et al. (2012), which solves the incompressible Navier-Stokes equations using a small number of vertical, boundary fitted, σ-layers. NHWAVE simulates wave generation by either rigid or deformable slides (Ma et al., 2012, 2013, 2015; Zhang et al., 2021a,b), including frequency dispersion effects (associated with vertical acceleration and non-hydrostatic pressure distribution). Terms describing the viscous and turbulent stress can be included in the NHWAVE model, but they were set to zero in the presented simulations. The code has been modified by Fornaciai et al. (2019) with respect to the original landslide treatment (imposing that the rigid body only follows straight trajectories on a constant slope and therefore with a fixed kinematics) in order to solve the landslide motion equation along the bathymetry. NHWAVE has been widely applied to simulate the wave generation stage of some real landslide-generated tsunami events with a RL model (Tappin et al., 2014; Grilli et al., 2015; Fornaciai et al., 2019). More recently, NHWAVE has been used to simulate the 2018 collapse of Anak Krakatau volcano and subsequent tsunami (Grilli et al., 2019), the 1908 Messina (Schambach et al., 2020), and the 2018 Palu (Schambach et al., 2021) tsunamis with a GL model. The NHWAVE model is parallelized using Message Passing Interface (MPI) with non-blocking communication, with domain-decomposition using ghost-cells.

The Multilayer-HySEA model implements one of the multilayer, non-hydrostatic models of the family introduced and described in Fernández-Nieto et al. (2018), in which the three-dimensional model equations are depth-averaged across a number of vertical layers. The governing equations, obtained by a process of depth-averaging, correspond to a semi-discretization for the vertical variable of the Euler equations and are mathematically equivalent to those of the NHWAVE model. The total pressure is decomposed into a sum of hydrostatic and non-hydrostatic pressures. In this process, the horizontal and vertical velocities are assumed to have a constant vertical profile. The proposed model admits an exact energy balance and, when the number of layers increases, the linear dispersion relation of the linear model converges to the same of Airy's theory (Fernández-Nieto et al., 2018). The motion of the bottom surface can be taken into account as a boundary condition. Therefore, this model can simulate the interaction with a slide in the case that the motion of the bottom is prescribed by a function, given by a set of data, or simulated by a numerical model. In the latter case, the bottom layer can represent the motion of either a rigid (RL) or granular (GL) landslide. The new version of Multilayer-HySEA incorporates the possibility of simulating the generation of tsunami produced by subaerial or submarine deformable landslides. The GL motion is modeled by a shallow-water Savage-Hutter type (Fernández-Nieto et al., 2008) model that is weakly coupled with the non-hydrostatic multilayer model through the boundary conditions (i.e., the modification of the pressure term associated with the wave height is neglected). Model description and validation tests are detailed in Macías et al. (2020a,b). The Multilayer-HySEA model can also be run in hydrostatic approximation (in which case, the multilayer formulation is equivalent to the non-linear shallow-Water equations). The Multilayer-HySEA numerical code is designed to run on Graphic Processing Unit (GPU) accelerated High-Performance Computing (HPC) architectures (Escalante et al., 2018, 2019).

Table 2 presents a list of the modeling approaches considered in this study, defining a hierarchy based on the complexity of the underlying physical model and highlighting the approximations and limitations. **Table 3** shows the numerical codes tested in this study and the different computational approaches implemented.

TABLE 3 | Numerical codes and modeling approaches tested in this work.

Numerical code	Underlying wave + landslide models	Numerical solver	Parallelization
NHWAVE	sNH-RL	Finite volumes	CPU-MPI*
Multilayer-HySEA non-hydrostatic	mNH-RL/GL	Finite volumes	GPU-CUDA**
Multilayer-HySEA hydrostatic	SW-RL/GL	Finite volumes	GPU-CUDA

**Central Processing Unit—Message Passing Interface, **Graphic Processing Units—Compute Unified Device Architecture.*

2.4. Computational Efficiency

The evaluation of the computational efficiency in the numerical simulation of a tsunami is a fundamental component, together with the accuracy of the approximations and of the numerical solution algorithm, for the choice of the strategy and the numerical model for early warning. Evaluating the suitability of a numerical application requires the identification of specific metrics to compare different models, considering three main factors: (1) accuracy of the model in the description of the phenomenon (physical problem); (2) accuracy of numerical approximations (mathematical problem); (3) efficiency of algorithms (implementation problem). It is indeed always possible to obtain extremely fast computational models by sacrificing the accuracy of the physical representation and/or by using coarser numerical methods, both in terms of spatial/temporal resolution and in terms of mathematical accuracy. In the present case, we make the choice of comparing execution times of the different solvers with the same physics, and on the same physical problem representing a real case. It is worth remarking, however, that such a comparison might be incomplete, because the models might have a different convergent rate to the solution (at decreasing grid size). To check this, a comparison with an analytical test solution should be done, which is left for a future study.

In **Table 4** we compare the execution time of the models described above for the simulation of the tsunami generation and propagation in the proximal domain around the Stromboli island. As expected, the hydrostatic models, with the same resolution, are much faster (by a factor of almost 10), since they can exploit efficient computational techniques for hyperbolic systems and do not require the solution of the more complex Poisson equation for the pressure. As for multilayer models, a linear dependence is observed between the number of layers and the execution time. Although MPI-based parallelization has the potential advantage of being more scalable for larger, memory-intensive applications, intrinsic speed-up limits are always associated with the overhead of the MPI, especially for relatively small-size problems. On the other hand, while GPUs are known to perform extremely fast for HPC problems, this is achieved at the price of a more complex programming paradigm and less flexibility in terms of memory usage. For the type and size of problem addressed in this work, resolution on GPU-based accelerated architectures is significantly more efficient. For this reason, we base most of the model sensitivity analysis on Multilayer-HySEA on GPUs.

2.5. Simulated Scenarios

We compare the simulation results with different wave and landslide models. Although a complete study on landslide modeling and parameterization is beyond the scope of the present work, we emphasize the importance of the source model in tsunami predictions, and we present a comparison of the influence of the landslide model on the resulting tsunami. The benchmark has been designed to ensure consistency with previous studies by Fornaciai et al. (2019). It relates to the initiation and propagation of the tsunami due to a submarine landslide, described as a rigid body of fixed volume propagating along the trajectory of maximum bathymetric slope, with a kinematic law prescribed by Equation (1). It is worth remarking that, although the volume of the rigid landslide remains the same during propagation, its shape may locally slightly vary because of the bathymetry changes on its bottom. As part of the work, the RL model was implemented in the Multilayer-HySEA code to ensure compatibility with the scenarios simulated by Fornaciai et al. (2019), in which the reference scenario for Stromboli was produced using the NHWAVE (3 layers) model. The geometric and physical parameters used to characterize the landslide kinematics are reported in **Table 5**. More details can be found in Fornaciai et al. (2019) and in the **Supplementary Material**. Please notice that the volumes reported in **Table 5** are those actually implemented in the simulation model. The values computed with the analytical formula proposed by Enet and Grilli (2007) in Fornaciai et al. (2019) (who reported 6, 10, and 15×10^6 m^3), were underestimated by about 15%. It is worth remarking that Enet and Grilli (2007)'s analytical formula has been recently corrected by Schambach et al. (2019).

Most of the numerical benchmark tests have been performed on a 10 m resolution mesh on a 9.2 × 6.6 km^2 domain, but the effect of the numerical resolution has also been tested. In particular, the error in maximum wave height moving from a horizontal resolution of 20–10 m was <5% in all simulated cases, whereas a grid of 40 m can lead to underestimate the wave height by about 30%. In **Table 4**, a list of tested resolutions is reported.

For each scenario, and for each model, the following outputs were compared: (1) the sampled waveforms at four different positions, corresponding to the two gauges installed in Stromboli offshore of Punta dei Corvi (gauge 1) and Punta Labronzo (gauge 2) and to two virtual gauges located one in front of Porto dei Balordi (gauge 3) and one near the Strombolicchio reef (gauge 4); (2) the runup, i.e., maximum height reached by the wave in the stretch that goes from Spiaggia Lunga to Porto; (3) the code execution time. The positions of the sampling points are indicated in **Figure 2** and reported in **Table 5**.

TABLE 4 | Computational effort for the benchmark test using different numerical models and grid resolutions.

Model	Number of layers	Architecture	Spatial resolution	Number of cells	Total simulated time	Approximate wall clock time
NHWAVE	3	Intel Xeon 192 cores*	10 m	920 × 660	600 s	12 h
Multilayer-HySEA NH-RL	1	NVIDIA P100**	10 m	920 × 660	600 s	1 h
	3		10 m			3 h
	5		10 m			5 h
	20		40 m	230 × 165		30 min
Multilayer-HySEA Hydro	1/3/5	NVIDIA P100**	10 m	920 × 660	600 s	<10 min

**16 × Intel(R) Xeon(R) CPU E5-2630 v3, 2.40 GHz, 192 cores, peak performance 2.5 TFLOPS (=10^9 Floating Point Operations Per Second). **NVIDIA Tesla P100 16GB, 3584 CUDA cores, peak performance 4.7 TFLOPS.*

TABLE 5 | Geometric and physical parameters characterizing the three scenarios of a submarine landslide studied by Fornaciai et al. (2019).

Parameter	Value
X, *Y* position of the lanslide center (WGS84, UTM 33)	517563, 4295449
Width, Length (m)	670, 670
Initial depth (m)	293
Thickness (m)	45.0 / 74.7 / 112.0
Volume (m^3)	7.1 / 11.8 / 17.6 $\times 10^6$
X, *Y* position of gauge 1 (WGS84, UTM 33)	516788, 4294437
X, *Y* position of gauge 2	518427, 4296006
X, *Y* position of gauge 3	520359, 4295865
X, *Y* position of gauge 4	521804, 4296463
Landslide density (kg/m^3)	2,600
Water density (kg/m^3)	1,000
*Global drag coefficient C_d	1.0
*Added mass coefficient C_m	1.0
*Coulomb friction coefficient C_n	0.0
**Pouliquen and Forterre (2002) friction coefficients μ	0.02–0.18
**Manning coefficient ξ	0.03

**Indicates parameters used for the RL model. ** Indicates parameters used only for the GL model.*

3. RESULTS

3.1. Waveforms

Because we take as a reference for our benchmark the scenarios discussed and simulations performed by Fornaciai et al. (2019) with the rigid landslide model, we first analyse the sensitivity of the numerical results to the wave model with the same rigid landslide source. **Figure 3** reports the simulated waves at the Punta dei Corvi proximal gauge (gauge 1), for the three simulated volumes of the rigid submarine landslide (7.1, 11.8, and 17.6 × 10^6 m^3). We first observe that the waveform amplitude is directly correlated with the landslide volume, whereas the frequency content is almost independent, showing almost identical sequences of local maxima and minima in the three scenarios. Independency of the wave form on the landslide volume is also observable at the more distal gauge (gauge 4 at Strombolicchio; **Figure 4**). Waveforms at gauges 2 and 3 are shown in the **Supplementary Material**.

3.1.1. Effect of the Algorithm and Implementation: NHWAVE vs. Multilayer-HySEA With 3 Layers

As described above, NHWAVE and Multilayer-HySEA models are equivalent from the point of view of the physical formulation (both for the wave and for the source). In particular, the viscous and turbulent viscosity terms (not present in Multilayer-HySEA) are set to zero in this application of NHWAVE. The numerical approximations can also be demonstrated to be mathematically equivalent (cf. Fernández-Nieto et al., 2018; Escalante et al., 2019). Differences between the results are therefore attributable mostly to the different numerical implementations, the accuracy of the discretization and the resolution algorithm.

Continuous black and red lines in **Figures 3**, **4** compare the results obtained, at a resolution of 10 m, with both models using 3 layers (as in Fornaciai et al., 2019), sampled at gauges 1 and 4. The waveforms obtained with the NHWAVE 3-layers and Multilayer-HySEA 3-layers models are very similar both in amplitude and over time, at least as regards the first peaks and the absolute maximum/minimum, for the three simulated triggering volumes. The same is observed for the two other sampling points shown in the **Supplementary Material**. This result was expected since the two models are mathematically equivalent. Differences observable in the rest of the wavetrain are possibly associated with reflections and the combined effect of the threshold of minimum depth for wet/dry condition, which was 1 m for NHWAVE and 0.01 m for Multilayer-HySEA. This is especially true at gauge 1, close to the shoreline. At gauge 4, wave oscillations are less influenced by near-shore effects but are influenced by diffraction by the corner of the island (at Punta Labronzo, near gauge 2—**Figure 2**).

3.1.2. Vertical Resolution Effects: Non-hydrostatic Multilayer-HySEA 1 vs. 3 Layers, With a Rigid Landslide

The comparison between the results of the Multilayer-HySEA non-hydrostatic model with different numbers of layers is aimed at evaluating the physical approximations (in particular, that of "long waves") in the presence of steep bathymetric slopes where three-dimensional effects and dispersive terms should be relevant. Indeed, adding more layers usually allow to relax the shallow-water approximation (Macías et al., 2020a). **Figures 3**, **4** show the comparisons obtained with the high-resolution models (10 m). Simulations with 20 layers (computationally

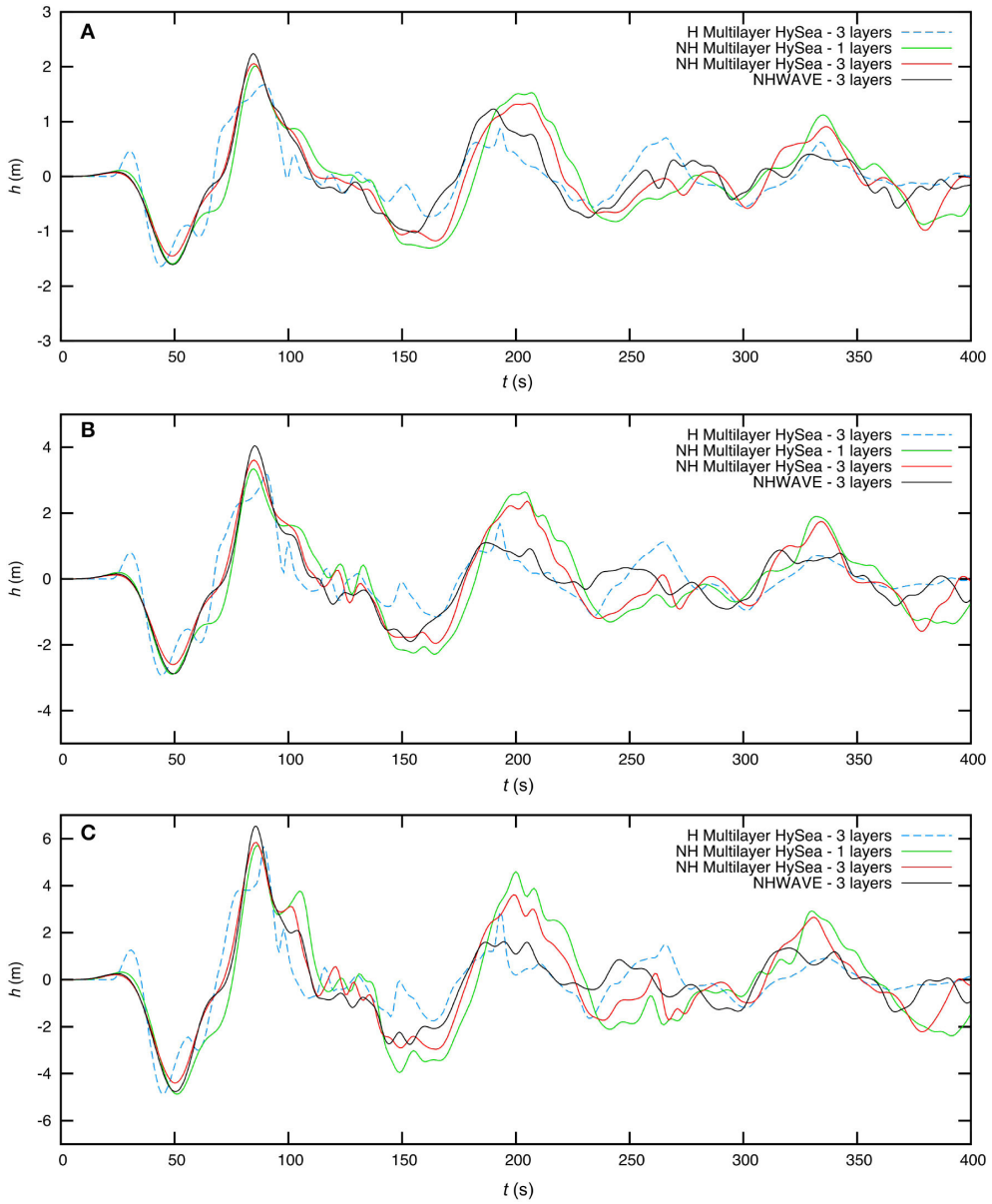

FIGURE 3 | Wave forms at gauge 1 simulated with different wave models with a rigid landslide **(A)** $V = 7.1 \times 10^6$ m^3, **(B)** $V = 11.8 \times 10^6$ m^3, and **(C)** $V = 17.6 \times 10^6$ m^3.

more demanding) are carried out only at low resolution (40 m) to ascertain the numerical convergence of the models to almost indistinguishable waveforms for $N > 3$ (cf. the **Supplementary Material**). Changing between 1 and 3 layers, differences in non-hydrostatic model results are relatively small for the first positive and negative peaks, but slightly increase for the subsequent oscillations in the proximal and more distal regions (for $t > 300$ s).

All non-hydrostatic models display a growing water crest above the submarine landslide, which moves at the same velocity and along the same trajectory of the landslide, without propagating in other directions. This effect is associated with the deepening of the bathymetry along the landslide trajectory, which makes the long-wave approximation weaker. It is due to the approximate dispersion laws in the dispersive, non-hydrostatic model, occurring for short wavelengths ($H/\lambda > 1$) (Escalante et al., 2019; Macías et al., 2020a). The phenomenon is greatly reduced by the use of a higher number of layers and, in this case and for the simulated domain, it almost disappears for $N > 5$.

3.1.3. Dispersive Effects: Multilayer-HySEA 3 Layers, Non-hydrostatic vs. Hydrostatic

The comparison between Multilayer-HySEA non-hydrostatic vs. hydrostatic, both with three vertical layers, is aimed at assessing

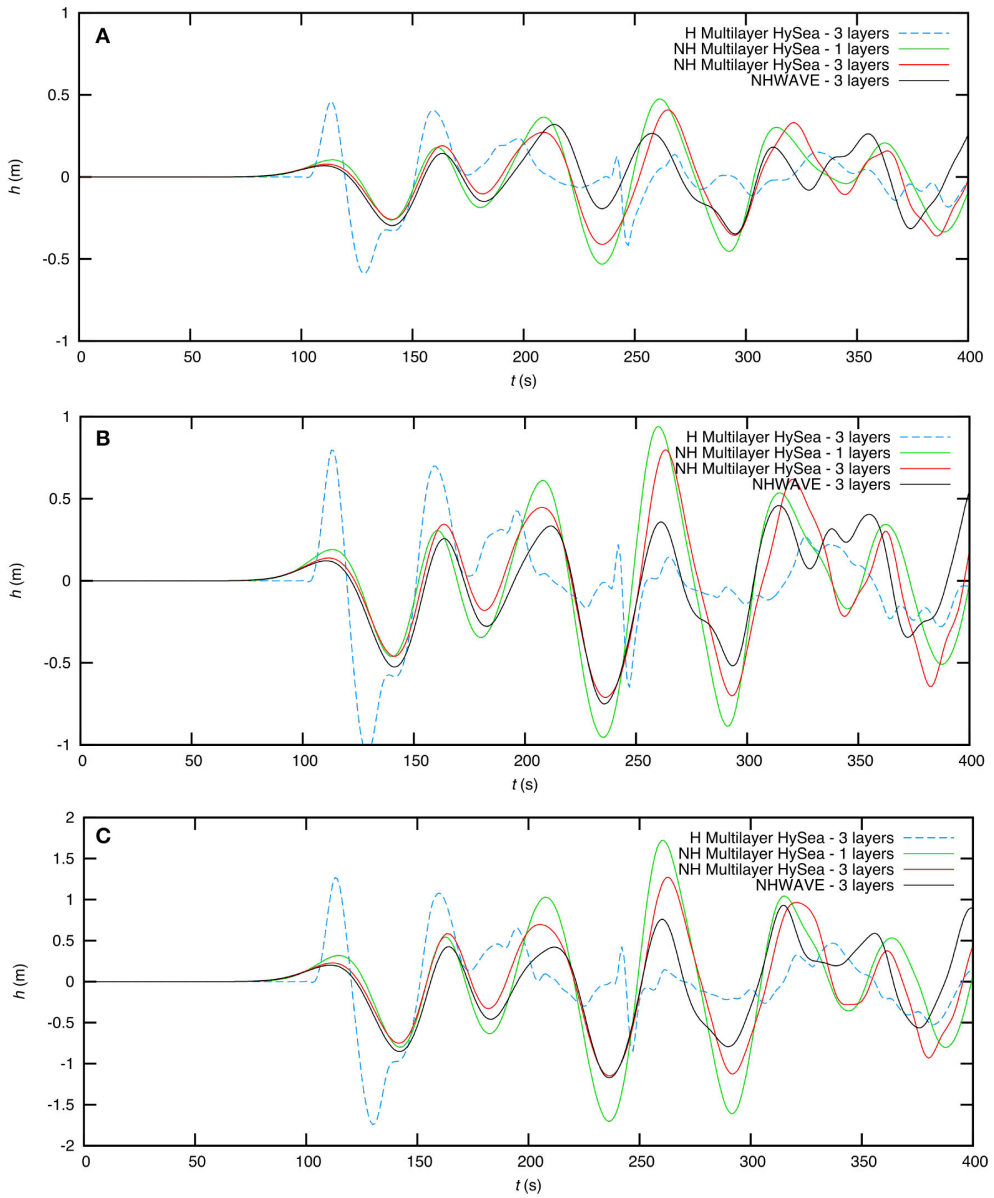

FIGURE 4 | Wave forms at gauge 4 simulated with different wave models with a rigid landslide **(A)** $V = 7.1 \times 10^6$ m^3, **(B)** $V = 11.8 \times 10^6$ m^3, and **(C)** $V = 17.6 \times 10^6$ m^3.

the suitability of the hydrostatic model (which is much more efficient from a computational point of view and attractive in the perspective of early-warning applications) for the simulation of near fields and waveforms. It should be noted that simulations with the 1, 3, or 5 layers hydrostatic model produce identical results, as regards to both the inundation height and waveforms. As expected, the waveforms generated by the hydrostatic models are significantly different from those obtained with the non-hydrostatic models. In particular, a significant increase of the first relative maximum of the leading crest is observed for the hydrostatic models (at about 40 s at gauge 1; **Figure 3**). This maximum is progressively amplified and becomes the absolute maximum at the most distal sampling points (**Figure 4**). Moreover, a general divergence of the waveforms is observed for longer times, as associated with the different phase velocity with respect to non-hydrostatic models.

To quantify the effect of the hydrostatic/non-hydrostatic approximation on the proximal (near-shore) waveforms (where monitoring gauges are installed), we have extracted the amplitude of wave minima and maxima and their time of arrival after the triggering of the landslide. In this analysis, we have not considered the positive local maximum of the first crest, since we have already noticed that hydrostatic models have the tendency to largely increase its amplitude. Moreover, to avoid considering

all the local amplitude fluctuations, we have set the minimum amplitude fluctuation to 0.66 m (0.55 m for hydrostatic models), which is approximately equal to the amplitude of the last maximum. **Table 6** reports the values of the first negative minimum and first positive maximum, and the amplitude and half period of the first, second, and third waves oscillations. Inspection of the results suggests that, beyond increasing the amplitude of the leading positive crest, the hydrostatic model overestimates the period of the first and largest oscillation, and it significantly decreases the amplitude of the second and third ones at the proximal locations.

3.1.4. Source Effects: Multilayer-HySEA Hydrostatic/Non-hydrostatic With Rigid or Granular Landslide

Figure 5 shows the comparison between waveforms obtained with either a RL or a GL model coupled with either the hydrostatic and non-hydrostatic Multilayer-HySEA wave model, at gauge 1, close to the landslide source. The initial geometric conditions (the volume and shape of the sliding mass, initially at rest) and vertical discretization (3 layers) are the same for the two models, and the friction and density contrasts are set within a comparable range: the differences between the simulated waveforms are only due to the different slide dynamics. For the RL model, the kinematics is prescribed by Equation (1) whereas the GL model computes the motion of a deformable granular fluid with Coulomb rheology.

The difference associated with the landslide (rigid or granular) source model is comparable to (but somehow larger than) that between the hydrostatic and non-hydrostatic results. At the most proximal gauge (**Figure 5**), the outcoming wave features a small leading crest followed by an intense depression, typical of submarine landslides. As expected, the leading crest is amplified by the hydrostatic model, more pronouncedly for the rigid landslide case. For the granular model, the first wave depression is deeper, but it is followed by a lower positive peak, resulting in a comparable wave height during the first oscillation. The main wave period appears to be comparable between the two models. As already discussed for **Figure 3**, the hydrostatic approximation, in both cases, produces a strong amplification of the leading crest.

3.1.5. Vertical Resolution Effects: Non-hydrostatic Multilayer-HySEA 3, 5, 10 Layers, With a Granular Landslide

As for the RL model, the use of many layers $N > 3$ for the GL model does not significantly change the waveform and the wave height, although some variations in the amplitude of minima and maxima can be noticed. **Table 7** reports the amplitude and time of the relative and absolute maxima and minima. To better quantify the influence of the vertical discretization on the wave features, in the **Supplementary Material** we show the waveforms obtained with Multilayer-HySEA with a granular landslide at gauge 1, with different vertical discretization from 3 to 10 layers. Amplitude of the first maximum can be up to 30% higher using 10 layers, but this is partly balanced by a slightly higher negative minimum. On the contrary, the time of the first maximum/minimum is almost identical in the three cases.

Figure 6 displays a rendering of the wave propagation and landslide position from 100 to 400 s, for the 17.6×10^6 m^3 granular landslide. The comparison among the three different volumes can be seen in the animated results provided in the **Supplementary Material**.

3.2. Maximum Surface Elevation and Potential Inundation

The simulation of the inundation process and the actual tsunami runup is very sensitive to the topo-bathymetric resolution, to sub-grid models describing turbulent processes at a scale smaller than the grid size (in our model, this is not considered), and to the minimum thickness threshold specified for the resolution of the wet/dry threshold. The use of a high threshold parameter (1 m thickness) was necessary in our study to ensure the convergence of the NHWAVE model on the complex topo-bathymetry of Stromboli, whereas the Multilayer-HySEA model converged with a thickness threshold of 0.01 m. **Figure 7** reports the maximum tsunami runup (i.e., the maximum surface elevation along a transect perpendicular to the coastline) along the coastline, simulated with Multilayer-HySEA and NHWAVE with a rigid landslide, for the three analyzed scenarios. The comparison between the maximum surface elevation simulated with NHWAVE 3 layers and Multilayer-HySEA 3 layers shows a good consistency in their average values. However, these models present some local differences where Multilayer-HySEA 3 layers, with respect to NHWAVE, seems to predict lower values.

At a qualitative level, it is observed that in both cases the best agreement with the observations on the field data (Maramai et al., 2005a; Tinti et al., 2005) is obtained with a volume of 17.6×10^6 m^3 (Fornaciai et al., 2019), consistent with the field estimates (Chiocci et al., 2008). In this region of the island, just behind Punta Labronzo headland, the wave height is very sensitive to the mechanism of reflection/diffraction, which in turn depends sensibly on the wet/dry threshold. Uncertainty of the results is therefore difficult to estimate. A detailed future study of the runups near the coast will clarify the role of this phenomenon in the runup estimates in Stromboli.

Results obtained with hydrostatic and non-hydrostatic formulations are comparable in amplitude and average value even if they are partially out of phase. The non-hydrostatic 1-layer model, compared to the 3-layer model in **Figure 7**, produces higher runups, probably due to inaccurate approximation of the phase velocity for short wavelengths onshore (Escalante et al., 2019; Macías et al., 2020a).

The GL model predicts smaller waves than the RL model, and a minor coastal inundation. To reproduce the inundation data reported by Fornaciai et al. (2019), a higher landslide volume of 25×10^6 m^3 was necessary. **Figure 8A** presents a map of maximum surface elevation and arrival times for a granular landslide of 17.6×10^6 m^3, to be compared with Figure 4 by Fornaciai et al. (2019). **Figure 8B** reports the maximum surface elevation at the coastline, together with the sampled runup at a number of sites (Maramai et al., 2005a; Tinti et al., 2005). Accordingly to this result, the best agreement with the observations is obtained with a volume of 25×10^6 m^3 (Fornaciai

TABLE 6 | Wave minima and maxima with respect to the average sea level at gauge 1, characterized by the time after landslide release (t) and surface elevation (h).

V (m^3)	Model	1st Min t (s), h (m)	1st Max t (s), h (m)	1st Δ Δt (s), Δh (m)	2nd Δ Δt (s), Δh (m)	3nd Δ Δt (s), Δh (m)
7.1×10^6	3H-RL	44, −1.65	90, 1.67	46, 3.32	32, 1.60	31, 1.26
	3NH-RL	49, −1.45	85, 2.06	36, 3.51	41, 2.51	101, 1.58
11.8×10^6	3H-RL	44, −2.93	90, 3.19	46, 6.12	28, 2.83	31, 2.24
	3NH-RL	49, −2.60	85, 3.61	36, 6.22	40, 4.33	98, 2.95
17.6×10^6	3H-RL	45, −4.87	89, 5.65	44, 10.52	29, 4.66	33, 3.13
	3NH-RL	50, −4.40	86, 5.84	36, 10.24	34, 6.57	93, 4.38

The Δ(·) refer to the difference between the first, second, and third minimum-maximum sequence. The period of each of these pulses is $T = 2\Delta t$. The results are obtained by using the Multilayer-HySEA (mH-RL and mNH-RL, 3 layers) for three different volumes of rigid landslides.

TABLE 7 | Wave minima and maxima with respect to the average sea level at gauge 1, characterized by the time after landslide release (t) and surface elevation (h).

V (m^3)	Model	1st Min t (s), h (m)	1st Max t (s), h (m)	1st Δ Δt (s), Δh (m)	2nd Δ Δt (s), Δh (m)	3nd Δ Δt (s), Δh (m)
7.1×10^6	3NH-GL	46, −1.93	96, 1.28	50, 3.21	30, 1.57	34, 1.00
	5NH-GL	46, −1.85	78, 1.49	32, 3.34	30, 1.58	34, 1.06
	10NH-GL	46, −1.78	78, 1.68	32, 3.46	30, 1.58	34, 1.11
11.8×10^6	3NH-GL	46, −3.43	96, 2.61	50, 6.04	30, 2.65	34, 1.71
	5NH-GL	46, −3.29	80, 2.64	34, 5.94	28, 2.59	34, 1.81
	10NH-GL	46, −3.18	80, 2.89	34, 6.07	30, 2.57	34, 1.89
17.6×10^6	3NH-GL	46, −5.65	96, 4.28	50, 9.93	28, 3.70	38, 2.44
	5NH-GL	46, −5.44	80, 4.24	34, 9.68	28, 3.61	36, 2.57
	10NH-GL	40, −5.27	80, 4.65	34, 9.92	30, 3.57	36, 2.63

The Δ(·) refer to the difference between the first, second, and third minimum-maximum sequence. The period of each of these pulses is $T = 2\Delta t$. The results are obtained by using the Multilayer-HySEA (mNH-GL, 3, 5, and 10 layers) for three different volumes of granular landslide.

et al., 2019), slightly larger but still consistent with the field estimates (Chiocci et al., 2008).

4. DISCUSSION

The comparison study carried out in this work is aimed at identifying the most effective modeling strategy to simulate the waveforms generated by submarine landslides occurring at the SdF, a necessary preliminary step to calibrate a warning system based on proximal sea level measurements. In the case of a tsunamigenic event, this approach would be used to reconstruct the source of the detected waves, and to quickly forecast the subsequent impact on the Island of Stromboli, on the nearby Aeolian Archipelago and on the Southern Tyrrhenian Sea shores.

The observation of a correlation between wave height and landslide volume is consistent with some historical observations (Murty, 2003) and theoretical predictions of landslide-generated tsunamis. In particular, Ruff (2003) demonstrated that submarine landslides produce wave heights related to block height, and have wavelengths that scale with block width. By considering a block with uniform thickness moving on a horizontal seabed with constant velocity, Haugen et al. (2005) also showed that the length of the block affects only the wavelength, while the wave height is determined by the thickness of the block, the landslide velocity, and the wave speed (which depends on the water depth). The same dependency was found by Løvholt et al. (2005), for landslides characterized by slow propagation or occurring in sufficiently deep water (i.e., low Froude number; Harbitz et al., 2006). The new results indicate that such a correlation might hold also for deformable (granular) landslides, whose dynamics is governed by gravity, internal and bottom friction, and interaction with the water column. In particular, the wave height scales with the landslide volume (or initial thickness), as predicted by simpler theories, whereas the wavelength is almost independent of the volume. The influence of the initial submergence of the slide, which is a key parameter for the tsunami generation (Løvholt et al., 2005), has not been addressed in this work (the initial position was fixed following the indications given by Chiocci et al., 2008, for the 2002 event).

Differently from subaerial landslides, which produce a first large positive wave, submarine slides produce a first negative wave that propagates as an edge wave around the island causing water to first withdraw (Romano et al., 2016). The animations provided in the **Supplementary Material** clearly show, as expected, a first negative wave propagating around the island, followed by the arrival of positive waves. The analysis of the waveforms indicates that non-hydrostatic models produce coherent predictions among each other, and that the use of more than 3 layers does not significantly change the features

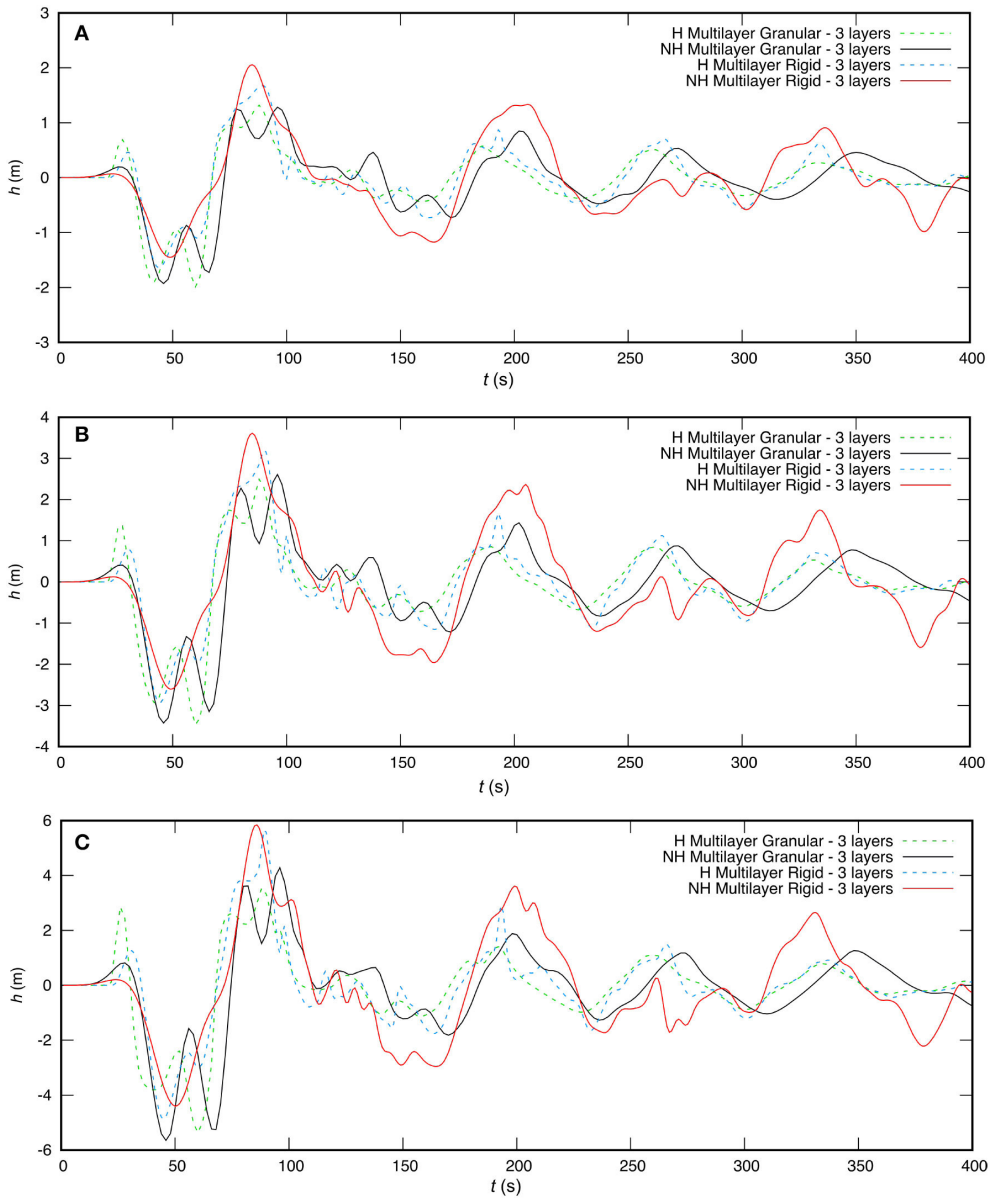

FIGURE 5 | Wave forms at gauge 1 simulated with a hydrostatic and non-hydrostatic Multilayer-HySEA model with either a rigid or a granular landslide, and three vertical layers. The three subplots are for different landslide volumes: **(A)** $V = 7.1 \times 10^6$ m^3, **(B)** $V = 11.8 \times 10^6$ m^3, and **(C)** $V = 17.6 \times 10^6$ m^3.

of the proximal waves. The hydrostatic model predicts a first minimum and maximum of the wave at the proximal gauges (which is usually the first peak) consistently with the non-hydrostatic models, but on the contrary it delays the wave propagation, producing different waveforms at later times and lower amplitudes. In addition, the hydrostatic model predicts a larger leading crest, whose amplitude increases with the distance. Although, a priori, it is difficult to evaluate which solution is physically better in a comparison study, the tests carried out on the LTMBW (2017) model benchmark (Macías et al., 2020a) confirm that the form of landslide-generated waves cannot be accurately reproduced by a hydrostatic model (shallow water equations) or even with a one-layer non-hydrostatic model. Schambach et al. (2019) also compared the landslide tsunami simulations with and without dispersion (i.e., hydrostatic vs. non-hydrostatic results for both NHWAVE and FUNWAVE) in the near- ad far-field. For the very large slide volumes considered, they showed moderate dispersive effects in the near-field but very large differences caused by dispersion in the far-field. In our simulations, non-hydrostatic models can introduce spurious shoaling phenomena when the water depth changes in response to bathymetric variations, due to the increase of the relative error in the phase dispersion relations when H/λ increases. This phenomenon (which locally causes wave maxima) is however

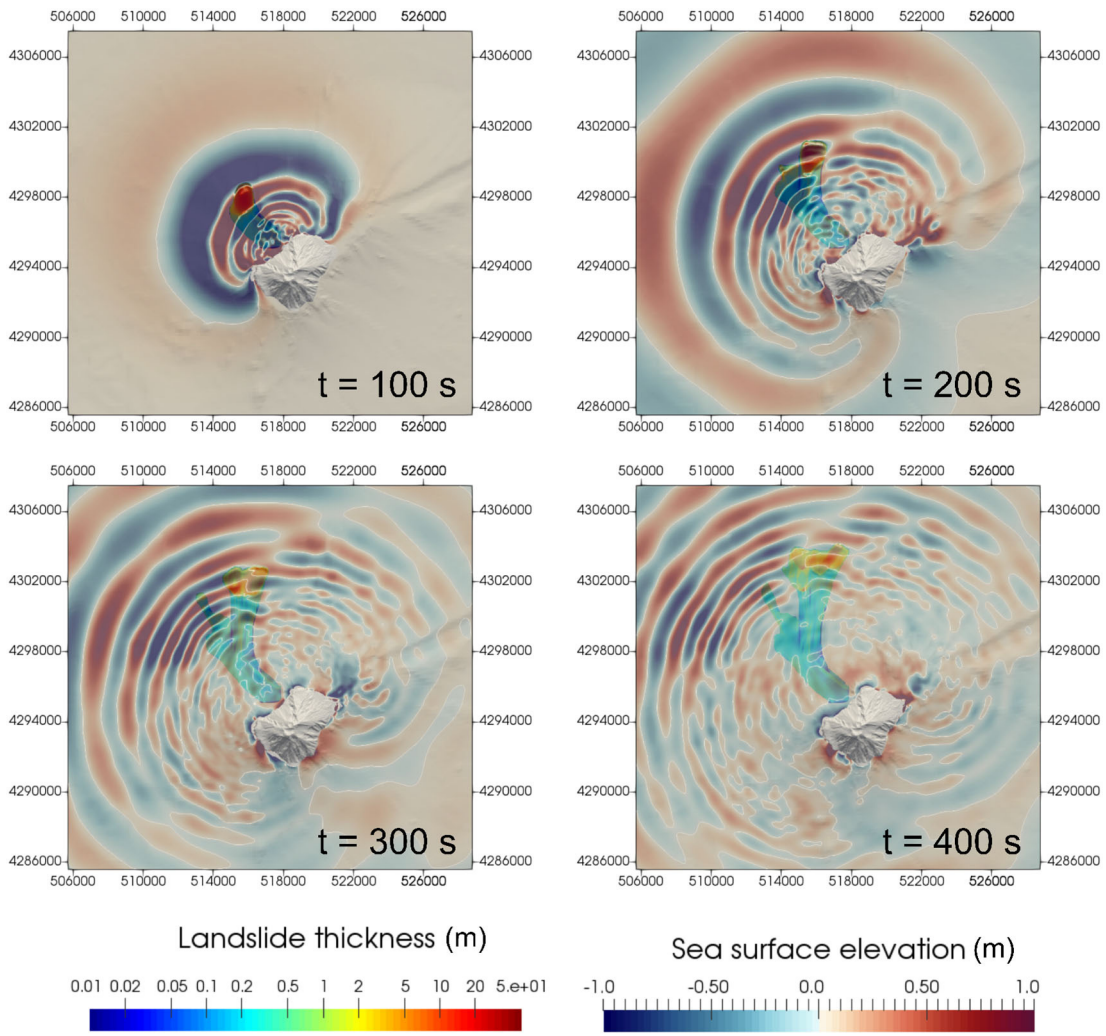

FIGURE 6 | Sea surface elevation and landslide thickness simulated with the Multilayer-HySEA-GL model, with a landslide volume of 17.6×10^6 m^3 and three vertical layers. At $t = 400$ s the landslide has reached its maximum runout and has almost completely stopped.

greatly reduced by using more than 5 layers, reducing the error to about 0.1% for kH up to 15 (k being the wavenumber), or $H/\lambda < 2.4$ (cf. Macías et al., 2020a) and it almost completely disappears with 10 layers.

The maximum surface elevation near the coastline is strongly affected by refraction and diffraction processes, and by shoaling effects (Ma et al., 2012), which justify the use of non-hydrostatic models able to account for a vertical component of the velocity (Zijlema and Stelling, 2008; Young and Wu, 2009). However, accurate modeling of near-shore dynamics might require the introduction of a turbulent stress term, to represent three-dimensional shear cascade and breaking of the fronts (Grilli and Watts, 2005). This will be the subject of future investigations.

The main comparisons in this work were made using a RL model. However, comparison of the results obtained with the RL and GL models shows that the two landslide models are not equivalent (although describing the same mobilized volume), and that the uncertainty associated with the trigger model is as relevant as that introduced by the water wave model (cf. **Figure 5**). The kinematic model for the rigid landslide was originally proposed by Watts (1998) not only for solid landslides but also for a deformable granular mass, with laboratory experiments (e.g., Grilli and Watts, 2005) suggesting that the center of mass motion in a deformable landslide moves in the same manner as a solid block. More recent results however report that RL models generally predict higher waves (Yavari-Ramshe and Ataie-Ashtiani, 2016; Schambach et al., 2019). Also in our simulations, for both the hydrostatic and non-hydrostatic cases the GL model shows a lower tsunamigenic potential. However, it is worth remarking that the amount of energy available to excite the wave obviously depends on the prescribed kinematics of the submarine rigid landslide. Analogously, for submarine granular landslides the rheological parameters (the angle of friction, the Manning coefficient;

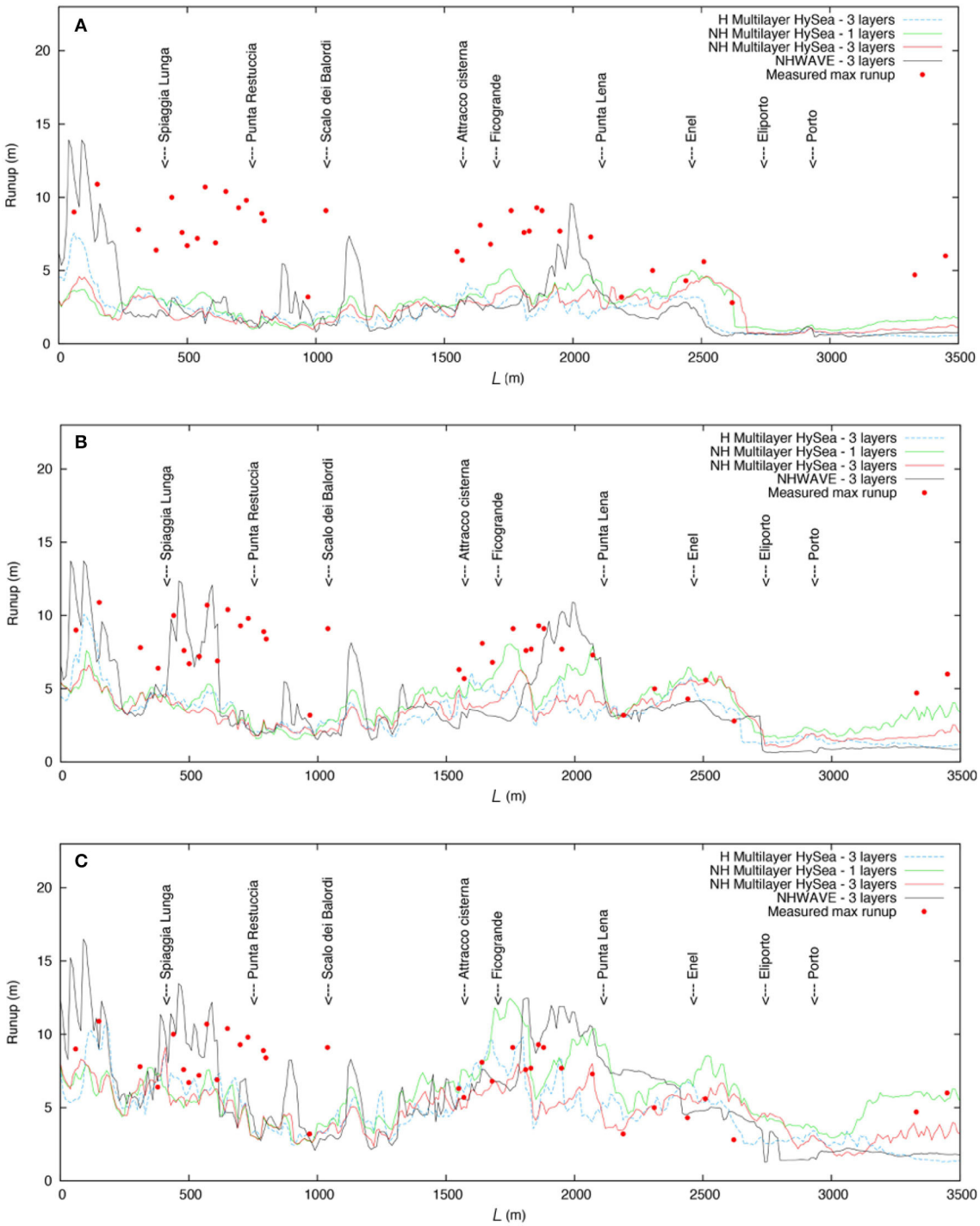

FIGURE 7 | Tsunami maximum runup along the stretch of coastline represented by the white solid line in **Figure 8**, obtained with different wave models with a RL model **(A)** $V = 7.1 \times 10^6$ m^3, **(B)** $V = 11.8 \times 10^6$ m^3, and **(C)** $V = 17.6 \times 10^6$ m^3.

Table 5) would require prior calibration. Whereas, for subaerial granular flows several experimental (Fritz et al., 2004; Heller and Hager, 2011; Mohammed and Fritz, 2012; Heller and Spinneken, 2013; Bougouin et al., 2020) and numerical (Ruffini et al., 2019) works exist, systematic studies on subacqueous deformable granular landslides are less developed (Yavari-Ramshe and Ataie-Ashtiani, 2017). Grilli et al. (2017) presented and modeled lab experiments for underwater granular flows. They and Schambach et al. (2019) compared the generation of tsunamis by solid and granular slides of same initial geometry and compared also

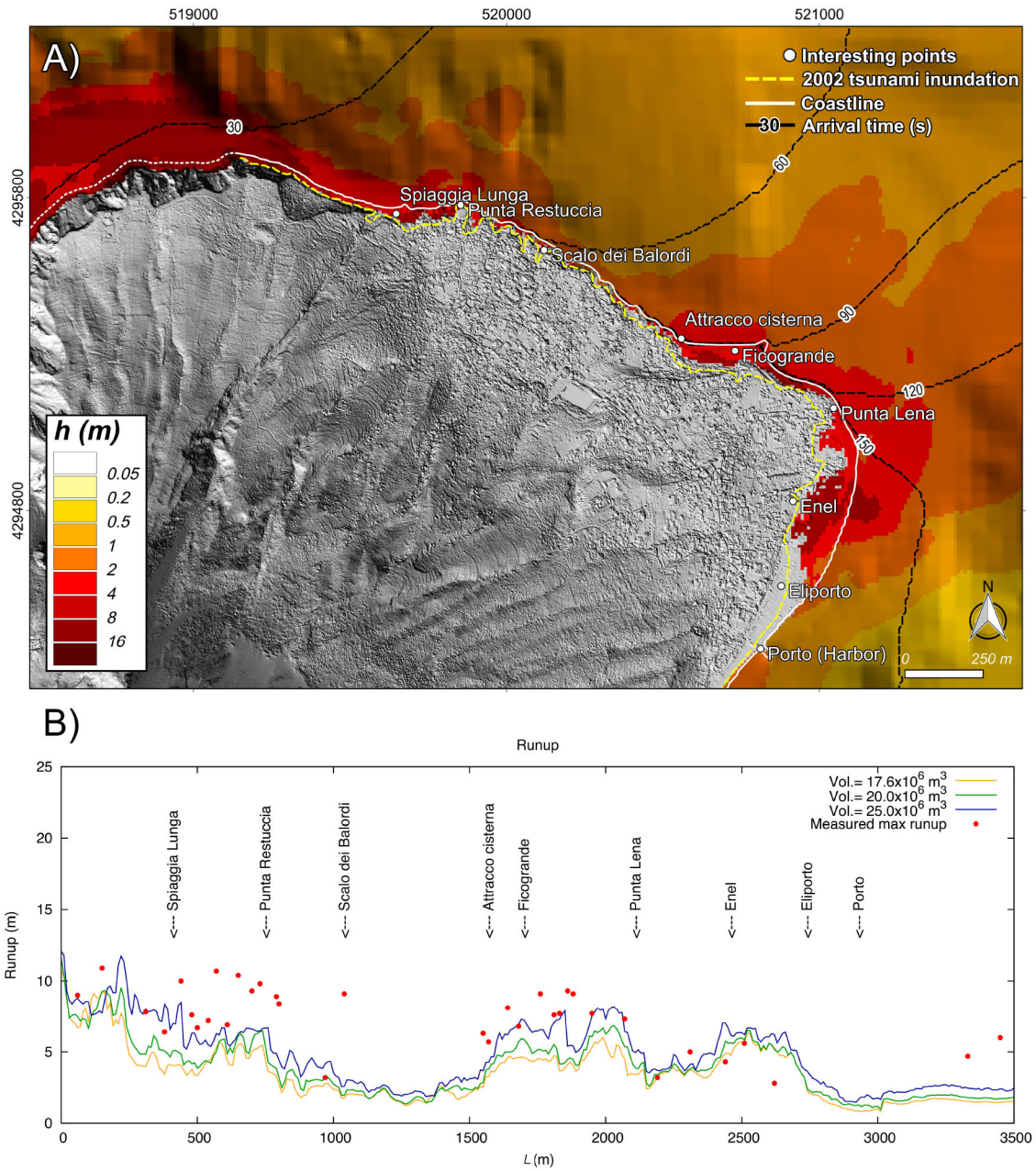

FIGURE 8 | (A) Maximum surface elevation of the tsunami generated by a submarine granular landslide of volume $V = 17.6 \times 10^6$ m^3. **(B)** Maximum runup obtained with Multilayer-HySEA and granular landslide volumes of $V = 17.6, 20.0$, and 25.0×10^6 m^3, with 3 layers. Red points represent the measurements reported by Tinti et al. (2006) of the tsunami runup for the 2002 event at Stromboli.

their center of mass motion. They showed that solid slides cause larger waves and runup. Although it is likely that the granular model provides a better representation of flow processes potentially generated by submarine landslides at Stromboli, it is still difficult to define a priori (in the absence of direct measures on the real phenomenon) which one is more realistic. For this reason, current line of research for future studies has been oriented toward developing validation studies for both the RL and GL models implemented in Multilayer-HySEA (Macías et al., 2020a,b).

Distal wave fields (>10 km) have not yet been addressed in this work. Extension of the domain to the whole Southern Tyrrhenian Sea would require nesting of different computational approaches, models and grid resolution to be effective (Fornaciai et al., 2019; Grilli et al., 2019). Simple scaling considerations suggest that the non-hydrostatic model would be necessary also to simulate

the wave propagation stage of landslide-generated tsunamis from Stromboli. Indeed, it is generally considered (cf. Bowden, 1983) that the long-wave approximation leading to the shallow-water (hydrostatic) model can be applied to regimes of $H/\lambda < 0.05$, i.e., in the case of the Southern Tyrrenian sea (with depths as those of **Figure 1**), a wavelength larger than 50–100 km. As seen, e.g., in **Figure 6**, a landslide from the Sciara del Fuoco would generate tsunamis with shorter wavelengths, increasing up to about 6 km on the domain boundaries. Even considering the further development of long-wave components by the effects of bathymetric variations and frequency dispersion, most of the wave propagation in the Southern Tyrrhenian Sea would likely occur in an intermediate regime $0.05 < H/\lambda \sim 1$. Fornaciai et al. (2019) estimated that waves generated by landslide at the SdF would be able to reach the first Stromboli populated beaches in just over 1 min and the harbor in <7 min. After about 30 min the whole Aeolian Arc would be impacted by maximum waves. After 1 h and 20 min, waves would encompass the whole Southern Tyrrhenian Sea arriving at Capri island. This leaves very little time for evacuating the coastal population, and makes it difficult to design an effective Tsunami Early Warning Systems (TEWS) (Selva et al., 2021).

Possible alternative approaches to the three-dimensional solution of the water equations and the granular landslide have been proposed by others, especially in the light of designing effective TEWS for landslide-generated tsunamis, also for volcanic islands. Ward (2001) has first proposed a linear solution for landslide-generated tsunami, based on the superposition of many small simple "square" slides for which a Green's function can be calculated analytically. This has been applied also to potential collapse of the Cumbre Vieja volcano (Ward and Day, 2001). A similar approach has recently been adopted by Wang et al. (2019) to reproduce the tsunami induced by the 1792 Unzen-Mayuyama mega-slide in Japan. Cecioni and Bellotti (2010) have proposed a near-field extension of the Bellotti et al. (2008)'s far-field propagation model based on the Mild Slope Equations, applied to tsunami propagation at Stromboli. Such an approach, based on the inclusion of a new wave source term representing the moving bottom boundary, has the advantage of giving an accurate solution in the far-field without needing many layers and to be accurate enough in the near-field. This is constrained by the approximate description of the source model and it has been tested only for a rigid landslide model. Another alternative approach is to use analytical models to describe the tsunami source, and using single layer wave models for the distal propagation (Liu et al., 2020). However, nowadays, numerical solvers exploiting GPUs allow to achieve unprecedented simulation speed-up and make it possible to approach three-dimensional (multilayer) simulations of tsunamis generated by a granular landslide at Stromboli, and their propagation across the Southern Tyrrhenian Sea. At the same time, three-dimensional simulations will potentially provide a way to interpret proximal waveforms registered by the two elastic gauges installed offshore the Sciara del Fuoco.

Data presented in **Table 4** are relative to simulations performed at high resolution and on a relatively small domain of a few square kilometers encompassing the island of Stromboli. Despite execution times are still too large for early-warning (real-time) applications, recent developments of multi-GPU computing for the numerical tsunami models (Escalante et al., 2018) have allowed to significantly speed-up the code execution. These developments will likely make the faster-than-real-time simulation of volcano-landslide-tsunami generation and propagation possible in the future, opening new avenues to urgent tsunami computing, probabilistic tsunami hazard assessment and tsunami early warning (Løvholt et al., 2019; Macías and de la Asunción, 2019).

5. CONCLUSION

We have presented a synthetic benchmark (or model inter-comparison) study aimed at quantifying the impact of different physical and numerical approximations on the resulting waveforms and tsunami inundation patterns at Stromboli, and identifying the most effective trade-off between computational cost and model accuracy. We have taken as a reference the 2002 scenario described by Fornaciai et al. (2019) and assessed the relative sensitivity of numerical predictions to the landslide and the wave models. Present results and comparison with previously published data clearly indicate that dispersive non-hydrostatic models are better suited to reproduce proximal wave forms of landslide-generated tsunamis, and that using multiple layers (three being the optimal compromise in our tests) improves the quality of predictions. To extend numerical prediction to larger domains (characterized by deeper water), different strategies should be adopted. Further studies and technological developments are needed to address this point. In any case, it is apparent that the uncertainty of numerical model predictions associated with the landslide source model is as large as that of the wave model approximation: the comparison between a RL and GL model produces sensibly different results, in terms of wave amplitude, frequencies and attenuation. In the perspective of assimilating in a numerical model the measurement of sea level at the two gauges near the shore of the SdF, to trigger a Stromboli Tsunami Early Warning, it would therefore be important to adopt a coupled non-hydrostatic, multilayer wave model (implemented on GPU to reduce the time of simulation) with an accurate GL model. Future research should particularly focus on validation and calibration of the latter. The results of numerical simulations can be used as a preliminary calibration of the detection system currently operating at Stromboli Island, when direct measurements of waves generated by submarine landslides are not available.

During the course of this study, on July 3rd and August 28th 2019, two paroxysmal events (Giordano and De Astis, 2020; Giudicepietro et al., 2020) generated a sequence of pyroclastic avalanches along the SdF, which entered the sea. Water waves as high as 1 m near the entrance point were detected by the two gauges operated by Università di Firenze, and by a low-frequency mareometer off the coast of the Ginostra village. In a forthcoming work, we will report about the use of the results of the present study to analyze the waveforms produced by the entrance in the sea of pyroclastic avalanches.

DATA AVAILABILITY STATEMENT

The raw data supporting the conclusions of this article will be made available by the authors, upon request without undue reservation.

AUTHOR CONTRIBUTIONS

TE, MM, and AF have conceived the study and coordinated the project with the Italian Department of Civil Protection. MC and BC have contributed to the analysis of the physical approximations, simulation runs, and data analysis. MF, AF, and LN have run the NHWAVE model and provided comparison with previously published data. JM, MJC, SO, JG-V, and CE have developed and made available the HySEA software, their expertise in the interpretation of numerical model results and some computer time. All authors contributed to the article and approved the submitted version.

FUNDING

This work has been produced within the 2012–2021 agreement between Istituto Nazionale di Geofisica e Vulcanologia (INGV) and the Italian Presidenza del Consiglio dei Ministri, Dipartimento della Protezione Civile (DPC), Convenzione B2, Ob. 5 Task 4 (2017), Ob. 4 Task 4 (2018) and WP2 Task 12 (2019-2021). HySEA codes development is supported by the Spanish Government-FEDER funded project MEGAFLOW (RTI2018-096064-B-C21).

ACKNOWLEDGMENTS

We thank: S. Calvari and G. Macedonio (INGV) for the coordination of activities at INGV Centro di Pericolosità Vulcanica; A. Neri (Director of INGV Departments of Volcanoes) for supporting the project activities; D. Mangione and A. Ricciardi (Italian Department of Civil Protection) for discussion about implications for tsunami hazard and risk mitigation; M. Ripepe and G. Lacanna (University of Florence) for information about the gauges installation, the discussion about the Stromboli tsunami alert system and the requirements for its calibration. We thank the Editor JB and three referees for their meticulous reviews and further reading suggestions.

SUPPLEMENTARY MATERIAL

The Supplementary Material for this article can be found online at: https://www.frontiersin.org/articles/10.3389/feart.2021.628652/full#supplementary-material

The Supplementary material reports additional plots, videos, and data to support the paper's conclusions. In particular:

- the benchmark results at gauges 2 and 3 for a rigid landslide;
- the waveforms predicted by Multilayer-HySEA at gauges 1, 2, 3, and 4 for a rigid landslide and 1, 3, 5, and 10 layers;
- animated results of Multilayer-HySEA with a granular landslide, for different slide volumes.

REFERENCES

Auker, M. R., Sparks, R. S. J., Siebert, L., Crosweller, H. S., and Ewert, J. (2013). A statistical analysis of the global historical volcanic fatalities record. *J. Appl. Volcanol.* 2, 57–24. doi: 10.1186/2191-5040-2-2

Béget, J. (2000). "Volcanic tsunamis," in *Encyclopedia of Volcanoes*, eds H. Sigurdsson, B. Houghton, H. Rymer, J. Stix, and S. McNutt (London, UK: Academic Press), 1005–1014.

Bellotti, G., Cecioni, C., and De Girolamo, P. (2008). Simulation of small-amplitude frequency-dispersive transient waves by means of the mild-slope equation. *Coast. Eng.* 55, 447–458. doi: 10.1016/j.coastaleng.2007.12.006

Bellotti, G., and Romano, A. (2017). Wavenumber-frequency analysis of landslide-generated tsunamis at a conical island. Part II: EOF and modal analysis. *Coast. Eng.* 128, 84–91. doi: 10.1016/j.coastaleng.2017.07.008

Bisson, M., Pareschi, M. T., Zanchetta, G., Sulpizio, R., and Santacroce, R. (2007). Volcaniclastic debris-flow occurrences in the Campania region (Southern Italy) and their relation to Holocene–Late Pleistocene pyroclastic fall deposits: implications for large-scale hazard mapping. *Bull. Volcanol.* 70, 157–167. doi: 10.1007/s00445-007-0127-4

Bonaccorso, A., Calvari, S., Garfì, G., Lodato, L., and Patanè, D. (2003). Dynamics of the December 2002 flank failure and tsunami at Stromboli volcano inferred by volcanological and geophysical observations. *Geophys. Res. Lett.* 30:1941. doi: 10.1029/2003GL017702

Bougouin, A., Paris, R., and Roche, O. (2020). Impact of fluidized granular flows into water: implications for tsunamis generated by pyroclastic flows. *J. Geophys. Res. Sol. Earth* 125, 319–317. doi: 10.1029/2019JB018954

Bowden, K. F. (1983). *Physical Oceanography of Coastal Waters*. Somerset: E. Horwood.

Branney, M. J., and Kokelaar, B. P. (2002). *Pyroclastic Density Currents and the Sedimentation of Ignimbrites*. London, UK: Geological Society of London.

Casalbore, D., Romagnoli, C., Bosman, A., and Chiocci, F. L. (2011). Potential tsunamigenic landslides at Stromboli Volcano (Italy): insight from marine DEM analysis. *Geomorphology* 126, 42–50. doi: 10.1016/j.geomorph.2010.10.026

Cecioni, C., and Bellotti, G. (2010). Inclusion of landslide tsunamis generation into a depth integrated wave model. *Nat. Hazards Earth Syst. Sci.* 10, 2259–2268. doi: 10.5194/nhess-10-2259-2010

Chiocci, F. L., Romagnoli, C., Tommasi, P., and Bosman, A. (2008). The Stromboli 2002 tsunamigenic submarine slide: characteristics and possible failure mechanisms. *J. Geophys. Res.* 113, 173–111. doi: 10.1029/2007JB005172

Clare, M. A., Le Bas, T., Price, D. M., Hunt, J. E., Sear, D., Cartigny, M. J. B., et al. (2018). Complex and cascading triggering of submarine landslides and turbidity currents at volcanic islands revealed from integration of high-resolution onshore and offshore surveys. *Front. Earth Sci.* 6:223. doi: 10.3389/feart.2018.00223

De Lange, W. P., Prasetya, G. S., and Healy, T. R. (2001). Modelling of tsunamis generated by pyroclastic flows (ignimbrites). *Nat. Hazards* 24, 251–266. doi: 10.1023/A:1012056920155

Enet, F., and Grilli, S. T. (2007). Experimental study of tsunami generation by three-dimensional rigid underwater landslides. *J. Waterway Port Coast. Ocean Eng.* 133, 442–454. doi: 10.1061/(ASCE)0733-950X(2007)133:6(442)

Escalante, C., de Luna, T. M., and Castro, M. J. (2018). Non-hydrostatic pressure shallow flows: GPU implementation using finite volume and finite difference scheme. *Appl. Math. Comput.* 338, 631–659. doi: 10.1016/j.amc.2018.06.035

Escalante, C., Fernández-Nieto, E. D., de Luna, T. M., and Castro, M. J. (2019). An efficient two-layer non-hydrostatic approach for dispersive water waves. *J. Sci. Comput.* 79, 273–320. doi: 10.1007/s10915-018-0849-9

Fernández-Nieto, E. D., Bouchut, F., Bresch, D., Castro Díaz, M. J., and Mangeney, A. (2008). A new Savage–Hutter type model for submarine avalanches and generated tsunami. *J. Comput. Phys.* 227, 7720–7754. doi: 10.1016/j.jcp.2008.04.039

Fernández-Nieto, E. D., Parisot, M., Penel, Y., and Sainte-Marie, J. (2018). A hierarchy of dispersive layer-averaged approximations of Euler

equations for free surface flows. *Comm. Math. Sci*. 16, 1169–1202. doi: 10.4310/CMS.2018.v16.n5.a1

Fornaciai, A., Favalli, M., and Nannipieri, L. (2019). Numerical simulation of the tsunamis generated by the Sciara del Fuoco landslides (Stromboli Island, Italy). *Sci. Rep*. 9:18542. doi: 10.1038/s41598-019-54949-7

Freundt, A. (2003). Entrance of hot pyroclastic flows into the sea: experimental observations. *Bull. Volcanol*. 65, 144–164. doi: 10.1007/s00445-002-0250-1

Fritz, H. M., Hager, W. H., and Minor, H. E. (2004). Near field characteristics of landslide generated impulse waves. *J. Waterway Port Coast. Ocean Eng*. 130, 287–302. doi: 10.1061/(ASCE)0733-950X(2004)130:6(287)

Giordano, G., and De Astis, G. (2020). The summer 2019 basaltic Vulcanian eruptions (paroxysms) of Stromboli. *Bull. Volcanol*. 83:1. doi: 10.1007/s00445-020-01423-2

Giudicepietro, F., pez, C. L. x., Macedonio, G., Alparone, S., Bianco, F., Calvari, S., et al. (2020). Geophysical precursors of the July-August 2019 paroxysmal eruptive phase and their implications for Stromboli volcano (Italy) monitoring. *Sci. Rep*. 10:10296. doi: 10.1038/s41598-020-67220-1

Glimsdal, S., Pedersen, G. K., Harbitz, C. B., and Løvholt, F. (2013). Dispersion of tsunamis: does it really matter? *Nat. Hazards Earth Syst. Sci*. 13, 1507–1526. doi: 10.5194/nhess-13-1507-2013

González-Vida, J. M., Macías, J., Castro, M. J., Sánchez-Linares, C., de la Asunción, M., Ortega-Acosta, S., et al. (2019). The Lituya Bay landslide-generated mega-tsunami–numerical simulation and sensitivity analysis. *Nat. Hazards Earth Syst. Sci*. 19, 369–388. doi: 10.5194/nhess-19-369-2019

Grilli, S. T., O'Reilly, C., Harris, J. C., Bakhsh, T. T., Tehranirad, B., Banihashemi, S., et al. (2015). Modeling of SMF tsunami hazard along the upper US East Coast: detailed impact around Ocean City, MD. *Nat. Hazards* 76, 705–746. doi: 10.1007/s11069-014-1522-8

Grilli, S. T., Shelby, M., Kimmoun, O., Dupont, G., Nicolsky, D., Ma, G., et al. (2017). Modeling coastal tsunami hazard from submarine mass failures: effect of slide rheology, experimental validation, and case studies off the US East Coast. *Nat. Hazards* 86, 353–391. doi: 10.1007/s11069-016-2692-3

Grilli, S. T., Tappin, D. R., Carey, S., Watt, S. F. L., Ward, S. N., Grilli, A. R., et al. (2019). Modelling of the tsunami from the December 22 2018 lateral collapse of Anak Krakatau volcano in the Sunda Straits, Indonesia. *Sci. Rep*. 9:11946. doi: 10.1038/s41598-019-48327-6

Grilli, S. T., and Watts, P. (2005). Tsunami generation by submarine mass failure. I: modeling, experimental validation, and sensitivity analyses. *J. Waterway Port Coast. Ocean Eng*. 131, 283–297. doi: 10.1061/(ASCE)0733-950X(2005)131:6(283)

Guyenne, P., and Grilli, S. T. (2003). "Computations of three-dimensional overturning waves in shallow water: dynamics and kinematics," in *Proceedings of The Thirteenth International Offshore and Polar Engineering Conference* (Honolulu, HI), 1–6.

Harbitz, C. B., Løvholt, F., and Bungum, H. (2013). Submarine landslide tsunamis: how extreme and how likely? *Nat. Hazards* 72, 1341–1374. doi: 10.1007/s11069-013-0681-3

Harbitz, C. B., Løvholt, F., Pedersen, G. K., and Masson, D. G. (2006). Mechanisms of tsunami generation by submarine landslides: a short review. *Norw. J. Geol*. 86, 255–264.

Haugen, K. B., Løvholt, F., and Harbitz, C. B. (2005). Fundamental mechanisms for tsunami generation by submarine mass flows in idealised geometries. *Mar. Petrol. Geol*. 22, 209–217. doi: 10.1016/j.marpetgeo.2004.10.016

Heller, V., and Hager, W. H. (2011). Wave types of landslide generated impulse waves. *Ocean Eng*. 38, 630–640. doi: 10.1016/j.oceaneng.2010.12.010

Heller, V., and Spinneken, J. (2013). Improved landslide-tsunami prediction: effects of block model parameters and slide model. *J. Geophys. Res. Oceans* 118, 1489–1507. doi: 10.1002/jgrc.20099

Horrillo, J., Grilli, S. T., Nicolsky, D., Roeber, V., and Zhang, J. (2015). Performance benchmarking tsunami models for NTHMP's inundation mapping activities. *Pure Appl. Geophys*. 172, 869–884. doi: 10.1007/s00024-014-0891-y

Hungr, O., Corominas, J., and Eberhardt, E. (2005). "Estimating landslide motion mechanism, travel distance and velocity," in *Landslide Risk Management* (London, UK: CRC Press), 109–138. doi: 10.1201/9781439833711-7

INGV (2019). *Comunicato Straordinario Stromboli 04/07/2019*. Press release n.16, Istituto Nazionale di Geofisica e Vulcanologia. Available online at: http://www.ingv.it/it/stampa-e-urp/stampa/comunicati-stampa-1/2019/37-comunicato-straordinario-stromboli-\hbox04--07-\hbox2019--09-00-utc-aggiornamento-sul-fenomeno-in-corso/file

Kirby, J., Grilli, S., Zhang, C., Horrillo, J., Nicolsky, D., and Liu, P. L. F. (2018). *The NTHMP Landslide Tsunami Benchmark Workshop, Galveston, January 9–11 2017*. Technical Report, Center for Applied Coastal Research.

Lacanna, G., and Ripepe, M. (2020). "Genesis of tsunami waves generated by pyroclastic flows and the early-warning system," in *Rittmann Conference 2020, Session S13. The Summer 2019 Stromboli Paroxysms:A Precious Opportunity to Expand the Knowledge on the Volcano* (Catania).

Latter, J. H. (1981). Tsunamis of volcanic origin: summary of causes, with particular reference to Krakatoa 1883. *Bull. Volcanol*. 44, 467–490. doi: 10.1007/BF02600578

LGS (2019a). *Esplosione parossistica del vulcano stromboli del 03/07/2019*. Report to the Italian Department of Civil Protection, Università di Firenze. Available online at: http://lgs.geo.unifi.it/index.php/reports/comunicati?view=document&id=7:esplosione-parossistica-03-07-2019&catid=14

LGS (2019b). *Esplosione parossistica del vulcano stromboli del 28/08/2019*. Report to the Italian Department of Civil Protection, Università di Firenze. Available online at: http://lgs.geo.unifi.it/index.php/reports/comunicati?view=document&id=8:esplosione-parossistica-28-08-2019&catid=14

Liu, P. L. F., Higuera, P., Husrin, S., Prasetya, G. S., Prihantono, J., Diastomo, H., et al. (2020). Coastal landslides in Palu Bay during 2018 Sulawesi earthquake and tsunami. *Landslides* 17, 2085–2098. doi: 10.1007/s10346-020-01417-3

Løvholt, F., Harbitz, C. B., and Haugen, K. B. (2005). A parametric study of tsunamis generated by submarine slides in the Ormen Lange/Storegga area off western Norway. *Marine Petrol. Geol*. 22, 219–231. doi: 10.1016/j.marpetgeo.2004.10.017

Løvholt, F., Lorito, S., Macías, J., Volpe, M., Selva, J., and Gibbons, S. (2019). "Urgent tsunami computing," in *2019 IEEE/ACM HPC for Urgent Decision Making (UrgentHPC)* (Denver, CO: IEEE), 45–50. doi: 10.1109/UrgentHPC49580.2019.00011

Løvholt, F., Pedersen, G., Harbitz, C. B., Glimsdal, S., and Kim, J. (2015). On the characteristics of landslide tsunamis. *Philos. Trans. R. Soc. A Math. Phys. Eng. Sci*. 373:20140376. doi: 10.1098/rsta.2014.0376

LTMBW (2017). *Landslide Tsunami Model Benchmarking Workshop, Galveston, Texas 2017*. Available online at: http://www1.udel.edu/kirby/landslide/index.html

Lube, G., Breard, E. C. P., Esposti Ongaro, T., Dufek, J., and Brand, B. (2020). Multiphase flow behaviour and hazard prediction of pyroclastic density currents. *Nat. Rev. Earth Environ*. 1, 348–365. doi: 10.1038/s43017-020-0064-8

Lynett, P. J., Gately, K., Wilson, R., Montoya, L., Arcas, D., Aytore, B., et al. (2017). Inter-model analysis of tsunami-induced coastal currents. *Ocean Model*. 114, 14–32. doi: 10.1016/j.ocemod.2017.04.003

Ma, G., Kirby, J. T., Hsu, T. J., and Shi, F. (2015). A two-layer granular landslide model for tsunami wave generation: theory and computation. *Ocean Model*. 93, 40–55. doi: 10.1016/j.ocemod.2015.07.012

Ma, G., Kirby, J. T., and Shi, F. (2013). Numerical simulation of tsunami waves generated by deformable submarine landslides. *Ocean Model*. 69, 146–165. doi: 10.1016/j.ocemod.2013.07.001

Ma, G., Shi, F., and Kirby, J. T. (2012). Shock-capturing non-hydrostatic model for fully dispersive surface wave processes. *Ocean Model*. 43–44, 22–35. doi: 10.1016/j.ocemod.2011.12.002

Macías, J., and de la Asunción, M. (2019). "Faster and faster tsunami simulations with ChEESE," in *AGU Fall Meeting, Session NH33A-06* (San Francisco, CA).

Macías, J., Escalante, C., and Castro, M. J. (2020a). Multilayer-HySEA model validation for landslide generated tsunamis. Part I rigid slides. *Nat. Hazards Earth Syst. Sci*. 21, 775–789. doi: 10.5194/nhess-21-775-2021

Macías, J., Escalante, C., and Castro, M. J. (2020b). Multilayer-HySEA model validation for landslide generated tsunamis. Part II Granular slides. *Nat. Hazards Earth Syst. Sci*. 21, 791–805. doi: 10.5194/nhess-21-791-2021

Macías, J., Vázquez, J. T., Fernández-Salas, L. M., González-Vida, J. M., Bárcenas, P., Castro, M. J., et al. (2015). The Al-Borani submarine landslide and associated tsunami. A modelling approach. *Marine Geol*. 361, 79–95. doi: 10.1016/j.margeo.2014.12.006

Maramai, A., Graziani, L., Alessio, G., Burrato, P., Colini, L., Cucci, L., et al. (2005a). Near- and far-field survey report of the 30 December 2002 Stromboli (Southern Italy) tsunami. *Marine Geol*. 215, 93–106. doi: 10.1016/j.margeo.2004.11.009

Maramai, A., Graziani, L., and Tinti, S. (2005b). Tsunamis in the Aeolian Islands (Southern Italy): a review. *Marine Geol.* 215, 11–21. doi: 10.1016/j.margeo.2004.03.018

Marani, M. P., Gamberi, F., Rosi, M., Bertagnini, A., and di Roberto, A. (2008). Subaqueous density flow processes and deposits of an island volcano landslide (Stromboli Island, Italy). *Sedimentology* 56, 1488–1504. doi: 10.1111/j.1365-3091.2008.01043.x

Masson, D. G., Harbitz, C. B., Wynn, R. B., Pedersen, G., and Løvholt, F. (2006). Submarine landslides: processes, triggers and hazard prediction. *Philos. Trans. R. Soc. A* 364, 2009–2039. doi: 10.1098/rsta.2006.1810

Mohammed, F., and Fritz, H. M. (2012). Physical modeling of tsunamis generated by three-dimensional deformable granular landslides. *J. Geophys. Res.* 117:C11015. doi: 10.1029/2011JC007850

Montagna, F., Bellotti, G., and Di Risio, M. (2011). 3D numerical modeling of landslide-generated tsunamis around a conical island. *Nat. Hazards* 58, 591–608. doi: 10.1007/s11069-010-9689-0

Murty, T. S. (2003). Tsunami wave height dependence on landslide volume. *Pure Appl. Geophys*. 160, 2147–2153. doi: 10.1007/s00024-003-2423-z

Paris, R. (2015). Source mechanisms of volcanic tsunamis. *Philos. Trans. R. Soc. A* 373:20140380. doi: 10.1098/rsta.2014.0380

Paris, R., Switzer, A. D., Belousova, M., Belousov, A., Ontowirjo, B., Whelley, P. L., et al. (2013). Volcanic tsunami: a review of source mechanisms, past events and hazards in Southeast Asia (Indonesia, Philippines, Papua New Guinea). *Nat. Hazards* 70, 447–470. doi: 10.1007/s11069-013-0822-8

Pistolesi, M., Bertagnini, A., di Roberto, A., Ripepe, M., and Rosi, M. (2020). Tsunami and tephra deposits record interactions between past eruptive activity and landslides at Stromboli volcano, Italy. *Geology* 48, 436–440. doi: 10.1130/G47331.1

Pouliquen, O., and Forterre, Y. (2002). Friction law for dense granular flows: application to the motion of a mass down a rough inclined plane. *J. Fluid Mech.* 453, 1–19. doi: 10.1017/S0022112001006796

Pudasaini, S. P., and Mergili, M. (2019). A multi-phase mass flow model. *J. Geophys. Res. Earth* 124, 2920–2942. doi: 10.1029/2019JF005204

Roche, O., Attali, M., Mangeney, A., and Lucas, A. (2011). On the run-out distance of geophysical gravitational flows: insight from fluidized granular collapse experiments. *Earth Planet. Sci. Lett.* 311, 375–385. doi: 10.1016/j.epsl.2011.09.023

Romano, A., Bellotti, G., and Di Risio, M. (2013). Wavenumber–frequency analysis of the landslide-generated tsunamis at a conical island. *Coast. Eng.* 81, 32–43. doi: 10.1016/j.coastaleng.2013.06.007

Romano, A., Di Risio, M., Bellotti, G., Molfetta, M. G., Damiani, L., and De Girolamo, P. (2016). Tsunamis generated by landslides at the coast of conical islands: experimental benchmark dataset for mathematical model validation. *Landslides* 13, 1379–1393. doi: 10.1007/s10346-016-0696-4

Rosi, M., Levi, S. T., Pistolesi, M., Bertagnini, A., Brunelli, D., x000F2, V. C., et al. (2019). Geoarchaeological evidence of middle-age tsunamis at Stromboli and consequences for the tsunami hazard in the Southern Tyrrhenian sea. *Sci. Rep.* 9:677. doi: 10.1038/s41598-018-37050-3

Rosi, M., Pistolesi, M., Bertagnini, A., Landi, P., Pompilio, M., and Di Roberto, A. (2013). Chapter 14 Stromboli volcano, Aeolian Islands (Italy): present eruptive activity and hazards. *Geol. Soc. Lond. Mem.* 37, 473–490. doi: 10.1144/M37.14

Ruff, L. J. (2003). Some aspects of energy balance and tsunami generation by earthquakes and landslides. *Pure Appl. Geophys.* 160, 2155–2176. doi: 10.1007/s00024-003-2424-y

Ruffini, G., Heller, V., and Briganti, R. (2019). Numerical modelling of landslide-tsunami propagation in a wide range of idealised water body geometries. *Coast. Eng.* 153:103518. doi: 10.1016/j.coastaleng.2019.103518

Savage, S. B., and Hutter, K. (1989). The motion of a finite mass of granular material down a rough incline. *J. Fluid Mech.* 199, 177–215. doi: 10.1017/S0022112089000340

Schambach, L., Grilli, S. T., Kirby, J. T., and Shi, F. (2019). Landslide tsunami hazard along the upper US east coast: effects of slide deformation, bottom friction, and frequency dispersion. *Pure Appl. Geophys.* 176, 3059–3098. doi: 10.1007/s00024-018-1978-7

Schambach, L., Grilli, S. T., and Tappin, D. R. (2021). New high-resolution modeling of the 2018 Palu tsunami, based on supershear earthquake mechanisms and mapped coastal landslides, supports a dual source. *Front. Earth Sci.* 8:598839. doi: 10.3389/feart.2020.598839

Schambach, L., Grilli, S. T., Tappin, D. R., Gangemi, M. D., and Barbaro, G. (2020). New simulations and understanding of the 1908 Messina tsunami for a dual seismic and deep submarine mass failure source. *Marine Geol.* 421:106093. doi: 10.1016/j.margeo.2019.106093

Selva, J., Amato, A., Armigliato, A., Basili, R., Bernardi, F., Brizuela, B., et al. (2021). Tsunami Risk Management From Crustal Earthquakes and Non-seismic Sources in Italy. *La Rivista del Nuovo Cimento*. doi: 10.1007/s40766-021-00016-9

Synolakis, C. E., Bernard, E. N., Titov, V. B., Kânoglu, U., and González, F. I. (2007). *Standards, Criteria, and Procedures for NOAA Evaluation of Tsunami Numerical Models*. Technical Report OAR PMEL-135, NOAA, Seattle, WA.

Tappin, D. R., Grilli, S. T., Harris, J. C., Geller, R. J., Masterlark, T., Kirby, J. T., et al. (2014). Did a submarine landslide contribute to the 2011 Tohoku tsunami? *Marine Geol.* 357, 344–361. doi: 10.1016/j.margeo.2014.09.043

Tibaldi, A. (2001). Multiple sector collapses at stromboli volcano, Italy: how they work. *Bull. Volcanol.* 63, 112–125. doi: 10.1007/s004450100129

Tinti, S., and Bortolucci, E. (2000). Energy of water waves induced by submarine landslides. *Pure Appl. Geophys.* 157, 281–318. doi: 10.1007/s000240050001

Tinti, S., Bortolucci, E., and Romagnoli, C. (2000). Computer simulations of tsunamis due to sector collapse at Stromboli, Italy. *J. Volcanol. Geotherm. Res.* 96, 103–128. doi: 10.1016/S0377-0273(99)00138-9

Tinti, S., Maramai, A., Armigliato, A., Graziani, L., Manucci, A., Pagnoni, G., et al. (2005). Observations of physical effects from tsunamis of December 30 2002 at Stromboli volcano, southern Italy. *Bull. Volcanol.* 68, 450–461. doi: 10.1007/s00445-005-0021-x

Tinti, S., Pagnoni, G., and Piatanesi, A. (2003a). Simulation of tsunamis induced by volcanic activity in the Gulf of Naples (Italy). *Nat. Hazards Earth Syst. Sci.* 3, 311–320. doi: 10.5194/nhess-3-311-2003

Tinti, S., Pagnoni, G., and Zaniboni, F. (2006). The landslides and tsunamis of the 30th of December 2002 in Stromboli analysed through numerical simulations. *Bull. Volcanol.* 68, 462–479. doi: 10.1007/s00445-005-0022-9

Tinti, S., Pagnoni, G., Zaniboni, F., and Bortolucci, E. (2003b). Tsunami generation in Stromboli island and impact on the south-east Tyrrhenian coasts. *Nat. Hazards Earth Syst. Sci.* 3, 299–309. doi: 10.5194/nhess-3-299-2003

Tinti, S., Zaniboni, F., Pagnoni, G., and Manucci, A. (2008). Stromboli island (Italy): scenarios of tsunamis generated by submarine landslides. *Pure Appl. Geophys.* 165, 2143–2167. doi: 10.1007/s00024-008-0420-y

Walder, J. S. (2003). Tsunamis generated by subaerial mass flows. *J. Geophys. Res.* 108:2236. doi: 10.1029/2001JB000707

Wang, J., Ward, S. N., and Xiao, L. (2019). Tsunami Squares modeling of landslide generated impulsive waves and its application to the 1792 Unzen-Mayuyama mega-slide in Japan. *Eng. Geol.* 256, 121–137. doi: 10.1016/j.enggeo.2019.04.020

Ward, S. N. (2001). Landslide tsunami. *J. Geophys. Res. Oceans* 106, 11201–11215. doi: 10.1029/2000JB900450

Ward, S. N., and Day, S. (2001). Cumbre Vieja Volcano—potential collapse and tsunami at La Palma, Canary Islands. *Geophys. Res. Lett.* 28, 3397–3400. doi: 10.1029/2001GL013110

Watts, P. (1998). Wavemaker curves for tsunamis generated by underwater landslides. *J. Waterway Port Coast. Ocean Eng.* 124, 127–137. doi: 10.1061/(ASCE)0733-950X(1998)124:3(127)

Watts, P., and Waythomas, C. F. (2003). Theoretical analysis of tsunami generation by pyroclastic flows. *J. Geophys. Res.* 108:2563. doi: 10.1029/2002JB002265

Yavari-Ramshe, S., and Ataie-Ashtiani, B. (2016). Numerical modeling of subaerial and submarine landslide-generated tsunami waves—recent advances and future challenges. *Landslides* 13, 1325–1368. doi: 10.1007/s10346-016-0734-2

Yavari-Ramshe, S., and Ataie-Ashtiani, B. (2017). A rigorous finite volume model to simulate subaerial and submarine landslide-generated waves. *Landslides* 14, 203–221. doi: 10.1007/s10346-015-0662-6

Young, C. C., and Wu, C. H. (2009). An efficient and accurate non-hydrostatic model with embedded Boussinesq-type like equations for surface wave modeling. *Int. J. Numer. Methods Fluids* 60, 27–53. doi: 10.1002/fld.1876

Zhang, C., Kirby, J. T., Shi, F., Ma, G., and Grilli, S. T. (2021a). A two-layer non-hydrostatic landslide model for tsunami generation on irregular bathymetry. 1. Theoretical basis. *Ocean Model.* 159:101749. doi: 10.1016/j.ocemod.2020.101749

Zhang, C., Kirby, J. T., Shi, F., Ma, G., and Grilli, S. T. (2021b). A two-layer non-hydrostatic landslide model for tsunami generation on irregular bathymetry. 2. Numerical discretization and model validation. *Ocean Model.* 160:101769. doi: 10.1016/j.ocemod.2021.101769

Zijlema, M., and Stelling, G. S. (2008). Efficient computation of surf zone waves using the nonlinear shallow water equations with non-hydrostatic pressure. *Coast. Eng.* 55, 780–790. doi: 10.1016/j.coastaleng.2008.02.020

Conflict of Interest: The authors declare that the research was conducted in the absence of any commercial or financial relationships that could be construed as a potential conflict of interest.

frontiers in Earth Science

ORIGINAL RESEARCH
published: 13 May 2021
doi: 10.3389/feart.2021.591383

Probabilistic Tsunami Hazard Assessment in Meso and Macro Tidal Areas. Application to the Cádiz Bay, Spain

Mauricio González[1], José A. Álvarez-Gómez[2], Íñigo Aniel-Quiroga[1], Luis Otero[3], Maitane Olabarrieta[4], Rachid Omira[5,6], Alberto Luceño[7], Robert Jelinek[8], Elisabeth Krausmann[9], Joern Birkman[10], Maria A. Baptista[5,11], Miguel Miranda[5,6] and Ignacio Aguirre-Ayerbe[1]*

[1] IHCantabria - Instituto de Hidráulica Ambiental de la Universidad de Cantabria, Santander, Spain, [2] Department of Geodynamics, Stratigraphy and Paleontology, Faculty of Geology, Complutense University of Madrid, Madrid, Spain, [3] Departamento de Física, Universidad del Norte, Colombia, Barranquilla, Colombia, [4] Department of Coastal Engineering, Engineering School of Sustainable Infrastructure and Environment, University of Florida, Gainesville, FL, United States, [5] Instituto Dom Luiz, University of Lisbon, IDL-FCUL, Lisbon, Portugal, [6] Instituto Português do Mar e da Atmosfera, Lisbon, Portugal, [7] Department of Applied Mathematics and Sciences of Computation, Universidad de Cantabria, Santander, Spain, [8] State Geological Institute of Dionýz Štúr, Bratislava, Slovakia, [9] European Commission, Joint Research Centre, Ispra, Italy, [10] Institute of Spatial and Regional Planning, University of Stuttgart, Stuttgart, Germany, [11] Instituto Superior de Engenharia de Lisboa, IPL, Lisbon, Portugal

OPEN ACCESS

Edited by:
Finn Løvholt, Norwegian Geotechnical Institute, Norway

Reviewed by:
Linlin Li, Sun Yat-sen University, China
Katsuichiro Goda, Western University, Canada

***Correspondence:**
Mauricio González
gonzalere@unican.es

Specialty section:
This article was submitted to Geohazards and Georisks, a section of the journal Frontiers in Earth Science

Received: *04 August 2020*
Accepted: *16 April 2021*
Published: *13 May 2021*

Citation:
González M, Álvarez-Gómez JA, Aniel-Quiroga Í, Otero L, Olabarrieta M, Omira R, Luceño A, Jelinek R, Krausmann E, Birkman J, Baptista MA, Miranda M and Aguirre-Ayerbe I (2021) Probabilistic Tsunami Hazard Assessment in Meso and Macro Tidal Areas. Application to the Cádiz Bay, Spain. Front. Earth Sci. 9:591383. doi: 10.3389/feart.2021.591383

Tsunami hazard can be analyzed from both deterministic and probabilistic points of view. The deterministic approach is based on a "credible" worst case tsunami, which is often selected from historical events in the region of study. Within the probabilistic approach (PTHA, Probabilistic Tsunami Hazard Analysis), statistical analysis can be carried out in particular regions where historical records of tsunami heights and runup are available. In areas where these historical records are scarce, synthetic series of events are usually generated using Monte Carlo approaches. Commonly, the sea level variation and the currents forced by the tidal motion are either disregarded or considered and treated as aleatory uncertainties in the numerical models. However, in zones with a macro and meso tidal regime, the effect of the tides on the probability distribution of tsunami hazard can be highly important. In this work, we present a PTHA methodology based on the generation of synthetic seismic catalogs and the incorporation of the sea level variation into a Monte Carlo simulation. We applied this methodology to the Bay of Cádiz area in Spain, a zone that was greatly damaged by the 1755 earthquake and tsunami. We build a database of tsunami numerical simulations for different variables: faults, earthquake magnitudes, epicenter locations and sea levels. From this database we generate a set of scenarios from the synthetic seismic catalogs and tidal conditions based on the probabilistic distribution of the involved variables. These scenarios cover the entire range of possible tsunami events in the synthetic catalog (earthquakes and sea levels). Each tsunami scenario is propagated using the tsunami numerical model C3, from the source region to the target coast (Cádiz Bay). Finally, we map the maximum values for a given probability of the selected variables (tsunami intensity

measures) producing a set of thematic hazard maps. 1000 different time series of combined tsunamigenic earthquakes and tidal levels were synthetically generated using the Monte Carlo technique. Each time series had a 10000-year duration. The tsunami characteristics were statistically analyzed to derive different thematic maps for the return periods of 500, 1000, 5000, and 10000 years, including the maximum wave elevation, the maximum current speed, the maximum Froude number, and the maximum total forces.

Keywords: tsunami, PTHA, montecarlo, tsunamigenic-sources, numerical modeling

INTRODUCTION

The mitigation of marine hazards on threaten coasts is a challenging scientific and engineering topic. Addressing such a challenge requires extensive preparation through the development of hazard and risk assessment methods. Tsunami is one of these marine hazards, for which the assessment methods have significantly progressed over the past 2-3 decades. However, as the tsunami historical catalogs are often inherently incomplete, obtaining a purely empirical hazard assessment remains difficult to achieve (Davies et al., 2018). Alternatively, methods combining data and numerical modeling have been developed (Geist and Lynett, 2014), gaining increasing improvement in the aftermath of the 2004 Indian Ocean tsunami (Grezio et al., 2017).

Existing tsunami hazard assessment methods for earthquake sources are basically developed in an analogous way to the seismic hazard assessment. They include the deterministic tsunami hazard assessment (DTHA) and the probabilistic tsunami hazard assessment (PTHA, or SPTHA from seismic probabilistic tsunami hazard assessment). Prior to the 2004 Indian Ocean tsunami, the DTHA method was the widely used among the tsunami scientific community (e.g., Tinti and Armigliato, 2003). Nevertheless, some few PTHA studies could also be found in the literature (Lin and Tung, 1982; Rikitake and Aida, 1988). The DTHA employs particular source scenarios (i.e., worst-case scenario) to numerically predict and map selected tsunami intensity measures (e.g., maximum wave height, flow depth, current velocity) (Tinti et al., 2005; Lorito et al., 2008). Although the DTHA is considered simple to conduct and provides easily interpreted results, it is very sensitive to the selection of the source scenario (Geist and Lynett, 2014). The PTHA, on the other hand, determines the likelihood of exceeding a tsunami intensity measure (e.g., wave height, runup height) at a particular location within a given time period by integrating the modeled hazard from all considered events (Geist and Parsons, 2006; Power et al., 2007; Grezio et al., 2017). In comparison to DTHA, PTHA is relatively complex and computationally demanding. The complexity of PTHA relies on the treatment of uncertainties that often leads to generate a large number of possible events. Annaka et al. (2007) distinguished two categories of PTHA uncertainties: aleatoric referring to the random nature of tsunami generation and its effects, and epistemic related to the insufficient knowledge on data and modeling accuracy. Covering all sources of uncertainties in PTHA remains highly challenging being the incorporation of uncertainties on the tsunami source one of the main difficulties (Basili et al., 2013; Lorito et al., 2015; Sepúlveda et al., 2019; Behrens et al., 2021).

A framework for modern PTHA was first presented in the pioneering work of Geist and Parsons (2006). This framework formed the basis for developing numerous PTHA research works (e.g., Burbidge et al., 2008; Otero, 2008; Taubenböck et al., 2008; Suppasri et al., 2012; Yadav et al., 2013; Horspool et al., 2014; Omira et al., 2015; Shin et al., 2015; El-Hussain et al., 2016; Griffin et al., 2016; Hoechner et al., 2016; Zamora and Babeyko, 2020). 7 years after the 2004 event, the massive 2011 Japan tsunami raised the need to consider the complexity of the earthquake rupture in the PTHA. Subsequently, PTHA studies incorporating heterogeneous slip distribution on the earthquake fault (Li et al., 2016; Sepúlveda et al., 2019) or rigidity depth-dependence (Davies and Griffin, 2019) have been conducted.

Probabilistic tsunami hazard analysis applies to different geographic scales. These scales include global-scale PTHA (Davies et al., 2018), regional-scale PTHA (Thio et al., 2007; Sorensen et al., 2012; Power et al., 2013; Lorito et al., 2015; Omira et al., 2015; Li et al., 2016; Zamora and Babeyko, 2020; Basili et al., 2021), national-scale PTHA (Grezio et al., 2012; Suppasri et al., 2012; Horspool et al., 2014; De Risi and Goda, 2016; El-Hussain et al., 2016; Davies and Griffin, 2019; Kotani et al., 2020), and local-scale PTHA (González et al., 2009; Omira et al., 2016; Volpe et al., 2019). Detailed PTHA of a specific coastal segment community (local-scale) often involves high-resolution inundation modeling and treatment of uncertainties from local effects, such as the tidal stage (Omira et al., 2016). Commonly, the sea level variation and the currents forced by the tidal motion are either disregarded or considered and treated as aleatory uncertainties in the numerical models (González et al., 2010; Omira et al., 2016). In some other cases, tidal elevations are added linearly to the maximum tsunami heights, without considering the non-linear shoaling and topo-bathymetry local effects. However, in zones with a macro and meso tidal regime, the effect of the tides on the probability distribution of tsunami hazard can be very important.

In this study, a PTHA methodology and its application to a costal site of the NE Atlantic, Cádiz Bay in Spain, is presented. Cádiz is characterized by a meso tidal regime (higher than 2 m and lower than 4 m, as defined in Davis et al., 1972) and, therefore, the study considers a combined statistical treatment of both tsunami hazard and sea level variation improving the existing mentioned approaches (sea level add linearly or a constant sea level). As a result, inundation maps expressing the

likelihood of exceeding tsunami intensity measures (maximum wave elevation, maximum current speed and maximum wave forces) are derived at given return periods.

Test Site Selection

The November 1st, 1755 Lisbon event is probably the earliest well documented tsunami, with references to all over the Atlantic basin, and one of the largest in European historical times. The tsunami was possibly generated by one of the many faults present in the area of the Gulf of Cádiz (Medialdea et al., 2004; Terrinha et al., 2009; Zitellini et al., 2009). This area is tectonically deformed by a slow (3.5 - 4 mm/year) ESE-WNW oblique convergence between the African and Eurasian lithospheric plates (Argus et al., 1989; Stich et al., 2006), which is translated into a relatively low seismic activity distributed over a wide deformation area. Although there are several seismic sources capable of generating major earthquakes, the slow strain rate causes a low frequency of large earthquakes. The historical record of tsunamis, therefore, is very limited in the area, although there are records of paleotsunamis with similar characteristics to that of 1755 (Luque et al., 2001, 2002; Ruiz et al., 2005; Morales et al., 2008; Baptista and Miranda, 2009).

The Bay of Cádiz is geographically located between the longitudes 6° W and 6° 25′ W and latitudes 36° 20′ N and 36° 40′ N, in the Southwest of Iberian Peninsula (**Figure 1**). It faces West to the Gulf of Cádiz and is landlocked around its Southwestern, Southern and Eastern margins by the mainland. This area is a natural protection zone with large tidal flats, tidal channels (mean spring tidal range $\sim$ 3.7 m) and several beaches. Cádiz city constitutes the municipality with the highest population in this area, with approximately 130 000 inhabitants. This city (**Figure 1**) occupies a small peninsula connected by a tombolo (a sandy isthmus or spit that connects the island to the mainland or to another island) to the Leon Island, where the San Fernando municipality is located. The main economic activities in Cádiz are related to tourism, naval construction and harbor activities. Due to its long and nice beaches, the warm weather and its historic heritage, tourism has increased considerably in the last decades.

Probabilistic Methodology

Probabilistic tsunami hazard analysis methods generally follow the PSHA (Probabilistic Seismic Hazard Analysis) method, originally developed by Cornell (1968). The PSHA is a widely used method for assessing the seismic hazard and has been described and extensively reviewed, as stated in various reports and documents (National Research Council, 1988, 1997; Senior Seismic Hazard Analysis Comittee, 1997), and several authors have discussed various aspects of it, such as the distinction between aleatory and epistemic uncertainties, the use of synthetic earthquake catalogs (Ward, 1991, 1996, 2000), the Monte Carlo methods (Savage, 1991, 1992; Cramer et al., 1996; Ebel and Kafka, 1999), and the use of Logic Trees (Coppersmith and Youngs, 1986).

Since the seismicity, and consequently the seismic generation of the tsunami is a stochastic phenomenon, it is necessary to use probabilistic analysis to estimate the hazard of these phenomena and their impact on the coast. The approach we used here is based on Monte Carlo techniques, which comprises the following steps:

- Building a database of numerical simulations of tsunamis for different variables: faults, seismic magnitudes, epicenter locations and sea levels.
- Generating a set of scenarios from synthetic seismic catalogs and tidal conditions based on the probabilistic distributions of the involved variables.
- Mapping the maximum values of the selected tsunami intensity measures to assess the hazard for a given probability.

Methods based on Monte Carlo techniques allow the processing of the work variables and their respective uncertainties in a robust way. The variables are treated by their probability density functions (PDF) and different values can be sampled from the distribution function for each simulation.

In the framework of the European FP6 TRANSFER project[1], we developed a PTHA methodology based on the generation of synthetic seismic catalogs and the incorporation of the sea level variation into a Monte Carlo simulation. In this work, we present the application of this methodology step-by-step to one of the project test-sites, the Bay of Cádiz area in Spain. The main novelty of the work is the combined statistical treatment of both tsunami hazard and tidal variation by incorporating the tidal state into the PTHA. The tide is included using a discrete set of constant sea level elevations, and the tsunami tidal current interaction is neglected.

This paper is structured as follows: first, the characterization of the seismic sources and the statistical analysis are presented. Second, the sea level characterization and statistical analysis are performed. Third, the methodology based on the Monte Carlo approach, which has been applied to obtain the synthetic seismic catalog, is described in detail. Fourth, the numerical database and the methodology to generate the probabilistic thematic maps are presented. Finally, the probabilistic thematic maps for the Bay of Cádiz area are derived from the application of the developed methodology.

TSUNAMIGENIC SOURCES CHARACTERIZATION

The tsunami origin accounts for a major source of uncertainty in PTHA. The importance of the seismic source characteristics into tsunami hazard has been shown in a number of works (Okal and Synolakis, 2004; Gica et al., 2007; Basili et al., 2013; Knighton and Bastidas, 2015; Davies and Griffin, 2019) and some approximations to deal with them from a probabilistic point of view have been proposed (e.g., Sørensen et al., 2012; Knighton and Bastidas, 2015; Lorito et al., 2015). The incorporation of variable or stochastic slip distribution functions (e.g., Goda et al., 2015; Li et al., 2016), as well as improved 3D geological rupture models (e.g., Yamada et al., 2013), into probabilistic analysis are part of the current development of the PTHA methodology.

[1] http://www.transferproject.eu/

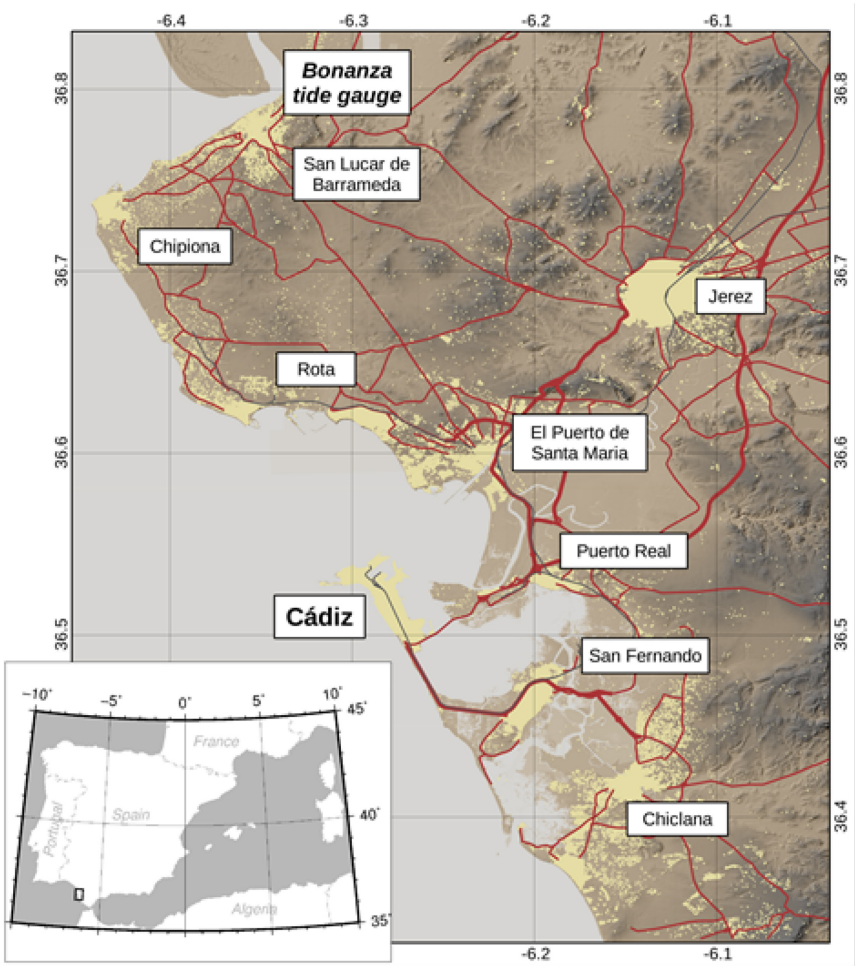

FIGURE 1 | Geographical localization of the Cádiz Bay and its main municipalities. Pale yellow polygons represent urban areas; red lines are the main roads and the gray line is the railroad.

Here, the characterization of tsunamigenic sources basically consists of identifying the seismic faults that can affect the studied region, and the probabilistic analysis of their parameters. This analysis is based on the historical earthquake data in the zone and can be divided into the following elements:

(1) Seismic zonation and identification of the main tectonic structures based on historic seismicity and geology. This zoning can include far-field and local sources.
(2) Determination of statistical parameters based on the Gutenberg-Richter Law.
(3) Determination of the geometrical parameters for the main fault ruptures and of the scaling relationships between the seismic moment and the source parameters.

Tectonic Structures

Tectonically, the study area can be defined as a diffuse plate boundary (Sartori et al., 1994), where the deformation is taking place by means of different structures distributed along a broad area. This area comprises the eastern edge of the Gloria and Tydeman transforms (where the deformation is mainly concentrated in these shear corridors), the Gorringe Bank, the Horseshoe Abyssal plain, the Portimao and Guadalquivir banks, and the western termination of the arcuated Gibraltar Arc (Medialdea et al., 2004; Zitellini et al., 2009). This deformation zone is the eastern edge of the Azores – Gibraltar seismic zone, being the present-day boundary between the Eurasian and African plates. Here, the strain is mainly compressive or transpressive, and changes to almost pure strike-slip along the Gloria Fault (Laughton and Whitmarsh, 1974; Borges et al., 2001). The relative motion between the two plates in this area is of the order of 3.5 - 4 mm/year (Argus et al., 1989; Stich et al., 2006).

Most damaging earthquakes and tsunamis that affected the coasts of Portugal, Morocco and Spain were probably generated in the SWIT (SW Iberian Transpressive Domain) zone, being the main active tectonic zone and plate boundary in the area (Zitellini et al., 2009; Martínez-Loriente et al., 2013), including the November 1st, 1755 massive tsunami. In the present study only the tsunamigenic areas in the SWIT region have been considered. This area of tectonic deformation is responsible for

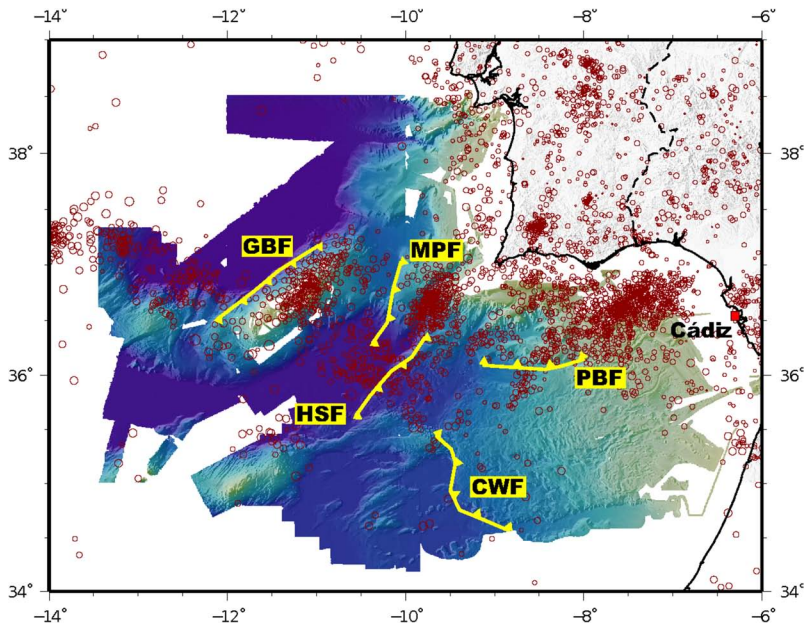

FIGURE 2 | Map of seismicity and geological structures used as sources in the present study. GBF, Gorringe Bank Fault; MPF, Marques de Pombal Fault; HSF, Horseshoe Fault; PBF, Portimao Bank Fault; CWF, Cádiz Wedge Fault. Circles show the epicenters of the Spanish National Seismic Network instrumental catalog, with the size proportional to the event magnitude. The colormap shows the SWIM high resolution bathymetry (Zitellini et al., 2009).

the offshore seismicity of Southwestern Iberia (**Figure 2**). The largest instrumental earthquake was the February 28th, 1969 Horseshoe Ms 8.0 (M_w 7.8) event (Fukao, 1973; Grandin et al., 2007) and the respective tsunami was recorded all over the North Atlantic (Gjevik et al., 1997; Baptista, 2019). Moreover, the SWIT was the place of several moderate size events that have been recorded in the last decades. Focal mechanisms and slip vectors show the coexistence of two different processes of deformation, on one hand the presence of mainly reverse and reverse-oblique faulting with N-S to NNW-SSE compression and on the other hand the occurrence of mainly strike-slip faulting with an associated direction of compression approximately NW-SE (Geissler et al., 2010; Stich et al., 2010). These characteristics are explained by the occurrence of strain partitioning in this area of diffuse deformation (Rosas et al., 2009; Terrinha et al., 2009).

As depicted in **Figure 2**, the seismicity can be grouped in clusters associated with the main geological structures. These structures are the main tsunamigenic sources in the Gulf of Cádiz and they are used in this work as maximum earthquake ruptures. These fault traces are parameterized in Álvarez-Gómez et al. (2008); Omira et al. (2009), Lima et al. (2010) and are described in greater detail in Zitellini et al. (2009). The seismicity associated with these structures is used to define its statistical parameters, basically the Gutenberg-Richter Law, as shown in the next section.

Statistical Analysis of the Seismicity

The Gutenberg-Richter Law relates the earthquake magnitude with its frequency:

$$log_{10}N = a - bM_w \tag{1}$$

where N represents the accumulated frequency of the earthquakes with a magnitude higher or equal to M_w. The a coefficient establishes the seismic activity in the zone, while the parameter b is related with the difference between the frequency of small and big earthquakes. The annual rate of earthquakes with a magnitude higher or equal to M_w (λM_W (N/T), where T refers to the time),

is given by the following equation:

$$\lambda_{M_W} = e^{(\alpha - \beta M_W)} \tag{2}$$

where $\alpha = a\ ln(10)$ and $\beta = b\ ln(10)$.

From the Gutenberg-Richter Law the following distribution function $F_{M0}\ (M_0)$ can be derived for the seismic moment M_0:

$$F_{Mo}\ (M_0) = \left[1 - \left(\frac{m_{0l}}{m_{0u}}\right)^{\beta}\right]^{-1} \left[1 - \left(\frac{m_{0l}}{M_0}\right)^{\beta}\right] \quad m_{0l} \le M_0 \le m_{0u} \tag{3}$$

The associated density function $f_{M0}\ (M_0)$ is the following:

$$f_{Mo}\ (M_0) = \left[1 - \left(\frac{m_{0l}}{m_{0u}}\right)^{\beta}\right]^{-1} \beta \left(\frac{m_{0l}^{\beta}}{M_0^{\beta+1}}\right) m_{0l} \le M_0 \le m_{0u} \tag{4}$$

where m_{0l} represents the lower limit of the considered earthquake seismic moment and m_{0u} represents the upper limit of the considered earthquake seismic moment. For each fault m_{0u} should be equal to the worst-case scenario seismic moment.

We have selected the time period between 1900 and 2002 in the IGN seismic catalog IGN (2011). In this interval the used magnitude m_b Lg (Mezcua and Martínez-Solares, 1983) is homogeneous. After 2002, the method to obtain the magnitude in

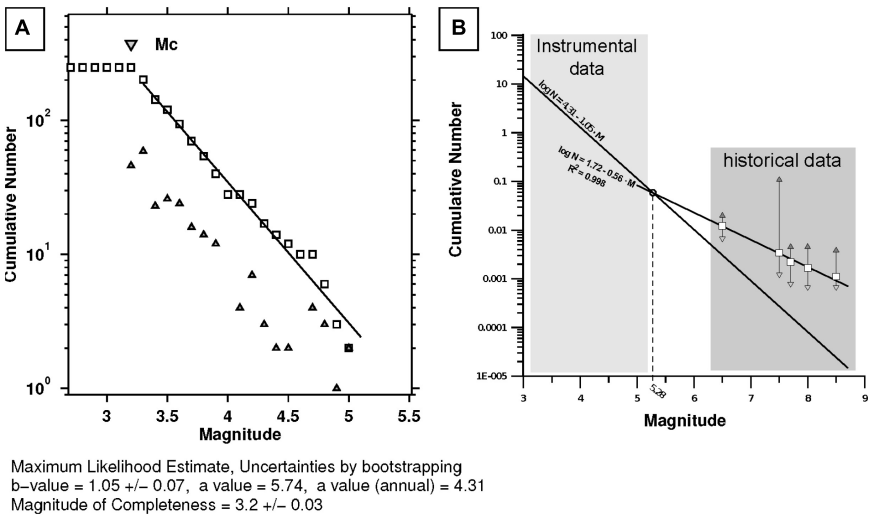

FIGURE 3 | (A) Gutenberg-Richter fit of the instrumental catalog after declustering of the catalog shown in **Figure 2** (see details in the text). Triangles show discrete frequencies while the squares show the cumulative distribution. **(B)** Plot comparing the Gutenberg-Richter Law fitted with instrumental data (thin line) and the historical data. Squares are the mean annual frequencies, light-gray downward triangles are minimum frequencies and dark-gray upward triangles are maximum frequencies. The fitted Gutenberg-Richter Law to the historical data is shown as a thick line. The intersection between both fits takes place on the magnitude value M_W = 5.28.

the Spanish seismic network changed, and no direct relationship between them has been calculated. This magnitude has been transformed to M_w using the relationship published by Rueda and Mezcua (2002) for Iberian earthquakes:

$$M_w = 0.311 + 0.637 m_b Lg + 0.061 m_b Lg^2 \quad (5)$$

The number of events increases exponentially with time, denoting the increase in sensitivity of the seismographs. To avoid this effect on the statistical framework, we have calculated the magnitude of completeness evolution through time using Gutenberg-Richter fits with a mobile window of 200 events. We obtained a magnitude of completeness of $M_W > 3.2$ since 1975, which was tested analyzing the cumulative distribution of events. To compute a synthetic catalog assuming a Poissonian model, all the "non-independent" events must be eliminated. We have used the declustering methodology of Gardner and Knopoff (1974), with time and space windows predefined as function of the event magnitude to eliminate the aftershocks. With the catalog filtered and declustered, we calculated the values a and b by means of a maximum likelihood method. The obtained values were $b = 1.05 \pm 0.07$, and $a = 4.31$ (**Figure 3A**). We used the software ZMAP (Wiemer, 2001) to perform these statistical analyses.

Although the fit is quite good, the magnitude interval in which the values are computed is very limited and we have no control over the fit for bigger earthquakes. To evaluate the validity of this relation for tsunamigenic earthquakes, we have estimated the annual frequency of great earthquakes from the historical data. We have used magnitudes estimated from the bibliography (Luque et al., 2001, 2002; Ruiz et al., 2005; Garcia-Orellana et al., 2006; IGN, 2009, 2011) and the minimum, maximum and mean annual frequencies have been computed.

In **Figure 3B** historical data are plotted over the previously calculated Gutenberg-Richter fit. As can be seen, the distribution of the mean frequencies can be fitted confidently by a Gutenberg-Richter Law (R^2 = 0.998) with values: a = 1.72, b = 0.56; intersecting the instrumental fit in the magnitude M_W = 5.28. This type of two-branch distribution has been proposed in different environments regarding the distribution of great earthquakes and implying for some authors a characteristic earthquake model (Schwartz and Coppersmith, 1984; Davison and Scholz, 1985; Wesnousky, 1994; Main, 2000; Zielke and Arrowsmith, 2008). In our approximation to the PTHA we are interested in earthquakes capable of generating tsunamis, in big and great earthquakes; and in our case, the second branch better describes the occurrence of the tsunamigenic earthquakes in the Gulf of Cádiz.

Once these parameters are known, the annual rate of earthquakes greater or equal to a given value can be obtained from the Gutenberg-Richter Law. For the SWIT zone we are constraining the minimum seismic moment magnitude for tsunamigenic earthquakes to 6.5. Therefore, earthquakes with smaller magnitudes have not been considered.

Geometrical Parameters and Scaling Relations

To define a set of potential earthquake ruptures with different magnitudes on the same fault, we have obtained first the aspect ratio of the largest rupture scenario in the synthetic catalog for each source and from its characteristics and the scaling relations we have derived those of the smaller events. The worst cases, as well as the fault traces that we used for the Cádiz Bay area, are similar to the ones described in Lima et al. (2010); but accounting for maximum earthquake magnitudes of M_w = 8.6 in the Cadiz

accretionary Wedge Fault (**Figure 2**). For the rest of the events, we have maintained constant the strike, dip and rake of the fault, as well as the length (L) - width (W) relation in order to have enough constraints to define the rest of the parameters from the event magnitude (M_w).

The scalar seismic moment equation (Aki, 1966) relates the size of the earthquake with the elastic properties of the media where the event is taking place, the dimensions of the rupture and the amount of slip on the fault plane:

$$M_0 = \mu S\overline{D} \tag{6}$$

where μ is the shear modulus of the upper lithosphere involved in the fault rupture, S is the area of the rupture that generates the earthquake, and D is the average displacement over the fault surface. In this study we have used a shear modulus of 3×10^{10} Pa, which is widely used for this area in the literature (Grandin et al., 2007; Gutscher et al., 2009; Omira et al., 2011; Roger et al., 2011), although higher values have also been proposed. To obtain the seismic moment we used the Kanamori (1977) relation:

$$M_w = \frac{2}{3}\left(log_{10}M_o - 9.1\right) \tag{7}$$

To obtain the source dimensions from the earthquake magnitude the common practice is the use of an empirical relation adequate for the tectonic environment (Stirling et al., 2013). Some of the most commonly used empirical relationships are mainly developed for earthquakes occurred in continental lithosphere (e.g., Wells and Coppersmith, 1994; Leonard, 2010) or subduction context (Blaser et al., 2010; Strasser et al., 2010; Murotani et al., 2013), while for oceanic lithosphere the empirical relations are scarce and related to normal faulting events (Strasser et al., 2010; Álvarez-Gómez et al., 2012). Scholz (2002) proposed a relation between the length of the fault (L) and the average slip of the rupture (D) as a function of the ratio L/W and the tectonic environment. We have maintained this ratio constant for each fault and assumed an oceanic intraplate environment, which is coherent for a distributed deformation boundary. The relation proposed by Scholz (2002) takes the form:

$$\overline{D}\,(m) = 6.5\ x\ 10^{-5}\ L\ (m) \tag{8}$$

The average displacement for the maximum magnitude event is obtained once the length of the fault is defined. The maximum length of the fault is constrained from the sea bottom mapping (**Figure 2**) while the width is limited by the maximum seismogenic depth. This depth varies from 50 km in the western area of the Gulf of Cádiz, where the oceanic lithosphere is coupled (Stich et al., 2005; Cunha et al., 2010; Geissler et al., 2010), to 25 km on its eastern edge where detachment levels exist at shallower depths in transitional or continental lithosphere (Medialdea et al., 2004; Pereira et al., 2011; Silva et al., 2017).

Once the L/W ratio is defined for each fault, combining eq. 8, L/W = constant for a fault and S = W.L in eq. 6, W can be obtained. All the parameters scales in relation with the source area defined from the earthquake magnitude (eq. 6).

SEA LEVEL STATISTICAL ANALYSIS

In this study the statistical treatment of the tidal variation is incorporated towards a PTHA. Based on the data measured by the tidal gauge closest to the study zone, the sea level probability distribution function is obtained. The net sea level variation is due to atmospheric processes, such as atmospheric pressure changes, the effect of wind and due to the astronomical effects. The former contribution has a random nature, while the astronomical tides are deterministic. Therefore, from the tide gauge data, conducting a harmonic analysis both contributions can be separated and treated as different processes.

The astronomical tide is characterized once the main tidal components are identified and their amplitudes and phases are known. The longest frequency that we are able to consider is the one corresponding to the nodal cycle, which has a period of 18.6 years. With the information derived from the harmonic analysis, 18.6 years of astronomical tide elevations (covering a nodal cycle) with a 1 h resolution are reconstructed.

The 20-year sea level data to perform the statistical analysis has been obtained from a tidal gauge located in Bonanza (**Figure 1**). The Bonanza tidal gage is part of the REDMAR network from Puertos del Estado, it is located just at the end of harbor breakwater in the mouth of the Guadalquivir river. The Bonanza station is selected for several reasons: (1) it is the closest station to Cadiz (30 km away), it has records of more than 25 years, it is a high-quality station taking measurements of sea level every 1 minute, it is a station included in the Spanish Tsunami Early Warning System in the IGN for tsunami detection, this is why its high temporal sampling in taking sea level data. The other two nearest tide stations are the one in Huelva, 90 km away from Cádiz, located also in a mouth of the Odiel river, just in the directional dike, and the Tarifa station at 85 km located in the Strait of Gibraltar, where it is already affected by the tidal wave of the Mediterranean and the Atlantic; (2) Given the large scale of spatial and temporal variation of the tidal wave, the tide is almost the same in Huelva as in Bonanza, there is only a slight temporal lag; (3) In regards the meteorological tide (storm surge) slight variations in the storm surge regime was obtained between the three gauges; and (4) The effect of Guadalquivir river floods in the sea level is really small, the river is being regulated by upstream dams, the average flow discharge is less than 5 mˆ3/s, and in floods in rain storms the flow discharge is controlled with maximal 40 mˆ3/s, being the effect on the sea level very small at the mouth. Therefore, the collected sea level records at the Bonanza station have high quality to characterize the harmonics of the tidal wave and the storm surge regime.

The main components arising from the harmonic analysis, after applying the Tide software, are shown in **Table 1**.

On the other hand, the meteorological tide needs a statistical treatment in order to apply this information in a Monte Carlo method. The distribution function of the meteorological tide can be fitted to different theoretical distribution functions, such as the Gumbel distribution, given by the following expression:

$$F_p = e^{-e^{\left(\frac{S_{mm}-\Lambda}{\Delta}\right)}} \tag{9}$$

TABLE 1 | Main components (amplitude and phase) in Bonanza.

Tidal component	Amplitude (m)	Phase (°)
O1	0.061	325.29
K1	0.064	60.50
N2	0.190	48.54
M2	0.927	64.41
S2	0.315	91.34
K2	0.089	88.40

where F_p represents the exceedance probability of a given meteorological tide S_{mm}, Λ represents the localization parameter and Δ the scale parameter.

Once the localization and scale parameters of the selected distribution function are obtained, all the information needed in the Monte Carlo simulations is known.

To derive the meteorological tide, the astronomical tide has been reconstructed along the same tidal gauge data series period. Reconstructed data has been subtracted from the total sea level variation measured by the tidal gauge. The residue corresponds to the meteorological tide. The distribution function of the meteorological tide and the fit to a Gumbel distribution function is shown in **Figure 4**. As can be seen, two different tendencies are apparent in the meteorological distribution function. Because of that, two different Gumbel distribution functions have been fitted, one in the upper part representing the extremal regime and the other in the mean and lower part, representing the mean regime. In **Table 2**, the values corresponding to the location parameters and to the scale parameters for both regimes are shown.

MONTE CARLO SIMULATION PROCEDURE

Based on the probabilistic characteristics of the sources, and by applying the Monte Carlo method, synthetic earthquake series are obtained for each of the considered faults. The time series corresponding to each fault are integrated to generate a global tsunamigenic earthquake and sea level catalog for the study region. The length of the time series in the present study was selected to 10000 years. To derive confidence bands, for each thematic map, we performed 1000 Monte Carlo simulations for each fault.

The steps followed in the Monte Carlo simulation for each fault (i) are the following (**Figure 5**):

(a) Generation of a random number for the probability of the seismic moment and computation of M_0 (Eq. 3).
(b) Computation of the fault dimensions, rupture width (Wi), length (Li) and Area ($Si = WixLi$) using the selected scaling relations (Eqs. 6, 7, 8).
(c) Computation of the focal depth (h_f) assuming surface rupture:

$$h_f = \frac{W_i}{2} sin\,(\delta) \tag{10}$$

where δ is the fault dip and W_i the rupture width.

(d) Computation of the epicenter. For a given rupture length Li a random number of locations is generated along the rupture zone, leaving a distance of Li /2 on both sides of the rupture (**Figure 6**). Once the point along the rupture zone has been generated, and assuming that the rupture reaches the surface, the location of the epicenter is computed with the following equations:

$$\begin{aligned} X_{0i} &= X_{fi} + \tfrac{L_i}{2} sin\,(\theta) + \sigma\,(L_{max} - L_i)\,sin\,(\theta) \\ Y_{0i} &= L_{fi} + \tfrac{L_i}{2} cos\,(\theta) + \sigma\,(L_{max} - L_i)\,cos\,(\theta) \end{aligned} \tag{11}$$

$$\begin{aligned} X_{ei} &= X_{0i} + \tfrac{W_i}{2} cos\,(\delta) \cdot \cos(-\theta) \\ Y_{ei} &= Y_{0i} + \tfrac{W_i}{2} cos\,(\delta) \cdot \sin(-\theta) \end{aligned} \tag{12}$$

where X_{0i} and Y_{0i} represent the longitude and the latitude of the middle point along the fault trace with length L_i; X_{ei}; and Y_{ei} represent the longitude and latitude of the epicenter for an earthquake with seismic moment Moi (**Figure 6**); σ is a random number between 0 and 1 (with uniform distribution); δ is the dip angle and θ is the strike angle and L_{max} is the maximum rupture length for the fault. Thus, l_e ($l_e = L_{max} - L_i$) is the effective distance along the trace (see **Figure 6**), where the point (X_{0i},Y_{0i}) associated to the epicenter can be located in a random way, for a given rupture length (L_i). If the fault length $L_i = L_{max}$ then only one point in the fault trace is possible and therefore only one epicenter location.

(e) Computation of the time interval from the last tsunamigenic earthquake event to the next. In the present methodology, earthquakes are assumed to be Poissonian processes; therefore, the probability $P(T)$ of having the next earthquake in a time interval of t or higher is given by the following equation:

$$P\,(T) = 1 - e^{(-\lambda t)} \tag{13}$$

Generating a random number for the probability, the time of the interval between two consecutive earthquakes can be obtained. λ is the annual rate of tsunamigenic earthquakes of magnitude M_{Wi} or higher. Eq. 13 can be expressed as a function of $P(T)$ to obtain the time t between two consecutive events:

$$t = \frac{\ln(1 - P\,(T))}{-\lambda} \tag{14}$$

(f) Generation of a random number for the time along a period of the 18.6 year astronomical sea level series. The astronomical tidal level corresponding to this random moment is considered as the tidal level coinciding with this earthquake event.
(g) Generation of a random number between 0 and 1 for the probability of the storm surge. With this random number, the storm surge S_{mm} can be derived according to the following expression (see Eq. 9):

$$S_{mm} = \Lambda - \Delta \cdot \ln(-\ln(F(x))) \tag{15}$$

where $F(x)$ is the cumulative probability.

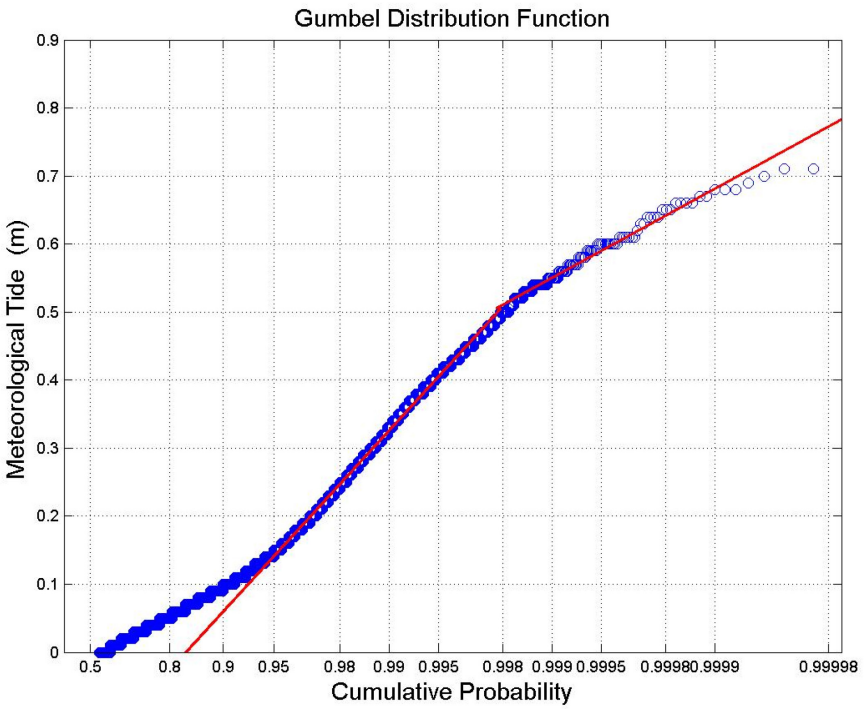

FIGURE 4 | Meteorological tide distribution function and its fit to a Gumbel distribution function. Open circles indicate the empirical distribution function of the meteorological tide and straight lines represent the two fitted Gumbel distribution functions.

TABLE 2 | Gumbel distribution function, localization, and scale parameters.

Regime	Mean		Extreme	
Parameter	Δ_m	Λ_m	Δ_e	Λ_e
Value	0.0633	−0.0341	0.0603	0.0448

(h) Computation of the net tidal level. In this step, the astronomic tidal level and the storm surge are linearly added.

We believe that the assumption of rupture to the surface in steps (c) and (d) concerns magnitudes higher than 6.5 is reasonable taking into account the mechanics of fracture of the schizosphere (the elasto-frictional upper layer of the crust). It is well recognized that major earthquakes nucleate at depth, where the strength of the rocks is higher due to thermo-mechanical conditions (Sibson, 1982). When an earthquake ruptures at depth, overcoming the high frictional strength of the faults, the amount of energy liberated during the earthquake is enough to allow the lateral and vertical propagation of the rupture, reaching the surface and propagating laterally (Scholz, 1998, 2002). Nevertheless, some of the modeled events, especially those with smaller magnitudes, where the surface rupture assumption could be more arguable, do not necessarily reach the surface in nature. Consequently this assumption could be a conservative bias in these cases. Nevertheless, being these events the smaller ones, and as we are using average uniform slip over the fault, this potential bias is reduced and is counterbalanced by the threat posed by the bigger events.

Steps "a" to "h" are repeated for each fault until a simulation of an established number of years is obtained (10000 years in our simulations). Once the synthetic earthquake series are derived for each fault, they all are joined in a single global synthetic catalog.

1000 different 10000-year long tsunamigenic seismic catalogs have been created for each fault. As an example, **Figure 7A** shows the evolution of one time series (10000-year) of the earthquakes (seismic moment magnitude) considering all the source regions. In **Figure 7B**, the sea levels corresponding to each of the simulated earthquake scenarios are represented. This figure shows that there are earthquakes that coincide with high sea levels, while others occur during the mean or low tide. These scenarios can create very different impacts on the coastal region.

The distribution of the total number of synthetic events from all sources, in the 1000-year series is shown in **Figure 8A**; it is worth noting the maximum generated magnitude M_W = 8.55. The epicenter location for each scenario is represented in **Figure 8B**.

NUMERICAL DATABASE

Once a synthetic catalog is generated (magnitude and epicenter location) based on (1) the synthetic earthquake series (magnitude and epicenter location) for each of the considered faults; and (2)

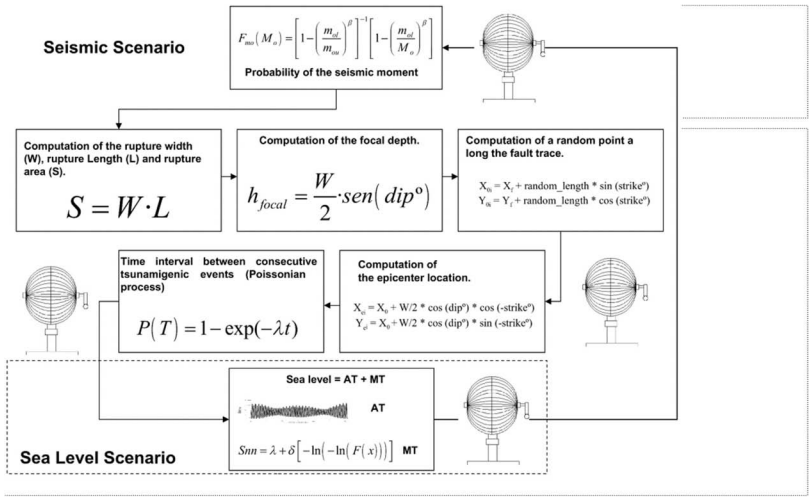

FIGURE 5 | Summary of the algorithm used to generate the synthetic catalog of tsunamis.

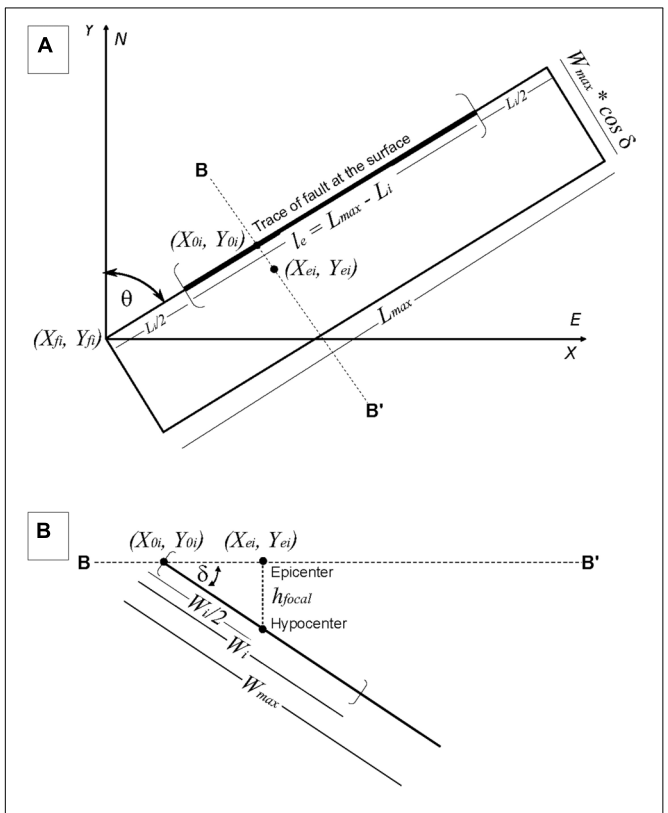

FIGURE 6 | Fault parameters. **(A)** Map view; **(B)** Cross section B - B′.

the synthetic sea level series, it is necessary to assign for each synthetic tsunamigenic event in the catalog a flooding scenario on the coast. Thus, a numerical database of scenarios is needed. These scenarios should cover the entire range of possible tsunami events in the synthetic catalog (earthquakes and sea levels). Each tsunami scenario is propagated using a tsunami numerical model, from the source region to the coast (study zone). In this section the numerical model and the simulated scenarios are described.

Numerical Model

We used the C3 (Cantabria-Comcot-Tsunami-Claw) numerical model to simulate the wave generation, propagation and coastal flooding (Olabarrieta et al., 2011). This model integrates finite difference and finite volumes model schemes, and solves the conservative form of the Non-Linear Shallow Water equations (NLSW), considering a Cartesian coordinate system.

These equations constitute a hyperbolic system that can be expressed by the following general conservation equation:

$$\frac{\partial q}{\partial t} + \frac{\partial f}{\partial x} + \frac{\partial g}{\partial y} = s \tag{16}$$

where q represents the vector of the conserved variables, f and g are the numerical flux vectors and s represents the source terms. These vectors are expressed in function of variables such as the water depth $H = (h + \xi)$ and the vertically integrated flow velocities (u, v)

$$\begin{aligned} q &= \begin{bmatrix} H \\ uH \\ vH \end{bmatrix} \\ f &= \begin{bmatrix} Hu \\ Hu^2 + \frac{1}{2}gH^2 \\ Huv \end{bmatrix} \\ g &= \begin{bmatrix} Hv \\ Huv \\ Hv^2 + \frac{1}{2}gH^2 \end{bmatrix} \\ s &= \begin{bmatrix} 0 \\ gh\frac{\partial h}{\partial x} - \frac{\tau_x}{\rho} \\ gh\frac{\partial h}{\partial y} - \frac{\tau_y}{\rho} \end{bmatrix} \end{aligned} \tag{17}$$

where ξ is the free surface elevation; x, y represent both components of the Cartesian coordinate system; g is the

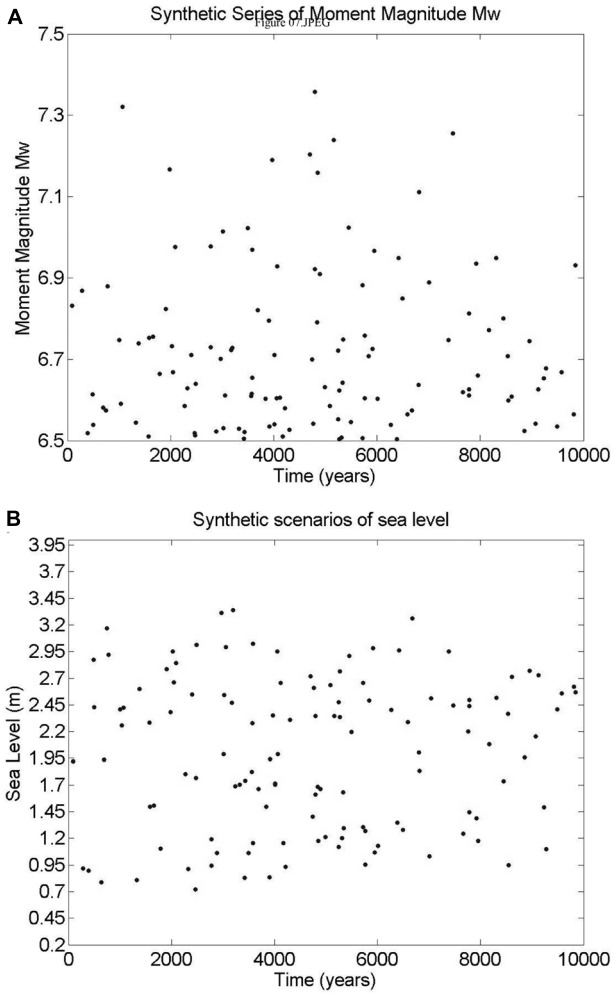

FIGURE 7 | Example of one time series of Moment magnitude (10000 years) for seismic events greater than 6.5 in all source regions **(A)** and associated sea levels **(B)**.

gravitational acceleration; ρ is the water density; *h* is the water depth at rest and τ*x*, τ*y* are the terms that represent the bottom shear stress.

The model solves the differential form of the mass and momentum conservation equations, applying a leap-frog scheme, based on the COMCOT numerical model of Liu et al. (1995). In the inner (detailed) nested grids a finite volume method (George and LeVeque, 2006) is applied to solve the integral form of the conservative equations. The C3 model (Olabarrieta et al., 2011) has been validated in the framework of the European Project TRANSFER using the standards and guidelines proposed by Synolakis et al. (2007).

The datasets used for the bathymetry and topography reconstruction are the Weatherall et al. (2015) database for the regional grids improved with the SWIM database (Zitellini et al., 2009). For the internal, more detailed bathymetric grids, we digitized the nautical charts of the Navy Hydrographic Institute of Spain. The topography and the geographical data used is from the National Geographic Institute of Spain (**Figure 9**).

Three different nested grids have been used to run the numerical model. From the regional bathymetry used to propagate the wave from the source, with a resolution of 864 m, to the detailed grid that includes the topography and local bathymetry with a cell size of 50 m. Between them we used an intermediate grid with a resolution of 216 m.

The submerged profile of the beaches in the area is characterized by the existence of a rocky slab at a water depth of about 5 m and several sandy shoals. In front of the Cádiz urban area there are several elongated shoals and rocky bars (**Figure 9**). These morphological features play an important role in the local tsunami wave propagation.

Simulated Scenarios

A set of tsunami scenarios are considered for tsunami propagation and for the creation of the tsunami datasets. These cases cover the entire range of possible tsunami scenarios in each zone (potential sources, earthquake magnitudes, and epicenter locations), together with all the possible sea levels.

To establish the tsunamigenic earthquake scenarios in each fault, the relation between the seismic moment magnitude and the rupture area has been taken into account. The width of the fault (W) is constrained by the L/W constant ratio for each fault and the momentum magnitude (eqs. 6-8). The relation between the momentum magnitude and the rupture area for each fault is shown as example for CWF Fault. A sensitivity analysis was carried out to define the minimal area of rupture that generates the earthquake and it was defined as 500 km^2. Based on a geological analysis of each fault, the maximal rupture area in this case for CWF fault was defined as 15.000 Km^2. Thus, the definition of moment magnitudes was obtained for areas between 500 km^2 and 15.000 km^2 each ΔS = 500 km^2, with minimal moment magnitude of 6.5 and maximal of 8.4, generating 31 magnitude events. As the magnitude increases, the area also increases exponentially. It is noteworthy that moment magnitudes selected are not equidistant, a change in the magnitude generates a higher variation in the area when the magnitude is large. Therefore, a larger number of scenarios have been considered for the big magnitudes.

On the other hand, in each fault, up to 4 different epicenter locations have been considered for each magnitude. The number of epicenter locations for a specific magnitude event, in a specific fault, depends on the moment magnitude (it defines the source size) and the maximal size of each fault. In the case of smaller magnitude events the size of the source is also small and more epicenter locations can be distributed along the fault. In the case of CWF fault, the largest fault in the area, 4 possible epicenters distributed along the fault were selected for magnitudes between 6.5 and 7.2, 3 for magnitudes 7.3 to 7.6, 2 for magnitudes 7.7 to 8.0 and just 1 epicenter location is possible for magnitudes larger than 8.0. The combination of magnitudes and epicenter locations on CWF fault led to 53 possible earthquake scenarios.

A sensitivity analysis was carried out to evaluate the sea level ranges based on numerical simulations and taking into account the computational time constraints. This analysis

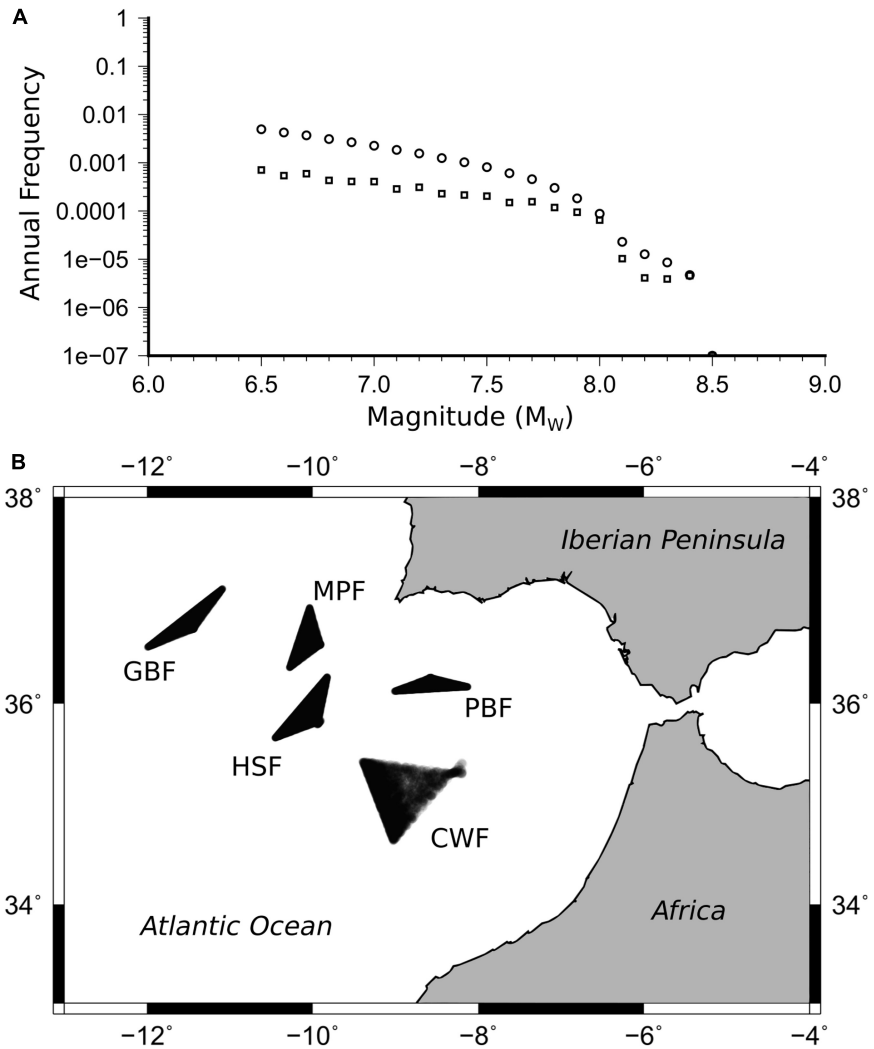

FIGURE 8 | (A) Distribution of all synthetic generated magnitudes M_w in discrete (squares) and cumulative(circles) form, and **(B)** location of the synthetically generated epicenters for all the tsunamigenic earthquake scenarios.

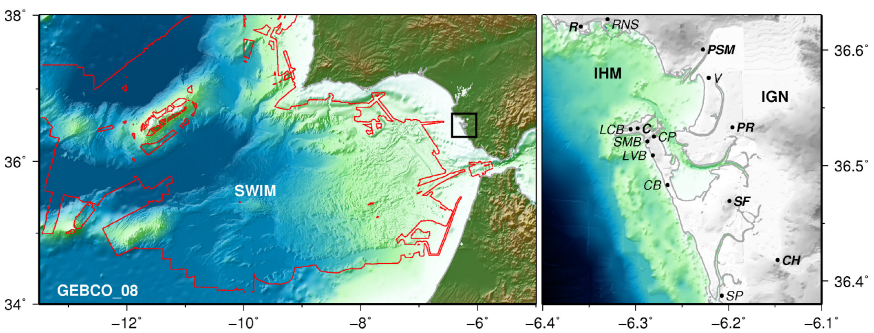

FIGURE 9 | Topo-bathymetric grids. GEBCO data, SWIM: Zitellini et al. (2009) bathymetric data (The red line is the limit of the high resolution SWIM bathymetry), IHM: Instituto Hidrográfico de la Marina (Navy Hydrographic Institute) data (the black square is the limit of the high resolution local bathymetry IHM), IGN: Instituto Geográfico Nacional (National Geographic Institute) data. Labels in italic font type show the locations commented in the text: R, Rota; RNS, Rota Naval Station; PSM, Puerto de Santa María; V, Valdelagrana; C, Cádiz; CP, Cádiz Port; LCB, La Caleta Beach; SMB, Santa María Beach; LVB, La Victoria Beach; CB, Cortadura Beach; PR, Puerto Real; SF, San Fernando; CH, Chiclana; SP, Sancti Petri.

allowed considering 4 sea level ranges (Δsl = 1.0 m). In **Table 3** the selected tidal levels are indicated where the reference level corresponds to the mean low spring tidal level.

Finally, the combination of magnitudes, epicenter location and sea levels for the CWF fault requires the simulation of 212 scenarios.

A total of 619 scenarios have been modeled (**Table 4**) using the C3 numerical model. The numerical simulations were performed in the Altamira Supercomputer which is part of the Spanish Supercomputation network. This supercomputer is operated by IFCA (Cantabrian Physics Institute) and it has 512 processors able to manage 4.5 billion of operations per second.

PROBABILISTIC THEMATIC HAZARD MAPS

Once the 1000 time series of tsunamigenic earthquake events, coinciding with a given sea level, are created in the Monte Carlo computation, the effect of each tsunami on the coast is obtained using the numerical database generated in the previous steps. An algorithm written in Matlab® was used for this purpose. For each scenario in the synthetic catalog, the closest case (sea level + earthquake) in the numerical database was identified. For the interpolation of the events of the synthetic catalog, we start from the basis of a 3D matrix of numerically modeled scenarios, with three inputs: magnitude, location of the epicenter and sea level. For a synthetic event of a given magnitude, the closest modeled magnitude is searched in the matrix, for this closest magnitude, the closest modeled epicenter to the synthetic catalog is searched among the modeled epicenters, and finally, the corresponding event with the closest sea level is searched in the matrix. Thus, the event of the synthetic series is associated with the closest simulated event in magnitude, location of the epicenter and sea level. The tsunami intensity measures corresponding to this numerical case (maximum current speed, maximum water depth, maximum wave elevation, maximum Froude number, and maximum force) are assigned to the tsunamigenic earthquake in the synthetic catalog. Total forces, consider hydrostatic and hydrodynamic forces as defined in FEMA (2000), and are associated with a drag coefficient *CD,* which represents the shear coefficient which depends on the bottom roughness, on the Reynolds number and on the geometry of the structures in the flooding area. *CD* is based on FEMA (2000); Synolakis (2003); Yeh (2006), which provided recommended shear coefficient values for various obstacle geometries.

TABLE 3 | Considered tidal level scenarios (the reference level corresponds to the mean low spring tidal level).

Tidal level scenario	Tidal level (m)	Representative range (m)
1	0.5	0.0 - 1.0
2	1.5	1.0 - 2.0
3	2.5	2.0 - 3.0
4	3.5	3.0 - 4.0

TABLE 4 | Number of considered scenarios in each fault.

Fault	Number of scenarios
CWF	212
GBF	128
HSF	120
MPF	82
PBF	77
Total	619

The time series of the tsunami intensity measures can be derived for the whole coastal region following the described procedure. Therefore, these time series of the maximum value can be used to perform a statistical analysis of the selected tsunami intensity measures and derive maps with an associated return period.

Once the time series are reconstructed in each high-resolution grid node, these data are sorted in an ascendant order. The cumulative probability is assigned to each organized scenario. This is given by its position, *i*:

$$P_i = \frac{i}{(m+1)} \tag{18}$$

where i represents the data position and m represents the total number of data. The distribution function of the analyzed parameter *vi* is given by the following expression:

$$FZ_i\,(v) = 1 - e^{-\lambda.(1-P_i)} \tag{19}$$

where *FZi (v)* is the annual exceedance probability and λ is the tsunamigenic earthquakes annual rate. For the computation of return period T_r the following expression is used:

$$T_r = \frac{1}{FZ(v_r)} \tag{20}$$

where T_r represents the mean number of years in which the variable v_r exceeds a given value.

For each return period and each synthetically generated catalog, a value of the study variable is obtained in all the grid nodes. Therefore, for a given return period, the analyzed variable can be mapped in the high-resolution grid. If several synthetically generated earthquake and sea level catalogs are used, the value of the analyzed parameter for a given return period will present a mean value and a variance. Computing the distribution function of the values obtained for the given return period, the value for a given return period with a given confidence can be obtained.

For a given return period it is possible in each grid point of the detailed mesh (the flooding area) to obtain the desired parameter (e.g., maximum water depth) using the grid point distribution function. The representation on a map of this parameter for all the grid points allow us to produce thematic maps for specific return periods.

In the present study, return periods of 500, 1000, 5000, and 10000 years with a confidence band of 99% have been considered. This confidence band is representative of the mean extreme events. Other confidence bands can easily be derived.

RESULTS

The probabilistic methodology applied to the Cádiz test-site enables the generation of different thematic maps in the study region. These maps do not represent the impact generated by a single tsunamigenic earthquake but the combined effect of different earthquakes in the area. For example, it is possible that an earthquake scenario generates a big impact in La Victoria beach but has a minor impact in Rota. However, another earthquake can generate a big impact in Rota and yet has a small effect in La Victoria. In these maps both Rota and La Victoria will appear to have a great impact, merging the effects of both earthquakes.

The maximum tsunami wave elevation is plotted only in those areas covering the intertidal zones and in those areas above this zone that are flooded due to tsunamis (**Figure 10**). For a 500-year return period the effects due to tsunamis are very low, and they are restricted to very specific areas. The area showing the highest sea surface elevations corresponds to the harbor of Cádiz and Rota. As expected, as the return period increases, the flooded area also increases, especially in the inner zone of Cádiz Bay as well as in the Sancti Petri zone. In Cádiz city, several beaches such as La Caleta, Santa María del Mar, Victoria, and Cortadura, are affected by the combined effect of sea level (tides) and tsunamis.

In **Figure 11**, the maximum current speed for different return periods has been plotted. For a return period of 500 years only the zone of Rota presents velocities exceeding the value of 0.5 m/s. For a return period of 1000 years, velocities higher than 4 m/s are achieved in the urban beaches of Cádiz and Rota. For higher return periods most of the coastal area present maximum current speeds higher than 9 m/s.

Figure 12 the maximum total forces, including the hydrostatic and hydrodynamic contributions with a drag coefficient of 2, have been plotted. For a 500-year return period the net force does not exceed the value of 1 ton/m in the study area. For the 1000-year return period the maximum observed net force increases to 4 tons/m. Rota and the urban beaches in Cádiz (Caleta, Santa María del Mar, Victoria and Cortadura) are the zones with the highest net forces. For higher return periods values of 5 tons/m are reached in large areas. In Rota and in the urban beaches of Cádiz, values of up to 10 tons/m are possible.

DISCUSSION

Method and Limitations

The PTHA methodology proposed here treats aleatoric uncertainties on the seismic source and tidal stage through

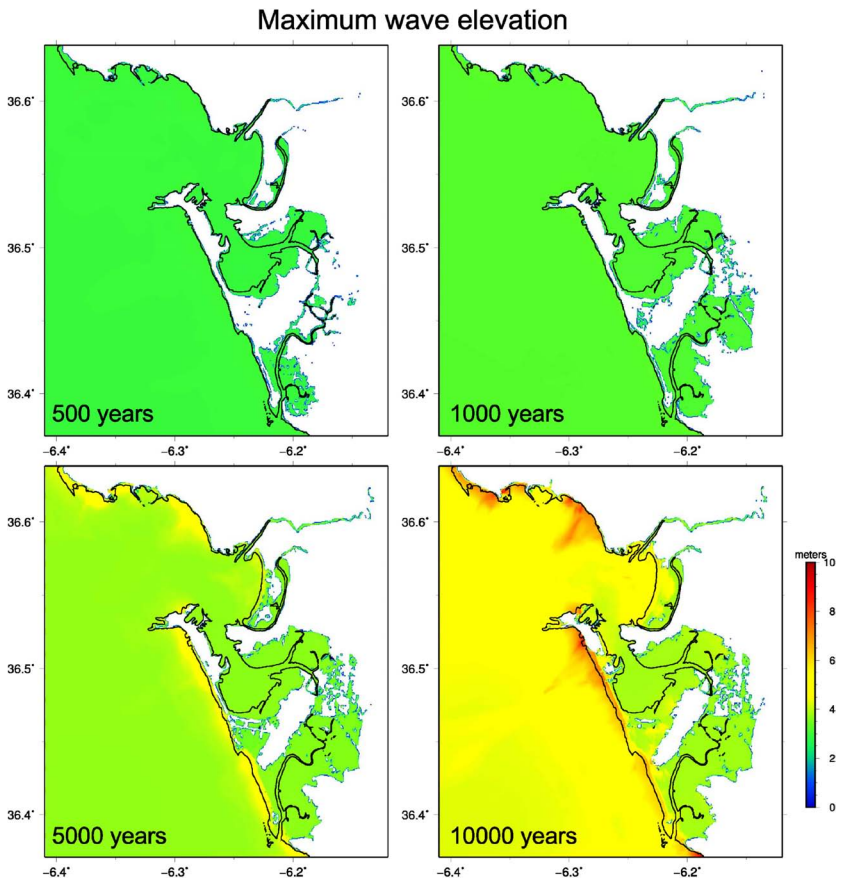

FIGURE 10 | Maximum wave elevation for different return periods. 99% confidence interval.

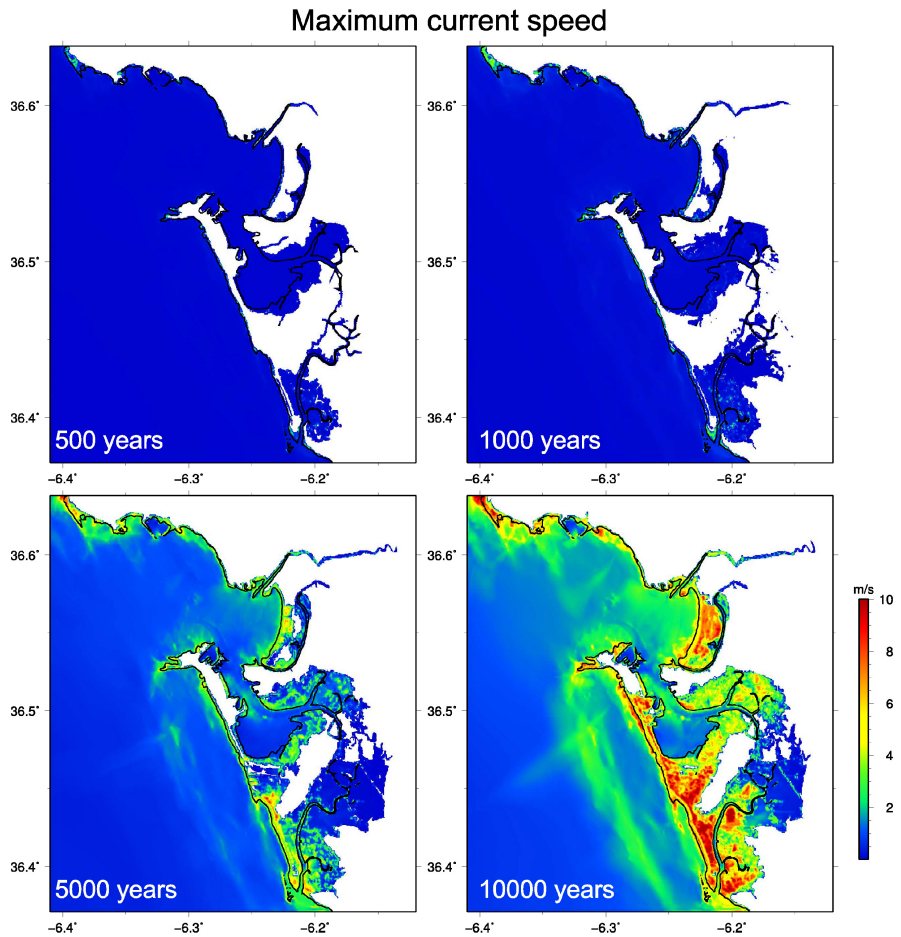

FIGURE 11 | Maximum current speed for different return periods. 99% confidence interval.

a Monte Carlo type framework. It, however, overlooks the epistemic uncertainties such as those related to the modeling of tsunami generation, propagation, and inundation and also those related to the accuracy of the bathymetric-topographic data. Our methodology allows deriving probabilistic coastal hazard maps (wave heights, current speed, and total force) for different return periods. It deals only with tsunamis of tectonic origin and can be applied to any tsunami-threatened coast where high-resolution DEM and records of tidal variations are available.

The PTHA developed here adopts a simple approximation to the source definition fixing some parameters of the earthquake faults (strike, dip, and rake angles) to constrain the variability of the models. This approximation is common in regional PTHA (e.g., Cheung et al., 2011; Heidarzadeh and Kijko, 2011; Power et al., 2012; Davies et al., 2018) but our methodological approximation can be extended to fully incorporate the aleatory uncertainties on the source definition by means of probability density functions using the Monte Carlo approach. Although the incorporation of these branches into the Monte Carlo approach would increase exponentially the number of simulations to compute, the use of GPU-optimized models can overcome this difficulty.

An important source of aleatoric uncertainty in the PTHA concerns the sea level when the tsunami waves reach the nearshore areas. However, this source of uncertainty is commonly disregarded in tsunami hazard assessments. On the other hand, tsunami-tide interaction has been a discussion topic in the literature. Several studies have been carried out to understand whether tide-tsunami interactions enhance/reduce tsunami elevation, flow speed, and arrival times. Based on observations and/or numerical experiments, various authors have found that tsunami inundation in rivers, inlets, harbors, and estuaries is strongly affected by tidal conditions (e.g., Kowalik et al., 2006; Kowalik and Proshutinsky, 2010; Zhang et al., 2011; Lee et al., 2015; Ayca and Lynett, 2016; Shelby et al., 2016; Tolkova, 2016; Ayca et al., 2017). Causes of tide-tsunami interaction are attributed to tidally induced currents and changes in the depth altering the background conditions during the propagation of the tsunami from its source (Weisz and Winter, 2005), both effects are small in the open ocean but increase as the tsunami shoals, mainly in coastal and bathymetric particular configurations as energetic tidal channels communicating large bodies of water or coastal configuration that can induce resonance effects between large scale shallow

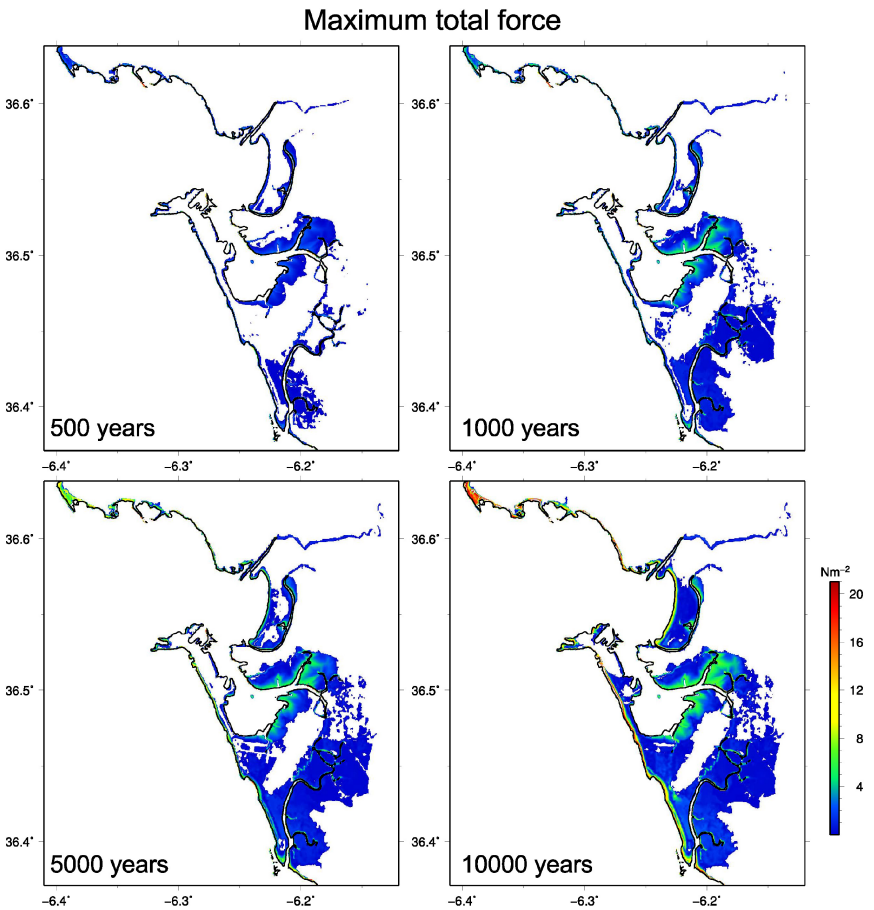

FIGURE 12 | Maximum forces for different return periods, per unit area of exposed element. 99% confidence interval.

shelfs, narrow channels, islands, etc. The hydrodynamic pattern of tsunamis occurring under strong tidal regimes can be assessed using different approaches with increasing levels of complexity, depending on the scope of the study and local conditions of the site. Our PTHA approach accounts for the uncertainty of the tide level when the tsunami reaches the coast off Cádiz by incorporating four tidal stages (0.5 m, 1.5 m, 2.5 m, and 3.5 m) into the Monte Carlo simulations. The sensitivity related to these tides levels has not been tested, and it is subject to future studies. The reference for the selected tidal levels corresponds to the mean low spring tidal level. While this approach allows reducing the computational time, it has the limitation of overlooking the non-linear interaction between the tsunami wave, the tidal wave and their induced currents, which could be important on a large spatial and temporal scales. However, in the city of Cádiz that is exposed to the open sea, there are no relevant bathymetry features to generate tsunami-tide interactions, that together with the very large dimensions and periods of the tide (1000 kms and hours) and the tsunami (100 kms and minutes), we assume a small tsunami-tide interaction. Thus, the tide is a boundary condition that can be assumed as instantaneous due to its low speed of variation (in hours), compared to the tsunami speed (in minutes). On the other hand, inside the bay a tsunami-tidal interaction could occur mainly in current speeds that have not been considered here. The study of this tsunami-tide interaction is a challenge that requires further investigation beyond the scope of this work.

Coastal Tsunami Impact

The impact of tsunamis generated in the SW Iberian Transpressive Domain is significant on the Bay of Cádiz and increases, as expected, with the increase of the return period as shown in the results. It is also expected that the incorporation of the sea level variation due to the local tide highly influences the tsunami hazard results on the Bay of Cádiz. To evidence the relevance and the influence of the sea level incorporation, numerical simulations conducted for an example of a large tsunami generated in CWF (Cadiz Wedge Fault) with a $M_w = 8.4$ in the study area of Cadiz are presented (**Figures 13A-C**). **Figure 13A** presents the maximum tsunami wave elevation for a simulation in a low tide sea level. **Figure 13B** shows the result of the same scenario but incorporating the sea level to the propagation (spring tide 3.5 m, characteristic of the area). And finally, **Figure 13C** depicts the resulting flooded area for the same scenario executed in low tide condition, and then adding linearly the tide sea level (3.5 m) after the numerical simulation,

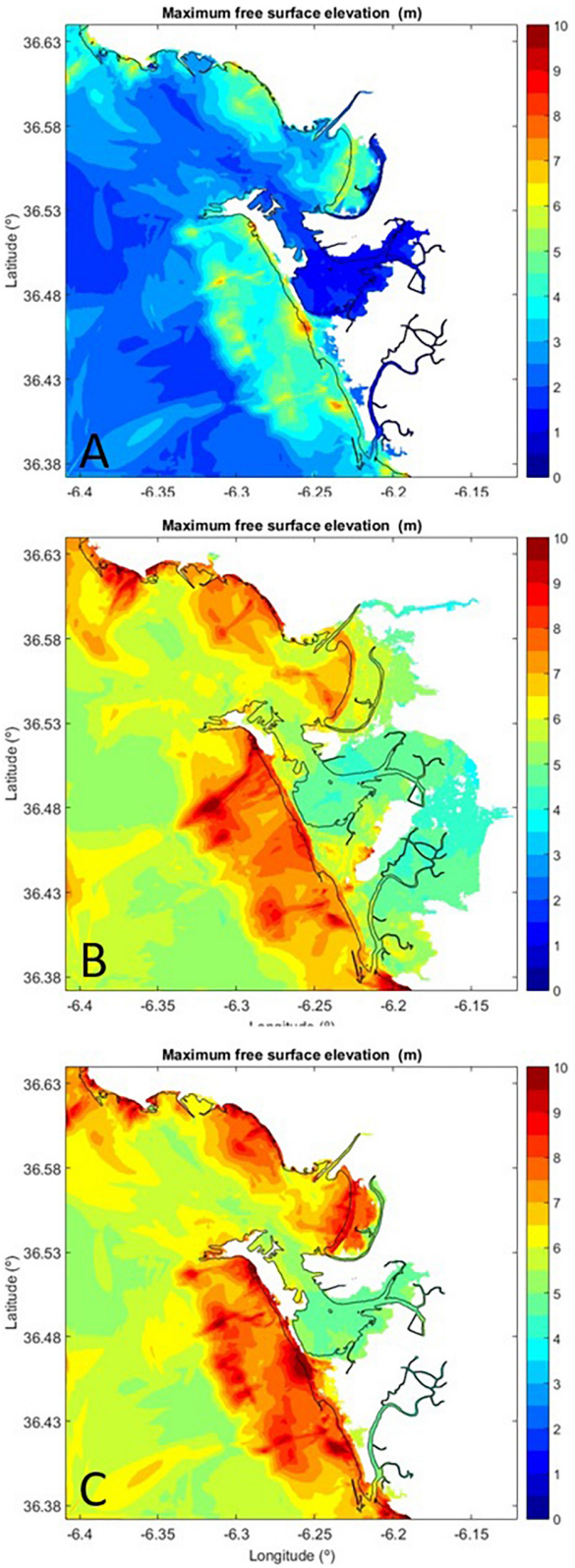

FIGURE 13 | Importance of using tides in the simulations. **(A)** low tide propagation. **(B)** high tide propagation. **(C)** low tide propagation and tide added linearly.

which is a common approximation to include the tidal effect in PTHA analysis. Two main remarks can be drawn from these results. First, the incorporation of the tide is relevant because the flooded area is larger, and second, this incorporation was made using different initial levels, not just adding tidal levels linearly. Thus, in order to reduce the uncertainty of the sea level in meso and macro tidal areas in a probabilistic analysis, it is required to include the sea level as another variable taking into account its probability of occurrence.

Another important issue concerns the use of deterministic and probabilistic thematic tsunami hazard maps. Whether deterministic (conservative scenario) or probabilistic analysis serves better increasing the tsunami resilience of coastal areas depends on the scale and scope of the study. **Figure 14** depicts a comparison of the aggregated results (envelope of the worst credible cases in each fault) for the high tide level obtained in a deterministic analysis with those obtained for the probabilistic results for a return period of 10000 years (confidence interval 99%). The comparison clearly indicates that the deterministic approach is very conservative. It is also noticeable that the aggregated results from the worst-case scenarios for each source of the deterministic approach (parameterized in Álvarez-Gómez et al., 2008; Omira et al., 2009; Lima et al., 2010) is associated with a return period longer than (Tr = 10000 years), as expected. Therefore, deterministic maps could be used to define those zones with no probability of being affected by a tsunami.

Both approaches can address different objectives in the analysis of the affected zone in a tsunami–prone area. Deterministic maps are more subjective but they are useful to establish inundation limits in areas where special infrastructures (nuclear plants, inflammable materials, pipelines) could be built or to assign the evacuation zones. On the other hand, the probabilistic maps are more valuable for vulnerability and risk assessments as well as for insurance purposes, as they provide a more complete picture of the hazard for a given zone with an associated return period. Additionally, building and infrastructure engineering design include probabilistic risk scenarios and risk return periods in the design.

To summarize, despite the limitations of the proposed PTHA methodology in dealing with limited sources of aleatoric uncertainty and disregarding the epistemic uncertainties it interestingly allows combining uncertainties in the generation parameters with the those of sea level in meso and maro tidal areas and performs high-resolution probabilistic tsunami hazard assessment. We believe that the method could highly benefit from further improvements. Particularly, the implementation in a specific case can be improved, with better probabilistic description of the different involved variables (definition of sources, geometrical parameters and scaling relations, Mw distribution, epicenter location in each fault, sea level distributions), and also, with higher resolution of the number of numerically modeled scenarios and higher grid resolutions inland taking into account the different source and sea level parameters, using more powerful and faster models using for example GPU techniques. However, the proposed methodology allows obtaining a reduction of the uncertainties for probabilistic

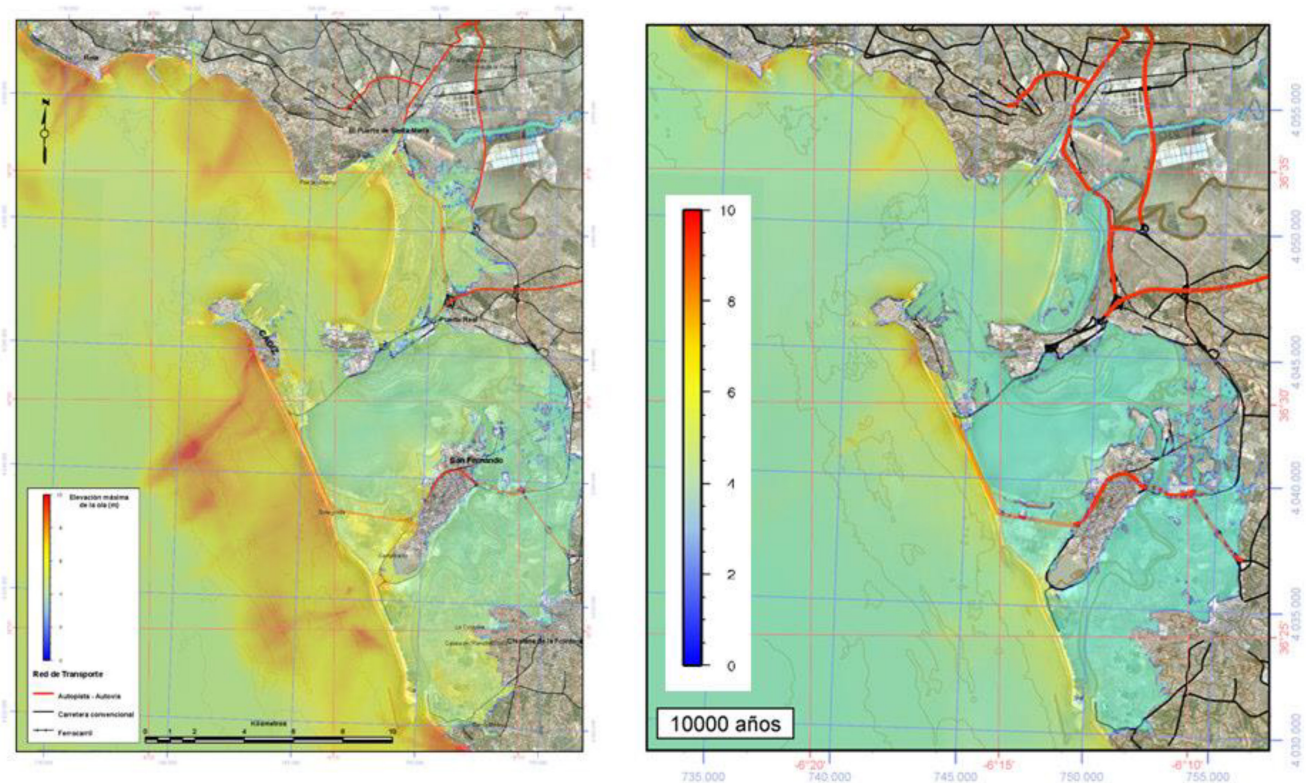

FIGURE 14 | Comparison of the aggregated maximum wave elevation obtained for the high tide condition in the deterministic and in the probabilistic approaches (Tr = 10000 years and a confidence interval of 99%).

flooding maps, achieving a distribution function of different tsunami intensity measures (max. water depth, max. wave elevation, max. current sped, max. forces, etc.) in each nodal grid point inland.

CONCLUSION

Deterministic or scenario-based approaches are based on tsunami events that could happen in the future, but have occurrence probabilities that are not well understood. In most deterministic assessments the tsunami scenario represents the worst tsunami case that can take place in the study region, often inferred from historical data. The most difficult task in this approach is to assign a return period to the considered scenario, which sometimes is impossible because of the time span of the seismic catalogs. Nevertheless, the results obtained from scenario-based approaches have been used for several applications, such as the establishment of inundation zones, evacuation maps (Geist and Parsons, 2006) and urban planning.

In this study, a new probabilistic method for the tsunami hazard estimation has been presented and its application to the Cádiz area has been described. This probabilistic method is combined with the application of high-resolution numerical simulations for tsunami propagation and inundation (in the present case the C3 model, Olabarrieta et al., 2011) to derive inundation and hazard maps for given return period and confidence interval. A novel characteristic of the present methodology, based on Monte Carlo simulations, is the statistical treatment of both tsunami hazard and sea level variation, including both astronomical and meteorological effects. Therefore, the present method does not assume that the tsunamigenic earthquake occurs at a given tidal level condition.

The application of the PTHA method described here requires *a priori* zoning of the source region and the identification of the different faults in each source region. In the specific case of the Cádiz area, only the tsunamigenic areas in the SWIT region were considered. The main tsunamigenic sources in the Gulf of Cádiz were identified as clusters of seismicity in the SWIT region, which represent the maximum earthquake ruptures. GBF (Gorringe Bank Fault), HSF (Horseshoe Fault), MPF (Marques de Pombal Fault), PBF (Portimao Bank Fault), and CWF (Cádiz Wedge Fault) were the five main earthquake ruptures identified in the analysis region. The *a* and *b* parameters of the Gutenberg-Ritcher Law for the SWIT region were obtained from the study of the instrumental and historical seismic catalog of the IGN. The tidal level probability distribution function and the characteristics of the main tidal harmonic constituents were obtained from a tidal gauge located near Cádiz. 1000 different time series of combined tsunamigenic earthquake and tidal levels were

synthetically generated using the Monte Carlo technique. Each time series had a 10000-year duration.

The C3 model was used to propagate the tsunami from the source region to the coast. The tsunami characteristics were analyzed statistically to derive different thematic maps for the return periods of 500, 1000, 5000, and 10000 years. The derived thematic maps include the maximum wave elevation, the maximum current velocity, the maximum Froude number, and the maximum total forces. The thematic maps obtained for a return period of 10000-year (confidence interval 99%) were compared to those derived from the aggregated deterministic worst-case scenarios for the Cádiz region. This deterministic scenario assumed that the worst-case scenarios for each considered source coincided with the maximum water level measured by the tidal gauge, which means that the probability of occurrence of this extreme event is very low. Thus, the deterministic approach was very conservative. Deterministic maps could be used to define those zones with a very low probability or with no probability of being affected by a tsunami. This is a useful information for visualizing the hazard and the establishment of the maximum limits of flooding, which is necessary for planning the evacuation zones and for defining those areas in which critical infrastructures (e.g., nuclear plants, flammable materials, pipelines) can be built. Ideally, deterministic approach should be linked to the probabilistic study. The probabilistic maps are more valuable for vulnerability and risk assessment and also for insurance proposes.

DATA AVAILABILITY STATEMENT

The raw data supporting the conclusions of this article will be made available by the authors, without undue reservation.

AUTHOR CONTRIBUTIONS

MG conceived the manuscript, did the probabilistic approximation, and managed the process. JÁ-G conducted the characterization of tsunamigenic sources. ÍA-Q computed the Numerical simulations. LO and MO compiled the Montecarlo procedure and created the database. RJ, EK, and JB provided some data and internal discussion on the probabilistic model and revised the manuscript. MB, RO, and MM wrote parts of the manuscript and participated in internal discussion. ÍA-A and AL reviewed the probabilistic model. All authors contributed to the article and approved the submitted version.

FUNDING

This research was part of the TRANSFER project (http://www.transferproject.eu/). AL acknowledges the support of the Spanish Grant MTM2008-00759. Some of the figures have been produced with the software GMT (Wessel and Smith, 1998). This is a contribution from the Environmental Hydraulics Institute (Universidad de Cantabria) and the Active Tectonics, Paleoseismology, and Associated Hazards research group (UCM-910368).

ACKNOWLEDGMENTS

We thank to the Environmental Ministry of Spain (Dirección General de Costas de Andalucia) for providing us the local bathymetry. We also thank to the Spanish Supercomputing Network the use of the Altamira IFCA supercomputer. We would like to thank to the TSUSY Project (IHCantabria).

REFERENCES

Aki, K. (1966). Generation and propagation of G waves from Niigata earthquake of June 16, 1964. Part 2. Estimation of earthquake moment, released energy, and stress-strain drop from the G wave spectrum. *Bull. Earthq. Res. Inst.* 44, 73–88.

Álvarez-Gómez, J. A., Gutiérrez, O. Q. G., Aniel-Quiroga, Í, and González, M. (2012). Tsunamigenic potential of outer-rise normal faults at the Middle America trench in Central America. *Tectonophysics* 574, 133–143. doi: 10.1016/j.tecto.2012.08.014

Álvarez-Gómez, J. A., Miranda, J. M., Carreño, E., Matías, L., Martínez-Solares, J. M., and Baptista, M. A. (2008). Review of tsunamigenic faults in the Gulf of Cádiz. *Geotemas* 10, 1425–1428.

Annaka, T., Satake, K., Sakakiyama, T., Yanagisawa, K., and Shuto, N. (2007). Logic-tree approach for probabilistic tsunami hazard analysis and its applications to the japanese coasts. *Pure Appl. Geophys.* 164, 577–592. doi: 10.1007/s00024-006-0174-3

Argus, D. F., Gordon, R. G., DeMets, C., and Stein, S. (1989). Closure of the Africa-Eurasia-North America plate motion circuit and tecton- ics of the gloria fault. *J. Geophys. Res.* 94, 5585–5602. doi: 10.1029/JB094iB05p05585

Ayca, A., and Lynett, P. J. (2016). Effect of tides and source location on nearshore tsunami-induced currents. *J. Geophys. Res. Oceans* 121, 8807–8820. doi: 10.1002/2016jc012435

Ayca, A., Lynett, P. J., and Wilson, R. (2017). Effects of tide and wave directionality on localized tsunami-induced currents in port and harbors. *Coast. Eng. Proc.* 1:8. doi: 10.9753/icce.v35.currents.8

Baptista, M. A. (2019). Tsunamis along the azores gibraltar plate boundary. *Pure Appl. Geophys.* 177, 1713–1724. doi: 10.1007/s00024-019-02344-8

Baptista, M. A., and Miranda, J. M. (2009). Revision of the Portuguese catalog of tsunamis. *Nat. Haz. Earth Syst. Sci.* 9, 25–42. doi: 10.5194/nhess-9-25-2009

Basili, R., Brizuela, B., Herrero, A., Iqbal, S., Lorito, S., Maesano, F. E., et al. (2021). The Making of the NEAM Tsunami Hazard Model 2018 (NEAMTHM18). *Front. Earth Sci.* 8:616594. doi: 10.3389/feart.2020.616594

Basili, R., Tiberti, M. M., Kastelic, V., Romano, F., Piatanesi, A., Selva, J., et al. (2013). Integrating geologic fault data into tsunami hazard studies. *Nat. Haz. Earth Syst. Sci.* 13, 1025–1050. doi: 10.5194/nhess-13-1025-2013

Behrens, J., Løvholt, F., Jalayer, F., Lorito, S., and Salgado-Gálvez, M. (2021). Probabilistic tsunami hazard and risk analysis -a review of research gaps. *Front. Earth Sci.* doi: 10.3389/feart.2021.628772

Blaser, L., Krüger, F., Ohrnberger, M., and Scherbaum, F. (2010). Scaling relations of earthquake source parameter estimates with special focus on subduction environment. *Bull. Seismol. Soc. Am.* 100, 2914–2926. doi: 10.1785/0120100111

Borges, J. F., Fitas, A. J., Bezzeghoud, M., and Teves-Costa, P. (2001). Seismotectonics of Portugal and its adjacent Atlantic area. *Tectonophysics* 331, 373–387. doi: 10.1016/s0040-1951(00)00291-2

Burbidge, D., Cummins, P. R., Mleczko, R., and Thio, H. K. (2008). A probabilistic tsunami hazard assessment for Western Australia. *Pure Appl. Geophys.* 165, 2059–2088. doi: 10.1007/978-3-0346-0057-6_6

Cheung, K. F., Wei, Y., Yamazaki, Y., and Yim, S. C. (2011). Modeling of 500-year tsunamis for probabilistic design of coastal infrastructure in the Pacific Northwest. *Coast. Eng.* 58, 970–985. doi: 10.1016/j.coastaleng.2011.05.003

Coppersmith, K. J., and Youngs, R. R. (1986). "Capturing uncertainty in probabilistic seismic hazard assessments within intraplate tectonic environments," in *Proceedings of the Third U.S. National Conference on Earthquake Engineering*, Charleston, SC, 301–312.

Cornell, C. A. (1968). Engineering seismic risk analysis. *Bull. Seismol. Soc. Am.* 58, 1583–1606.

Cramer, C. H., Petersen, M. D., and Reichle, M. S. (1996). A Monte Carlo approach in estimating uncertainty for a seismic hazard assessment of Los Angeles, Ventura, and Orange Counties, California. *Bull. Seismol. Soc. Am.* 86, 1681–1691.

Cunha, T., Watts, A., Pinheiro, L., and Myklebust, R. (2010). Seismic and gravity anomaly evidence of large-scale compressional deformation off SW Portugal. *Earth Planet. Sci. Lett.* 293, 171–179. doi: 10.1016/j.epsl.2010.01.047

Davies, G., and Griffin, J. (2019). Sensitivity of probabilistic tsunami hazard assessment to far-field earthquake slip complexity and rigidity depth-dependence: case study of Australia. *Pure Appl. Geophys.* 177, 1521–1548. doi: 10.1007/s00024-019-02299-w

Davies, G., Griffin, J., Løvholt, F., Glimsdal, S., Harbitz, C., Thio, H. K., et al. (2018). A global probabilistic tsunami hazard assessment from earthquake sources. *Geol. Soc. Spec. Publ.* 456, 219–244. doi: 10.1144/sp456.5

Davis, R. A., Fox, W. T., Hayas, M. O., and Boothroyd, J. C. (1972). Comparison of ridge and runnel systems in tidal and non-tidal environments. *J. Sediment. Petrol.* 42, 413–421.

Davison, F. C., and Scholz, C. H. (1985). Frequency-moment distribution of earthquakes in the Aleutian Arc: a test of the characteristic earthquake model. *Bull. Seismol. Soc. Am.* 75, 1349–1361.

De Risi, R., and Goda, K. (2016). Probabilistic earthquake-tsunami multi-hazard analysis: application to the Tohoku region, Japan. *Front. Built Environ.* 2, 2–25. doi: 10.3389/fbuil.2016.00025

Ebel, J. E., and Kafka, A. L. (1999). A Monte Carlo approach to seismic hazard analysis. *Bull. Seismol. Soc. Am.* 89, 854–866.

El-Hussain, I., Omira, R., Deif, A., Al-Habsi, Z., Al-Rawas, G., Mohamad, A., et al. (2016). Probabilistic tsunami hazard assessment along Oman coast from submarine earthquakes in the Makran subduction zone. *Arab. J. Geosci.* 9:668. doi: 10.1007/s12517-016-2687-0

FEMA (2000). *Coastal Construction Manual, Tech. Rep. 55*. Washington, DC: Federal Emergency Management Agency.

Fukao, Y. (1973). Thrust faulting at a lithospheric plate boundary the portugal earthquake of 1969. *Earth Planet. Sci. Lett.* 18, 205–216. doi: 10.1016/0012-821x(73)90058-7

Garcia-Orellana, J., Gràcia, E., Vizcaino, A., Masqué, P., Olid, C., Martínez- Ruiz, F., et al. (2006). Identifying instrumental and historical earthquake records in the SW Iberian margin using 210Pb turbidite chronology. *Geophys. Res. Lett.* 33:L24601. doi: 10.1029/2006GL028417

Gardner, J. K., and Knopoff, L. (1974). Is the sequence of earthquakes in Southern California, with aftershocks removed, Poissonian? *Bull. Seismol. Soc. Am.* 64, 1363–1367.

Geissler, W. H., Matias, L., Stich, D., Carrilho, F., Jokat, W., Monna, S., et al. (2010). Focal mechanisms for sub-crustal earthquakes in the Gulf of Cadiz from a dense OBS deployment. *Geophys. Res. Lett.* 37:L18309. doi: 10.1029/2010GL044289

Geist, E., and Parsons, T. (2006). Probabilistic analysis of tsunami hazards. *Nat. Hazards* 37, 277–314. doi: 10.1007/s11069-005-4646-z

Geist, E. L., and Lynett, P. J. (2014). Source processes for the probabilistic assessment of tsunami hazards. *Oceanography* 27, 86–93.

George, D. L., and LeVeque, R. J. (2006). Finite volume methods and adaptive refinement for global tsunami propagation and local inundation. *Sci. Tsunami Hazards* 24, 319–328.

Gica, E., Teng, M. H., Liu, P. L. F., Titov, V., and Zhou, H. (2007). Sensitivity analysis of source parameters for earthquake-generated distant tsunamis. *J. Waterw. Port Coast. Ocean Eng.* 133, 429–441. doi: 10.1061/(asce)0733-950x(2007)133:6(429)

Gjevik, B., Pedersen, G., Dybesland, E., Harbitz, C. B., Miranda, P. M. A., Baptista, M. A., et al. (1997). Modeling tsunamis from earthquake sources near Gorringe Bank southwest of Portugal. *J. Geophys. Res. Oceans* 102, 27931–27949. doi: 10.1029/97jc02179

Goda, K., Yasuda, T., Mori, N., and Mai, P. M. (2015). Variability of tsunami inundation footprints considering stochastic scenarios based on a single rupture model: application to the 2011 T ohoku earthquake. *J. Geophys. Res. Oceans* 120, 4552–4575. doi: 10.1002/2014jc010626

González, F. I., Geist, E. L., Jaffe, B., Kânoglu, U., Mofjeld, H., Synolakis, C. E., et al. (2009). Probabilistic tsunami hazard assessment at seaside, Ore- gon, for near- and far-field seismic sources. *J. Geophys. Res.* 114:C11023. doi: 10.1029/2008JC005132

González, M., Medina, R., Olabarrieta, M., and Otero, L. (2010). Tsunami hazard assesment in the Southern coast of Spain. *Turk. J. Earth Sci.* 19, 351–366.

Grandin, R., Borges, J. F., Bezzeghoud, M., Caldeira, B., and Carrilho, F. (2007). Simulations of strong ground motion in SW Iberia for the 1969 February 28 (Ms= 8.0) and the 1755 November 1 (M $\sim$ 8.5) earthquakes – II. Strong ground motion simulations. *Geophys. J. Int.* 171, 807–822. doi: 10.1111/j.1365-246x.2007.03571.x

Grezio, A., Babeyko, A., Baptista, M. A., Behrens, J., Costa, A., Davies, G., et al. (2017). Probabilistic tsunami hazard analysis: multiple sources and global applications. *Rev. Geophys.* 55, 1158–1198. doi: 10.1002/2017RG000579

Grezio, A., Sandri, L., Marzocchi, W., Argnani, A., and Gasparini, P. (2012). Probabilistic tsunami hazard assessment for messina strait area (Sicily, Italy). *Nat. Hazards* 64, 329–358. doi: 10.1007/s11069-012-0246-x

Griffin, J., Pranantyo, I. R., Kongko, W., Haunan, A., Robiana, R., Miller, V., et al. (2016). Assessing tsunami hazard using heterogeneous slip models in the Mentawai Islands, Indonesia. *Geol. Soc. Spec. Publ.* 441, 47–70. doi: 10.1144/SP441.3

Gutscher, M.-A., Dominguez, S., Westbrook, G. K., and Leroy, P. (2009). Deep structure, recent deformation and analog modeling of the Gulf of Cadiz accretionary wedge: implications for the 1755 Lisbon earthquake. *Tectonophysics* 475, 85–97. doi: 10.1016/j.tecto.2008.11.031

Heidarzadeh, M., and Kijko, A. (2011). A probabilistic tsunami hazard assessment for the Makran subduction zone at the northwestern Indian Ocean. *Nat. Hazards* 56, 577–593. doi: 10.1007/s11069-010-9574-x

Hoechner, A., Babeyko, A. Y., and Zamora, N. (2016). Probabilistic tsunami hazard assessment for the Makran region with focus on maximum magnitude assumption. *Nat. Hazards Earth Syst. Sci.* 16, 1339–1350. doi: 10.5194/nhess-16-1339-2016

Horspool, N., Pranantyo, I., Griffin, J., Latief, H., Natawidjaja, D. H., Kongko, W., et al. (2014). A probabilistic tsunami hazard assessment for Indonesia. *Nat. Hazards Earth Syst. Sci.* 14, 3105–3122. doi: 10.5194/Nhess-14-3105-2014

IGN (2009). *Catálogo de Tsunamis en las Costas Españolas*. Madrid: Instituto Geográfico Nacional.

IGN (2011). *Catálogo Sísmico*. Madrid: Instituto Geográfico Nacional.

Kanamori, H. (1977). The energy release in great earthquakes. *J. Geophys. Res.* 82, 2981–2987. doi: 10.1029/jb082i020p02981

Knighton, J., and Bastidas, L. A. (2015). A proposed probabilistic seismic tsunami hazard analysis methodology. *Nat. Hazards* 78, 699–723. doi: 10.1007/s11069-015-1741-7

Kotani, T., Tozato, K., Takase, S., Moriguchi, S., Terada, K., Fukutani, Y., et al. (2020). Probabilistic tsunami hazard assessment with simulation-based response surfaces. *Coast. Eng.* 160:103719. doi: 10.1016/j.coastaleng.2020.103719

Kowalik, Z., and Proshutinsky, A. (2010). Tsunami–tide interactions: a cook inlet case study. *Cont. Shelf Res.* 30, 633–642. doi: 10.1016/j.csr.2009.10.004

Kowalik, Z., Proshutinsky, T., and Proshutinsky, A. (2006). Tide-tsunami interactions. *Sci. Tsunami Hazards* 24, 242–256.

Laughton, A. S., and Whitmarsh, R. B. (1974). *The Azores-Gibraltar Plate Boundary*. Dordrecht: Reidel Publishing, 63–81.

Lee, H. S., Shimoyama, T., and Popinet, S. (2015). Impacts of tides on tsunami propagation due to potential Nankai Trough earthquakes in the Seto Inland Sea, Japan. *J. Geophys. Res. Oceans* 120, 6865–6883. doi: 10.1002/2015jc010995

Leonard, M. (2010). Earthquake fault scaling: self-consistent relating of rupture length, width, average displacement, and moment release. *Bull. Seismol. Soc. Am.* 100, 1971–1988. doi: 10.1785/0120090189

Li, L., Switzer, A. D., Chan, C.-H., Wang, Y., Weiss, R., and Qiu, Q. (2016). How heterogeneous coseismic slip affects regional probabilistic tsunami hazard assessment: a case study in the South China Sea. *J. Geophys. Res.* 121, 6250–6272. doi: 10.1002/2016jb013111

Lin, I.-C., and Tung, C. C. (1982). A preliminary investigation of tsunami hazard. *Bull. Seismol. Soc. America Am.* 72, 2323–2337.

Lima, V. V., Miranda, J. M., Baptista, M. A., Catalão, J., Gonzalez, M., Otero, L., et al. (2010). Impact of a 1755-like tsunami in Huelva, Spain. *Nat. Hazards Earth Syst. Sci.* 10, 139–148. doi: 10.5194/nhess-10-139-2010

Liu, P. L.-F., Cho, Y.-S., Briggs, M. J., Kanoglu, U., and Synolakis, C. E. (1995). Runup of solitary waves on a circular island. *J. Fluid Mech.* 302, 259–285. doi: 10.1017/s0022112095004095

Lorito, S., Selva, J., Basili, R., Romano, F., Tiberti, M. M., and Piatanesi, A. (2015). Probabilistic hazard for seismically induced tsunamis: accuracy and feasibility of inundation maps. *Geophys. J. Int.* 200, 574–588. doi: 10.1093/gji/ggu408

Lorito, S., Tiberti, M. M., Basili, R., Piatanesi, A., and Valensise, G. (2008). Earthquake generated tsunamis in the Mediterranean Sea: scenarios of potential threats to southern Italy. *J. Geophys. Res. Solid Earth* 113, 1978–2012.

Luque, L., Lario, J., Civis, J., Silva, P. G., Zazo, C., Goy, J. L., et al. (2002). Sedimentary record of a tsunami during Roman times, Bay of Cadiz, Spain. *J. Quat. Sci.* 17, 623–631. doi: 10.1002/jqs.711

Luque, L., Lario, J., Zazo, C., Goy, J. L., Dabrio, C. J., and Silva, P. G. (2001). Tsunami deposits as paleoseismic indicators: examples from the Spanish coast. *Acta Geol. Hisp.* 36, 197–211.

Main, I. (2000). Apparent breaks in scaling in the earthquake cumulative frequency- magnitude distribution: fact or artifact? *Bull. Seismol. Soc. Am.*, 90, 86–97. doi: 10.1785/0119990086

Martínez-Loriente, S., Gràcia, E., Bartolome, R., Sallarès, V., Connors, C., Perea, H., et al. (2013). «Active deformation in old oceanic lithosphere and significance for earthquake hazard: seismic imaging of the coral patch ridge area and neighboring abyssal plains (SW Iberian Margin)». *Geochem. Geophys. Geosy.* 14, 2206–2231. doi: 10.1002/ggge.20173

Medialdea, T., Vegas, R., Somoza, L., Vázquez, J., Maldonado, A., del Río, V. D., et al. (2004). Structure and evolution of the "Olistostrome" complex of the Gibraltar Arc in the Gulf of Cádiz (east- ern Central Atlantic): evidence from two long seismic cross-sections. *Mar. Geol.* 209, 173–198. doi: 10.1016/j.margeo.2004.05.029

Mezcua, J., and Martínez-Solares, J. M. (1983). *Sismicidad en el Área Ibero-Mogrebí, Publicación Técnica 203*. Madrid: Instituto Geográfico Nacional.

Morales, J. A., Borrego, J., Miguel, E. G. San, López-González, N., and Carro, B. (2008). Sedimentary record of recent tsunamis in the Huelva Estuary (southwestern Spain). *Quat. Sci. Rev.* 27, 734–746. doi: 10.1016/j.quascirev.2007.12.002

Murotani, S., Satake, K., and Fujii, Y. (2013). Scaling relations of seismic moment, rupture area, average slip, and asperity size for M˜ 9 subduction-zone earthquakes. *Geophys. Res. Lett.* 40, 5070–5074. doi: 10.1002/grl.50976

National Research Council (1988). *Probabilistic Seismic Hazard Analysis, Tech. Rep*. Washington, DC: National Academy press.

National Research Council (1997). *Review of Recommendations for Probabilistic Seismic Hazard Analysis: Guidance on Uncertainty and Use of Experts, Tech. rep*. Washington, DC: National Academy press.

Okal, E. A., and Synolakis, C. E. (2004). Source discriminants for near-field tsunamis. *Geophys. J. Int.* 158, 899–912. doi: 10.1111/j.1365-246x.2004.02347.x

Olabarrieta, M., Medina, R., Gonzalez, M., and Otero, L. (2011). C3: a finite volume- finite difference hybrid model for tsunami propagation and runup, computers andamp. *Geosciences* 37, 1003–1014. doi: 10.1016/j.cageo.2010.09.016

Omira, R., Baptista, M. A., and Matias, L. (2015). Probabilistic tsunami hazard in the northeast atlantic from near-and far-field tectonic sources. *Pure Appl. Geophys.* 172, 901–920. doi: 10.1007/s00024-014-0949-x

Omira, R., Baptista, M. A., Matias, L., Miranda, J. M., Catita, C., Carrilho, F., et al. (2009). Design of a sea-level tsunami detection network for the Gulf of Cadiz. *Nat. Hazards Earth Syst. Sci.* 9, 1327–1338. doi: 10.5194/nhess-9-1327-2009

Omira, R., Baptista, M. A., and Miranda, J. M. (2011). Evaluating tsunami impact on the Gulf of Cadiz Coast (Northeast Atlantic). *Pure Appl. Geophys.* 168, 1033–1043. doi: 10.1007/s00024-010-0217-7

Omira, R., Matias, L., and Baptista, M. A. (2016). Developing an event-tree probabilistic tsunami inundation model for NE Atlantic coasts: application to a case study. *Pure Appl. Geophy.* 173, 3775–3794. doi: 10.1007/s00024-016-1367-z

Otero, L. (2008). *Metodología Para Evaluar la Peligrosidad Debido a Tsunamis en Zonas Costeras*. Ph.D. thesis. Santander: University of Cantabria.

Pereira, R., Alves, T. M., and Cartwright, J. (2011). Post-rift compression on the SW Iberian margin (eastern North Atlantic): a case for prolonged inversion in the ocean–continent transition zone. *J. Geol. Soc.* 168, 1249–1263. doi: 10.1144/0016-76492010-151

Power, W., Wallace, L., Wang, X., and Reyners, M. (2012). Tsunami hazard posed to New Zealand by the Kermadec and southern New Hebrides subduction margins: an assessment based on plate boundary kinematics, interseismic coupling, and historical seismicity. *Pure Appl. Geophys.* 169, 1–36.

Power, W., Downes, G., and Stirling, M. (2007). Estimation of tsunami hazard in New Zealand due to South American earthquakes. *Pure Appl. Geophys.* 164, 547–564.

Power, W., Wang, X., Lane, E. M., and Gillibrand, P. A. (2013). A probabilistic tsunami hazard study of the Auckland region, Part I: propagation modelling and tsunami hazard assessment at the shoreline. *Pure Appl. Geophys.* 170, 16–21. doi: 10.1007/s00024-012-0543-z

Rikitake, B. T., and Aida, I. (1988). Tsunami hazard probability in Japan. *Bull. Seismol. Soc. Am.* 78, 1268–1278.

Roger, J., Baptista, M. A., Sahal, A., Accary, F., Allgeyer, S., and Hébert, H. (2011). The Transoceanic 1755 Lisbon tsunami in Martinique. *Pure Appl. Geophys.* 168, 1015–1031.

Rosas, F., Duarte, J., Terrinha, P., Valadares, V., and Matias, L. (2009). Morphotectonic characterization of major bathymetric lineaments in Gulf of Cadiz (Africa– Iberia plate boundary): insights from analogue modelling experiments. *Mar. Geol.* 261, 33–47.

Rueda, J., and Mezcua, J. (2002). Estudio del terremoto de 23 de septiembre de 2001 en Pego (Alicante). Obtención de una relación m_bLg - M_W para la Península Ibérica. *Rev. Soc. Geol. Esp.* 15, 159–173.

Ruiz, F., Rodríguez-Ramírez, A., Cáceres, L. M., Vidal, J. R., Carretero, M. I., Abad, M., et al. (2005). Evidence of high-energy events in the geological record: mid-holocene evolution of the southwestern Doñana National Park (SW Spain). *Palaeogeogr. Palaeoclimatol. Palaeoecol.* 229, 212–229.

Sartori, R., Torelli, L., Zitellini, N., Peis, D., and Lodolo, E. (1994). Eastern segment of the Azores-Gibraltar line (central-eastern Atlantic): an oceanic plate boundary with diffuse compressional deformation. *Geology* 22, 555–558.

Savage, J. C. (1991). Criticism of some forecasts of the National Earthquake Prediction Evaluation Council. *Bull. Seismol. Soc. Am.* 81, 862–881.

Savage, J. C. (1992). The uncertainty in earthquake conditional probabilities. *Geophys. Res. Lett.* 19, 709–712.

Scholz, C. H. (1998). «Earthquakes and friction laws». *Nature* 391, 37–42.

Scholz, C. H. (2002). *The Mechanics of Earthquakes and Faulting*, 2nd Edn. Cambridge: Cambridge University Press, 471.

Schwartz, D. P., and Coppersmith, K. J. (1984). Fault behavior and characteristic earthquakes: examples from the wasatch and san andreas fault zones. *J. Geophys. Res.* 89, 5681–5698. doi: 10.1029/JB089iB07p05681

Senior Seismic Hazard Analysis Comittee (1997). *Recommendations for Probabilistic Seismic Hazard Analysis: Guidance on Uncertainty and Use of Experts, Tech. rep*. Rockville, MD: U. S. Nuclear Regulatory Commission.

Sepúlveda, I., Liu, P. L. F., and Grigoriu, M. (2019). Probabilistic tsunami hazard assessment in South China Sea with consideration of uncertain earthquake characteristics. *J. Geophys. Res. Solid Earth* 124, 658–688. doi: 10.1029/2018JB016620

Shelby, M., Grilli, S. T., and Grilli, A. R. (2016). Tsunami hazard assessment in the Hudson River Estuary based on dynamic tsunami-tide simulations. *Pure Appl. Geophys.* 173, 3999–4037.

Shin, J. Y., Chen, S., and Kim, T.-W. (2015). Application of Bayesian Markov Chain Monte Carlo method with mixed gumbel distribution to estimate extreme magnitude of tsunamigenic earthquake. *J. Civ. Eng.* 19, 366–375. doi: 10.1007/s12205-015-0430-0

Sibson, R. H. (1982). «Fault zone models, heat flow, and the depth distribution of earthquakes in the continental crust of the United States». *Bull. Seismol. Soc. Am.* 72, 151–163.

Silva, S., Terrinha, P., Matias, L., Duarte, J. C., Roque, C., Ranero, C. R., et al. (2017). Micro-seismicity in the Gulf of Cadiz: is there a link between micro-seismicity, high magnitude earthquakes and active faults? *Tectonophysics* 717, 226–241. doi: 10.1016/j.tecto.2017.07.026

Sørensen, M. B., Spada, M., Babeyko, A., Wiemer, S., and Grunthal, G. (2012). Probabilistic tsunami hazard in the Mediterranean Sea. *J. Geophys. Res.* 117:B01305. doi: 10.1029/2010JB008169

Sorensen, M. B., Spada, M., Babeyko, A., Wiemer, S., and Grunthal, G. (2012). Probabilistic tsunami hazard in the Mediterranean Sea. *J. Geophys. Res.* 117:B01305. doi: 10.1029/2010JB008169

Stich, D., de Lis Mancilla, F., and Morales, J. (2005). Crust-mantle coupling in the Gulf of Cadiz (SW-Iberia). *Geophys. Res. Lett.* 32:L13306.

Stich, D., Martín, R., and Morales, J. (2010). Moment tensor inversion for Iberia–Maghreb earthquakes 2005–2008. *Tectonophysics* 483, 390–398.

Stich, D., Serpelloni, E., de Lis Mancilla, F., and Morales, J. (2006). Kinematics of the Iberia–Maghreb plate contact from seismic moment tensors and GPS observations. *Tectonophysics* 426, 295–317.

Stirling, M., Goded, T., Berryman, K., and Litchfield, N. (2013). Selection of earthquake scaling relationships for seismic-hazard analysis. *Bull. Seismol. Soc. Am.* 103, 2993–3011.

Strasser, F. O., Arango, M. C., and Bommer, J. J. (2010). Scaling of the source dimensions of interface and intraslab subduction-zone earthquakes with moment magnitude. *Seismol. Res. Lett.* 81, 941–950. doi: 10.1785/gssrl.81.6.941

Suppasri, A., Imamura, F., and Koshimura, S. (2012). Probabilistic tsunami hazard analysis and risk to coastal populations in Thailand. *J. Earthq. Tsunami* 06:1250011. doi: 10.1142/S179343111250011x

Synolakis, C. E. (2003). *Tsunami and Seiche, pp. 9.1–9.99, Earthquake Engineering Handbook*. New York, NY: CRC Press.

Synolakis, C. E., Bernard, E. N., Titov, V. V., Kanoglu, U., and GonzáLez, F. I. (2007). *Standard, Criteria, and Procedures for NOAA Evaluation Of Tsunami Numerical Models, Technical Memorandum PMEL-135*. Washington, DC: NOAA.

Terrinha, P., Matias, L., Vicente, J., Duarte, J., Luís, J., Pinheiro, L., et al. (2009). Morphotectonics and strain partitioning at the Iberia–Africa plate boundary from multibeam and seismic reflection data. *Mar. Geol.* 267, 156–174.

Taubenböck, H., Post, J., Roth, A., Zosseder, K., Strunz, G., and Dech, S. (2008). A conceptual vulnerability and risk framework as outline to identify capabilities of remote sensing. *Nat. Hazard. Earth Syst. Sci.* 8, 409–420. doi: 10.5194/nhess-8-409-2008

Thio, H. K., Somerville, P., Polet, J., and Ichinose, G. (2007). "Probabilistic tsunami hazard analysis for ports and harbors. Ports 2007: 30 Years of Sharing Ideas 1977-2007," in *Proceedings of the Eleventh Triennial International Conference.* doi: 10.1061/40834(238)103

Tinti, S., and Armigliato, A. (2003). The use of scenarios to evaluate the tsunami impact in southern Italy. *Mar. Geol.* 199, 221–243.

Tinti, S., Armigliato, A., Pagnoni, G., and Zaniboni, F. (2005). Scenarios of giant tsunamis of tectonic origin in the Mediterranean. *ISET J. Earthq. Technol.* 42, 171–188.

Tolkova, E. (2016). Tsunami penetration in tidal rivers, with observations of the Chile 2015 tsunami in rivers in Japan. *Pure Appl. Geophys.* 173, 389–409.

Volpe, M., Lorito, S., Selva, J., Tonini, R., Romano, F., and Brizuela, B. (2019). From regional to local SPTHA: efficient computation of probabilistic tsunami inundation maps addressing near-field sources. *Nat. Hazard. Earth Syst. Sci.* 19, 455–469.

Ward, S. N. (1991). A synthetic seismicity model for the middle America trench. *J. Geophys. Res.* 96, 433–421.

Ward, S. N. (1996). A synthetic seismicity model for southern California: cycles, probabilities, and hazard. *J. Geophys. Res.* 101, 393–322.

Ward, S. N. (2000). San Francisco Bay Area earthquake simulations: a step toward a standard physical earthquake model. *Bull. Seismol. Soc. Am.* 90, 370–386.

Weisz, R., and Winter, C. (2005). "Tsunami, tides and run-up: a numerical study," in *Proceedings of the International Tsunami Symposium*, eds G. A. Papadopoulos and K. Satake, Chania, 322.

Wells, D. L., and Coppersmith, K. J. (1994). New empirical relationships among magnitude, rupture length, rupture width, rupture area, and surface displacement. *Bull. Seismol. Soc. Am.* 84, 974–1002.

Wesnousky, S. G. (1994). The Gutenberg-Richter or characteristic earthquake distribution, which is it? *Bull. Seismol. Soc. Am.* 84, 1940–1959.

Wessel, P., and Smith, W. H. F. (1998). New improved version of generic mapping tools released. *EOS Trans. Am. Geophys. Union* 79:579.

Weatherall, P., Marks, K. M., Jakobsson, M., Schmitt, T., Tani, S., Arndt, J. E., et al. (2015). A new digital bathymetric model of the world's oceans. *Earth Space Sci.* 2, 331–345. doi: 10.1002/2015EA000107

Wiemer, S. (2001). A software package to analyze seismicity: ZMAP. *Seismol. Res. Lett.* 72, 373–382.

Yadav, R. B. S., Tsapanos, T. M., Bayrak, Y., and Koravos, G. C. (2013). Probabilistic appraisal of earthquake hazard parameters deduced from a bayesian approach in the northwest frontier of the himalayas. *Pure Appl. Geophys.* 170, 283–297. doi: 10.1007/s00024-012-0488-2

Yamada, Y., Masui, R., and Tsuji, T. (2013). Characteristics of a tsunamigenic megasplay fault in the Nankai Trough. *Geophys. Res. Lett.* 40, 4594–4598.

Yeh, H. (2006). "Tsunami forces in the runup zone," in *NSF Caribbean Tsunami Workshop*, eds A. Mercado-Irizarry and P. L.-F. Liu (Singapore: World Scientific).

Zamora, N., and Babeyko, A. Y. (2020). Probabilistic tsunami hazard assessment for local and regional seismic sources along the Pacific coast of Central America with emphasis on the role of selected uncertainties. *Pure Appl. Geophys.* 177, 1471–1495.

Zhang, Y. J., Witter, R. C., and Priest, G. R. (2011). Tsunami–tide interaction in 1964 Prince William Sound tsunami. *Ocean Model.* 40, 246–259.

Zielke, O., and Arrowsmith, J. R. (2008). Depth variation of coseismic stress drop explains bimodal earthquake magnitude-frequency distribution. *Geophys. Res. Lett.* 35, L24301. doi: 10.1029/2008GL036249

Zitellini, N., Gràcia, E., Matias, L., Terrinha, P., Abreu, M., DeAlteriis, G., et al. (2009). The quest for the Africa–Eurasia plate boundary west of the Strait of Gibraltar. *Earth Planet. Sci. Lett.* 280, 13–50.

Conflict of Interest: The authors declare that the research was conducted in the absence of any commercial or financial relationships that could be construed as a potential conflict of interest.

The handling editor declared a past co-authorship with several of the authors MB and RO.

frontiers in Earth Science

ORIGINAL RESEARCH
published: 28 May 2021
doi: 10.3389/feart.2021.671378

Anatomy of a Catastrophe: Reconstructing the 1936 Rock Fall and Tsunami Event in Lake Lovatnet, Western Norway

Nicolas Waldmann[1]†, Kristian Vasskog[2,3]†, Guy Simpson[4], Emmanuel Chapron[5], Eivind Wilhelm Nagel Støren[3,6], Louise Hansen[7], Jean-Luc Loizeau[8], Atle Nesje[6] and Daniel Ariztegui[4]*

[1] Dr. Moses Strauss Department of Marine Geosciences, Charney School of Marine Sciences, University of Haifa, Haifa, Israel, [2] Department of Geography, University of Bergen, Bergen, Norway, [3] Bjerknes Center for Climate Research, University of Bergen, Bergen, Norway, [4] Department of Earth Sciences, University of Geneva, Geneva, Switzerland, [5] Laboratory Geographie De l'Environnement (GEODE), University of Toulouse Jean Jaurès, Toulouse, France, [6] Department of Earth Science, University of Bergen, Bergen, Norway, [7] Geological Survey of Norway, Trondheim, Norway, [8] Department F.-A. Forel for Environmental and Aquatic Science, University of Geneva, Geneva, Switzerland

OPEN ACCESS

Edited by:
Finn Løvholt, Norwegian Geotechnical Institute, Norway

Reviewed by:
Michael Strupler, Swiss Seismological Service, ETH Zurich, Switzerland
Alessandro Romano, Sapienza University of Rome, Italy

***Correspondence:**
Nicolas Waldmann
nwaldmann@univ.haifa.ac.il

† These authors have contributed equally to this work

Specialty section:
This article was submitted to Geohazards and Georisks, a section of the journal Frontiers in Earth Science

Received: *23 February 2021*
Accepted: *26 April 2021*
Published: *28 May 2021*

Citation:
Waldmann N, Vasskog K, Simpson G, Chapron E, Støren EWN, Hansen L, Loizeau J-L, Nesje A and Ariztegui D (2021) Anatomy of a Catastrophe: Reconstructing the 1936 Rock Fall and Tsunami Event in Lake Lovatnet, Western Norway. Front. Earth Sci. 9:671378. doi: 10.3389/feart.2021.671378

Rock falls and landslides plunging into lakes or small reservoirs can result in tsunamis with extreme wave run-ups. The occurrence of these natural hazards in populated areas have encouraged a recent sharp increase of studies that aim to mitigate their impact on human lives and assess infrastructure lost. This paper amalgamates in a novel fashion and at an unprecedented detail *in situ* historic measurements, geological data and numerical modeling of a rock fall event and associated tsunami wave that occurred in Lake Lovatnet (western Norway) in September 1936. Historical records report an event that released ca. 1 million m^3 of rocks and debris from Ramnefjellet Mountain at an altitude of 800 m above Lake Lovatnet. The fragmented material plunged into the lake, causing a tsunami that reached a maximum run-up of 74 m and killed 74 people. In fact, the settlements of Bødal and Nesdal were wiped out as a result of the catastrophic wave. Sediments resulting from the 1936 rock fall and associated tsunami were identified in the subsurface of Lake Lovatnet by shallow geophysical investigations and were retrieved using gravity coring equipment. A set of high resolution physical and geochemical measurements were carried out on the cores with the aim of reproducing a highly detailed reconstruction of this catastrophic event in order to better understand and learn about the processes involved. The cores were retrieved in the northwestern sub-basin of the lake and its chronology was constrained by ^{210}Pb and radiocarbon dating. A specially tailored physically based mathematical model was applied to better understand the tsunami event. Integration of the geophysical record, the sedimentological data and numerical modeling provide a comprehensive background to better understand the effects of such event in a deep fjord-like lacustrine basin and to generate information for better mitigation of similar events elsewhere.

Keywords: mass transport deposits, geohazard, numerical modeling, tsunami deposit, lacustrine sediments, shallow geophysics, cryogenic processes

INTRODUCTION

Subaerial and subaqueous landslides, rock falls and associated sediment mass movements in or near aquatic bodies have been responsible for many tsunamis in high-relief coastal areas around the globe. While these events represent an important landscape-forming factor and serve as major conduits for sediment transport from elevated topography to sedimentary basins, the associated tsunamis pose a considerable hazard to human lives and they have the potential to cause major loss of infrastructure (e.g., Nadim et al., 2006; Shipp et al., 2011; Tanikawa et al., 2014). When the descending masses strike lakes or fjords, the resulting wave activity may last for hours, increasing the hazard and destructiveness (Clague et al., 2003; Pelinovsky, 2006; Harbitz et al., 2014; Mountjoy et al., 2019). In fact, the resulting catastrophic waves occurring in lakes (e.g., Bussmann and Anselmetti, 2010; Kremer et al., 2012, 2015; Gylfadóttir et al., 2017; Leithold et al., 2018) can be comparable to their marine counterparts in terms of both magnitude and strength. A well-documented example for the great ferocity of such hazards is given by the July 9 1958 Lituya Bay tsunami event in Alaska (Fritz, 2001; among others). This event was produced by a magnitude 7.9 earthquake that triggered the detachment of a ca. 5–10 $\times$ 10^6 m^3 subaerial rockslide into a fjord inlet. This generated a tsunami with a maximum run-up height of 524 m, which probably stands as the most prominent event recorded in modern history (Miller, 1960; Lander, 1996).

Mass-movement induced tsunamis occurring in lakes differ from their open ocean counterparts as they (a) affect areas near the wave source, (b) have higher run-ups, (c) strike more rapidly, and (d) pose a greater local hazard, as the degree of confinement of the water body prevents the tsunami energy from escaping, while concurrently inducing stronger and longer seiche (Siegenthaler et al., 1987; Chapron et al., 1999; Schnellmann et al., 2006). Although rock fall- or landslide-generated tsunamis are more localized than those generated by earthquakes (Ruff, 2003), they can produce remarkably high waves, particularly when trapped within small lakes, fjords, semi-enclosed bays or narrow inlets, such as Lituya Bay. Aside from earthquakes, a range of other conditioning factors may trigger landslides or rock falls, including physicochemical deterioration of the substratum by thermal and cryogenic forcing (Draebing et al., 2017), variability in ground humidity (Whiteley et al., 2019) or variability in the precipitation gradients (Hong et al., 2006; Jakob and Lambert, 2009), evaporite dissolution or disintegration of carbonate rocks at depth (Gutiérrez et al., 2008; Benac et al., 2009), biological intervention (Jahn, 1988; Scheidl et al., 2020) and subsurface degassing associated with volcanic complexes (Luckett et al., 2002; Hibert et al., 2011).

Previous studies have shown that the fjords of western Norway are prone to generate major rock falls and landslide events with a magnitude similar to that of Lituya Bay (Furseth, 2006; Jaedicke et al., 2009). In fact, the degree of destruction caused by devastating mass wasting-generated tsunami events in Norwegian fjords and lakes is the highest in the world, as a large percentage of the country's population inhabits the coastline (Hermanns et al., 2014). Although not a tsunami, the largest natural event known to have impacted the population in Norway appears to be the landslide dam burst and associated flood catastrophe that occurred in September 1345 in the Gauldalen valley (**Figure 1A**). Contemporaneous written reports, oral tradition and geological interpretations express divergent opinions about both its exact location and development. However, all agree that the amount of people killed in that disaster was estimated to ca. 500 (Rokoengen et al., 2001). Historical records of tsunami events associated with rock falls include the 1756 Tjellefonna event (Sandøy et al., 2017), the 1934 Tafjord event (Kaldhol and Kolderup, 1936) and the 1905, 1936, and 1950 series of events in Lake Lovatnet (Grimstad, 2006; **Figures 1A,B**). Other identified events in Loen include snow avalanches that destroyed settlements at Breng and Hellsete in 1500 and 1755, respectively, and a series of rock falls that hit settlements at Raudi in 1614 and 1743, with a destructive event on March 2nd 1885 at Kvithammaren (Furseth, 2006; **Figure 1C**). The latter caused the final abandonment of the settlement. Historical records indicate that the fjord region of western Norway has undergone about two to three large-scale catastrophic events every century (Blikra et al., 2006). Thus, for mitigation purposes and in order to study the impact of such an event in generation of possible tsunamis, the Norwegian government has put large efforts during the past decade into studying and monitoring unstable rock slopes such as the Åkneset cliff on the western side of the Sunnylvsfjorden fjord (Sćlevik et al., 2009; **Figure 1B**).

In many aspects, the most notorious and devastating series of rock fall and rock-avalanche events imprinted in modern Norwegian history are those that occurred in Lake Lovatnet. The stained reputation of this site comes from the fact that not one, but a series of events occurred at the same location (Ramnefjellet Mountain; **Figure 1D**), with the most destructive of them occurring in 1905 and 1936 summing a combined death toll of 134 human lives. Despite the numerous events that have struck the fjord area of western Norway, the severity and destructive pattern of these two events coupled with the fact that they occurred at the exact same locality, resulted in a wide-scale repercussion through national broadcasting services, leading to a deeply carved memory in modern Norwegian history.

It is the purpose of the present study to improve the understanding of mechanisms and processes involved in the 1936 rock fall-tsunami event in Lovatnet, through amalgamation of a variety of datasets that include sub-surface imaging, sediment coring and analyses, and numerical modeling based on the shallow water equations. The insight gained here may help to raise awareness concerning similar catastrophes both in Norway and elsewhere in the world.

LAKE LOVATNET

Geological and Hydrological Setting

Lake Lovatnet [ca. 10 km^2 and 52 m above mean sea level (msl)] is a freshwater glacier-fed lake situated in the Lodalen Valley at the head of Nordfjord (**Figures 1B,C**). Given that the local marine limit is at least 80 m above msl (Rye et al., 1997), the Lovatnet basin was part of the fjord for some time following deglaciation.

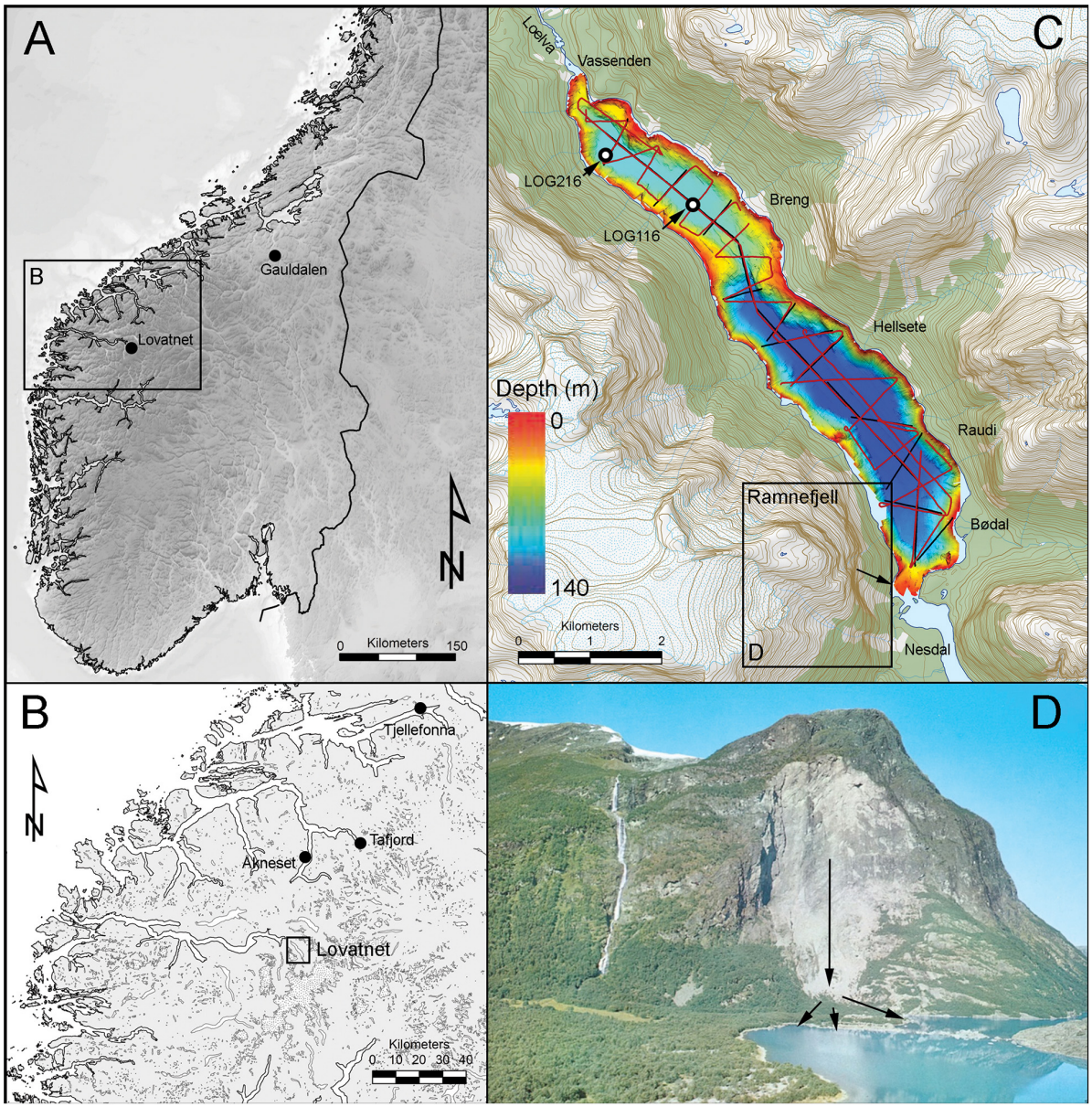

FIGURE 1 | (A) Map of southern Norway, the study area of inner Nordfjord and surrounding region is marked. **(B)** Location of Lake Lovatnet marked by a black square in inner Nordfjord. Sites with known records of rock fall events and associated tsunamis are marked by black dots (see text for more details). **(C)** Swath bathymetric map of Lovatnet showing pinger- (red) and airgun (black) seismic profiles. Sites of cores LOG216 and LOG116 are shown as a white circle in the NW sub-basin. The Ramnefjell slide scar is indicated with an arrow. Lake Lovatnet occupies the entire area of Lodalen Valley. **(D)** Picture of Ramnefjell with the location of the rock fall (Normann, 1963).

The over-deepened character of the basin, with up to 1,000 m high steep valley sides and a typical U-shaped basin floor, was formed by repeated carving of the local glaciers during the Pleistocene glaciations into Cambrian-Silurian schists (e.g., Nesje et al., 1991). The catchment of Lake Lovatnet is 235 km^2 in extent, of which 33% is glaciated, with the lake itself featuring three main river inlets (the Bødalselva, Kjenndalselva and Utigardselva) and a single outlet (Loelva) that drains the lake waters toward Nordfjord. The lake's incoming rivers are fed by three main glaciers: Bødalsbreen, Kjendalsbreen, and Ruteflotbreen, which are all tongues of the major Jostedalsbreen icecap (**Figure 1B**). Previous studies have measured combined sediment and water discharges in the nearby Erdalen valley, pointing to an average of 3.5 m^3/s, with peak flows reaching up to 30 m^3/s (Beylich and Laute, 2015; Beylich et al., 2017).

Previous works using a high-resolution sonar data show that Lake Lovatnet is divided into two sub-basins separated by a morphological high (**Figure 1C**; Hansen et al., 2016). The central

part of the lake floor in each sub-basin is nearly planar, with 90 and 140 m water depth in the northern and southern sub-basins, respectively. Steep marginal slopes rim each sub-basin and are characterized by the total absence of sediments or by a thin sedimentary cover that is directly deposited over the metamorphic bedrock. High-resolution sonar reveals a lake-floor morphology characterized by signs of historic and prehistoric rock falls and landslides (Hansen et al., 2016), pointing to an active source-to-sink lacustrine system with vigorous mass wasting activity. A recent study carried out on a neighboring lake shows that suspended sedimentation with a singular main source (the adjacent glaciers) dominates the limnic depositional system (Storms et al., 2020). Moreover, a study from nearby Lake Oldevatnet shows that the active source-to-sink processes of avalanches and flood activity is more widespread than previously thought, contributing more than 50% of the total lacustrine sedimentation budget at sites located near active avalanche tracks (Vasskog et al., 2011).

The History of Rock Falls in Lake Lovatnet

The event of 1905 happened in the night between January 15th and 16th, when a total volume of 350,000 m^3 of rocks and glacial debris collapsed into the lake from an altitude of ca. 500 m at the eastern side of Mt. Ramnefjellet (Reusch, 1907; Grimstad, 2006). A maximum height of the devastating wave was measured in Nesodden (40.5 m) and reached 14.5 and 15.5 m in the villages of Bødal and Nesdal, respectively (Reusch, 1907; **Figure 2A**). It appears that the tsunami wave wiped clean an entire strip of land along the shoreline of Nesdal and killed 61 from the original population of 122 people (Nesdal, 1983). The wave seiche affected the whole lake reaching a maximum height of 5.8 m at the outlet, which according to historical records caused the destruction of a local bridge over Loelva. A number of subsequent rock falls occurred in the following months, although no lives were lost (Bjerrum and Jørstad, 1968). The mass movement events caused major morphological changes in some parts of the lake. For example, as Sundet (at the southernmost end of the lake), the bathymetry was covered with 5.5 m of debris over an area of ca. 62,500 m^2 (Reusch, 1907). Studies showed that the 1905 rock fall was a consequence of extremely low temperature conditions that caused the water trapped in the sub-vertical joints to freeze and thus to expand and crack, promoting detachment and further collapse of the cliff (Bugge, 1937). Several days after the Loen disaster *Aftenposten* (Norway's largest printed newspaper at the time) chose to use the disaster to make a political statement during a period of constitutional crisis that eventually led to the dissolution of the union with Sweden and creation of the Kingdom of Norway, later in October the same year (Svensen, 2009).

The second event occurred on September 13th 1936, at 5:00 a.m., when a ca. 1 million m^3 block was detached from an altitude of 800 m above Lake Lovatnet, from the same area of Ramnefjellet Mt. (Furseth, 2006; **Figures 1C**, **2B**). The block fragmented and plunged into the lake causing a tsunami wave that reached a maximum run-up of 74 m near the rock-fall site (Jørstad, 1968). The towns of Nesdal and Bødal that were rebuilt after the previous tsunami of 1905 (**Figure 2C**), were again wiped out by the surging catastrophic tsunami wave, leading to a death toll of 74 victims (Hatledal, 2014). In fact, historical records show that only a few houses in the village of Bødal (a dairy and some farm barns) were not affected by the rising waves, probably because they stood further up the hill (Nesdal, 1983). Several verbal narratives were transmitted in local families, such as that of Mr. Anders Bødal, who was 12 years old at the time of the catastrophe. Anders later wrote in a school essay that he was in the garden of his house when he saw the wave arriving over Nesodden. Anders survived, according to his story because he took shelter behind a large rock that protected him, yet the rest of his family members who stayed in the house perished (Hatledal, 2014). The rescue team that was gathered following the 1936 event meticulously mapped the maximum height of the tsunami wave around the entire coastline of Lake Lovatnet (Jørstad, 1968; **Figure 3**) producing an undisputable highly valuable historical documentation of the event that is rarely seen for other sites around the world.

Following the disaster of September 13th, 1936, three additional, smaller landslides were recorded in the same year: (1) on the 21st of September when ca. 10^5 m^3 of rocks fell down and generated a wave that washed up to 40 m in height above the lake; (2) on the 6th of October when an unknown volume of rock fell and generated a wave that sunk several boats; and (3) on the 11th of November with an unregistered volume of rock and no recorded destruction. It is estimated that the total volume of rocks that fell in these three rock fall events was far greater than 1 million m^3 (Grimstad, 2006). The last recorded event occurred on the 22nd of June 1950 at 4:00 p.m., when the crack formed at Mt. Ramnefjellet following the 1936 rock

FIGURE 2 | (A) The settlement of Bødal in CE 1890. **(B)** The Mt. Ramnefjelll slide scar following the 1936 rock fall, with remains of Bødal in the foreground. **(C)** Remains of the settlement Bødal following the rock fall and tsunami event in CE 1936. Following the two events, the settlement was rebuilt 50 m above its past location in order to avoid destruction from a future event. All pictures are from Martinussen and Berg (1937).

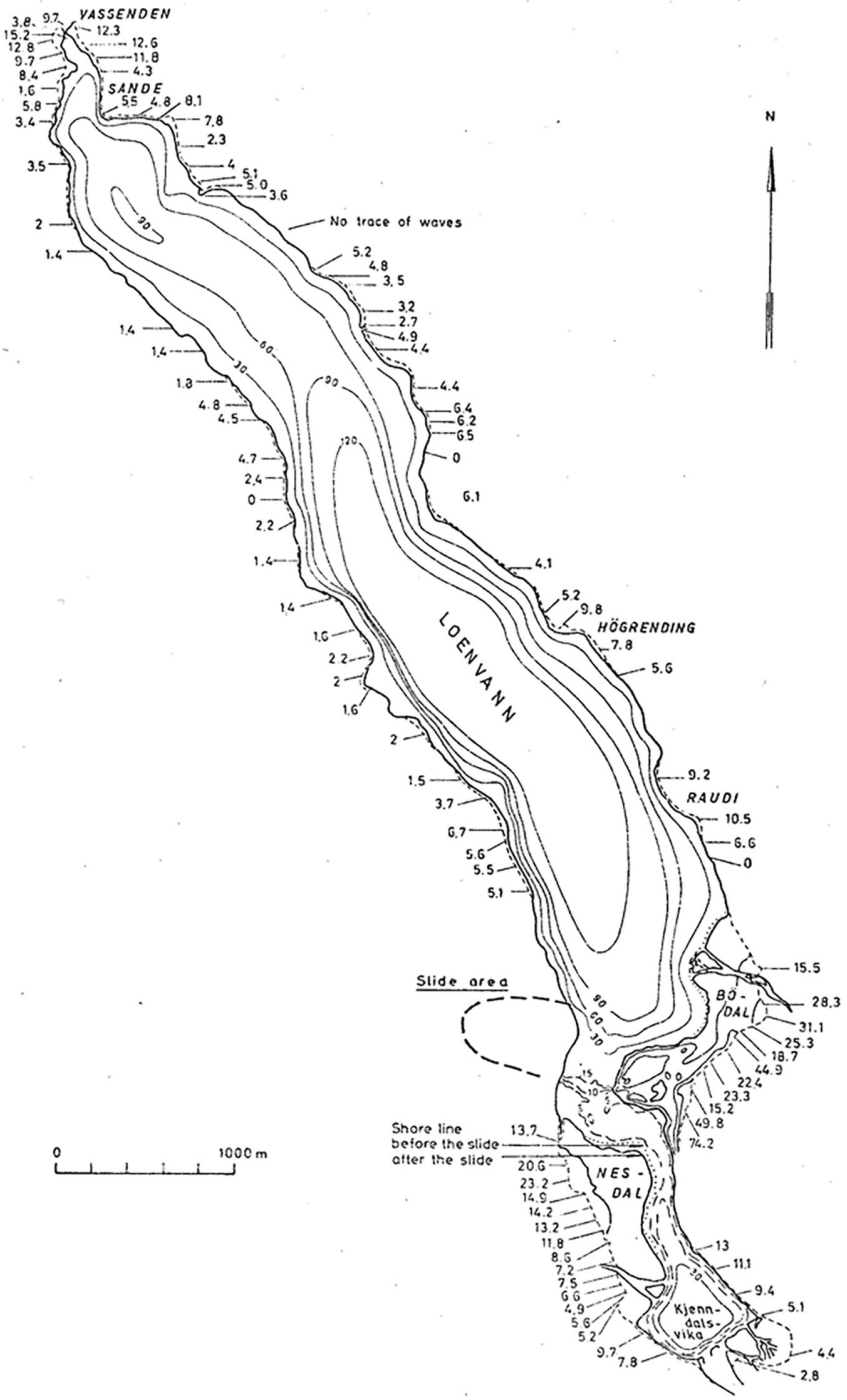

FIGURE 3 | Historical map of Lake Lovatnet with the run-up information measured at high precision following the 1936 tsunami event. Map modified and adapted from Jørstad (1968).

falls expanded and consequently released an estimated volume of ca. 1 million m^3. Considering the shallow water environment below Mt. Ramnefjellet (8–10 m water depth), the wave reached a maximum height of only 15 m (Jørstad, 1954). The settlements of Nesdal and Bødal, which were destroyed twice during the previous events, were built at higher grounds and therefore were situated beyond the wave impact. Historical records show that the 1950 tsunami wave reached a height of 7–8 m at Vassenden at the lake mouth, causing minimal destruction to local infrastructure, including a road and a 30 m long bridge (Jørstad, 1968).

Proposed Triggering Mechanisms for the Lake Lovatnet Rock Falls

During the early Paleozoic Caledonian orogeny, the rocks that are now part of western Norway were intensely deformed, resulting in a series of complex parallel to sub-parallel faults, fractures and lineaments. These features have been continually reactivated through time, and they appear to have played an important role in controlling the location of slope instabilities in more recent times. Equally important with respect to slope instabilities is the Quaternary period during which the region was intensely glaciated, and the steep-sided valleys were formed. As the Scandinavian ice sheet retreated following the last glacial period, the region has undergone significant isostatic uplift, which has provided additional relief along fjords and lakes. Together with the destabilizing effect of glacial debuttressing (e.g., Ballantyne, 2002), this has made the region of western Norway even more susceptible to mass wasting.

The inherited structural framework of the Caledonian orogeny dominates the Ramnefjellet region and has served as an important modulator for slope instabilities and landscape evolution (Redfield and Osmundsen, 2009). A first set of fractures can be followed for several km to the S of the mountain in an often discontinuous fashion, with a spacing ranging between 0.5 and 2 m (Grimstad, 2006). In several cases the vertical protruding fractures run several tens of m below the surface widening toward their tops, from a few cm to > 2 m. A second set of fractures has a NE-SW orientation, a spacing of 0.1 and 0.5 m and dips varying from ca. 35–40° to 22–36° in the northern and southern parts of the fracture, respectively. A less frequent third fracture set can be identified in a vertical direction, almost perpendicular to the mountain side and with a spacing of 30 m to more than 100 m. Historical documents provide valuable information from eyewitnesses during the 1936 event that describe "sudden outbursts of water under high pressure occurring from certain places just above the fractures that delimit the uppermost boundary of the 1905 slide" (Bugge, 1937). Moreover, the documents portray as well "a pulsating water outburst cycle, with each pulse lasting for 1–2 and at 6–7 min intervals." It is estimated that the fractures served as conduits for ground water, which pulsated under increasing high water pressure conditions (Grimstad, 2006). Moreover, it appears that the morphology of the sub-vertical fractures allowed for the storage of large amounts of water during heavy rainfall or snow melting periods, which consequently froze at low temperatures and induced their expansion, further promoting the consequential destabilization of the wall and imminent collapse (**Figure 4**). The rock fall of 1905 provoked the formation of an overhanging shaped edge of ca. 100 m above the bottom of the scar, which consequently fell during the rock fall events of 1936 and 1950 (**Table 1**).

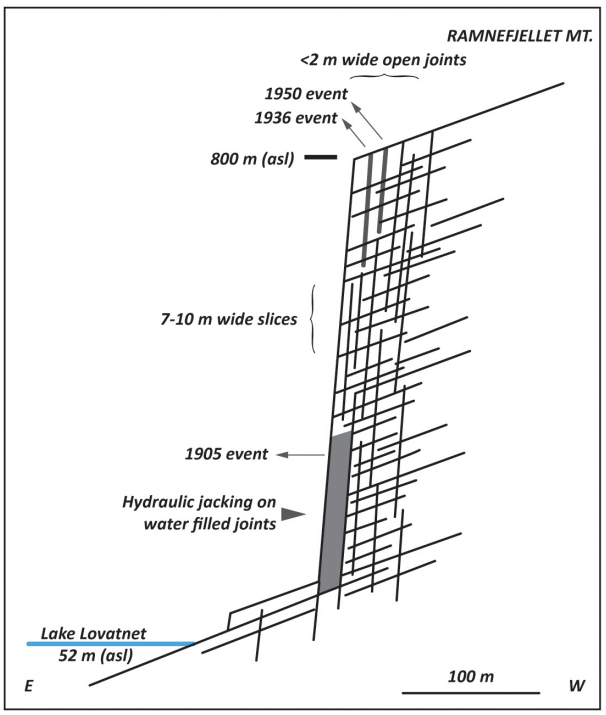

FIGURE 4 | Simplified cross-section across Mt. Ramnefjellet in a W-E direction, describing the general inherited fracture patterns and development of associated series of rock fall events [figure modified from Grimstad (2006)].

APPROACH

In order to better understand the degree of destructiveness associated with a rock fall and accompanying tsunami event in a relatively small but deep lacustrine basin, we carried out a high-resolution study of the event that struck Lake Lovatnet in 1936. A detailed description and analysis of the sedimentary unit (tsunamite) identified in the subsurface of the lake by both shallow geophysical mapping and piston cores was done. Moreover, a description of the processes behind its formation is proposed, while concurrently producing a numerical model of the generated tsunami. The results of this study are framed by historical records hence providing a comprehensive examination of the 1936 rock fall and tsunami event with implications to understand previous events such as the one that occurred in 1905.

Swath Bathymetry

High-resolution bathymetric data was collected in 2005 from Lovatnet using a 125 kHz GeoSwath interferometric side-scan sonar from GeoAcoustics, which was mounted on a locally rented boat. Data was collected at a speed around 4 knots and with a general line spacing of 100 m. Sound velocity profiles (SVP) were measured using a Valeport 650 SVP. Water level during the survey was measured digitally using a submerged Valeport 740 instrument. A base station was used for a positioning on dm-scale (RTK) and a gyroscope was used to adjust navigation. In locations with poor signal coverage, primarily due to the high relief, a differential GPS was used for positioning, giving a horizontal accuracy of ±1 m. The accuracy of depth measurements during data acquisition was on dm-scale. Processing was conducted using the GeoSwath software and included sound velocity correction and calibration to reduce

TABLE 1 | List of historical rock fall events occurring in the Lovatnet Valley (Jørstad, 1968).

Date	Total volume (m^3)	Height of the rock fall (m above lake)	Maximum measured wave height (m)	Lives lost
15/01/1905	350,000	500	40.5	61
20/09/1905	∼15,000	400	>15	0
13/09/1936	∼100,000	800	74.2	74
21/09/1936	1 million	800	∼40	0
6/10/1936	?	800	?	0
11/11/1936	> 1 million	800	>74	0
22/6/1950	∼1 million	800	∼15	0

signal-to-noise ratios. Merging of data and calculation of a 1 m grid was also carried out in the GeoSwath software.

Seismic Survey

The seismic survey was carried out in summer of 2006, simultaneously combining a multi-channel airgun (Sercel) and a single channel high-resolution 3.5 kHz pinger profiling system (Geoacoustic), both attached to a local trawler boat (to the stern and port side, respectively, navigation grid shown in **Figure 1C**).

The deployed airgun used a dominant frequency of 400 Hz and a nominal pressure of 80 bar, with data recorded using a 12-channel streamer (1 hydrophone per channel), a 24-bit seismograph (Geometrics Strataview), and positioned by an onboard GPS with an average accuracy of ± 5 m. The survey was conducted with an average constant boat speed of ca. 4 knots, allowing the airgun to fire at 5 m horizontal intervals under the control of a computer-driven triggering system that adjusts the firing rate according to the boat's velocity (Pugin et al., 1999). Receiver, shot, and offset spacing were all 7 m, which yielded a nominal sixfold data coverage and a nominal common depth-point (CDP) spacing of 3.5 m. Following acquisition, processing of the data was carried out utilizing the open system Seismic Unix utility (developed by CWP) and considering parameters as described in Beres et al. (2008).

For the pinger system, an Octopus acquisition unit was used for imaging the obtained seismic signal on board and for later processing. The pinger data was band-pass filtered (2–6 kHz) and gained with an Automated Gain Control (AGC; 100 ms). For both airgun and pinger data, seismic profiles were digitally recorded in SEG-Y format, and a water bottom mute was applied with constant shallow noise digitally removed. Acoustic velocities of 1,470 and 1,500 m/s were assumed for the water column and the sedimentary infill, respectively. All seismic data was interpreted using Kingdom Suite software packages, developed by Information Handling Services (IHS, Inc.).

Core Retrieval, Sedimentology, and Chronology

Based on the seismic data interpretation, two gravity cores were retrieved (LOG116 and LOG216) from Lake Lovatnet in autumn of 2016 utilizing an Uwitec gravity corer (**Figure 1C**). Both cores were retrieved from the NW sub-basin utilizing a rigid aluminum raft supported by two inflatable Zodiac boats. Core LOG116 was obtained at water depths of 89 m near the main depocenter and core LOG216 was retrieved more distal to the rock fall area and closer to the western shore at water depths of 92.5 m (see location in **Figures 1C**, 5B). Following fieldwork, the cores were transported to the University of Bergen to be stored under 4°C in dark conditions. The cores were analyzed at the University of Bergen EARTHLAB laboratory facilities, where they were first cut lengthwise into halves, photographed, and visually described in detail, prior to carrying out further analytical measurements. One of the core halves was stored for future reference (archive halves), while the other (working halves) was scanned with a Geotek^{TM} multi-sensor core logger (MSCL) to obtain gamma-ray attenuation (γ-ray) density and surface magnetic susceptibility (MS), and an ITRAX core scanner (Croudace et al., 2006) to obtain geochemical X-Ray Fluorescence (XRF) data. XRF measurements were performed at 500 μm (LOG116) and 200 μm resolution (LOG216) using a molybdenum X-ray source at 30 kV and 50 mA for an exposure time of 10 s. Geotek measurements were performed with a downcore resolution of 0.5 cm in LOG116 and 0.2 cm in LOG216.

In order to determine sediment accumulation rates in the recent sedimentary sequence, natural and artificial radionuclides (^{241}Am, ^{210}Pb, and ^{137}Cs) were measured at the Department F.-A. Forel for Environmental and Aquatic Science, University of Geneva (Switzerland). The samples were subsampled from core LOG116 every half cm down to 10.5 cm depth and every cm between 45.5 and 54.5 cm. Each sample was weighed, freeze-dried and weighed again to measure water content and ensure a dry weight between 2 and 5 g (minimum weight 2.75 g, maximum 4.99 g). ^{137}Cs, ^{210}Pb, and ^{241}Am activity profiles were obtained using a HPGe well gamma spectrometer (Ortec EG&G) measuring gamma emissions at 46.5 and 662 keV. Prior to ^{210}Pb analysis, samples were sealed in a glass tube to prevent any loss of ^{222}Rn and stored for a period of 3 weeks to ensure secular equilibrium between ^{226}Ra and ^{214}Pb. Excess ^{210}Pb was calculated as the difference between total ^{210}Pb and the supported ^{210}Pb determined by ^{214}Pb measurement (Appleby, 2001). The detection efficiency was corrected for geometry and density using Monte Carlo simulation software (Gespecor 4.1, Sima et al., 2001). ^{210}Pb ages were calculated considering the Constant Rate of Supply model (CRS, Appleby, 2001). Sediment accumulation rates (g cm^{-2} y^{-1}) were calculated using sediment bulk dry density (Sanchez-Cabeza and Ruiz-Fernández, 2012). The radioactive fallouts from nuclear weapon tests in the atmosphere and from the Chernobyl accident were used as markers to test the ^{210}Pb chronological model (Appleby, 2001).

A single sample of terrestrial plant macrofossils was extracted from a depth of 77.5–80 cm depth in core LOG216, in order to constrain the full age range covered by the cores. The sample (Poz-93757) was submitted to the Poznan Radiocarbon Laboratory (Poland) for AMS radiocarbon dating, and calibrated in OxCal using the IntCal20 atmospheric calibration curve (Reimer et al., 2020).

Tsunami Modeling

We modeled the wave propagation associated with the 1936 rock fall in Lake Lovatnet using the shallow water equations in two dimensions (Simpson and Castelltort, 2006). The paleo-bathymetry for the model was estimated by interpreting high resolution seismic profiles. Modeling the processes involved when a rock fall enters a lake is a complex task that requires different specific tools, such as full 3D CFD techniques (e.g., Chen et al., 2020; Romano et al., 2020; Rauter et al., 2021) or 2D-3D experimental models (Fritz et al., 2004; Evers et al., 2019), both not presently used as our study is based on a simpler and less computationally demanding approach. Here we treat only the movement of an assumed known volume of material within the lake, while we neglect effects related to the impact of the slide mass on the surface. Thus, our models are expected to significantly underestimate wave heights. We also treat the edge of the lake as a solid boundary, which does not permit us to compute inundation and run-up distances, as done by others (Lindstrøm et al., 2014; Heller and Spinneken, 2015; Løvholt et al., 2015a,b; Bellotti and Romano, 2017). This solid boundary approximation might be a reasonable along steep portions of the lake, but it will tend to exaggerate boundary reflections relative to a model that treats run-up correctly. Reflected edge waves tend to be dispersive and are expected to slow the lateral propagation of the wave. Nevertheless, we expect our model to provide a reasonable first order estimate of lateral propagation of the first wave across the lake.

The wave in our models was generated by instant adding of a mass of sediments and rocks to the base of the lake, thus locally modifying the bathymetry near the rock fall. Please note that we did not treat the impact of the slide mass on the surface of the lake, since this would require a more complicated 3d model. The area and volume of the mass movement were constrained from historical data, but we considered a range of volumes from 10^5 to 10^7 m^3. The mass movement is initiated in the lake at the base of Mt. Ramnefjellet where the water depth is currently 122 m. The velocity at which the rock mass moves within the lake was computed using a simple empirical relationship (Ward and Day, 2002):

$$v = (gL_c sin(\alpha)/8)^{\frac{1}{2}}$$

where L_c is the slide length and α is the initial angle of the slide surface.

This relationship is certainly a strong simplification of the complex processes involved in subaqueous mass-movements as it tends to overestimate the velocity, ignores frictional deceleration and neglects the influence of the possible contribution of additional dislocated sediments as a consequence of seiche waves (Thorpe, 1998). Nevertheless, it provides a first order estimate of the slide velocity and its dependence on mean slope angle and run out distance.

RESULTS

Bathymetric Data

The floor of Lake Lovatnet displays several debris lobes from failures along the lateral slopes (Hansen et al., 2016), with the most prominent identified around the area between Ramnefjellet and Nesodden (**Figure 5A**). The whole deposit appears to extend ca. 1.8 km northwards, including ca. 1 km along the basin floor plain. Here, two major debris lobes make up a total volume of at least 1.2×10^6 m^3 (Hansen et al., 2016). Some debris are also present along the lateral slopes to the west and near Bødalsdelta to the east (**Figure 5A**). In the area of the lake's outlet, furrows appear at the bottom that can be followed from the Vassenden area into the deep basin. Here, minor lobes occupy the basin floor, and an array of small debris mounds can be followed far into the lake (**Figure 5B**). The distance from Vassenden to the southernmost tip of the debris is ca. 1.5 km. One of the southernmost debris mounds includes a 15 m long and 1 m high feature, which could potentially be the remains of the vessel Lodølen that disappeared during the 1936 event (Hansen et al., 2016).

Seismic Reflection Data

The airgun survey provided excellent imaging of the deeper units, including the bedrock morphology, while the pinger survey offered seismic stratigraphic information of the shallow subsurface sediments (up to a depth of ca. 10 m). Based on the seismic stratigraphy analysis of the airgun data acquired in Lake Lovatnet, six seismic units were identified: LOV-S1 to LOV-S6, from bottom to top, respectively (**Figure 6A**). At 250 ms [two-way travel time (TWTT)] seismic energy faded and prevented good visualization of possible deeper substratum units. Unit LOV-S1 is characterized by chaotic and discontinuous internal refractions, bounded on top by discontinuous high-amplitude shattered reflections with a prominent rough surface of irregular morphology. The overlying LOV-S2 unit can be occasionally identified as discontinuous internal strong refractions that onlap the top of LOV-S1 in a clear truncation. The unit is not prominent and was identified only on scattered areas of the basin. Seismic units LOV-S3 to LOV-S6 show a much clearer internal morphology, and indicate the initiation of a different sedimentation pattern, probably pointing to a limnic-(or glacio-marine)-style basin infill. LOV-S3 is characterized by semi-transparent to transparent facies with occasional medium-energy parallel discontinuous internal semi-parallel to parallel reflections. The overlying seismic unit LOV-S4 shows continuous internal reflections occasionally changing spatially to more chaotic closer to the central promontory that divides the basin into two sub-basins. The LOV-S5 unit, however, is chaotic with significant lateral thickness variations that ponds toward the deeper basin depocenter. The topmost seismic unit LOV-S6 drapes all previous units and consists of very clear and strong

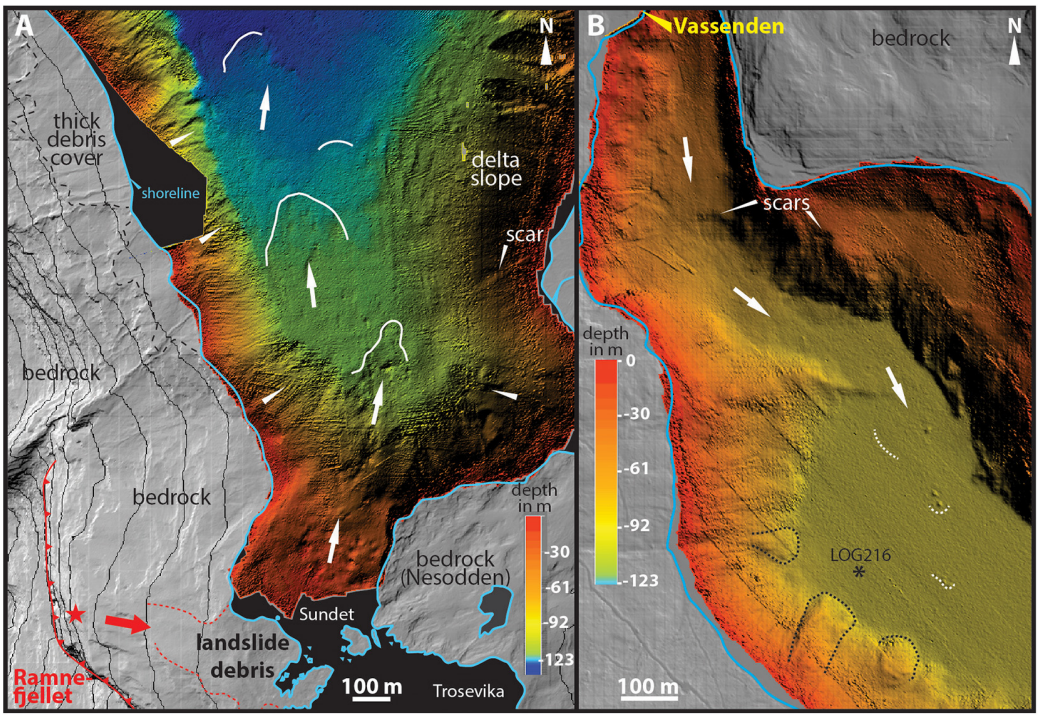

FIGURE 5 | Detailed shaded-relief images from the southern and northern ends of Lake Lovatnet. The images are based on high resolution topographical data from LiDAR and high-resolution swath bathymetry (modified from Hansen et al., 2016). **(A)** The escarpment at Ramnefjellet is highlighted in red. The path of landslide debris from the rock-slope and into the lake is shown by the large white arrows, with the front of distinct interpreted MTD lobes shown in white lines. Additional debris was entrained from the lateral slopes (small white arrows). **(B)** The northern part of Lovatnet displays an array of minor lobes and debris. North of the array are furrows that can be followed to shallow water near Vassenden. Location of core LOG216 is marked.

continuous reflections that intercalate with low-amplitude to transparent ponded intervals, which greatly increase in thickness toward the deeper parts of the basin. Seismic units LOV-S5 and S6 are clearly identified in the pinger seismic profiles (**Figures 6B,C,F**), where a great increase in thicknesses (up to 10 m) is revealed in the central parts of both sub-basins. In this areas, LOV-S6 includes internal sub-units characterized by stacked, chaotic and transparent seismic facies divided by clear strongly undulated and rough reflectors (**Figures 6B–F**). At least five of these stacked chaotic and semi-transparent sub-units are well identified and named LOV-S6a to LOV-S6f, although more of these units can also locally be recognized. Some of such intervals locally increase in their thicknesses (e.g., LOV-S6e, **Figures 6D,E**), which might reflect contribution from local processes.

Sedimentological Data

Both cores LOG116 and LOG216 show a very similar lithostratigraphic pattern, with alternating dark and light gray laminae, occasionally disturbed by thicker dark brown units of variable thickness topped by light gray mud caps (**Figure 7**). Three main sedimentary facies were recognized in core LOG116 and LOG216, here numbered as Facies I–III:

- **Facies I** consists of a light gray, laminated, highly minerogenic, clayey silt, interpreted to reflect the continuous "background" pelagic-type sedimentation in Lovatnet. As about one third of Lake Lovatnet's catchment is covered by glaciers, a large part of the background sedimentation may thus come from contemporaneous glacier erosion. However, a significant part may also be derived from re-mobilization of different kinds of unconsolidated materials in the catchment, such as till or colluvium. Some of the lamina are several mm in thickness, and might be related to episodic sedimentation events.
- **Facies II** appear as dark gray to brown layers, ranging in thickness from 1 to 3 cm. The dark, brownish color is due to high organic content, mainly in the form of plant macrofossils, although in some cases the organic detritus can be very fine, similar to gyttja. Most of the facies II layers contain coarser minerogenic grains than the background sediments, either scattered in a matrix of organic material or as massive sand layers that are usually overlain by more organic-rich layers. Facies II layers are interpreted as Mass Transport Deposits (MTDs) resulting from (snow-) avalanches, flood events, and sub-aquatic slope processes, similar to what was found in nearby Lake Oldevatnet (Vasskog et al., 2011). In core LOG216 some of the facies II deposits are capped by a light gray layer of clayey silt.
- **Facies III** represents a more complex sedimentary succession found between 43.5 and 10.5 cm depth in core LOG116 and 28–9 cm in core LOG-216, and has

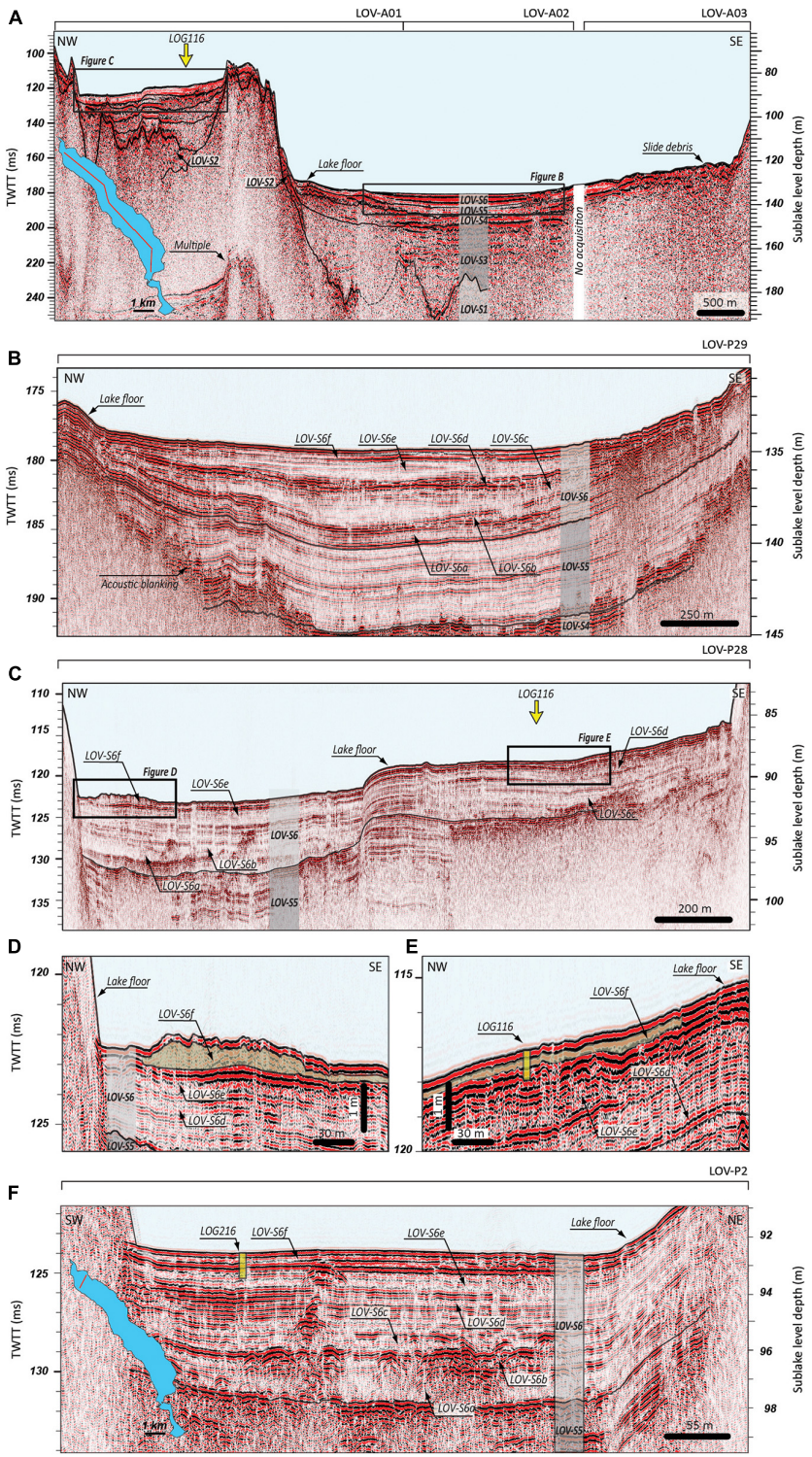

FIGURE 6 | (A) Longitudinal airgun seismic profile across the lake axis (NW-SE). Location of the airgun line is marked in the map. **(B)** Pinger profile P29 across the SE sub-basin, with location marked in **(A)** by a black square. Internal stacked sub-units are marked (LOV-S6a to LOV-S6f) and stands for a series of rock falls and debris flows (see discussion for more detail). **(C)** Pinger profile in the shallow sub-basin (location in **A**). **(D)** Zoomed area in **(C)** near the lake's outlet highlighting the local increase in thickness of LOV-S6f, probably as a result of the seiche effect and local contribution to the debris. **(E)** Zoomed area in the location of the cores retrieved in the lake, with highlight of LOV-S6f. **(F)** Pinger profile P2 across the NW sub-basin, location marked in the inlet figure. Location of core LOG216 is marked, as well as the stacked subunits of LOV-S6 (LOV-S6a to LOV-S6f).

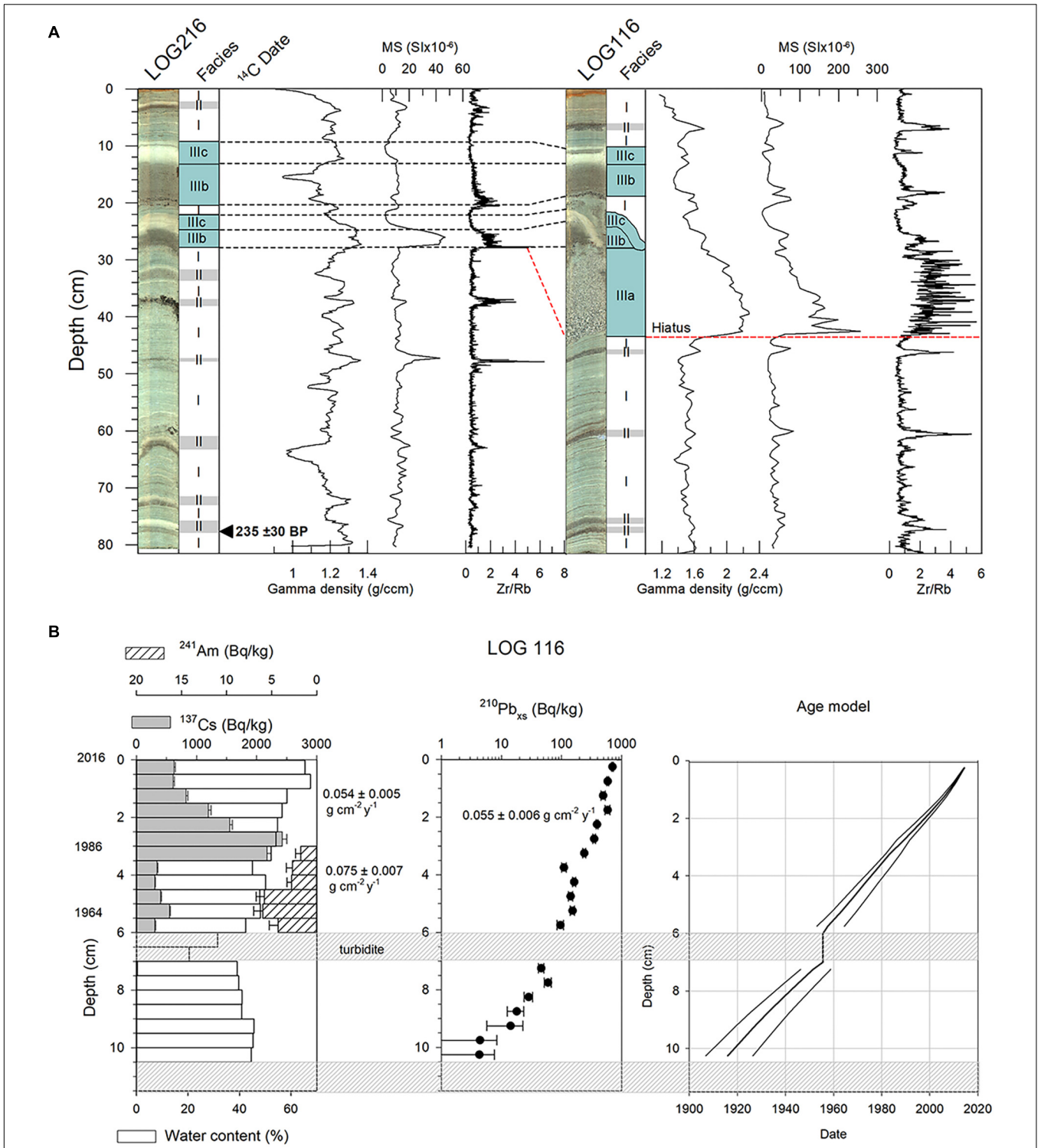

FIGURE 7 | (A) Photographs of LOG216 (left) and LOG116 (right) with corresponding measurements of gamma ray density, Magnetic Susceptibility (MS), and Zr/Rb-ratios from the XRF scanning. **(B)** Age-depth model for the upper section of LOG116 based on ^{137}Cs, ^{210}Pb, and ^{241}Am.

therefore been divided into three sub-facies (**Figure 7**). **Facies IIIa** is only found in LOG-116, and comprises a normally graded unit that is fining upwards from very fine gravel (2.5 mm) at the base to medium sand in the top. The overlying **facies IIIb** features a dark brown layer of concentrated plant macrofossils in the base, overlain by a lighter brown, organic-rich silt with a high content of small plant macrofossils throughout. The uppermost **facies IIIc** consists of a light, clayey silt. Facies III is interpreted as a more complex MTD than facies II. Two repeating sequences of facies IIIb–IIIc is recognized in both cores, separated by a 3–5 cm section of facies I. This facies I-section, together with the lowermost facies IIIc layer, is strongly deformed in core LOG116, probably due to disturbance during coring.

Facies II and III layers, here interpreted as episodic sedimentation events or MTDs, are well captured by the MS and XRF data (**Figure 7A**) with particularly distinct spikes seen in the Zr/Rb ratio. This ratio is thought to reflect grain-size, as resistant Zr minerals are typically enriched in coarser grain-sizes and consequently known to peak in turbidites (Rothwell et al., 2006).

A radiocarbon age of 235 ± 30 a BP was obtained for the sample at 78–77.5 cm depth in LOG216 (Poz-93757), which produced multiple modes of possible ages after calibration due to large fluctuations in the calibration curve over the last few hundred years (Reimer et al., 2020). The two most likely calibrated age ranges returned at a 95% confidence level were 1634–1684 CE (48.4% likelihood) and 1735–1804 CE (39.7% likelihood). Broadly speaking, this indicates that the LOG216 core covers the period from somewhere between 1634 and 1804 CE until present, and by lithostratigraphic correlation LOG116 should cover a similar age range. Thus, the radiocarbon dating indicates that the sedimentary signals of the historical rock fall and tsunami events of 1905, 1936, and 1950 should be captured within the retrieved cores. Using the average facies-I bulk dry density measured in LOG116 (0.84 g cm^{-3}), and the most likely age range of the radiocarbon date (1634–1684 CE), an average dry Sediment Accumulation Rate (SAR) of 0.11 ± 0.01 g cm^{-2} y^{-1} can be calculated for LOG216 background sedimentation (facies I).

An age model based on ^{210}Pb indicates an average SAR of 0.055 ± 0.006 g cm^{-2} y^{-1} for the upper 6 cm of LOG116, and 0.04 ± 0.011 g cm^{-2} y^{-1} between 7 and 10.5 cm, i.e., below the facies II layer at 6–7 cm (marked as turbidite in **Figure 7B**). The measured ^{137}Cs-content in the uppermost sediments shows two spikes at 2.75 and 5.25 cm, which are inferred to reflect fallout from the Chernobyl accident (1986 CE) and peak nuclear bomb testing (1964 CE), respectively. A corresponding peak in ^{241}Am at 5.25 cm supports the inferred age of 1964 CE for this depth. From this, the artificial radionuclides agree well with the ^{210}Pb model in the upper 2.75 cm of LOG116, where they indicate a SAR of 0.054 ± 0.005 g cm^{-2} y^{-1}. Below this level, however, they deviate, with ^{137}Cs and ^{241}Am suggesting a SAR of 0.075 ± 0.007 g cm^{-2} y^{-1} for the period between the Chernobyl accident and peak nuclear fallout. **Figure 7B** shows an age model based on the artificial radionuclide tie-points between 0 and 6 cm, and extrapolation of the same SAR further downwards to 10.5 cm. With these assumptions, the model indicates an approximate age of 1956 (1951–1962) CE for the facies II layer at 6–7 cm depth and an age of 1914 (1904–1924) CE for the facies III succession below 10.5 cm.

Simulation of the 1936 Tsunami Event

As stated in section "Tsunami Modeling," the simplicity of our numerical model does not permit to compute run-up distances or realistic wave amplitudes. However, our model is of use to estimating how the first wave spreads across the lake with time. Our models show that lateral propagation of the wave is mainly controlled by the geometry and bathymetry of the lake, both of which are quite well constrained with geophysics. In such a small mass of water, wave arrival times are extremely short, often on the order of minutes for sites located close to the initiation site. In Lake Lovatnet, the most distal sites appear to have received the first wave after a little more than 10 min (**Figure 8**). This estimate is consistent with eyewitness accounts of the Tsunami.

DISCUSSION

The primary objective of the current contribution is to study the sedimentary imprint and model the rock fall and associated tsunami wave that occurred in Lake Lovatnet in September 1936. The amalgamation of geophysical imaging (pinger), with results obtained from the sediment cores and framed by a robust chronology, allows us to model the impact of the 1936 tsunami and to correlate with the historical records.

Seismic Interpretation

The qualitative construction of an event stratigraphy record based on our pinger sub-bottom profiler is constrained by some limiting factors, which needs to be taken into account. This includes both external elements (such as the nature of the slide and resulting sedimentary facies) and internal elements (such as decisions taken during retrieval of the seismic data). While some of these factors were partially addressed during processing of the seismic data, others such as the vertical resolution of a specific event layer (dm scale) or the survey grid density (few hundred m), impede detection of very thin and/or spatially limited MTDs. Thus, a record of MTDs based solely on subsurface geophysical imaging may lack several types of events, such as those that left a limited sedimentary imprint on the lake bottom or those with the same lithology as the surrounding pelagic environment. Moreover, the density of the seismic grid influences the mapping and volume calculations of the identified MTDs (Clare et al., 2018). Possible improvements include a densification of the dataset and post-processing of high-quality seismic data, such as the one acquired by 3D sub-bottom profiler (Vardy et al., 2017). Moreover, a secondary component that needs to be taken into account is the low signal-to-noise ratio and signal masking in deeper parts of the sedimentary infill due to the gradual decrease of transmitted (and reflected) seismic energy with depth and the potential presence of gas-rich levels. These two depth-related

factors have a major effect in the calculated amount of MTDs in the lower parts of the seismic profiles.

The lithology produced at the lake floor as a consequence of the rock fall event may also generate some restrictions when producing a rigorous stratigraphy. For instance, increase in grain size may impede proper imaging of the unit boundaries and prevent the acoustic signal to penetrate the layer (Girardclos et al., 2007). Moreover, the presence of repeated events can lead to the generation of stacked MTDs with unclear boundaries (e.g., Lindhorst et al., 2016), which is especially true in case of erosive events that impede the proper separation of each generated unit. In those cases, the proper identification is carried out on the distal part of the basin, where the units are typically non-erosive and bear fewer fluid escape features. The last factor which needs to be considered is the operator prejudice in the assignment of stratigraphic levels and identification of MTDs. In several cases, the interpretation of the seismic profiles leads to grouping some MTDs on a single level, whereas in reality they may relate to closely spaced levels. Such bias is difficult to account for, but may be reduced by allowing different persons to interpret the data or by a standardized protocol (e.g., Oswald et al., 2021).

In Lake Lovatnet, the signal penetration is restricted to only few dm beneath the lake floor in the areas near Ramnefjell where the rock fall originated (**Figure 6A**), probably as a result of the local presence of slide debris composed of coarser material, which inhibit the acoustic signal to return a clear image of the subsurface. Moreover, the seismic architecture of unit LOV-6S is characterized by a series of irregular stacked MTDs across the whole deep part of the SE basin (**Figure 6B**), which in turn complicates any attempt to properly identify and separate each single event. We identify six MTDs in the deeper LOV-S6 sequence (sub-units LOV-S6a to LOV-S6f), which should be considered a minimum estimate, as some events might have been missed and left unidentified due to methodological restrictions. Nevertheless, we propose that sub-unit LOV-S6f corresponds to the 1936 tsunami event, as it is estimated by merging our seismic interpretation with the information retrieved from the two cores and their respective chronologies. Unfortunately, an accurate volume calculation for sub-unit LOV-S6f (and thus for the 1936 event) could not be generated. This exercise might have led to misinterpretations as disentangling between the 1905 and 1936 events in the seismic data is below the resolution of the acquisition system. Yet, our event stratigraphy model proposes that the 1936 catastrophe might have not been the sole to occur in Lake Lovatnet that has left a meaningful impact in the deep lacustrine environment, yet we do not have the sufficient information to propose their chronologies or triggering mechanisms.

Chronological and Sedimentological Interpretations

We have analyzed two short gravity cores from Lake Lovatnet (LOG116 and LOG216) to investigate whether the major rock fall and tsunami event of 1936 CE left a distinguishable sedimentary imprint in the lake deposits. Dating results from ^{137}Cs and ^{241}Am were only in agreement with ^{210}Pb down to a depth of 2.75 cm in LOG116, after which they deviate, with the artificial radionuclides suggesting an increasing SAR with depth and ^{210}Pb suggesting the opposite. Here, we have chosen to rely more on

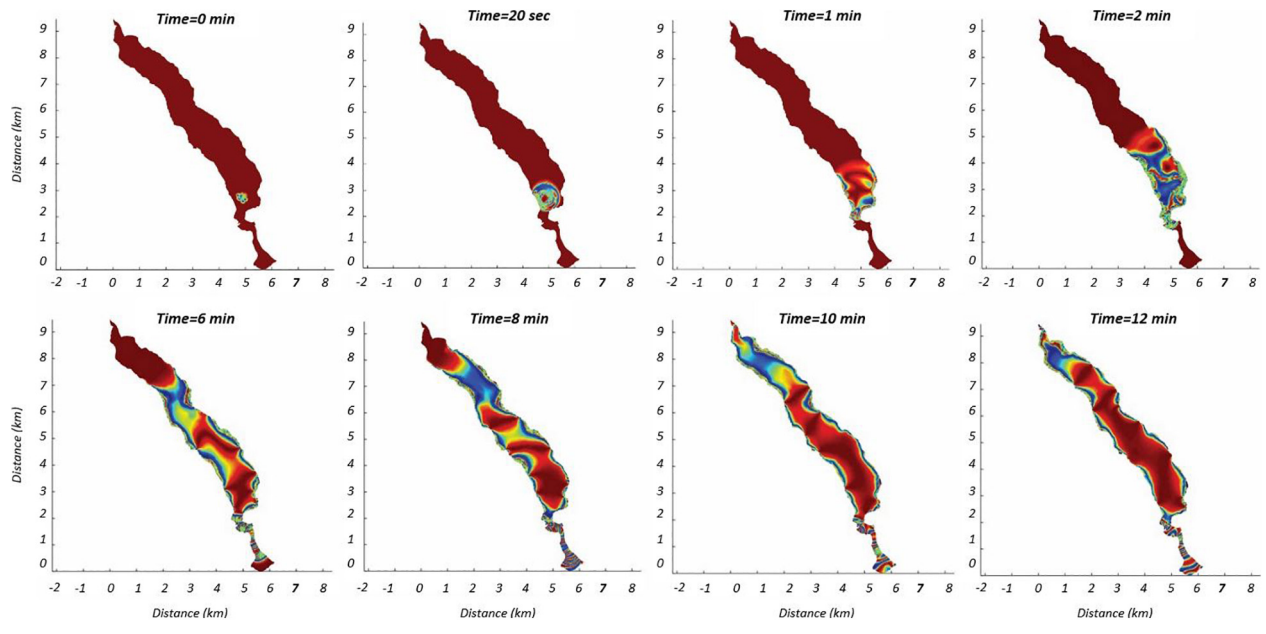

FIGURE 8 | Maps of Lake Lovatnet showing the result of the numerical model reconstruction of the 1936 tsunami waves caused by the rock fall at different modeled times (time = zero). The model corroborates historical records conserving the time that passed since the first tsunami wave was generated until it reached the other extreme of the lake (10 min). Please note that the vertical scale of the tsunami is not shown on purpose, since the model is too simplified to provide an accurate prediction.

the artificial radionuclides, because an increasing SAR with depth seems most reasonable. This argument is based on the regional glacier history, which indicates that glacial activity and associated erosion and delivery of glacio-fluvial sediment to Lake Lovatnet should increase as we move back in time toward the local "Little Ice Age" period (Vasskog et al., 2012). A detailed reconstruction of the Briksdalsbreen glacier in the neighboring Oldedalen Valley shows a distinct retreat phase between 1934 and 1950 CE (Nesje, 2005), and it is reasonable to believe that the glaciers draining into Lake Lovatnet followed a similar pattern, although with small variations based on different response times of individual glaciers. The SAR indicated by artificial radionuclides at depths of 2.75–5.25 cm (0.075 ± 0.007 g cm^{-2} y^{-1}) is also approaching the overall SAR for the entire LOG216 core based on radiocarbon dating (0.11 ± 0.01 g cm^{-2} y^{-1}), further supporting the idea of an increasing SAR downcore. As we no longer have tie-points from artificial radionuclides below 7 cm, our extrapolated age model (**Figure 7B**) might still overestimate the age of the facies III layer at 10.5 cm at 1904–1924 CE, given the probability of a further increasing SAR. If we employ the most likely radiocarbon-based SAR in the extrapolation, however, we obtain an age of 1939–1923 CE for the upper facies-III succession in LOG116. This allows for the possibility that this succession was deposited by the historical 1936 CE rock fall and tsunami event, and we will further argue that this is the case based on sedimentological evidence.

Clearly, episodic MTDs form an important part of Lake Lovatnet's sedimentation budget, with facies II and III making up almost half of the sediments contained in LOG116 and LOG216. Facies III layers are distinguished from facies II layers because they are thicker and have a clear internal succession of sub-facies, in addition to the fact that the facies IIIb and IIIc-layers appear near identical in the two cores, which are separated by a distance of 1.6 km. Tentative correlations can be made between some of the smaller facies-II layers, but they do not appear identical in both cores, and are therefore more likely to represent locally sourced MTDs, possibly from (snow-) avalanches, floods and subaqueous slope failures. The events that deposited the two repeating successions of facies IIIb–IIIc must, on the other hand, have affected the entire northern sub-basin of Lake Lovatnet in a similar manner during emplacement of these MTDs, which together with the thickness of these deposits suggest events of a considerable magnitude. Facies IIIa is only identified in the lower succession of LOG116, which suggests the contribution of local sources at this site during this event. Normally graded sand layers similar to that of facies IIIa are common units following tsunami events with contributing material sourced from the coastal areas that are hit by the wave (Dawson and Shi, 2000). Similar layers have been previously identified in several lake settings in western Norway and correlated with the Storegga tsunami (Bondevik et al., 1997b; Vasskog et al., 2013). Similarly, facies IIIb might be analogous to the organic detritus found in deposits from the Storegga tsunami, termed facies 7 by Bondevik et al. (1997a), which also represent material washed into the lake from onshore areas. Facies IIIc (light gray mud capping the sequence) has been attributed to suspension fallout following subaqueous density flows (Mulder and Alexander, 2001), but have also been correlated with seiche effects following tsunami events (e.g., Waldmann et al., 2011; Vasskog et al., 2013; Kempf et al., 2015; Nigg et al., 2021). Based on the above points, we suggest that the facies III successions represent major tsunami events that affected the whole lake basin. While the reasons facies IIIa only occurs within the lowermost event are still unclear, we postulate that these sediments originated from a local source (e.g., exposed sandy glacio-fluvial deposits), which might have not been present when the latter event occurred.

To summarize: we interpret the facies III succession found at 43–25 cm and 28–22 cm in cores LOG116 and LOG216, respectively, as deposits from the 1905 CE rock fall and tsunami, whereas the succession found at 20–10.5 cm and 20–9 cm in cores LOG116 and LOG216, respectively, to correspond to the 1936 rock fall and tsunami. As far as we know, the 1905 and 1936 events are unparalleled in magnitude over the period covered by our sediment cores, and from the sedimentological evidence it therefore seems likely that these two prominent facies III successions indeed reflect the historical events. While the chronology of the cores is not sufficiently precise to pinpoint the exact age of these deposits, it places them roughly within the correct age bracket, thereby strengthening our sedimentological interpretation.

Modeling the Tsunami of 30 September 1936

Determination of arrival times modeled for the Lake Lovatnet 1936 tsunami is critically important for proposing early warnings, for planning evacuation efforts, and for mitigation avenues. Moreover, these calculations serve as example for prevention of similar catastrophes in comparable lacustrine basins elsewhere in the world. The arrival times are determined by wave celerity, which in case of a linear wave propagation velocity is controlled by the wave-length and the water depth, taking into consideration a linear dispersion relation (Mohammed and Fritz, 2012). In the present numerical model, while the first and second basin-wide waves fall into a linear regime, the near field waves are non-linear due to the very shallow depth of the water (few meters) and the extreme volume of the added rock mass (1 M m^3). Moreover, it should be considered that individual crests and troughs of the rock fall-generated tsunami wave have independent wavelengths and propagate with different velocities. Interestingly, despite the limitations of our model, results show that the arrival time of the first wave generated by the 1936 tsunami event to the lake's outlet happened 10 min after its initial generation by the rock fall (**Figure 8**). This suggests a mean linear wave velocity of 13.3 m s^{-1}, which is in concordance with previous observations elsewhere (Truong, 2012) and taking into consideration the confined, deep and narrow basin that characterizes Lake Lovatnet. The arrival time of the first wave at different sites in the lake shoreline seems to be in good concordance with historical records (Bugge, 1937). Together, these results imply that early warning is extremely challenging in small water bodies. Although the current model does not address the impact of the tsunami wave and associated seiche on the lake surroundings, we believe that our model results could be merged with the historical record

(**Figure 3**) and produce a more complex 3D fluid dynamics model as a potential topic for future studies.

SUMMARY AND CONCLUSION

In the current study, we present a wide spectrum of information that includes geological, geophysical, and historical datasets concerning the 1936 rock fall and associated tsunami event that occurred in Lake Lovatnet. The following points summarize our study:

- A series of rock fall events associated with tsunamis occurred in Lake Lovatnet (inner Nordfjord region, western Norway) in 1905, 1936, and 1950, with the first two events being catastrophic and causing a combined loss of 134 human lives.
- A high-resolution shallow geophysical survey (pinger) was carried out in the lake aiming to identify the imprint of the 1936 event in the sedimentary infill. Meticulous seismic stratigraphy analysis allows to identify a series of units down to tens of dm in thickness, which are interpreted as MTDs. Among these units, two appear to correspond to the 1905 and 1936 rock fall and tsunami events.
- Based on high resolution seismic stratigraphy interpretation, two gravity cores (LOG216 and LOG116) were retrieved in the shallower NW sub-basin of the lake aiming to penetrate these MTD units. The cores lithology shows intercalations of alternating dark and light gray laminae, in which events layers are occasionally identified as thicker dark brown units topped by light gray mud caps (interpreted to results from the seiche effect following the tsunamis).
- The cores were logged for geochemistry and petrophysics and subsequently sampled for constraining their chronology through amalgamation of radiocarbon and radionuclides measurements (^{137}Cs and ^{210}Pb). Only through the combination of these dating techniques, were we able to constrain the ages of the MTD events identified in the cores and to provide explanations for the processes that were involved in their formation.
- A numerical model was produced combining the geophysical and historical data in order to reproduce the tsunami generated by the 30 of September 1936 rock fall. Our model, based on the shallow water equations, shows that the size and magnitude of the 1936 event is comparable to similar events that have occurred in other similar settings. Thus, our study provides valuable data that help to better understand the mechanisms and processes involved in rock fall-tsunami events. Finally, we expect that the current study will provide valuable information that in the long perspective, might help to raise the awareness and mitigate similar catastrophes both in western Norway and elsewhere in the world.
- The current study provides valuable information concerning the relative short time the tsunami wave generated during the 1936 rock fall traveled the whole length of the lake (10 min). This information is in concordance with measurements carried out in similar settings elsewhere and enlighten with valuable information on how to mitigate for possible generation of similar geohazards in Norway and in worldwide similar settings.

DATA AVAILABILITY STATEMENT

The original contributions presented in the study are included in the article/**Supplementary Material**, further inquiries can be directed to the corresponding author/s.

AUTHOR CONTRIBUTIONS

NW, EC, AN, and DA participated in fieldwork, gathered the data, and conceived of the presented idea. KV collected the sediment cores. NW and KV contributed equally to the writing of the manuscript with partial support of DA. J-LL performed the chronological analyses. GS developed the theory and performed the computations and modeling. LH contributed with the multibeam map of the lake. Sediment cores were analyzed by KV and ES. All authors discussed the results and contributed to the final manuscript.

FUNDING

KV was partly funded by the EISCLIM project (Research Council of Norway, Grant No. 229788). All sediment core analyses were done at the EARTHLAB National Infrastructure (Grant No. NRC 226171), University of Bergen. This work was supported by the Swiss National Science Foundation (Grant Nos. 200021-100668/1 and 200020-111928/1 to DA).

ACKNOWLEDGMENTS

We would like to thank Jostein Bakke (University of Bergen, Norway), Laura Sanna (Consiglio Nazionale delle Ricerche, Italy), Flavio Anselmetti (University of Bern, Switzerland), and Richard Gyllencreutz (Stockholm University, Sweden) for the invaluable help they provided in the field, lab and for many long and fruitful scientific discussions. We thank IHS for granting academic licenses for Kingdom Suite (universities of Geneva and Haifa).

SUPPLEMENTARY MATERIAL

The Supplementary Material for this article can be found online at: https://www.frontiersin.org/articles/10.3389/feart.2021.671378/full#supplementary-material

Supplementary Movie 1 | Moving visual simulation of the 1936 tsunami event.

REFERENCES

Appleby, P. G. (2001). "Chronostratigraphic techniques in recent sediments," in *Tracking Environmental Change Using Lake Sediments. Volume I: Basin Analysis, Coring, and Chronological Techniques*, eds W. M. Last and J.-P. Smol (Dordrecht: Kluwer Academic Publishers), 171–203. doi: 10.1007/0-306-47669-X_9

Ballantyne, C. (2002). Paraglacial geomorphology. *Q. Sci. Rev.* 21, 1935–2017. doi: 10.1016/S0277-3791(02)00005-7

Bellotti, G., and Romano, A. (2017). Wavenumber-frequency analysis of landslide-generated tsunamis at a conical island. Part II: EOF and modal analysis. *Coast. Eng.* 128, 84–91. doi: 10.1016/j.coastaleng.2017.07.008

Benac, È, Dugonjić, S., Arbanas, Ž, Oštrić, M., and Jurak, V. (2009). "The origin of instability phenomena along the karst-flysch contacts," in *ISRM International Symposium Rock Engineering in Difficult Ground Conditions: Soft Rock and Karst*, ed. I. Vrkljan (Cavtat: CRC Press), 757–761.

Beres, M., Gilli, A., Ariztegui, D., and Anselmetti, F. S. (2008). The Lago Cardiel Basin, Argentina (49 S): origin and evolution revealed by high-resolution multichannel seismic reflection studies. *J. South Am. Earth Sci.* 25, 74–85. doi: 10.1016/j.jsames.2007.08.001

Beylich, A. A., and Laute, K. (2015). Sediment sources, spatiotemporal variability and rates of fluvial bedload transport in glacier-connected steep mountain valleys in western Norway (Erdalen and Bødalen drainage basins). *Geomorphology* 228, 552–567. doi: 10.1016/j.geomorph.2014.10.018

Beylich, A. A., Laute, K., and Storms, J. E. (2017). Contemporary suspended sediment dynamics within two partly glacierized mountain drainage basins in western Norway (Erdalen and Bødalen, inner Nordfjord). *Geomorphology* 287, 126–143. doi: 10.1016/j.geomorph.2015.12.013

Bjerrum, I., and Jørstad, F. (1968). *Stability of Natural Rock Slopes in Norway*, Tech. Rep. 79. Oslo: Norwegian Geotechnical Institute (NGI).

Blikra, L., Longva, O., Braathen, A., Anda, E., Dehls, J., and Stalsberg, K. (2006). *Rock Slope Failures in Norwegian Fjord Areas: Examples, Spatial Distribution and Temporal Pattern, Landslides From Massive Rock Slope Failure*. Berlin: Springer, 475–496. doi: 10.1007/978-1-4020-4037-5_26

Bondevik, S., Svendsen, J. I., and Mangerud, J. (1997a). Tsunami sedimentary facies deposited by the Storegga tsunami in shallow marine basins and coastal lakes, western Norway. *Sedimentology* 44, 1115–1131. doi: 10.1046/j.1365-3091.1997.d01-63.x

Bondevik, S., Svendsen, J. I., Johnsen, G., Mangerud, J., and Kaland, P. E. (1997b). The Storegga tsunami along the Norwegian coast, its age and runup. *Boreas* 26, 29–53. doi: 10.1111/j.1502-3885.1997.tb00649.x

Bugge, A. (1937). Fjellskred fra topografisk og geologisk synspunkt. *Norsk Geogr. Tidssk.* 6, 342–360. doi: 10.1080/00291953608551553

Bussmann, F., and Anselmetti, F. S. (2010). Rossberg landslide history and flood chronology as recorded in Lake Lauerz sediments (Central Switzerland). *Swiss J. Geosci.* 103, 43–59. doi: 10.1007/s00015-010-0001-9

Chapron, E., Beck, C., Pourchet, M., and Deconinck, J.-F. (1999). 1822 earthquake-triggered homogenite in Lake Le Bourget (NW Alps). *Terra Nova* 11, 86–92. doi: 10.1046/j.1365-3121.1999.00230.x

Chen, F., Heller, V., and Briganti, R. (2020). Numerical modelling of tsunamis generated by iceberg calving validated with large-scale laboratory experiments. *Adv. Water Resour.* 142:103647. doi: 10.1016/j.advwatres.2020.103647

Clague, J. J., Munro, A., and Murty, T. (2003). Tsunami hazard and risk in Canada. *Nat. Hazards* 28, 435–463. doi: 10.1023/A:1022994411319

Clare, M. A., Le Bas, T., Price, D. M., Hunt, J. E., Sear, D., Cartigny, M. J., et al. (2018). Complex and cascading triggering of submarine landslides and turbidity currents at volcanic islands revealed from integration of high-resolution onshore and offshore surveys. *Front. Earth Sci.* 6:223. doi: 10.3389/feart.2018.00223

Croudace, I. W., Rindby, A., and Rothwell, R. G. (2006). ITRAX: description and evaluation of a new multi-function X-ray core scanner. *Geol. Soc. Lond. Spec. Publ.* 267, 51–63. doi: 10.1144/GSL.SP.2006.267.01.04

Dawson, A. G., and Shi, S. (2000). Tsunami deposits. *Pure Appl. Geophys.* 157, 875–897. doi: 10.1007/s000240050010

Draebing, D., Krautblatter, M., and Hoffmann, T. (2017). Thermo−cryogenic controls of fracture kinematics in permafrost rockwalls. *Geophys. Res. Lett.* 44, 3535–3544. doi: 10.1002/2016GL072050

Evers, F., Heller, V., Fuchs, H., Hager, W. H., and Boes, R. (2019). Landslide-generated Impulse waves in reservoirs: basics and computation. *VAW Mitteil.* 11:254.

Fritz, H. M. (2001). Lituya Bay case rockslide impact and wave run-up. *Sci. Tsun. Hazards* 19, 3–22.

Fritz, H. M., Hager, W. H., and Minor, H.-E. (2004). Near field characteristics of landslide generated impulse waves. *J. Water. Port Coast. Ocean Eng.* 130, 287–302. doi: 10.1061/(ASCE)0733-950X(2004)130:6(287)

Furseth, A. (2006). *Skredulykker i Norge*. Oslo: Tun Forlag, 207.

Girardclos, S., Schmidt, O. T., Sturm, M., Ariztegui, D., Pugin, A., and Anselmetti, F. S. (2007). The 1996 AD delta collapse and large turbidite in Lake Brienz. *Mar. Geol.* 241, 137–154. doi: 10.1016/j.margeo.2007.03.011

Grimstad, E. (2006). "The Loen rock slide-an analysis of the stability," in *Proceedings of the 11th International Conference and Field Trip on Landslides, Norway, September 2005: Landslides and Avalanches*, eds K. Senneset, K. Flaate, and J. O. Larsen (London: Taylor & Francis).

Gutiérrez, F., Calaforra, J., Cardona, F., Ortí, F., Durán, J., and Garay, P. (2008). Geological and environmental implications of the evaporite karst in Spain. *Environ. Geol.* 53, 951–965. doi: 10.1007/s00254-007-0721-y

Gylfadóttir, S. S., Kim, J., Helgason, J. K., Brynjólfsson, S., Höskuldsson, Á, Jóhannesson, T., et al. (2017). The 2014 Lake Askja rockslide-induced tsunami: optimization of numerical tsunami model using observed data. *J. Geophys. Res. Oceans* 122, 4110–4122. doi: 10.1002/2016JC012496

Hansen, L., Waldmann, N., Storms, J. E. A., Eilertsen, R. S., Ariztegui, D., Chapron, E., et al. (2016). Morphological signatures of mass wasting and delta processes in a fjord-lake system: insights from Lovatnet, western Norway. *Norweg. J. Geol.* 96, 9–29. doi: 10.17850/njg96-3-02

Harbitz, C. B., Glimsdal, S., Løvholt, F., Kveldsvik, V., Pedersen, G. K., and Jensen, A. (2014). Rockslide tsunamis in complex fjords: from an unstable rock slope at Åkerneset to tsunami risk in western Norway. *Coast. Eng.* 88, 101–122. doi: 10.1016/j.coastaleng.2014.02.003

Hatledal, E.-M. (2014). *Raset frå Ramnefjell: Reaksjonar og Tiltak Etter Lodalsulykka i 1936, Department of Archaeology, Conservation and History*. M. Sc. dissertation. Oslo: University of Oslo.

Heller, V., and Spinneken, J. (2015). On the effect of the water body geometry on landslide–tsunamis: Physical insight from laboratory tests and 2D to 3D wave parameter transformation. *Coast. Eng.* 104, 113–134. doi: 10.1016/j.coastaleng.2015.06.006

Hermanns, R. L., Oppikofer, T., Roberts, N. J., and Sandøy, G. (2014). *Catalogue of Historical Displacement Waves and Landslide-Triggered Tsunamis in Norway, Engineering Geology for Society and Territory*, Vol. 4. Berlin: Springer, 63–66. doi: 10.1007/978-3-319-08660-6_13

Hibert, C., Mangeney, A., Grandjean, G., and Shapiro, N. (2011). Slope instabilities in Dolomieu crater, Réunion Island: From seismic signals to rockfall characteristics. *J. Geophys. Res. Earth Surf.* 116:F04032. doi: 10.1029/2011JF002038

Hong, Y., Adler, R., and Huffman, G. (2006). Evaluation of the potential of NASA multi-satellite precipitation analysis in global landslide hazard assessment. *Geophys. Res. Lett.* 33:8010. doi: 10.1029/2006GL028010

Jaedicke, C., Lied, K., and Kronholm, K. (2009). Integrated database for rapid mass movements in Norway. *Nat. Hazards Earth Syst. Sci.* 9, 469–479. doi: 10.5194/nhess-9-469-2009

Jahn, J. (1988). "Deforestation and rockfall," in *Proceedings of the International Congress, Interpraevent*, Graz, 185–198.

Jakob, M., and Lambert, S. (2009). Climate change effects on landslides along the southwest coast of British Columbia. *Geomorphology* 107, 275–284. doi: 10.1016/j.geomorph.2008.12.009

Jørstad, F. A. (1954). *Beretning over Norges Geotekniske Institutts Virksomhet fra 1. Januar 1954 til 31. Desember 1955, NGI-Report*. Oslo: Norges Geotekniske Institutts.

Jørstad, F. A. (1968). *Waves Generated by Landslides in Norwegian Fjords and Lakes*. Oslo: Norwegian Geotechnical Institute Publication, 22.

Kaldhol, H., and Kolderup, N.-H. (1936). *Skredet i Tafjord 7. april 1934. Bergens Museums Årbok 1936 Naturvitenskapelig Rekke*, Vol. 11. Bergen: Bergens Museum, 1–15.

Kempf, P., Moernaut, J., Van Daele, M., Vermassen, F., Vandoorne, W., Pino, M., et al. (2015). The sedimentary record of the 1960 tsunami in two coastal

lakes on Isla de Chiloé, south central Chile. *Sedimen. Geol.* 328, 73–86. doi: 10.1016/j.sedgeo.2015.08.004

Kremer, K., Hilbe, M., Simpson, G., Decrouy, L., Wildi, W., and Girardclos, S. (2015). Reconstructing 4000 years of mass movement and tsunami history in a deep peri-Alpine lake (Lake Geneva, France-Switzerland). *Sedimentology* 62, 1305–1327. doi: 10.1111/sed.12190

Kremer, K., Simpson, G., and Girardclos, S. (2012). Giant Lake Geneva tsunami in AD 563. *Nat. Geosci.* 5, 756–757. doi: 10.1038/ngeo1618

Lander, J. F. (1996). *Tsunamis Affecting Alaska, 1737-1996*. Boulder, CO: National Geophysical Data Center, 196.

Leithold, E. L., Wegmann, K. W., Bohnenstiehl, D. R., Smith, S. G., Noren, A., and O'Grady, R. (2018). Slope failures within and upstream of Lake Quinault, Washington, as uneven responses to Holocene earthquakes along the Cascadia subduction zone. *Q. Res.* 89:178. doi: 10.1017/qua.2017.96

Lindhorst, K., Krastel, S., and Baumgarten, H. (2016). *Mass Wasting History Within Lake Ohrid Basin (Albania/Macedonia) Over the Last 600 ka, Submarine Mass Movements and their Consequences*. Berlin: Springer, 291–300. doi: 10.1007/978-3-319-20979-1_29

Lindstrøm, E. K., Pedersen, G. K., Jensen, A., and Glimsdal, S. (2014). Experiments on slide generated waves in a 1: 500 scale fjord model. *Coast. Eng.* 92, 12–23. doi: 10.1016/j.coastaleng.2014.06.010

Løvholt, F., Glimsdal, S., Lynett, P., and Pedersen, G. (2015a). Simulating tsunami propagation in fjords with long-wave models. *Nat. Hazard. Earth Syst. Sci.* 15, 657–669. doi: 10.5194/nhess-15-657-2015

Løvholt, F., Pedersen, G., Harbitz, C. B., Glimsdal, S., and Kim, J. (2015b). On the characteristics of landslide tsunamis. *Philos. Transact. R. Soc. A Math. Phys. Eng. Sci.* 373:20140376. doi: 10.1098/rsta.2014.0376

Luckett, R., Baptie, B., and Neuberg, J. (2002). The relationship between degassing and rockfall signals at Soufriere Hills Volcano, Montserrat. *Geol. Soc. Lond. Mem.* 21, 595–602. doi: 10.1144/GSL.MEM.2002.021.01.28

Martinussen, H., and Berg, F. G. S. (1937). *Naturkatastrofer i Norge, Nasjonalbiblioteket Digital 2009-09-21*. Bergen: Nasjonalbiblioteket.

Miller, D. J. (1960). Giant waves in Lituya Bay, Alaska. *Bull. Seismol. Soc. Am.* 50, 253–266. doi: 10.3133/pp354C

Mohammed, F., and Fritz, H. M. (2012). Physical modeling of tsunamis generated by three-dimensional deformable granular landslides. *J. Geophys. Res. Oceans* 117:7850. doi: 10.1029/2011JC007850

Mountjoy, J. J., Wang, X., Woelz, S., Fitzsimons, S., Howarth, J. D., Orpin, A. R., et al. (2019). "Tsunami hazard from lacustrine mass wasting in Lake Tekapo, New Zealand," in *Subaqueous Mass Movements and their Consequences: Assessing Geohazards, Environmental Implications and Economic Significance of Subaqueous Landslides*, eds D. G. Lintern, D. C. Mosher, L. G. Moscardelli, P. T. Bobrowsky, C. Campbell, J. D. Chaytor, et al. (London: The Geological Society of London), 413–426. doi: 10.1144/SP477.21

Mulder, T., and Alexander, J. (2001). The physical character of subaqueous sedimentary density flows and their deposits. *Sedimentology* 48, 269–299. doi: 10.1046/j.1365-3091.2001.00360.x

Nadim, F., Kjekstad, O., Peduzzi, P., Herold, C., and Jaedicke, C. (2006). Global landslide and avalanche hotspots. *Landslides* 3, 159–173. doi: 10.1007/s10346-006-0036-1

Nesdal, S. (1983). *Lodalen, Fager og Fårleg*. Tønsberg: Ekspresstrykk, 125.

Nesje, A. (2005). Briksdalsbreen in western Norway: AD 1900-2004 frontal fluctuations as a combined effect of variations in winter precipitation and summer temperature. *Holocene* 15, 1245–1252. doi: 10.1191/0959683605hl897rr

Nesje, A., Kvamme, M., Rye, N., and Løvlie, R. (1991). Holocene glacial and climate history of the Jostedalsbreen region, Western Norway; evidence from lake sediments and terrestrial deposits. *Q. Sci. Rev.* 10, 87–114. doi: 10.1016/0277-3791(91)90032-P

Nigg, V., Wohlwend, S., Hilbe, M., Bellwald, B., Fabbri, S. C., de Souza, G. F., et al. (2021). A tsunamigenic delta collapse and its associated tsunami deposits in and around Lake Sils, Switzerland. *Nat. Hazards* 21, 1–15. doi: 10.1007/s11069-021-04533-y

Normann (1963). *Ramnefjellet på Austsida av Lodalsvatnet*. Stryn Municipality: Fylkesarkivet i Sogn og Fjordane.

Oswald, P., Strasser, M., Hammerl, C., and Moernaut, J. (2021). Seismic control of large prehistoric rockslides in the Eastern Alps. *Nat. Commun.* 12:1059. doi: 10.1038/s41467-021-21327-9

Pelinovsky, E. (2006). "Hydrodynamics of tsunami waves," in *Waves in Geophysical Fluids. CISM International Centre for Mechanical Sciences*, eds J. Grue and K. Trulsen (Vienna: Springer).

Pugin, A., Pullan, S. E., Burns, R., Douma, M., and Good, R. (1999). "High-resolution, multichannel, marine seismic surveying using a small airgun source," in *Proceedings of the 12th EEGS Symposium on the Application of Geophysics to Engineering and Environmental Problems*, (Houten: European Association of Geoscientists & Engineers). doi: 10.3997/2214-4609-pdb.202.1999_028

Rauter, M., Hoße, L., Mulligan, R. P., Take, W., and Løvholt, F. (2021). Numerical simulation of impulse wave generation by idealized landslides with OpenFOAM. *Coast. Eng.* 165:103815. doi: 10.1016/j.coastaleng.2020.103815

Redfield, T., and Osmundsen, P. (2009). The Tjellefonna fault system of Western Norway: linking late-Caledonian extension, post-Caledonian normal faulting, and Tertiary rock column uplift with the landslide-generated tsunami event of 1756. *Tectonophysics* 474, 106–123. doi: 10.1016/j.tecto.2009.02.006

Reimer, P. J., Austin, W. E., Bard, E., Bayliss, A., Blackwell, P. G., Ramsey, C. B., et al. (2020). The IntCal20 Northern Hemisphere radiocarbon age calibration curve (0–55 cal kBP). *Radiocarbon* 62, 725–757. doi: 10.1017/RDC.2020.41

Reusch, H. (1907). Skredet i Loen 15 de januar 1905. Norges geologiske undersøkelse. *Aarbok* 1907, 3.

Rokoengen, K., Jespersen, M. N., Kleiv, R. A., and Sćterbø, E. (2001). The 1345 slide and flood disaster in the Gauldalen valley, Mid-Norway: a new interpretation. *Norsk Geograf. Tidsskr.* 55, 57–70. doi: 10.1080/00291950121138

Romano, A., Lara, J., Barajas, G., Di Paolo, B., Bellotti, G., Di Risio, M., et al. (2020). Tsunamis generated by submerged landslides: numerical analysis of the near-field wave characteristics. *J. Geophys. Res. Oceans* 125:e2020JC016157. doi: 10.1029/2020JC016157

Rothwell, R. G., Hoogakker, B., Thomson, J., Croudace, I. W., and Frenz, M. (2006). Turbidite emplacement on the southern Balearic Abyssal Plain (western Mediterranean Sea) during Marine Isotope Stages 1–3: an application of ITRAX XRF scanning of sediment cores to lithostratigraphic analysis. *Geol. Soc. Lond. Spec. Publ.* 267, 79–98. doi: 10.1144/GSL.SP.2006.267.01.06

Ruff, L. (2003). *Some Aspects of Energy balance and tsunami generation by earthquakes and landslides, Landslide Tsunamis: Recent Findings and Research Directions*. Berlin: Springer, 2155–2176. doi: 10.1007/978-3-0348-7995-8_18

Rye, N., Nesje, A., Lien, R., Blikra, L. H., Eikenaes, O., Hole, P., et al. (1997). Glacial geology and deglaciation chronology of the area between inner Nordfjord and Jostedalsbreen Strynefjellet, western Norway. *Norsk Geol. Tidsskr.* 77, 51–63.

Sćlevik, G., Jensen, A., and Pedersen, G. (2009). Experimental investigation of impact generated tsunami; related to a potential rock slide, Western Norway. *Coast. Eng.* 56, 897–906. doi: 10.1016/j.coastaleng.2009.04.007

Sanchez-Cabeza, J., and Ruiz-Fernández, A. (2012). 210Pb sediment radiochronology: an integrated formulation and classification of dating models. *Geochim. Cosmochim. Acta* 82, 183–200. doi: 10.1016/j.gca.2010.12.024

Sandøy, G., Oppikofer, T., and Nilsen, B. (2017). Why did the 1756 Tjellefonna rockslide occur? A back-analysis of the largest historic rockslide in Norway. *Geomorphology* 289, 78–95. doi: 10.1016/j.geomorph.2016.08.016

Scheidl, C., Heiser, M., Vospernik, S., Lauss, E., Perzl, F., Kofler, A., et al. (2020). Assessing the protective role of alpine forests against rockfall at regional scale. *Eur. J. For. Res.* 20, 1–12.

Schnellmann, M., Anselmetti, F. S., Giardini, D., and Mckenzie, J. A. (2006). 15,000 Years of mass-movement history in Lake Lucerne: implications for seismic and tsunami hazards. *Eclo. Geol. Helvet.* 99, 409–428. doi: 10.1007/s00015-006-1196-7

Shipp, R. C., Weimer, P., and Posamentier, H. W. (2011). *Mass-Transport Deposits in Deepwater Settings*. Tulsa, OK: SEPM Soc for Sed Geology. doi: 10.2110/sepmsp.096

Siegenthaler, C., Finger, W., Kelts, K., and Wang, S. (1987). Earthquake and seiche deposits in Lake Lucerne, Switzerland. *Eclo. Geol. Helvet.* 80, 241–260.

Sima, O., Arnold, D., and Dovlete, C. (2001). GESPECOR: a versatile tool in gamma-ray spectrometry. *J. Radioanal. Nuclear Chem.* 248, 359–364. doi: 10.1023/A:1010619806898

Simpson, G., and Castelltort, S. (2006). Coupled model of surface water flow, sediment transport and morphological evolution. *Comput. Geosci.* 32, 1600–1614. doi: 10.1016/j.cageo.2006.02.020

Storms, J. E., Beylich, A. A., Hansen, L., and Waldmann, N. (2020). Source to Sink Reconstruction of a Holocene Fjord-infill: depositional patterns, suspended sediment yields, wind-induced circulation patterns and trapping efficiency for Lake Strynevatnet, inner Nordfjord, Norway. *Deposit. Record* 6, 471–485. doi: 10.1002/dep2.101

Svensen, H. (2009). *The End is Nigh: A History of Natural Disasters*. London: Reaktion Books.

Tanikawa, H., Managi, S., and Lwin, C. M. (2014). Estimates of lost material stock of buildings and roads due to the Great East Japan Earthquake and tsunami. *J. Industr. Ecol.* 18, 421–431. doi: 10.1111/jiec.12126

Thorpe, S. (1998). Some dynamical effects of internal waves and the sloping sides of lakes. *Phys. Proces. Lakes Oceans* 98, 441–460. doi: 10.1029/CE054p0441

Truong, H. V. P. (2012). "Wave-propagation velocity, tsunami speed, amplitudes, dynamic water-attenuation factors," in *Proceedings of World Conference on Earthquake Engineering* (Red Hook, NY: Curran Associates, Inc.), 1–10.

Vardy, M. E., Vanneste, M., Henstock, T. J., Clare, M. A., Forsberg, C. F., and Provenzano, G. (2017). State-of-the-art remote characterization of shallow marine sediments: the road to a fully integrated solution. *Near Surf. Geophys.* 15, 387–402. doi: 10.3997/1873-0604.2017024

Vasskog, K., Nesje, A., Støren, E. N., Waldmann, N., Chapron, E., and Ariztegui, D. (2011). A Holocene record of snow-avalanche and flood activity reconstructed from a lacustrine sedimentary sequence in Oldevatnet, western Norway. *Holocene* 21, 597–614. doi: 10.1177/0959683610391316

Vasskog, K., Paasche, Ø, Nesje, A., Boyle, J. F., and Birks, H. (2012). A new approach for reconstructing glacier variability based on lake sediments recording input from more than one glacier. *Q. Res.* 77, 192–204. doi: 10.1016/j.yqres.2011.10.001

Vasskog, K., Waldmann, N., Bondevik, S., Nesje, A., Chapron, E., and Ariztegui, D. (2013). Evidence for Storegga tsunami run-up at the head of Nordfjord, western Norway. *J. Q. Sci.* 28, 391–402. doi: 10.1002/jqs.2633

Waldmann, N., Anselmetti, F. S., Ariztegui, D., Austin, J. A. Jr., Pirouz, M., Moy, C. M., et al. (2011). Holocene mass-wasting events in Lago Fagnano, Tierra del Fuego (54° S): implications for paleoseismicity of the Magallanes-Fagnano transform fault. *Basin Res.* 23, 171–190. doi: 10.1111/j.1365-2117.2010.00489.x

Ward, S. N., and Day, S. (2002). *Suboceanic landslides. Yearbook of Science and Technology*. New York, NY: McGraw-Hill, 1.

Whiteley, J., Chambers, J., Uhlemann, S., Wilkinson, P., and Kendall, J. (2019). Geophysical monitoring of moisture-induced landslides: a review. *Rev. Geophys.* 57, 106–145. doi: 10.1029/2018RG000603

Conflict of Interest: The authors declare that the research was conducted in the absence of any commercial or financial relationships that could be construed as a potential conflict of interest.

frontiers in Built Environment

ORIGINAL RESEARCH
published: 11 June 2021
doi: 10.3389/fbuil.2021.674659

Evolution of Pneumatic Tsunami Simulators–From Concept to Proven Experimental Technique

Ian Chandler[1], *William Allsop*[2], *David Robinson*[3] *and Tiziana Rossetto*[4]*

[1]HR Wallingford, Wallingford, United Kingdom, [2]William Allsop Consulting Ltd, Abingdon, United Kingdom, [3]EPICentre, Department of Civil, Environmental and Geomatic Engineering, University College London, London, United Kingdom, [4]EPICentre, Civil, Environmental and Geomatic Engineering, University College London, London, United Kingdom

This paper describes the evolution through three generations of pneumatic Tsunami Simulators for physical model tests of realistic tsunami. The pneumatic method, originally developed for tidal modeling in the Fifties, has been modernized to generate extraordinarily long waves in a controlled manner, with accurate reproduction of recorded free-surface tsunami field data. The paper describes how the simulator designs were developed and how they performed in the laboratory. Example results are presented from selected research studies that have validated their performance and then used to quantify tsunami effects. Having described each of the first, second, and third generation Tsunami Simulators, the paper discusses how to calibrate the wave generation control to model tsunami with model periods 20–240 s duration (equivalent to 2–20 min duration in prototype at 1:50 scale), many of which are far too long to "fit into the test flume." The evolution of a composite approach to wave calibration is described with examples from second and third generation devices, demonstrated by successful simulation of both the 2004 Boxing Day, and the 2011 Great Eastern Japan (Tohoku) Tsunami at 1:50 scale.

Keywords: tsunami, physical modeling, wavemaker, tsunami simulator, N-waves

OPEN ACCESS

Edited by:
Spyros Hirdaris, Aalto University, Finland

Reviewed by:
Ahmet Cevdet Yalciner, Middle East Technical University, Turkey
Vanessa Katsardi, University of Thessaly, Greece

***Correspondence:**
Tiziana Rossetto
t.rossetto@ucl.ac.uk

Specialty section:
This article was submitted to Coastal and Offshore Engineering, a section of the journal Frontiers in Built Environment

Received: *29 March 2021*
Accepted: *18 May 2021*
Published: *11 June 2021*

Citation:
Chandler I, Allsop W, Robinson D and Rossetto T (2021) Evolution of Pneumatic Tsunami Simulators–From Concept to Proven Experimental Technique. Front. Built Environ. 7:674659. doi: 10.3389/fbuil.2021.674659

INTRODUCTION

Accurate modeling of tsunami propagation and interaction with coastlines is vital to develop informed tsunami defense, public advice and warning systems, and to manage disaster relief. Tsunamis are generated by an earthquake, a landslide (above or below the ocean), a volcanic eruption, or a major debris slide, any of which caused a rapid displacement of a large body of water, generating a long gravity wave. Tsunami are parameterized according to period (T), wavelength (L), wave height (H) and the components of the wave height positive and negative amplitude (a+ and a−).

Tsunami waves reach the coastline in a variety of different shapes due to the long distance propagation, complex bottom and coastal bathymetry and their initial shape (Sriram et al., 2019). Tsunami reaching the shore may be broadly classified in the following three categories (e.g. Shuto, 1985):

- Non-breaking waves that act as a rapidly rising tide, often observed during small and moderate tsunami events;
- Breaking bore or hydraulic jump, observed as a result of wave breaking during large tsunami events;

- Undular bore, sometimes observed after long distance propagation (in terms of wavelength) caused by the disintegration of the tsunami into a series of solitons.

It is therefore vital for researchers to understand which type of tsunami they are representing within their experiments. The few field measurements of tsunami free-surface elevation that have been recorded in recent years, (e.g. the trace recorded by the yacht "Mercator" of the 2004 Indian Ocean Tsunami at a water depth of 14 m) show that the solitary and N-wave approximations are poor representations of real tsunami signals. This is demonstrated clearly in (Figure 2 of Schimmels et al., 2016) where they compare the trace recorded by the yacht "Mercator" and one from the 2011 East Coast tsunami with a solitary wave.

A unique advantage of the pneumatic tsunami generation method for physical modeling described here is that it enables the displacement of very large volumes of water in a controlled manner. This method makes it possible to generate waves of very long wavelength and, crucially, has been shown to accurately reproduce free surface profiles from recorded tsunami field data. This paper aims to draw together the lessons learnt from over ten years of research, designing, constructing and testing world-leading pneumatic Tsunami Simulators for scaled laboratory modeling.

This paper documents the development of a laboratory modeling technique that can reproduce at appropriate scales, subduction zone tsunami, for example, those measured in the 2004 Indian Ocean and 2011 Japan East Coast tsunami. This paper will concentrate on the pneumatic tsunami generation method, describing how designs were developed, how they work, and presenting research results validating their performance to quantify tsunami effects.

PREVIOUS WORK TO GENERATE TSUNAMI IN LABORATORIES

Testing of tsunami in hydraulics laboratories has been relatively rare, so advances in tsunami generation at laboratory scale are similarly few. Previous tsunami simulation approaches can be grouped under four main headings:

- those that generate waves by reproducing the physical triggering mechanism of a tsunami, landslide or motion of the seabed;
- simulating a part of a tsunami wave trace, primarily by dam-break or similar;
- generating a much shorter wave such as a soliton;
- simulating a full time series using some form of Tsunami Simulator.

Reproduction of the Prototype Tsunami Trigger

In the past, reproducing the physical triggering of tsunami was considered the most appropriate approach to simulating tsunami-like waves. In the early 1970s at California Institute of Technology where (Hammack. 1972; 1Hammack, 1973) used a moving section (0.3 m or 0.6 m) of a test flume floor, raised or lowered suddenly by a hydraulic ram to reproduce sub-sea bed motion. Potentially a good way to simulate effects of sub-seabed movement, this approach was only ever used in relatively shallow depths, and had not been repeated until a series of recent micro-experiments at Dundee, see (Lu et al., 2017a; 2Lu et al., 2017b).

Thunsyanthan and Madabhushi, (2008) attempted to generate a scaled tsunami by dropping a 100 kg rectangular block vertically into the deeper end of an ultra-short (4.5 m) flume in an attempt to recreate a sudden sea-bed motion in reverse. The waves generated were however, equivalent to H = 2.5 m, T = 7.5 s at 1:25 scale, which is far too short a period to bear any significant similarity with realistic tsunami waves.

Practically all studies on landslide-triggered tsunami involve the tsunami waves being generated using a physically realistic (if simplified) landslide to displace the water in a flume/basin. A useful review (of work mainly in the United States) is given by Enet and Grilli, (2007). Wiegel, (1955) studied landslide-generated waves in a flume using a wedge-shaped box sliding down a plane. This "moving block" method is still the most common way of modeling landslide-triggered waves, often with sand or gravel filled boxes sliding down a slope under gravity. Buoyant wedge paddles driven/controlled by electric or hydraulic rams have been used to generate solitary waves in the Tsunami Basin under the United States Network for Earthquake Engineering Simulation (NEES) program, Yim et al. (2004), McFall and Fritz, 2016. Each sliding wedge piston (29 no.) is driven by electric motors to give wave periods of 0.5–10 s (model), and maximum wave heights of 0.8 m in up to 1 m depth. Landslide-triggered tsunami have also been modeled at the University of Rhode Island using a Gaussian shaped underwater shape sliding down a 15° slope, and similar experiments were conducted in a wave basin at Bari by Di Risio et al. (2009). A pneumatically controlled landslide generator was developed at the Swiss Federal Institute of Technology in Zurich, Switzerland, and was used to generate a high-speed granular slide at 1:675 of Lituya Bay, (Fritz et al., 2001).

A major drawback of all these approaches is that they only allow the study of tsunami or tsunami impact for near source events.

Wave Paddles

The most common and robust attempt to reproduce subduction zone tsunami waves in the laboratory has previously been a piston paddle. This has been used in various laboratories, particularly in the large Hydro-Geo Flume at Port and Air Research Institute (PARI) described by Shimosako et al. (2002), and in the Large Wave Flume (Großer Wellenkanal, GWK) described by Schimmels et al. (2016). The PARI flume used a piston paddle producing up to significant wave height, H_s = 1.4 m at T = 5.5 s, but it is understood that the capacity may have been increased in recent years. The GWK uses a piston type wave maker with a 4 m stroke. In its usual mode, it can generate wave heights of up to 2 m at typical periods between 3 s and 8 s in water depths between 4 and 5 m. The tsunami tests described by Schimmels et al. (2016)

however, used a water depth reduced to 1 m to generate waves of periods up to 100 s, corresponding to typical tsunami durations of 1,000 s at 1:100 scale. The maximum achievable wave heights were about 6 cm, corresponding to 6 m at that scale.

Dam-Breaks

Several researchers have used a dam-break approach to generating tsunami bore-fronts, see particularly Nouri et al. (2010), Al-Faesly et al. (2012), Kihara et al. (2015). This method is effective in generating a violent bore-front, but few comparisons have been made with the full length of recorded tsunami profiles. This may limit the application of this method to the investigation of the initial tsunami impact loads only.

A pump-driven flow generator has been developed at Franzius-Institute at the University of Hannover, using a set of pumps to control depths and incoming/outgoing currents. Generation of different kinds of waves are claimed by Goseberg et al. (2013), Bremm et al. (2015), Drähne et al. (2016), including single cycle sinusoidal waves, solitary waves and N-waves. They present results from wave periods 20 s–100 s, with wave heights from 20 to 40 mm. Within the limitations of the system, a pumped system gives a robust way to add water volume to the test section, although installing new pump capacity in any existing facility to give the volumes and peak flows required by realistic tsunami may be extremely expensive.

Pneumatic Tanks

A 3-part tsunami generator 45 m × 4 m, has been developed at Kyoto University's Ujikawa Open Laboratory of the Disaster Prevention Research Institute (http://www.kyoto-u.ac.jp/cutting-edge/project/page04.html) with results reported by Hiraishi et al. (2015) and Tomiczek et al. (2016a, 2016b). The generator combines a piston-based wave maker with a moderate (2.5 m) stroke, a current generator, and an overhead water tank, to allow flexibility in the profile of the waves generated. The current generator, in particular, is needed to produce the long period tsunami flows that follow initial bore-type waves. The water tank, meanwhile, can reproduce other effects of tsunami subduction zone movements, including those driven by two linked sources.

A tsunami generator was created at the Laboratory of Hydraulic Constructions (LCH) at Ecole Polytechnique Federale de Lausanne (EPFL) in Switzerland that uses a vertical release technique to generate surges and long waves, Wüthrich et al. (2018). An upper reservoir was connected to a lower reservoir, through three submerged pipes. When the generation system was activated, a difference in the head between the upper and lower reservoir was established, resulting in a gravitational flow through the pipes. Since the lower basin was completely filled with water, the incoming discharge resulted in an upward flow at the channel inlet, and subsequently, a free-surface wave formed and propagated downstream in the flume.

Early examples of pneumatic tsunami generators include (Togashi, 1986) and Palmer and Funasaki. (1967). These facilities had a very similar generation technique to the facility described within this paper, but with considerably smaller Froude-scaling.

FIRST GENERATION OF PNEUMATIC TSUNAMI SIMULATOR

Introduction

The first generation of pneumatic Tsunami Simulator was conceived by HR Wallingford following the Indian Ocean tsunami in 2004. At the time, the most popular method for generating tsunami within laboratories was the paddle method, based on methods used in laboratories across the world to generate (shorter) wind waves. By increasing the stroke length of a typical paddle wind wave generator, the period of the waves could be increased so much that they might match the extraordinarily long wavelengths of tsunami.

Unfortunately, in 2004, there was a practical limit to stroke length that most laboratories could accommodate, and many researchers had tried and failed to use this method to reproduce full duration, and particularly trough-led, tsunami at that time.

In creating the pneumatic Tsunami Simulator, the HR Wallingford team intended to extend the technology of tide generation to produce an alternative tsunami generation method avoiding mechanical stroke length limitations. Rather than generating a very long wind wave, they hoped to use advancements in vacuum pump and control technologies to produce a very short tide.

The precursor of HR Wallingford (Hydraulics Research Station, HRS) developed the tide generation method over fifty years previously, Wilkie and Young (1952). In the 3 decades after its development, this method was used extensively in physical modeling at HR Wallingford, most notably within the large area model for the Third London Airport (HRS, 1974) producing a 12.5 h tide in 7.5 min. Eventually though, this method was made redundant by the advancement of large area numerical tidal models.

The 2004 Indian Ocean tsunami had a duration of approximately 20 min. At a scale of 1:50, this would require a laboratory-scale wave of just under 3 min period. If the tide generation technology of the Fifties was to be repurposed to create a tsunami wave, it would require a 3x increase of speed of that system. In discussion with the UCL researchers, the Wallingford team agreed that this was a reasonable ambition, and set to designing the first generation pneumatic Tsunami Simulator (TS).

Concept Design

The methods described by Wilkie and Young (1952) were the initial starting point for the concept design. A vacuum pump is used to draw air out continuously of a steel box or tank. An outlet underwater into the flume allows water to move into or out of the tank. An air valve on the top of the tank is then used to regulate the pressure inside the tank, raising and lowering the water level inside (Tank Water Level, TWL). In the new systems, control of this air valve, via computer software, allows the wave form generated to be closely controlled.

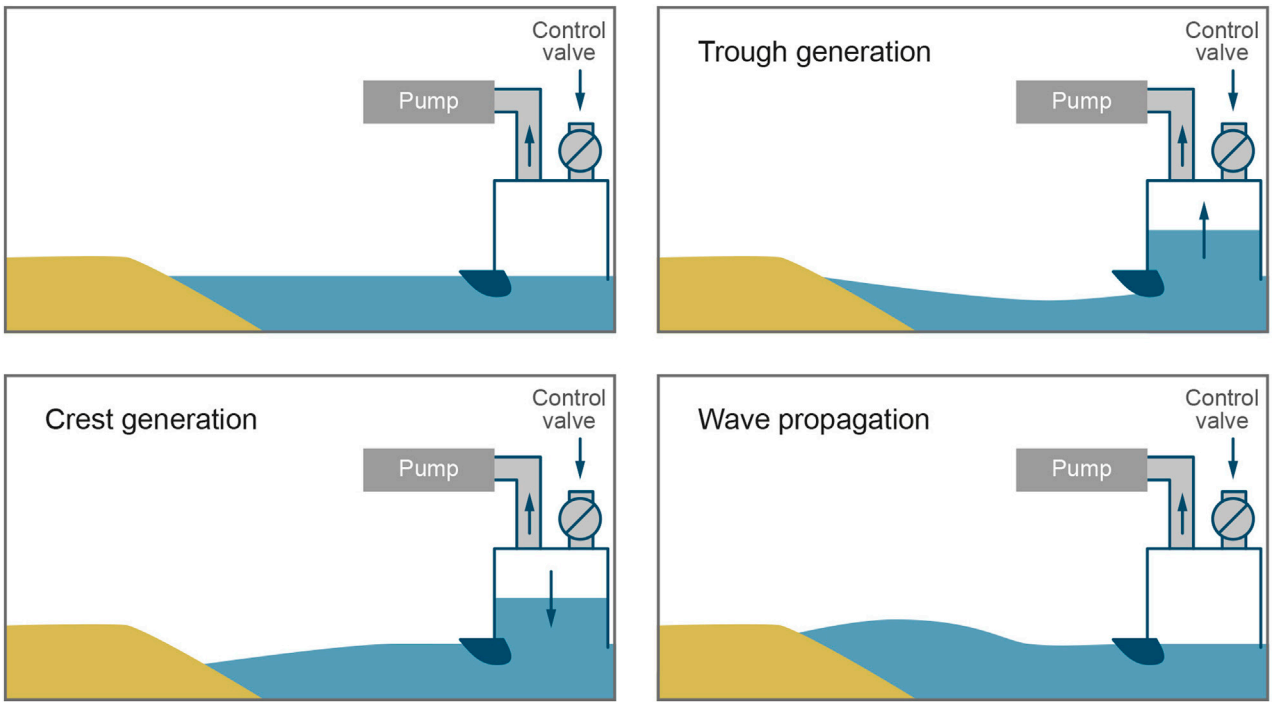

FIGURE 1 | Schematic diagram of pneumatic Tsunami Simulator wave generation. From top left to bottom right: pump on and control valve open; pump on and control valve closed creating wave trough; pump on and control valve open creating wave crest; wave propagating along flume.

The wave from the TS is created by changing the relative vacuum inside the TS and hence the TWL. Raising the TWL creates a depression in the free-surface in the flume, creating a wave trough. Lowering the TWL increases the flume water level creating a wave crest. The control system involved changing the angle of the computer-controlled inlet air valve. This process is summarized in **Figure 1**.

Detailed Design and Construction

The first generation Tsunami Simulator at Wallingford was constructed in spring 2008, funded by EPSRC through the EPICentre grant (No. EP/F012179/1). This Tsunami Simulator was designed to fit in either of HR Wallingford's Flumes one or two in the Froude Modeling Hall. These flumes are each 45 m long and 1.2 m wide. Approach bathymetry and shoreline within the flume were formed in cement mortar on top of compacted fill. For the EPICentre experiments (Charvet, 2011), they were shaped to represent a 1:20 coastal slope followed by a horizontal "inland" inundation area (3.3 m long). The toe of the 1:20 slope was situated 15.2 m from the outlet of the TS.

The design of the first generation TS (Allsop et al., 2008; Robinson, 2009) was conducted with the aim of creating a TS tank with sufficient strength to resist the developed pressures, but also to allow rapid deployment, removal and storage. A modular system of steel panels was chosen which created a 4.8 ml x 1.8 mH × 1.15 mW tank (length x height x width). Internal bracing was included to avoid distortion under the pressure difference between inside and outside the TS. Internal baffles were also included to reduce longitudinal sloshing within the TS tank, perhaps exacerbated by the single offset air inlet and outlet. The front panel of the first generation TS was adjustable to create different outlet heights. A plastic cylinder (115 mm diameter) was placed over the bottom edge of the panel to reduce turbulence created by the sharp steel edge during peak flows.

The first generation TS tank was connected to a two-stage side-channel vacuum pump (7.5 kW Zepher™) RT-84086, and two 4 inch butterfly valves. The first valve acted as a safety valve, that was to be opened in cases of emergency to avoid the pump being flooded. The second valve was connected to a computer via a servo-motor operated by an open-loop control system, calibrated to produce the required wave profiles. The size of the valves and pump were chosen by recreating air-flow calculations by Wilkie and Young (1952). The published valve and pump performance characteristics were combined with the flume and tank dimensions to estimate pressures, water levels and flow-rates into the tank. These calculations were repeated for different configurations for optimum use of the available space.

The TS (of any generation) can theoretically be controlled by either a closed or open-loop system (Rossetto et al., 2011). With open-loop control, the user prescribes a control valve position time series during wave generation. This gives greater certainty of the wave generated, but requires calibration for each desired wave profile. A closed-loop control system uses a Proportional Integral Derivative (PID) feedback loop to update the valve position based on the difference between a measured and target variable, such as the water level inside the TS tank, Tank Water Level (TWL). The choice of the input variable is critical to the success of the feedback system (Goseberg et al., 2013). A perfect closed-loop

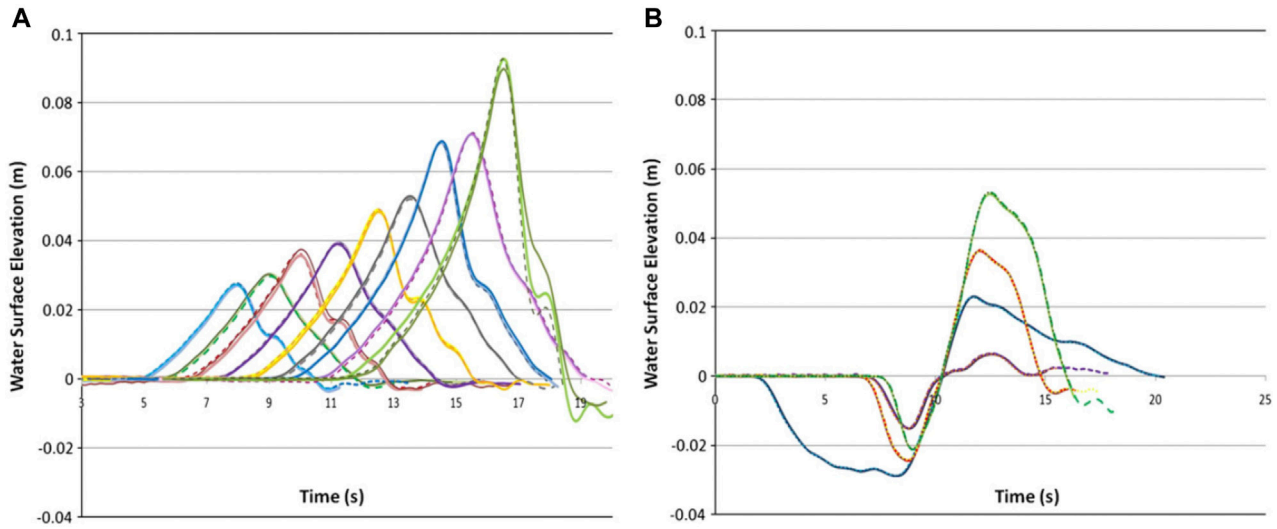

FIGURE 2 | Repeatability of elevated and N-waves with the first generation TS (Rossetto et al., 2011), the profiles obtained from three tests for each of nine different solitary wave heights **(A)** and **(B)** the profiles obtained for three tests for four different N-waves. Different line styles represent different repeat tests (solid, opaque and dashed).

system does not require individual wave calibrations because the system should produce the desired wave first time. An open-loop system requires an iterative calibration process in order to simulate the desired waveform. The first generation TS used an open-loop control based on the LabVIEW software. Some initial investigations into closed-loop control were conducted, but the use of "water level only" control produced some "undesired wave behavior in the flume" (Rossetto et al., 2011).

Testing

Initial testing of the first generation Tsunami Simulation was performed during the EPICentre project. It was split into two main stages: wave run-up tests; and measuring forces on a single building. The first stage included identifying the range of waves that could be simulated and their repeatability (**Figure 2**). Sine, solitary (elevated) and trough-led N-waves were generated, ranging in period from 5 to 18 s (model), with positive amplitudes up to 0.1 m. The ability to simulate stable trough-led waves is a unique ability of the pneumatic generation system. An attempt was made to calibrate the Mercator wave trace from the 2004 Boxing Day Tsunami at 1:50 scale (see Rossetto et al., 2011). The trough and the front face of the crest were well reproduced, however, the wave tail was not reproduced quite as well.

The first research conducted with the TS investigated the run-up of various elevated and N-waves. This work is described in Charvet. (2011), and Charvet et al. (2013), and resulted in a new predictive equation for wave run-up, perhaps now superseded by McGovern et al (2018).

The second stage of the EPICentre project measured the forces acting on a single idealized office or hotel building and are reported in Lloyd. (2016). Lloyd focused on measuring total body force and pressures acting on a square (plan) building at different orientations to the incoming tsunami wave. A range of solitary (elevated) and N-waves were used, with the body force measured using a 3-axis load-cell and arrays of pressure transducers used to measure pressures on the different faces.

Comments on the first Generation Tsunami Simulator

The work done on the TS under the EPICentre project demonstrated the capability of the pneumatic Tsunami Simulator technique, but also highlighted areas for improvement. These included the flume length (too short), the height of the TS tank (should be increased to allow greater volume and head of water to be used) and turbulence created at the outlet during wave generation, particularly crest generation. The introduction of an active wave absorption system and closed-loop control were also desirable.

Follow-Up Numerical Study and Design Improvements

Despite success with the generation of the 2004 Mercator time series at 1:50 scale using the first generation Tsunami Simulator, particular wave shapes/heights showed significant distortion. As part of HYDRALAB IV, a 2-dimensional (2D) numerical model of the Tsunami Simulator was created to:

- Identify factors and/or processes that reduced efficiency, perhaps sloshing within the tank, eddies from the outlet, or other phenomena;
- Identify inherent generation limits; and hence
- Investigate ways of increasing the generation window.

The (2D) numerical model was created using the OpenFOAM® computational fluid dynamics (CFD) platform

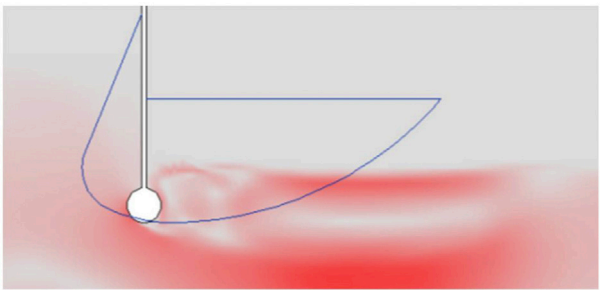

FIGURE 3 | Illustration of final design of the new outlet flow shaper (blue line) superimposed on velocity field (gray to red scale where red is high velocity and turbulence) from a numerical model of the original outlet (white circle) during crest generation (flow out of the first generation TS into the flume, left to right).

(see Weller et al., 1998). The size and shape of the domain were created to match that of the first generation Tsunami Simulator, 4.8 m long and 1.8 m high. The model used the interFoam solver and replicated the tank control system using a time dependent pressure boundary condition at the tank roof. Further model details are described by Allsop et al (2014).

Initial testing confirmed that the CFD model could reproduce the idealized tsunami waves generated in the lab showing suitable agreement with the recorded wave gauge data. The OpenFOAM model was therefore used to investigate the limits of the Tsunami Simulator, in particular identifying the maximum height for generated waves, and the maximum steepness of wave that the tank could generate.

The numerical model simulations showed that an increase in the height of the target signal did not necessarily leads to an equivalent increase in wave height. As the steepness of the wave increased, the wave was seen to separate into a series of sharp peaks. This suggested that throttling at the outlet was imposing a limit to the outflow rate, and thus to the rate of rise of the tsunami wave.

The numerical model demonstrated that the outlet of the first tank led to substantial reverse-flow eddies at peak flow conditions. Incremental improvements to the flow-shaper in the numerical model created a smooth contraction of the flow through the outlet and a controlled expansion downstream. A further project (under HYDRALAB IV) supported validation of the numerical model by direct comparison between physical and numerical tests using pressures measured at the top of the TS tank as input to the numerical model. The tank was raised, and the flow-shaper was installed (**Figure 3**). The Mercator time series was generated at an undistorted Froude scale of 1:50 (**Figure 4**) and the improved performance characteristics were reported by Allsop. (2014).

SECOND GENERATION OF PNEUMATIC TSUNAMI SIMULATOR

Introduction

The second generation Tsunami Simulator was constructed in a flume ~100 m long. This different flume had the added benefit of greater width, 1.8 m, so more 3-dimensional experiments could be run with flows through breaches in seawalls, or around groups of buildings. The construction of the second generation Tsunami Simulator within this especially long flume looked to limit (some of) the effects of wave reflection. Local limitations forced the Tsunami Simulator tank to be shorter, and coupled with the desire to increase the rate of rise, the new tank was made taller at 3.5 m vs 1.8 m. This had the significant advantage of increasing the maximum outlet flows, so (potentially) steepening the rising part of the tsunami time trace. Results from the second generation device in the 100 m long flume were presented by Chandler et al (2016) and McGovern et al (2016). Interestingly, these experiments provided insight into the 'flume length vs wave length' problem, and suggested ways by which the effects of reflections might be reduced. The research performed during this stage of research was funded by the European Research Council (ERC) URBANWAVES grant (No. 336084).

Design and Construction

The CFD model developed to design the flow shaper for the first generation TS was used extensively in the design of the second generation TS. The effect of changing tank height and length were investigated as well as the influence of the outlet height and the still water level (SWL) in the flume at the start of wave generation. The numerical model was also used to estimate the potential performance of the second generation TS. One of the findings from the numerical modeling was that for a TS tank less than

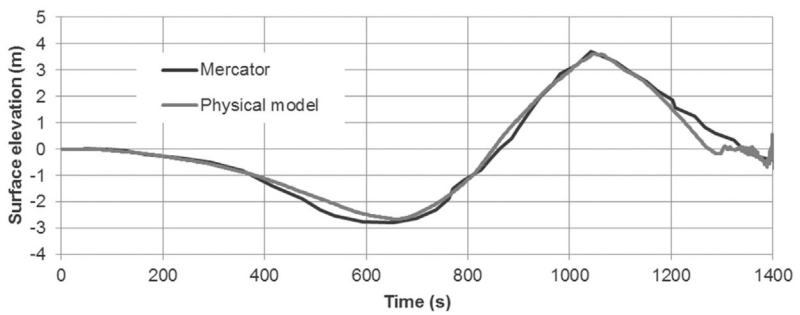

FIGURE 4 | Mercator time series at 1:50 scale with measurements in improved first generation Tsunami Simulator.

4.5 m long, there was no discernible sloshing within the tank during wave generation, even without the presence of baffles. For tanks longer than 4.5 m a longitudinal slosh could develop if baffles were not used. This gave a desirable length of TS of 4.0–4.5 m. The width of the TS is governed by the width of the flume into which it is placed. The height of the TS is governed by the available head room above the flume and the maximum head difference achievable with the vacuum pumps used. Greater head differences (partial vacuum pressures) start to require more complex and more expensive pumps.

For the second generation TS, a tank length of 4.0 m was chosen as this did not need internal baffles, simplifying design and fabrication. The headroom above the flume dictated a maximum tank height of 3.5 m. The second generation TS was designed to be deployed in HR Wallingford's Flume 3, which is 1.8 m wide, 100 m long and 1.8 m deep, which in turn dictated the maximum width of the second generation TS at 1.8 m. Due to access constraints to Flume 3, the second generation TS required a different construction method to the first generation, which had been constructed outside the flume and lifted into position. The second generation TS was constructed *in-situ* from long narrow channel section panels. Each panel was 0.465 m wide and varied in length depending in its intended location (side panels were 3.5 m long; front, back and top panels were 1.5 m long). All steel design was accorded with Eurocode 3 (BS EN, 1993). The TS does not come under the Pressure Equipment Directive (Directive, 97/23/EC) as the vacuum inside it insufficient, but these regulations were still consulted during the design phase for best practice information.

Numerical modeling had demonstrated that the outlet height did not influence the wave generated unless it was too close to the SWL in the flume, and might therefore allow air into the outlet during trough generation. An outlet height of 0.4 m was chosen as this allowed the greatest range of flume depths (SWL's) to be used. The design of the front panels allowed the outlet height to be changed in fixed increments by removing panels and moving the lowest panel up. The same design of outlet flow shaper developed for the first generation TS (see **Figure 3**) was used on the second generation TS. Each of the eight top panels were pre-cut with an 8 inch (0.203 m) diameter hole, which allowed instrumentation, vacuum hoses and control valves to be fitted. Un-used holes were later blanked off. A 5 inch (0.127 m) internal diameter 45° butterfly valve was used for the second Generation TS in combination with the Zepher^{UK} RT-84086 vacuum pump from the first generation TS coupled with a new RT-95330 vacuum pump (Zepher, 2016).

The control system for the second generation TS used a Beckhoff EtherCAT based system, governed by a programmable logic controller, PLC, and a. NET application. The PLC does most of the work, and is where the main functionality was set. The. NET application was effectively used as a graphical interface for users to communicate with the PLC on the controller. The control software allowed the vacuum pumps to be switched on and off remotely and to control the angle of the air valve in two different ways. The first, and simplest method of controlling the valve was by setting a desired angle and a speed (°/s) at which the valve should move to reach this position from its current one. This was used to set the initial water level inside the TS (Tank Water Level, TWL) and during the commissioning stage to explore the response of the TS system. The second method of controlling the valve position was through a valve time series, given to the control application in a two column. csv file. Various safety protocols were implemented through the PLC, including a safe switch off procedure when an emergency stop button was pressed and procedures to prevent water from being drawn up into the vacuum pumps.

HR Wallingford's Flume 3 has a hinged flap wave paddle mounted at the upstream end of the flume and this could not be removed for the deployment of the TS. The TS, therefore, sat downstream of that wave paddle, ~2.0 m from the end wall of the flume, reducing slightly the available 100 m flume length. The experimental setup of the second generation TS for the initial URBANWAVES experiments is shown in **Figure 5**. Twin wire resistance wave gauges were placed at various distances from the front of the TS on the constant depth region of the flume and along the 1:20 bathymetry slope. Wave gauges were typically sampled at 100 Hz throughout testing.

Testing

A series of wave calibrations were performed and presented in (Chandler et al., 2016). This included elevated (crest only) and trough-led N-type waves. The calibrated elevated waves and N-waves are summarized in **Table 1** and **Figure 6**. The calibration process was iterative, based on a degree of trial-and-error.

For shorter period waves, the propagation of the waves could be tracked along the flume. The propagation of a 20 s elevated wave is shown in **Figure 7**. The wave was unchanged as it propagated over the area of constant depth ("offshore" region), and then shoaled when it reached the 1:20 slope (WG_05 and 06). The reflection from a vertical wall present at the top of the 1:20 slope during this test can be seen in the second half of WG_06 traveling back along the flume to WG_05, arriving at approximately 45 s. The wave fissions as it propagates against the continued arrival of the incident wave.

For longer period waves (T > 45 s) the generation is not complete before the reflections from the bathymetry (and any structures present) reach the TS. Through the calibration process in Flume 3, these reflections are accounted for by altering the valve motion, creating a manual, pre-defined absorption system. Due to the geometry and generation method employed by the TS, a significant amount of "self-correction" occurred during wave generation. Both "absorption" methods worked best for long period waves due to the inherent response time of the TS. The combination of these methods allowed the generation of waves significantly longer than the experimental facility, discussed at some length by McGovern et al (2018).

The presence of a 22 s period resonance within the wave flume can be seen on the longer wave periods (**Figure 6**). The amplitude of this resonance was 2 mm and did not influence the generated wave or the tests conducted. There was however, still a desire to remove this resonance from the long waves generated. This led to an exploratory study of active absorption on the third generation TS described in *Third Generation of Pneumatic Tsunami Simulator*.

There is further discussion on the validity of the waves generated by the second generation TS in McGovern et al.

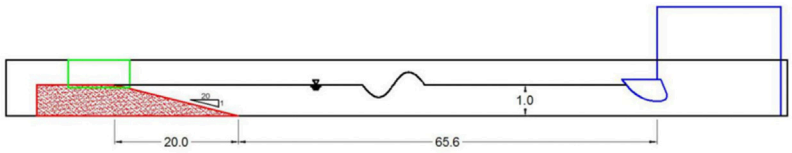

FIGURE 5 | Schematic of the second generation TS for URBANWAVES phase 1 testing, bathymetry in red on the left with the flume window in green and the second generation TS in blue on the right.

TABLE 1 | Calibrated crest only (elevated) waves and N-waves using second generation TS.

Name	Period, T (s)	Crest amplitude, A_c (m)	Trough amplitude, A_t (m)	Calculated wave length, L (m)
Elevated_T = 160 s	160	0.056	–	500
Elevated_T = 80 s	80	0.066	–	250
Elevated_T = 45 s	45	0.085	–	140
Elevated_T = 20 s	20	0.089	–	63
Nwave_T = 240 s	240	0.036	−0.041	750
Nwave_T = 200 s	200	0.040	−0.043	630
Nwave_T = 166 s	166	0.041	−0.041	520
Nwave_T = 111 s	111	0.053	−0.045	350
Nwave_T = 80 s	80	0.044	−0.039	250
Nwave_T = 80 s_max	80	0.075	−0.065	250
Nwave_T = 70 s_max	70	0.075	−0.067	220
Nwave_T = 40 s	40	0.033	−0.054	125
Nwave_T = 20 s	20	0.053	−0.049	63

Note: Wave length calculated using the shallow water approximation.

(2018), focusing particularly on the generation of waves that are much longer that the wave flume. The 240 s N-wave has a calculated wave length of ≈750 m, more than 10 times the distance between the TS and the bathymetry.

Discussion on Tsunami Wave Calibration Tests

The key finding that came from the calibration process was the importance of the choice of calibration point when dealing with such long waves. When using a single point to define a single wave, the position of that point relative to any reflective surfaces, such as the 1:20 slope or any tested seawall, becomes important and can significantly influence the apparent wave form and amplitude (Chandler et al., 2016). This finding is also important when looking at tsunami wave forms measured in prototype, such as the Mercator trace, as this may not itself be a "clean" signal of the incident tsunami wave alone as it has probably been influenced by reflections from the coastline, especially the later part of the signal.

THIRD GENERATION OF PNEUMATIC TSUNAMI SIMULATOR

Introduction

The third generation of pneumatic Tsunami Simulator took advantage of the availability of HR Wallingford's new Fast Flow Facility (FFF) (Whitehouse et al., 2014). The FFF was much wider (4 m) than the flumes for generations 1 and 2. This created an opportunity to investigate three-dimensional effects onshore, but the wider tank required much greater air flow rates for operation than for the second generation TS. The generally good experience in running the two (dissimilar) pumps for the second generation device suggested that it would be simple to again mount two vacuum pumps in parallel, hence an additional RT-95330 was purchased to increase the peak flow rate. Experience of the second generation device was used to improve the control and generation of the tsunami length waves. This stage of development was funded by the ERC URBANWAVES project.

Despite using a rather different facility, design of the third generation TS was built on the developments of the previous two generations. The design of the third generation TS tank followed a similar strategy to the second generation, with multiple small bolted sections, rather than the larger panels with welded bracing used in the first generation. The tank design again obeyed Eurocode 3 (BS EN, 1993), and used lessons from the second generation to increase panel stiffness by greater reverse folding at the edges, and by reducing the number of bolts required by changing panel cross sections.

Design and Construction

The third generation TS tank was 3.96 m wide, 4.0 m tall and 4.45 m long. It was positioned on a 1:10 approach slope within the Fast Flow Facility, just in front of the existing wave maker

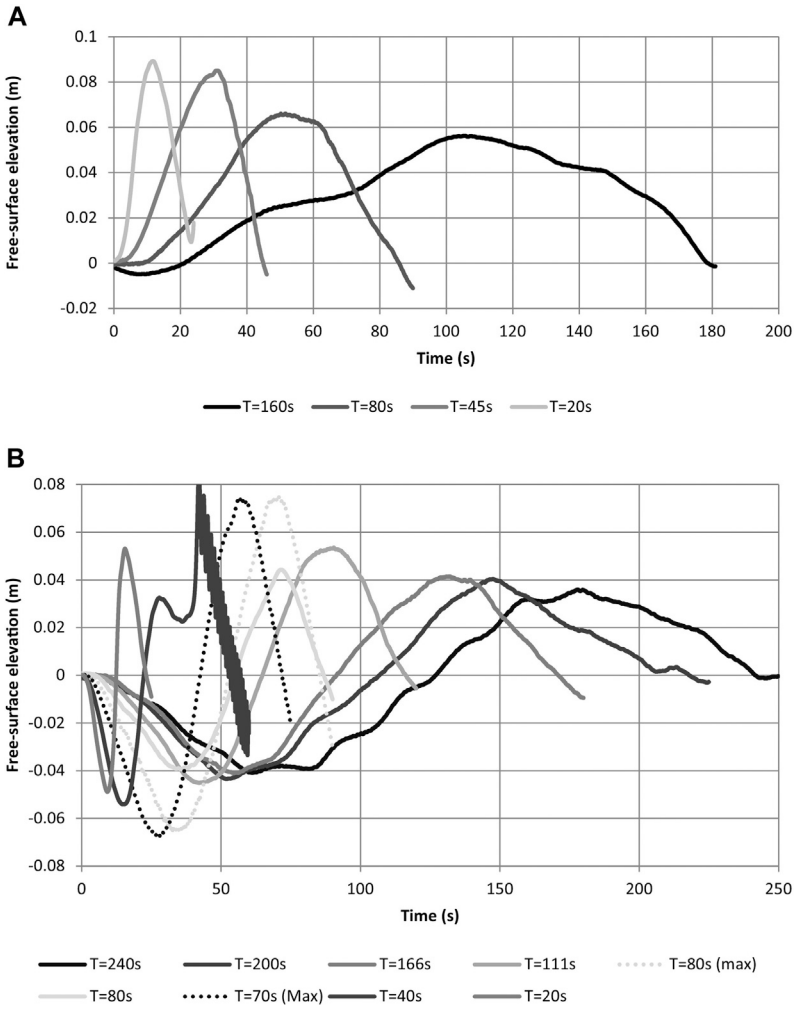

FIGURE 6 | Calibrated crest only (elevated) waves **(A)** and N-waves **(B)** using the second generation TS, measured at the toe of the bathymetry.

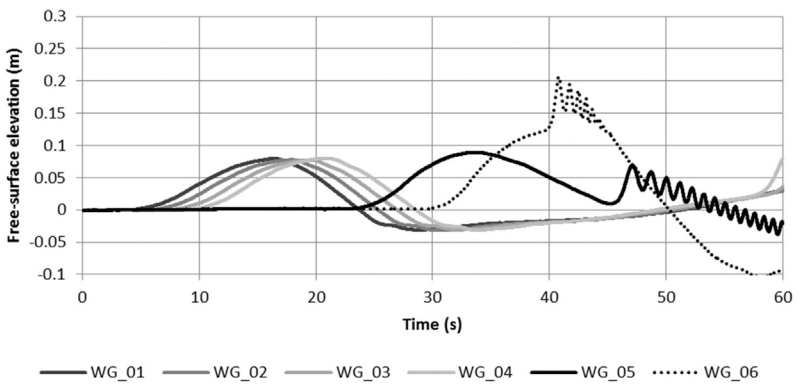

FIGURE 7 | T = 20 s elevated wave propagating along the flume, WG_01 to 04 in a constant depth (7.0, 12.0, 17.0 and 22.0 m from TS respectively, h = 1.0 m), WG_05 at the toe of the 1:20 slope (65.6 m from TS, h = 1.0 m) and WG_06 on the 1:20 slope (75.6 m from TS, h = 0.5 m).

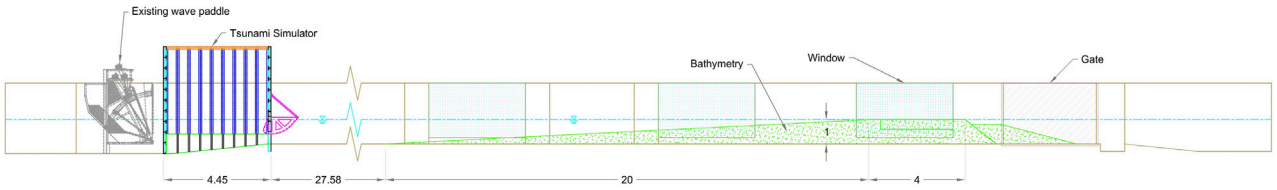

FIGURE 8 | Setup of the third generation TS for URBANWAVES phase 2 testing, from left to right: flume bottom hinge wave paddle (gray), third generation TS (blue with flow shaper in magenta), bathymetry (green), flume windows (blue) and flume gate (gray hatch).

(bottom hinge type, **Figure 8**). A tapered base panel created a horizontal platform from which the rest of the TS was constructed. The OpenFOAM CFD model was used to assess the impact of placing the TS on the approach slope and whether a horizontal false floor was needed inside the TS. The CFD model showed that there was no discernible difference between waves generated with a sloping floor in the TS and a horizontal floor. The third generation TS used two Zepher^{UK} RT-95330 vacuum pumps and a 7 inch (0.178 m) internal diameter 45° butterfly valve, operated by the same Beckhoff AS1050 stepper motor used in the second generation TS (*Design and Construction*). The third generation TS was instrumented with a 3.5 m Temposonics magnetostrictive float gauge inside the tank, a negative (vacuum) pressure transducer in the top of the tank measuring air pressure (0 to −500 mbar), and a pressure transducer (0–0.5 bar) 0.65 m mounted at the flume floor in the center of the back panel of the TS.

The bathymetry installed in the FFF consisted of a 1:20 slope, starting 27.6 m from the front of the TS (**Figure 8**). The slope rose to a height of 1.0 m above the flume floor, after which a 4.0 m horizontal area allowed building arrays, coastal defenses (at the seaward edge) and other structures to be placed and tested. The central 3.0 m section of the horizontal area could be removed to allow a mobile bed to be placed for scour experiments. Over-wash from the wave generation flowed over the back of the bathymetry and into the secondary (back) part of the "race-track" flume. Only

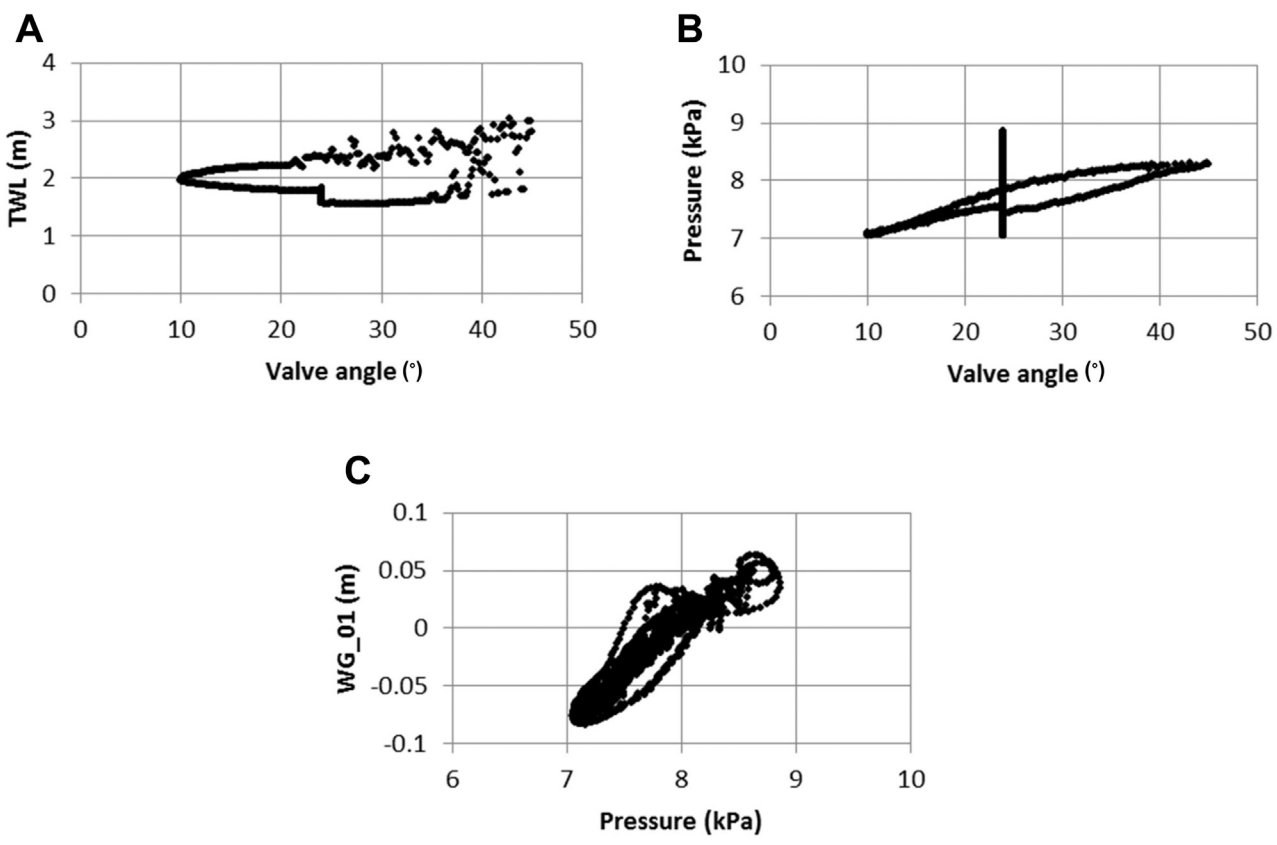

FIGURE 9 | Comparison of time co-incident values for **(A)** valve angle and tank water level, **(B)** valve angle and pressure at the base of the TS and **(C)** pressure at the base of the TS and free-surface elevation at WG_01 (0.25 m from TS) for second generation TS.

for the largest waves does enough volume of water enter this secondary loop to create back-wash over the horizontal section back into the main part of the flume. Twin wire resistance wave gauges were placed along the flume in the constant depth region and on the 1:20 bathymetry slope.

The control system for the third generation TS was also upgraded from the second generation. The main advance was the implementation of closed-loop control using a proportional-integral-derivative (PID) feedback loop, instead of the open-loop control of the second generation TS. This is similar to the work by Goseberg et al. (2013) for their pumped Tsunami Simulator who used a "real" PID control system to control their water pumps, based on pressures measured in the flume. Goseberg et al. (2013) found that the pressure sensor needed to be placed close to the pumps, otherwise a long delay time was introduced into the system which caused unstable oscillatory behavior. They also found that the *p*, I and D variables needed to be tuned for each wave generated using trial-and-error. A moving average filter was applied to the pressure signal to reduce the influence of residual oscillations.

Experience with the second generation TS (Chandler et al., 2016) suggested that pressures from the transducer at the base of the TS would be a good parameter on which to base the PID feedback. This tank pressure showed a good correlation with both the free-surface elevation (FSE) in the flume and with the valve motion (**Figure 9**). Initial thoughts were to use either the TWL or one of the wave gauges in the flume. There is no strong correlation between the TWL and the FSE in the flume, so this was not a good parameter to use. A wave gauge in the flume would be ideal because it is directly measuring the parameter that we want to control (FSE), however, there is a time delay in the signal measured by any of the wave gauges and TS. This would lead to the problems described by Goseberg et al. (2013) when moving their pressure transducer away from the water pumps.

During the commissioning phase of the third generation TS, a set of PID values was established that allowed the system to respond quickly enough to generate the desired wave form, but not to become unstable. System responses were different when

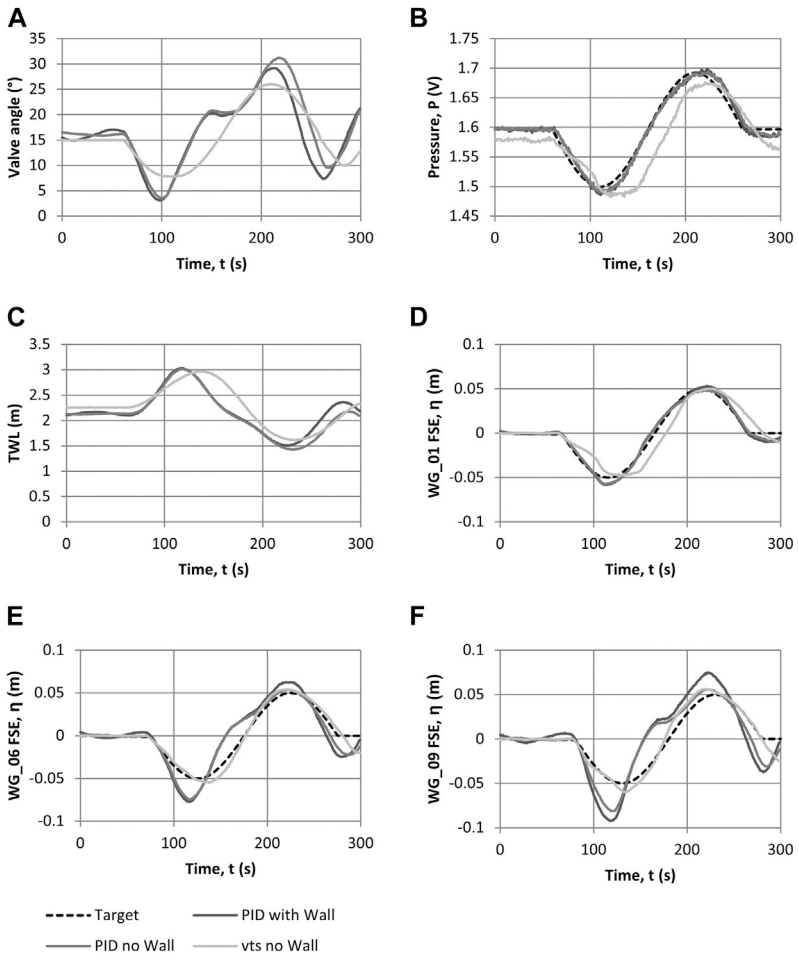

FIGURE 10 | Comparison of the three calibration runs (PID control with seawall, PID control without seawall and open-loop (valve time series, vts) control) of N200 wave for **(A)** valve angle, **(B)** pressure at base of TS, **(C)** tank water level (TWL), **(D)** free-surface elevation (FSE) for WG_01 (0.25 m from TS, h = 1.0 m), e) FSE for WG_06 (toe of the bathymetry, 27.47 m from TS, h = 1.0 m) and f) FSE for WG_09 (closest to shore, 42.47 m from TS, h = 0.25 m).

the air valve closes or opens, so different PID values were prescribed depending on the valve motion.

Testing

Wave calibrations occurred in three stages:

- The first stage used the closed-loop PID control to generate the full suite of waves, with no trial-and-error to match the desired FSE. This matched the set-up used in the calibration of the second Generation TS.
- The second stage repeated this process, but without a seawall at the top of the 1:20 slope, so with lower reflections,
- The third phase of the calibration procedure required manual modification of each PID derived valve time series, where necessary, to achieve the desired free-surface elevation within the flume.

During the first stage, the closed PID control system converted the desired FSE into a pressure time series desired at the TS, which was then supplied to the control software. The PID system then determined the valve motion required to match the desired pressure. The results from this first phase of calibration were mixed. Excellent agreement was achieved between target and desired pressure time series, but this did not always result in the desired free-surface elevation at the calibration gauge. The differences were due in part to the distance between the calibration gauge and the TS, and due to the inability of the feedback system to determine the direction of the wave and consequent inability to distinguish when a reflected component is traveling back against the generated wave. This resulted in truncated crests at the calibration gauge, but apparently 'correct' pressure signal at the TS due to reflected earlier parts of the crest.

The removal of the seawall for the second stage of calibration did not significantly change the findings from the first phase, suggesting that most of the reflection originates from the 1:20 slope. In the first phase of calibration the seawall was reached by all waves and overtopped by the majority. A comparison of various TS instruments and flume wave gauges for the three phases of the calibration exercise are shown for the N200 wave in **Figure 10**, where the effectiveness of the PID system at following the desired pressure signal is clearly observable. The free-surface elevation at the toe of the slope is significantly different, particularly the trough and the rise up to the crest (**Figure 10E**) with the PID control compared to the target and the final calibrated time series.

The third stage enabled a better determination of the valve time series, and a much greater understanding of the system response based on the PID wave generation results. The open-loop control results are also shown in **Figure 10**. The difference in valve motion and in free-surface elevation is clear between open and closed-loop control. Open-loop control was used during the third Generation TS testing because it gave greater confidence in what was being generated by the TS and propagating down the flume. This method is similar to that used by Bremm et al (2015).

The family of waves calibrated is presented in **Table 2** and **Figure 11** for elevated waves and N-waves. The Mercator time series from the Indian Ocean Boxing Day Tsunami in 2004 was also recreated at 1:50 scale (**Figure 12A**) as was one of the traces from the Tohoku tsunami in 2011 (**Figure 12B**). As with the elevated and N-type waves, these real tsunami time series were initially generated using the closed-loop system and then refined using open-loop control.

DISCUSSION

The most striking difference between the second and third generation TS is the different system response, both in terms

TABLE 2 | Calibrated crest only (elevated) waves and N-waves using third generation TS.

Name	Period, T (s)	Crest amplitude, A_c (m)	Trough amplitude, A_t (m)	Calculated wave length, λ (m)
E20	24	0.055	–	63
E20_max	31	0.113	–	63
E45	54	0.065	–	141
E80	75[a]	0.04	–	235
E80_max	86[a]	0.118	–	270
E160	150[a]	0.047	–	470
E160_max	146[a]	0.115	–	457
N20	20	0.084	–0.053	63
N40	42	0.048	–0.057	131
N50	50	0.052	–0.047	155
N50_max	49	0.061	–0.060	154
N80	87	0.040	–0.038	274
N80_max	87	0.070	–0.087	272
N120	129	0.047	–0.042	406
N120_max	129	0.072	–0.089	403
N160	170	0.052	–0.050	532
N160_max	168	0.080	–0.123	527
N200	208	0.054	–0.055	652
N240	245	0.056	–0.058	769

Note: Wave length calculated using the shallow water approximation
[a]*indicates period affected by reflections at calibration point.*

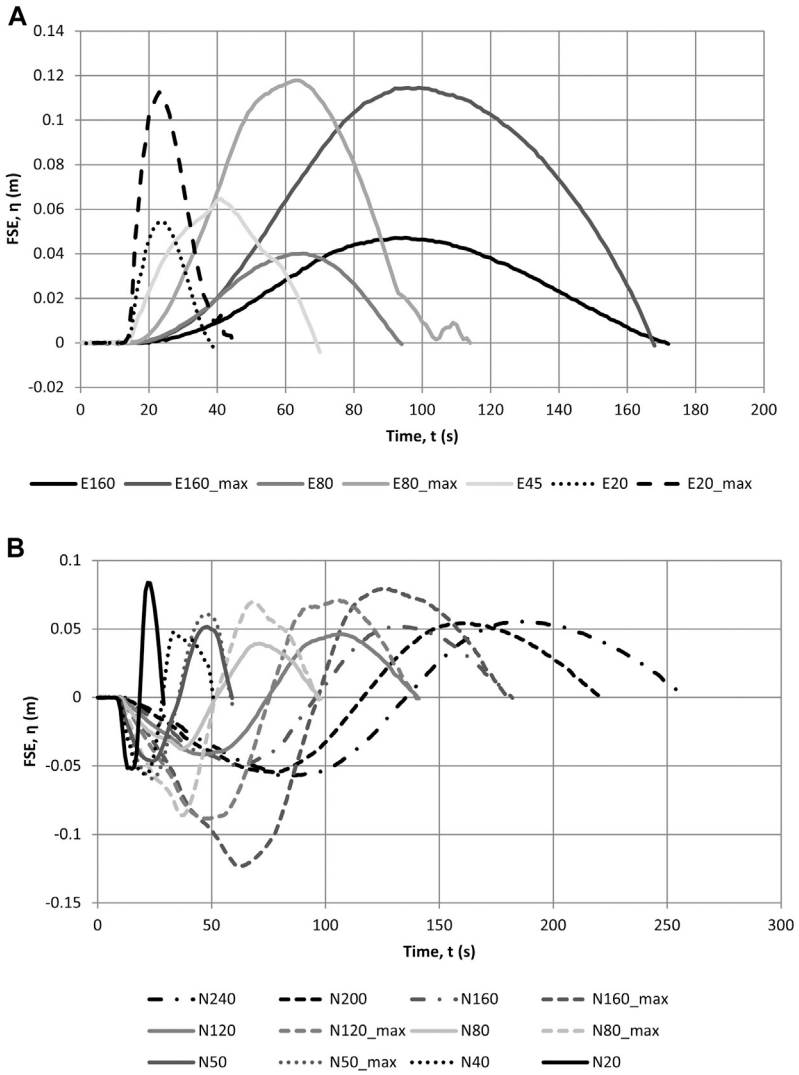

FIGURE 11 | Calibrated crest only (elevated) waves **(A)** and N-waves **(B)** using third generation TS, measured at the toe of the bathymetry.

of the TS directly and with the flume in which it sits. The valve angle, TWL and free-surface elevation at the calibration point for and N240 waves generated with both the second and third generation TS are shown in **Figure 13**. The wave form generated by both TS's closely resembles the target (with a slightly lower amplitude for the smaller third generation TS). The corresponding TWL profiles are very similar between the two generations (**Figure 13B**), but the valve motion used to create this TWL change is very different (**Figure 13A**). This is due to the different valve and pump characteristics of the second and third generation TS and the effect of the different flume lengths.

The combination of the length and height of each of the tanks (their cross-sectional area) is where the difference in wave amplitude seen in **Figure 13C** originates. A larger cross-sectional area allows greater wave amplitudes to be generated for a given period, i.e., more capacity to draw in water for the trough and more water to put into a crest. The width of the TS has much less bearing on the waves generated as the waves span the width of the flume, as does the TS, and only comes into consideration when selecting a vacuum pump (or pumps) to move the required volume of air in the required time. As long as the pumps are sufficiently capable, only the cross-sectional area of the TS and the flume length govern the size of the waves.

The flume length influences the generated waves through the travel time of the wave and therefore the interaction of any reflections that may occur with the later parts of the wave. For a very short flume, the reflections will return to the TS almost immediately and would then re-reflect (if not accounted for) from the TS. These re-reflections can be incorporated into the wave generation to enhance the amplitude of the wave. In a very long flume, reflections would not return to the TS before the wave had finished being generated, so would not be able to be incorporated in the generation to enhance the wave amplitude. Further

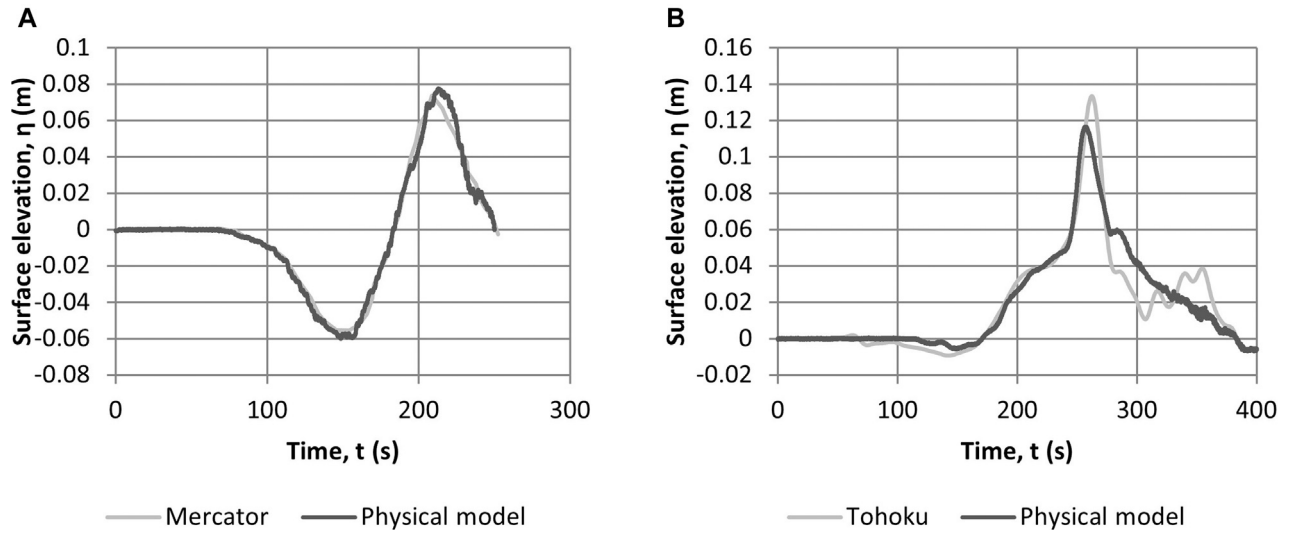

FIGURE 12 | Calibrated Mercator **(A)** and Tohoku **(B)** tsunami time series at 1:50 scale using third Generation TS.

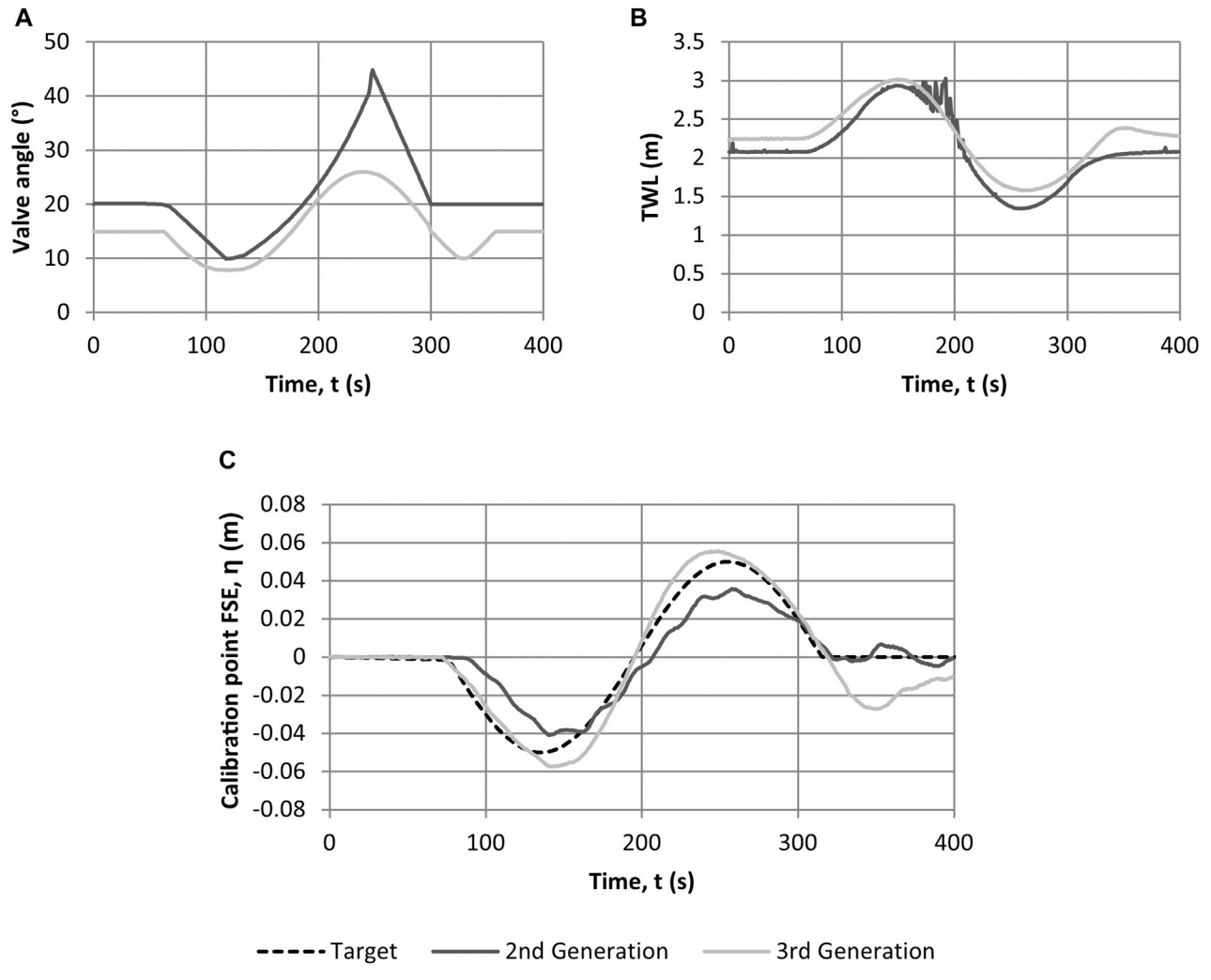

FIGURE 13 | Comparison of **(A)** valve angle, **(B)** tank water level (TWL) and **(C)** free-surface elevation at the calibration point for second and third generation TS (N240 wave), target (desired) profile indicated with dashed line.

discussion on the influence of reflections on wave generation is given in McGovern et al (2018).

As discussed in *Testing*, the PID control system in the third generation TS, using a single pressure measurement within the TS could not determine the direction of reflections and therefore struggled to account for them correctly when looking at the wave measured at the calibration point much further up the flume. This required manual adjustment of the valve time series and the running of the system during testing in open-loop control mode, but using the PID derived valve time series as a starting point.

CONCLUSION

This paper has described the development and evolution of the HR Wallingford pneumatic Tsunami Simulator (TS), which is based on a pneumatic system. A unique advantage of the method is that waves of very long wavelength can be generated, due to its ability to displace very large volumes of water in a controlled manner. The paper describes how, through an ERC grant (URBANWAVES, grant no. 336084), two EPSRC grants (EPICentre and CRUST, grant nos. EP/F012179/1 and EP/M001067/1) and internally funded research by HR Wallingford, three generations of TS have been designed, built, tested and improved within a 10 years time span. The three generations of TS reflect the increased understanding of the technology, with the development of numerical modeling to accompany the design of the TS, the flow shapers at the TS outlets, detailed studies conducted on the effects of location in the flume for calibration, and a control software for the improved damping of reflections. It is noted that the three TS developed over this period, have been upgraded to have the same control software as was developed for the third generation.

The TS has moved from a prototype to a mature technology, with proven capacity for reproducing free surface profiles of recorded tsunami field data. It can be applied directly to new and innovative research and practical design studies. In particular, the TS has unique capabilities in terms of its generation of stable trough-led waves and tsunami-like wavelengths for scales of 1:50. The latter makes the facility particularly useful for understanding tsunami inundation interaction with coastal infrastructure and especially scour phenomena, where the duration of the inundation flow plays a critical role.

DATA AVAILABILITY STATEMENT

The raw data supporting the conclusion of this article will be made available by the authors, without undue reservation.

AUTHOR CONTRIBUTIONS

WA and TR contributed to the original concepts behind tsunami simulator. TR was principal investigator on the research grants funding the tsunami simulator development over 10 years. WA led the development of the tsunami simulators. IC and DIR conducted numerical modeling and physical testing to prove the capabilities of the tsunami simulators, and contributed to optimization of the design. WA and TR contributed to physical testing of simulator, and managed the development team from HR Wallingford and research team from University College London, respectively. IC and WA took leadership in drafting the paper, which was contributed to and reviewed by DIR and TR.

FUNDING

The authors acknowledge European Research Council (ERC) funding for the URBANWAVES project (Grant No. 336084) and the Engineering and Physics Research Council (EPSRC) funding for the EPICentre and CRUST grants, nos. EP/F012179/1 and EP/M001067/1, respectively.

ACKNOWLEDGMENTS

The authors acknowledge European Research Council (ERC) funding for the URBANWAVES project (Grant No. 336084) and the Engineering and Physics Research Council (EPSRC) funding for the EPICentre project (Grant No. EP/F012179/1) and CRUST project (Grant No. EP/M001067/1). We acknowledge the support of numerous staff at HR Wallingford, particularly Dr. S Richardson, Mr O Harris and Mr I Payne: visiting researchers, particularly Pierre-Henri Bazin, Alice Barthel, Mario Zaccaria, Ignacio Barranco-Granged, and Roberta Riva; and students and staff of UCL especially Prof. Ian Eames, Dr. T Robinson, Dr. D McGovern, Dr. C. Klettner, Dr. A Foster, Dr. C Petrone, Dr. Ingrid Charvet and Dr. Tristan Lloyd.

REFERENCES

Al-Faesly, T., Palermo, D., Nistor, I., and Cornett, A. (2012). Experimental Modelling of Extreme Hydrodynamic Forces on Structural Models. *Int. Jo. Protective Structures* 3 (4), 477. doi:10.1260/2041-4196.3.4.477

Allsop, W., Chandler, I., and Zaccaria, M. (2014). "Improvements in the Physical Modelling of Tsunami and Their Effects," in Proc. 5th Int. Conf. on Application of Physical Modelling to Port and Coastal Protection (Varna: Coastlab14).

Allsop, W. (2014). *Improving the Generation of Tsunami Waves in Physical Modelling.* Report DDS0336-RT001 (Wallingford: HR Wallingford for HYDRALAB IV).

Allsop, W., Robinson, D., Charvet, I., Rossetto, T., and Abernethy, R. (2008). *A Unique Tsunami Generator for Physical Modelling of Violent Flows and Their Impact*. Beijing: Proc. 14th World Conf. on Earthquake Engineering.

Bremm, G., Goseberg, N., Schlurmann, T., and Nistor, I. (2015). Long Wave Flow Interaction with a Single Square Structure on a Sloping beach. *J. Mar. Sci. Eng.* 3, 821–844. doi:10.3390/jmse3030821

BS EN (1993). *Eurocode 3: Design of Steel Structures*. London: British Standards Institution.

Chandler, I., Allsop, W., Barranco Granged, I., and McGovern, D. J. (2016). "Understanding Wave Generation in Pneumatic Tsunami Simulators," in Proc. 6th Int. Conf. on Application of Physical Modelling to Port and Coastal Protection (Ottawa: Coastlab16).

Charvet, I. (2011). "Experimental Modelling of Long Elevated and Depressed Waves Using a New Pneumatic Wave Generator," (London: University College London). PhD thesis.

Charvet, I., Eames, I., and Rossetto, T. (2013). New Tsunami Runup Relationships Based on Long Wave Experiments. *Ocean Model.* 69, 79–92. doi:10.1016/j.ocemod.2013.05.009

Di Risio, M., De Girolamo, P., Bellotti, G., Panizzo, A., Aristodemo, F., Molfetta, M. G., et al. (2009). Landslide-generated Tsunami Runup at the Coast of a Conical Island: New Physical Model Experiments. *J. Geophys. Res. Oceans* 114, 1. doi:10.1029/2008JC004858

Directive (97/23/EC). Directive 97/23/EC of the European Parliament and of the Council of 29 May 1997 on the Approximation of the Laws of the Member States Concerning Pressure Equipment. *Official J. L* 181, 1, 97/23/EC . Available at: https://eur-lex.europa.eu/eli/dir/1997/23/oj

Drähne, U., Goseberg, N., Vater, S., Beisiegel, N., and Behrens, J. (2016). An Experimental and Numerical Study of Long Wave Run-Up on a Plane beach. *Jo. Mar. Sci. Eng.* 4, 1. doi:10.1029/2008jc004858

Enet, F., and Grilli, S. T. (2007). Experimental Study of Tsunami Generation by Three-Dimensional Rigid Underwater Landslides. *J. Waterway, Port, Coastal, Ocean Eng.* 133, 442–454. doi:10.1061/(asce)0733-950x(2007)133:6(442)

Fritz, H. M., Hager, W. H., and Minor, H-E. (2001). Lituya Bay Case: Rockslide Impact and Wave Run-Up. *Int. Jo. Tsunami Soc.* 19 (1), 3–22.

Goseberg, N., Wurpts, A., and Schlurmann, T. (2013). Laboratory-scale Generation of Tsunami and Long Waves. *Coastal Eng.* 79, 57–74. doi:10.1016/j.coastaleng.2013.04.006

Hammack, J. L. (1972). *Tsunami: A Model of Their Generation and Propagation*. Pasadena: London: W.M .Keck Lab. Hydraul. and Water Res., Calif. Inst. Tech. Rep. KH-R-28.

Hammack, J. L. (1973). A Note on Tsunamis: Their Generation and Propagation in an Ocean of Uniform Depth. *J. Fluid Mech.* 60 (4), 769–799. doi:10.1017/s0022112073000479

Hiraishi, T., Mori, N., Yyasuda, T., Azuma, R., Mase, H., Prasteyo, A., et al. (2015). Characteristics of Tsunami Generator Newly Implemented with Three Generation Modes. *J. Jpn. Soc. Civil Eng. Ser. B2 (Coastal Engineering)* 71 (2), I_349. 1883-8944. doi:10.2208/kaigan.71.i_349

HRS (1974). *Maplin Investigation – Report on the Outer Thames Physical Model Studies*. Report EX 657 (Wallingford: Hydraulics Research Station).

Kihara, N., Niida, Y., Takabatake, D., Kaida, H., Shibayama, A., and Miyagawa, Y. (2015). Large-scale Experiments on Tsunami-Induced Pressure on a Vertical Tide wall. *Coastal Eng.* 99, 46–63. doi:10.1016/j.coastaleng.2015.02.009

Lloyd, T. (2016). "An Experimental Investigation of Tsunami Forces on Coastal Structures," (London: University College London). PhD thesis.

Lu, H., Park, Y. S., and Cho, Y-S. (2017a). Investigation of Long Waves Generated by Bottom-Tilting Wave Maker. *Coastal Eng. J.* 59 (4), 1750018-1–1750018-23. doi:10.1142/s0578563417500188

Lu, H., Park, Y. S., and Cho, Y.-S. (2017b). Modelling of Long Waves Generated by Bottom-Tilting Wave Maker. *Coastal Eng.* 122, 1–9. doi:10.1016/j.coastaleng.2017.01.007

McFall, B. C., and Fritz, H. M. (2016). Physical Modelling of Tsunamis Generated by Three-Dimensional Deformable Granular Landslides on Planar and Conical Island Slopes. *Proc. R. Soc. A.* 472, 20160052. doi:10.1098/rspa.2016.0052

McGovern, D. J., Chandler, I., and Rossetto, T. (2016). "Experimental Study of the Runup of Tsunami Waves on a Smooth Sloping beach," in Proc. 6th Int. Conf. on Application of Physical Modelling to Port and Coastal Protection (Ottawa: Coastlab16).

McGovern, D. J., Robinson, T., Chandler, I. D., Allsop, W., and Rossetto, T. (2018). Pneumatic Long-Wave Generation of Tsunami-Length Waveforms and Their Runup. *Coastal Eng.* 138, 80–97. doi:10.1016/j.coastaleng.2018.04.006

Nouri, Y., Nistor, I., Palermo, D., and Cornett, A. (2010). Experimental Investigation of Tsunami Impact on Free Standing Structures. *Coastal Eng. J.* 52 (1), 43–70. doi:10.1142/s0578563410002117

Palmer, R. Q., and Funasaki, G. T. (1967). The Hilo Harbor Tsunami Model. *Coastal Eng.* 1966, 1227–1248.

Robinson, D. (2009). "Development of the HRW Tsunami Generator: Conceptual Design and Preparatory Modelling Studies," Report IT585 (Wallingford: HR Wallingford).

Rossetto, T., Allsop, W., Charvet, I., and Robinson, D. I. (2011). Physical Modelling of Tsunami Using a New Pneumatic Wave Generator. *Coastal Eng.* 58 (6), 517–527. doi:10.1016/j.coastaleng.2011.01.012

Schimmels, S., Sriram, V., and Didenkulova, I. (2016). Tsunami Generation in a Large Scale Experimental Facility. *Coastal Eng.* 110, pp32–41. doi:10.1016/j.coastaleng.2015.12.005

Shimosako, K., Takahashi, S., Suzuki, K., and Kang, Y. K. (2002). Large Hydro-Geo Flume and its Use for Coastal Engineering Research. *Tech. Note Natl. Inst. Land Infrastructure Manage* 41, 81–89.

Shuto, N. (1985). The Nihonkai-Chubu Earthquake Tsunami on the North Akita Coast. *Coastal Eng. Jpn.* 28, 255–264. doi:10.1080/05785634.1985.11924420

Sriram, V., Didenkulova, I., Sergeeva, A., and Schimmels, S. (2019). Tsunami Evolution and Run-Up in a Large Scale Experimental Facility. *Coastal Eng.* 111, 1–12. doi:10.1016/j.coastaleng.2015.11.006

Thusyanthan, N. I., and Madabhushi, S. P. G. (2008). Tsunami Loading on Coastal Houses: a Model Approach. *Proc. ICE* 161, 77–86. doi:10.1680/cien.2008.161.2.77

Togashi, H. (1986). *Wave Force of Tsunami Bore on a Vertical Wall*. Nagasaki: Reports of the Faculty of Engineering, Nagasaki University, 16–26.

Tomiczek, T., Prasetyo, A., Mori, N., Yasuda, T., and Kennedy, A. (2016b). "Experimental Modelling of Macro-Roughness Effects on Tsunami-Induced Pressure in Idealized Urban Environments," in Proc. 6th Int. Conf. Physical Modelling in Coastal and Port Eng (Ottawa: Coastlab16).

Tomiczek, T., Prasetyo, A., Mori, N., Yasuda, T., and Kennedy, A. (2016a). Physical Modelling of Tsunami Onshore Propagation, Peak Pressures, and Shielding Effects in an Urban Building Array. *Coastal Eng.* 117, 97–112. doi:10.1016/j.coastaleng.2016.07.003

Weller, H. G., Tabor, G., Jasak, H., and Fureby, C. (1998). A Tensorial Approach to Computational Continuum Mechanics Using Object-Oriented Techniques. *Comput. Phys.* 12 (6), 620. doi:10.1063/1.168744

Whitehouse, R., SutherlandPowell, J. K., and Harris, J. (2014). "Fast Flow Facility for Sediment and Morphology Testing," in Proc. 5th Int. Coast. Editors V. Penchev and F. T. Pinto (Bulgaria: Lab Conf. Varna), 104–113.2.

Wiegel, R. L. (1955). Laboratory Studies of Gravity Waves Generated by the Movement of a Submerged Body. *Trans. AGU* 36 (5), 759–774. doi:10.1029/TR036i005p00759

Wilkie, M. J., and Young, G. A. J. (1952). *Pneumatic Tide Generator*, 25, 133–137. London: The Engineer.

Wüthrich, D., Pfister, M., Nistor, I., and Schleiss, A. J. (2018). Experimental Study of Tsunami-like Waves Generated with a Vertical Release Technique on Dry and Wet Beds. *Proc. Asce, Jo. Waterway, Port, Coastal, Ocean Eng.* 144, 4. doi:10.1061/(asce)ww.1943-5460.0000447

Yim, S., Yeh, H., Cox, D., and Pancake, C. (2004). "A Shared-Used Large-Scale Multidirectional Wave basin for Tsunami Research, Paper 1517," in Proc. 13th World Conf. on Earthquake Eng (Vancouver: International Association for Earthquake Engineering (IAEE)). doi:10.1061/40733(147)75

Zepher (2016). Product Brochure. Available at: http://zepher-uk.com/side_channel/side_channel.html (Accessed March 15, 2016).

Conflict of Interest: IC was employed by the company HR Wallingford. DR was employed by the company HR Wallingford and by academic institution University College London. Professor WA is employed by WA Consulting Ltd, and donated his time to writing this paper pro bono.

The remaining author declares that the research was conducted in the absence of any commercial or financial relationships that could be construed as a potential conflict of interest.

frontiers in Earth Science

ORIGINAL RESEARCH
published: 24 June 2021
doi: 10.3389/feart.2021.626844

3D Linked Subduction, Dynamic Rupture, Tsunami, and Inundation Modeling: Dynamic Effects of Supershear and Tsunami Earthquakes, Hypocenter Location, and Shallow Fault Slip

Sara Aniko Wirp[1], Alice-Agnes Gabriel[1,2], Maximilian Schmeller[3], Elizabeth H. Madden[4], Iris van Zelst[5], Lukas Krenz[3], Ylona van Dinther[6] and Leonhard Rannabauer[3]*

[1] Department of Earth and Environmental Sciences, Institute of Geophysics, Ludwig-Maximilians-University, Munich, Germany, [2] Institute of Geophysics and Planetary Physics, Scripps Institution of Oceanography, University of California, San Diego, San Diego, CA, United States, [3] Department of Informatics, Technical University of Munich, Garching, Germany, [4] Observatório Sismológico, Instituto de Geociências, Universidade de Brasília, Brasilia, Brazil, [5] Institute of Geophysics and Tectonics, School of Earth and Environment, University of Leeds, Leeds, United Kingdom, [6] Department of Earth Sciences, Utrecht University, Utrecht, Netherlands

OPEN ACCESS

Edited by:
Tiziana Rossetto, University College London, United Kingdom

Reviewed by:
Yuichiro Tanioka, Hokkaido University, Japan
Thorne Lay, University of California, Santa Cruz, United States

***Correspondence:**
Sara Aniko Wirp
sara.wirp@geophysik.uni-muenchen.de

Specialty section:
This article was submitted to Geohazards and Georisks, a section of the journal Frontiers in Earth Science

Received: *06 November 2021*
Accepted: *26 May 2021*
Published: *24 June 2021*

Citation:
Aniko Wirp S, Gabriel A-A, Schmeller M, H. Madden E, van Zelst I, Krenz L, van Dinther Y and Rannabauer L (2021) 3D Linked Subduction, Dynamic Rupture, Tsunami, and Inundation Modeling: Dynamic Effects of Supershear and Tsunami Earthquakes, Hypocenter Location, and Shallow Fault Slip. Front. Earth Sci. 9:626844. doi: 10.3389/feart.2021.626844

Physics-based dynamic rupture models capture the variability of earthquake slip in space and time and can account for the structural complexity inherent to subduction zones. Here we link tsunami generation, propagation, and coastal inundation with 3D earthquake dynamic rupture (DR) models initialized using a 2D seismo-thermo-mechanical geodynamic (SC) model simulating both subduction dynamics and seismic cycles. We analyze a total of 15 subduction-initialized 3D dynamic rupture-tsunami scenarios in which the tsunami source arises from the time-dependent co-seismic seafloor displacements with flat bathymetry and inundation on a linearly sloping beach. We first vary the location of the hypocenter to generate 12 distinct unilateral and bilateral propagating earthquake scenarios. Large-scale fault topography leads to localized up- or downdip propagating supershear rupture depending on hypocentral depth. Albeit dynamic earthquakes differ (rupture speed, peak slip-rate, fault slip, bimaterial effects), the effects of hypocentral depth (25–40 km) on tsunami dynamics are negligible. Lateral hypocenter variations lead to small effects such as delayed wave arrival of up to 100 s and differences in tsunami amplitude of up to 0.4 m at the coast. We next analyse inundation on a coastline with complex topo-bathymetry which increases tsunami wave amplitudes up to ≈1.5 m compared to a linearly sloping beach. Motivated by structural heterogeneity in subduction zones, we analyse a scenario with increased Poisson's ratio of $\nu = 0.3$ which results in close to double the amount of shallow fault slip, ≈1.5 m higher vertical seafloor displacement, and a difference of up to ≈1.5 m in coastal tsunami amplitudes. Lastly, we model a dynamic rupture "tsunami earthquake" with low rupture velocity and low peak slip rates but twice as high tsunami potential energy. We triple fracture energy which again doubles the amount of shallow fault slip, but also causes a

2 m higher vertical seafloor uplift and the highest coastal tsunami amplitude (≈7.5 m) and inundation area compared to all other scenarios. Our mechanically consistent analysis for a generic megathrust setting can provide building blocks toward using physics-based dynamic rupture modeling in Probabilistic Tsunami Hazard Analysis.

Keywords: earthquake rupture dynamics, tsunami generation and inundation modeling, high performance computing, physics-based hazard assessment, seismic cycle modeling, subduction zone dynamics

1. INTRODUCTION

Earthquake sources are governed by highly non-linear multi-physics and multi-scale processes leading to large variability in dynamic and kinematic properties such as rupture speed, slip rate, energy radiation, and slip distribution (e.g., Oglesby et al., 2000; Kaneko et al., 2008; Gabriel et al., 2012; Bao et al., 2019; Ulrich et al., 2019a; Gabriel et al., 2020). Such variability may impact the generation, propagation, and inundation of earthquake-generated tsunami or secondary tsunami generation mechanisms such as triggered landslides (e.g., Sepúlveda et al., 2020). For example, unexpectedly large slip at shallow depths may generate large tsunami (Lay et al., 2011; Romano et al., 2014; Lorito et al., 2016).

To model earthquake-generated tsunami, sources can be approximated from earthquake generated uplift (Behrens and Dias, 2015, and references therein). Analytical solutions (e.g., Okada, 1985) describe seafloor displacements sourced by uniform rectangular dislocations within a homogeneous elastic half space. Models of tsunami generated by large earthquakes can routinely and quickly use kinematic finite fault models constrained by inversion of seismic, geodetic, and other geophysical data (Geist and Yoshioka, 1996; Ji et al., 2002; Babeyko et al., 2010; Maeda et al., 2013; Allgeyer and Cummins, 2014; Mai and Thingbaijam, 2014; Bletery et al., 2016; Jamelot et al., 2019), but are challenged by the inherent non-uniqueness of kinematic source models (Mai et al., 2016).

Probabilistic Tsunami Hazard Analysis (PTHA) requires the computation of thousands or millions of tsunami scenarios for each specific area of interest (González et al., 2009; Geist and Oglesby, 2014; Horspool et al., 2014; Geist and Lynett, 2014; Lorito et al., 2015; Selva et al., 2016; Grezio et al., 2017; Mori et al., 2018; Sepúlveda et al., 2019; Glimsdal et al., 2019). Stochastic source models (McCloskey et al., 2008; Davies and Griffin, 2019) statistically vary slip distributions (Andrews, 1980) and are specifically suited for PTHA in combination with efficient tsunami solvers (e.g., Berger et al., 2011; Nakano et al., 2020). For instance, Goda et al. (2014) highlights strong sensitivities of tsunami height to slip distribution and variations in fault geometry in stochastic random-field slip models for the 2011 Tohoku-Oki earthquake and tsunami. Recently, Scala et al. (2019) use stochastic slip distributions for PTHA in the Mediterranean area.

3D Dynamic earthquake rupture modeling can provide mechanically viable tsunami source descriptions on complex faults or fault systems on the scale of megathrust events (Galvez et al., 2014; Murphy et al., 2016; Uphoff et al., 2017; Murphy et al., 2018; Ma and Nie, 2019; Saito et al., 2019; Ulrich et al., 2020). Such simulations can exploit modern numerical methods and high-performance computing (HPC) to shed light on the dynamics and severity of earthquake behavior and potentially complement PTHA. For example, in dynamic rupture models shallow slip amplification can spontaneously emerge due to up-dip rupture facilitated by along-depth bi-material effects (Rubin and Ampuero, 2007; Ma and Beroza, 2008; Scala et al., 2017) and free-surface reflected waves within the accretionary wedge (Nielsen, 1998; Lotto et al., 2017a; van Zelst et al., 2019). Dynamic rupture earthquake models can yield stochastic slip distributions, too, under the assumption of stochastic loading stresses (Geist and Oglesby, 2014). Such physics-based models can be directly linked to tsunami models by using the time-independent or time-dependent seafloor displacements (and potentially velocities) as the tsunami source (Kozdon and Dunham, 2013; Ryan et al., 2015; Lotto et al., 2017b; Saito et al., 2019; Madden et al., 2020). For instance, time-dependent 3D displacements from observational constrained dynamic rupture scenarios of the 2018 Palu, Sulawesi earthquake and the 2004 Sumatra-Andaman earthquake are linked to a hydrostatic shallow water tsunami model by Ulrich et al. (2019b). Bathymetry induced amplification of horizontal displacements are thereby accounted for by following Tanioka and Satake (1996).

Observational and numerical studies show that megathrust geometry and hypocenter location influence earthquake rupture characteristics. Ye et al. (2016) state that megathrust earthquakes across faults that are longer horizontally than they are deep vertically (with an aspect ratio of three or larger) tend to exhibit primarily unilateral behavior. Also, events with an asymmetric hypocenter location on the fault favor rupture propagation along strike to its far end (Harris et al., 1991; McGuire et al., 2002; Hirano, 2019). Weng and Ampuero (2019) show the energetics of elongated ruptures is radically different from that of conventional circular crack models. Bilek and Lay (2018) find that the complexity of slip as well as bi- or unilateral rupture preferences of large earthquakes highly depend on the depth location of the hypocenter.

Subduction zones worldwide are associated with tectonic, frictional, and structural heterogeneity along depth and along-arc impacting megathrust earthquake and tsunami dynamics (Kirkpatrick et al., 2020, e.g.,). Kanamori and Brodsky (2004) show that fracture energy varies between subduction zone earthquakes. A special case are so called tsunami earthquakes (Kanamori, 1972) that may require a large amount of fracture energy, low rupture velocity and low radiation efficiency. Structural heterogeneity in subduction zones includes variations

in Poisson's ratio (V_p/V_s) (e.g., Liu and Zhao, 2014; Niu et al., 2020)), while dynamic rupture and seismic wave propagation models often adopt an idealized Poisson's ratio of ν =0.25 governing seismic wave propagation (e.g., Kozdon and Dunham, 2013).

The initial conditions of dynamic rupture simulations that control earthquake rupture nucleation, propagation, and arrest include fault loading stresses, frictional strength, fault geometry, and subsurface material properties (e.g., Kame et al., 2003; Gabriel et al., 2013; Galis et al., 2015; Bai and Ampuero, 2017). These initial conditions may be observationally and empirically informed (e.g., Aochi and Fukuyama, 2002; Aagaard et al., 2004; Murphy et al., 2018; Ulrich et al., 2020) but remain difficult to constrain. Particularly in subduction zones where observational data are sparse, space and time scales vary over many orders of magnitude and both geometric and rheological megathrust complexities are likely to control rupture characteristics. Recently, initial conditions for 2D and 3D megathrust dynamic rupture earthquake models have been informed from 2D geodynamic long-term subduction and seismic cycle models (van Zelst et al., 2019; Madden et al., 2020; van Zelst et al., 2021). This approach provides self-consistent initial fault loading stresses and frictional strength, fault geometry and material properties on and surrounding the megathrust, as well as consistency with crustal, lithospheric, and mantle deformation and deformation in the subduction channel over geological time scales. Such subduction-initialized heterogeneous dynamic rupture models lead to complex earthquakes with multiple rupture styles (Gabriel et al., 2012), shallow slip accumulation and fault reactivation.

We apply the 2D geodynamical subduction and seismic cycle (SC) model from van Zelst et al. (2019) to inform realistic 3D dynamic rupture (DR) megathrust earthquake models within a complex, self-consistent subduction setup along with their consequent tsunami, following the subduction to tsunami run-up linking approach described in Madden et al. (2020). In this study we introduce a number of important differences to previous work. 2D linking including approximations to match SC and DR fracture energy during slip events leads to differences in slip magnitude between the SC and DR modeling and large magnitudes and high rupture speed in dynamic rupture scenarios (van Zelst et al., 2019). In contrast, we here constrain fracture energy independently from the long-term model. In Madden et al. (2020), a different long-term geodynamic and seismic cycle simulation was used, specifically, assuming different shear moduli. We here change the geometrical 3D extrapolation of the 2D fault geometry compared to the large blind dynamic earthquake scenario of M_W9.0 of Madden et al. (2020), to be consistent with empirical earthquake source scaling relations for M_W8.5 megathrust events (Strasser et al., 2010).

We use complex 3D dynamic rupture modeling to first study trade-offs and effects of along-strike unilateral vs. bilateral rupture and variations in hypocentral depth in subduction zone earthquakes (McGuire et al., 2002). By varying the hypocentral location along arc and along depth, we generate 12 distinct unilateral and bilateral earthquakes with depth-variable slip distribution, rupture direction, bimaterial, and geometrical effects in the dynamic slip evolution. We analyse the consequent time-dependent variations in seafloor uplift affecting tsunami propagation and inundation patterns. We define as reference model a bilateral, deeply nucleating earthquake. To this reference model we add a complex and more realistic coastline in the tsunami simulation and study the effects on tsunami arrival time and wave height at the coast.

The linkage from long-term geodynamic to co-seismic dynamic rupture modeling requires assumptions with respect to the incompressibility and visco-elasto-plastic, plane-strain conditions of the subduction model vs. the compressible, elastic conditions of the earthquake model. In two additional scenarios we analyse variations in the energy balance of the subduction-initialized dynamic rupture scenarios. We increase fracture energy in the reference model by changing the frictional critical slip distance within the dynamic rupture model and adapting nucleating energy accordingly. The increase in fracture energy leads to large uplift, low radiation efficiency and low rupture velocities, characterizing a tsunami earthquake (Kanamori, 1972). Lastly, we analyze the effect of a higher Poisson's ratio throughout the dynamic rupture reference model and the effect on tsunami genesis and inundation.

This leads to a total of 15 subduction-initialized 3D dynamic rupture-tsunami scenarios: 12 dynamic rupture models with varying hypocenters. For one "reference model" (model 3B) of these 12 we vary fracture energy or Poisson's ratio, or coastline bathymetry.

2. METHODS

Here, we summarize the computational methods used for simulating subduction-initialized dynamic earthquake rupture linked to tsunami generation, propagation, and inundation (**Figure 1**). For an in-depth description of the virtual laboratory for modeling tsunami sources arising from 3D co-seismic seafloor displacements generated by dynamic earthquake rupture models, we refer to Madden et al. (2020). We compute 3D dynamic earthquake rupture and seismic wave propagation with SeisSol (https:/seissol.org). Tsunami propagation and inundation uses sam(oa)^2-flash, which is part of the open-source software sam(oa)^2 (https://gitlab.lrz.de/samoa/samoa). Both codes use highly optimized and parallel implementations of discontinuous Galerkin (DG) schemes. All simulations were performed on SuperMUC-NG at the Leibniz Supercomputing Centre Garching, Germany.

To link input and output data in massively parallel simulations, we use ASAGI (pArallel Server for Adaptive GeoInformation), an open source library with a simple interface to access Cartesian material and geographic datasets (Rettenberger et al., 2016, www.github.com/TUM-I5/ASAGI). ASAGI translates a snapshot of the 2D subduction model into 3D initial conditions for the earthquake model and bathymetry data and seafloor displacements from the earthquake model into initial conditions for the tsunami model. ASAGI organizes Cartesian data sets for dynamically adaptive simulations by

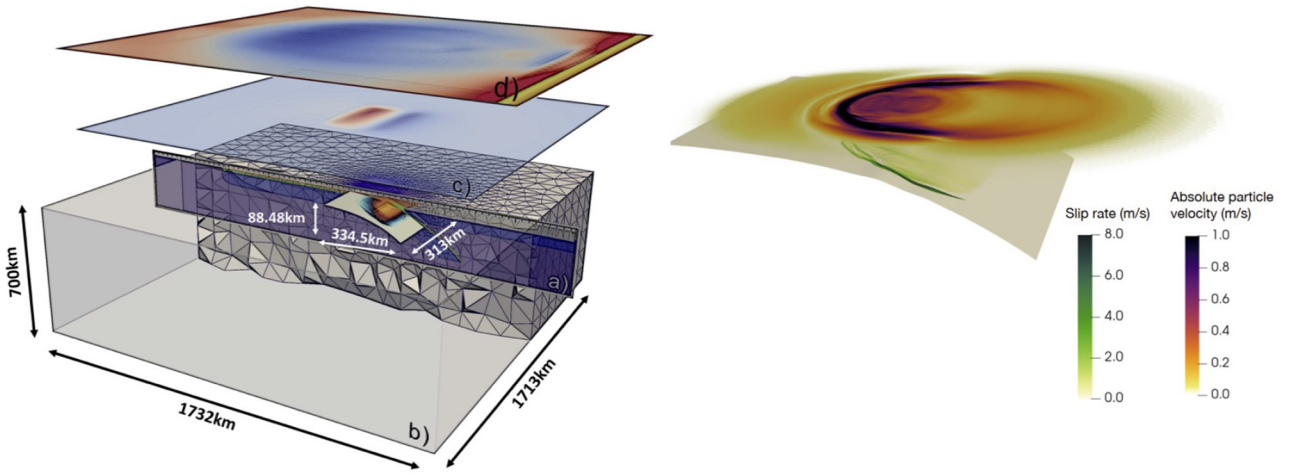

FIGURE 1 | (Left): Adapted from Madden et al. (2020) (a) sketch and dimensions of the one-way linked 2D geodynamic subduction model, (b) the 3D dynamic rupture earthquake model, (c) the dynamic rupture seafloor displacement, and (d) the 2D tsunami model, modified from Madden et al. (2020). The 3D unstructured tetrahedral mesh of the dynamic rupture model (b) is shown in gray. **(Right)** Snapshot of slip rate across the 3D subducting interface (greenish colors) and the seismic wavefield recorded at the free surface in terms of absolute velocity (warm colors). This snapshot is extracted from model 3B after 40 s simulation time.

automatically migrating the corresponding data tiles across compute nodes as required for efficient access.

2.1. 3D Earthquake Dynamic Rupture Modeling With SeisSol

Physics-based 3D earthquake modeling captures how faults yield, slide and interact (e.g., Ulrich et al., 2019a; Palgunadi et al., 2020) and can provide mechanically viable tsunami-source descriptions (Ryan et al., 2015; Ma and Nie, 2019; Ulrich et al., 2019b, 2020). We use SeisSol (de la Puente et al., 2009; Pelties et al., 2012, 2014) to solve simultaneously for frictional failure across prescribed fault surfaces and high-order accurate seismic wave propagation in space and time (illustrated in **Figure 1**, right). SeisSol uses a discontinuous Galerkin (DG) scheme with Arbitrary high-order DERivative (ADER) time stepping on unstructured tetrahedral grids with static mesh adaptivity (Dumbser and Käser, 2006; Käser and Dumbser, 2006). It is thereby particularly suited for modeling complex geometries such as those in the vicinity of subducting slabs. SeisSol is optimized for current petascale supercomputers (Breuer et al., 2014; Heinecke et al., 2014; Rettenberger et al., 2016; Uphoff and Bader, 2020; Dorozhinskii and Bader, 2021) and uses an efficient local time-stepping algorithm (Breuer et al., 2016; Uphoff et al., 2017; Wolf et al., 2020). Its accuracy is verified against a wide range of community benchmarks (Harris et al., 2011, 2018), including dipping and branching faults with heterogeneous off-fault material and initial on-fault stresses (Pelties et al., 2014; Wollherr et al., 2018; Gabriel et al., 2020). We note that on-fault initial conditions such as frictional parameters or initial fault stresses are assigned with sub-elemental resolution (at each DG Gaussian integration point). However, within each off-fault element, all material properties are constant. We create a 3D complex structural model in GoCad (Holding, 2018) and discretize it with the meshing software Simmodeler by Simmetrix (Simmetrix Inc., 2017).

Within SeisSol, frictional failure is treated as an internal boundary condition for which the numerical solution of the elastodynamic wave equation is modified. In the dynamic rupture scenarios of our study, fault strength, i.e., its yielding and subsequent frictional weakening, is governed by the widely adopted linear slip weakening (LSW) friction law (Ida, 1972). Over a critical slip weakening distance D_c the effective friction coefficient μ decreases linearly from static μ_s until reaching dynamic μ_d. We note that this is different to the rate-weakening friction used in the long-term geodynamic SC model. The process zone width is the inherent length scale defining the minimum resolution required on-fault, and is defined as the area behind the rupture tip in which shear stress decreases from its static to its dynamic value (Day et al., 2005).

2.2. Subduction Seismic Cycle Modeling for Earthquake Initial Conditions

Figure 2 depicts the inferred 3D initial conditions from the subduction seismic cycle model for all dynamic rupture scenarios. These include highly heterogeneous initial shear stress and strength as well as fault geometry and material structure that together govern earthquake nucleation, propagation, and arrest. The underlying 2D seismo-thermo-mechanical geodynamic seismic cycle (SC) model simulates subduction dynamics over millions of years and earthquake cycles over several hundreds of years (e.g., Van Dinther et al., 2013, 2014) (**Figure 2A**). The long-term phase of the simulation builds up stress as well as self-consistent strength and fault geometries across the subduction interface and forearc. The geodynamic SC model includes 70 megathrust events that rupture almost the entire fault and nucleate near the downdip seismogenic zone limit. The same representative event as in van Zelst et al. (2019) is here chosen and linked to the newly designed dynamic rupture model applying the techniques described in Madden et al. (2020). We note, that at the

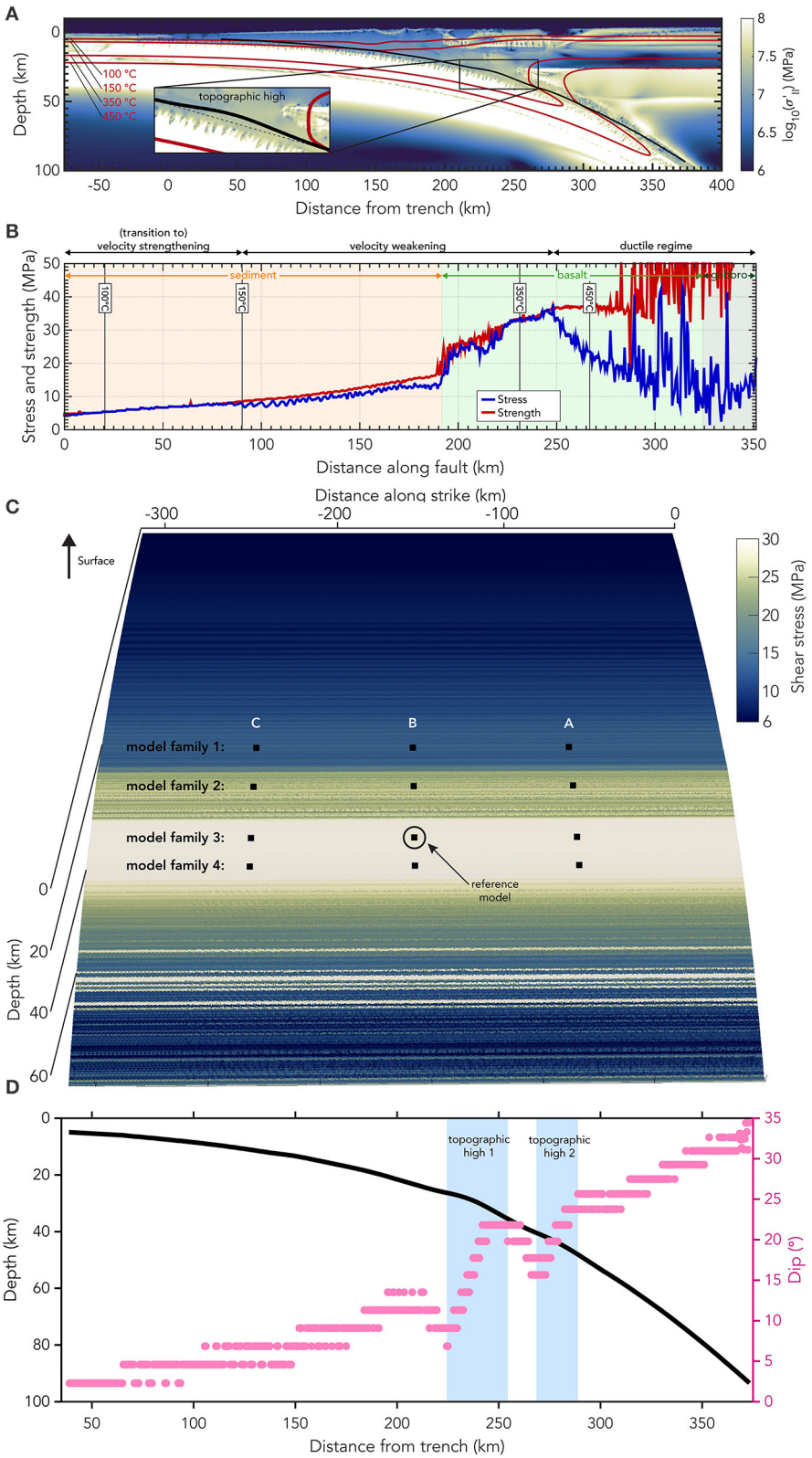

FIGURE 2 | Subduction model initial conditions for the dynamic rupture earthquake simulations. **(A)** Snapshot of stresses evolving during the 2D long-term geodynamic subduction and seismic cycle simulation at the time-step right before a slip event occurs (adapted from van Zelst et al., 2019). The stresses are expanded to the third dimension assuming plane strain conditions. **(B)** On-fault shear stress and fault strength in the SC model at the coupling time-step. The fault

(Continued)

FIGURE 2 | yields and failure occurs when both align. **(C)** Pre-processed (see text) initial shear stress in the three-dimensional dynamic rupture model at timestep t = 0 s in the DR model. The black squares indicate nucleation locations that are used for model families 1–4. The hypocenter of the reference model 3B is marked. **(D)** Fault geometry in 2D and dip angle of the fault. Regions of increasing dip are highlighted in blue and indicate local topographic highs (1 and 2) in the fault plane.

chosen SC time step, the dominant deformation mechanism in the seismogenic zone is elastic behavior, which is consistent with the deformation mechanism in the dynamic rupture model. All material properties, stresses, and fault geometries are exported from the SC model at that timestep. Material density and fault strength can be adapted to be used in the DR model. Cohesion varies between 2.5 and 20 MPa and increases with deeper lithologies. At nucleation depth, cohesion is set to 5 MPa. The curved, blind megathrust interface evolves during this slip event and is characterized by large-scale fault roughness including characteristic topographic highs ("bumps") in terms of a distinct change in local gradients of the curved non-planar interface related to sediment intrusion on geodynamic time scales (zoom-in box of **Figure 2A**).

In contrast to van Zelst et al. (2019) and Madden et al. (2020), the critical slip weakening distance D_c is here not inferred from the geodynamic SC model directly but is assigned to be a constant value (D_c = 0.1 m for 13 out of 14 dynamic rupture models) along the entire fault. Increasing the critical slip weakening distance D_c, over which effective friction is reduced to its dynamic value, results in a higher fracture energy G_c according to $G_c = 1/2\mu_s P_n - \mu_d P_n D_c$ with P_n being the initial fault normal stress (Venkataraman and Kanamori, 2004). The fracture energy consumed within the frictional process zone indicates how much energy is necessary to initiate and sustain rupture propagation. A high fracture energy results in higher fault slip, higher stress drop and a higher moment magnitude for comparable dynamic rupture scenarios (given the nucleation energy is adopted accordingly). In one model, model 5, we triple the model-wide constant D_c from 0.1 to 0.3 m while keeping all other parameters constant, thus, tripling fracture energy.

All material properties are extrapolated into the third dimension as constant along arc, for simplicity. We use a plane strain assumption, as in the 2D subduction model, to determine the out-of-plane normal and shear stress components in 3D. This implies that we omit eventual oblique subduction components by setting the out-of-plane shear stresses to zero and the out-of-plane normal stress component to be a function of the two in-plane normal stresses and Poisson's ratio ν. In the SC subduction model a Poisson's ratio of $\nu = 0.5$ is used, which is an appropriate assumption for large time scales. This Poisson's ratio needs to be reassigned within the DR model to represent compressible rocks and to solve the linear elastic wave equations. The choice of ν affects the material properties as they are transferred from the subduction model to the earthquake model since Lame's parameter is calculated from the re-assigned ν and the shear modulus G is taken from the subduction model. In all besides one dynamic rupture models we assume $\nu = 0.25$ (Poisson solid, $\lambda = G$). In one 3D dynamic rupture (model 6, modified from reference model 3B), we use a larger Poisson's ratio of $\nu = 0.3$, which is in the range observations of basaltic rocks (Gercek, 2007).

Using the imported on-fault conditions from the geodynamic SC model directly would lead to multiple locations of instantaneous failure on the fault (**Figure 2B**). We thus use a pre-processing static relaxation step in which we relax the initial fault loading stresses to be just below fault strength before applying them to the DR model following Wollherr (2018). Spontaneous earthquake rupture is commonly initialized by assigning an over-stressed or frictionally weaker predefined hypocentral "nucleation" area. We here assign a locally lower static friction coefficient within a circular patch of an empirically determined minimum required size to initiate spontaneous rupture. We choose frictional coefficients μ_s and μ_d within this patch constrained from the geodynamic SC model. We prescribe all but the shallowest (model family 1) hypocentral nucleation depths at locations which are close to failure (low strength excess, **Figure 2B**) in the SC model. The reference geodynamic SC slip event nucleates at 40 km depth, corresponding to model family 3 in this study.

2.3. Tsunami and Inundation Modeling With Samoa

Tsunami are modeled with a limited second order Runge-Kutta discontinuous Galerkin solver (Cockburn and Shu, 1998; Giraldo and Warburton, 2008) for the two dimensional depth-integrated hydrostatic non-linear Shallow Water Equations (SWE, LeVeque et al., 2011) in the sam(oa)^2-flash framework (Madden et al., 2020). The SWE are a simplification of the incompressible Navier-Stokes equations, under the assumption that vertical scales are negligible compared to horizontal scales. As a result, hydro-static pressure and the conservation of mass and momentum are part of the equations, while vertical velocity and turbulence are neglected. Manning friction is included in the model with an additional source term (Liang and Marche, 2009). To allow accurate and robust wetting and drying, the model uses a Barth-Jaspersen type limiter that guarantees the conservation of steady states (well-balancedness), mass conservation and positivity preservation of the water-depth (Vater and Behrens, 2014; Vater et al., 2015, 2019).

The framework sam(oa)^2-flash simulates hyperbolic PDEs on dynamically adaptive triangular meshes (Meister et al., 2016). It is based on the Sierpinsky Space filling curve, which allows cache efficient traversals of mesh-cells and -edges with a stack and stream approach. Cell-level adaptive mesh refinement in every time step and a water-depth based refinement criterion, allow for multiple levels of refinement for the tracking of wave fronts and other areas of interest (i.e., coasts). While tsunami are usually sourced by setting a perturbation to the seafloor and water surface as initial condition, sam(oa)^2-flash can include the full spatio-temporal evolution of the seafloor displacement in the

simulation. sam(oa)^2-flash has been validated against a suite of benchmarks (Synolakis et al., 2008).

2.4. Dynamic Rupture Modeling for Tsunami Initial Conditions

The time-dependent seafloor displacement generated in the dynamic rupture model is used as input for the tsunami model. Since these displacements are written in form of a triangular unstructured grid by SeisSol, rasterization is required to obtain a regular grid that can be read by sam(oa)^2-flash . The resulting grid is comprised of rectangular cells of size $\Delta x \times \Delta y =$ 500 m $\times$ 500 m. The geometric center of each cell is used to sample the triangular grid using a nearest-neighbor approach. Since all our examples share a relatively large source area and a short process-time, compared to the ocean depth (2 km), we here omit corrections required for landslide-induced tsunami (Kajiura, 1963) and neglect the effects of water flow from seafloor to sea-surface (Saito and Furumura, 2009; Wendt et al., 2009). We directly use the seafloor deformation as time-dependent (or static, for comparison) initial sea-surface perturbation.

The seafloor deformation data contains the seismic wavefield and the dominant static displacement, which remains unchanged after dynamic rupture propagation ceased since we do not account for post-seismic relaxation. Saito et al. (2019) shows that seismic waves have an effect on tsunami generation, but do not affect the solution in the far field. However, our earthquake scenarios also include reverberating seismic waves, e.g., trapped within the accretionary wedge. Simulating long enough for such complex seismic waves to stop imprinting on the time-dependent near-source seafloor deformation requires significantly longer simulation times. We here limit computational costs by stopping the DR earthquake simulation after the fault stopped slipping and the dominant static displacement remains constant. We apply the time-dependent seafloor deformation to source the tsunami model during that period and keep the seafloor elevation constant afterwards. In the presence of transient seismic waves, however, this approach may lead to artifacts such as spurious gravity-waves in the tsunami simulation. Thus, we here remove reverberating seismic waves using a filter-based approach on the seafloor perturbation.

We apply a Fourier filter approach that we base on an analytical test-bed in which we can separate the significant frequency-wavenumber coefficients of the permanent displacement from the ones of seismic waves (Madden et al., 2020). In the wavenumber representation for the displacement field we can identify the coefficients belonging to seismic waves clearly as radial symmetric lines in the wavenumber space (**Supplementary Figure 1**). Our analytical testbed confirms that these lines propagate in the frequency-wavenumber domain with the inverse velocity with which seismic waves propagate in time and space. Coefficients of the permanent displacement on the other hand are dominant close to the origin. To erase seismic waves from the seafloor perturbation we design a kernel to zero-out the radial symmetric waves in the frequency-wavenumber representation depending on their velocity. Close to the origin we leave the representation as it is, to keep the dominant coefficients of permanent displacement. To avoid rolling effects, the kernel is smoothed. As a result, seismic waves of chosen frequencies are effectively damped in the time-dependent displacement field (**Supplementary Figure 2**). The effects of seismic wave damping on the permanent displacement are negligible.

3. EARTHQUAKE AND TSUNAMI MODEL SETUP

3.1. 3D Heterogeneous Megathrust Dynamic Rupture Models

In DR modeling, rupture can only propagate across predefined fault interfaces. In distinction, fault geometry spontaneously arises during slip events in the SC model. The fault geometry for the chosen slip event at the coupling time step is shown in **Figure 2A**. The locations of the highest visco-plastic strain rate represent the fault. A moving average scheme is used to smooth this 2D fault geometry, which is then uniformly extruded along-arc to construct the 3D DR fault plane (van Zelst et al., 2019; Madden et al., 2020). The 3D dynamic rupture fault (**Figure 2C**) does not intersect the surface but ends ≈5 km below the seafloor and extends to 93.5 km depth. The fault length in the along-arc y-direction is chosen to agree with the average scaling of the source dimensions of interface and intraslab subduction-zone earthquakes with moment magnitude (Strasser et al., 2010). We here aim to model typical size tsunamigenic earthquakes of magnitudes close to M_W=8.5, and thus choose a fault width of ≈313 km. The curved fault is characterized by large scale roughness. Noticeable are two topographic highs shown in terms of sharp increases of fault dip in **Figure 2D**. We use a constant element edge length of 1 km along the fault. We ensure that this element size along the fault is sufficient to capture the median process zone width following all error criteria of Day et al. (2005) in a series of models with different size elements following the analysis in Wollherr et al. (2018). We measure the median process zone width as 1,386 m for the reference model 3B and 1,224 m for model 1B. For a polynomial basis function of order $p = 5$ (Wollherr et al., 2018) estimate the minimum required resolution to be 1.65 elements per median process zone width. A polynomial basis function of $p = 5$ leads to 6th order numerical accuracy in space and time in the seismic wave propagation solution. We note that each tetrahedral element fault interface is discretized by $(p + 2)^2$ Gaussian points. In **Supplementary Figure 3** we detail two exemplary higher resolution versions (h=500 m, p=5) of the reference model 3B and of model 1B which has the shortest median process zone width. Compared to the coarser resolution of h = 1 km, we quantify the error to be <1% for the maximum vertical seafloor displacement, <6% for the rupture velocity, <5% for the average peak slip rate and <2.5% for the average fault slip which agree with the criteria for well-resolved models by Day et al. (2005). We note that in contrast to the simple depth-dependent setup in Wollherr et al. (2018), the peak slip rate and not the average fault slip is most sensitive here.

The 3D model domain extends from x = −657 to x = 1,075 km and y = −1,023 to y = 700 km and to a depth of z = −700 km. The large model size prevents that waves reflected from non-perfect

absorbing boundary conditions interfere with the rupture itself. To limit computational cost, the unstructured tetrahedral mesh is statically coarsened. The sea floor is flat in the DR model (but not in the tsunami simulations) and assigned a free surface boundary condition. The mesh size is 7.8 million elements. Each simulation took 1:10 h on 75 nodes, with 48 Intel Xeon Skylake cores each, of Supermuc-NG.

To analyze the effects of material directivity and complex initial conditions, as well as uni- and bilateral rupture behavior in the DR models, and the resulting tsunami, we vary the hypocenter location along arc and depth. We choose fault locations which are close to failure in the 2D SC model, at 30, 40, and 45 km depth (**Figure 2B**). To analyze shallower earthquake nucleation locations, we additionally nucleate 3D DR scenarios at 25 km depth (**Figure 2C**). The reference dynamic rupture model (Model 3B) is nucleated at the origin location of the slip event in the SC model, that is, at a depth of 40 km and at the center of the fault along strike (x = 267.25 km, y = −156.5 km). The static friction coefficient is reduced to $\mu_s = 0.019$ within a patch of radius 2 km, which represents the minimum value in the SC model within the nucleation area (**Table 1**). For all earthquake model families, the assigned nucleation parameters, that is locally reduced static friction coefficients μ_s and patch radii r, are listed in **Table 1**. To evaluate effects in lateral direction, we move the hypocenter from y = −156.5 km (fault width center) to y = −78.25 km (25% of the fault width) and y = −234.75 km (75% of the fault width), exploring observational and statistical inferences of large ruptures being predominantly unilateral or bilateral (McGuire et al., 2002; Mai et al., 2005) (see **Figure 2C**). We note that larger nucleation energy (larger radii, lower local strength) are required in fault regions further from failure than the reference model (hypocentral depth of 40 km).

3.2. Tsunami Model Setup

The tsunami modeling area extends from x = −600 to x = 600 km and from y = −750 to y = 450 km, the ocean depth being at a constant 2 km. A linearly sloping beach is placed with its toe at x = 500 km with an inclination of 5%, which results in the coastline being located at x = 540 km in most models (see **Figure 3**, left). We additionally analyze the inundation behavior along a more realistic coastline in one model (model 4D). To this end a non-linear coastline is included in model 3B (**Figure 3**, right). We adapt the coastal topo-bathymetry of the Okushiri benchmark (Yeh, 1996; Honal and Rannabauer, 2020) and stretch it along the full y-direction model length. Every tsunami is generated using the time-dependent (dynamic) seafloor displacements generated in the 3D DR models from 0 to 200 s.

Depending on the used DR model setups, different tsunami modeling refinement levels and output configurations are required. The minimum spatial resolution in sam(oa)^2-flash is defined as $\Delta x = \textit{domain-width} \cdot (1/2)^{d/2}$. We use a minimum refinement level of d = 18 for all tsunami simulation runs, yielding a minimum spatial resolution of Δx = 2.34 km. To obtain detailed inundation patterns, we use a refinement of d = 30 (Δx = 36.62 m) near the coast and a maximum refinement of d = 26 (Δx = 146.5 m) in the remainder of the domain. On SuperMUC-NG, these simulations took 2:43 h on 100 nodes sourced by dynamic displacement. This corresponds to roughly 13,000 CPUh, respectively. Simulation outputs are in general written every 10 s of simulation time. If only sea surface height tracing measurements along a few axes are needed, a run with a maximum refinement of $d = 24$ ($\Delta x = 293.0$ m) takes approximately 27 min across 100 nodes (2,187 CPUh) with dynamic displacement. Output of the full wavefield with a maximum of $d = 24$ took 1:21 h across 32 nodes (2,074 CPUh) for dynamic displacements, writing outputs every 100 s of simulation time between t = 0 and t = 3,000. We note that in all our tsunami models, including a slow "tsunami earthquake," the ratio of tsunami source width/ (source time × tsunami wave speed), in water depth of 2 km is >>1, indicating that the tsunami does not propagate over the source duration (Abrahams et al., 2021). We find differences of up to 10% in the tsunami system energy balance of kinetic and potential energy when comparing static with dynamic sources and source all tsunami in the following from the dynamic seafloor displacement.

TABLE 1 | Model families 1–4 defined by hypocentral location.

Model family	Hypocenter Depth [km]	Radius nucleation zone [km]	Static friction Coeff.
Model 1	25	15.0	0.013
Model 2	30	3.3	0.019
Model 3	40	2.0	0.019
Model 4	45	3.5	0.019
Model 5	40	10.0	0.019
Model 6	40	1.8	0.019

*Each model family includes three dynamic rupture scenarios with varying lateral hypocenter location **(A–C)**. Nucleation characteristics vary between the dynamic rupture model families. The material properties that are imported from the seismic cycle model and used as initial conditions vary with depth. Thus, different static friction coefficients and radii have to be chosen to enable nucleation at different depths. Model 5 is adapted from the reference model 3B friction law with higher fracture energy. Model 6 is the reference model 3B with a higher Poisson's ratio of 0.3.*

4. RESULTS

4.1. Dynamic Rupture Models

We first investigate the effects of varying earthquake hypocenter locations in complex subduction initialized dynamic rupture models. We vary the hypocentral depth between 25, 30, 40, and 45 km, which resembles one shallow earthquake and three low strength excess regions in the geodynamic subduction and seismic cycle model. It has been inferred that hypocenters of large earthquakes are not arbitrarily distributed across fault planes, but located close by regions of large slip (Mai et al., 2005). Additionally, large subduction zone events may propagate preferably unilateral (McGuire et al., 2002) or bilateral (Mai et al., 2005) and rupture dynamics of subduction earthquakes may be significantly affected by bimaterial contrasts (Ma and Beroza, 2008). In our 12 scenarios listed in **Table 1**, different hypocenter depths lead to pronounced differences in dynamic rupture propagation. The models differ in their propagation direction,

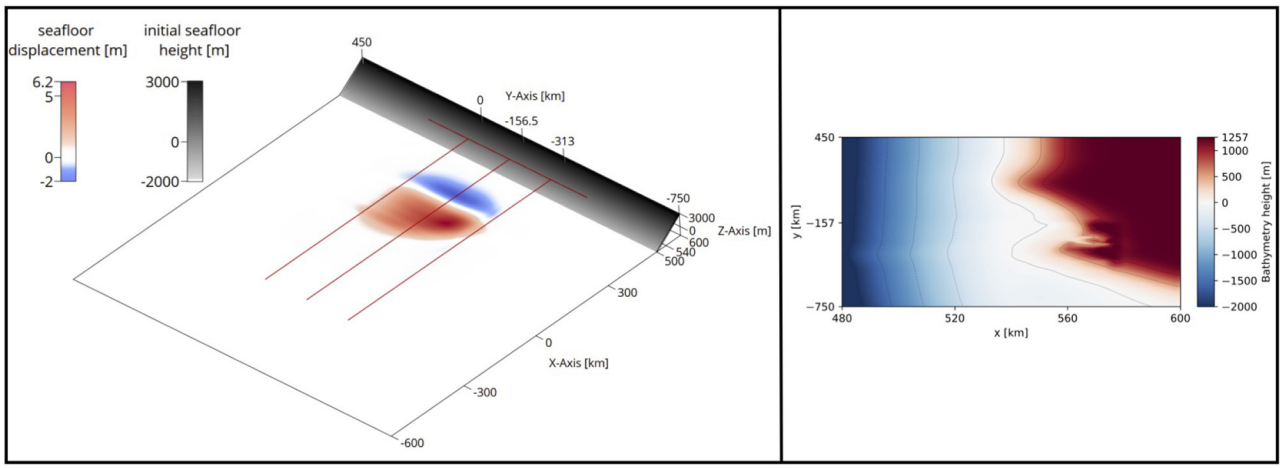

FIGURE 3 | (Left) Sketch of the tsunami model setup for most scenarios for sam(oa)^2-flash with a linearly sloping beach starting at x = 500 km. Red and blue colors are an exemplary snapshot of seafloor uplift and subsidence resulting from a DR model that are used to source the tsunami model. **(Right)** Zoom-in of the non-linear height profile of the complex beach used in one tsunami scenario (model 4.D) adapted from the Okushiri benchmark. The position and slope are designed to be comparable to the linear beach **(left)**. The depth profile is illustrated by blue and red colors. Contour lines are shown every 500 m.

slip rates and rupture velocities, and include localized supershear rupture at different simulation times and fault locations.

Figures 4–6 compare snapshots of slip rate and rupture velocity as well as the accumulated fault slip of all 12 models. Animations of slip rate are provided in the **Supplementary Material**. **Supplementary Figure 4** shows the peak slip rate of all 12 models. **Table 2** summarizes all rupture characteristics.

In model family 1 (shallowest hypocenter) nucleation is initiated at a depth of 25 km which is located above topographic high 1 on the megathrust. We observe complex dynamic rupture behavior, including supershear transition at topographic high 2, localized high slip rates within the fault depression and reactivation of fault slip at a late stage. Rupture propagates at low slip rates before reaching the edge of the first topographic high, where the slip rate increases. As the main rupture front hits the second topographic high (10 s), supershear rupture initiates in downdip direction (**Figure 4**).

For model family 2, we observe complex downdip propagating dynamic rupture behavior with supershear rupture being triggered at the second topographic high. The hypocenter is located at the edge of topographic high 1 (**Figure 2**). As the rupture front passes topographic high 1, slip rate increases, similar to model family 1. Supershear rupture is triggered in downdip direction at 15 s simulation time (**Figures 4**, **5**).

The nucleation location in model family 3 corresponds to spontaneous failure in the 2D SC model. It is located on the lowermost point of the geometric depression of the fault, at 40 km depth. Slip evolves circularly and propagates away from the hypocenter. After 8 s simulation time, supershear rupture initiates in updip direction at topographic high 1 (see **Figures 4**, **5**).

For model family 4, the hypocenter was placed at a depth of 45 km, which lies at the edge of the second topographic high. A circular rupture front evolves during 9 s simulation time. Supershear rupture arises in updip direction after 13 s, when the rupture front hits the first topographic high (**Figures 4**, **5**).

In all 12 models, rupture fronts reach the lower limit of the seismogenic zone at x = 282.25 km after passing the second topographic high. In the SC model, ductile behavior begins to dominate here which is expressed as strength increase in the DR model. Rupture propagation is spontaneously arrested at this depth. Thus, in all 12 models, slip stops at the same depth. At the lateral edges of the prescribed megathrust fault, rupture is geometrically stopped, and no tapering of initial stress or strength is applied. Close to the surface, in the shallowest part of the fault, the sedimentary region allows for small slip while smoothly stopping rupture.

Bilateral rupture evolution appears to be symmetrical for centered hypocenters, despite bimaterial contrasts above and beneath the fault potentially affecting strike-slip faulting contributions (Harris and Day, 2005). For asymmetric hypocenter locations (models A and C of each model family), unilateral dynamic rupture propagation is identical to bilateral models within the first seconds until stopping phases from the closer fault edge affect rupture dynamics. In both cases (A and C), rupture dynamics appear minor symmetric with slight bimaterial effects (see rupture characteristics summarized in **Table 2**). Larger slip is accumulated at the respective far side of the fault (**Figure 6**). The highest absolute slip is observed in the models with hypocenter locations at y = −234.75 km (C models) and the lowest absolute fault slip is observed for models with hypocenters placed in the center of the fault (B models).

In all 12 models we observe localized weak reactivation of slip after approximately 100 s simulation time due to dynamic triggering caused by trapped waves. Waves are trapped within the accretionary wedge between the uppermost part of the fault and the surface until the end of the simulation (200 s). They are reflected at the free surface boundary and propagate back to the fault, which leads to very small amounts of shallow slip

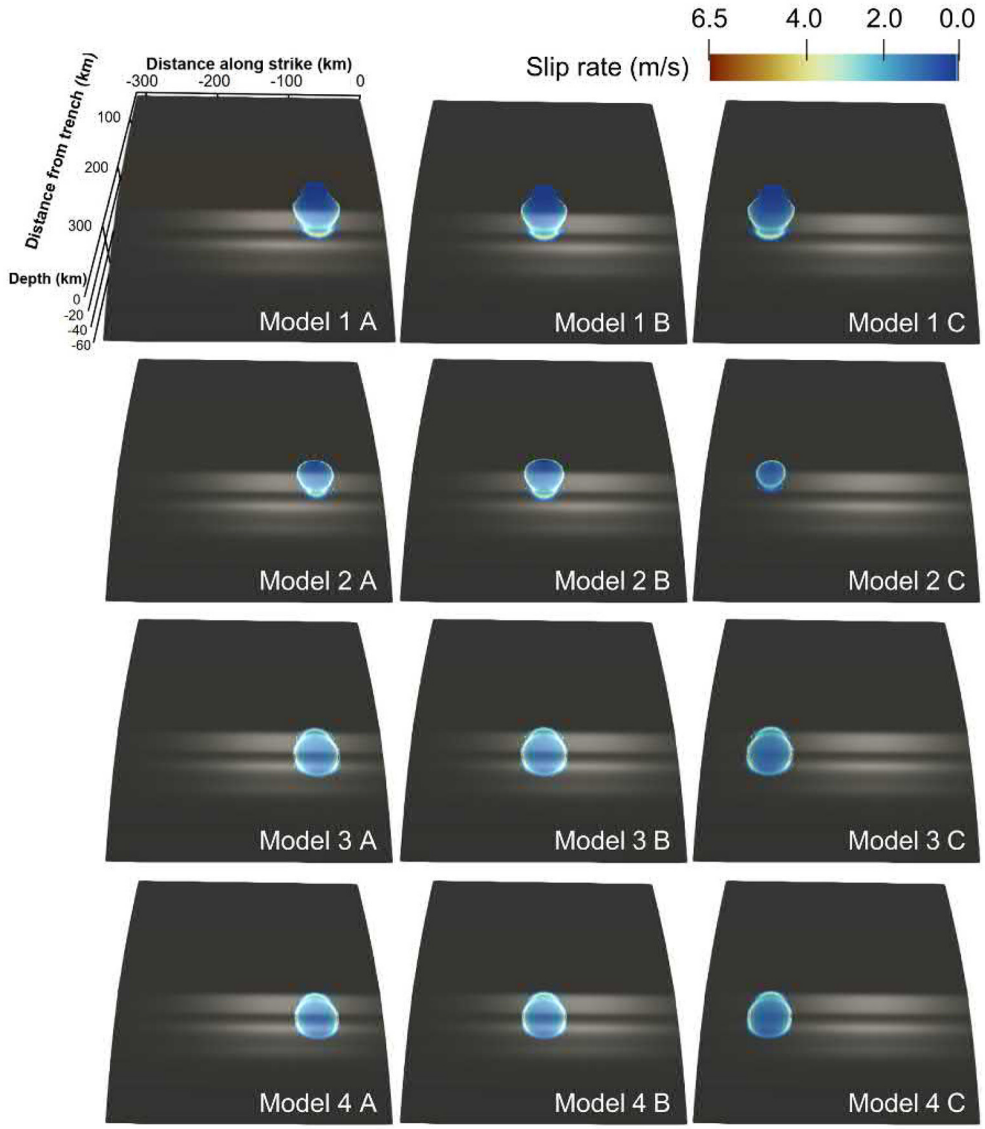

FIGURE 4 | Slip rate at the timestep t = 12 s (model 1), t = 16 s (model 2), t = 10 s (model 3), and t = 14 s (model 4), capturing down-dip and up-dip propagating supershear rupture being triggered by one of the two topographic highs in the fault geometry depending on hypocentral depth. The white reflections highlight the uneven geometry of the fault. The hypocentral locations vary with depth (25, 30, 40, and 45 km) and laterally on the fault (y = −78.25 km, y = −156.5 km, y = −234.75 km). For model 1 and 2 supershear rupture evolves in downdip direction, whereas for model 3 and 4 in updip direction.

in the order of centimeters. As noted before, in the tsunami linking step any artificial contribution of these waves to seafloor displacements will be filtered.

Across all 12 models, the highest peak slip rate (PSR) occurs on the lower part of the fault, inside the geometric depression at ≈40 km depth, and spread out in along-strike direction (**Supplementary Figure 4**, **Table 2**). Model family 2 produces the highest PSR (model 2A, 27.29 m/s). Deeper earthquakes produce lower peak slip rates, such that the earthquakes with the deepest hypocenter (model family 4) exhibits the lowest PSR (model 4A, 23.06 m/s). Along-arc, PSR first increases while rupture propagates away from the hypocenter. Then it decreases due to dynamic interaction with the free surface and other fault edges. At the hypocenter, the PSR is low.

The overall highest absolute slip of 34.31 m is observed for model 4C (see **Table 2**) and the lowest absolute fault slip is observed for model 1B (32.40 m). For models with the same hypocentral depth, the maximum accumulated fault slip is consistently observed when the hypocenter location is located laterally at y = −234.75 km. At the same time, these earthquakes show relatively low peak slip rates. The lowest maximum absolute fault slip for models with the same hypocenter depth is observed for a laterally centered hypocenter. Moment magnitudes vary from M_W = 8.87 (model 3B) to M_W = 8.89 (model 4B, **Table 2**).

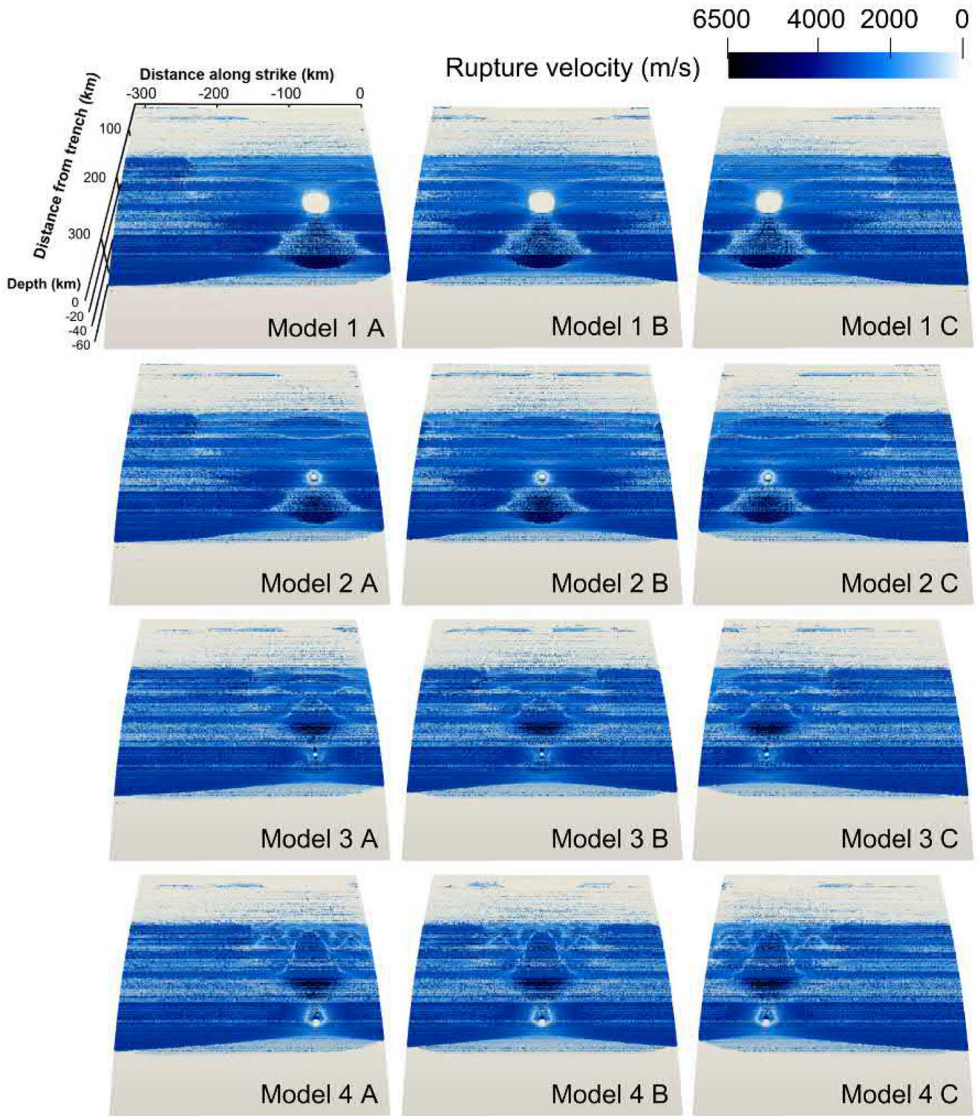

FIGURE 5 | Rupture velocity for 12 dynamic rupture simulations with varying hypocenter locations. Note the difference in nucleation radii according to **Table 1**. Most parts of the fault rupture at speeds around 3,000 m/s. Much lower velocities are visible in the shallower fault part. Supershear rupture is visible as dark blue areas in downdip direction for nucleation locations at a depth of 25 and 30 km and in updip direction for nucleation depths of 40 and 45 km. The rupture velocity is very inhomogeneous due to the complex and heterogeneous material properties on the fault.

4.2. Tsunami Simulations

At 200 s simulation time, the filtered vertical sea-surface uplift has a maximum of ≈4 m which is located above the buried dynamic rupture fault plane for all 12 models (see **Supplementary Figure 5**). The sea surface uplift and subsidence reflect the patterns of accumulated slip in **Figure 6**. Thus, despite the stark dynamic differences in rupture dynamics between the 12 models, including supershear rupture evolution in up- or downdip direction, the static sea surface disturbance is nearly the same. For models of one family, we see lateral differences in the spatial extend of the sea surface uplift which are related to laterally varying hypocenter locations. For models with asymmetric on-fault slip distributions, we observe the same pattern in the sea surface uplift.

Supplementary Figure 6 illustrates the dynamically sourced tsunami propagation toward the simulation domain boundaries. After 2,300 s simulation time, the tsunami arrive at the coast with wave heights of up to ≈5.5 m. At the coast, we observe differences in the tsunami arrival times for laterally varying hypocenter locations of up to 100 s (**Figure 7**). The time delay between the tsunami waves caused by an earthquake with a centered hypocenter (B) and an earthquake with a hypocenter located at y = −78.25 km (A) are always some tens of seconds higher than the time delay between events with a centered

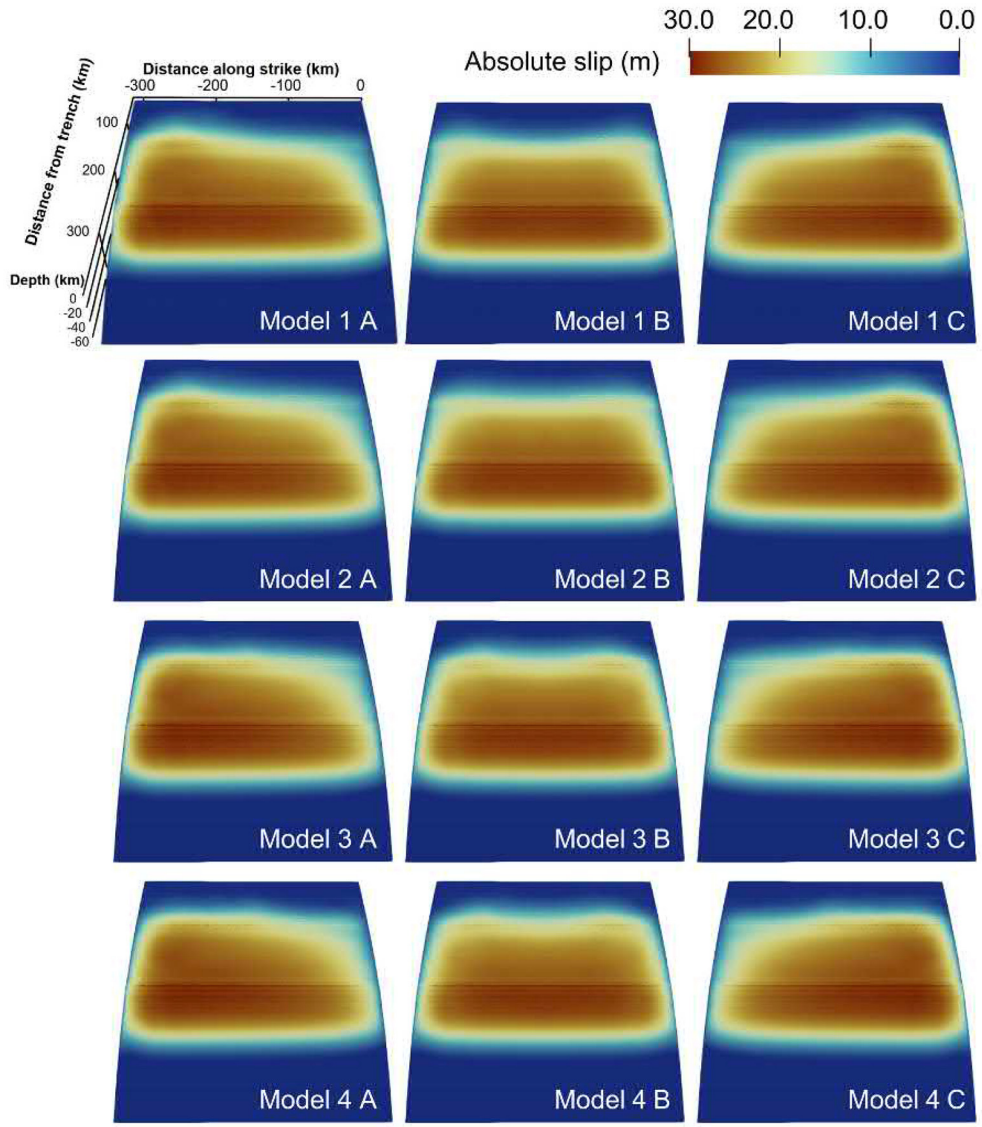

FIGURE 6 | Accumulated fault slip at the end of the simulation, after 200 s for 12 dynamic rupture models. The hypocenter locations vary with depth (25, 30, 40, and 45 km) and laterally on the fault (y = −78.25 km, y = −156.5 km, y = −234.75 km).

hypocenter (B) and a hypocenter location of y = −234.75 km (C) (see **Supplementary Figures 7–9**). We observe only insignificant differences in the tsunami arrival time at the coast with varying hypocentral depths (**Supplementary Figures 10–12**). Tsunami that were generated by deeper earthquakes arrive few seconds later than those being generated by shallower ones.

Figure 7 shows the sea surface height (ssh) of the tsunami when arriving at the coast. We observe non-symmetric differences in coastal ssh in dependence of earthquake along-strike hypocentral location. A maximum wave height of ≈5.5 m can be observed in all 12 simulations. The difference in the tsunami height (Δssh) of models with a centered hypocentral location (B) and a hypocenter located at y = −78.25 km (A) present higher values of approximately 0.25–0.4 m than the Δssh of earthquakes with a centered hypocenter location (B) and earthquakes located at y = −234.75 km (C) (Δssh is ≈ 0.1 m). This agrees with the differences in tsunami arrival at the coast. For larger time delays we observe larger differences in the tsunami height accordingly. In summary, comparing all model families 1A-C, 2A-C, 3A-C, and 4A-C, the largest difference of 6 cm in coastal sea-surface heights can be observed between the shallowest earthquakes (models 1A-C) and earthquakes nucleating at 40 km depth (models 3A-C) (see **Supplementary Figures 13–18**).

We calculate the potential energy transferred by the earthquake rupture to the sea surface (the "tsunami potential

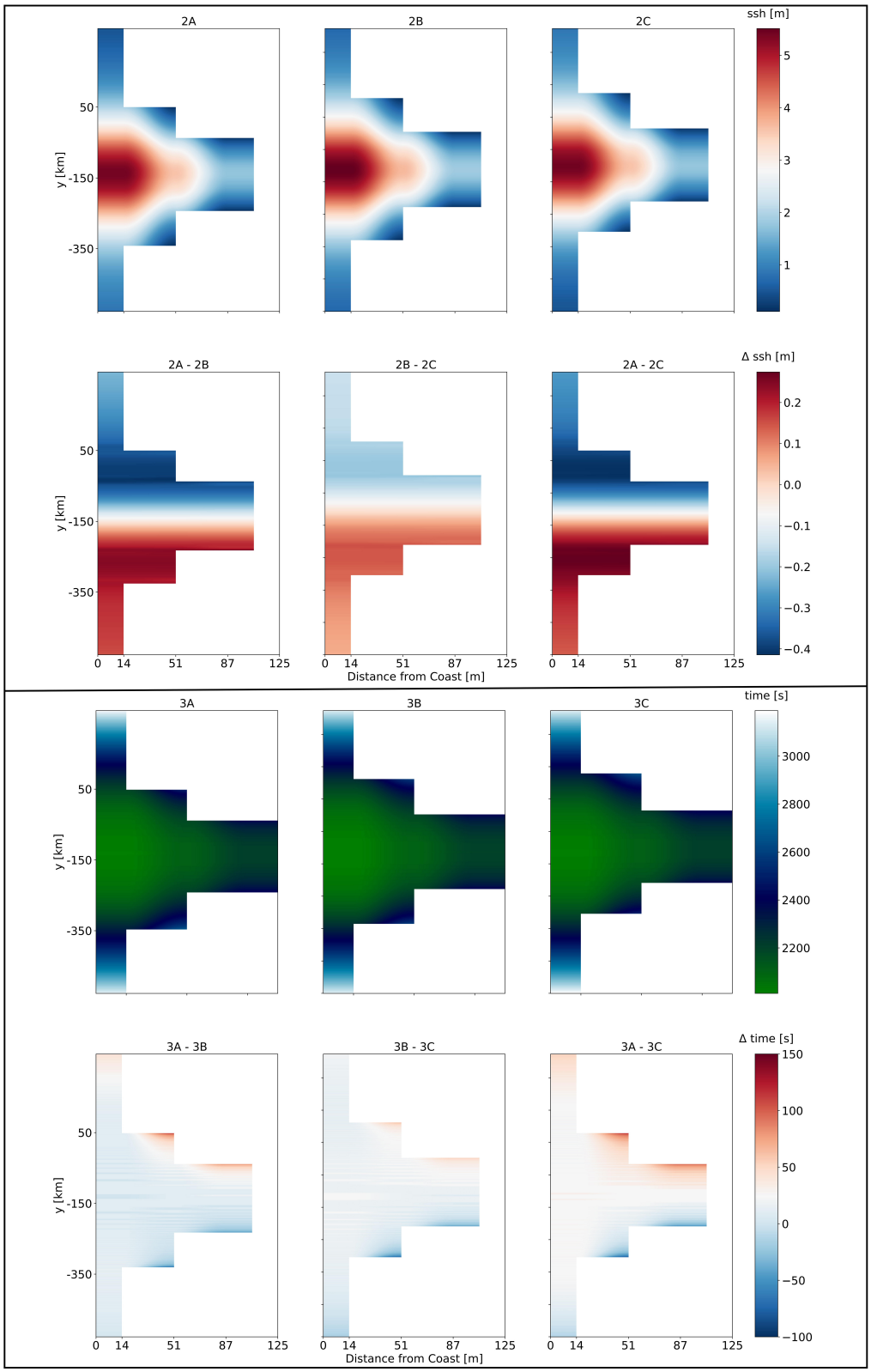

FIGURE 7 | (Top) Comparison of sea surface height (ssh) for tsunami fronts arriving at the coast for the models 2A–2C (upper row). The difference in arrival times between the models is shown as Δssh (lower row). **(Bottom)** Inundation comparison for models 3A–3C. The green to white color scale shows the time delay for the tsunami fronts arriving at the coast (upper row). The difference in inundation between respective models is plotted as Δt (lower row).

energy") (Melgar et al., 2019; Crempien et al., 2020):

$$E_T = \frac{1}{2}\rho g \int\int_A \eta^2 dA, \quad (1)$$

where η is the vertical, static sea-floor deformation of the DR model (corresponding to the sea surface heights after 200 s shown in **Tables 2**, **3**), with a water density of ρ=1,000kg/m^3 and the gravitational acceleration being g=10m/s. The deepest earthquake (model 4B) produces the highest tsunami potential with ≈3,150 TJ which marginally differs from the tsunami potential of model 3B (**Table 2**). The tsunami resulting from shallower hypocenter depths (models 1B and 2B) have slightly smaller tsunami potentials of 3,078 and 3,062 TJ. Within model families 1 and 2, a centered hypocenter location leads to the highest tsunami potential, while for model family 3 and 4, the centered hypocenter causes the smallest tsunami potential. Within each model family, tsunami simulations with a hypocenter location at y = −78.25 km (A) always present lower tsunami potentials than models with hypocenter locations at y = −234.75 km (C).

4.3. Tsunami Simulation With Complex Coastal Topo-Bathymetry

We perform an additional tsunami simulation, model 3D, which is adapting model 3B by replacing the linearly sloping beach with a complex coastline (see **Figure 3**, right). We adapt the coastal topo-bathymetry of the Okushiri benchmark (Honal and Rannabauer, 2020) and stretch it along the full y-direction model length (section 3.2). The resulting sea-surface height and inundation area are displayed in **Figure 8**. Tsunami inundation is observed along the entire length of the coast. While the coastal parts at the far-ends of the domain are hit by a shallow wave of approximately 1 or 2 m, its central part is hit by high wave amplitudes of up to 8 m. In this model, the tsunami amplitudes

TABLE 3 | Dynamic rupture and tsunami characteristics for model 3B, 5, and 6 with centered hypocenter locations.

	Model 3B	Model 5	Model 6
Max. absolute fault slip [m]	32.82	67.76	65.72
Mean absolute fault slip [m]	15.63	33.51	32.23
Max. peak slip rate [m/s]	24.12	12.59	24.80
Mean peak slip rate [m/s]	4.15	2.73	4.48
Magnitude [1]	8.87	9.03	9.04
Mean rupture velocity [m/s]	2124.0	1352.0	1936.0
Mean stress drop [MPa]	5.16	6.10	6.24
Max. seafloor displacement [m]	4.60	6.55	6.09
Tsunami potential energy [TJ]	3133.15	6949.16	6182.48

TABLE 2 | Dynamic rupture and tsunami characteristics for model 1–4 with centered and lateral varying hypocenter locations.

	Model 1			Model 2		
	1.A	1.B	1.C	2.A	2.B	2.C
Lateral hypocenter location [km]	-78.25	-156.5	-234.75	-78.25	-156.5	-234.75
Max. absolute fault slip [m]	33.13	32.40	33.31	33.21	32.43	33.39
Mean absolute fault slip [m]	15.29	15.27	15.31	15.20	15.16	15.24
Max. peak slip rate [m/s]	26.61	26.75	26.71	27.29	27.18	27.19
Mean peak slip rate [m/s]	4.11	4.24	4.08	4.11	4.21	4.09
Magnitude [1]	8.88	8.88	8.88	8.88	8.88	8.88
Mean rupture velocity [m/s]	2,083	2,042	2,086	2,134	2,095	2,137
Mean stress drop [MPa]	5.19	5.23	5.16	5.10	5.12	5.08
Seafloor displacement [m]	4.58	4.54	4.58	4.59	4.58	4.61
Tsunami potential [TJ]	3018.81	3078.00	3026.03	2995.31	3062.01	3003.95
	Model 3			**Model 4**		
	3.A	**3.B**	**3.C**	**4.A**	**4.B**	**4.C**
Lateral hypocenter location [km]	-78.25	-156.5	-234.75	-78.25	-156.5	-234.75
Max. absolute fault slip [m]	33.80	32.82	34.23	33.82	32.91	34.31
Mean absolute fault slip [m]	15.51	15.63	15.54	15.73	15.92	15.75
Max. peak slip rate [m/s]	23.69	24.12	24.36	23.06	23.27	23.41
Mean peak slip rate [m/s]	4.08	4.15	4.07	4.04	4.12	4.02
Magnitude [1]	8.88	8.87	8.88	8.88	8.89	8.88
Mean rupture velocity [m/s]	2,119	2,124	2,118	2,116	2,120	2,115
Mean stress drop [MPa]	5.13	5.16	5.12	5.23	5.28	5.27
Max. seafloor displacement [m]	4.66	4.60	4.64	4.66	4.62	4.67
Tsunami potential [TJ]	3045.13	3133.15	3052.87	3067.32	3149.63	3074.53

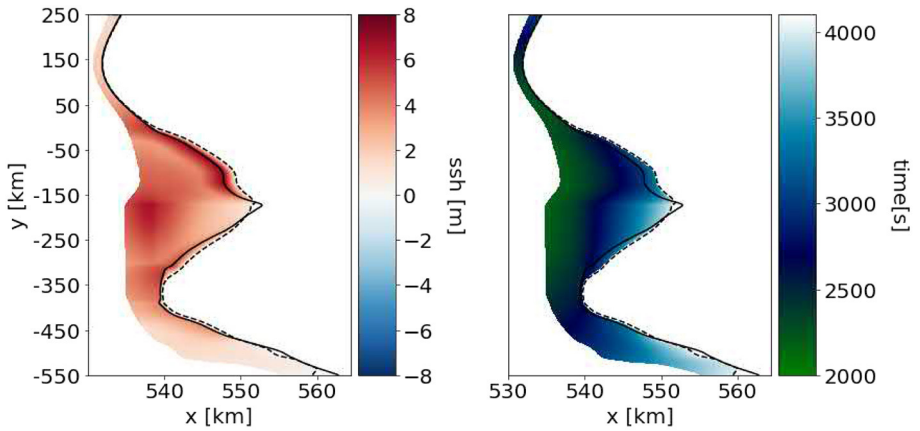

FIGURE 8 | Sea-surface height of the waves at the coast (**left**) and inundation area and time (**right**) for the tsunami scenario with a complex coast (**Figure 3**, right). Note the different x-axis scale compared to **Figure 7** which is necessary to resolve the complex coastline at the beginning of the simulation (solid black line) accurately. The dotted line illustrates how far in-land the tsunami inundates.

are ≈2.5 m higher, compared to absolute sea-surface heights of ≈5.5 m for the linearly sloping beach.

4.4. Simulations With Increased Fracture Energy and Poisson's Ratio

We here analyse two additional dynamic rupture models based on reference model 3B varying on-fault or off-fault rheology. Firstly, we triple the critical slip weakening distance D_c from 0.1 to 0.3 m (model 5) which triples fracture energy and generates a "tsunami earthquake." Secondly, Poisson's ratio is increased from ν=0.25 to ν=0.3 (model 6) everywhere in the domain. Both models result in shallow slip about twice as high as the reference model 3B (see **Table 3**). **Table 1** shows the adapted nucleation characteristics that were necessary to initiate rupture on the fault. We do not further decrease the static friction coefficient, but increase the nucleation radius from 3.5 to 10.0 km (model 5). In model 6 a smaller nucleation area of only 1.8 km is sufficient. For the high fracture energy model 5, rupture dynamics evolve very differently to model 3B, specifically at much lower rupture velocities of max. 1,352 m/s. There is no supershear rupture triggered during the entire simulation time. In model 6 the dynamic rupture evolution is similar to model 3B and supershear rupture evolves in updip direction after 9 s.

For both models, 5 and 6, trapped waves are observed until the end of the simulation (200 s) dynamically interacting with the shallow part of the fault.

Figure 9 displays the rupture characteristics of model 3B, model 5, and model 6. Compared to the reference model 3B, both adapted models accumulate large shallow slip. The maximum and average fault slip of models 5 and 6 are about twice as high as in the reference model 3B (see **Table 3**), which reflects in increased earthquake magnitudes of M_W=9.03 (model 5) and M_W=9.04 (model 6). Also, their dynamic stress drops are higher and the maximum vertical dynamic seafloor displacement is increased by up to ≈2 m. Model 5 shows a much smaller PSR (12.59 m/s) and rupture velocity (1,352 m/s) then model 3B (24.12 and 2,124 m/s), while the PSR (24.80 m/s) and rupture velocity (1,936 m/s) of model 6 are similar to the reference model. The maximum PSR for all three models is always observed at the same depth which is located within the fault depression at ≈ 40 km depth.

Figure 10, top, compares the sea-surface height of models 5 and 6 after 200 s, corresponding to the end time of the DR simulation. The overall tsunami waveforms in models 5 and 6 appear to be broader than in model 3B (**Supplementary Figure 7**) and the trajectories in **Figure 10**, bottom, show much higher tsunami amplitudes. After 1,400 s simulation time, the wave amplitudes of model 3B reach extrema of +2 and −3 m, whereas the tsunami in models 5 and 6 reach values of +2 and −5 m. After 2,300 s simulation time, the wavefronts hit the coast and result in maximum tsunami heights of over 7.5 m. This is ≈2.0 m higher than in the reference model 3B. An important difference between models 5 and 6 is the difference in rupture speed. While model 6 produces supershear rupture, the overall rupture velocity of model 5 is ≈1,352 m/s. Thus, although the model 5 earthquake scenario has a slightly smaller stress drop and magnitude than model 6, it produces the highest tsunami amplitudes.

As the waves hit the coast there is a time delay of 100 s and a difference in tsunami height of ≈0.5 m between models 6 and 5 (see **Figure 11**). Due to the overall higher tsunami waves of models 5 and 6, the water inundates further on-shore and reaches higher distances from the coast than for model 3B. Model 5 has the highest tsunami potential with roughly 6,950 TJ and model 6 has a tsunami potential of 6182.48 TJ (**Table 3**). The tsunami potential of model 5 is twice as high as the one of reference model 3B.

4.5. Dynamic Effects During Tsunami Generation by Supershear and Tsunami Earthquakes

Figure 12, top, shows snapshots of the unfiltered DR seafloor displacements of models 1B (supershear rupture in downdip direction), 3B (supershear rupture in updip direction), and

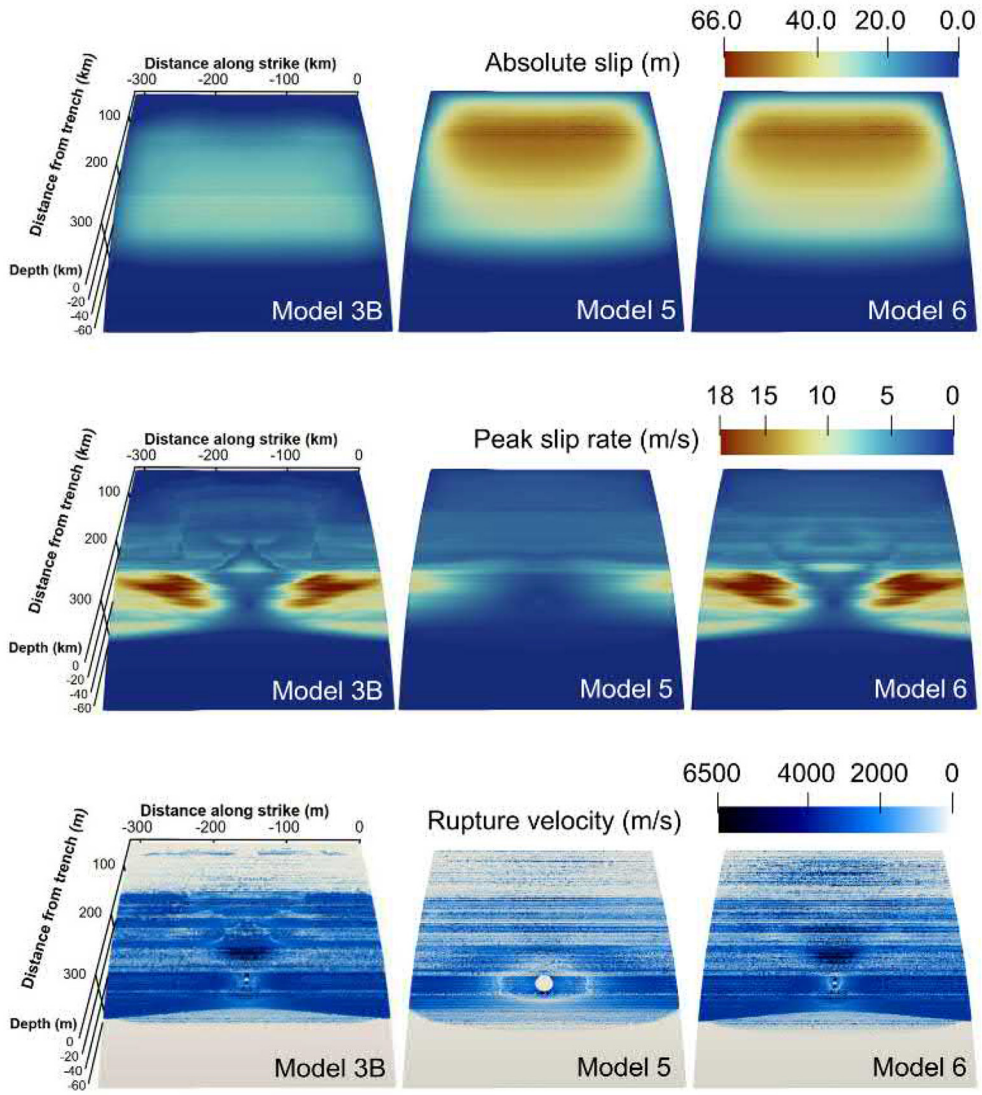

FIGURE 9 | Fault slip, peak slip rate, and rupture velocity for the dynamic rupture models 3, 5 (increased fracture energy), and 6 (higher Poisson's ratio) after 200 s at the end of the DR simulation.

5 (tsunami earthquake, no supershear rupture) after 100 s simulation time. Localized, sharp uplifting fronts are visible in the dynamic displacement off-set from the centrally located hypocenter overprinting the static deformation signal. The ocean response recorded within the source region during the tsunami generation process of all 3 models (**Figure 12**, bottom) reflect the seismic, and near-field displacements around a rupture front at 100 s simulation time. The time series shown is recorded at x = −100 km and y = −150 km, which is well inside the DR modeling domain.

In our models, co-seismic ocean response phases appear for supershear earthquakes as well as for the "tsunami earthquake" propagating at sub-Rayleigh speed during the duration of earthquake slip and within the DR model, i.e., for the dynamic tsunami generation process. We here do not observe a faster, instantaneous supershear mach cone ocean response signature (e.g., identified in Elbanna et al. (2020) for strike-slip events). Additionally, due to our filtering approach, trapped seismic waves are effectively damped, also inside the near-fault region once rupture stops. We then do not observe dynamic phases propagating (**Supplementary Figures 5, 6**).

5. DISCUSSION

5.1. Simplifying Model Assumptions

In this study, we link 3D dynamic rupture initial conditions to a chosen slip event in a 2D long-term geodynamic subduction and seismic cycle. The linked initial conditions include a curved, blind fault geometry, spatially heterogeneous fault stresses, strength, and material properties. The SC 2D material properties,

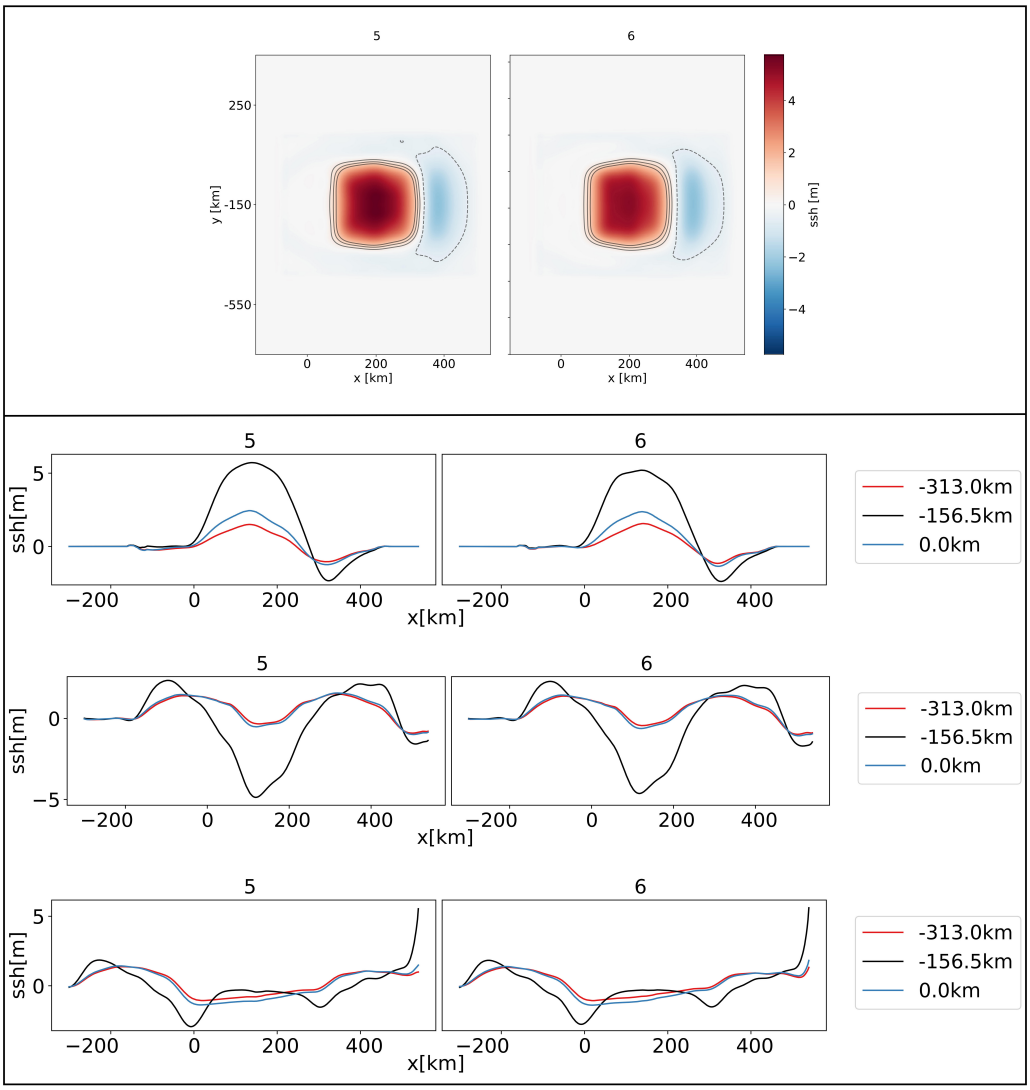

FIGURE 10 | (Top) Sea surface height (ssh) for models 5 and 6 at t = 200 s with contours at −0.5, 0.5, 1.0, and 1.5 m, at the end of the DR earthquake simulations. **(Bottom)** Trajectories of the sea surface height for dynamically sourced tsunami (model 5 and 6) measured at y = 0.0, −156.5, and −313.0 km. Directly after the earthquake at t = 200 s (top), during the wave propagation at 1,400 s (middle), and at the time of coastal inundation at t = 2,200 s (bottom).

fault geometry, as well as stresses and strength are extruded into the third dimension without adding additional along-strike variability. While limiting complexity, we can in this manner isolate sensitivities, e.g., of hypocentral location, and their effects on rupture dynamics and tsunami generation, propagation and inundation.

In linking from the SC to the DR model, we adopt several simplifying assumptions to bridge the incompressibility and visco-elasto-plastic, plane-strain conditions of the subduction model to the compressible, elastic conditions of the earthquake model. The resulting 3D dynamic rupture is linked with the tsunami model through the time-dependent seafloor displacements, following the same methods as detailed in Madden et al. (2020). All resulting rupture models are characterized by uniformity along strike, rendering the dynamic earthquake source differences to be associated with along-dip variability in rupture dynamics controlled by the nucleation position relative to the two bands of topography on the megathrust. Future work may extend our analysis to include along-arc variations in stress, strength, rheology, and geometry across the megathrust as suggested by detailed imaging of fault geometry and shown to impact earthquake and tsunami dynamics (e.g., Galvez et al., 2019; Ulrich et al., 2020). The adopted "bumpy" fault geometry develops self-consistently with stress, strength and rheology in the SC model. Its along-depth dimensions aligns with conceptual asperity models governing megathrust fault slip. Future work may study the dynamic effects of subducted seamounts (e.g., Cloos, 1992) ensuring to adapt initial stresses consistently.

We use fully elastic material response in combination with linear slip weakening friction. The complexity of the DR model could be increased by including more complex physics, such as

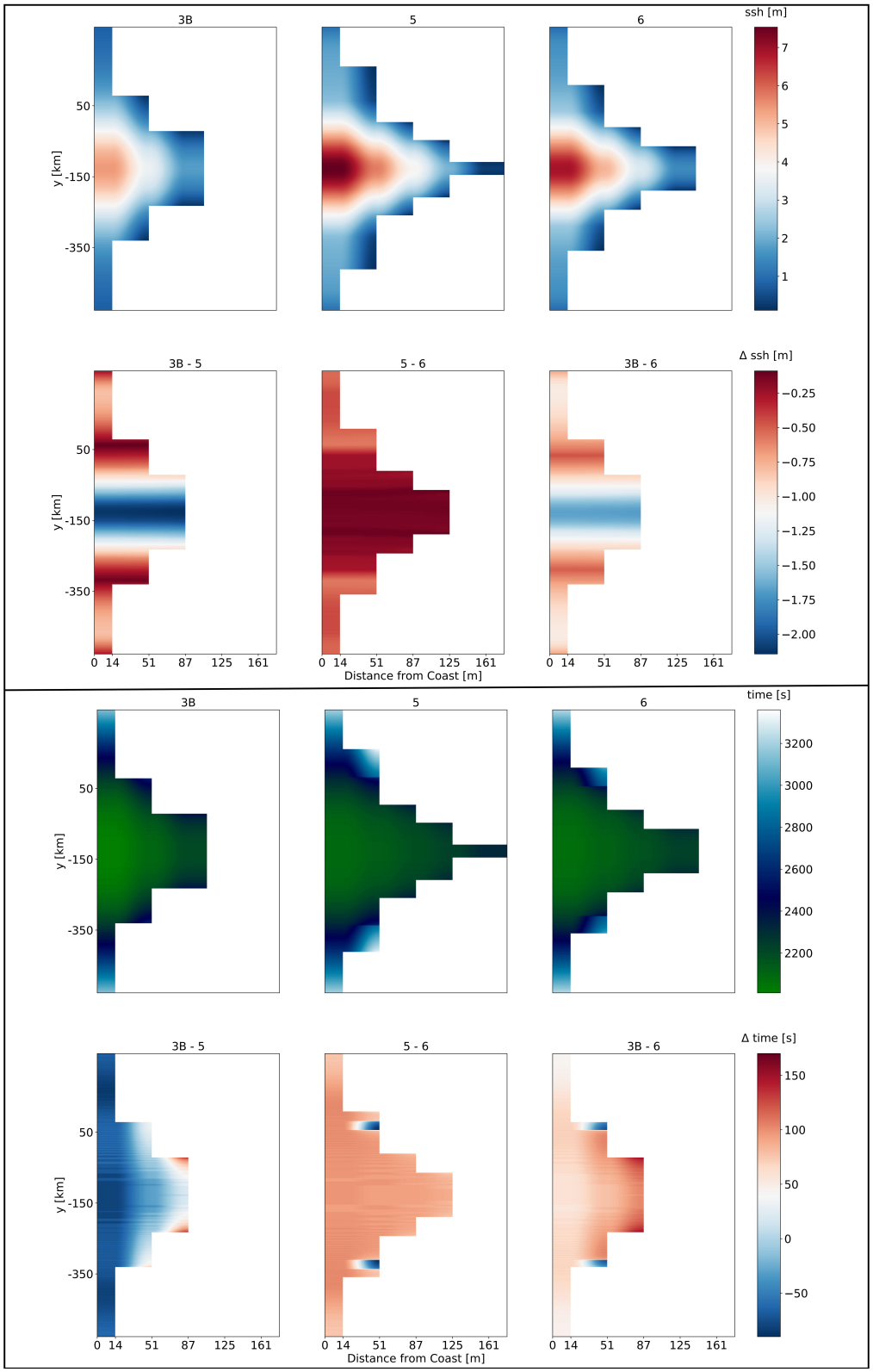

FIGURE 11 | (Top) Comparison of sea surface height for tsunami fronts arriving at the coast for the models 3B, 5, and 6. The difference between the models is shown as Δssh. In contrast to **Figure 11** the x-axis (distance from coast) indicates higher values. This is due to the greater inundation area of model 5 which exceeds 161 m distance. **(Bottom)** Inundation comparison for models 3B, 5, and 6. The green to white color scale shows the time delay for the wave fronts arriving at the coast. The difference between the models is plotted as Δt with a blue (negative values) to red (p color-scale, respectively.

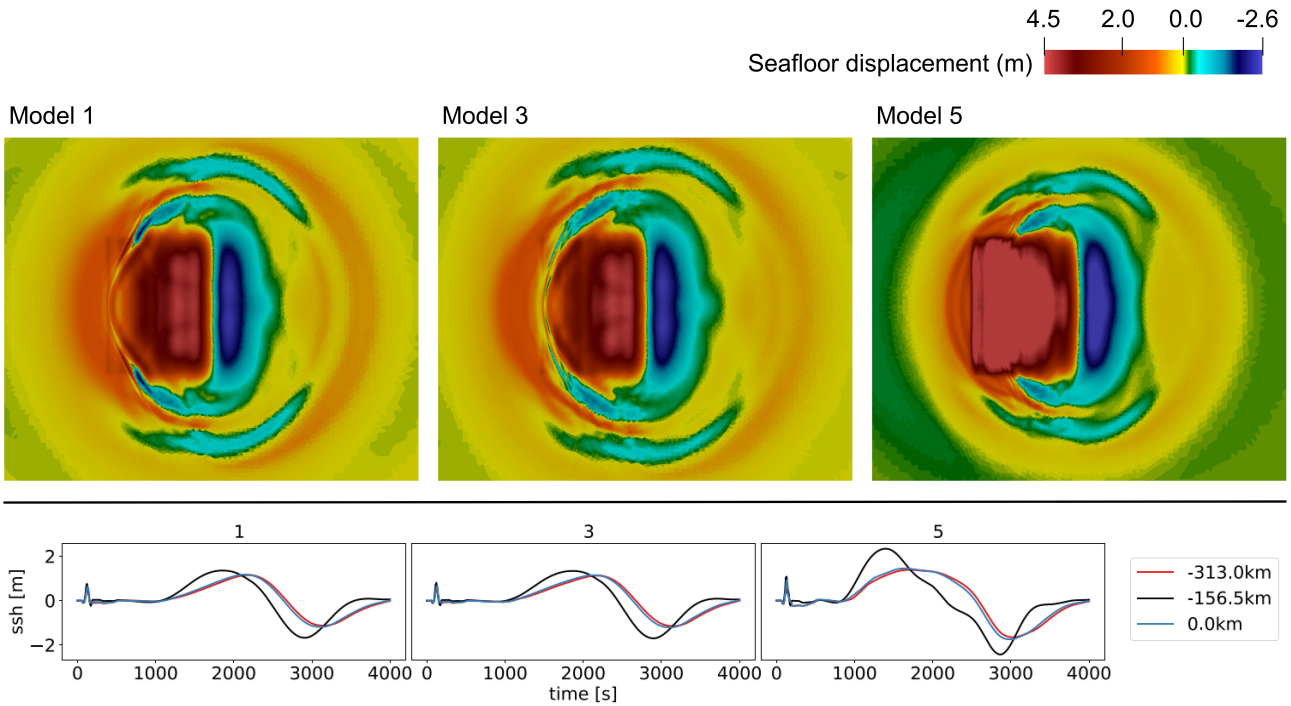

FIGURE 12 | (Top) Unfiltered seafloor displacements from dynamic rupture model 1B (supershear rupture in downdip direction), 3B (supershear rupture in updip direction), and 5 (tsunami earthquake) at a simulation time of 100 s. **(Bottom)** Tsunami generation sea surface height timeseries for model 1B, 3B, and 5 at x = −100 km, y = −150 km.

rapid velocity weakening rate-and state friction (Ulrich et al., 2019a), thermal pressurization of pore fluids (Gabriel et al., 2020), or off-fault plasticity (Wollherr et al., 2018; Ma and Nie, 2019).

In the linking step from the DR model to the tsunami model, we filter the seafloor displacements using a spatial-temporal Fourier-transform (section 4.5). Detailed analysis of the effects of relatively small coseismic phases on tsunami genesis, propagation, and inundation is here challenging due to the filter we apply. Future studies may use the unfiltered seafloor displacement as input to the tsunami model to analyse the fully dynamic interaction of the seafloor movements with the tsunami and inundation dynamics. sam(oa)^2-flash 's hydrostatic shallow water tsunami model enables the simulation of tsunami genesis, propagation, and inundation at the coast. The approach is limited by the assumption of long wavelengths. Additionally, it does not take the interaction of wind with the water interface into account. Overall, the usage of the shallow water equations might overestimate wave amplitudes.

Our DR models do not account for seafloor bathymetry. A more realistic bathymetry would translate the horizontal earthquake motion into vertical displacements, such that the tsunami amplitude might be amplified (Tanioka and Satake, 1996; Lotto et al., 2018; Saito et al., 2019; Ulrich et al., 2019a). Recent work in van Zelst et al. (2021) complement this paper by using the exact subduction bathymetry and topography arising from the 2D seismic cycle model and include it in 2D DR simulation. The resulting seafloor displacement is linked to a one-dimensional shallow water tsunami model. The resulting maximum tsunami amplitude is 6.5 m, larger than our comparable 3D reference model 3B. It is here left for future work to combine their findings with our 3D sensitivity analysis.

The computational costs of each of the presented 15 linked scenarios (see sections 3.1 and 3.2) is well within the scope of the allocation typically available to users of supercomputing centers. While hundreds of such simulations are readily possible, fully physics-based dynamic rupture models rather complement than replace cheaper (e.g., kinematic) source descriptions used for millions of PTHA forward models. Specifically, for narrowing down the high-dimensional and often non-unique source parameter space in conjunction with observational or long-term modeling constraints and for sensitivity analysis of other parameters influencing rupture behavior and tsunami generation and propagation.

5.2. Hypocentral Depth and Up-Dip vs. Down-Dip Supershear Rupture Propagation

We vary the hypocenter location across four depths (25, 30, 40, 45 km) to study the effects on rupture dynamics and tsunami evolution, propagation, and coastal inundation. Earthquakes with shallower hypocentral depths (25 and 30 km depth) generally generate lower slip than earthquakes with deeper hypocenters (40 and 45 km depth). The lower accumulated on-fault slip for events with shallower hypocenters leads to

comparably lower vertical seafloor displacement. In our SC initialized models, however, these differences are relatively minor and have small impact on tsunami generation, propagation and inundation, in contrast to what is typically observed from observational data (Bilek and Lay, 2018).

For simulations with shallower hypocenter locations, we observe supershear rupture propagating in the downdip direction, while hypocenters located at 40 and 45 km depth lead to supershear rupture in the updip direction. In either case, the slab geometry (topographic highs) and rheology influences the nucleation and direction of supershear rupture propagation significantly. In all our simulations, supershear rupture initiates when the rupture front hits a topographic high on the fault plane. The first topographic high (1) is related to a pile up of subducted sediments. The weaker material at the depth of the topographic high 1 might facilitate supershear rupture. Supershear rupture is also triggered by the second topographic high highlighting the complex dynamic effects of the long-term self-consistently developing fault roughness, stress, and rheology heterogeneities. The direction of supershear rupture propagation is determined by whether the updip or downdip rupture front interacts with the rough fault geometry (Bruhat et al., 2016; Bao et al., 2019; Tadapansawut et al., 2021). Megathrust supershear rupture is challenging to identify observationally but has been suggested in back-projection analysis of the Tohoku-Oki megathrust earthquake (Meng et al., 2011) and was analyzed in Cascadia 2D dynamic rupture models by Ramos and Huang (2019) who observe down-dip supershear rupture propagation near the ETS region caused by normal stress gradients (similar to the conditions governing our topographic highs).

Independent of where the earthquakes nucleate, the highest peak slip rate is consistently observed at the same location on the fault: inside the depression that separates the two local fault topographic highs, although the intensity of the slip rate decreases with increasing hypocentral depth. The calculated tsunami potential energy varies in the range of $\Delta E_T \approx 78$ TJ for earthquakes nucleating at different depths. This is caused by a difference in the maximum seafloor displacement of approx. $\Delta = 0.13$ m.

5.3. Bilateral vs. Unilateral Rupture on a Complex Bimaterial Megathrust

To study unilateral vs. bilateral rupture effects on rupture dynamics (Hirano, 2019; McGuire et al., 2002) and tsunami generation, we shifted rupture nucleation from a centered hypocenter to 25% (A) and 75% (C) of the fault width (y = −78,25 and y = −234,75 km). Overall, differences are small. However, we note that earthquakes with a centered hypocentral location (B) consistently produce the highest stress drops and lowest accumulated slip on the fault, which lead to the lowest vertical seafloor displacement. The simulations with a nucleation patch at 75% (C) of the fault width show the highest accumulated slip for earthquakes at the same depth, but relatively low PSR. Due to the high amount of accumulated slip, we would expect the seafloor displacement to be the highest as well, but this is not the case for all model families, due to bimaterial effects (Brietzke et al., 2009). These effects lead to (minor) differences in amplitudes of the resulting tsunami at the coast and the (short) time delay between the arriving wave fronts. The higher sea surface uplift is also seen in the trajectories of the different models (**Supplementary Figure 7**).

We note again, that in difference to Madden et al. (2020), we here use the 2D geodynamic SC model developed in van Zelst et al. (2019) which has twice larger shear moduli. All our earthquakes show a higher stress drop of roughly 5 MPa compared to 2.2 MPa in Madden et al. (2020), whereas the rupture velocity remains the same ($\approx 2,100\ m/s$). They also show a comparably lower maximum slip of 32.8 m (Madden et al., 2020 observe a slip of 42.2 m) on the fault plane, which is visible in the lower seafloor displacement as well (4.60 m compared to 28.1 m). Overall, our earthquake and tsunami scenario agree with observational scaling, resulting in a typical tsunami generating earthquake magnitude of $M_W = 8.8$ and a tsunami wave height of roughly 5.5 m at the coast. For all 12 models with hypocenter variations, we find that high earthquake magnitudes (or high fault slip) correspond to the highest seafloor displacements and result in greater tsunami heights, as expected.

5.4. Comparison of Tsunami Behavior for Linear and Complex Coastline

To analyze the effect of coastal complexity on inundation, we included a non-linear coastline in model 3B (see **Figure 3**). The results show that the complex and more realistic setup yields higher tsunami amplitudes (up to 8 m, **Figure 8**) than the model with a linear beach (sea-surface height of up to 5 m, **Figures 7**, **11**). The overall distribution of sea-surface heights along a non-linear coast is much more complex. Between y = 50 and y = −160 km, the distance between fault and coast increases. Beyond y = −160 km until y = −350 km this distance decreases. While the part between y = 50 and y = −160 km is hit by tsunami heights of up to 8 m, the sea-surface heights at the coast between y = −160 and y = −350 km are ≈2 m lower. This effect may be enhanced when combining a complex coastline with lateral varying earthquake source characteristics. Even though the waves of both, model 3B and the scenario with the complex beach arrive nearly simultaneously at the coast, they need ca. 1,000 seconds longer to reach the farthest onshore point in the non-linear case.

5.5. Large Shallow Slip

Most earthquakes of high magnitudes tend to have a large stress drop, accompanied with a high radiation energy (Festa et al., 2008). Venkataraman and Kanamori (2004) state that this is different for a special class of megathrust events, "tsunami earthquakes," which have a comparably small radiation efficiency. We here model this dynamically by increasing the critical slip distance, the amount of slip over which the static friction coefficient in the dynamic rupture model decreases to the dynamic friction coefficient. Polet and Kanamori (2000) state that tsunami earthquakes tend to rupture the shallow portions of a fault, which results in a large amount of shallow slip. The increased D_c value in model 5 leads to a lower rupture velocity

of 1,352 m/s compared to the rupture speed in the initial model 3B of 2,124 m/s. The mean velocity of 1,352 m/s is lower than 80% of the S-wave speed (van Zelst et al., 2019), which specifies this earthquake by definition as a tsunami earthquake (Kanamori, 1972; Bilek and Lay, 1999). As the rupture propagates updip, we observe high slip on the shallow fault. The slip is twice as high as in the initial model 3B, which leads to a higher max. vertical seafloor displacement (1.5 times the displacement of 3B) and a higher tsunami height (see **Figure 11**). This behavior is reflected in the tsunami potential of model 5, which is double the tsunami potential in model 3B.

In model 6, we increase the Poisson's ratio from $\nu = 0.25$ to $\nu = 0.3$. The increase in Poisson's ratio results in a reduction of the critical maximal shear stress on the fault (Xie et al., 2009). This means that rupture initiation is facilitated. Whereas, van Zelst et al. (2019) observe a decrease in slip with increasing Poisson's ratio, we find higher slip on the fault, together with a higher stress drop; model 6 has also double the amount of slip of model 3B, just as the "tsunami earthquake" model 5. This causes a higher vertical seafloor displacement and thus a higher tsunami. At the same time the rupture velocity remains nearly the same as in model 3B. Due to the high magnitude and accumulated shallow slip, the tsunami potential of model 6 is nearly twice as high as in model 3B. The differences in rupture dynamics between van Zelst et al. (2019) and our model 6 from varying the Poisson's ratio is due to the different choices in linking frictional parameters (we here assume constant D_c) which leads to differences in stress drop. While the stress drop in van Zelst et al. (2019) remains the same with increasing ν, we observe an increase of 1.08 MPa.

The main difference between model 5 and 6 are summarized in **Tables 2**, **3**. In model 6, the peak slip rate and stress drop get amplified, leading to a similar rupture behavior than in model 3B with a higher magnitude and absolute slip, resulting in higher tsunami amplitudes. In model 5, the rupture velocity gets reduced and the rupture characteristics change. Although model 5 produces an earthquake with a slightly lower magnitude and stress drop, it produces a seafloor displacement that is 46 cm higher than for model 6. The tsunami earthquake (model 5) generates the highest tsunami amplitude of all these models and consequently the greatest inundation area at the coast, while the waves arrive significantly later due to the lower rupture velocity. The effect of a Poisson's ratio increase in model 6 is not quite as large as the change of the rupture dynamics and tsunami generation in model 5. While in model 5 rupture propagates at sub-shear speeds, supershear rupture still evolves in model 6. Nevertheless, an increasing critical slip weakening distance D_c just as a change in the material properties in the earthquake rupture model can drastically change the rupture dynamics and influence tsunami generation and propagation (see **Figure 11**). We note that for future analysis of the effects of enhanced shallow slip such as occurring in both models 5 and 6, it will be crucial to combine our analysis with 3D non-constant water depth in the source region, since a realistic subduction zone geometry (van Zelst et al., 2021) will place shallow slip in deeper water and cause additional effects due to horizontal motions and steep topography contrasts.

6. CONCLUSION

We investigate the influence of hypocentral depth, rupture propagation direction and bimaterial effects, as well as the influence of fracture energy and Poisson's ratio on rupture behavior and tsunami generation and propagation. We analyse 15 subduction-initialized 3D dynamic earthquake rupture tsunami propagation and tsunami run-up scenarios. We vary the hypocentral depth between 25, 30, 40, and 45 km, which resembles four low strength excess regions in the geodynamic subduction and seismic cycle model. In all models, supershear rupture is triggered once the earthquake rupture front crosses one of two distinct topographic highs in the megathrust geometry, which are related to sediment subduction on geodynamic time scales. Earthquakes from shallow hypocenters exhibit supershear rupture in the downdip direction, whereas supershear rupture propagates updip for earthquakes that nucleate deeper. Albeit dynamic earthquakes differ (rupture speed, peak slip-rate, fault slip, bimaterial effects), the effects of hypocentral depth on tsunami dynamics are negligible. Earthquakes with deeper hypocenters accumulate higher slip during up-dip rupture compared to shallow hypocenters, in which rupture mainly propagates downdip. Larger fault slip correlates with larger vertical seafloor displacement by up to 13 cm, which is reflected in the tsunami potentials. These tendencies barely affect the tsunami run-up behavior at the coast, where the maximum difference in tsunami height is only a few centimeters and the wave arrival times vary by few seconds.

Lateral hypocenter variations lead to small effects such as delayed wave arrival of up to 100 s and differences in tsunami amplitude of up to 0.4 m at the coast. To study unilateral vs. bilateral directivity effects on dynamic megathrust rupture, tsunami generation, propagation, and inundation, we varied the hypocenter location along-strike at all of above depth locations. We find that the highest fault slip is always observed for unilateral rupture with hypocenters located at 75% of the fault width (at y = −234.75 km), whereas a centered rupture initiation leads to purely bilateral rupture including the lowest dynamically accumulated slip. In between models of one model family, fault slip varies up to ≈1.5 m. We find only minor bimaterial effects; models with hypocenters located at 25% of the fault width mostly mirror those with hypocenters at 75% of the fault width.

We dynamically generate a "tsunami earthquake" by increasing the critical slip distance, and thus increasing the amount of fracture energy and decreasing radiation efficiency of the bilateral, 40 km deep dynamic earthquake rupture model. This results in lower rupture velocities (average rupture velocities in model 5 are 64% of those in model 3B) and doubles the amount of on-fault slip which is then, in contrast to the initial model, concentrated on the shallow part of the fault. This leads to a ≈2 m higher vertical seafloor displacement and a ≈2 m higher tsunami amplitude at the coast. Increasing Poisson's ratio has a similarly large effect on shallow fault slip, but less on tsunami height and run-up. Increasing ν from 0.25 to 0.3 doubles the amount of fault slip and favors shallow slip, leading to a vertical seafloor uplift of ≈6 m, which is an increase of 1.5 m and a difference of up to ≈1.5 m in coastal tsunami amplitudes.

Our sensitivity analysis based on 15 physics-based linked earthquake and tsunami and inundation models for a generic megathrust setting can provide building blocks toward dynamic rupture modeling complementing Probabilistic Tsunami Hazard Analysis (PTHA). Virtual laboratories, such as we use here, using computationally efficient and open source earthquake and tsunami computational models enable hypothesis testing and physics-based plausibility assessment of linked tsunami and earthquake models of varying complexity.

DATA AVAILABILITY STATEMENT

All data is available under https://doi.org/10.5281/zenodo.4686551.

AUTHOR CONTRIBUTIONS

SW further post-processed the geodynamic seismic cycle (SC) data, designed the DR models, analyzed the DR data and visualized it, and wrote the initial draft of the study. A-AG initiated the study, revised the draft, supervised SW, and acquired the financial support for the ChEESE project leading to this publication. MS performed tsunami simulations and contributed substantially to the manuscript. EM provided tools (used in Madden et al., 2020) to analyze the data of the SC model and to format the data in a way such that they can be used as input for the dynamic rupture model (DR), helped designing the DR models, and critically reviewed the manuscript. IvZ provided firstly postprocessed data output from SC model, contributed to and critically reviewed the manuscript. LK co-supervised MS and contributed a conversion tool from dynamic rupture to tsunami models and provided critical feedback on the manuscript. YvD provided critical comments on the manuscript. LR designed the tsunami studies together with SW, A-AG, and MS analyzed and visualized the tsunami model output, analyzed and post-processed the DR models and co-supervised MS. All authors contributed to the article and approved the submitted version.

FUNDING

This research has been supported by the European Union's Horizon 2020 Research and Innovation Programme under the projects ChEESE, grant no. 823844 and TEAR, grant no. 852992. IvZ was funded by the Royal Society (UK) through Research Fellows Enhancement Award RGF\EA\181084. Computing resources were provided by the Institute of Geophysics of LMU Munich and the Leibniz Supercomputing Centre (projects no. pr63qo, pr45fi, and pn68fi).

ACKNOWLEDGMENTS

We thank Thorne Lay, Yuichiro Tanioka and the editorial office whose comments and suggestions improved this manuscript. We thank Thomas Ulrich and Taufiqurrahman who provided expertise that greatly assisted to overcome technical issues.

SUPPLEMENTARY MATERIAL

The Supplementary Material for this article can be found online at: https://www.frontiersin.org/articles/10.3389/feart.2021.626844/full#supplementary-material

REFERENCES

Aagaard, B. T., Anderson, G., and Hudnut, K. W. (2004). Dynamic Rupture Modeling of the Transition from Thrust to Strike-Slip Motion in the 2002 Denali Fault Earthquake, Alaska. *Bull. Seismol. Soc. Am.* 94, S190–S201. doi: 10.1785/0120040614

Abrahams, L., Dunham, E., Krenz, L., Saito, T., and Gabriel, A.-A. (2021). Comparison of techniques for coupled earthquake and tsunami modeling. *Earth Space Sci. Open Arch*. 49. doi: 10.1002/essoar.10506178.1

Allgeyer, S., and Cummins, P. (2014). Numerical tsunami simulation including elastic loading and seawater density stratification. *Geophys. Res. Lett*. 41, 2368–2375. doi: 10.1002/2014GL059348

Andrews, D. (1980). A stochastic fault model: 1. Static case. *J. Geophys. Res*. 85, 3867–3877. doi: 10.1029/JB085iB07p03867

Aochi, H, and Fukuyama, E. (2002). Three-dimensional nonplanar simulation of the 1992 Landers earthquake. *J. Geophys. Res*. 107, ESE.4-1–ESE.4-12. doi: 10.1029/2001JB000448

Babeyko, A., Hoechner, A., and Sobolev, S. V. (2010). Source modeling and inversion with near real-time GPS: a GITEWS perspective for Indonesia. *Nat. Hazards Earth Syst. Sci*. 10, 1617–1627. doi: 10.5194/nhess-10-1617-2010

Bai, K., and Ampuero, J.-P. (2017). Effect of seismogenic depth and background stress on physical limits of earthquake rupture across fault step overs. *J. Geophys. Res*. 122, 10–280. doi: 10.1002/2017JB014848

Bao, H., Ampuero, J.-P., Meng, L., Fielding, E. J., Liang, C., Milliner, C. W., et al. (2019). Early and persistent supershear rupture of the 2018 magnitude 7.5 Palu earthquake. *Nat. Geosci*. 12, 200–205. doi: 10.1038/s41561-018-0297-z

Behrens, J., and Dias, F. (2015). New computational methods in tsunami science. *Philos. Trans. R. Soc. A Math. Phys. Eng. Sci*. 373:20140382. doi: 10.1098/rsta.2014.0382

Berger, M. J., George, D. L., LeVeque, R. J., and Mandli, K. T. (2011). The GeoClaw software for depth-averaged flows with adaptive refinement. *Adv. Water Resour*. 34, 1195–1206. doi: 10.1016/j.advwatres.2011.02.016

Bilek, S. L., and Lay, T. (1999). Rigidity variations with depth along interplate megathrust faults in subduction zones. *Nature* 400, 443–446. doi: 10.1038/22739

Bilek, S. L., and Lay, T. (2018). Subduction zone megathrust earthquakes. *Geosphere* 14, 1468–1500. doi: 10.1130/GES01608.1

Bletery, Q., Sladen, A., Jiang, J., and Simons, M. (2016). A Bayesian source model for the 2004 great Sumatra-Andaman earthquake. *J. Geophys. Res*. 121, 5116–5135. doi: 10.1002/2016JB012911

Breuer, A., Heinecke, A., and Bader, M. (2016). "Petascale Local Time Stepping for the ADER-DG Finite Element Method," in *2016 IEEE International Parallel and Distributed Processing Symposium (IPDPS)* (Chicago, IL), 854–863. doi: 10.1109/IPDPS.2016.109

Breuer, A., Heinecke, A., Rettenberger, S., Bader, M., Gabriel, A.-A., and Pelties, C. (2014). "Sustained Petascale Performance of Seismic Simulations with SeisSol on Supermuc," in *International Supercomputing Conference, Lecture Notes in Computer Science,* Vol. 8488, eds J. M. Kunkel, T. Ludwig, and H. W. Meuer (Cham: Springer), 1–18. doi: 10.1007/978-3-319-07518-1_1

Brietzke, G. B., Cochard, A., and Igel, H. (2009). Importance of bimaterial interfaces for earthquake dynamics and strong ground motion. *Geophys. J. Int*. 178, 921–938. doi: 10.1111/j.1365-246X.2009.04209.x

Bruhat, L., Fang, Z., and Dunham, E. M. (2016). Rupture complexity and the supershear transition on rough faults. *J. Geophys. Res. Solid Earth,* 121, 210–224. doi: 10.1002/2015JB012512

Cloos, M. (1992). Thrust-type subduction-zone earthquakes and seamount asperities: A physical model for seismic rupture. *Geology* 20, 601–604. doi: 10.1130/0091-7613(1992)020<0601:TTSZEA>2.3.CO;2

Cockburn, B., and Shu, C.-W. (1998). The Runge-Kutta Discontinuous Galerkin Method for Conservation Laws V: Multidimensional Systems. *J. Comput. Phys.* 141, 199–224. doi: 10.1006/jcph.1998.5892

Crempien, J. G. F., Urrutia, A., Benavente, R., and Cienfuegos, R. (2020). Effects of earthquake spatial slip correlation on variability of tsunami potential energy and intensities. *Sci. Rep*. 10:8399. doi: 10.1038/s41598-020-65412-3

Davies, G., and Griffin, J. (2019). Sensitivity of Probabilistic Tsunami Hazard Assessment to Far-Field Earthquake Slip Complexity and Rigidity Depth-Dependence: Case Study of Australia. *Pure Appl. Geophys*. 177, 1521–1548. doi: 10.1007/s00024-019-02299-w

Day, S. M., Dalguer, L. A., Lapusta, N., and Liu, Y. (2005). Comparison of finite difference and boundary integral solutions to three-dimensional spontaneous rupture. *J. Geophys. Res*. 110:B12307. doi: 10.1029/2005JB003813

de la Puente, J., Ampuero, J.-P., and Käser, M. (2009). Dynamic rupture modeling on unstructured meshes using a discontinuous Galerkin method. *J. Geophys. Res*. 144, 148–227. doi: 10.1029/2008JB006271

Dorozhinskii, R., and Bader, M. (2021). "Seissol on Distributed Multi-GPU Systems: CUDA Code Generation for the Modal Discontinuous Galerkin Method," in *The International Conference on High Performance Computing in Asia-Pacific Region* (New York, NY), 69–82. doi: 10.1145/3432261.3436753

Dumbser, M., and Käser, M. (2006). An arbitrary high-order discontinuous Galerkin method for elastic waves on unstructured meshes—II. The three-dimensional isotropic case. *Geophys. J. Int*. 167, 319–336. doi: 10.1111/j.1365-246X.2006.03120.x

Elbanna, A., Abdelmeguid, M., Ma, X., Amlani, F., Bhat, H. S., Synolakis, C., et al. (2020). Anatomy of strike slip fault Tsunami-genesis. *Proc. Natl. Acad. Sci. USA* 118:e2025632118. doi: 10.1073/pnas.2025632118

Festa, G., Zollo, A., and Lancieri, M. (2008). Earthquake magnitude estimation from early radiated energy. *Geophys. Res. Lett*. 35:L22307. doi: 10.1029/2008GL035576

Gabriel, A.-A., Ampuero, J.-P., Dalguer, L. A., and Mai, P. M. (2012). The transition of dynamic rupture styles in elastic media under velocity-weakening friction. *J. Geophys. Res*. 117:B09311. doi: 10.1029/2012JB009468

Gabriel, A.-A., Ampuero, J.-P., Dalguer, L. A., and Mai, P. M. (2013). Source properties of dynamic rupture pulses with off-fault plasticity. *J. Geophys. Res*. 118, 4117–4126. doi: 10.1002/jgrb.50213

Gabriel, A.-A., Li, D., Chiocchetti, S., Tavelli, M., Peshkov, I., Romenski, E., et al. (2020). A unified first order hyperbolic model for nonlinear dynamic rupture processes in diffuse fracture zones. *Philos. Trans. R. Soc. A*. 379:20200130. doi: 10.1098/rsta.2020.0130

Galis, M., Pelties, C., Kristek, J., Moczo, P., Ampuero, J.-P., and Mai, P. M. (2015). On the initiation of sustained slip-weakening ruptures by localized stresses. *Geophys. J. Int*. 200, 890–909. doi: 10.1093/gji/ggu436

Galvez, P., Ampuero, J. P., Dalguer, L. A., Somala, S. N., and Nissen-Meyer, T. (2014). Dynamic earthquake rupture modelled with an unstructured 3-D spectral element method applied to the 2011 M9 Tohoku earthquake. *Geophys. J. Int*. 198, 1222–1240. doi: 10.1093/gji/ggu203

Galvez, P., Somerville, P., Petukhin, A., Ampuero, J.-P., and Peter, D. (2019). Earthquake Cycle Modelling of Multi-segmented Faults: Dynamic Rupture and Ground Motion Simulation of the 1992 Mw 7.3 Landers Earthquake. *Pure Appl. Geophys*. 177, 2163–2179. doi: 10.1007/s00024-019-02228-x

Geist, E., and Yoshioka, S. (1996). Source parameters controlling the generation and propagation of potential local tsunamis along the cascadia margin. *Nat. Hazards* 13, 151–177. doi: 10.1007/BF00138481

Geist, E. L., and Lynett, P. J. (2014). Source processes for the probabilistic assessment of tsunami hazards. *Oceanography* 27, 86–93. doi: 10.5670/oceanog.2014.43

Geist, E. L., and Oglesby, D. D. (2014). *Tsunamis: Stochastic Models of Occurrence and Generation Mechanisms*. New York, NY: Springer. doi: 10.1007/978-3-642-27737-5_595-1

Gercek, H. (2007). Poisson's ratio values for rocks. *Int. J. Rock Mech. Mining Sci*. 44, 1–13. doi: 10.1016/j.ijrmms.20,06.04.011

Giraldo, F. X., and Warburton, T. (2008). A high-order triangular discontinuous Galerkin oceanic shallow water model. *Int. J. Numer. Methods Fluids* 56, 899–925. doi: 10.1002/fld.1562

Glimsdal, S., Løvholt, F., Harbitz, C. B., Romano, F., Lorito, S., Orefice, S., et al. (2019). A New Approximate Method for Quantifying Tsunami Maximum Inundation Height Probability. *Pure Appl. Geophys*. 176, 3227–3246. doi: 10.1007/s00024-019-02091-w

Goda, K., Mai, P., Yasuda, T., and Mori, N. (2014). Sensitivity of tsunami wave profiles and inundation simulations to earthquake slip and fault geometry for the 2011 Tohoku earthquake. *Earth Planet Space* 66, 1–20. doi: 10.1186/1880-5981-66-105

González, F., Geist, E. L., Jaffe, B., Kânoğlu, U., Mofjeld, H., Synolakis, C., et al. (2009). Probabilistic tsunami hazard assessment at Seaside, Oregon, for near-and far-field seismic sources. *J. Geophys. Res*. 114:C11023. doi: 10.1029/2008JC005132

Grezio, A., Babeyko, A., Baptista, M. A., Behrens, J., Costa, A., Davies, G., et al. (2017). Probabilistic Tsunami Hazard Analysis: Multiple sources and global applications. *Rev. Geophys*. 55, 1158–1198. doi: 10.1002/2017RG000579

Harris, R. A., Archuleta, R. J., and Day, S. M. (1991). Fault steps and the dynamic rupture process: 2-D numerical simulations of a spontaneously propagating shear fracture. *Geophys. Res. Lett*. 18, 893–896. doi: 10.1029/91GL01061

Harris, R. A., Barall, M., Aagaard, B., Ma, S., Roten, D., Olsen, K., et al. (2018). A Suite of Exercises for Verifying Dynamic Earthquake Rupture Codes. *Seismol. Res. Lett*. 89, 1146–1162. doi: 10.1785/0220170222

Harris, R. A., Barall, M., Andrews, D. J., Duan, B., Ma, S., Dunham, E. M., et al. (2011). Verifying a Computational Method for Predicting Extreme Ground Motion. *Seismol. Res. Lett*. 82, 638–644. doi: 10.1785/gssrl.82.5.638

Harris, R. A., and Day, S. M. (2005). Material contrast does not predict earthquake rupture propagation direction. *Geophys. Res. Lett*. 32:L23301. doi: 10.1029/2005GL023941

Heinecke, A., Breuer, A., Rettenberger, S., Bader, M., Gabriel, A., Pelties, C., et al. (2014). "Petascale High Order Dynamic Rupture Earthquake Simulations on Heterogeneous Supercomputers," in *SC '14: Proceedings of the International Conference for High Performance Computing, Networking, Storage and Analysis*, (New Orleans, LA), 3–14. doi: 10.1109/SC.2014.6

Hirano, S. (2019). Modeling of unilateral rupture along very long reverse faults. *J. Geophys. Res*. 124, 1057–1071. doi: 10.1029/2018JB016511

Holding, E. P. (2018). GOCAD: A computer aided design program for geological applications.

Honal, C., and Rannabauer, L. (2020). *Comparing the Numerical Results in [Vater S., N. Beisiegel, and J. Behrens, 2019] to Results Produced by the FLASH Implementation in Samoa2*.

Horspool, N., Pranantyo, I., Griffin, J., Latief, H., Natawidjaja, D., Kongko, W., et al. (2014). A probabilistic tsunami hazard assessment for Indonesia. *Nat. Hazards Earth Syst. Sci*. 14:3105. doi: 10.5194/nhess-14-3105-2014

Ida, Y. (1972). Cohesive force across the tip of a longitudinal-shear crack and Griffith's specific surface energy. *J. Geophys. Res*. 77, 3796–3805. doi: 10.1029/JB077i020p03796

Jamelot, A., Gailler, A., Heinrich, P., Vallage, A., and Champenois, J. (2019). Tsunami Simulations of the Sulawesi Mw 7.5 Event: Comparison of Seismic Sources Issued from a Tsunami Warning Context Versus Post-Event Finite Source. *Pure Appl. Geophys*. 176, 3351–3376. doi: 10.1007/s00024-019-02274-5

Ji, C., Wald, D. J., and Helmberger, D. V. (2002). Source Description of the 1999 Hector Mine, California, Earthquake, Part I: Wavelet Domain Inversion Theory and Resolution Analysis. *Bull. Seismol. Soc. Am*. 92, 1192–1207. doi: 10.1785/0120000916

Kajiura, K. (1963). The leading wave of a tsunami. *Bull. Earthq. Res. Instit. Univ. Tokyo*, 41, 535–571.

Kame, N., Rice, J. R., and Dmowska, R. (2003). Effects of prestress state and rupture velocity on dynamic fault branching. *J. Geophys. Res*. 108, 2265. doi: 10.1029/2002JB002189

Kanamori, H. (1972). Mechanism of tsunami earthquakes. *Phys. Earth Planet. Inter*. 6, 346–359. doi: 10.1016/0031-9201(72)90058-1

Kanamori, H., and Brodsky, E. E. (2004). The physics of earthquakes. *Rep. Prog. Phys*. 67:1429. doi: 10.1088/0034-4885/67/8/R03

Kaneko, Y., Lapusta, N., and Ampuero, J.-P. (2008). Spectral element modeling of spontaneous earthquake rupture on rate and state faults: Effect of velocity-strengthening friction at shallow depths. *J. Geophys. Res.* 113:B09317. doi: 10.1029/2007JB005553

Käser, M., and Dumbser, M. (2006). An arbitrary high-order discontinuous Galerkin method for elastic waves on unstructured meshes-I. The two-dimensional isotropic case with external source terms. *Geophys. J. Int*. 166, 855–877. doi: 10.1111/j.1365-246X.2006.03051.x

Kirkpatrick, J. D., Edwards, J. H., Verdecchia, A., Kluesner, J. W., Harrington, R. M., and Silver, E. A. (2020). Subduction megathrust heterogeneity characterized from 3D seismic data. *Nat. Geosci*. 13, 369–374. doi: 10.1038/s41561-020-0562-9

Kozdon, J. E., and Dunham, E. M. (2013). Rupture to the Trench: Dynamic Rupture Simulations of the 11 March 2011 Tohoku Earthquake. *Bull. Seismol. Soc. Am*. 103, 1275–1289. doi: 10.1785/0120120136

Lay, T., Ammon, C. J., Kanamori, H., Yamazaki, Y., Cheung, K. F., and Hutko, A. R. (2011). The 25 October 2010 Mentawai tsunami earthquake (Mw 7.8) and the tsunami hazard presented by shallow megathrust ruptures. *Geophys. Res. Lett*. 38:L06302. doi: 10.1029/2010GL046552

LeVeque, R. J., George, D. L., and Berger, M. J. (2011). Tsunami modelling with adaptively refined finite volume methods. *Acta Numer*. 20:211. doi: 10.1017/S0962492911000043

Liang, Q., and Marche, F. (2009). Numerical resolution of well-balanced shallow water equations with complex source terms. *Adv. Water Resour*. 32, 873–884. doi: 10.1016/j.advwatres.2009.02.010

Liu, X., and Zhao, D. (2014). Structural control on the nucleation of megathrust earthquakes in the Nankai subduction zone. *Geophys. Res. Lett*. 41, 8288–8293. doi: 10.1002/2014GL062002

Lorito, S., Romano, F., and Lay, T. (2016). "Tsunamigenic major and great earthquakes (2004-2013): Source processes inverted from seismic, geodetic, and sea-level data," in *Encyclopedia of Complexity and Systems Science*, ed R. A. Meyers (New York, NY: Springer), 978. doi: 10.1007/978-3-642-27737-5_641-1

Lorito, S., Selva, J., Basili, R., Romano, F., Tiberti, M., and Piatanesi, A. (2015). Probabilistic hazard for seismically induced tsunamis: accuracy and feasibility of inundation maps. *Geophys. J. Int*. 200, 574–588. doi: 10.1093/gji/ggu408

Lotto, G. C., Dunham, E. M., Jeppson, T. N., and Tobin, H. J. (2017a). The effect of compliant prisms on subduction zone earthquakes and tsunamis. *Earth Planet. Sci. Lett*. 458, 213–222. doi: 10.1016/j.epsl.2016.10.050

Lotto, G. C., Jeppson, T. N., and Dunham, E. M. (2018). Fully coupled simulations of megathrust earthquakes and tsunamis in the Japan Trench, Nankai Trough, and Cascadia Subduction Zone. *Pure Appl. Geophys*. 176, 4009–4041. doi: 10.1007/s00024-018-1990-y

Lotto, G. C., Nava, G., and Dunham, E. M. (2017b). Should tsunami simulations include a nonzero initial horizontal velocity? *Earth Planets Space* 69, 1–14. doi: 10.1186/s40623-017-0701-8

Ma, S., and Beroza, G. C. (2008). Rupture Dynamics on a Bimaterial Interface for Dipping Faults. *Bull. Seismol. Soc. Am*. 98, 1642–1658. doi: 10.1785/0120070201

Ma, S., and Nie, S. (2019). Dynamic wedge failure and along-arc variations of tsunamigenesis in the Japan Trench margin. *Geophys. Res. Lett*. 46, 8782–8790. doi: 10.1029/2019GL083148

Madden, E., Bader, M., Behrens, J., Van Dinther, Y., Gabriel, A.-A., Rannabauer, L., et al. (2020). Linked 3-D modelling of megathrust earthquake-tsunami events: from subduction to tsunami run up. *Geophys. J. Int*. 224, 487–516. doi: 10.1093/gji/ggaa484

Maeda, T., Furumura, T., Noguchi, S., Takemura, S., Sakai, S., Shinohara, M., et al. (2013). Seismic- and Tsunami-Wave Propagation of the 2011 Off the Pacific Coast of Tohoku Earthquake as Inferred from the Tsunami-Coupled Finite-Difference Simulation. *Bull. Seismol. Soc. Am*. 103, 1456–1472. doi: 10.1785/0120120118

Mai, P. M., Schorlemmer, D., Page, M., Ampuero, J. P., Asano, K., Causse, M., et al. (2016). The Earthquake-Source Inversion Validation (SIV) Project. *Seismol. Res. Lett*. 87, 690–708. doi: 10.1785/0220150231

Mai, P. M., Spudich, P., and Boatwright, J. (2005). Hypocenter Locations in Finite-Source Rupture Models. *Bull. Seismol. Soc. Am*. 95, 965–980. doi: 10.1785/0120040111

Mai, P. M. and Thingbaijam, K. K. (2014). SRCMOD: An Online Database of Finite-Fault Rupture Models. *Seismol. Res. Lett*. 85, 1348–1357. doi: 10.1785/0220140077

McCloskey, J., Antonioli, A., Piatanesi, A., Sieh, K., Steacy, S., Nalbant, S., et al. (2008). Tsunami threat in the Indian Ocean from a future megathrust earthquake west of Sumatra. *Earth Planet. Sci. Lett*. 265, 61–81. doi: 10.1016/j.epsl.2007.09.034

McGuire, J. J., Zhao, L., and Jordan, T. H. (2002). Predominance of Unilateral Rupture for a Global Catalog of Large Earthquakes. *Bull. Seismol. Soc. Am*. 92, 3309–3317. doi: 10.1785/0120010293

Meister, O., Rahnema, K., and Bader, M. (2016). Parallel Memory-Efficient Adaptive Mesh Refinement on Structured Triangular Meshes with Billions of Grid Cells. *ACM Trans. Math. Softw*. 43, 1–27. doi: 10.1145/2947668

Melgar, D., Williamson, A. L., and Salazar-Monroy, E. F. (2019). Differences between heterogenous and homogenous slip in regional tsunami hazards modelling. *Geophys. J. Int*. 219, 553–562. doi: 10.1093/gji/ggz299

Meng, L., Inbal, A., and Ampuero, J.-P. (2011). A window into the complexity of the dynamic rupture of the 2011 Mw 9 Tohoku-Oki earthquake. *Geophys. Res. Lett*. 38:L00G07. doi: 10.1029/2011GL048118

Mori, N., Goda, K., and Cox, D. (2018). "Recent Process in Probabilistic Tsunami Hazard Analysis (PTHA) for Mega Thrust Subduction Earthquakes," in *The 2011 Japan Earthquake and Tsunami: Reconstruction and Restoration*, eds V. Santiago-Fandiño, S. Sato, N. Maki, and K. Iuchi (Cham: Springer), 469–485. doi: 10.1007/978-3-319-58691-5_27

Murphy, S., Scala, A., Herrero, A., Lorito, S., Festa, G., Trasatti, E., et al. (2016). Shallow slip amplification and enhanced tsunami hazard unravelled by dynamic simulations of mega-thrust earthquakes. *Sci. Rep*. 6, 1–12. doi: 10.1038/srep35007

Murphy, S., Toro, G. D., Romano, F., Scala, A., Lorito, S., Spagnuolo, E., et al. (2018). Tsunamigenic earthquake simulations using experimentally derived friction laws. *Earth Planet. Sci. Lett*. 486, 155–165. doi: 10.1016/j.epsl.2018.01.011

Nakano, M., Murphy, S., Agata, R., Igarashi, Y., Okada, M., and Hori, T. (2020). Self-similar stochastic slip distributions on a non-planar fault for tsunami scenarios for megathrust earthquakes. *Prog. Earth Planet. Sci*. 7, 1–13. doi: 10.1186/s40645-020-00360-0

Nielsen, S. B. (1998). Free surface effects on the propagation of dynamic rupture. *Geophys. Res. Lett*. 25, 125–128. doi: 10.1029/97GL03445

Niu, X., Zhao, D., Isozaki, Y., Nishizono, Y., and Inakura, H. (2020). Structural heterogeneity and megathrust earthquakes in southwest Japan. *Phys. Earth Planet. Int*. 298:106347. doi: 10.1016/j.pepi.2019.106347

Oglesby, D. D., Archuleta, R. J., and Nielsen, S. B. (2000). The Three-Dimensional Dynamics of Dipping Faults. *Bull. Seismol. Soc. Am*. 90, 616–628. doi: 10.1785/0119990113

Okada, Y. (1985). Surface deformation due to shear and tensile faults in a half-space. *Bull. Seismol. Soc. Am*. 75, 1135–1154.

Palgunadi, K. H., Gabriel, A., Ulrich, T., López-Comino, J. Á., and Mai, P. M. (2020). Dynamic Fault Interaction during a Fluid-Injection-Induced Earthquake: The 2017 M_w 5.5 Pohang Event. *Bull. Seismol. Soc. Am*. 110, 2328–2349. doi: 10.1785/0120200106

Pelties, C., de la Puente, J., Ampuero, J.-P., Brietzke, G. B., and Käser, M. (2012). Three-dimensional dynamic rupture simulation with a high-order discontinuous Galerkin method on unstructured tetrahedral meshes. *J. Geophys. Res*. 117:B02309. doi: 10.1029/2011JB008857

Pelties, C., Gabriel, A.-A., and Ampuero, J.-P. (2014). Verification of an ADER-DG method for complex dynamic rupture problems. *Geosci. Model Dev*. 7, 847–866. doi: 10.5194/gmd-7-847-2014

Polet, J., and Kanamori, H. (2000). Shallow subduction zone earthquakes and their tsunamigenic potential. *Geophys. J. Int*. 142, 684–702. doi: 10.1046/j.1365-246x.2000.00205.x

Ramos, M. D., and Huang, Y. (2019). How the transition region along the Cascadia megathrust influences coseismic behavior: insights from 2-D dynamic rupture simulations. *Geophys. Res. Lett*. 46, 1973–1983. doi: 10.1029/2018GL080812

Rettenberger, S., Meister, O., Bader, M., and Gabriel, A.-A. (2016). "ASAGI: A Parallel Server for Adaptive Geoinformation," in *Proceedings of the Exascale Applications and Software Conference 2016, EASC'16*, (New York, NY: Association for Computing Machinery), 1–9. doi: 10.1145/2938615.2938618

Romano, F., Trasatti, E., Lorito, S., Piromallo, C., Piatanesi, A., Ito, Y., et al. (2014). Structural control on the Tohoku earthquake rupture process investigated by 3D FEM, tsunami and geodetic data. *Sci. Rep*. 4, 1–11. doi: 10.1038/srep05631

Rubin, A. M., and Ampuero, J.-P. (2007). Aftershock asymmetry on a bimaterial interface. *J. Geophys. Res*. 112:B05307. doi: 10.1029/2006JB004337

Ryan, K. J., Geist, E. L., Barall, M., and Oglesby, D. D. (2015). Dynamic models of an earthquake and tsunami offshore Ventura, California. *Geophys. Res. Lett*. 42, 6599–6606. doi: 10.1002/2015GL064507

Saito, T., Baba, T., Inazu, D., Takemura, S., and Fukuyama, E. (2019). Synthesizing sea surface height change including seismic waves and tsunami using a dynamic rupture scenario of anticipated Nankai trough earthquakes. *Tectonophysics* 769:228166. doi: 10.1016/j.tecto.2019.228166

Saito, T., and Furumura, T. (2009). Three-dimensional tsunami generation simulation due to sea-bottom deformation and its interpretation based on the linear theory. *Geophys. J. Int*. 178, 877–888. doi: 10.1111/j.1365-246X.2009.04206.x

Scala, A., Festa, G., and Vilotte, J.-P. (2017). Rupture dynamics along bimaterial interfaces: a parametric study of the shear-normal traction coupling. *Geophys. J. Int*. 209, 48–67. doi: 10.1093/gji/ggw489

Scala, A., Lorito, S., Romano, F., Murphy, S., Selva, J., Basili, R., et al. (2019). Effect of Shallow Slip Amplification Uncertainty on Probabilistic Tsunami Hazard Analysis in Subduction Zones: Use of Long-Term Balanced Stochastic Slip Models. *Pure Appl. Geophys*. 177, 1497–1520. doi: 10.1007/s00024-019-02260-x

Selva, J., Tonini, R., Molinari, I., Tiberti, M. M., Romano, F., Grezio, A., et al. (2016). Quantification of source uncertainties in Seismic Probabilistic Tsunami Hazard Analysis (SPTHA). *Geophys. J. Int*. 205, 1780–1803. doi: 10.1093/gji/ggw107

Sepúlveda, I., Haase, J. S., Carvajal, M., Xu, X., and Liu, P. L. (2020). Modeling the sources of the 2018 Palu, Indonesia, tsunami using videos from social media. *J. Geophys. Res*. 125:e2019JB018675. doi: 10.1029/2019JB018675

Sepúlveda, I., Liu, P. L.-F., and Grigoriu, M. (2019). Probabilistic tsunami hazard assessment in South China Sea with consideration of uncertain earthquake characteristics. *J. Geophys. Res*. 124, 658–688. doi: 10.1029/2018JB016620

Simmetrix Inc. (2017). *SimModeler: Simulation Modeling Suite 11.0 Documentation*. Technical Report, Simmetrix Inc.

Strasser, F. O., Arango, M., and Bommer, J. J. (2010). Scaling of the Source Dimensions of Interface and Intraslab Subduction-zone Earthquakes with Moment Magnitude. *Seismol. Res. Lett*. 81, 941–950. doi: 10.1785/gssrl.81.6.941

Synolakis, C. E., Bernard, E. N., Titov, V. V., Kânoğlu, U., and González, F. I. (2008). Validation and Verification of Tsunami Numerical Models. *Pure Appl. Geophys*. 165, 2197–2228. doi: 10.1007/s00024-004-0427-y

Tadapansawut, T., Okuwaki, R., Yagi, Y., and Yamashita, S. (2021). Rupture process of the 2020 Caribbean earthquake along the Oriente transform fault, involving supershear rupture and geometric complexity of fault. *Geophys. Res. Lett*. 48:e2020GL090899. doi: 10.1029/2020GL090899

Tanioka, Y., and Satake, K. (1996). Tsunami generation by horizontal displacement of ocean bottom. *Geophys. Res. Lett*. 23, 861–864. doi: 10.1029/96GL00736

Ulrich, T., Gabriel, A.-A., and Madden, E. (2020). Stress, rigidity and sediment strength control megathrust earthquake and tsunami dynamics. doi: 10.31219/osf.io/9kdhb

Ulrich, T., Gabriel, A. A., Ampuero, J. P., and Xu, W. (2019a). Dynamic viability of the 2016 Mw 7.8 Kaikoura earthquake cascade on weak crustal faults. *Nat. Commun*. 10:1213. doi: 10.1038/s41467-019-09125-w

Ulrich, T., Vater, S., Madden, E. H., Behrens, J., van Dinther, Y., Van Zelst, I., et al. (2019b). Coupled, Physics-Based Modeling Reveals Earthquake Displacements are Critical to the 2018 Palu, Sulawesi Tsunami. *Pure Appl. Geophys*. 176, 4069–4109. doi: 10.1007/s00024-019-02290-5

Uphoff, C., and Bader, M. (2020). Yet another tensor toolbock for discontinous galerkin methods and other applications. *ACM Trans. Math. Softw*. 46, 1–40. doi: 10.1145/3406835

Uphoff, C., Rettenberger, S., Bader, M., Madden, E., Ulrich, T., Wollherr, S., et al. (2017). "Extreme Scale Multi-Physics Simulations of the Tsunamigenic 2004 Sumatra Megathrust Earthquake," in *Proceedings of the International Conference for High Performance Computing, Networking, Storage and Analysis, SC 2017* (New York, NY), 1–16. doi: 10.1145/3126908.3126948

Van Dinther, Y., Gerya, T., Dalguer, L., Mai, P. M., Morra, G., and Giardini, D. (2013). The seismic cycle at subduction thrusts: insights from seismo-thermo-mechanical models. *J. Geophys. Res*. 118, 6183–6202. doi: 10.1002/2013JB010380

Van Dinther, Y., Mai, P. M., Dalguer, L., and Gerya, T. (2014). Modeling the seismic cycle in subduction zones: The role and spatiotemporal occurrence of off-megathrust earthquakes. *Geophys. Res. Lett*. 41, 1194–1201. doi: 10.1002/2013GL058886

van Zelst, I., Rannabauer, L., Gabriel, A.-A., and van Dinther, Y. (2021). Earthquake rupture on multiple splay faults and its effect on tsunamis. doi: 10.31223/X5KC74

van Zelst, I., Wollherr, S., Gabriel, A.-A., Madden, E. H., and van Dinther, Y. (2019). Modeling megathrust earthquakes across scales: one-way coupling from geodynamics and seismic cycles to dynamic rupture. *J. Geophys. Res*. 124, 11414–11446. doi: 10.1029/2019JB017539

Vater, S., and Behrens, J. (2014). "Well-Balanced Inundation Modeling for Shallow-Water Flows with Discontinuous Galerkin Schemes," in *Finite Volumes for Complex Applications VII-Elliptic, Parabolic and Hyperbolic Problems, Springer Proceedings in Mathematics & Statistics*, Vol. 78, eds J. Fuhrmann, M. Ohlberger, and C. Rohde (Cham: Springer), 965–973. doi: 10.1007/978-3-319-05591-6_98

Vater, S., Beisiegel, N., and Behrens, J. (2015). A limiter-based well-balanced discontinuous Galerkin method for shallow-water flows with wetting and drying: One-dimensional case. *Adv. Water Resour*. 85, 1–13. doi: 10.1016/j.advwatres.2015.08.008

Vater, S., Beisiegel, N., and Behrens, J. (2019). A limiter-based well-balanced discontinuous Galerkin method for shallow-water flows with wetting and drying: Triangular grids. *Int. J. Numer. Methods Fluids* 91, 395–418. doi: 10.1002/fld.4762

Venkataraman, A., and Kanamori, H. (2004). Observational constraints on the fracture energy of subduction zone earthquakes. *J. Geophys. Res*. 109:B05302. doi: 10.1029/2003JB002549

Wendt, J., Oglesby, D. D., and Geist, E. L. (2009). Tsunamis and splay fault dynamics. *Geophys. Res. Lett*. 36:L15303. doi: 10.1029/2009GL038295

Weng, H., and Ampuero, J.-P. (2019). The dynamics of elongated earthquake ruptures. *J. Geophys. Res*. 124, 8584–8610. doi: 10.1029/2019JB017684

Wolf, S., Gabriel, A., and Bader, M. (2020). "Optimization and Local Time Stepping of an ADER-DG Scheme for Fully Anisotropic Wave Propagation in Complex Geometries," in *International Conference on Computational Science – ICCS 2020,* Vol. 12139, ed V. V. Krzhizhanovskaya (Cham: Springer). doi: 10.1007/978-3-030-50420-5_3

Wollherr, S. (2018). *Inelastic material response in multi-physics earthquake rupture simulations* (Ph.D. thesis). Geomechanically constrained dynamic rupture models of subduction zone earthquakes with plasticity. Ludwig-Maximilians-Universität-München, Munich, Germany.

Wollherr, S., Gabriel, A.-A., and Uphoff, C. (2018). Off-fault plasticity in three-dimensional dynamic rupture simulations using a modal Discontinuous Galerkin method on unstructured meshes: implementation, verification and application. *Geophys. J. Int*. 214, 1556–1584. doi: 10.1093/gji/ggy213

Xie, Z., Hu, C., Cai, Y., and Wang, C.-Y. (2009). Effect of Poisson?s ratio on stress state in the Wenchuan M_s 8.0 earthquake fault. *Earthq. Sci*. 22, 603–607. doi: 10.1007/s11589-009-0603-3

Ye, L., Lay, T., Kanamori, H., and Rivera, L. (2016). Rupture characteristics of major and great ($M_w \geq$ 7.0) megathrust earthquakes from 1990 to 2015: 1. Source parameter scaling relationships. *J. Geophys. Res*. 121, 826–844. doi: 10.1002/2015JB012426

Yeh, L.-P. (1996). *Benchmark Problem 4. The 1993 Okushiri Data, Conditions and Phenomena*. World Scientific Publishing Co. Pte. Ltd.

Conflict of Interest: The authors declare that the research was conducted in the absence of any commercial or financial relationships that could be construed as a potential conflict of interest.

Advantages of publishing in Frontiers

OPEN ACCESS
Articles are free to read for greatest visibility and readership

FAST PUBLICATION
Around 90 days from submission to decision

HIGH QUALITY PEER-REVIEW
Rigorous, collaborative, and constructive peer-review

TRANSPARENT PEER-REVIEW
Editors and reviewers acknowledged by name on published articles

Frontiers
Avenue du Tribunal-Fédéral 34
1005 Lausanne | Switzerland

Visit us: www.frontiersin.org
Contact us: frontiersin.org/about/contact

REPRODUCIBILITY OF RESEARCH
Support open data and methods to enhance research reproducibility

DIGITAL PUBLISHING
Articles designed for optimal readership across devices

FOLLOW US
@frontiersin

IMPACT METRICS
Advanced article metrics track visibility across digital media

EXTENSIVE PROMOTION
Marketing and promotion of impactful research

LOOP RESEARCH NETWORK
Our network increases your article's readership